Tuning the donor properties of bipyridyl-substituted phosphines by metal ion encapsulation

&

Photocatalytic synthesis of 6*H*-benzo[*c*]chromenes from *S*-aryl sulfonium salts

Dissertation

zur Erlangung des mathematisch-naturwissenschaftlichen Doktorgrades

„Doctor rerum naturalium“

der Georg-August-Universität Göttingen

im Promotionsprogramm: Chemie

der Georg-August-University School of Science (GAUSS)

vorgelegt von

Steve Karreman

aus Wolfenbüttel, Deutschland

Göttingen 2022

Betreuungsausschuss:

Prof. Dr. M. Alcarazo, Institut für Organische und Biomolekulare Chemie, Tammannstraße 2, 37077 Göttingen

Prof. Dr. S. Schneider, Institut für Anorganische Chemie, Tammannstraße 4, 37077 Göttingen

Mitglieder der Prüfungskommission:

Referent: Prof. Dr. Manuel Alcarazo, Institut für Organische und Biomolekulare Chemie, Tammannstraße 2, 37077 Göttingen

Korreferent: Prof. Dr. Sven Schneider, Institut für Anorganische Chemie, Tammannstraße 4, 37077 Göttingen

Weitere Mitglieder der Prüfungskommission:

Jun.-Prof. Dr. Johannes C. L. Walker, Institut für Organische und Biomolekulare Chemie, Tammannstraße 2, 37077 Göttingen

Jun.-Prof. Dr. Nadja A. Simeth, Institut für Organische und Biomolekulare Chemie, Tammannstraße 2, 37077 Göttingen

PD Dr. Michael John, Institut für Organische und Biomolekulare Chemie, Tammannstraße 2, 37077 Göttingen

Dr. Holm Frauendorf, Institut für Organische und Biomolekulare Chemie, Tammannstraße 2, 37077 Göttingen

Tag der mündlichen Prüfung: 30. September 2022

Die vorliegende Arbeit entstand unter Anleitung von Prof. Dr. Manuel Alcarazo in der Zeit von Juli 2017 bis September 2022 an der Georg-August-Universität Göttingen.

Teile dieser Arbeit wurden bereits veröffentlicht:

S. Karreman, S. B. H. Karnbrock, S. Kolle, C. Golz, M. Alcarazo, *Organic Letters* **2021**, *23*, 1991.

Hiermit versichere ich, dass ich die eingereichte Dissertation selbständig verfasst, keine anderen als die angegebenen Quellen und Hilfsmittel benutzt, sowie Zitate kenntlich gemacht habe.

Göttingen,

……

Steve Karreman

Acknowledgements

Zuallererst möchte ich mich bei Prof. Dr. Manuel Alcarazo bedanken, welcher mir die Möglichkeit gab der Arbeitsgruppe beizutreten und meine Dissertation in den letzten Jahren betreute. Vielen Dank für die immerwährende Unterstützung, die zahlreichen Diskussionen und Ratschläge, sowie die Chance auch eigene Ideen zu verfolgen.

Mein Dank gilt außerdem Prof. Dr. Sven Schneider, welcher mir während der jährlichen Berichte häufig einen anderen Blickwinkel auf meine Forschung gab und mir weitere Ideen aufzeigte diese fortzuführen.

Des Weiteren möchte ich Jun.-Prof. Dr. Johannes C. L. Walker, Jun.-Prof. Dr. Nadja A. Simeth, PD Dr. Michael John und Dr. Holm Frauendorf für die Teilnahme an meinem Disputationskomitee danken.

Ich danke der NMR- und der Massenspektrometrie Abteilung für die unzähligen gemessenen Proben und Hilfestellungen bei allen Fragen rundum die entsprechende Analytik.

Der Studienstiftung des deutschen Volkes danke ich sowohl für die finanzielle als auch die ideelle Unterstützung. Insbesondere möchte ich mich hier bei Prof. Dr. Anja Lobenstein-Reichmann und den restlichen Mitgliedern der Stipendiatengruppe für die gemeinsamen Treffen und Ausflüge bedanken.

Den Mitarbeitern des AK Alcarazo danke ich für die gute Arbeitsatmosphäre und der ein oder anderen Party. Besonders möchte ich mich hier bei meinen Laborkollegen Thierry Hartung, Dr. Leo Nicholls, Sven Timmann, Rafael Machleid für die gute Stimmung und Musik im Labor 4.121 bedanken. Außerdem bin ich dankbar für die unterhaltsamen Gespräche im Office mit Dr. Kai F. G. Averesch, die Expertise zu Carbenen und das ein oder andere NMR tube von Jun.-Prof. Dr. Max M. Hansmann, spätes Arbeiten mit Patrick Antoni, Unterhaltungen über Kunst, Politik (und NMR) mit Anne Kreyenschmidt oder Wissenswertes über Tschechien mit Dr. Soňa Krajčovičová.

Bedanken möchte ich mich auch bei meinen Praktikanten/Bacheloranden Sebastian Kolle, Simon Maroldt und Jiri Kollmann für die super Unterstützung im Labor.

Danke an die „Spanier“-Gruppe bestehend aus Martí Recort Fornals, Pablo Redero Garcia, Zeyu Feng, Jaime Tostado, Dr. Carmen Garcia Lopez, Dr. Xavier Marset, Dr. Juan Miguel Lopez Soria, und Dr. Valentina Pelliccioli für jede Menge „Unterhaltung“ und Aufmunterung im Labor und gelungene „Schnitzelpartys“.

Danke an Franziska Sophia Kremser Koch, Felix Struck, Franziska Otto, Ha-My Pham, Henning Duwe, Niklas Hörbelt, Marvin Schmitz, Antonia Lüdeke und Markus Wetterich für das „Willkommen-Heißen“ in Göttingen und die vielen Mittwochabende in der Innenstadt, wo Chemie kein Thema war.

Dr. Christopher Golz danke ich für die Unterstützung bei allen Fragen rund um Kristallographie und für das Korrekturlesen dieser Arbeit.

Simon B. H. Karnbrock danke ich für das tolle Zusammenarbeiten im Labor, fachbezogene Diskussionen, lustige Abende in Göttingen und das Korrekturlesen dieser Arbeit.

Besonders möchte ich mich bei Ilona Ussoltsev bedanken. Danke für die Thannersbesuche, Aufmunterung bei jedem Stress im Labor oder beim Schreiben, sowie Unterstützung bei allen großen und kleinen Problemen des Lebens.

Meinen Eltern und meiner Schwester danke ich dafür, dass ich mich immer auf euch verlassen konnte und ihr mir in allen Lebenslagen mit Rat und Tat zur Seite standet.

Abbreviations

$\%V_{Bur}$	percent buried volume	MeLi	methyllithium
)))	sonicate	MeOH	methanol
°	degree	Mes	2,4,6-trimethylphenyl (mesityl)
°C	degree Celsius	mesna	2-mercaptoethane sulfonate Na
Å	angstrom	mg	milligram
Ac	acetyl	MHz	megahertz
AIBN	azobisisobutyronitrile	min	minute
aq	aqueous	mL	milliliter
Ar	aryl	MLCT	metal-to-ligand charge-transfer
ArF	C_6F_5	mmol	millimole
ATR	attenuated total reflection	MO	molecular orbital
BArF	Tetrakis[3,5-bis(trifluoromethyl)phenyl]borate	MS	mass spectrometry
BDE	bond-dissociation energy	mV	millivolt
BHT	butylated hydroxytoluene	mV/s	millivolt per second
Bn	benzyl	Naph	naphthyl
bpy	2,2′-bipyridine	NBD	norbornadiene
Bu	butyl	^{n}Bu	*n*-Butyl
c	concentration	^{n}BuLi	*n*-Butyllithium
CAAC	cyclic(alkyl)(amino)carbene	NHC	N-heterocyclic carbene
calc.	calculated	nm	nanometer
cat.	catalytic	NMR	nuclear magnetic resonance
cf.	confer/ compare	NOE	nuclear Overhauser effect
cm	centimeters	Nu	nucleophile
COSY	correlation spectroscopy	*o*	*ortho*
CV	cyclic voltammetry	oct (NMR)	octet
Cy	Cyclohexyl	*p*	*para*
d	day	p (NMR)	pentet/quintet
d (NMR)	doublet	PC	*photocatalyst*
DBT	dibenzothiophene	PCC	pyridinium chlorochromate
DBU	1,8-diazabicyclo[5.4.0]undec-7-ene	Ph	phenyl
DCE	1,2-dichloroethane	PhD	doctor of philosophy
DCM	dichloromethane	pK_a	negative common logarithm of K_a
DFT	density-functional theory	pK_b	negative common logarithm of K_b
DIPEA	N,N-diisopropylethylamine/Hünig's base	PPh_3	triphenylphosphine
DMF	dimethylformamide	ppm	parts per million
DMS	dimethyl sulfide	ppy	2-phenylpyridine
DMSO	dimethyl sulfoxide	Pr	propyl
dppf	1,1′-bis(diphenylphosphino)ferrocene	PTB	9-phosphatriptycene-10-phenylborate
e^-	electron	PTH	10-phenylphenothiazine
e.g.	exempli gratia/for example	Py	pyridyl
EI	electron ionization	q	quartet
EPC	electrophilic phosphonium cation	quant.	quantitative
EPR	electron paramagnetic resonance	R	generic substituent
equiv.	equivalents	rac	racemic
ESI	electrospray ionization	R_F	retardation factor
Et	ethyl	RMSD	root-mean-square deviation
et al.	*et alii*/and others	rt	room temperature
eV	electronvolt	s	second
fac	facial	s (NMR)	singlet
Fc	ferrocene	SCE	saturated calomel electrode
Fc^+	ferrocenium cation	SET	single-electron transfer
FID	flame ionization detector	sext (NMR)	sextet/hextet
g	gram	S_N	nucleophilic substitution
G	Gibbs free energy	S_NAr	nucleophilic aromatic substitution
G (EPR)	gauss	SOMO	singly occupied molecular orbital
GC	gas chromatography	Sphos	2-dicyclohexylphosphino-2',6'-dimethoxybiphenyl
h	hour	SPS	solvent purification system

HAT	hydrogen atom transfer	t	time
HCTD	heptacyclotetradecane	t (NMR)	triplet
HMBC	heteronuclear multiple bond correlation	T	temperature
HMDS	hexamethyldisilazane	TAP	trigonal antiprismatic/octahedral
HOMO	highest occupied molecular orbital	^{t}Bu	*tert*-butyl
HOTf	trifluoromethanesulfonic acid	TEMPO	(2,2,6,6-tetramethylpiperidin-1-yl)oxyl
HPLC	high-performance liquid chromatography	TEP	Tolman electronic parameter
HR	high-resolution	Tf	trifluormethylsulfonyl
hs	high spin	Tf_2O	trifluoromethanesulfonic anhydride
HSAB	hard and soft Lewis acids and bases	TFAA	trifluoroacetic anhydride
HSQC	heteronuclear single quantum coherence	TfO^-	trifluoromethanesulfonate/triflate
Hz	hertz	TFP	tri-(2-furyl)-phosphine
hν	light irradiation	THF	tetrahydrofuran
IMes	1,3-bis-(2,4,6-trimethylphenyl)imidazol-2-ylidene	TLC	thin-layer chromatography
^{i}Pr	isopropyl	TM	transition metal
IPr	1,3-bis-(2,6-diisopropylphenyl)imidazol-2-ylidene	TMS	trimethylsilyl
IR	infrared spectroscopy	TOF	turnover frequency
ISC	intersystem crossing	TON	turnover number
J	joule	TP	trigonal prismatic
J	coupling constant	TPPTS	tris(3-sulfophenyl)phosphine trisodium salt
JohnPhos	(2-biphenyl)di-*tert*-butylphosphine	triflate	trifluoromethanesulfonate
k	kilo	*trig*	trigonal
K	kelvin	TRIP	9-phospha-10-silatriptycene
K_a	acid dissociation constant	Ts	toluenesulfonyl
K_b	base dissociation constant	UV	ultraviolettstrahlung
K_{SV}	Stern–Volmer constant	vdW	van der Waals
L	ligand	*vic*	vicinal
LED	light-emitting diode	Vis	visible
ls	low spin	*vs.*	*versus*
LUMO	lowest unoccupied molecular orbital	VSEPR	valence shell electron pair repulsion (theory)
M	molar	W	watt
m	*meta*	X	generic substituent/heteroatom
M	generic metal	δ	chemical shift
m.p.	melting point	ε	molar attenuation coefficient
m/z	mass-to-charge ratio	κ	denticity
*m*CPBA	*meta*-chloroperoxybenzoic acid	λ	wavelength
Me	methyl	µmol	micromole
MeCN	acetonitrile	$\tilde{\nu}$	wavenumber

Contents

1 Introduction I: Phosphines and π-acid catalysis

1.1 π-acid catalysis

Over the past 70 years, homogeneous catalysis using organometallic complexes has evolved as a powerful tool for the construction of complex molecular scaffolds, enabling highly selective and efficient reaction pathways.[1] In this context, organometallic chemistry and coordination chemistry represent an essential groundwork for understanding the role of corresponding complexes in catalysis.

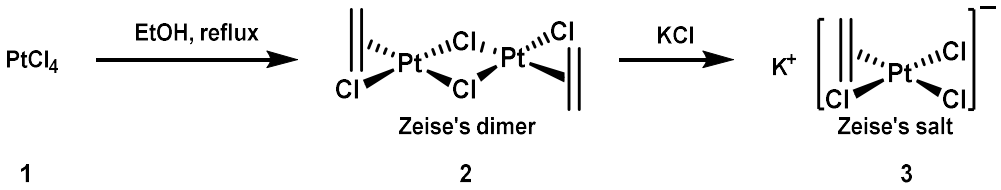

Scheme 1: Zeise's salt

In the years between 1825 and 1830 William Christopher Zeise synthesized the first olefin π-complex by boiling platinum salts such as $PtCl_4$ in ethanol and treating the resulting compound with KCl (Scheme 1).[2,3] The yellow potassium salt $K[C_2H_4PtCl_3]*H_2O$ obtained in this process is still known today as Zeise's salt and represents a milestone in organometallic chemistry.[4] The nature of the binding of the platinum(II) to the η^2-ethylene ligand was hotly debated in the following years and could not be explained until a century later, in 1951, by Michael Dewar.[3,5]

To this day, the bonding situation between a transition metal such as platinum or gold and an olefin (Figure 1 a,b) or alkyne (Figure 1 a-d) is usually described by the Dewar–Chatt–Duncanson model.

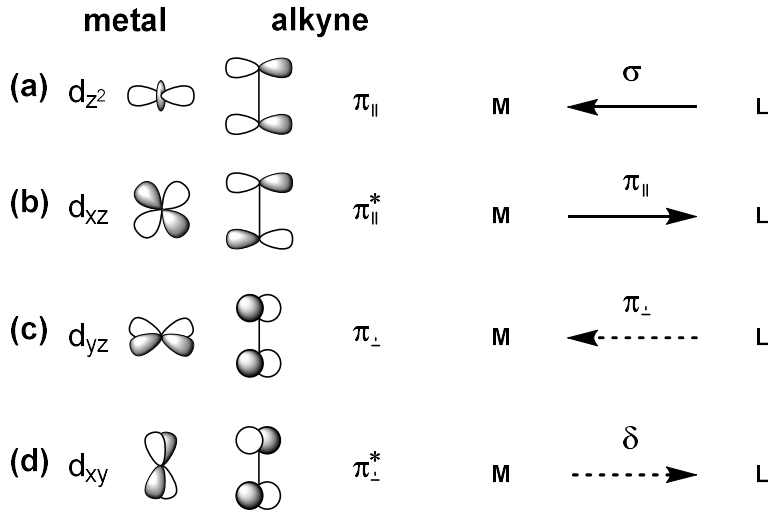

Figure 1: Dewar-Chatt-Duncanson model of TM and alkyne[6]

The bond is characterized by the interaction of metal d orbitals and alkene/alkyne π-orbitals of suitable symmetry. For platinum(II) and gold(I), the major contribution arises from the σ-bond resulting from a overlap of the alkene's or alkyne's HOMO and the empty d_{z^2} orbital of the metal (**a**).[6] Beside the σ-interaction, also π-symmetric back donation from an occupied metal d orbital to an antibonding π* orbital of the alkene/alkyne contributes to the bonding situation, but to a smaller extent (**b**). In the case of an alkyne further interactions can be achieved by the overlap of orthogonal out-of-plane π and π* orbitals with d orbitals of suitable symmetry. The former leads to a weak π-donation from the alkyne to the metal (**c**), while the latter results in a δ-bond with almost negligible strength (**d**). In case of a significant π-back donation from the metal center to the olefin/alkyne, the bonding situation is often

considered to have a metallacyclopropanes/propene character (e.g., $Pt^{(0)}$), while in the case of Pt(II) the π-back donation tends to be weaker and the bonding situation can be better described as dative metal ligand bond.

Due to the strong σ-bond to the metal and the lack of acceptor properties of the olefin/alkyne in a Pt(II) complex, this bond is best described as a donor-acceptor interaction in which the olefin (or alkyne) donates two electrons to the metal. In this case, the metal has an empty orbital and assumes the role of an electron acceptor (Lewis acid), while the olefin (or alkyne) provides this electron pair (Lewis base). This concept goes back to Gilbert N. Lewis, who first described species with an unoccupied orbital or a low-lying LUMO as "Lewis acid".[7] Later this concept was extended by Ralph G. Pearson, who recognized polarizability as an important measure of the interaction between Lewis acid and base.[8] Thus, hard Lewis acids often show a stronger affinity to hard Lewis bases and soft Lewis acids to soft Lewis bases (hard and soft Lewis acids and bases/"HSAB" concept).

In Zeise's salt **3**, the soft Lewis acidic platinum fragment with its chloride spectator ligands removes electron density from the soft Lewis base ethylene. The activated ethylene is now more prone to nucleophilic attack.[6,9] This activation can now be used in catalysis in that metal fragments with empty orbitals not only activate the substrate, but can also dissociate after further reaction and emerge unchanged. Of particular interest in organic synthesis are soft carbophilic Lewis acids, which have no preference for hard heteroelements but for soft carbon─carbon bonds. Examples of such soft Lewis acids are Au^{+}, Hg^{2+} and Pt^{2+}.

The chemistry of all three elements is strongly influenced by relativistic effects.[10] If the nuclear charge of an element exceeds 70, the electrons located close to the nucleus *e.g.* the 6s orbital reach radial velocities near the speed of light and therefore can no longer be described by non-relativistic physics. Compared to a "non-relativistic electron", the mass increases strongly and the inversely proportional Bohr radius decreases. The contraction of the 6s orbital, on the other hand, causes larger shielding of the 5d and 5f orbitals, which in turn expand. The contraction of the 6s orbital also causes a lowering of the LUMO of the metal fragment compared to metals of the same group. The lowering of the LUMO is now manifested by the increased Lewis acidity. Therefore, Au^{+} as well as Pt^{2+} and Hg^{2+} can be considered as strong soft Lewis acids.

1.1.1 Lewis acid catalysis vs. Brønsted acid catalysis

With the corresponding costs for ligands and noble metals, the question arises why one cannot simply use proton catalysis instead (Brønsted acid catalysis). A proton is after all isolobal to the LAu^{+} and Hg^{2+} fragments. An evident difference is the contrasting hardness according to the Pearson concept.[6] Protons are hard Lewis acids, while mentioned metal fragments are soft Lewis acids. This difference leads to the fact that protons often need harsh reaction conditions and are less selective. The softer metal fragments, however, have higher affinity to soft substrates and therefore require less harsh conditions and react in higher selectivity. Besides this evident difference, the use of metal fragments also allows the possibility of stabilizing carbene-like intermediates and to unlock their reactivity. In the case of gold(I), this topic is highly controversial, and resonances of gold carbenes or gold-stabilized carbocations are discussed (→"carbenoid"[6] or "carbene"[11], Scheme 2).[11,12]

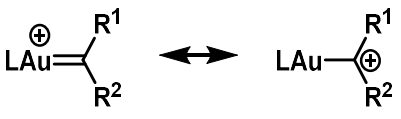

4 5

Scheme 2: Gold carbene[11]

Nevertheless, the bonding model developed by Toste and Goddard is often used to explain certain reactivities (Figure 2).[12,13]

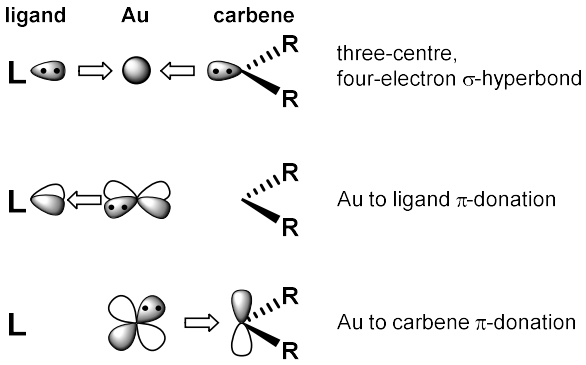

Figure 2: Gold carbene complex bonding model by Toste and Goddard[12]

In the three-center, four-electron σ-hyperbond, electron density is transferred from both the spectator ligand and the carbene to the empty 6s orbital of the gold. Meanwhile, a filled gold 5d orbital donates electron density back to the two acceptor orbitals of the carbene and the ligand. Since both parties overlap with the same metal orbital, the carbene and ligand compete for corresponding electron density. While a strong σ-donor ligand weakens the hyperbond to the carbene, a good π-donor increases the π backbonding to the carbene. This also underlines the importance of the nature of both ligands.

In the following, we will focus on catalysis with Au(I) and Pt(II). These metals are significantly less toxic than Hg^{2+} and at the same time possess a kinetically more labile carbon-metal bond.[6] In the case of Hg^{2+}, this carbon-metal bond is often kinetically too stable for catalytic reactions (*e.g.* of alkenes) and bond cleavage by additional workup is required (*e.g.* oxymercuration reaction).

For carbophilic activation of multiple bonds with both platinum(II) and gold(I), the following mechanism can be assumed (Scheme 3):[14,15]

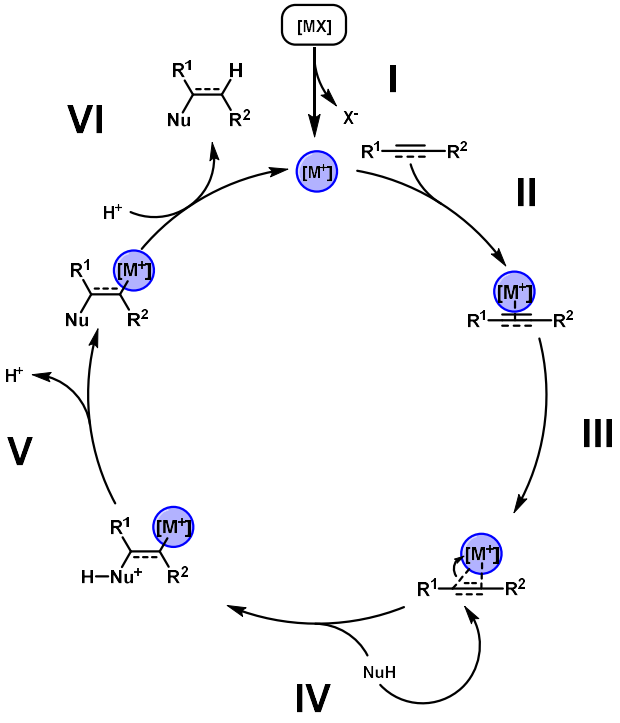

Scheme 3: General mechanism of carbophilic activation of multiple bonds[15]

The precatalyst [MX], which is a linear two-coordinate complex in the case of gold(I) (or often a four-coordinate square-planar complex in the case of platinum(II)), is turned into an active catalyst by ligand abstraction (**I**). The abstracted ligand is often a halide that can be removed by addition of silver salts, and the spectator ligand is frequently a carbene or phosphine. After activation, the LAu^+ fragment ($[M^+]$) is now capable of coordinating an alkyne (or olefin, allene) to form a η^2 π-complex (**II**). The electrophilicity of the activated multiple bond is increased by deformation to a η^1-coordination ("slippage", **III**), making it easier for the nucleophile to attack in anti-fashion (**IV**). The "slippage" is therefore a crucial step that determines the regioselectivity, but also strongly depends on substrate and ligands. Moreover, "slippage" in some cases unlocks the reactivity of *vic*-carbenes (and after [1,2] migration of Au vinylidene complexes, Scheme 4).[16]

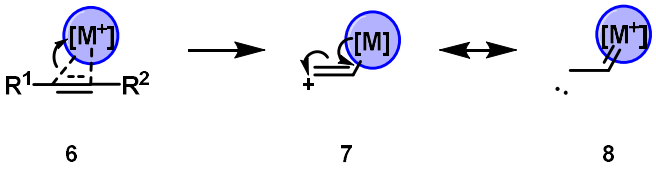

Scheme 4: Activation of alkynes: "slippage"[6]

After deprotonation (**V**), the vinyl gold intermediate formed is now susceptible to reactions with electrophiles, usually protons, leading to protodeauration (or protodemetalation) and product formation (**IV**). During this process, the catalytically active species $[M^+]$ is released/regenerated for further conversions. The mechanism is widely adopted in the literature to explain gold(I) catalytic reactions. Likewise, many two-coordinated gold(I) alkene[17] and alkyne[18] η^2 π-complexes have been synthesized in the past that support it.

1.1.2 Gold(I)-Catalysis

Almost no other topic in gold(I) catalysis has received as much attention synthetically as well as mechanistically as the cycloaddition of 1,n-enynes. Here, the nucleophile attacking the activated alkyne is an olefin.

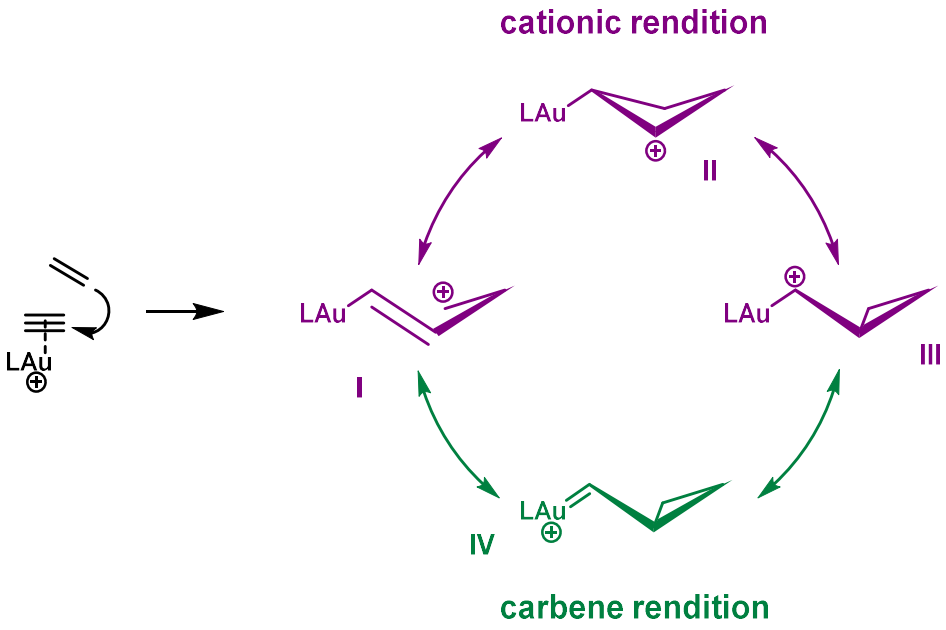

Scheme 5: Mesomeric „carbenoid" structures formed during enyne reactions[15]

The reactive carbenoid intermediate ("non-classical" cation) formed can now be described by different resonance forms (Scheme 5).[12,15] As already stated the carbenoid exhibits cationic carbene/α-

metallocarbenium character stabilized by the gold(I). To predict reactivity, all dichotomic resonance extremes must be considered, which can be difficult because of the strong dependence on substrates and ligands. On the other hand, prediction is facilitated by the fact that metal-based redox steps are unlikely and the alkyne, rather than the olefin, continues to react as an electrophile once activated by the gold (alkynophilicity). The latter may seem surprising, since olefins bind more strongly to gold(I) than alkynes, but nucleophilic attacks are thermodynamically favored in the alkyne due to the low lying LUMO of the C≡C bond in the activated state.[19]

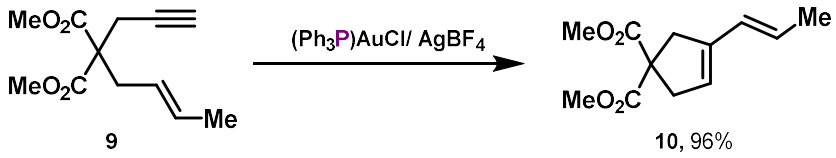

Scheme 6: Gold(I) catalyzed 1,6-enyne cyclization[20]

The first gold(I) catalyzed 1,6-enyne cyclization was reported by Echavarren[20] in 2004 (Scheme 6). The reaction uses a gold(I) precatalyst, which exhibits a phosphine (PPh_3) spectator ligand. After chloride abstraction by $AgBF_4$ the activated gold(I) complex $[Au(PPh_3)]^+$ is able to reorganize enyne **9** into cyclized product **10** in 96% yield in 10 min at 23 °C. This outperforms comparable platinum(II) catalysts.[21]

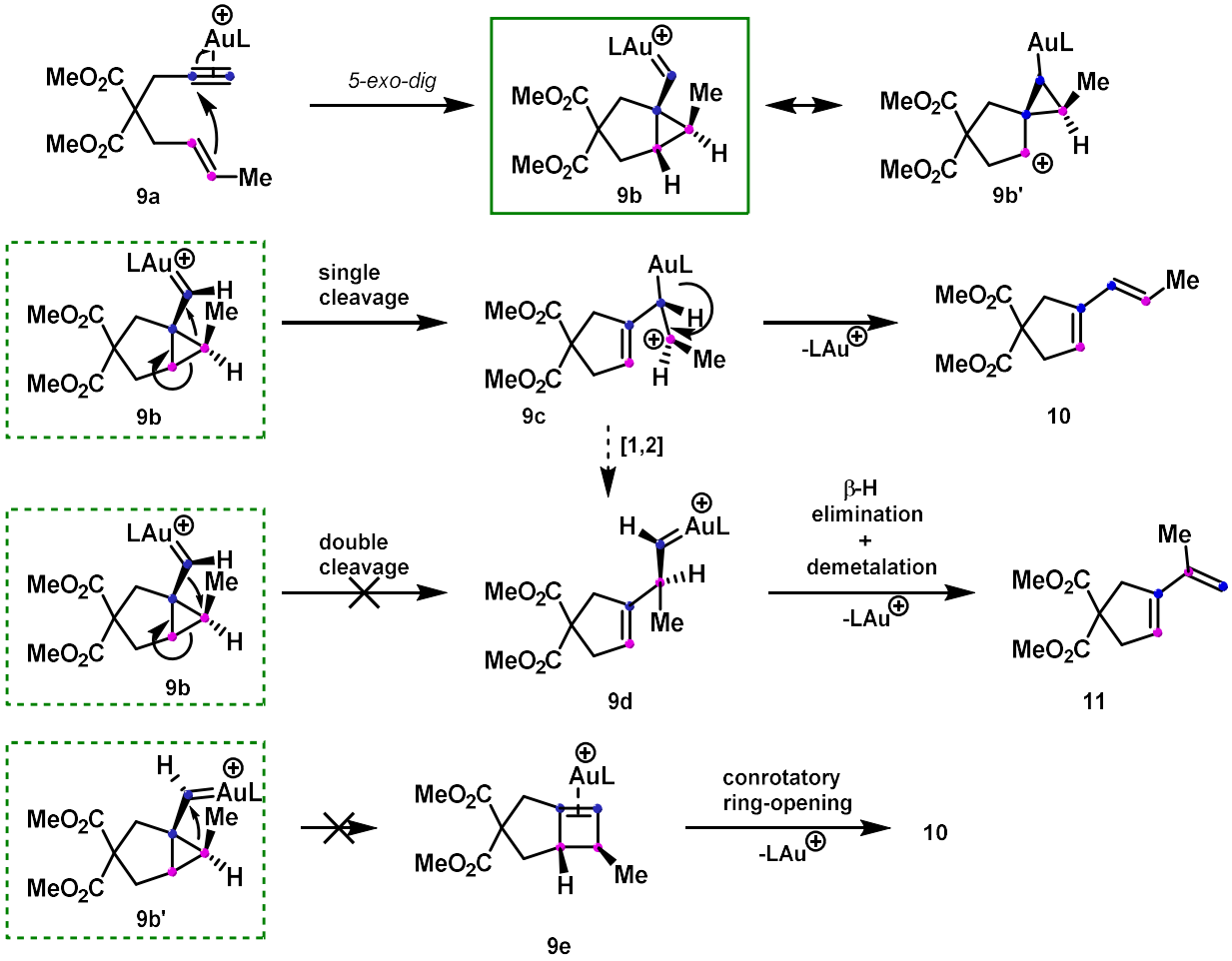

Scheme 7: 1,6-enyne cyclization: Conceivable mechnanisms based on a 5-exo-cyclization[22]

Although the reaction appears quite simple, prediction of the product is difficult (Scheme 7). Calculations support a mechanism based on a *5-exo*-cyclization in combination with a "single *exo*-cleavage" skeletal rearrangement.[21,22,23] In this process, the cyclopropyl-metal carbene **9b** is first formed *via 5-exo-dig* cyclization from the gold(I) activated alkyne complex **9a**. Starting from cyclopropyl-metal carbene **9b**, the cation **9c** can be formed *via* skeletal rearrangement and, after elimination, release the catalyst and the product ("single *exo*-cleavage").

Depending on the substrate, the "double *exo*-cleavage" pathway is also accessible, in which after a 1,2 shift of the metal carbene and distal C─C cleavage in the cyclopropane, an α-metallocarbenium ion **9d** forms, which can be converted to a double bond by β-H elimination and demetalation. Note, however, that beside "double *exo*-cleavage" skeletal rearrangements also *6-endo-dig* cyclizations (instead of the *5-exo-dig*) and cyclobutene intermediates **9e** (formed by rearrangement of **9b**) are also conceivable. The variety of possible mechanisms makes a large number of products feasible, depending on the substitution pattern on the alkyne or olefin and the linker or catalyst used. Furthermore, various intermediates can also be trapped *e.g.* by nucleophiles or demetalation, which further increases the product range and gives access to small ring structures e.g. cyclopropanes or cyclobutenes.[24,25]

One example for a trapping of an electrophilic gold(I)-carbenoid intermediate similar to **9b**, is the oxygen atom transfer from sulfoxides published by Toste and coworkers (Scheme 8).[25]

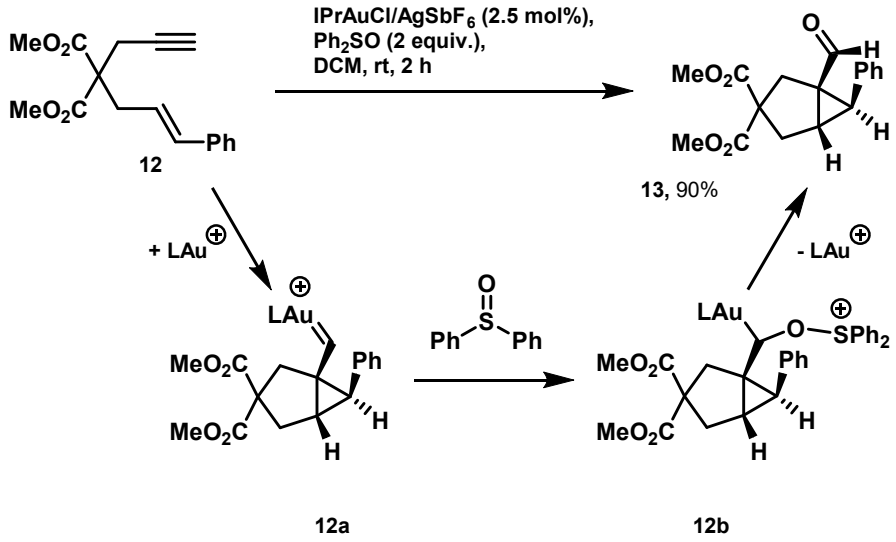

Scheme 8: Gold(I)-catalyzed oxidative rearrangement[25]

The gold(I) catalyst used is based on a N-heterocyclic carbene ligand [1,3-bis(2,6-diisopropylphenyl)imidazol-2-ylidene = IPr], which was giving superior yields compared to the triphenylphosphine gold(I) complex. One can see that product **13** is a direct result of substituting the gold(I) catalyst of intermediate **12a**, giving access to cyclopropane structures.

In addition to the application of gold(I) catalyzed enyne cyclizations in the synthesis of small molecules, it especially offers the possibility to build highly complex natural products, since due to the selectivity of the soft gold(I) the methodology tolerates many functional groups (Scheme 9).

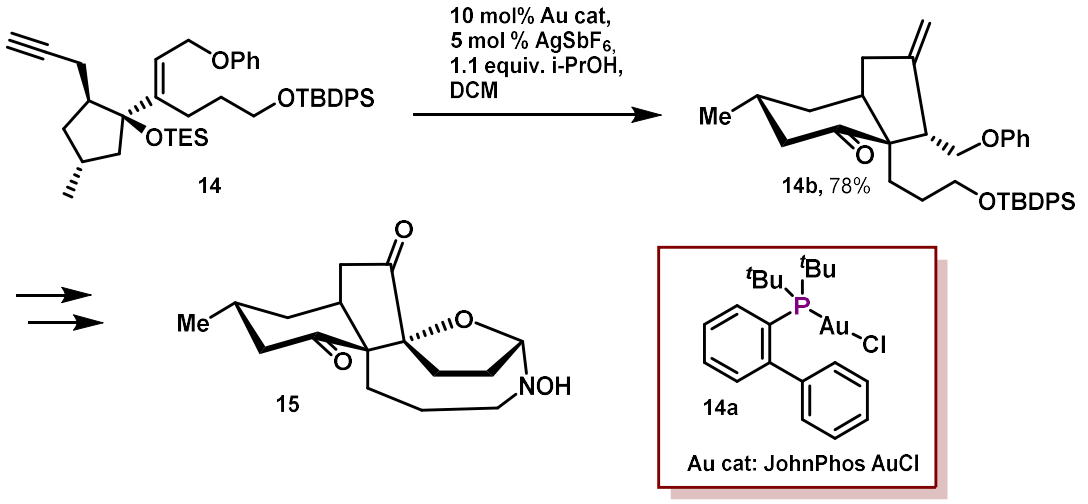

Scheme 9: Total synthesis of (+)-Sieboldine A[26]

An example of such a natural product is (+)-Sieboldine A[26] (**15**), whose key step in its total synthesis is based on a pinacol-terminated 1,6-enyne cyclization published by Kirsch and Rhee[27]. The catalyst used is a gold(I) complex **14a** of the Buchwald-type phosphine JohnPhos.

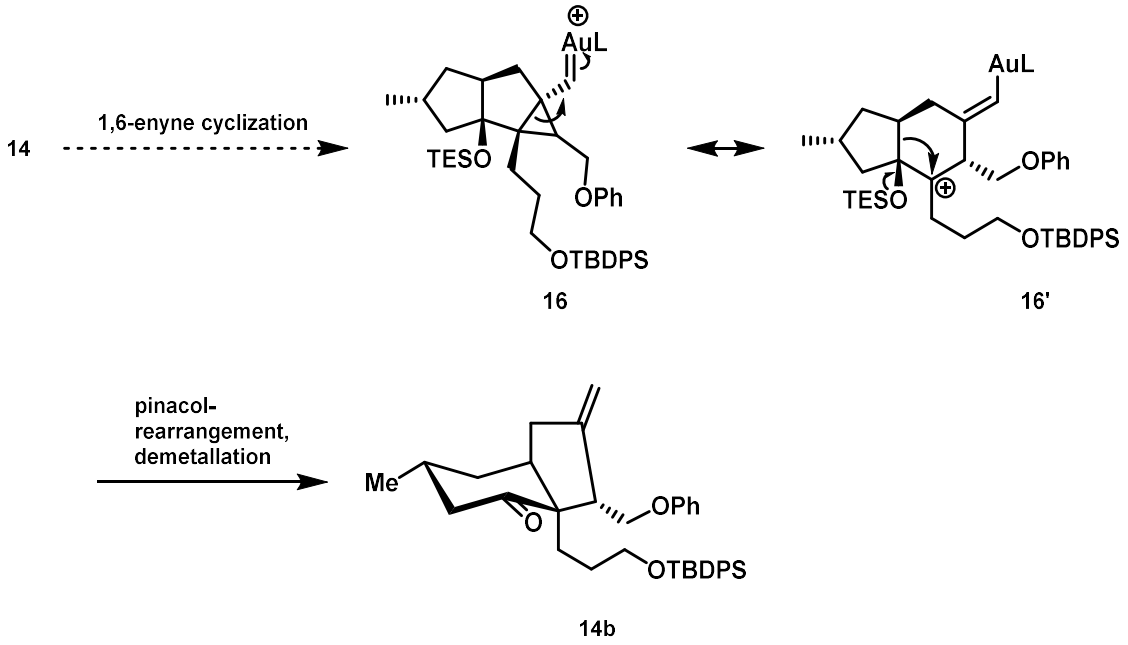

Scheme 10: Key step in the synthesis of (+)-Sieboldine: 1,6-enyne cyclization and pinacol-rearrangement[26,27]

The mechanism is based on an intermediate **16** (similar to **9b**) which in turn can be interpreted as its "mesomeric" form of **16'** (Scheme 10). The structure **16'** now readily reveals a pinacol rearrangement leading to product **14**.

In addition to the application of gold(I) catalysts in enyne reactions, there are plenty of other reaction types that benefit from the use of gold(I) catalysts.[28] For example, one significant reaction type is the hydroarylation (or hydroheteroarylation) of alkynes. Two reaction mechanisms are particularly relevant here: Reactions similar to Friedel-Crafts alkenylation or *via* metal cyclopropyl carbene intermediates similar to those of 1,n-enyne cyclizations (**9b**).[29]

In 2000, Hashmi was able to develop an elegant method of converting alkynyl furans into phenols by Au(III) catalysis (Scheme 11).[30]

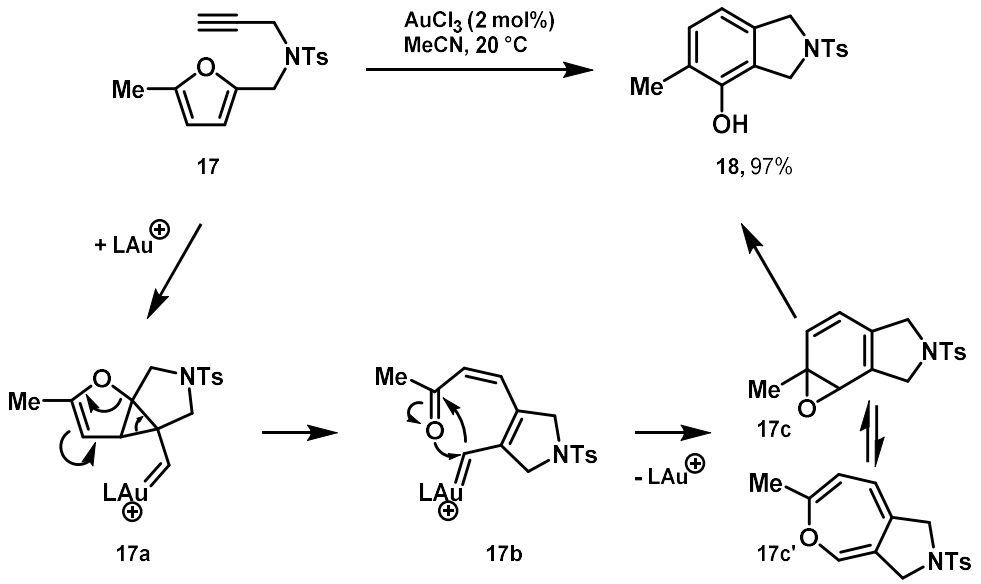

Scheme 11: Gold(I) or Gold(III) catalysed intramolecular phenol synthesis[31]

The reaction proceeds *via* cyclopropyl carbene intermediate **17a** (*cf*. **9b**).[31] In this process, however, the furan is not directly rearomatized and reformed as in classical hydroarylations, but ring opening and formation of the stabilized carbene **17b** takes place. Afterwards carbene **17b** cyclizes and forms the benzene-oxide/oxepin equilibrium, which can then isomerize to the final product. Despite the fact that the original reaction was published using an Au(III) catalyst, numerous Au(I) catalysts are now available which also lead to the desired phenol.[32]

A more classical hydroarylation published by Fürstner in 2002 leads to the synthesis of phenanthrenes (Scheme 12).[33]

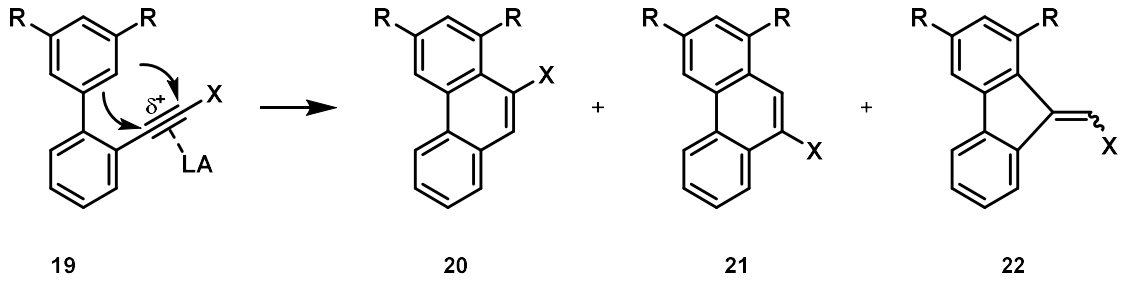

Scheme 12: Phenanthrenes synthesized by Lewis acid catalyzed cycloisomerization[33,34]

This synthesis is reminiscent of an intramolecular Friedel-Crafts alkenylation but might also proceed *via* a metal cyclopropyl carbene intermediate.[6,33] The alkyne can be activated by various Lewis acids (**LA**) and after positive polarization initiate cyclization. Interestingly, the products of the cyclization are strongly dependent on the substitution pattern of the alkyne and the catalyst used. Three different products are conceivable (**20**, **21**, **22**). If $PtCl_2$ is used as catalyst and R=Me and X=Me, the *6-endo-dig* isomer **20** (R=Me, X=Me) is formed exclusively, while the exchange of X=Me by X=COOMe, leads almost exclusively to the *5-exo-dig* isomer **22** (R=Me, X=COOMe). The electron-withdrawing moiety thus changes not only the reaction rate but also the selectivity by shifting the position of the partial positive charge in the activated alkyne intermediate **19**.

It also becomes particularly interesting when a halogen such as X=Cl, Br or I, which is capable of migration, is used instead of an organic group on the alkyne.[34] Here, $PtCl_2$ no longer serves as an effective catalyst and AuCl and $InCl_3$ were used. Both show *6-endo-dig* selectivity, but differences can

be observed on the halophenanthrene products with respect to halide retention (**20**, $InCl_3$) or 1,2-halide migration (**21**, AuCl).

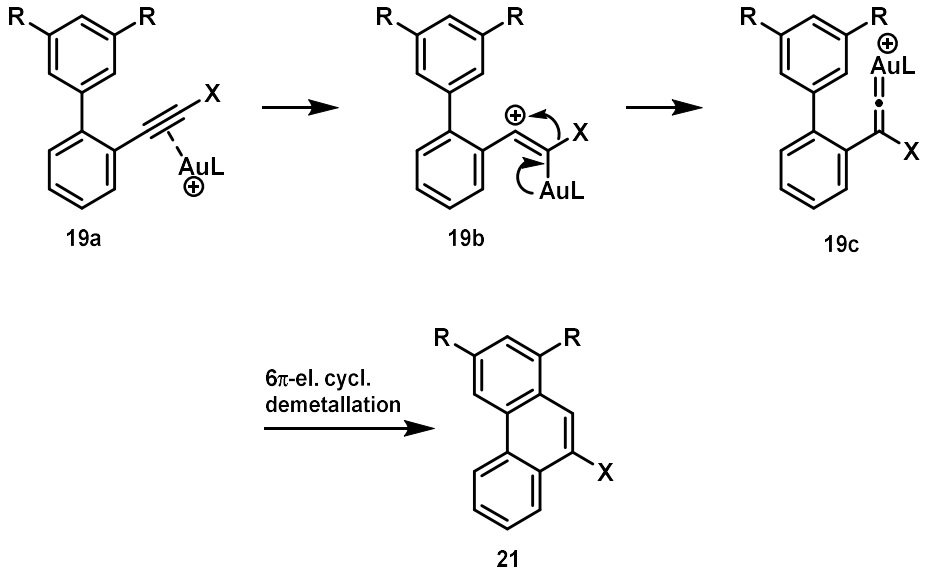

Scheme 13: 9-halophenanthrenes by 1,2-halide migration[34]

In the case of the AuCl catalyst, the halide walk can be explained by the *vic*-carbene reactivity (Scheme 4), which triggers the 1,2-halide migration and generates a gold(I) vinylidene species **19c** (Scheme 13). After 6π-electrocyclization and demetalation the regioisomer (**21**) is obtained. In(III) does not exhibit such reactivity due to its high oxidation state and thus leads to hydroarylation with halide retention (**20**).

1.1.3 Platinum-Catalysis

Like gold(I), platinum(II) is also used in the carbophilic activation of multiple bonds. However, gold(I) catalysts are often more effective.[35] This is due to the less pronounced backbonding as well as higher electrophilicity caused by the more present relativistic effects in gold(I) complexes. On the other hand, platinum(II), besides its Lewis acidity, also shows redox behavior but due to kinetically inhibited oxidative addition and reductive elimination in combination with high platinum-ligand bond dissociation energies often cannot compete in reactivity to lighter group 10 metals. The further abilities to stabilize carbene intermediates and activate inert bonds makes platinum(II) complexes catalysts that combine the properties of soft Lewis acids and palladium-like redox events, unlocking reaction mechanisms such as that of carbophilic activation (Scheme 3), but also such as the Chalk-Harrod mechanism for *e.g.* hydrosilylation (Scheme 14):[6,36]

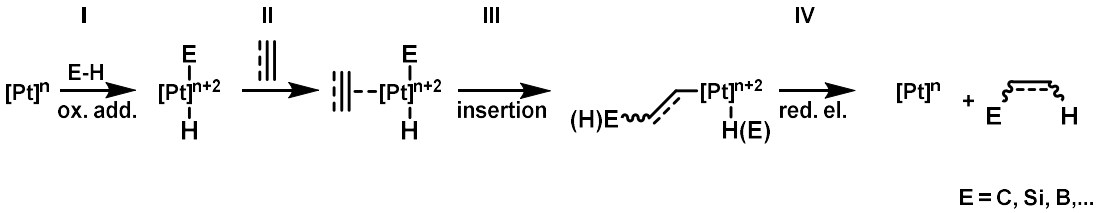

Scheme 14:Chalk-Harrod mechanism[36]

The latter mechanism is composed of oxidative addition (**I**) followed by ligand association (**II**), insertion (**III**) and reductive elimination (**IV**). As a side reaction, mainly β-hydride elimination is present. Because of its ability to activate inert bonds, platinum(II) is also used in the activation of methane, which represents a classic example of C–H activation (Shilov system).[37] Methanol and chloromethane can

be obtained in this process. In the following, however, we will focus on cationic or low-electron count Pt complexes, which are used in Lewis acid catalysis.

The applications and intermediates of platinum(II) Lewis acid catalysis are often similar to those of gold(I) catalysis, but the corresponding reactions require higher temperatures and reaction times. Therefore, innovative approaches are needed to improve the electrophilic character of the platinum catalyst and increase the reaction rate.

One such approach was published by Fürstner in 2005.[38]

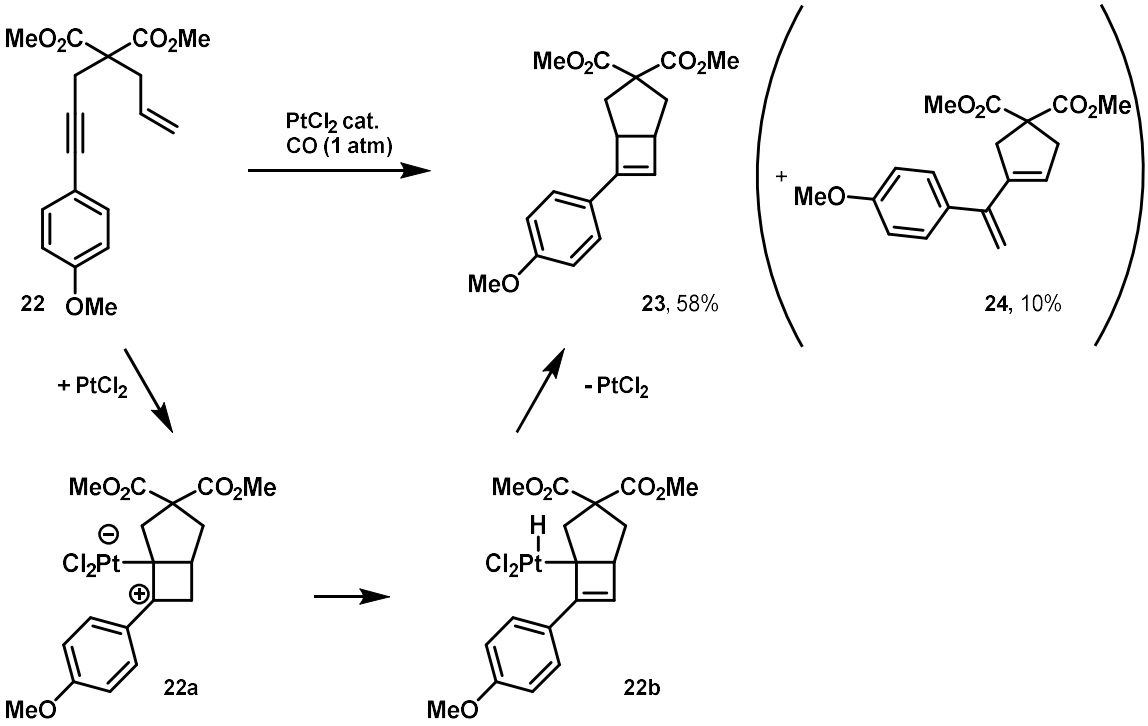

Scheme 15: Synthesis of cyclobutenes by platinum(II)-catalyzed cycloisomerization of enynes[38]

Two different products are formed during the platinum(II) catalyzed cycloisomerization of enyne **22**. One product (**24**) corresponds to that of the gold(I) catalysis already presented (single cleavage, Scheme 6). However, the diene **24** represents only the minor product, since the aromatic substituent (*p*-$MeOC_6H_4$-) on the alkyne stabilizes the intermediate **22a** (*cf.* **9e**, Scheme 7) and favors the formation of a cyclobutene **23**. To avoid the formation of a bridgehead olefin, the redox-capable platinum(II) intermediate **22a** can now initiate the formation of the Bredt isomer **23** by formation of the platinum hydride **22b** and reductive elimination. However, the reaction progresses slowly and requires more than 16 h. To address this issue, Fürstner and co-workers changed the atmosphere of the reaction to carbon monoxide. The strongly π-acidic CO coordinates to the metal center and increases its electrophilicity, accelerating the reaction to 2 hours. The acceleration clearly shows the strong influence ligands can have on a reaction and that the reactivity of Platinum(II) can be tuned to a level of cationic gold(I) systems.

Another approach to tune the electrophilicity of a metal center is the use of non-innocent Z-type ligands.[39–41] With the d shell partially filled, transition metals are not only capable of π-backbonding but also of acting as pure Lewis bases in the presence of Z-type ligands.

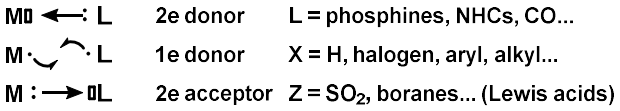

Figure 3: Types of 2-center metal–ligand interactions[39]

These Lewis acidic ligands reverse the electron density distribution compared to conventional L-ligands and act as two-electron acceptors in the 2-center metal-ligand interaction (sigma-acceptors, Figure 3). To circumvent alternative coordination modes, Z-type ligands are often supported by multiple donor buttresses, for example in the form of pincer ligands. Z-type ligands are now able to increase the Lewis acidity of the coordinated metal at the free coordination site trans to the Z-type ligand by depleting electron density from the filled d-orbitals and stabilizing a vacant p-orbital. This fact motivated Gabbaï and co-workers to use Z-type ligands in platinum catalysis.[40]

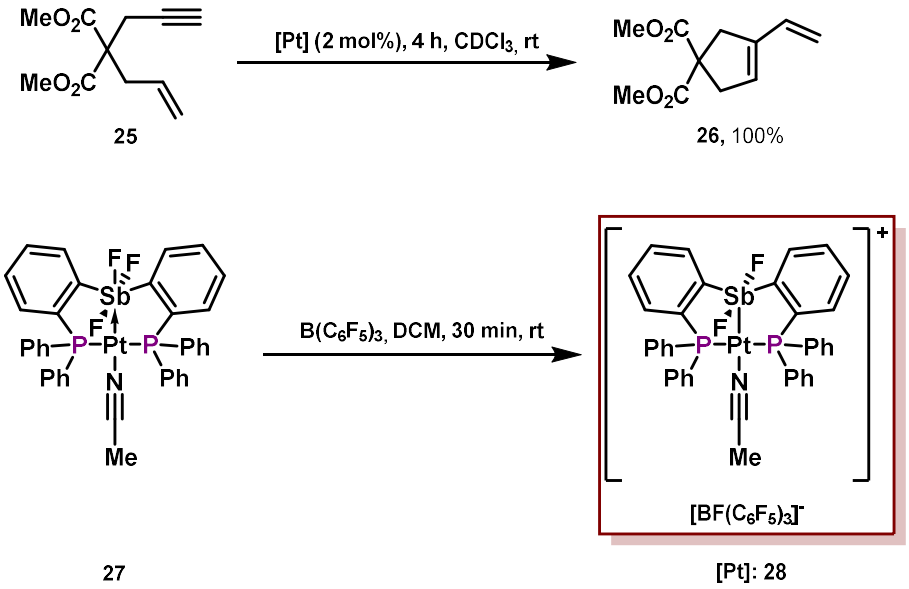

Scheme 16: Enyne cyclization catalyzed by platinum complexes based on Z-type ligand[40]

As a Z-type ligand they used an antimony Lewis acid, which, by interacting with platinum ($Pt^0 \rightarrow Sb^V$), withdrew electron density from the latter while still remaining modulatable *via* reorganization of the halide ligands (**27**, Scheme 16). However, the platinum center remained too electron-rich to catalyze 1,6-enyne isomerization of **25**. Note, that the platinum exhibits a d^{10} configuration and thus appears as Pt^0. To further increase the electrophilicity of the platinum center, the authors decided to enhance the Lewis acidity of the Z-type ligand by abstracting a fluorine, resulting in complex **28**. The strongly Lewis acidic diaryldifluorostibonium moiety in **28** can now form an even stronger Pt→Sb interaction, which is covalent in nature and thereby further increases the electrophilic character of the platinum. With **28**, the authors were now able to successfully cycloisomerize enyne **25** in only 4 h and demonstrate the utility of Z-type ligands in platinum catalysis.

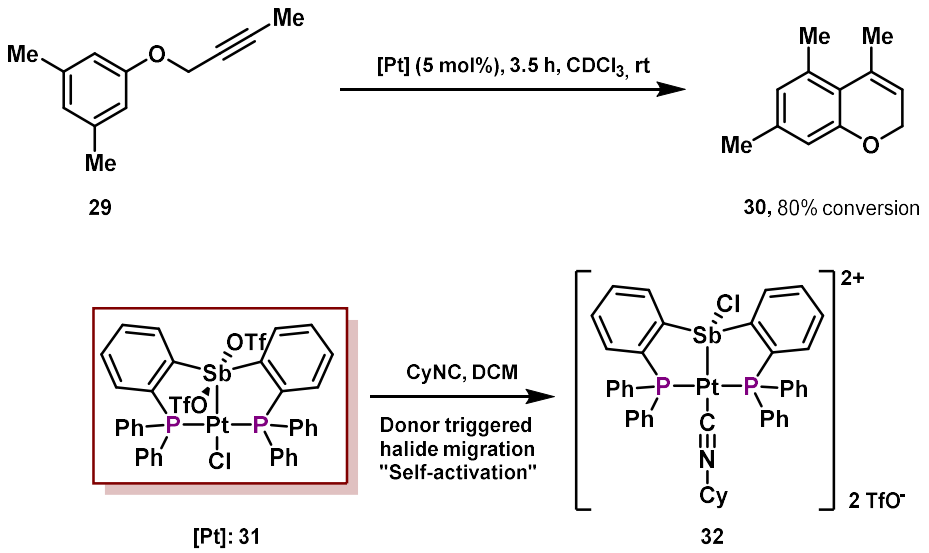

Scheme 17: Hydroarylierung catalyzed by "self-activating" catalyst[42]

The same group also published a related system of a "self-activating" catalyst **31** (Scheme 17).[42] Here, the antimony-based Lewis acid served as a kind of activator that can abstract the chloride of the platinum and subsequently serves as a π-acceptor ligand that withdraws electron density from the platinum enabling it to catalyze the hydroarylation of **29**. The activation is triggered by the nucleophilic attack of the substrate. Attack and halide migration could be imitated by the isonitrile surrogate CyNC leading to complex **32** and confirming the proposed "self-activation".

However, the general idea of reducing the electron density of a platinum center by using π-acidic ligands is not new and is reminiscent of Fürstner's use of carbon monoxide. Similar approaches have been pursued by the use of electron-deficient bpy ligands[43], cationic arsines[44] or cationic phosphines[45] (*cf.* chapter 1.3.2.3, Scheme 36).

1.2 Phosphines

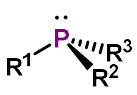

Phosphines, along with cyclopentadienyls and N-heterocyclic carbenes, represent one of the most important classes of substances used as spectator ligands.[46] This is mainly due to their Lewis basic character of intermediate hardness in combination with easily tunable electronic and steric properties *via* the substituents.

Once bound to a metal, the L-type phosphine ligand stabilizes many different oxidation states of the metal center, even if these change during a reaction. This is particularly desirable in homogeneous organometallic catalysis and it is therefore not surprising that phosphines in the form of their palladium complexes are used in cross-coupling reactions such as the Suzuki–Miyaura reaction (Scheme 18).[47]

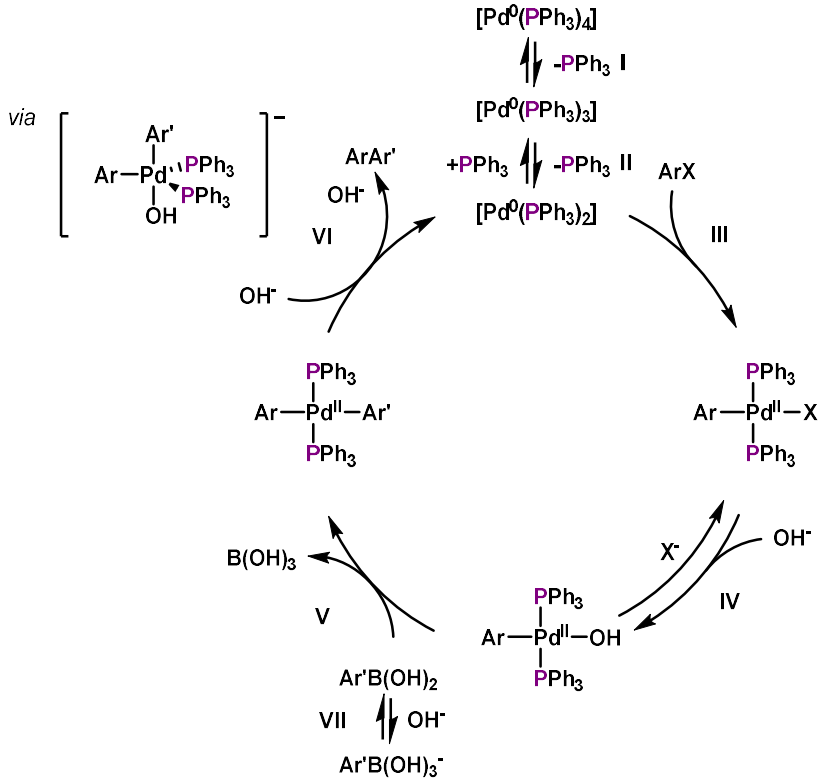

Scheme 18: Mechanism of the Suzuki-Miyaura reaction[47]

Here, one of the most popular precatalysts is tetrakis(triphenylphosphine)palladium(0), which is converted into the actual catalyst after dissociation of two phosphine ligands (**I**, **II**). The palladium(0) species can now undergo oxidative addition and inserts into the Ar–X bond leading to a palladium(II) species (**III**). After ligand exchange (**IV**) and transmetalation by the boronic acid (**V**), reductive elimination (**VI**) results in the formation of the product ArAr' and returns the active palladium(0) catalyst. It is believed that the base, in this case the hydroxide ion, positively influences the catalytic cycle by forming a Pd–OH species (**IV**), thus facilitating the transmetalation (**V**).[47] Furthermore it assists in the reductive elimination process of the *trans*-[ArPdAr'(PPh_3)$_2$] complex (**VI**) by forming a fivefold coordinated palladate(II) species. On the other hand, the base also has a negative effect by generating a resting state (**VII**) capturing the boronic acid as an unreactive borate. The reaction, which represents a tool for constructing biaryl compounds, was awarded with a Nobel Prize in 2010 (Palladium-catalyzed cross couplings in organic synthesis: Heck, Negishi, Suzuki) and illustrates the utility of phosphine ligands in modern chemistry. The ability of phosphines to stabilize corresponding palladium intermediates arises from their good σ-donor (and moderate π-acceptor) capabilities.

1.2.1 Electronic properties of phosphine ligands

The bond between a transition metal and a phosphine ligand can be described in a simplified way by the Dewar-Chatt-Duncanson model (Figure 4).[48,49]

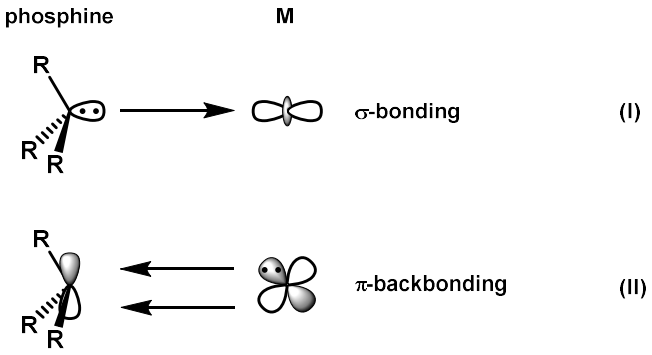

Figure 4: Dewar-Chatt-Duncanson model of TM and phosphine[49]

The sigma bond is formed by the overlap of the phosphorus lone pair exhibiting a strong s character (often corresponding to the HOMO) and the empty metal d_{z^2}-orbital (**I**). The backbonding results from the overlap of a filled metal d-orbital with an empty antibonding σ*-orbital of the phosphorus (P─R) (**II**, often corresponding to the LUMO). In early work, the backbonding was thought to be based on electron density transfer from a filled metal d-orbital to an empty phosphorus d-orbital (or pd hybrid orbital). Nowadays, modern theoretical works have shown, that d-orbital contribution is neglectable in main group elements, thus backbonding is assumed to occur almost exclusively into orbitals of the phosphorus with 3p character.[48]

As mentioned above, one of the great advantages of phosphine ligands is their easy tunability by changing the substituents. Not only the sterics but also the electronics of the phosphine ligands can be altered significantly. Introducing an electronegative substituent can decrease the σ-donor ability and increase the π-acceptor character of a phosphine.

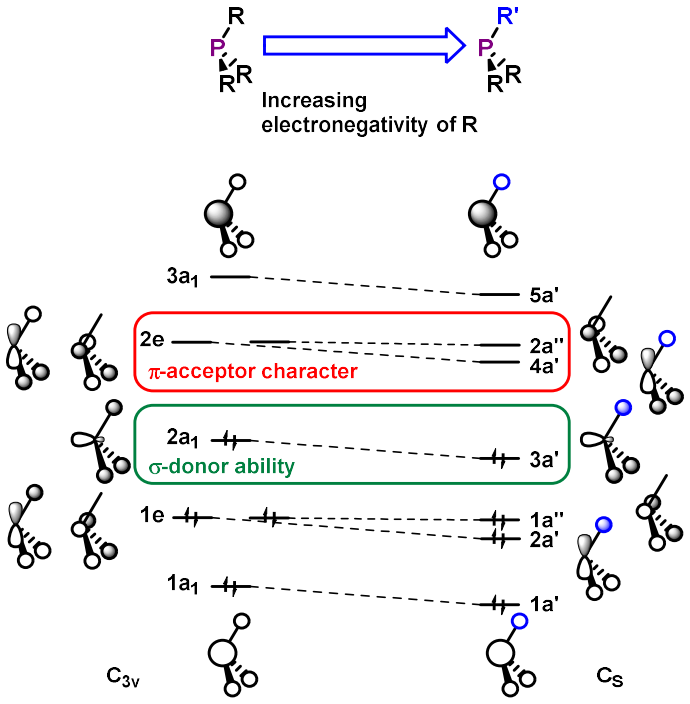

Figure 5: Molecular orbital diagram of a phosphine (left) and of a perturbed system in which a substituent has been replaced by a more electron-withdrawing substituent (right)[50]

Figure 5 elegantly illustrates the effect of replacing one substituent of a C_{3v} symmetric phosphine by a more electron-withdrawing one.[46,50] As soon as a more electronegative substituent R' is introduced, both the energy of the HOMO (green, P lone pair) and the LUMO [red, σ*(P─R')] decrease. The decrease in the energy of the HOMO now makes it more difficult to transfer electron density from the phosphine lone pair to the metal (weaker σ-donor), while the lowered LUMO facilitates the back-bonding from the metal to the phosphine σ*(P─R') orbital (better π-acceptor). The latter results not only from the lowering of the LUMO energy, but also from the more phosphorus centered σ*(P─R') orbitals.[46] The lowering of the LUMO energy can be explained by the fact that the more stable atomic orbital of a more electronegative moiety results in a more stable σ*(P─R') orbital. However, while more electronegative atoms have higher coefficients in binding MOs, the less electronegative atoms have higher coefficients for antibonding MOs, thus, if the energy gap between the atomic orbitals of the phosphorus and the electronegative group increases, the phosphorus also contributes more to the σ*(P─R') bond. The higher contribution is expressed by an increase in the size of the σ*-orbital lobe next to the phosphorus, which is then more readily available for overlap with the d-orbitals of the metal.

1.2.2 Experimental determination of net donor abilities

To quantify the electronic properties of various ligands, Tolman developed a scale based on the A_1 band of IR spectra of nickel carbonyl complexes with the general formula $[Ni(CO)_3L]$ which is nowadays referred to as the Tolman electronic parameter χ (TEP).[51,52] In solutions of $[Ni(CO)_3L]$, the CO ligand exhibits a CO stretching frequency χ that depends strongly on the nature of the ligand L and is smaller than in free CO (2143 cm^{-1}). This can be explained by the special bonding situation of CO ligands in metal carbonyls (Figure 6).[46]

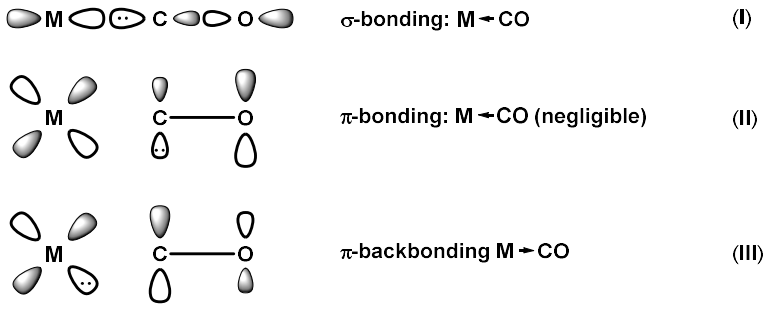

Figure 6: Dewar-Chatt-Duncanson model of TM and CO[4]

The C(sp) lone pair of the CO coordinates to an empty metal $d_σ$-orbital forming a σ-bond (**I**). However, bond formation to the metal only slightly affects the CO bond, since the lone pair is nonbonding (or weakly anti-bonding). On the other hand, the metal $d_π$-orbital donates electron density into the CO π* orbital, lowering the bond order of the CO bond [π-backbonding, (**III**)]. Thus, the decrease on the bond order of the CO bond is stongly dependend on the tendency for π-backbonding/ π-basicity of the metal (Scheme 19).

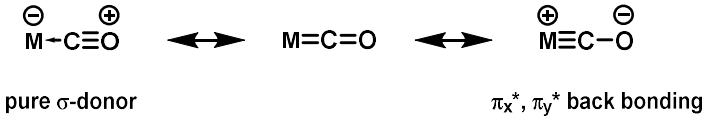

Scheme 19: Resonance forms of metal CO bonding[46]

As known from the quantum harmonic oscillator, a bond order decrease leads to a bathochromic shift of the CO-stretching frequency. Therefore, the binding of the CO to a metal with π-backbonding is expected to lead to a frequency decrease compared to the free CO (exceptions are nonclassical carbonyls with weak π-backbonding). However, the π-basicity of the metal depends not only on its

oxidation state and nature but also on its ligands. If only one of the ligands L is systematically changed {[Ni(CO)$_3$L]}, these ligands can be compared on the basis of their donor abilities. If a ligand with strong donor properties transfers more electron density to the nickel, better π-backbonding from the nickel to the CO ligand can take place and a relative low frequency χ is obtained. The Tolman electronic parameter χ is thus a measure of the net donating ability (interplay of σ-donor ability and π-acceptor character) of a ligand L (Figure 7).[53]

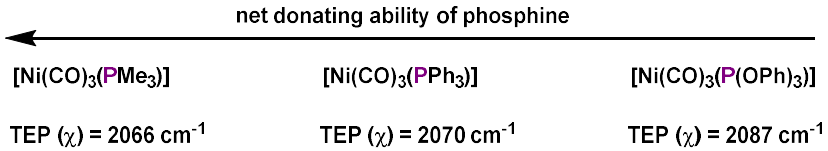

Figure 7: TEP of different phosphines[53]

However, in the recent past, nickel carbonyls have been used less and less due to their toxicity and have been replaced by other metal carbonyls that follow the same concept. This leads to other scales based on transition metal carbonyls, which can be partially correlated.[53]

In addition to metal carbonyl-based IR concepts, methods that use NMR parameters such as chemical shifts (*e.g.* ^{13}C) or coupling constants (*e.g.* $^1J_{PB}$, $^1J_{PPt}$, $^1J_{PSe}$) to determine the donor ability of a phosphine have also been employed.[53] Of particular interest for multidentate heterophosphines is the determination of their basicity *via* their $^1J_{PSe}$ NMR coupling constants of the corresponding phosphine selenides (Scheme 20).[54,55]

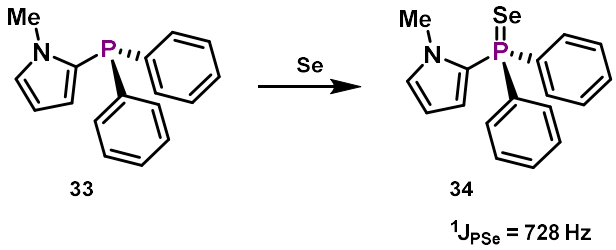

Scheme 20: Oxidation of phosphines to phosphine selenides[55]

Since the J-coupling constant contains information about the electronic environment, bonding situation and hybridization of ^{31}P (I = ½) and ^{77}Se (I = ½) *via* the Fermi contact interaction, it is also strongly influenced by the polarization of the P─Se bond. If electron pushing substituents are chosen on the phosphorus, the coupling constant $^1J_{PSe}$ decreases, while electron withdrawing substituents result in high coupling constants. In other words, the coupling constant decreases as the basicity of the corresponding unoxidized phosphine increases (Scheme 21).

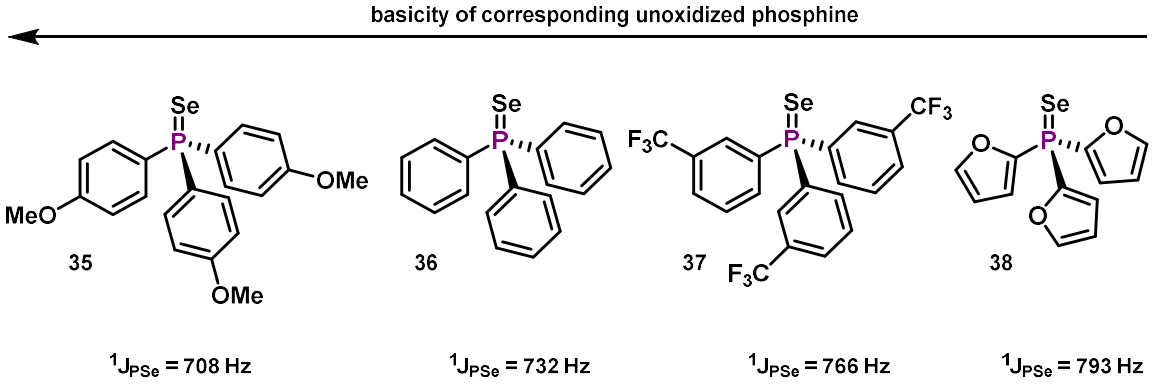

Scheme 21: Correlation of the basicity of a phosphine and $^1J_{PSe}$ of the corresponding phosphine selenide[55]

The method is compatible with many different phosphines. Phosphines can be studied whose basicities cannot be easily determined *via* titration (pk_b) due to other basic substituents, or whose net donor capabilities cannot be easily determined by carbonyl complexes because multiple coordination modes are a problem. In addition, it is usually possible to achieve selective oxidation at the phosphorus (Scheme 20). In contrast to these advantages, it should be mentioned that long ^{31}P NMR measurement times are often required to visualize the ^{77}Se satellites, since Se has only one NMR active isotope with a natural abundance of 7.63%. In addition, the coupling constants seem to be affected by the nature of NMR solvent used or the steric bulk of the substituents at the phosphorus.[56] Care should be taken to use the same NMR solvent and to compare phosphines of similar steric demand.

1.2.3 Steric measure of phosphines

The steric demand of a phosphine ligand can be described by the cone angle θ defined by Tolman.[51] For symmetrical phosphines of the type PR_3, the cone angle describes the apex angle starting at a real or putative metal atom M at a distance of 2.28 Å from the phosphorus and tangentially touching the van der Waals radii of the two outermost ligand atoms. In the case of asymmetrically substituted phosphines of the $PR^1R^2R^3$ type, an averaging and doubling of the corresponding half cone angles θ_i can be used (Figure 8, Equation 1).

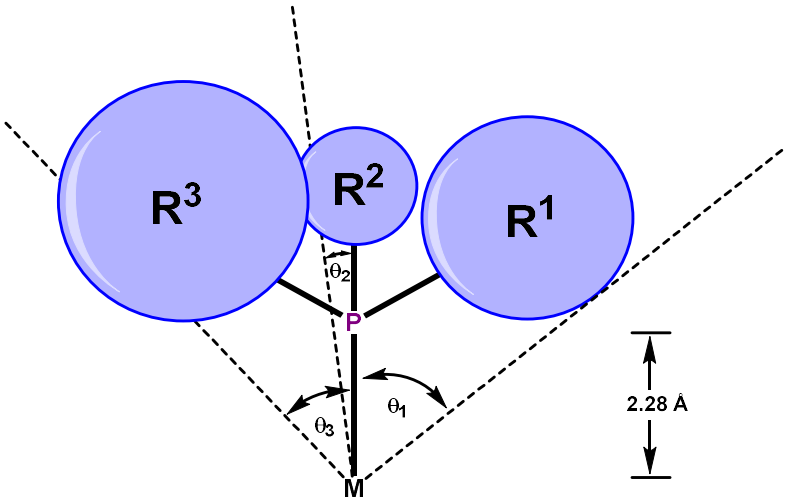

Figure 8: Cone angle for unsymmetrical phosphines[51]

$$\theta = \frac{2}{3}\sum_{i=1}^{3}\theta_i \qquad (1)$$

Equation 1: Averaging of the corresponding half cone angles[51,57]

To simplify the determination of the cone angle θ and to easiyl excess half cone angles θ_i from X-ray structural data, an adapted method for phosphines with organic substituents has been published (Figure 9).[57]

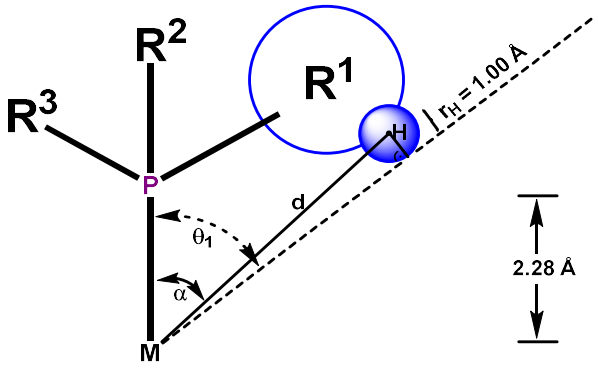

Figure 9: Calculating θ_1 from crystallographic parameters such as d(M-H) and α(≮MPH)[57]

Although the cone angle θ is also obtained by averaging and doubling the half-angles θ_i (Equation 1), the latter are not measured directly but calculated beforehand from the crystallographic coordinates by geometric considerations *via* Equation 2 (*cf.* Figure 9).

$$\theta_i = \alpha + \frac{180}{\pi} \sin^{-1} \frac{r_H}{d} \qquad (2)$$

Equation 2:Calculation of half-angles θ_i by trigonometry

For this purpose, the metal-hydrogen distance d and the phosphorus-metal-hydrogen angle α are determined for each hydrogen at the first substituent R^1 and θ_i is calculated for each assuming a van der Waals radius of hydrogen r_H of 1.00 Å. The largest half-angle θ_1 is now determined and added to those half-angles θ_2, θ_3 of the other substituents R^2 and R^3 (which are determined in the same way) using Equation 1.

By plotting the Tolman electronic parameter χ and the Tolman cone angle θ for different phosphines, a Toman stereoelectronic map can be obtained (see chapter 1.3.2, Figure 15, page 24).

Beside the Tolman cone angle θ also other methods have been developed descibing the steric measure of a ligand. A modern method, which also allows comparisons of different ligand types, is the calculation of the percent buried volume $\%V_{bur}$ published by Nolan and coworkers (Figure 10).[58]

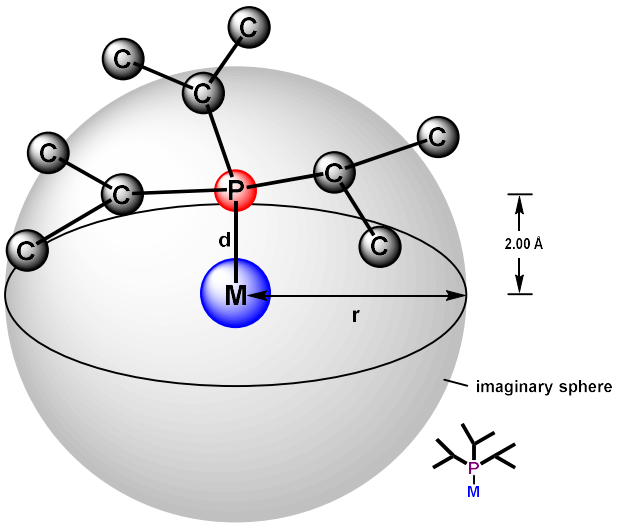

Figure 10: Percent buried volume $\%V_{bur}$[59]

In this method an imaginary sphere with a certain volume and a fixed radius **r** is formed around a metal (or putative metal) with a certain distance to a ligand d (for example, to the phosphorus of a phosphine

ligand, 2.00 Å). Now the ligand (*e.g.* a phosphine) occupies a part of the volume of this imaginary sphere because its atoms overlap with the sphere (%V_{bur}). The amount of this buried volume is a measure of the steric demand of the ligand. Thus, the bulkier a ligand is the more volume of the sphere is occupied and the higher the %V_{bur} will be. For the calculation X-ray structures or DFT optimized geometries of both the free ligand or of the corresponding metal complexes can be used. When metal complexes are used the radius of the metal is omitted to ensure that only the ligand contributes to the volume buried. The great advantage of Nolan's method is not only the compatibility with e.g. carbenes, but also the automatability and reliability, which were realized in the form of a web application (Samb*V*ca).[60] In addition to the absolute value of the %V_{bur}, the web application also provides a topographic steric map that can be used to identify catalytic pockets (Figure 11).

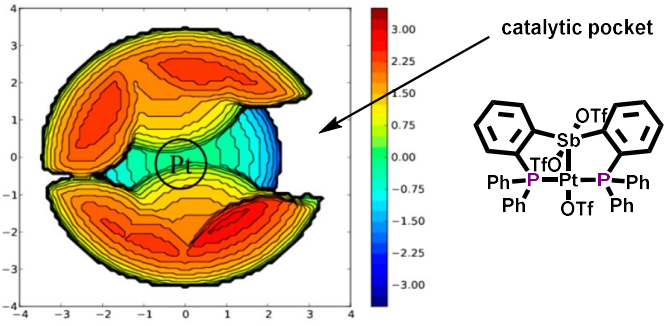

Figure 11: Topographic steric map of a phosphino-antimony ligand (taken from literature[61])

Nevertheless, it should be noted that different metal complexes (or the use of the free ligand) lead to partially different results, since the different metal atoms have different effects on the geometry of a ligand. Furthermore, different M–P distances d are often used in the literature, which thus give different %Vbur for the same ligand.

1.3 Modification of donor properties of phosphines

1.3.1 Changing the substituents

Changing the donor properties of phosphines is an important tool to tune catalysts in a certain direction (see chapter 1.1.3). Their influence to the metal center can facilitate reactions or even enable new selectivities. Most phosphines have, because of their electron pushing substituents, strong donor abilities and a lack of π-acceptor properties. Changing the phosphine to a more electron poor one by introduction of electron-withdrawing substituents might increase the electrophilicity of the coordinated metal center and therefore accelerate reactions. On the other hand making the metal center more electron deficient can slow down the reaction depending on substrate and rate determining step of the reaction. Different key steps in the catalytic cycle are accelerated by different types of phosphines. This is a major issue in π-acid catalysis, especially in Au(I) catalysis. Adjusting the substituents on the phosphorus can lead to higher catalyst stability, higher conversions and reaction rates (ligand effect).

Au(I) catalysis typically goes through three major steps[62,63] (see chapter 1.1.1, Scheme 3) consisting of

1) Electronic activation of the alkyne or allene moiety in the substrate
2) Attack of a nucleophile, which can either proceed intra- or intermolecularly
3) Protodeauration/demetalation

Beside these three steps usually decomposition or deactivation occurs. All of these processes benefit from different ligands.

A ligand being a good π-acceptor but weak σ-donor will lead to more electron density transferred from the olefin, allene or alkyne to the electron poor metal center during activation. This is a result of the substrate and the ligand competing for electron density in the two π-bonds, backdonating electron density from gold d-orbitals into π acceptor orbitals of ligand and substrate (*cf.* chapter 1.1.1, Figure 2). This will result in a more activated or electronically depleted alkyne/allene being more prone to nucleophilic attack. On the other hand a ligand which is a good σ-donor giving more electron density to the gold 6s orbital will activate the substrate less but will perform much better in protodeauration. Both, good π-acceptors and weak σ-donors, will lead to an increase of the Au–$C_{substrate}$ bond length (*trans* influence).[13,64]

The ligand effects and designs in Au(I) catalysis were studied by Xu *et al*.[14] They differentiate between four scenarios:

1) Protodeauration is the rate determining step
2) Electronic activation is the rate determining step
3) Protodeauration is the rate determining step but accompanied by significant catalyst deactivation
4) Electronic activation is the rate determining step but accompanied by significant catalyst deactivation

By separating individual scenarios into different reactions it could be shown that the reaction rate of the protodeauration of vinyl gold complexes is decreased with phosphines bearing electron withdrawing groups (Scenario 1). On the other hand electron poor ligands lead to an acceleration in the electronic activation of alkynes (Scenario 2, Figure 12).

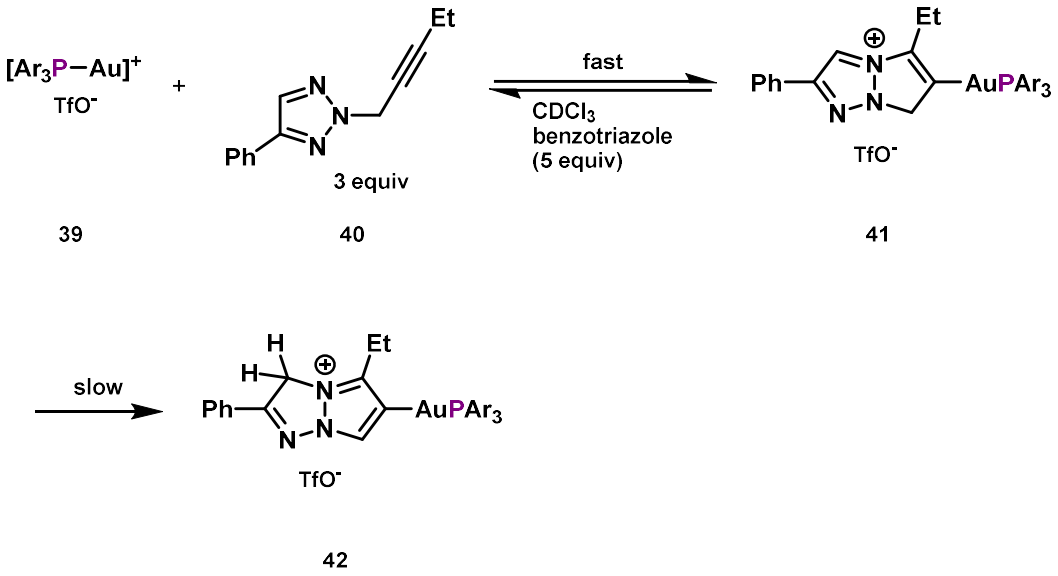

Scheme 22:Triazole-yne 5-endo-dig cyclization yielding stable vinyl-Au complexes[14]

Using a triazole-yne 5-endo-dig cyclization with very slow protodemetalation leaves the electronic activation step untouched by side reactions (Scenario 2, Scheme 22).[14,65] Modifying the substituents in the used arylphosphine based $[Au(PAr_3)]^+$ catalyst shows significant increase in reaction rate by adding trifluoromethyl groups, making the phosphine electron-deficient (Figure 12, blue curve).

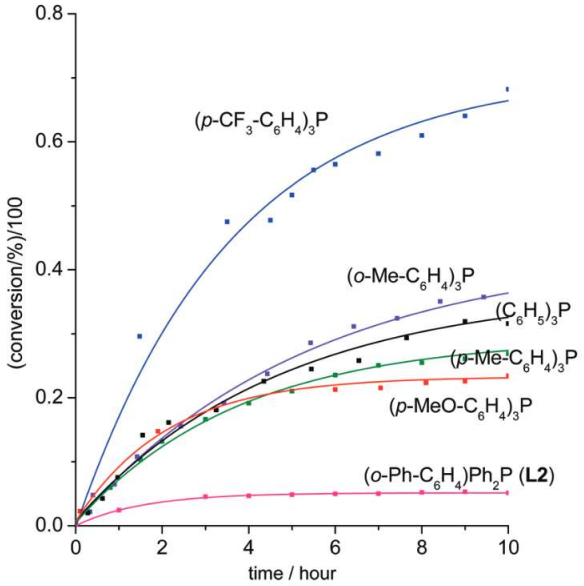

Figure 12: Ligand effect in triazole-yne 5-endo-dig cyclization (taken from literature[14])

This result clearly indicates the benefit from electron deficient phosphines in the activation step of alkynes. Both scenario 1 and scenario 2 can now be combined with significant catalyst deactivation (scenario 3 and scenario 4), which makes it in some reactions helpful to modify the phosphine even more by adding phenyl groups in strategic positions (Buchwald-type ligands) to stabilize the cationic gold.

This result also shows the synthetic benefit from electron-deficient ligands in reactions with less reactive alkynes or allenes and weak nucleophiles making the activation the rate determining step. One example for this kind of catalytic reaction is the intermolecular hydroamination of allenes published by Toste and coworkers (Scheme 23).[66]

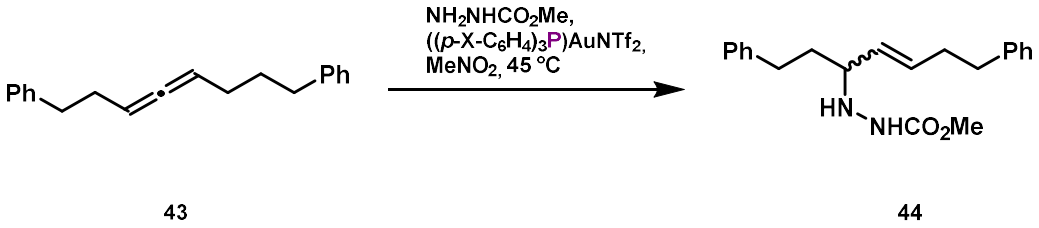

Scheme 23: Intermolecular hydroamination of allenes[66]

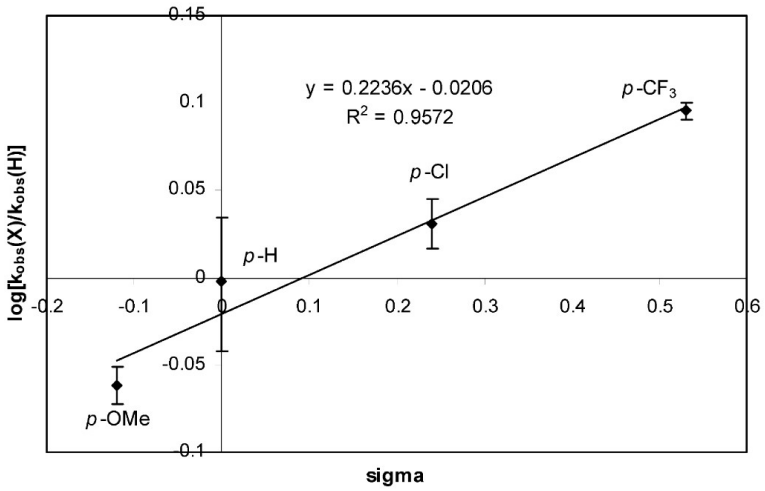

Figure 13: Hammett plot of k_{obs} for hydroamination of allenes in the presence of $Ar_3PAuNTf_2$ (taken from literature[66])

This example represents a combination of a hydrazide, being a weak nucleophile and an allene (**43**), being hard to activate compared to an alkyne. The reaction seems to be a good candidate for the scenario 2 mentioned above. Experiments could show the reaction behaves first order in Au(I) catalyst and allene **43** indicating both of them are involved in the turnover limiting transition state. Using phosphines with weak donor and good acceptor properties should increase the reaction rate. The Hammett analysis supports this assumption (Figure 13). Triphenylphosphines substituted with electron withdrawing moieties like Cl and CF_3 (positive Hammett parameter sigma) give higher rates then methoxy substitution (negative Hammett parameter sigma).

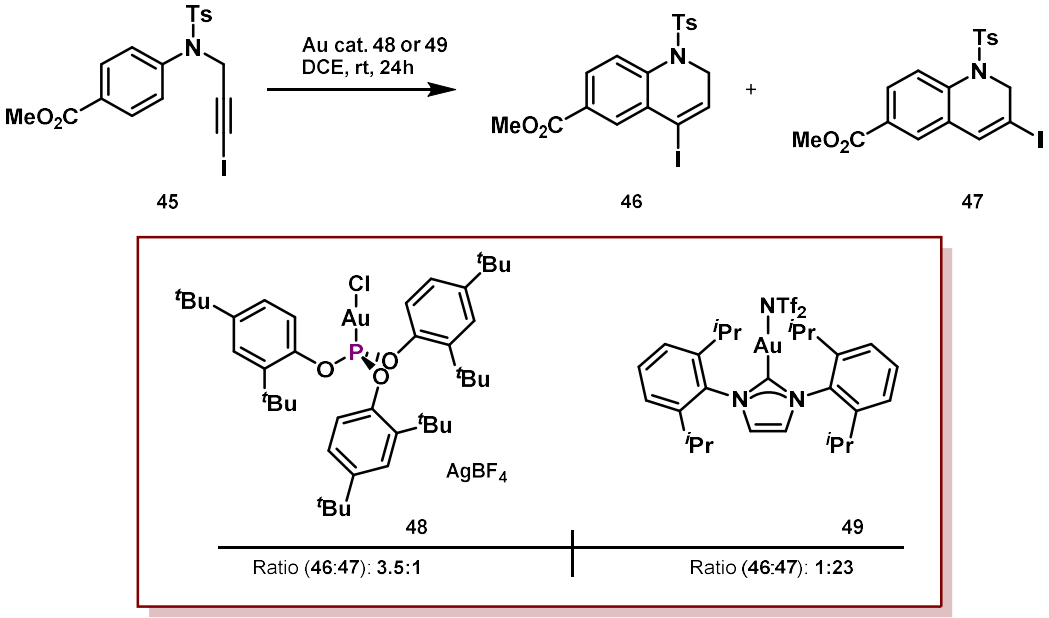

Scheme 24: Gold(I)-catalyzed cyclization of N-(3-iodoprop-2-ynyl)-N-tosylanilines[67]

Similar improvements can be seen in the ring expansion of 1-alkynyl cyclopropanols[68] and aminoauration of alkenes.[64] These findings point out the importance of ligand design by changing phosphine substituents. Interestingly, not only the reaction rates but also the outcome of a reaction can be altered. Ligands having strong π-acceptor but weak σ-donor properties support carbocation-like reactivity, whereas strong donor ligands support carbene-like reactivity (see chapter 1.1.2, Scheme 5).[13] In the cyclization of N-(3-iodoprop-2-ynyl)-N-tosylanilines this change in reactivity by replacing a good donor ligand IPr **49** for an electron-poor phosphite ligand **48** results in different product distributions or regioselectivity (Scheme 24, *cf.* chapter 1.1.2, Scheme 13).[67]

1.3.2 Introducing charge to the substituents

Introducing charge on the substituents of a phosphine not only has influence on the electronic but also on the physicochemical properties such as solubility or volatility.[50] This mainly depends on the nature, position, distance and electronic delocalizability of the charge. So it is not surprising that before modifying the donor abilities of the phosphine charge was already used to increase the solubility of phosphines or catalyst in polar solvents (Scheme 25). The most prominent example is probably the tris(3-sulfophenyl)phosphine trisodium salt (TPPTS, **50**). This phosphine is used in the hydroformylation of propene to synthesize butanal in a two phase process.[69,70] Due to the anionic phosphine TPPTS the rhodium catalyst is water soluble and stays during the process in the aqueous phase. Product und substrate are dissolved in the organic phase. This process came on stream in 1986 and was commercialized by Ruhrchemie (today: OQ Werk Ruhrchemie) following previous work at Rhône-Poulenc. The huge advantage is the separation of a homogenous catalyst and the product, which can be easily achieved by phase separation. Also according to Hoechst-Ruhrchemie this process does not lead to any detectable losses of rhodium.

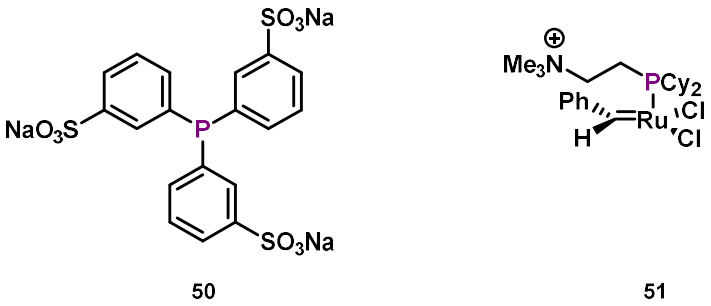

50 51

Scheme 25: Charged phosphines[69,71]

Beside the purification aspect also analytical information can be obtained by using charged phosphines. For example, the cationic phosphine **51** was used in olefin metathesis to achieve high levels of sensitivity in electrospray ionization mass spectrometry due to its charged tags.[71,72] The cationic phosphine also shows different solubility behavior thanks to the ammonium moiety. But on the other hand the cationic charge does not have a direct influence to the electronic situation of the phosphorus, because the linker in between (ethyl group) is aliphatic and not electronically communicative.

To change this situation the cationic charge can be placed directly next to the phosphorus in α-position leading to α-cationic phosphines. The result can be rationalized by Figure 14 and the two secondary interactions therein (**I**, **II**). The π* orbitals of the cationic aromatic system, adjacent to the phosphorus, can now overlap with its lone pair (**I**). This leads to a stabilization and therefore to a limitation of the σ-donor properties of the phosphine (lowering of the HOMO). Another interaction that strongly changes the electronic properties of the phosphine is the overlap of the in plane π* orbitals with an antibonding σ*(P─R) orbital (**II**). This leads to an energy decrease of the latter and thus to an enhancement of the acceptor properties (lowering of the LUMO).[50]

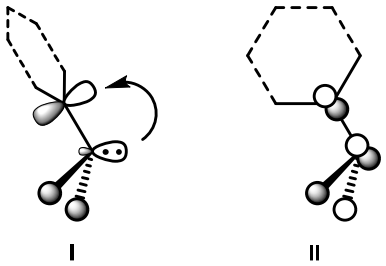

Figure 14: Secondary interactions of phosphorus and cationic substituents in α-position[50]

With the adjacent positive charge the demand for stronger π-acceptors than phosphites can be met circumventing the use of sensitive and highly toxic polyhalogenated phosphines.[50,73] Especially this is of interest in π-acid catalysis, where the electrophilicity of the metal center can be further increased with strong π-acceptor ligands, superior to the electron-poor phosphines mentioned in the last chapter.

The net donor abilities of cationic phosphines can be easily compared with neutral phosphines by using the Tolman stereoelectronic map (Figure 15).[45] Phosphines are represented in orange, phosphites in violet, arsines in pink and cationic ligands in green. Calculated TEPs are shown in form of blue points while experimental TEPs are shown in red.

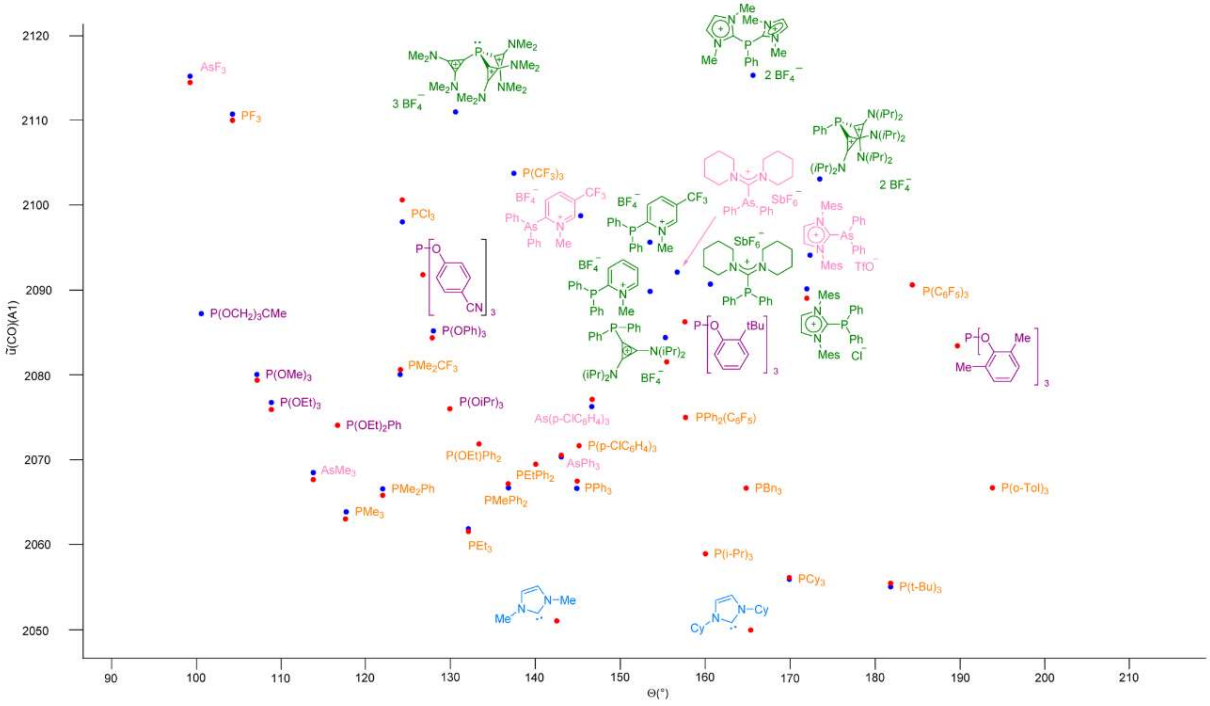

Figure 15: Tolman stereoelectronic map of cationic and neutral phosphines (taken from literature[45])

The TEP values of the cationic phosphines surpass the ones of neutral phosphines and are located between electron poor phosphites and PF_3. Interestingly not only the number of cationic charges determines the TEP value but also the nature of the charged substituent. This theory can also be supported by DFT calculations at the B3LYP-D3/def2-TZVP level (Figure 16).

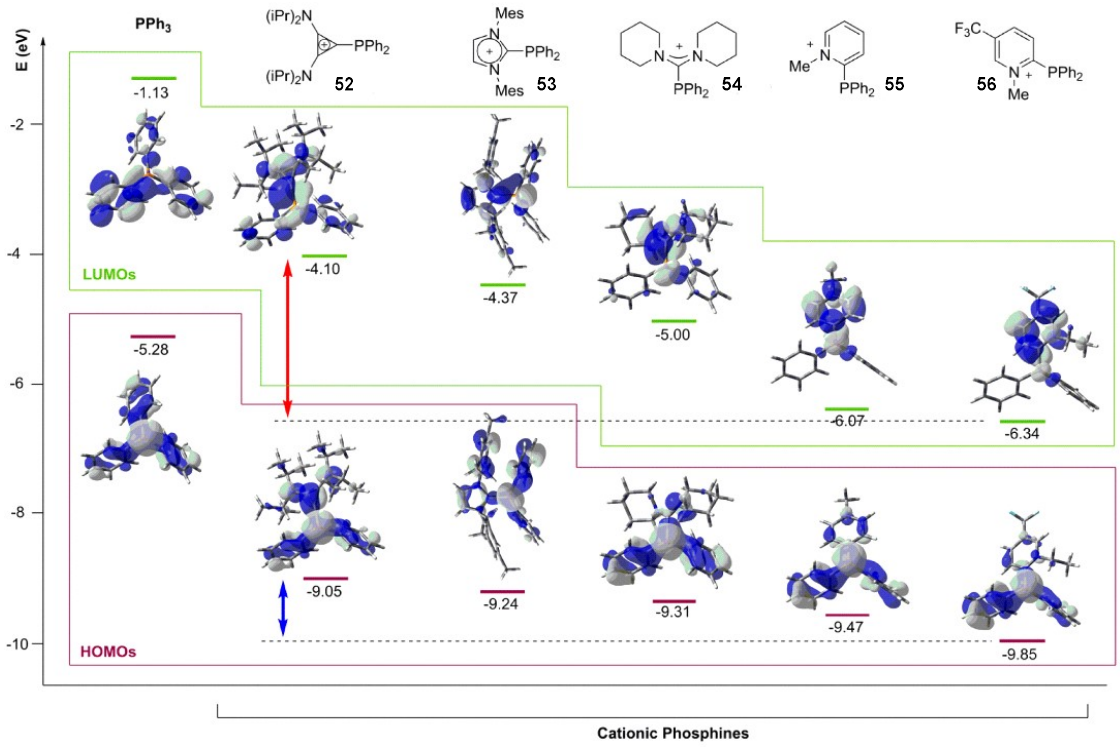

Figure 16: Comparison of the frontier orbital energies for monocationic phosphines of a different nature (taken from literature[45])

The HOMO energy levels of the cationic phosphines (**52**-**56**) are in all cases much lower than triphenylphosphine. But the HOMO energies of the differently substituted cationic phosphines are very similar to each other, indicating that also the σ-donation is comparable. This implies that the donor ability is more dependent on the amount of cationic charge than on the nature of the cationic substituent. On the other hand the LUMO energy representing the π-acceptor properties is lowered in all cationic cases by a very different amount. This shows the relevance of the nature of the cationic substituent. The TEP values are giving now a mixture of the donor and acceptor properties. Following this reasoning phosphines with pyridinum architecture show higher TEPs than cyclopropenium substituted phosphines.

1.3.2.1 Synthesis of α-cationic phosphines

α-Cationic phosphines can be synthesized by different strategies. Basically three different disconnection approaches are known in the literature[74]:

1) a neutral nucleophile or Lewis base (*e.g.* a carbene, pyridine) attacking a phosphorus electrophile releasing an anion (Scheme 26)
2) transforming a neutral substituent of the phosphorus into a cationic one (Scheme 27)
3) having a nucleophilic phosphorus attacking a positively charged electrophile (Scheme 28)

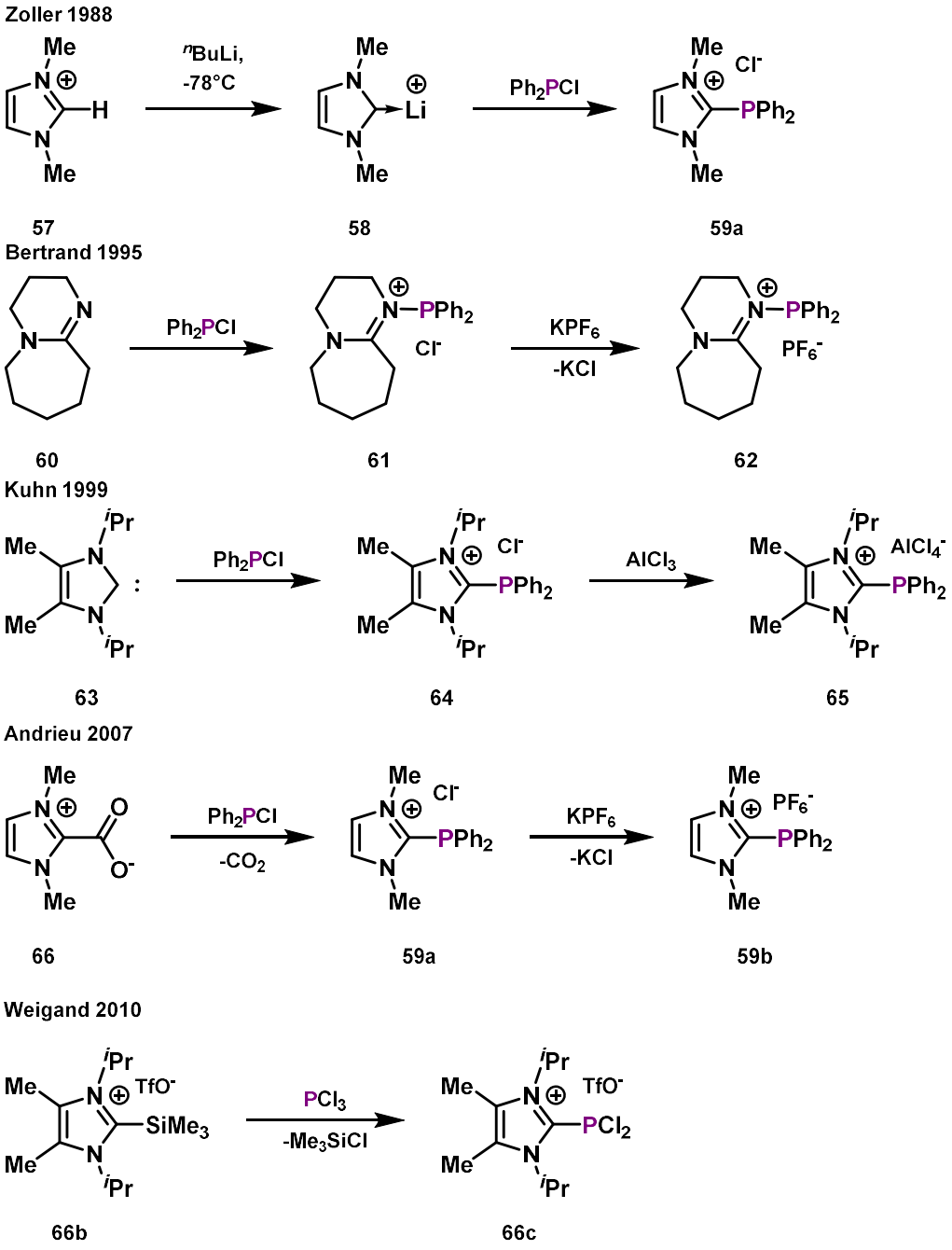

Scheme 26: Synthesis of monocationic phosphines via first approach[75–78]

The first approach was already published by Zoller and coworkers in 1988 (Scheme 26).[75] They reacted an imidazole-based carbene lithium adduct **58** with a phosphorus chloride to obtain a 2-phosphinated imidazolium salt **59**. A similar approach was also developed in 1999 by Kuhn[76] using a free carbene **63**. Due to the fact that free carbenes are very sensitive more methods were developed starting from more stable substrates. Examples for these precursors are imidazolium carboxylates **66** (Andrieu[77]), which decarboxylate during reaction, or TMS protected imidazolium salts (Weigand[79]), which release TMS-halides. But still the synthesis of cationic phosphines by using free carbenes *e.g.* CAACs is in use.[80] Also, an interesting class of cationic phosphines which exhibit an onio-motif can be obtained by the reaction of phosphorus chlorides with a base like DBU **60** (Bertrand[78]) following still the first disconnection approach.

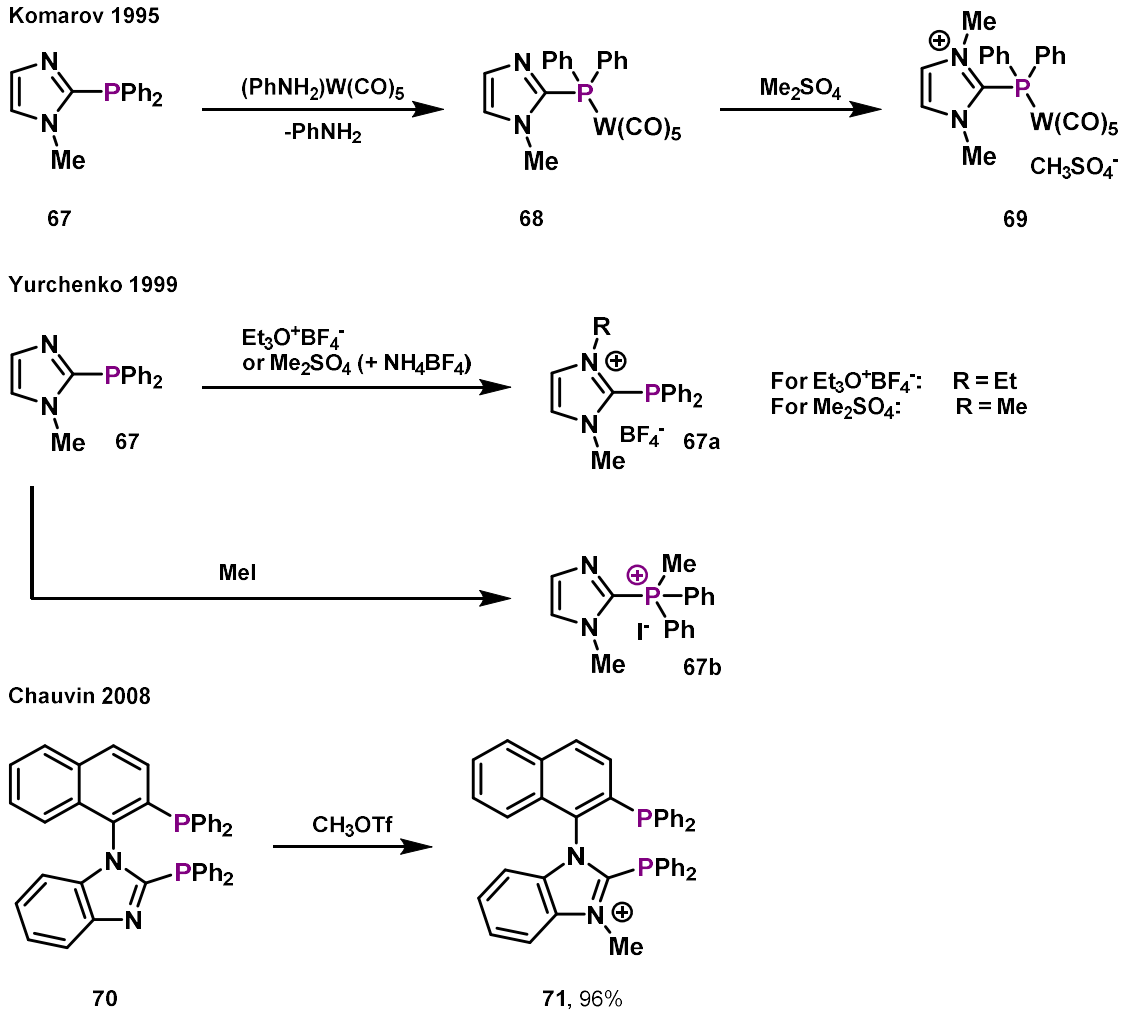

Scheme 27: Synthesis of monocationic phosphines via second approach[81,82]

The second disconnection approach, transforming a neutral substituent of phosphorus into a cationic one, is most of the time achieved by alkylation of an imidazole substituent at the phosphorus (Scheme 27). This method was used to synthesize the first cationic phosphine metal complex **69** by Komarov back in 1995 without even isolating the free cationic phosphine.[81] In the synthesis of the free phosphine this method is bearing the risk of alkylating the phosphorus (Yurchenko[83]). Nevertheless, by choosing the right alkylating agent Yurchenko and coworkers were capable to synthesize compound **67a**. Furthermore, Chauvin managed to synthesize a cationic atropo-stereogenic diphosphane **71** in 96% yield by using the hard methylating agent (MeOTf).[82]

The last approach was mainly developed by our group. Changing the disconnection approach from a nucleophilic carbene to a nucleophilic phosphorus has many advantages. The opposite retrosynthetic heterolysis of the phosphorus carbon bond makes it possible to attach substituents which carbene counterparts are not known or stable. This opens a wider range of different cationic moieties which can be applied to the synthetic protocol (Scheme 28). Also, circumventing the use of free carbenes can improve selectivity (*cf.* first approach) and the already pre-prepared cationic substituents, *e.g.* chloropyridinium, do not suffer the risk of alkylating the phosphorus during postfunctionalization (*cf.* second approach).

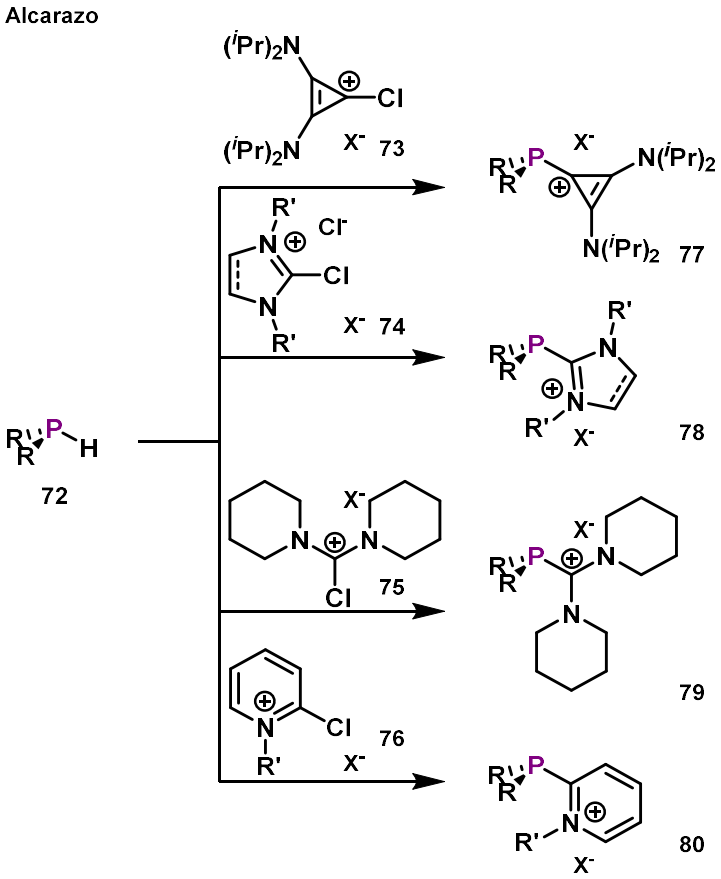

Scheme 28: Synthesis of monocationic phosphines via third approach[45]

With this method at hand not only imidazolium[84] **78** but also cyclopropenium[85] **77**, amidinium[84] **79** and pyridinium[86] **80** substituted phosphines could be received. The synthetic procedure is starting from corresponding Vilsmeier-type salts like chloroimidazol(in)ium **74**, chlorocyclopropenium **73**, chloroamidinium **75** or chloropyridinium salts **76** and a secondary phosphine **72**. The secondary phosphine is then attacking the chlorosubstituted aromatic or heteroaromatic system *via* S_NAr reaction substituting the chloride. For this substitution sometimes deprotonation of the phosphine is necessary. Also, an exchange of the halide counter ion for a weakly coordinating anion is used to prearrange the ligand for use in π-acid catalysis.

Pyridinio phosphines like **80** are of particular interest, as they can reach net donor abilities close to the ones of dicationic phosphines (see Tolman stereoelectronic map, Chapter 1.3.2, Figure 15, page 24), but having just one positive charge. Also, due to the low lying LUMO of the resulting phosphine the π-acceptor properties surpass the other monocationic phosphines by far. Thanks to the improved synthetic approach by Alcarazo and coworkers, fine tuning of this ligand type can now be easily achieved. Different neutral ligands can be inserted into the architecture by using different secondary phosphines as starting material. Also, combining cationic phosphines with the outstanding architecture of Buchwald type ligands[22,87] and their advantages in selectivity and activity can be realized.[88] Therefore N-substituents at the pyridine are introduced by a Zincke reaction (Scheme 29).

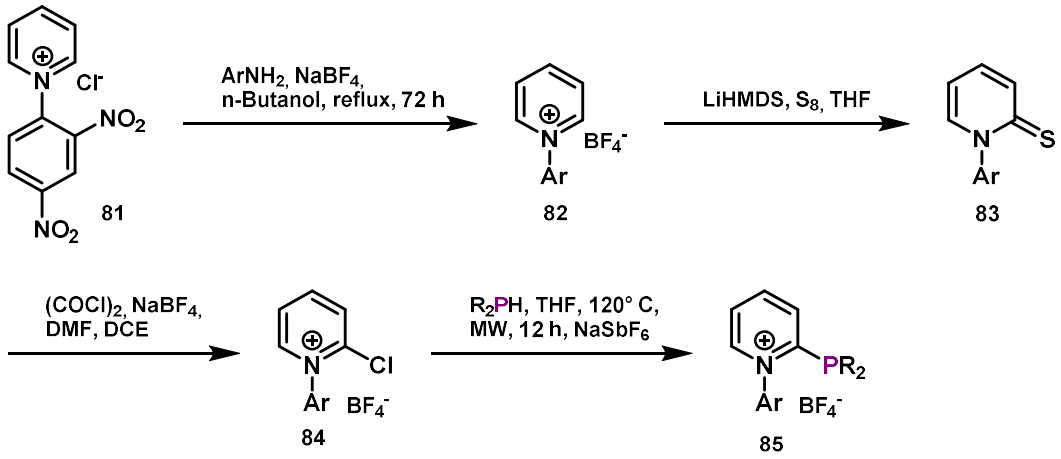

Scheme 29: Synthesis of Buchwald type monocationic phosphines using Zincke reaction[88]

1.3.2.2 Synthesis of α-Polycationic phosphines

Thinking of the positive influence of cationic charges on the acceptor properties of a phosphine, one might come to the conclusion to substitute a second or third moiety by a cationic one leading to α-dicationic or tricationic phosphines. In theory all synthetic strategies from the field of monocationic phosphines are conceivable for this purpose.

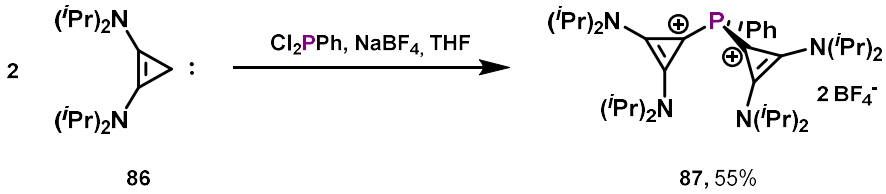

Scheme 30: Synthesis of dicationic phosphines from a free carbene source[89]

In 2009 Andrieu and coworkers were the first synthesizing a dicationic phosphine.[90] They used a very similar method to that described for monocatic phosphines using imidazolium carboxylates and dichlorophenylphosphine in a 2:1 ratio (approach 1). The product could just be purified after an anion exchange and seems to be quite water stable. Later, also other methods for preparing dicationic phosphines similar to those of monocationic phoshines were developed. Chauvin *et al*.[91] used the already approved method by methylation of an bisimidazole substituted phosphine (approach 2), while Alcarazo and coworkers could show that bis(cyclopropenium)phosphines can be synthesized by using the Umpolung-strategy combining one equivalent of primary phosphines with two equivalents of chlorocyclopropenium salts (approach 3).[92] For this method the base KHMDS is needed to deprotonate the monocationic intermediate. Another method to prepare bis(cyclopropenium)phosphine **87** starts from a free carbene and phosphorus chloride and was developed by the group of Chauvin (Scheme 30, approach 2).[89] While metal complexes of monodentate dicationic phosphines relying on an imidazolium architecture are unknown due to their reduced donor capacity, gold and platinum complexes of bis(cyclopropenium)phosphines can be synthesized and used in catalysis. The only way to attach imidazolium based dicationic phosphines to metal centers is to combine the cationic phosphine with a neutral phosphine in form of a chelate ligand. These neutral phosphine moiety acts then as an anchor keeping the ligand attached to the metal, while also binding to the cationic part. With this strategy coordination of Rh, Mo, Pt and Pd could be achieved.[93]

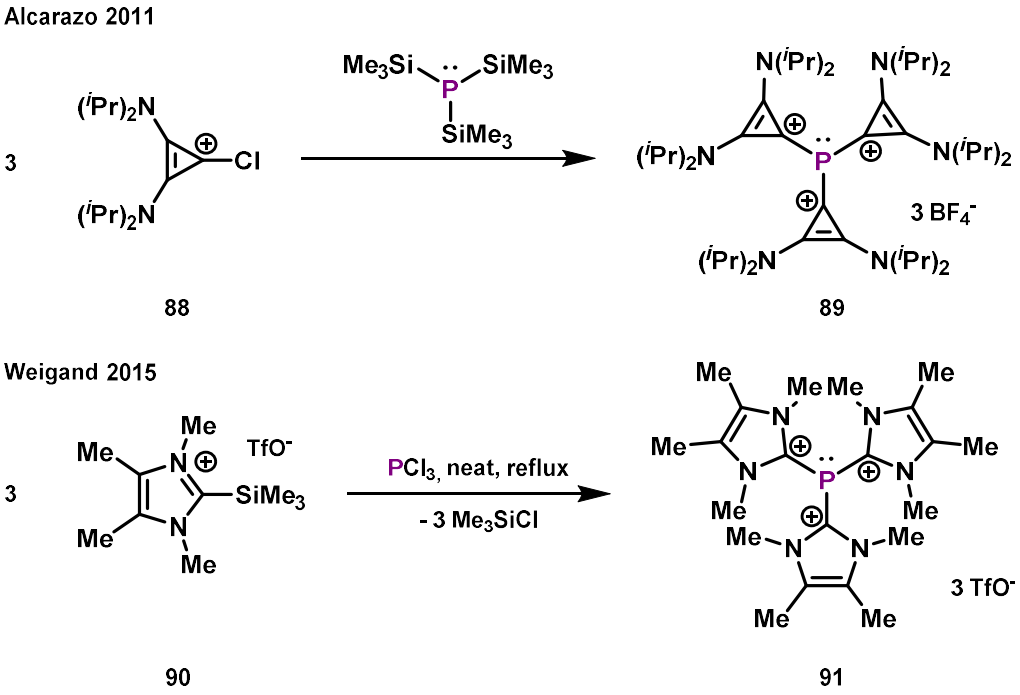

Scheme 31: Synthesis of tricationic phosphines[63,94]

Tricationic phosphines could be realized by a new synthetic strategy using $P(TMS)_3$. $P(TMS)_3$ is a substitute for gaseous monophosphane and reacts in a similar way with chlorocyclopropenium salts **88** in a S_NAr fashion releasing TMS-chloride as a driving force (Alcarazo, Scheme 31).[63]

Despite their electron deficiency, these ligands could be coordinated to palladium(II) and platinum(II). Tris(imidazolium)phosphines like **91** can be addressed by the reaction of three equivalents of silylimidazolium salt with PCl_3 using an opposite disconnection approach, but suffer from highly reduced donor capacity and therefore do not coordinate any metals (Weigand, Scheme 31).[94]

Reducing the net donor ability of phosphines by introducing more charge is possible, but it is often accompanied by a lack of solubility or inability to coordinate metals.

1.3.2.3 Application of α-cationic phosphines

α-Cationic phosphines are used in various research areas. By oxidation, for example, they can be transformed into electrophilic phosphonium cations (EPCs). In this context, cationic phosphines can replace polyfluorinated phosphines, for example in the hydrosilylation of olefins (**a**), hydrodeoxygenation of ketones (**b**), reduction of phosphine oxides (**c**) or the catalytic reduction of amides to amines (**d**) (Scheme 32).[95]

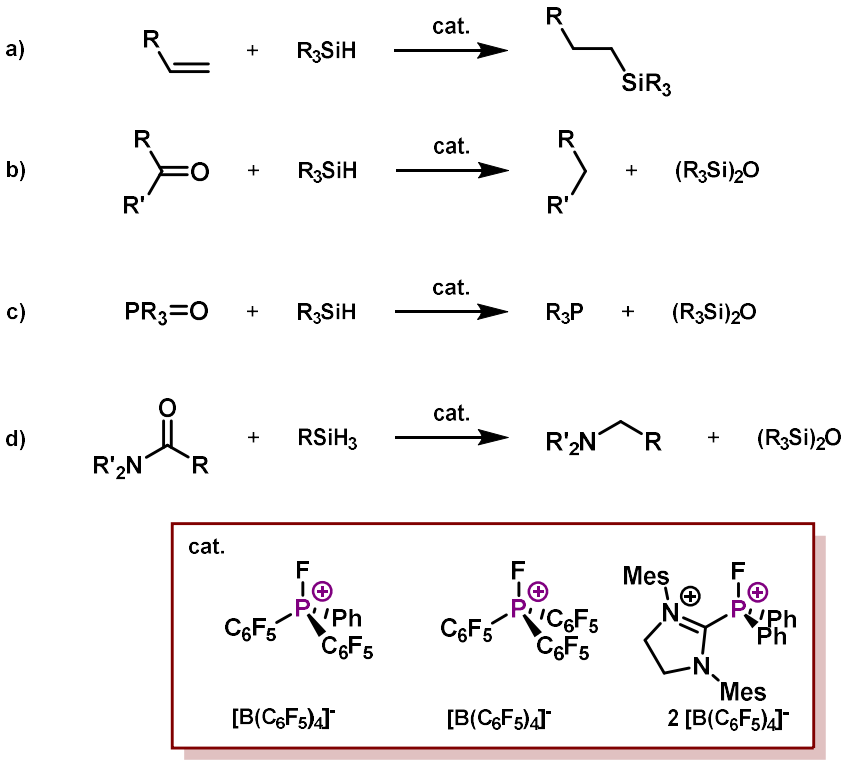

Scheme 32: EPC catalysed reactions of polyfluorinated and monocationic phosphines[95]

The latter (**d**) proceeds *via* "Frustrated Lewis pair-type" hydrosilylation mechanism, starting with the electrophilic phosphonium cation weakening the Si—H bond of $PhSiH_3$ (Scheme 33, **I**). After the attack of the amide-carbonyl to the silicon center (**II**), followed by hydrosilylation (**III**), the silylether is further reduced (**IV**) and the amine and the catalyst (EPC) are released.

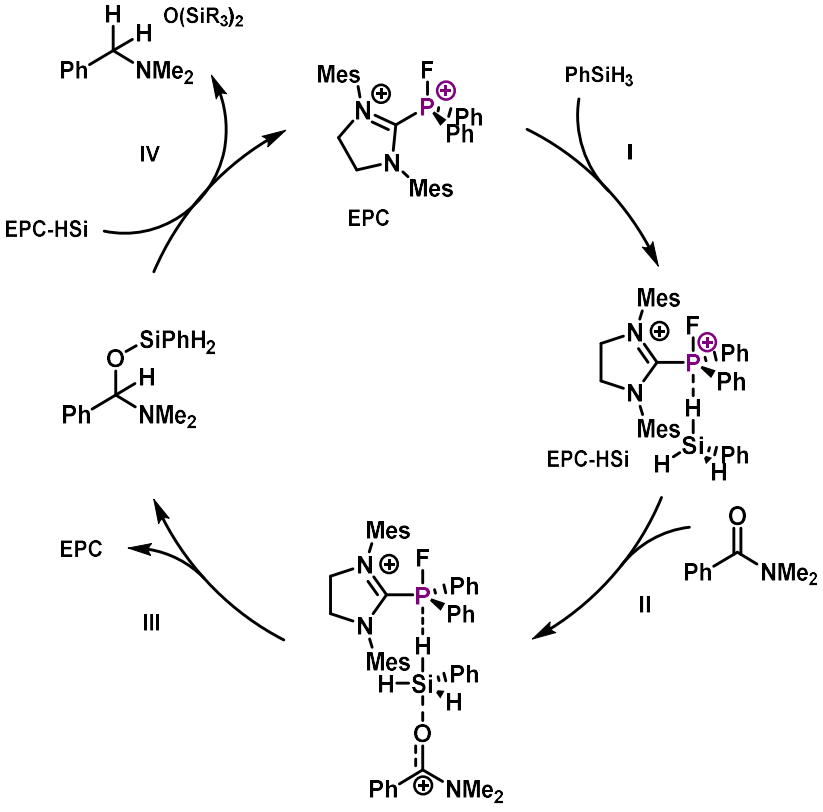

Scheme 33: Proposed mechanism for EPC-catalyzed amide reduction (d)[95]

In addition to these rather specialized applications, the greatest potential of electron-deficient phosphines lies in their ability to coordinate metals and their use as ligands. Coordinating monocationic ligands to rhodium opens the opportunity to use these corresponding complexes as hydroformylation catalyst of *e.g*. 1-octene. This was tried by Stelzer and coworkers mixing [$Rh(CO)_2$(acac)] *in situ* with a monocationic imidazolium based ligand.[96] The cationic complex performed much better in terms of TOF than a comparative phosphine ligand of lower proximity of the positive charge. This result again shows the benefit of positive proximate charges in ligand design.[97]

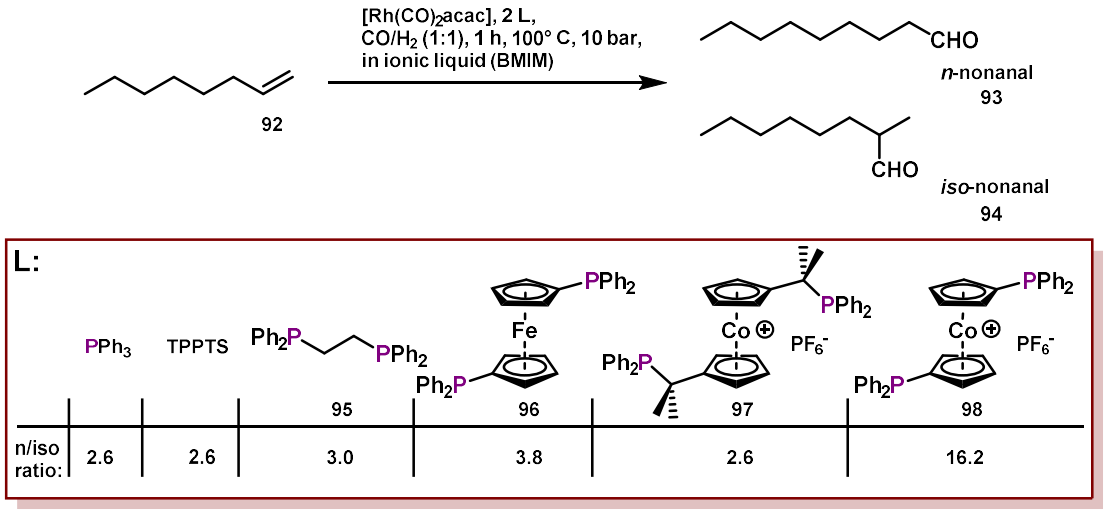

Scheme 34: Hydroformylation of 1-octene using neutral, anionic, and cationic phosphines[98]

Beside this classical imidazolium based cationic phosphines Wasserscheid, Salzer and coworkers tried positive charged metallocene-based phosphines (**97**, **98**) and their performance in hydroformylation of 1-octene **92** (Scheme 34).[98] Different ligands were compared including one with the phosphine directly attached to a cobaltocenium **98** and one with a non-conducting propylene-linker **97**. The catalyst without linker **98** showed much better performance, having a higher TOF and selectivity towards the n-isomeric nonanal product **93** than the one exhibiting a linker **97**. Furthermore **98** combines the advantages of cationic charge being easy to separate in the biphasic reaction, having superior electronic properties and higher selectivity.

Alcarazo and coworkers could show the special ligand effect of cationic phosphines **103** and **104** in π-acid catalysis (Scheme 35).[85] Therefore, they synthesized the corresponding cationic Au(I) complex by a ligand exchange reaction using (Me_2S)AuCl. With the gold catalysts at hand they tested these in a cycloisomerization reaction of an allene-diene system **99**. The reaction which was chosen by the authors is very sensitive towards the electronic properties of the ligand used. The ratio of the reaction products indicates the overall donor abilities of the ligand. As already mentioned before, do electron-poor ligands push the reactivity of **100** towards a carbocationic-like behavior (1,2-alkyl shift), while good electron donating carbenes like IMes **105** support carbene-like reactivity (1,2-hydride migration). The same product preference (**102**) of electron poor phosphite ligands $P(OPh)_3$ and cyclopropenium-phosphines shows that the donor properties of both phosphine classes need to be similar.

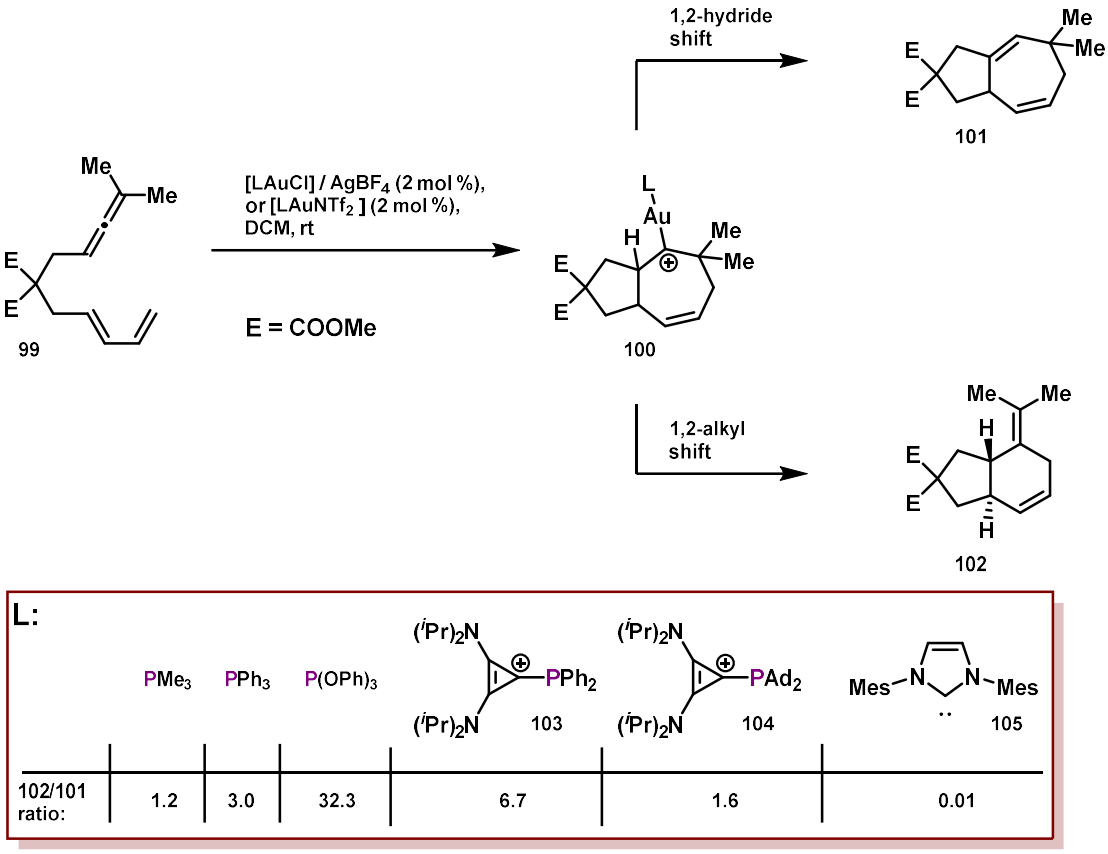

Scheme 35: Gold(I)-catalyzed cyclization of allene dienes[85]

Continuing with monocationic phosphines of the pyridinium architecture, even more reaction acceleration in π-acid catalysis should be possible. This results from the low lying π*-orbitals of the pyridinium interacting with the phosphorus making it very electron poor.

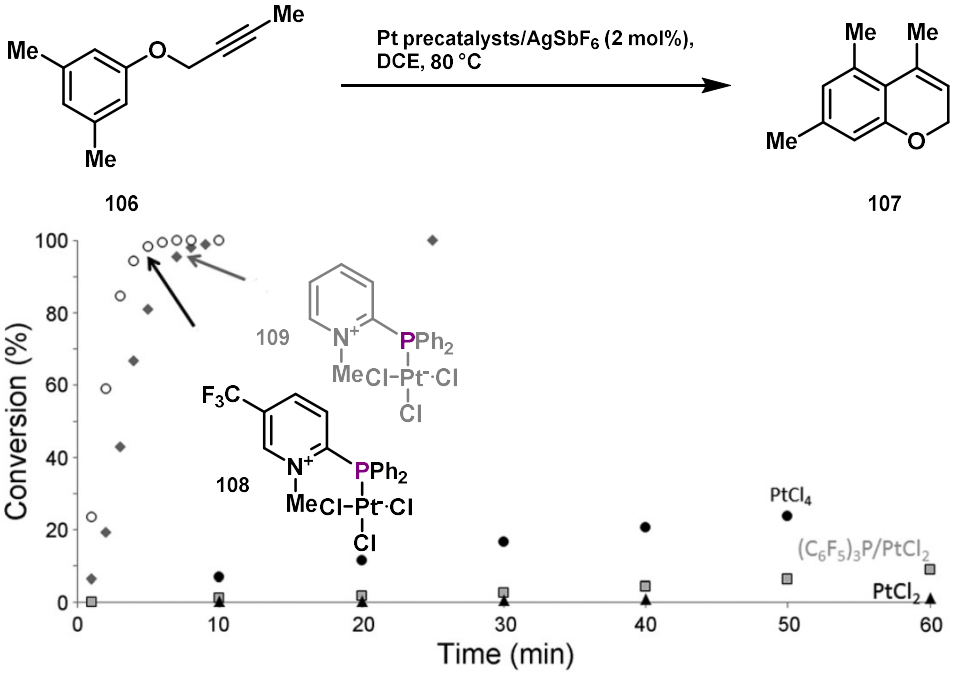

Scheme 36: Ligand effect in Pt(II) catalyzed hydroarylation of propargyl aryl ethers(taken from literature[86])

Alacrazo and coworkers could show with their modular synthetic route that fine tuning of these ligands can be easily achieved by changing different moieties on phosphorus or pyridinum backbone.[86] After coordinating the ligands to platinum by using the Pt(II)-precursor $K_2[PtCl_4]$ the authors applied the complexes **108** and **109** in the hydroarylation of propargyl aryl ether **106** to form the corresponding chromene **107** (Scheme 36). In this reaction the π-acidity of the platinum center is crucial, leading to full conversion in less than 10 min when using cationic ligands (*cf.* chapter 1.1.3, Scheme 17). The kinetic coefficients are way higher for platinum complexes of cationic ligands then these of electron poor polyfluorinated phosphines. Also, they surpass platinum species of higher oxidation state indicating the strong accepting properties of cationic phosphines. Similar results could also be shown by the platinum catalyzed cycloisomerization of enynes to cyclobutenes (Scheme 37) or the gold catalyzed hydroarylation of phenylacetylene with mesitylene. In both reactions cationic ligands easily surpass phosphites.

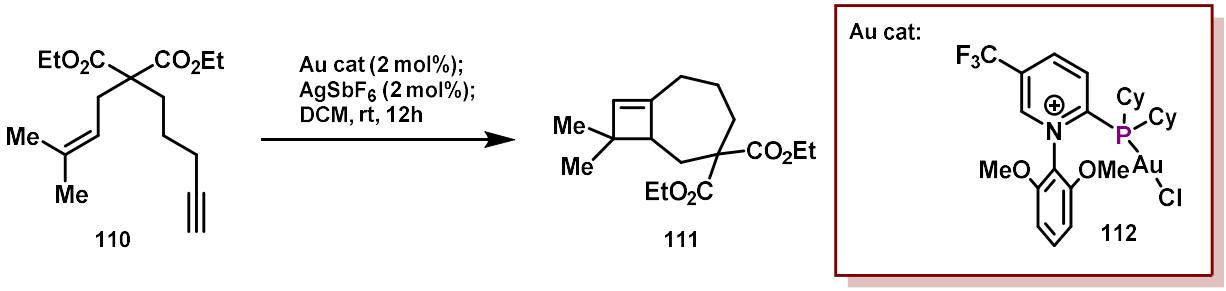

Scheme 37: Formal [2 +2] cycloaddition of an 1,8-enyne using Buchwald-type cationic phosphines[88]

In Au(I) catalysis these cationic phosphines suffer from a fast decay. Therefore in 2018 the same group published a modified version of this ligand exchanging the methyl substitution on the pyridinium for aryl groups to achieve Buchwald-type ligands like **112**.[88] These ligands show higher robustness due to the stabilizing effect of the electronic interaction of the aryl π-system and the Au. This stabilization tries to compensate the drawbacks of using cationic ligands. Cationic ligands suffer from a weak bond towards the gold resulting from a weak σ-donation and Coulomb repulsion of the ligand-charge and the activated cationic gold. With ligand **112,** a catalyst loading of up to 0.2% could be achieved in a [2+2] cycloaddition of an 1,8-enyne, but still being superior in reaction rate to neutral Buchwald type ligands (SPhos).

Besides using only cationic charges, also implementing an electron poor phosphole backbone results in a low lying LUMO accessible for the back donation of the metal center.[80] This approach differs from the others, because instead of just tuning the acceptor properties by different cationic moieties, starting from an already electron poor phosphole system and then attaching the exocyclic positive charge can result in even higher π-acceptor properties. This can be proven by the already mentioned sensitive cyclisation of N-(3-iodoprop-2-ynyl)-N-tosylanilines to 1,2-dihydroquinolines with Au(I) complexes (Scheme 38).[67] After the activation of the gold complexes, the carbocation like reactivity is much more present in case of an α-cationic phosphole with CAAC architecture **118** then in case of the phosphite **121**. Furthermore, the selectivity of **118** towards regioisomer **114** exceeds the cyclopropenium-based catalysts **117** and **120** indicating the strong withdrawing nature of the CAAC architecture.

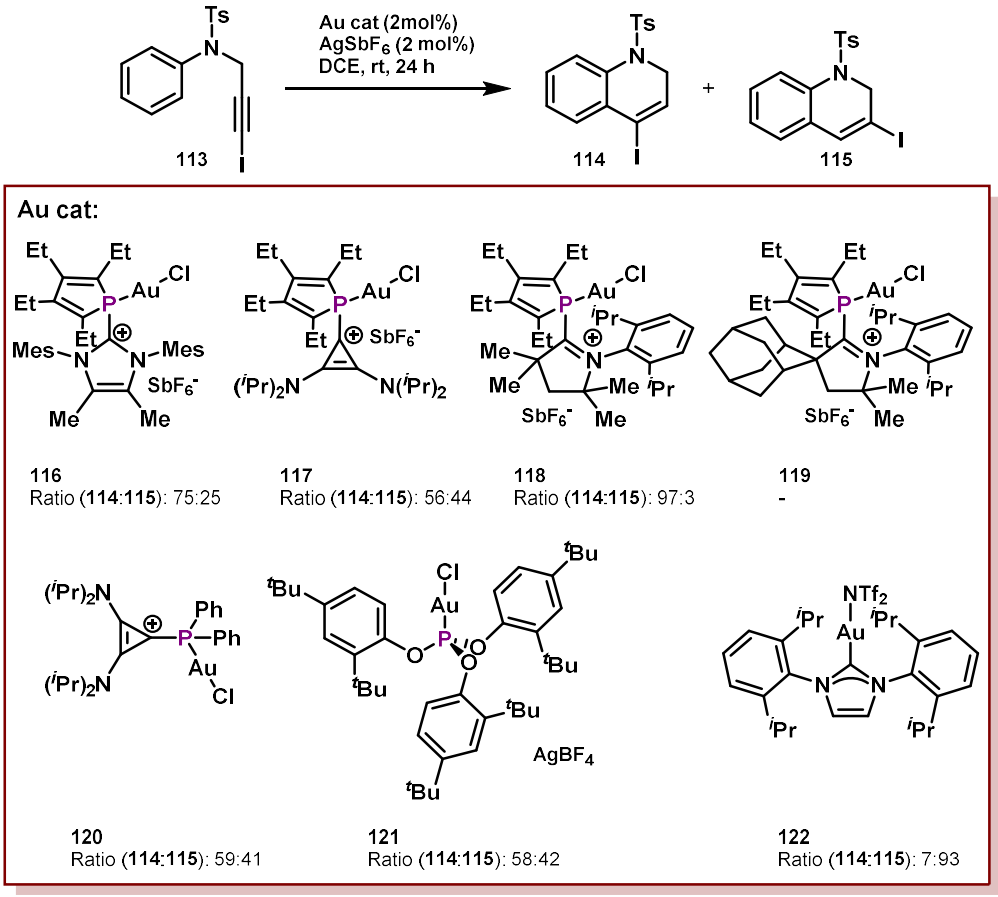

Scheme 38: Regioselectivity of Au(I)-catalyzed cyclisation of N-(3-iodoprop-2-ynyl)-N-tosylanilines[80]

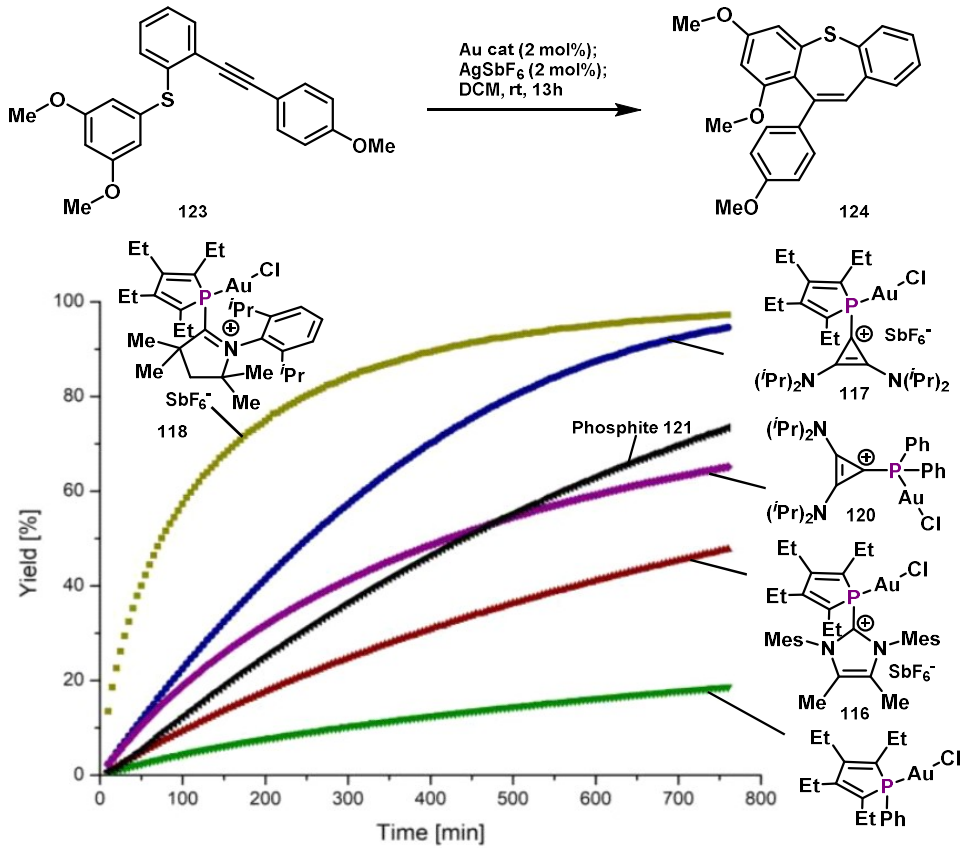

*Scheme 39: Ligand effect in the hydroarylation of sulfide **123** forming thiepine **124** (taken from literature[80])*

While little difference in performance can be detected between catalyst **117** and **120** in the cyclization of N-(3-iodoprop-2-ynyl)-N-tosylanilines, the influence of the phosphole backbone is evident in the intramolecular hydroarylation of sulfide **123** forming thiepine **124** (7-*exo-dig* cyclisation, Scheme 39). Here, complex **117** shows higher reactivity than **120**. Moreover, the lifetime of the active catalysts of **117** appears to exceed that of catalyst **120**. The CAAC-based catalyst **118**, which already stood out before, also shows the highest reactivity in this reaction, while the imidazolium-based catalyst **116** showed very little turnover in the same time, indicating its high steric demand.

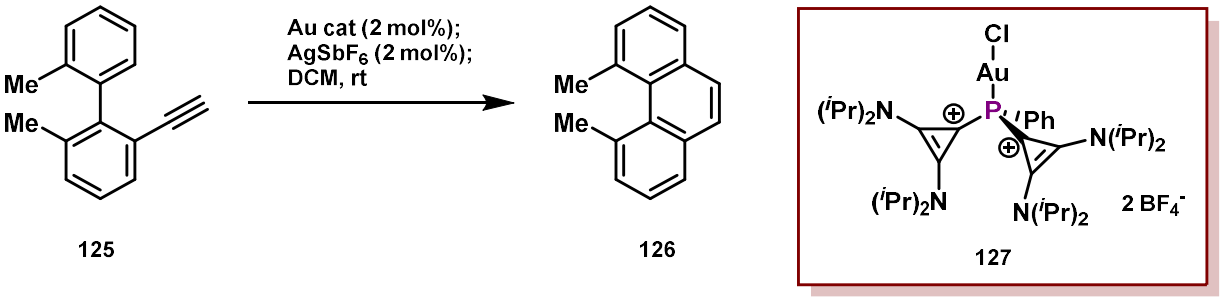

125 126 127

Scheme 40: Synthesis of strained phenantrenes by hydroarylation[92]

Dicationic systems have also been applied to gold catalysis (**127**). Due to the fact that these gold(I) complexes are limited to phosphines with cyclopropenium moiety, this architecture was used to synthesize strained phenanthrenes by hydroarylation.[92] Also a strong ligand effect could be detected here. The second charge makes this ligand class have much higher conversion numbers in shorter time than phosphites. The scope of 14 entries and the synthesis of natural products like bulbophylantrin, coeloginin, and calanquinone C indicate the reliability of cationic ligands in this methodology.

As already explained in the last chapter (chapter 1.3.2.2) one method to coordinate imidazolium based dicationic phosphines to metal centers is by applying a second neutral phosphine anchor rigidly connected to the dicationic phosphine. With this ligand at hand rhodium complexes could be synthesized and used in the hydroarylation of dienes with electron rich arenes.[93] This is possible because of the enhanced Lewis acidity of the rhodium catalyst.

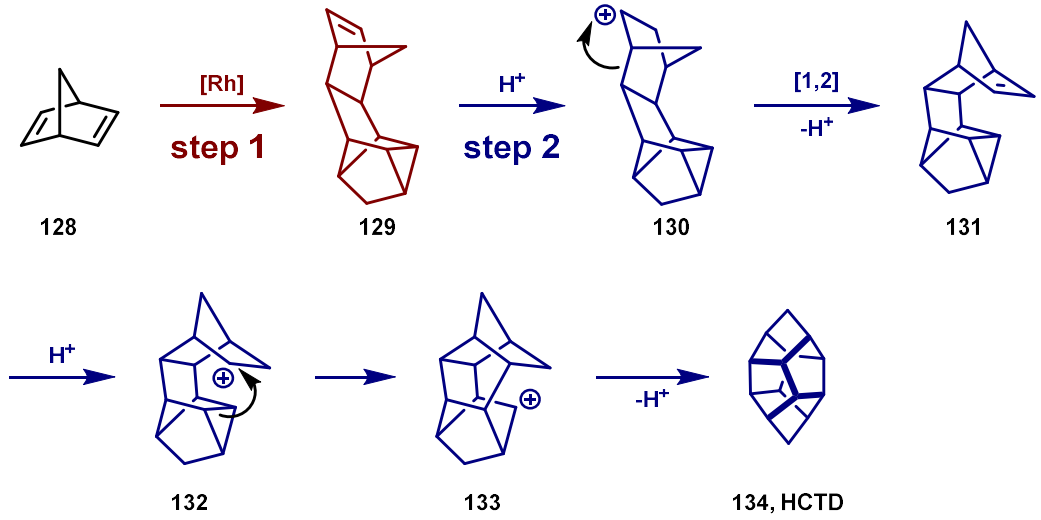

128 129 130 131 132 133 134, HCTD

Scheme 41: Two-Step Synthesis of HCTD from norbornadiene[99]

Recently similar rhodium catalysts were also used to build up HCTD **134** by a two-step procedure (Scheme 41).[99] Therefore it was necessary to get hold of the *exo-cis-endo* dimer **129** of norbornadiene (NBD) **128** which can later be transformed to HCTD **134** by proton catalysis (step 2).

The dimer can be achieved by an exo-[2+2+2] cyclization of NBD (step 1, Scheme 42). This can just be realized by the expansion of the coordination sphere of rhodium from four to five. With five coordinating sites two positions can be blocked by the pincer ligand and three are free to coordinate two NBDs facilitating the non-concerted homo-Diels-Alder cyclization (**128b**, **128c**).

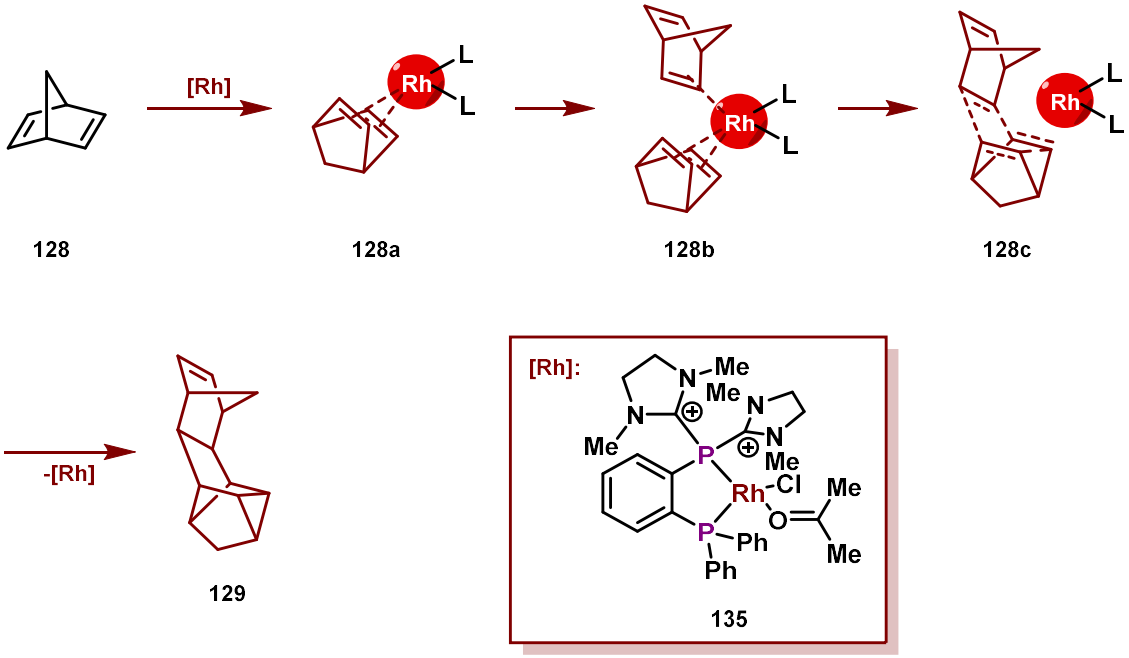

Scheme 42: Step 1: Selective [2+2+2] Homo-Diels-Alder cyclization[99]

The dicationic nature in this process is of great significance, because making the rhodium so electron deficient enables the coordination of another ligand. Also it was stated by the authors that the asymmetry of the ligand in combination with the steric bulk of the cationic phosphine part is expected to favor the *exo* cyclization. The low solubility of dicationic phosphines was also a problem in this case, but could be overcome by using $NaB(C_6F_5)_4$, which increased solubility by anion exchange and had the positive side effect of also abstracting the chloride ligand of the rhodium precatalyst.

1.3.3 Changing the geometry

The last chapters showed the huge impact on the stereoelectronic properties of phosphines by simply changing the substituents. The impact by changing the geometry, especially the pyramidalization at the phosphorus, was much less studied.[100] But this change in pyramidalization can be easily achieved by using a bridged/caged phosphorus system which exhibits geometrically constrained structures.[101] Considering an isovalent hybridization in the sp^3 hybridized phosphorus and taking Bent's rule to account the free electron pair of the phosphorus already shows high s character. This s character can be increased by reducing the ∡C–P–C angle (changing the pyramidalization) hampering hybridization.[102]

1.3.3.1 9-Phosphatriptycenes

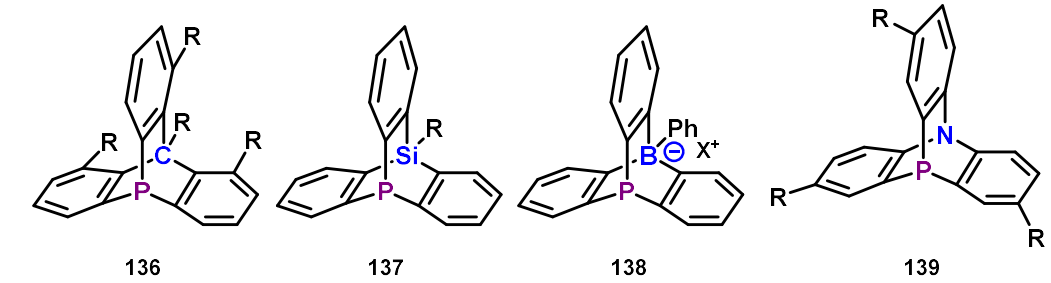

136 137 138 139

Bickelhaupt 1974 (R=H)
Kawashima 2004 (R=OMe)

Tsuji and Tamao 2006

Sawamura 2018
Peters 2018

Hellwinkel 1969 (R=H)
Sadighi 2019 (R=^{t}Bu)

Scheme 43: Phosphatriptycene derivatives[100]

In the last few years in particular 9-phosphatriptycenes are growing in interest (Scheme 43). Classical 9-phosphatriptycenes (**136**) were first synthesized by Bickelhaupt and coworkers in 1974.[103] They could achieve 35% yield by ring closure reaction of a carbanion and a benzyne moiety (**143**) leading to the C_3 symmetric rigid structure (Scheme 44).

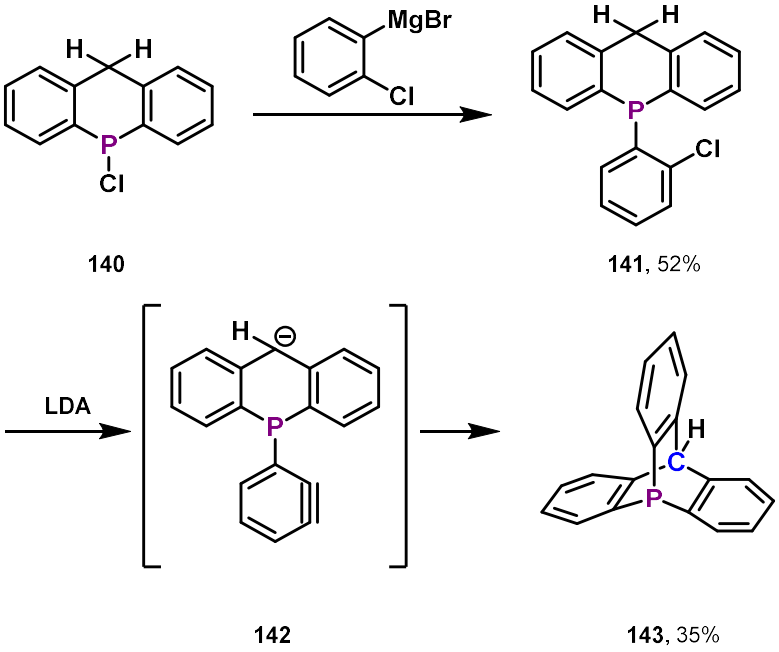

140 **141**, 52%

142 **143**, 35%

Scheme 44: Synthesis of classical 9-phosphatriptycenes[103]

In 2003 the group of Kawashima presented a novel synthetic route to multi-substituted 9-phosphatriptycenes using *ortho*-lithiation as a key step starting from a phosphine oxide **144** (Scheme 45).[104] The formed phosphine oxide **146** was afterwards reduced in a two-step procedure.

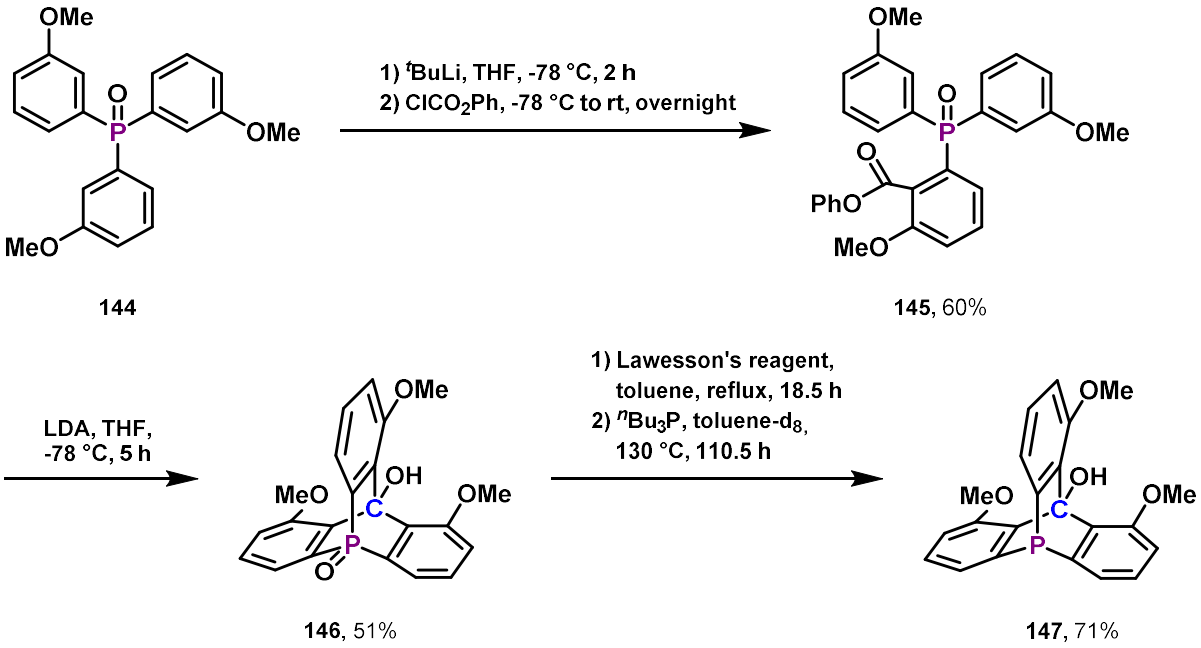

Scheme 45: Synthetic route towards 9-phosphatriptycenes by Kawashima[104]

In 2004 the same group also tried to evaluate the electronic properties of a similar ligand **148** (Scheme 46).[105] They discovered that not only was the oxidation potential shifted to more positive potentials than for PPh_3 but also measuring the $^1J_{PSe}$-coupling constant of the corresponding selenide in NMR (828 Hz) revealed a much higher coupling constant than in $Se{=}PPh_3$ (736 Hz). This coupling constant, which reflects the σ-donor ability, even surpasses the one of electron poor tri-(2-furyl)-phosphine (TFP, 788 Hz) making **148** an even weaker σ-donor. By synthesizing the first metal complexes of these phosphine-class by reacting them with $W(CO)_5$(thf) the TEP of the corresponding tungsten complexes revealed significantly less overall donor ability of **148** compared to PPh_3. The bathochromic shift was almost the same as with the ligand $SbPh_3$.

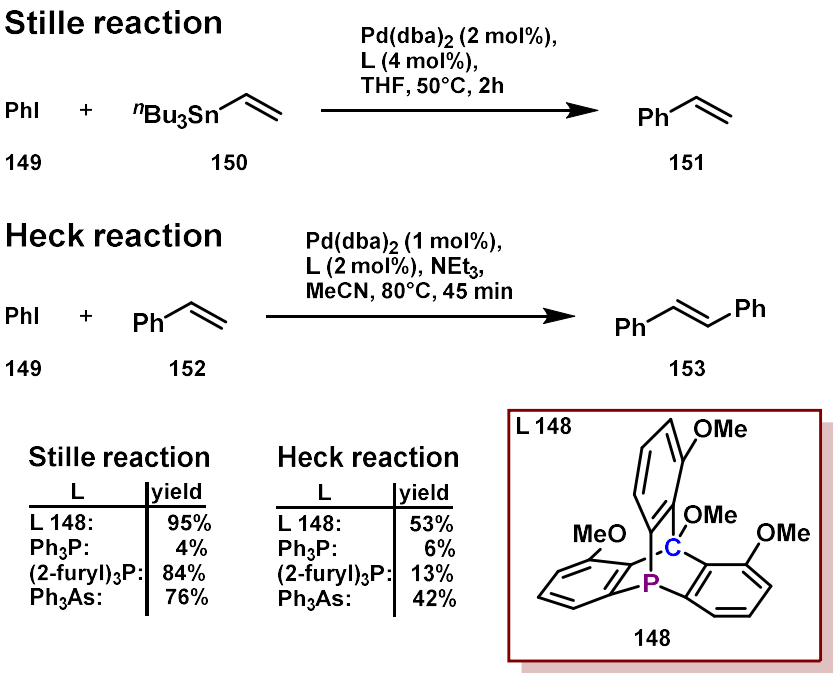

*Scheme 46: Stille and Heck reactions using 9-Phosphatriptycene **148** as ligand[105]*

Due to its electron deficient nature the 9-phosphatriptycene was used in palladium catalyzed Stille and Heck reactions (Scheme 46). By using PhI (**149**), which simplifies oxidative addition, the rate determining step in Stille coupling was the transmetalation step. In the tested Heck reaction it was the migratory-insertion of the alkene. Both rate determining steps profit from weak σ-donating ligands. Thus, it could be shown that both reactions can be accelerated by using the 9-phosphatriptycene ligand instead of more σ-donating PPh_3 and TFP.

Following in Bickelhaupts footsteps the group of Robiette and Berionni synthesized the classic carbon-based 9-phosphatriptycene **143** and sterically hindered *ortho*-substituted phosphatriptycenes but by a triple halogen/lithium approach cyclizing (tris)lithio-triphenylmethanes with PCl_3 or (tris)lithio-triphenylphosphines with a carbon electrophile.[100,106] They analyzed the Brønsted and Lewis basicity of the classic 9-phosphatriptycene by computing proton affinity, pK_a value and calculating Lewis basicity parameters of selected equilibriums of association reactions. It could therefore be concluded that 9-phosphatriptycene is 5 orders of magnitude less Brønsted-basic and 10^6 times weaker Lewis basic than PPh_3. Also the CO stretching frequency of the Rh(acac)CO(9-phosphatriptycene) complex (1985 cm^{-1}) showed that speaking about overall donor properties 9-phosphatriptycene is more similar to *para*-CF_3-triphenylphosphine (1986 cm^{-1}) than to PPh_3. Compared to PPh_3 9-phosphatriptycene exhibits a lower energy of the lone pair in combination with a higher s-orbital contribution and is aside from that more bulky (crystallographic cone angle). The cone angle can also be tuned by installing *ortho*-substituents, while the electronic properties stay, due to absence of conjugation of the aryl groups with the lone pair, the same. Furthermore, it could be shown that enantiopure P-chirogenic triarylphosphines with configurational stability can be achieved by unsymmetrical substitutions because rotation, inversion and flipping can be neglected at the phosphorus. Also Au(I) and Rh(I) complexes of this bulky phosphatriptycene could be synthesized but were up until now not used for any application like catalysis.

Even before Bickelhaupt synthesized the first classical carbon-based 9-phosphatriptycene, Schenk, Hellwinkel and coworkers published in 1969 a method to synthesize analog Azaphosphatriptycenes.[107] They mentioned the interesting up-field shifted ^{31}P signals in NMR and found a logarithmic relation between the ∡C─P─C angle in the molecule and the chemical shift in NMR.[108] Also, they came to the conclusion that the s-orbital character in these molecules' lone pair needs to be higher than in unstrained phosphine systems giving the phosphorus center a more magnetically shielded environment. The rhodium carbonyl complexes of azaphosphatriptycenes [high ν_{CO} LRh(CO)(acac) of 1985 cm^{-1}] later found application in the hydroformylation of cyclic enol ethers by Sadighi and coworkers[109], while two slightly modified azaphosphatriptycenes coordinated to one Pt(II) stator were used in the development of a switchable molecular gear by Shionoya and coworkers[110].

Beside carbon and nitrogen, also other elements on the other bridgehead position have been studied. For example the heavier element congeners of group 14 could be implemented into the architecture. Bickelhaupt and coworkers synthesized the Ge/P mixed group 14/15 triptycenes,[111] while Tsuji and Tamao later synthesized also the silicon variant of this phosphatriptycene motif.[112] The latter group synthesized 9-Phospha-10-silatriptycenes *via* an halogen-lithium exchange reaction generating a trilithio species, which could be reacted further with silicon tetrachloride (Scheme 47). By synthesizing the phosphine selenides they could show that the s-character of the lone pair of phosphorus ($^1J_{PSe}$=795 Hz) is higher than in PPh_3 but still lower than in carbon-based 9-phosphatriptycenes. This finding is comprehensible taking to account that increasing the radius of the bridgehead element results in a bigger ∡C─P─C angle as well as lower s-character of the lone pair.

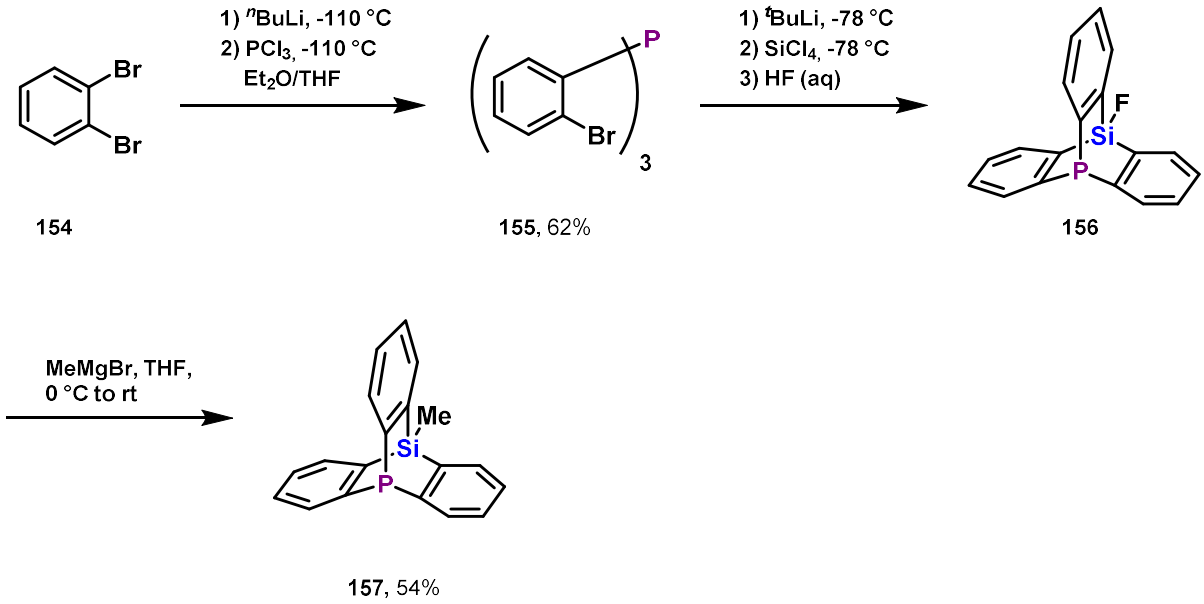

154 **155**, 62% **156**

157, 54%

Scheme 47: Synthesis of 9-Phospha-10-silatriptycenes[112]

A modified version of Tsujis and Tamaos synthetic protocol was later used by Sawamura and coworkers to craft a silicon-chloride based 9-phosphatriptycene on silica gel (**164**).[113] The heterogeneous ligand system (Silica-TRIP, **164**) was further used in Rh-catalyzed *ortho*-selective C─H borylation of arenes by addition of $[Rh(OH)cod)]_2$ and showed its advantages especially with imine-type directing groups. The authors claimed that immobilized constrained phosphines are less prone to encounter significant steric hindrance on the silica surface and thereof surpass the catalytic activity of silica-crafted triphenylphosphine analogs. Later the same group could show that the same Silica-TRIP system could also site-selectively borylate N-adjacent $C(sp^3)$−H bonds of amides, ureas, and 2-amino-pyridines by adding $[Rh(OMe)cod)]_2$ as a rhodium source.[114] Furthermore the Silica-TRIP system was used in iridium catalyzed site-selective $C(sp^3)$−H activation[115] and Pd-catalyzed Suzuki–Miyaura cross-coupling of chloroarenes.[116] The latter seems to be counterintuitive using an electron poor ligand to activate relatively inert chloroarenes, but taking $PdCl_2(Py)_2$ as a palladium precursor and taking to account how spread the ligands on the silica surface are this can only lead to mono-P-ligated palladium species[117] of the type $PdCl_2(py)$(Silica-TRIP), which are known to be highly catalytically active regardless of the moderate electron donor power. Thus, the choice of 9-phosphatriptycene as a ligands in this research topic is not about donor abilities but of limiting the mobility of the ligand. By choosing a rigid linker the steric hindrance of the solid surface toward the active site is reduced and reactive mono-P-ligated palladium species are formed.

In 2018 the group of Sawamura implemented for the first time charge into the caged structure.[118] Instead of using a neutral silicon─phenyl bridgehead they used a negatively charged phenyl─boron moiety, creating a mixture of a triptycene and a BArF like motif (**167**, **168**). They claimed that long-range orbital interaction and the anionic charge in this rigid structures will increase the donor power of the phosphorus lone pair. Despite the smaller ∡C─P─C angle compared to silicon-based systems the anionic charge enabled much lower $^1J_{PSe}$ coupling constants in the corresponding phosphorus selenide indicating strong σ-donor properties. Furthermore, this new negatively charged ligands showed a smaller cone angle due to the boron atom being smaller than the silicon atom. DFT studies revealed that the negative charge is distributed throughout the aromatic rings, making the borate-phosphine ligand a phosphine with strong electron donor abilities suitable for mono-P-ligated palladium catalysis. The mono-P-ligation thereby is caused by electrostatic repulsion between the negatively charged phosphines. The homogeneous borate-phosphine ligands **167** and **168** showed

good performance in Suzuki-Miyaura coupling of aryl chlorides (Scheme 48), which was comparable to XPhos **162** (homogeneous) and Silica-TRIP **164** (heterogeneous) and superior to PPh_3 **161**, Ph-TRIP **163** and other non-caged borate-based anionic phosphines (**165**, **166**). The latter indicates a much bigger influence of the negative charge in **167** and **168** compared to non-caged systems (**165**, **166**).

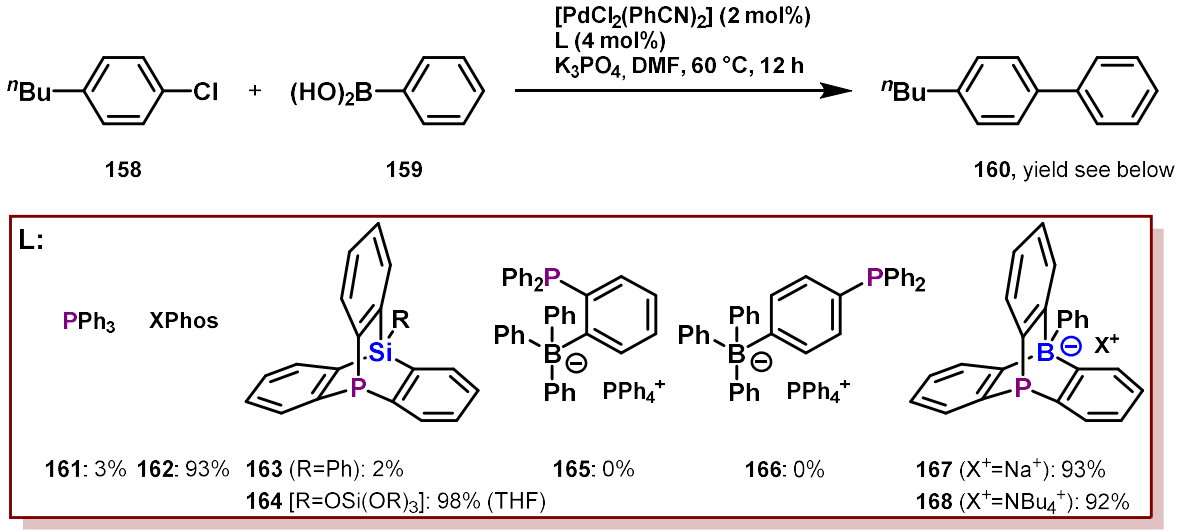

Scheme 48: Ligand effect of PTB in Suzuki–Miyaura reaction[118]

Two weeks later the same ligand was published by Peters and coworkers showing that also complexes of platinum (II), cobalt (II), iron (II) and pentakis(carbonyl)tungsten (0) can be synthesized.[119] The latter, in addition to oxidation potentials and selenium coupling constants, was used to evaluate the donor properties of the 9-phosphatriptycene-10-phenylborate (PTB) anion. Also here, PTB demonstrated its strong donor character.

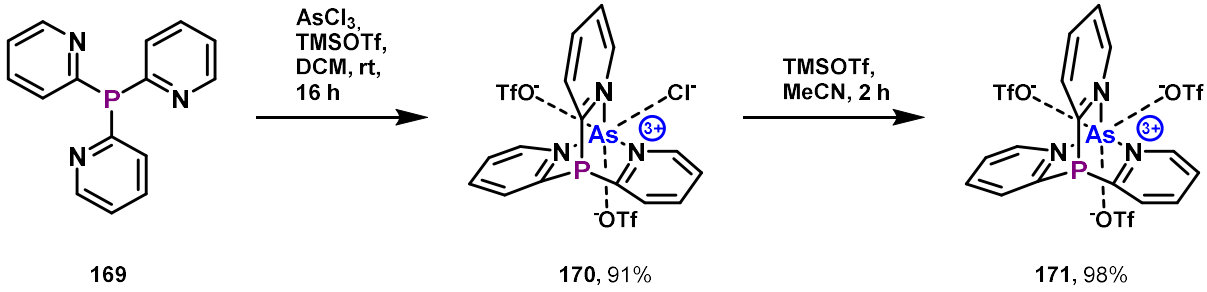

Scheme 49: Synthesis of a tricationic caged phosphine[120]

A related tricationic caged phosphine was published by Suter, Burford and coworkers in 2017.[120] They were able to coordinate tris(2-pyridyl)phosphine **169** to As^{3+} to form compound **171** in two steps by chloride abstraction starting from $AsCl_3$. However, the substituting triflate anions remain in the coordination sphere of the arsenic and have distances smaller than the corresponding van der Waals radii. Calculations have shown that the positive charge is mainly present on the arsenic but also partly distributed on the phosphorus. Nevertheless, both axial lone pairs remain electronically separated and no electron density is directly donated from one pnictogen lone pair to the other and thus no transannular P–As bond is formed.[120,121]

The selective tripodal-N,N',N''-κ^3 coordination of the multidentate ligand **169** is not self-evident. Softer metal centers like $Mo(CO)_n$ show *e.g.* competition between phosphorus and nitrogen coordination.[122] This is reminiscent of the selectivity problems in the generation of cationic phosphines by alkylation of a phosphorus substituent (see Chapter 1.3.2.1, Scheme 27). However, in this regard, the ligand of Holm

172 provides more controlled conditions due to higher denticity (Scheme 50).[123] Here, Fe^{2+}, Co^{2+}, Ni^{2+} and Cu^{2+} could be selectively κ^6 encapsulated and the risk of additional coordinated anions is much lower.

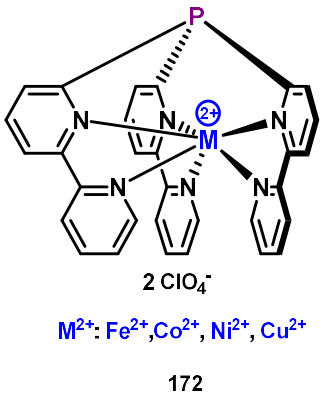

172

Scheme 50: Encapsulating phosphines published by Holm in 1972[123]

But to our knowledge, neither the mentioned "tricationic ligands" of Suter and Burford **171**[120] nor the mentioned "dicationic ligands" of Holm **172**[123] were used in homogeneous catalysis. Furthermore, the ligands of Holm were never used to coordinate a second metal showing catalytic activity. Here the group of Holm was mainly focused on the geometry differences between trigonal prismatic and trigonal antiprismatic structures and the phosphines represented only one compound class of the many to be investigated in their stereochemistry.

2 Results and Discussion I: Cationic PNN pincer and encapsulating phosphine ligands

2.1 Project I: Dicationic PNN pincer ligands - Motivation

Due to their low donor ability and their Coulomb repulsion classic dicationic ligands are limited to a few metals they can coordinate [Au(I) and Pt(II)]. To address this limitation the group of Alcarazo installed a rigid phenylene-linker backbone and a neutral strong σ-donating anchor diphenylphosphine moiety making the formed chelate ligand able to coordinate even Mo, Pd and Rh.[93,99] Combination of a rigid backbone and neutral phosphine anchor now forces the dicationic phosphine substituent to enter the coordination sphere of the metal center leading to coordinate itself. But also this approach is limited. Coordination of 3d-metals has not yet been possible, but is of great interest, especially because the replacement of noble metals by cheap and accessible base-metals is a recent trend in catalysis research.[124] In order to achieve this goal it was considered to move away from bidentate chelating ligands to PNN pincer ligands (Scheme 51).

For this approach a very rigid backbone is needed (**173**). The architecture of the backbone should circumvent the coordination of all neutral N,N ligand parts without also binding to the dicationic phosphine. In this context a substituted quinoline seemed to be very suitable. Substituting it at the 8-position with the dicationic phosphine and installing a pyridine moiety at the 2-position circumvents the phosphine to point away from the metal center and offers a strong chelation.

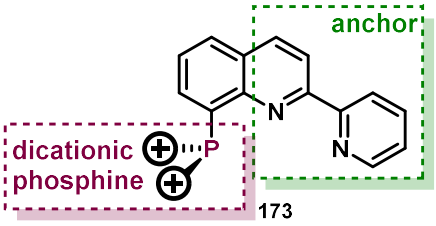

Scheme 51: Quinoline based dicationic PNN pincer ligand

2.2 Synthesis of dicationic PNN pincer ligands

The pyridyl bromoquinoline backbone **178**, which was required as a precursor for the rigid PNN pincer ligand, was already known in the literature and can be synthesized by two different strategies.[125,126]

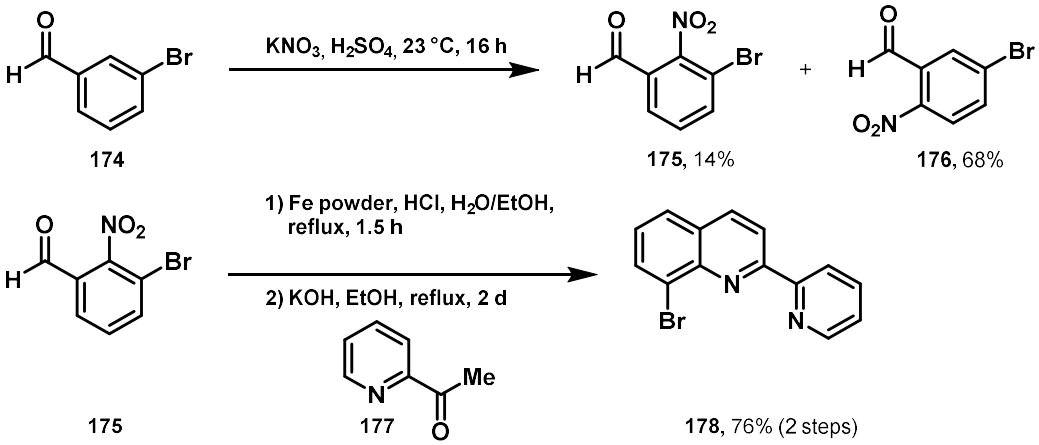

Scheme 52: Synthesis of pyridyl bromoquinoline published by Thummel and coworkers[125,127]

The first strategy was published by Thummel and coworkers in 2014 and starts from 3-bromo-2-nitrobenzaldehyde **175** (Scheme 52).[125] Reduction with Fe powder and condensing the corresponding aniline with 2-acetylpyridine **177** in a Friedländer synthesis yields quinoline **178**. However, the synthesis of the 3-bromo-2-nitrobenzaldehyde **175** itself turns out to be difficult because of a lack of regioselectivity of the nitration giving the desired compound only as a minor product **175** in 14% yield.[127] Therefore, we used the second strategy, which was published by Thummel and coworkers in 2015.[126,128] Our results are shown in Scheme 53.

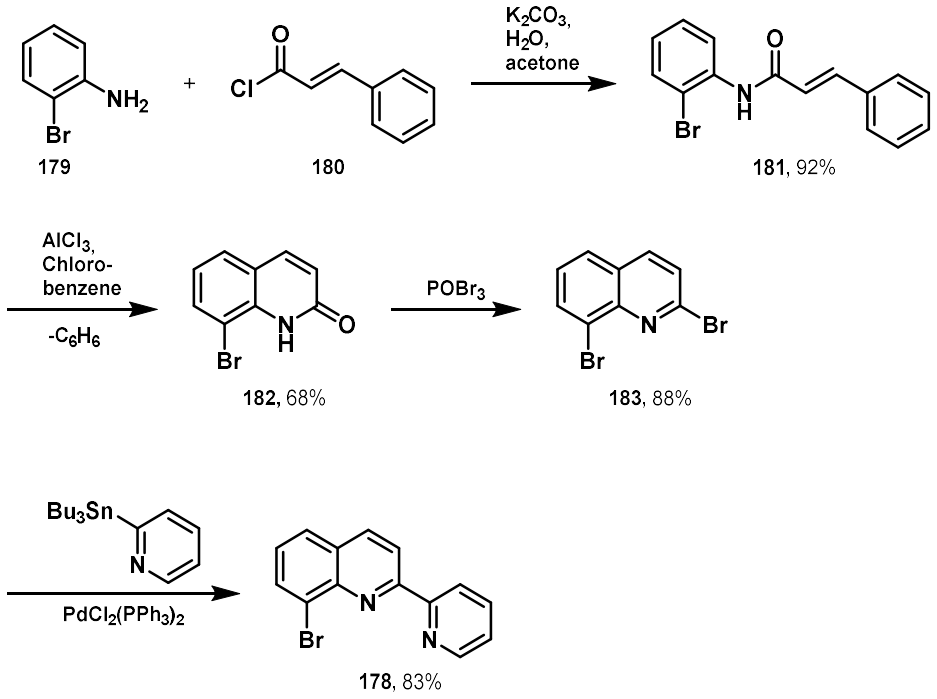

Scheme 53: Synthesis of pyridyl bromoquinoline[126]

Starting from 2-bromoaniline **179**, we could synthesize the corresponding amide **181** by condensation with cinnamoyl chloride **180** in 92% yield. Amide **181** could then be thermally converted to 2,8-dibromoquinoline **182** by intramolecular Friedel–Crafts acylation in combination with an elimination

of benzene followed by bromination using phosphorus oxybromide. After Stille coupling the target pyridyl bromoquinoline backbone **178** was achieved.

With this bromoquinoline **178** at hand various phosphorus compounds can be synthesized *via* lithium-halogen exchange and reaction of the resulting 8-lithio-2-(pyrid-2′-yl)quinoline with phosphorus chlorides. First, the reaction was tried with Ph_2PCl, which resulted in 8-(diphenylphosphaneyl)-2-(pyridin-2-yl)quinoline **184** (Scheme 54).

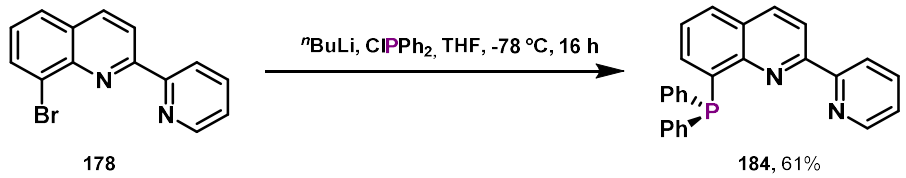

Scheme 54: Synthesis of neutral PNN pincer ligand with pyridyl bromoquinoline backbone

This ligand was tried to coordinate towards Co(II) but during the investigation similar attempts were published by Rauchfuss and coworkers[129,130] and later on also an identical diphenylsubstituted phosphine ligand **184** was published by Nakazawa and coworkers.[131] However, this result shows that phosphorus electrophiles can be easily attached, which is important for the synthesis of a dicationic analog.

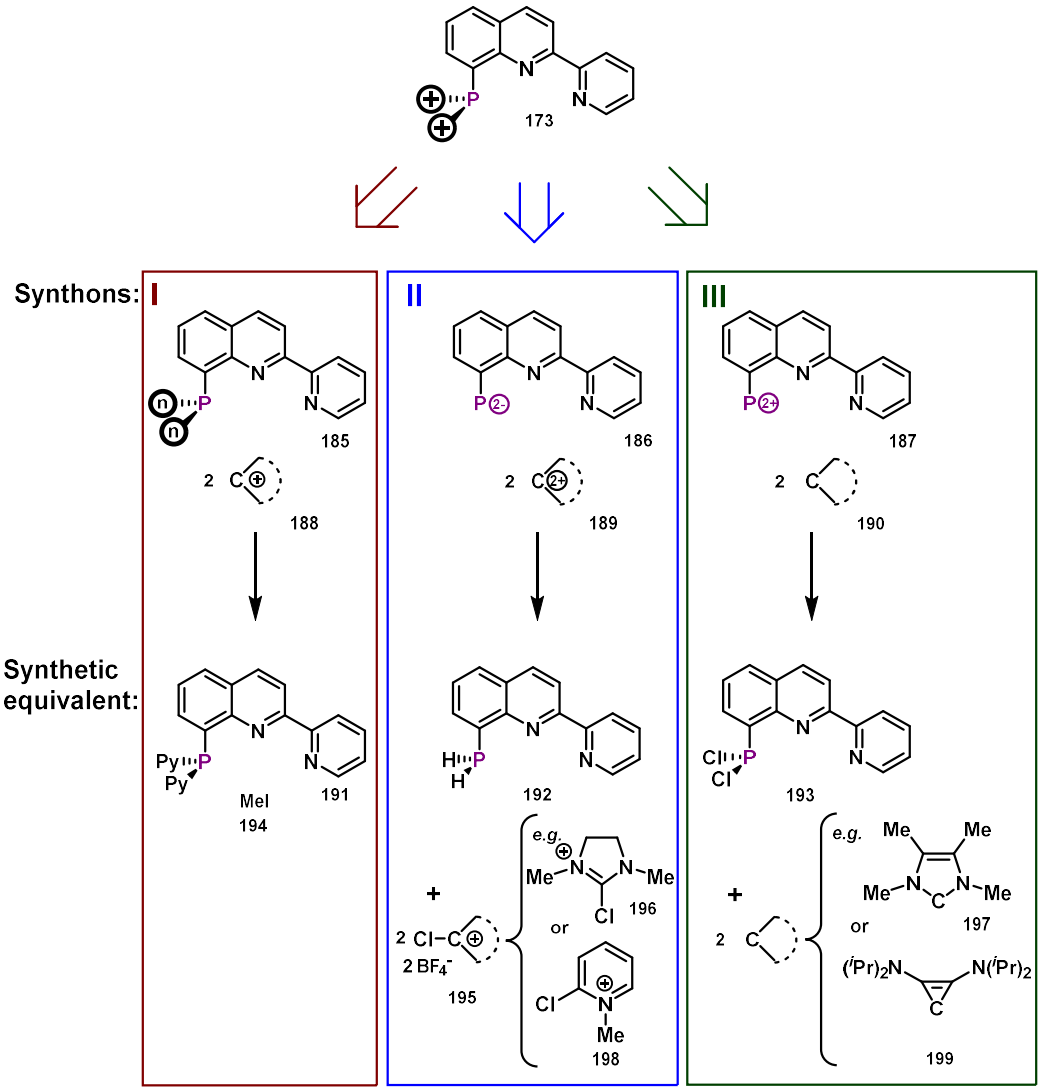

Scheme 55: Disconnection approach of dicationic PNN pincer ligand

As already mentioned before, the synthesis of cationic phosphines mainly relies on three different heterolytic disconnection approaches (Scheme 55):

1) transforming a neutral substituent of the phosphorus into a cationic one (**I**, red)
2) having a nucleophilic phosphorus attacking a positively charged electrophile (**II**, blue)
3) a neutral nucleophile or Lewis base (*e.g.* a carbene, pyridine) attacking a phosphorus electrophile releasing an anion (**III**, green)

The first approach (Scheme 55, **I**) relies on a late stage functionalization of neutral substituents at the phosphorus by for example methylation of pyridine moieties (**191**, **194**). This approach seems difficult to realize in **191** due to the fact that, additional to the pyridine moieties at the phosphorus, there are further nucleophilic centers at the backbone. This could result in a methylation of the phosphorus or nitrogen of the pyridine or quinoline backbone.

In this context, the second approach (Scheme 55, **II**) seems more promising. By formally disconnecting the positive charges giving the electron pair towards the phosphorus an organophosphide synthon **186** and two carbodicationic synthons **189** are received. Transferring this disconnection to synthetic equivalents will end up with a primary phosphine **192** and Vilsmeier type salts *e.g.* chlorodihydroimidazolinium **196** or 2-chloropyridinium salt **196**. Various Vilsmeier type salts are known to literature and α-dicationic chelating phosphine ligands could already be synthesized by this method using phosphonate intermediates.[93]

The third approach is based on the synthesis of free carbenes (e.g. **197**, **199**) and phosphorus chlorides **193**, furthermore it has limitations in the possible cationic substituents on the phosphorus (pyridinium is not possible) and was therefore excluded at the beginning.

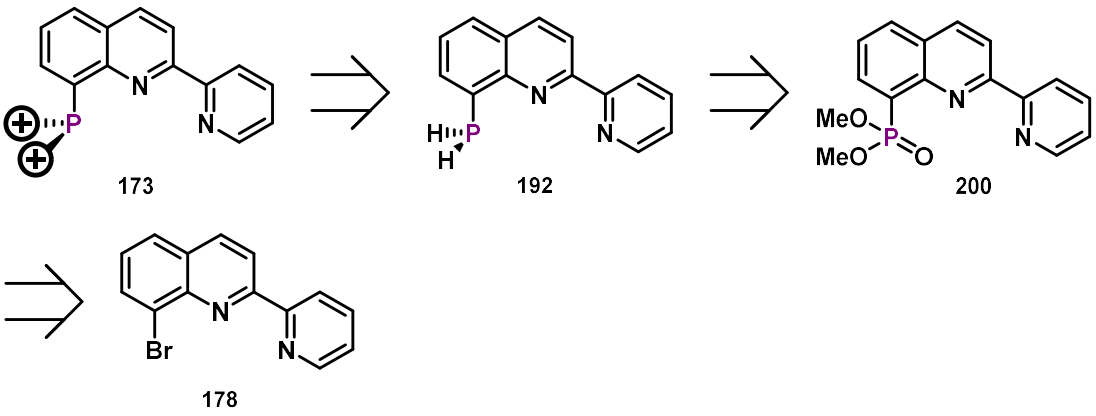

Scheme 56: Three step reaction sequence using disconnection approach II

Based on approach II, dicationic phosphine **173** should therefore be accessible *via* a linear three step reaction sequence starting from 8-bromo-2-(pyridin-2-yl)quinoline **178**. However, to obtain a primary phosphine such as **192**, a direct lithiation approach cannot be chosen, and therefore the indirect route *via* phosphonate **200** is frequently used.[93] From the primary phosphine **192** it should then be only one step to the dicationic phosphine **173**.

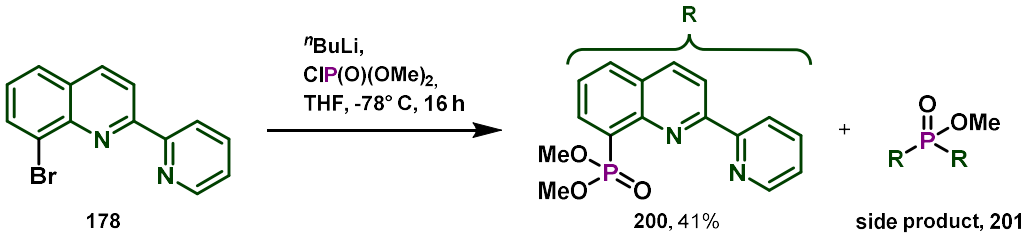

*Scheme 57: Synthesis of phosphonate **200***

Phosphonate **200** was prepared by lithium-halogen exchange using ^{n}BuLi in THF and quenching of the metalated species with dimethylchlorophosphate in 41% yield (Scheme 57). The low yield can be explained by side product **201**. The disubstituted phosphonate **201** could be identified *via* ^{1}H-NMR and ^{31}P-NMR and is a result of two lithiated quinoline-backbones (green) reacting with only one dimethylchlorophosphate. Addressing this selectivity problem can be done by either changing the order of addition by adding the lithiated species to the dimethylchlorophosphate in a diluted solution, or changing the reaction type or product. The later was tried by using a palladium-catalyzed cross-coupling between aryl bromide and H-phosphonate dimethylester (Scheme 58) or using again the lithiation-approach but with a more sterically hindered chlorophosphate (diethylchlorophosphate, Scheme 59).

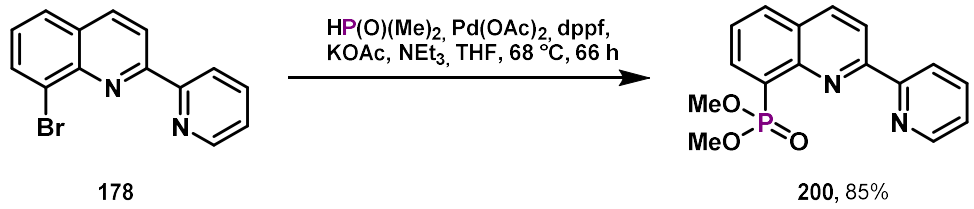

*Scheme 58: Synthesis of phosphonate **200** via acetate-promoted cross-coupling*

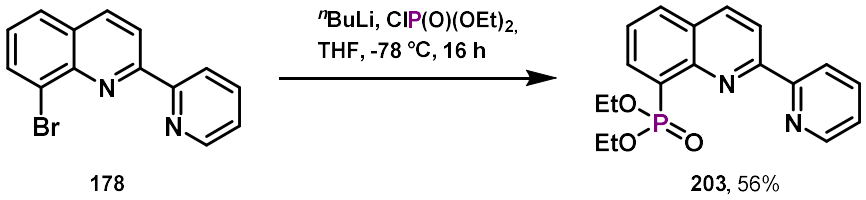

*Scheme 59: Synthesis of phosphonate **203** via lithiation approach*

While the lithiation attempt using diethylchlorophosphate as electrophile only gave 56% yield the acetate-promoted cross-coupling gave 85% yield towards the desired phosphonate **200**.

With the phosphonate available the next step towards a cationic phosphine involves the reduction from phosphonate to primary phosphine. This usually is enabled by the usage of $LiAlH_4$.[93] Unfortunately, neither the dimethyl nor the diethyl phosphonate lead to the desired product when reduced with excess $LiAlH_4$ (3 equiv.). Furthermore the quinoline backbone of the phosphonate was not stable towards reduction. The obtained mixture of products after drying and filtering through Celite contained different phosphorus species.

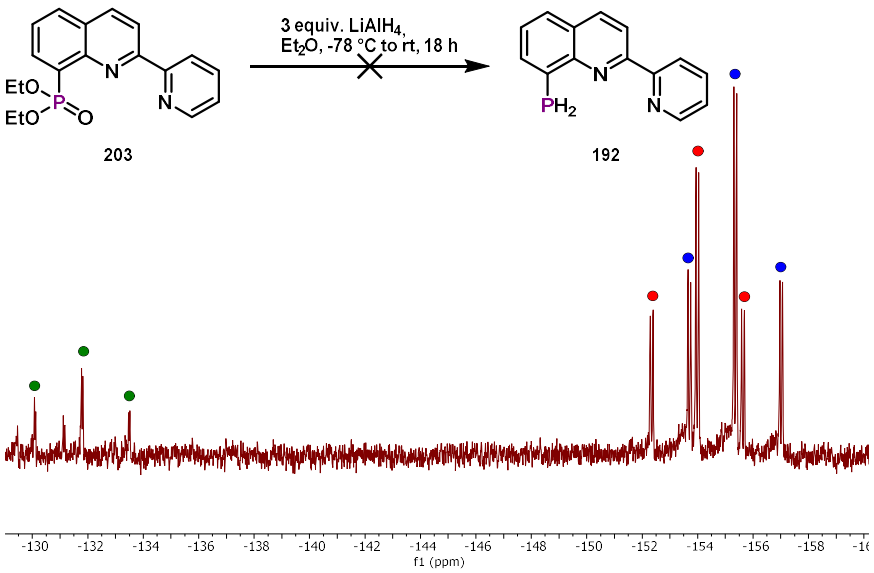

Figure 17: ^{31}P NMR Spectrum of crude reaction mixture suggesting a mixture of different primary phosphines.

These could be identified *via* proton-coupled ^{31}P-NMR (Figure 17). For each phosphorus-species there was nearly the same ^{31}P triplet of doublets pattern with $^{1}J_{PH}$ coupling constants of over 200 Hz (blue, red: 201 Hz, green: 206 Hz) but with different chemical shifts. This leads to the conclusion that the reduction of the phosphonate to a primary phosphine worked, but different reductions of the ligand backbone caused different phosphorus-species. Even with modified procedures by using less equivalents of $LiAlH_4$ or different reducing agents (e.g. $HSiCl_3$, TMS─Cl/$LiAlH_4$) the selectivity could not be increased to a degree that one pure primary phosphine could be isolated.

Although the synthesis of dicationic phosphines by using primary phosphines as nucleophiles is a reliable method, in this case the reducible quinoline-backbone makes it unsuitable. Therefore, we switched to approach III.

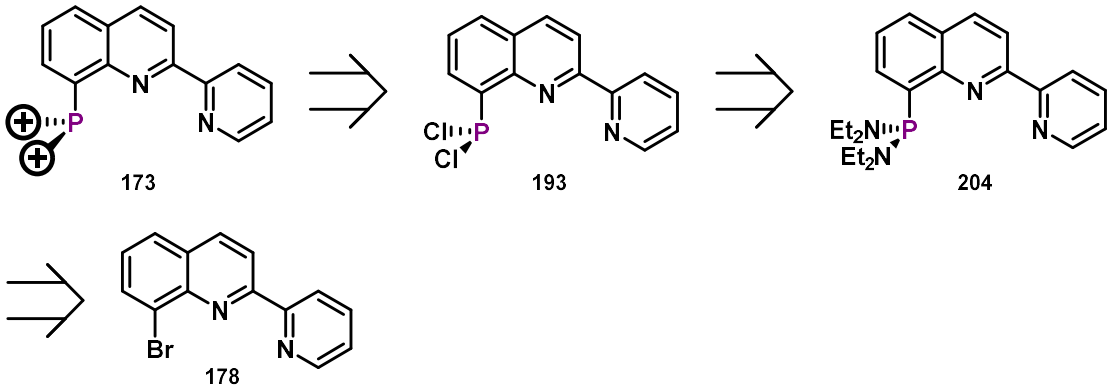

Scheme 60: Three step reaction sequence using disconnection approach III

Approach III inverts the polarity at the phosphorus from a nucleophilic to an electrophilic center using phosphorus chloride **193**, which can then be attacked by carbenes (Scheme 60). This method involves one extra step, since direct conversion of bromide **178** to phosphorus chloride **193** is unselective (over-substitution). An indirect route *via* the phosphonous diamide **204** is therefore reasonable. The phosphonous diamide **204** can now be selectively synthesized from the bromide **178** by a lithiation approach and then converted into the phosphorus chloride **193** by acidolysis.

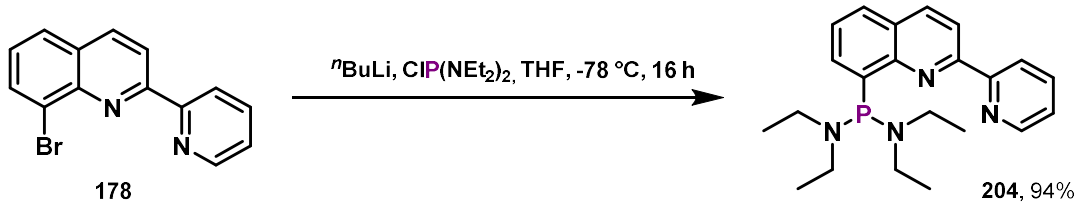

*Scheme 61: Synthesis of phosphonous diamide **204***

The synthesis of phosphonous diamide **204** proceeds *via* halogen metal exchange and reaction of the lithiated quinoline with bis(diethylamino)chlorophosphine (Scheme 61). The pentane soluble product **204** can then be easily separated from the reaction mixture by extraction techniques in very good yield.

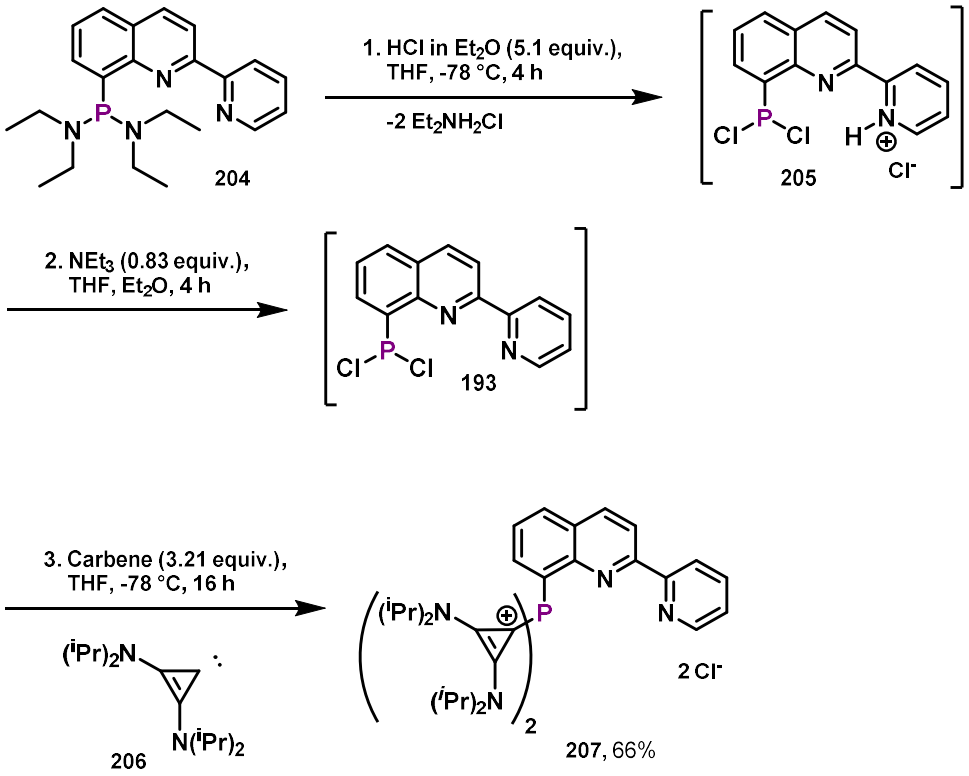

*Scheme 62: Synthesis of dicationic PNN pincer ligand **207***

With the phosphonous diamide **204** at hand acidolysis can be accomplished by treatment with HCl in ether (Scheme 62). The *in situ* generated phosphorus chloride **193** was then reacted with bis(diisopropylamino)cyclopropenylidene[132] **206** to phosphine **207** in 66% yield. The substitution of both chlorides leads to a dicationic phosphine with two chloride counterions. This example clearly shows the benefits of this methodology (approach III), when the primary phosphine analog of a phosphine ligand cannot be synthesized or the primary phosphine lacks reactivity towards Vilsmeier-type salts. Unfortunately, also this approach was limited to the use of cyclopropenylidene **206**. Other carbenes with little steric hindrance like 1,3,4,5-tetramethyl-imidazol-2-ylidene **197**[133] did not form the desired product.

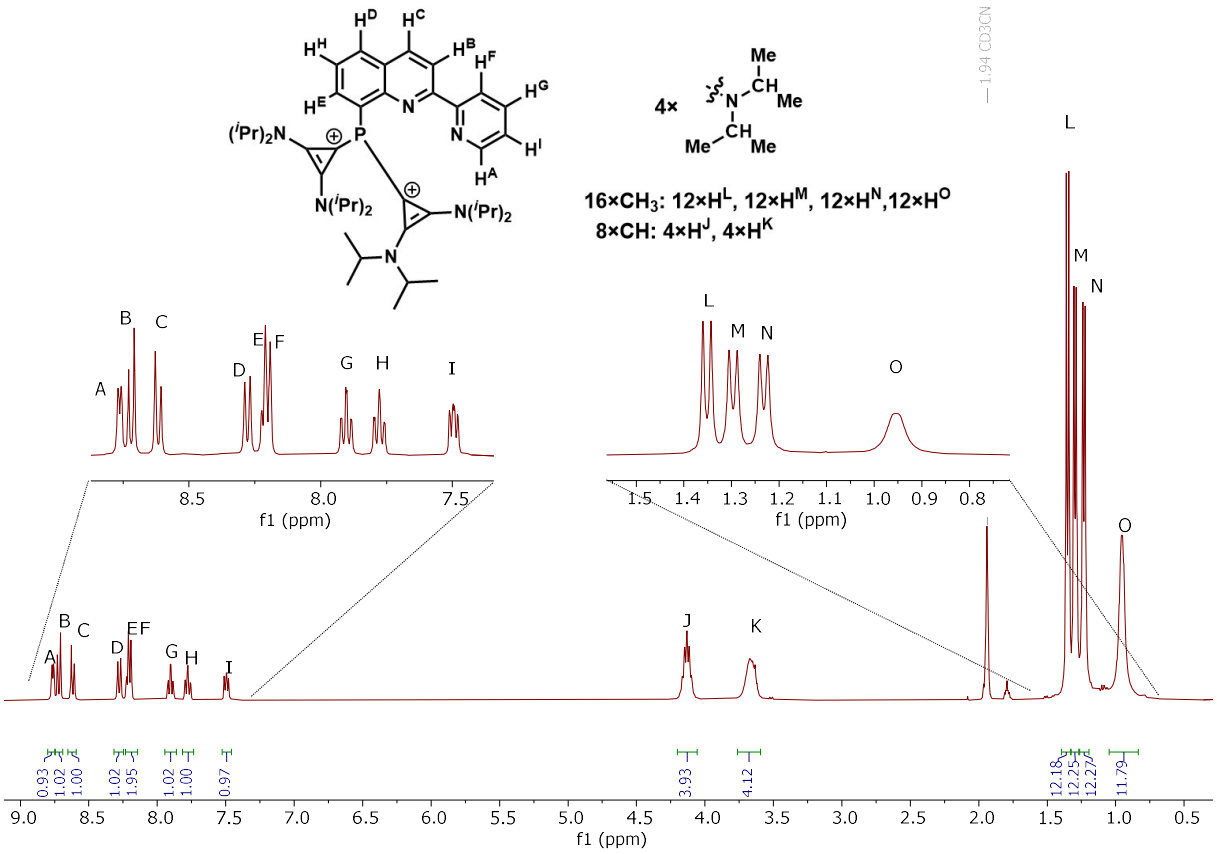

*Figure 18: ^{1}H NMR Spectrum of dicationic PNN pincer ligand **207***

The ^{1}H-NMR of **207** shows the typical downfield signal **A** of the pyridine proton $\mathbf{H^A}$ in 2-position (Figure 18). Also the quinoline backbone was not reduced during reaction. This is indicated by the AB system of the signals **B** and **C**, which can be easily identified by their roofing and identical coupling constants. The signal for proton $\mathbf{H^E}$ in *ortho*-position to the phosphorus (**E**) is superimposed with a signal from the pyridine moiety **F**. All aromatic signals can be assigned to the corresponding protons in dicationic phosphine **207** *via* 2D NMR analysis [(^{1}H-^{1}H) COSY, (^{1}H-^{13}C) HSQC, (^{1}H-^{13}C) HMBC] and are shown in Figure 18.

The analysis of the aliphatic signals is more complicated. In the ^{1}H spectrum, two signals for the eight methine groups (**CH**) can be identified (**J** and **K**). This indicates either a rotational barrier or the loss of C_s-symmetry of the molecule in solution. Based on the mesomeric structure **207'** (Scheme 63), a slow rotation on the NMR time scale[134] of the cyclopropenyl–N bond seems most likely.

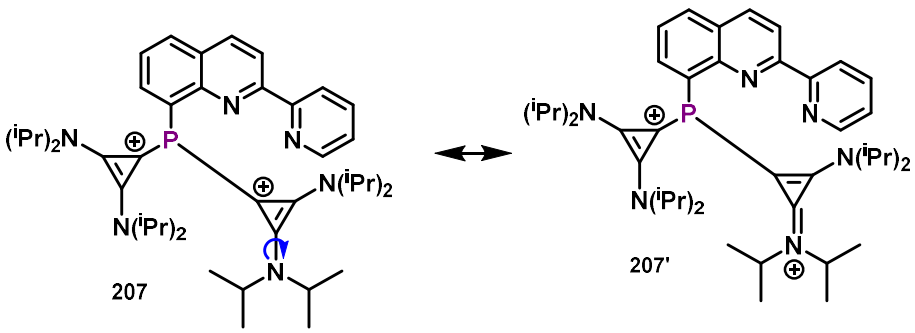

*Scheme 63: Rotational barrier of dicationic PNN pincer ligand **207***

Further evidence is provided by the (^{1}H-^{13}C) HMBC. Here, the ^{1}H signal of the $\mathbf{H^J}$ protons correlate with the α-^{13}C signal of protons $\mathbf{H^K}$. The protons $\mathbf{H^J}$ and $\mathbf{H^K}$ need to be connected *via* the same sp^2-hybridized

nitrogen. A loss of symmetry or a rotational barrier around a P─C bonds can thus be excluded as the reason for the two signals **J** and **K**. Consistent with a cyclopropenyl─N rotational barrier, also four proton signals (L, M, N, O) were found for the 16 methyl groups (48 protons: 12×$\mathbf{H^L}$, 12×$\mathbf{H^M}$, 12×$\mathbf{H^N}$, 12×$\mathbf{H^O}$). Thus, on one N(iPr)$_2$ group there are four diastereotopic methyl groups and two diastereothopic methine groups, which can be converted into the remaining aliphatic methyl/methine groups by free rotation (homotopic protons) and mirroring (enantiotopic protons).

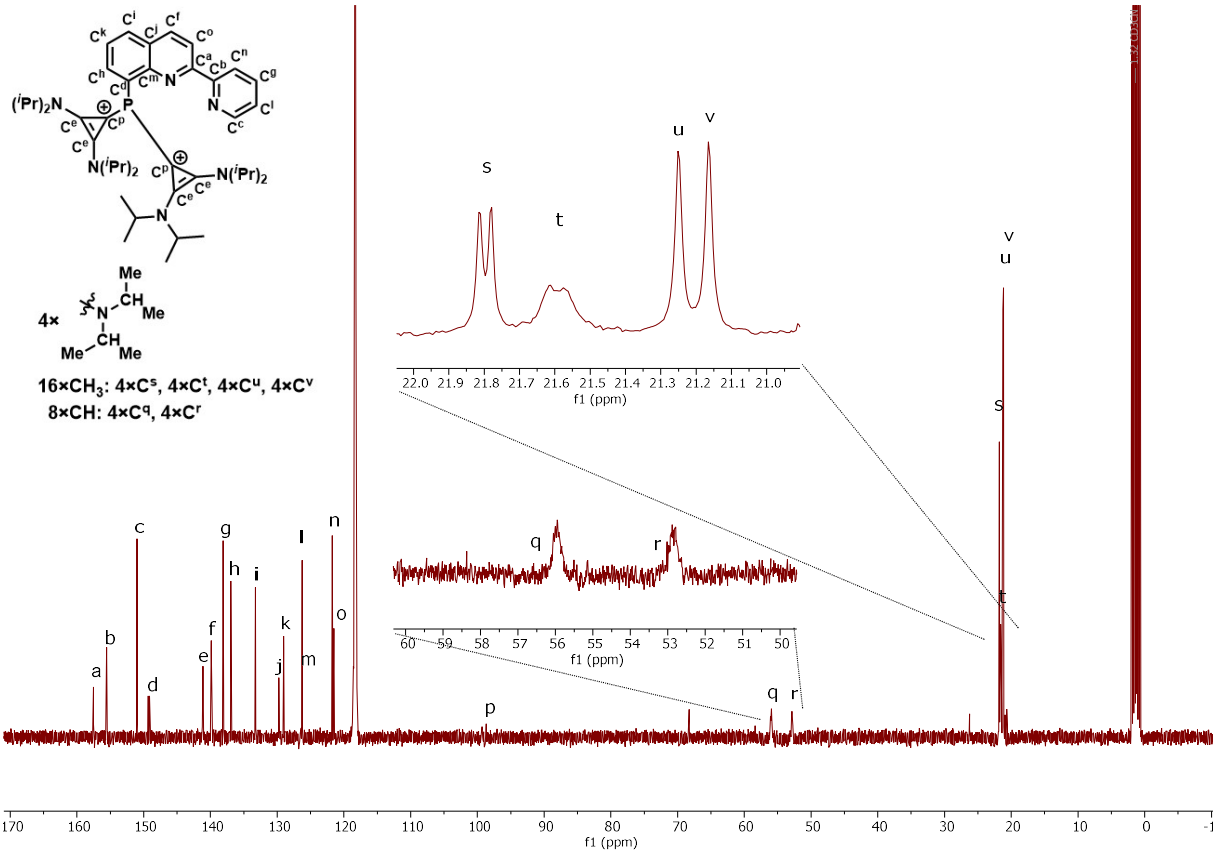

*Figure 19: ^{13}C NMR Spectrum of dicationic PNN pincer ligand **207***

The situation is similar for the ^{13}C signals. All ^{13}C signals could be assigned to the corresponding carbons *via* 2D NMR analysis [(^{1}H-^{1}H) COSY, (^{1}H-^{13}C) HSQC, (^{1}H-^{13}C) HMBC] and are shown in Figure 19. While all four C atoms $\mathbf{C^e}$ together give one signal and thus exclude a symmetry breaking or P─C rotation barrier in solution, the eight methine C atoms $\mathbf{C^q}$ and $\mathbf{C^r}$ give two ^{13}C signals, which again suggest a N─C rotation barrier. Corresponding to the four methyl signals in the ^{1}H NMR, there are also four ^{13}C signals for the methyl groups [(^{1}H-^{13}C) HSQC]. However, a coupling is observed in two of the four signals **s** and **t**, which can only be explained by a ‘‘through-space’’ ^{31}P,^{13}C spin coupling.[135] Therefore, mediated by the rotation of cylopropenyl─P bond, eight methyl groups should be located in close proximity to the phosphorus.

For crystallographic analysis of **207**, an anion exchange was carried out, swapping Cl^- for SbF_6^- to dramatically improve crystallization behavior as well as the stability in terms of storage (Scheme 64).

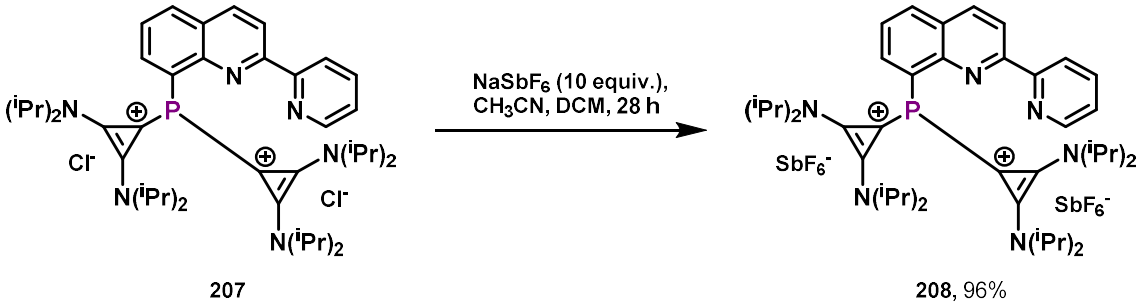

*Scheme 64: Anion exchange of dicationic PNN pincer ligand **207***

The exchange of the chloride anions by a less coordinating hexafluoroantimonate-ion was accomplished in 96% yield using excess $NaSbF_6$, which itself can easily be separated by precipitation in DCM. As expected, the NMR spectrum of this compound looks very similar to its starting material. The ^{13}C signals indicative of a ''through-space'' $^{31}P,^{13}C$ spin coupling are also present in **208** and do not significantly alter when NMR spectrometers of different magnetic fields are used (indication that the doublets are caused by coupling and not by a rotational barrier[136]). Also, both phosphorus signals of **207** and **208** in ^{31}P-NMR match, pointing out that even the more coordinating chloride anion is dissociated from the dicationic phosphine. Both signals are about -56 ppm which is very upfield shifted compared to a neutral triaryl phosphine. On the other hand, this is a very common chemical shift among cationic phosphines, where the shielding of the phosphorus center is a result of its cationic nature.[92] Beside this strong NMR-based evidence, definitive proof of the structure could be achieved by X-ray crystallography (Figure 20, left).

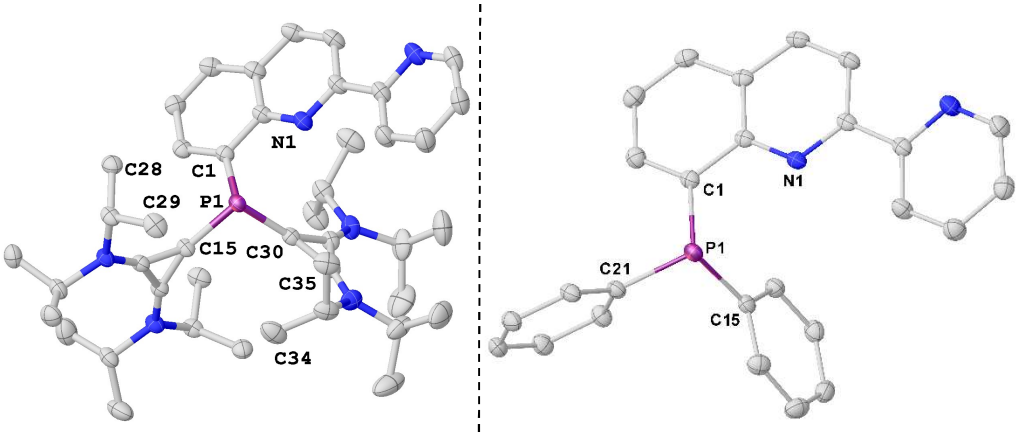

*Figure 20: Molecular structures of **208**[1] (left) and **184**[2] (right). Thermal ellipsoids at 50% probability level. Hydrogen atoms, non-coordinating counter anions and co-crystallized solvent molecules omitted for clarity. Selected bond length (Å) and angles (°) for **208**: P1—C1 1.823(3), P1—C15 1.818(3), P1—C30 1.807(3), P1—C34 3.863(4), P1—C35 3.872(4), P1—C29 3.841(3), P1—C28 3.776(3), ∡C1—P1—C15 102.5(1), ∡C15—P1—C30 102.1(1), ∡C30—P1—C1 102.6(1); for **184**: P1—C1 1.830(1), P1—C15 1.833(1), P1—C21 1.837(1), ∡C1—P1—C15 103.4(1), ∡C15—P1—C21 100.0(1), ∡C21—P1—C1 101.6(1).*

Compound **208** was crystallized by slowly evaporating a DCM solution to obtain colorless blocks. Compound **184** was crystallized similarly from DCM and also yielded colorless blocks. The P—C bond

[1] **Crystal Data** for **208** ($C_{26}H_{19}N_2P$; *M* =390.40 g/mol): monoclinic, space group $P2_1/c$ (no. 14), *a* = 9.4673(7) Å, *b* = 9.4429(7) Å, *c* = 22.5342(17) Å, *β* = 99.214(3)°, *V* = 1988.5(3) Å^3, *Z* = 4, *T* = 99.98 K, μ(MoKα) = 0.153 mm^{-1}, *Dcalc* = 1.304 g/cm^3, 30026 reflections measured (4.686° ≤ 2Θ ≤ 59.226°), 5587 unique (R_{int} = 0.0223, R_{sigma} = 0.0170) which were used in all calculations. The final R_1 was 0.0347 (I > 2σ(I)) and wR_2 was 0.0947 (all data).

[2] **Crystal Data** for **184** ($C_{26}H_{19}N_2P$; *M* =390.40 g/mol): monoclinic, space group $P2_1/c$ (no. 14), *a* = 9.4673(7) Å, *b* = 9.4429(7) Å, *c* = 22.5342(17) Å, *β* = 99.214(3)°, *V* = 1988.5(3) Å^3, *Z* = 4, *T* = 99.98 K, μ(MoKα) = 0.153 mm^{-1}, *Dcalc* = 1.304 g/cm^3, 30026 reflections measured (4.686° ≤ 2Θ ≤ 59.226°), 5587 unique (R_{int} = 0.0223, R_{sigma} = 0.0170) which were used in all calculations. The final R_1 was 0.0347 (I > 2σ(I)) and wR_2 was 0.0947 (all data).

lengths in the cationic **208** are slightly shortened relative to those in the corresponding neutral diphenyl derivative **184**. In comparison with other bis[(diisopropylamino)cyclopropenium]-substituted dicationic phosphines the bond lengths are nearly identical.[92] Especially the P─C(Carbene) distances in both cases are shortened but just slightly compared to a regular P─C single bond. However, the P─C distances still are much longer than P─C double bonds. This leads to the conclusion that back-donation of the phosphorus lone pair to the carbene moieties is negligible.[137] Further evidence is provided by the compound **208**, remaining in a pyramidal geometry, and having just marginal less pyramidalization[138] compared to the neutral phenyl-substituted analog **184** as apparent from the sum of angles ∡C─P─C of 307.2(1) and 305.0(1) ° for **208** and **184**, respectively.

The close proximity of the methyl groups to the phosphorus, which was already suspected from the NMR data, is confirmed by the X-ray structural data. The lowest P···C(Methyl) separation is 3.776(3) Å, which is in a range where "through-space" couplings have already been observed (*cf.* 3.64 Å[135]). However, in solution, in contrast to the solid state, there is free rotatability around the P─C bond, and the PC interaction involves not only four but eight methyl groups.

In relation to future applications beside the structural aspects also the electronic properties are of interest. *Via* cyclic voltammetry relevant insights into radical stabilizing properties or non-innocent redox behavior can be gained. The cyclic voltammogram was recorded in an electrolyte solution (0.1 M $[NBu_4][PF_6]$ in MeCN) at a scan rate of 100 mV/s under nitrogen atmosphere.

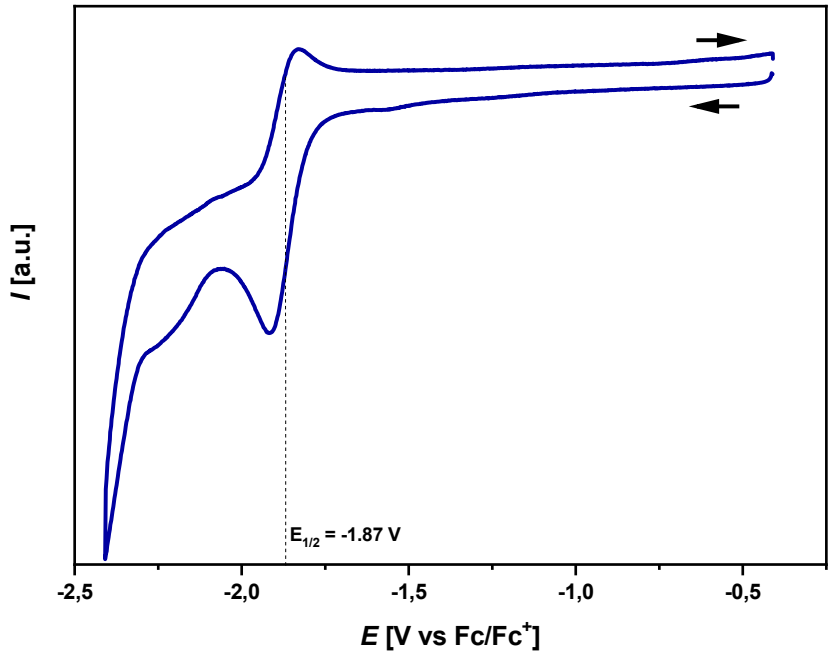

*Figure 21: Cylic voltammogram of **208***

In the potential window of the electrolyte (-2.4 V to 1.6 V vs. Fc/Fc^+) no oxidation potential could be measured (see experimental section). This fact makes it difficult to rank the donor properties of this ligand by its oxidation potential. Direct reduction of the ligand reveals a partial reversible redox process at a potential of -1.87 V vs. Fc/Fc^+ (Figure 21). This partial reversibility makes the synthesis of corresponding stabile α-radical phosphines like the CAAC –based monocationic phosphines known to literature[80,139] questionable but could enable the ligand to "store" electrons during transition metal catalysis. For further investigation, however, a coordination to a metal is required.

2.3 Coordination chemistry of dicationic PNN pincer ligands

One main goal of this project was to study the coordination ability of dicationic ligands towards 3d transition metals and test the corresponding first-row transition metal complexes in catalysis to see if there is a benefit from the positive charge towards reactivity or selectivity. In recent years, the hydrogenation, hydrosilylation and hydroboration was of great interest to upgrade alkynes and alkenes, especially using earth-abundant transition metal catalysts, such as cobalt, iron or nickel.[140] Starting from a Co(II) precatalyst a planar tridentate ligand could stabilize a low-spin Co(I) catalyst after reduction.[129] Having this advantage combined in a dicationic PNN pincer ligand, this complex could show interesting metal-ligand cooperativity, activate even electron poor alkenes/alkynes or facilitate the coordination of alkenes/alkynes during catalysis. Another issue, which can be addressed, is the tendency for autoionization, which was reported for Fe-catalysts.[129,141] Two dicationic ligands can hardly bind to the same metal center due to strong Coulomb repulsion, therefore autoionization should not occur.

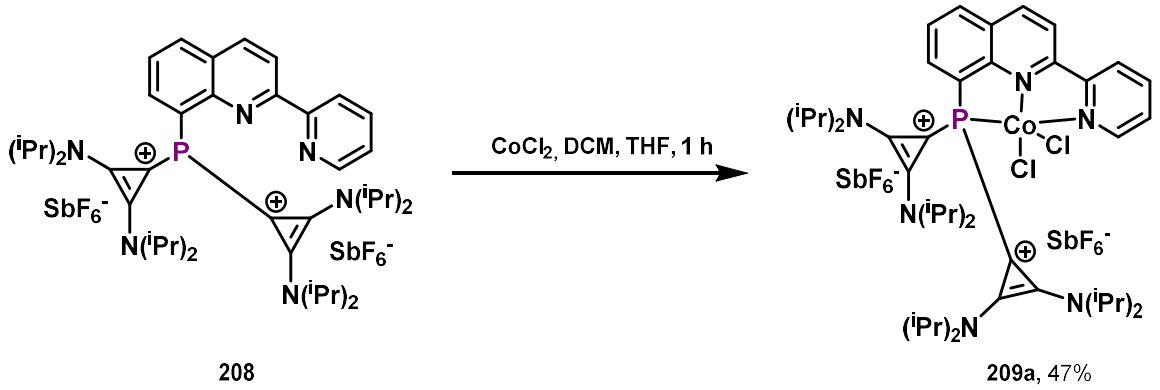

208 **209a**, 47%

*Scheme 65: Coordinating dicationic PNN pincer ligand **208** to Co(II)*

To synthesize the Co(II)-precatalyst, $CoCl_2$ was reacted with THF to obtain a suitable metal precursor to further react with ligand **208** (Scheme 65). The ligand was therefore dissolved in DCM and slowly added to the $Co_4Cl_8(THF)_6$ solution[142] to circumvent two ligands coordinating the same metal. After adding further THF to the mixture the green crystalline complex **209a** could be obtained in 47% yield.

Single crystals of **209a** suitable for X-ray diffraction could be obtained by slowly evaporating a solution of tetrahydrofuran and dichloromethane (Figure 22, left). The thus obtained green plates were systematically non-merohedrically twinned with a challenging unit cell determination due to long and overlapping unit cell axes. The final unit cell used was rather large and determined in a hexagonal crystal system and space group R-3. The asymmetric unit consists of two equivalents of molecule **209a**, four SbF_6 anions of which two are on general positions and the other two split on several special positions with 1/3 or 2/3 occupancies, breaking possible symmetry, and presumably two equivalents of dichloromethane. The DCM position however is obscured by problematic disorder and model refinement led to occupancy less than 1 for one of the two positions, leading to the non-integer sum formula. The two crystallographically independent molecules of **209a** are chemically identical and coincide well in their geometries, with only slight differences in the conformations of the terminal CH_3-groups. Hence, only the geometry of one is used in the course of this further discussion.

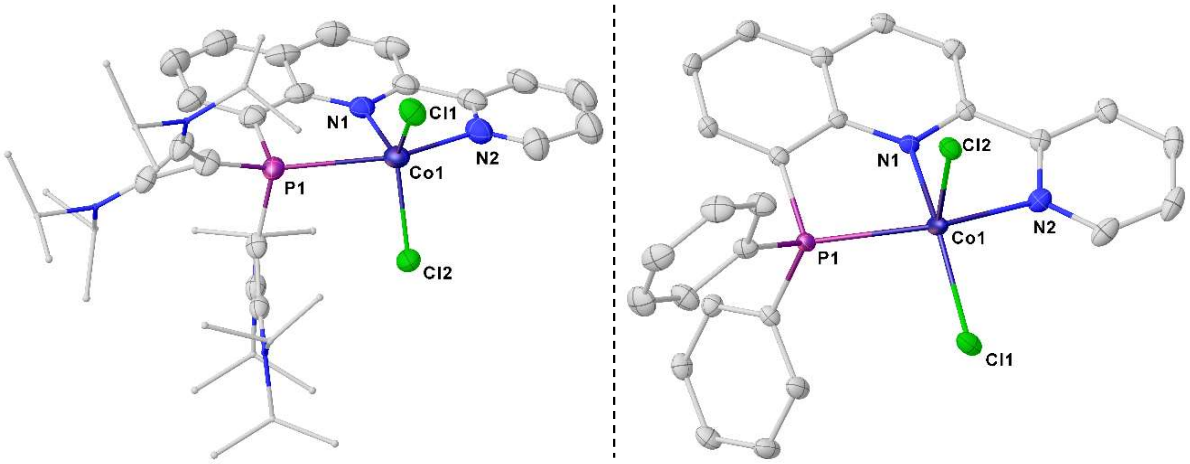

*Figure 22: Molecular structures of **209a**[3] (left) and corresponding neutral biphenyl complex **209b**[4] (right). Thermal ellipsoids at 50% probability level. Hydrogen atoms, non-coordinating counter anions, co-crystallized solvent molecules and second molecule in asymmetric unit in both cases omitted for clarity.*

Table 1: Comparison of molecular geometry metrics (Figure 22).

	209a	**209b**	**209c**[129]	**209d**[129]
M–P [Å]	2.667(3)[/2.670(3)]	2.375(1)/2.460(1)	2.442(1)	2.506(1)
M–N(quinoline) [Å]	2.074(8)[/2.078(9)]	2.046(2)/2.130(2)	2.097(1)	2.086(3)
M–N(Py) [Å]	2.070(8)[/2.073(8)]	2.072(2)/2.105(2)	2.138(1)	2.100(3)
M–Cl^{axial} [Å]	2.255(2)[/2.255(2)]	2.328(1)/2.301(1)	2.318(1)	2.342(1)
M–Cl^{basal} [Å]	2.245(3)[/2.244(3)]	2.267(1)/2.308(1)	2.300(1)	2.304(1)
Geometry index τ_5	0.5853/0.5865	0.0303/0.048	0.4396	0.2676
RMSD [Å]	0.046/0.046	0.049/0.078	0.038	0.040

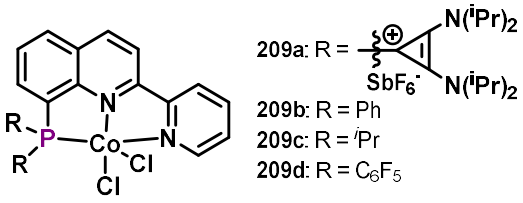

[3] **Crystal Data** for **209a** ($C_{44.166667}H_{65.333333}Cl_{2.833333}CoF_{12.000556}N_6PSb_2$; *M* =1342.21 g/mol): trigonal, space group R3 (no. 146), *a* = 21.0339(13) Å, *c* = 66.548(5) Å, *V* = 25498(4) Å^3, *Z* = 18, *T* = 100.01 K, μ(MoKα) = 1.473 mm^{-1}, *Dcalc* = 1.573 g/cm^3, 67603 reflections measured (4.286° ≤ 2Θ ≤ 53.998°), 24644 unique (R_{int} = 0.0237, R_{sigma} = 0.0286) which were used in all calculations. The final R_1 was 0.0657 (I > 2σ(I)) and wR_2 was 0.1960 (all data).

[4] **Crystal Data** for **209b** ($C_{26}H_{19}Cl_2CoN_2P$; *M* =520.23 g/mol): monoclinic, space group $P2_1/c$ (no. 14), *a* = 16.018(6) Å, *b* = 15.183(6) Å, *c* = 18.598(5) Å, *β* = 90.017(8)°, *V* = 4523(3) Å^3, *Z* = 8, *T* = 99.96 K, μ(MoKα) = 1.083 mm^{-1}, *Dcalc* = 1.528 g/cm^3, 64376 reflections measured (4.296° ≤ 2Θ ≤ 59.236°), 12677 unique (R_{int} = 0.0478, R_{sigma} = 0.0395) which were used in all calculations. The final R_1 was 0.0379 (I > 2σ(I)) and wR_2 was 0.0817 (all data).

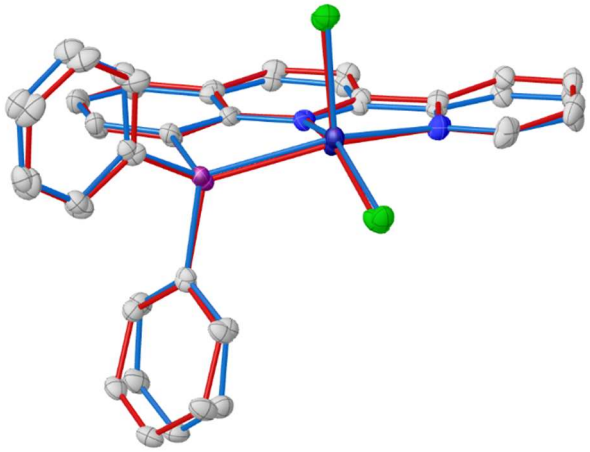

*Figure 23: Overlay of both crystallographically independent molecules of **209b** in the solid state.*

Compound **209b** was crystallized from DCM by slow evaporation to yield green blocks. The unit cell contains two equivalents of **209b** that upon close inspection reveal dissimilarities in their geometries. This is especially apparent from the molecular overlay (see Figure 23). The molecule featuring the longer P─Co, Cl─Co and N─Co bonds is in high-spin state, while the other one is in low-spin. This is a rare but not unprecedented phenomenon, known in literature for other 3d-metal complexes.[143]

To study the influence of the cationic charges the crystal structures of **209a** is compared with the diphenyl substituted analog **209b**. Furthermore, a comparison with the ^{i}Pr (**209c**) and ArF (**209d**) substituted analogs submitted by Rauchfuss and coworkers during my research using the identical backbone will be drawn.[129]

For d^7 five-coordinate Co(II) complexes high, low and equilibrium (crossover) spin states are known to literature.[129,144] The spin state correlates strongly with the nephelauxetic effect of the donor atoms e.g. the halides. Using chlorides frequently results in high-spin complexes. The geometries also differ from square pyramidal and trigonal bipyramidal to intermediate geometries influenced by the sterics of the ligand.

All complexes reported herein share a $[N_2PCl_2]$ pentacoordinate environment, but also differ in their geometry. To describe their structure, which as expected is positioned between square pyramidal and trigonal bipyramidal, the geometry index τ_5 proposed by Addison *et al*. is used.[145] τ_5 can adopt values between 0 and 1 indicating if the structure is more similar toward a square pyramid or a trigonal bipyramid, respectively. As can be seen in Table 1 the electronic nature of the substituent at the phosphorus does not clearly correlate with the geometry. However, it can be hypothesized that the very bulky cyclopropenylidenium moiety in the dicationic phosphine leads to a more trigonal bipyramidal structure (τ_5 = 0.5853) to release steric strain. The trend that the better π-accepting properties lead to a less predominant square pyramidal structures can be discarded due to that fact that the isopropyl substituted ligand results also in a more trigonal bipyramidal structure (τ_5 = 0.4396[129]). This might also be a result of sterics but depending on the literature reference the steric bulk of two phenyl vs. two isopropyl groups is hard to compare.[146] Comparing the M─P bond lengths, the influence of the substituents becomes evident. The better π-accepting phosphines with electron withdrawing substituents show elongated Co─P distances (**209a** and **209d**). Furthermore, in the case of the dicationic phosphine the distance of the other donor atoms N1,N2;Cl1,Cl2 to the Co center shrinks compared to the others to compensate the enhanced electrophilicity at the metal center.

A suitable measure of the planarity of these ligands is the root mean square distance (RMSD) of the atoms P1─C─C─N1─C─C─N2 to their common plane.[129] In all cases the RMSD values are close to zero, confirming the coplanarity and rigidity of the ligand motif.

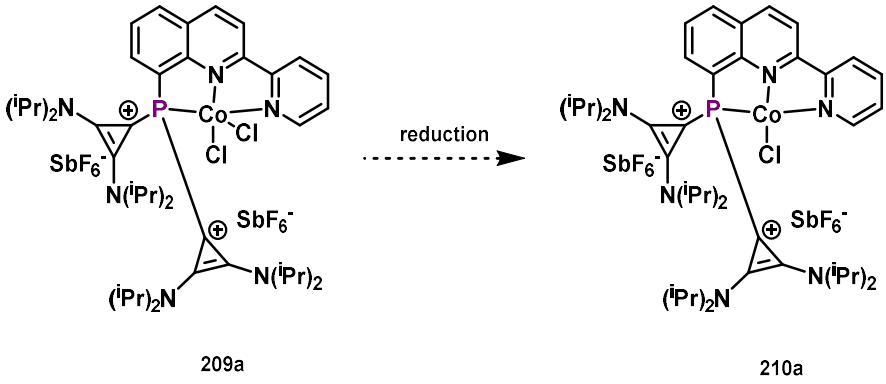

*Scheme 66: Reduction of compound **209***

With the dicationic Co(II) precatalyst **209a** at hand, the reducibility towards an active Co(I) catalyst **210a** could be investigated (Scheme 66). Therefore cyclic voltammetry was applied to complex **209a** giving insights into its redox behavior. The cyclic voltammogram was recorded in an electrolyte solution (0.1 M $[NBu_4][PF_6]$ in MeCN) at a scan rate of 100 mV/s under nitrogen.

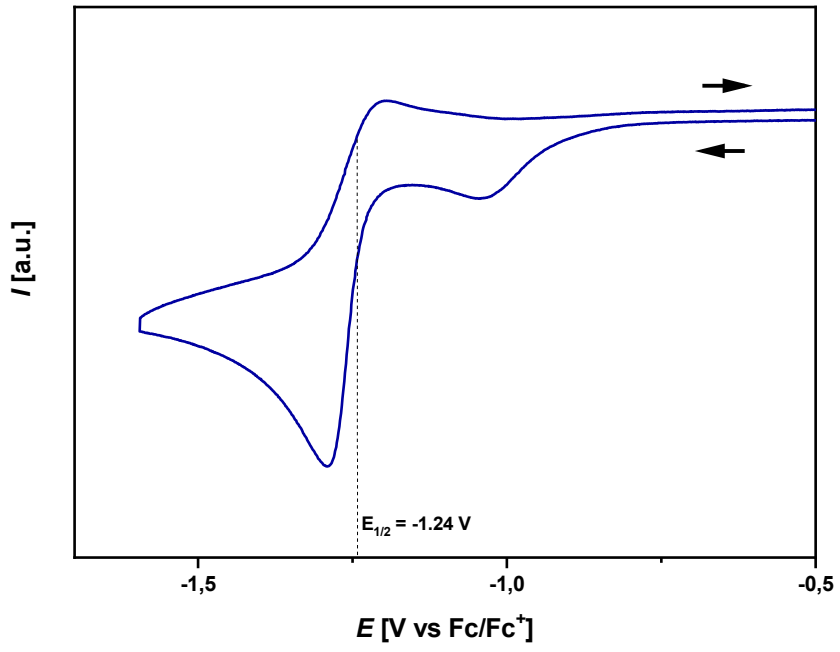

*Figure 24: Cylic voltammogram of **209a** at a scan rate of 100 mV/s*

The voltammogram shows three reductions (see experimental section). The first reduction (shown in Figure 24) is irreversible ($E_{1/2}$=-1.24 V vs. Fc/Fc^+), while the two following reductions seem to be quasi-reversible ($E_{1/2}$=-1.86 V, $E_{1/2}$=-2.06 V vs. Fc/Fc^+). Assuming that the first reduction is the Co(II) to Co(I) reduction, which is accompanied by the dissociation of one chloride ligand, the irreversibility can be rationalized.

To reduce the actual compound **209a** to a useful catalyst for hydrosilylation or hydroboration different reagents were tried, which have been reported as successful in literature. To our regret neither $NaBH_4$ nor $NaHBEt_3$ nor Zn could lead to the target complex **210a**. Especially the increased solubility of the resulting mixtures in non-polar solvents made it unlikely that the cationic charged cyclopropenylium moieties survived the reducing reaction conditions. To get further insights into the reaction and potential products the reaction mixture of the zinc reduction was dissolved in dichloromethane and crystallization forced by diffusing pentane into the solution. Tiny single crystals of **210a** were obtained, however their suitability for diffraction experiments was rather limited for their poor diffraction properties. Thus, the presented molecular structure represents only a preliminary result and is to be viewed with care, a detailed geometry analysis will not be attempted here. **210a** crystallizes in space group *C*2/c as a perfectly C2-symmetric complex with half of the molecule, as well as the anion and one dichloromethane, constituting the asymmetric unit (Figure 25, left).

Crystals of **210b** were obtained as opaque blocks by reduction of **209b** with Zinc and subsequent layering of the deep black THF solution with pentane. Due to technical limitations at that time, the data collection was performed at room temperature (Figure 25, right).

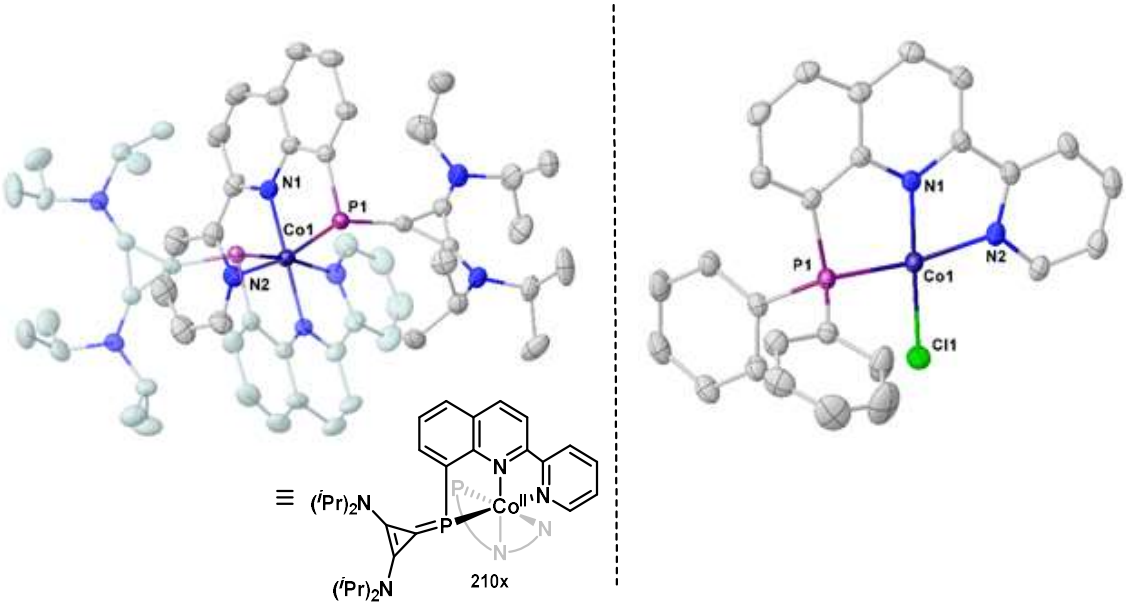

*Figure 25: Molecular structures of **210x**[5] (left) and corresponding reduced neutral biphenyl Co(I) complex **210b**[6] (right). Thermal ellipsoids at 20% and 30% probability level, respectively. Hydrogen atoms, non-coordinating counter anions and co-crystallized solvent molecules omitted for clarity; second half of the C2 symmetric **210a** generated by symmetry drawn translucent. Selected bond length (Å) and angles (°) for **210b**: P1—Co1 2.163(1), P1—Cl1 2.196(1), P1—N1 1.832(1), P1—N2 1.943(1), ∡P1—Co1—N1 86.4(1), ∡N1—Co1—N2 82.1(1).*

As can be seen in Figure 25 (left) the complex **209a** was reduced to **210x**. However, the reduction was not metal-based as expected, but one of the cyclopropenylium moieties was reductively cleaved from

[5] **Crystal Data** for **210x** ($C_{59}H_{76}Cl_2CoF_{12}N_8P_2Sb_2$; *M* =1560.54 g/mol): monoclinic, space group C2/c (no. 15), *a* = 33.1838(18) Å, *b* = 11.2289(5) Å, *c* = 25.8131(15) Å, *β* = 123.2400(10)°, *V* = 8044.7(7) Å^3, *Z* = 4, *T* = 298.65 K, μ(MoKα) = 1.041 mm^{-1}, *Dcalc* = 1.288 g/cm^3, 24706 reflections measured (4.68° ≤ 2Θ ≤ 52.866°), 8170 unique (R_{int} = 0.0899, R_{sigma} = 0.0932) which were used in all calculations. The final R_1 was 0.1164 (I > 2σ(I)) and wR_2 was 0.3876 (all data).

[6] **Crystal Data** for **210b** ($C_{26}H_{19}ClCoN_2P$; *M* =484.78 g/mol): monoclinic, space group $P2_1/n$ (no. 14), *a* = 10.3651(9) Å, *b* = 16.8319(12) Å, *c* = 12.3935(11) Å, *β* = 96.483(4)°, *V* = 2148.4(3) Å^3, *Z* = 4, *T* = 298.04 K, μ(MoKα) = 1.014 mm^{-1}, *Dcalc* = 1.499 g/cm^3, 28704 reflections measured (4.84° ≤ 2Θ ≤ 61.052°), 6552 unique (R_{int} = 0.0201, R_{sigma} = 0.0179) which were used in all calculations. The final R_1 was 0.0300 (I > 2σ(I)) and wR_2 was 0.0844 (all data).

the molecule and two PNN pincer ligands now coordinate towards one Co(II). Of course this result does not represent the whole mixture of compounds in solution but gives a hint towards the instability of the P─C (cyclopropenylidene) bond towards reduction or metals in low oxidation states.[147,148] The stability of the ligand backbone could be verified by the reduction of the diphenylsubstituted cobalt complex **209b** to give **210b**. The crystals show a successful reduction towards the Co(I) d^8-species in a square planar geometry (τ_4[149]= 0.1116, τ_4'[150]=0.0778).

To summarize, it could be shown that dicationic phosphorus ligands can be coordinated towards 3d metals by installing two more coordinating donor atoms to achieve a tridentate pincer ligand. But on the other hand the cyclopropenylidene substituted phosphine were prone to C─P bond cleavage during reduction or use of a metal in low oxidation states.[147] Beside the low stability they also suffer from an elaborate synthesis and are not so easy to modify. Exchanging the cyclopropenylidene moieties for different carbene substituents with stronger P─C bonds could not be achieved, so their use in catalysis with metals in low oxidation states is questionable. Furthermore, the ligand backbone was already investigated and published by Rauchfuss and coworkers.

2.4 Project II: Cationic encapsulating phosphines - Motivation

With the limited success of the PNN pincer system in the intent of building an α-cationic phosphine ligand, and the encountered problems in its synthetic feasibility, the basic premise was partially changed. Instead of installing cationic groups, which were the main cause of the problems, a bimetallic system is envisaged, where the first metal (M_1^{n+}) "charges" the system and enables the phosphorus, until then not yet included in ligation, to coordinate a second metal (M_2) generating a catalytically active center (Scheme 67).

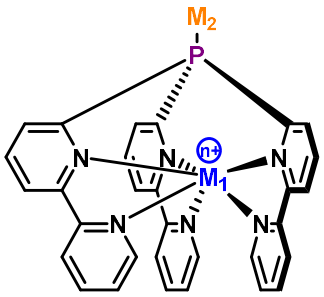

210

Scheme 67: Cationic encapsulating phosphines as ligands

The first metal (M_1^{n+}) is therefore responsible for adjusting the electronic properties of the phosphine and has an indirect influence on the catalytically active metal center (M_2). The bimetallic system should be easily fine-tuned without much synthetic effort. Thus, the encapsulated metal (M_1^{n+}) can be exchanged for another (M'_1^{n+}), or redox-switched in the case of redox active encapsulate metal (M_1^{n+x}). The positive charge of M_1^{n+} and the change in pyramidalization resulting from the encapsulation, should lead to cationic phosphine ligands with weak σ-donor abilities and strong π-acceptor abilities, which then make the catalytically active metal center M_2 particularly electrophilic and suitable for π acid catalysis (Au, Pt).

2.5 Synthesis of encapsulating preligands

To synthesize this bimetallic complexes **210** different strategies are possible, but all of them start from the hexadentate cryptand-like phosphine **212** which was already published by Holm and coworkers in only 17% yield.[123,151]

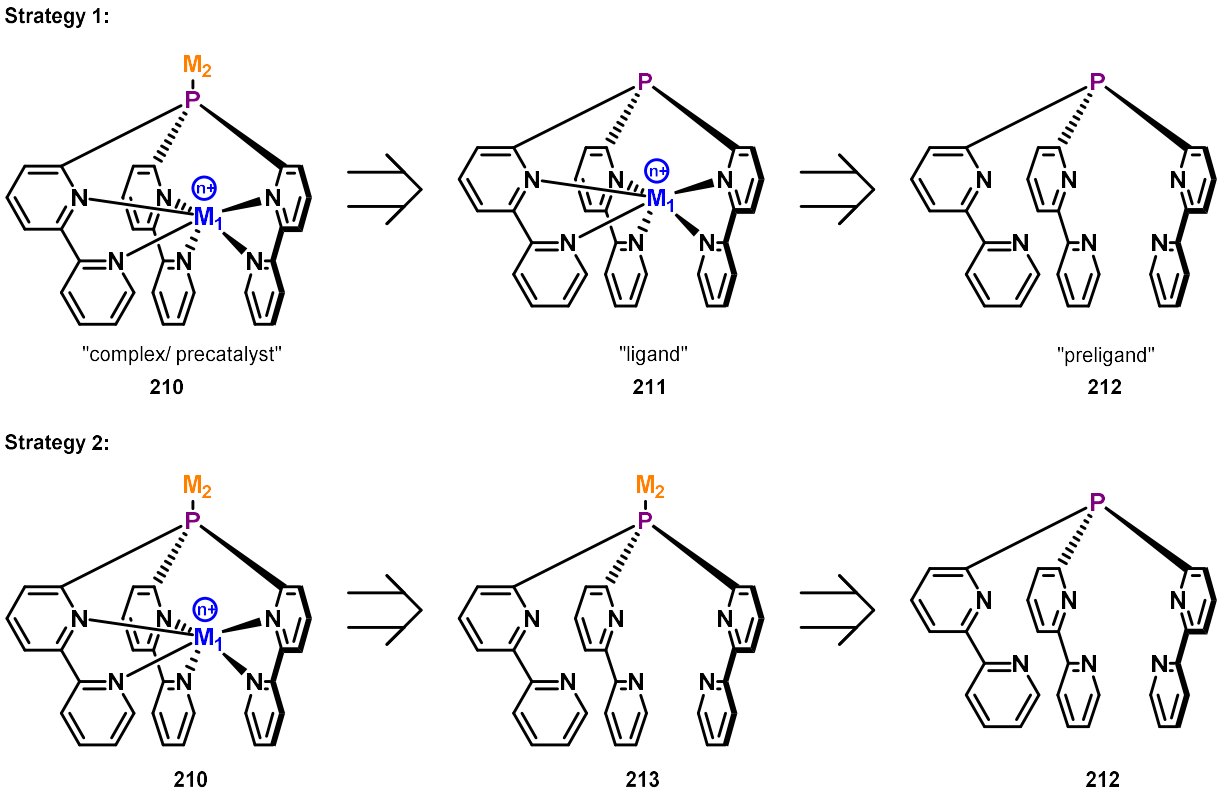

Scheme 68: Synthetic strategies for bimetallic complexes

Both presented strategies show benefits and should be tested (Scheme 68). The first strategy allows to synthesize a library of different ligands, which can be used in combination with different metals M_2, while strategy 2 allows the modification of the ligand while already attached to a catalytic metal. For the first approach we will focus on strategy 1, but also show later that strategy 2 is valid. To easier identify each synthon the hexadentate cryptand-like phosphine will be called preligand **212**, while the combination of preligand and M_1^{n+} **211** will be called ligand of the later attached M_2.

The low yield of the preligand with only 17% yield is a problem, which needs to be addressed first, because the price of a catalyst is not only determined by the metal used but also by the price of the ligand. Therefore we wanted to improve the method of Holm and coworkers and also to develop a completely new one to easily access a preligand in less steps.

The most straightforward method to start with is the heterolytic disconnection leading to a formal P^{3+} cation (Scheme 69, left, red). This approach was also used by Holm and coworkers.[123] The synthetic equivalent of P^{3+} would be PCl_3, which can be attacked by 6-lithio-2,2'-bipyridine **216** as nucleophile.

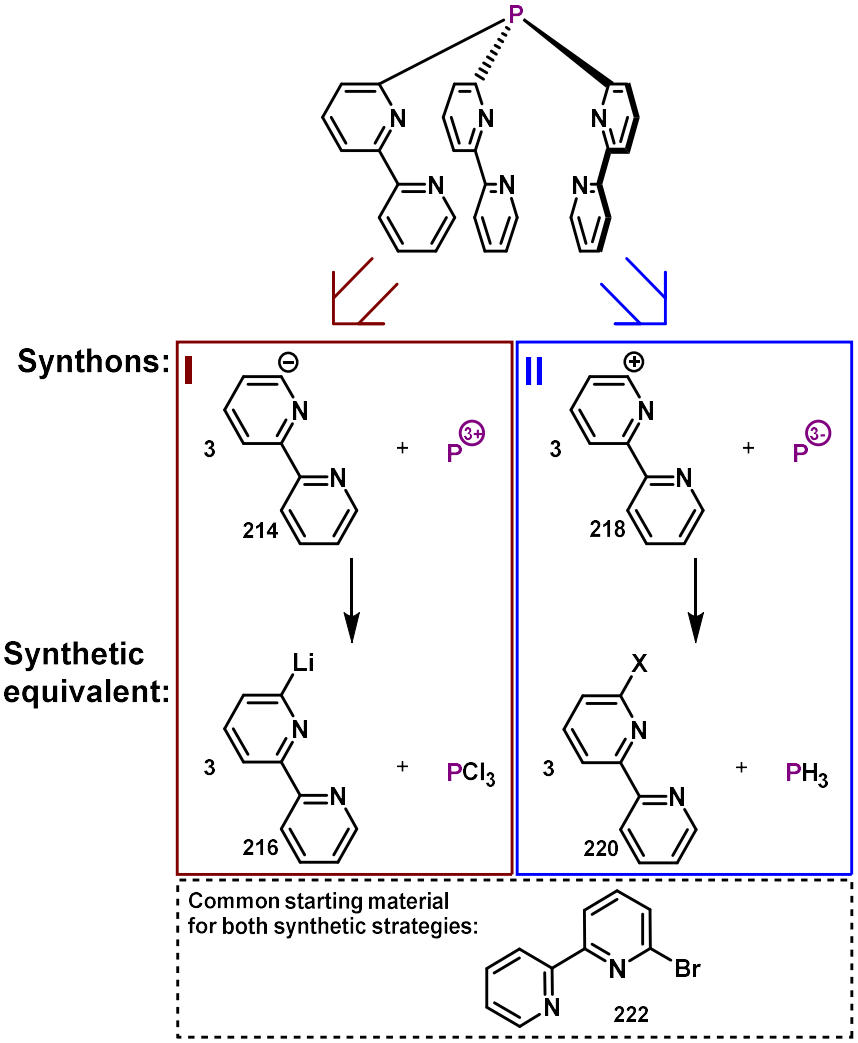

*Scheme 69: Disconnection approach of preligand **212***

The protocol of Holm and co-workers was modified by changing the reaction temperature and altering the purification procedure, thereby increasing the yield to 44% (Scheme 70). To work up the raw material column chromatography is needed. Due to the fact that the compound is prone to oxidation, purification on air needs to be performed quickly. As the starting material for the lithiated 2,2'-bipyridine both, Holm and us, started from 6-bromo-2,2'-bipyridine **222** treated with ^{n}BuLi in diethyl ether.

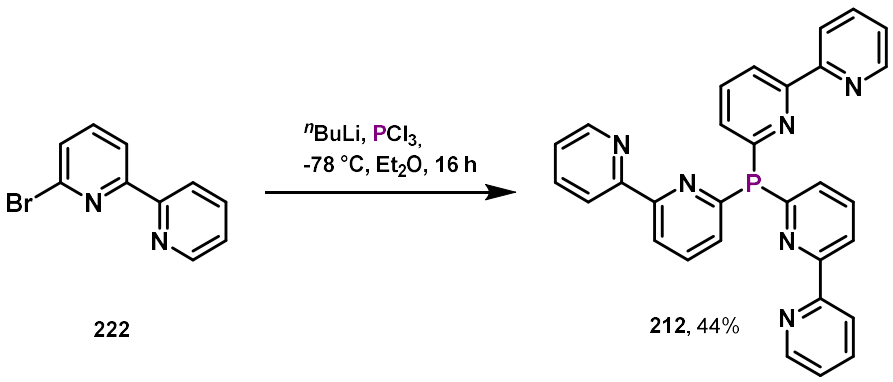

*Scheme 70: Synthesis of preligand **212**.*

The second heterolytic disconnection approach leads to a P^{3-} synthon or PH_3 synthetic equivalent (Scheme 69, right, blue). The use of phosphine gas in laboratory is rare, because it is highly toxic, hard to handle and under most synthetic conditions pyrophoric. Therefore in the laboratories of Trofimov a protocol for the synthesis of phosphines was developed starting directly from red or white phosphorus.[152–154] This method based on the Trofimov–Gusarova reaction conditions is assumed to proceed *via* P─P bond cleavage by the superbasic media (KOH/DMSO). Nucleophilic attack of *in situ* generated polyphosphide **226** and polyphosphinite **227** particles towards 2-bromopyridine **229** can then lead to *e.g.* tri(2-pyridyl)phosphine **232** or its phosphine oxide **233** (Scheme 71).[154] Using red phosphorus and the right electrophile can suppress the formation of phosphine oxides.

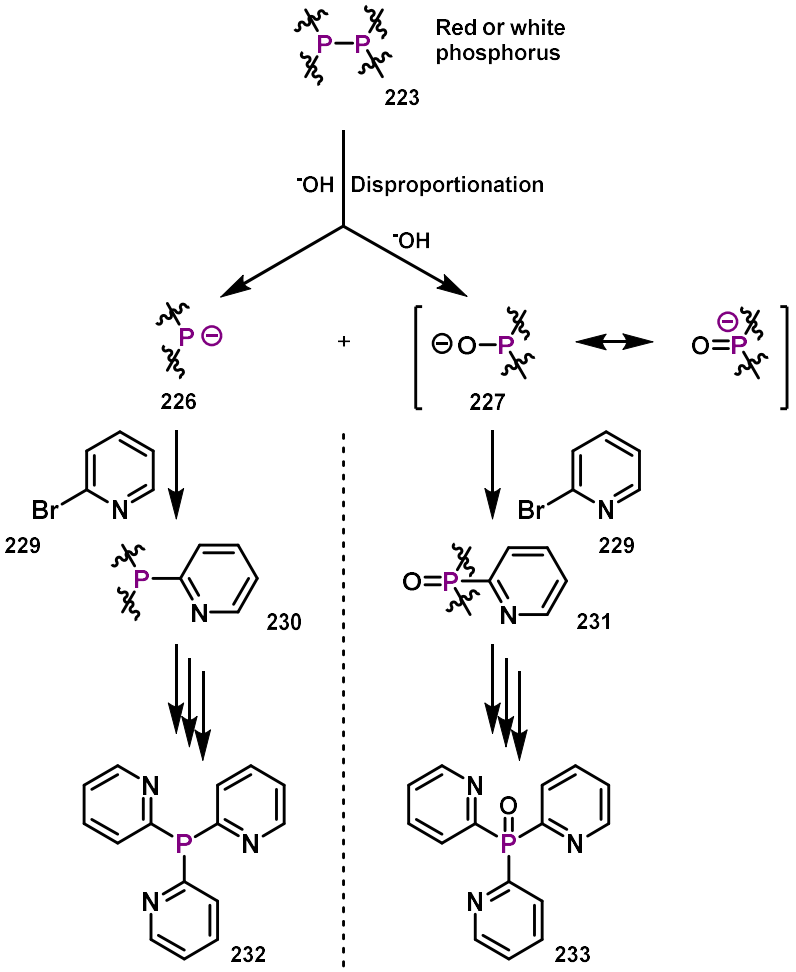

Scheme 71: Mechanism of Trofimov–Gusarova reaction using tri(2-pyridyl)phosphine as an example[154]

A similar approach was now developed and optimized for 6-bromo-2,2'-bipyridine. The preligand **212** could be isolated in 46% yield (Scheme 72). The corresponding phosphine oxide was also formed during the reaction but just as the minor product, which could be removed by recrystallization from toluene. The crystals obtained in the form of colorless plates were suitable for X-ray diffraction and the connectivity of **212** could be confirmed.

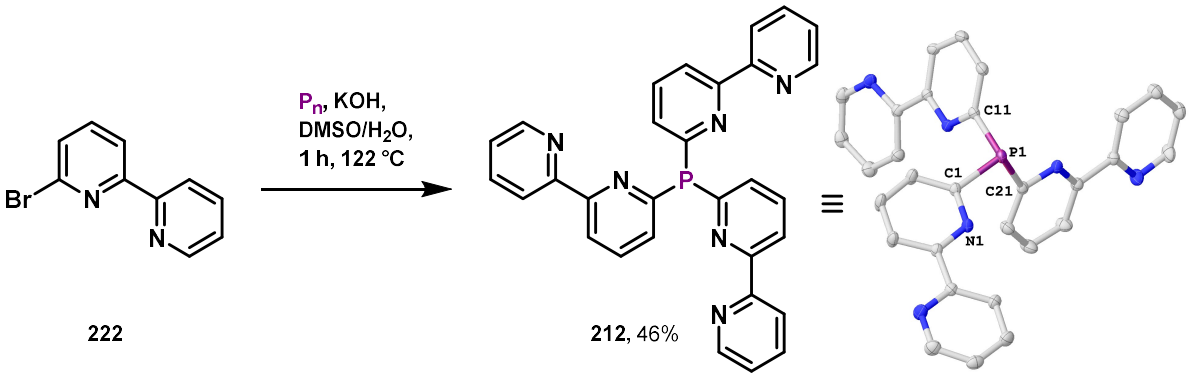

*Scheme 72: Synthesis of preligand **212** via Trofimov–Gusarova reaction. Molecular structure of **212**[7] (right). Thermal ellipsoids at 50% probability level. Hydrogen atoms omitted for clarity. Selected bond length (Å) and angles (°) for **212**: P1—C1 1.838(1), P1—C11 1.844(1), P1—C21 1.841(1), ∡C1—P1—C11 101.8(1), ∡C11—P1—C21 96.8(1), ∡C1—P1—C11 103.8(1), Cone angle 175°, %V_{Bur} = 32.1 (2.00 Å) [27.3 (2.28 Å)].*

Both methods start with 6-bromo-2,2'-bipyridine **222**. This starting material can either be synthesized *via* Stille coupling of 2,6-dibromopyridine **225** and 2-(tributylstannyl)pyridine **224** (79%[155], Strategy I, Scheme 73), which involves toxic stannanes, the use of Pd(0) and the need to also synthesize the stannane itself or it can be synthesized by a three step sequence of methylation (79%[156]), oxidation (77%[156]) and bromination (86%[156]) staring from 2,2'-bipyridine **228a** (Strategy II, Scheme 73).

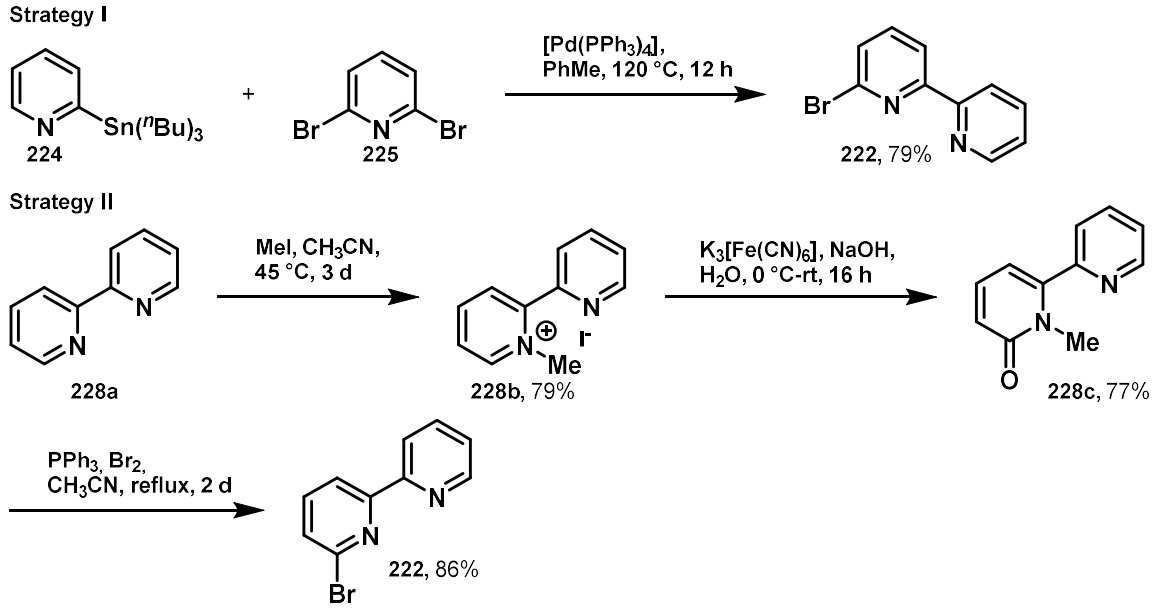

*Scheme 73: Strategies towards **222**, yields taken from literature[155,156]*

Therefore, apart from κ⁶-preligand **212**, κ⁶-preligand **237** was developed, which has strategically installed methyl groups and thus combines fewer synthesis steps and higher yields.

[7] **Crystal Data** for **212** ($C_{30}H_{21}N_6P$; *M* =496.50 g/mol): monoclinic, space group $P2_1/n$ (no. 14), *a* = 12.8993(14) Å, *b* = 11.5311(11) Å, *c* = 17.2403(19) Å, *β* = 105.668(4)°, *V* = 2469.1(5) Å³, *Z* = 4, *T* = 100.02 K, μ(MoKα) = 0.143 mm^{-1}, *Dcalc* = 1.336 g/cm³, 80015 reflections measured (4.3° ≤ 2Θ ≤ 63.046°), 8222 unique (R_{int} = 0.0252, R_{sigma} = 0.0139) which were used in all calculations. The final R_1 was 0.0370 (I > 2σ(I)) and wR_2 was 0.1056 (all data).

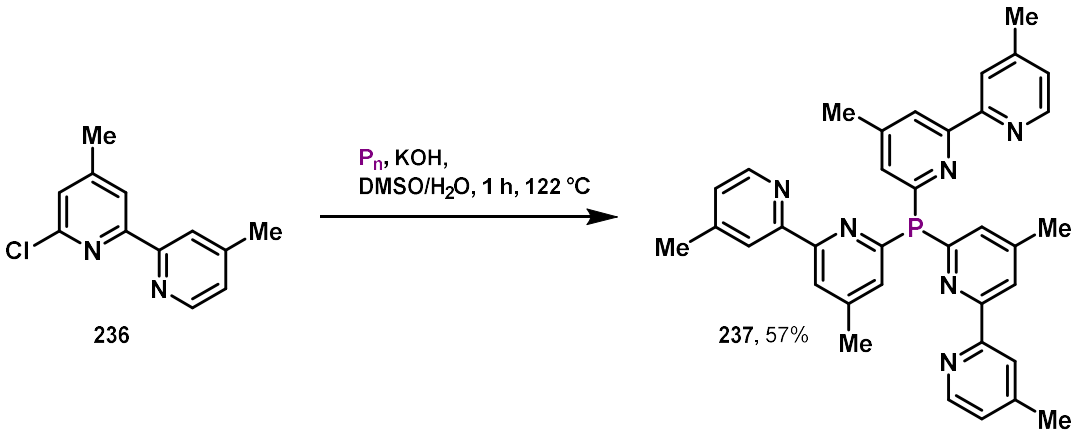

Scheme 74: Synthesis of preligand 237 via Trofimov–Gusarova reaction

Starting from 6-chloro-4,4'-dimethyl-2,2'-bipyridine **236** instead of 6-bromo-2,2'-bipyridine combines multiple benefits. It has been shown that using chlorides instead of bromides suppresses the formation of phosphine oxides during Trofimov–Gusarova reaction.[154] Furthermore, 6-chloro-4,4'-dimethyl-2,2'-bipyridine is easy to synthesize *via* a two-step procedure of oxidation (77%[157]) and chlorination (80%[157]) without the need of palladium catalysis nor toxic stannanes (Scheme 75).

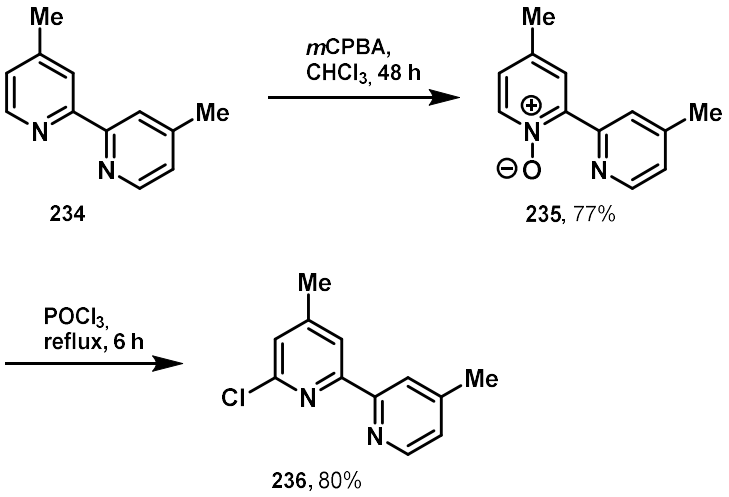

*Scheme 75: Synthesis of starting material **236** via two step procedure, yields taken from literature[157]*

Beside the fact that the methyl groups reduce the amount of steps needed to synthesize 6-chloro-4,4'-dimethyl-2,2'-bipyridine by blocking the 4 and 4' positions, they also make the preligand **237** quite soluble in non-polar solvents. This positive side-effect might become important later, when highly charged complexes used in π-acid catalysis need to stay in solution even after activation. The new preligand **237** could be synthesized by Trofimov–Gusarova reaction in even better yields, removing the small amounts of phosphine oxide formed by washing with cold methanol.

2.6 Synthesis, geometry, steric measure and switchability of cationic phosphine ligands with encapsulated metals

With the κ^6-preligands at hand, different metals can be encapsulated. This was already shown by Holm and coworkers using preligand **212**.[123] They could synthesize complexes encapsulating Fe(II), Co(II), Ni(II) and Cu(II). The bridging phosphorus atom serves as a connector/ anchoring atom between the three 2,2'-bipyridin-6-yl moieties, implying rigidity in the ligand structure, and was only used to compare structural trends between trigonal-prismatic and trigonal-antiprismatic (octahedral) motifs in their clathrochelates. For their comparison (also to other hexadentate complexes) stereochemic and electronic considerations were taken and tried to proof with electronic spectra, polarography, Mössbauer spectra and paramagnetic NMR. This resulted in proposed structures in solution. None of the above mentioned complexes was either used as a ligand nor did they provide any X-ray structural data regarding these complexes. In the following chapter, the coordination capabilities of preligand **212** as well as the new preligand **237** will be analyzed and extended to other metals. Furthermore, the synthesis, switchability, solid-state structure and steric measure of the encapsulating hexadentate complexes as ligands will be discussed.

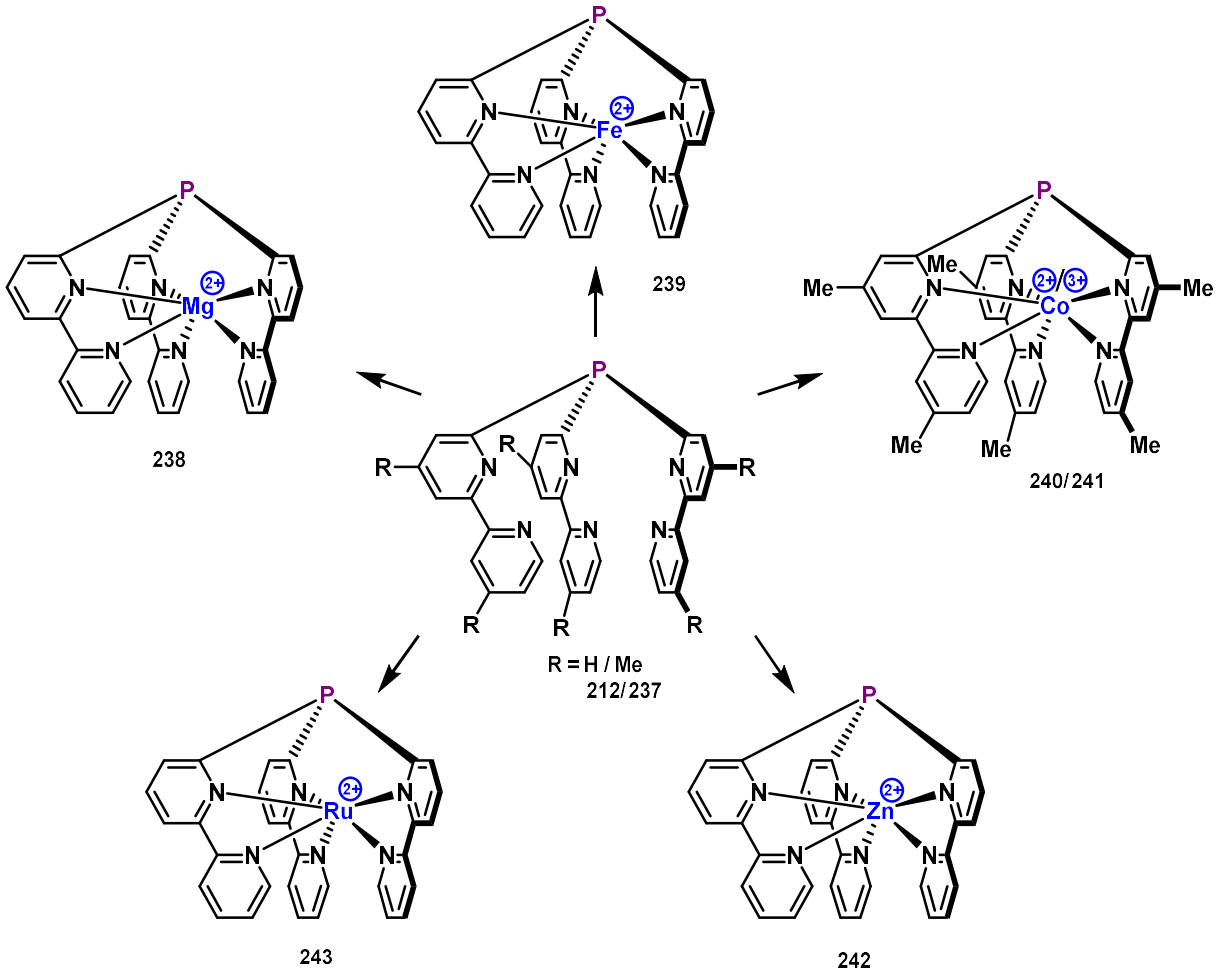

Scheme 76: Cationic phosphine ligands with encapsulated metals

In this context Na^+, Mg^{2+}, Fe^{2+}, Co^{2+}, Co^{3+}, Zn^{2+}, Ru^{2+}, Ca^{2+}, Sc^{3+} Cu^+ and La^{3+} could be coordinated. While the solid structure of the sodium ligand stays unknown, the others could be crystallized and studied with single-crystal X-ray diffraction. Ligands of the Elements Mg^{2+}, Fe^{2+}, Co^{2+}, Co^{3+}, Zn^{2+} and Ru^{2+} represent structures between trigonal-prismatic (TP) and trigonal-antiprismatic (TAP) motifs while Sc^{3+}

Cu^{+} and La^{3+}differ from these by coordinating additional triflates or preferring a phosphorus coordination. In the following, we will therefore first discuss the TP and TAP structures and then move on to the more complex structures.

2.6.1 Trigonal prismatic and trigonal antiprismatic encapsulation

2.6.1.1 Synthesis and characterization in solution

2.6.1.1.1 Encapsulation of Mg^{2+}

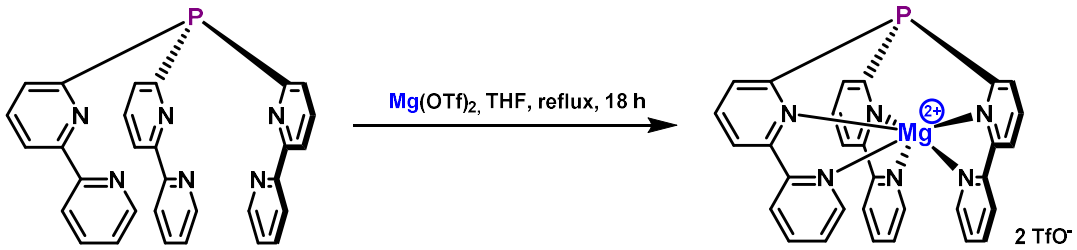

212 **238**, 87%

*Scheme 77: Synthesis of **238***

Beside alkali metals like sodium (in form of $NaBArF_{24}$) also alkaline earth metal can be coordinated (Scheme 77). Therefore a slightly under-stoichiometric amount of corresponding metal triflate and the preligand **212** are refluxed in THF. Starting from $Mg(OTf)_2$ the magnesium based ligand can be obtained in 87% yield. The ^{1}H-NMR reveals a highly symmetric structure of the product in solution, which can be either of C_3- (based on a TAP structure) or C_{3v}-(based on a TP structure) symmetry. The proton-coupled ^{31}P-NMR shows an upfield shifted quartet at -36.07 ppm, which indicates a more magnetically shielded environment of the phosphorus center similar to previously reported cationic phosphines or 9-phosphatriptycenes. This shielding can be explained by the high s-orbital character at the phosphorus lone pair caused by the strained geometry. The quartet pattern indicates the intact P─C bonds to the three 2,2'-bipyridyl moieties by showing ^{3}J-couplings towards the protons in 5 position at the 2,2'-bipyridyl substituent. The ^{19}F-NMR shows a sharp signal at -79.31 ppm, which implies fully dissociated triflates at least in solution.

2.6.1.1.2 Encapsulation of Fe^{2+}

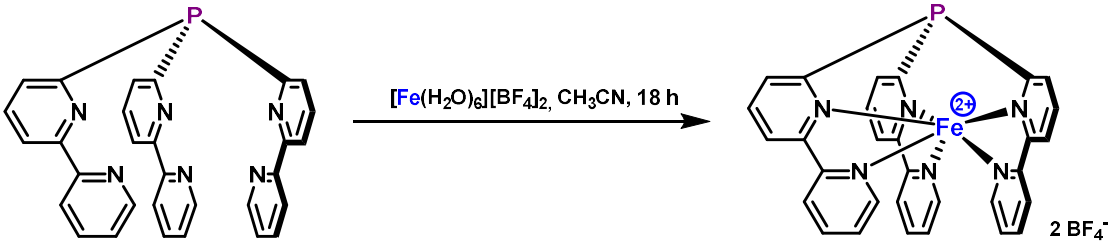

212 **239**, 85%

*Scheme 78: Synthesis of **239***

The iron-based ligand was originally synthesized in form of its perchlorate salt by Holm and coworkers.[123] To circumvent this potentially explosive chemical $[Fe(H_2O)_6][BF_4]$ was used as a metal precursor successfully leading to ligand **239** in 85% yield (Scheme 78). The ^{1}H-NMR reveals a narrow chemical shift range, but with broadened signals. This might be a result of a low-spin d^6-spin system with tendencies for thermally induced spin crossover due to relatively small ligand field splitting and

distortion.[158] (Measuring the ^{1}H-NMR spectrum at lower temperatures might result in a much sharper spectrum.)

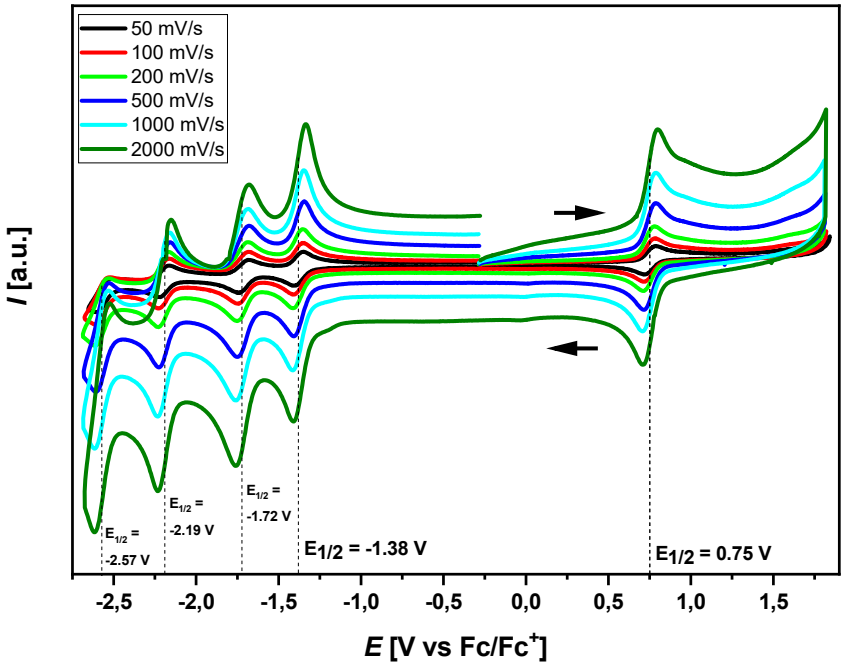

*Figure 26: Cyclic voltammogram of **239** at different scan rates (50 mV/s, 100 mV/s, 200 mV/s, 500 mV/s, 1000 mV/s and 2000 mV/s)*

By using a redox-active metal center, it seems possible to post-synthetically modify the stereoelectronic properties of the ligand by oxidation or reduction. The redox-switchability of the ligand was tested *via* cyclic voltammetry (0.1 M $[NBu_4][PF_6]$ in MeCN, Figure 26). The spectrum shows one reversible oxidation at $E_{1/2}$ = 0.75 V versus the ferrocene (II/III) couple (1.13 V vs. SCE[159]), which is related to the Fe(II)/Fe(III) oxidation. This result is comparable to the potential reported by Holm *via* polarography (*cf.* 1.16 V vs. SCE[123]) and very similar to the $E_{1/2}$ of the redox couple $[Fe(bpy)_3]^{2+}/Fe[(bpy)_3]^{3+}$ (*cf.* 0.71 V vs. Fc^{+}/Fc[160]). Additionally to the oxidation the cyclic voltammogram exhibits three reversible reductions ($E_{1/2}$ = -1.38 V, -1.72 V, -2.19 V vs. Fc^{+}/Fc) followed by a quasi-reversible fourth reduction ($E_{1/2}$ = -2.57 V vs. Fc^{+}/Fc). The former probably belongs to three ligand based reductions, which start at higher potentials compared to $[Fe(bpy)_3]^{2+}$ (*cf.* -1.75 V, -1.95 V, -2.19 V vs. Fc^{+}/Fc[160]). The redox processes (except the fourth reduction) show high reversibility and the peak-to-peak separation is relatively small and close to the optimal limit of 56 mV (20 °C, n=1, $\Delta E_p = 2.218\frac{RT}{nF}$). Moreover, the peak height/current shows a linear correlation to the square root of the scan rate, suggesting that the voltammetric current is governed by the Randles–Ševćik equation and the redox processes are chemically reversible (see experimental section).[161] These results may be an indication that the Fe^{2+}-based ligand can be tuned by oxidation to drive the acceptor properties towards the extremes resulting in a tricationic phosphine.

2.6.1.1.3 Encapsulation of Co^{2+} and Co^{3+}

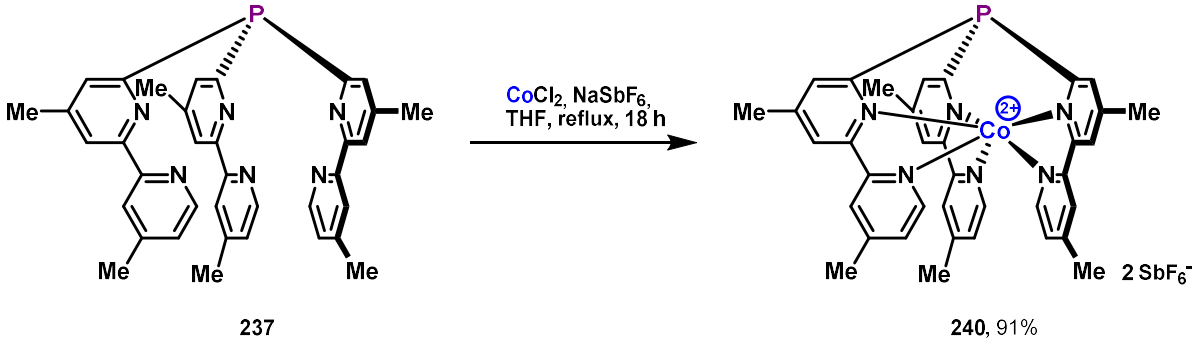

237 **240**, 91%

*Scheme 79: Synthesis of **240***

To prove the redox-switchability of this ligand class in a synthetic way a dicationic d^7 high-spin system was chosen, which can than later be oxidized to a tricationic d^6 low-spin system. To adress possible solubility issues in organic solvents the preligand was chosen to be **237**. A d^7 high-spin complex based on Co^{2+} with 3/2 ground-state spin was already published using preligand **212** by Holm.[123] They claimed an intermediate geometry between TP and TAP in solution based on ligand-field spectral data.

The ligand **240** was synthesized by heating $CoCl_2$ in THF forming a $Co_4Cl_8(THF)_6$ solution[142], which was further used to react with preligand **237** in presence of $NaSbF_6$ to obtain ligand **240** in 91% yield. The ^{1}H-NMR showed shifts from 1.09 to 366.09 ppm indicating the ligand's paramagnetic nature but due to the similarity to the system of Holm we refrained from further investigation on the susceptibility (*e.g.* by Evans method). Also, the ^{31}P-NMR spectrum showed one single downfield signal with strong deshielding at 316.57 ppm. The NMR analysis indicates a C_3-symmetric structure in solution.

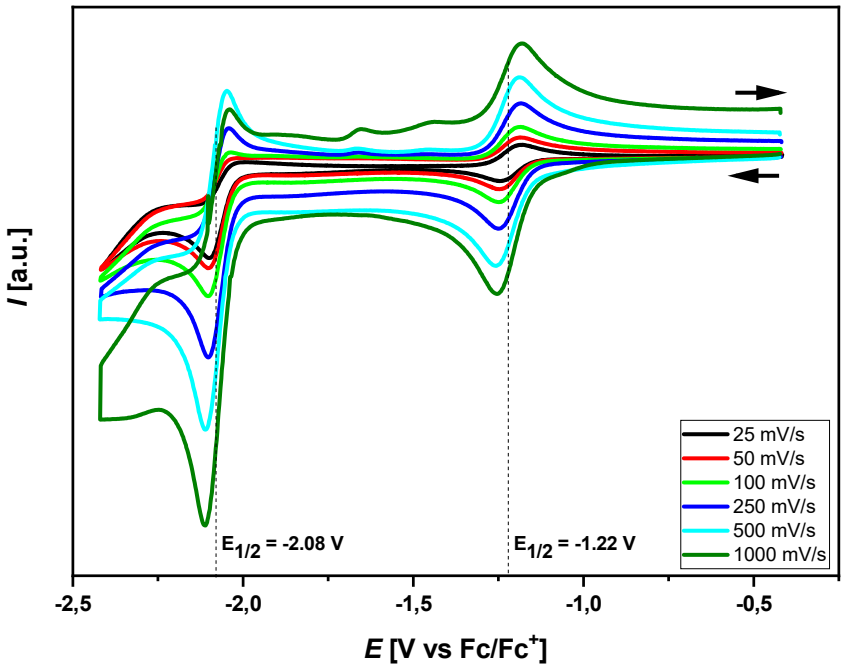

*Figure 27: Cyclic voltammogram of **240** at different scan rates (25 mV/s, 50 mV/s, 100 mV/s, 250 mV/s, 500 mV/s and 1000 mV/s)*

The cyclic voltammogram shows two reductions (Figure 27) and one oxidation (Figure 29) of the ligand (0.1 M $[NBu_4][PF_6]$ in MeCN). The reductions are at half wave potentials of -1.22 V and -2.08 V vs. the ferrocene/ferrocenium couple (-0.84 V and -1.70 V vs. SCE[159]). While the second one is an irreversible multiple electron reduction, the first one is quasi-reversible exceeding the 56 mV optimal peak-to-peak separation. The reversibility of the first Co(II) to Co(I) reduction can be increased by excluding the second reduction leading to the cyclic voltammogram in Figure 28.

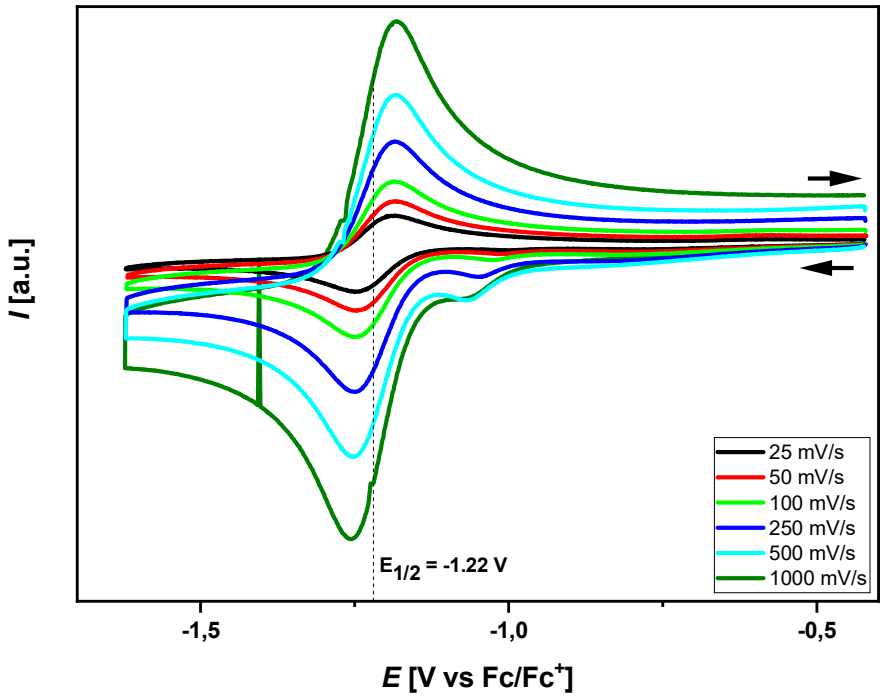

*Figure 28: Cyclic voltammogram, first reduction of **240** at different scan rates (25 mV/s, 50 mV/s, 100 mV/s, 250 mV/s, 500 mV/s and 1000 mV/s)*

The magnitude of the voltammetric current shows the expected linear behavior towards the square root of the scan rate (Randles–Ševćik equation, see experimental section).[161] According to Holm and coworkers the first reduction of $Co^{2+}(L{-}L)_3$ complexes is related to their stereochemistry.[123] In this case this finding is hard to rationalize because our results are difficult to compare to the polarography results reported (-0.66V vs. SCE for the first reduction of the unmethylated complex[123]).

To perform the planned oxidation of the ligand to tune its donor abilities, the Co(II)/Co(III) half wave potential is of high interest (Figure 29). The quasi-reversible oxidation is in the area of 0.20 V vs. the Fc/Fc^+ couple (0.58 V vs. SCE[159]). The peak-to-peak separation by far exceeds 56 mV and therefore cannot electrochemically be called strictly reversible.

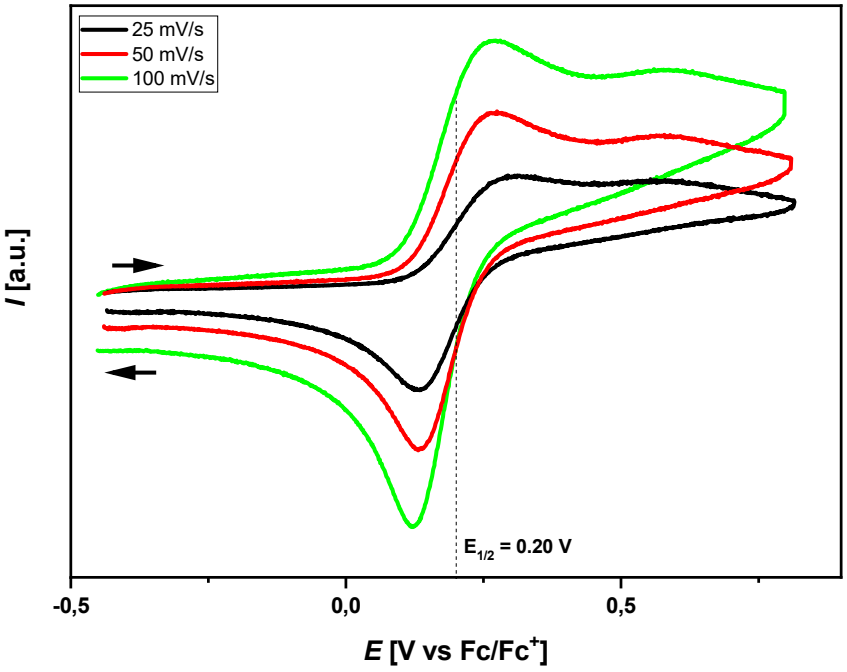

*Figure 29: Cyclic voltammogram, oxidation of **240** at different scan rates (25 mV/s, 50 mV/s and 100 mV/s)*

The solvent dependence of $E_{1/2}$, tends to be negligible for larger, coordinatively saturated compounds, therefore it should not change by using a different solvent than acetonitrile.[162] Hence, suitable oxidation agents to oxidize the Co(II) ligand to a Co(III) ligand are *e.g.* Ag^+, $NOSbF_6$ and magic blue in DCM.

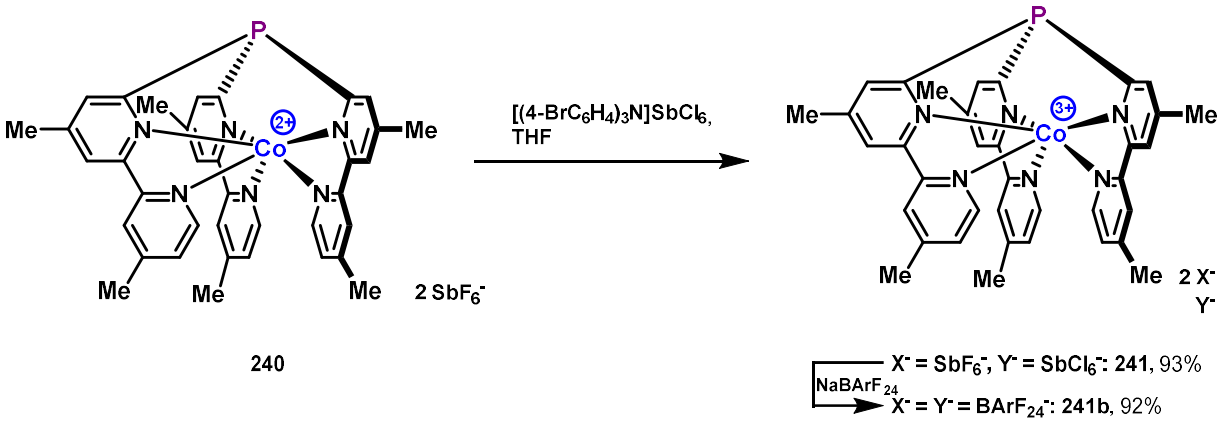

*Scheme 80: Synthesis of **241***

Since Ag^+ in DCM just leads to slow and incomplete oxidation and $NOSbF_6$ in multiple solvents shows side reactions, magic blue in THF was chosen to oxidize and directly precipitate the product. This attempt was successful and gave product **241** in 93% yield. The magic blue used as an oxidant was commercially available in form of its $SbCl_6^-$ salt leading to a product with mixed anions. An acetonitrile solution of the Co(III) ligand kept in the dark slowly decomposes, but the decomposition rate rapidly increases when exposed to light. Unfortunately, the solubility in DCM for this compound is negligible, but can be increased by exchanging the anions for $BArF_{24}^-$ (complex **241b**). The corresponding $BArF_{24}$-

salt itself is soluble in DCM, while retaining its light sensitivity. A NMR-Sample of this compound **241b** in d^2-DCM was irradiated with blue LEDs over 10 minutes and showed full conversion towards its Co(II) analog **240**.

Compound **241** itself exhibits sharp ^{1}H-NMR signals from 2.68 to 8.51 ppm indicating a C_3-symmetric diamagnetic d^6 low-spin system with high ligand field splitting. Interestingly, the ^{31}P-NMR signal shows strong deshielding (12.94 ppm) compared to its Mg^{2+} analog **238**. However, the ^{31}P-NMR signals reveal a strong correlation with the coordination geometry (TAP vs. TP) of the ligands and will thus be discussed in Chapter 2.6.1.2.

2.6.1.1.4 Encapsulation of Zn^{2+}

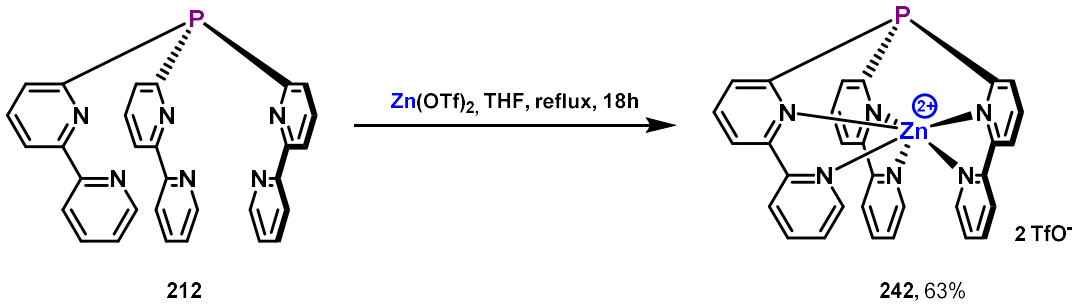

212 **242**, 63%

*Scheme 81: Synthesis of **242***

Starting from $Zn(OTf)_2$ and preligand **212** Zn^{2+}-ligand **242** can be obtained in 63% yield. The ^{1}H-NMR implies a C_3-symmetric molecule in solution. In ^{31}P-NMR one signal at -50.87 ppm can be found, which is, similar to the Mg^{2+}-ligand **238**, strongly shielded. This might be a result of the high pyramidalization (lone pair exhibits strong s orbital character).

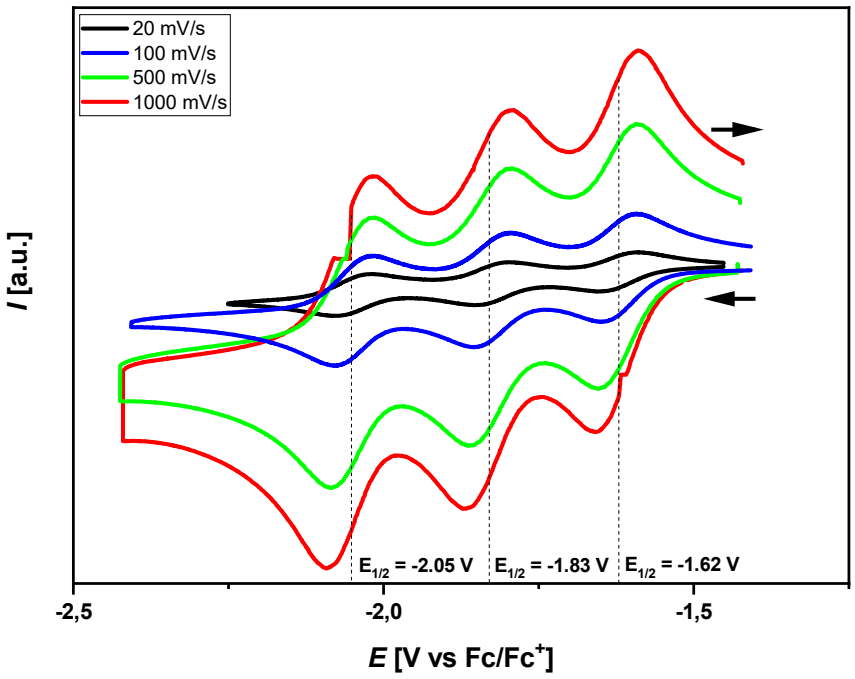

*Figure 30: Cyclic voltammogram of **242** at different scan rates (20 mV/s, 100 mV/s, 500 mV/s and 1000 mV/s)*

Cyclic voltammetry was originally planned to determine the oxidation potential as a parameter to rank the electronic properties of the ligand. Instead of finding an irreversible oxidation, which probably exceeds the solvent window for a dicationic phosphine, three quasi-reversible reductions were found (0.1 M $[NBu_4][PF_6]$ in MeCN). They probably are preligand-based and located at -1.62 V, -1.83 V and -2.05 V versus Fc^+/Fc. All three reductions surpass the theoretical peak separation value of 56 mV (20 °C) and cannot be considered as strictly reversible.

2.6.1.1.5 Encapsulation of Ru^{2+}

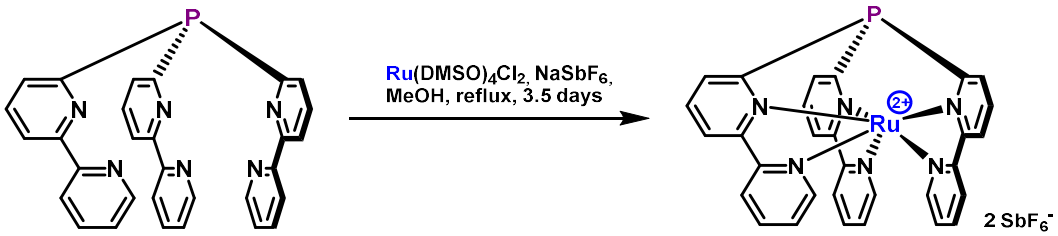

212 **243**, 67%

*Scheme 82: Synthesis of **243***

Initial attempts to synthesise **243** with various metal precursors $[RuCl_2(PPh_3)_3]$, $[Ru(NCCH_3)_6][BF_4]_2$, $RuCl_3$ and $[RuCl_3(H_2O)_3]$ failed, until $[Ru(dmso)_4Cl_2]$ was found to be a suitable substrate. The desired molecule **243** could be obtained by using preligand **212**, $NaSbF_6$ and $[Ru(dmso)_4Cl_2]$ in refluxing methanol over 3.5 days. The diamagnetic low-spin d^6 complex was analyzed *via* $^1H/^{13}C$-NMR, having seven sharp chemically non-equivalent proton- and ten sharp chemically non-equivalent carbon-signals indicating a C_3 symmetric molecule in solution. The ^{31}P NMR showed a deshielded signal at 11.85 ppm, which might indicate a related structure to the Co^{3+} ligand **241** (see Chapter 2.6.1.2).

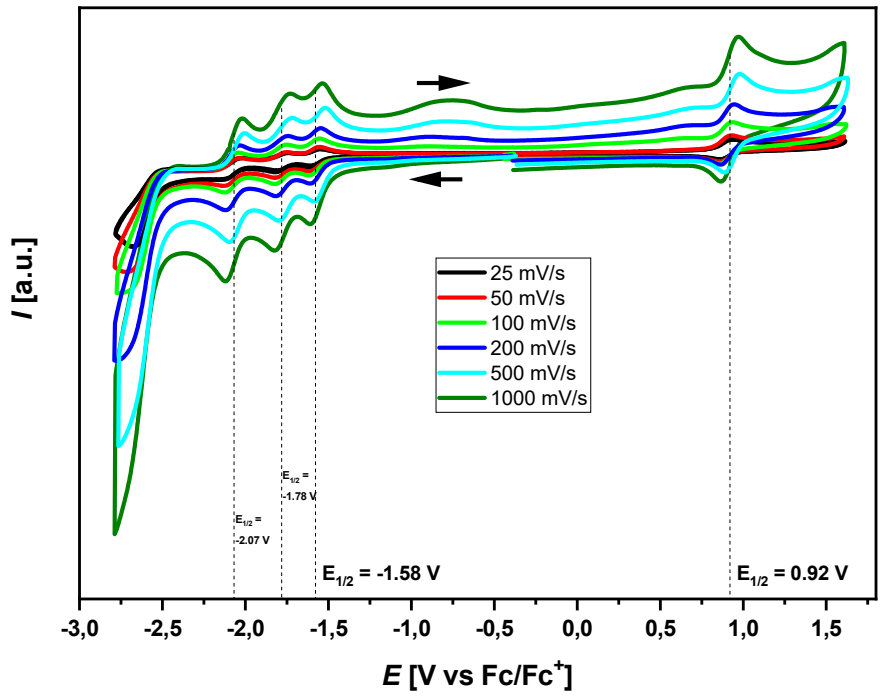

*Figure 31: Cyclic voltammogram of **243** at different scan rates (25 mV/s, 50 mV/s, 100 mV/s, 200 mV/s, 500 mV/s and 1000 mV/s)*

In the case of ligand **243**, redox-switchability is also conceivable. The cyclic voltammogram (0.1 M $[NBu_4][PF_6]$ in MeCN) reveals four different redox events ($E_{1/2}$ = 0.92 V, -1.58 V, -1.78 V, -2.07 V vs. Fc/Fc^+), which can be considered as quasi-reversible exceeding 56 mV peak-to-peak separation at 20 °C. The oxidation wave belongs to the metal oxidation from formal oxidation state +II to +III, while the three one-electron reduction waves most likely belong to preligand reduction. The oxidation potential is nearly identical to the one of $[Ru(bpy)_3]^{2+}$.

Due to its structural similarity to $[Ru(bpy)_3]^{2+}$ and the great potential of the deep reddish phosphine **243** to be used in visible light photoredox catalysis merged with gold(I) catalysis[163], ligand **243** was further analyzed by UV–visible spectrophotometry and fluorescence spectroscopy (Figure 32). While the fluorescence spectrum remained silent, which might be caused by non-radiative transitions caused by distortion, the UV–visible spectrophotometry revealed the typical metal-to-ligand charge-transfer band (MLCT: 488 nm) and two preligand-based π–π* (bpy) transitions (268 nm, 289 nm) similar to $[Ru(bpy)_3]^{2+}$.[164] Beside the ligand itself also its gold(I) complex **271** (see Chapter 2.9.1) was subjected to UV-Vis spectroscopy (MLCT: 483 nm, π–π*: 288 nm, Figure 33).

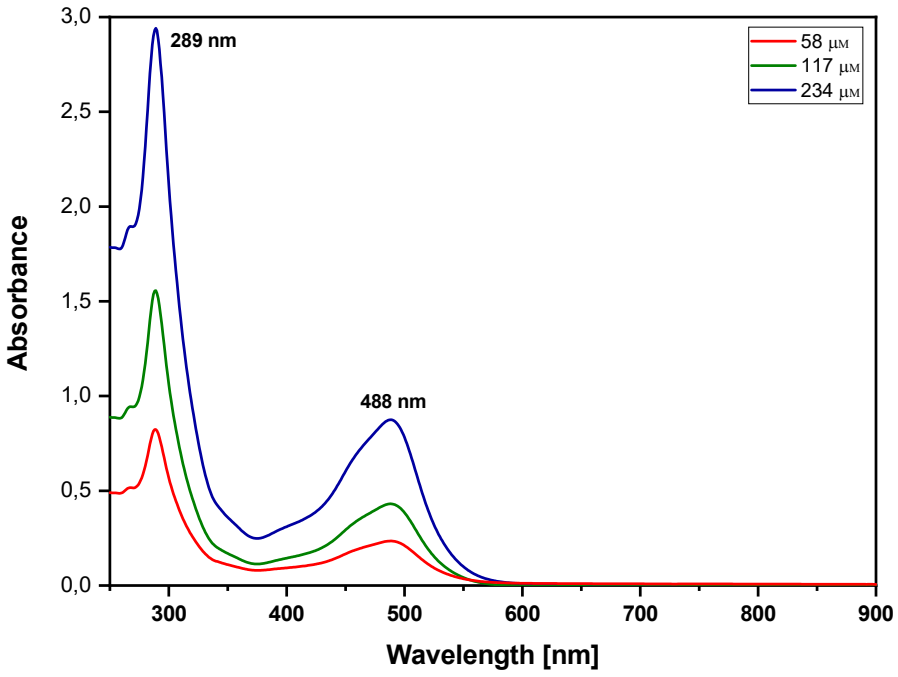

*Figure 32: UV-Vis absorption spectrum of **243** at different concentrations*

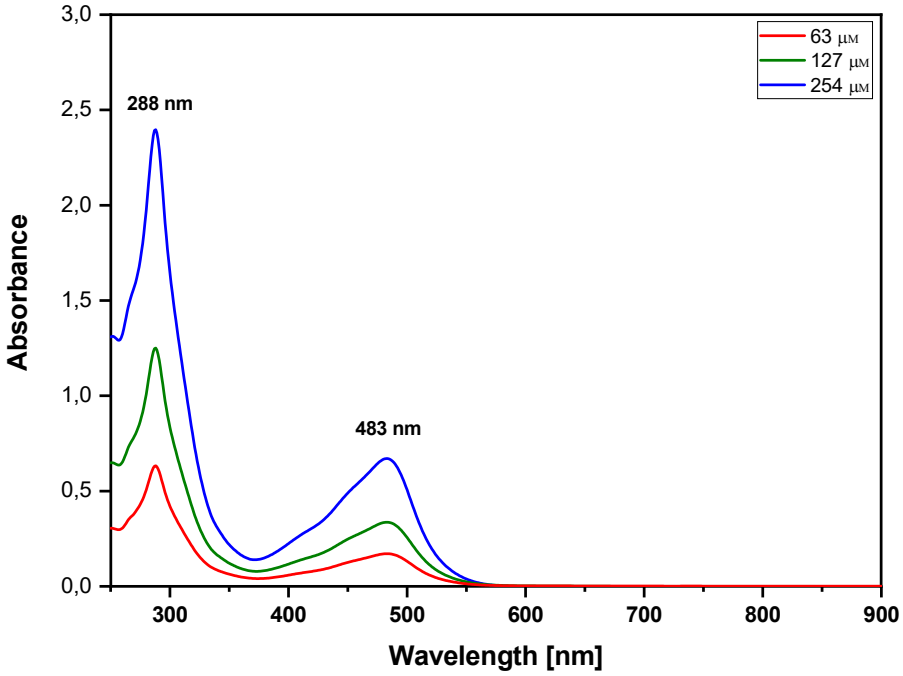

*Figure 33: UV-Vis absorption spectrum of **271** at different concentrations*

In accordance with the Beer-Lambert law the molar attenuation coefficient ε could then be determined *via* a concentration series and linear regression of absorbance and concentration. For ligand **243** ε was determined to be 3670.4 $M^{-1}cm^{-1}$ (488 nm, Figure 34), while gold complex **271** revealed a value of 2626.4 $M^{-1}cm^{-1}$ (483 nm, Figure 35). Both molar attenuation coefficients are much smaller compared to the one of $[Ru(bpy)_3]^{2+}$ [>10000 $M^{-1}cm^{-1}$ (MLCT)[164]].

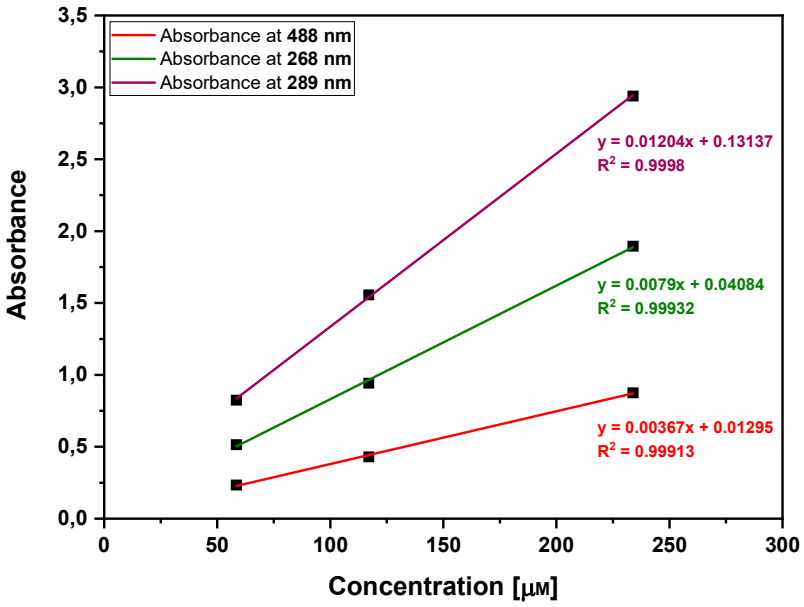

*Figure 34: Determining the attenuation coefficient ε for different maxima of the UV-Vis absorption spectrum of **243** by linear regression*

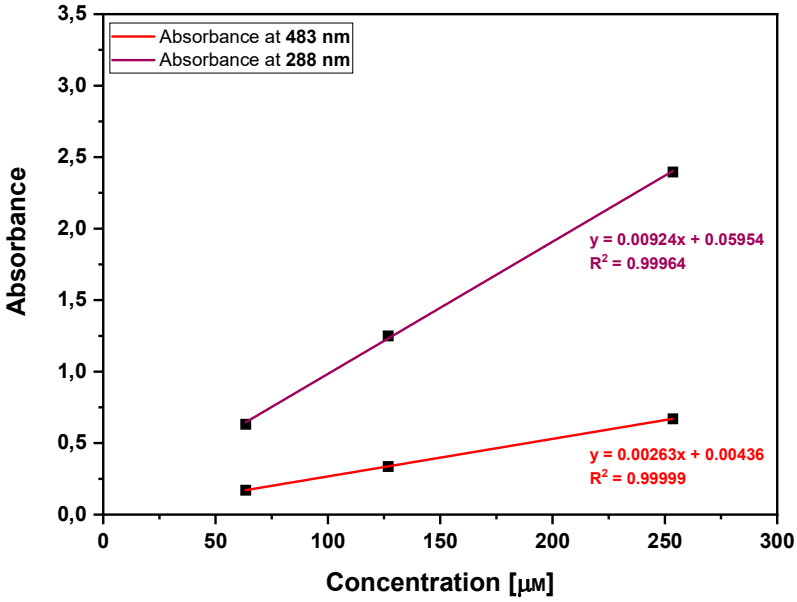

*Figure 35: Determining the attenuation coefficient ε for different maxima of the UV-Vis absorption spectrum of **271** by linear regression*

To test the capabilities of these compounds to use them as photoredox catalysts and to examine the general feasibility to substitute $[Ru(bpy)_3]^{2+}$, compound **243** and compound **271** were used in photocatalytic [2+2] enone cycloaddition[165] and gold and photoredox dual catalyzed oxyarylation of alkenes with aryldiazonium salts[166], respectively, but without success. This might be a direct result of a short lifetime of the excited state.[167]

2.6.1.2 Crystal structures, Tolman cone angles and percent buried volume %Vbur

With the synthesis and characterization of the ligands in solution established in the last chapter the next step is the concomitant analysis of the structures by means of single crystal X-ray diffraction. In the following, first the crystallization and elemental features of the crystal structures are presented to follow up in a detailed comparative analysis of the geometry encountered at each of the encapsulated metals.

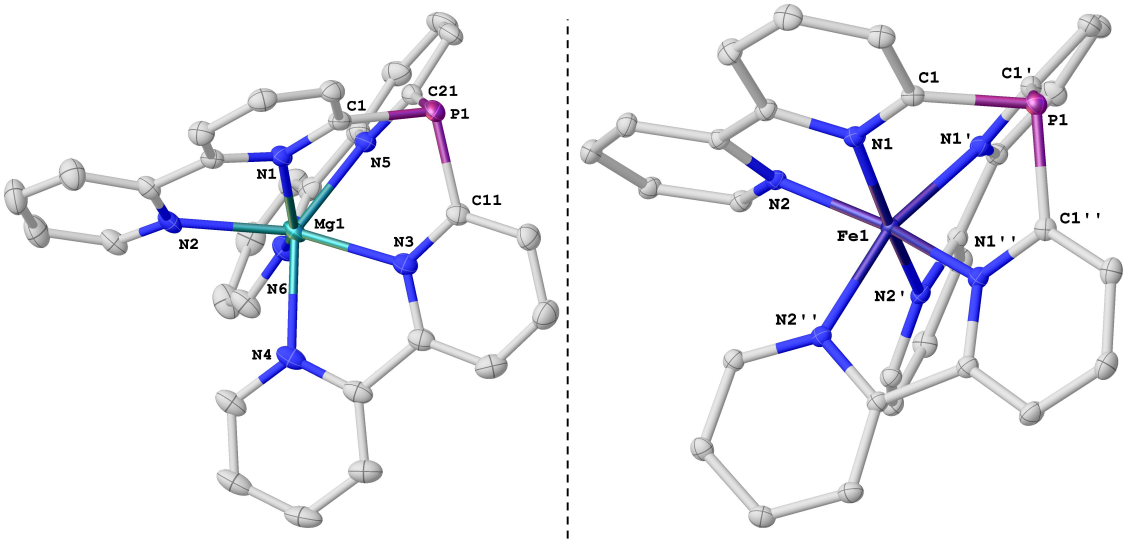

*Figure 36: Molecular structures of **238**[8] (left) and **239**[9] (right). Thermal ellipsoids at 50% probability level. Hydrogen atoms, non-coordinating counter anions and co-crystallized solvent molecules omitted for clarity. **239**, Z'=1/3 structure generated by symmetry code: '= 2-y, 1+x-y, +z; '' = 1+y-x, 2-x, +z. Selected bond length (Å) and angles (°) for **238** and **239** are summarized in Table 2.*

Compound **238** and **239** were crystallized by acetonitrile/diethyl ether vapor diffusion as colorless needles. The asymmetric unit of **238** also contains one half molecule of co-crystallized diethyl ether on a special position. In contrast to the Mg-ligand the Fe-ligand features a higher symmetry with a perfect C3 symmetric molecule and Z'=1/3. **238** crystallizes in the non-centrosymmetric space group *P*3 with meaningful absolute structure factors [Hooft 0.000(3)], but merohedral twinning was found during refinement with the twin law (010 / 100 / 00-1) and a refined batch scale factor of 0.0979(11). This draws the conclusion that the single crystal is enantiopure (right-handed (Δ) helical symmetry), while on the batch scale a racemic conglomerate is present. The relatively small Fe─N distances (Table 2) indicate a low-spin complex at 100 K (ground state), which might lead to entropy-driven spin transition populating a high-spin state at higher temperatures (see 2.6.1.1.2).[158,167]

[8] **Crystal Data** for **238** ($C_{68}H_{52}F_{12}Mg_2N_{12}O_{13}P_2S_4$; *M* =1712.01 g/mol): monoclinic, space group C2/c (no. 15), *a* = 19.138(9) Å, *b* = 14.306(4) Å, *c* = 27.811(11) Å, *β* = 105.757(15)°, *V* = 7328(5) Å^3, *Z* = 4, *T* = 100.04 K, μ(MoKα) = 0.293 mm^{-1}, *Dcalc* = 1.552 g/cm^3, 22385 reflections measured (4.14° ≤ 2Θ ≤ 55.66°), 8657 unique (R_{int} = 0.0400, R_{sigma} = 0.0582) which were used in all calculations. The final R_1 was 0.0568 (I > 2σ(I)) and wR_2 was 0.1437 (all data).

[9] **Crystal Data** for **239** ($C_{30.003}H_{21.0021}B_{2.0002}F_{8.0008}FeN_{6.0006}P$; *M* =726.04 g/mol): trigonal, space group P3 (no. 143), *a* = 9.538(2) Å, *c* = 8.899(2) Å, *V* = 701.2(3) Å^3, *Z* = 0.9999, *T* = 99.99 K, μ(MoKα) = 0.685 mm^{-1}, *Dcalc* = 1.719 g/cm^3, 17503 reflections measured (4.578° ≤ 2Θ ≤ 62.986°), 3119 unique (R_{int} = 0.0262, R_{sigma} = 0.0187) which were used in all calculations. The final R_1 was 0.0191 (I > 2σ(I)) and wR_2 was 0.0498 (all data).

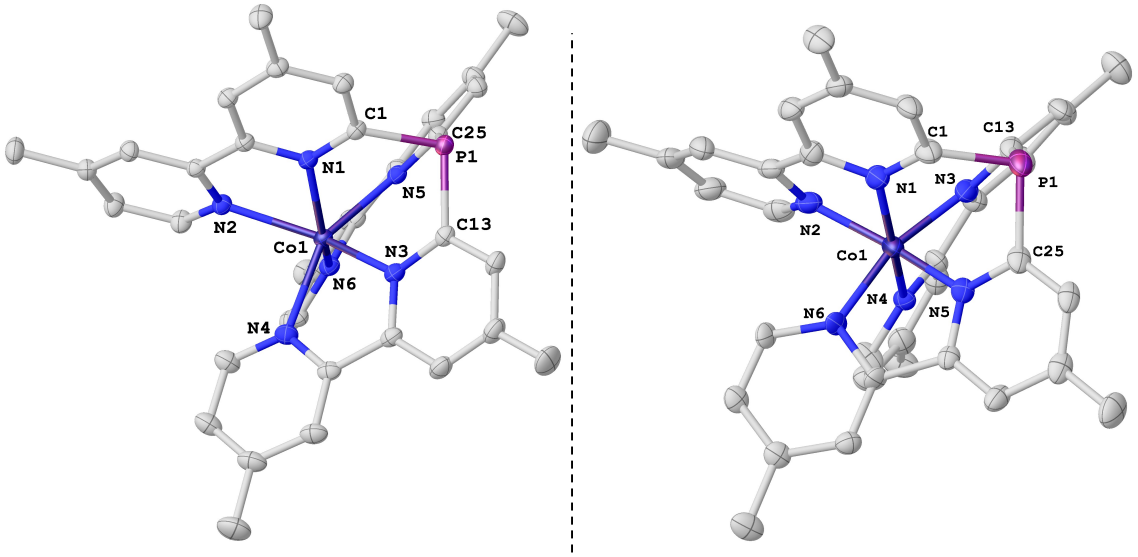

*Figure 37: Molecular structures of **240**[10] (left) and **241**[11] (right). Thermal ellipsoids at 50% probability level. Hydrogen atoms, non-coordinating counter anions and co-crystallized solvent molecules omitted for clarity. Selected bond length (Å) and angles (°) for **240** and **241** are summarized in Table 2.*

Compound **240** crystallizes in triclinic crystal system in space group *P*-1 by acetonitrile/diethyl ether vapor diffusion as yellow blocks. The asymmetric unit contains two equivalents of **240**, four SbF_6^--anions of which two show positional disorder, three equivalents of acetonitrile of which one shows positional disorder and one molecule of diethyl ether. These contents seem to explain already the occurrence of Z'=2 in this case, since the odd number of co-crystallized solvents break any possible symmetry. However, close inspection reveals geometric dissimilarities between the two crystallographically independent molecules of **240**. Both molecules show relatively long Co─N bond lengths (Table 2) indicating a high-spin complex at 100 K.[167,168]

Unfortunately, the Co(III) analogue **241** on the other hand features significantly worse structural data. Again, by acetonitrile/diethyl ether vapor diffusion orange blocks were obtained. The asymmetric unit consists of the full **241**, two molecules of $SbCl_6^-$ on general positions, each a half of SbF_6^- and $SbCl_6^-$ on special positions and one molecule of acetonitrile. The anions show some poorly resolved positional disorder which is assumed to be the main cause of the poor R indices, with R1 at 11.7%, since these constitute the major scattering centers. Due to that, detailed geometry discussion is to be taken with special wariness in the following. If higher quality of refinement is needed, the $BArF_{24}$-salt or an sample with exclusively SbF_6^- anions (oxidizer of the same anion: *e.g.* magic blue with SbF_6^- anion[169]) might be crystallized.

[10] **Crystal Data** for **240** ($C_{84}H_{88}Co_2F_{24}N_{16}OP_2Sb_4$; *M* =2460.50 g/mol): triclinic, space group P-1 (no. 2), *a* = 13.9725(6) Å, *b* = 17.4714(8) Å, *c* = 22.1473(9) Å, *α* = 106.5790(10)°, *β* = 99.0290(10)°, *γ* = 107.9820(10)°, *V* = 4747.3(4) Å^3, *Z* = 2, *T* = 100.00 K, μ(MoKα) = 1.598 mm^{-1}, *Dcalc* = 1.721 g/cm^3, 233866 reflections measured (3.878° ≤ 2Θ ≤ 65.4°), 34498 unique (R_{int} = 0.0296, R_{sigma} = 0.0180) which were used in all calculations. The final R_1 was 0.0313 (I > 2σ(I)) and wR_2 was 0.0784 (all data).

[11] **Crystal Data** for **241** ($C_{38}H_{36}Cl_{15}CoF_3N_7PSb_3$; *M* =1634.64 g/mol): orthorhombic, space group Pccn (no. 56), *a* = 38.7202(18) Å, *b* = 19.7571(9) Å, *c* = 14.3388(7) Å, *V* = 10969.2(9) Å^3, *Z* = 8, *T* = 100.00 K, μ(MoKα) = 2.567 mm^{-1}, *Dcalc* = 1.980 g/cm^3, 209333 reflections measured (3.664° ≤ 2Θ ≤ 59.174°), 15342 unique (R_{int} = 0.0470, R_{sigma} = 0.0212) which were used in all calculations. The final R_1 was 0.1174 (I > 2σ(I)) and wR_2 was 0.2560 (all data).

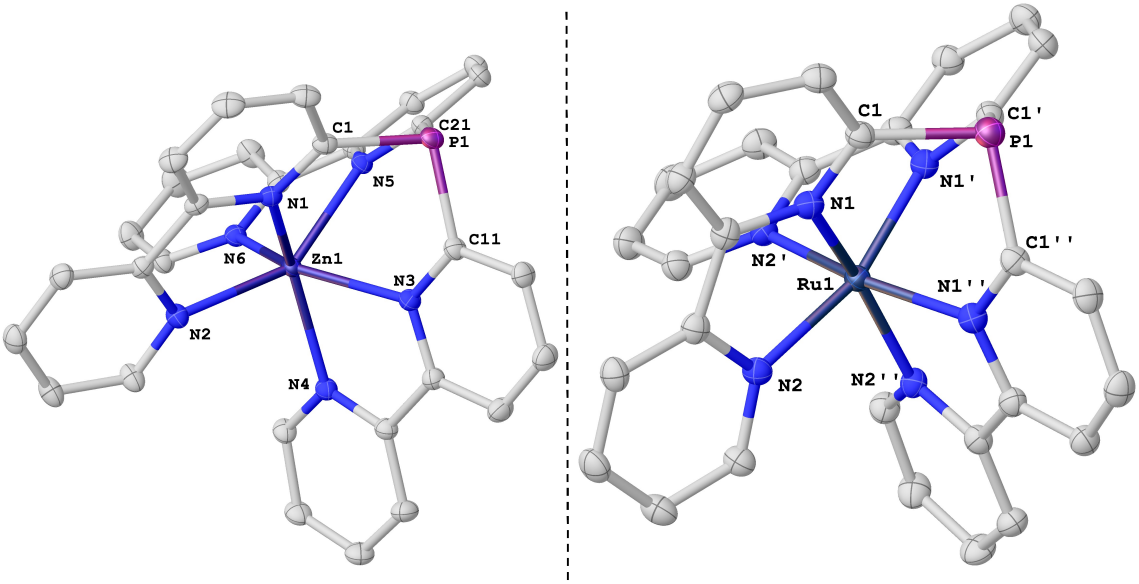

*Figure 38: Molecular structures of **242**[12] (left) and **243**[13] (right). Thermal ellipsoids at 50% probability level. Hydrogen atoms, non-coordinating counter anions and co-crystallized solvent molecules omitted for clarity. Selected bond length (Å) and angles (°) for **242** and **243** are summarized in Table 2.*

Compound **242** was similarly to the Mg-analogue **238** crystallized from acetonitrile/diethyl ether vapor diffusion as colorless blocks. Indeed, both were found to be isostructural, as may be expected from the similarity between the two encapsulated metals.

Compound **243** crystallized by acetonitrile/diethyl ether vapor diffusion as red twinned plates. The twinning was resolved by twin indexation and using the detwinned hklf4 for further refinement. This was done, because, additionally, inversion twinning was found and treated with the twin law (-100/0-10/00-1) as an ideal case. The asymmetric unit consists of two crystallographically independent SbF_6^- anions and three separate thirds of perfect C_3-symmetrical molecule **243**. During refinement, prominent residual densities were observed in proximity to each phosphorus, which is consistent with partly occupied oxygen atoms. These were found to freely refine to occupancy factors of 0.300, 0.149 and 0.143 respectively. In consequence, ca. 20% of compound **243** was found oxidized in solid state. Interestingly, attempts to crystallize **242** in absence of air and moisture, no crystal growth was obtained, leading to the assumption that the crystallization propensity of partly oxidized **243** is enhanced.

[12] **Crystal Data** for **242** ($C_{68}H_{52}F_{12}N_{12}O_{13}P_2S_4Zn_2$; M =1794.13 g/mol): monoclinic, space group C2/c (no. 15), a = 19.0320(11) Å, b = 14.2485(8) Å, c = 27.6486(14) Å, β = 105.530(2)°, V = 7223.9(7) Å^3, Z = 4, T = 100.00 K, μ(MoKα) = 0.928 mm^{-1}, *Dcalc* = 1.650 g/cm^3, 93941 reflections measured (4.154° ≤ 2Θ ≤ 65.22°), 13001 unique (R_{int} = 0.0265, R_{sigma} = 0.0157) which were used in all calculations. The final R_1 was 0.0366 (I > 2σ(I)) and wR_2 was 0.0955 (all data).

[13] **Crystal Data** for **243** ($C_{30}H_{21}F_{12}N_6O_{0.201667}PRuSb_2$; M =1072.29 g/mol): trigonal, space group P31c (no. 159), a = 17.7830(12) Å, c = 18.1227(13) Å, V = 4963.2(8) Å^3, Z = 6, T = 99.96 K, μ(MoKα) = 2.223 mm^{-1}, *Dcalc* = 2.153 g/cm^3, 19575 reflections measured (4.582° ≤ 2Θ ≤ 61.064°), 10101 unique (R_{int} = 0.0204, R_{sigma} = 0.0201) which were used in all calculations. The final R_1 was 0.0252 (I > 2σ(I)) and wR_2 was 0.0665 (all data).

*Table 2: Summarized crystallographic data and ^{31}P-NMR shifts of **238**-**243**. Only crystallographic independent/unique parameters are shown. If the asymmetric unit contains more than one formula unit of the corresponding compound (Z'>1), the different crystallographic data is separated by slash ("/"). For methyl substituted compounds **240** and **241** C11 and C21 correspond to C13 and C25.*

	Mg^{2+} **238**	Fe^{2+} **239**	Co^{2+} **240**	Co^{3+} **241**	Zn^{2+} **242**	Ru^{2+} **243**
^{31}P-shift [ppm]	-36.07	-	316.57	12.94	-50.87	11.85
∡(C1—P1—C11) [°]	97.4(1)	98.1(1)	98.9(1) /99.2(1)	98.3(6)	98.6(1)	99.7(2) /100.6(2)/99.7(2)
∡(C11—P1—C21) [°]	99.0(1)	-	101.4(1) /97.9(1)	95.9(6)	97.1(1)	-
∡(C21—P1—C1) [°]	104.2(1)	-	98.2(1) /100.6(1)	97.2(5)	103.6(1)	-
pyramidalization [°]	300.7	294.4	298.5 /297.7	291.4	299.3	299.2 /301.8/299.1
P1—C1 distance [Å]	1.844(3)	1.834(2)	1.843(2) /1.834(2)	1.831(13)	1.839(2)	1.842(4) /1.838(5)/1.849(4)
P1—C11 distance [Å]	1.849(3)	-	1.838(2) /1.845(2)	1.850(14)	1.840(2)	-
P1—C21 distance [Å]	1.845(3)	-	1.839(2) /1.837(2)	1.849(12)	1.837(2)	-
M—P1 distance [Å]	3.581(2)	3.327(1)	3.517(1) /3.512(1)	3.372(4)	3.575(1)	3.333(2) /3.344(2)/3.333(2)
M—N1 distance r [Å]	2.191(2)	1.924(1)	2.144(1) /2.122(2)	1.903(10)	2.164(1)	1.998(3) /2.005(3)/1.998(3)
M—N3 distance r [Å]	2.258(3)	-	2.123(1) /2.139(2)	1.933(10)	2.247(1)	-
M—N5 distance r [Å]	2.183(2)	-	2.132(1) /2.125(1)	1.920(9)	2.171(1)	-
M—N2 distance r [Å]	2.213(2)	1.999(1)	2.172(1) /2.130(2)	1.964(10)	2.195(1)	2.079(3) /2.067(4)/2.075(3)
M—N4 distance r [Å]	2.237(3)	-	2.173(1) /2.182(2)	1.972(9)	2.197(1)	-
M—N6 distance r [Å]	2.210(2)	-	2.160(1) /2.180(1)	1.966(9)	2.182(1)	-
bite angle α_1 ∡(N1—M—N2) [°]	74.3(1)	80.0(1)	74.8(1) /76.1(1)	80.6(4)	75.2(1)	78.2(2) /78.3(2)/78.2(1)
bite angle α_2 ∡(N3—M—N4) [°]	72.6(1)	-	75.3(1) /74.4(1)	81.8(4)	73.0(1)	-
bite angle α_3 ∡(N5—M—N6) [°]	74.5(1)	-	75.0(1) /75.4(1)	81.1(4)	75.3(1)	-
twist angle ϕ_1 ∡[p(N1,M,P1)-p(N2,M,P1)][°]	15.5(1)	41.4(1)	22.3(1) /20.6(1)	42.6(5)	17.8(1)	41.1(1) /41.4(2)/41.4(2)
twist angle ϕ_2 ∡[p(N3,M,P1)-p(N4,M,P1)][°]	16.0(1)	-	20.8(1) /23.3(1)	41.9(5)	17.1(1)	-
twist angle ϕ_3 ∡[p(N5,M,P1)-p(N6,M,P1)][°]	16.3(1)	-	20.9(1) /21.8(1)	43.7(5)	17.4(1)	-

	Mg^{2+} **238**	Fe^{2+} **239**	Co^{2+} **240**	Co^{3+} **241**	Zn^{2+} **242**	Ru^{2+} **243**
Mean twist angle ϕ	15.9	41.4	21.3 /21.9	42.7	17.4	41.1 /41.4/41.4
geometry index τ_6 [%]	73.5	30.9	64.5 /63.5	28.8	71.0	31.5 /31.0/31.0
Tolman cone angle [°]	163	159	169 /166	165	163	161 /160/160
%V_{Bur} (2.00 Å) [%]	34.6	33.1	34.3 /33.8	32.6	34.5	33.6 /33.4/33.4
%V_{Bur} (2.28 Å) [%]	29.9	28.4	29.6 /29.1	28.0	29.7	28.9 /28.7/28.7

Table 2 shows the geometric parameters taken from compounds **238**-**243**. However, before going deeper into the comparison of the compounds, individual parameters require further explanation. Many geometries of the encapsulating ligands can be interpreted as a Bailar twisted octahedral [TAP, M(L─L)$_3$, local D_3-symmetry] or distorted trigonal prismatic [TP, M(L─L)$_3$, local D_{3h}-symmetry] structure. The geometry can be described by a set of parameters, which are based on the work of Schäffer[170] and Holm[123]. One of the most indicative parameters to classify the limits of TAP or TP structures is the mean twist angle ϕ, which is defined as the averaged angle of ϕ_1, ϕ_2 and ϕ_3 (see Table 2). Where ϕ_1 corresponds to the included angle between the two p(N1,M,P1) and p(N2,M,P1) planes of the same 2,2'-bipyridin-6-yl moiety (Figure 39). The analogous angles for the other 2,2'-bipyridin-6-yl substituents lead to ϕ_2 and ϕ_3. Note, that in compounds of perfect C_3 symmetry $\phi_1 = \phi_2 = \phi_3$ and N2 and N3 correspond to N1' and N1''.

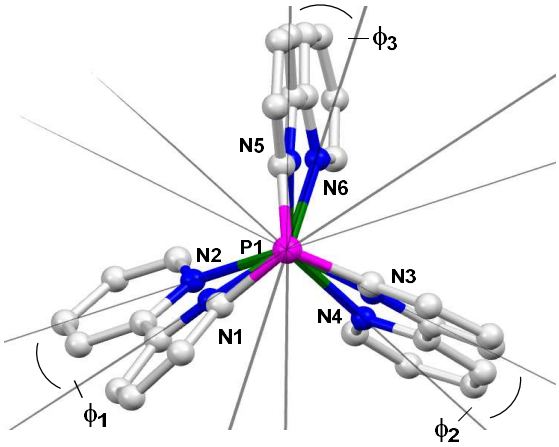

*Figure 39: Twist angles ϕ_1, ϕ_2 and ϕ_3 for **238**. Top view.*

Twist angle ϕ is expected to be between 0° (TP) and 60° (TAP), so that a geometry index τ_6 can be defined as:[171]

$$\tau_6 = \frac{5}{3}(60 - \phi) \qquad (3)$$

Equation 3

τ_6 serves as an indicator, whether a geometry is TP or TAP and ranges between 0, perfectly TAP, and 100%, perfectly TP.

The three bite angles α_1,α_2 and α_3 refer to the included angle between the two nitrogen atoms and the metal (∡N─M─N) for each individual 2,2'-bipyridin-6-yl substituent.

Beside geometrical aspects the solid state structure can also give insights into the steric measure of phosphines themselves. Excellent descriptors for this purpose are the Tolman cone angle[57] and the percent buried volume %V_{Bur} [59,60] (Table 2). Both descriptors have already been outlined in the Chapter 1.2.3. While for the Tolman cone angle the construction of Figure 9 in combination with Equation 1 and Equation 2 was used, the percent buried volume %V_{Bur} was determined *via* the web application SambVca 2.1[172] applying the parameters specified in the experimental section.

Pyramidalization

The phosphabarrelene-like structure stretched between the bridgehead metal ion and the P atom (M─P1 distance, Table 2) causes already mentioned geometric strain, which can be expressed by the amount of pyramidalization [sum of angles ∡(C─P─C)]. In all cases (**238**-**243**) the pyramidalization is higher than that of the corresponding preligand **212** (sum of angles ∡(C─P─C) = 302.5°), but still lower compared to classical carbon-based 9-phosphatriptycenes. The latter is a direct result of the encapsulated metal ions having larger ion sizes than carbon. Comparing the pyramidalization among the ligands (**238**-**243**), one finds a trend with the corresponding effective ionic radii[173,174] of the encapsulated metal ion. Thus, ligands encapsulating highly oxidized [Co^{3+}(ls), **241**] or low-spin 3d metal ions [Fe^{2+}(ls), **239**], with small effective ionic radii, have a higher pyramidalization(<295°) than the others [Mg^{2+} **238**, Co^{2+}(hs) **240**, Zn^{2+} **242**, Ru^{2+}(ls) **243**]. Note, however, that this trend is only rough, since effective ionic radii assume a purely ionic interaction and neglect the covalent character of the M─N bonds and that the reported value for pyramidalization of Ru^{2+} ligand **243** might be overestimated as a result of partial oxidation.

Geometry

The coordination geometry of the encapsulated metals in the ligands varies between the TAP and TP limits (geometry index τ_6, Table 2). The structure is largely determined by three parameters: the effective ionic radius, the constrained preligand system and the metal directional effect based on the electron configuration of the metal ion. While a large ionic radius and the nature of the preligand push the geometry towards the TP limit, electron configurations such as a low-spin d^6 system have a strong metal directional effect leading to a structure with TAP character.[171] The metal directional effect of different d-electron configurations was already calculated by Holm and coworkers for a $M(L{-}L)_3$ system using an angular overlap model based analysis, but corresponding trends have also been confirmed in more recent publications:[123,171]

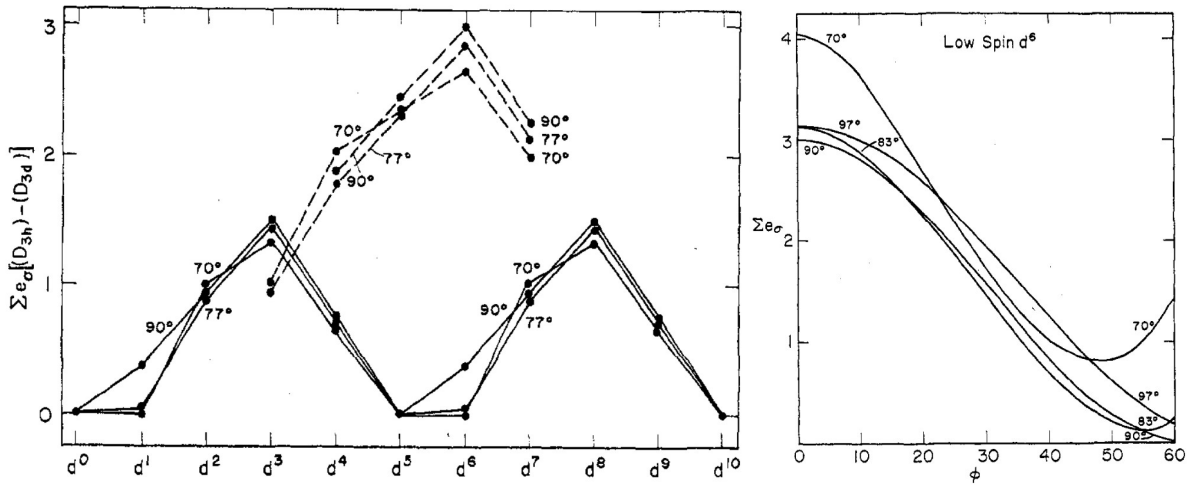

Figure 40: d-electron destabilization energies (TAP vs. TP) as a function of the number of d electrons (left). Sums of one-electron σ-bonding energies for a low-spin d^6 system as a function of the twist angle ϕ (right).Both figures taken from the literature[123]

In Figure 40 (left) the differences in total d-electron energies between TP (D_{3h}) and TAP (D_{3d}) geometry (σ-bonding) are plotted as a function of the number of d-electrons.[123] The dashed line represents $M(L{-}L)_3$ complexes of low-spin state while the solid line indicates a high-spin configuration. The different graphs are labeled with the corresponding bite angle α (in our case: averaged bite angle α of the 2,2'-bipyridin-6-yl substituents, Table 2). As it can be seen for the low-spin d^6 case, a displacement towards the TAP geometry can be expected. On the other hand the sum of the one-electron d-orbital energies for a low-spin d^6 complex (Figure 40, right) demonstrates that for bite angles smaller than 90° twist angles ϕ of 60° cannot be reached.

Thus, in the cases of a d^6 low spin system like in Fe^{2+} (**239**), Co^{3+} (**241**) and Ru^{2+} (**243**), structures can be expected to approach the TAP limit but not reach it due to the nature of the preligand. The crystal structures confirm this prognosis. All twist angles of the ligands **239**, **241** and **243** are above 40° indicating a strong TAP character, but still being far from optimal TAP geometry (60°). This is also expressed by the geometry index τ_6, which is about 30% for the mentioned ligands. As the TAP character increases, also the bite angles (α_1, α_2, α_3) increase. Furthermore, the ligands close to the TAP limit exhibit small M─P distances, since the helical twist of the 2,2'-bipyridin-6-yl substituents centers the metal and forces it towards the phosphorus. The TAP character is particularly pronounced for Co^{3+}-ligand **241** (τ_6 = 28.8, Table 2). This can be explained by the large ligand field splitting and the small effective ionic radius in highly oxidized Co^{3+}, which further push the ligand into a TAP structure.

In contrast to the low-spin d^6 metal ions, ligands **238** (Mg^{2+}) and **242** (Zn^{2+}) exhibit a strong TP character (τ_6 < 70°, ϕ < 20°, Table 2) . This fact can be explained by the nature of the preligand, which forces the geometry near the TP limit. Since the Mg^{2+} and Zn^{2+} ions have a closed-shell configuration, there is no driving force to reach the TAP limit. The small twist angle, which is nevertheless observed, serves to optimize the M─N distances. Due to the only small twist angle in the TP geometry, the bite angle is decreased while the distance M─P is increased.

In the case of Co^{2+} (**240**), several trends are now competing with each other. While the large effective ionic radius of high spin Co^{2+} and the nature of the preligand favor a TP structure, ligand **240** also exhibits a driving force to adopt the TAP structure due to the metal directional effect (high-spin d^7, Figure 40 left). However, the metal directional effect is smaller compared to the low-spin d^6 case and as a result ligand **240** reveals an intermediate TP/TAP structure with an intermediate geometry index τ_6 of about 64% (twist angle ϕ > 20°, Table 2). With an intermediate τ_6 also an intermediate M─P distance is found.

Geometry and chemical shift in ^{31}P NMR

A closer look at Table 2 reveals that when comparing the ligands of pure diamagnetic nature, the ligands with TP geometry exhibit the expected strongly shielded signals (*cf.* 9-phosphatriptycenes and cationic phosphines, chapter 1.3), while the ligands with TAP geometry show strongly deshielded signals.

The TAP-geometry and the high pyramidalization stand in contrast to the downfield ^{31}P-shift in NMR. For a highly constrained system with high pyramidalization, the lone pair should exhibit high s character and therefore lead to a strong shielding. However, beside the hybridization the chemical shift also depends on bond overlap, atomic charge and average electronic excitation energy. Which leads to three dominant factors in ^{31}P chemical shift differences of similar compound classes: differences in electronegativity, change in π-electron overlap and change in σ-bond angle.[175] While the ring current (remotely induced fields) should be similar in all cases, the influence of the metal center increases with increasing TAP geometry (M─P distance shrinks). Hence, the strong deshielding effect might in this case be less the change in σ-bond angle rather than the increased electronegativity

by the metal center in combination with the increased tilt angle of the 2,2'-bipyridin-6-yl substituents leading to higher π-electron overlap of the phosphorus to the pyridine (acceptor interaction).[176] Furthermore, a paramagnetic deshielding (electronic excitation energy) can be considered for the shift-difference depending on the HOMO-LUMO gap, which should be geometry dependent and decreased in the case of a TAP-ligand. However, further research is required for an accurate explanation of this interesting phenomenon.

Steric measure

To determine the steric demand of the different ligands, the Tolman cone angle and the percent buried volume %V_{Bur} were used. Similar to the pyramidalization at the phosphorus, the Tolman cone angle and %V_{Bur} are only slightly affected by the encapsulation of different metals. All ligands therefore exhibit nearly the same small steric bulk between 32.6 and 34.6 %V_{Bur} (Tolman cone angle: 160°-169°) and free accessibility of the phosphorus for coordination (Table 2). This makes it easier to adjust the phosphines electronic properties without changing its sterics. The methyl groups of ligands **240** and **241** have no effect on the %V_{Bur} and only a small effect on the Tolman cone angle, because they are too far away from the phosphorus. Hence, due to bending back of the 2,2'-bipyridin-6-yl moieties, installing substituents on the aryl rings next to the phosphorus[106] or using much bulkier substituents like ^{t}Bu-groups are the only chances to drastically increase steric bulk.

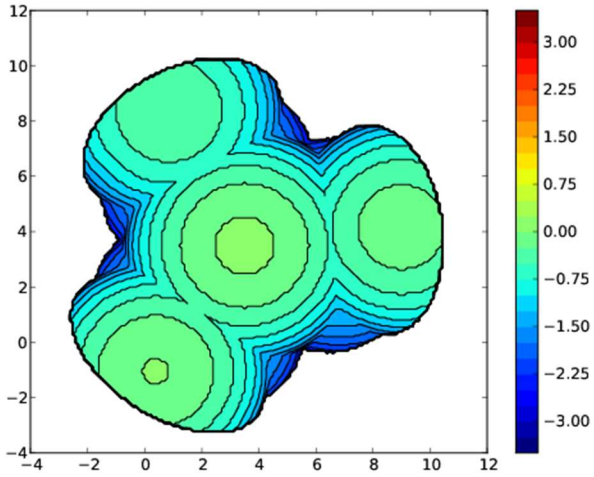

*Figure 41: Topographic steric map of **238** (SambVca 2.1[172])*

In addition to the %V_{Bur}, the web application SambVca 2.1[172]also provides a topographic steric map of the corresponding ligand. Figure 41 shows the topographic map of the Mg^{2+} ligand **238** as an example. The topographic steric map exhibits a pseudo-threefold axis like the ligand itself, distributing the steric bulk nearly evenly in the sphere. In ligand **238** no hot spots of steric bulk can be detected nor does the ligand seem to be very sterically demanding. The topographic steric maps of the other ligands look very alike showing free accessibility of the phosphorus (see experimental section).

To carry over this information obtained from the solid state structures of the free phosphines to homogenous catalysis one has to admit that the conformation can drastically change upon coordination of a second metal or solvation. Even though, due to the rigid nature of the barrelene-like architecture, the conformation should not be effected much. This makes the percent buried volume %V_{Bur} and Tolman cone angle of the free ligands important tools to get a rough idea of the steric bulk even later in homogeneous catalysis.

2.6.2 Ligands beyond trigonal prismatic and trigonal antiprismatic encapsulation

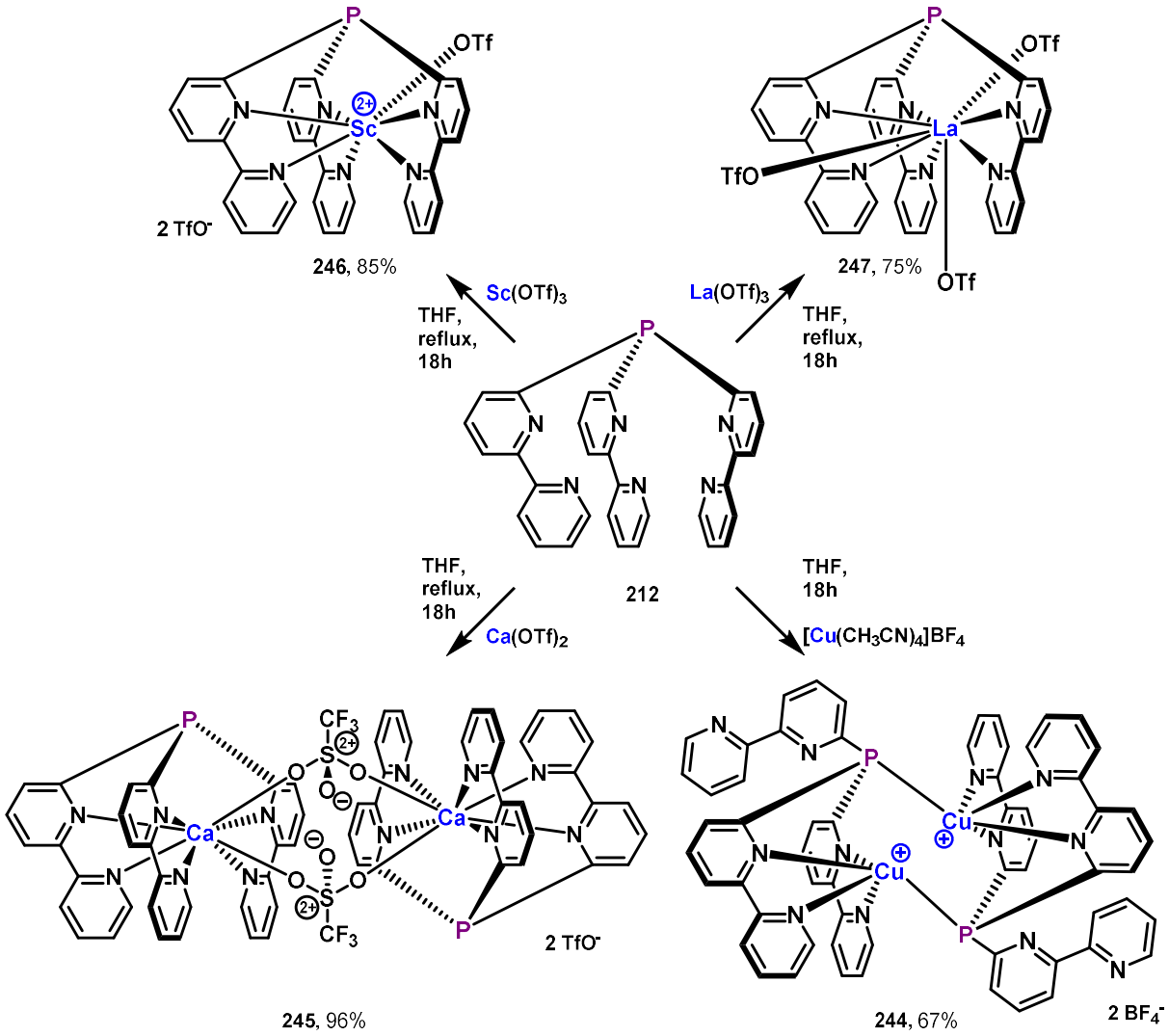

Scheme 83: Cationic phosphine ligands beyond trigonal prismatic and trigonal antiprismatic encapsulation

The Ca(II), Sc(III) and La(III) ligands were synthesized from their metal triflates, whereas tetrakis(acetonitrile)copper(I) tetrafluoroborate was used as a metal precursor to obtain compound **244** (Scheme 83). Beside the expected TAP and TP structures, Ca(II)-, Sc(III)-, Cu(I)- and La(III)-ligands show different solid state coordination environments. All ligands (**244**-**247**) could be crystallized and will be described below based on the elemental features of the crystal structures.

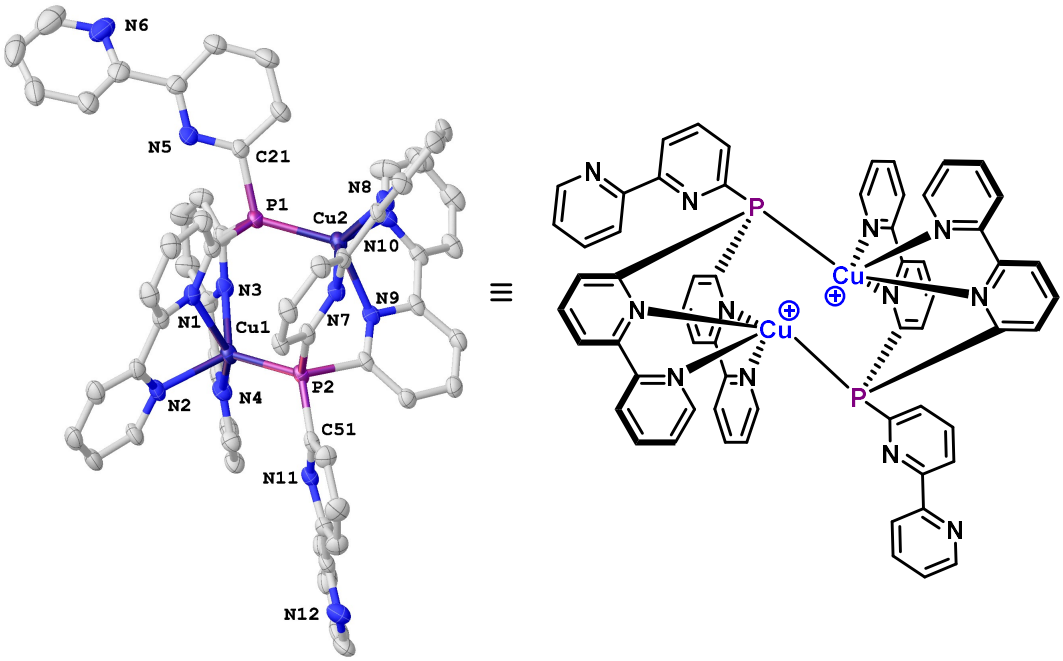

*Figure 42: Molecular structure of **244**[14]. Thermal ellipsoids at 50% probability level. Hydrogen atoms, non-coordinating counter anions and co-crystallized solvent molecules omitted for clarity. Selected bond length (Å) and greatest valence angles of both coordination centers (°) for **244**: Cu1—P2 2.2091(15), Cu1—N1 2.286(5), Cu1—N2 2.188(5), Cu1—N3 2.221(5), Cu1—N4 2.157(5), Cu2—P1 2.182(2), Cu2—N7 2.338(5), Cu2—N8 2.139(5), Cu2—N9 2.162(5), Cu2—N10 2.157(5), ∢N1—Cu1—N4 145.6(2), ∢P2—Cu1—N3 123.5(1), ∢N7—Cu2—N10 146.4 (2), ∢P1—Cu2—N9 126.2(1), τ_5 = 0.3670 (Cu1)/0.3353(Cu2).*

Compound **244** crystallizes in a triclinic crystal system in space group *P*-1 by acetonitrile/diethyl ether vapor diffusion as orange needles (Figure 42). The asymmetric unit consists of the molecule **244**, two molecules of BF_4^- on general positions showing positional disorder and one molecule of acetonitrile. The two Cu(I) centers in complex **244** reveal a pentacoordinate environment where the soft Cu^+ is not only coordinated by two 2,2′-bipyridin-6-yl moieties but also additionally to a phosphorus of another Cu^+ complex.[122] The resulting dimeric structure exhibits two Cu(I) centers in a distorted tetragonal pyramidal configuration (τ_5 = 0.3670/0.3353[145]). The nearly centrosymmetric arrangement is symmetry-broken by the different orientations of the two dangling 2,2′-bipyridin-6-yl moieties and the different tetragonal pyramidal distortion of the two Cu^+ centers.

The dimeric structure can be easily dissociated by addition of coordinating solvent. Thus, in contrast to the solid state structure the ^{1}H-NMR and ^{13}C-NMR show a molecule of C_3 symmetry in CD_3CN having seven chemically non-equivalent proton- and ten chemically non-equivalent carbon-signals. Fluctuation in coordination, with ligand dissociation and association on a faster time scale than the NMR experiment leads to the observed averaged signals. These dynamic processes can be also seen in the ^{31}P spectrum of **244** exhibiting a very broad signal at -4.63 ppm.

[14] **Crystal Data** for **244** ($C_{62}H_{45}B_2Cu_2F_8N_{13}P_2$; *M* =1334.75 g/mol): triclinic, space group P-1 (no. 2), *a* = 9.992(2) Å, *b* = 12.717(2) Å, *c* = 23.241(5) Å, *α* = 84.103(6)°, *β* = 89.849(7)°, *γ* = 87.319(8)°, *V* = 2934.4(10) Å^3, *Z* = 2, *T* = 150.0 K, μ(MoKα) = 0.859 mm^{-1}, *Dcalc* = 1.511 g/cm^3, 121147 reflections measured (4.08° ≤ 2Θ ≤ 57.986°), 15435 unique (R_{int} = 0.0686, R_{sigma} = 0.0424) which were used in all calculations. The final R_1 was 0.0952 (I > 2σ(I)) and wR_2 was 0.2372 (all data).

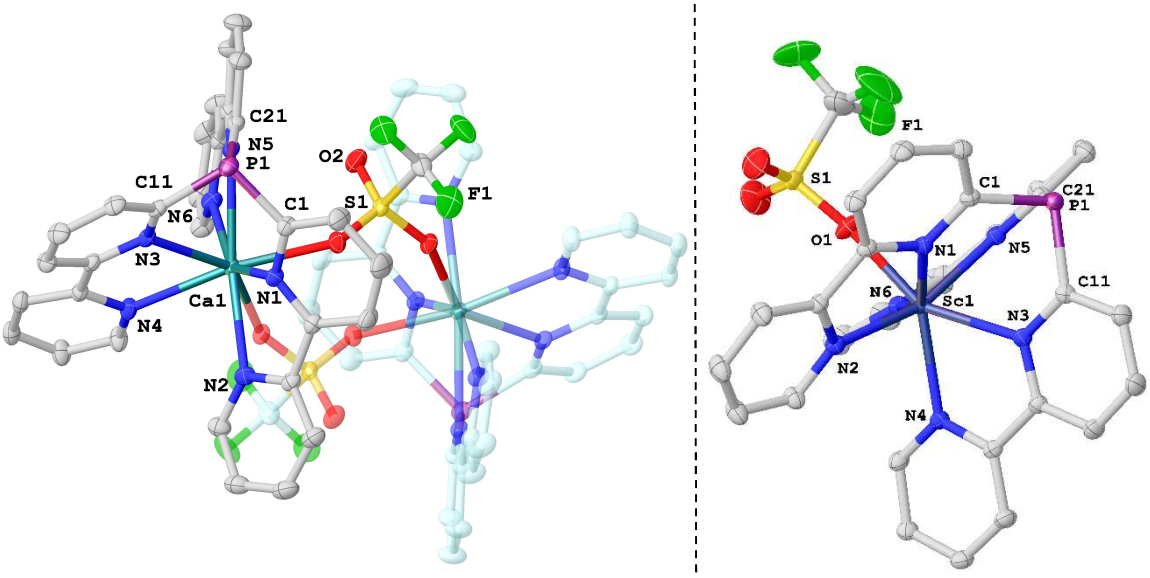

*Figure 43: Molecular structures of **245**[15] (left) and **246**[16] (right). Thermal ellipsoids at 50% probability level. Hydrogen atoms, non-coordinating counter anions and co-crystallized solvent molecules omitted for clarity; second half of the centrosymmetric **245** generated by symmetry drawn translucent (symmetry code: '=1-x, 1-y, 1-z). Selected bond length (Å) and angles (°) for **245** and **246** are summarized in Table 3.*

Compound **245** and **246** were crystallized by acetonitrile/diethyl ether vapor diffusion as colorless blocks and plates, respectively (Figure 43). In the case of **245**, the encapsulation of the corresponding Ca^{2+} is non-enclosing, leaving enough space for two bridging triflates and the two Ca^{2+} centers to form a centrosymmetric dimeric aggregate. The asymmetric unit now consists of half a molecule of this full dinuclear aggregate (Z'=0.5), two molecules of acetonitrile, and another disordered uncoordinated triflate. Compound **246** crystallizes in a monoclinic crystal system in space group $P2_1/c$. Again, the coordination sphere of the metal center (Sc^{3+}) is extended by the coordination of a triflate, but no dinuclear aggregates are formed. The asymmetric unit therefore consists of one molecule **246** with one coordinated triflate, two uncoordinated triflates in general positions and one acetonitrile in a general position. In contrast to the soft Cu^{+}, the two hard Lewis acidic metal centers Ca^{2+} and Sc^{3+} prefer the coordination of hard triflates in addition to the chelating κ^6-coordination of the preligand. Thereby, the coordination sphere of the Ca^{2+} center (**245**) adopts a distorted octacoordinated bicapped trigonal prismatic /distorted square antiprismatic intermediate structure, while the Sc^{3+} center of ligand **246** resembles a distorted capped trigonal prism.[177,178]

However, as can already be assumed, the bonds to the triflates are extremely labile in both cases, which can be confirmed by the NMR spectra in deuterated acetonitrile. Both ligands (**245**, **246**) exhibit averaged signals of seven chemically non-equivalent proton- and eleven chemically non-equivalent carbon-nuclei. Also they show sharp singlets in ^{19}F and $^{31}P\{H\}$ NMR indicating a fluctuation in

[15] **Crystal Data** for **245** ($C_{36}H_{27}CaF_6N_8O_6PS_2$; *M* =916.82 g/mol): triclinic, space group P-1 (no. 2), *a* = 12.3954(14) Å, *b* = 13.5925(15) Å, *c* = 13.9772(14) Å, *α* = 76.642(3)°, *β* = 64.708(3)°, *γ* = 69.307(3)°, *V* = 1982.9(4) Å^3, *Z* = 2, *T* = 100 K, μ(MoKα) = 0.389 mm^{-1}, *Dcalc* = 1.536 g/cm^3, 186985 reflections measured (4.108° ≤ 2Θ ≤ 63.236°), 13262 unique (R_{int} = 0.0322, R_{sigma} = 0.0141) which were used in all calculations. The final R_1 was 0.0386 (I > 2σ(I)) and wR_2 was 0.1037 (all data).

[16] **Crystal Data** for **246** ($C_{35}H_{24}F_9N_7O_9PS_3Sc$; *M* =1029.72 g/mol): monoclinic, space group $P2_1/c$ (no. 14), *a* = 13.7123(4) Å, *b* = 16.5738(4) Å, *c* = 19.0349(4) Å, *β* = 106.8050(10)°, *V* = 4141.22(18) Å^3, *Z* = 4, *T* = 100.0 K, μ(MoKα) = 0.471 mm^{-1}, *Dcalc* = 1.652 g/cm^3, 73236 reflections measured (4.648° ≤ 2Θ ≤ 63.074°), 13807 unique (R_{int} = 0.0351, R_{sigma} = 0.0259) which were used in all calculations. The final R_1 was 0.0390 (I > 2σ(I)) and wR_2 was 0.1073 (all data).

coordination, with triflate dissociation and association on a faster time scale than the NMR experiment.

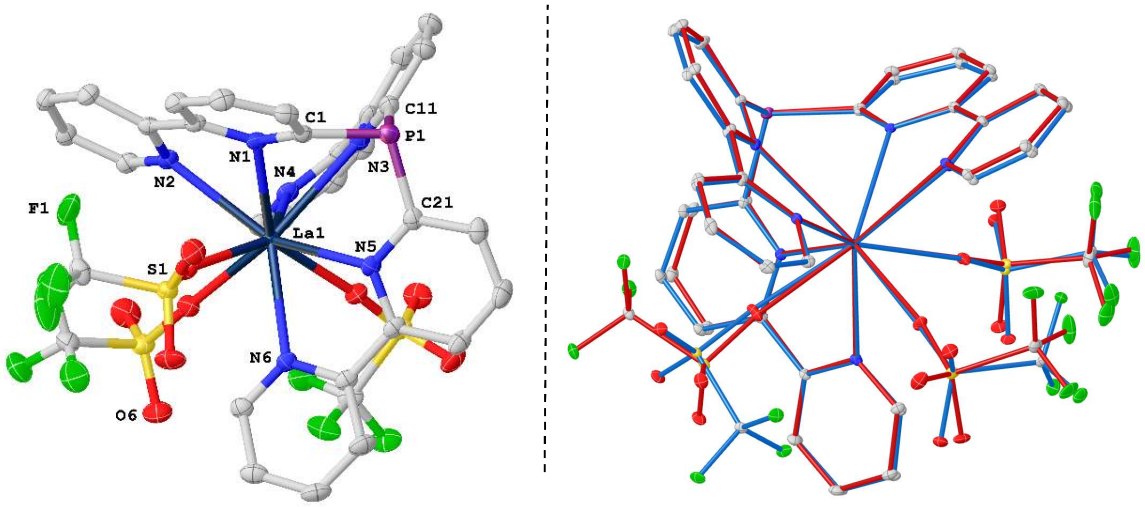

*Figure 44: Molecular structure (left) and overlay of both crystallographically independent molecules (right) of **247**[17]. Left: Thermal ellipsoids at 50% probability level. Hydrogen atoms omitted for clarity. Asymmetric unit contains two formula units of the corresponding compound **247**, one unit has been omitted for clarity. Selected bond length (Å) and angles (°) for **247** are summarized in Table 3.*

Single crystals of **247** suitable for X-ray diffraction were grown by vapor diffusion (acetonitrile/diethyl ether) and obtained as colorless plates. The asymmetric unit contains two equivalents of **247** (Z'=2), each coordinating additional three triflates (Figure 44, left). The coordinated triflate anions are distinguished by their different conformations and positional disorder in the two crystallographically independent molecules. The resulting symmetry breaking therefore leads to the observed Z'=2 asymmetric unit, but the overall geometry differs only slightly (see Figure 44, right).

The κ^6-preligand and the three monodentate triflates lead to a nonacoordinated La^{3+} center similar to that in $La(H_2O)_9^{3+}$.[179] Leaving out not coordinated atoms the geometry of the coordination polyhedral can be best described as distorted tricapped trigonal prismatic.[178,180]

Again, the triflates are only weakly bound and averaged (^{1}H-, ^{13}C-, ^{19}F-) NMR signals of a formal C_3-symmetric molecule are observed in solution (acetonitrile).

[17] **Crystal Data** for **247** ($C_{33}H_{21}F_9LaN_6O_9PS_3$; M =1082.62 g/mol): monoclinic, space group $P2_1/c$ (no. 14), a = 22.8133(13) Å, b = 19.5884(10) Å, c = 17.8485(10) Å, β = 106.423(2)°, V = 7650.6(7) Å^3, Z = 8, T = 100.03 K, μ(MoKα) = 1.430 mm^{-1}, *Dcalc* = 1.880 g/cm^3, 94756 reflections measured (4.264° ≤ 2Θ ≤ 63.23°), 25511 unique (R_{int} = 0.0397, R_{sigma} = 0.0420) which were used in all calculations. The final R_1 was 0.0325 (I > 2σ(I)) and wR_2 was 0.0768 (all data).

*Table 3: Summarized crystallographic data and ^{31}P-NMR shifts of **245**-**247**. Only crystallographic independent/unique parameters are shown. If the asymmetric unit contains more than one formula unit of the corresponding compound (Z'>1), the different crystallographic data is separated by slash ("/").*

	Ca^{2+} **245**	Sc^{3+} **246**	La^{3+} **247**
^{31}P-shift [ppm]	-4.16	-17.63	7.27
∡(C1—P1—C11) [°]	102.6(1)	97.3(1)	102.2(1)/101.0(1)
∡(C11—P1—C21) [°]	100.4(1)	97.9(1)	99.8(1)/102.9(1)
∡(C21—P1—C1) [°]	104.9(1)	106.7(1)	107.1(1)/107.0(1)
pyramidalization [°]	307.94	301.85	309.05/310.78
P1—C1 distance [Å]	1.832(1)	1.832(2)	1.836(2)/1.837(2)
P1—C11 distance [Å]	1.846(1)	1.839(2)	1.838(2)/1.839(2)
P1—C21 distance [Å]	1.837(1)	1.841(2)	1.834(2)/1.826(2)
M—P1 distance [Å]	3.854(1)	3.637(1)	3.981(1)/4.004(1)
M—N1 distance r [Å]	2.542(1)	2.281(1)	2.679(2)/2.693(2)
M—N3 distance r [Å]	2.575(1)	2.311(1)	2.788(2)/2.797(2)
M—N5 distance r [Å]	2.622(1)	2.276(1)	2.700(2)/2.729(2)
M—N2 distance r [Å]	2.602(1)	2.320(1)	2.677(2)/2.672(2)
M—N4 distance r [Å]	2.519(1)	2.320(1)	2.757(2)/2.762(2)
M—N6 distance r [Å]	2.572(1)	2.286(1)	2.700(2)/2.666(2)
M—O distance [Å]	2.391(1)	2.133(1)	2.563(1)/2.441(2)
M—O distance [Å]	-	-	2.514(2)/2.555(2)
M—O distance [Å]	-	-	2.434(2)[2.498(10)]/2.517(2)
bite angle α ∡(N1—M—N2) [°]	62.2(1)	71.3(1)	60.3(1)/59. 9(1)
bite angle α ∡(N3—M—N4) [°]	65.4(1)	70.7(1)	60.5(1)/60.4(1)
bite angle α ∡(N5—M—N6) [°]	63.5(1)	71.6(1)	60.5(1)/60.1(1)
twist angle ϕ_1 ∡[p(N1,M,P1)-(N2,M,P1)][°]	26.2(1)	18.8(1)	22.2(1)/24.1(1)
twist angle ϕ_2 ∡[p(N3,M,P1)-p(N4,M,P1)][°]	2.4(1)	10.8(1)	1.4(1)/1.2(1)
twist angle ϕ_3 ∡[p(N5,M,P1)-p(N6,M,P1)][°]	11.3(1)	2.4(1)	16.1(1)/15.6(1)
Mean twist angle ϕ	13.3	10.7	13.2/13.6
geometry index τ_6 [%]	77.8	82.2	78.0/77.3
Tolman cone angle [°]	166	165	165/169
$\%V_{Bur}$ (2.00 Å) [%]	36.1	35.2	36.3/37.0
$\%V_{Bur}$ (2.28 Å) [%]	31.2	30.5	31.5/32.1

While complex **244** is less relevant for the further discussion in this work, due to the phosphorus already being coordinated, complexes **245**, **246** and **247** still provide potential ligands to form binuclear complexes. Table 3 therefore lists the crystallographic parameters of these ligands for comparison. Due to the coordinated triflate anions, the C_3 symmetry of the molecules is no longer given and therefore the geometric parameter τ_6 is only listed for the sake of completeness. The three strongly different twist angles ($\phi_1 \neq \phi_2 \neq \phi_3$) of each structure illustrate the strong distortion from the otherwise adopted TAP or TP geometry (*cf.* **238**-**243**, Table 2). Among the ligands **245**, **246** and **247** the pyramidalization decreases with increasing effective ionic radius[173] of the metal ion (Table 3). In all three cases, the pyramidalization is significantly lower than in the ligands of TP and TAP geometry. This is partly due to the triflates occupying space, but also to the significantly larger effective ionic radii compared to the encapsulated metal ions of ligands **238**-**243**. Due to the size of the metal ions and the additional coordination of the triflates, the metal is less centered in the preligand and the M—P distance is increased in all three ligands. The M—N bond lengths are also significantly larger in all three cases than in the TP/TAP ligands and provide smaller bite angles. The harder metal ions also prefer the coordination of the harder triflate anions, which can be seen from the shortened M—O bonds.

The large effective ionic radius and the triflate coordination in **245**-**247** also affect the steric measures of the ligands. Both the Tolman cone angle and $\%V_{Bur}$ are slightly increased compared to the TP/TAP ligands. However, the effect is small, since the influence of the triflate is just by indirect distortion of the geometry and not by really extending into the phosphorus environment and the effect of the metal ions are significantly reduced by the leverage effect of the 2,2'-bipyridin-6-yl moieties.

2.7 Stereoelectronic properties of cationic phosphine ligands with encapsulated metals

2.7.1 Rhodium(I) complexes and Tolman electronic parameters

Beside the concepts to describe the steric demand of phosphines like Tolman cone angles and percent buried volume there are also many concepts to describe the electron-donating ability of the phosphorus. The most prominent concept is probably using ν(CO) stretching frequencies of corresponding metal carbonyls. This method is based on the idea of Tolman to quantify the influence of substituents on phosphorus using carbonylnickel(0) complexes of the formula [Ni(CO)$_3$L] resulting in the Tolman electronic parameter.[51] To circumvent highly toxic tetracarbonylnickel(0) thereafter also other series of transition metal complexes were prepared and correlated to the TEP.[53] One system which shows high correlation to the original TEPs is based on [Rh(acac)(CO)L] complexes and was developed by Nolan and coworkers.[181]

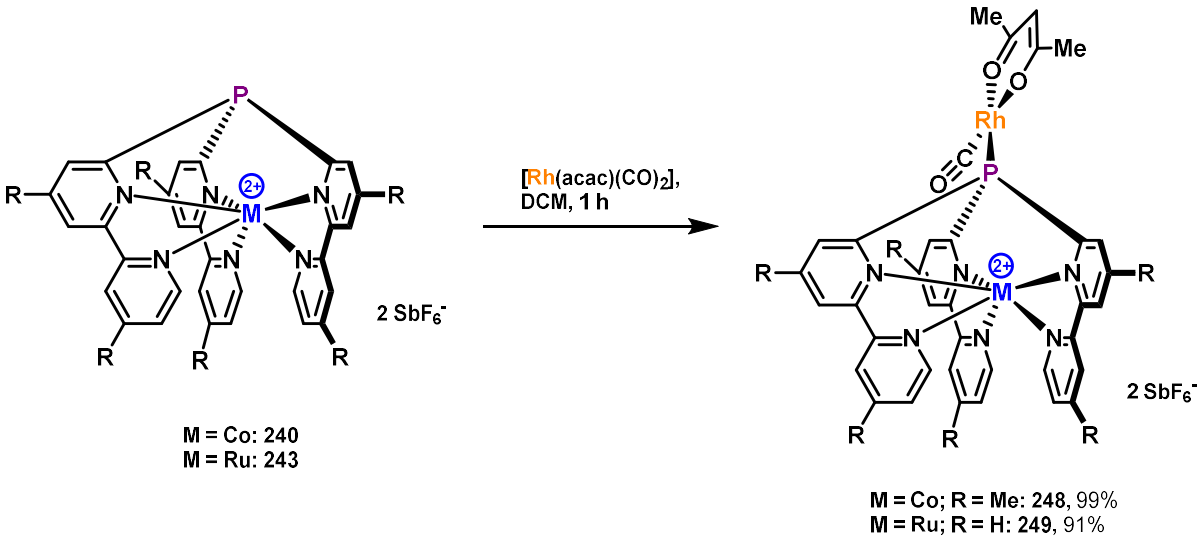

Scheme 84: Synthesis of [Rh(acac)(CO)L] complexes

The therefore needed bimetallic rhodium(I) complexes could be easily synthesized in the case of Co^{2+} (**248**) and Ru^{2+} (**249**) by ligand substitution starting from [Rh(acac)(CO)$_2$] (Scheme 84). The products can be readily identified by their doublet signals caused by $^1J_{P-Rh}$ coupling of the phosphorus nuclei to ^{103}Rh in the ^{31}P{H} NMR sprectrum. The diamagnetic Ru^{2+} binuclear rhodium(I) complex **249** shows a deshielded signal (compared to the free ligand **243**) at 60.20 ppm and a coupling constant $^1J_{P-Rh}$ of 197.3 Hz, while the Co^{2+} analog **248** exhibits a shielded signal (compared to the free ligand **240**) at 273.08 ppm and a coupling constant $^1J_{P-Rh}$ of 183.4 Hz. These asymmetric hetero-binuclear complexes represent the first use of the encapsulated dicationic ligands to modify the electronic situation of a second metal. Although their synthesis was just taken into consideration to evaluate the electron-donating ability of the phosphorus, one could also bear in mind a catalytic application in hydroformylation.[109]

In accordance to literature, DCM solutions of binuclear complexes **248** and **249** were analyzed *via* infrared spectroscopy. Both complexes revealed a bathochromic shift compared to other neutral electron-rich phosphines. The high CO stretching frequencies for the Co-based binuclear complex **248** (2001 cm^{-1}) and Ru-based binuclear complex **249** (2004 cm^{-1}) are comparable to electron poor phosphites like P(OPh)$_3$ (2008 cm^{-1}) or phosphines like N-pyrrolyl substituted phosphine P(C$_4$H$_4$N)$_2$(C$_6$H$_5$) (2003 cm^{-1}), but exceed *e.g.* PPh$_3$ by far (1978 cm^{-1}). The only small differences in sterics should not have a significant impact on the CO stretching frequencies according to the percent

buried volume measured, but it should be mentioned that distortions from the ideal square planar geometry of the Rh complexes can cause CO stretching frequency variations.

The measured CO stretching frequencies can now be correlated to the TEP according to Kühl[53] by Equation 4 with an correlation coefficient R of 0.981:

$$TEP = 0.535\, \nu CO_{Rh} + 1012;\ R = 0.981 \qquad (4)$$

Equation 4

$$TEP_{Co} = 2083\ cm^{-1}$$

$$TEP_{Ru} = 2084\ cm^{-1}$$

The results should be used with care, because the formula is only accurate for poor π-acceptors. However, this value perfectly fits the TEP of $P(OPh)_3$ and might therefore serve for comparison to other phosphines. It must be stressed that a comparison within the [Rh(acac)(CO)L] series should be preferred.

Interestingly the geometry of the ligand (TP vs. TAP) seems not to have a large impact on the TEP, which is nearly identical for both complexes **248** and **249**. However, they do have the same charge. To quantify the influence of charge on the overall donor ability a comparison of the Co^{2+} binuclear rhodium(I) complex to a Co^{3+} binuclear rhodium(I) complex was planned. Unfortunately, starting from the DCM-soluble Co^{3+} ligand **241b**, where the anions have been exchanged for $BArF_{24}^-$, no rhodium(I) could be coordinated. This result is in agreement with the literature, where Alcarazo and coworkers already stated the difficulty of tricationic ligands to coordinate metals other than anionic platinum.[92] In the hope that we can passively determine the TEP by electrochemical oxidation and using IR-spectroelectrochemistry to analyze the Co^{2+} binuclear rhodium(I) complex, we recorded a cyclic voltammogram (0.1 M $[NBu_4][PF_6]$ in DCM, 500 mV/s) of **248**.

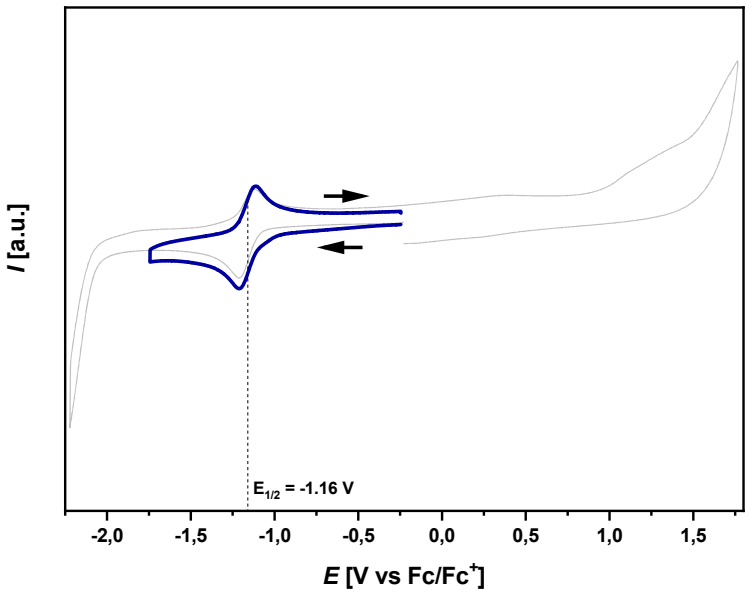

*Figure 45: Cylic voltammogram of **248** at a scan rate of 500 mV/s*

As it can be seen, no oxidation wave was obtained in the potential windows of solvent stability. On the other hand a quasi-reversible reduction at a potential $E_{1/2}$ of -1.16 V vs. Fc/Fc^+ was found. This result

might not correspond to a ligand oxidation, but can also be used in the future to be subjected to IR spectroelectrochemistry and unravel the quantitative influence of the encapsulated charges on the phosphines donor abilities.

Without being an absolute measure, the TEP values are nevertheless a valid indication of the strong influence of the cationic charges leading to a decrease in the overall donor ability of both ligands (**248** and **249**). This statement can be rationalized by comparison to other phosphine ligands. The bathochromic shift in CO stretching frequencies cannot be explained by higher pyramidalization alone. However, this method has its limitation. The solvent is limited to polar solvents, which can dissolve cations of high charge to determine the CO stretching frequency. On the other hand a coordinating solvent like acetonitrile cannot be used, because binuclear complexes like **248** show decomposition in solution most likely by ligand substitution. This fact leads to problems if the binuclear rhodium(I) complex is not soluble in DCM. Furthermore, the multitopic nature of the preligand made it impossible to synthesize clean binuclear complexes for the ligands of *e.g.* Mg^{2+}, Ca^{2+} and La^{3+}. Here, probably N coordination of 2,2'-bipyridin-6-yl moieties to the Rh takes place. Nevertheless, a reliable method for determining the donor properties or basicity of the encapsulating ligands that also allows comparison and is easy to synthesize would be desirable.

2.7.2 Phosphine selenides and $^1J_{PSe}$ coupling constants

For many multidentate heterophosphines the basicity (pK_b) cannot be determined *via* titration because *e.g.* nitrogen atoms are stronger Brønsted bases.[54] This is also the case for our ligand system, which in some cases probably would be protonated at the nitrogen releasing the encapsulated metal. Furthermore, as already pointed out, the phosphorus of the ligand is not necessarily the only atom reacting as a Lewis base towards a second metal ion[122], which makes $^1J_{PPt}$ spin–spin coupling constants towards ^{195}Pt in some cases also a bad choice for quantifying donor properties. A more suitable system involves the oxidation of a phosphine to its phosphine selenide and analyzing the $^1J_{PSe}$ spin–spin coupling constants *via* ^{31}P-NMR.[54–56,182,183] The methodology shows good correlation to the TEP and basicity of the phosphine and shows high selectivity towards phosphorus oxidation. However, to ensure its validity bulky moieties at the phosphorus and hydrogen bonds towards the selenium should be avoided. Furthermore, the P=Se group shows active and passive interactions with the NMR solvent, especially when the phosphine is charged. The reason is, that not only inductive (through-bond) but also electrostatic (through-space) effects contribute to the donor strength, whereas the latter depends on the dielectrics of the medium. This can be visualized by the two limiting resonance structure for the phosphorus-selenium bond: $Se^-{-}P^+R_3$ and $Se{=}PR_3$, where the latter structure is more favored for electron withdrawing R but also for strong coulomb interactions between selenium and a positively charged R. Having diamagnetic cationic phosphine ligands, which are very similar in steric demand, this methodology is perfectly suited, when retaining the same solvent. For neutral phosphines the electrostatic effect does not play such an important role, so they are often reported in various solvents but predominantly in DCM-d_2. For better comparison to other phosphine classes $^1J_{PSe}$ of DCM-soluble ligands will be reported in DCM-d_2 (or $CDCl_3$), while for comparison within the same encapsulating phosphine class, including DCM-insoluble ligands, $^1J_{PSe}$ will be measured in CD_3CN.

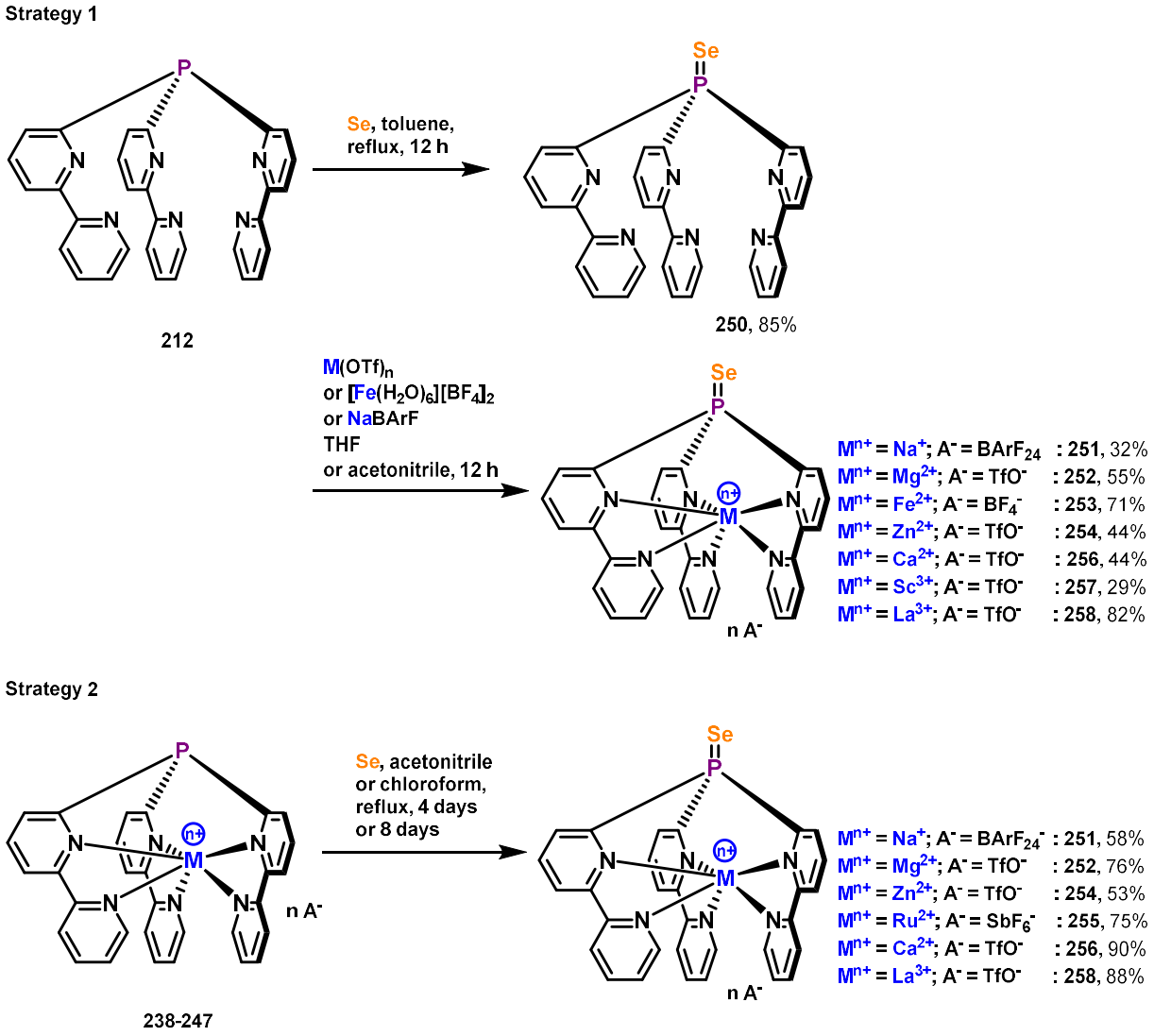

Scheme 85: Strategies towards phosphine selenides

For the synthesis of the phosphine selenides two strategies were used. The first strategy is based on precursor **250**, which can be obtained by oxidation of the preligand **212** with gray selenium. This precursor can be coordinated to different metal triflates, or if the encapsulated metal is Fe^{2+} or Na^{+} to corresponding tetrafluoroborate {$[Fe(H_2O)_6][BF_4]_2$} or tetrakis[3,5-bis(trifluoromethyl)phenyl]borate ($NaBArF_{24}$), respectively. The second strategy is based on the classic oxidation of the ligand itself by gray selenium. Therefore the ligands are dissolved in acetonitrile (or chloroform in case of **251**) and refluxed for a few days, which is possible due to their thermal stability (Unfortunately not the Co^{3+}-based ligand, which lacks thermal stability). The benefit of this method is clearly the higher yields. However, the reaction times to oxidize these electron poor ligands are long (4 days), especially for the Ru^{2+}-ligand this process takes more than an entire week. The obtained products (**251**, **252**, **254**-**258**) could then be analyzed *via* NMR, while some of them (**252**, **253**, **254**, **256**, **258**) could also be crystallized revealing structural data by single-crystal X-ray diffraction (Figure 46, Figure 47 and Figure 48).

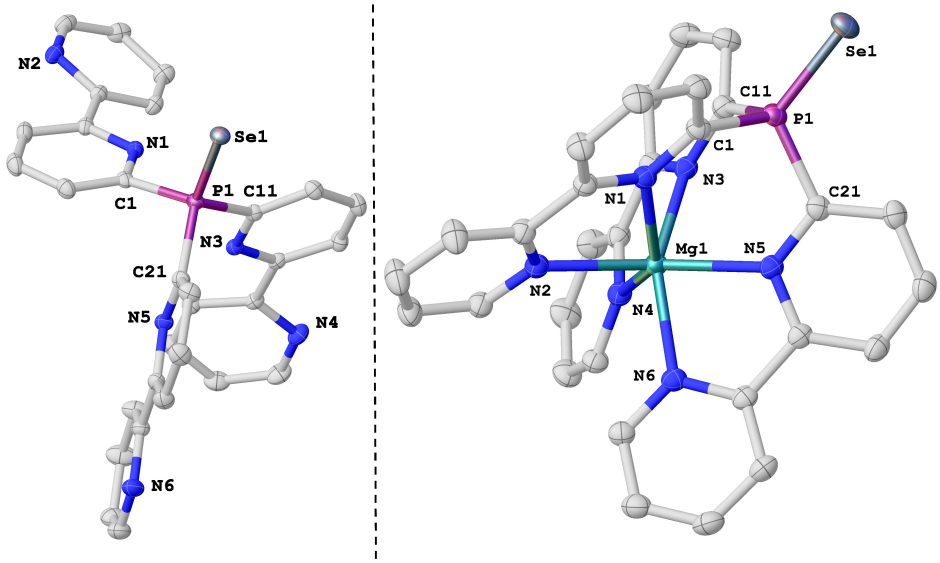

Figure 46: Molecular structures of ***250***[18] *(left) and* ***252***[19] *(right). Thermal ellipsoids at 50% probability level. Hydrogen atoms, non-coordinating counter anions and co-crystallized solvent molecules omitted for clarity.*

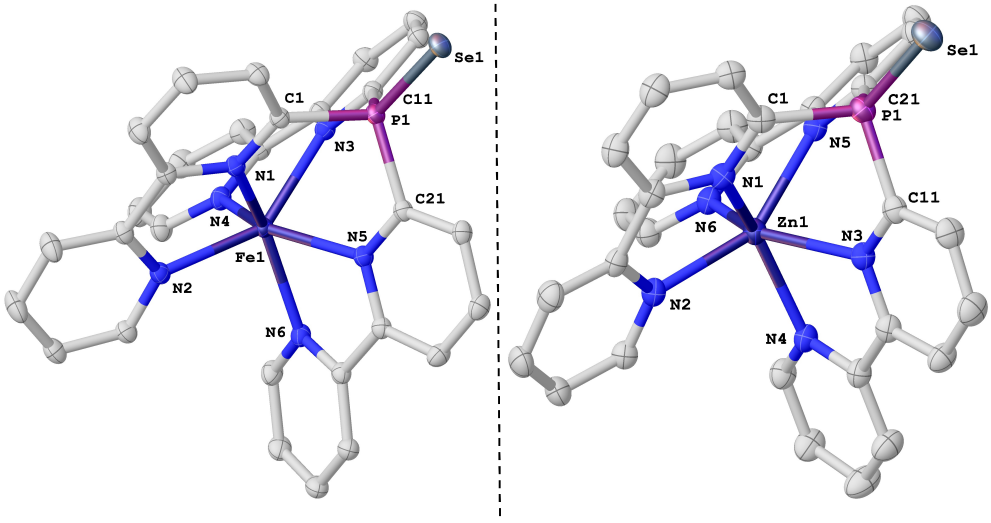

Figure 47: Molecular structures of ***253***[20] *(left) and* ***254***[21] *(right). Thermal ellipsoids at 50% probability level. Hydrogen atoms, non-coordinating counter anions and co-crystallized solvent molecules omitted for clarity.*

[18] **Crystal Data** for **250** ($C_{30}H_{21}N_6PSe$; *M* =575.46 g/mol): triclinic, space group P-1 (no. 2), *a* = 8.4515(6) Å, *b* = 11.7706(8) Å, *c* = 13.5596(9) Å, *α* = 91.842(2)°, *β* = 96.535(2)°, *γ* = 104.198(2)°, *V* = 1296.67(15) Å^3, *Z* = 2, *T* = 100.01 K, μ(MoKα) = 1.542 mm^{-1}, *Dcalc* = 1.474 g/cm^3, 23695 reflections measured (4.83° ≤ 2Θ ≤ 65.182°), 7809 unique (R_{int} = 0.0168, R_{sigma} = 0.0195) which were used in all calculations. The final R_1 was 0.0250 (I > 2σ(I)) and wR_2 was 0.0711 (all data).

[19] **Crystal Data** for **252** ($C_{34}H_{24}F_6MgN_7O_6PS_2Se$; *M* =1070.95 g/mol): monoclinic, space group $P2_1/c$ (no. 14), *a* = 17.9189(6) Å, *b* = 17.8810(6) Å, *c* = 14.2629(5) Å, *β* = 110.7900(10)°, *V* = 4272.4(3) Å^3, *Z* = 4, *T* = 100.03 K, μ(MoKα) = 1.138 mm^{-1}, *Dcalc* = 1.665 g/cm^3, 129994 reflections measured (5.07° ≤ 2Θ ≤ 61.114°), 13016 unique (R_{int} = 0.0286, R_{sigma} = 0.0165) which were used in all calculations. The final R_1 was 0.0383 (I > 2σ(I)) and wR_2 was 0.1036 (all data).

[20] **Crystal Data** for **253** ($C_{33}H_{25.5}B_2F_8FeN_{7.5}PSe$; *M* =866.51 g/mol): monoclinic, space group C2/c (no. 15), *a* = 21.8613(10) Å, *b* = 12.4042(6) Å, *c* = 25.4288(13) Å, *β* = 101.743(2)°, *V* = 6751.3(6) Å^3, *Z* = 8, *T* = 99.99 K, μ(MoKα) = 1.656 mm^{-1}, *Dcalc* = 1.705 g/cm^3, 68833 reflections measured (4.284° ≤ 2Θ ≤ 63.058°), 10771 unique (R_{int} = 0.0233, R_{sigma} = 0.0162) which were used in all calculations. The final R_1 was 0.0264 (I > 2σ(I)) and wR_2 was 0.0683 (all data).

[21] **Crystal Data** for **254** ($C_{32}H_{21}F_6N_6O_6PS_2SeZn$; *M* =1112.01 g/mol): monoclinic, space group $P2_1/c$ (no. 14), *a* = 17.9209(7) Å, *b* = 17.9062(7) Å, *c* = 14.2484(6) Å, *β* = 110.6650(10)°, *V* = 4278.1(3) Å^3, *Z* = 4, *T* = 100.0 K,

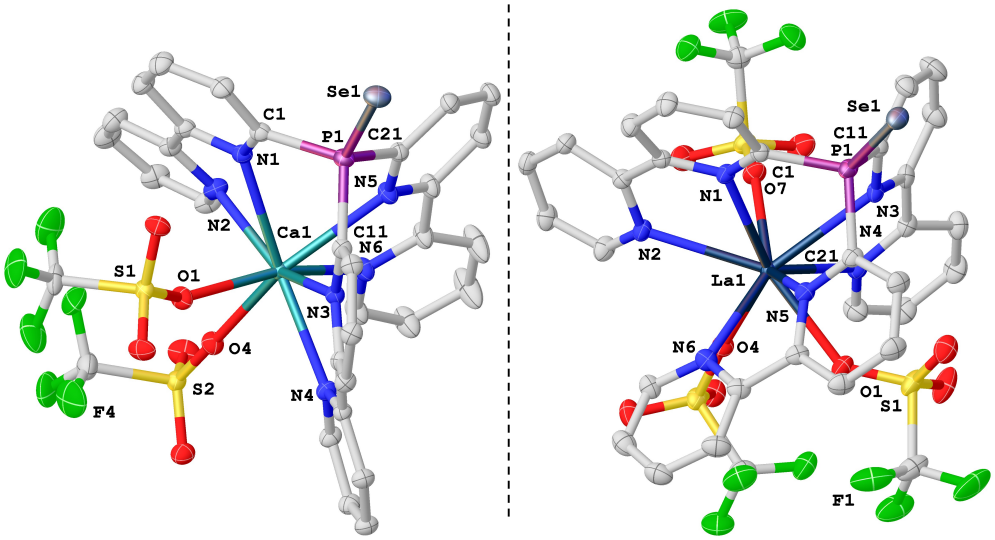

*Figure 48: Molecular structures of **256**[22] (left) and **258**[23] (right). Thermal ellipsoids at 50% probability level. Hydrogen atoms, non-coordinating counter anions and co-crystallized solvent molecules omitted for clarity.*

While compound **250** was crystallized from hot toluene, crystals suitable for X-ray diffraction of the ligands **252**, **253**, **254**, **256** and **258** could be obtained from acetonitrile/diethyl ether by vapor diffusion. All compounds retain their basic molecular structure prior to oxidation. The structures show occasional disorder, but apart from that they are crystallographically unremarkable. Disorders were found in the corresponding anions (**252**, **253**), coordinated triflates (**256**, **258**) or one pyridyl segment (**256**).

The crystallographic parameters of the individual compounds are summarized in Table 4. Additionally, corresponding NMR data is listed. In the following, the corresponding NMR data will first be discussed and then correlated with the crystal structure parameters. Finally, special features of the solid state structure and the geometries of the individual molecules will be briefly outlined.

μ(MoKα) = 1.669 mm^{-1}, *Dcalc* = 1.727 g/cm^3, 100373 reflections measured (4.858° ≤ 2Θ ≤ 54.236°), 9434 unique (R_{int} = 0.0303, R_{sigma} = 0.0154) which were used in all calculations. The final R_1 was 0.0403 (I > 2σ(I)) and wR_2 was 0.0986 (all data).

[22] **Crystal Data** for **256** ($C_{34.135}H_{24.4}CaF_{5.93}N_{7.065}O_6PS_{1.975}Se$; *M* =955.53 g/mol): triclinic, space group P-1 (no. 2), *a* = 11.9266(8) Å, *b* = 12.0896(9) Å, *c* = 13.8290(7) Å, *α* = 103.091(2)°, *β* = 97.731(2)°, *γ* = 95.302(2)°, *V* = 1908.8(2) $Å^3$, *Z* = 2, *T* = 100.0 K, μ(MoKα) = 1.352 mm^{-1}, *Dcalc* = 1.662 g/cm^3, 283398 reflections measured (4.046° ≤ 2Θ ≤ 65.218°), 13931 unique (R_{int} = 0.0193, R_{sigma} = 0.0068) which were used in all calculations. The final R_1 was 0.0256 (I > 2σ(I)) and wR_2 was 0.0722 (all data).

[23] **Crystal Data** for **258** ($C_{41}H_{33}F_9LaN_{10}O_9PS_3Se$; *M* =1325.79 g/mol): triclinic, space group P-1 (no. 2), *a* = 11.8645(5) Å, *b* = 14.0467(6) Å, *c* = 15.9396(8) Å, *α* = 79.8440(10)°, *β* = 89.095(2)°, *γ* = 71.4750(10)°, *V* = 2477.03(19) $Å^3$, *Z* = 2, *T* = 100.01 K, μ(MoKα) = 1.854 mm^{-1}, *Dcalc* = 1.778 g/cm^3, 15747 reflections measured (4.498° ≤ 2Θ ≤ 64.908°), 15747 unique (R_{int} = N/A, R_{sigma} = 0.0354) which were used in all calculations. The final R_1 was 0.0387 (I > 2σ(I)) and wR_2 was 0.0850 (all data).

*Table 4: NMR and X-ray characteristics of **250-258.** * measured in $CDCl_3$*

	250	Na^+ **251**	Mg^{2+} **252**	Fe^{2+} **253**	Zn^{2+} **254**	Ru^{2+} **255**	Ca^{2+} **256**	Sc^{3+} **257**	La^{3+} **258**
^{31}P-shift (CD_3CN) [ppm]	29.96	26.57	10.98	-	4.17	28.7	24.96	29.72	35.83
^{77}Se-shift (CD3CN) [ppm]	-307.9*	-388*	-487.86	-	-502.42	-472.85	-359.6	-	-309.69
$^1J_{P-Se}$ (CD_3CN) [Hz]	753	769.1	842.5	-	842.9	851.7	800.2	782.7	817.7
$^1J_{P-Se}$ (CD_2Cl_2) [Hz]	746.3*	785.4*	852.7	-	852.9	866.4	-	-	815.4
P1—Se1 [Å]	2.108(1)	-	2.078(1)	2.080(1)	2.077(1)	-	2.100(1)	-	2.095(1)
∡(C1—P1—C11) [°]	104.1(1)	-	102.1(1)	105.6(1)	101.6(1)	-	109.5(1)	-	105.4(1)
∡(C11—P1—C21) [°]	105.2(1)	-	106.7(1)	103.4(1)	102.6(1)	-	105.8(1)	-	109.1(1)
∡(C21—P1—C1) [°]	106.3(1)	-	101.3(1)	103.3(1)	106.2(1)	-	104.2(1)	-	103.6(1)
pyramidalization [°]	315.5	-	310.2	312.3	310.4	-	319.5	-	318.0
P1—C1 distance [Å]	1.825(1)	-	1.833(2)	1.825(1)	1.826(3)	-	1.828(1)	-	1.835(3)
P1—C11 distance [Å]	1.830(1)	-	1.830(2)	1.828(1)	1.830(3)	-	1.834(1)	-	1.823(3)
P1—C21 distance [Å]	1.830(1)	-	1.827(2)	1.828(1)	1.829(3)	-	1.840(1)	-	1.825(3)
M—P1 distance [Å]	-	-	3.488(1)	3.456(1)	3.486(1)	-	3.842(1)	-	3.947(1)
M—N1 distance r [Å]	-	-	2.247(2)	2.181(1)	2.190(2)	-	2.633(1)	-	2.815(2)
M—N3 distance r [Å]	-	-	2.178(2)	2.205(1)	2.250(2)	-	2.616(1)	-	2.724(2)
M—N5 distance r [Å]	-	-	2.197(2)	2.206(1)	2.166(2)	-	2.644(1)	-	2.715(2)
M—N2 distance r [Å]	-	-	2.249(2)	2.186(1)	2.152(2)	-	2.537(1)	-	2.720(2)
M—N4 distance r [Å]	-	-	2.195(2)	2.201(1)	2.232(2)	-	2.554(1)	-	2.703(2)
M—N6 distance r [Å]	-	-	2.185(2)	2.218(1)	2.166(2)	-	2.567(1)	-	2.672(2)
M—O distance [Å]	-	-	-	-	-	-	2.422(1)	-	2.500(2)
M—O distance [Å]	-	-	-	-	-	-	2.432(1)	-	2.460(2)
M—O distance [Å]	-	-	-	-	-	-	-	-	2.478(3) [2.48(1)]
bite angle α ∡(N1—M—N2) [°]	-	-	72.2(1)	74.2(1)	75.2(1)	-	62.4(1)	-	61.5(1)
bite angle α ∡(N3—M—N4) [°]	-	-	74.9(1)	73.6(1)	72.6(1)	-	64.1(1)	-	62.1(1)
bite angle α ∡(N5—M—N6) [°]	-	-	74.6(1)	73.2(1)	75.4(1)	-	64.5(1)	-	60.1(1)
twist angle ϕ ∡[p(N1,M,P1)-(N2,M,P1)][°]	-	-	18.6(1)	17.1(1)	18.2(1)	-	23.3(1)	-	0.5(1)
twist angle ϕ ∡[p(N3,M,P1)-p(N4,M,P1)][°]	-	-	16.9(1)	15.4(1)	19.8(1)	-	15.3(1)	-	9.7(1)

	250	Na^+ **251**	Mg^{2+} **252**	Fe^{2+} **253**	Zn^{2+} **254**	Ru^{2+} **255**	Ca^{2+} **256**	Sc^{3+} **257**	La^{3+} **258**
twist angle ϕ ∡[p(N5,M,P1)-p(N6,M,P1)][°]	-	-	16.9(1)	19.2(1)	18.3(1)	-	1.4(1)	-	24.9(1)
Mean twist angle ϕ	-	-	17.5	17.3	18.8	-	13.3	-	11.69
geometry index τ_6 [%]	-	-	70.9	71.3	68.7	-	77.8	-	80.5

In the corresponding $^{31}P\{H\}$ NMR spectra of all diamagnetic phosphine selenides one signal with small ^{77}Se satellites can be seen, indicating successful synthesis. Due to oxidation the ^{31}P-chemical shifts are deshielded compared to the unoxidized ligands. The satellites result from the small natural abundance of ^{77}Se (7.63%), which is the only of the six natural isotopes being NMR active (spin ½ nucleus). These satellites can now be used to determine the $^1J_{P-Se}$ spin–spin coupling constants (Table 4). The $^1J_{P-Se}$ coupling constants (CD_3CN) clearly outline the influence of the cationic charge on the donor ability of the phosphine. While the oxidized neutral preligand shows the lowest coupling constant, the monocationic oxidized ligand of Na^+ exhibits a slightly increased one. The phosphine selenides of Ca^{2+} and La^{3+} show coordinated triflates in their solid state structures compensating the positive charge. From the Sc^{3+} ligand the crystal structure is unknown, but it can be assumed, that, like in the unoxidized ligand, at least one triflate is coordinated. The structures of these ligands in solution stay unknown, but a fluctuation in coordination, with triflates dissociation and association on a faster time scale than the NMR can be expected. This process can be visualized in case of the oxidized La^{3+} ligand **258**. If the ^{19}F NMR is measured in DCM-d^2 instead of coordinating CD_3CN, the sharp ^{19}F signal splits into two broad signals. This fluctuation effect results in Ca^{2+}, La^{3+}, Sc^{3+} ligands, whose phosphorus does not experience the full impact of their cationic charge, leading to coupling constants higher than monocationic phosphine selenides, but less than coordinatively saturated dicationic phosphine selenides. These in turn (Mg^{2+}, Zn^{2+}, Ru^{2+}) show the highest coupling constants. Unfortunately, the coupling constant of the corresponding Fe^{2+} selenide **253** could not be determined due to its paramagnetism. The $^1J_{PSe}$ spin–spin coupling constant increases with s character of the lone pair and decreases with basicity (donor properties) at the phosphorus of a phosphine. Therefore, the relative tendency for weak donor abilities is: Ru^{2+}>Zn^{2+}>Mg^{2+}>La^{3+}>Ca^{2+}>Sc^{3+}>Na^+>preligand. Due to the fact that Ru^{2+}, Zn^{2+} and Mg^{2+}-ligands have similar weak donor abilities, being coordinatively saturated and having the largest cationic charge, seems to be more important than geometric influences by TAP and TP structures.

For the better comparison towards other ligand classes and to analyze the influence of the NMR solvent used, $^1J_{PSe}$ spin–spin coupling constant were also determined in DCM-d^2 (or $CDCl_3$, marked with an asterisk). Unfortunately, the Ca^{2+} and Sc^{3+} phosphine selenides did not exhibit the required solubility in DCM. However, using a solvent with smaller dielectrics should decrease the medium's ability to shield the charge, which should result in an increase of the $^1J_{PSe}$ spin–spin coupling constant for cationic charges (electrostatic effect).[183] This effect should not be present for neutral phosphines or reversed for anionic phosphines. The increase of $^1J_{PSe}$ can be seen in the case of Na^+, Mg^{2+}, Zn^{2+} and Ru^{2+}. Surprisingly, this was not the case for the La^{3+} phosphine selenide, which might be explained by the coordination of the triflates making it neutral or coordination of acetonitrile in the CD_3CN solution changing its electronic properties. The decrease in $^1J_{PSe}$ for the neutral ligand might be explained by stronger interactions of CD_3CN compared to DCM-d^2 with the P─Se bond.

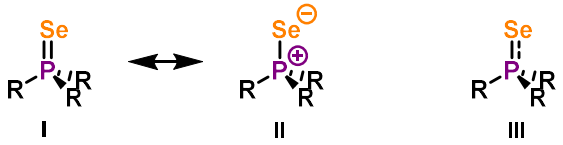

Scheme 86: Resonance forms for P—Se bond[184]

The P—Se bond length obtained from the crystallographic data is shortened for all crystallized ligands compared to the preligand. The P—Se bond (III, Scheme 86) can be best described as a composition of a zwitterionic resonance form (II, Scheme 86) and a resonance form featuring a double bond (I, Scheme 86). Counterintuitively, the P—Se bond strength decreases with decrease in bond length (decreased P—Se BDE).[184] The positive charges encapsulated in the ligands mentioned and the electron withdrawing effect of the substituents on the phosphorus destabilize the zwitterionc resonance form and lead to a shortening of the Se=P bond, which might also indicate a very weak P—Se bond in case of the cationic phosphine selenides.[184] An application as chalcogen atom transfer reagent is conceivable. The literature also reported a correlation between the BDE and the ^{77}Se shift, which indicated for electron donating R a stabilization of zwitterionic species II and therefore a stronger shielding of the selenium. This result contradicts with the strong shielded ^{77}Se shifts obtained for our electron poor phosphine selenides. Furthermore, a contrary trend can be seen. With decreasing ^{77}Se chemical shift the bond distances also decrease. On the other hand, the expected distance correlation of the $^{1}J_{PSe}$ spin–spin coupling constant can be found for all ligands of which both values are known (Figure 49).

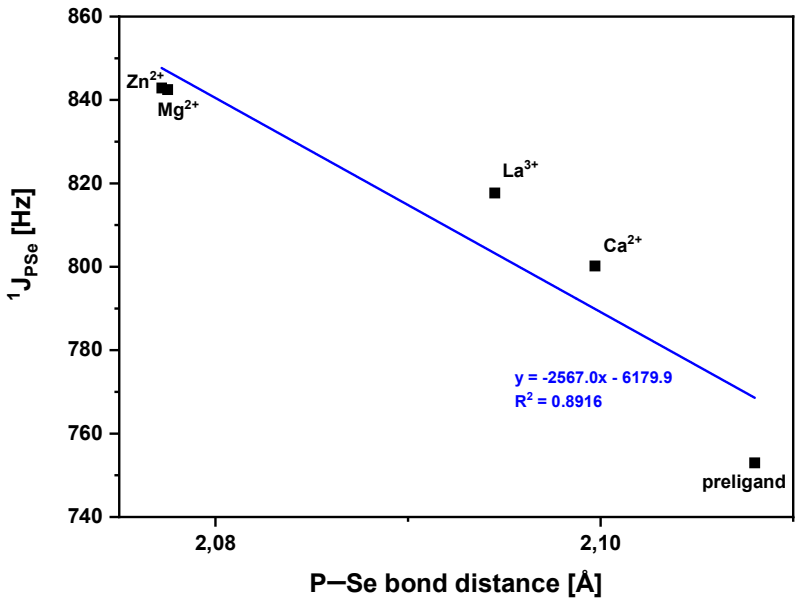

Figure 49: Correlation of $^{1}J_{PSe}$ and P—Se bond distance

A second look at the crystal structures and comparing them with their corresponding unoxidized ligands reveals some geometric differences. The Ca^{2+} structure is not dimeric any more but exhibits a monomeric structure with two coordinated triflates, while the oxidized La^{3+}-ligand keeps three coordinated triflates. In all crystal structures the P—C distances are shortened and the pyramidalization is decreased, which can be explained by the P(III)→P(V) oxidation with selenium. Furthermore, the increase in pyramidalization does not change the preferred geometry (general TP vs. TAP trends are maintained), but leads to a more distorted structure towards the TAP limit in every crystallized

coordinatively saturated case except for Fe^{2+}. The structure of the Fe^{2+} phosphine selenide might be confusing, because starting from an unoxidized ligand very close to the TAP limit and ending up with an oxidized ligand closer to the TP limit than Mg^{2+} and Zn^{2+} might be counterintuitive. Consequently, a spin cross over caused by the perturbation of the pyramidalization from the d^6 low-spin to the d^6 high-spin configuration must have happened, resulting in a strong tendency to achieve the TP limit.[171] The broad proton NMR signals for the unoxidized Fe^{2+} ligand **239** close to a spin crossover, the impossibility to obtain even a proton NMR spectrum of **253** and especially the large M─N distances in **253**[158] also suggest this.

2.8 Steric and Stereoelectronic properties in comparison to related ligands

To classify these encapsulating phosphine ligands one has to compare them to phosphines exhibiting similar environments (Scheme 87). The easiest way is the comparison of the dicationic encapsulating phosphine ligands of Co^{2+} (**240**), Zn^{2+} (**242**) and Ru^{2+} (**243**) to dicationic ligands already published in our group. The inability of those to coordinate metals other than Pt(II) and Au(I) makes it difficult to find comparable experimental data. However, the π-acceptor properties of the Co^{2+} and Ru^{2+} encapsulating dicationic phosphine ligands cannot compete with the calculated TEP of ligand **87**[92] (2101 cm^{-1}, Scheme 87). This is probably due to the more localized cationic charges next to the phosphorus in ligand **87**.

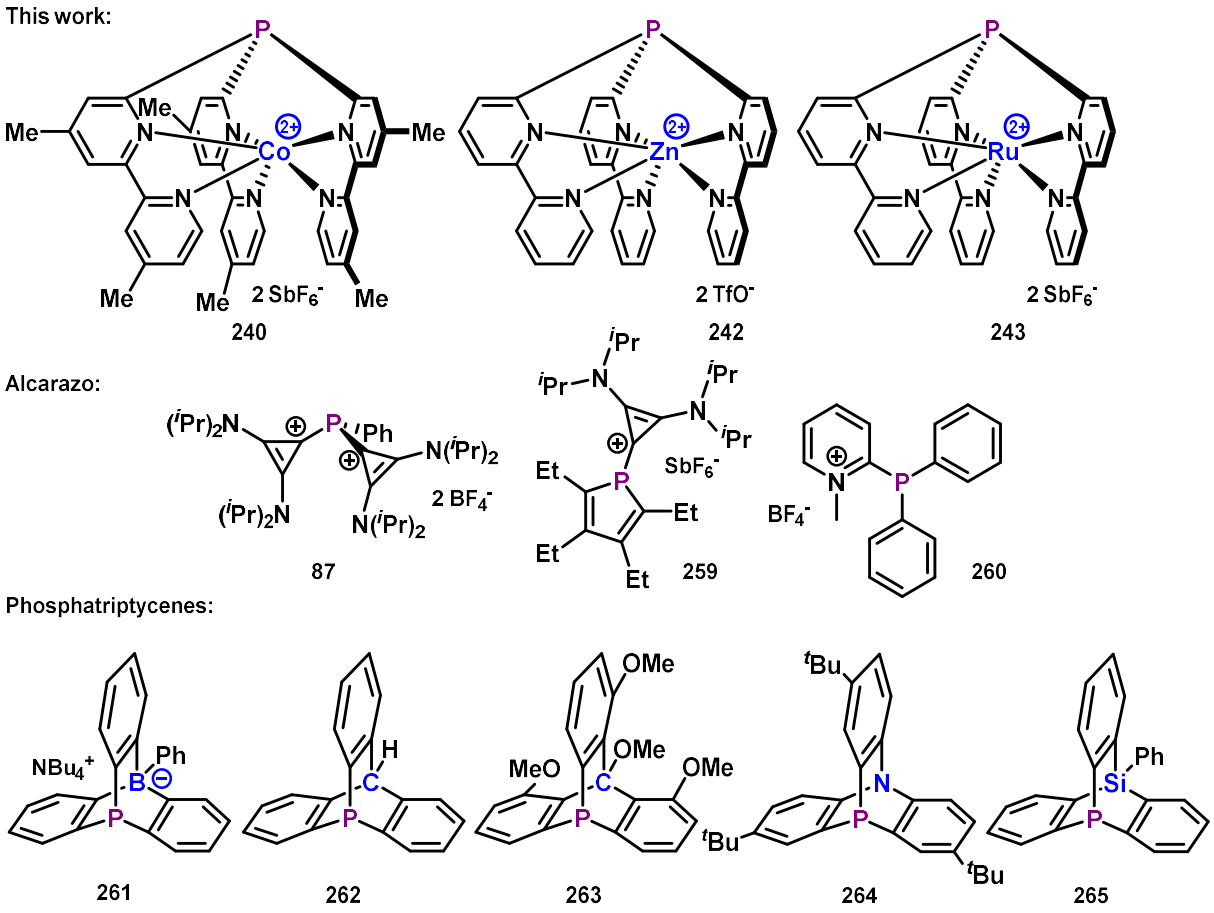

Scheme 87: Comparison between different strained and cationic phosphines

Table 5: Characteristics of different strained and cationic phosphines

	Co^{2+} **240**	Zn^{2+} **242**	Ru^{2+} **243**	259[80]	260[86]	261[118]	262[100,106]	263[105]	264[109]	265[112,118]
Pyramidalization <(C—P—C) [°]	298	299	300	304	305	288	284	-	285	297
$^1J_{P-Se}$ (CD_2Cl_2) [Hz]	-	853	866	763	-	-	-	-	-	-
$^1J_{P-Se}$ ($CDCl_3$) [Hz]	-	-	-	-	-	719	-	828	-	793
$^1J_{P-Se}$ (CD_3CN) [Hz]	-	843	852	-	-	-	-	-	-	-
$\nu_{CO}^{[Rh(acac)(CO)L]}$ [cm^{-1}]	2001	-	2004	-	-	-	1985	-	1985	-
$\nu_{CO}^{trans\text{-}[RhCl(CO)L2]}$ [cm^{-1}]	-	-	-	1984	1996	-	-	-	-	-
cone angle [°]	166 /169	163	160 /160 /161	-	-	157	160	-	151	161
buried volume %VBur (2.00 Å) [%]	34.3 /33.8	34.5	33.4 /33.4 /33.6	51.3	-	32.5	30.7	-	30.6	33.6
buried volume %VBur (2.28 Å) [%]	29.6 /29.1	29.7	28.7 /28.7 /28.9	46.7	-	27.8	26.2	-	26.0	28.9

Nevertheless, a comparison to monocationic phosphines (**260**), constrained monocationic phosphines (**259**), neutral 9-phosphatriptycenes (**262**, **263**, **264**, **265**) and anionic 9-phosphatriptycenes (**261**) of different pyramidalization should visualize the effect of charge and geometric constrain. Furthermore, a comparison to more classical phosphine PPh_3 and phosphite $P(OPh)_3$ is of interest.

First it needs to be said that TEP and related metal carbonyl methodologies quantify the net donating ability of phosphines. Although in literature high TEPs are often referred to phosphines with weak σ-donor and good π-acceptor, the separation of σ-donor and π-acceptor properties with just one parameter (*e.g.* TEP) is not accurate and neglects the existence of *e.g.* phosphines with weak σ-donor and weak π-acceptor properties.[53] In literature the $^1J_{P-Se}$ coupling constants are very often used as quantification of pure σ-donor properties of a phosphine. This fact can be rationalized, when one considers that the $^1J_{P-Se}$ coupling constants correlates with the basicity (pk_b) of a phosphine, which itself is a measure of the σ-donor properties.[54,185]

While the net donor ability for the Co^{2+} ($\nu_{CO}^{[Rh(acac)(CO)L]}$ 2001 cm^{-1}) and Ru^{2+} ($\nu_{CO}^{[Rh(acac)(CO)L]}$ = 2004 cm^{-1}) ligands is much less than for PPh_3 (*cf.* $\nu_{CO}^{[Rh(acac)(CO)L]}$ = 1978 cm^{-1} [53]) the CO stretching frequency is almost the same compared to $P(OPh)_3$ (*cf.* $\nu_{CO}^{[Rh(acac)(CO)L]}$ = 2008 cm^{-1} [53]). However, at the same time the $^1J_{P-Se}$ coupling constant for the corresponding triphenylselenophosphate of $P(OPh)_3$ ($^1J_{P-Se}$ = 1016 Hz ($CDCl_3$) [186]) is much higher than for the phosphine selenide of Ru^{2+} ($^1J_{P-Se}$ = 866 Hz(CD_2Cl_2)). The lower basicity of $P(OPh)_3$ at similar net donor ability might indicate the presence of strong π-accepting properties in the Ru^{2+} ligand if steric effects and additional electronic factors are neglected.

The 9-phosphatriptycenes are an interesting phosphine class exhibiting low σ-donor properties due to their high pyramidalization causing high s-character of their lone pair. Exchanging the second bridging

atom from a carbon to another p-block element can alter the donor abilities directly by their charge or indirectly by the ionic radius defining the pyramidalization. As it can be seen in Table 5, the carbon and nitrogen based 9-phosphatriptycenes (**262**, **264**) exhibit decreased net donating ability compared to PPh_3 but still are stronger overall donors than the ligands of Ru^{2+} (**243**)and Co^{2+} (**240**). This fact already shows the huge impact of the positive charge on the donor abilities: Both ligands (Ru^{2+} and Co^{2+}) show less pyramidalization but still have an even more decreased net donating ability than **262** and **264**. Comparing the low σ-donating abilities of the encapsulating phosphines (Co^{2+}, Zn^{2+}, Ru^{2+}) *via* $^1J_{P-Se}$ coupling constant shows that encapsulating phosphines outcompete even Si-based 9-phosphatriptycenes **265** of similar pyramidalization or C-based 9-phosphatriptycenes with higher pyramidalization and electron withdrawing groups (**263**). The reversed influence of charge in phosphatriptycenes can also be visualized by borate-phosphine ligand **261** holding one of the highest pyramidalizations but exhibiting increased basicity due to the negative charge spread out toward the four aromatic rings.

A comparison to monocationic phosphines (**260**, **259**) is problematic, not only because of the usage of a different reference system determining the CO stretching frequencies, but also because the distortion of the used square pyramidal Vaska's complexes [RhCl(CO)L_2], which might underestimate their potential (*cf.* $P(OPh)_3$: $\nu_{CO}^{trans\text{-}[RhCl(CO)L_2]}$ = 2012 cm^{-1} [187]). Nevertheless, calculations and experimental TEPs of similar monocationic phosphines estimate their net donating ability close to $P(OPh)_3$. This might suggest that the overall donor abilities are very similar to our Ru^{2+}-ligand, but compared to **259** the basicity ($^1J_{P-Se}$) of the Ru^{2+}-ligand is much smaller. Furthermore, the steric measure compared to **259** is according to the percent buried volume much smaller ($\%V_{Bur}$ of **259** was recalculated from the free ligand and it's provided crystallographic data[80]). This makes the Ru^{2+}-ligand a weak σ-donor and strong π-acceptor with a steric demand comparable to PPh_3 and $P(OPh)_3$.[59]

2.9 Coordination chemistry - Au(I) complexes

2.9.1 Synthesis of Au(I) complexes

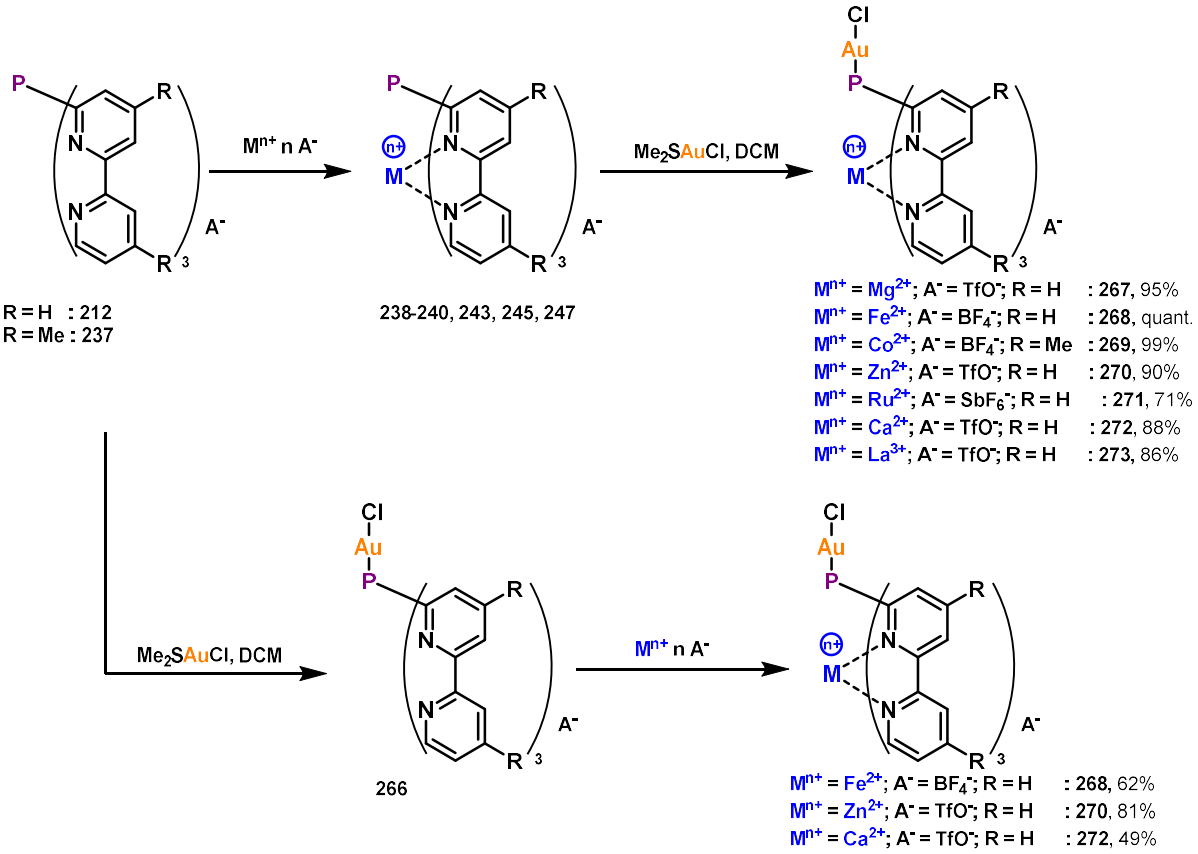

Scheme 88: Synthesis of Au(I) complexes

For initial screenings gold(I) catalysis seemed to be the right choice, due to the frequently reported ligand effect of strong acceptor ligands. To apply the cationic encapsulating phosphines in π-acid catalysis the corresponding chlorogold(I) complexes are required. These precatalysts should form an active catalyst after activation with *e.g.* silver salts.

The binuclear gold(I) complexes **267**-**273** could be synthesized *via* two different synthetic routes. The first strategy uses the already synthesized cationic encapsulating phosphines and reacts them with a gold(I) precursor [$(CH_3)_2SAuCl$] in DCM. However, due to the high selectivity of the soft gold(I) for phosphorus coordination, also the preligand **212** can be reacted with $(CH_3)_2SAuCl$ forming a phosphine chlorogold(I) complex **266**. Afterwards, a second metal can be encapsulated leading also to the binuclear gold(I) complexes **268**, **270** and **272**. The second approach highlights the easy switchability of this ligand class by exchanging the metal center. The success of the reaction is indicated by a shift of the phosphorus signal in ^{31}P-NMR. All diamagnetic compounds exhibit the expected deshielding of the signal while the paramagnetic compound of Co^{2+} **269** shows a more shielded signal.

The solid-state structures of some gold(I)complexes could be obtained from crystals grown by slow evaporation of a diethyl ether solution (**266**) or by slow vapor diffusion of diethyl ether into a acetonitrile solution (Mg^{2+} **267**, Fe^{2+} **268**, Zn^{2+} **270** and Ca^{2+} **272**).

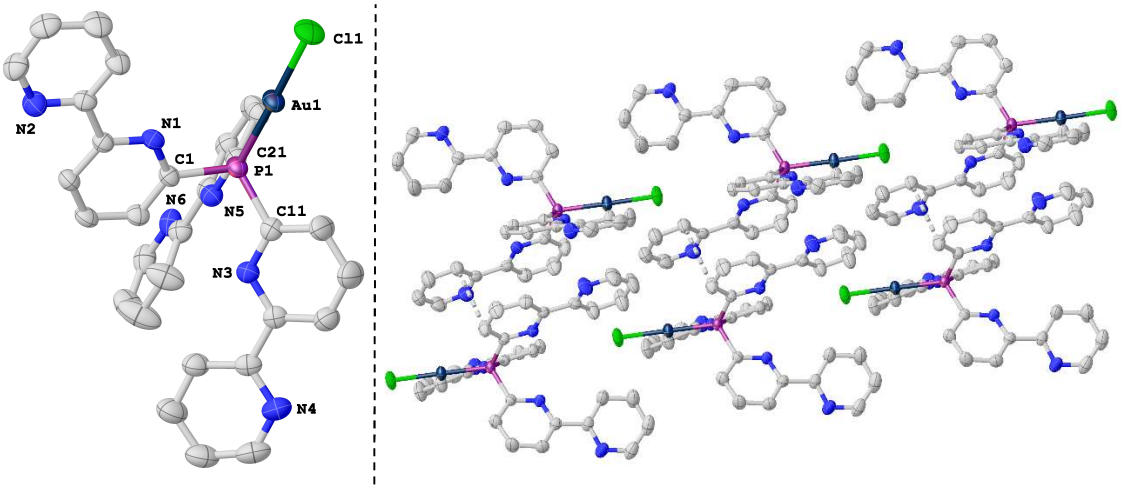

*Figure 50: Molecular structures of **266**[24](left), Illustration of π-stacking (right). Thermal ellipsoids at 50% probability level. Hydrogen atoms omitted for clarity; Asymmetric unit contains two formula units of the corresponding compound **266** (left), one unit has been omitted for clarity. Selected bond length (Å) and angles (°) for **266** are summarized in Table 6.*

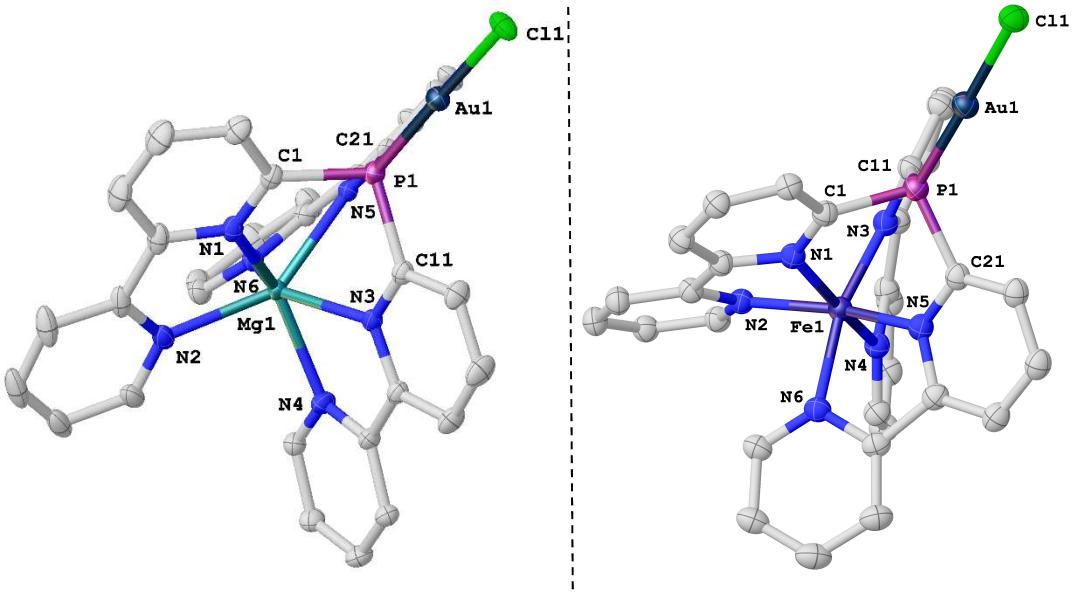

*Figure 51: Molecular structures of **267**[25] (left) and **268**[26] (right). Thermal ellipsoids at 50% probability level. Hydrogen atoms, non-coordinating counter anions and co-crystallized solvent molecules omitted for clarity. Selected bond length (Å) and angles (°) for **267** and **268** are summarized in Table 6.*

[24] **Crystal Data** for **266** ($C_{30}H_{21}AuClN_6P$; *M* =728.91 g/mol): monoclinic, space group $P2_1/c$ (no. 14), *a* = 10.6032(4) Å, *b* = 27.4329(9) Å, *c* = 23.9847(11) Å, *β* = 90.679(2)°, *V* = 6976.1(5) Å^3, *Z* = 8, *T* = 199.98 K, μ(MoKα) = 4.365 mm^{-1}, *Dcalc* = 1.388 g/cm^3, 82508 reflections measured (4.118° ≤ 2Θ ≤ 61.344°), 21377 unique (R_{int} = 0.0256, R_{sigma} = 0.0251) which were used in all calculations. The final R_1 was 0.0275 (I > 2σ(I)) and wR_2 was 0.0789 (all data).

[25] **Crystal Data** for **267** ($C_{36}H_{27}AuClF_6MgN_8O_6PS_2$; *M* =1133.47 g/mol): monoclinic, space group $P2_1/n$ (no. 14), *a* = 14.0320(5) Å, *b* = 14.4151(5) Å, *c* = 20.3948(7) Å, *β* = 91.9850(10)°, *V* = 4122.8(2) Å^3, *Z* = 4, *T* = 100.0 K, μ(MoKα) = 3.872 mm^{-1}, *Dcalc* = 1.826 g/cm^3, 237732 reflections measured (4.052° ≤ 2Θ ≤ 66.34°), 15601 unique (R_{int} = 0.0303, R_{sigma} = 0.0138) which were used in all calculations. The final R_1 was 0.0219 (I > 2σ(I)) and wR_2 was 0.0546 (all data).

[26] **Crystal Data** for **268** ($C_{32}H_{24}AuB_2ClF_8FeN_7P$; *M* =999.44 g/mol): triclinic, space group P-1 (no. 2), *a* = 11.6881(7) Å, *b* = 12.3876(9) Å, *c* = 12.9242(7) Å, *α* = 89.801(3)°, *β* = 72.710(4)°, *γ* = 68.357(3)°, *V* = 1648.82(19) Å^3, *Z* = 2, *T* = 100.01 K, μ(MoKα) = 5.097 mm^{-1}, *Dcalc* = 2.013 g/cm^3, 120907 reflections measured (4.18° ≤ 2Θ ≤ 65.382°), 12084 unique (R_{int} = 0.0238, R_{sigma} = 0.0113) which were used in all calculations. The final R_1 was 0.0324 (I > 2σ(I)) and wR_2 was 0.0835 (all data).

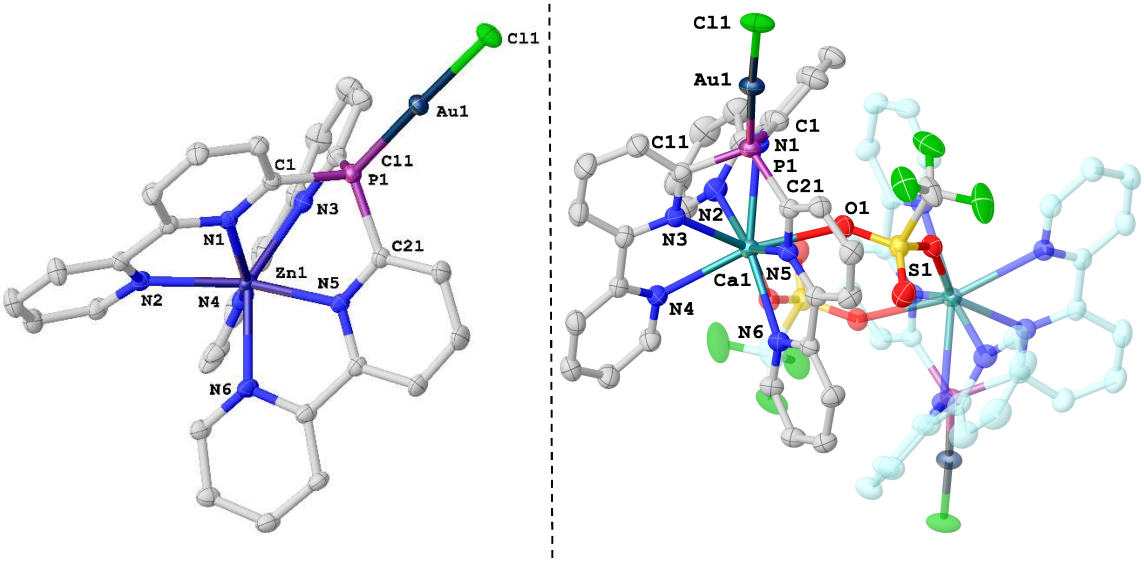

*Figure 52: Molecular structures of **270**[27] (left) and **272**[28] (right). Thermal ellipsoids at 50% probability level. Hydrogen atoms, non-coordinating counter anions and co-crystallized solvent molecules omitted for clarity; second half of the centrosymmetric **272** generated by symmetry drawn translucent (symmetry code: '=1-x,1-y,1-z). Selected bond length (Å) and angles (°) for **270** and **272** are summarized in Table 6.*

The crystal structures of **267**, **268** and **270** shown, exhibit the expected geometry and are crystallographically unremarkable Z'=1 structures except for disordering of one pyridyl segment and the triflate anions in **267** and **270**. However, **266** and **272** are Z'=2 and Z'=0.5, respectively, which needs to be investigated in more detail. Due to technical limitations at that time, the data collection was performed at 200 K for **266**. The asymmetric unit contains two molecules of **266** that undergo π-stacking between two respective 2,2'-bipyridin-6-yl units leading to a loss of potential C_3 symmetry. In the case of **272**, the encapsulation of the corresponding Ca^{2+} is non-enclosing like in **245**, leaving enough space for two bridging triflates thus forming a centrosymmetric dimeric aggregate. The asymmetric unit now consists of half a molecule of this full dinuclear aggreagete (Z'=0.5), two molecules of co-crystallized acetonitrile and one molecule of co-crystallized diethyl ether at special positions, and one uncoordinated triflate.

The NMR and crystallography data are now summarized in Table 6 to allow further comparison.

[27] **Crystal Data** for **270** ($C_{36}H_{27}AuClF_6N_8O_6PS_2Zn$; *M* =1174.53 g/mol): monoclinic, space group $P2_1/n$ (no. 14), *a* = 13.9820(5) Å, *b* = 14.4313(6) Å, *c* = 20.4194(8) Å, *β* = 92.3160(10)°, *V* = 4116.8(3) Å^3, *Z* = 4, *T* = 100.0 K, μ(MoKα) = 4.431 mm^{-1}, *Dcalc* = 1.895 g/cm^3, 226250 reflections measured (4.058° ≤ 2Θ ≤ 66.342°), 15512 unique (R_{int} = 0.0255, R_{sigma} = 0.0125) which were used in all calculations. The final R_1 was 0.0217 (I > 2σ(I)) and wR_2 was 0.0560 (all data).

[28] **Crystal Data** for **272** ($C_{36}H_{29}AuCaClF_6N_7O_{6.5}PS_2$; *M* =1145.25 g/mol): monoclinic, space group $P2_1/c$ (no. 14), *a* = 11.5902(13) Å, *b* = 14.7946(14) Å, *c* = 25.274(3) Å, *β* = 91.069(3)°, *V* = 4333.0(8) Å^3, *Z* = 4, *T* = 100.0 K, μ(MoKα) = 3.788 mm^{-1}, *Dcalc* = 1.756 g/cm^3, 16970 reflections measured (4.24° ≤ 2Θ ≤ 61.05°), 16970 unique (R_{int} = ?, R_{sigma} = 0.0283) which were used in all calculations. The final R_1 was 0.0398 (I > 2σ(I)) and wR_2 was 0.1301 (all data).

*Table 6: Characteristics of Au(I) complexes. * measured in $CDCl_3$; ** measured in CD_2Cl_2*

	266	Mg^{2+} **267**	Fe^{2+} **268**	Co^{2+} **269**	Zn^{2+} **270**	Ru^{2+} **271**	Ca^{2+} **272**	La^{3+} **273**
^{31}P-shift (CD_3CN) [ppm]	32.82*	15.72	23.58	251.78	5.21	44.88	34.27	47.36**
P—Au [Å]	2.224(1) /2.225(1)	2.217(1)	2.211(1)	-	2.217(1)	-	2.223(1)	-
Au—Cl [Å]	2.274(1) /2.278(1)	2.278(1)	2.275(1)	-	2.280(1)	-	2.275(1)	-
∡P—Au—Cl angle [°]	178.7(1) /177.8(1)	178.1(1)	178.7(1)	-	178.4(1)	-	177.8(1)	-
∡(C1—P1—C11) [°]	109.4(1) /100.7(1)	103.3(1)	103.4(1)	-	104.6(1)	-	105.0(2)	-
∡(C11—P1—C21) [°]	102.5(1) /105.3(1)	102.7 (1)	100.8(1)	-	103.6(1)	-	106.0(2)	-
∡(C21—P1—C1) [°]	105.6(1) /110.7(1)	105.5(1)	99.7(1)	-	102.9(1)	-	106.7(2)	-
pyramidalization [°]	317.5 /316.7	311.5	303.9	-	311.0	-	317.7	-
P1—C1 distance [Å]	1.824(3) /1.826(2)	1.822(2)	1.809(2)	-	1.819(2)	-	1.824(5)	-
P1—C11 distance [Å]	1.829(3) /1.821(2)	1.822(2)	1.820(2)	-	1.819(2)	-	1.828(5)	-
P1—C21 distance [Å]	1.837(3) /1.828(2)	1.819(2)	1.821(2)	-	1.820(2)	-	1.823(5)	-
Mean P—C distance [Å]	1.830 /1.825	1.821	1.817	-	1.819	-	1.825	-
M—P1 distance [Å]	-	3.479(1)	3.260(1)	-	3.468(1)	-	3.798(2)	-
M—N1 distance r [Å]	-	2.209(2)	1.937(2)	-	2.161(1)	-	2.576(5)	-
M—N3 distance r [Å]	-	2.239(1)	1.928(2)	-	2.207(2)	-	2.583(4)	-
M—N5 distance r [Å]	-	2.184(1)	1.933(2)	-	2.217(1)	-	2.654(4)	-
M—N2 distance r [Å]	-	2.186(2)	2.008(2)	-	2.205(1)	-	2.569(5)	-
M—N4 distance r [Å]	-	2.234(2)	1.999(2)	-	2.151(2)	-	2.545(5)	-
M—N6 distance r [Å]	-	2.210(2)	1.999(2)	-	2.201(1)	-	2.548(4)	-
M—O distance [Å]	-	-	-	-	-	-	2.390(4)	-
bite angle α ∡(N1—M—N2) [°]	-	74.4(1)	79.9(1)	-	74.8(1)	-	62.1(2)	-
bite angle α ∡(N3—M—N4) [°]	-	72.7(1)	80.5(1)	-	74.6(1)	-	65.7(1)	-
bite angle α ∡(N5—M—N6) [°]	-	74.3(1)	80.4(1)	-	73.5(1)	-	63.1(1)	-

	266	Mg^{2+} **267**	Fe^{2+} **268**	Co^{2+} **269**	Zn^{2+} **270**	Ru^{2+} **271**	Ca^{2+} **272**	La^{3+} **273**
twist angle ϕ ∡[p(N1,M,P1)-(N2,M,P1)][°]	-	14.1(1)	41.0(1)	-	18.2(1)	-	25.3(2)	-
twist angle ϕ ∡[p(N3,M,P1)-p(N4,M,P1)][°]	-	17.7 (1)	40.6(1)	-	15.7(1)	-	2.1(2)	-
twist angle ϕ ∡[p(N5,M,P1)-p(N6,M,P1)][°]	-	16.1(1)	42.8(1)	-	19.5(1)	-	11.9(2)	-
Mean twist angle ϕ	-	15.9	41.4	-	17.8	-	13.1	-
geometry index τ_6 [%]	-	73.5	30.9	-	70.3	-	78.2	-
Tolman cone angle [°]	192/190	168	162	-	168	-	169	-
$\%V_{Bur}$ (2.00 Å) [%]	37.4 /37.2	35.9	34.0	-	35.7	-	37.0	-
$\%V_{Bur}$ (2.28 Å) [%]	32.7 /32.5	31.1	29.3	-	30.9	-	32.1	-
$\%V_{Bur}$ (P—Au) [%]	33.7 /33.4	32.2	30.4	-	32.0	-	33.1	-

Compared to the neutral preligand-gold(I)complex the P—Au distances of the cationic encapsulating binuclear gold(I) complexes are shortened, while the Au—Cl distance nearly stays the same. The shortening of the P—Au distance can be explained by the decreased donor ability of the phosphine.

The measured mean P—C bond lengths for the binuclear gold(I) complexes are also slightly shortened compared to the ones measured for the free encapsulating cationic phosphines. Furthermore, the pyramidalization is decreased compared to the free ligands (exception: Ca^{2+} **267**, coordinated triflate!). Both findings cannot be explained by the different measurement-temperatures alone (100 K vs. 200 K), but by the enhanced importance of σ-bonding and decreased importance of π-bonding in late transition metals. The σ-bonding shortens the P—C bond distances by reducing the P(lone pair)–R(bonding pair) repulsions, while the lack of π-back bonding ability of the gold(I) does not compensate this shortening and leads to a lower pyramidalization.[46,188]

The geometry of the P—Au—Cl fragment in all binuclear gold(I) complexes is just slightly distorted from perfect linearity. The geometries of the encapsulated phosphines coordinated to the gold(I) follow the trend of free encapsulating ligands very accurately. While Mg^{2+} and Zn^{2+} binuclear gold(I) complexes have structures close to the TP limit and the Fe^{2+} binuclear gold(I) complex to the TAP limit, the Ca^{2+} binuclear gold(I) complex shows a dimeric and centrosymmetric solid state structure. These similar geometries also lead to nearly identical buried volumes but slightly increased Tolman cone angles for the free ligand and the corresponding binuclear gold(I) complexes. This fact makes it likely that due to the rigid nature of the encapsulating phosphines the steric measure should not be strongly affected by the metal coordinated to the phosphorus.

2.9.2 Applications in Au(I) catalysis

Having the binuclear gold(I) complexes at hand different model reactions were chosen to investigate their catalytic activity.

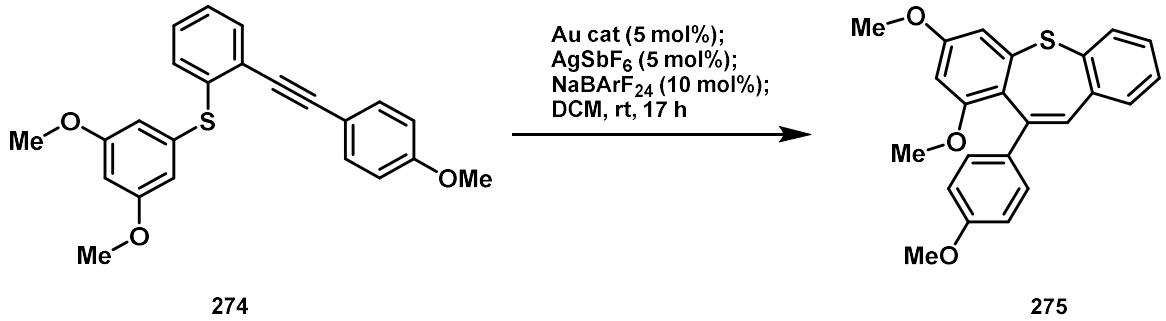

274 275

Scheme 89: Model reaction 1

At first the Zn^{2+} binuclear gold(I) complex (5 mol%) was tested in a literature known 7-endo-dig cyclisation of 1-thioaryl-2-ethynylbenzenes to dibenzothiepine structures, where electron poor ligands demonstrate their advantage over electron-rich phosphines (Scheme 89).[80,189]

To activate the precatalyst one equivalent of $AgSbF_6$ [or $AgBArF_{24}$ or $AgCB_{11}H_6Cl_6$ (carborane)] was used. Unfortunately, even after 17 h reaction time and extra addition of $NaBArF_{24}$, to increase the solubility of the catalyst, the product was just formed in traces. The use of silver and sodium salts of non-coordinating anions with high solubility is necessary, since the active catalyst should be tricationic and will otherwise most likely not stay in a DCM solution. To ensure solubility, the following experiments were performed using the Zn^{2+} binuclear gold(I) complex and 3 equivalents of $AgCB_{11}H_6Cl_6$. While screening different reactions, we adhered to the Zn^{2+} binuclear gold(I) complex, due to the low donor ability of the encapsulating ligand **242** and the readily availability of the encapsulated metal (Zn^{2+}) used.

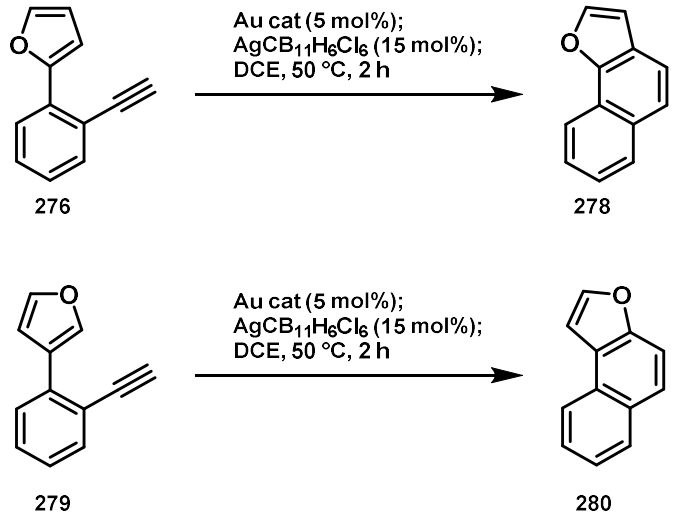

276 278

279 280

Scheme 90: Model reaction 2 and 3

The next reaction we tried was the literature known hydroarylation of 1-furyl-2-alkynyl benzenes to naphtho[1,2-b]furanes (Scheme 90).[190] The reaction is known to benefit from the use of dicationic phosphines in gold(I) catalysis. To our disappointment even with higher catalyst loading (5 mol%) than the literature (2 mol%) no product **278** was formed after 2 h. This represents a lower catalyst activity than that of gold(I) complexes of PPh_3 and $P(OPh)_3$. Also, just traces of the product **280** could be detected in NMR after 2 h starting from 3-(2-ethynylphenyl)furan.

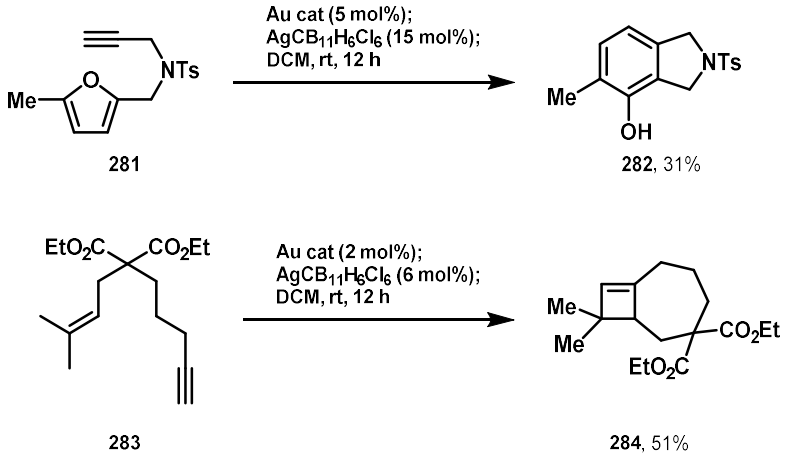

Scheme 91: Model reaction 4 and 5

In the Hashmi transformation of alkynyl furan **281** to a phenol **282**[30] the Zn^{2+} binuclear gold(I) complex/ $AgCB_{11}H_6Cl_6$ mixture cannot compete with $PPh_3AuCl/AgSbF_6$ (*cf*. 3 mol% cat, 89%[191]), even with higher catalyst loading and longer reaction times. Moreover, in enyne cyclizations the Zn^{2+} binuclear gold(I) complex **270** could not build on the success of cationic phosphines.

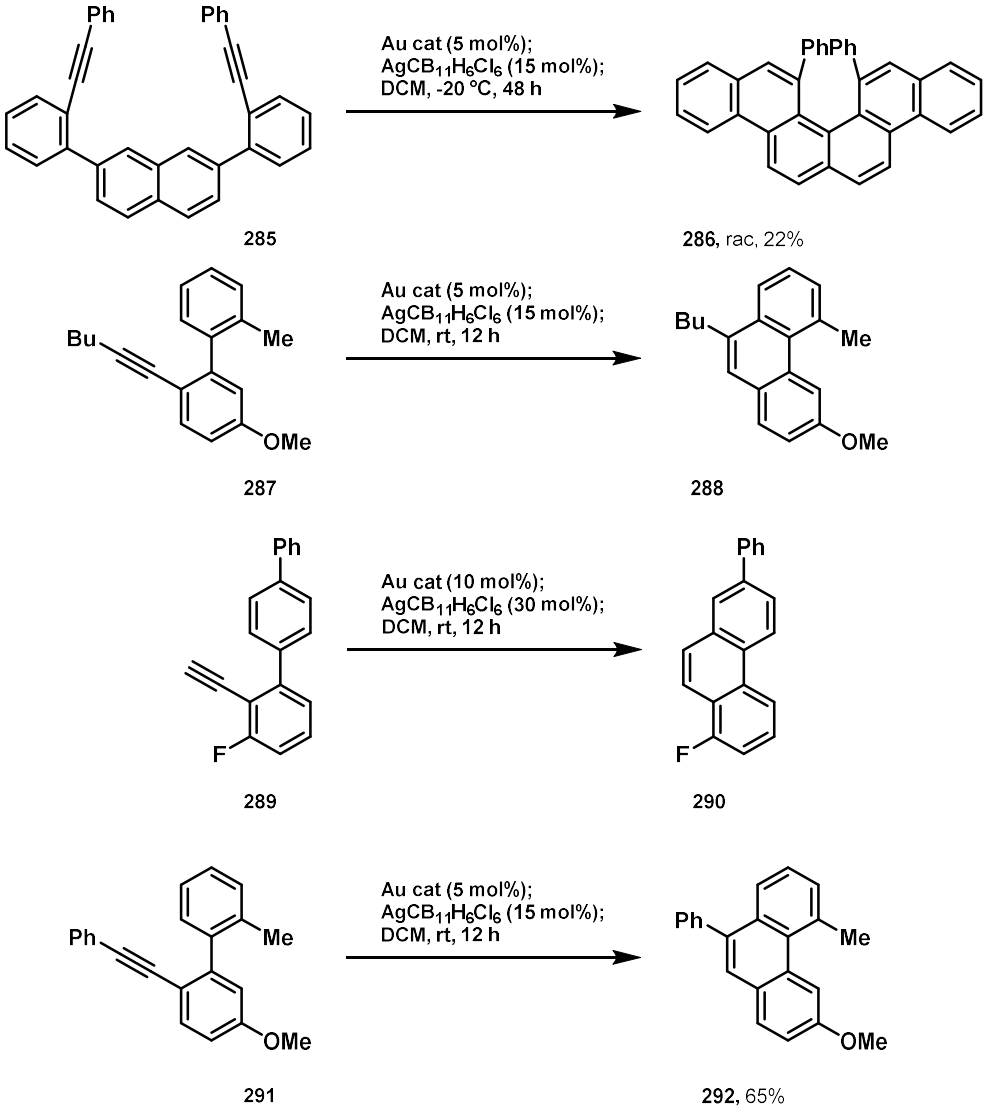

Scheme 92: Model reaction 6, 7, 8 and 9

Further cycloisomerizations were examined, where cationic phosphines show a strong ligand effect.[192] The formation of helicene **286** was only achieved in 22% yield, while the hydroarylation of **287** and **289** lead to 50 different compounds apparent in HPLC analysis and nearly no conversion, respectively. The only successful cycloisomerization was detected in compound **291** leading to phenanthrene **292** in 65% yield. This reaction was further investigated by kinetic studies, to analyze the performance of the catalyst, compare it to others and to identify possible issues during the reaction (Figure 53).

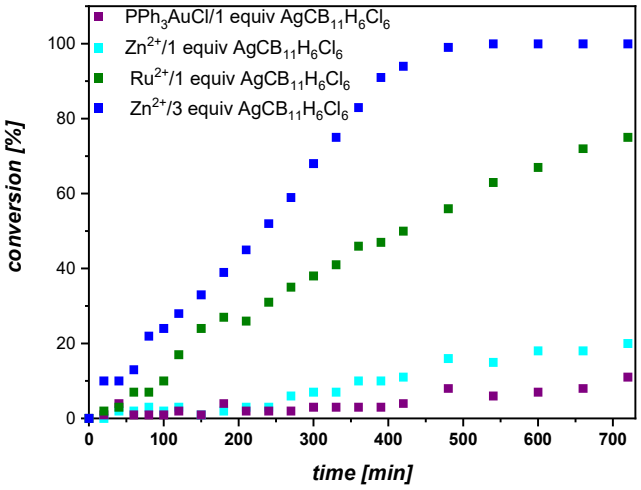

*Figure 53: Kinetik studies on the conversion of **291** by catalyst **270***

The data was taken from the Bachelor's thesis of S. Kolle.[193] The samples were analyzed *via* GC-FID, anthracene was used as an internal standard and 5 mol% was the loading of each catalyst. It can be seen that using Zn^{2+} binuclear gold(I) complex **270** and 3 equivalent of $AgCB_{11}H_6Cl_6$ nearly full conversion is reached after 480 min (99%). The catalytic activity is clearly superior to PPh_3AuCl together with one equivalent $AgCB_{11}H_6Cl_6$ (11% after 12 h). However, when using the Zn^{2+} binuclear gold(I) complex **270** in combination with just one equivalent of $AgCB_{11}H_6Cl_6$ the activity dropped a lot (20% after 12 h). This might indicate a lack of solubility of the activated Zn^{2+} binuclear gold(I) complex **270**, silver assisted gold catalysis[194] or absence of activation in combination with catalysis of an unknown Ag/Au species (decomposition, nanoparticels *etc*.). It should be emphasized, that the $AgCB_{11}H_6Cl_6$ itself did not show any catalytic activity, while the more soluble Ru^{2+} binuclear gold(I) complex **271** in combination with one equivalent of $AgCB_{11}H_6Cl_6$ achieved 75% conversion after 12 h. This was a surprising result, because we tested the Ru^{2+} based catalyst **271** before in the cyclisation of N-(3-iodoprop-2-ynyl)-N-tosylanilines to 1,2-dihydroquinolines[67], where it showed nearly no conversion after 24h (5 mol% cat, 3 equiv. $NaBArF_{24}$, 1 equiv $AgSbF_6$).

2.9.3 Problems in Au(I) catalysis

The many failed reactions, where cationic phosphines usually unfold their full potential, and the strong silver effect in the cycloisomerization of compound **291** were starting to make us wonder. The focus was shifted towards the activation of the binuclear gold(I) complexes. In order to test the possibility of activation and to synthesize complexes reactive without additional Ag^+, attempts were made to abstract the chloride by Ag^+ salts and substitute it by acetonitrile. Hence, the binuclear gold(I) complex of Zn^{2+}, Mg^{2+} and Co^{2+} were dissolved in CD_3CN, treated with silver salts and analyzed *via* ^{31}P-NMR.

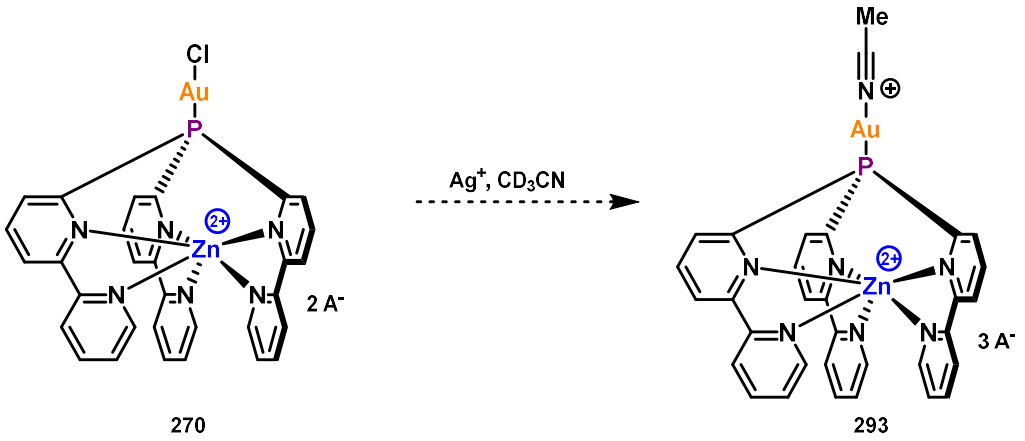

270 293

*Scheme 93: Treating precatalyst **270** with silver salts in acetonitrile*

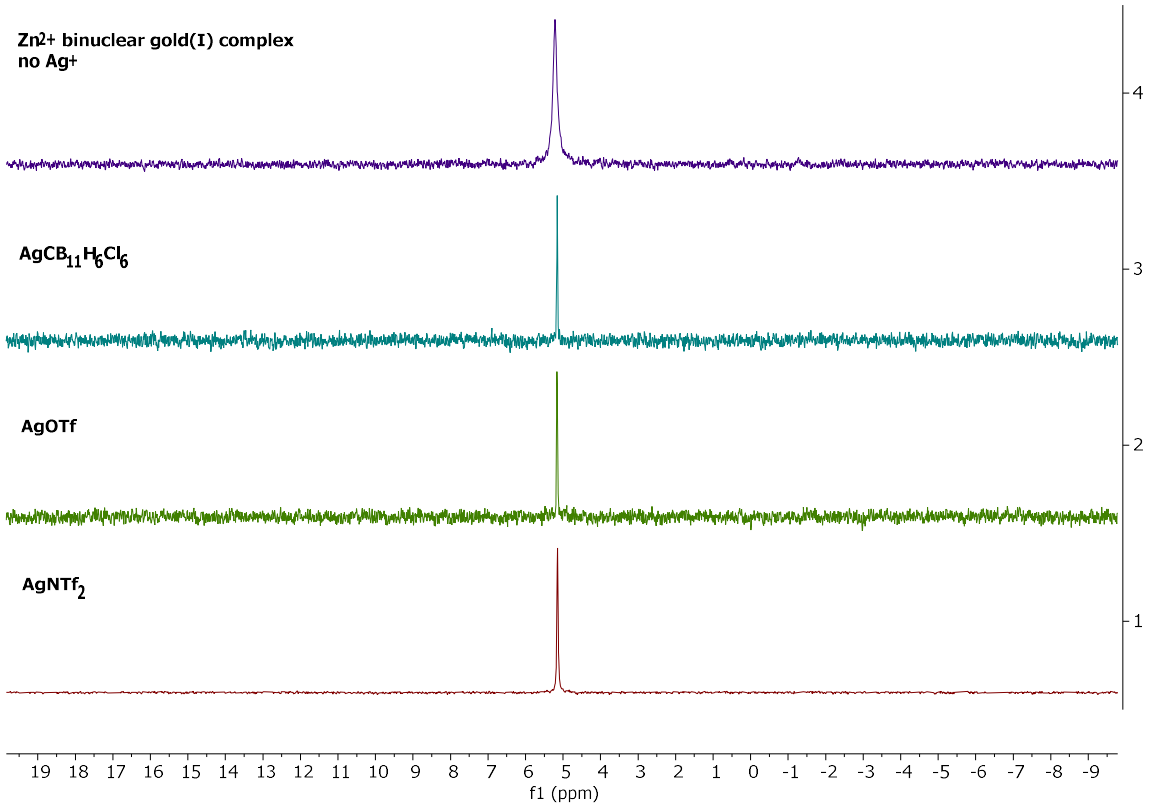

*Figure 54: $^{31}P\{H\}$-NMR of **270** before and after addition of silver salts*

As can be seen in Figure 54 the phosphorus signal of the Zn^{2+} binuclear gold(I) complex does not change upon addition of silver salts. The same result was obtained for Mg^{2+} and Co^{2+} in combination with $AgNTf_2$. The Co^{2+} binuclear gold(I) complex however showed after longer reaction times (18 h) a signal at 13.23 ppm, but this is most likely the free Co^{3+} ligand **241** obtained by oxidation (reduction: $Ag^{+} \rightarrow Ag^{0}$), which would also explain the gold mirror formed. The low σ-donor ability of the encapsulating phosphine-ligands (trans effect) and the Coulomb interactions seem to impede the chloride substitution.

In the case of the Ru^{2+} binuclear gold(I) complex we tried to simulate real reaction conditions and analyzed the shift of the phosphorus signal upon addition of $AgCB_{11}H_6Cl_6$ in DCM-d_2 (20 min). The $^{31}P\{H\}$-NMR signal gets upfield shifted by 3 ppm and broadened. This might be a new tricationic gold(I) species but could also indicate dynamical processes or the presence of nanoparticles. Also no visible

AgCl was formed during the reaction. This fact and the small chemical shift difference makes the formation of the tricationic gold(I) species highly questionable.

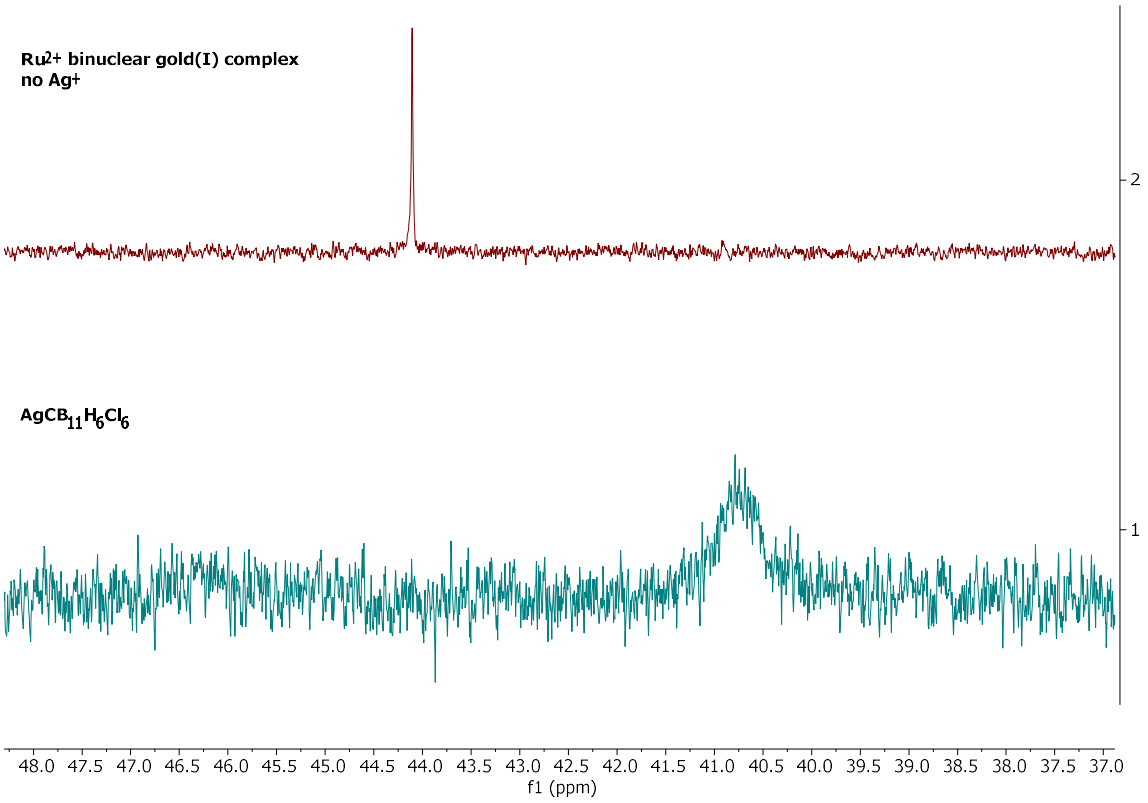

*Figure 55: $^{31}P\{H\}$-NMR of **271** before and after addition of silver salt*

Besides the usual activation of gold(I) chloride complexes by silver salts there are plenty other activation methods of gold(I) complexes. To name a few examples: One can use preactivated gold(I) bis(trifluoromethanesulfonyl)imidates[195], methyl gold complexes in combination with Brønsted acids[196], gold(I) chloride complexes in combination with $Cu(OTf)_2$[197] or one can start from gold(I) complexes with coordinated by N-heterocycles *e.g.* pyridine.[198] While preactivation with silver salts did not seem to be promising and even the highly DCM soluble Ru^{2+} binuclear gold(I) complex **271** was not soluble enough in THF to be methylated with MeLi, we tried to synthesize the Ru^{2+} binuclear gold(I) complex with coordinated pyridine.

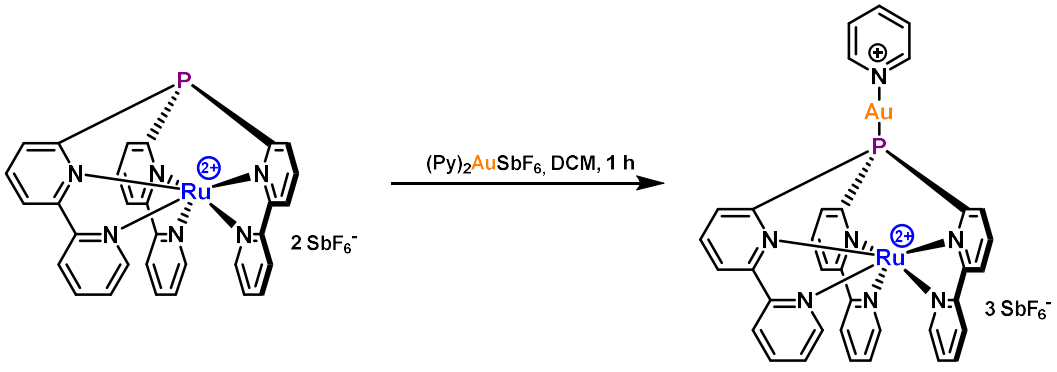

243 294

*Scheme 94: Synthesis of catalyst **294***

Therefore we substituted one pyridine ligand of bis(pyridine)gold(I)hexafluoroantimonate by Ru^{2+} ligand **243** in DCM (Scheme 94). According to the literature[198], pyridine gold(I) complexes enjoy great advantages in gold(I)-catalyzed oxazole synthesis, so the obtained binuclear gold(I) complex **294** was examined in the synthesis of **297** (Scheme 95).

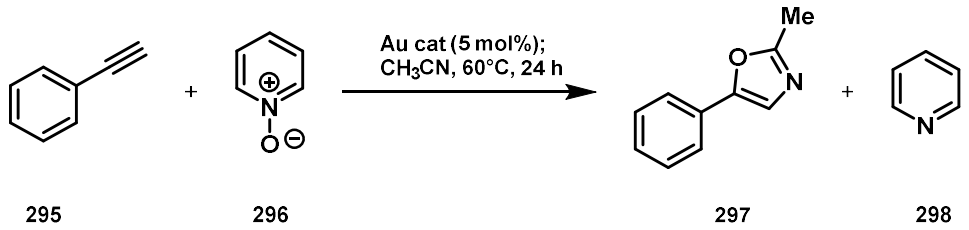

295 296 297 298

Scheme 95: Gold(I)-catalyzed oxazole synthesis

Unfortunately, also after 24h of heating just traces of the product were obtained, while PPh_3-based gold(I) complexes show full conversion after this time.[198] We also tried the catalyst **294** in the cyclisation of N-(3-iodoprop-2-ynyl)-N-tosylanilines but also without success.

2.10 Coordination chemistry - Pt(II) complexes

To address the solubility and activation problems of our ligand class in π acid catalysis we thought of changing the active metal center from gold(I) (L—AuCl) to platinum(II) (L—$PtCl_3^-$). In case of platinum(II), complexes of a dicationic L^{2+} should be monocationic before or dicationic after activation. This replacement should therefore lead to increased solubility and a facilitated activation.

2.10.1 Synthesis of Pt(II) complexes

The Co^{2+} (**240**) and Ru^{2+} (**243**) ligands do not suffer from rearrangement of the bipyridine moieties towards other metals, they are coordinatively saturated, stable and their TEPs are known. Furthermore, also their gold(I) complexes showed good solubility in DCM. Therefore they were chosen to be coordinated towards platinum(II) and subsequently tested in π acid catalysis.

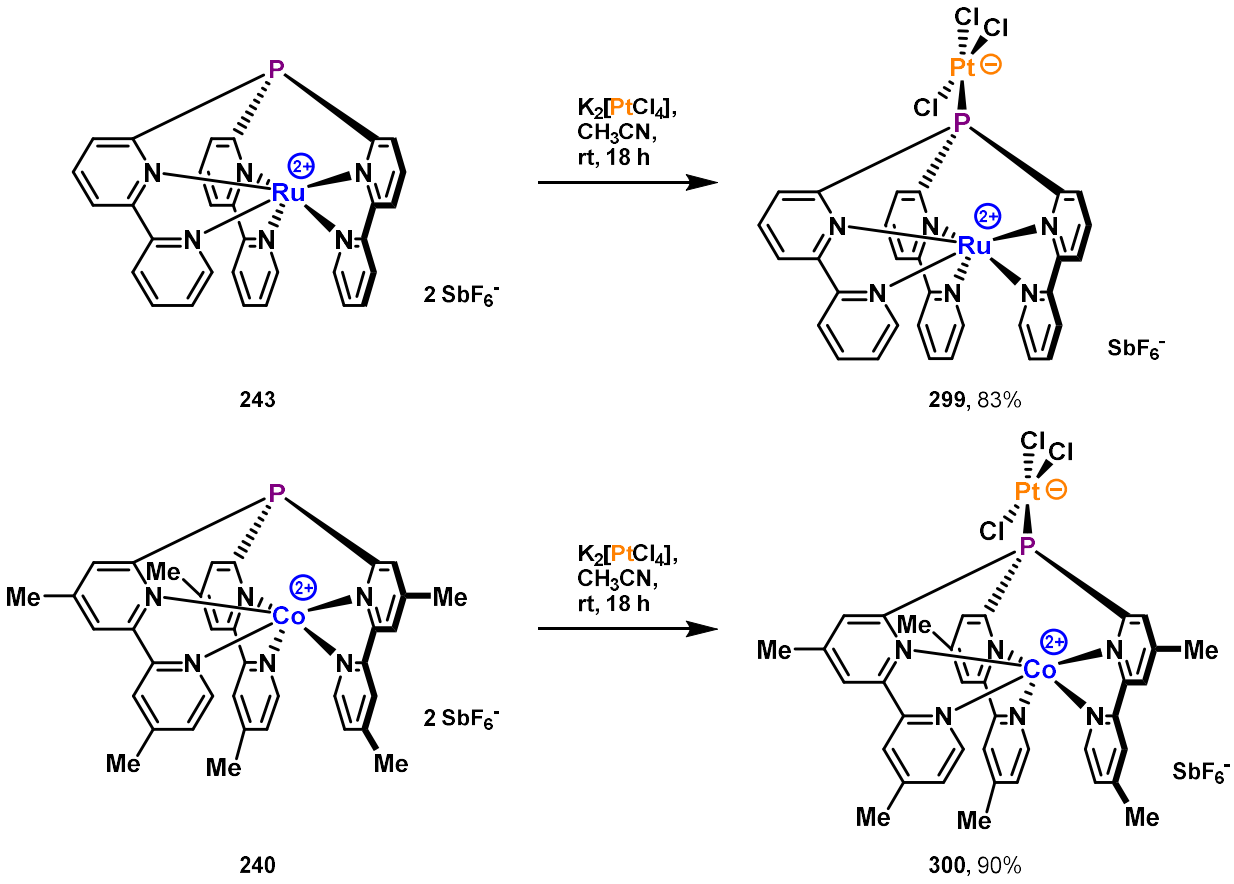

*Scheme 96: Synthesis of Pt(II) complexes **299** and **300**.*

The trichloroplatinum(II) complexes were synthesized from $K_2[PtCl_4]$ and could be easily identified by their ^{195}Pt satellites in ^{31}P-NMR. The $^1J_{PPt}$-coupling constants (Ru^{2+}: $^1J_{PPt}$ = 4200 Hz; Co^{2+}: $^1J_{PPt}$ = 4209 Hz) are exceptionally high[84,190,199] which might be attributed to the ligands' low donor abilities (Scheme 96).[55]

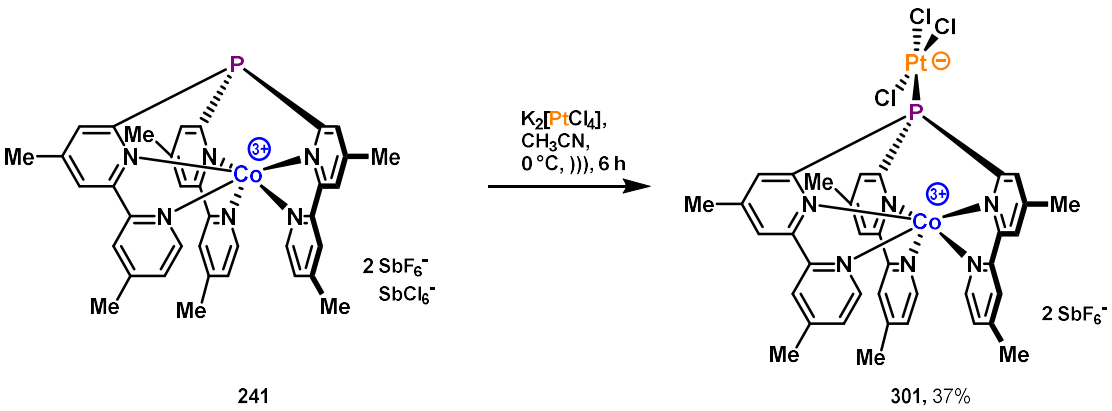

241 301, 37%

*Scheme 97: Synthesis of Pt(II) complex **301***

Also, due to the excellent π-back-donation capabilities of the anionic platinum(II)-moiety and the coulombic attractive interactions, a trichloroplatinum(II) complex of the tricationic Co^{3+} ligand could be synthesized (Co^{3+}: $^{1}J_{PPt}$ = 4384 Hz, Scheme 97).[84,92] However, due to the slowly proceeding reaction ($K_2[PtCl_4]$ is nearly insoluble in CH_3CN) and the decomposition of the tricationic Co^{3+} ligand in solution, the reaction needed to be cooled and sonicated. Unfortunately, the reaction product **301** was not soluble in DCM.

2.10.2 Applications in Pt(II) catalysis

Before starting with a model reaction to test the Pt(II) catalysts, the Ru^{2+} and Co^{2+} trichloroplatinum(II) complexes **299** and **300** were tried to be activated *via* Ag^{+}. Therefore a solution of the Ru^{2+} trichloroplatinum(II) complex **299** in CD_3CN was treated with a substoichiometric amount $AgSbF_6$ and analyzed by ^{31}P-NMR.

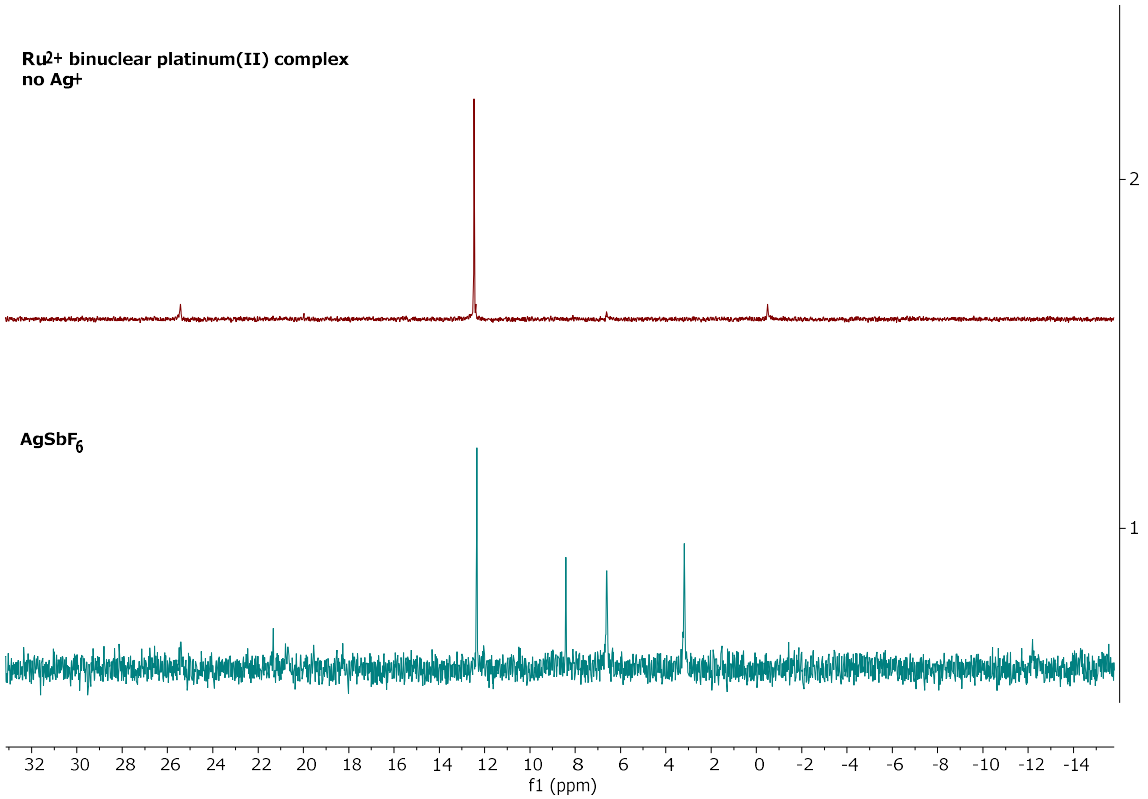

*Figure 56: $^{31}P\{H\}$-NMR of **299** before and after addition of silver salt*

Three further signals appeared, which were interpreted as signs for the substitution of chlorides.

The same experiment was also repeated for the Co^{2+} trichloroplatinum(II) complex in CD_3CN but with a stoichiometric amount $AgSbF_6$. In doing so, it was not just important to verify a possible activation, but also see if this activation is much faster than a possible oxidation of the ligand. As it can be concluded from the silver(I)-treatment of the corresponding gold(I) complex, an oxidation seems possible when the complex is exposed to silver(I) for a long time. However, it needs to be noted that the oxidation potential especially of Ag^+ is solvent dependent and is much higher in *e.g.* DCM.

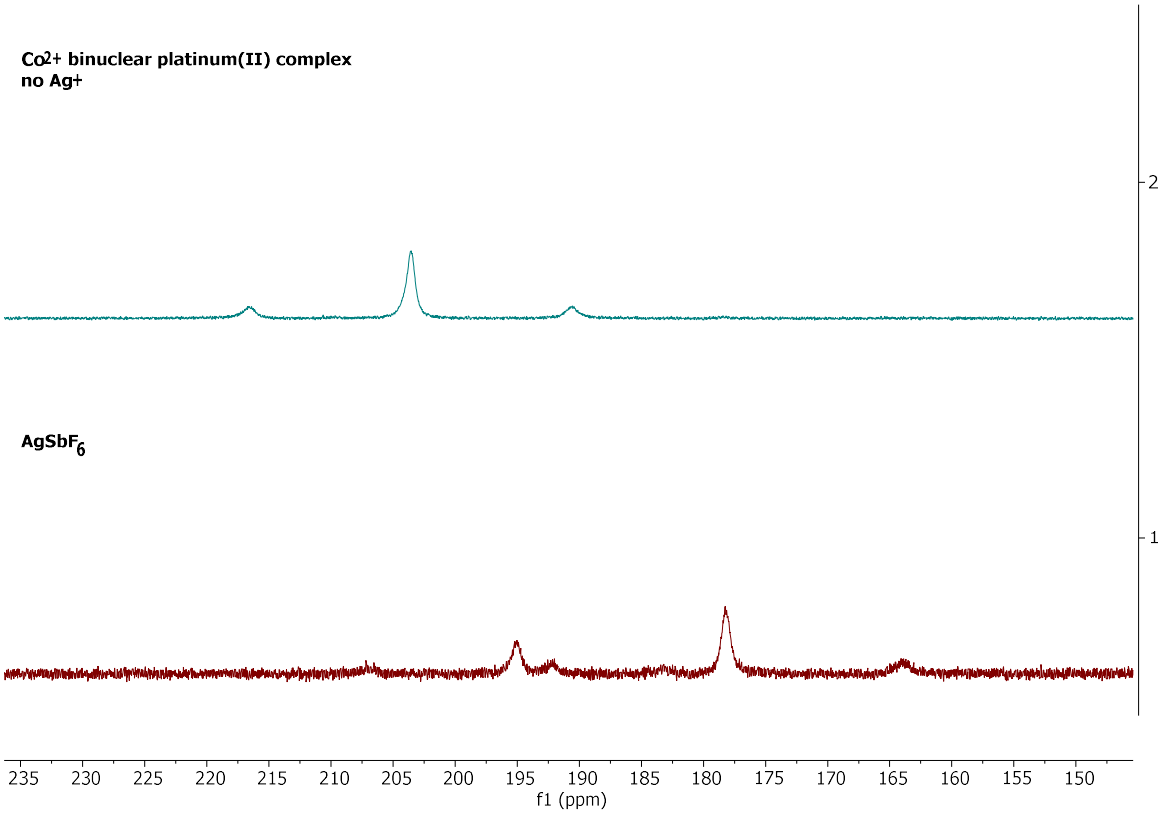

*Figure 57: $^{31}P\{H\}$-NMR of **300** before and after addition of silver salt*

As one can see, the major ^{31}P signal is shifted by 25 ppm leading to a signal with a $^1J_{PPt}$ = 4584 Hz indicating a successful substitution of one chloride. No signal of a diamagnetic Co^{3+} species (*e.g.* Co^{3+} trichloroplatinum(II) complex **241**) was detected.

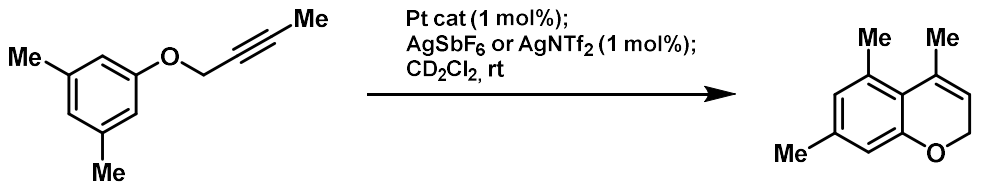

302 303

*Scheme 98: Hydroarylation of propargyl ether **302***

As a model reaction we tested the literature known hydroarylation of propargyl ether **302** to chromene **303** with our Co^{2+}-based trichloroplatinum(II) precatalyst **300** and recorded a conversion vs. time curve *via* ^{1}H-NMR.[84,200] To have a better comparison to other cationic phosphines we took the same reaction conditions as reported in the PhD thesis of Hendrik Tinnermann.[201]

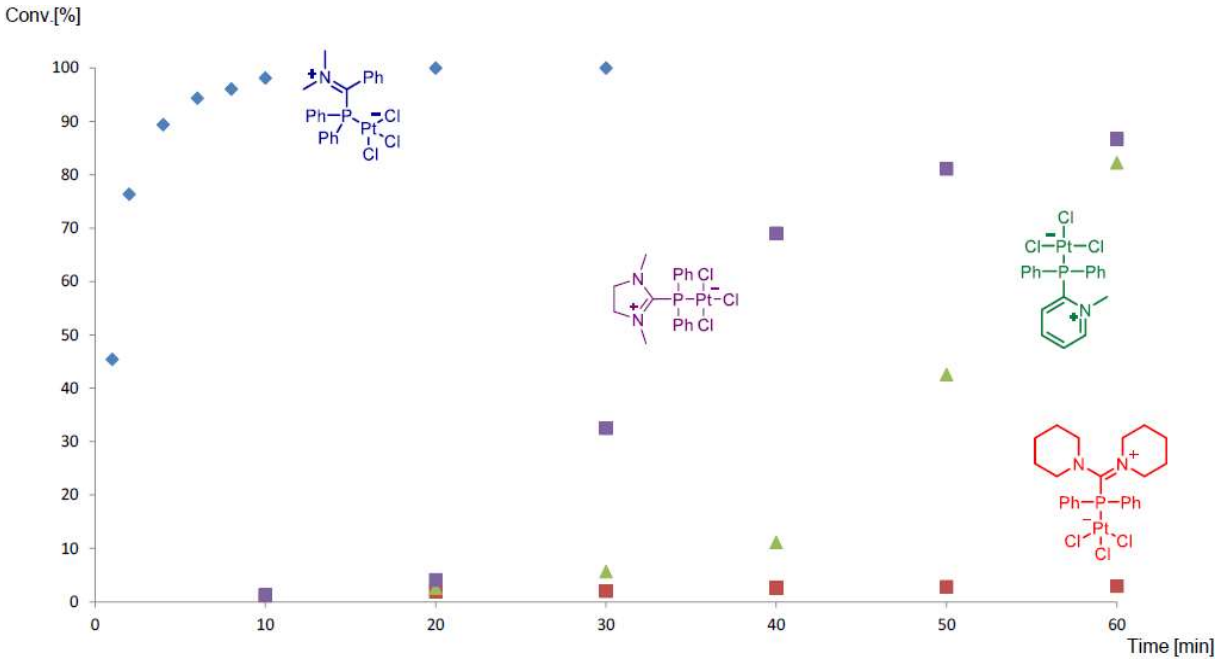

*Figure 58: Conversion vs. time curve of hydroarylation of propargyl ether **302** using different Pt(II) precatalysts owning monocationic phosphine ligands (taken from literature[201])*

The conversion vs. time curve (taken from this PhD thesis and modified[201]) he presented shows the ligand effect of monocationic ligands on platinum catalysis. By choosing the right ligand (dimethyl-amidinium ligand) the reaction gets accelerated and full conversion can be reached within 10 min. Also the imidazolinium and pyridinium ligands in form of their platinum(II) complexes show high catalytic activity. However, the sigmoid correlation might indicate a low solubility of the precatalysts.[201]

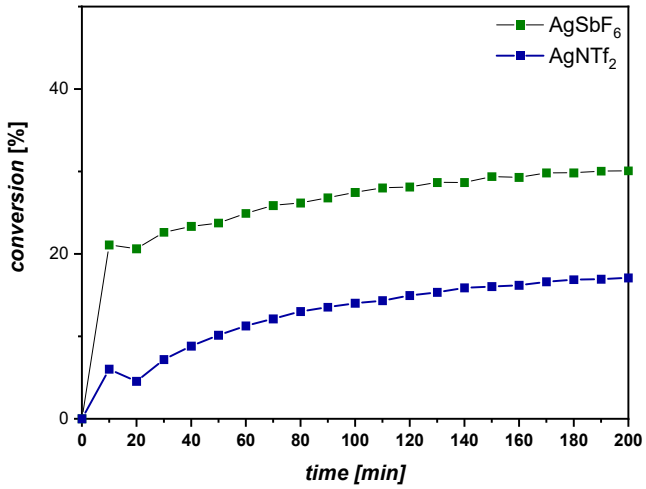

*Figure 59: Conversion vs. time curve of hydroarylation of propargyl ether **302** using precatalyst **300** (Conversions determined by ^{1}H NMR, internal standard: naphthalene)*

Taking the same reaction conditions, our Co^{2+} trichloroplatinum(II) precatalyst in combination with $AgSbF_6$ (green) presents a completely different correlation. The activation seems to be fast. The activated catalyst has a high averaged turnover frequency (TOF) of 2.1 min^{-1} within the first 10 min, which is much higher than that of the imidazolinium and pyridinium ligands, but after the first 10 min the TOF drops rapidly. This results in a low TON. After 3 h the TON barely increases and reaches 33.0

after 9 h, which indicates a fast deactivation of the catalyst. This phenomenon was already reported in literature for dicationic ligands but at higher temperatures and catalyst loadings (2 mol% cat, 80 °C, DCE) and might be a result of the low tendency of dicationic phosphines to coordinate a neutral $PtCl_2$ species.[84] The TOF of the dimethyl-amidinium system in the first 10 min is higher compared to ours, but due to the lack of data points the TOF within the first minutes cannot be easily compared.

The kinetic data clearly demonstrates the ability of the electron poor encapsulating ligand to enhance the π-acidity of the Pt center resulting in a high TOF. It must be pointed out that systems based on electron poor neutral phosphines require higher temperatures and proceed much slower.[84] The dicationic charge achieves the desired effect and offers reactivity of a cationic phosphine ligand in combination with tunability by the encapsulated metal. To address the stability issue of this catalytic system we tried to use $AgNTf_2$ instead of $AgSbF_6$ hoping that this change might result in a more stable active catalyst. However, the platinum(II) catalyst activated *via* $AgNTf_2$ clearly shows a lower TOF (0.6 min^{-1} within the first 10 min) and TON (20.2 after 9 h).

302 303

*Scheme 99: Hydroarylation of propargyl ether **302** using higher catalyst loading of precatalyst **300***

302 303

*Scheme 100: Hydroarylation of propargyl ether **302** using precatalyst **299***

Beside the Co^{2+} trichloroplatinum(II) precatalyst also the Ru^{2+} trichloroplatinum(II) precatalyst was shown to be catalytically active by Sebastian Kolle using the same reaction conditions as Haldón et al.[84,193] After one hour of reaction at least 20% conversion was achieved. However, the high temperatures in DCE might not be the best choice for our catalytic system.

The trichloroplatinum(II) complex of the tricationic Co^{3+} ligand is not soluble in DCM but still should be considered as a potential catalyst, when two equivalents of $NaBArF_{24}$ are added in addition to the Ag^+-activator. The tricationic encapsulating ligand should enhance the π-acidity of the Pt center even more. Research in this direction is still pending.

3 Summary I

In conclusion, two cationic phosphine ligand systems could be established. The first system, a dicationic PNN pincer ligand, was successfully synthesized and coordinated subsequently to the base metal cobalt(II).

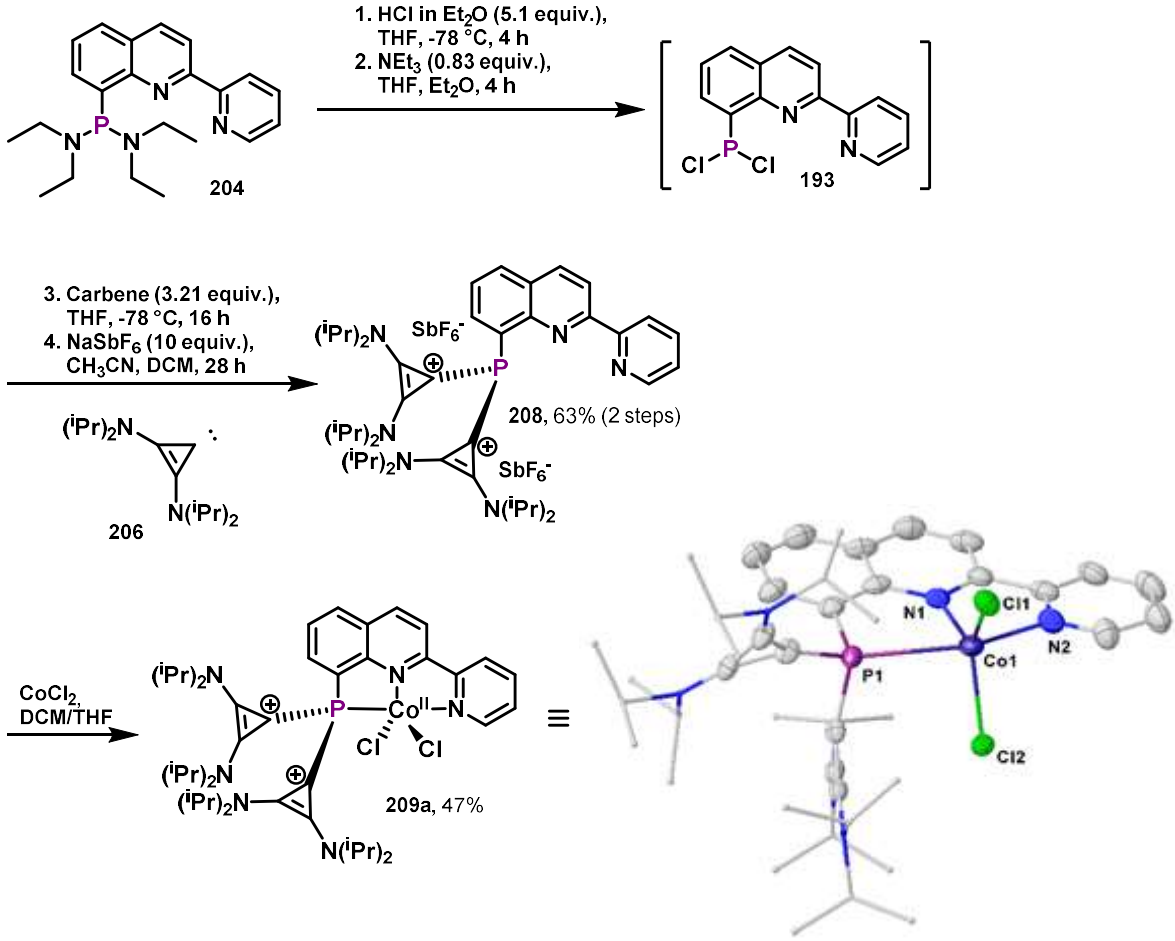

Scheme I: Synthesis of a dicationic PNN pincer ligand

Starting from phosphonous diamide **204**, dicationic PNN pincer ligand **208** was synthesized in a two-step approach with 63% yield. The first step consists of acidolysis of the phosphonous diamide **204** to generate a phosphorus chloride intermediate, which reacts with bis(diisopropylamino)cyclopropenylidene **206** under chloride substitution. The second step involves the anion exchange of chloride by hexafluoroantimonate (96%). Phosphonous diamide **204** was easily accessible *via* a lithiation approach starting from the corresponding bromide[125,126] and bis(diethylamino)chlorophosphine in 94% yield. The structure of **208** could be confirmed by NMR, mass spectrometry and single crystal X-ray diffraction.

Dicationic phosphine **208** could then be successfully coordinated to cobalt(II). This represented a major innovation, as dicationic phosphines were previously unable to coordinate 3d metals due to their low donor properties. The example shows that the use of a rigid backbone like quinoline, which serves as an anchor and forces the dicationic phosphine into the coordination sphere of the Co(II), successfully compensates for this low donor properties. Ligand **208** thus combines the advantages of both worlds, PNN pincer ligands and cationic phosphines. However, in an attempt to reduce the Co(II) complex and find an application in catalysis, we observed that the P–C bonds towards the cationic moieties are easily cleaved, making the complex unsuitable for the use in Co(I)-catalysis.

Since the ligand scaffold had already been published in the meantime by another group[129], we decided to build a second cationic ligand system, which could be modulated and synthesized with less effort.

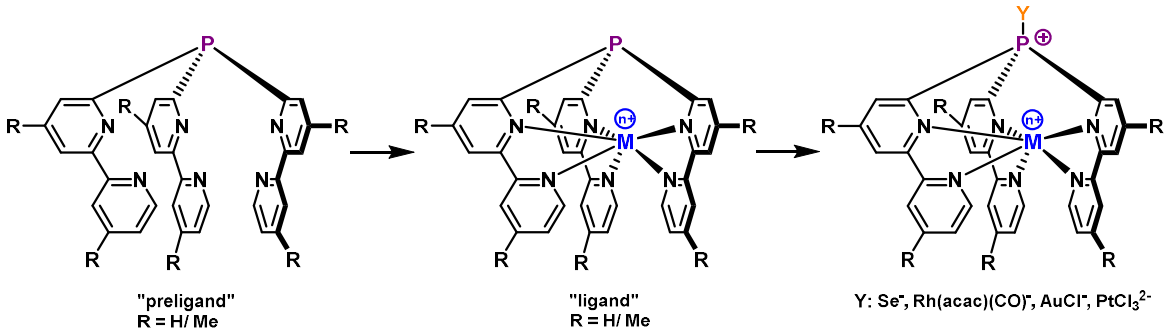

Scheme II: Encapsulating phosphine ligands

This ligand system is based on two multidentate heterophosphines ("preligands"), which are capable of encapsulating a cationic metal ion and thereby changing the electronic and structural properties at the uncoordinated phosphorus. The preligand (R=H) known from the literature[123] was modified in such a way that it can be synthesized from commercially available chemicals within three synthetic steps (R=Me, Trofimov–Gusarova reaction). The metals Mg^{2+}, Fe^{2+}[123], Co^{2+}, Co^{3+}, Zn^{2+}, Ru^{2+}, Ca^{2+}, Sc^{3+} and La^{3+} were successfully incorporated in the preligands and the resulting cationic ligands were investigated for their solid-state structure *via* single-crystal X-ray diffraction. The geometries differ by fully enclosed metals of trigonal antiprismatic (TAP: Fe^{2+}, Co^{3+}, Ru^{2+}) or trigonal prismatic (TP: Mg^{2+}, Co^{2+}, Zn^{2+}) structure or incompletely enclosed metals with additionally coordinated counter ions (coordinated triflates: Ca^{2+}, Sc^{3+}, La^{3+}). Furthermore, using the Tolman electronic parameter TEP [Y = Rh(acac)(CO)] and $^1J_{PSe}$ selenium coupling constants (Y = Se), the influence of the cationic charge of the encapsulated metal on the donor ability of the phosphine could be demonstrated. The net donor ability is thus low for all analyzed ligands and, according to the $^1J_{PSe}$ coupling constants of the diamagnetic compounds, increases in the following order:

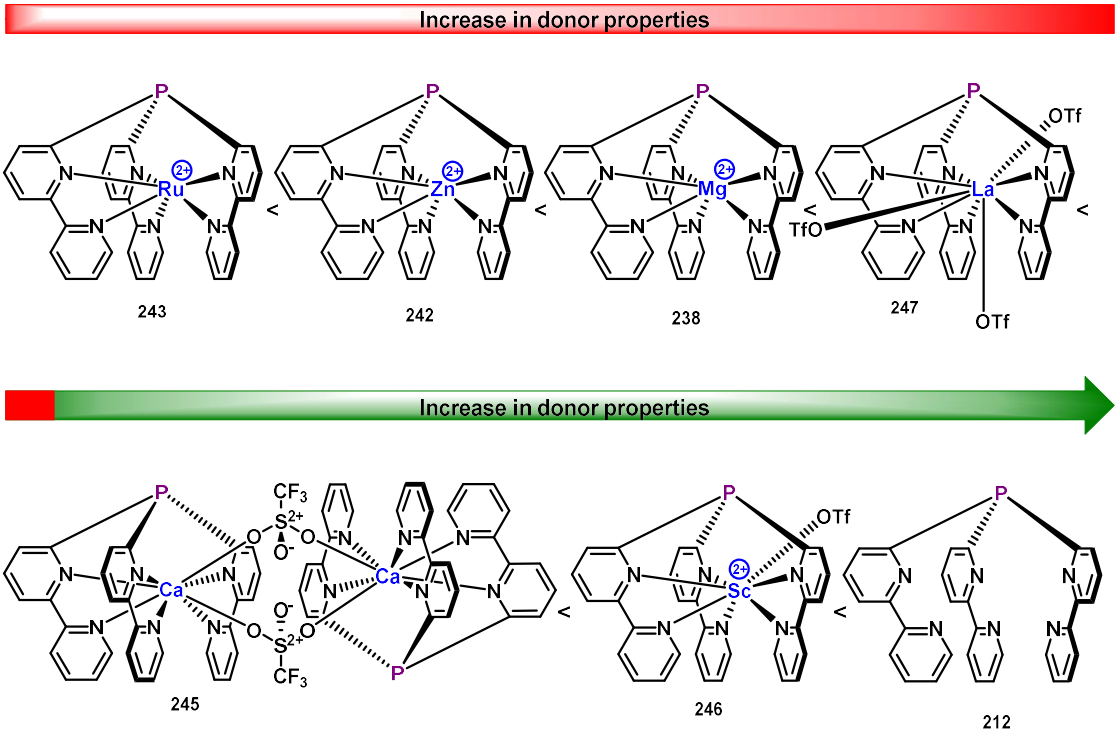

Scheme III: Increase in donor properties

Thereby, the steric measure (Tolman cone angle, $\%V_{bur}$) changes only slightly among the encapsulating ligands. The ligands could be subsequently coordinated to metals such as gold(I) or platinum(II). While the bimetallic gold(I) complexes showed little to no catalytic activity in π-acid catalysis, due to impeded activation by means of the silver salt activator, the synthesized platinum complexes were able to exhibit the reactivity known from dicationic phosphine ligands. Thus, in the case of the bimetallic cobalt/platinum complex, these show high TOFs but on the other hand low TONs in the hydroarylation of propargyl ethers.

4 Introduction II: Photoredox catalysis & sulfonium salts

4.1 Photoredox catalysis

Photoredox catalysis has become an important tool in synthetic organic chemistry over the last 15 years. The groundwork was established by the work of Yoon[165], MacMillan[202] and Stephenson[203] and is based on the ability of a photocatalyst (metal complex or organic dye) to participate in bimolecular single-electron transfer reactions (SET) after excitation by visible light.[204] However, this requires a sufficiently long-lived excited state of the catalyst. The catalyst in the excited state then possesses properties of an oxidant as well as a reductant. This provides synthetic access to common radical chemistry, interesting radical ion intermediates and reactivities that combine oxidation and reduction (overall redox neutral reactions) in ways that would otherwise be difficult to achieve. The aforementioned reactivities are particularly interesting from a synthetic point of view because they take place under mild reaction conditions. Room temperature is not uncommon in these reactions and visible light can be used instead of high energy UV radiation. The latter is particularly interesting for the transformation of organic molecules, since these absorb only little visible light and high-energy radiation can otherwise trigger side reactions.

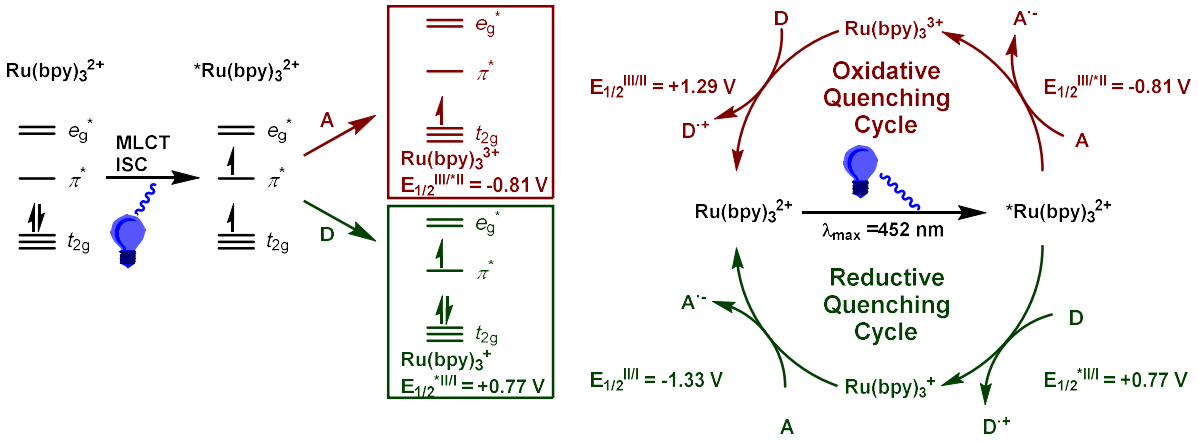

Figure 60: $Ru(bpy)_3^{2+}$: Reductive and oxidative quenching cycle[204]

One of the most commonly used photocatalysts is the metal complex $Ru(bpy)_3^{2+}$ (Figure 60). When excited by a photon, an electron is excited from the metal-centered t_{2g} orbitals into a ligand-centered π* orbital (MLCT, Figure 60 left).[204] The resulting species $*Ru(bpy)_3^{2+}$, after intersystem crossing (ISC) to the triplet state, is then capable of being both more reducing, due to the high-energy electron in π* orbital (reduced ligand framework), and more oxidizing, due to the low-energy hole in t_{2g} orbital (Ru^{III} center), than the ground state complex. Subsequent redox processes can therefore also take place *via* reductive or oxidative quenching (Figure 60 right). In the reductive quenching cycle (green) the excited-state species $*Ru(bpy)_3^{2+}$ first oxidizes an electron donor (**D**) *via* SET to give radical cation $\mathbf{D}^{\bullet+}$ and $Ru(bpy)_3^{+}$. $Ru(bpy)_3^{+}$ itself is now a good reducing agent capable of reducing an electron acceptor (**A**) regenerating the photocatalyst. In the oxidative quenching cycle (red) the excited-state species $*Ru(bpy)_3^{2+}$ first donates an electron to an electron acceptor (**A**) generating an radical anion ($\mathbf{A}^{\bullet-}$). The resulting $Ru(bpy)_3^{3+}$ is now a good oxidant being able to oxidize an electron donor (**D**) and thereby reforms the photocatalyst. Note, however, that different half-wave potentials $E_{1/2}$ are involved in each process. The dual nature of $*Ru(bpy)_3^{2+}$ leads to two potentials, one in the oxidative quenching (red) of $E_{1/2}^{III/*II}$ = -0.81 V and one in the reductive quenching (green) of $E_{1/2}^{*II/I}$ = +0.77 V. The oxidized and reduced catalysts ($Ru(bpy)_3^{3+}$ and $Ru(bpy)_3^{+}$) then have potentials of $E_{1/2}^{III/II}$ = +1.29 V and $E_{1/2}^{II/I}$ = -1.33 V, respectively. To determine whether the quenching cycle is of reductive or oxidative nature can be distinguished by fluorescence quenching experiments (*e.g.* Stern–Volmer plot). The Stern–Volmer studies use the emission of the photocatalyst under irradiation. If no quencher is present, the emission

intensity corresponds to I_0. If a quencher is present, SET and emission processes compete for the deactivation of the excited state of the photocatalyst. Thus, the emission intensity **I** decreases when the quencher molecule is able to participate in SET processes with the photocatalyst. If the relative intensity I_0/I in the presence of the quencher is plotted against the quencher concentration, then ideally, if the quencher is capable of participating in SET processes, a linear relationship should be found whose slope corresponds to the Stern–Volmer constant K_{SV}. In the case of a tertiary amine as a (reductive) quencher molecule, this would indicate a reductive quenching cycle, since the tertiary amine is thus able to quench the excited state *e.g.* $*Ru(bpy)_3^{2+}$ successfully as a reductant/electron donor.

In addition to the classification by mechanism into reductive and oxidative quenching cycles, photoredox catalysis is subdivided primarily on the basis of the organic substrate and whether it is net reduced, oxidized or redox neutrally transformed.

4.1.1 Net reductive reactions

For photocatalytic reactions yielding products corresponding to a net reduction, an additional electron donor is usually required, which is added as a stoichiometric reducing agent.[204]

An example of such a reaction is the recently published photocatalytic 5-*exo* radical cyclization by Jui, Blakey and co-workers.[205]

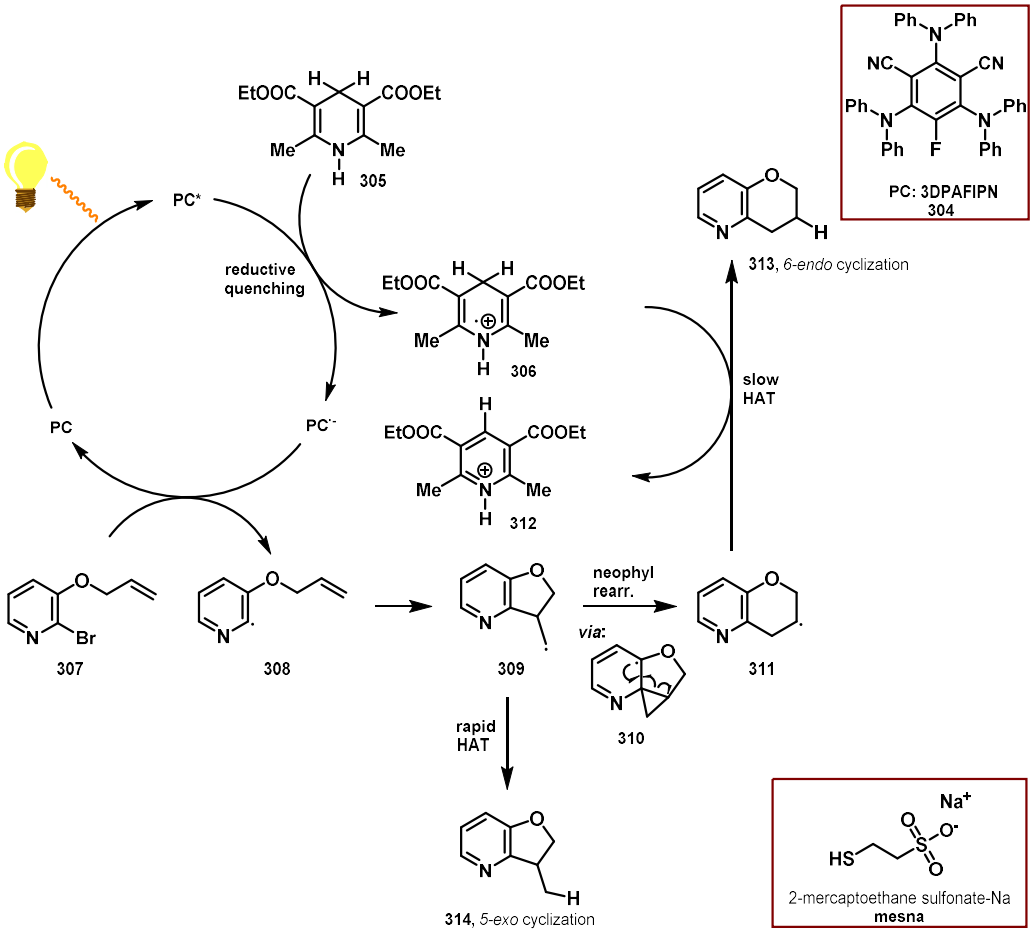

Scheme 101: Photocatalytic 5-exo radical cyclization by Jui, Blakey (Condition slow HAT:[205] Photocatalyst 3DPAFIPN (1 mol%), Hantzsch ester (1.5 equiv.), 50% H_2O/MeCN, blue LED, 23 °C, 16h; Condition rapid HAT:[205,206] Photocatalyst: 4CzIPN (1 mol%), mesna (20 mol%), $NaHCO_2$ (5 equiv.), HCO_2H (5 equiv.), DMSO, blue LED, 23 °C, 16h)

Here, the stoichiometric reducing agent corresponds to Hantzsch ester **305**, while the photocatalyst **304** is a donor-acceptor cyanoarene[207]. Note, that the Hantzsch ester not only fulfills the function of the stoichiometric reductant, but is also used as a hydrogen atom transfer reagent (HAT).[208]

After excitation of the photocatalyst by a photon, the excited photocatalyst 3DPAFIPN* (**PC***) can be reductively quenched by the Hantzsch ester **305**. The corresponding radical cation of the Hantzsch ester **306** is formed. The reduced photocatalyst 3DPAFIPN$^{\bullet-}$ (**PC**$^{\bullet-}$) can now cleave the bromopyridine bond of **307** *via* SET and release the pyridyl radical **308**. The pyridyl radical, in turn, can cyclize *via* a kinetically favored 5-*exo* mechanism to **309**. Due to the chosen reaction conditions (only 1.5 equiv. of Hantzsch ester in a solvent mixture of MeCN/H_2O (1:1), in which the Hantzsch ester is poorly soluble), an inefficient HAT reagent is generated, and the hydrogen atom transfer is slow compared to the neophyl rearrangement of **309**. Therefore, the lifetime of **309** is high enough to rearrange to the thermodynamically more stable radical **311** and afterwards abstracts a hydrogen from radical cation **306** giving preferably *6-endo* product **313**. The formation of the protonated Hantzsch pyridinium salt **312** is a driving force in the reaction enabling the 3DPAFIPN$^{\bullet-}$ to reduce bromopyridine **307**, although the reduced photocatalyst lacks sufficient reducing power.

By using a different protocol[205,206] and a more efficient thiol-based HAT reagent mesna (an inexpensive alkyl thiol), the radical **309** can be trapped and thus the *5-exo* product **314** can be selectively obtained. However, it should be noted that this is not a classical photocatalyzed reaction. The photocatalyst is only used for initiation of a radical chain and the actual catalyst is the thiol-based HAT catalyst mesna (polarity-reversal catalysis[209]). After hydrogen atom transfer from mesna to radical **309**, the resulting electrophilic thiyl radical can abstract a H$^{\bullet}$ of the formate ($NaHCO_2$). The formed $CO_2^{\bullet-}$ is then able to reductively cleave the bromopyridine bond of **307** and thus propagating the radical chain without the necessity of a photocatalyst.

Both reaction conditions lead to a net reduction of the substrate, while the first reaction oxidizes Hantzsch ester **305**, the latter approach oxidizes formate to CO_2.

4.1.2 Net oxidative reactions

Net oxidative reactions require the presence of a stoichiometric electron acceptor and involve transformations in which the substrate is formally oxidized.[204]

One example of for a net oxidative reaction is the oxidative generation of an iminium ion and it's trapping published by the group of Stephenson.[210]

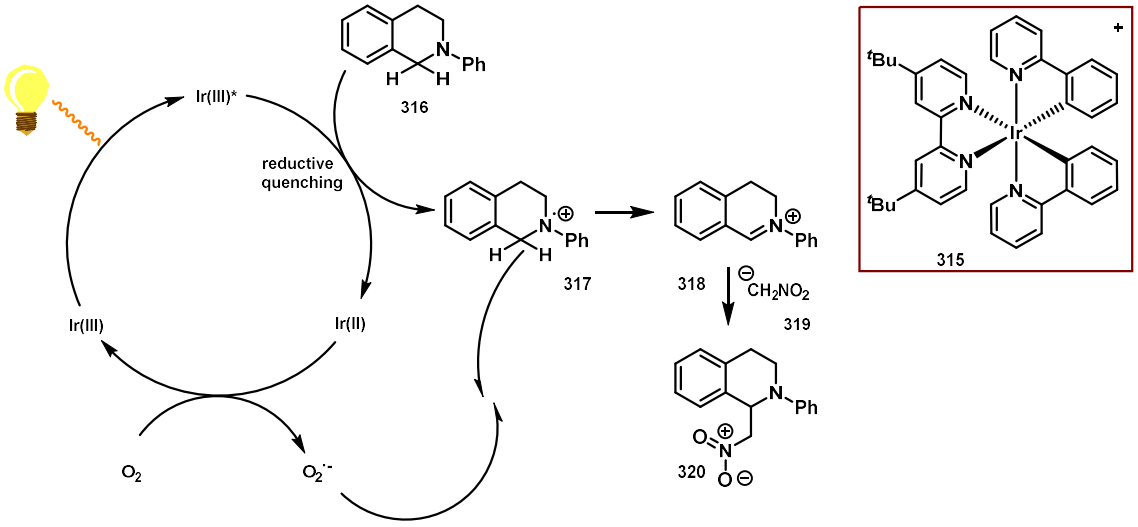

Scheme 102: Proposed mechanism for the photoredox catalysed aza-Henry reaction[210]

The photcatalytic conversion takes place over several steps. First, the $[Ir(dtbbpy)(ppy)_2]PF_6$ catalyst is excited by a photon. This is followed by reductive quenching of the catalyst and corresponding oxidation of the amine **316** to the radical cation **317**. The SET converts the catalyst into a strong Ir(II) reducing agent. Now the catalyst is able to reduce either oxygen or the solvent nitromethane to recover the Ir(III) photocatalyst. The radical anion derived from *e.g.* the oxygen is now able to abstract a hydrogen atom in α-position to the ammonium radical cation (lowered BDE) and afterwards deprotonates the nitromethane. The formed iminium ion is now susceptible to the addition of **319** reminiscent of a Henry reaction leading to product **320**. The reaction is also possible with $Ru(bpy)_3^{2+}$, but the mechanism is debated whether it proceeds *via* an oxidative quenching cycle (Ru(II)/Ru(III)) or *via* a reductive quenching cycle [Ru(I)/Ru(II)].[211] Stephenson published in a subsequent paper that the general methodology is not limited to nitromethane, but also other nucleophiles can be used.[212] The group showed that using a suitable stoichiometric oxidant $BrCCl_3$ instead of oxygen in DMF and $Ru(bpy)_3^{2+}$ as a photocatalyst in combination with triethylamine[213], iminium ions can be obtained much faster by catalytic oxidation of α-amino C–H bonds and further reacted with nucleophiles such as nitroalkanes, cyanides, indoles, methallyl trimethylsilane, silyl enol ethers, siloxyfuranes, malonates and copper acetylides.

4.1.3 Redox neutral reactions

In redox neutral reactions, the substrate undergoes both oxidation and reduction due to the dual nature of the photocatalyst, therefore no stoichiometric reagents are needed to serve as an electron source or reservoir. The net oxidation state of the substrate does not change, as the SET processes of oxidation and reduction finally balance each other out.[204]

An example from 1984, the early days of photocatalysis, is the net redox neutral Pschorr reaction of aryldiazonium salts, which provides access to phenanthrenes.[214,215]

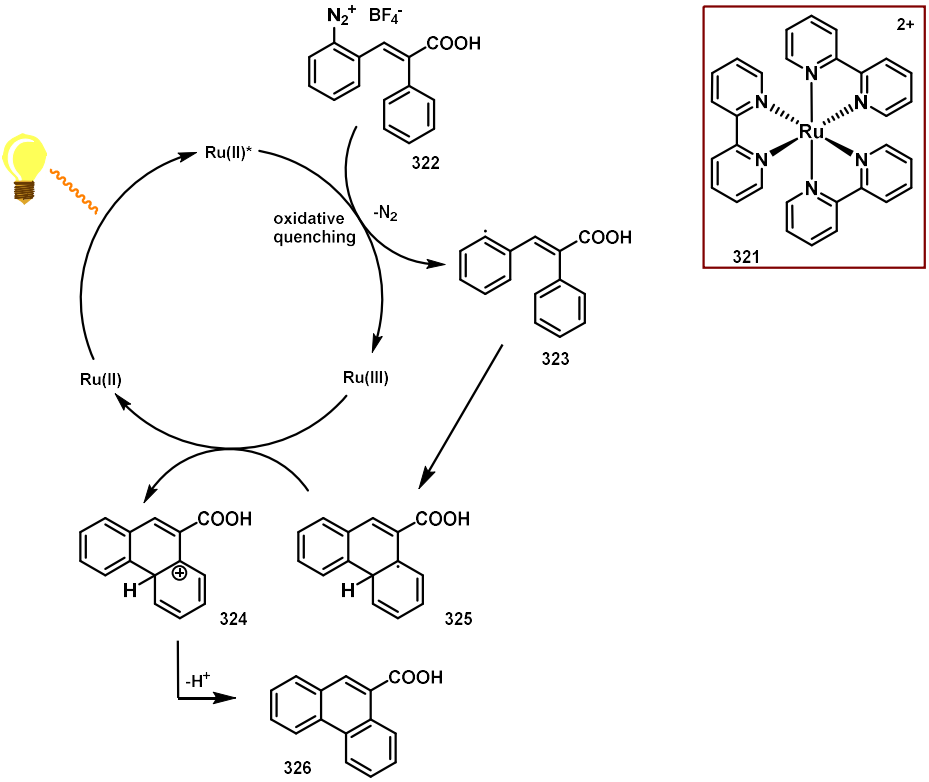

Scheme 103: Syntheisis of phenanthrenes using a photocatalytic Pschorr reaction[204,215]

Here, the excited photocatalyst is oxidatively quenched by the aryldiazonium salt **322**. The SET reduces the diazonium salt **322** and releases dinitrogen. The generated aryl radical can then add to the pendent aromatic moiety. The intramolecular coupling is completed by subsequent reoxidation of the radical **325** to the carbocation **324** and successive rearomatization/ deprotonation.

4.1.4 Energy transfer reactions

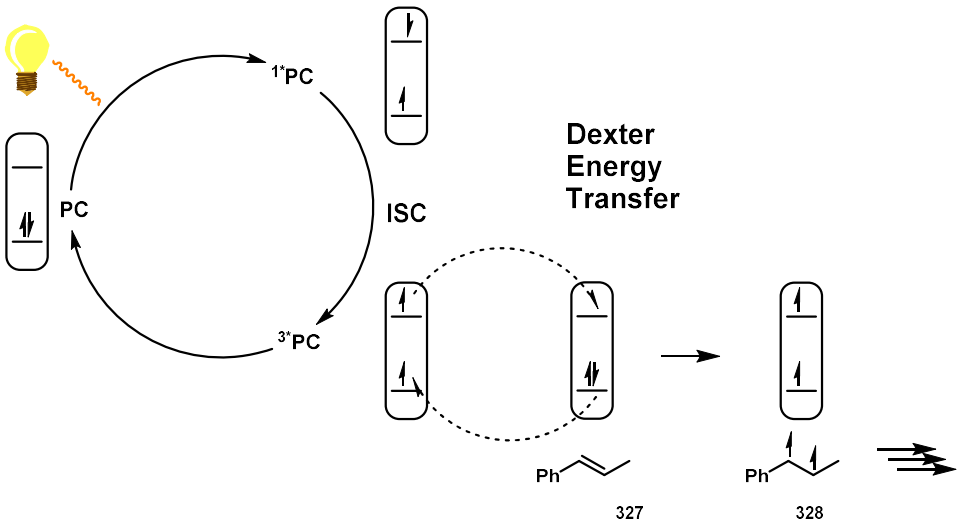

Scheme 104: Energy transfer photocatalysis: Dexter-type energy transfer[216]

In contrast to the electron transfer photocatalysis presented so far, which is based on the high redox activity of the excited photocatalyst and induced SET processes, energy transfer catalysis focuses on the transfer of energy of the excited-state photocatalyst (donor) to the ground-state substrate (acceptor).[216,217] Thus, the substrate is not directly excited by the light, but indirectly "sensitized" *via* the photocatalyst. In the context of pure energy transfer, the catalyst is often referred to as a photosensitizer, while catalysts for SET processes are often referred to as photoredox catalysts. However, many photoredox catalysts are also good photosensitizers, and the same is true vice versa. The general idea of electron transfer photocatalysis is to convert the substrate into a highly reactive triplet state by using visible light and a photosensitizer, which can then open up new excited-state reactivities. For the energy transfer from the excited photosensitizer to the substrate, three mechanisms are conceivable: A Mechanism *via* emission and absorption, Förster resonance energy transfer or Dexter energy transfer. However, the latter is the more predominant one in the energy transfer catalysis of organic molecules (Scheme 104). Here, the photocatalyst is transferred to the excited singlet state by light. Subsequently, the photocatalyst can enter the triplet state by inter system crossing (ISC). The triplet state of the photocatalyst (donor) can now be transferred to a substrate (acceptor) in a bimolecular quenching process by a concurrent two-electron exchange mechanism. This requires a long triplet state lifetime with high triplet energy (large energy gap between the triplet state and the ground state) of the catalyst and the formation of an encounter complex between substrate and triplet-state photosensitizer.

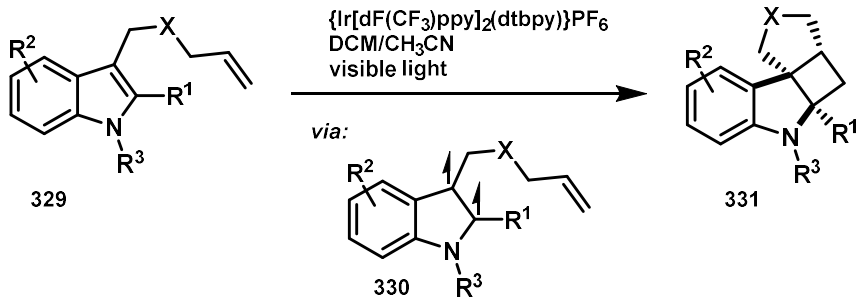

Scheme 105: Tetracyclic spiroindolines via indole dearomatization[218]

The most prominent substrate class in energy transfer catalysis are olefins.[216] These often require very high energy radiation to directly transfer them to an excited singlet state. However, the triplet state of an olefin, whose hypersurface is energetically significantly lower than the singlet state, can be achieved under certain conditions by energy transfer photocatalysis. This requires lowering the excited triplet energy of the olefin by implementing a conjugated or cyclic system in the substrate to reach an energy level that matches that of common photosensitizers. With the olefin in the triplet state, for example, [2+2] cycloadditions, which are thermally forbidden by the Woodward-Hoffmann rules, are now accessible. However, the reaction does not proceed in a concerted manner like "real" [2+2] cycloadditions, but stepwise *via* a 1,4-biradical intermediate. The biradical can now be converted into a cyclobutane *via* ISC and radical recombination. An example of such a cycloaddition is the indole dearomatization of You (Scheme 105).[218] They could show that not only alkenes but also aromatic double bonds can be converted into complex scaffolds with high stereoselectivity, excellent yields and mild reaction conditions using energy transfer photocatalysis. However, the reaction requires a suitable substitution on the indole substrate to reduce the energy gap between the triplet state and the ground state. This was achieved mainly by using phenyl substituents in the position of R^1 bearing electron-withdrawing groups. After subsequent screening of photocatalysts and solvent mixtures, a protocol was developed using $\{Ir[dF(CF_3)ppy]_2(dtbpy)\}PF_6$ as a photosensitizer with appropriate triplet energy and DCM/acetonitrile (3:1) as a solvent mixture, resulting in yields up to 99%. A Stern–Volmer plot could show that the indole is the corresponding quencher of the photosensitizer. In comparison of the different photocatalysts, there was no correlation between reactivity and redox properties of the catalyst, which largely rules out SET processes involved in the mechanism. Furthermore, it could be shown that the reaction is inhibited by the addition of a further triplet quencher and that the yields of the reaction are strongly related to the corresponding energy gap of the triplet and the ground state of the substrate. These factors suggest that the catalyst in this reaction acts as an energy transfer and not as a photoredox catalyst.

4.2 Sulfonium salts and their synthetic applications

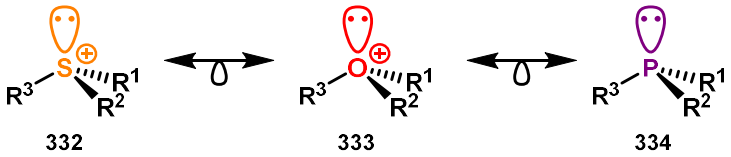

Scheme 106: Sulfonium salts, oxonium salts and phosphines

Sulfonium salts **332** represent an interesting substance class of positively charged organosulfur reagents, which are widely used in chemistry.[219] This is due to their higher stability and structural diversity compared to corresponding isoelectronic oxonium compounds **333** of the lighter homolog oxygen. However, sulfonium salts of the general formula $[R_3S]^+X^-$, where X^- is an non-coordinated counter ion, are not only related to oxonium salts but also to phosphines **334** already discussed in chapter 1.2. Because of the three substituents and the free electron pair on sulfur, and in agreement with the VSEPR rules, the sulfonium salts adopt a similar pyramidal geometry as the phosphines. Thus, phosphines and sulfonium salts are both isoelectronic and isostructural.

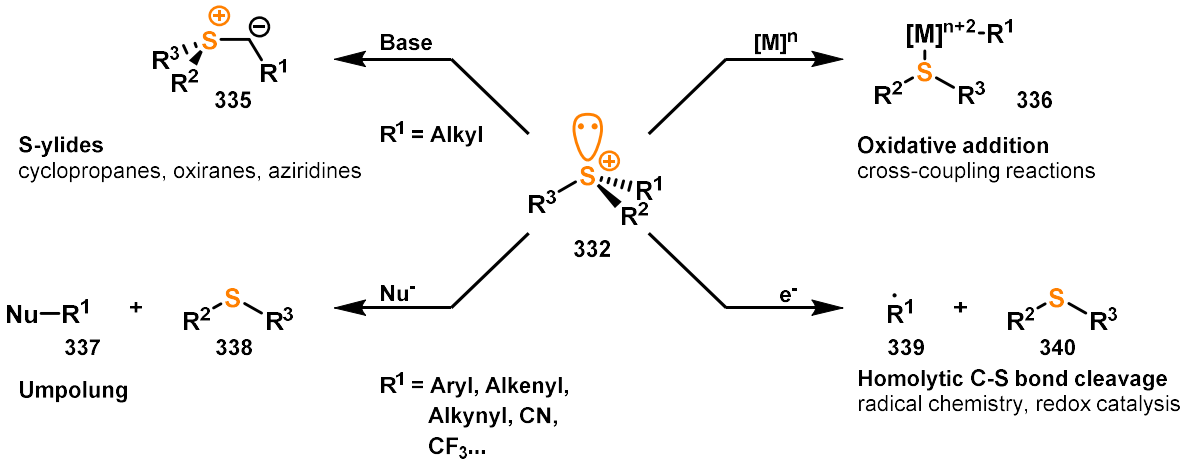

Scheme 107: Sulfonium salts and their applications[219]

Unlike phosphines, however, sulfonium salts are not used as spectator ligands, with a few exceptions.[220] Due to their increased reactivity, as a result of the cationic charge, they are rather used as stoichiometric reagents in synthesis (Scheme 107).[219] For example, sulfonium salts can be used as starting materials for *S*-ylides **335** due to their α-CH-acidity.[221] Subsequent Corey-Chaykovsky reactions can then be used to build up three-membered ring systems. Furthermore, the sulfonium unit represents a good leaving group. This can be used, for example, in nickel or palladium catalyzed couplings, since metals in low oxidation states can insert particularly easily into one of the R–S bonds (**336**).[222,223] The low-lying σ*(S–R) orbital also facilitates an attack of nucleophiles on the positively charged sulfur. Subsequent reductive elimination and coupling of two sulfur ligands yields products in which the sulfonium moiety, as a good leaving group, has been formally replaced by a nucleophile (**337**).[224] In this context, sulfonium salts resemble hypervalent I(III) reagents, which represent a privileged class of substances in Umpolung reactions. In contrast to these, however, sulfonium salts do not bear the risk of being potentially explosive. A well-established example of such an electrophilic transfer reagent is the Umemoto reagent **343**[225], which is capable of trifluoromethylating various nucleophiles.

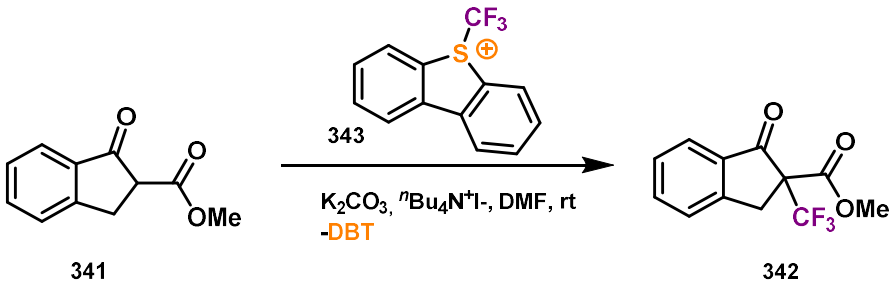

Scheme 108: Trifluoromethylation of β-ketoesters[226]

The reagent allows for the trifluoromethylation of β-ketoesters providing α-substituted α-trifluoromethyl β-ketoesters **342** using the phase-transfer catalyst $^{n}BuN^{+}I^{-}$ (Scheme 108).[226] However, the reaction mechanism of the Umemoto reagent with enols is controversial, since not only already discussed ionic processes in which the sulfonium fragment is substituted by a nucleophile are conceivable, but also radical mechanisms.[227] This results from the fact that nucleophiles can also act as a SET reductant and thus perform a one electron reduction of the sulfonium salt releasing an $^{\bullet}CF_3$ radical (Scheme 107, **339**).

The susceptibility of sulfonium salts to electron reductions can now also be utilized in a more controlled synthetic manner.[228] For this purpose, photocatalysis is particularly suitable, in which the Umemoto reagent can serve as a radical source (Scheme 109).

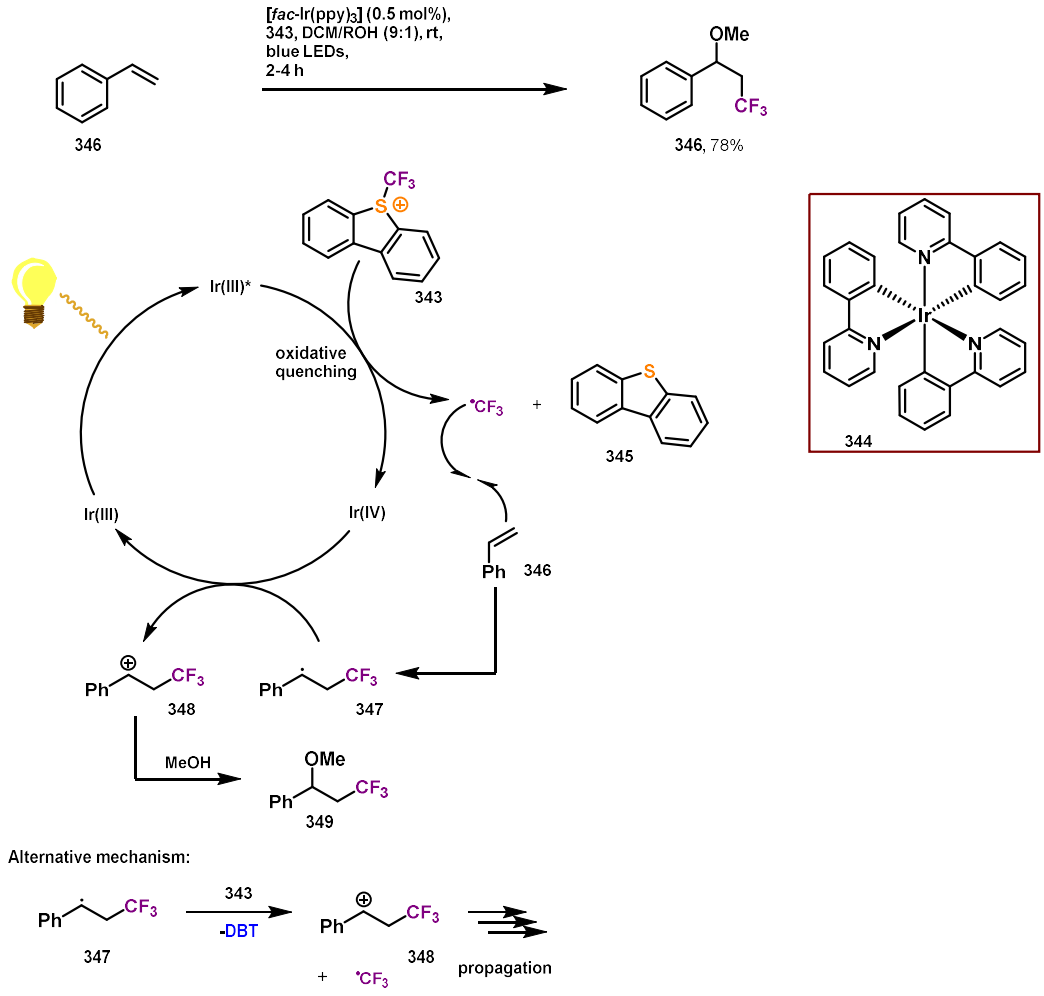

Scheme 109: Oxytrifluoromethylation of styrene[229]

Akita, Koike and coworkers were able to show that $^{\bullet}CF_3$ radicals can be generated photocatalytically as well as added to styrene **346**.[229] In this process, the photocatalyst [*fac*-Ir(ppy)$_3$] **344** is first excited and then oxidatively quenched by the Umemoto reagent **343**. Due to the homolytic C–S bond cleavage, the joint product DBT **345** is formed along with the $^{\bullet}CF_3$ radical in stoichiometric amounts. After addition of $^{\bullet}CF_3$ to the styrene **346**, the photocatalyst can now reoxidize the benzylic radical **347** to benzylic carbocation **348**. The overall process is thus net redox neutral. Methanol can now serve as a nucleophile and attack the formed cation **348** to complete the oxytrifluoromethylation. Although the reaction takes place exclusively under irradiation, an alternative mechanism in which the Umemoto reagent **343** is reduced by the benzylic radical **347** cannot be completely ruled out. Thus, a radical propagation is also conceivable.

However, the idea of generating radicals from sulfonium salts by photocatalysis is not completely new. For example, one of the first photocatalytic conversions was based on the reduction of sulfonium salts and was published by Kellogg and co-workers in 1978 (Scheme 110).[230]

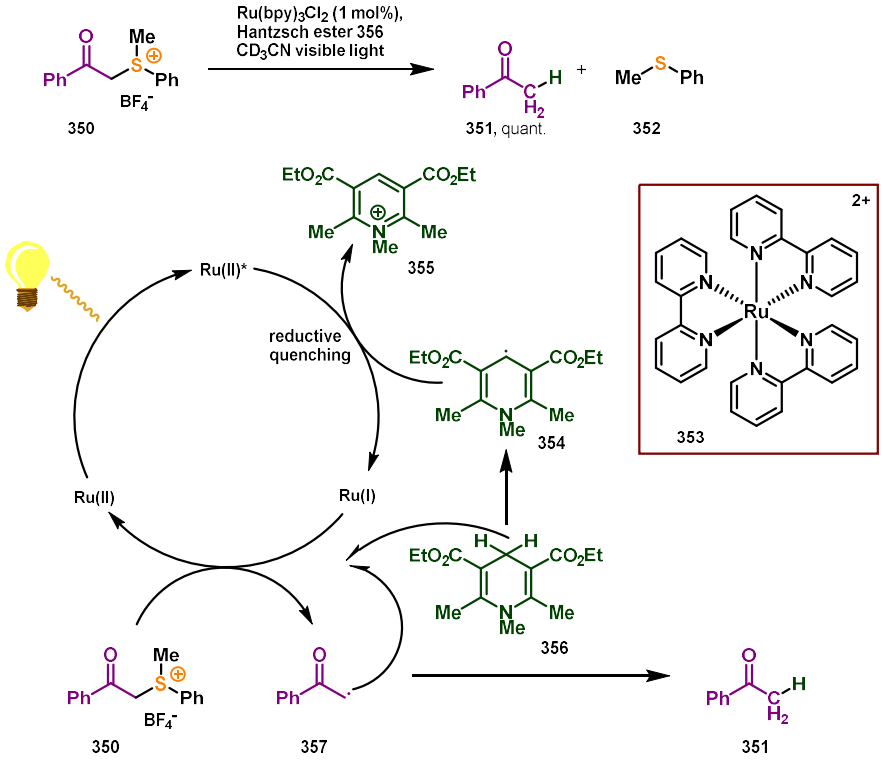

Scheme 110: Photocatalytic reduction of phenylacylsulfonium salts[204,231]

The reaction represents a reduction of phenylacylsulfonium **350** to ketone **351**, which is accelerated by the presence of a photocatalyst and light.[204,231] Hantzsch ester **356** is used as stoichiometric reductant and HAT reagent, while Ru(bpy)$_3$ serves as the photocatalyst. However, Stern–Volmer experiments showed that neither the Hantzsch ester nor the phenylacylsulfonium salt could successfully quench the excited photocatalyst. Therefore, reductive quenching can be assumed to proceed *via* a catalytically generated amount of radical **354**. The radical **354** is formed repeatedly by the α-carbonyl radical **357** directly abstracting a hydrogen from the Hantzsch ester **356**. The radical **357** in turn is the result of the reduction of the sulfonium salt **350**. At the beginning of the reaction, in which radical **354** is not yet present, Hantzsch ester radical **354** is presumably formed by photoexcitation of the Hantzsch ester **356** and subsequent SET reaction with the sulfonium salt **350**. The reduction of **350** and subsequent HAT process from Hantzsch ester **356** to radical **357** completes the photocatalytic cycle and releases product **351** and photocatalyst. The reaction serves as a conceptual example, but is of limited synthetic use.

4.3 *S*-(Aryl) Sulfonium salts

Due to the lack of α-CH acidity and the inability to form ylides, the possible applications of triarylsulfonium salts focus on the other three research topics of sulfonium salts mentioned above (Scheme 107).[219] These are metal-catalyzed cross-coupling reactions[222], non-catalyzed nucleophilic aromatic substitutions[232] and the formation of aryl radicals after reduction with one electron.[233] Besides these three fundamental applications in academia, triarylsulfonium salts are also used in industry as cationic photoinitiators and acid generators.[219,234] In the following, however, we will focus mainly on the synthesis of arylsulfonium salts, their properties and their application in the formation of aryl radicals in photocatalysis. The latter is particularly appealing since a number of photocatalytic systems have recently been published which allow interesting transformations.[233,235]

4.3.1 *S*-(Aryl) Sulfonium salts - Synthesis

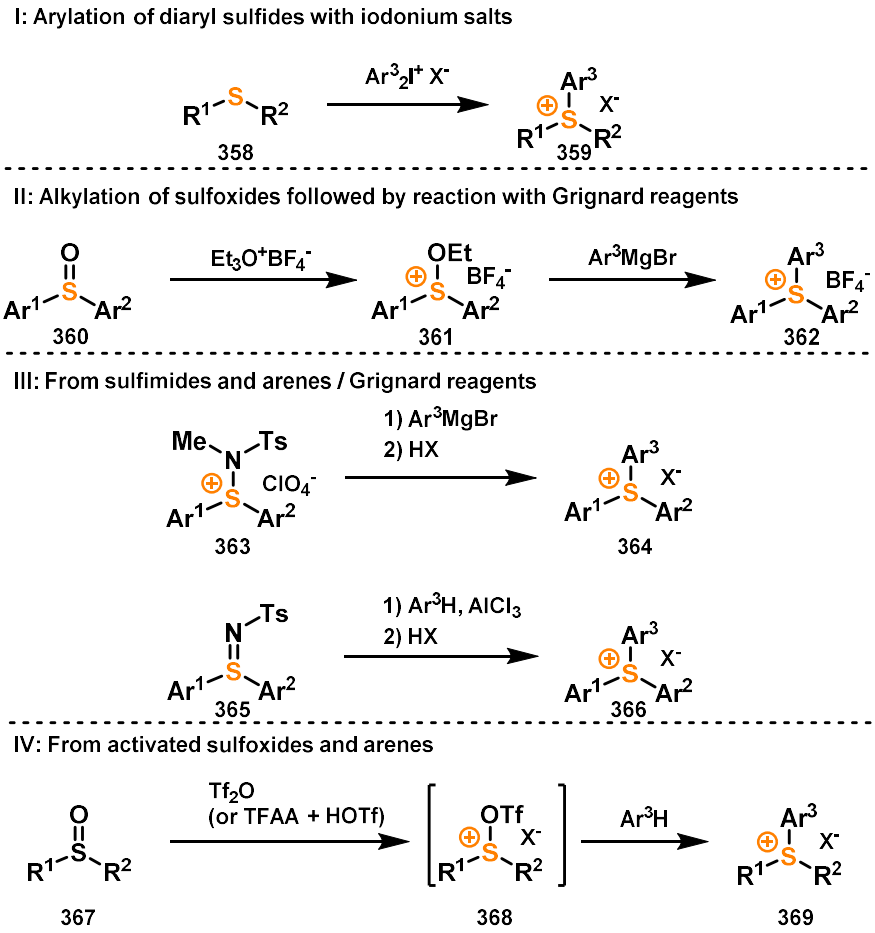

Scheme 111: Synthetic strategies for the preparation of S-aryl sulfonium salts[219]

S-Arylsulfonium salts can be prepared from four different starting materials (Scheme 111). Direct conversion of diaryl sulfides to *S*-arylsulfonium salts can be achieved by arylation using iodonium salts (Scheme 111, **I**). For this purpose, a mixture of the I(III) species and diphenyl sulfide is heated at 180 °C for 35 hours[236], or the same mixture is heated at 120-125 °C for only 3 hours with copper(II) benzoate as a catalyst.[237] The copper(II) catalyst drastically lowers the temperature of the decomposition of the iodonium salts and therefore allows transfer of the aryl group to the sulfide at much lower temperatures if only non-nucleophilic counterions such as BF_4^-, AsF_6^-, and PF_6^- are present. The methodology can be used to convert not only diaryl sulfides but also diaryl selenides to the corresponding onium compounds. However, the practicability of the reaction is limited by the fact that I(III) transfer reagents are required to synthesize a sulfur- or selenium-based transfer reagent.

In this sense, the synthetic utility can be improved by using a sulfur-based precursor [*e.g.* diaryl(alkoxy) sulfonium salts **361** or sulfimides **363**], which can then react with various Grignard reagents to obtain corresponding sulfonium salts (Scheme 111, **II** and **III**). For example, Andersen *et al.* were able to obtain triarylsulfonium salts **362** by activating diaryl sulfoxides **360** with Meerwein salts (triethyloxonium tetrafluoroborate) and subsequently reacting the diaryl(alkoxy) sulfonium precursor **361** formed with Grignard reagents.[238] Instead of Meerwein salts, other activators such as TMSOTf[239] and TMSCl[240] can be used with similar success. Starting from sulfinimines instead of diaryl(alkoxy)sulfonium precursors, either a similar route *via* Grignard reaction can be chosen or they can be further activated by addition of $AlCl_3$, enabling them to directly functionalize C–H bonds of aromatic compounds.[219,241]

Another particularly elegant approach to aryl sulfonium salts is the activation of aryl sulfoxides using acid anhydrides and subsequent C–H bond functionalization of arenes in form of an electrophilic aromatic substitution (Scheme 111, **IV**).

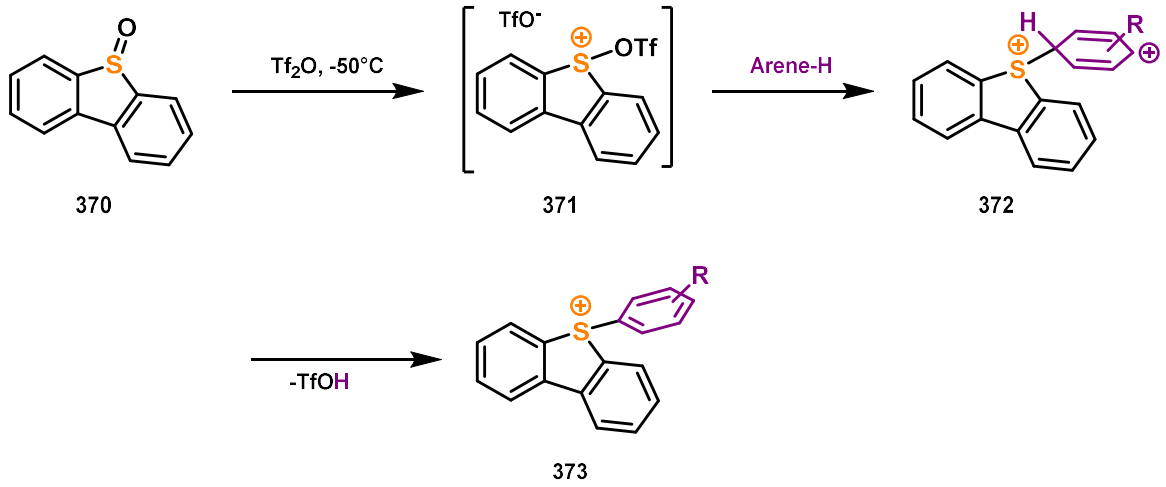

Scheme 112: Sulfonium salt formation via electrophilic aromatic substitution[222]

This approach was used by the group of Alcarazo and the group of Ritter, who used Tf_2O (or mixtures of TFAA and HOTf) as an activator, which, when combined with the sulfoxide **370**, forms the corresponding S(IV) bistriflate **371** *in situ* (Scheme 112).[222,232] The bistriflate **371** is now capable to react as an electrophile, when an arene is added. After subsequent rearomatization, one equivalent trifluoromethanesulfonic acid is released and the product **373** is formed. The methodology has broad functional group tolerance (ethers, esters, halogens, and heteroaromatic compounds), and does not rely on corresponding Grignard reagents. The selectivity corresponds to that of common electrophilic aromatic substitutions and is strongly dependent on the substituents of the arene. Limitations of this methodology are very electron-poor substrates, which reduce the nucleophilicity of the arene and thus give poor yields, or very electron-rich arenes, which run the risk of being oxidized by the strongly oxidizing bistriflate **371**. Apart from this, the released HOTf occasionally causes problems with acid labile functional groups, which can be addressed by the addition of base.[242]

The use of cyclic scaffolds like **373** in which two aromatic substituents of the sulfur are bridged offers synthetic advantages in subsequent reactions, when chemoselective transfer of only one particular substituent is required. Therefore, arylthianthrenium or aryldibenzothiophenium salts like **373** are often used in the literature. It should be noted, however, that although the mechanism of electrophilic aromatic substitution is proposed for the synthesis of aryldibenzothiophenium salts such as **373**, the mechanism cannot be generalized and is highly dependent on the type of sulfenylating agent used. Thus, for the formation of the corresponding arylthianthrenium salts, a SET/radical mechanism is hypothesized.[243]

4.3.2 *S*-Aryl sulfonium salts with cyclic scaffolds – Structure and reactivity of debenzothiophenium based sulfonium salts

S-(Aryl) sulfonium salts with cyclic frameworks, such as sulfonium salt **374**, have a pyramidal geometry with an angular sum of about 300°, as do most sulfonium salts.[219] Calculations have shown that their positive charge is almost completely localized at the sulfur.[219,222] The α-carbon atom of the sulfur C^1 involved in the S–Ar exocyclic bond bears a negative partial charge. Due to the interaction of anionic triflates and the positively charged sulfur, O–S short contacts are often found in the crystal structures of corresponding sulfonium salts.

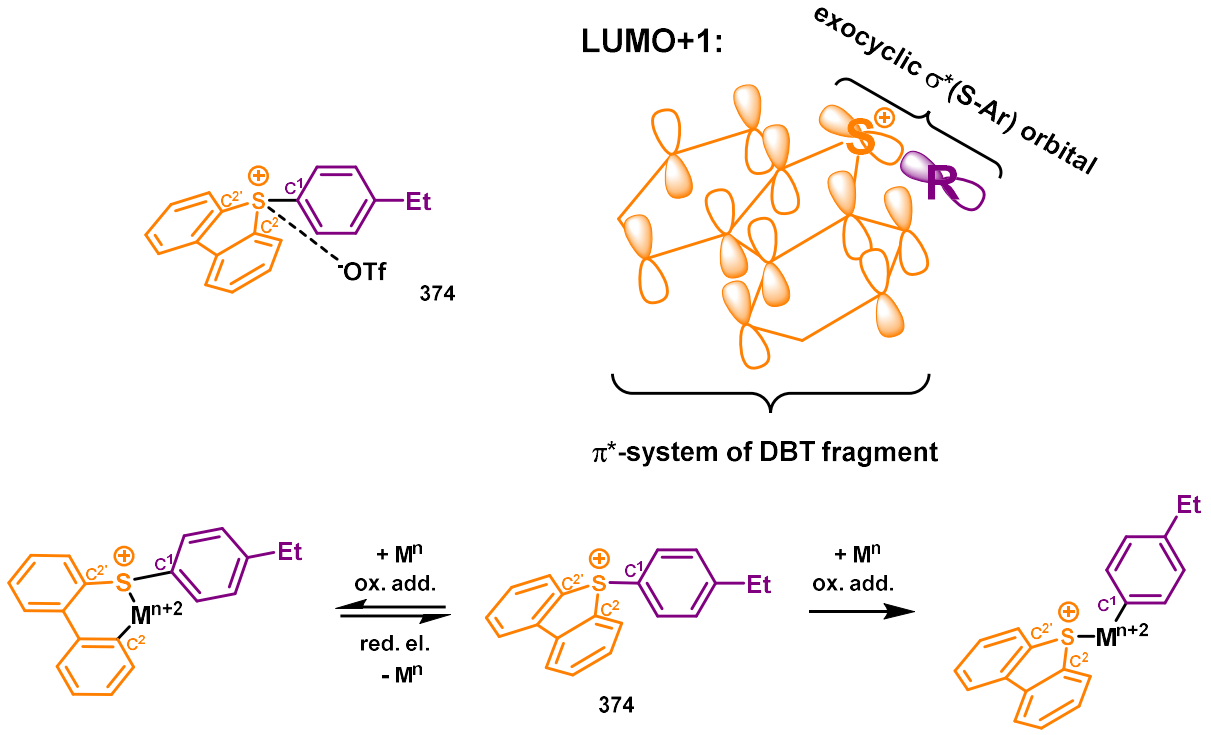

*Figure 61: Simplified molecular orbital diagram (LUMO+1) of compound **374**.* [219]

As already mentioned, the use of cyclic scaffolds has an application-related synthetic benefit.[219] The preferential transfer of the aryl substituent of the exocyclic bond can now be explained in terms of the structure. In metal-catalyzed reactions of a sulfonium salt (*e.g.* **374**), an oxidative insertion of the metal into one of the two cyclic S–C^2 bonds and thus the formation of a six-membered ring would be conceivable (Figure 61). However, this six-membered ring species formed is in equilibrium with the starting material, which in turn is regenerated *via* reductive elimination to the five-membered ring. Thus, a further reaction is hindered, unlike in the case of an insertion into the S–C^1 exocyclic bond. The effect that the "monodentate" arene (bound to the sulfur *via* one carbon atom) is preferentially transferred instead of the "bidentate" biaryl (bound to the sulfur *via* two carbon atoms) is reminiscent of the stabilization in chelating ligands. It is therefore possible to transfer a certain arene and to leave the other two bridged ones untouched.

A similar effect also occurs in SET processes, where the bond to the exocyclic arene is also preferentially homolytically cleaved after one-electron reduction.[219] The corresponding aryl radical of the exocyclic substituent is released and the dibenzothiophene backbone remains unaffected. To understand this phenomenon, one must consider the LUMO+1 that is populated during the one electron reduction. The corresponding MO diagram of the LUMO+1 is shown in a highly simplified form in Figure 61 (based on DFT calculations from literature[219]). The LUMO+1 consists of a combination of the π* orbital of the dibenzothiophene fragment and the σ*(S–Ar) orbital of the exocyclic S–Ar bond. Thus, a population

of this orbital leads to a weakening of said σ* (S–Ar) bond and therefore to the selective release of the exocyclic arene radical. This fact makes sulfonium salts based on the dibenzothiophene motif so interesting for photocatalytic applications and explains their advantages over halides.

4.3.3 *S*-Aryl Sulfonium salts in photocatalysis

The first triarylsulfonium salts to find application in photocatalysis were published by Fensterbank, Goddard, Ollivier and co-workers in 2013.[244]

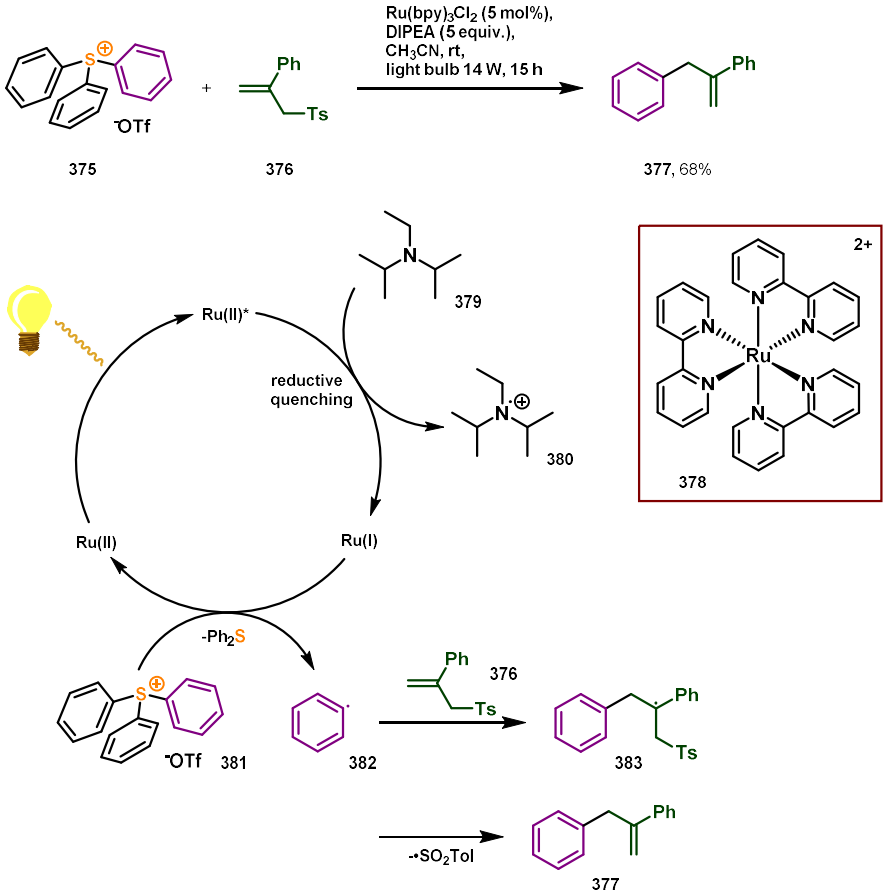

Scheme 113: Proposed mechanism for photoreductive allylation of trarylsulfonium salts[244]

They were able to show that not only sp^3-carbon-centered radicals as published by Kellogg or Akita and Koike (see chapter 4.2), but also aryl radicals are accessible *via* photocatalytic SET reactions when starting from arylsulfonium salts.[244] For this purpose, they reacted triarylsulfonium salts under reductive photocatalytic conditions and were able to use the released aryl radicals for carbon-carbon bond formations. One of these bond formations, for example, is the allylation of the corresponding phenyl radical **382**. The proposed mechanism is shown in Scheme 113. The applied photocatalyst $Ru(bpy)_3^{2+}$ **378** is irradiated with light. The excited photocatalyst is then reductively quenched by the stoichiometric reducing agent DIPEA **379**. The reduced photocatalyst with its enhanced reduction potential can now transfer an electron to the arylsulfonium salt **381**. After SET, the sulfonium salt releases an aryl radical and diphenyl sulfide under homolytic S–Ar bond cleavage. The aryl radical **382** can now be trapped by the allyl sulfone **376**. After subsequent β-fragmentation of the $^{\bullet}SO_2Tol$ radical, the olefin **377** is obtained. The authors stated that no reaction occurred in the absence of light, photocatalyst or DIPEA.

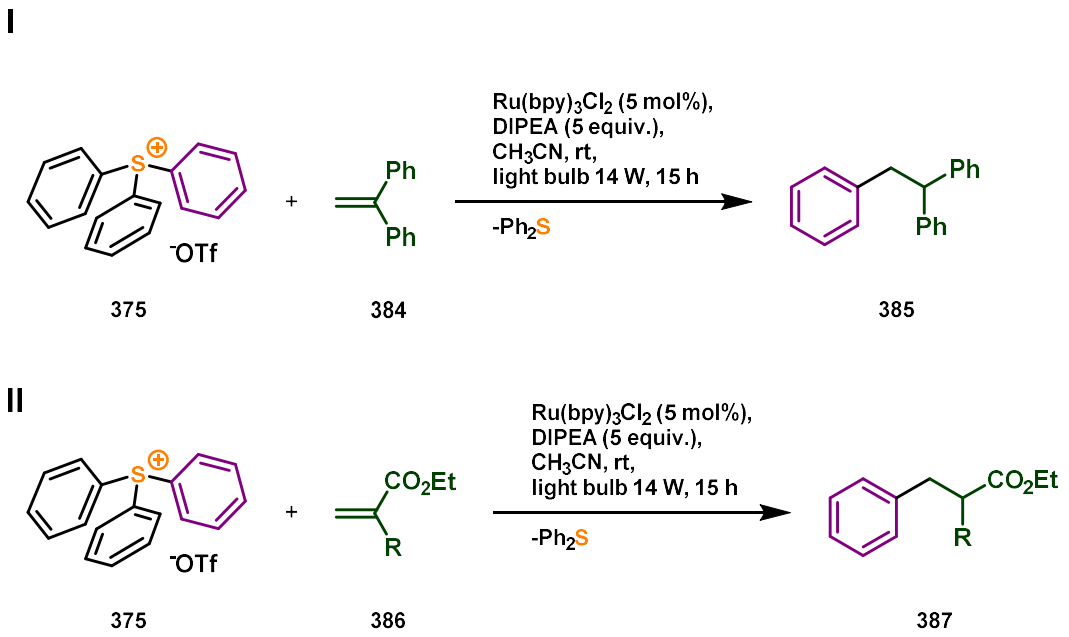

Scheme 114: Hydroarylation of activated olefins[244]

In addition to allyl sulfone, the group also tested other radical acceptors such as 1,1-diphenylethylene **384** (Scheme 114, **I**) and acrylates **386** (Scheme 114, **II**) to intercept the phenyl radical **382**.[244] Since there is no leaving group like in allyl sulfones, trapping of the phenyl radical is followed by HAT of the DIPEA radical cation **380** to give hydroarylation products **385** and **387** (Scheme 114), in which the phenyl-fragment formally adds to the double bond of the 1,1-diphenylethylene or acrylates. The methodology was also robust to variations in the aryl substituents at the sulfur (*p*-MeC_6H_4, *p*-$^tBuC_6H_4$, p-FC_6H_4) and variations of the corresponding anions of the sulfonium salt (TfO^-, BF_4^-, PF_6^-, Br^-). In the latter case, only poorly soluble sulfonium bromides led to significantly reduced yields.

During our research on the applicability of dibenzothiophenium salts for photocatalytic carbon–carbon bond formation, a similar approach was published by Procter and coworkers in 2020.

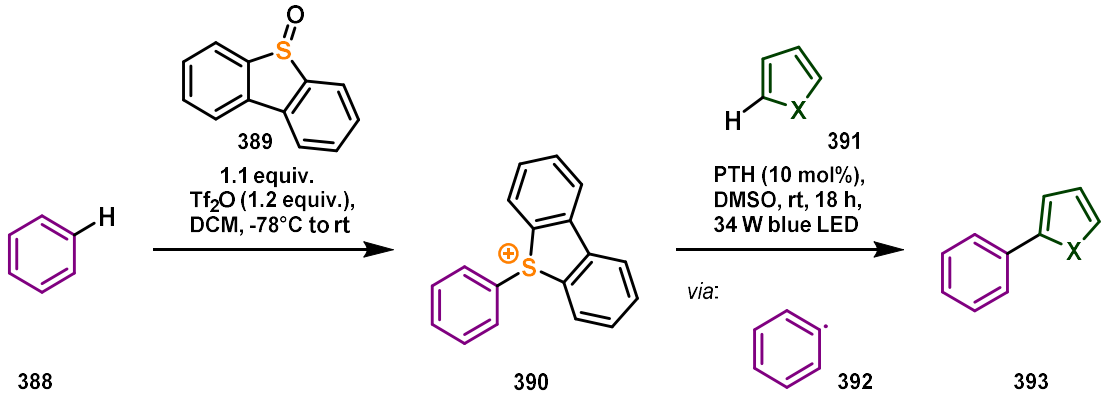

Scheme 115: Metal-free photoredox-catalyzed formal C–H/C–H coupling[233]

The group demonstrated that arenes (**388** and **391**) can be formally C–H/C–H coupled by a one-pot synthesis without the use of a transition metal (Scheme 115).[233] The one-pot approach thereby merges two synthetic steps, a functionalization/sulfenylation of **388** and a photocatalytic cross-coupling step of **390** and acceptor **391**. The photocatalytic cross-coupling step in Procter's approach is reminiscent of the aryl radical trapping reactions published by Fensterbank, Goddard, Ollivier and co-workers. In contrast to Fensterbank, Goddard, Ollivier and co-workers, however, Procter's group starts

from a cyclic dibenzothiophenium oxide **390**, which makes it possible not only to late stage functionalize a given arene **388** (violet) but also to chemoselectively transfer this specific *exo*-aryl group (violet) of the formed dibenzothiophenium salt **390** in the subsequent coupling (*cf.* Chapter 4.3.1 and 4.3.2). For the subsequent photocatalytic cross-coupling, the sulfonium salt **390** does not need to be further purified and can react with the added non-functionalized (hetero)arene acceptor **391** *via* the corresponding aryl radical **392**. Furthermore, Procter's approach uses an organic photocatalyst **PTH** (10-Phenylphenothiazine) and performs the coupling *via* a redox-neutral reaction pathway, which eliminates the need for stoichiometric reducing agents. However, as a major drawback, the reaction requires a large excess (20 equiv.) of the (hetero)arene acceptor **391** (20 equiv.).

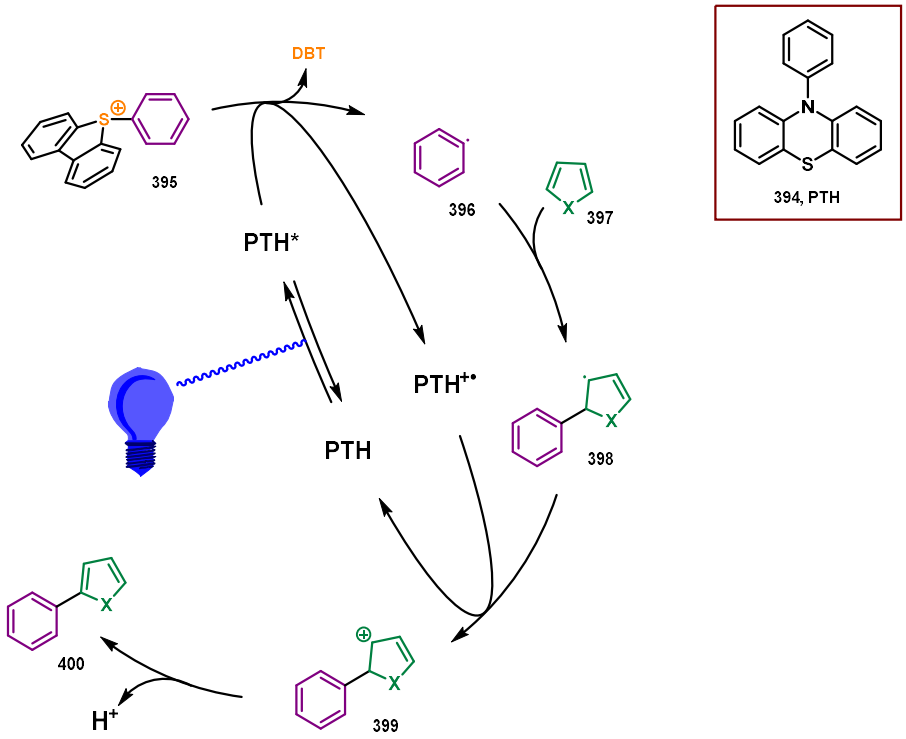

Scheme 116: Proposed mechanism for the photoredox-catalyzed formal C–H/C–H coupling[233]

The proposed mechanism for the photocatalytic cross-coupling is supported by several studies (Scheme 116). Cyclic voltammetry experiments showed that the excited photocatalyst **PTH*** is able to reduce the dibenzothiophenium salt **395**. Furthermore, Stern–Volmer experiments demonstrated that dibenzothiophenium salt **395** is also capable of successfully quenching the excited photocatalyst **PTH***. It therefore seems relatively certain that the first key step of the mechanism is the SET reduction of sulfonium salt **395** by the excited photocatalyst **PTH***. The aryl radical **396** released by reduction of sulfonium **395** and its trapping by the added arene acceptor **397** represent the next steps of the catalytic cycle. The radical nature of the processes was demonstrated by the fact that product **400** formation can be prevented by the addition of radical scavengers such as TEMPO and 1,1-diphenylethylene. Subsequent reoxidation of the radical intermediate **398** by the oxidized photocatalyst **PTH** $^{\bullet+}$ and rearomatization of **399** yields the product **400**.

In order to exclude a radical propagation, in which, for example, radical **398** is capable of reducing sulfonium **395** and thus triggers a radical chain, the quantum yield of the reaction was determined. The quantum yield Φ represents the number of photochemical conversions to product **400** that occur per absorbed photon.[245]

$$\Phi = \frac{\text{amount of reactant consumed or product formed}}{\text{amount of photons absorbed}} \qquad (5)$$

Equation 5: Quantum yield

Therefore, the quantum yield for photochemical reactions, in which radical chains do not dominate, should be less than 1. In the case of the photocatalytic cross-coupling step published by Procter, the quantum yield was determined to be 0.18, thus a process in which chain reactions dominate can be excluded.

4.4 Intramolecular addition of (aryl) radicals to arenes

Intramolecular radical cyclizations are a popular tool to establish C─C bonds between two aryl substituents in a molecule. One examples of such a reaction is the photocatalytic Pschorr reaction which has already been described in chapter 3.1.3. Also intermolecular reactions of similar fashion are represented by the methodology developed by Procter or Fensterbank, Goddard, Ollivier and co-workers. In the following chapter, however, the various methods of initiating an intramolecular radical cyclization and the possible products that can be formed in the radical addition to an arene as well as the corresponding mechanisms will be discussed in a historical context.

The basis for this methodology goes back to the work of Hey *et al.* from the 1960s and 1970s.

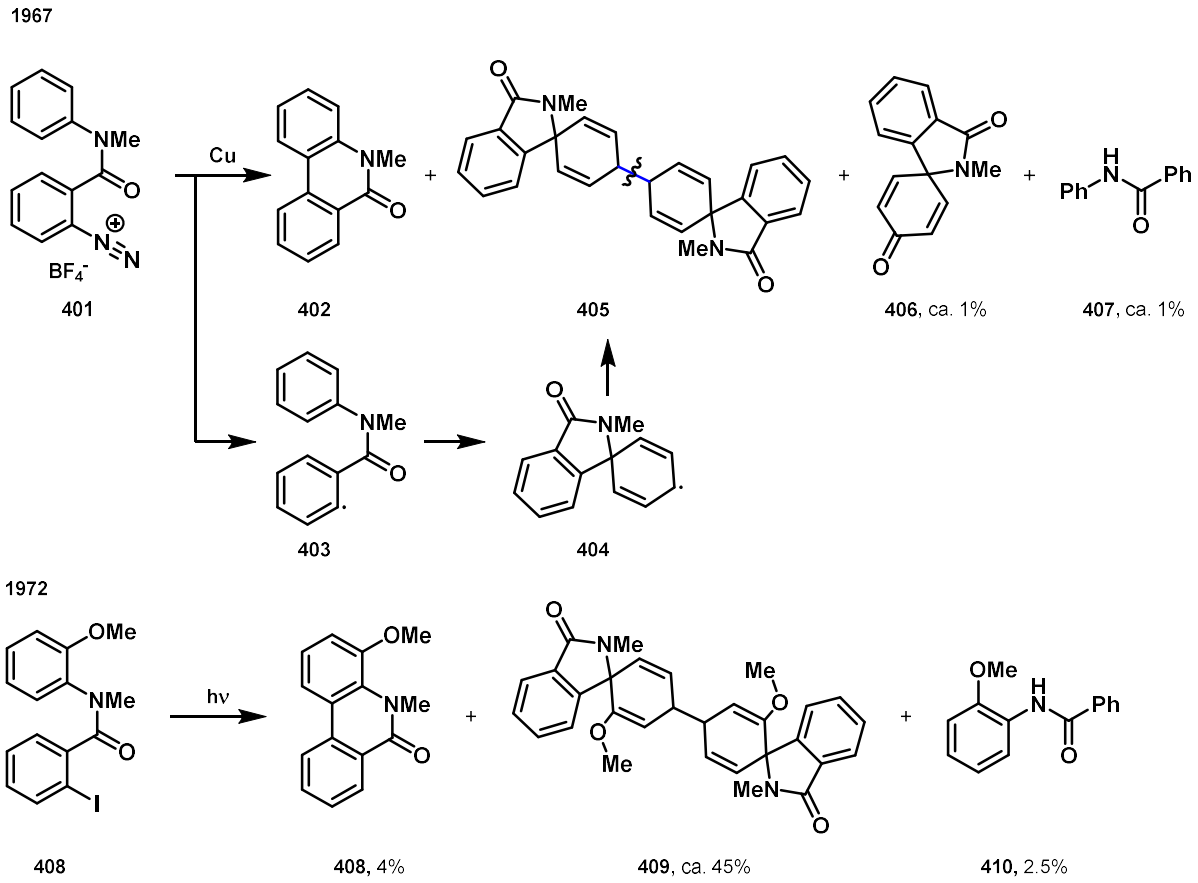

Scheme 117: Radical cyclization initiated by decomposition of diazonium fluoroborates[246]

In 1967 Hey *et al.* published a copper catalyzed cyclization of diazonium fluoroborates.[246] Here, a one-electron reduction by the copper initiates the formation of an aryl radical **403** able to cyclize in different fashions. The resulting product mixture consists to a large extent of phenanthridinone **402** and **405**. The latter is a dimer of the intermediary cyclohexadienyl radical **404**, which can be rationalized by homolytic bond cleavage at the indicated bond. The last two products, which are present in about 1% each, are formed by quenching of the said radical **404** with oxygen and dehydration of the hydroperoxide (**406**) or by deamination and demethylation (**407**). Later Hey *et al.* could show that similar products can be achieved by the photolysis of aryl iodides **408** using a mercury lamp.[247] Again, an isomeric mixture of a cyclohexadienyl dimers **409** is obtained after the homolytic C─I bond cleavage.

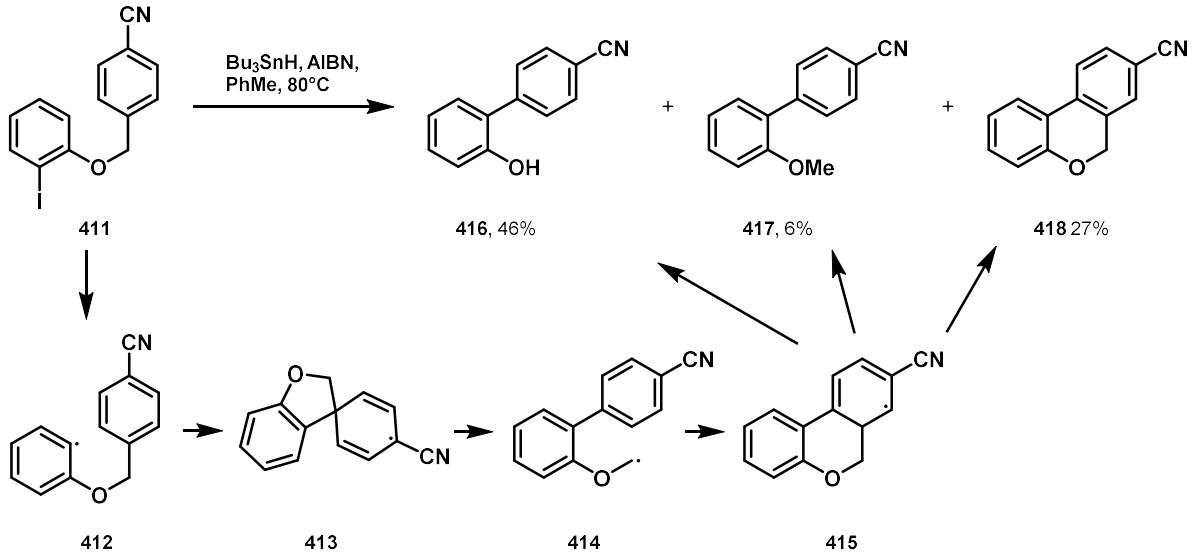

Scheme 118: Synthesis of biaryls from benzyl iodoaryl ethers[248]

In addition to the amide-based tether, benzyl ether-based systems can also be cyclized.[249] In 2000, for example, Bowman and co-workers successfully obtained 6*H*-benzo[*c*]chromen-6-ones *via* Bu_3SnH-mediated cyclization of aryl iodides (or bromides) followed by oxidation of the resulting 6*H*-benzo[*c*]chromenes with PCC.[250] A similar approach based on Bu_3SnH was used by the group of Harrowven to synthesize biarylic phenols **416** (Scheme 118).[248] Also here 6*H*-benzo[*c*]chromenes like **418** could be isolated, but only as a minor product. Their connectivity could be proven by NOE NMR studies and suggests an intermediate **414**, which cyclizes in a 6-*endo/exo*-trig course leading to benzo[*c*]chromene **418** *via* **415**. Also the second minor product **417** can be rationalized by intermediate **414** abstracting a hydrogen from Bu_3SnH. The outcome of the reaction strongly depends on the substitution pattern at the attacked aryl ring. While arenes bearing electron withdrawing moieties (*e.g.* compound **411**, CN) lead to phenol formation (**416**), radical stabilizing moieties (*e.g.* phenyl) predominantly lead to benzo[*c*]chromene formation (**418**, 50%). Both, Bowman and Harrowven, generate the initial radical by abstraction of a leaving group through a $Bu_3Sn\bullet$-radical. After cyclization towards intermediates like **415**, however, the reaction proceeds predominantly by oxidation (e.g. by loss of $H^\bullet$) rather than reduction by abstraction of a hydrogen from Bu_3SnH.[250] Therefore, the radical chain is interrupted and both the radical initiator AIBN and toxic Bu_3SnH must be used overstoichiometrically. Furthermore, the reaction is not very selective and product mixtures are often obtained.

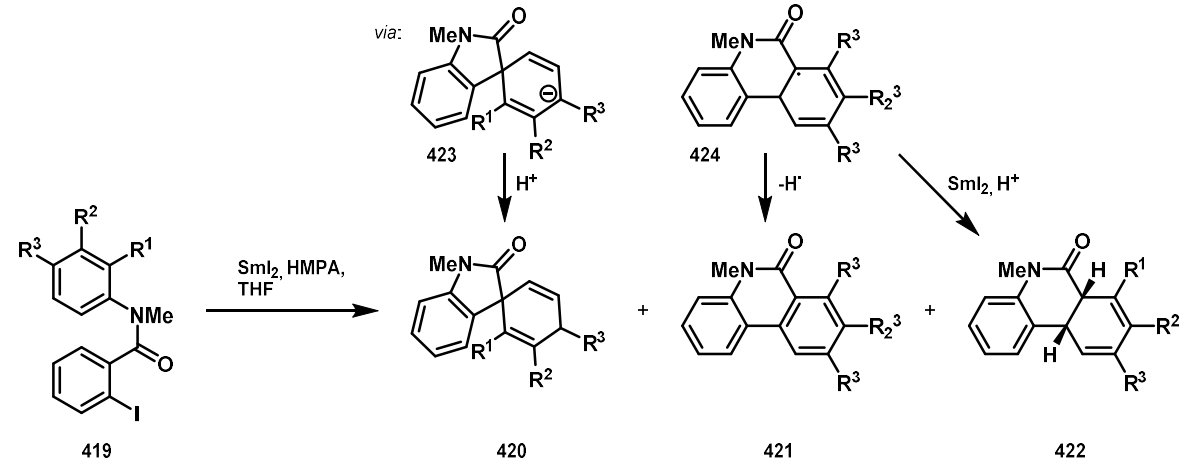

Scheme 119: Samarium(II) mediated aryl radical cyclization[251]

In 2004 Tanaka and coworkers published a tunable method for the cyclization of benzanilide derivatives.[251] In this case, the initial aryl radical is generated by the reduction of aryl iodide **419** with SmI_2 in HMPA (Scheme 119). In the absence of ^{i}PrOH, 15-60% of the phenanthridinone **421** can be obtained, depending on the substituents. In contrast, if ^{i}PrOH is added to the reaction, product mixtures of Birch-type reduced compound **420** and dihydrophenanthridinone **422** are obtained in ratios that depend strongly on the substitution pattern. The different products can be explained by the intermediates **423** and **424**. After cyclization of the initially formed aryl radical to a spirocyclohexadienyl radical, this spirocyclohexadienyl radical can either be trapped by a further reduction to the anion **423** or rearrange to intermediate **424**. In the absence of ^{i}PrOH hydrogen abstraction of **424** leads to phenanthridinone **421**, while in the presence of protic ^{i}PrOH anionic intermediates like **423** or **424**, after another reduction step, are trapped giving products **420** and **422**, respectively.

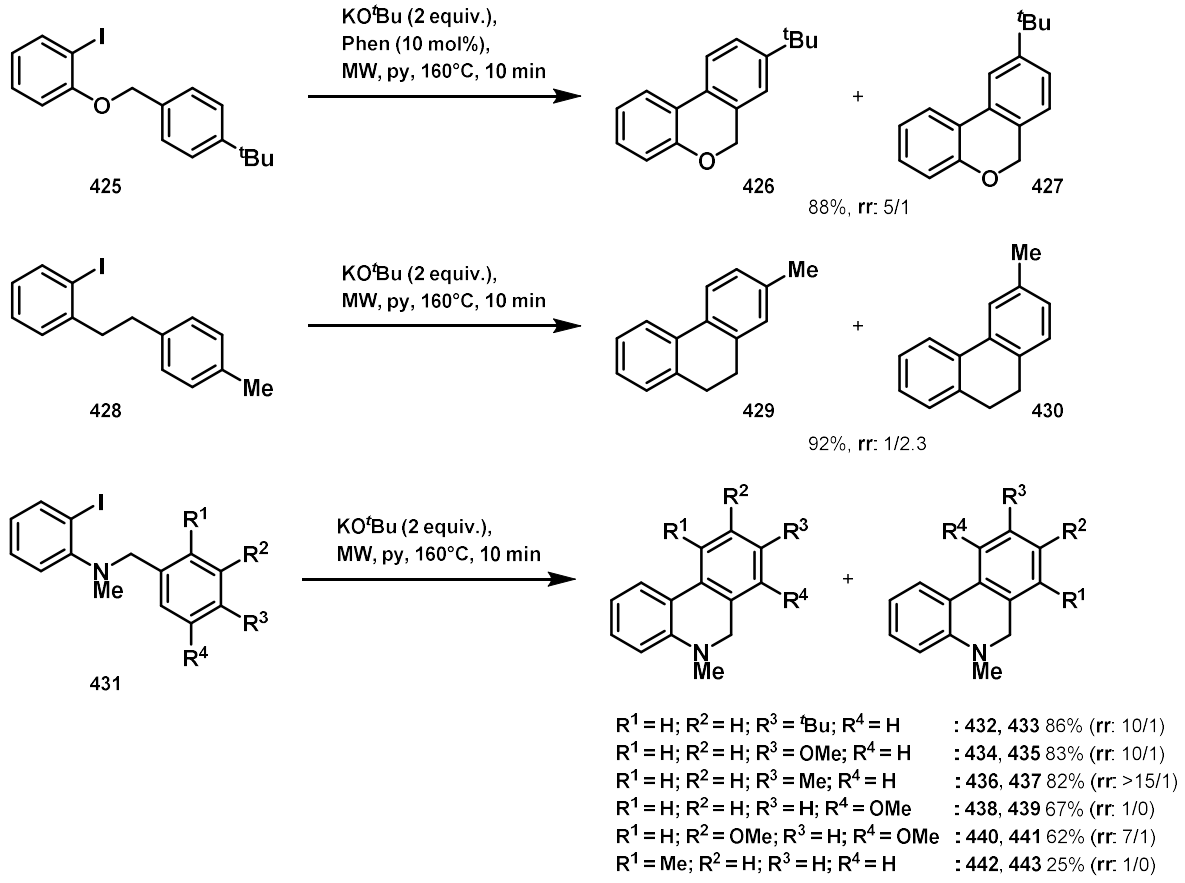

Scheme 120: Substitution effect on regioselectivity of methodology published by Charette[252]

In 2011 Charette and coworkers published an intramolecular cyclization of aryl ethers, amines, amides and ethylene bridged aryls like **428** based on an initial radical formation by single-electron transfer from KO^{t}Bu to an aryl iodide.[252] In some cases, a catalytic SET mediator such as phenanthroline (phen) is required for the microwave-assisted reaction in pyridine. While exploring different substitution patterns the authors observed different regioisomeric products (Scheme 120). Furthermore, they noticed an intrinsic electrophilicity[253] of the generated radical, which causes electron-deficient anilines with *e.g.* a pyridine acceptor arene to be poor substrates (therefore not included in the list of Scheme 120).

The exact mechanism of electron transfer to the aryl iodide does not appear to be clear, but the generated radical anion cleaves into an aryl radical, which cyclizes *via* a kinetically preferred *5-exo-trig*

manner to **448** (Scheme 121). From there, the subsequent ring expansion with two possible migrations determines the regioisomeric product.

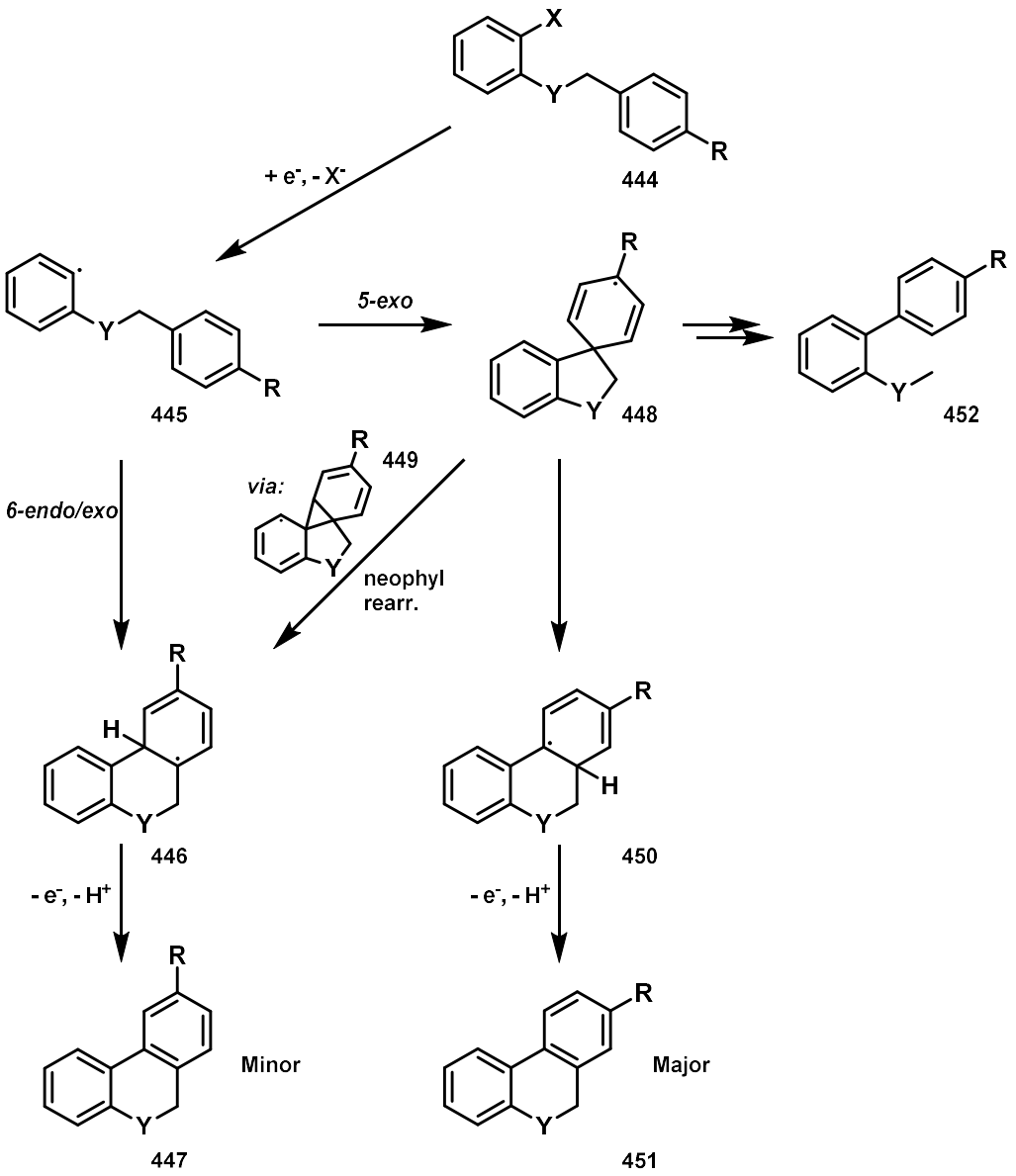

Scheme 121: Proposed radical cyclization machanism[252]

The proposed mechanism starts with the generation of aryl radical **445**.[252] After the already mentioned *5-exo-trig ipso* attack spirocyclohexadienyl radical **448** is obtained. Concerted ring expansion with alkyl migration can then lead to compound **450**, which can rearomatize to the major regioisomer **451** *via* loss of an electron and proton. The formation of the minor product can be explained by the neophyl rearrangement[254] of spirocyclohexadienyl radical **448** or a *6-endo/exo* cyclization of aryl radical **446**. According to the product distribution (Scheme 120) the alkyl migration to the major product **451** seems to be the predominant pathway, when stabilizing heteroatom lone pairs are involved. Biarylic compounds like **452** could not be detected, since β-scission of spirocyclohexadienyl radical **448** seems to be a slow process.

In addition to the reduction of aryl halides using stoichiometric reductants, visible-light photocatalytic methods for the generation of radicals and subsequent addition to aromatic systems have recently become established.

In 2018 the group of Sun could synthesize 6*H*-benzo[*c*]chromenes by a visible-light induced cascade radical addition/cyclization of biphenyl vinyl ethers (Scheme 122).[255]

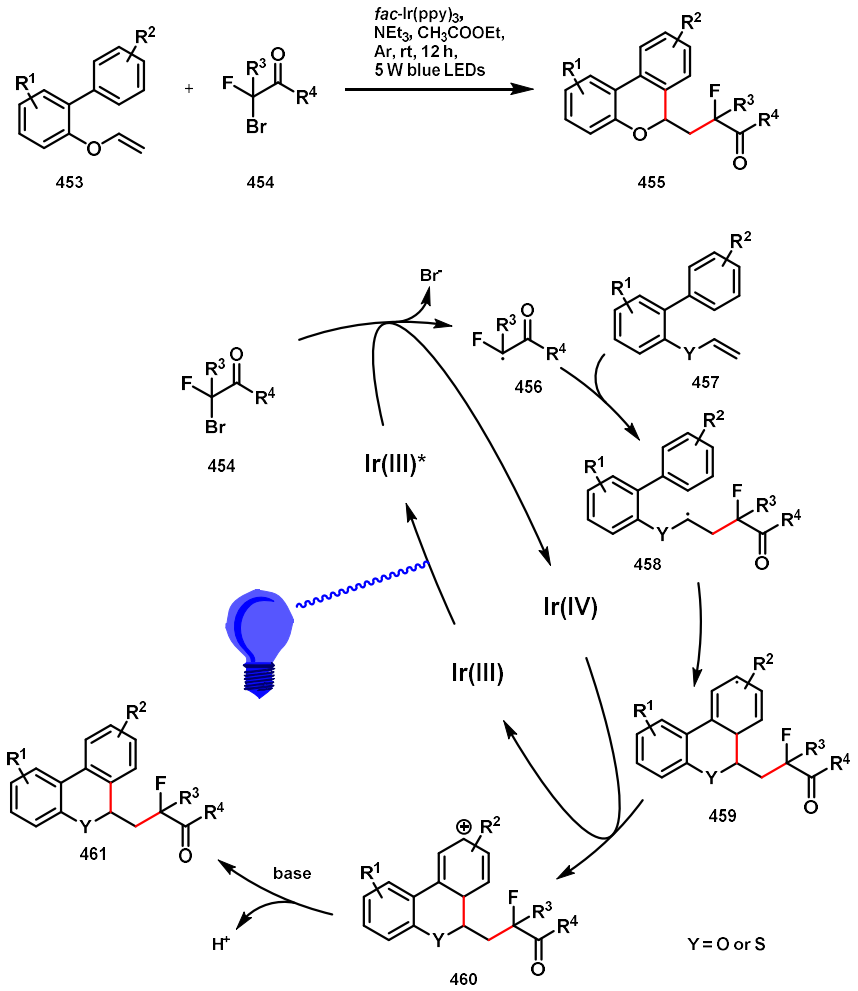

Scheme 122: Visible-light promoted radical addition/cyclization of biaryl vinyl ethers to 6H-benzo[c]chromenes – proposed mechanism[255]

The group succeeded in optimizing the reaction conditions to achieve yields between 42% and 93%. *fac*-Ir(ppy)$_3$ was identified as the best performing photocatalyst and triethylamine as the best performing essential base. The yields showed dependence on the substitution pattern and the attacked aryl-substituent used. While electron-rich acceptor arenes showed the highest yields, aryls such as pyridyl or phenyl groups with electron-withdrawing substituents R^2 showed reduced yields. The methodology could be applied not only to vinyl ethers resulting in benzochromenes but also to vinyl thioethers resulting in benzothiochromenes. Also the substituents at the bromo- and fluoro-substituted acetic acid derivatives could be modified (R^3).

The proposed mechanism starts with the excitation of the *fac*-Ir(ppy)$_3$ photocatalyst *via* blue light. The excited photocatalyst Ir(III)* can now reduce the bromo- and fluoro-substituted acetic acid derivative **454** *via* SET to a fluoroactyl radical **456**, which can add to the carbon-carbon double bond of the vinyl ether **457**. After intramolecular cyclization, reoxidation by Ir(IV) and deprotonation by triethylamine the desired product **461** and the Ir(III) photocatalyst are released. The proposed mechanism is

supported by light on/off experiments and Stern–Volmer kinetic studies. Furthermore, the reaction is not possible without bromo- and fluoro-substituted acetic acid derivatives **454** or without photocatalyst or in the presence of TEMPO. If additives such as 1,1-diphenylethene are added, the radical **456** adds to the latter instead of the vinyl ether. The methodology differs from the previously mentioned, since an alkyl radical and not an aryl radical adds to the aryl substituent. The disconnection approach to obtain benzochromenes is therefore different from that of Charette.

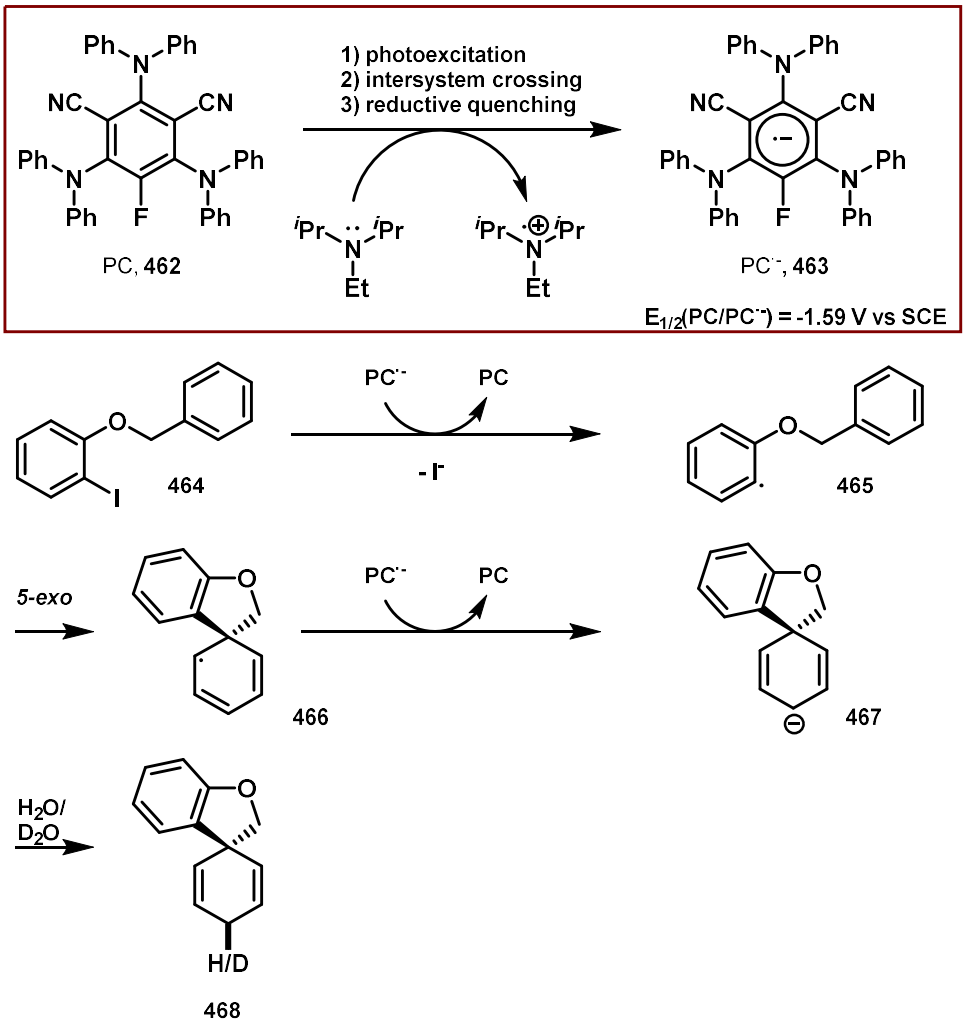

Scheme 123: Proposed mechanism for dearomative hydroarylation. Reaction conditions: 5 mol% PC, DIPEA (3 equiv.) MeCN/H2O (1:1), blue LEDs, 23 °C, 16h.[256]

In 2020, Jui and coworkers published an approach to synthesize spirocyclic cyclohexadienes similar to those of Tanaka (Scheme 123).[256] By using a photocatalytic approach, the reductant can be generated more targeted, thus creating higher selectivity to the dearomized product **468**. The reductant ($PC^{\bullet-}$) is formed by photoexcitation of the Adachi-type photocatalyst (PC) and reductive quenching with Hünig's base. The reduction of the aryl iodide **464** with $PC^{\bullet-}$ then proceeds in the usual way to the cyclohexadienyl radical **466**. However, the cyclohexadienyl radical **466** is subsequently trapped by further reduction, and unwanted radical side reactions are prevented by reductive radical-polar crossover. Since the solvent used is a 1:1 mixture of water and acetonitrile, the formed anion **467** is then protonated. In this way, the aromaticity of the acceptor arene can be broken, even under mild conditions. Thus, the method requires only 5 mol% photocatalyst, 3 equivalents DIPEA and 15 W blue LED irradiation to realize the spirocyclization of various halides with different tethers (ether, amide, amine) and substitution patterns in yields between 46% and 94%.

5 Results and Discussion II: Photoredox catalysis with *S*-(aryl) sulfonium salts

5.1 Project III: Two-step cyclization tool based on sulfenylation and subsequent photocatalytic coupling - Motivation

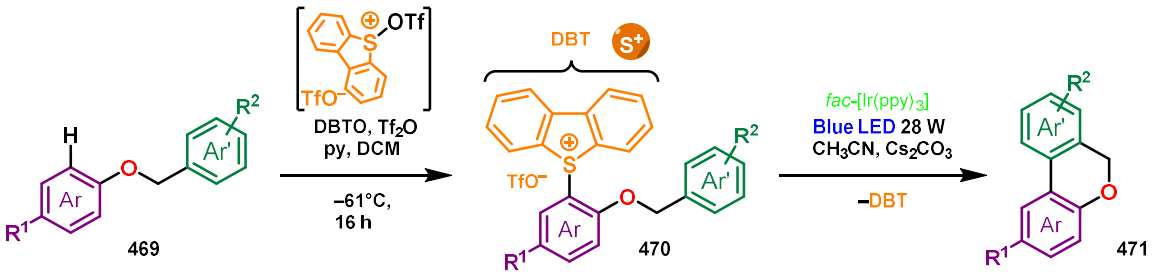

Scheme 124: Two-step cyclization tool[242]

Inspired by the research of Fensterbank, Goddard, Ollivier and co-workers and supported by the publication of Procter (Chapter 4.3.3), our goal was to develop a two-step cyclization tool that formally C–H/C–H couples two linked arenes. The methodology should therefore consist of a regioselective functionalization step in which an appropriately designed arene is sulfenylated, followed by a subsequent photocatalytic cyclization step, which leads selectively to one cyclized product. Due to the selectivity issues discussed in Section 4.4 for reactions involving intramolecular addition to arenes caused by different reaction mechanisms, the focus of the cyclization tool development should also be on mechanism exploration. The following results have already been published in corresponding literature in 2021.[242]

5.2 Synthesis and requirements of benzylic ethers

To develop an efficient cyclization tool by combining C–H sulfenylation with Ar-radical generation one has first to design a polyaromatic substrate suitable for this purpose.

The substrate should contain two aromatic parts connected *via* a linker which will be intramolecularly C–H/C–H coupled by the two step sulfenylation/Ar-radical cyclization approach (Scheme 125). To avoid product mixtures one aromatic part needs to be more nucleophilic then the other to selectively undergo electrophilic aromatic substitution (sulfenylation). Furthermore the exact position of the sulfenylation is crucial and must be forced to a position geometrically allowing subsequent cyclization. A solution that meets these requirements is the use of an asymmetric linker. By choosing an oxymethylene linker the aryl benzyl ethers should be selectively sulfenylated at the phenolic part (violet arene).

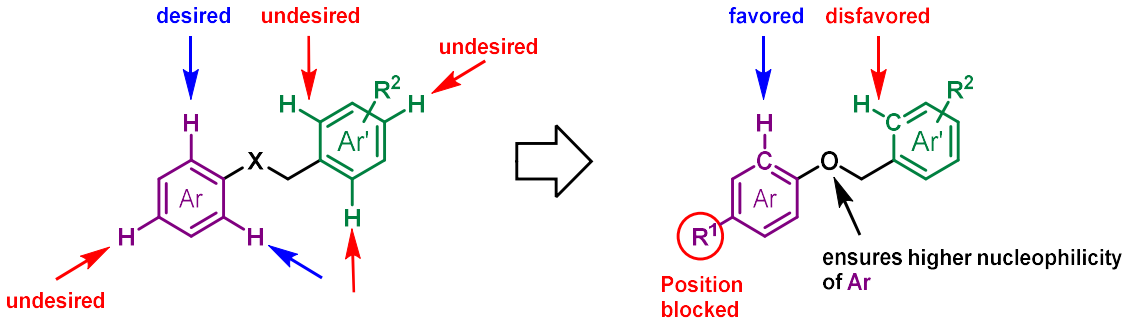

Scheme 125: Substrate design[242]

The most reactive positions for electrophilic aromatic substitution are marked with arrows. The two homotopic *ortho*-positions (blue arrow) are the ones, that once sulfenylated, will lead to a subsequent cyclization, while the more sterically accessible *para*-position (red arrow) will not and needs to be blocked by R^1. The expected C–H/C–H coupling will proceed between the C–H groups marked.

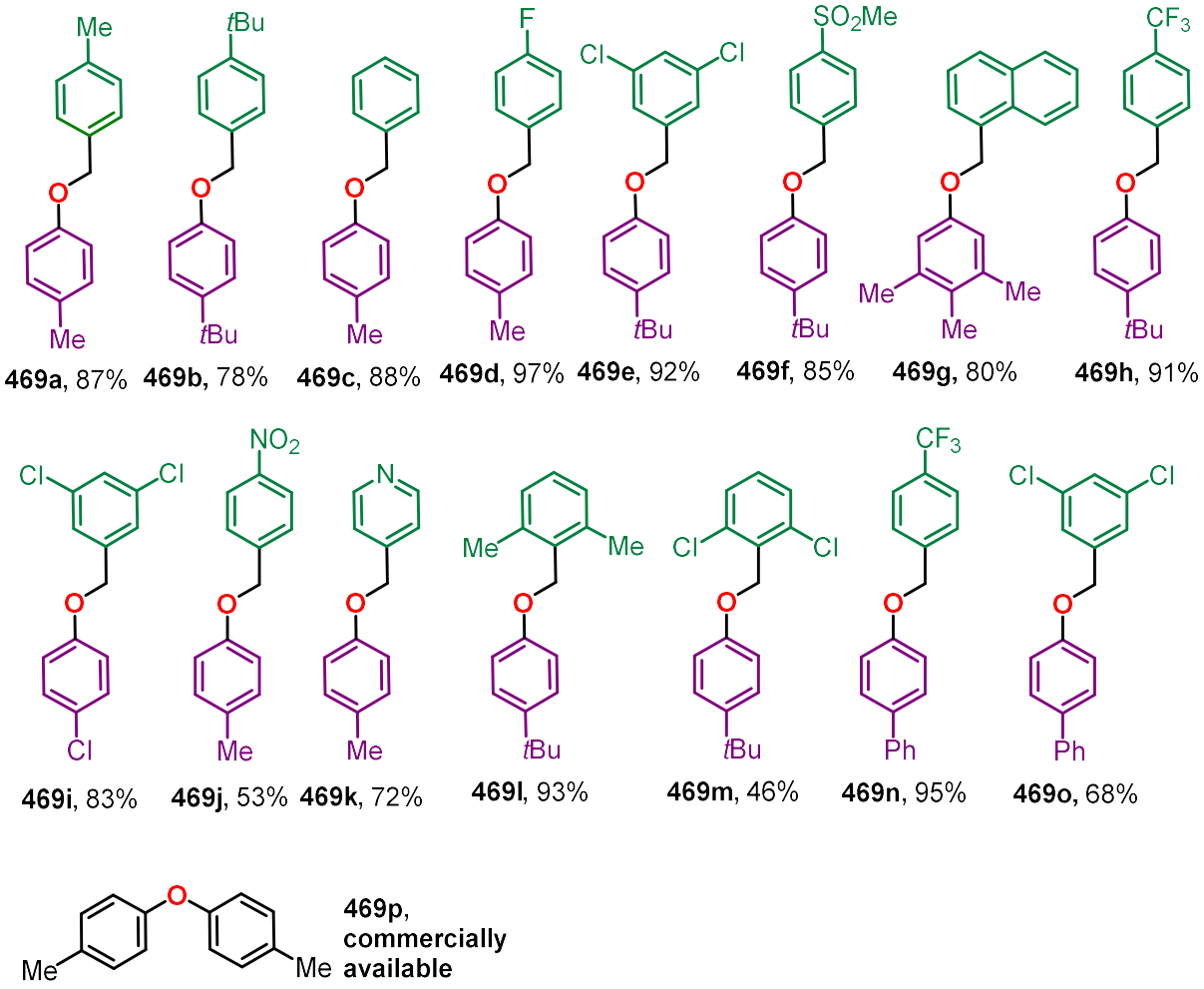

469a, 87% **469b**, 78% **469c**, 88% **469d**, 97% **469e**, 92% **469f**, 85% **469g**, 80% **469h**, 91%

469i, 83% **469j**, 53% **469k**, 72% **469l**, 93% **469m**, 46% **469n**, 95% **469o**, 68%

469p, **commercially available**

Scheme 126: O-benzylated phenols[242]

To examine the behavior of *O*-benzylated phenols subjected to our cyclization methodology a set of them were synthesized (Scheme 126). On the electron rich ring (violet) various moieties (R^1) were installed to block the *para*-position (Me, Cl, ^{t}Bu, Ph), while on the less activated ring (green) different (hetero)arenes (Ph, Naph, Py) bearing diverse functional groups were placed (R^2: Me, ^{t}Bu, F, Cl, SO_2Me, CF_3, NO_2). On the one hand functional groups (R^2) were placed at positions not interfering with the subsequent cyclization (**469a-k**,**n-p**), but on the other hand in some examples substitution patterns were chosen to impede the later cyclization and analyze the reaction of the system to this disturbance (**469l,m**). Beside the *O*-benzylated phenols also the commercially available diphenyl ether **469p** was considered as a possible substrate for further investigations.

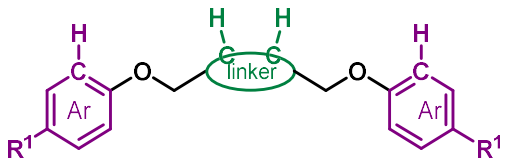

Scheme 127: Schematic representation of substrates suitable for double cyclization[242]

Furthermore we wanted to extend the scope also on substrates capable of double cyclization leading to more complex but highly symmetrical products (Scheme 127). Hence, it was necessary to expand the linker by an aromatic system offering the required C–H functionality capable for cyclization (green) and to install two phenolic rings exhibiting a substitution pattern being able to undergo sulfenylation (violet). Systems that meet the requirements are shown in Scheme 128.

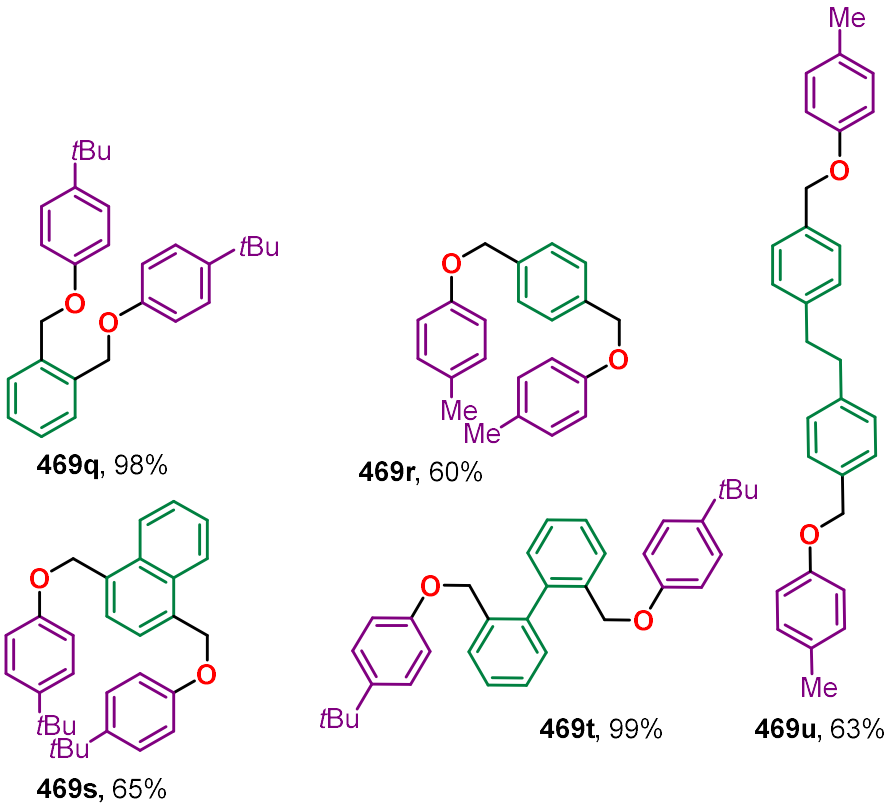

Scheme 128: Substrates suitable for double cyclization[242]

Most of the compounds were synthesized using the classical Williamson ether synthesis starting from phenols (**469a-d,j,r,u**) or phenolates (**469e-i,l-o,q,s,t**) and benzylic halides. Starting from phenolates in refluxing DMF has the advantage of significantly reducing reaction times, which can make a difference of days (vs 15 min) in the case of **469s** and **469t**. For compound **469k** we used *p*-cresol and pyridin-4-ylmethanol as starting materials in a Mitsunobu reaction.

5.3 Synthesis and properties of the corresponding dibenzothiophenium salts

The first attempt for the sulfenylation of the benzylic ethers was using a procedure published in literature[222]. Therefore the *O*-benzyl-phenol **469a** was added to a solution of benzothiophene-*S*-oxide activated *via* triflic acid anhydride.

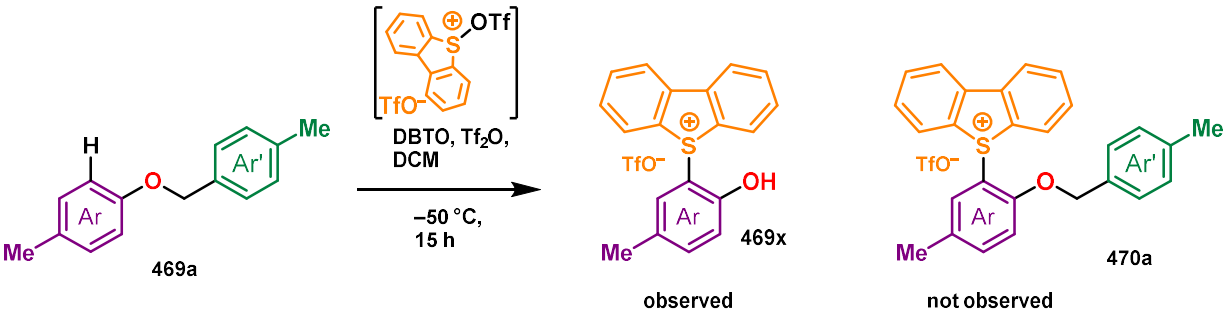

Scheme 129: Sulfenylation of the benzylic ethers without base[242]

To our surprise the crude ^{1}H-NMR revealed that a cationic species had formed but not as expected product **470a** but species **469x** (Scheme 129). This result can be explained by the release of stoichiometric amounts of triflic acid by the electrophilic aromatic substitution, which then catalyzes the cleavage of the benzylic ether. After washing with diethyl ether, mainly compound **469x** remained and could be detected. In order to maintain the benzylic ether a Brønsted base is needed to capture the released triflic acid. For this task phosphates, carbonates, aliphatic amines, di-*tert*-butylpyridine and pyridine were considered. While carbonates and phosphates did not bring the requested effect, amines probably did not withstand the oxidative environment and di-*tert*-butylpyridine was too prone to electrophilic aromatic substitution; only the addition of pyridine resulted in the correct product **470a**.

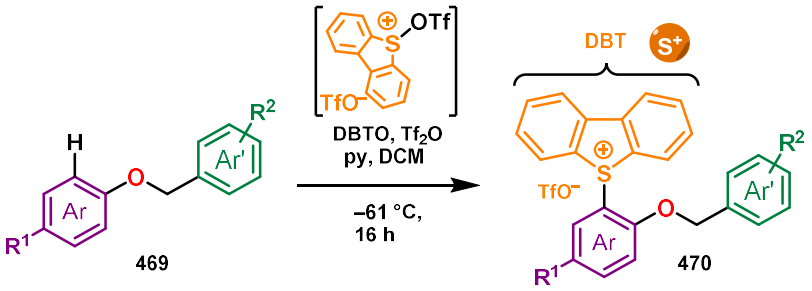

Scheme 130: Protocol for selective sulfenylation[242]

A new protocol was developed using a slight excess of pyridine as base (Scheme 130). This protocol was then applied to the *O*-benzylated phenols of Scheme 126.

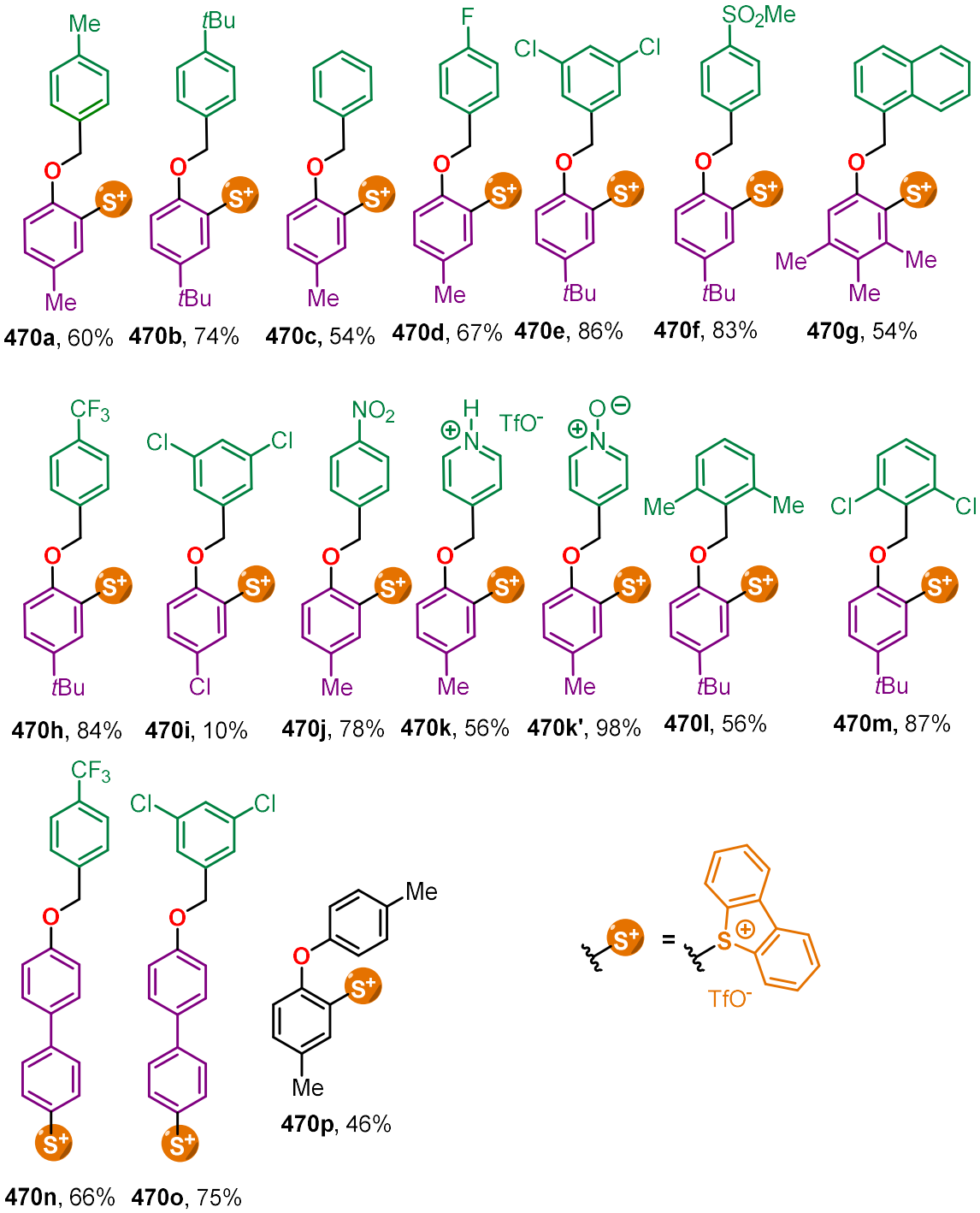

Scheme 131: Scope of sulfenylation suitable for single cyclization[242]

While all the other dibenzothiophene sulfonium salts were directly synthesized *via* this protocol (yield: 10% - 87%), pyridine-*N*-oxide **470k'** was synthesized by the oxidiation of **470k** by *m*CPBA in 98% yield indicating the stability of dibenzothiophenium salts towards oxidizing agents. The synthesis of **470k** itself did not require additional pyridine as a base.

A number of sulfonium salts could be synthesized with the correct regioselectivity. The substitution at the *o*-position of the oxygenated substituent is a direct result of the blocking group R^1. If R^1 corresponds to an alkyl group, high selectivity is achieved, while phenyl groups or halides are not suitable for this task. While the former are sulfenylated themselves (**470n**, **470o**) making a subsequent cyclization impossible, the latter provide significantly reduced yields (**470i**). This dependence on alkyl groups for

blocking the *para*-position of the electron-rich ring system corresponds to a limitation of this methodology.

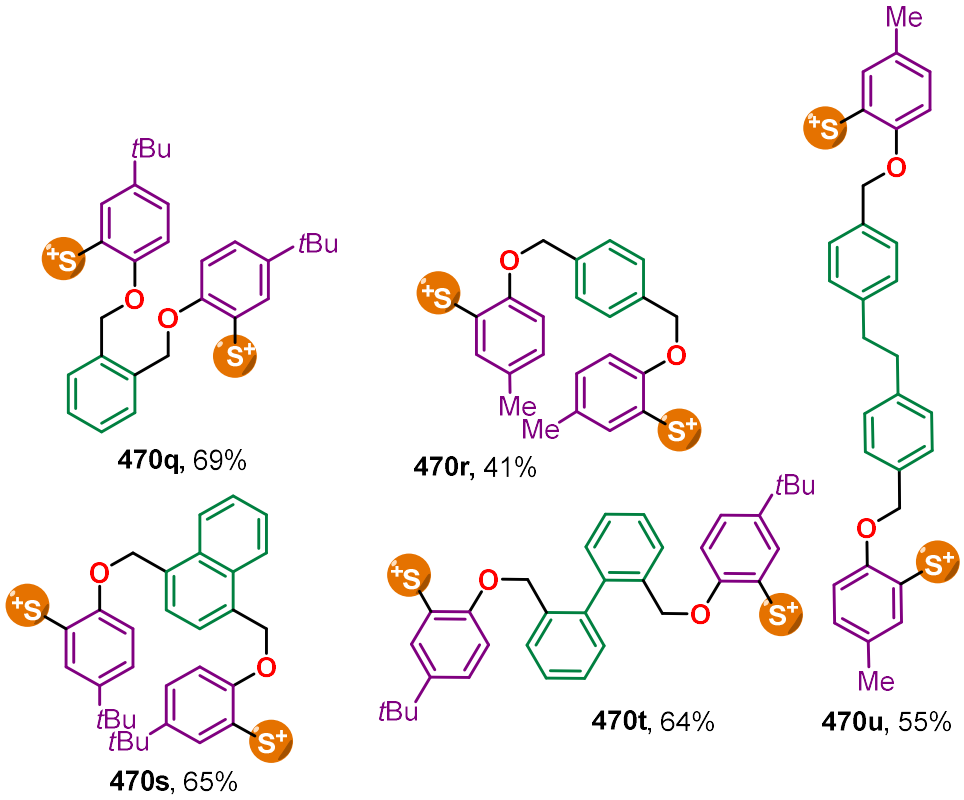

Scheme 132: Scope of sulfenylation suitable for double cyclization[242]

The benzyl ethers capable of double cyclization could be successfully sulfenylated at both oxygenated substituents using two equivalents of dibenzothiophene *S*-oxide and triflic anhydride. Also, in this case 2.1 equivalent of pyridine as a base are required. The success of the sulfenylations according to the structures shown in Scheme 131 and Scheme 132 could be ensured by ^{1}H-, ^{13}C-, ^{19}F- NMR analysis and [ESI(+)]HRMS.

Beside NMR and mass spectrometry analysis, also single-crystal X-ray diffraction was used to determine structural parameters. Single crystals suitable for X-ray diffraction could be obtained by vapor diffusion (acetonitrile/diethyl ether) and verify the proposed structures of **470a**, **470e**, **470f**, **470h**, **470j**, **470l**, **470n**, **470p** (Figure 62). While most of the structures are crystallographically unremarkable Z'=1 structures with occasional disorder, **470e** has an asymmetric unit with Z'=2. This can be explained by a different spatial orientation of the triflates interacting with the sulfur, which has a symmetry-breaking effect. The most important crystallographic parameters of **470a**, **470e**, **470f**, **470h**, **470j**, **470l**, **470n**, **470p** are summarized in Table 7.

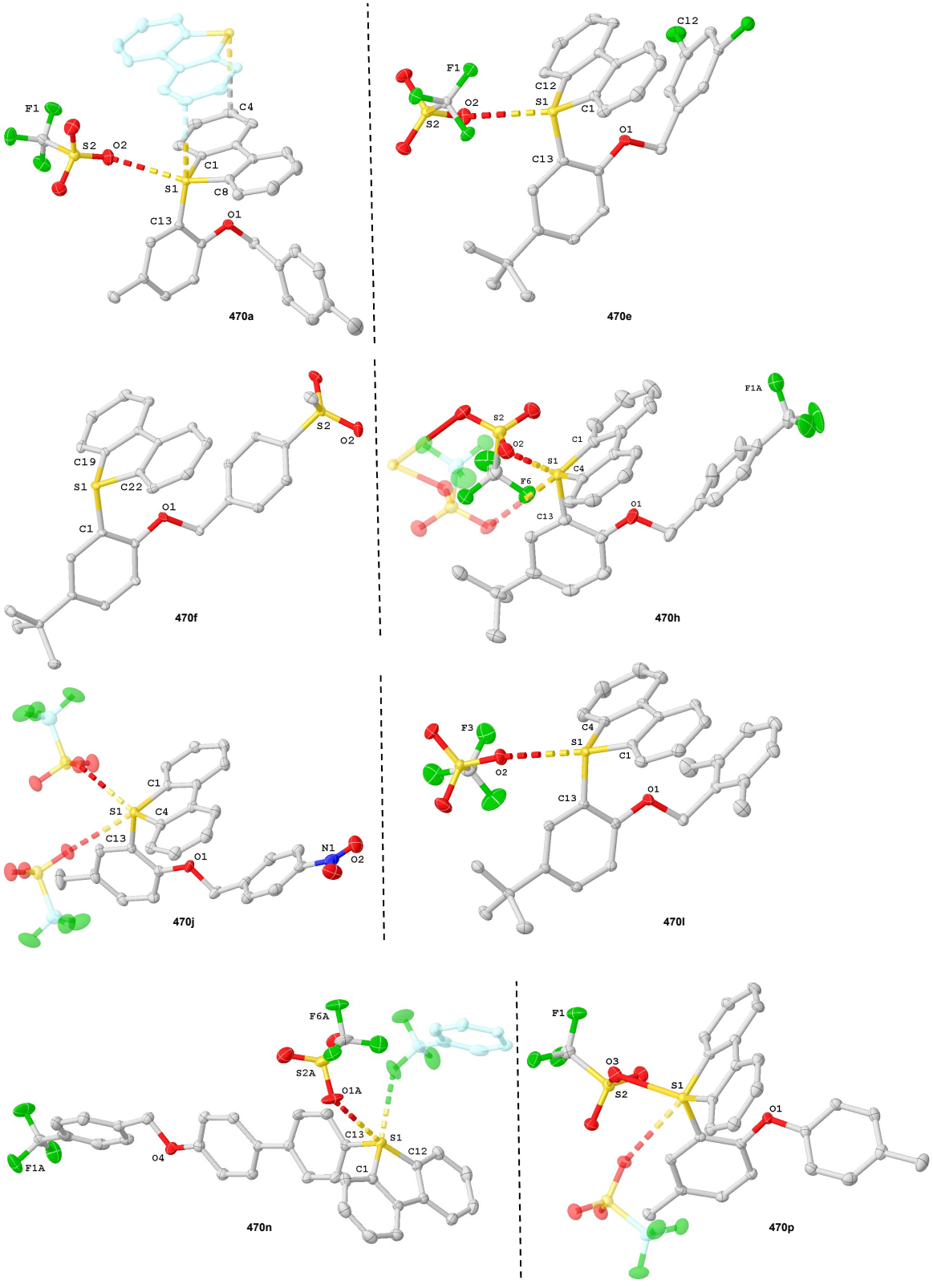

Figure 62: Molecular structures of ***470a***[29], ***470e***[30], ***470f***[31], ***470h***[32], ***470j***[33], ***470l***[34], ***470n***[35], ***470p***[36]. *Thermal ellipsoids at 50% probability level. Hydrogen atoms, non-coordinating counter anions and co-crystallized solvent molecules omitted for clarity; interactions exceeding the asymmetric unit generated by symmetry are drawn translucent. Selected bond length (Å) and angles (°) are summarized in Table 7. Asymmetric unit of* ***470e*** *contains two formula units of the corresponding compound, one unit has been omitted for clarity.*

[29] **Crystal Data** for **470a** ($C_{29}H_{25}Cl_2F_3O_4S_2$; *M* =629.51 g/mol): triclinic, space group P-1 (no. 2), *a* = 10.3968(8) Å, *b* = 10.5814(7) Å, *c* = 13.6257(9) Å, *α* = 91.537(3)°, *β* = 102.506(3)°, *γ* = 102.648(2)°, *V* = 1423.58(17) Å^3, *Z* = 2, *T* = 99.97 K, μ(MoKα) = 0.429 mm^{-1}, *Dcalc* = 1.469 g/cm^3, 61800 reflections measured (4.546° ≤ 2Θ ≤ 57.446°), 7347 unique (R_{int} = 0.0222, R_{sigma} = 0.0131) which were used in all calculations. The final R_1 was 0.0370 (I > 2σ(I)) and wR_2 was 0.0980 (all data).

[30] **Crystal Data** for **470e** ($C_{30}H_{25}Cl_2F_3O_4S_2$; *M* =641.52 g/mol): triclinic, space group P-1 (no. 2), *a* = 12.288(2) Å, *b* = 13.457(2) Å, *c* = 17.735(2) Å, *α* = 87.935(5)°, *β* = 88.466(5)°, *γ* = 81.486(5)°, *V* = 2898.0(8) Å^3, *Z* = 4, *T* = 100.0 K, μ(MoKα) = 0.423 mm^{-1}, *Dcalc* = 1.470 g/cm^3, 76807 reflections measured (4.106° ≤ 2Θ ≤ 59.292°), 16230 unique (R_{int} = 0.0375, R_{sigma} = 0.0310) which were used in all calculations. The final R_1 was 0.0336 (I > 2σ(I)) and wR_2 was 0.0811 (all data).

[31] **Crystal Data** for **470f** ($C_{31}H_{29}F_3O_6S_3$; *M* =650.72 g/mol): triclinic, space group P-1 (no. 2), *a* = 10.4015(5) Å, *b* = 11.4555(5) Å, *c* = 14.4789(8) Å, *α* = 99.272(2)°, *β* = 106.979(2)°, *γ* = 111.023(2)°, *V* = 1470.30(13) Å^3, *Z* = 2, *T* = 100.0 K, μ(MoKα) = 0.316 mm^{-1}, *Dcalc* = 1.470 g/cm^3, 80472 reflections measured (3.99° ≤ 2Θ ≤ 68.674°), 10974 unique (R_{int} = 0.0210, R_{sigma} = 0.0154) which were used in all calculations. The final R_1 was 0.0289 (I > 2σ(I)) and wR_2 was 0.0793 (all data).

[32] **Crystal Data** for **470h** ($C_{31}H_{26}F_6O_4S_2$; *M* =640.64 g/mol): monoclinic, space group $P2_1/c$ (no. 14), *a* = 12.7942(18) Å, *b* = 18.753(3) Å, *c* = 12.5933(19) Å, *β* = 106.529(4)°, *V* = 2896.6(7) Å^3, *Z* = 4, *T* = 100.0 K, μ(MoKα) = 0.259 mm^{-1}, *Dcalc* = 1.469 g/cm^3, 54576 reflections measured (4.344° ≤ 2Θ ≤ 56.032°), 6957 unique (R_{int} = 0.0494, R_{sigma} = 0.0308) which were used in all calculations. The final R_1 was 0.0537 (I > 2σ(I)) and wR_2 was 0.1178 (all data).

[33] **Crystal Data** for **470j** ($C_{27.5}H_{21}ClF_3NO_6S_2$; *M* =618.02 g/mol): triclinic, space group P-1 (no. 2), *a* = 8.5295(9) Å, *b* = 11.5788(15) Å, *c* = 14.6028(18) Å, *α* = 72.127(4)°, *β* = 81.483(3)°, *γ* = 76.786(4)°, *V* = 1331.5(3) Å^3, *Z* = 2, *T* = 99.98 K, μ(MoKα) = 0.367 mm^{-1}, *Dcalc* = 1.541 g/cm^3, 96536 reflections measured (4.924° ≤ 2Θ ≤ 59.244°), 7486 unique (R_{int} = 0.0228, R_{sigma} = 0.0123) which were used in all calculations. The final R_1 was 0.0443 (I > 2σ(I)) and wR_2 was 0.1317 (all data).

[34] **Crystal Data** for **470l** ($C_{32}H_{31}F_3O_4S_2$; *M* =600.69 g/mol): monoclinic, space group $P2_1/c$ (no. 14), *a* = 12.2978(7) Å, *b* = 17.7425(9) Å, *c* = 13.6378(6) Å, *β* = 95.691(2)°, *V* = 2961.0(3) Å^3, *Z* = 4, *T* = 100.0 K, μ(MoKα) = 0.234 mm^{-1}, *Dcalc* = 1.347 g/cm^3, 73673 reflections measured (4.592° ≤ 2Θ ≤ 61.034°), 9040 unique (R_{int} = 0.0269, R_{sigma} = 0.0162) which were used in all calculations. The final R_1 was 0.0336 (I > 2σ(I)) and wR_2 was 0.0914 (all data).

[35] **Crystal Data** for **470n** ($C_{33}H_{22}F_6O_4S_2$; *M* =660.62 g/mol): monoclinic, space group Cc (no. 9), *a* = 10.9573(10) Å, *b* = 18.3080(16) Å, *c* = 14.6355(12) Å, *β* = 101.241(3)°, *V* = 2879.6(4) Å^3, *Z* = 4, *T* = 100.0 K, μ(MoKα) = 0.263 mm^{-1}, *Dcalc* = 1.524 g/cm^3, 28697 reflections measured (4.394° ≤ 2Θ ≤ 59.284°), 8020 unique (R_{int} = 0.0204, R_{sigma} = 0.0215) which were used in all calculations. The final R_1 was 0.0311 (I > 2σ(I)) and wR_2 was 0.0803 (all data).

[36] **Crystal Data** for **470p** ($C_{27}H_{21}F_3O_4S_2$; *M* =530.56 g/mol): triclinic, space group P-1 (no. 2), *a* = 8.4140(7) Å, *b* = 11.8431(13) Å, *c* = 13.3560(12) Å, *α* = 69.169(4)°, *β* = 80.816(4)°, *γ* = 73.350(4)°, *V* = 1189.3(2) Å^3, *Z* = 2, *T* = 99.99 K, μ(MoKα) = 0.281 mm^{-1}, *Dcalc* = 1.482 g/cm^3, 26453 reflections measured (5.522° ≤ 2Θ ≤ 57.55°), 6150 unique (R_{int} = 0.0234, R_{sigma} = 0.0205) which were used in all calculations. The final R_1 was 0.0304 (I > 2σ(I)) and wR_2 was 0.0835 (all data).

*Table 7: X-ray structural parameters of **470a, 470e, 470f, 470h, 470j, 470l, 470n, 470p***

	470a	**470e**	**470f**	**470h**	**470j**	**470l**	**470n**	**470p**
DBT ∡(C–S–C) [°]	91.4(1)	91.6(1) /91.5(1)	91.4(1)	91.1(1)	91.6(1)	91.5(1)	91.7(1)	91.5(1)
exo ∡(C–S–C) (1) [°]	105.9(1)	107.6(1) /106.6(1)	108.0(1)	106.4(1)	108.5(1)	109.2(1)	105.3(1)	107.3(1)
exo ∡(C–S–C) (2) [°]	109.1(1)	107.8(1) /108.2(1)	106.6(1)	107.4(1)	104.6(1)	106.7(1)	104.3(1)	104.8(1)
Pyramidalization Σ∡(C–P–C) [°]	306.4	306.9 /306.3	306.0	304.9	304.7	307.4	301.3	303.6
S–C distance (1) [Å]	1.783(1)	1.779(1) /1.780(1)	1.781(1)	1.785(2)	1.781(1)	1.780(1)	1.776(2)	1.781(1)
S–C distance (2) [Å]	1.778(1)	1.779(1) /1.784(1)	1.780(1)	1.787(2)	1.777(1)	1.783(1)	1.780(2)	1.782(1)
exo S–C distance [Å]	1.768(1)	1.772(1) /1.771(1)	1.771(1)	1.773(2)	1.772(1)	1.768(1)	1.779(2)	1.769(1)
Mean S–C distance [Å]	1.777(6)	1.777(4) /1.778(6)	1.777(5)	1.782(6)	1.777(4)	1.777(7)	1.778(2)	1.777(6)
S–OTf short contact (1) [Å]	3.220(1)	3.146(1) /3.190(1)	-	3.203(2)	3.154(2)	3.152(1)	3.235(5) [3.214(13)]	3.145(1)
S–X short contact (2) [Å]	C: 3.386(1)	-	-	3.293(2)	3.221(1)	-	F: 3.031(4)	3.179(1)
∡C–S–OTf angle (1) [°]	161.9(4)	161.2(1) /172.4(1)	-	167.8(1)	153.3(1)	175.5(1)	162.5(1) [156.6(3)]	160.5(4)
∡C–S–X angle (2) [°]	165.3(6)	-	-	172.2(1)	172.5(1)	-	164.5(1)	168.0(1)

Due to the free electron pair and in accordance with the VSEPR rules the threefold substituted central sulfur atom in the sulfonium salts adopts pyramidal geometry.[219] This represents their isoelectronic and isostructural nature to trivalent pnictogen atoms. The crystallographic data reveals also for the sulfonium salts **470a**, **470e**, **470f**, **470h**, **470j**, **470l**, **470n** and **470p** distorted pyramidal geometries with a pyramidalization slightly exceeding 300°. Being all *S*-(Aryl) sulfonium salts, also their S–C distances are nearly identical. Similar to trivalent pnictogen atoms, also for sulfonium salts with three covalent bonds three σ-holes can be expected, which should be located opposite to the three S–C bonds and be able to undergo noncovalent interactions to negative sites (*e.g.* counter ions).[257] Due to the positive charge of the sulfur these chalcogen bonds are expected to be charge assisted and formed between the sulfur and the triflates. In the crystal structures of our sulfonium salts up to two chalcogen bonds per sulfonium can be identified. While structure **470f** exhibits no short contacts to the sulfonium center, **470e** and **470l** exhibit one (S···:⁻OTf) and **470a**, **470h**, **470j**, **470n** and **470p** two chalcogen contacts shorter than the corresponding sum of van-der-Waals-radii. In the case of **470h**, **470j** and **470p** both chalcogen contacts are based on noncovalent interactions between the sulfur and triflates. **470a** and **470n** show one sulfur-triflate contact but also a second one between S–C and S–F, respectively. In the crystal structure of **470a** the contact between S and C can be explained by the π-stacking of two dibenzothiophenium moieties of two different molecules, while in case of **470n** the negative site of one triflate is exchanged by a F atom of a CF_3 group of a second molecule.

The C─S···:$^{-}$OTf angles range from 150°-180° making the chalcogen bond nearly linear. The distortion from perfect linearity can be explained by the hydrogen bonding of the triflates towards aryl protons nearby. The low sulfur triflate distances underline the electrophilicity of the sulfur in this compound class.

With the sulfonium salts at hand our next step was to unleash their potential to generate aryl radicals. Therefore we needed to find the approximated one-electron reduction potential for populating the exocyclic σ*(S─Ar) orbital and to homolytically cleave the already weakened S─Ar bond.[219,258] The most suitable tool for this task was cyclic voltammetry (0.1 M $[NBu_4][PF_6]$ in MeCN, 100 mV/s).

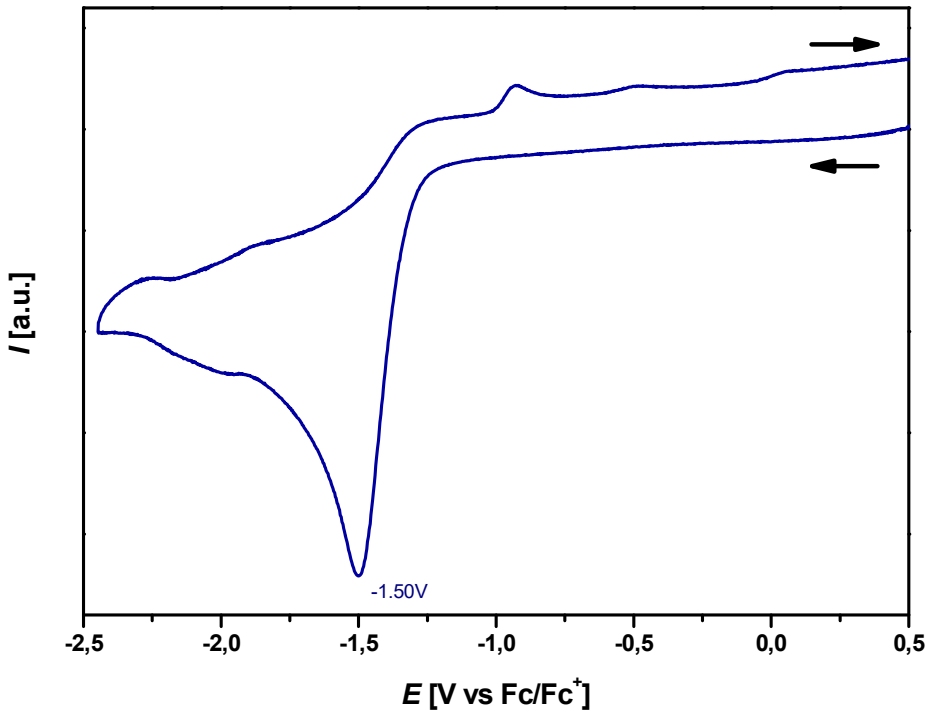

*Figure 63: Cyclic voltammogram of compound **470a**[242]*

The corresponding cyclic voltammogram of compound **470a** revealed a reduction peak at -1.50 V referenced to the Fc/Fc^+ couple (-1.12 V vs. SCE[159]). The reduction causing the S─Ar bond cleavage is as expected irreversible. This fact makes it difficult to determine the exact potential, but at least allows a rough classification.

5.4 Photocatalytic S—Ar bond cleavage and first mechanistic insights

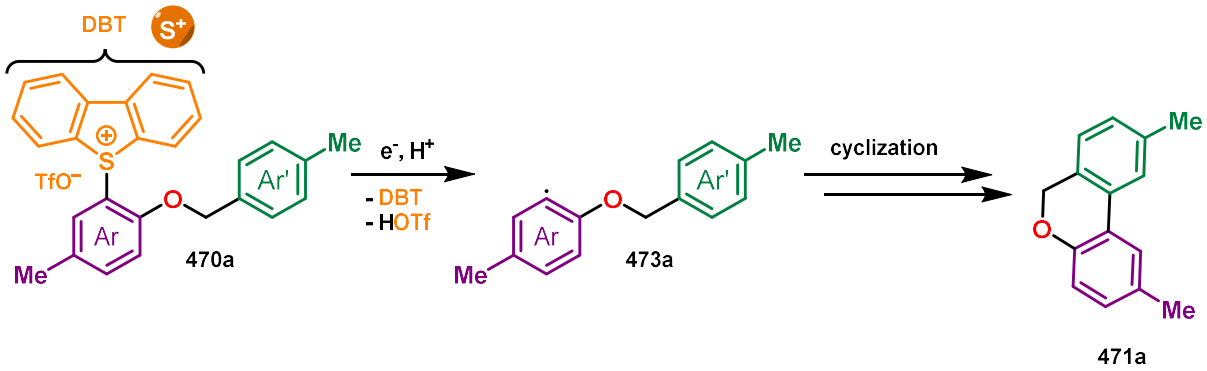

Scheme 133: Aryl radical generation via photoreduction[242]

To enable a photocatalytic cyclization one has to first find a photocatalyst capable of reducing the sulfonium salt **470a** (approx. -1.12 V vs. SCE) in order to generate an aryl radical **473a** (Scheme 133). According to the literature[204] the photocatalyst *fac*-[Ir(ppy)$_3$] (1 mol%, $E_{1/2}^{IV/III*}$ = −1.73 vs. SCE[204]) should be suitable for this task. Together with the radical formation/cyclization, joint products like dibenzothiophene and triflic acid are formed. While dibenzothiophene does not pose a problem during the reaction and can be removed afterwards *via* column chromatography, the triflic acid needs to be removed while the reaction proceeds, otherwise a degradation of the ether backbone would hamper progress. To scavenge the triflic acid a base was added (Cs_2CO_3) to the protocol and the whole reaction performed in CH_3CN using blue LEDs as irradiation source (28 W, 4 h).

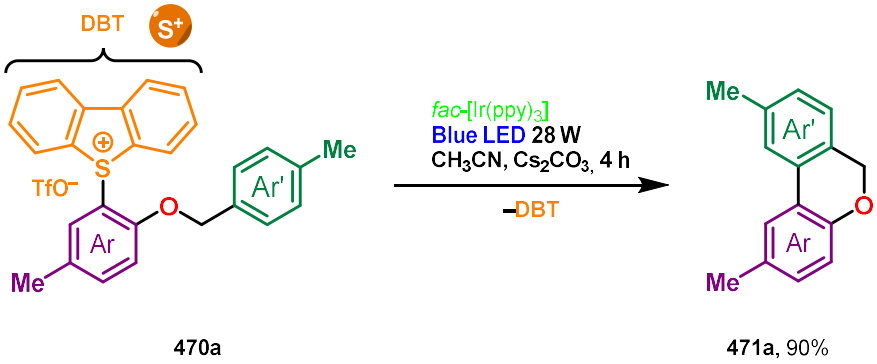

*Scheme 134: Protocol for photocatalyzed cyclization of sulfonium salt **470a**[242]*

To our delight, this protocol was already quite optimal, giving product **471a** in 90% yield (34.0 mg, 165 µmol). Neither changing the solvent (DMSO, DMF or DCM) nor the base (K_3PO_4) could cause an improvement. Under the same conditions the photocatalyst $[Ru(bpy)_3]^{2+}$ (5 mol%, $E_{1/2}^{III/II*}$ = −0.81 vs. SCE[204]) was tried but as expected the reduction potential of the excited photocatalyst was not strong enough to initiate radical formation and the starting material was reisolated. When adding additional DIPEA the reduction potential of $[Ru(bpy)_3]^{2+}$ can be increased by entering a reductive quenching cycle. In this cycle the excited photocatalyst $[Ru(bpy)_3]^{2+*}$ gets first reduced by an electron donor (*e.g.* DIPEA) and can then with a more negative potential of $E_{1/2}^{II/I}$ = −1.33 vs. SCE[204] be enabled to reduce the sulfonium salt **470a**. When catalytic amounts of DIPEA are used a redox-neutral catalytic cycle consisting of first reduction of **470a** and then reoxidation of the cyclized radical is generated leading to **471a** (like in the case of *fac*-[Ir(ppy)$_3$]). However, if an excess of DIPEA is used, these reductive conditions may result in the formation of reaction intermediates not being oxidized and thus can be identified. Following this idea, we cyclized **470a** in the presence of five equivalents of DIPEA (making the use of additional Cs_2CO_3 obsolete) and 5 mol% $[Ru(bpy)_3]^{2+}$.

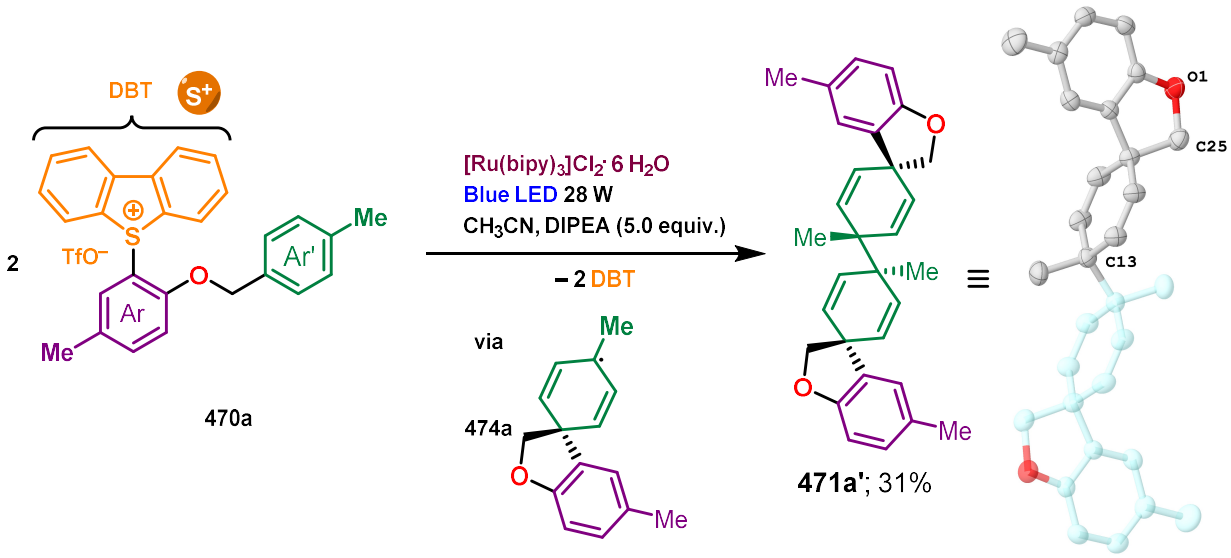

*Scheme 135: Photocatalyzed cyclization of sulfonium salt **470a** under reductive conditions.[242] Molecular structures of **471a'**[37]. Thermal ellipsoids at 50% probability level. Hydrogen atoms omitted for clarity; second half of the centrosymmetric **471a'** generated by symmetry drawn translucent (Z'=0.5, symmetry code: '=1-x,2-y,1-z). Selected bond length (Å) for **471a'**: C13—C13' 1.593(3), O1—C25 1.453(2).*

During the 30 min of irradiation crystals suitable for X-ray diffraction precipitated. The acetonitrile insoluble product **471a'** could therefore be easily separated and characterized.

The crystal structure reveals a centrosymmetric dimeric structure, with an asymmetric unit containing half a molecule **471a'** (Z'=0.5), indicating that two *bis*-allylic spirocyclohexadienyl radicals **474a** reacted. The *bis*-allylic radicals **474a** are formed after the cyclization of the generated aryl-radical **473a**. The cyclization proceeds *via* a *5-exo-trig* pathway and not a *6-endo/exo-trig* pathway as one might suspect at first. The *bis*-allylic radical then accumulates, because the reductant DIPEA prevents reoxidation, and dimerizes. Interestingly, the dimerization is diastereoselective and cannot be stopped by additive HAT reagents (DIPEA, Hantzsch ester, BHT, $^{n}Bu_3SnH$, Cyclohexa-1,4-diene and 9,10-dihydroanthracene).

[37] **Crystal Data** for **471a'** ($C_{15}H_{15}O$; *M* =211.27 g/mol): orthorhombic, space group Pbca (no. 61), *a* = 13.2616(3) Å, *b* = 8.2331(2) Å, *c* = 21.3930(5) Å, *V* = 2335.78(9) Å^3, *Z* = 8, *T* = 150 K, μ(MoKα) = 0.073 mm^{-1}, *Dcalc* = 1.202 g/cm^3, 39949 reflections measured (4.892° ≤ 2Θ ≤ 55.784°), 2783 unique (R_{int} = 0.0253, R_{sigma} = 0.0103) which were used in all calculations. The final R_1 was 0.0511 (I > 2σ(I)) and wR_2 was 0.1512 (all data).

The knowledge gained from photocatalysis with reductive conditions {$[Ru(bpy)_3]^{2+}$ / 5 equiv. DIPEA} can now be applied to the redox-neutral process {*fac*-$[Ir(ppy)_3]$ / Cs_2CO_3}, allowing us to propose the following mechanism (Scheme 136):

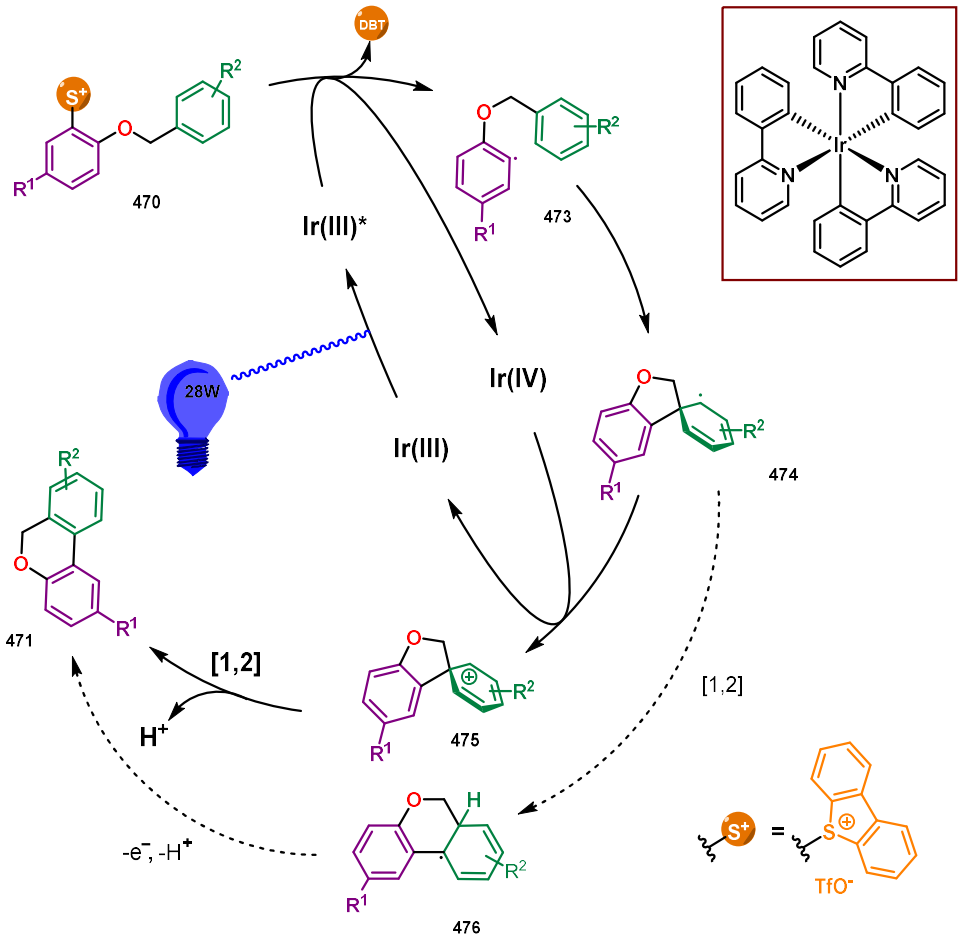

Scheme 136: Proposed mechanism for the photocatalyzed cyclization of sulfonium salts by fac-$[Ir(ppy)_3]$[242]

At first the photocatalyst {*fac*-$[Ir(ppy)_3]$} absorbs a photon. The photoexcited species Ir(III)* then reduces the sulfonium salt **470,** while itself being oxidized [Ir(III)*→Ir(IV)]. After homolytic cleavage of the S–Ar bond the aryl radical **473** cyclized *via* kinetically favored *5-exo-trig ipso* attack to the *bis*-allylic radical **474**. The *bis*-allylic radical is now able to reduce the Ir(IV) to Ir(III) forming the diallylic cation **475** making the process redox-neutral. (In the case of the reductive conditions {$[Ru(bpy)_3]^{2+}$ / 5 equiv. DIPEA} the DIPEA assumes the role of the reducing agent reducing of Ir(IV) to Ir(III).) The positive charge in **475** now triggers a Wagner–Meerwein rearrangement {[1,2]-shift}, which leads to 6*H*-benzo[*c*]chromenes after the loss of a proton.

The Wagner–Meerwein rearrangement plays a crucial role in this catalytic cycle, as it determines the regioselectivity of the reaction. Starting from cation **475** two different products are conceivable (**471a** and **471a''**, Scheme 137) *via* migration of different substituents at the spiro center. Shifting of the sp^2-carbon of the aryl substituent (**a**) leads to product **471a**, while shifting the sp^3-carbon of the alkyl substituent (**b**) results in **471a''**. Interestingly, the reaction {*fac*-$[Ir(ppy)_3]$ / Cs_2CO_3} is highly regioselective towards product **471a** and no **471a''** could be detected. This can be explained by the migratory abilities of the two substituents **a** and **b**. The aryl substituent (**a**) tends to shift as an anion in a Wagner–Meerwein rearrangement, while this anionic shift is unfavorable in the case of the alkyl carbon (**b**). On the other hand alkyl carbon (**b**) reveals a higher migratory ability as a radical. In the doubly-allylic cation **475** pathway **A** is much more likely than **B** and no **471a''** is formed.

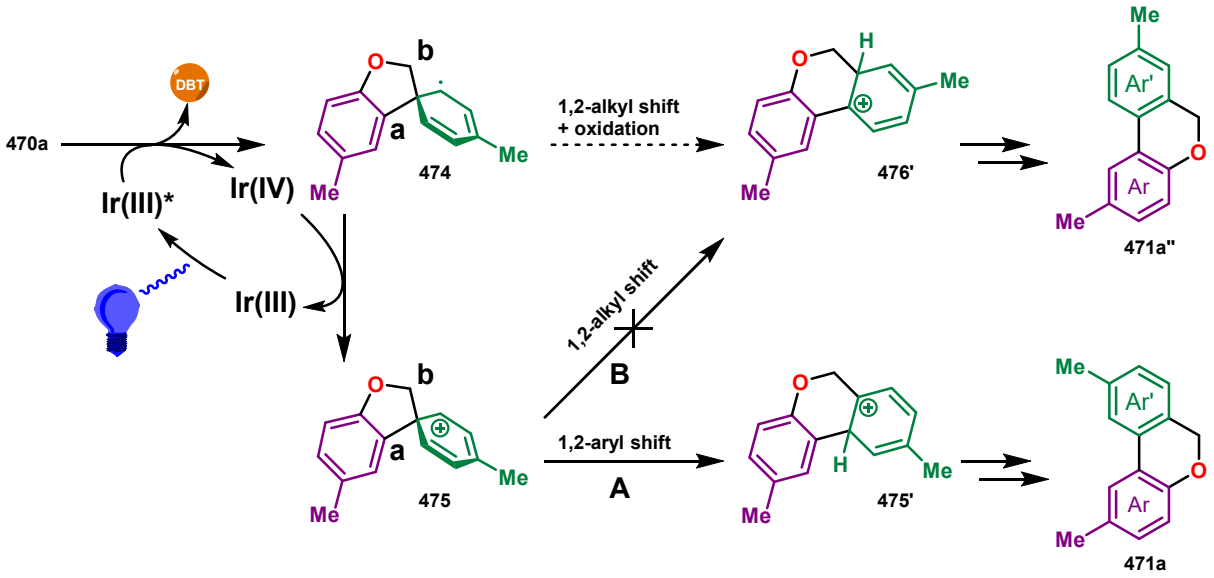

*Scheme 137: Regioselectivity in the photocatalyzed cyclization of sulfonium salt **470a**[242]*

However, in a related radical cyclization Charette and coworkers proposed a reaction mechanism based on the a concerted radical ring expansion or a 3-*exo* closure in combination with neophyl rearrangement of a *bis*-allylic spirocyclohexadienyl radical similar to **474** leading to compounds similar to **471a** and **471a''**, respectively.[252] This radical mechanism seems to be less likely in our case based on the facts that even in a reductive procedure the *bis*-allylic spirocyclohexadienyl radical is stable enough to form dimers and that our major product in the redox-neutral cyclization **471a** is the contrary isomer to theirs[252] (similar to **471a''**). However, a radical mechanism involving an intermediate such as **476** (see Scheme 136) cannot be ruled out and could also depend strongly on the substituents R^2, which, in the case of very electron-withdrawing groups, could destabilize the radical **474** in a manner that a radical pathway becomes more likely.

5.5 Further evidence supporting the proposed mechanism

5.5.1 Stern–Volmer-Plot

To further investigate the mechanism and to provide more evidence that the mechanism consist of an oxidative quenching cycle with intermediates similar to **474** and **475** we designed a couple of experiments.

First we performed a Stern–Volmer analysis to prove that substrate **470a** engages in single-electron transfer with the photocatalyst (oxidative quenching). Therefore we mixed a *fac*-[Ir(ppy)$_3$] (CH_3CN) stock solution with a dilution series of quencher **470a** in CH_3CN, irradiated the samples at 372.8 nm, and plotted the relative intensity of the observed emission maximum ($\mathbf{I_0/I}$) against the concentration of **470a**.

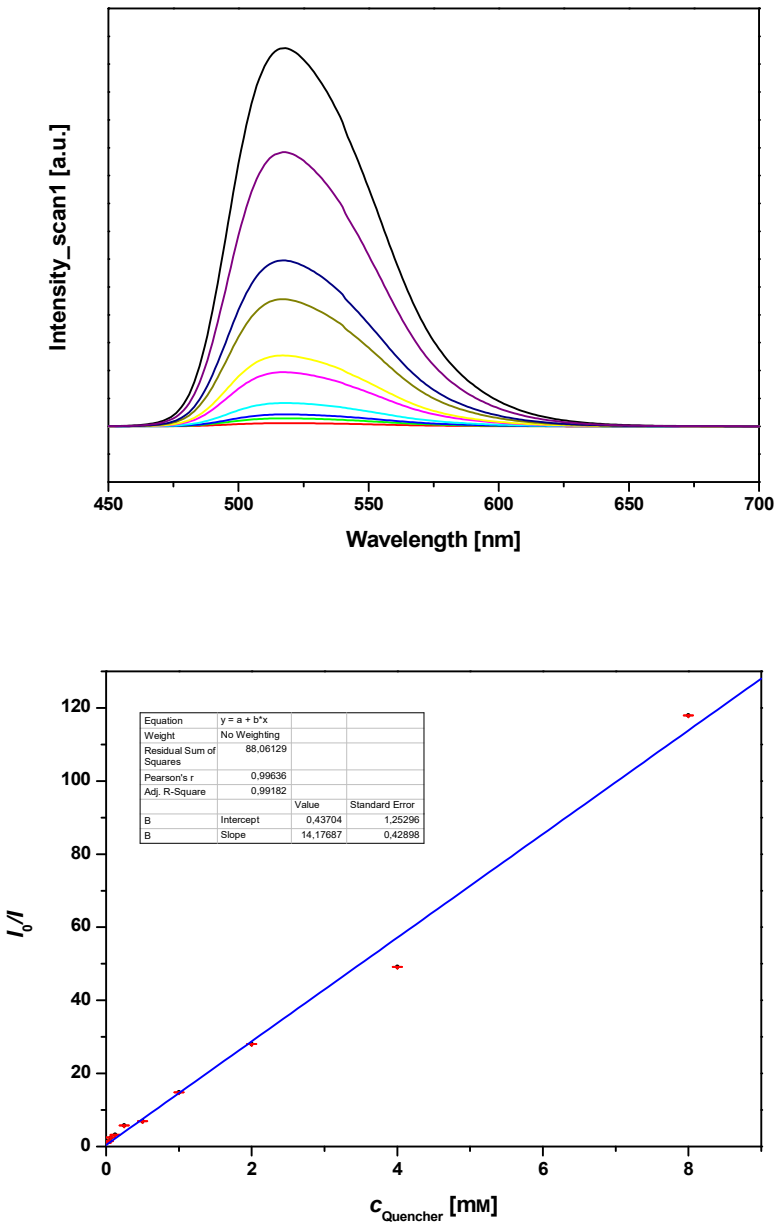

Figure 64: Stern–Volmer plot[242]

If no quencher (**470a**) is present, the intensity corresponds to $\mathbf{I_0}$, otherwise the quencher decreases the intensity (**I**) by intermolecular deactivation *via* electron-transfer pathways. This decrease in intensity can be seen in Figure 64 (top). Plotting $\mathbf{I_0/I}$ against the concentration of **470a** ($\mathbf{c_{Quencher}}$) now results in a linear correlation, which can be best described by the Stern–Volmer equation (Figure 64, bottom).

$$\frac{I_0}{I} = 1 + k_q \tau_0 [Q] \qquad (6)$$

Equation 6

In this equation $\mathbf{k_q}$ represents the quenching rate constant by the quencher **470a**, $\boldsymbol{\tau_0}$ the excited-state lifetime in the absence of quencher and **[Q]** is the concentration of the quencher **470a**. The higher the concentration of quencher **470a** the less intense is the observed phosphorescence and the higher $\mathbf{I_0/I}$ gets. This correlation provides strong evidence that the reaction proceeds *via* oxidative quenching of the excited *fac*-[Ir(ppy)$_3$] photocatalyst. Furthermore, the slope of the regression line represents the product of the excited-state lifetime $\boldsymbol{\tau_0}$ and quenching rate constant $\mathbf{k_q}$ (Stern–Volmer constant: $\boldsymbol{\tau_0 k_q}$ = 14.177 (±0.43) $m^3 \cdot mol^{-1}$ = 14177 (±430) M^{-1}). With this information $\mathbf{k_q}$ should be accessible with a literature reported excited-state lifetime $\boldsymbol{\tau_0}$ of the photocatalyst *fac*-[Ir(ppy)$_3$]. Note that $\boldsymbol{\tau_0}$ is the lifetime of the excited state in the absence of the quencher **470a**, but not the lifetime at infinite dilution. Therefore, $\boldsymbol{\tau_0}$ is not only strongly dependent on the solvent, but also on the concentration of the photocatalyst, due to self-quenching. Literature matching our conditions is hard to find, especially with the relatively high photocatalyst concentration of our system (19.85 × 10^{-5} M). The lifetimes reported in literature[259] were measured in acetonitrile, but for concentrations ranging from 0 M to 6 × 10^{-5} M, so extrapolation to our *fac*-[Ir(ppy)$_3$] concentration leads only to a very imprecise approximation of $\mathbf{k_q}$ (after recalculating k_q[259] from the reported data: $\mathbf{k_q} \approx 3.3 \times 10^{10}$ $M^{-1}s^{-1}$).

5.5.2 Isolation of a persistent radical intermediate

Since we have strong evidence for an oxidative quenching cycle, we wanted to follow up the next steps of the catalytic cycle and confirm the existence of intermediate **474**. Unfortunately, intermediate **474** was not detectable in the reaction mixture and the sample remained EPR silent under blue light irradiation. Therefore, we wanted to develop a sulfonium salt that can form a persistent radical after its reduction and cyclization. One of the most prominent persistent radicals is (2,2,6,6-Tetramethylpiperidin-1-yl)oxyl (TEMPO), which owes its stability, among other things, to the delocalization in the two-center three-electron N–O bond.

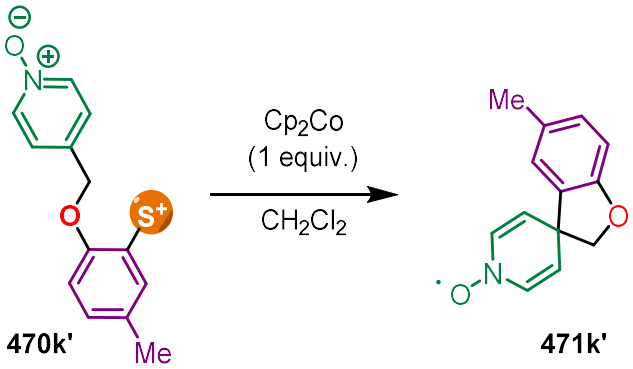

*Scheme 138: Chemical reduction of **470k'** to generate a persistent radical **471k'**[242]*

Following the idea, we installed the N–O group in compound **470k'** and added equimolar amounts of the one-electron reducing agent cobaltocene, simulating the photoreduction process (Scheme 138).

After filtration the DCM solution revealed a well resolved EPR spectrum, which perfectly fits the simulated one (Figure 65).

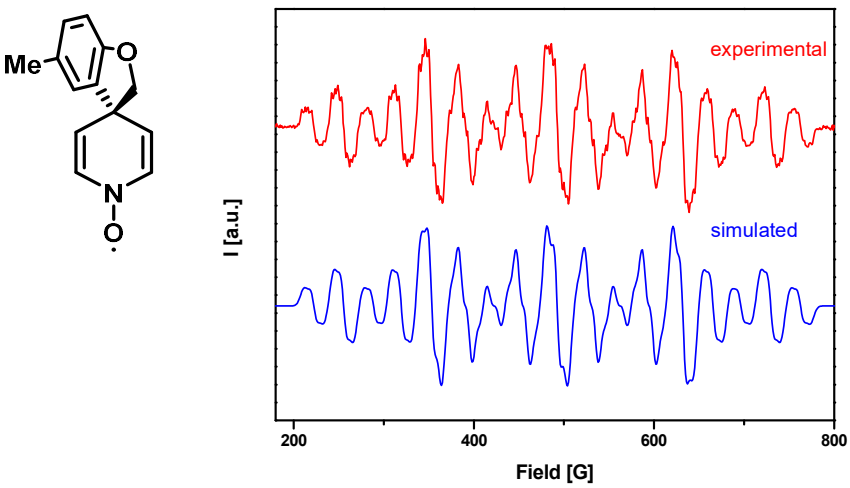

*Figure 65: EPR spectrum of **471k'** (simulated and experimental)*[242]

The EPR spectrum exhibits a multiplet at a g-factor of g = 2.0054 (*cf.* literature[260]) and hyperfine coupling to the N atom a(N) = 8.39 G and two pairs of enantiotopic protons [a(H) = 5.83 (2H), 1.99 (2H) G]. This resolved hyperfine coupling clearly indicates a C_s symmetric molecule with a radical also delocalized over the adjacent π-bonds. This finding can be seen as a strong evidence for a cyclization *via* kinetically favored *5-exo-trig ipso* attack giving a similar product to intermediate **474**. However, this radical **471k'** suffers from slow decay. In addition, the reversible nitroxyl/oxoammonium redox process of **470k'** expected in cyclic voltammetry, which is observed in the case of TEMPO[261], did not occur even after several scans. Therefore, from a synthetic point of view, sterically demanding moieties should be installed next to the nitrogen to increase the steric protection.

5.5.3 Trapping of a cationic intermediate

To further investigate the mechanism after the formation of intermediate **474**, we tried to stop the reaction after photooxidation.

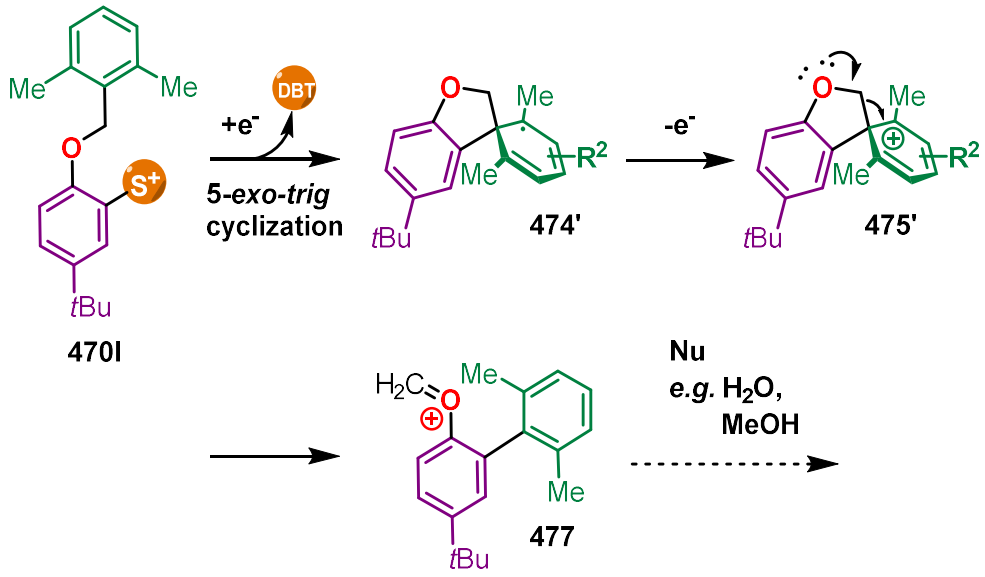

*Scheme 139: Trapping of cationic intermediate **475'***[242]

Therefore, we have incorporated two methyl groups that make a 1,2-shift impossible (Scheme 139). Starting from **470l** the carbenium ion **475'** formed is now unable to undergo Wagner–Meerwein rearrangement. However, intermediate **475'** should not be very stable and try to rearomatize, leading to the formation of the oxocarbenium ion **477**.

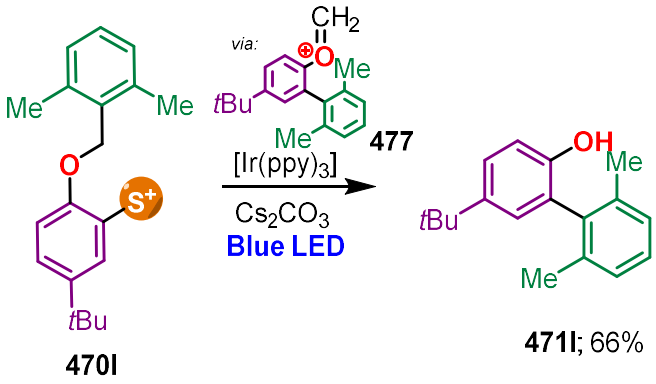

*Scheme 140: Photocatalyzed cyclization of sulfonium salt **470l**[242]*

When the compound **470l** is subjected to the protocol developed by us, compound **471l** can be isolated after column chromatography (Scheme 140). Biphenyl **471l** is not the oxonium species **477**, but can be considered as its hydrolysis product, since species **477** tends to hydrolyze on formaldehyde emission and is difficult to isolate. However, product **471l** could also be a result of a radical pathway similar to that described by Harrowven synthesizing biarylic phenols (Scheme 118).

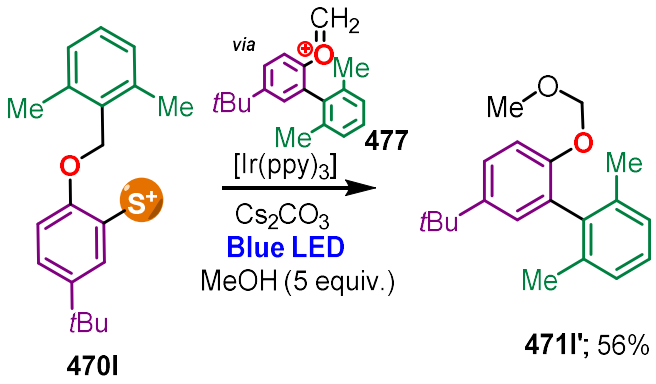

*Scheme 141: Photocatalyzed cyclization of sulfonium salt **470l** in presence of methanol[242]*

Therefore, stronger evidence for the existence of compound **477** is gained by adding methanol during the reaction (Scheme 141). Methanol traps species **477** and forms an methoxymethyl ether (acetal-) protecting group (MOM) leading to compound **471l'**. This compound can then be easily isolated *via* column chromatography and serves as evidence on species **477**, which itself is indicative of compound **475'** and its trend towards rearomatization.

5.5.4 Quantum yield measurement

As a final step, we wanted to ensure that the catalytic cycle was a closed catalytic loop in which no radical chain processes predominated.[262] Since radical chain processes can often occur on the order of seconds or subseconds, it is not sufficient to merely state that this reaction does not occur in the dark. Therefore, we have performed quantum yield measurements, which provide a useful instrument for detecting photochemical reactions involving radical chains. As an irradiation source we used a

spectrofluorometer and determined its photon flux by standard ferrioxalate actinometry at λ = 436 nm (flux = 5.40 × 10^{-9} Einstein/s).[233,263]

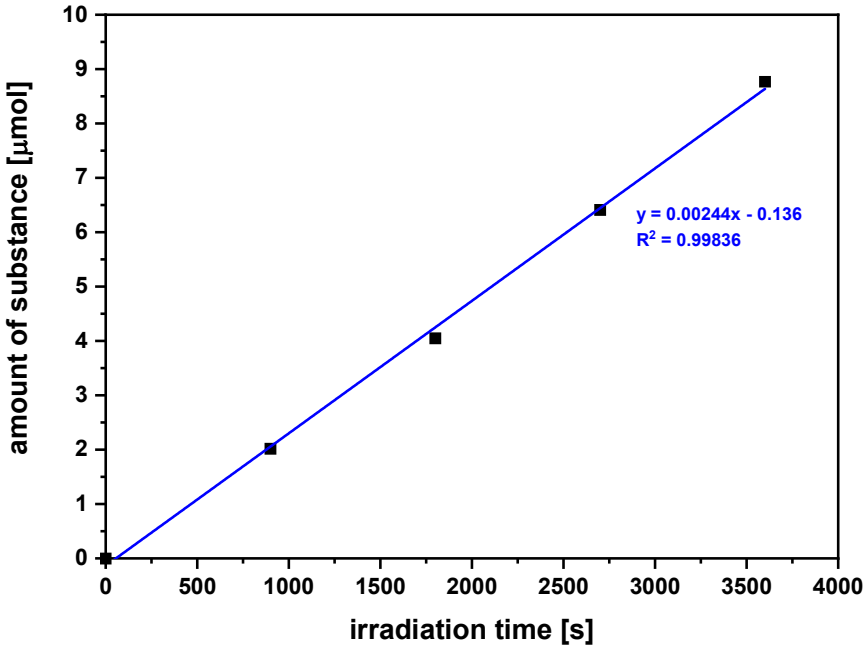

*Figure 66: Quantum yield measurement: amount of substance **471a** vs. irradiation time*[242]

Now we irradiated our reaction mixture containing **470a**, *fac*-[Ir(ppy)$_3$] and Cs_2CO_3 at the same concentrations in CH_3CN as in our protocol for different times. Using CH_2Br_2 (added afterwards) as an internal standard, we were then able to determine by ^{1}H-NMR the amount of **471a** [n(product)] formed during these times. The amount of **471a** was then plotted against the irradiation time (Figure 66) and clearly shows the expected linear relationship. Having n(product), reaction time (t) and the photon flux of the spectrofluorometer at hand we just needed to determine the fraction of light absorbed by photocatalyst *fac*-[Ir(ppy)$_3$] (0.9233) to calculate the quantum yield Φ *via* Equation 7 to be 47%.

$$\Phi = \frac{n(product)}{flux \cdot t \cdot f} \cdot 100 = 47\% \qquad (7)$$

Equation 7

With the quantum yield Φ being smaller than unity a strong product-forming chain can be excluded. Therefore, having a quantum yield Φ of 47% a radical chain process cannot predominate. The quantum yield is higher than that of comparable reactions (*cf.* intermolecular: 18%[233]), but this can be explained by the intramolecular nature of the reaction.

In summary, we could show that the presented mechanism is plausible and most likely also proceeds through the mentioned intermediates. The dimer **471a'** isolated under reductive conditions shows the stability and existence of intermediate **474**. Furthermore, the 5-*exo*-*trig* attack could be verified to a large extent by the synthesis of the permanent radical **471k'**. The initiation of the reaction by the photocatalyst was thereby confirmed by Stern–Volmer analysis. Intermediate **475** could not be detected directly but indirectly by hydrolysis products of the oxocarbenium ion **477** formed under disturbance. Furthermore, the reaction seems to proceed for the most part *via* a closed loop (quantum yield Φ<1).

5.6 Reaction scope and limitations - 6*H*-benzo[*c*]chromenes

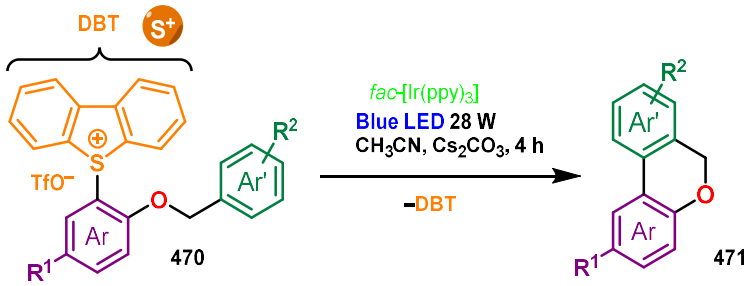

Scheme 142: General protocol for photocatalyzed cyclization of sulfonium salts[242]

Having studied the mechanism of the reaction in more detail, we wanted to focus to a greater extent on the synthetic utility of our reaction protocol (Scheme 142). To do this, we first scaled up our reaction tenfold to verify scalability [using 1 g (1.84 mmol) of **470a**]. After the reaction gave identical yields (90%), we also tried to reisolate the dibenzothiophene formed to show that it can be recycled. To our delight, the dibenzothiophene was recovered in 96%. These findings demonstrate not only scalability of the reaction, but also an improvement in atomic economy when dibenzothiophene formed is reisolated, reoxidized, and used to synthesize new dibenzothiophenium salts.

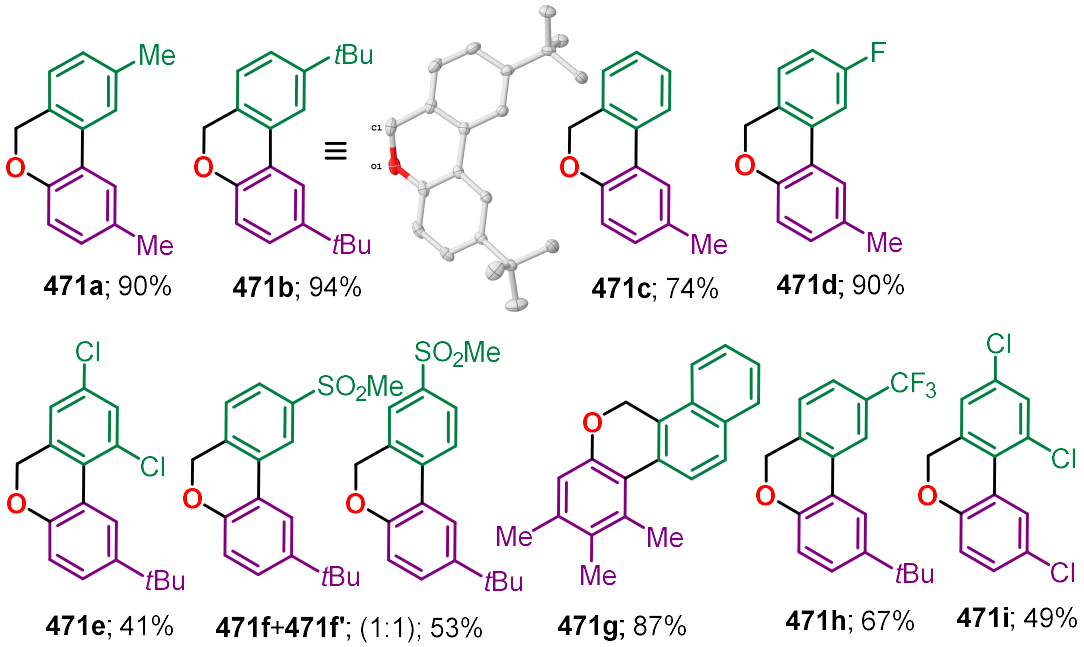

*Scheme 143: Scope of the photocatalyzed cyclization (single cyclization). Molecular structure of **471b**[38].[242] Thermal ellipsoids at 50% probability level. Hydrogen atoms and co-crystallized solvent molecules omitted for clarity. Asymmetric unit contains two formula units of the corresponding compound **471b** (Z'=2), one unit has been omitted for clarity.*

In addition to **470a**, **470b**-**470i** were also successfully cyclized in good to excellent yields giving 6*H*-benzo[*c*]chromenes **471a**-**471i**. Outstanding yields were obtained in particular for compound **471b** (94%). Here, the correct connectivity and selectivity could be determined not only by NMR analysis but also by growing single crystals in hot methanol for X-ray diffraction analysis (Scheme 143).

[38] **Crystal Data** for **471b** ($C_{21}H_{26}O$; M =294.42 g/mol): triclinic, space group P-1 (no. 2), a = 5.8629(10) Å, b = 16.941(3) Å, c = 17.277(3) Å, α = 92.461(5)°, β = 90.992(8)°, γ = 92.986(5)°, V = 1711.8(5) Å^3, Z = 4, T = 100.0 K, μ(MoKα) = 0.068 mm^{-1}, *Dcalc* = 1.142 g/cm^3, 117019 reflections measured (4.72° ≤ 2Θ ≤ 63.146°), 11374 unique (R_{int} = 0.0274, R_{sigma} = 0.0187) which were used in all calculations. The final R_1 was 0.0506 (I > 2σ(I)) and wR_2 was 0.1284 (all data).

The standard protocol also showed the desired regioselectivity for all the other sulfonium salts (**470a**-**470e**, **470g**-**470i**), except in the case of **470f**. The mixture of products **471f** and **471f'** obtained upon cyclization of **470f** can be explained by the instability of a radical intermediate similar to intermediate **474**. The electron-withdrawing sulfone substituent destabilizes the bis-allylic spirocyclohexadienyl radical, impeding reoxidation and opening a competitive radical migration that can lead to different product distributions.

The cyclization shows a high functional group tolerance, which enables the cyclization even in the presence of halogens (F, CF_3 and Cl) or sulfones. However, the protocol also shows its limitations, besides obviously non-cyclizable sulfonium salts like **470l**, **470m**, **470n** and **470o**, also sulfonium salts containing a nitro group (**470j**), are based on pyridine (**470k**, **470k'**) or requiring cyclization *via* a 5-*exo/endo-trig* attack (**470p**) could not be cyclized. The problems that arise with electron-deficient substrates (**470j**, **470k**, **470k'**) might suggest an intrinsic electrophilicity of the aryl radical (low-energy SOMO).[252,253] Therefore, reactions should proceed faster with high-energy HOMOs (SOMO/HOMO interaction). However, the HOMO in the cases of **470j**, **470k** and **470k'** is of low-energy and thus interferes with the reaction.

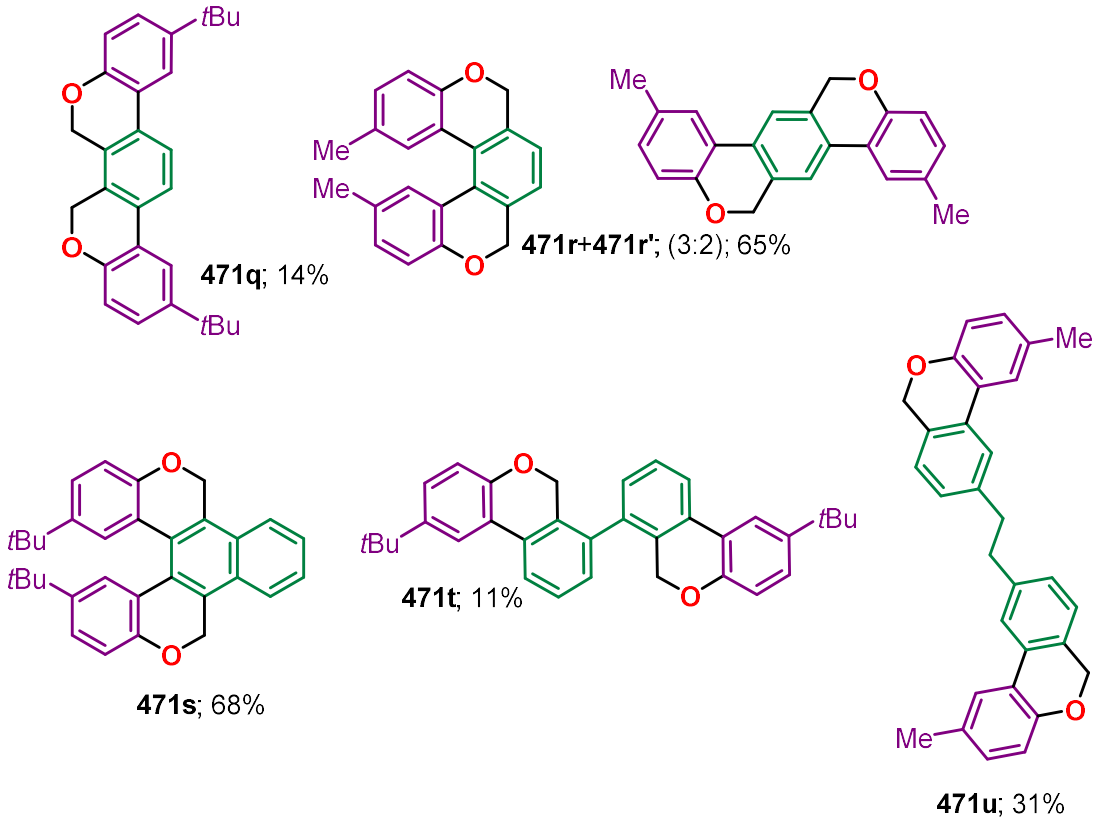

Scheme 144: Scope of the photocatalyzed cyclization (double cyclization)[242]

Apart from the single cyclization, the double cyclization was also successful. However, it was necessary to change the solvent from acetonitrile to DMF to eliminate solubility problems. The change of solvent was accompanied by a strong decrease in reaction time (2 h) with the same amount of catalyst. However, the yields fell short of expectations in the cases **471q**, **471t** and **471u**. A by-product (**471q'**), which was also isolated during the synthesis of **471q**, allows some conclusions to be drawn (Scheme 145).

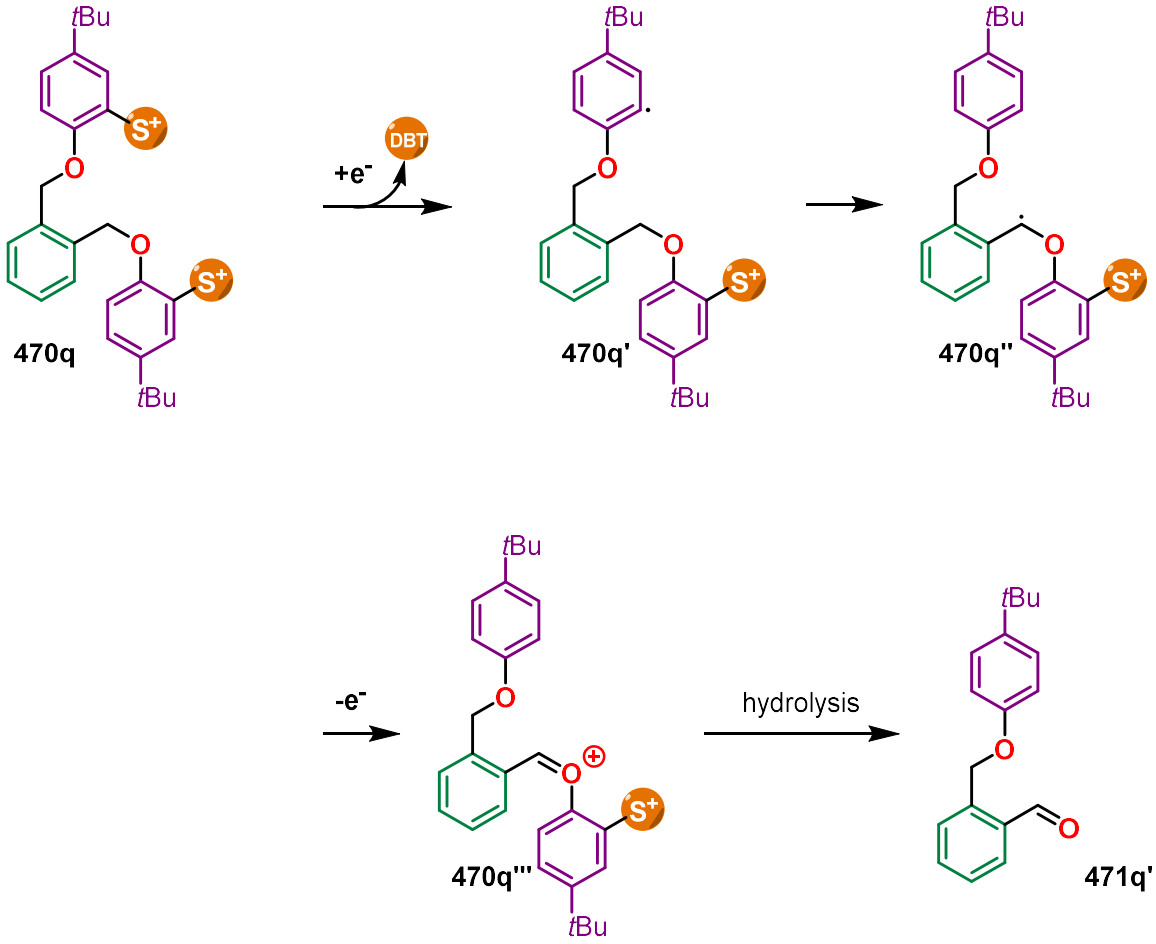

*Scheme 145: Proposed mechanism for the formation of by-product **471q'**[242]*

The aldehyde **471q'** might be a result of an intramolecular hydrogen atom transfer. Therefore, the reactive aryl radical (**470q'**) formed after photoreduction abstracts a nearby benzylic hydrogen, resulting in a more stable benzylic radical. After reoxidation by the oxidized photocatalyst this oxocarbenium ion **470q'''** can now be hydrolyzed forming compound **471q'**. This alternative to the intrameolecular 5-*exo/endo-trig* attack inevitably leads to yield losses. A similar process might have happened also in case of biaryl **471t**.

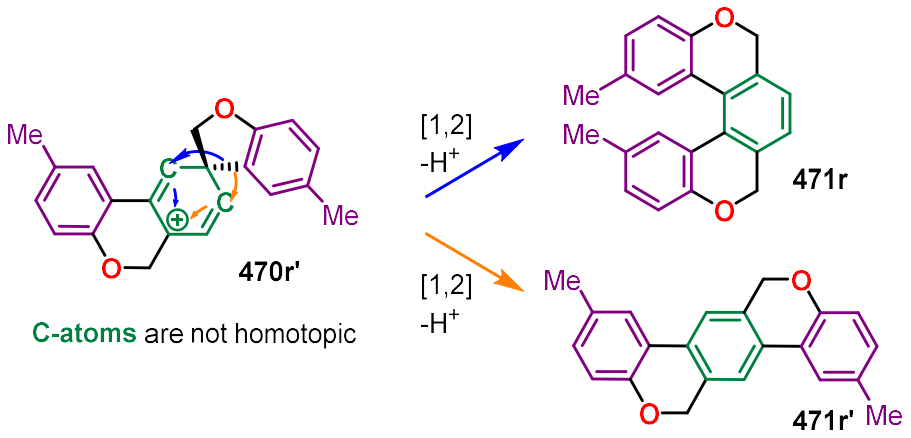

*Scheme 146: Regioselectivity problems during formation of **471r**[242]*

Compound **470r** was designed to undergo double cyclization releasing a helicoidal structure (**471r**). However, the second [1,2]-rearrangement of intermediate **470r'** lacks regioselectivity and beside **471r**

also forms the linear isomer **471r'**. In the other cases (**471q,s,t,u**), the high regioselectivity is achieved by blocking one of the C-atoms or by two homotopic C-atoms in the close proximity of the spirocenter. Then the migration of the aryl group is clearly defined in the cationic intermediate.

The helicoidal and linearly cyclized regioisomer **471r** and **471r'** can be clearly differentiated by the shape of the benzylic CH_2 signal in ^{1}H-NMR. In case of a "true" helicene with high inversion barrier this two protons would be diastereotopic and lead to two different doublets. Because the inversion barrier of **471r** is low and the molecule racemizes on the NMR time scale, the CH_2 signal appears as a broadened singlet. In case of the non-helicoidal molecule **471r'** there is no racemization barrier so the enantiotopic protons appear as a sharp singlet.

To have further evidence single crystals suitable for X-ray diffraction of **471r** and **471r'** were obtained by cooling a hot, saturated solution of methanol or toluene, respectively, confirming the proposed structures.

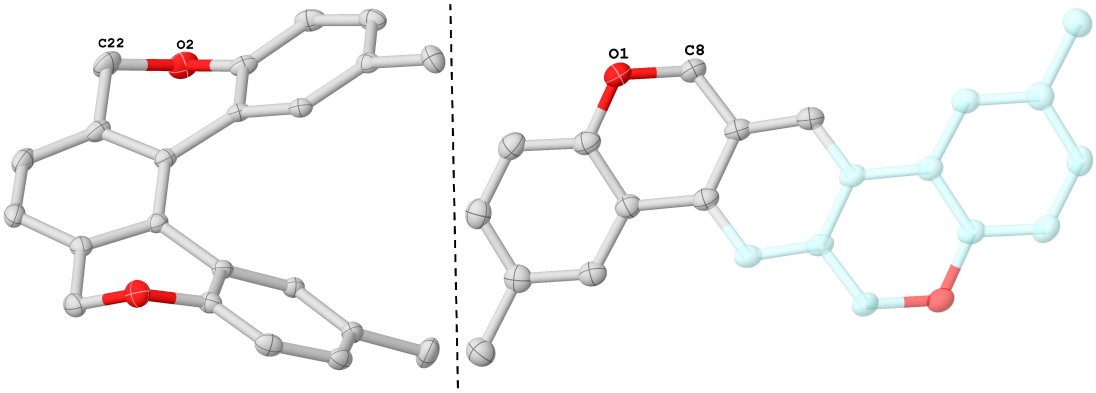

*Figure 67: Molecular structures of **471r**[39] (left) and **471r'**[40] (right). Thermal ellipsoids at 50% probability level. Hydrogen atoms and co-crystallized solvent molecules omitted for clarity. Second half of the centrosymmetric **471r'** generated by symmetry drawn translucent (Z'=0.5, symmetry code: '=1-x,2-y,1-z).*

The problems with regioselectivity and rapid isomerization in case of **471r** led us to the idea of developing the helicoidal compound **471s**. Using a naphthalene backbone instead of a phenylene one and replacing the R^1 substituents by ^{t}Bu should result in a higher inversion barrier and regioselectivity. Compound **471s** could be synthesized selectively in 68% yield. Insight into its solid state structure was obtained by growing monocrystals suitable for X-ray diffraction analysis from MeCN and H_2O by diffusion crystallization.

[39] **Crystal Data** for **471r** ($C_{22}H_{18}O_2$; *M* =314.36 g/mol): monoclinic, space group $P2_1/n$ (no. 14), *a* = 10.6570(8) Å, *b* = 9.3242(8) Å, *c* = 16.6165(11) Å, *β* = 101.178(3)°, *V* = 1619.8(2) Å^3, *Z* = 4, *T* = 100.0 K, μ(MoKα) = 0.081 mm^{-1}, *Dcalc* = 1.289 g/cm^3, 72705 reflections measured (4.2° ≤ 2Θ ≤ 57.406°), 4173 unique (R_{int} = 0.0212, R_{sigma} = 0.0081) which were used in all calculations. The final R_1 was 0.0410 (I > 2σ(I)) and wR_2 was 0.1102 (all data).

[40] **Crystal Data** for **471r** ($C_{22}H_{18}O_2$; *M* =314.36 g/mol): monoclinic, space group $P2_1/n$ (no. 14), *a* = 8.1303(10) Å, *b* = 7.7477(9) Å, *c* = 12.6640(16) Å, *β* = 99.953(4)°, *V* = 785.71(17) Å^3, *Z* = 2, *T* = 100.0 K, μ(MoKα) = 0.084 mm^{-1}, *Dcalc* = 1.329 g/cm^3, 37879 reflections measured (5.55° ≤ 2Θ ≤ 57.436°), 2028 unique (R_{int} = 0.0277, R_{sigma} = 0.0105) which were used in all calculations. The final R_1 was 0.0551 (I > 2σ(I)) and wR_2 was 0.1378 (all data).

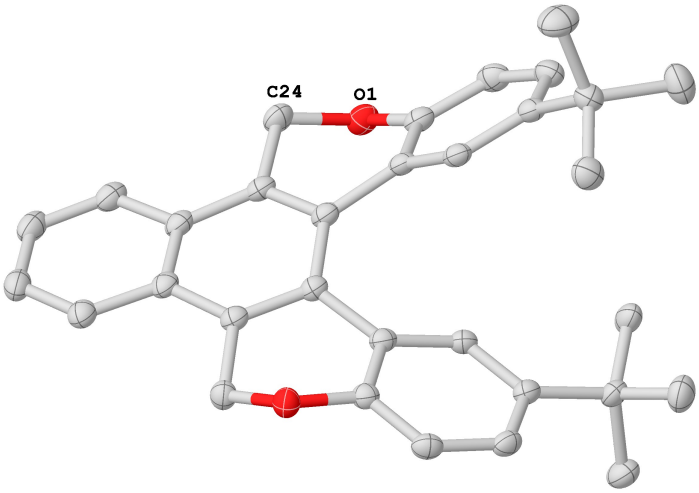

*Figure 68: Molecular structure of **471s**. Thermal ellipsoids at 50% probability level. Hydrogen atoms and co-crystallized solvent molecules omitted for clarity. Asymmetric unit contains two formula units of the corresponding compound **471s**, one unit has been omitted for clarity.*

The asymmetric unit contains two molecules (Z'=2) that clearly outline the helicoidal nature of **471s** (Figure 68). The best way to describe this helicoidal nature is by the interplanar angle of the peripheral rings, the torsional angles of the inner helix or the inner pitch (distance of peripheral carbons at the inner helix) which are shown in Table 8 and Scheme 147. Note, that differences between the molecules can be caused by crystal packing effects.

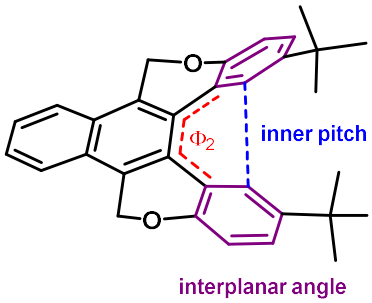

Scheme 147: Interplanar angle, torsional angles and inner pitch

*Table 8: Structural parameters of **471s***

	Molecule 1	Molecule 2
Inner pitch [Å]	3.010(2)	3.038(2)
Interplanar angle [°]	46.72(6)	47.91(6)
Torsional angle Φ_1 [°]	29.2(3)	27.9(3)
Torsional angle Φ_2 [°]	23.0(3)	19.9(3)
Torsional angle Φ_3 [°]	21.4(3)	27.6(3)

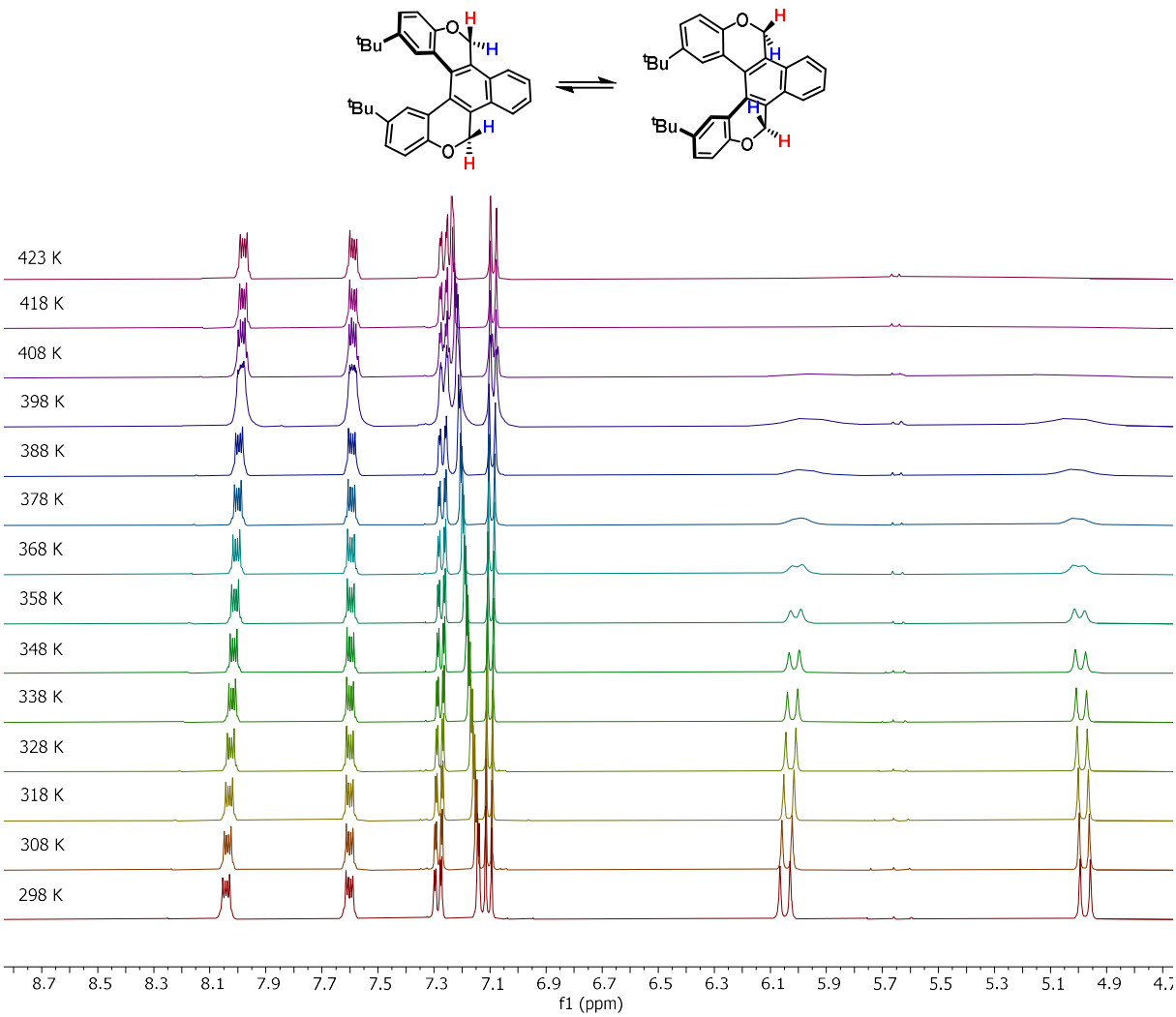

*Figure 69: Dynamic NMR experiment of **471s** in DMSO-d_6*[242]

The free energy barrier of the inversion was estimated *via* temperature-dependent NMR (Figure 69). Due to the symmetry breaking helicoidal structure the blue and red benzylic protons are diastereotopic and experience a different chemical shift and as a result couple to each other. When a solution of **471s** in DMSO-d_6 is heated the Heisenberg uncertainty principle leads to lifetime broadened benzylic proton peaks, which merge into one broad peak at the coalescence temperature.[134] At this point the free energy of activation $\Delta G^{\ddagger}$ can be estimated via the following equations:

$$k_c = 2.22\sqrt{\Delta n^2 + 6J_{AB}^2} = 956\ s^{-1} \qquad (8)$$

Equation 8

$$\Delta G^{\ddagger} = 19.14 T_c \left(10.32 + log\left(\frac{T_c}{k_c}\right)\right) = 81.2\ \frac{kJ}{mol} \qquad (9)$$

Equation 9

Where T_c is the coalescence temperature in K, J_{AB} the mutual coupling of exchanging nuclei in Hz, Δn the separation between the peaks of exchanging nuclei in Hz, k_c the rate of exchange at coalescence temperature in s^{-1} and $\Delta G^{\ddagger}$ the Gibbs energy of activation in J/mol. According to the Eyring equation, a free energy barrier of 81.2 kJ/mol corresponds to a half-life of 33 seconds at 20 °C, which makes a separation of the enantiomers pointless.

5.7 Application of benzo[*c*]chromenes in the synthesis of pyrylium salts

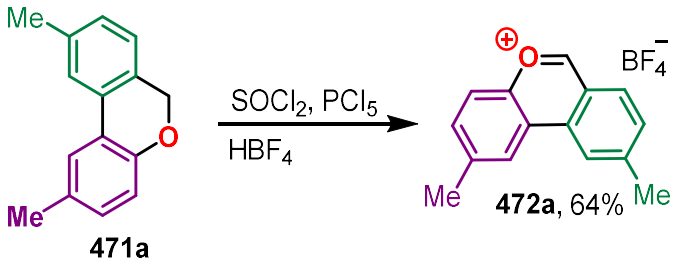

*Scheme 148: Synthesis of pyrylium salt **472a**[242]*

Beside helicoidal compounds like **471s** and 6*H*-benzo[*c*]chromenes like **471a** also pyrylium salts like **472a** become easily attainable through a combination of our methodology with a protocol for oxidation of cyclic ethers (Scheme 148).[264] These salts not only represent an interesting class of compounds by themselves, but can also be transformed into pyridines, phosphinines, pyridinium salts and thiopyrylium salts.[265]

Dibenzopyrylium salt **472a** was obtained in 64% yield by oxidation with $SOCl_2/PCl_5$ followed by an anion exchange for BF_4^-. The connectivity could be verified by NMR and X-ray diffraction analysis. The corresponding single crystals were prepared by diffusion crystallization (MeCN and Et_2O). Dibenzopyrylium salt **472a** was found to exhibit a notable π-stacking interactions, where antiparallelly arranged pyrylium-cations form columns along the a-axis. The distance between the pyrylium-cation mean-plane to the next stacking partner is only 3.373(1) Å, making this interaction remarkably short. Possibly, this is due to their cationic nature leading to a contraction of the π-electrons and the ability to act as excellent π-hole donors.[266]

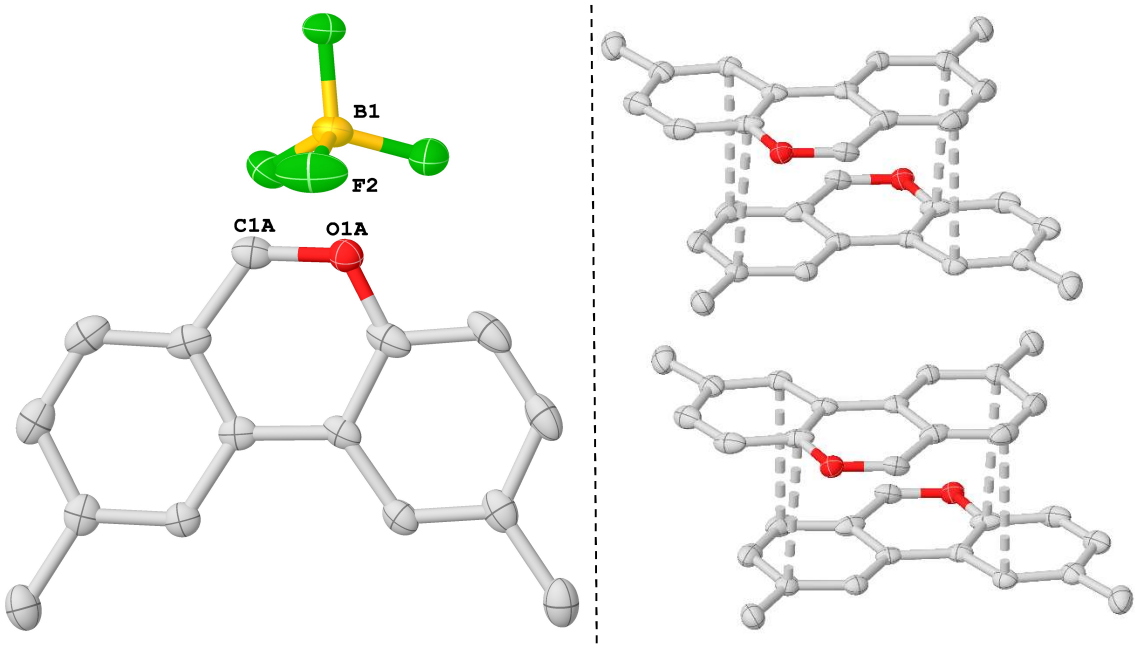

*Figure 70: Molecular structure of **472a**[41] (left). Thermal ellipsoids at 50% probability level. Hydrogen atoms omitted for clarity. Illustration of π-stacking (right). Thermal ellipsoids at 50% probability level. Hydrogen atoms and non-coordinating counter anions omitted for clarity*

[41] **Crystal Data** for **472a** ($C_{15}H_{13}BF_4O$; *M* =296.06 g/mol): monoclinic, space group $P2_1/n$ (no. 14), *a* = 6.9285(6) Å, *b* = 18.8834(14) Å, *c* = 10.2997(6) Å, *β* = 96.754(2)°, *V* = 1338.20(17) Å^3, *Z* = 4, *T* = 100.0 K, μ(MoKα) = 0.127 mm^{-1}, *Dcalc* = 1.470 g/cm^3, 3776 reflections measured (4.314° ≤ 2Θ ≤ 59.164°), 3776 unique (R_{int} = ?, R_{sigma} = 0.0130) which were used in all calculations. The final R_1 was 0.0389 (I > 2σ(I)) and wR_2 was 0.1190 (all data).

6 Summary II

In summary, a two-step protocol was developed that converts specially designed benzyl phenyl ethers into tricyclic 6*H*-benzo[*c*]chromenes. After selective C–H sulfenylation, the formed aryl sulfonium salts can undergo a high yielding cyclization enabled by visible light photoredox catalysis.

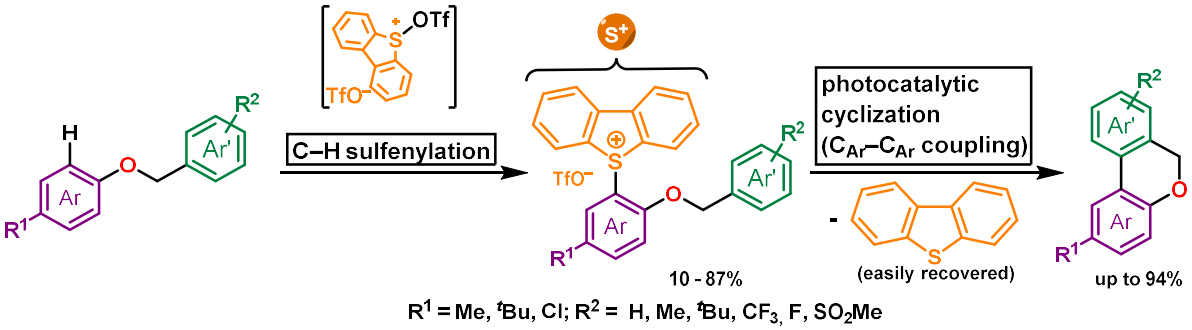

Scheme IV: Synthesis of 6H-benzo[c]chromenes via two-step protocol[242]

To ensure selective C–H-sulfenylation, benzyl phenyl ethers with specifically blocked positions (R^1) were synthesized. The transformation into corresponding sulfonium salts was enabled using a literature procedure[222] in combination with a base, since the existing protocol was incompatible with the acid labile benzyl ether motif. With the modified procedure at hand yields up to 87% could be realized. All sulfonium salts were fully characterized by standard methods and their structure was elucidated by single crystal X-ray diffraction on selected examples. Charge-assisted chalcogen bonds were found between the cationic sulfur and the triflate anions, which are typical for the substance class.

Selected sulfonium salts could then be converted into the corresponding 6*H*-benzo[*c*]chromenes using the photocatalyst *fac*-[Ir(ppy)$_3$]. It was also shown that DBT formed during the reaction can be easily recovered. The cyclization occurs in a highly regioselective manner (with one exception) and tolerates functional groups such as halogens (F, CF_3 and Cl) or sulfones.

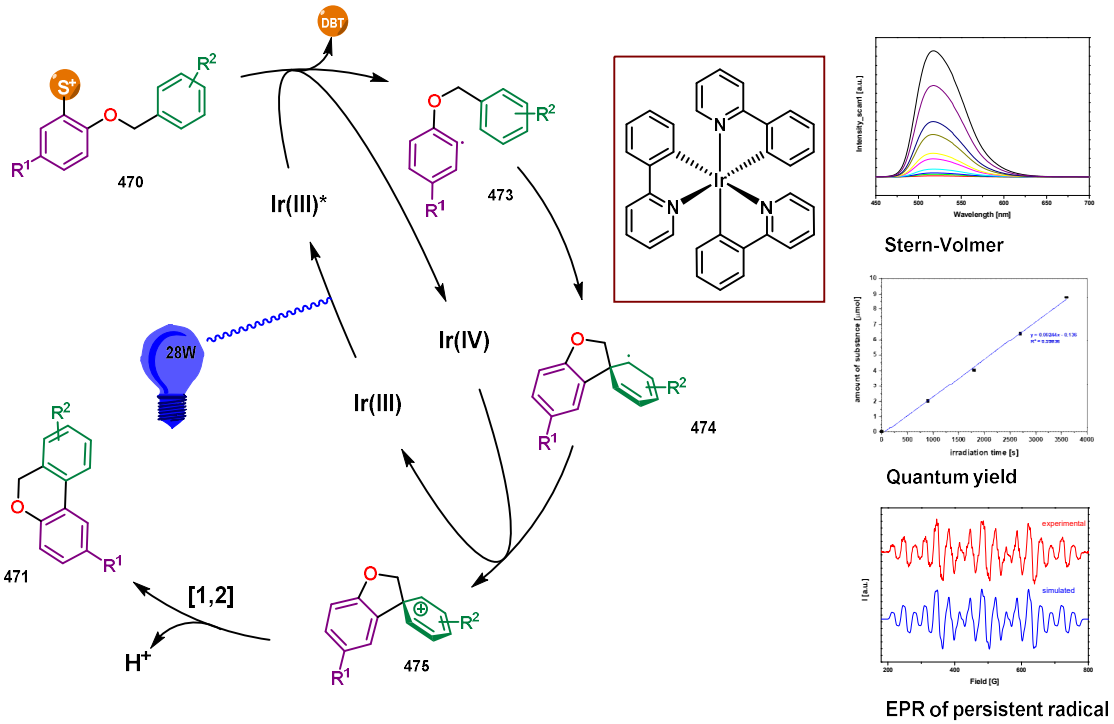

Scheme V: Proposed mechanism[242]

The photocatalytic cyclization proceeds predominantly *via* a reaction pathway consisting of a one-electron reduction of the sulfonium salt, selective S–Ar_{exo} bond cleavage resulting in aryl radical **473** and subsequent radical 5-*exo*-*trig* cyclization (**474**). After reoxidation (**475**), ring expansion and rearomatization the product **471** is formed. The proposed mechanism is supported by several studies. These include Stern–Volmer studies, quantum yield measurements, EPR measurements of a related persistent radical and trapping of intermediates. For the regioselectivity, the Wagner–Meerwein rearrangement in **475** to **471** is crucial leading to a selective aryl group migration in almost all cases.

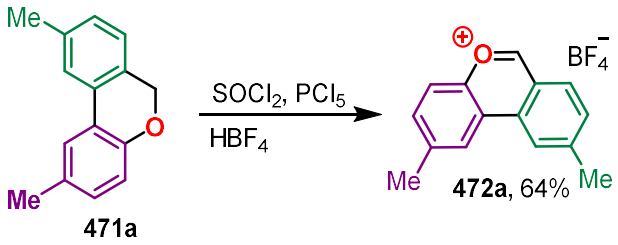

Scheme VI: Oxidation of 6H-benzo[c]chromenes to pyrylium salts[242]

6*H*-benzo[*c*]chromenes are not only a common motif in natural products, but also provide the basis for the synthesis of pyrylium salts, which in turn can be converted into various pyridines, phosphinines, pyridinium salts and thiopyrylium salts. The possibility of easily converting 6*H*-benzo[*c*]chromenes into the corresponding pyrylium salts by oxidation was demonstrated using the example **471a**.

Furthermore, the methodology could be used to enable double cyclizations (5 examples). A notable example was the double cyclization of **470s**, which was used to selectively build up helicoidal structures.

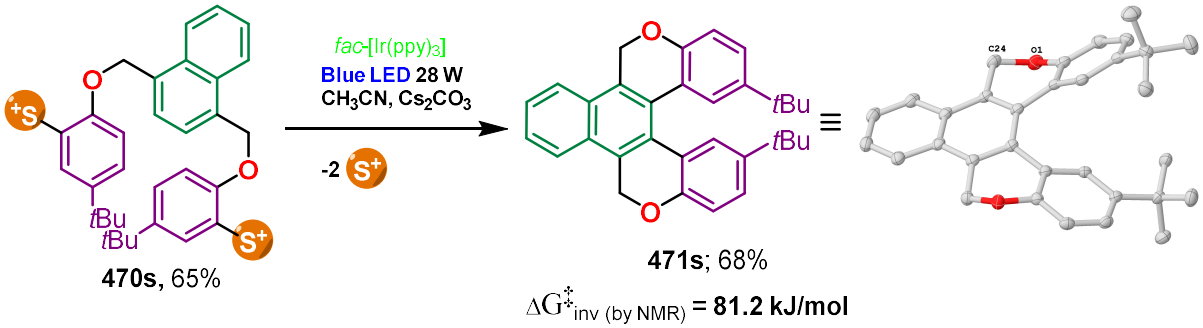

Scheme VII: Double cyclization of ***470s***[242]

Compound **471s** serves as a conceptual example demonstrating the potential of the presented two-step protocol to generate complex molecules.

7 Experimental

Experimental Procedures

Dry and degassed solvents were obtained *via* distillation over the appropriate drying agents and stored under nitrogen or argon. Alternatively, dry solvents were obtained using a MBraun MB-SPS-800 solvent purification system (acetonitrile, dichloromethane, diethyl ether, pentane, tetrahydrofuran, toluene). Flash chromatography was performed on Macherey Nagel 60 (40-63 µm) silica gel. Reactions were controlled by thin-layer chromatography (TLC) analysis, performed using polygram SIL G/UV254 TLC-plates from Macherey Nagel, and visualized by UV irradiation (λ = 254 nm) or staining with a 5% phosphomolybdic acid solution in EtOH.

Starting materials

Unless otherwise stated, all reagents were used as received from commercial suppliers (ABCR, Acros Organics, Alfa Aesar, Chempur GmbH, J and K Scientific, Sigma Aldrich, Thermo Fisher Scientific, Tokyo Chemical Industry).

General analytical methods

NMR: spectra were recorded on Bruker Avance III HD 300, Bruker Avance III 300, Bruker Avance III HD 400, Bruker Avance III 400, Bruker Avance Neo 400, Bruker Avance III HD 500, Bruker Avance Neo 600 or Varian Inova 500 spectrometers; ^{1}H and ^{13}C chemical shifts (δ) are given in ppm relative to TMS, using the residual solvent signals as references and converting the chemical shifts to the TMS scale. ^{19}F chemical shifts (δ) are given in ppm relative to $CFCl_3$, while ^{31}P chemical shifts (δ) are given in ppm relative to H_3PO_4 (external standard). Coupling constants (*J*) are given in Hz. Solvents for NMR spectroscopy used as received from Eurisotop.

HR-MS: Bruker Daltonik maXis Q-TOF (ESI), Bruker Daltonik micrOTOF (ESI), Thermo Scietific LTQ Orbitrap XL (ESI), Thermo Scietific Exactive GC-Orbitrap-MS (EI) or Jeol AccuTOF (EI). Dimensionless mass-to-charge ratios (*m/z*) are given.

IR: FT/IR-4600 (Jasco), wavenumbers ($\tilde{\nu}$) in cm^{-1}.

Preparative HPLC: preparative separations were carried out on an Interchim PuriFlash 4250 using either an Agilent ZORBAX SB-C18, 21.2×250 mm, 7 µm column (up to 50 mg) or an Agilent ZORBAX 7 SB-C18, 50.0×250 mm, 7µm column (>50 mg).

UV/Vis: spectra were conducted using either a Jasco V-630 or Jasco J-1500 spectrometer using a 1 cm quartz sample cell.

Fluorescence: spectra were conducted using a Jasco FP-8500 spectrofluorometer using a 10×2 mm quartz sample cell.

EPR: Bruker EMX mikro X-Band EPR using Bruker Xenon Software.

Single crystal X-ray diffraction analysis: Data collection was done on two dual source equipped *Bruker D8 Venture* four-circle-diffractometer from *Bruker AXS GmbH*; used X-ray sources: microfocus *IµS 2.0* Cu/Mo and microfocus *IµS 3.0* Ag/Mo from *Incoatec GmbH* with mirror optics *HELIOS* and single-hole collimator from *Bruker AXS GmbH;* used detector: *Photon III CE14* (Cu/Mo) and Photon III HE (Ag/Mo) from *Bruker AXS GmbH*. Used programs: *APEX3 Suite* (v2019.1-0) for data collection and therein integrated programs *SAINT* V8.38A (Integration) und *SADABS* 2016/2 (Absorption correction) from *Bruker AXS GmbH*; structure solution was done with *SHELXT*[267], refinement with *SHELXL*-2018/3[267]; $OLEX^2$ was used for data finalization[268].Special Utilities: *SMZ1270* stereomicroscope from *Nikon Metrology GmbH* was used for sample preparation; crystals were mounted on *MicroMounts* or *MicroLoops* from *MiTeGen* in NVH oil; for sensitive samples the *X-TEMP 2 System* was used for picking of crystals[269]; crystals were cooled to given temperature with *Cryostream 800* from *Oxford Cryosystems.*

Tuning the donor properties of bipyridyl-substituted phosphines by metal ion encapsulation

Compound **184**

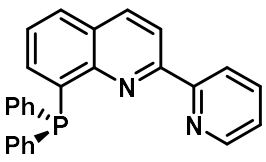

An oven-dried Schlenk flask was equipped with a stirring bar and charged with 8-bromo-2-(pyridin-2-yl)quinoline[125,126] (0.66 g, 2.31 mmol, 1.00 equiv.). The flask was evacuated and back-filled with nitrogen three times. Dry degassed THF (26 mL) was added under nitrogen. The suspension was stirred until all solids dissolved, cooled to –78 °C, and ^{n}BuLi (1.6 M in hexanes, 1.45 mL, 2.31 mmol, 1.0 equiv.) was added dropwise. After the addition was completed, the red reaction mixture was stirred for an additional 60 min at the same temperature. Afterwards, chlorodiphenylphosphane (0.51 g, 2.31 mmol, 1.00 equiv.) was added dropwise, and the reaction mixture was stirred for 16 h while being allowed to warm up to ambient temperature. A saturated aqueous solution of NH_4Cl was added, and the mixture was stirred for 5 min at ambient temperature. The mixture was extracted with CH_2Cl_2 (3 × 50 mL) and the CH_2Cl_2 extracts dried over Na_2SO_4. Volatile compounds were evaporated under reduced pressure. The residue was purified by flash-chromatography (SiO_2, pentane:EA 3:1) to give the target compound as a colorless solid (0.55 g, 1.41 mmol, 61%).

^{1}H NMR (300 MHz, $CDCl_3$) δ 8.62 (ddd, *J* = 4.8, 1.8, 1.0 Hz, 1H), 8.55 (d, *J* = 8.6 Hz, 1H), 8.27 (dd, *J* = 8.7, 0.7 Hz, 1H), 8.05 (dt, *J* = 8.0, 1.1 Hz, 1H), 7.82 (dt, *J* = 8.1, 1.2 Hz, 1H), 7.65 (ddd, *J* = 8.0, 7.5, 1.8 Hz, 1H), 7.47 – 7.38 (m, 5H), 7.37 – 7.30 (m, 6H), 7.24 (ddd, *J* = 7.5, 4.8, 1.2 Hz, 1H), 7.11 (ddd, *J* = 7.1, 3.9, 1.4 Hz, 1H); **^{13}C{H} NMR** (101 MHz, $CDCl_3$) δ 156.2, 154.9 (d, *J* = 1.6 Hz), 148.9, 148.6 (d, *J* = 15.9 Hz), 139.3 (d, *J* = 11.8 Hz), 137.7 (d, *J* = 9.7 Hz), 137.1 (d, *J* = 1.9 Hz), 136.9, 134.6, 134.4, 134.1 (d, *J* = 1.4 Hz), 128.7, 128.6, 128.5, 128.4, 127.9 (d, *J* = 1.8 Hz), 126.9, 124.1, 122.4, 119.0; **^{31}P{H} NMR** (121 MHz, $CDCl_3$) δ -12.7; **IR (ATR)** [cm^{-1}]: $\tilde{\nu}$ = 3067, 3049, 3027, 3011, 2998, 1599, 1548, 1496, 1471, 1418, 1291, 1090, 846, 781, 762, 742, 696, 621, 584, 541, 507, 482, 442; **HR-MS-ESI(+)** calc. $C_{26}H_{20}N_2P^+$ $[M+H]^+$ 391.1359; found 391.1360.

Preparation of compound **184** was described in the literature; however, without characterization.[131]

Compound **200**

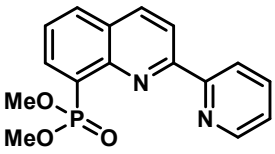

An oven-dried Schlenk flask was equipped with a stirring bar and charged with 8-bromo-2-(pyridin-2-yl)quinoline[125,126] (100.0 mg, 0.35 mmol, 1.00 equiv.). The flask was evacuated and back-filled with nitrogen three times. Dry degassed THF was added under nitrogen. The suspension was stirred until all solids dissolved, cooled to –78 °C, and ^{n}BuLi (1.6 M in hexanes, 0.22 mL, 0.35 mmol, 1.0 equiv.) was added dropwise. After the addition was completed, the reaction mixture was stirred for an additional 60 min at the same temperature. Afterwards, dimethyl chlorophosphate (50.7 mg, 0.35 mmol, 1.00 equiv.) was added dropwise, and the reaction mixture was stirred for 16 h while being allowed to warm up to ambient temperature. A saturated aqueous solution of NH_4Cl was added, and the mixture was stirred for 5 min at ambient temperature. The mixture was extracted with CH_2Cl_2 (3 × 20 mL) and the CH_2Cl_2 extracts dried over Na_2SO_4. Volatile compounds were evaporated under reduced pressure. The residue was purified by flash-chromatography (SiO_2, EA) to give the target compound as a colorless solid (45 mg, 0.14 mmol, 41%).

The syntheses were carried out using a modified literature procedure.[270]

An oven-dried Schlenk flask was equipped with a stirring bar and charged with $Pd(OAc)_2$ (39.4 mg, 0.18 mmol, 0.05 equiv.), dppf (194.4 mg, 0.35 mmol, 0.10 equiv.) and KOAc (74.6 mg, 0.76 mmol, 0.22 equiv.). The flask was evacuated and back-filled with nitrogen three times. Dry degassed THF

(10 mL) and triethylamine (851.7 mg, 8.42 mmol, 2.40 equiv.) were added under nitrogen. The mixture was stirred and heated to 68 °C for 15 min. Afterwards, dimethyl phosphonate (771.9 mg, 7.01 mmol, 2.00 equiv.) and 8-bromo-2-(pyridin-2-yl)quinoline[125,126] (1 g, 3.51 mmol, 1.00 equiv.) were added and the reaction mixture was stirred and heated to 68 °C for 66 h. Volatile compounds were evaporated under reduced pressure. The residue was purified by flash-chromatography (SiO_2, EA) to give the target compound as a colorless solid (933 mg, 2.97 mmol, 85%).

^{1}H NMR (300 MHz, $CDCl_3$) δ 8.89 (d, *J* = 8.0 Hz, 1H), 8.79 – 8.70 (m, 2H), 8.45 – 8.31 (m, 2H), 8.07 (dt, *J* = 8.2, 1.4 Hz, 1H), 7.95 (t, *J* = 7.3 Hz, 1H), 7.63 (ddd, *J* = 8.1, 7.1, 3.6 Hz, 1H), 7.42 (dd, *J* = 7.2, 5.1 Hz, 1H), 3.91 (d, *J* = 11.4 Hz, 6H); **^{13}C{H} NMR** (75 MHz, $CDCl_3$) δ 156.7 (d, *J* = 1.0 Hz), 156.0, 149.1, 147.9 (d, *J* = 6.6 Hz), 137.3, 137.2 (d, *J* = 3.5 Hz), 137.1 (d, *J* = 2.1 Hz), 132.9 (d, *J* = 3.5 Hz), 128.3 (d, *J* = 10.8 Hz), 127.2 (d, *J* = 187.6 Hz), 126.0 (d, *J* = 16.3 Hz), 124.5, 122.8, 119.5, 53.1 (d, *J* = 5.9 Hz); **^{31}P{H} NMR** (121 MHz, $CDCl_3$) δ 20.24; **IR (ATR)** [cm^{-1}]: $\tilde{\nu}$ = 3060, 2998, 2946, 2845, 1598, 1555, 1496, 1472, 1446, 1421, 1243, 1222, 1151, 1054, 1028, 872, 849, 818, 794, 753, 677, 621, 591, 562, 477, 458, 434; **HR-MS-ESI(+)** calc. $C_{16}H_{15}N_2O_3P^+$ $[M+H]^+$ 315.0893; found 315.0895.

Compound **203**

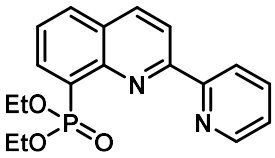

An oven-dried Schlenk flask was equipped with a stirring bar and charged with 8-bromo-2-(pyridin-2-yl)quinoline[125,126] (174.1 mg, 0.61 mmol, 1.00 equiv.). The flask was evacuated and back-filled with nitrogen three times. Dry degassed THF was added under nitrogen. The suspension was stirred until all solids dissolved, cooled to –78 °C, and ^{n}BuLi (1.6 M in hexanes, 0.38 mL, 0.61 mmol, 1.0 equiv.) was added dropwise. After the addition was completed, the reaction mixture was stirred for an additional 60 min at the same temperature. Afterwards, diethyl chlorophosphate (105.4 mg, 0.61 mmol, 1.00 equiv.) was added dropwise, and the reaction mixture was stirred for 16 h while being allowed to warm up to ambient temperature. A saturated aqueous solution of NH_4Cl was added, and the mixture was stirred for 5 min at ambient temperature. The mixture was extracted with CH_2Cl_2 (3 × 20 mL) and the CH_2Cl_2 extracts dried over Na_2SO_4. Volatile compounds were evaporated under reduced pressure. The residue was purified by flash-chromatography (SiO_2, EA) to give the target compound as a colorless solid (118.0 mg, 0.34 mmol, 56%).

^{1}H NMR (300 MHz, $CDCl_3$) δ 8.89 (dt, *J* = 8.1, 1.2 Hz, 1H), 8.73 (ddd, *J* = 4.9, 1.8, 1.0 Hz, 1H), 8.67 (d, *J* = 8.6 Hz, 1H), 8.38 (ddd, *J* = 15.7, 7.1, 1.5 Hz, 1H), 8.31 (dd, *J* = 8.7, 2.4 Hz, 1H), 8.04 (dt, *J* = 8.2, 1.5 Hz, 1H), 7.89 (ddd, *J* = 8.0, 7.5, 1.8 Hz, 1H), 7.60 (ddd, *J* = 8.2, 7.1, 3.6 Hz, 1H), 7.37 (ddd, *J* = 7.4, 4.8, 1.2 Hz, 1H), 4.44 – 4.17 (m, 4H), 1.33 (td, *J* = 7.1, 0.6 Hz, 6H); **^{13}C{H} NMR** (75 MHz, $CDCl_3$) δ 156.4, 156.1, 149.1, 147.9 (d, *J* = 6.6 Hz), 137.2, 137.2 (d, *J* = 2.0 Hz), 137.0 (d, *J* = 7.5 Hz), 132.7 (d, *J* = 3.3 Hz), 128.3 (d, *J* = 10.5 Hz), 128.1 (d, *J* = 187.0 Hz), 126.0 (d, *J* = 16.0 Hz), 124.5, 122.8, 119.4, 62.4, 62.3, 16.7, 16.6; **^{31}P{H} NMR** (121 MHz, $CDCl_3$) δ 17.15; **IR (ATR)** [cm^{-1}]: $\tilde{\nu}$ = 3452, 3054, 2979, 2928, 2901, 2867, 1597, 1554, 1496, 1474, 1421, 1236, 1157, 1021, 958, 845, 783, 744, 621, 589, 556, 404; **HR-MS-ESI(+)** calc. $C_{18}H_{20}N_2O_3P^+$ $[M+H]^+$ 343.1206; found 343.1207.

Compound **204**

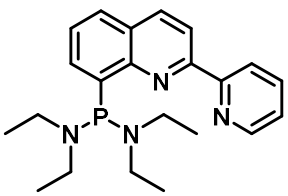

An oven-dried Schlenk flask was equipped with a stirring bar and charged with 8-bromo-2-(pyridin-2-yl)quinoline[125,126] (1.47 g, 5.17 mmol, 1.00 equiv.). The flask was evacuated and back-filled with nitrogen three times. Dry degassed THF (20 mL) was added under nitrogen. The suspension was stirred until all solids dissolved, cooled to –78 °C, and ^{n}BuLi (1.6 M in hexanes, 3.23 mL, 5.17 mmol, 1.0 equiv.) was added dropwise. After the

addition was completed, the reaction mixture was stirred for an additional 60 min at the same temperature. Afterwards, the red solution of 8-lithio-2-(pyrid-2'-yl)quinoline was added to a cooled solution of bis(diethylamino)chlorophosphine (1.09 g, 5.17 mmol, 1.00 equiv.) in 20 mL THF at -78 °C, and the reaction mixture was stirred for 16 h while being allowed to warm up to ambient temperature. 6 mL degassed water and 20 mL of pentane were added, and the mixture was stirred for 5 min at ambient temperature. The organic phase was separated and the aqueous solution further extracted with pentane (2 × 20 mL). The combined THF/pentane extracts were dried over Na_2SO_4 and filtered. Volatile compounds were evaporated under reduced pressure to give the target compound as an orange oil (1.86 g, 4.88 mmol, 94%).

^{1}H NMR (400 MHz, $CDCl_3$) δ 8.81 (dt, *J* = 8.1, 1.1 Hz, 1H), 8.70 (ddd, *J* = 4.7, 1.8, 1.0 Hz, 1H), 8.57 (d, *J* = 8.7 Hz, 1H), 8.23 (d, *J* = 8.7 Hz, 1H), 7.87 – 7.80 (m, 2H), 7.76 (dt, *J* = 8.1, 1.6 Hz, 1H), 7.52 (ddd, *J* = 8.2, 7.0, 1.3 Hz, 1H), 7.32 (ddd, *J* = 7.5, 4.8, 1.2 Hz, 1H), 3.22 – 3.09 (m, 8H), 1.05 (t, *J* = 7.0 Hz, 12H); **^{13}C{H} NMR** (101 MHz, $CDCl_3$) δ 156.7, 154.5 (d, *J* = 2.2 Hz), 149.0, 148.5 (d, *J* = 16.9 Hz), 142.0 (d, *J* = 12.8 Hz), 137.0 (d, *J* = 2.2 Hz), 136.7, 132.4 (d, *J* = 5.5 Hz), 128.3, 128.0 (d, *J* = 2.2 Hz), 126.6, 124.0, 122.5, 118.5, 44.1 (d, *J* = 18.7 Hz), 15.1 (d, *J* = 2.9 Hz); **^{31}P{H} NMR** (162 MHz, $CDCl_3$) δ 94.39; **IR (ATR)** [cm^{-1}]: $\tilde{\nu}$ = 3050, 2963, 2926, 2864, 2821, 2774, 2749, 2726, 2481, 2389, 1599, 1470, 1184, 1013, 908, 783; **HR-MS-ESI(+)** calc. $C_{22}H_{30}N_4P$ $[M+H]^+$ 381.2203; found 381.2214.

Compound **207**

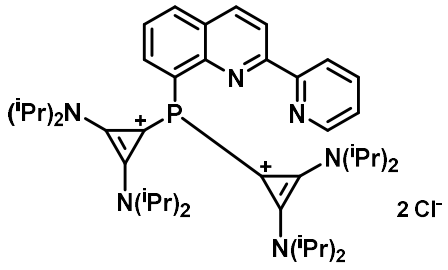

An oven-dried Schlenk flask was equipped with a stirring bar and charged with N,N,N',N'-tetraethyl-1-(2-(pyridin-2-yl)quinolin-8-yl)phosphanediamine **204** (1.01 g, 2.65 mmol, 1.00 equiv.). The flask was evacuated and back-filled with nitrogen three times. Dry degassed THF (25 mL) was added under nitrogen. The emulsion was stirred until both liquids mixed, cooled to –78 °C, and hydrogen chloride solution (2.0 M in diethyl ether, 6.77 mL, 13.54 mmol, 5.1 equiv.) was added dropwise. Afterwards, the reaction mixture was stirred for 16 h while being allowed to warm up to ambient temperature. The colorless precipitate was filtered off, washed with THF and dried in vacuum to obtain 2-(8-(dichlorophosphaneyl)quinolin-2-yl)pyridin-1-ium chloride **205** as a 1:2 mixture with diethylammonium chloride. To separate the impurities and free the 8-(dichlorophosphaneyl)-2-(pyridin-2-yl)quinoline dry degassed THF (25 mL), Et_2O (10 mL) and triethylamine (0.22 g, 2.20 mmol, 0.83 equiv.) were added and the mixture stirred for 4 h. Then, the supernatant solution was cooled to -78 °C and added dropwise to a solution of bis(diisopropylamino)cyclopropenylidene[132] (2.01 g, 8.52 mmol, 3.21 equiv.) in THF (250 mL) at -78 °C *via* cannula filtration. The resulting reaction mixture was stirred for 16 h while being allowed to warm up to ambient temperature. During this time a white precipitate formed, which was filtered off and washed with THF. After drying *in vacuo* the product was obtained as a colorless solid (1.36 g, 1.74 mmol, 66%).

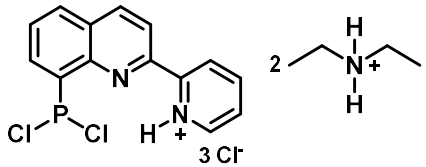

205: **^{1}H NMR** (400 MHz, $CDCl_3$) δ 9.46 (dd, *J* = 8.6, 1.0 Hz, 1H), 9.11 – 9.07 (m, 2H), 8.65 (d, *J* = 8.8 Hz, 1H), 8.60 (ddd, *J* = 8.4, 7.6, 1.6 Hz, 1H), 8.54 (dt, *J* = 7.2, 1.5 Hz, 1H), 8.16 (dt, *J* = 8.4, 1.4 Hz, 1H), 8.03 (ddd, *J* = 7.9, 5.7, 1.5 Hz, 1H), 7.88 (ddd, *J* = 8.2, 7.2, 1.0 Hz, 1H); **^{13}C{H} NMR** (101 MHz, $CDCl_3$) δ 149.9, 148.0 (d, *J* = 20.9 Hz), 146.4, 146.0, 142.3, 139.5 (d, *J* = 2.6 Hz), 138.8 (d, *J* = 60.2 Hz), 133.6 (d, *J* = 4.4 Hz), 132.1 (d, *J* = 2.2 Hz), 129.5, 128.8, 126.9, 126.5, 121.4; **^{31}P{H} NMR** (162 MHz, $CDCl_3$) δ 158.16; **IR (ATR)** [cm^{-1}]: $\tilde{\nu}$ = 3034, 2973, 2959, 2913, 2866, 2820, 2773, 2750, 2726, 2709, 2478, 2386, 1610, 1592, 1556, 1529,

1495, 1457, 1390, 1279, 1227, 1146, 1084, 1036, 999, 961, 869, 842, 814, 785, 769, 732, 707, 619, 580, 537, 507, 463, 426; **HR-MS-ESI(+)** calc. n.a.

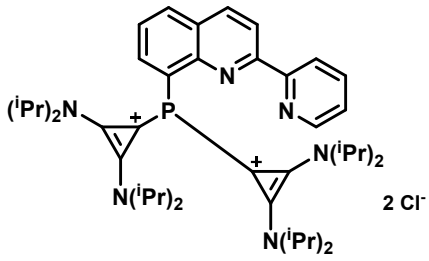

207: **^{1}H NMR** (400 MHz, CD_3CN) δ 8.76 (d, *J* = 4.7 Hz, 1H), 8.72 (d, *J* = 8.7 Hz, 1H), 8.62 (d, *J* = 8.7 Hz, 1H), 8.28 (d, *J* = 8.2 Hz, 1H), 8.25 – 8.17 (m, 2H), 7.90 (td, *J* = 7.8, 1.9 Hz, 1H), 7.78 (td, *J* = 8.6, 8.0, 1.9 Hz, 1H), 7.49 (ddd, *J* = 7.7, 4.9, 0.8 Hz, 1H), 4.14 (hept, *J* = 6.9 Hz, 4H), 3.67 (m, 4H), 1.35 (d, *J* = 6.9 Hz, 12H), 1.30 (d, *J* = 6.9 Hz, 12H), 1.23 (d, *J* = 6.8 Hz, 12H), 1.04 – 0.83 (m, 12H); **^{13}C{H} NMR** (101 MHz, CD_3CN) δ 157.6 (d, *J* = 2.3 Hz), 155.6, 151.0, 149.2 (d, *J* = 19.5 Hz), 141.1 (d, *J* = 2.0 Hz, 4C), 139.9 (d, *J* = 2.7 Hz), 138.1, 136.9, 133.2, 129.8 (d, *J* = 2.3 Hz), 129.0 (d, *J* = 1.8 Hz), 126.3, 126.2 (d, *J* = 2.3 Hz), 121.7, 121.5 (d, *J* = 1.4 Hz), 99.0 (d, *J* = 63.4 Hz, 2C), 55.9 (4C), 52.9 (4C), 21.8 (d, *J* = 3.3 Hz, 4C), 21.6 (d, *J* = 4.3 Hz, 4C), 21.3 (4C), 21.2 (4C); **^{31}P{H} NMR** (162 MHz, CD_3CN) δ -56.07; **IR (ATR)** [cm^{-1}]: $\tilde{\nu}$ = 3465, 3390, 2976, 2933, 2872, 1856, 1550, 1455, 1347, 1148, 1039, 859, 826, 791, 687, 642, 573; **HR-MS-ESI(+)** calc. $C_{44}H_{65}N_6P^{2+}$ $[M–2Cl]^{2+}$ 354.2499; found 354.2503.

Compound **208**

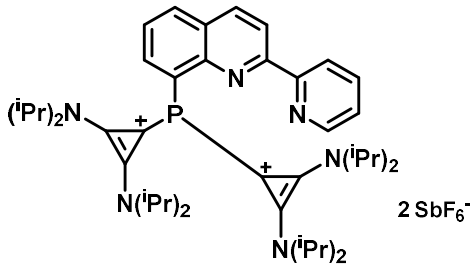

An oven-dried Schlenk flask was equipped with a stirring bar and charged with 1,1'-((2-(pyridin-2-yl)quinolin-8-yl)phosphanediyl)bis(2,3-bis(diisopropylamino)cycloprop-2-en-1-ylium) chloride **207** (189.6 mg, 0.24 mmol, 1.00 equiv.) and $NaSbF_6$ (629.0 mg, 2.43 mmol, 10.00 equiv.). The flask was evacuated and back-filled with nitrogen three times. Dry degassed acetonitrile (10 mL) was added under nitrogen and the suspension was stirred for 16 h. Afterwards, the solvent was removed *in vacuo* and DCM (10 mL) was added. After stirring for 12 h at ambient temperature excess $NaSbF_6$ was filtered off, extracted with DCM and the combined extracts evaporated under reduced pressure to give the target compound as a colorless solid (274.9 mg, 0.23 mmol, 96%).

^{1}H NMR (400 MHz, CD_3CN) δ 8.76 (dq, *J* = 4.7, 1.0 Hz, 1H), 8.73 (d, *J* = 8.7 Hz, 1H), 8.60 (dd, *J* = 8.7, 1.2 Hz, 1H), 8.27 (dt, *J* = 8.3, 1.3 Hz, 1H), 8.21 (dt, *J* = 8.0, 1.2 Hz, 1H), 7.95 (ddd, *J* = 7.3, 4.7, 1.4 Hz, 1H), 7.90 (td, *J* = 7.8, 1.8 Hz, 1H), 7.77 (ddd, *J* = 8.7, 7.1, 1.8 Hz, 1H), 7.50 (ddd, *J* = 7.6, 4.7, 1.2 Hz, 1H), 4.11 (hept, *J* = 6.8 Hz, 4H), 3.66 (s, 4H), 1.35 (d, *J* = 6.9 Hz, 12H), 1.29 (d, *J* = 6.8 Hz, 12H), 1.23 (d, *J* = 6.8 Hz, 12H), 1.01 – 0.91 (m, 12H); **^{13}C{H} NMR** (101 MHz, CD_3CN) δ 157.7 (d, *J* = 2.3 Hz), 155.6, 151.0, 149.2 (d, *J* = 19.5 Hz), 141.1 (d, *J* = 2.6 Hz, 4C), 139.9 (d, *J* = 2.3 Hz), 138.1, 136.3, 133.4, 129.8 (d, *J* = 2.7 Hz), 128.9 (d, *J* = 1.8 Hz), 126.3, 126.3 (d, *J* = 1.8 Hz), 121.8, 121.6, 99.0 (d, *J* = 61.3 Hz, 2C), 55.9 (4C), 53.0 (4C), 21.8 (d, *J* = 3.4 Hz, 4C), 21.6 (d, *J* = 4.4 Hz, 4C), 21.2 (4C), 21.1 (4C); **^{13}C NMR** (75 MHz, CD_3CN) δ 157.6 (d, *J* = 2.2 Hz), 155.5, 151.0, 149.3 (d, *J* = 19.7 Hz), 141.1 (d, *J* = 2.6 Hz), 139.9 (d, *J* = 2.5 Hz), 138.2, 136.3, 133.4, 129.8 (d, *J* = 2.7 Hz), 128.9 (d, *J* = 1.1 Hz), 126.3, 126.3 (d, *J* = 2.2 Hz), 121.8, 121.6 (d, *J* = 1.1 Hz), 99.0 (d, *J* = 61.5 Hz), 55.9, 53.0, 21.8 (d, *J* = 3.3 Hz), 21.6 (d, *J* = 4.8 Hz), 21.3, 21.2; **^{31}P{H} NMR** (162 MHz, CD3CN) δ -56.24; **^{19}F NMR** (282 MHz, CD_3CN) δ -123.87 (hex, *J* = 1931.7 Hz), -123.88 (oct, *J* = 1048.3 Hz); **IR (ATR)** [cm^{-1}]: $\tilde{\nu}$ = 2878, 1851, 1549, 1457, 1377, 1347, 1203, 1179, 1145, 1037, 1011, 891, 855, 820, 783, 743, 684, 653, 592, 580, 541, 433; **HR-MS-ESI(+)** calc. $C_{44}H_{65}F_6SbN_6P^+$ $[M–SbF_6]^+$ 943.3945; found 943.3941.

Compound **209a**

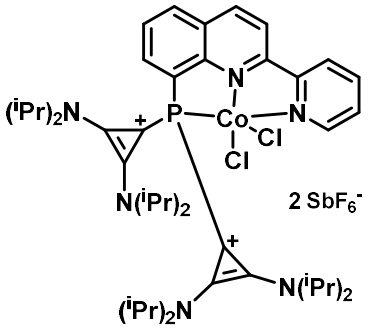

An oven-dried Schlenk flask was equipped with a stirring bar and charged with 1,1'-((2-(pyridin-2-yl)quinolin-8-yl)phosphanediyl)bis(2,3-bis(diisopropylamino)cycloprop-2-en-1-ylium) hexafluoroantimonate **208** (66.8 mg, 0.57 mmol, 1.00 equiv.). The flask was evacuated and back-filled with nitrogen three times. Dry degassed DCM (10 mL) was added under nitrogen. The suspension was stirred until all solids dissolved and slowly added to a solution of $CoCl_2$ (7.4 mg, 0.57 mmol, 1.00 equiv.) in THF (5 mL) (prepared by heating $CoCl_2$ in THF, 1h, reflux). After the addition was completed, the reaction mixture was stirred for an additional 60 min at ambient temperature, and layered with THF (10 mL) to obtain the target compound as a crystalline green solid (35.1 mg, 0.27 mmol, 47%).

^{1}H NMR (400 MHz, CD_3CN) δ 7.36 (s), 4.40 – 3.57 (m), 1.81 – 0.14 (m); Due to the paramagnetic nature of **209a**, only incomplete, broad and unstructured resonances were observed. **IR (ATR)** [cm^{-1}]: $\tilde{\nu}$ = 2980, 2942, 2882, 1855, 1557, 1455, 1378, 1355, 1183, 1149, 1028, 892, 850, 817, 776, 654, 593, 419; **HR-MS-ESI(+)** calc. $C_{44}H_{65}Cl_2CoN_6P^{2+}$ $[M–2SbF_6]^{2+}$ 418.6853; found 418.6856.

Compound **212**

The syntheses were carried out using a modified literature procedure.[123]

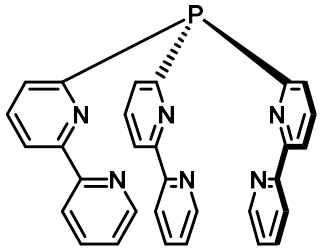

An oven-dried Schlenk flask was equipped with a stirring bar and charged with 6-bromo-2,2'-bipyridine[156] (10.68 g, 45.43 mmol, 3.00 equiv.). The flask was evacuated and back-filled with nitrogen three times. Dry degassed diethyl ether (100 mL) was added under nitrogen. The suspension was stirred until all solids dissolved, cooled to –78 °C, and ^{n}BuLi (2.5 M in hexanes, 18.60 mL, 46.49 mmol, 3.07 equiv.) was added fast. After the addition was completed, the reaction mixture was stirred for an additional 60 min at the same temperature. Afterwards, PCl_3 (2.08 g, 15.14 mmol, 1.00 equiv.) was slowly added dropwise, and the reaction mixture was stirred for 16 h while being allowed to warm up to ambient temperature. Degassed methanol and water were added successively, and the mixture was stirred for 5 min at ambient temperature. The diethyl ether was removed *in vacuo* and the residue extracted with CH_2Cl_2 (3 × 50 mL) and dried over Na_2SO_4. Volatile compounds were evaporated under reduced pressure. The residue was purified by **fast** flash-chromatography (SiO_2, pentane:EA 1:1 (+1 vol%[fraction] NEt_3), R_F = 0.2, stains used beside UV light: ceric ammonium molybdate solution and sat. acetone solution of $Fe(BF_4)_2$•$6H_2O$ (colorless→deep violet)) to give the target compound as a colorless solid (3.28 g, 6.61 mmol, 44%), which is prone to oxidation.

The syntheses were carried out using a modified literature procedure.[152–154]

An oven-dried 100mL three-necked round-bottom flask was equipped with a stirring bar, reflux condenser (+Tee connector with bubbler and nitrogen-inlet) and an adapter with stopcock and connector (nitrogen-side-inlet). The bubbler was connected with an absorbent bottle containing saturated aqueous $CuSO_4$*$5H_2O$ solution *via* tubing. The flask was charged with a grinded mixture of 6-bromo-2,2'-bipyridine[156] (100 mg, 0.43 mmol, 1.00 equiv.), red phosphorus powder (33 mg, 1.06 mmol, 2.50 equiv.) and powdered KOH (60 mg, 1.06 mmol, 2.50 equiv.) and evacuated and back-filled with nitrogen three times. Degassed DMSO/H_2O (0.6 mL, 20/1 v/v) was added under nitrogen. The suspension was vigorously stirred and placed in a pre-heated oil bath (oil bath temperature 122 °C) for 1 h. During this time a slow nitrogen stream was flushed through the bubbler by the tee connector.

Afterwards, the oil bath was removed and the whole apparatus cooled to ambient temperature. Before disconnecting the reflux condenser, the round bottom flask was flushed with nitrogen through the side inlet, water was added, and again flushed with nitrogen to remove traces of PH_3. 20 mL of DCM were added and the mixture filtered through Celite®. Volatile compounds were evaporated under reduced pressure. The residue was purified by **fast** flash-chromatography [SiO_2, pentane:EA 1:1 (+1 vol% NEt_3), Rf = 0.2 , stains used beside UV light: ceric ammonium molybdate solution and sat. acetone solution of $Fe(BF_4)_2 \bullet 6H_2O$ (colorless→deep violet)], followed by recrystallization from hot toluene to give the target compound as a colorless solid (32.6 mg, 0.07 mmol, 46%), which is prone to oxidation.

^{1}H NMR (300 MHz, $CDCl_3$) δ 8.65 (ddd, *J* = 4.8, 1.8, 0.9 Hz, 3H), 8.38 (dt, *J* = 8.0, 1.1 Hz, 3H), 8.31 (dt, *J* = 8.0, 1.1 Hz, 3H), 7.75 (td, *J* = 7.8, 2.1 Hz, 3H), 7.70 (td, *J* = 7.8, 1.8 Hz, 3H), 7.46 (dt, *J* = 7.7, 1.2 Hz, 3H), 7.27 (ddd, *J* = 7.5, 5.0, 1.2 Hz, 3H); **^{13}C{H} NMR** (101 MHz, $CDCl_3$) δ 161.6 (d, *J* = 4.1 Hz), 156.4 (d, *J* = 12.0 Hz), 156.1, 149.1, 137.0, 136.6 (d, *J* = 3.6 Hz), 129.3 (d, *J* = 18.2 Hz), 123.9, 121.6, 120.0; **^{31}P{H} NMR** (121 MHz, $CDCl_3$) δ -0.67; **IR (ATR)** [cm^{-1}]: $\tilde{\nu}$ = 3057, 1547, 1473, 1420, 1255, 1159, 1070, 1040, 985, 770, 619, 509; **HR-MS-ESI(+)** calc. $C_{30}H_{22}N_6P^+$ $[M+H]^+$ 497.1638; found 497.1644.

Preparation of compound **212** was described in the literature; however, without characterization.[123,151]

Compound **237**

The syntheses were carried out using a modified literature procedure.[152–154]

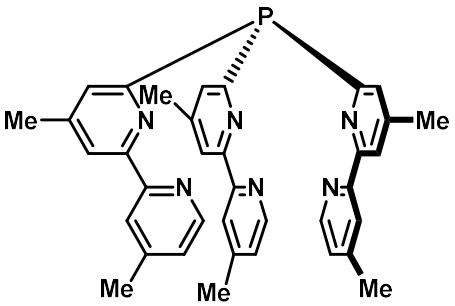

An oven-dried 100mL three-necked round-bottom flask was equipped with a stirring bar, reflux condenser (+Tee connector with bubbler and nitrogen-inlet) and an adapter with stopcock and connector (nitrogen-side-inlet). The bubbler was connected with an absorbent bottle containing saturated aqueous $CuSO_4 * 5H_2O$ solution *via* tubing. The flask was charged with a grinded mixture of 6-chloro-4,4'-dimethyl-2,2'-bipyridine[157] (2.87 g, 13.13 mmol, 1.00 equiv.), red phosphorus powder (1.02 g, 32.81 mmol, 2.50 equiv.) and powdered KOH (1.84 g, 32.81 mmol, 2.50 equiv.) and evacuated and back-filled with nitrogen three times. Degassed DMSO/H_2O (17.22 mL, 20/1 v/v) was added under nitrogen. The suspension was vigorously stirred and placed in a pre-heated oil bath (oil bath temperature 122 °C) for 1 h. During this time a slow nitrogen stream was flushed through the bubbler by the tee connector. Afterwards, the oil bath was removed and the whole apparatus cooled to ambient temperature. Before disconnecting the reflux condenser, the round bottom flask was flushed with nitrogen through the side inlet, water was added, and again flushed with nitrogen to remove traces of PH_3. 100 mL of DCM were added and the mixture filtered through Celite®. The DCM phase was washed with water (20 mL) and concentrated *in vacuo*. Diethyl ether (300 mL) was added and the mixture washed with water (3 × 20 mL). The organic phase was dried (Na_2SO_4) and all volatile compounds were evaporated under reduced pressure. The residual solid was suspended in cold methanol (30 mL), sonicated, and filtered off to obtain compound **237** as a colorless powder (1.46 g, 2.51 mmol, 57%). (Alternative: Recrystallization from toluene/*n*-octane at 120 °C)

^{1}H NMR (400 MHz, $CDCl_3$) δ 8.49 (d, *J* = 5.0 Hz, 3H), 8.20 (s, 3H), 8.15 (s, 3H), 7.29 (s, 3H), 7.08 (d, *J* = 5.0 Hz, 3H), 2.37 (s, 9H), 2.30 (s, 9H); **^{13}C{H} NMR** (101 MHz, $CDCl_3$) δ 161.3 (d, *J* = 4.6 Hz), 156.3 (d, *J* = 12.5 Hz), 156.1, 148.8, 148.1, 147.6 (d, *J* = 3.6 Hz), 130.3 (d, *J* = 18.5 Hz), 124.8, 122.7, 121.0, 21.5, 21.3; **^{31}P{H} NMR** (162 MHz, $CDCl_3$) δ -0.82; **IR (ATR)** [cm^{-1}]: $\tilde{\nu}$ = 3051, 3008, 2977, 2953, 2916, 2856, 1585,

1541, 1473, 1441, 1394, 1367, 1251, 1173, 1144, 1109, 1038, 987, 896, 862, 822, 786, 739, 686, 635, 549, 524, 508, 423; **HR-MS-ESI(+)** calc. $C_{36}H_{34}N_6P^+$ $[M+H]^+$ 581.2577; found 581.2548.

Compound **237x**

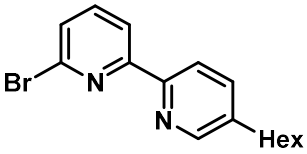

To a solution of 2,6-dibromopyridine (1.42 g, 5.98 mmol, 1.20 equiv.) and tetrakis(triphenylphosphine)palladium(0) (288 mg, 0.249 mmol, 0.05 equiv.) in dry toluene (30 mL) 5-Hexyl-2-(tributylstannyl)pyridine (3.47 g, purity 59 wt%, 4.53 mmol, 1.00 equiv.,) was added at room temperature. The reaction mixture was stirred for 42.5 h at 120 °C. The cooled reaction mixture was concentrated *in vacuo* and n-pentane (20 mL) was added. The mixture was extracted with hydrochloric acid (8 x 20 mL, 6 M). The organic layer was extracted with ammonia solution (20 mL, 2 M). The aqueous ammonia layer was extracted with n-pentane (2 x 20 mL). The combined organic layers were dried over anhydrous sodium sulfate, filtered and concentrated *in vacuo*. The crude product was purified by silica gel column chromatography twice using a mixture of n-pentane and EA (20:1) as eluent with an addition of 1 vol% triethylamine. 872 mg (Rf =0.23, 2.73 mmol, yield 60 %) of 6'-Bromo-5-hexyl-2,2'-bipyridine were obtained.

^{1}H NMR (300 MHz, $CDCl_3$) δ 8.48 (d, *J* = 2.2 Hz, 1H), 8.38 – 8.26 (m, 2H), 7.64 (t, *J* = 7.8 Hz, 1H), 7.62 (dd, *J* = 8.1, 2.3 Hz, 1H), 7.46 (dd, *J* = 7.9, 0.9 Hz, 1H), 2.66 (m, 2H), 1.63 (m, 2H), 1.43 – 1.22 (m, 6H), 0.96 – 0.82 (m, 3H); **^{13}C NMR** (75 MHz, $CDCl_3$) δ 157.7, 152.3, 149.6, 141.7, 139.3, 139.1, 137.0, 127.7, 121.3, 119.5, 33.0, 31.8, 31.2, 28.9, 22.7, 14.2; **IR (ATR)** [cm^{-1}]: $\tilde{\nu}$ = 2960, 2925, 2854, 1566, 1542, 1483, 1427, 1390, 1185, 1153, 1122, 1063, 1026, 986, 847, 804, 781, 768, 754, 724, 668, 615, 606, 541, 480, 403; **HR-MS-ESI(+)** calc. $C_{16}H_{20}N_2Br^+$ $[M+H]^+$ 395.1464; found 395.1465.

Compound **237y**

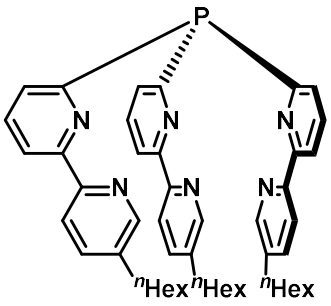

An oven-dried Schlenk flask was equipped with a stirring bar and charged with 6'-Bromo-5-hexyl-2,2'-bipyridine (497 mg, 1.57 mmol, 1.00 equiv.). The flask was evacuated and back-filled with nitrogen three times. Dry degassed diethyl ether (70 mL) was added under nitrogen. The suspension was stirred until all solids dissolved, cooled to –78 °C, and ^{n}BuLi (1.57 mmol, 0.63 mL, 2.5 M in n-hexane, 1.00 equiv.) was added fast. After the addition was completed, the reaction mixture was stirred for an additional 60 min at the same temperature. Afterwards, PCl_3 (45 µL, 0.517 mmol, 0.33 equiv.) was slowly added dropwise, and the reaction mixture was stirred for 16 h while being allowed to warm up to ambient temperature. Degassed methanol (10 mL) and water (50 mL) were added successively, and the mixture was stirred for 5 min at ambient temperature. The diethyl ether was removed *in vacuo* and the residue extracted with CH_2Cl_2 (3 × 50 mL) and dried over Na_2SO_4. Volatile compounds were evaporated under reduced pressure. The residue was purified by **fast** flash-chromatography (SiO_2, pentane:EA 15:1→10:1 (+1 vol%[fraction] NEt_3), Rf = 0.22 (15:1)) and recrystallization from toluene/diphenylsilane (33.6 equiv.) to give the target compound as a colorless solid (25.5 mg, 0.03 mmol, 6%), which is prone to oxidation.

^{1}H NMR (400 MHz, $CDCl_3$) δ 8.46 (d, *J* = 1.9 Hz, 3H), 8.33 (d, *J* = 8.0 Hz, 3H), 8.22 (d, *J* = 8.6 Hz, 3H), 7.72 (td, *J* = 7.9, 2.2 Hz, 3H), 7.51 (dd, *J* = 8.1, 2.3 Hz, 3H), 7.41 (dt, *J* = 7.6, 1.2 Hz, 3H), 2.63 (t, *J* = 7.6 Hz, 6H), 1.61 (q, *J* = 7.7, 7.3 Hz, 6H), 1.40 – 1.18 (m, 18H), 0.99 – 0.72 (m, 9H); **^{13}C{H} NMR** (101 MHz, $CDCl_3$) δ 161.7 (d, *J* = 4.4 Hz), 156.6 (d, *J* = 12.5 Hz), 153.9, 149.3, 138.5, 136.9, 136.6, 129.0 (d, *J* = 17.6 Hz), 121.3, 119.7, 33.0, 31.8, 31.2, 28.9, 22.7, 14.2; **^{31}P{H} NMR** (162 MHz, $CDCl_3$) δ -0.75; **IR (ATR)** [cm^{-1}]: $\tilde{\nu}$ = 2955, 2925, 2853, 1563, 1547, 1485, 1462, 1436, 1399, 1377, 1246, 1163, 1079, 1024, 987, 864,

810, 762, 741, 670, 640, 623, 492, 445; **HR-MS-ESI(+)** calc. $C_{48}H_{58}N_6P^+$ [M+H]$^+$ 749.4455; found 749.4435.

Compound **237z**

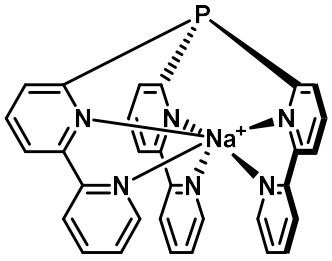

Under nitrogen atmosphere in a glovebox, an oven-dried Schlenk flask was equipped with a stirring bar and charged with preligand tri([2,2'-bipyridin]-6-yl)phosphane **212** (100.0 mg, 201.40 µmol, 1.00 equiv.) and $NaBArF_{24}$ (Sodium tetrakis[3,5-bis(trifluoromethyl)phenyl]borate, 178.49 mg, 201.40 µmol, 1.00 equiv.). Dry degassed DCM (15 mL) was added under nitrogen. Afterwards, the soution was stirred for 1 h and concentrated *in vacuo*. The residue was then washed with diethyl ether and dried *in vacuo* to give the target compound as a colorless solid (85.7 mg, 38.16 µmol, 19%).

^{1}H NMR (300 MHz, CD_3CN) δ 8.67 (ddd, *J* = 4.8, 1.8, 1.0 Hz, 3H), 8.36 (dt, *J* = 8.0, 1.1 Hz, 3H), 8.18 (dt, *J* = 8.0, 1.1 Hz, 3H), 7.87 (td, *J* = 7.8, 2.2 Hz, 3H), 7.79 (td, *J* = 7.8, 1.8 Hz, 3H), 7.72 – 7.63 (m, 12H), 7.54 (ddd, *J* = 7.7, 2.2, 1.1 Hz, 3H), 7.37 (ddd, *J* = 7.5, 4.8, 1.2 Hz, 3H); **^{1}H NMR** (400 MHz, $CDCl_3$) δ 8.86 (s, 3H), 8.05 (d, *J* = 5.0 Hz, 3H), 7.98 – 7.77 (m, 12H), 7.72 (s, 8H), 7.48 (s, 4H), 7.40 (s, 3H); **^{13}C NMR** (101 MHz, CD_3CN) δ 162.6 (dd, *J* = 99.7, 49.9 Hz), 161.3, 157.3 (d, *J* = 8.7 Hz), 156.4, 150.6, 138.6, 138.6, 135.7, 131.7 (d, *J* = 30.7 Hz), 129.9 (qdd, *J* = 31.8, 5.8, 2.9 Hz), 125.5 (q, *J* = 271.8 Hz), 125.4, 122.4, 122.0, 118.7 (p, *J* = 4.0 Hz). **^{13}C NMR** (101 MHz, $CDCl_3$) δ 161.9 (dd, *J* = 99.6, 49.8 Hz), 158.0, 156.3, 156.2, 155.4, 149.6, 138.4, 138.1 (d, *J* = 22.6 Hz), 134.9, 133.9 (d, *J* = 59.0 Hz), 129.1 (qdd, *J* = 31.6, 5.8, 2.9 Hz), 124.9, 124.7 (q, *J* = 272.5 Hz), 122.8, 117.6 (p, *J* = 4.0 Hz); **^{31}P{H} NMR** (121 MHz, CD_3CN) δ -1.12; **^{31}P{H} NMR** (121 MHz, $CDCl_3$) δ -6.17; **^{19}F NMR** (282 MHz, CD_3CN) δ -63.27; **^{19}F NMR** (377 MHz, $CDCl_3$) δ -62.4; **^{11}B NMR** (96 MHz, CD_3CN) δ -6.67; **^{11}B NMR** (96 MHz, $CDCl_3$) δ -6.59; **IR (ATR)** [cm^{-1}]: $\tilde{\nu}$ = 3062, 3017, 2962, 1557, 1434, 1353, 1273, 1115, 999, 886, 839, 773, 744, 713, 669, 624, 580, 533; **HR-MS-ESI(+)** calc. $C_{30}H_{21}N_6PNa^+$ [M–BArF]$^+$ 519.1458; found 519.1456.

Compound **238**

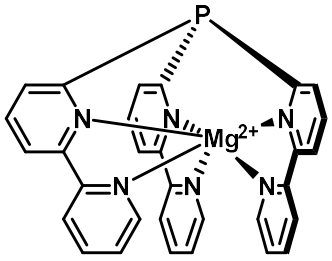

Under nitrogen atmosphere in a glovebox, an oven-dried Schlenk flask was equipped with a stirring bar and charged with the corresponding metal triflate $Mg(OTf)_2$ (61.9 mg, 191.81 µmol, 1.00 equiv.) and preligand tri([2,2'-bipyridin]-6-yl)phosphane **212** (100.0 mg, 201.40 µmol, 1.05 equiv.). Dry degassed THF (1 mL) was added under nitrogen and the reaction mixture was stirred under reflux for 18 h using a pre-heated oil bath. After cooling to room temperature, 4 mL of dry degassed toluene were added. The colorless precipitate was filtered off, washed with dry degassed pentane and dried *in vacuo* to give the target compound as a colorless solid (137.2 mg, 167.53 µmol, 87%).

^{1}H NMR (300 MHz, CD_3CN) δ 8.46 (t, *J* = 7.2 Hz, 6H), 8.37 – 8.28 (m, 9H), 8.24 (td, *J* = 7.8, 2.8 Hz, 3H), 7.78 (dd, *J* = 7.6, 5.3 Hz, 3H); **^{13}C{H} NMR** (101 MHz, CD_3CN) δ 156.5 (d, *J* = 16.8 Hz), 154.5, 152.7, 150.8, 143.2, 142.5 (d, *J* = 14.9 Hz), 136.7 (d, *J* = 52.3 Hz), 128.6, 124.7, 124.5, 122.1 (q, *J* = 320.6 Hz); **^{31}P{H} NMR** (121 MHz, CD_3CN) δ -36.06; **^{31}P NMR** (162 MHz, CD_3CN) δ -36.07 (q, *J* = 9.0 Hz); **^{19}F NMR** (282 MHz, CD_3CN) δ -79.31; **IR (ATR)** [cm^{-1}]: $\tilde{\nu}$ = 3087, 1588, 1490, 1435, 1304, 1209, 1159, 1025, 825, 777, 629, 580, 513; **HR-MS-ESI(+)** calc. $C_{31}H_{21}MgN_6PF_3O_3S^+$ [M–TfO]$^+$ 669.0903; found 669.0933.

Compound **239**

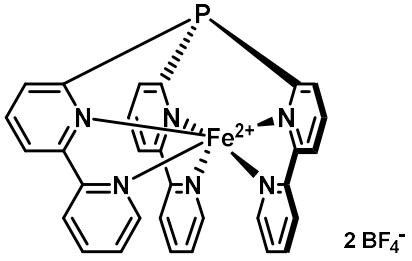

Under nitrogen atmosphere in a glovebox, an oven-dried Schlenk flask was equipped with a stirring bar and charged with hexaaquairon(II) tetrafluoroborate (22.6 mg, 67 µmol, 0.95 equiv.) and preligand tri([2,2'-bipyridin]-6-yl)phosphane **212** (36.0 mg, 73 µmol, 1.00 equiv.). Dry degassed MeCN was added under nitrogen and the reaction mixture was stirred for 18 h. The solvent was removed *in vacuo* and the residue washed with small amounts of diethyl ether and pentane. After drying *in vacuo* the target compound was obtained as a red/violet solid (44 mg, 62 µmol, 85%).

^{1}H NMR (300 MHz, CD_3CN) δ 14.51 – 9.33 (m, 15H), 7.01 (s, 3H), 6.16 (s, 3H).
IR (ATR) [cm^{-1}]: $\tilde{\nu}$ = 3080, 1605, 1441, 1319, 1296, 1245, 1167, 1025, 813, 772, 700, 603, 554, 518; **HR-MS-ESI(+)** calc. $C_{30}H_{21}N_6PFe^{2+}$ $[M–2BF_4]^{2+}$ 276.0452; found 276.0454.

Preparation of the corresponding perchlorate salt of **239** was described in the literature; however, without characterization.[123]

Compound **240**

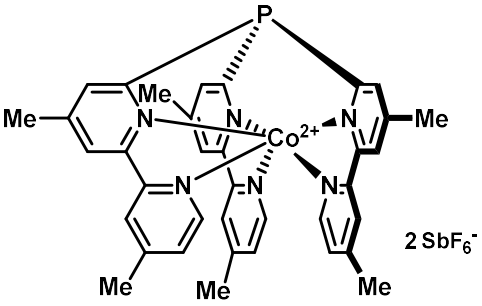

Under nitrogen atmosphere in a glovebox, an oven-dried Schlenk flask was equipped with a stirring bar and charged with $CoCl_2$ (46.3 mg, 356.48 µmol, 1.00 equiv.), $NaSbF_6$ (184.5 mg, 712.96 µmol, 2.00 equiv.) and preligand tris(4,4'-dimethyl-[2,2'-bipyridin]-6-yl)phosphane **237** (207.0 mg, 356.48 µmol, 1.00 equiv.). Dry degassed THF (1 mL) was added under nitrogen and the reaction mixture was stirred under reflux for 18 h using a pre-heated oil bath. After cooling to room temperature, volatile compounds were evaporated under reduced pressure. The remaining solid was extracted with DCM. Afterwards, the combined organic extracts were concentrated *in vacuo*. The residue was washed several times with dry degassed toluene and diethyl ether and dried *in vacuo* to give the target compound as a yellow solid (362.1 mg, 325.89 µmol, 91%).

^{1}H NMR (400 MHz, CD_3CN) δ 366.09 (s, 3H), 94.34 (s, 3H), 82.91 (s, 3H), 34.89 (s, 3H), 24.21 (s, 3H), 4.51 (s, 9H), 1.09 (s, 9H); **^{31}P{H} NMR** (162 MHz, CD_3CN) δ 316.57; **^{19}F NMR** (377 MHz, CD_3CN) δ -123.56 (sext, *J* = 1932.6 Hz), -123.56 (oct, *J* = 1050.3 Hz); **IR (ATR)** [cm^{-1}]: $\tilde{\nu}$ = 3666, 3653, 3646, 3626, 3584, 3564, 3090, 3080, 3068, 2976, 2964, 2927, 2866, 2858, 1617, 1603, 1545, 1488, 1444, 1393, 1297, 1248, 1013, 935, 870, 835, 736, 651, 540, 514, 425; **HR-MS-ESI(+)** calc. $C_{36}H_{33}CoF_6N_6PSb^+$ $[M–SbF_6]^+$ 874.0773; found 874.0779.

Compound **241**

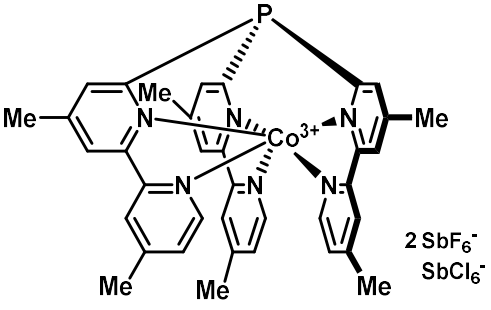

Under nitrogen atmosphere in a glovebox, an oven-dried Schlenk flask was equipped with a stirring bar and charged with compound **237** (300.0 mg, 270.00 µmol, 1.00 equiv.). Dry degassed THF (10 mL) was added under nitrogen. Afterwards, a solution of magic blue (Tris(4-bromophenyl)ammoniumyl hexachloroantimonate, 220.5 mg, 270.00 µmol, 1.00 equiv.) in 5 mL THF was added dropwise to the suspension. After the addition was

complete, the pink precipitate was filtered off, washed with THF and DCM, and dried *in vacuo* to give target compound as a pink(/orange) solid (362.6 mg, 250.84 µmol, 93%).

^{1}H NMR (400 MHz, CD_3CN) δ 8.51 (s, 3H), 8.38 (d, *J* = 8.5 Hz, 3H), 8.33 (s, 3H), 7.51 (d, *J* = 5.6 Hz, 3H), 6.13 (d, *J* = 5.5 Hz, 3H), 2.69 (s, 9H), 2.68 (s, 9H); **^{13}C{H} NMR** (101 MHz, CD_3CN) δ 160.5, 158.7, 158.3 (d, *J* = 12.2 Hz), 157.7, 154.2 (d, *J* = 24.1 Hz), 151.9, 138.3 (d, *J* = 44.2 Hz), 132.0, 129.7, 127.6, 21.9, 21.6; **^{31}P{H} NMR** (162 MHz, CD_3CN) δ 12.94; **^{19}F NMR** (377 MHz, CD_3CN) δ -123.81 (sext, *J* = 1933.8 Hz), -123.35 (m, *J* = 1048.5 Hz); **IR (ATR)** [cm^{-1}]: $\tilde{\nu}$ = 3130, 3075, 2976, 2932, 2866, 2857, 1619, 1543, 1449, 1293, 1254, 1029, 871, 833, 757, 651, 587, 528, 451, 413; **HR-MS-ESI(+)** calc. $C_{36}H_{33}CoCl_6F_6N_6PSb_2^+$ $[M–SbF_6]^+$ 1208.7915; found 1208.7846.

Compound **241b**

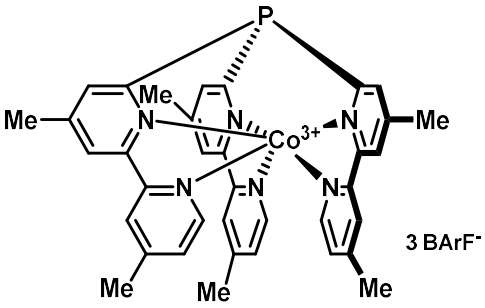

Under nitrogen atmosphere in a glovebox, an oven-dried Schlenk flask was equipped with a stirring bar and charged with compound **241** (50.0 mg, 34.59 µmol, 1.00 equiv.) and $NaBArF_{24}$ (Sodium tetrakis[3,5-bis(trifluoromethyl)phenyl]borate, 92.0 mg, 103.77 µmol, 3.00 equiv.). Dry degassed DCM (15 mL) was added under nitrogen. Afterwards, the suspension was stirred for 1h, filtered, and the combined organic extracts concentrated *in vacuo*. The pink residue was then washed with diethyl ether and dried *in vacuo* to give the target compound as a pink solid (103.3 mg, 31.99 µmol, 92%).

^{1}H NMR (400 MHz, CD_2Cl_2) δ 8.35 (d, *J* = 6.9 Hz, 6H), 8.15 (s, 3H), 7.66 (s, 24H), 7.48 (s, 15H), 6.02 (s, 3H), 2.67 (s, 18H); **^{13}C{H} NMR** (101 MHz, CD_2Cl_2) δ 162.1 (q, *J* = 49.9 Hz), 160.4 (d, *J* = 12.2 Hz), 160.3, 159.4, 156.6, 153.2 (d, *J* = 26.4 Hz), 150.7, 138.9 (d, *J* = 44.3 Hz), 135.2, 132.6, 129.3, 129.2 (qq, *J* = 31.5, 2.8 Hz), 127.5, 124.9 (q, *J* = 272.7 Hz), 117.9 (q, *J* = 7.4, 5.6 Hz), 22.4, 22.2; **^{31}P{H} NMR** (162 MHz, CD_2Cl_2) δ 12.56; **^{19}F NMR** (377 MHz, CD_2Cl_2) δ -62.75; **^{11}B NMR** (96 MHz, CD_2Cl_2) δ -6.67; **IR (ATR)** [cm^{-1}]: $\tilde{\nu}$ = 3075, 1619, 1609, 1445, 1354, 1272, 1109, 940, 885, 838, 745, 712, 681, 668, 626, 583, 527, 449, 435, 416; **HR-MS-ESI(+)** calc. $C_{68}H_{45}CoF_{24}N_6PB^+$ $[M–2BArF]^+$ 1502.2491; found 1502.2464; calc. $C_{36}H_{33}CoN_6P^{3+}$ $[M–3BArF]^{3+}$ 213.0607; found 213.0609.

Compound **242**

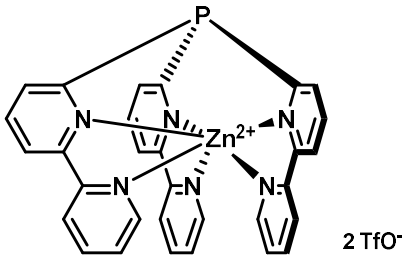

Under nitrogen atmosphere in a glovebox, an oven-dried Schlenk flask was equipped with a stirring bar and charged with the corresponding metal triflate $Zn(OTf)_2$ (69.7 mg, 191.81 µmol, 1.00 equiv.) and preligand tri([2,2'-bipyridin]-6-yl)phosphane **212** (100.0 mg, 201.40 µmol, 1.05 equiv.). Dry degassed THF (1 mL) was added under nitrogen and the reaction mixture was stirred under reflux for 18 h using a pre-heated oil bath. After cooling to room temperature, 4 mL of dry degassed toluene were added. The colorless precipitate was filtered off, washed with dry degassed pentane and dried *in vacuo* to give the target compound as a colorless solid (104.4 mg, 121.39 µmol, 63%).

^{1}H NMR (300 MHz, CD_3CN) δ 8.55 – 8.43 (m, 6H), 8.39 – 8.28 (m, 6H), 8.24 (td, *J* = 7.8, 2.8 Hz, 3H), 8.10 (d, *J* = 5.2 Hz, 3H), 7.79 (ddd, *J* = 7.5, 5.3, 1.2 Hz, 3H); **^{13}C{H} NMR** (101 MHz, CD_3CN) δ 155.3 (d, *J* = 17.1 Hz), 152.1, 150.4, 149.9, 143.1, 142.4 (d, *J* = 14.4 Hz), 137.0 (d, *J* = 51.1 Hz), 128.8, 124.8, 124.4, 122.2 (q, *J* = 320.9 Hz); **^{31}P{H} NMR** (121 MHz, CD_3CN) δ -50.87; **^{19}F NMR** (282 MHz, CD_3CN) δ -79.30; **IR (ATR)** [cm^{-1}]: $\tilde{\nu}$ = 3074, 3012, 2975, 2871, 2852, 1605, 1590, 1557, 1488, 1442, 1256, 1224, 1191, 1148, 1097,

1030, 1012, 919, 833, 800, 780, 755, 653, 635, 572, 543, 516, 418; **HR-MS-ESI(+)** calc. $C_{31}H_{21}CaN_6PF_3O_3S^+$ $[M–TfO]^+$ 709.0372; found 709.0370.

Compound **242b**

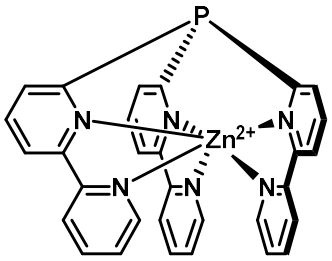

Under nitrogen atmosphere in a glovebox, an oven-dried Schlenk flask was equipped with a stirring bar and charged with compound **242** (17.9 mg, 21 µmol, 1.00 equiv.) and $NaBArF_{24}$ (Sodium tetrakis[3,5-bis(trifluoromethyl)phenyl]borate, 36.9 mg, 42 µmol, 2.00 equiv.). Dry degassed DCM (15 mL) was added under nitrogen. Afterwards, the suspension was stirred for 18 h, filtered, and the combined organic extracts concentrated *in vacuo*. The residue was then washed with small amounts of chloroform and dried *in vacuo* to give the target compound as a colorless solid (29 mg, 13 µmol, 60%).

^{1}H NMR (600 MHz, CD_3CN) δ 8.47 (dt, *J* = 8.3, 1.0 Hz, 3H), 8.45 (dt, *J* = 8.2, 1.2 Hz, 3H), 8.31 (dtd, *J* = 18.5, 7.7, 1.3 Hz, 6H), 8.21 (td, *J* = 7.9, 2.7 Hz, 3H), 8.07 (d, *J* = 4.9 Hz, 3H), 7.76 (ddd, *J* = 7.6, 5.3, 1.2 Hz, 3H), 7.70 (dt, *J* = 5.0, 2.3 Hz, 16H), 7.65 (s, 8H); **^{13}C{H} NMR** (126 MHz, CD_3CN) δ 162.4 (dd, *J* = 99.6, 49.8 Hz), 155.1 (d, *J* = 17.4 Hz), 151.9, 150.2, 149.6, 142.9, 142.2 (d, *J* = 14.5 Hz), 136.8 (d, *J* = 51.0 Hz), 135.5, 129.8 (qdd, *J* = 31.5, 5.7, 3.0 Hz), 128.6, 125.3 (q, *J* = 271.4 Hz), 124.6, 124.2, 118.5 (tt, *J* = 9.1, 4.9 Hz); **^{31}P{H} NMR** (121 MHz, CD_3CN) δ -50.86; **^{19}F NMR** (282 MHz, CD_3CN) δ -63.25; **^{11}B NMR** (96 MHz, CD_3CN) δ -6.66; **IR (ATR)** [cm^{-1}]: $\tilde{\nu}$ = 3089, 3048, 3021, 2966, 1605, 1446, 1354, 1271, 1110, 1039, 1016, 886, 839, 775, 745, 713, 682, 669, 634, 618, 580, 519; **HR-MS-ESI(+)** calc. $C_{62}H_{33}ZnN_6PBF_{24}^+$ $[M–BArF]^+$ 1423.1510; found 1423.1522.

Compound **243**

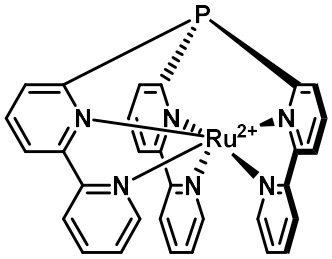

Under nitrogen atmosphere in a glovebox, an oven-dried Schlenk flask was equipped with a stirring bar and charged with $[Ru(DMSO)_4Cl_2]$ (111.2 mg, 229.60 µmol, 1.00 equiv.), $NaSbF_6$ (297.0 mg, 1.15 mmol, 5.00 equiv.) and preligand tri([2,2'-bipyridin]-6-yl)phosphane **212** (114.0 mg, 229.60 µmol, 1.00 equiv.). Dry degassed methanol (10 mL) was added under nitrogen and the reaction mixture was stirred under reflux for 3.5 days using a pre-heated oil bath. After cooling to room temperature, volatile compounds were evaporated under reduced pressure. Dry degassed DCM (20 mL) was added and the deep red suspension stirred for 4h. Afterwards, the reaction mixture was filtered and the residue further extracted with DCM. The combined organic extracts were concentrated *in vacuo* to give the target compound as a red solid (165.3 mg, 154.62 µmol, 67%) after flash-chromatography (neutral Al_2O_3, MeOH/DCM 1:10).

^{1}H NMR (400 MHz, CD_3CN) δ 8.61 (ddd, *J* = 8.2, 1.3, 0.7 Hz, 3H), 8.45 (ddd, *J* = 9.1, 7.5, 1.2 Hz, 3H), 8.37 (dt, *J* = 8.2, 1.3 Hz, 3H), 8.19 – 8.12 (m, 6H), 7.58 (ddd, *J* = 7.6, 5.7, 1.4 Hz, 3H), 6.89 (ddd, *J* = 5.7, 1.5, 0.8 Hz, 3H); **^{13}C{H} NMR** (126 MHz, CD_3CN) δ 159.1, 158.0, 151.3, 149.7 (d, *J* = 20.8 Hz), 139.0, 137.4 (d, *J* = 14.2 Hz), 135.5 (d, *J* = 49.1 Hz), 128.4, 125.9, 124.9; **^{31}P{H} NMR** (162 MHz, CD_3CN) δ 11.85; **^{19}F NMR** (376 MHz, CD_3CN) δ -123.88 (sext, J = 1932.3 Hz), -123.88 (oct, *J* = 1053.8 Hz); **IR (ATR)** [cm^{-1}]: $\tilde{\nu}$ = 3666, 3653, 3646, 3626, 3583, 3574, 3563, 3093, 2962, 2926, 2854, 1604, 1473, 1442, 1375, 1289, 1259, 1092, 1013, 806, 767, 745, 702, 650, 605, 554, 481, 457; **HR-MS-ESI(+)** calc. $C_{30}H_{21}RuN_6PF_6Sb^+$ $[M–SbF_6]^+$ 832.9555; found 832.9533.

Compound **244**

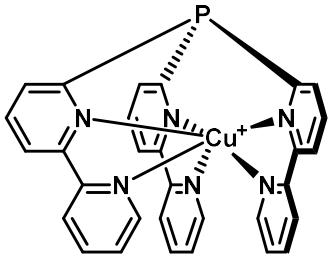

Under nitrogen atmosphere in a glovebox, an oven-dried Schlenk flask was equipped with a stirring bar and charged with tetrakis(acetonitrile)copper(I) tetrafluoroborate (30.1 mg, 95 mmol, 1.00 equiv.) and preligand tri([2,2'-bipyridin]-6-yl)phosphane **212** (50.0 mg, 100 µmol, 1.00 equiv.). Dry degassed THF was added under nitrogen and the reaction mixture was stirred for 18 h. The solvent was removed *in vacuo* and the residue washed with small amounts of THF. Afterwards, the orange/brown solid was dried *in vacuo* to give the target compound (41 mg, 67 µmol, 67%).

^{1}H NMR (300 MHz, CD_3CN) δ 8.83 (dt, *J* = 4.8, 1.4 Hz, 3H), 8.24 (dt, *J* = 8.5, 1.1 Hz, 3H), 8.04 – 7.97 (m, 3H), 7.91 (td, *J* = 7.7, 1.7 Hz, 3H), 7.78 (td, *J* = 7.9, 3.0 Hz, 3H), 7.49 (ddd, *J* = 7.5, 4.9, 1.2 Hz, 3H), 7.29 (dd, *J* = 7.8, 3.6 Hz, 3H); **^{13}C NMR** (101 MHz, CD_3CN) δ 156.6, 156.1, 155.7 (d, *J* = 11.2 Hz), 153.9, 150.7 (d, *J* = 1.8 Hz), 139.2, 131.1 (d, *J* = 20.4 Hz), 126.6, 123.1 (2C); **^{31}P{H} NMR** (203 MHz, CD_3CN) δ -4.63; **^{19}F NMR** (376 MHz, CD_3CN) δ -151.79, -151.84; **^{11}B NMR** (96 MHz, CD_3CN) δ -1.17; **IR (ATR)** [cm^{-1}]: $\tilde{\nu}$ = 6068, 2961, 1552, 1424, 1260, 1167, 1034, 1003, 906, 773, 618, 520; **HR-MS-ESI(+)** calc. $C_{30}H_{21}CuN_6P^+$ $[M–BF_4]^+$ 559.0856; found 559.0854.

Compound **245**

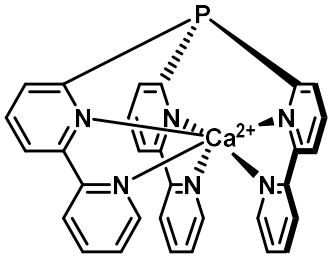

Under nitrogen atmosphere in a glovebox, an oven-dried Schlenk flask was equipped with a stirring bar and charged with the corresponding metal triflate $Ca(OTf)_2$ (64.9 mg, 191.81 µmol, 1.00 equiv.) and preligand tri([2,2'-bipyridin]-6-yl)phosphane **212** (100.0 mg, 201.40 µmol, 1.05 equiv.). Dry degassed THF (1 mL) was added under nitrogen and the reaction mixture was stirred under reflux for 18 h using a pre-heated oil bath. After cooling to room temperature, 4 mL of dry degassed toluene were added. The colorless precipitate was filtered off, washed with dry degassed pentane and dried *in vacuo* to give the target compound as a colorless solid (153.5 mg, 183.89 µmol, 96%).

^{1}H NMR (300 MHz, CD_3CN) δ 9.13 (dd, *J* = 5.2, 1.6 Hz, 3H), 8.34 – 8.23 (m, 6H), 8.20 (d, *J* = 8.5 Hz, 3H), 8.15 – 8.05 (m, 6H), 7.66 (ddd, *J* = 7.4, 5.2, 1.2 Hz, 3H); **^{13}C{H} NMR** (101 MHz, CD_3CN) δ 157.3 (d, *J* = 13.9 Hz), 156.7 (d, *J* = 1.4 Hz), 155.0, 151.8, 140.9, 140.9 (d, *J* = 16.6 Hz), 136.0 (d, *J* = 59.7 Hz), 126.6, 124.7, 124.2, 121.6 (q, *J* = 320.3 Hz); **^{31}P{H} NMR** (121 MHz, CD_3CN) δ -4.16; **^{19}F NMR** (282 MHz, CD_3CN) δ -79.43; **IR (ATR)** [cm^{-1}]: $\tilde{\nu}$ = 3073, 2116, 1556, 1484, 1434, 1252, 1157, 1028, 1004, 773, 629, 572, 516; **HR-MS-ESI(+)** calc. $C_{31}H_{21}CaN_6PF_3O_3S^+$ $[M–TfO]^+$ 685.0706; found 685.0706.

Compound **246**

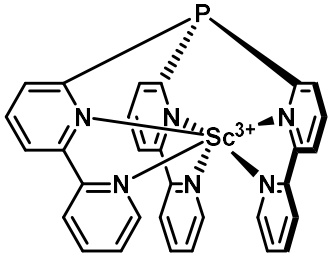

Under nitrogen atmosphere in a glovebox, an oven-dried Schlenk flask was equipped with a stirring bar and charged with the corresponding metal triflate $Sc(OTf)_3$ (94.4 mg, 191.81 µmol, 1.00 equiv.) and preligand tri([2,2'-bipyridin]-6-yl)phosphane **212** (100.0 mg, 201.40 µmol, 1.05 equiv.). Dry degassed THF (1 mL) was added under nitrogen and the reaction mixture was stirred under reflux for 18 h using a pre-heated oil bath. After cooling to room temperature, 4 mL of dry degassed toluene were added. The colorless precipitate was filtered off, washed with dry degassed pentane and dried *in vacuo* to give the target compound as a colorless solid (161.6 mg, 163.45 µmol, 85%).

^{1}H NMR (300 MHz, CD_3CN) δ 9.06 (d, *J* = 5.5 Hz, 3H), 8.57 – 8.31 (m, 15H), 7.97 (ddd, *J* = 7.2, 5.6, 1.3 Hz, 3H); **^{13}C{H} NMR** (101 MHz, CD_3CN) δ 156.3, 154.8 (d, *J* = 20.3 Hz), 153.4, 149.8, 144.8, 144.3 (d, *J* = 15.8 Hz), 138.0 (d, *J* = 54.9 Hz), 129.3, 126.0, 125.5, 121.3 (q, *J* = 320.0 Hz); **^{31}P{H} NMR** (162 MHz, CD_3CN) δ -17.63; **^{19}F NMR** (282 MHz, CD_3CN) δ -79.51; **IR (ATR)** [cm^{-1}]: $\tilde{\nu}$ = 3083, 1606, 1558, 1441, 1328, 1251, 1207, 1161, 1026, 776, 693, 633, 573, 515; **HR-MS-ESI(+)** calc. $C_{32}H_{21}ScN_6PF_6O_6S_2^+$ $[M–TfO]^+$ 839.0159; found 839.0149.

Compound **247**

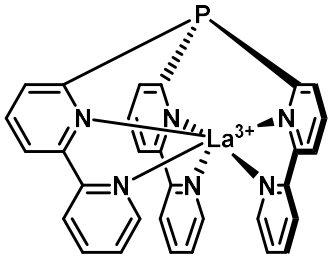

Under nitrogen atmosphere in a glovebox, an oven-dried Schlenk flask was equipped with a stirring bar and charged with the corresponding metal triflate $La(OTf)_3$ (112.4 mg, 191.81 µmol, 1.00 equiv.) and preligand tri([2,2'-bipyridin]-6-yl)phosphane **212** (100.0 mg, 201.40 µmol, 1.05 equiv.). Dry degassed THF (1 mL) was added under nitrogen and the reaction mixture was stirred under reflux for 18 h using a pre-heated oil bath. After cooling to room temperature, 4 mL of dry degassed toluene were added. The colorless precipitate was filtered off, washed with dry degassed pentane and dried *in vacuo* to give the target compound as a colorless solid (155.9 mg, 144.00 µmol, 75%).

^{1}H NMR (400 MHz, CD_3CN) δ 9.25 (d, *J* = 5.4 Hz, 3H), 8.47 – 8.32 (m, 6H), 8.29 – 8.18 (m, 6H), 8.18 – 8.10 (m, 3H), 7.76 – 7.57 (m, 3H); **^{13}C{H} NMR** (101 MHz, CD_3CN) δ 158.5, 155.7 (d, *J* = 17.1 Hz), 155.0, 151.5, 142.1 (d, *J* = 17.4 Hz), 141.6, 137.4 (d, *J* = 62.2 Hz), 127.0, 126.3, 125.2, 121.0 (q, *J* = 319.4 Hz); **^{31}P{H} NMR** (162 MHz, CD_3CN) δ 7.27; **^{19}F NMR** (377 MHz, CD_3CN) δ -79.38; **IR (ATR)** [cm^{-1}]: $\tilde{\nu}$ = 3088, 1588, 1490, 1435, 1305, 1210, 1159, 1025, 825, 776, 629, 581, 512; **HR-MS-ESI(+)** calc. $C_{32}H_{21}LaN_6PF_6O_6S_2^+$ $[M–TfO]^+$ 932.9664; found 932.9653.

Compound **247b**

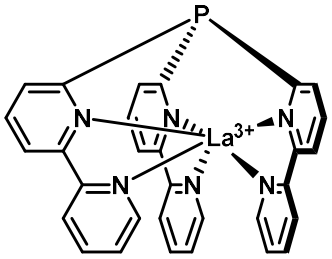

Under nitrogen atmosphere in a glovebox, an oven-dried Schlenk flask was equipped with a stirring bar and charged with compound **247** (20.0 mg, 18 µmol, 1.00 equiv.) and $NaBArF_{24}$ (Sodium tetrakis[3,5-bis(trifluoromethyl)phenyl]borate, 49.1 mg, 55 µmol, 3.00 equiv.). Dry degassed DCM (15 mL) was added under nitrogen. Afterwards, the suspension was stirred for 18 h, filtered, and the combined organic extracts concentrated *in vacuo*. The residue was then washed with small amounts of chloroform and dried *in vacuo* to give the target compound as a colorless solid (29 mg, 11 µmol, 60%).

^{1}H NMR (300 MHz, CD_3CN) δ 9.18 (dd, *J* = 5.5, 1.7 Hz, 3H), 8.45 – 8.34 (m, 6H), 8.29 – 8.21 (m, 6H), 8.18 (td, *J* = 7.8, 1.7 Hz, 3H), 7.77 – 7.67 (m, 27H), 7.66 (s, 12H); **^{13}C{H} NMR** (75 MHz, CD_3CN) δ 162.6 (dd, *J* = 99.8, 49.8 Hz), 158.3 (d, *J* = 5.2 Hz), 155.7 (d, *J* = 17.6 Hz), 154.9, 151.3, 142.5 (d, *J* = 17.3 Hz), 141.9, 137.5 (d, *J* = 61.8 Hz), 135.6, 129.9 (qdd, *J* = 31.5, 5.9, 2.9 Hz), 127.3, 126.4, 125.5, 125.4 (q, *J* = 271.7 Hz), 118.6 (tt, *J* = 8.0, 3.5 Hz); **^{31}P{H} NMR** (121 MHz, CD_3CN) δ 7.14; **^{19}F NMR** (282 MHz, CD_3CN) δ -63.21; **^{11}B NMR** (96 MHz, CD_3CN) δ -6.66; **IR (ATR)** [cm^{-1}]: $\tilde{\nu}$ = 2962, 2283, 1602, 1438, 1354, 1272, 1110, 1010, 932, 886, 839, 775, 713, 668, 633, 581, 519; **HR-MS-ESI(+)** calc. $C_{30}H_{21}N_6LaP^{2+}$ $[M–2BArF]^{2+}$ 749.0638; found 749.0625.

Compound **248**

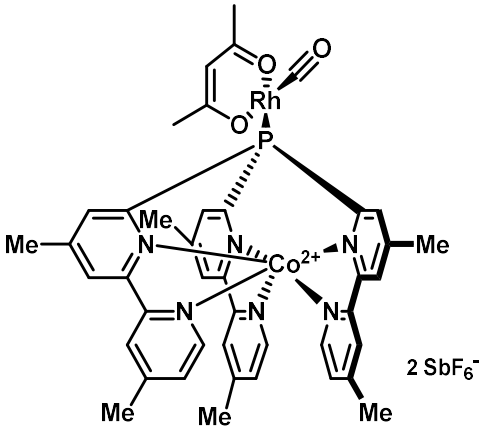

Under nitrogen atmosphere in a glovebox, an oven-dried Schlenk flask was equipped with a stirring bar and charged with [Rh(acac)(CO)$_2$] (12.2 mg, 47.25 µmol, 1.05 equiv.). Dry degassed DCM (1 mL) was added under nitrogen. Afterwards, a solution of phosphine ligand **240** (50.0 mg, 45.00 µmol, 1.00 equiv.) in 1 mL DCM was added dropwise to the reaction mixture. After the addition was complete, the reaction mixture was stirred for 1 h. All volatile compounds were evaporated under reduced pressure and the residue was washed with diethyl ether. Drying *in vacuo* gave the target compound as a yellow solid (59.5 mg, 44.37 µmol, 99%).

^{1}H NMR (400 MHz, CD_2Cl_2) δ 362.36 (s, 3H), 99.25 (s, 3H), 82.82 (s, 3H), 31.63 (s, 3H), 26.19 (s, 3H), 18.01 (s, 1H), 13.90 (s, 3H), 12.88 (s, 3H), 5.53 (s, 9H), 0.97 (s, 9H); **^{31}P{H} NMR** (162 MHz, CD_2Cl_2) δ 273.08 (d, *J* = 183.4 Hz); **^{19}F NMR** (377 MHz, CD_2Cl_2) δ -106.68 – -138.86 (m); **IR (ATR)** [cm^{-1}]: $\tilde{\nu}$ = 3085, 3072, 2971, 2924, 2857, 1985, 1618, 1604, 1574, 1521, 1495, 1435, 1383, 1299, 1274, 1251, 1164, 1014, 937, 879, 836, 735, 696, 653, 599, 544, 513, 465, 447, 414; **IR (DCM)** [cm^{-1}]: $\tilde{\nu}$ = 2001 (CO); **HR-MS-ESI(+)** calc. $C_{42}H_{40}CoF_6N_6PRhSb^+$ [M–SbF_6]$^+$ 1104.0223; found 1104.0222.

Compound **249**

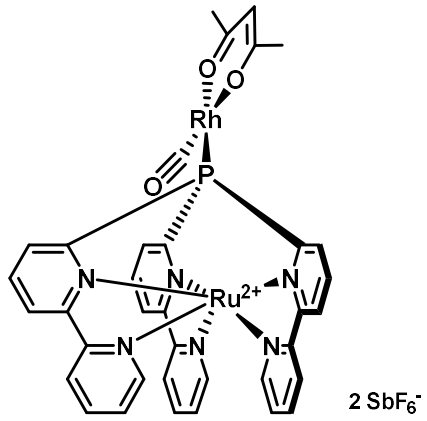

Under nitrogen atmosphere in a glovebox, an oven-dried Schlenk flask was equipped with a stirring bar and charged with [Rh(acac)(CO)$_2$] (2.5 mg, 9.82 µmol, 1.05 equiv.). Dry degassed DCM (1 mL) was added under nitrogen. Afterwards, a solution of phosphine ligand **243** (10.0 mg, 9.35 µmol, 1.00 equiv.) in 1 mL DCM was added dropwise to the reaction mixture. After the addition was complete, the reaction mixture was stirred for 1h. All volatile compounds were evaporated under reduced pressure and the residue was washed with diethyl ether. Drying *in vacuo* gave the target compound as a red solid (11.1 mg, 8.54 µmol, 91%).

^{1}H NMR (300 MHz, CD_2Cl_2) δ 9.44 (t, *J* = 8.0 Hz, 3H), 8.62 (d, *J* = 8.1 Hz, 3H), 8.41 (dt, *J* = 8.2, 1.6 Hz, 3H), 8.33 – 8.17 (m, 6H), 7.67 (ddd, *J* = 7.4, 5.7, 1.3 Hz, 3H), 6.86 (d, *J* = 5.7 Hz, 3H), 5.83 (s, 1H), 2.30 (s, 3H), 2.07 (s, 3H); **^{13}C{H} NMR** (101 MHz, CD_2Cl_2) δ 189.4, 187.1 (dd, *J* = 70.9, 27.4 Hz), 185.6, 158.6 (d, *J* = 4.5 Hz), 156.6, 150.9, 147.2 (dd, *J* = 50.2, 2.6 Hz), 139.4, 137.4 (d, *J* = 31.5 Hz), 137.4 (d, *J* = 11.8 Hz), 128.8, 125.8, 125.0, 102.1 (d, *J* = 2.6 Hz), 27.8 (d, *J* = 6.2 Hz), 27.1; **^{31}P{H} NMR** (162 MHz, CD_2Cl_2) δ 60.20 (d, *J* = 197.3 Hz); **^{19}F NMR** (376 MHz, CD_3CN) δ -123.40 (m); **IR (ATR)** [cm^{-1}]: $\tilde{\nu}$ = 3657, 3580, 3090, 2960, 2922, 2852, 1992, 1565, 1521, 1442, 1373, 1259, 1017, 954, 806, 768, 703, 652, 607, 592, 563, 506, 470, 446, 429; **IR (DCM)** [cm^{-1}]: $\tilde{\nu}$ = 2004 (CO); **HR-MS-ESI(+)** calc. $C_{36}H_{28}O_3RuN_6PF_6SbRh^+$ [M–SbF_6]$^+$ 1062.9007; found 1062.8990.

Compound **250**

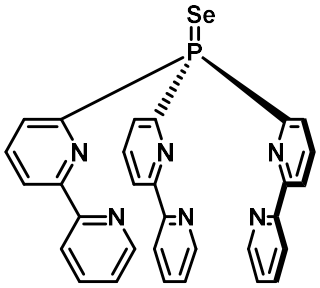

Under nitrogen atmosphere in a glovebox, an oven-dried Schlenk flask was equipped with a stirring bar and charged with preligand tris(4,4'-dimethyl-[2,2'-bipyridin]-6-yl)phosphane **212** (125 mg, 251.8 µmol, 1.00 equiv.) and gray selenium (39.76 mg, 503.5 µmol, 2.00 equiv.). Dry degassed toluene (10 mL) was added under nitrogen and the reaction mixture was stirred under reflux for 12h using a pre-heated oil bath. After cooling to room temperature, the solution was filtered and volatile compounds were evaporated under reduced pressure. The residue was dried *in vacuo* to give the target compound as a colorless solid (123.2 mg, 214.0 µmol, 85%).

^{1}H NMR (400 MHz, $CDCl_3$) δ 8.61 (dd, *J* = 4.8, 1.5 Hz, 3H), 8.52 (ddd, *J* = 8.0, 3.0, 1.2 Hz, 3H), 8.40 (ddd, *J* = 7.4, 6.0, 1.1 Hz, 3H), 8.06 (dt, *J* = 8.0, 1.2 Hz, 3H), 7.98 (td, *J* = 7.9, 4.8 Hz, 3H), 7.49 (td, *J* = 7.8, 1.8 Hz, 3H), 7.22 (ddd, *J* = 7.6, 4.8, 1.3 Hz, 3H); **^{13}C{H} NMR** (101 MHz, $CDCl_3$) δ 155.7 (d, *J* = 18.6 Hz), 155.4, 154.1 (d, *J* = 106.9 Hz), 149.1, 137.2 (d, *J* = 10.2 Hz), 136.9, 129.3 (d, *J* = 25.9 Hz), 124.2, 122.1 (d, *J* = 3.1 Hz), 121.6; **^{31}P{H} NMR** (162 MHz, CD_3CN) δ 29.96 (d, *J* = 753.0 Hz), 29.96; **^{31}P{H} NMR** (162 MHz, $CDCl_3$) δ 30.1 (d, *J* = 746.3 Hz), 30.1; **^{77}Se NMR** (76 MHz, $CDCl_3$) δ -307.90 (d, *J* = 746.4 Hz); **IR (ATR)** [cm^{-1}]: $\tilde{\nu}$ = 3048, 2962, 1588, 1574, 1550, 1476, 1446, 1422, 1382, 1258, 1070, 1013, 986, 924, 894, 865, 796, 785, 770, 739, 699, 691, 627, 615, 602, 557, 510; **HR-MS-ESI(+)** calc. $C_{30}H_{22}N_6PSe^+$ $[M+H]^+$ 577.0805; found 577.0807.

Compound **250x**

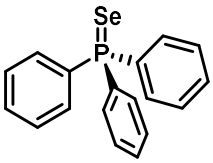

Under nitrogen atmosphere in a glovebox, an oven-dried Schlenk flask was equipped with a stirring bar and charged with triphenylphosphine (100 mg, 381 µmol, 1.00 equiv.) and gray selenium (60 mg, 762 µmol, 2.00 equiv.). Dry degassed toluene (10 mL) was added under nitrogen and the reaction mixture was stirred under reflux for 12 h using a pre-heated oil bath. After cooling to room temperature, the solution was filtered and volatile compounds were evaporated under reduced pressure. The residue was dried *in vacuo* to give the target compound as a colorless solid (90 mg, 267 µmol, 70%).

^{1}H NMR (400 MHz, CD_3CN) δ 7.75 – 7.67 (m, 7H), 7.61 – 7.55 (m, 3H), 7.54 – 7.47 (m, 7H); **^{13}C NMR** (101 MHz, CD_3CN) δ 133.4 (d, J = 10.7 Hz), 132.9 (d, J = 3.1 Hz), 132.8 (d, J = 77.2 Hz), 129.7 (d, J = 12.4 Hz); **^{31}P NMR** (162 MHz, CD_3CN) δ 35.03 (d, J = 736.7 Hz), 35.03; **^{77}Se NMR** (76 MHz, CD_3CN) δ -277.22 (d, J = 736.2 Hz). **IR (ATR)** [cm^{-1}]: $\tilde{\nu}$ = 3053, 2962, 1583, 1572, 1477, 1432, 1330, 1305, 1259, 1179, 1157, 1093, 1066, 1023, 996, 928, 865, 854, 797, 743, 710, 687, 618, 558, 500, 450, 428; **HR-MS-ESI(+)** calc. $C_{18}H_{16}PSe^+$ $[M+H]^+$ 343.0149; found 343.0150.

Analytical data are in accordance with those previously published in the literature.[271]

Compound **251**

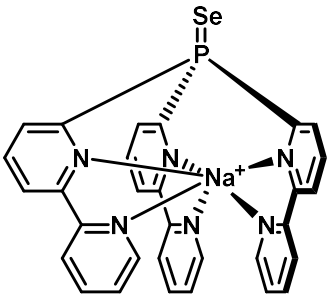

Procedure 1: Under nitrogen atmosphere in a glovebox, an oven-dried Schlenk flask was equipped with a stirring bar and charged with the $NaBArF_{24}$ (46.2 mg, 52.1 µmol, 1.00 equiv.) and tri([2,2'-bipyridin]-6-yl)phosphine selenide **250** (30.0 mg, 52.1 µmol, 1.00 equiv.). Dry degassed THF (3 mL) was added under nitrogen and the reaction mixture was stirred for 12 h. Afterwards, all volatile compounds were evaporated under reduced pressure. The colorless residue was washed with dry degassed diethyl ether

and pentane and dried *in vacuo* to give the target compound as a colorless solid (24.4 mg, 16.7 µmol, 32%).

Procedure 2: Under nitrogen atmosphere in a glovebox, an oven-dried Schlenk flask was equipped with a stirring bar and charged with the corresponding phosphine ligand **237z** (10.0 mg, 7.23 µmol, 1.00 equiv.) and gray selenium (2.9 mg, 36.16 µmol, 5.00 equiv.). Dry degassed chloroform (1 mL) was added under nitrogen and the reaction mixture was stirred under reflux for 4 days using a pre-heated oil bath. After cooling to room temperature, the solution was filtered and volatile compounds were evaporated under reduced pressure. The colorless residue was washed with dry degassed diethyl ether and dried *in vacuo* to give the target compound as a colorless solid (6.1 mg, 4.17 µmol, 58%).

^{1}H NMR (400 MHz, $CDCl_3$) δ 9.06 (t, *J* = 8.2 Hz, 3H), 8.84 (d, *J* = 5.0 Hz, 3H), 8.06 (td, *J* = 8.0, 4.4 Hz, 3H), 7.98 (dd, *J* = 8.1, 2.8 Hz, 3H), 7.86 (dd, *J* = 19.4, 7.8 Hz, 6H), 7.70 (p, *J* = 2.3 Hz, 8H), 7.46 (s, 4H), 7.42 (t, *J* = 6.4 Hz, 3H); **^{13}C{H} NMR** (101 MHz, CD_3CN) δ 162.6 (q, *J* = 49.9 Hz), 156.6 (d, *J* = 16.8 Hz), 155.5, 154.4 (d, *J* = 101.7 Hz), 150.9, 139.8 (d, *J* = 11.0 Hz), 139.1, 135.7, 130.7 (d, *J* = 27.3 Hz), 130.0 (qdd, *J* = 31.7, 5.6, 2.7 Hz), 126.0, 125.5 (d, *J* = 271.8 Hz), 124.6 (d, *J* = 3.0 Hz), 123.3, 118.7 (dt, *J* = 7.8, 3.8 Hz); **^{13}C NMR** (101 MHz, $CDCl_3$) δ 161.8 (dd, *J* = 99.7, 49.8 Hz), 155.3 (d, *J* = 14.8 Hz), 154.4, 153.2 (d, *J* = 97.1 Hz), 149.6, 139.1 (d, *J* = 12.0 Hz), 138.8, 134.9, 130.7 (d, *J* = 28.9 Hz), 129.1 (qdd, *J* = 31.6, 5.7, 2.5 Hz), 125.4, 124.6 (q, *J* = 272.6 Hz), 124.1, 123.2, 117.6 (p, *J* = 4.0 Hz); **^{31}P{H} NMR** (162 MHz, CD_3CN) δ 26.58, 26.57 (d, *J* = 769.1 Hz); **^{31}P{H} NMR** (162 MHz, $CDCl_3$) δ 23.68 (d, *J* = 785.4 Hz), 23.68; **^{19}F NMR** (377 MHz, CD_3CN) δ -63.28; **^{19}F NMR** (376 MHz, $CDCl_3$) δ -62.45; **^{11}B NMR** (128 MHz, CD_3CN) δ -6.66; **^{11}B NMR** (96 MHz, $CDCl_3$) δ -6.58; **^{77}Se NMR** (76 MHz, $CDCl_3$) δ -388.00 (d, *J* = 786.1 Hz); **IR (ATR)** [cm^{-1}]: $\tilde{\nu}$ = 2962, 1610, 1592, 1579, 1556, 1479, 1446, 1433, 1355, 1309, 1277, 1259, 1091, 1014, 928, 885, 838, 795, 775, 743, 712, 681, 669, 645, 623, 601, 579, 520, 473, 447, 432; **HR-MS-ESI(+)** calc. $C_{30}H_{21}NaN_6PSe^+$ $[M–BArF]^+$ 599.0625; found 599.0632.

Compound **252**

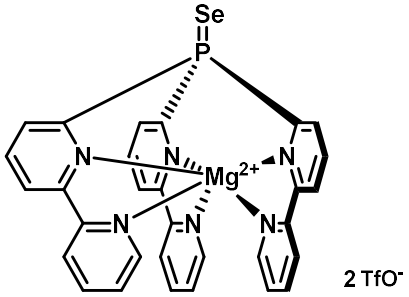

Procedure 1: Under nitrogen atmosphere in a glovebox, an oven-dried Schlenk flask was equipped with a stirring bar and charged with the corresponding metal triflate $Mg(OTf)_2$ (5.32 mg, 16.5 µmol, 0.95 equiv.) and tri([2,2'-bipyridin]-6-yl)phosphine selenide **250** (10.0 mg, 17.4 µmol, 1.00 equiv.). Dry degassed acetonitrile (3 mL) was added under nitrogen and the reaction mixture was stirred for 12 h. Afterwards, all volatile compounds were evaporated under reduced pressure. The colorless residue was washed with dry degassed diethyl ether and pentane and dried *in vacuo* to give the target compound as a colorless solid (8.6 mg, 9.6 µmol, 55%).

Procedure 2: : Under nitrogen atmosphere in a glovebox, an oven-dried Schlenk flask was equipped with a stirring bar and charged with the corresponding phosphine ligand **238** (10.0 mg, 12.21 µmol, 1.00 equiv.) and gray selenium (4.8 mg, 61.05 µmol, 5.00 equiv.). Dry degassed acetonitrile (1 mL) was added under nitrogen and the reaction mixture was stirred under reflux for 4 days using a pre-heated oil bath. After cooling to room temperature, the solution was filtered and volatile compounds were evaporated under reduced pressure. The colorless residue was washed with dry degassed diethyl ether and dried *in vacuo* to give the target compound as a colorless solid (8.3 mg, 9.24 µmol, 76%).

^{1}H NMR (400 MHz, CD_3CN) δ 8.93 (ddd, *J* = 10.0, 7.8, 1.0 Hz, 3H), 8.58 (ddd, *J* = 8.3, 2.4, 1.0 Hz, 3H), 8.53 (dt, *J* = 8.1, 1.0 Hz, 3H), 8.43 (td, *J* = 8.0, 4.0 Hz, 3H), 8.35 (td, *J* = 7.9, 1.6 Hz, 3H), 8.28 (ddd, *J* = 5.3, 1.6, 0.9 Hz, 3H), 7.82 (ddd, *J* = 7.6, 5.3, 1.2 Hz, 3H); **^{13}C{H} NMR** (101 MHz, CD_3CN) δ 154.0 (d, *J* = 11.1 Hz), 152.0, 151.1 (d, *J* = 91.2 Hz), 151.0, 143.6, 143.5 (d, *J* = 11.7 Hz), 132.6 (d, *J* = 24.3 Hz), 129.1, 125.7

(d, *J* = 2.7 Hz), 125.3, 122.0 (q, *J* = 320.8 Hz); **^{31}P{H} NMR** (162 MHz, CD_3CN) δ 10.98 (d, *J* = 842.5 Hz), 10.98; **^{31}P{H} NMR** (162 MHz, CD_2Cl_2) δ 10.89 (d, *J* = 852.7 Hz), 10.89; **^{19}F NMR** (376 MHz, CD_3CN) δ -79.34; **^{77}Se NMR** (76 MHz, CD_3CN) δ -487.86 (d, *J* = 842.6 Hz); **IR (ATR)** [cm^{-1}]: $\tilde{\nu}$ = 3094, 2962, 2252, 1666, 1605, 1590, 1576, 1556, 1488, 1455, 1439, 1393, 1244, 1224, 1153, 1115, 1095, 1057, 1027, 1014, 813, 778, 758, 695, 634, 617, 604, 582, 573, 516, 499, 433; **HR-MS-ESI(+)** calc. $C_{31}H_{21}MgN_6PF_3O_3SSe^+$ $[M–TfO]^+$ 749.0098; found 749.0102.

Compound **253**

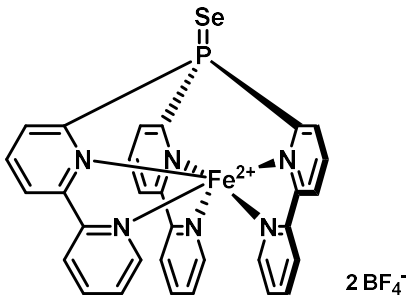

Under nitrogen atmosphere in a glovebox, an oven-dried Schlenk flask was equipped with a stirring bar and charged with hexaaquairon(II)tetrafluorborate (10.1 mg, 30.0 µmol, 0.95 equiv.) and tri([2,2'-bipyridin]-6-yl)phosphine selenide **250** (18.2 mg, 31.6 µmol, 1.00 equiv.). Dry degassed acetonitrile (3 mL) was added under nitrogen and the reaction mixture was stirred for 12 h. Afterwards, all volatile compounds were evaporated under reduced pressure. The red residue was washed with dry degassed diethyl ether and pentane and dried *in vacuo* to give the target compound as a red/violet solid (18.1 mg, 22.4 µmol, 71%).

IR (ATR) [cm^{-1}]: $\tilde{\nu}$ = 2962, 1774, 1637, 1603, 1591, 1575, 1554, 1488, 1454, 1438, 1390, 1307, 1253, 1168, 1010, 814, 776, 743, 695, 652, 635, 616, 604, 583, 521, 499, 482, 443, 427; **HR-MS-ESI(+)** calc. $C_{30}H_{21}FeN_6PSe^+$ $[M–2BF_4]^+$ 316.0036; found 316.0039.

Compound **254**

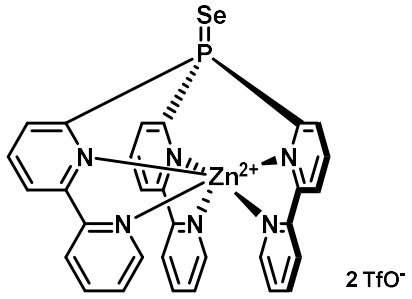

Procedure 1: Under nitrogen atmosphere in a glovebox, an oven-dried Schlenk flask was equipped with a stirring bar and charged with the corresponding metal triflate $Zn(OTf)_2$ (20.0 mg, 51.1 µmol, 1.00 equiv.) and tri([2,2'-bipyridin]-6-yl)phosphine selenide **250** (30.0 mg, 51.1 µmol, 1.00 equiv.). Dry degassed THF (3 mL) was added under nitrogen and the reaction mixture was stirred for 12 h. Afterwards, all volatile compounds were evaporated under reduced pressure. The colorless residue was washed with dry degassed diethyl ether and pentane and dried *in vacuo* to give the target compound as a colorless solid (31.3 mg, 22.5 µmol, 44%).

Procedure 2: : Under nitrogen atmosphere in a glovebox, an oven-dried Schlenk flask was equipped with a stirring bar and charged with the corresponding phosphine ligand **242** (10.0 mg, 11.63 µmol, 1.00 equiv.) and gray selenium (4.6 mg, 58.14 µmol, 5.00 equiv.). Dry degassed acetonitrile (1 mL) was added under nitrogen and the reaction mixture was stirred under reflux for 4 days using a pre-heated oil bath. After cooling to room temperature, the solution was filtered and volatile compounds were evaporated under reduced pressure. The colorless residue was washed with dry degassed diethyl ether and dried *in vacuo* to give the target compound as a colorless solid (5.8 mg, 6.18 µmol, 53%).

^{1}H NMR (400 MHz, CD_3CN) δ 8.91 (dd, *J* = 10.1, 7.7 Hz, 3H), 8.62 (dd, *J* = 8.2, 2.3 Hz, 3H), 8.58 (d, *J* = 8.1 Hz, 3H), 8.42 (td, *J* = 8.0, 3.9 Hz, 3H), 8.35 (td, *J* = 7.9, 1.6 Hz, 3H), 8.13 – 8.05 (m, 3H), 7.83 (dd, *J* = 7.7, 5.2 Hz, 3H); **^{13}C{H} NMR** (101 MHz, CD_3CN) δ 151.5 (d, *J* = 10.6 Hz), 150.6 (d, *J* = 91.6 Hz), 150.0, 149.8, 143.5, 143.4 (d, *J* = 11.7 Hz), 132.7 (d, *J* = 23.5 Hz), 129.3, 125.5 (d, *J* = 2.8 Hz), 125.4 (TfO^- missing); **^{31}P{H} NMR** (162 MHz, CD_3CN) δ 4.17, 4.17 (d, *J* = 842.9 Hz); **^{31}P{H} NMR** (162 MHz, CD_2Cl_2) δ 3.96 (d, *J* = 852.9 Hz), 3.96; **^{19}F NMR** (376 MHz, CD_3CN) δ -79.25; **^{77}Se NMR** (76 MHz, CD_3CN) δ -502.42 (d, *J* = 843.7 Hz); **IR (ATR)** [cm^{-1}]: $\tilde{\nu}$ = 3075, 2962, 1604, 1589, 1556, 1487, 1439, 1257, 1223, 1140, 1087,

1057, 1012, 865, 779, 696, 662, 652, 634, 614, 604, 572, 516, 497, 483, 457, 446; **HR-MS-ESI(+)** calc. $C_{31}H_{21}CaN_6PF_3O_3SSe^+$ $[M–TfO]^+$ 788.9534; found 788.9516.

Compound **255**

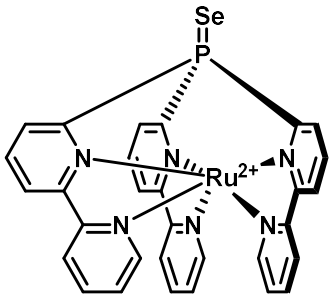

Under nitrogen atmosphere in a glovebox, an oven-dried Schlenk flask was equipped with a stirring bar and charged with the corresponding phosphine ligand **243** (10.0 mg, 9.35 µmol, 1.00 equiv.) and gray selenium (3.7 mg, 46.77 µmol, 5.00 equiv.). Dry degassed acetonitrile (1 mL) was added under nitrogen and the reaction mixture was stirred under reflux for 8 days using a pre-heated oil bath. After cooling to room temperature, the solution was filtered and volatile compounds were evaporated under reduced pressure. The colorless residue was washed with dry degassed diethyl ether and dried *in vacuo* to give the target compound as a colorless solid (8.0 mg, 6.97 µmol, 75%).

^{1}H NMR (400 MHz, CD_3CN) δ 8.78 (t, *J* = 8.4 Hz, 3H), 8.66 (d, *J* = 8.1 Hz, 3H), 8.48 (dd, *J* = 8.1, 2.2 Hz, 3H), 8.34 (td, *J* = 7.9, 3.8 Hz, 3H), 8.21 (t, *J* = 7.8 Hz, 3H), 7.62 (t, *J* = 6.7 Hz, 3H), 6.86 (d, *J* = 5.7 Hz, 3H); **^{13}C{H} NMR** (101 MHz, CD_3CN) δ 159.9 (d, *J* = 8.6 Hz), 157.1, 151.7, 145.3 (d, *J* = 95.3 Hz), 139.8, 138.9 (d, *J* = 11.4 Hz), 133.3 (d, *J* = 23.6 Hz), 129.2, 126.4, 126.2 (d, *J* = 2.6 Hz); **^{31}P{H} NMR** (162 MHz, CD_3CN) δ 28.70, 28.70 (d, *J* = 851.7 Hz); **^{31}P{H} NMR** (162 MHz, CD_2Cl_2) δ 28.71 (d, *J* = 866.4 Hz), 28.71; **^{19}F NMR** (377 MHz, CD_3CN) δ -123.96 (sext, *J* = 1937.1 Hz), -123.96 (oct, *J* = 1050.0 Hz); **^{77}Se NMR** (76 MHz, CD_3CN) δ -472.85 (d, *J* = 851.9 Hz); **IR (ATR)** [cm^{-1}]: $\tilde{\nu}$ = 3089, 2961, 2925, 2855, 1604, 1442, 1377, 1294, 1258, 1147, 1025, 953, 810, 768, 703, 650, 603, 576, 495, 431; **HR-MS-ESI(+)** calc. $C_{30}H_{21}RuN_6PF_6SbSe^+$ $[M–SbF_6]^+$ 912.8727; found 912.8731.

Compound **256**

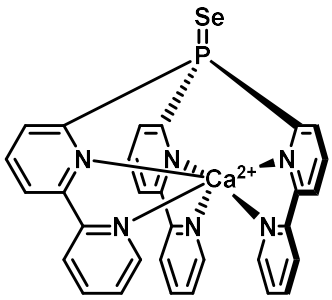

Procedure 1: Under nitrogen atmosphere in a glovebox, an oven-dried Schlenk flask was equipped with a stirring bar and charged with the corresponding metal triflate $Ca(OTf)_2$ (5.58 mg, 16.51 µmol, 0.95 equiv.) and tri([2,2'-bipyridin]-6-yl)phosphine selenide **250** (10.0 mg, 17.4 µmol, 1.00 equiv.). Dry degassed acetonitrile (3 mL) was added under nitrogen and the reaction mixture was stirred for 12 h. Afterwards, all volatile compounds were evaporated under reduced pressure. The colorless residue was washed with dry degassed diethyl ether and pentane and dried *in vacuo* to give the target compound as a colorless solid (7.0 mg, 7.26 µmol, 44%).

Procedure 2: : Under nitrogen atmosphere in a glovebox, an oven-dried Schlenk flask was equipped with a stirring bar and charged with the corresponding phosphine ligand **245** (10.0 mg, 11.98 µmol, 1.00 equiv.) and gray selenium (4.7 mg, 59.90 µmol, 5.00 equiv.). Dry degassed acetonitrile (1 mL) was added under nitrogen and the reaction mixture was stirred under reflux for 4 days using a pre-heated oil bath. After cooling to room temperature, the solution was filtered and volatile compounds were evaporated under reduced pressure. The colorless residue was washed with dry degassed diethyl ether and dried *in vacuo* to give the target compound as a colorless solid (9.8 mg, 10.73 µmol, 90%).

^{1}H NMR (400 MHz, CD_3CN) δ 9.19 – 9.12 (m, 6H), 8.39 (ddd, *J* = 8.2, 2.8, 1.1 Hz, 3H), 8.29 (td, *J* = 8.0, 4.2 Hz, 3H), 8.24 (dt, *J* = 8.0, 1.0 Hz, 3H), 8.12 (td, *J* = 7.8, 1.7 Hz, 3H), 7.70 (ddd, *J* = 7.5, 5.2, 1.1 Hz, 3H); **^{13}C{H} NMR** (101 MHz, CD_3CN) δ 156.1 (d, *J* = 13.8 Hz), 154.3, 152.3 (d, *J* = 93.8 Hz), 151.8, 141.6 (d, *J* = 11.9 Hz), 141.2, 132.9 (d, *J* = 27.6 Hz), 127.0, 126.4 (d, *J* = 2.9 Hz), 124.8, 121.3 (q, *J* = 318.7 Hz); **^{31}P{H} NMR** (162 MHz, CD_3CN) δ 24.96 (d, *J* = 800.2 Hz), 24.95; **^{19}F NMR** (376 MHz, CD_3CN) δ -79.35; **^{77}Se NMR**

(76 MHz, CD_3CN) δ -359.6 (d, *J* = 800.9 Hz); **IR (ATR)** [cm^{-1}]: $\tilde{\nu}$ = 2962, 1432, 1257, 1150, 1084, 1057, 1007, 865, 787, 689, 662, 635, 628, 619, 575, 561, 513, 500, 478, 465, 444, 430, 408; **HR-MS-ESI(+)** calc. $C_{31}H_{21}CaN_6PF_3O_3SSe^+$ $[M–TfO]^+$ 764.9873; found 764.9873.

Compound **257**

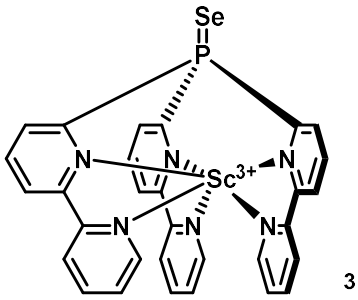

Under nitrogen atmosphere in a glovebox, an oven-dried Schlenk flask was equipped with a stirring bar and charged with the corresponding metal triflate $Sc(OTf)_3$ (16.25 mg, 33.02 µmol, 0.95 equiv.) and tri([2,2'-bipyridin]-6-yl)phosphine selenide **250** (20.0 mg, 34.8 µmol, 1.00 equiv.). Dry degassed THF (3 mL) was added under nitrogen and the reaction mixture was stirred for 12 h. Afterwards, all volatile compounds were evaporated under reduced pressure. The colorless residue was washed with dry degassed diethyl ether and pentane and dried *in vacuo* to give the target compound as a colorless solid (10.60 mg, 10.1 µmol, 29%).

^{1}H NMR (400 MHz, CD_3CN) δ 8.74 – 8.54 (m, 12H), 8.47 (dd, *J* = 7.9, 3.4 Hz, 3H), 8.32 (dq, *J* = 8.0, 4.0 Hz, 3H), 8.03 (dt, *J* = 9.5, 5.3 Hz, 3H); **^{13}C{H} NMR** (101 MHz, CD_3CN) δ 155.1 (d, *J* = 103.9 Hz), 149.3, 147.9, 147.6 (d, *J* = 18.4 Hz), 143.3, 141.0 (d, *J* = 9.7 Hz), 133.8 (d, *J* = 24.9 Hz), 128.8, 126.0, 125.9 (d, *J* = 2.9 Hz), 121.3 (q, *J* = 318.4 Hz); **^{31}P{H} NMR** (162 MHz, CD_3CN) δ 29.72, 29.72 (d, *J* = 782.7 Hz); **^{19}F NMR** (282 MHz, CD_3CN) δ -79.23; **IR (ATR)** [cm^{-1}]: $\tilde{\nu}$ = 3103, 2962, 2252, 1624, 1608, 1579, 1561, 1535, 1444, 1401, 1257, 1223, 1159, 1076, 1009, 864, 782, 687, 661, 637, 573; **HR-MS-ESI(+)** calc. $C_{32}H_{21}ScN_6PF_6O_3S_2Se^+$ $[M–TfO]^+$ 918.9326; found 918.9317.

Compound **258**

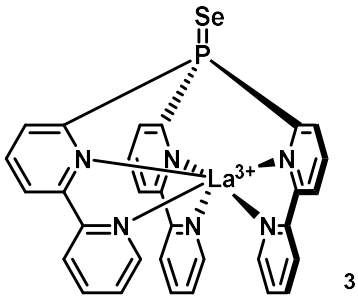

Procedure 1: Under nitrogen atmosphere in a glovebox, an oven-dried Schlenk flask was equipped with a stirring bar and charged with the corresponding metal triflate $La(OTf)_3$ (10.2 mg, 17.4 µmol, 1.00 equiv.) and tri([2,2'-bipyridin]-6-yl)phosphine selenide **250** (10.0 mg, 17.4 µmol, 1.00 equiv.). Dry degassed THF (3 mL) was added under nitrogen and the reaction mixture was stirred for 12 h. Afterwards, all volatile compounds were evaporated under reduced pressure. The colorless residue was washed with dry degassed diethyl ether and pentane and dried *in vacuo* to give the target compound as a colorless solid (16.6 mg, 14.3 µmol, 82%).

Procedure 2: : Under nitrogen atmosphere in a glovebox, an oven-dried Schlenk flask was equipped with a stirring bar and charged with the corresponding phosphine ligand **247** (10.0 mg, 9.24 µmol, 1.00 equiv.) and gray selenium (3.7 mg, 46.18 µmol, 5.00 equiv.). Dry degassed acetonitrile (1 mL) was added under nitrogen and the reaction mixture was stirred under reflux for 4 days using a pre-heated oil bath. After cooling to room temperature, the solution was filtered and volatile compounds were evaporated under reduced pressure. The colorless residue was washed with dry degassed diethyl ether and dried *in vacuo* to give the target compound as a colorless solid (9.4 mg, 8.09 µmol, 88%).

^{1}H NMR (400 MHz, CD_3CN) δ 9.25 – 9.13 (m, 6H), 8.45 (dd, *J* = 8.0, 2.0 Hz, 3H), 8.37 (td, *J* = 8.0, 3.8 Hz, 3H), 8.25 (d, *J* = 8.1 Hz, 3H), 8.17 (td, *J* = 7.9, 1.7 Hz, 3H), 7.69 (dd, *J* = 7.4, 5.6 Hz, 3H); **^{1}H NMR** (400 MHz, CD_2Cl_2) δ 9.43 (dd, *J* = 5.2, 1.4 Hz, 3H), 9.29 (ddd, *J* = 10.4, 7.3, 1.7 Hz, 3H), 8.33 – 8.18 (m, 6H), 8.13 – 7.97 (m, 6H), 7.65 (ddd, *J* = 7.1, 5.3, 2.1 Hz, 3H); **^{13}C{H} NMR** (101 MHz, CD_3CN) δ 157.7 (d, *J* = 13.3 Hz), 154.5, 151.6 (d, *J* = 91.4 Hz), 151.5, 142.9 (d, *J* = 11.9 Hz), 141.8, 134.3 (d, *J* = 27.1 Hz), 128.2 (d, *J* = 2.4 Hz), 127.2, 125.9, 121.0 (q, *J* = 319.1 Hz); **^{31}P{H} NMR** (162 MHz, CD_3CN) δ 35.83 (d, *J* = 817.7

Hz), 35.83; **^{31}P{H} NMR** (162 MHz, CD_2Cl_2) δ 35.97 (d, *J* = 815.4 Hz), 35.97; **^{19}F NMR** (376 MHz, CD_3CN) δ -79.25; **^{19}F NMR** (376 MHz, CD_2Cl_2) δ -78.00, -79.04; **^{77}Se NMR** (76 MHz, CD_3CN) δ -309.69 (d, *J* = 816.1 Hz); **^{77}Se NMR** (76 MHz, CD_2Cl_2) δ -300.43 (d, *J* = 815.9 Hz); **IR (ATR)** [cm^{-1}]: $\tilde{\nu}$ = 2962, 1599, 1585, 1554, 1431, 1315, 1305, 1258, 1232, 1201, 1180, 1168, 1085, 1011, 865, 795, 782, 773, 690, 661, 631, 606, 572, 513; **HR-MS-ESI(+)** calc. $C_{32}H_{21}LaN_6PF_6O_3S_2Se^+$ $[M–TfO]^+$ 1012.8830; found 1012.8817.

Compound **266**

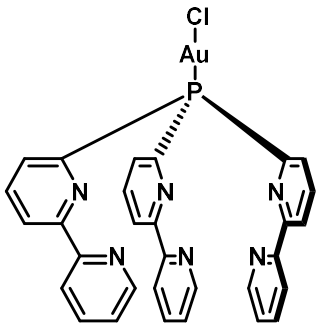

Under nitrogen atmosphere in a glovebox, an oven-dried Schlenk flask was equipped with a stirring bar and charged with tri([2,2'-bipyridin]-6-yl)phosphane **212** (100 mg, 210 mmol, 1.00 equiv.). Dry degassed DCM (10 mL) was added under nitrogen. Afterwards, a solution of chloro(dimethylsulfide)gold(I) (59.3 mg, 210 mmol, 1.00 equiv.) in 10 mL DCM was added to the reaction mixture at -20 °C. After the addition was complete, the reaction mixture was stirred for 2h at room temperature. The reaction mixture was filtered and all volatile compounds were evaporated under reduced pressure. The residue was further dried *in vacuo* give the target compound as a colorless solid (122 mg, 174 mmol, 83%).

^{1}H NMR (300 MHz, $CDCl_3$) δ 8.61 (dd, *J* = 4.9, 1.7 Hz, 3H), 8.53 (ddt, *J* = 7.8, 2.4, 1.0 Hz, 3H), 8.18 (dd, *J* = 8.0, 1.2 Hz, 3H), 8.02 – 7.83 (m, 6H), 7.65 (td, *J* = 7.8, 1.8 Hz, 3H), 7.26 (dd, *J* = 7.7, 5.1 Hz, 3H); **^{13}C{H} NMR** (75 MHz, $CDCl_3$) δ 157.2 (d, *J* = 17.2 Hz), 154.8, 152.4 (d, *J* = 87.1 Hz), 149.2, 137.5 (d, *J* = 9.4 Hz), 137.3, 130.9 (d, *J* = 27.0 Hz), 124.5, 122.7 (d, *J* = 2.5 Hz), 121.6; **^{31}P{H} NMR** (162 MHz, $CDCl_3$) δ 32.82; **IR (ATR)** [cm^{-1}]: $\tilde{\nu}$ = 3053, 3007, 2922, 2855, 1576, 1550, 1472, 1446, 1421, 1260, 1147, 1075, 1033, 986, 822, 771, 732, 699, 617, 539, 505; **HR-MS-ESI(+)** calc. $C_{30}H_{22}N_6PAuCl^+$ $[M+H]^+$ 729.0992; found 729.0984.

Compound **267**

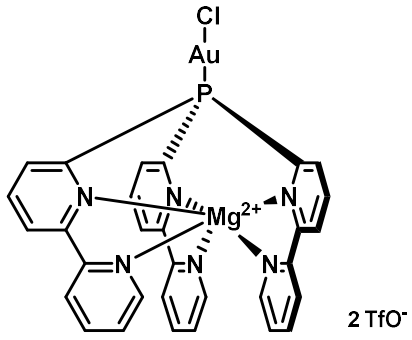

Under nitrogen atmosphere in a glovebox, an oven-dried Schlenk flask was equipped with a stirring bar and charged with phosphine ligand **238** (53.0 mg, 64.72 µmol, 1.00 equiv.). Dry degassed DCM (1 mL) was added under nitrogen. Afterwards, a solution of chloro(dimethylsulfide)gold(I) (10.06 mg, 64.72 µmol, 1.00 equiv.) in 1 mL DCM was added to the reaction mixture at 0 °C. After the addition was complete, the reaction mixture was stirred for 1 h at room temperature. The reaction mixture was filtered and all volatile compounds were evaporated under reduced pressure. The residue was washed with diethyl ether and dried *in vacuo* give the target compound as a colorless solid (64.7 mg, 61.54 µmol, 95%).

^{1}H NMR (300 MHz, CD_3CN) δ 8.72 (ddd, *J* = 11.5, 7.6, 1.0 Hz, 3H), 8.57 (ddd, *J* = 8.4, 2.3, 1.0 Hz, 3H), 8.51 (dt, *J* = 8.0, 1.0 Hz, 3H), 8.46 – 8.24 (m, 9H), 7.82 (ddd, *J* = 7.5, 5.4, 1.2 Hz, 3H); **^{13}C{H} NMR** (101 MHz, CD_3CN) δ 155.4 (d, *J* = 8.6 Hz), 151.9, 151.0, 150.0 (d, *J* = 72.6 Hz), 143.5, 143.2 (d, *J* = 13.7 Hz), 137.6 (d, *J* = 35.6 Hz), 129.1, 126.2 (d, *J* = 2.4 Hz), 125.2, 122.0 (q, *J* = 320.3 Hz); **^{31}P{H} NMR** (121 MHz, CD_3CN) δ 15.72; **^{19}F NMR** (282 MHz, CD_3CN) δ -79.33; **IR (ATR)** [cm^{-1}]: $\tilde{\nu}$ = 3472, 3078, 3061, 3011, 1604, 1591, 1556, 1489, 1438, 1395, 1255, 1225, 1197, 1145, 1085, 1028, 1014, 817, 776, 755, 732, 701, 653, 634, 618, 597, 572, 516, 435, 408; **HR-MS-ESI(+)** calc. $C_{31}H_{21}MgN_6PF_3O_3SAuCl^+$ $[M–TfO]^+$ 901.0285; found 901.0275.

Compound **268**

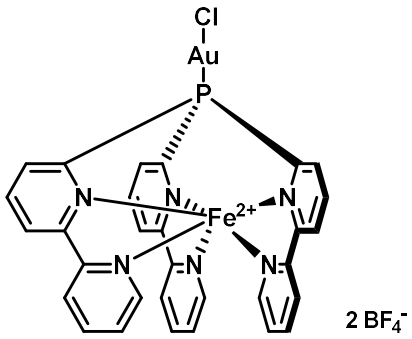

Procedure 1: Under nitrogen atmosphere in a glovebox, an oven-dried Schlenk flask was equipped with a stirring bar and charged with chloro(dimethylsulfide)gold(I) (3.6 mg, 12 µmol, 1.00 equiv.). Dry degassed DCM (1 mL) was added under nitrogen. Afterwards, a solution of phosphine ligand **239** (8.8 mg, 12 µmol, 1.00 equiv.) in 1 mL DCM was added to the reaction mixture at -15 °C. After the addition was complete, the reaction mixture was stirred for 1 h at room temperature. The reaction mixture was filtered and all volatile compounds were evaporated under reduced pressure. The residue was washed with diethyl ether and dried *in vacuo* give the target compound as a red/violet solid (9.5 mg, 12 µmol, quant.).

Procedure 2: Under nitrogen atmosphere in a glovebox, an oven-dried Schlenk flask was equipped with a stirring bar and charged with hexaaquairon(II)tetrafluorborate (35.2 mg, 109.8 µmol, 1.00 equiv.) and tri([2,2'-bipyridin]-6-yl)phosphinegold(I) chloride **266** (80.00 mg, 109.8 µmol, 1.00 equiv.). Dry degassed acetonitrile (3 mL) was added under nitrogen and the reaction mixture was stirred for 12 h. Afterwards, all volatile compounds were evaporated under reduced pressure. The red/violet residue was washed with dry degassed diethyl ether and pentane and dried *in vacuo* to give the target compound as a red/violet solid (64.9 mg, 68.1 µmol, 62%).

^{1}H NMR (500 MHz, CD_3CN, 238K) δ 12.42 – 7.81 (m, 5H), 7.54 (s, 1H), 6.13 (s, 1H); **^{13}C NMR** (126 MHz, CD_3CN, 238K) δ 162.4, 158.5, 154.4, 151.9, 140.3, 138.7, 135.5, 128.2, 126.2, 124.7; **^{31}P NMR** (203 MHz, CD_3CN, 238K) δ 23.58; **^{19}F NMR** (471 MHz, CD_3CN, 238K) δ -150.66, -150.71; **IR (ATR)** [cm^{-1}]: $\tilde{\nu}$ = 3081, 1600, 1440, 1378, 1284, 1242, 1025, 812, 777, 699, 598, 563, 515, 435; **HR-MS-ESI(+)** calc. $C_{30}H_{21}FeN_6PBF_4AuCl^+$ $[M–BF_4]^+$ 871.0299; found 871.0284.

Compound **269**

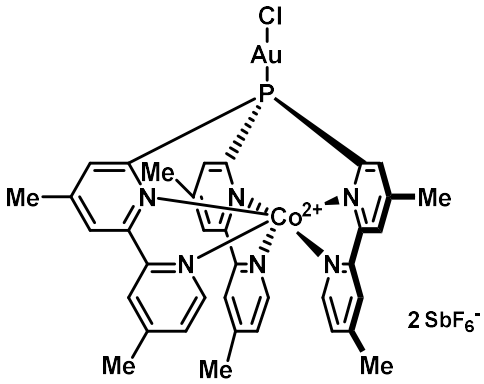

Under nitrogen atmosphere in a glovebox, an oven-dried Schlenk flask was equipped with a stirring bar and charged with phosphine ligand **240** (26.0 mg, 23.40 µmol, 1.00 equiv.). Dry degassed DCM (1 mL) was added under nitrogen. Afterwards, a solution of chloro(dimethylsulfide)gold(I) (6.9 mg, 23.40 µmol, 1.00 equiv.) in 1 mL DCM was added to the reaction mixture at 0 °C. After the addition was complete, the reaction mixture was stirred for 1 h at room temperature. The reaction mixture was filtered and all volatile compounds were evaporated under reduced pressure. The residue was washed with diethyl ether and dried *in vacuo* give the target compound as a yellow solid (31.0 mg, 23.07 µmol, 99%).

^{1}H NMR (400 MHz, CD_3CN) δ 369.00 (s, 3H), 95.89 (s, 3H), 82.64 (s, 3H), 31.51 (s, 3H), 26.46 (s, 3H), 4.40 (s, 9H), 1.42 (s, 9H); **^{31}P{H} NMR** (162 MHz, CD_3CN) δ 251.78; **^{19}F NMR** (376 MHz, CD_3CN) δ -124.15 (sext, *J* = 1934.2 Hz), -124.15 (oct, *J* = 1049.4 Hz); **IR (ATR)** [cm^{-1}]: $\tilde{\nu}$ = 3068, 2987, 2963, 2925, 2852, 1617, 1600, 1544, 1486, 1444, 1414, 1397, 1299, 1252, 1168, 1132, 1012, 935, 872, 839, 734, 702, 687, 650, 603, 547, 515, 472, 456, 432, 412; **HR-MS-ESI(+)** calc. $C_{36}H_{33}CoF_6N_6PAuClSb^+$ $[M–SbF_6]^+$ 1108.0126; found 1108.0120.

Compound **270**

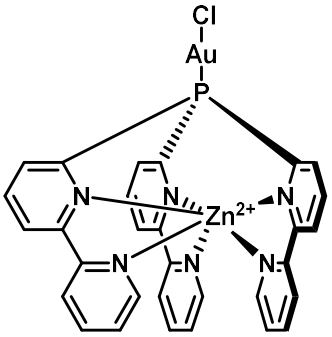

Procedure 1: Under nitrogen atmosphere in a glovebox, an oven-dried Schlenk flask was equipped with a stirring bar and charged with phosphine ligand **242** (54.4 mg, 63.25 µmol, 1.00 equiv.). Dry degassed DCM (1 mL) was added under nitrogen. Afterwards, a solution of chloro(dimethylsulfide)gold(I) (18.6 mg, 63.25 µmol, 1.00 equiv.) in 1 mL DCM was added to the reaction mixture at 0 °C. After the addition was complete, the reaction mixture was stirred for 1 h at room temperature. The reaction mixture was filtered and all volatile compounds were evaporated under reduced pressure. The residue was washed with diethyl ether and dried *in vacuo* give the target compound as a yellow solid (62.5 mg, 57.21 µmol, 90%).

Procedure 2: Under nitrogen atmosphere in a glovebox, an oven-dried Schlenk flask was equipped with a stirring bar and charged with the corresponding metal triflate $Zn(OTf)_2$ (29.9mg, 82.3µmol, 1.00 equiv.) and tri([2,2'-bipyridin]-6-yl)phosphinegold(I) chloride **266** (60 mg, 82.3 µmol, 1.00 equiv.). Dry degassed THF (3 mL) was added under nitrogen and the reaction mixture was stirred for 12 h. Afterwards, all volatile compounds were evaporated under reduced pressure. The colorless residue was washed with dry degassed diethyl ether and pentane and dried *in vacuo* to give the target compound as a colorless solid (72.5 mg, 66.7 µmol, 81%).

^{1}H NMR (300 MHz, CD_3CN) δ 8.70 (dd, *J* = 11.5, 7.6 Hz, 3H), 8.61 (dd, *J* = 8.2, 2.2 Hz, 3H), 8.55 (d, *J* = 8.0 Hz, 3H), 8.45 – 8.30 (m, 6H), 8.11 (d, *J* = 5.3 Hz, 3H), 7.83 (dd, *J* = 7.4, 5.6 Hz, 3H); **^{13}C{H} NMR** (101 MHz, CD_3CN) δ 153.0 (d, *J* = 8.2 Hz), 150.1, 149.7, 149.3 (d, *J* = 73.2 Hz), 143.5, 143.0 (d, *J* = 13.5 Hz), 137.7 (d, *J* = 34.5 Hz), 129.3, 126.1 (d, *J* = 2.5 Hz), 125.3, 122.2 (d, *J* = 321.3 Hz); **^{31}P{H} NMR** (121 MHz, CD_3CN) δ 5.21; **^{19}F NMR** (282 MHz, CD_3CN) δ -79.29; **IR (ATR)** [cm^{-1}]: $\tilde{\nu}$ = 3080, 2962, 2855, 1604, 1578, 1557, 1489, 1455, 1439, 1394, 1254, 1225, 1197, 1166, 1094, 1058, 1026, 1013, 902, 866, 781, 757, 695, 651, 635, 617, 597, 571, 515, 499, 463, 446, 432; **HR-MS-ESI(+)** calc. $C_{31}H_{21}ZnN_6PF_3O_3SAuCl^+$ [M–TfO]$^+$ 940.9726; found 940.9720.

Compound **270b**

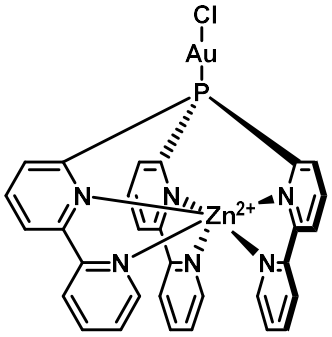

Under nitrogen atmosphere in a glovebox, an oven-dried Schlenk flask was equipped with a stirring bar and charged with phosphine ligand **242b** (28.7 mg, 13 µmol, 1.00 equiv.). Dry degassed DCM (1 mL) was added under nitrogen. Afterwards, a solution of chloro(dimethylsulfide)gold(I) (3.7 mg, 13 µmol, 1.00 equiv.) in 1 mL DCM was added to the reaction mixture at -15 °C. After the addition was complete, the reaction mixture was stirred for 1 h at room temperature. The reaction mixture was filtered and all volatile compounds were evaporated under reduced pressure. The residue was washed with diethyl ether and dried *in vacuo* give the target compound as a colorless solid (10.9 mg, 4 µmol, 34%).

^{1}H NMR (300 MHz, CD_3CN) δ 8.72 (dd, *J* = 11.4, 7.6 Hz, 3H), 8.61 – 8.55 (m, 3H), 8.52 (d, *J* = 8.1 Hz, 3H), 8.43 – 8.30 (m, 6H), 8.09 (d, *J* = 5.3 Hz, 3H), 7.81 (ddd, *J* = 7.7, 5.3, 1.2 Hz, 3H), 7.69 (p, *J* = 2.2 Hz, 16H), 7.65 (s, 8H); **^{13}C{H} NMR** (75 MHz, CD_3CN) δ 162.6 (dd, *J* = 99.8, 49.7 Hz), 152.9 (d, *J* = 8.5 Hz), 150.0, 149.7, 149.3 (d, *J* = 72.6 Hz), 143.5, 143.1 (d, *J* = 13.5 Hz), 137.8 (d, *J* = 34.5 Hz), 135.6, 129.9 (qdd, *J* = 31.8, 5.7, 2.7 Hz), 129.3, 126.1 (d, *J* = 2.5 Hz), 125.5 (q, *J* = 271.8 Hz), 125.3, 118.7 (dt, *J* = 8.1, 3.9 Hz); **^{31}P{H} NMR** (121 MHz, CD_3CN) δ 5.13; **^{19}F NMR** (282 MHz, CD_3CN) δ -63.20; **^{11}B NMR** (96 MHz, CD_3CN)

δ -6.67; **IR (ATR)** [cm^{-1}]: $\tilde{\nu}$ = 3090, 2966, 1606, 1354, 1274, 1115, 887, 840, 775, 745, 711, 681; **HR-MS-ESI(+)** calc. $C_{62}H_{33}ZnN_6PBF_{24}AuCl^+$ [M–BArF]$^+$ 1657.0828; found 1657.0843.

Compound **271**

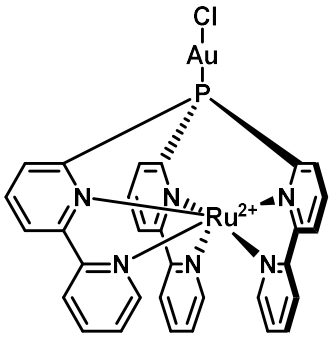

Under nitrogen atmosphere in a glovebox, an oven-dried Schlenk flask was equipped with a stirring bar and charged with phosphine ligand **243** (40.0 mg, 37.4 µmol, 1.00 equiv.). Dry degassed DCM (10 mL) was added under nitrogen. Afterwards, a solution of chloro(dimethylsulfide)gold(I) (11.0 mg, 37.4 µmol, 1.00 equiv.) in 10 mL DCM was added to the reaction mixture. After the addition was complete, the reaction mixture was stirred for 12 h. The reaction mixture was filtered and all volatile compounds were evaporated under reduced pressure. The residue was washed with diethyl ether and dried *in vacuo* give the target compound as a red solid (34.60 mg, 26.6 µmol, 71%).

^{1}H NMR (400 MHz, CD_3CN) δ 8.76 (ddd, *J* = 10.7, 7.6, 1.2 Hz, 3H), 8.66 (ddd, *J* = 8.2, 1.3, 0.7 Hz, 3H), 8.50 (ddd, *J* = 8.3, 2.3, 1.2 Hz, 3H), 8.31 (ddd, *J* = 8.2, 7.6, 3.5 Hz, 3H), 8.22 (ddd, *J* = 7.7, 1.5 Hz, 3H), 7.62 (ddd, *J* = 7.7, 5.7, 1.4 Hz, 3H), 6.85 (ddd, *J* = 5.7, 1.5, 0.7 Hz, 3H); **^{13}C{H} NMR** (101 MHz, CD_3CN) δ 160.5 (d, *J* = 6.6 Hz), 157.3, 151.7, 143.9 (d, *J* = 74.1 Hz), 139.8, 138.4 (d, *J* = 13.1 Hz), 137.3 (d, *J* = 33.9 Hz), 129.2, 126.7, 126.6 (d, *J* = 2.4 Hz); **^{31}P{H} NMR** (162 MHz, CD_3CN) δ 44.88; **^{19}F NMR** (376 MHz, CD_3CN) δ -123.85 (sext, *J* = 1935.4 Hz), -123.85 (oct, *J* = 1052.8 Hz); **IR (ATR)** [cm^{-1}]: $\tilde{\nu}$ = 2962, 1604, 1443, 1377, 1292, 1258, 1085, 1013, 865, 793, 768, 744, 703, 651, 603, 592, 570, 516, 475, 458; **HR-MS-ESI(+)** calc. $C_{30}H_{21}RuN_6PF_6SbAuCl^+$ [M–SbF_6]$^+$ 1066.8904; found 1066.8893.

Compound **272**

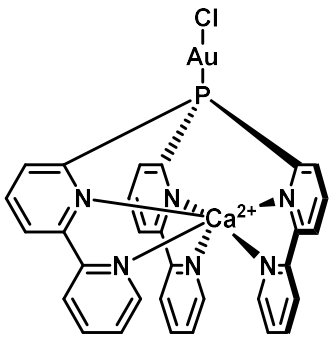

Procedure 1: Under nitrogen atmosphere in a glovebox, an oven-dried Schlenk flask was equipped with a stirring bar and charged with phosphine ligand **245** (70.4 mg, 84.34 µmol, 1.00 equiv.). Dry degassed DCM (1 mL) was added under nitrogen. Afterwards, a solution of chloro(dimethylsulfide)gold(I) (24.9 mg, 84.34 µmol, 1.00 equiv.) in 1 mL DCM was added to the reaction mixture at 0 °C. After the addition was complete, the reaction mixture was stirred for 1 h at room temperature. The reaction mixture was filtered and all volatile compounds were evaporated under reduced pressure. The residue was washed with diethyl ether and dried *in vacuo* give the target compound as a colorless solid (79.3 mg, 74.31 µmol, 88%).

Procedure 2: Under nitrogen atmosphere in a glovebox, an oven-dried Schlenk flask was equipped with a stirring bar and charged with the corresponding metal triflate $Ca(OTf)_2$ (18.6 mg, 54.9 µmol, 1.00 equiv.) and tri([2,2'-bipyridin]-6-yl)phosphinegold(I) chloride **266** (40 mg, 54.9 µmol, 1.00 equiv.). Dry degassed THF (3 mL) was added under nitrogen and the reaction mixture was stirred for 12 h. Afterwards, all volatile compounds were evaporated under reduced pressure. The colorless residue was washed with dry degassed diethyl ether and pentane and dried *in vacuo* to give the target compound as a colorless solid (29 mg, 26.9 µmol, 49%).

^{1}H NMR (400 MHz, CD_3CN) δ 9.14 (ddd, *J* = 5.1, 1.7, 0.9 Hz, 3H), 8.82 (ddd, *J* = 11.9, 7.6, 1.0 Hz, 3H), 8.41 (ddd, *J* = 8.4, 2.7, 1.1 Hz, 3H), 8.33 – 8.22 (m, 6H), 8.13 (td, *J* = 7.8, 1.7 Hz, 3H), 7.71 (ddd, *J* = 7.5, 5.2, 1.2 Hz, 3H); **^{13}C{H} NMR** (101 MHz, CD_3CN) δ 157.5 (d, *J* = 10.7 Hz), 154.2, 151.9, 150.7 (d, *J* = 75.9 Hz), 141.6 (d, *J* = 14.9 Hz), 141.2 (d, *J* = 2.2 Hz), 137.6 (d, *J* = 41.1 Hz), 127.1, 126.8, 124.7, 121.5 (q, *J* =

319.9 Hz); **^{31}P{H} NMR** (162 MHz, CD_3CN) δ 34.27; **^{19}F NMR** (376 MHz, CD_3CN) δ -79.48; **IR (ATR)** [cm^{-1}]: $\tilde{\nu}$ = 3067, 1589, 1554, 1432, 1280, 1234, 1221, 1156, 1028, 1001, 814, 777, 743, 625, 563, 509, 416; **HR-MS-ESI(+)** calc. $C_{31}H_{21}CaN_6PF_3O_3SAuCl^+$ $[M–TfO]^+$ 917.0060; found 917.0044.

Compound **273**

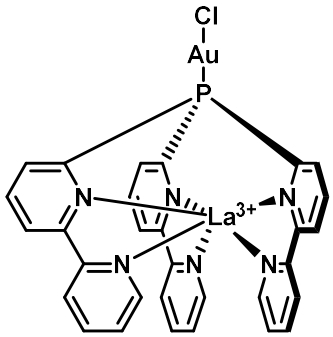

Under nitrogen atmosphere in a glovebox, an oven-dried Schlenk flask was equipped with a stirring bar and charged with phosphine ligand **247** (83.2 mg, 76.85 µmol, 1.00 equiv.). Dry degassed DCM (1 mL) was added under nitrogen. Afterwards, a solution of chloro(dimethylsulfide)gold(I) (22.6 mg, 76.85 µmol, 1.00 equiv.) in 1 mL DCM was added to the reaction mixture at 0 °C. After the addition was complete, the reaction mixture was stirred for 1 h at room temperature. The reaction mixture was filtered and all volatile compounds were evaporated under reduced pressure. The residue was washed with diethyl ether and dried *in vacuo* give the target compound as a colorless solid (87.3 mg, 66.39 µmol, 86%).

^{1}H NMR (300 MHz, CD_2Cl_2) δ 9.46 (dt, *J* = 5.3, 1.2 Hz, 3H), 8.98 (ddd, *J* = 12.8, 7.3, 1.4 Hz, 3H), 8.36 (ddd, *J* = 8.4, 2.8, 1.5 Hz, 3H), 8.29 (ddd, *J* = 8.4, 7.3, 3.3 Hz, 3H), 8.15 – 8.01 (m, 6H), 7.69 (ddd, *J* = 7.1, 5.4, 2.0 Hz, 3H); **^{13}C{H} NMR** (101 MHz, CD_2Cl_2) δ 159.5 (d, *J* = 7.7 Hz), 153.4, 151.7, 148.5 (d, *J* = 72.6 Hz), 141.3 (d, *J* = 15.0 Hz), 140.5, 138.0 (d, *J* = 43.1 Hz), 127.8, 126.8, 124.6 (TfO^- missing); **^{31}P{H} NMR** (121 MHz, CD_2Cl_2) δ 47.36; **^{19}F NMR** (282 MHz, CD_2Cl_2) δ -78.82; **IR (ATR)** [cm^{-1}]: $\tilde{\nu}$ = 3351, 3078, 1590, 1556, 1490, 1434, 1310, 1232, 1204, 1163, 1058, 1021, 813, 773, 744, 631, 559, 513, 419; **HR-MS-ESI(+)** calc. $C_{32}H_{21}LaN_6PF_6O_6S_2AuCl^+$ $[M–TfO]^+$ 1164.9018; found 1164.9003.

Compound **294**

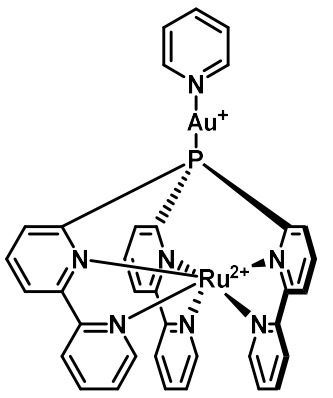

Under nitrogen atmosphere in a glovebox, an oven-dried Schlenk flask was equipped with a stirring bar and charged with phosphine ligand **243** (50.0 mg, 46.77 µmol, 1.00 equiv.). Dry degassed DCM (1 mL) was added under nitrogen. Afterwards, a solution of bis(pyridine)gold(I) hexafluoroantimonate[272] (27.6 mg, 46.77 µmol, 1.00 equiv.) in 1 mL DCM was added to the reaction mixture at 0 °C. After the addition was complete, the reaction mixture was stirred for 12 h at room temperature. Afterwards, the red precipitate was filtered off, washed with DCM, and dried *in vacuo* to give target compound as a red solid (69.7 mg, 44.09 µmol, 94%).

^{1}H NMR (400 MHz, CD_3CN) δ 8.93 – 8.78 (m, 5H), 8.69 (d, *J* = 8.1 Hz, 3H), 8.53 (dd, *J* = 8.4, 2.3 Hz, 3H), 8.34 (td, *J* = 7.8, 3.5 Hz, 3H), 8.24 (tdd, *J* = 7.9, 5.9, 1.5 Hz, 4H), 7.91 – 7.83 (m, 2H), 7.64 (ddd, *J* = 7.4, 5.7, 1.4 Hz, 3H), 6.88 (dt, *J* = 5.6, 1.1 Hz, 3H); **^{13}C{H} NMR** (101 MHz, CD_3CN) δ 160.7 (d, *J* = 6.4 Hz, 2C), 157.3, 151.8, 151.7, 142.8, 139.9, 138.4 (d, *J* = 13.1 Hz), 137.3 (d, *J* = 33.4 Hz), 129.2, 127.5, 126.7 (s, 2C); **^{31}P{H} NMR** (162 MHz, CD_3CN) δ 41.47; **^{19}F NMR** (376 MHz, CD_3CN) δ -123.80 (sext, *J* = 1937.9 Hz), -123.80 (oct, *J* = 1048.5 Hz); **IR (ATR)** [cm^{-1}]: $\tilde{\nu}$ = 3647, 3575, 3108, 3095, 1611, 1444, 1380, 1295, 1246, 1220, 1149, 1074, 1022, 813, 769, 649, 605, 595, 572, 475, 423; **HR-MS-ESI(+)** calc. $C_{30}H_{21}RuN_6PF_6SbAuCl^+$ $[M–Py–SbF_6+Cl]^+$ 1066.8905; found 1066.8925.

Compound **299**

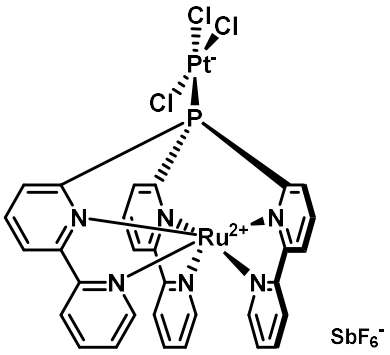

Under nitrogen atmosphere in a glovebox, an oven-dried Schlenk flask was equipped with a stirring bar and charged with finely ground K_2PtCl_4 (4.3 mg, 10.29 µmol, 1.10 equiv.) and phosphine ligand **243** (10.0 mg, 9.35 µmol, 1.00 equiv.). Dry degassed acetonitrile (1 mL) was added under nitrogen and the suspension was stirred for 18 h. Afterwards, all volatile compounds were evaporated under reduced pressure. The red residue was extracted with dry degassed DCM, filtered and the remaining residue further extracted with DCM. The combined organic extracts were concentrated *in vacuo* to give the target compound as a red solid (8.8 mg, 7.75 µmol, 83%).

^{1}H NMR (400 MHz, CD_3CN) δ 9.67 (td, *J* = 7.9, 1.2 Hz, 3H), 8.60 (dt, *J* = 8.1, 1.1 Hz, 3H), 8.41 (dt, *J* = 8.2, 1.6 Hz, 3H), 8.24 (td, *J* = 8.0, 3.5 Hz, 3H), 8.16 (td, *J* = 7.9, 1.5 Hz, 3H), 7.56 (ddd, *J* = 7.4, 5.7, 1.4 Hz, 3H), 6.77 (dt, *J* = 5.6, 1.1 Hz, 3H); **^{13}C{H} NMR** (101 MHz, CD_3CN) δ 159.2, 157.6, 151.4, 146.1 (d, *J* = 67.5 Hz), 139.4, 138.1 (d, *J* = 27.4 Hz), 137.1 (d, *J* = 11.3 Hz), 128.7, 126.1, 125.5 (d, *J* = 2.1 Hz); **^{31}P{H} NMR** (162 MHz, CD_3CN) δ 12.47, 12.46 (d, *J* = 4200.4 Hz); **^{19}F NMR** (282 MHz, CD_3CN) δ -124.01 (hex, *J* = 1933.6 Hz), -124.02 (oct, *J* = 1050.3 Hz).; **IR (ATR)** [cm^{-1}]: $\tilde{\nu}$ = 3501, 3084, 2954, 2925, 2853, 1604, 1442, 1376, 1240, 1153, 1016, 809, 768, 653, 568, 501, 430, 405; **HR-MS-ESI(+)** calc. $C_{30}H_{21}RuN_6PPtCl_2^+$ $[M–SbF_6]^+$ 431.9808; found 431.9814.

Compound **300**

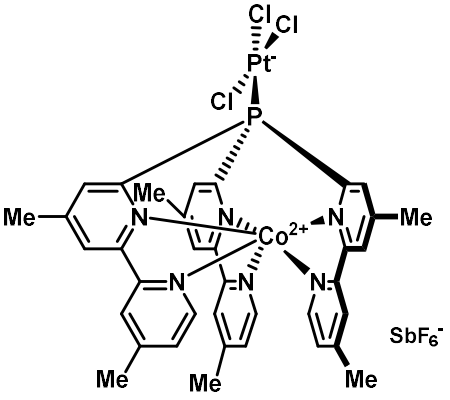

Under nitrogen atmosphere in a glovebox, an oven-dried Schlenk flask was equipped with a stirring bar and charged with finely ground K_2PtCl_4 (21.8 mg, 52.47 µmol, 1.10 equiv.) and phosphine ligand **240** (53.0 mg, 47.70 µmol, 1.00 equiv.). Dry degassed acetonitrile (3 mL) was added under nitrogen and the suspension was stirred for 18 h. Afterwards, all volatile compounds were evaporated under reduced pressure. The residue was extracted with dry degassed DCM, filtered and the remaining residue further extracted with DCM. The combined organic extracts were concentrated *in vacuo* to give the target compound as a yellow solid (50.4 mg, 42.83 µmol, 90%).

^{1}H NMR (400 MHz, CD_3CN) δ 358.92 (s, 3H), 99.66 (s, 3H), 82.30 (s, 3H), 30.67 (s, 3H), 26.45 (s, 3H), 5.95 (s, 9H), 1.03 (s, 9H); **^{31}P{H} NMR** (162 MHz, CD_3CN) δ 203.59 (d, *J* = 4208.8 Hz), 203.56; **^{19}F NMR** (376 MHz, CD_3CN) δ -123.77 (sext, *J* = 1933.9 Hz), -123.77 (oct, *J* = 1048.7 Hz); **IR (ATR)** [cm^{-1}]: $\tilde{\nu}$ = 3066, 2958, 2922, 2852, 1615, 1544, 1393, 1251, 1012, 935, 879, 832, 653, 597, 544, 512, 431; **HR-MS-ESI(+)** calc. $C_{36}H_{33}N_6PPtCl_3^+$ $[M–SbF_6]^+$ 940.0500; found 940.0522.

Compound **301**

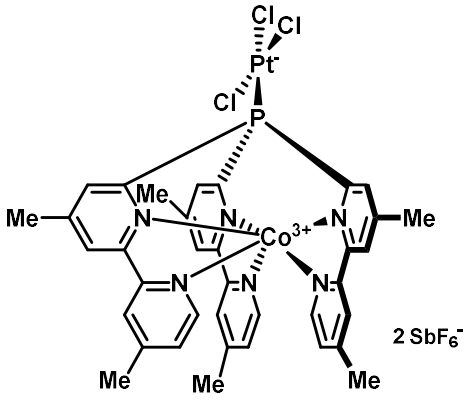

Under nitrogen atmosphere in a glovebox, an oven-dried Schlenk flask was equipped with a stirring bar and charged with finely ground K_2PtCl_4 (72.4 mg, 174.33 µmol, 2.00 equiv.) and phosphine ligand **241** (126.0 mg, 87.16 µmol, 1.00 equiv.). Dry degassed acetonitrile (1 mL, small amount!) was added under nitrogen and the suspension was sonicated for 6h at 0 °C. The suspension was filtered and all volatile compounds were evaporated under reduced pressure. The residue was washed with DCM and dried *in vacuo* give the target compound as an orange solid (84.9 mg, 31.83 µmol, 37%).

^{1}H NMR (400 MHz, CD_3CN) δ 9.46 (d, *J* = 8.5 Hz, 3H), 8.57 (s, 3H), 8.44 (s, 3H), 7.56 (d, *J* = 5.5 Hz, 3H), 6.17 (d, *J* = 5.2 Hz, 3H), 2.75 (s, 9H), 2.72 (s, 9H); **^{13}C NMR** (101 MHz, CD_3CN) δ 159.7 – 159.4 (m), 158.0, 157.2 (d, *J* = 9.7 Hz), 156.3, 151.0, 148.2 (d, *J* = 59.9 Hz), 139.5 (d, *J* = 24.1 Hz), 131.4, 129.0, 127.3, 21.0, 21.0; **^{31}P{H} NMR** (162 MHz, CD_3CN) δ 13.33 (d, *J* = 4383.9 Hz), 13.33; **^{19}F NMR** (376 MHz, CD_3CN) δ -123.87 (sext, *J* = 1932.5 Hz), -123.87 (oct, *J* = 1050.5 Hz); **IR (ATR)** [cm^{-1}]: $\tilde{\nu}$ = 3068, 2929, 1620, 1437, 1294, 1255, 1032, 828, 653, 601, 515, 455; **HR-MS-ESI(+)** calc. $C_{36}H_{33}N_6PPtCl_3SbF_6^+$ $[M– SbF_6]^+$ 1176.9473; found 1176.9468.

Cyclic Voltammetry

A three electrode setup, consisting of a working electrode (glassy carbon), counter electrode (Pt) and a pseudo-reference electrode (Ag/AgCl) combined with a VersaSTAT 4 potentiostat was used to record the cyclic voltammograms of the following compounds. The voltammograms were later on referenced to the Fc/Fc^+ couple.

Compound **208** (electrolyte solution: 0.1 M $[NBu_4][PF_6]$ in MeCN, scan rate: 100 mV/s, under nitrogen)

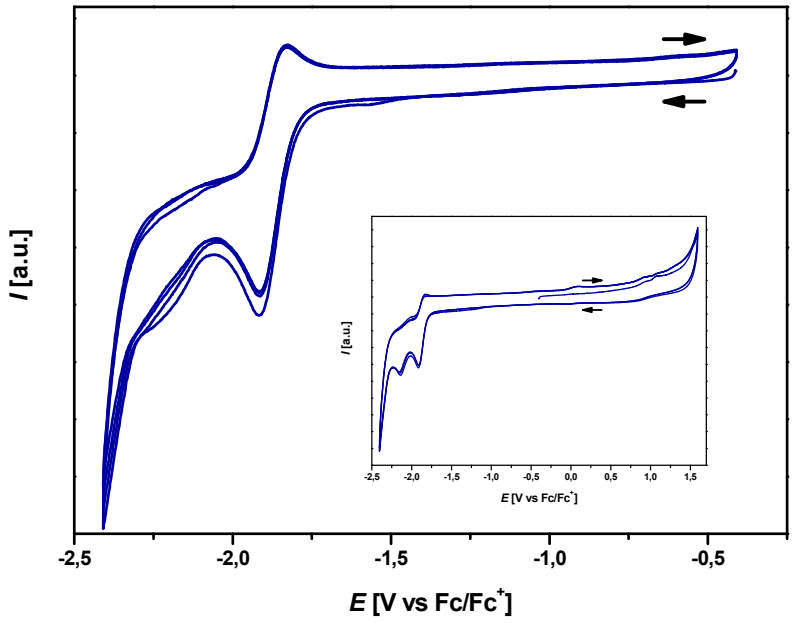

Compound **209** (electrolyte solution: 0.1 M $[NBu_4][PF_6]$ in MeCN, scan rate: 100 mV/s, under nitrogen)

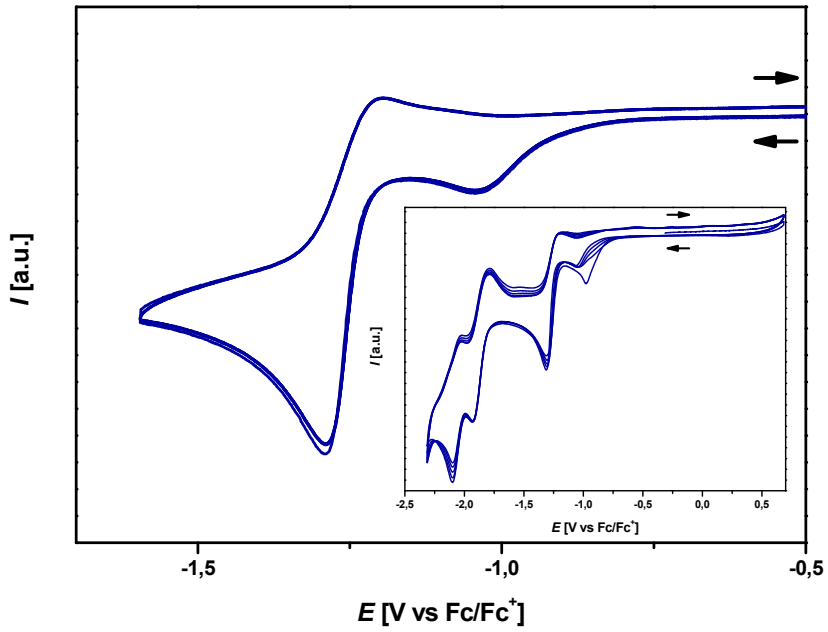

Compound **239** (electrolyte solution: 0.1 M $[NBu_4][PF_6]$ in MeCN, scan rates: 50 mV/s, 100 mV/s, 200 mV/s, 500 mV/s, 1000 mV/s and 2000 mV/s, under nitrogen)

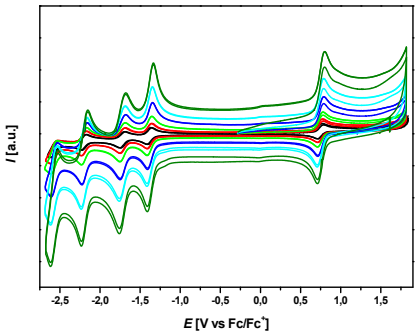

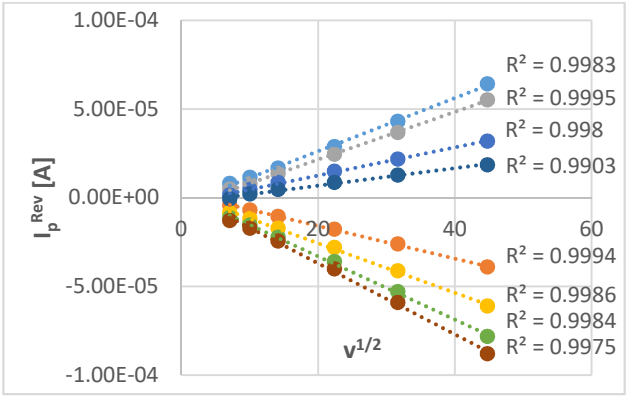

Compound **240** (electrolyte solution: 0.1 M $[NBu_4][PF_6]$ in MeCN, scan rates: 25 mV/s, 50 mV/s, 100 mV/s, 250 mV/s, 500 mV/s and 1000 mV/s, under nitrogen)

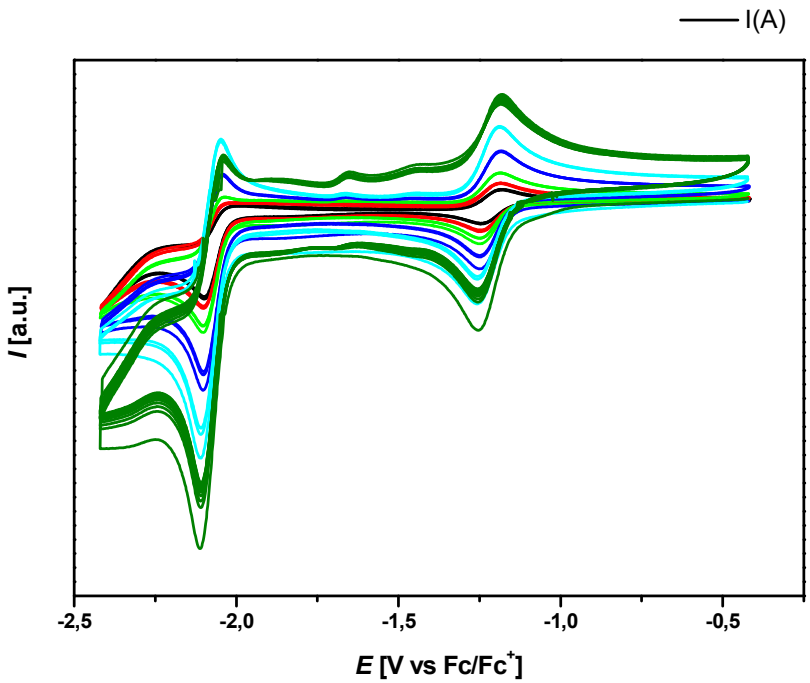

First reduction of **240** (electrolyte solution: 0.1 M $[NBu_4][PF_6]$ in MeCN, scan rates: 25 mV/s, 50 mV/s, 100 mV/s, 250 mV/s, 500 mV/s and 1000 mV/s, under nitrogen)

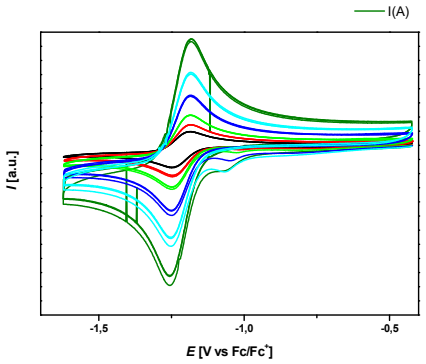

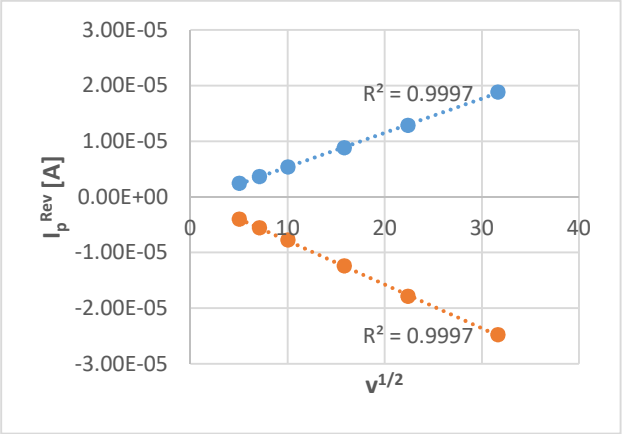

Oxidation of **240** (electrolyte solution: 0.1 M $[NBu_4][PF_6]$ in MeCN, scan rates: 25 mV/s, 50 mV/s and 100 mV/s, under nitrogen)

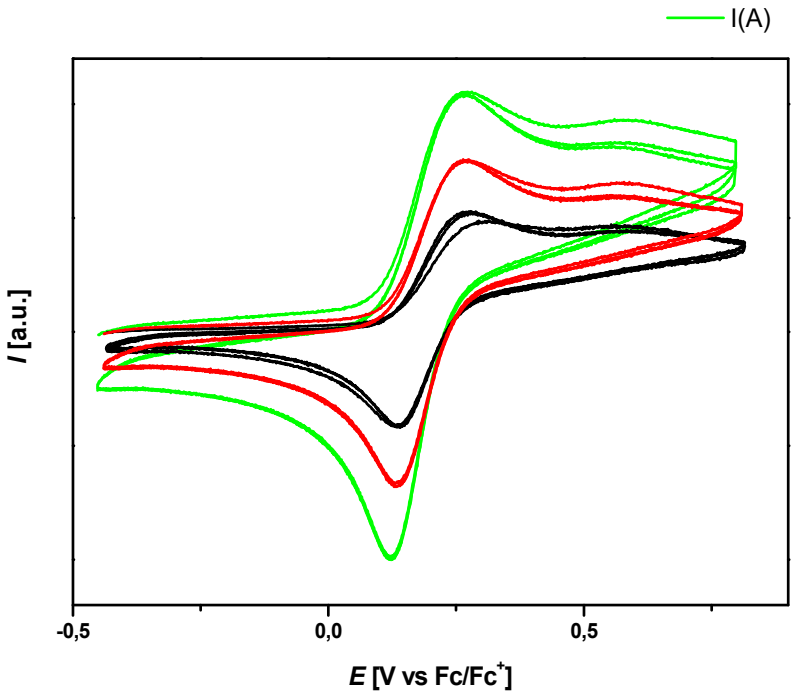

Compound **242** (electrolyte solution: 0.1 M $[NBu_4][PF_6]$ in MeCN, scan rates: 20 mV/s, 100 mV/s, 500 mV/s and 1000 mV/s, under nitrogen)

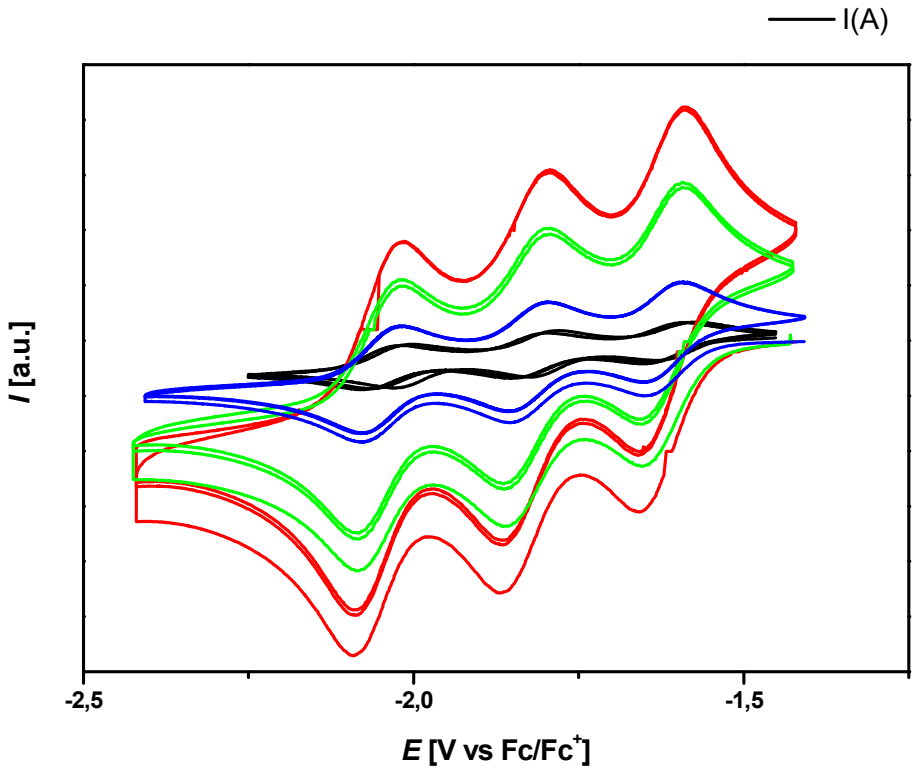

Compound **243** (electrolyte solution: 0.1 M $[NBu_4][PF_6]$ in MeCN, scan rates: 25 mV/s, 50 mV/s, 100 mV/s, 200 mV/s, 500 mV/s and 1000 mV/s, under nitrogen)

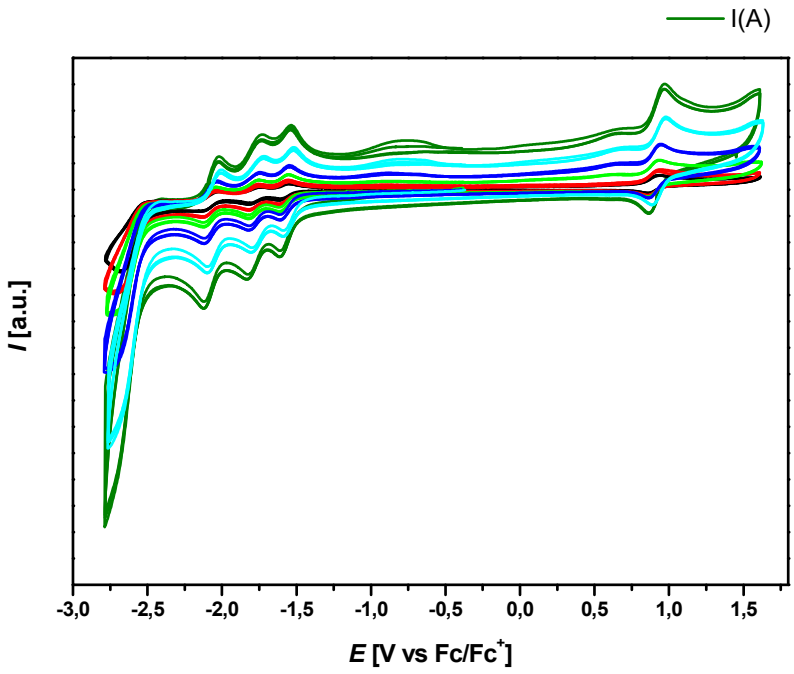

Compound **248** (electrolyte solution: 0.1 M $[NBu_4][PF_6]$ in DCM, scan rate: 500 mV/s, under nitrogen)

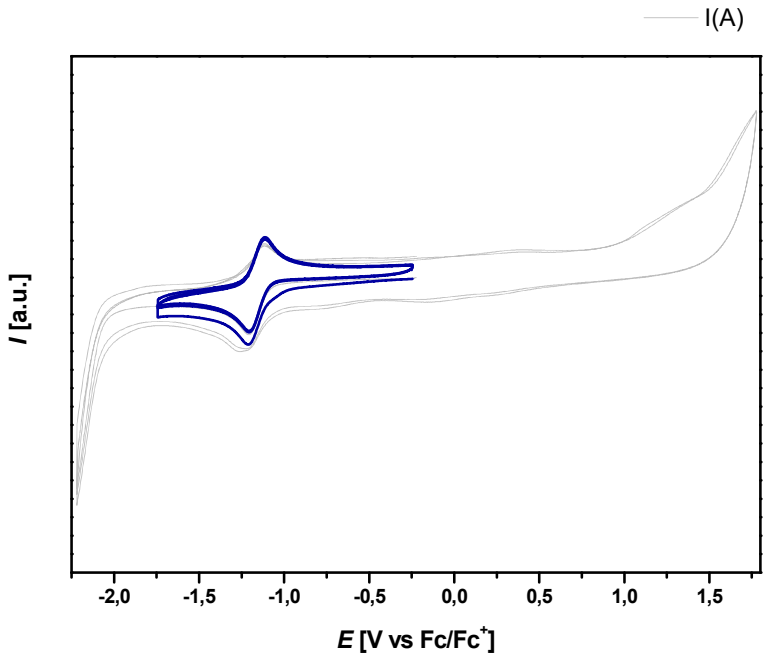

UV-VIS spectroscopy

UV-Vis absorption spectrum of **243**

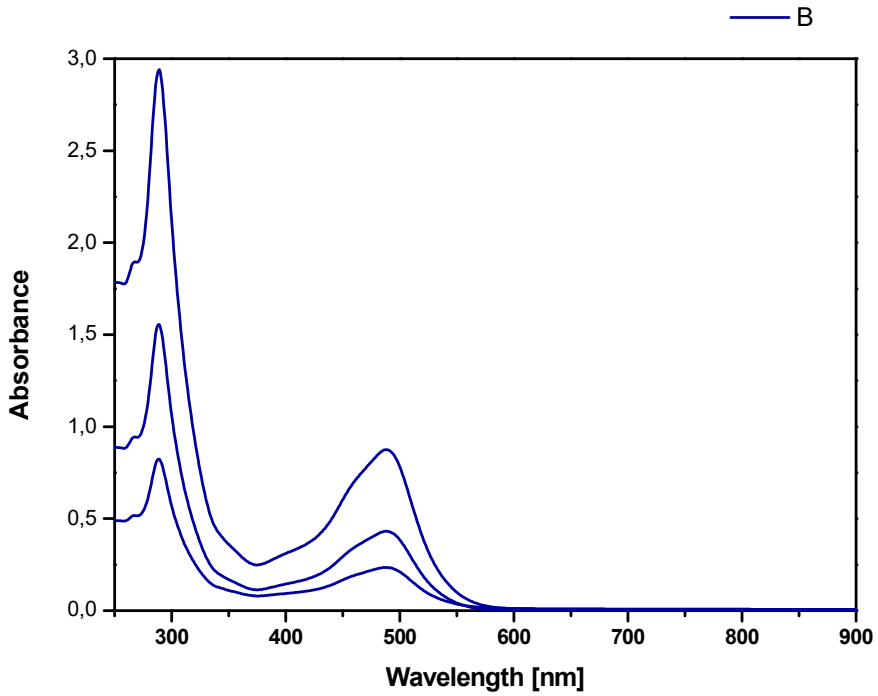

UV-Vis absorption spectrum of **271**

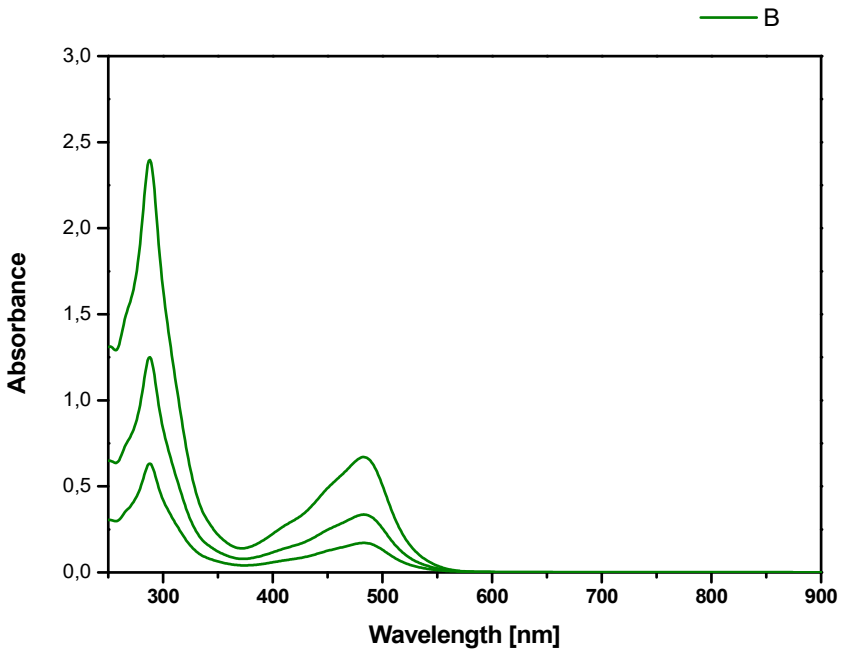

Topographic steric map

The percent buried volume $\%V_{Bur}$ was determined using the following parameters:

The atom that coordinates to the metal was chosen to be the P atom, the three C atoms bonded to the P atom where used to define the z axis, the xy plane was defined through one of the C atoms bond to the P atom, Bondi radii were scaled by 1.17, the radius of the sphere was set to 3.5 Å and 0.05 Å were used for the mesh spacing. While omitting the H atoms, the $\%V_{Bur}$ was calculated for the distances between the coordinated atom and the putative metal center of d = 2.00 Å and 2.28 Å. Topographic steric maps are shown for a distance of d = 2.00 Å.

Compound **212** (left) and **238** (right)

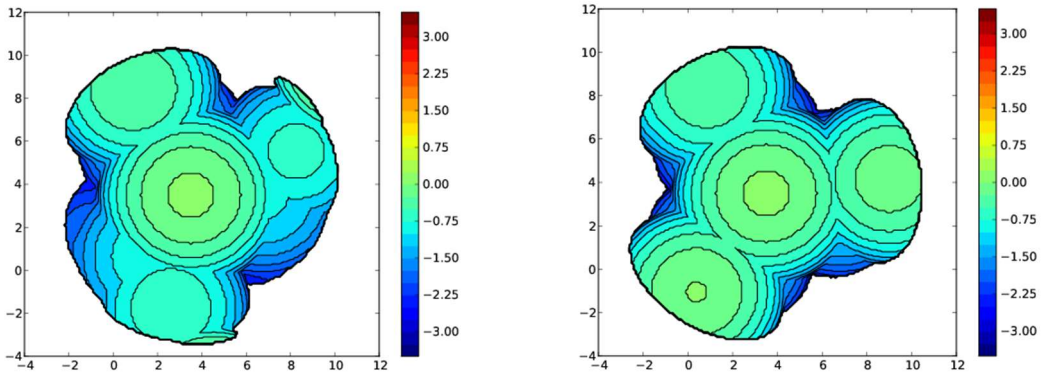

Compound **239** (left) and **240** (right)

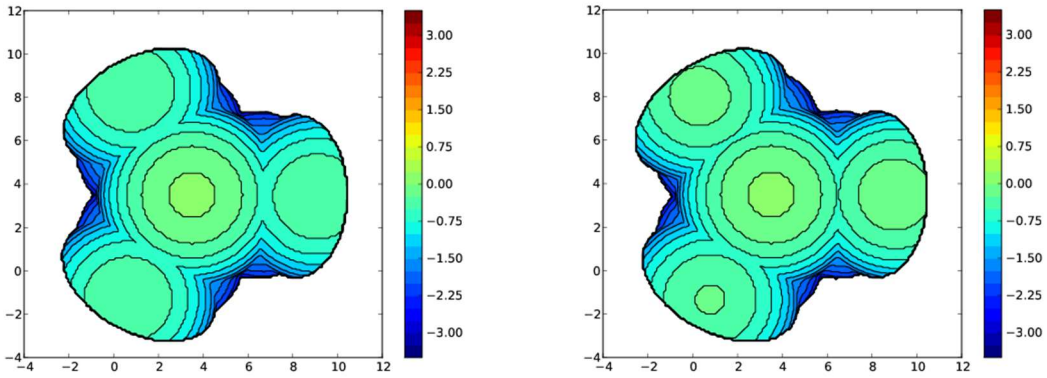

Compound **241** (left) and **242** (right)

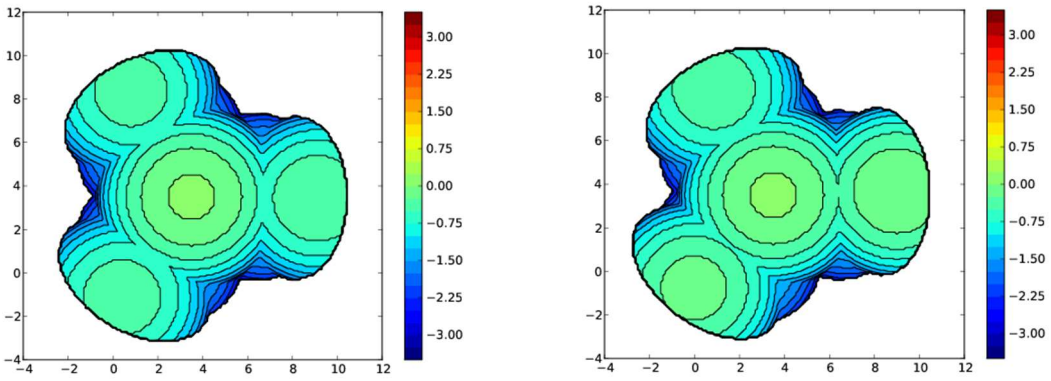

Compound **243**

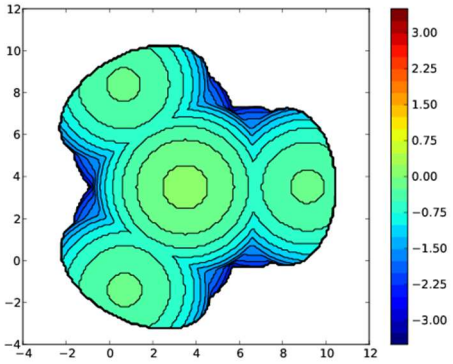

Photocatalytic synthesis of 6*H*-benzo[*c*]chromenes from *S*-aryl sulfonium salts[242]

Photoreactor Set-Up

5m dimmable LED strip, 460-465 nm wavelength (blue), maximum rated power 72 W, dimmed to 28 W (dimmer, 24 V transformer). Supplier: revoArt GmbH.

LED strip was mounted on a cylindrical metal case to control diffuse light scattering. Stirring was achieved by magnetic stirrer. Constant temperature was ensured by ventilation slots and a 20 cm computer fan.

Procedures

General procedure A:

Starting from Monohalides

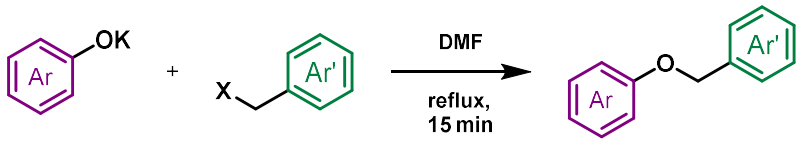

The syntheses were carried out using a modified literature procedure.[273]

A round-bottom flask equipped with a stirring bar and charged with the appropriate potassium phenolate[274] (1 equiv.), appropriate benzyl halide (1 equiv.) in DMF was heated under reflux for 15 min using a pre-heated oil bath. After cooling to ambient temperature, all volatile compounds were evaporated under reduced pressure and the residue dissolved in CH_2Cl_2. The solution was washed with H_2O and dried over $MgSO_4$. The solvent was removed *in vacuo*, and the resulting solid was purified by flash-chromatography (SiO_2, pentane:EtOAc), unless otherwise noted.

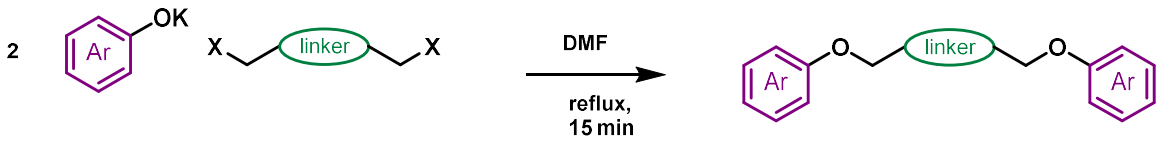

Starting from Dihalides

The syntheses were carried out using a modified literature procedure.[273]

A round-bottom flask equipped with a stirring bar and charged with the corresponding potassium phenolate[274] (2 equiv.), corresponding benzyl halide (1 equiv.) in DMF was heated under reflux for 15 min using a pre-heated oil bath. After cooling to ambient temperature, all volatile compounds were evaporated under reduced pressure and the residue was dissolved in CH_2Cl_2. The solution was washed with H_2O and dried over $MgSO_4$. The solvent was removed *in vacuo*, and the resulting solid purified by flash-chromatography (SiO_2, pentane:EtOAc), unless otherwise noted.

Benzyl ethers:

1-Methyl-4-[(4-methylbenzyl)oxy]benzene (469a)

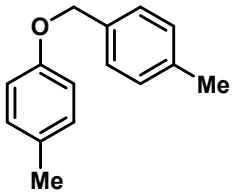

K_2CO_3 (17.09 g, 123.65 mmol, 2 equiv.) was added to a solution of *p*-cresol (6.685 g, 61.82 mmol, 1 equiv.) and 1-(bromomethyl)-4-methylbenzene (11.44 g, 61.82 mmol, 1.00 equiv.) in acetone (300 mL), and the reaction mixture was stirred under reflux for 12 h using a pre-heated oil bath. After cooling to ambient temperature, the solvent was removed *in vacuo*. Water was added to the residue, and the mixture was extracted with CH_2Cl_2 (3 × 100 mL). The combined organic phases were washed with brine and dried over $MgSO_4$. All volatile compounds were removed under reduced pressure, and the residue was purified by flash-chromatography (SiO_2, pentane/EtOAc) affording the target compound as a colorless solid (11.38 g, 53.61 mmol, 87%).

^{1}H NMR (400 MHz, $CDCl_3$) δ 7.32 (d, *J* = 8.2 Hz, 2H), 7.19 (d, *J* = 7.8 Hz, 2H), 7.08 (d, *J* = 8.2 Hz, 2H), 6.92 – 6.80 (m, 2H), 5.00 (s, 2H), 2.36 (s, 3H), 2.29 (s, 3H); **^{13}C{H} NMR** (101 MHz, $CDCl_3$) δ 156.9, 137.8, 134.4, 130.2, 130.0, 129.4, 127.7, 114.9, 70.2, 21.3, 20.6.

Analytical data are in accordance to those reported in the literature.[275]

1-(*tert*-Butyl)-4-{[4-(*tert*-butyl)benzyl]oxy}benzene (469b)

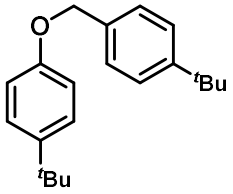

K_2CO_3 (18.25 g, 132.05 mmol, 2 equiv.) was added to a solution of 4-(*tert*-butyl)phenol (9.92 g, 66.04 mmol, 1 equiv.) and 1-(bromomethyl)-4-(*tert*-butyl)benzene (15.00 g, 66.04 mmol, 1.00 equiv.) in acetone (300 mL), and the reaction mixture was stirred under reflux for 3 d using a pre-heated oil bath. After cooling to ambient temperature, the solvent was removed *in vacuo*. Water was added to the residue, and the mixture was extracted with CH_2Cl_2 (3 × 100 mL). The combined organic phases were washed with brine and dried over $MgSO_4$. All volatile compounds were removed under reduced pressure and the residue was purified by recrystallization from hot MeOH yielding the target compound as a colorless solid (15.19 g, 51.24 mmol, 78%).

^{1}H NMR (300 MHz, $CDCl_3$) δ 7.46 – 7.36 (m, 4H), 7.36 – 7.29 (m, 2H), 6.98 – 6.89 (m, 2H), 5.02 (s, 2H), 1.34 (s, 9H), 1.32 (s, 9H); **^{13}C{H} NMR** (75 MHz, $CDCl_3$) δ 156.9, 151.1, 143.6, 134.4, 127.6, 126.4, 125.7, 114.4, 70.0, 34.7, 34.2, 31.7, 31.5.

Analytical data are in accordance to those reported in the literature.[276]

1-(Benzyloxy)-4-methylbenzene (469c)

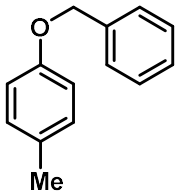

K_2CO_3 (10.10 g, 73.08 mmol, 2.50 equiv.) was added to a solution of *p*-cresol (3.48 g, 32.18 mmol, 1.10 equiv.) and benzyl bromide (5.00 g, 29.23 mmol, 1.00 equiv.) in MeCN (100 mL), and the reaction mixture was stirred under reflux for 3 d using a pre-heated oil bath. After cooling to ambient temperature, the solvent was removed *in vacuo*. Water was added to the residue, and the mixture was extracted with CH_2Cl_2 (3 × 100 mL). The combined organic phases were washed with brine and dried over $MgSO_4$. All volatile compounds were removed under reduced pressure, and the residue was purified by flash-chromatography [SiO_2, pentane:EtOAc (20:1)] affording the target compound as a colorless solid (5.09 g, 25.67 mmol, 88%).

^{1}H NMR (300 MHz, $CDCl_3$) δ 7.50 – 7.30 (m, 5H), 7.15 – 7.07 (m, 2H), 6.95 – 6.87 (m, 2H), 5.07 (s, 2H), 2.32 (s, 3H).

The spectrum corresponds to those reported in the literature.[277]

1-Fluoro-4-[(*p*-tolyloxy)methyl]benzene (469d)

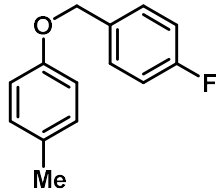

1-(Bromomethyl)-4-fluorobenzene (5.00 g, 26.45 mmol, 1.00 equiv.) and *p*-cresol (3.15 g, 29.13 mmol, 1.10 equiv.) were dissolved in MeCN (100 mL), and K_2CO_3 (9.14 g, 66.13 mmol, 2.50 equiv.) was added. The reaction mixture was stirred under reflux for 3 d using a pre-heated oil bath. After cooling to ambient temperature, the solvent was removed *in vacuo*. Water was added to the residue, and the mixture was extracted with CH_2Cl_2 (3 × 100 mL). The combined organic phases were washed with brine and dried over $MgSO_4$. All volatile compounds were removed under reduced pressure, and the residue was purified by recrystallization from hot MeOH. The supernatant was evaporated to dryness, and the residue was recrystallized again from hot MeOH. The solids were combined and dried under reduced pressure furnishing the target compound as a colorless crystalline solid (5.55 g, 25.66 mmol, 97%).

^{1}H NMR (300 MHz, $CDCl_3$) δ 7.44 – 7.36 (m, 2H), 7.13 – 7.01 (m, 4H), 6.89 – 6.82 (m, 2H), 5.00 (s, 2H), 2.29 (s, 3H).

The spectral data matches literature reports.[278]

1-{[4-(*tert*-Butyl)phenoxy]methyl}-3,5-dichlorobenzene (469e)

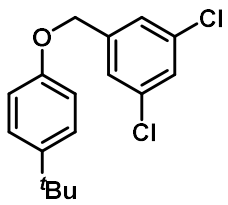

According to general procedure A, compound **469e** was obtained from potassium 4-(*tert*-butyl)phenolate (1.13 g, 6.00 mmol, 1.00 equiv.) and 1-(bromomethyl)-3,5-dichlorobenzene (1.44 g, 6.00 mmol, 1.00 equiv.) after flash-chromatography (SiO_2, pentane:EtOAc) as a colorless solid (1.70 g, 5.50 mmol, 92%).

m.p. 73 °C; **^{1}H NMR** (300 MHz, $CDCl_3$) δ 7.35 – 7.29 (m, 5H), 6.93 – 6.85 (m, 2H), 4.99 (s, 2H), 1.31 (s, 9H); **^{13}C{H} NMR** (101 MHz, $CDCl_3$) δ 156.1, 144.4, 141.0, 135.3, 128.1, 126.6, 125.6, 114.4, 68.7, 34.2, 31.6; **IR (ATR)** [cm^{-1}]: $\tilde{\nu}$ = 2960, 2904, 2866, 1593, 1570, 1510, 1459, 1431, 1364, 1298,1182, 1115, 1102, 1024, 850, 826, 797, 668, 552, 431; **HR-MS-EI** calc. $C_{17}H_{18}Cl_2O^+$ $[M]^+$ 308.0729; found 308.0727.

1-(*tert*-Butyl)-4-{[4-(methylsulfonyl)benzyl]oxy}benzene (469f)

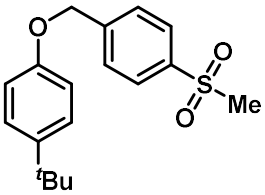

According to general procedure A, compound **469f** was obtained from potassium 4-(*tert*-butyl)phenolate (0.91 g, 4.83 mmol, 1.00 equiv.) and 4-(methylsulfonyl)benzyl bromide (1.20 g, 4.82 mmol, 1.00 equiv.) after flash-chromatography (SiO_2, pentane:EtOAc) as a colorless solid (1.30 g, 4.08 mmol, 85%).

m.p. 165 °C; **^{1}H NMR** (300 MHz, $CDCl_3$) δ 7.96 (d, *J* = 8.4 Hz, 2H), 7.64 (d, *J* = 8.1 Hz, 2H), 7.33 (d, *J* = 8.8 Hz, 2H), 6.90 (d, *J* = 8.8 Hz, 2H), 5.15 (s, 2H), 3.06 (s, 3H), 1.31 (s, 9H); **^{13}C{H} NMR** (75 MHz, $CDCl_3$) δ 156.1, 144.3, 143.9, 140.0, 127.9, 127.8, 126.5, 114.4, 69.0, 44.7, 34.2, 31.6; **IR (ATR)** [cm^{-1}]: $\tilde{\nu}$ = 3041, 3005, 2949, 2925, 2903, 2871, 1605, 1514, 1461, 1415, 1311, 1294, 1239, 1184, 1146, 1089, 1036, 961, 870, 826, 762, 687, 537, 513; **HR-MS-ESI(+)** calc. $C_{18}H_{23}O_3S^+$ $[M+H]^+$ 319.1362; found 319.1359.

1-[(3,4,5-Trimethylphenoxy)methyl]naphthalene (469g)

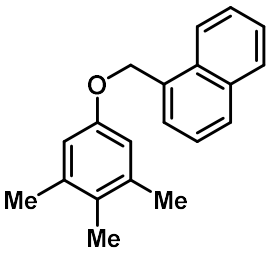

According to general procedure A, compound **469g** was obtained from potassium 3,4,5-trimethylphenolate (3.94 g, 22.61 mmol, 1.00 equiv.) and 1-(bromomethyl)naphthalene (5.00 g, 22.61 mmol, 1.00 equiv.) after flash-chromatography (SiO_2, pentane:EtOAc) as a colorless solid (5.00 g, 18.09 mmol, 80%).

m.p. 87 °C; **^{1}H NMR** (300 MHz, $CDCl_3$) δ 8.11 – 8.02 (m, 1H), 7.93 – 7.88 (m, 1H), 7.88 – 7.83 (m, 1H), 7.61 (dd, *J* = 7.0, 1.2 Hz, 1H), 7.57 – 7.42 (m, 3H), 6.77 (s, 2H), 5.46 (s, 2H), 2.29 (s, 6H), 2.14 (s, 3H); **^{13}C{H} NMR** (75 MHz, $CDCl_3$) δ 156.5, 137.8, 133.9, 132.9, 131.7, 129.0, 128.8, 127.7, 126.6, 126.5, 126.0, 125.5, 124.0, 114.1, 68.7, 21.0, 14.8; **IR (ATR)** [cm^{-1}]: $\tilde{\nu}$ = 3058, 3012, 2965, 2917, 2857, 2729, 1598, 1485, 1315, 1205, 1169, 1149, 1073, 1000, 849, 827, 789, 768, 699, 647, 531, 439, 407; **HR-MS-ESI(+)** calc. $C_{20}H_{21}O^+$ $[M+H]^+$ 277.1587; found 277.1584.

1-(*tert*-Butyl)-4-{[4-(trifluoromethyl)benzyl]oxy}benzene (469h)

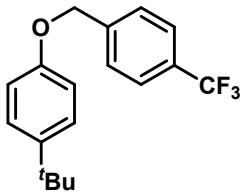

According to general procedure A, compound **469h** was obtained from potassium 4-(*tert*-butyl)phenolate (1.13 g, 6.01 mmol, 1.00 equiv.) and 4-(trifluoromethyl)benzyl bromide (1.44 g, 6.02 mmol, 1.00 equiv.) after flash-chromatography (SiO_2, pentane:EtOAc) as a colorless solid (1.68 g, 5.45 mmol, 91%).

m.p. 68 °C; **^{1}H NMR** (300 MHz, $CDCl_3$) δ 7.69 – 7.51 (m, 4H), 7.36 – 7.29 (m, 2H), 6.93 – 6.87 (m, 2H), 5.11 (s, 2H), 1.30 (s, 9H); **^{13}C{H} NMR** (101 MHz, $CDCl_3$) δ 156.3, 144.2, 141.6, 130.2 (q, C-F, $^2J_{C\text{-}F}$ = 32.5 Hz), 127.5, 126.5, 125.7 (q, C-F, $^3J_{C\text{-}F}$ = 3.7 Hz), 124.3 (q, C-F, $^1J_{C\text{-}F}$ = 271.7 Hz), 114.4, 69.3, 34.3, 31.7; ^{19}F NMR (377 MHz, $CDCl_3$) δ -62.53; **IR (ATR)** [cm^{-1}]: $\tilde{\nu}$ = 2965, 2907, 2870, 1514, 1325, 1238, 1159, 1107, 1046, 1049, 1026, 1015, 821, 592, 552; **HR-MS-EI** calc. $C_{18}H_{19}F_3O^+$ $[M]^+$ 308.1383; found 308.1385.

Preparation of compound 4h was described in the literature; however, without characterization.[279]

1,3-dichloro-5-((4-chlorophenoxy)methyl)benzene (469i)

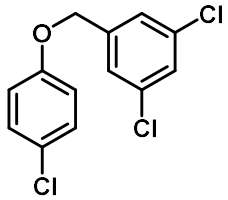

According to general procedure A, compound **469i** was obtained from potassium 4-chlorophenolate (2.56 g, 15.36 mmol, 1.00 equiv.) and 1-(bromomethyl)-3,5-dichlorobenzene (3.69 g, 15.36 mmol, 1.00 equiv.) after flash-chromatography (SiO_2, pentane:EtOAc) as a colorless solid (3.67 g, 12.76 mmol, 83%).

m.p. 51 °C; **^{1}H NMR** (300 MHz, $CDCl_3$) δ 7.34 – 7.29 (m, 3H), 7.28 – 7.22 (m, 2H), 6.93 – 6.81 (m, 2H), 4.98 (s, 2H); **^{13}C{H} NMR** (75 MHz, $CDCl_3$) δ 156.9, 140.2, 135.4, 129.7, 128.3, 126.6, 125.6, 116.2, 68.9; **IR (ATR)** [cm^{-1}]: $\tilde{\nu}$ = 3076, 1597, 1571, 1489, 1435, 1376, 1281, 1235, 1179, 1101, 1024, 1005, 873, 855, 812, 797, 703, 661, 602, 541, 516, 502, 429; **HR-MS-EI** calc. $C_{13}H_9Cl_3O^+$ $[M]^+$ 285.9713; found 285.9711.

1-methyl-4-[(4-nitrobenzyl)oxy]benzene (469j)

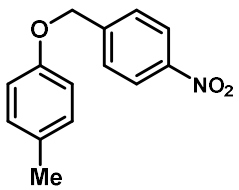

K_2CO_3 (3.23 g, 23.41 mmol, 2 equiv.) was added to a solution of *p*-cresol (1.90 g, 17.55 mmol, 1.5 equiv.) and 1-(bromomethyl)-4-nitrobenzene (2.53 g, 11.70 mmol, 1.00 equiv.) in acetone (100 mL), and the reaction mixture was stirred under reflux for 12 h using a pre-heated oil bath. After cooling to ambient temperature, the solvent was removed *in vacuo*. Water was added to the residue, and the mixture was extracted with CH_2Cl_2 (3 × 100 mL). The combined organic phases were washed with brine and dried over $MgSO_4$. All volatile compounds were removed

under reduced pressure, and the residue was purified by flash-chromatography (SiO_2, pentane/EtOAc) affording the target compound as a colorless solid (1.50 g, 6.17 mmol, 53%).

^{1}H NMR (400 MHz, CDCl3) δ 8.30 – 8.20 (m, 2H), 7.60 (ddt, *J* = 8.4, 2.3, 1.1 Hz, 2H), 7.16 – 7.06 (m, 2H), 6.92 – 6.81 (m, 2H), 5.15 (s, 2H), 2.30 (s, 3H); **^{13}C NMR** (101 MHz, CDCl3) δ 156.2, 147.7, 145.0, 131.0, 130.2, 127.7, 124.0, 114.8, 68.9, 20.6; **IR (ATR)** [cm^{-1}]: $\tilde{\nu}$ = 3108, 3075, 3027, 2925, 2851, 1607, 1583, 1509, 1457, 1340, 1299, 1238, 1175, 1108, 1051, 843, 822, 801, 738, 683, 656, 512, 461; **HR-MS-ESI(+)** calc. $C_{14}H_{14}O_3N^+$ $[M+H]^+$ 243.0890, found 243.0888.

4-[(*p*-Tolyloxy)methyl]pyridine (469k)

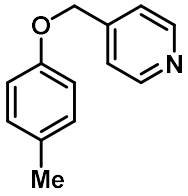

The synthesis was carried out using a modified literature procedure.[280]

An oven-dried Schlenk flask was equipped with a stirring bar and charged with *p*-cresol (6.00 g, 55.49 mmol, 1.00 equiv.), PPh_3 (16.01 g, 61.04 mmol, 1.1 equiv.) and pyridin-4-ylmethanol (6.66 g, 61.03 mmol, 1.1 equiv.). The flask was evacuated and back-filled with nitrogen three times. Dry degassed CH_2Cl_2 was added under nitrogen. The suspension was stirred until all solids dissolved, and DEAD (10.63 g, 61.03 mmol, 1.1 equiv.) was added dropwise at room temperature. After the addition was completed, the mixture was stirred for an additional 12 h at the same temperature. The solvent was removed *in vacuo*, and the residue was purified by flash-chromatography (SiO_2, pentane:EtOAc) to afford the target compound as a colorless solid (8.00 g, 40.15 mmol, 72%).

m.p. 78 °C; **^{1}H NMR** (300 MHz, $CDCl_3$) δ 8.65 – 8.57 (m, 2H), 7.39 – 7.31 (m, 2H), 7.15 – 7.04 (m, 2H), 6.90 – 6.79 (m, 2H), 5.06 (s, 2H), 2.29 (s, 3H); **^{13}C{H} NMR** (75 MHz, $CDCl_3$) δ 156.2, 150.0, 146.7, 130.9, 130.2, 121.6, 114.7, 68.3, 20.6; **IR (ATR)** [cm^{-1}]: $\tilde{\nu}$ = 3032, 2920, 2900, 2857, 1604, 1563, 1511, 1449, 1414, 1386, 1324, 1288, 1253, 1175, 1112, 1090, 1048, 994, 805, 755, 601, 514, 486; **HR-MS-ESI(+)** calc. $C_{13}H_{14}NO^+$ $[M+H]^+$ 200.1070; found 200.1072.

Preparation of compound 4j was described in the literature; however, without characterization.[281]

2-{[4-(*tert*-Butyl)phenoxy]methyl}-1,3-dimethylbenzene (469l)

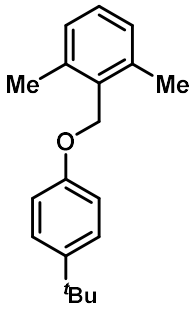

According to general procedure A, compound **469l** was obtained from potassium 4-(*tert*-butyl)phenolate (3.13 g, 16.62 mmol, 1.00 equiv.) and 2-(chloromethyl)-1,3-dimethylbenzene (2.57 g, 16.62 mmol, 1.00 equiv.) after flash-chromatography (SiO_2, pentane:EtOAc) as a colorless solid (4.16 g, 15.52 mmol, 93%).

m.p. 69 °C; **^{1}H NMR** (300 MHz, $CDCl_3$) δ 7.42 – 7.34 (m, 2H), 7.19 (dd, *J* = 8.6, 6.3 Hz, 1H), 7.10 (d, *J* = 7.5 Hz, 2H), 7.04 – 6.96 (m, 2H), 5.05 (s, 2H), 2.42 (d, *J* = 0.8 Hz, 6H), 1.35 (s, 9H); **^{13}C{H} NMR** (75 MHz, $CDCl_3$) δ 157.2, 143.7, 138.3, 133.1, 128.7, 128.5, 126.4, 114.2, 64.7, 34.2, 31.7, 19.7; **IR (ATR)** [cm^{-1}]: $\tilde{\nu}$ = 3041, 2956, 2900, 2866, 1607, 1512, 1470, 1364, 1294, 1236, 1182, 1032, 1005, 870, 829, 768, 694, 553; **HR-MS-EI** calc. $C_{19}H_{24}O$ $[M]^+$ 268.1822; found 268.1823.

2-((4-(tert-butyl)phenoxy)methyl)-1,3-dichlorobenzene (469m)

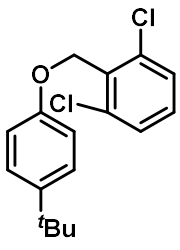

According to general procedure A, compound **469m** was obtained from potassium 4-(*tert*-butyl)phenolate (2.90 g, 15.42 mmol, 1.00 equiv.) and 2-(bromomethyl)-1,3-dichlorobenzene (3.70 g, 15.42 mmol, 1.00 equiv.) after flash-chromatography (SiO_2, pentane:EtOAc) as a colorless solid (2.18 g, 7.05 mmol, 46%).

^{1}H NMR (300 MHz, $CDCl_3$) δ 7.45 – 7.36 (m, 4H), 7.30 (dd, *J* = 6.8, 2.1 Hz, 1H), 7.08 – 6.96 (m, 2H), 5.31 (s, 2H), 1.37 (s, 9H); **^{13}C NMR** (75 MHz, $CDCl_3$) δ 156.8, 144.1, 137.2,

132.5, 130.5, 128.6, 126.4, 114.5, 65.2, 34.3, 31.7; **IR (ATR)** [cm^{-1}]: $\tilde{\nu}$ = 2960, 2896, 2865, 1606, 1583, 1563, 1510, 1467, 1437, 1382, 1362, 1292, 1237, 1184, 1092, 1020, 998, 873, 827, 805, 783, 766, 730, 677, 551; **HR-MS-EI(+)** calc. $C_{17}H_{18}Cl_2O^+$ $[M]^+$ 308.0729, found 308.0730.

4-{[4-(Trifluoromethyl)benzyl]oxy}-1,1'-biphenyl (469n)

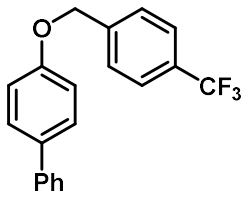

According to general procedure A, compound **469n** was obtained from potassium [1,1'-biphenyl]-4-olate (6.10 g, 29.28 mmol, 1.00 equiv.) and 1-(bromomethyl)-4-(trifluoromethyl)benzene (7.00 g, 29.29 mmol, 1.00 equiv.) after flash-chromatography (SiO_2, pentane:EtOAc) as a colorless solid (9.10 g, 27.72 mmol, 95%).

m.p. 137 °C; **^{1}H NMR** (400 MHz, $CDCl_3$) δ 7.68 (d, *J* = 8.1 Hz, 2H), 7.62 – 7.52 (m, 6H), 7.44 (dd, *J* = 8.5, 6.9 Hz, 2H), 7.37 – 7.29 (m, 1H), 7.05 (d, *J* = 8.8 Hz, 2H), 5.18 (s, 2H); **^{13}C{H} NMR** (101 MHz, $CDCl_3$) δ 158.1, 141.2 (q, C-F, $^4J_{C\text{-}F}$ = 1.5 Hz), 140.8, 134.6, 130.3 (q, C-F, $^2J_{C\text{-}F}$ = 32.4 Hz), 128.9, 128.4, 127.5, 127.0, 126.9, 125.7 (q, C-F, $^3J_{C\text{-}F}$ = 3.7 Hz), 124.2 (q, C-F, $^1J_{C\text{-}F}$ = 272.1 Hz), 115.2, 69.3; **^{19}F NMR** (377 MHz, $CDCl_3$) δ -62.51; **IR (ATR)** [cm^{-1}]: $\tilde{\nu}$ = 3097, 3081, 3064, 3050, 3037, 3010, 2925, 2886, 2856, 1606, 1522, 1488, 1459, 1331, 1270, 1251, 1150, 1106, 1067, 1049, 1015, 855, 827, 761, 711, 689, 645, 591, 579, 495; **HR-MS-ESI(+)** calc. $C_{20}H_{15}F_3O^+$ $[M]^+$ 328.1070; found 328.1068.

4-[(3,5-Dichlorobenzyl)oxy]-1,1'-biphenyl (469o)

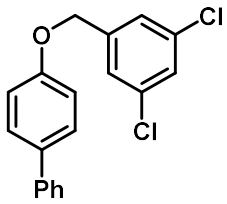

According to general procedure A, compound **469o** was obtained from potassium [1,1'-biphenyl]-4-olate (3.18 g, 15.27 mmol, 1.00 equiv.) and 1-(bromomethyl)-3,5-dichlorobenzene (3.66 g, 15.26 mmol, 1.00 equiv.) after flash-chromatography (SiO_2, pentane:EtOAc) as a colorless solid (3.43 g, 10.42 mmol, 68%).

m.p. 113 °C; **^{1}H NMR** (300 MHz, $CDCl_3$) δ 7.61 – 7.49 (m, 4H), 7.49 – 7.38 (m, 2H), 7.38 – 7.28 (m, 4H), 7.07 – 6.98 (m, 2H), 5.06 (s, 2H); **^{13}C{H} NMR** (75 MHz, $CDCl_3$) δ 157.9, 140.7, 140.7, 135.4, 134.8, 128.9, 128.5, 128.2, 127.0, 126.9, 125.7, 115.2, 68.7; **IR (ATR)** [cm^{-1}]: $\tilde{\nu}$ = 3083, 3074, 3052, 3033, 3003, 2913, 2896, 2863, 2853, 2726, 1569, 1523, 1485, 1430, 1366, 1272, 1243, 1102, 1041, 917, 830, 795, 762, 727, 693, 668, 638, 550, 486, 431; **HR-MS-EI** calc. $C_{19}H_{14}Cl_2O^+$ $[M]^+$ 328.0416; found 328.0416.

1,2-Bis{[4-(*tert*-butyl)phenoxy]methyl}benzene (469q)

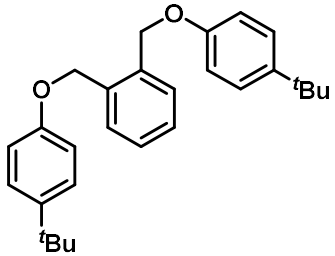

According to general procedure A, compound **469q** was obtained from potassium 4-(*tert*-butyl)phenolate (2.14 g, 11.36 mmol, 2.00 equiv.) and 1,2-bis(bromomethyl)benzene (1.50 g, 5.68 mmol, 1.00 equiv.) after flash-chromatography (SiO_2, pentane:EtOAc) as a colorless solid (2.23 g, 5.54 mmol, 98%).

m.p. 95 °C; **^{1}H NMR** (300 MHz, $CDCl_3$) δ 7.52 (dd, *J* = 5.6, 3.5 Hz, 2H), 7.40 – 7.33 (m, 2H), 7.33 – 7.27 (m, 4H), 6.95 – 6.87 (m, 4H), 5.15 (s, 4H), 1.30 (s, 18H); **^{13}C{H} NMR** (75 MHz, $CDCl_3$) δ 156.4, 143.8, 135.4, 128.9, 128.4, 126.3, 114.3, 68.0, 34.1, 31.5; **IR (ATR)** [cm^{-1}]: $\tilde{\nu}$ = 3060, 3036, 2962, 2952, 2902, 2861, 1607, 1511, 1453, 1364, 1296, 1244, 1183, 1115, 1043; **HR-MS-ESI(+)** calc. $C_{28}H_{35}O_2^+$ $[M+H]^+$ 403.2632; found 403.2623.

1,4-Bis[(*p*-tolyloxy)methyl]benzene (469r)

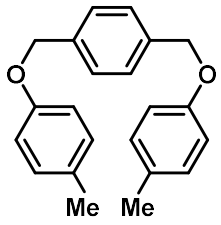

α,α′-Dibromo-*p*-xylene (3.7 g, 14.02 mmol, 1.00 equiv.) and *p*-cresol (3.33 g, 30.80 mmol, 2.20 equiv.) were dissolved in DMF (70 mL), and K_2CO_3 (9.69 g, 70.11 mmol, 5.00 equiv.) was added. The reaction mixture was stirred at 60 °C for 3 d using a pre-heated oil bath and afterwards poured into H_2O. The mixture was extracted with CH_2Cl_2, (3 × 50 mL). The combined organic phases were washed with brine and dried over $MgSO_4$. Evaporation of all volatile components and recrystallization from a hot toluene/heptane solution yielded the target compound as colorless solid (2.67 g, 8.39 mmol, 60%).

m.p. 170 °C; **^{1}H NMR** (300 MHz, $CDCl_3$) δ 7.45 (s, 4H), 7.13 – 7.06 (m, 4H), 6.92 – 6.84 (m, 4H), 5.05 (s, 4H), 2.30 (s, 6H); **^{13}C{H} NMR** (75 MHz, $CDCl_3$) δ 156.8, 137.1, 130.3, 130.1, 127.8, 114.8, 69.9, 20.6; **IR (ATR)** [cm^{-1}]: $\tilde{\nu}$ = 3032, 2919, 2863, 1884, 1609, 1581, 1508, 1376, 1221, 1174. 1012, 809, 784, 508; **HR-MS-ESI(+)** calc. $C_{22}H_{22}NaO_2^+$ $[M+Na]^+$ 341.1512; found 341.1499.

Analytical data are in accordance to the previously published in the literature.[282]

1,4-Bis{[4-(*tert*-butyl)phenoxy]methyl}naphthalene (469s)

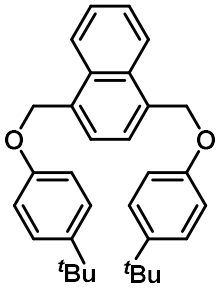

According to general procedure A, compound **469s** was obtained from potassium 4-(*tert*-butyl)phenolate (2.04 g, 10.83 mmol, 2.00 equiv.) and 1,4-bis(bromomethyl)naphthalene[283] (1.70 g, 5.41 mmol, 1.00 equiv.) after recrystallization from MeOH as a colorless solid (1.60 g, 3.53 mmol, 65%).

m.p. 145 °C; **^{1}H NMR** (300 MHz, $CDCl_3$) δ 8.17 – 8.07 (m, 2H), 7.62 – 7.53 (m, 4H), 7.41 – 7.29 (m, 4H), 7.08 – 6.94 (m, 4H), 5.49 (s, 4H), 1.32 (s, 18H); **^{13}C{H} NMR** (75 MHz, $CDCl_3$) δ 156.7, 144.0, 133.5, 132.0, 126.5, 126.5, 126.2, 124.6, 114.5, 68.8, 34.3, 31.7; **IR (ATR)** [cm^{-1}]: $\tilde{\nu}$ = 2957, 2901, 2867, 1607, 1510, 1363, 1292, 1239, 1181, 1001, 828, 813, 757, 553; **HR-MS-ESI(+)** calc. $C_{32}H_{36}NaO_2^+$ $[M+Na]^+$ 475.2608; found 475.2609.

2,2'-Bis{[4-(*tert*-butyl)phenoxy]methyl}-1,1'-biphenyl (469t)

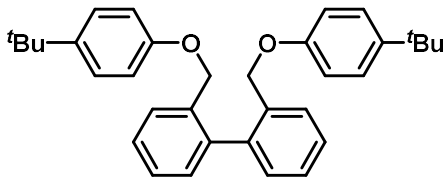

According to general procedure A, compound **469t** was obtained from potassium 4-(*tert*-butyl)phenolate (5.65 g, 30.00 mmol, 2.00 equiv.) and 2,2'-bis(bromomethyl)-1,1'-biphenyl (5.10 g, 15.00 mmol, 1.00 equiv.) after flash-chromatography (SiO_2, pentane:EtOAc) as a colorless solid (7.16 g, 14.95 mmol, 99%).

m.p. 69 °C; **^{1}H NMR** (300 MHz, $CDCl_3$) δ 7.68 – 7.59 (m, 2H), 7.42 (td, *J* = 7.6, 1.9 Hz, 2H), 7.36 (td, *J* = 7.4, 1.7 Hz, 2H), 7.29 – 7.19 (m, 6H), 6.80 – 6.72 (m, 4H), 4.81 (s, 4H), 1.28 (s, 18H); **^{13}C{H} NMR** (75 MHz, $CDCl_3$) δ 156.6, 143.6, 139.4, 135.3, 129.9, 128.8, 128.2, 127.8, 126.3, 114.4, 68.1, 34.2, 31.6; **IR (ATR)** [cm^{-1}]: $\tilde{\nu}$ = 3060, 3037, 2957, 2902, 2866, 1606, 1510, 1462, 1362, 1295, 1237, 1180, 1117, 1010, 825, 755, 680; **HR-MS-ESI(+)** calc. $C_{34}H_{39}O_2^+$ $[M+H]^+$ 479.2945; found 479.2937.

1,2-Bis{4-[(*p*-tolyloxy)methyl]phenyl}ethane (469u)

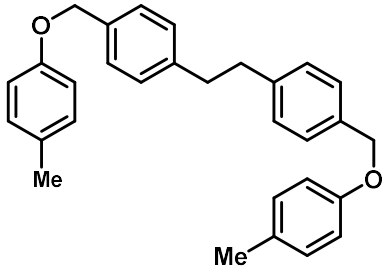

1,2-Bis[4-(bromomethyl)phenyl]ethane[284] (11.40 g, 30.97 mmol, 1.00 equiv.) and *p*-cresol (8.37 g, 77.41 mmol, 2.50 equiv.) were dissolved in MeCN (100 mL), and K_2CO_3 (10.70 g, 77.42 mmol, 2.50 equiv.) was added. The reaction mixture was stirred at 90 °C for 60 h using a pre-heated oil bath. After cooling to ambient temperature, the solvent was removed *in vacuo*. Water was added to the residue, and the mixture was extracted with CH_2Cl_2 (3 × 100 mL). The combined organic phases were washed with brine and dried over $MgSO_4$. All volatile compounds were removed under reduced pressure and the residue was purified by flash-chromatography (SiO_2, pentane:EtOAc) affording the target compound as a colorless solid (8.19 g, 19.38 mmol, 63%).

m.p. 164 °C; **^{1}H NMR** (300 MHz, $CDCl_3$) δ 7.38 – 7.31 (m, 4H), 7.23 – 7.16 (m, 4H), 7.13 – 7.05 (m, 4H), 6.92 – 6.84 (m, 4H), 5.01 (s, 4H), 2.93 (s, 4H), 2.29 (s, 6H); **^{13}C{H} NMR** (75 MHz, $CDCl_3$) δ 156.9, 141.6, 135.0, 130.2, 130.0, 128.8, 127.8, 114.9, 70.1, 37.7, 20.6; **IR (ATR)** [cm^{-1}]: $\tilde{\nu}$ = 3034, 2945, 2918, 2858, 2727, 1612, 1509, 1295, 1245, 1174, 1014, 872, 816, 778, 570, 527; **HR-MS-ESI(+)** calc. $C_{30}H_{30}NaO_2^+$ $[M+Na]^+$ 445.2144; found 445.2138.

General procedure B:

Dibenzothiophenium trifluoromethanesulfonates

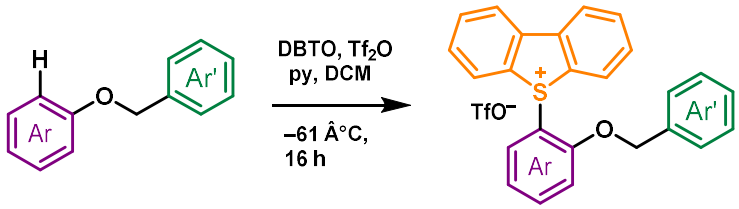

The syntheses were carried out using a modified literature procedure.[222]

An oven-dried Schlenk flask was equipped with a stirring bar and charged with dibenzothiophene *S*-oxide (1.00 equiv.). The flask was evacuated and back-filled with nitrogen three times. Dry degassed CH_2Cl_2 was added under nitrogen. The suspension was stirred until all solids dissolved, cooled to -61 °C, and triflic anhydride (1.00 equiv.) was added dropwise. After the addition was completed, the reaction mixture was stirred for an additional 10 min at the same temperature. Afterwards, a solution of the corresponding benzyl ether (1.00 equiv.) and pyridine (1.10 equiv.) in DCM was added dropwise, and the reaction mixture was stirred for 16 h while being allowed to warm up to ambient temperature. A saturated aqueous solution of $NaHCO_3$ was added, and the mixture was stirred for 30 min at ambient temperature to deprotonate the pyridinium triflate. The mixture was extracted with CH_2Cl_2, washed with brine and dried over Na_2SO_4. Volatile compounds were evaporated under reduced pressure. If not otherwise stated, the residue was purified by flash-chromatography (SiO_2, gradient elution: CH_2Cl_2; acetone:CH_2Cl_2 1:4) to give the target compound.

Bis(dibenzothiophenium) trifluoromethanesulfonates

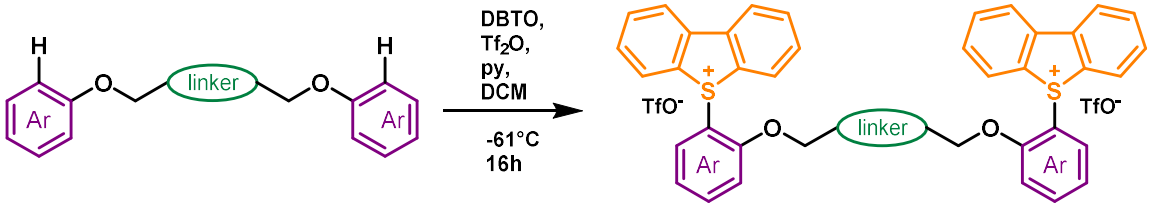

The syntheses were carried out using a modified literature procedure.[222]

An oven-dried Schlenk flask was equipped with a stirring bar and charged with dibenzothiophene *S*-oxide (2.00 equiv.). The flask was evacuated and back-filled with nitrogen three times. Dry degassed CH_2Cl_2 was added under nitrogen. The suspension was stirred until all solids dissolved, cooled to -61 °C, and triflic anhydride (2.00 equiv.) was added dropwise. After the addition was completed, the reaction mixture was stirred for additional 10 min at the same temperature. Afterwards, a solution of the corresponding benzyl ether (1.00 equiv.) and pyridine (2.10 equiv.) in DCM was added dropwise, and the reaction mixture was stirred for 16 h while being allowed to warm up to ambient temperature. A saturated aqueous solution of $NaHCO_3$ was added and the mixture was stirred for 30 min at ambient temperature to deprotonate the pyridinium triflate. The suspension was filtered and the filtrate extracted with CH_2Cl_2. The precipitate was washed with water and combined with the CH_2Cl_2 extracts. Volatile compounds were evaporated under reduced pressure. If not otherwise stated, the resulting solid was purified by flash-chromatography (SiO_2, gradient elution: acetone:CH_2Cl_2 1:4; acetone:CH_2Cl_2 2:3) to give the target compound.

Dibenzothiophenium trifluoromethanesulfonates:

5-{5-Methyl-2-[(4-methylbenzyl)oxy]phenyl}-5*H*-dibenzo[*b*,*d*]thiophen-5-ium Trifluoromethanesulfonate (470a)

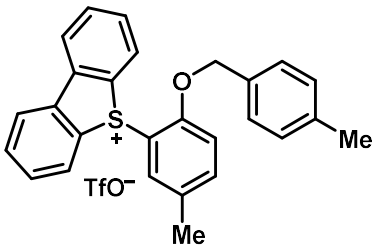

According to general procedure B, compound **470a** was obtained from 1-methyl-4-[(4-methylbenzyl)oxy]benzene (**469a**) (6.00 g, 28.26 mmol, 1.00 equiv.) and corresponding amounts of other reagents in CH_2Cl_2 (100 mL) after recrystallization from THF/hexane as a colorless solid (9.27 g, 17.02 mmol, 60%).

m.p. 190 °C; **^{1}H NMR** (400 MHz, $CDCl_3$) δ 8.04 (d, *J* = 8.1 Hz, 2H), 7.80 (d, *J* = 7.8 Hz, 2H), 7.70 (t, *J* = 7.5 Hz, 2H), 7.67 (s, 1H), 7.58 (td, *J* = 7.8, 1.5 Hz, 2H), 7.44 (dd, *J* = 8.5, 2.2 Hz, 1H), 7.11 (d, *J* = 8.2 Hz, 2H), 6.98 (d, *J* = 8.5 Hz, 1H), 6.79 (d, *J* = 7.9 Hz, 2H), 4.75 (s, 2H), 2.40 (s, 3H), 2.33 (s, 3H); **^{13}C{H} NMR** (101 MHz, $CDCl_3$) δ 156.2, 139.5, 139.0, 138.4, 134.4, 133.6, 133.5, 131.1, 131.1, 129.7, 129.5, 128.7, 128.1, 123.7, 121.1 (q, C-F, $^1J_{C\text{-}F}$ = 320.8 Hz), 114.5, 110.9, 71.9, 21.4, 20.4; **^{19}F NMR** (376 MHz, CDCl3) δ -78.15; **IR (ATR)** [cm^{-1}]: $\tilde{\nu}$ = 3085, 3055, 3012, 2951, 2925, 1496, 1449, 1254, 1224, 1146, 1028, 984, 814, 784, 761, 706, 634, 572, 552, 515, 479, 418; **HR-MS-ESI(+)** calc. $C_{27}H_{23}OS^+$ [M–TfO]$^+$ 395.1464; found 395.1465.

5-[5-(*tert*-Butyl)-2-{[4-(*tert*-butyl)benzyl]oxy}phenyl]-5*H*-dibenzo[*b,*d]thiophen-5-ium Trifluoromethane-sulfonate (470b)

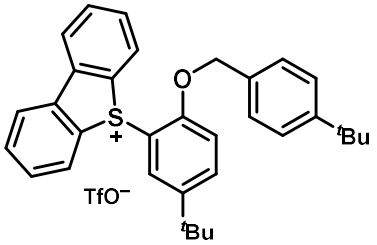

According to general procedure B, compound **470b** was obtained from 1-(*tert*-butyl)-4-{[4-(*tert*-butyl)benzyl]oxy}benzene (**469b**) (6.00 g, 20.24 mmol, 1.00 equiv.) and corresponding amounts of other reagents in CH_2Cl_2 (100 mL) after recrystallization from THF/hexane as a colorless solid (9.40 g, 14.95 mmol, 74%).

m.p. 196 °C; **^{1}H NMR** (400 MHz, $CDCl_3$) δ 8.01 (d, *J* = 8.0 Hz, 2H), 7.99 (d, *J* = 2.4 Hz, 1H), 7.72 – 7.64 (m, 5H), 7.57 (ddd, *J* = 8.7, 6.7, 2.0 Hz, 2H), 7.30 (d, *J* = 8.4 Hz, 2H), 7.02 (d, *J* = 8.8 Hz, 1H), 6.78 – 6.70 (m, 2H), 4.66 (s, 2H), 1.38 (s, 9H), 1.31 (s, 9H); **^{13}C{H} NMR** (101 MHz, $CDCl_3$) δ 156.0, 152.2, 146.6, 139.4, 135.3, 133.5, 132.0, 131.0, 130.9, 129.5, 128.6, 127.9, 125.6, 123.6, 121.0 (q, C-F, $^1J_{C\text{-}F}$ = 320.6 Hz), 114.2, 109.9, 71.6, 34.9, 34.8, 31.5, 31.2; **^{19}F NMR** (282 MHz, CD_3CN) δ -79.32; **IR (ATR)** [cm^{-1}]: $\tilde{\nu}$ = 3090, 3063, 2952, 2905, 2868, 1504, 1489, 1465, 1448, 1387, 1363, 1256, 1149, 1028, 987, 822, 756, 635, 571, 516, 488, 418; **HR-MS-ESI(+)** calc. $C_{33}H_{35}OS^+$ [M−TfO]$^+$ 479.2403; found 479.2404.

5-[2-(Benzyloxy)-5-methylphenyl]-5*H*-dibenzo[*b*,*d*]thiophen-5-ium Trifluoromethanesulfonate (470c)

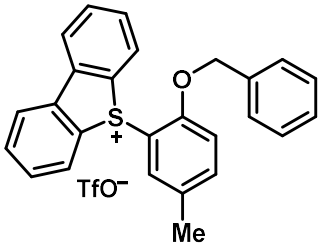

According to general procedure B, compound **470c** was obtained from 1-methyl-4-(phenoxymethyl)benzene (**469c**) (1.00 g, 5.04 mmol, 1.00 equiv.) and corresponding amounts of other reagents in CH_2Cl_2 (50 mL) after flash-chromatography as a colorless solid (1.43 g, 2.70 mmol, 54%).

m.p. 186 °C; **^{1}H NMR** (300 MHz, CD_3CN) δ 8.04 – 7.94 (m, 4H), 7.83 (td, *J* = 7.6, 1.1 Hz, 2H), 7.72 – 7.63 (m, 2H), 7.61 – 7.52 (m, 1H), 7.45 – 7.31 (m, 4H), 7.19 (d, *J* = 8.6 Hz, 1H), 7.07 – 7.00 (m, 2H), 4.93 (s, 2H), 2.27 (s, 3H); **^{13}C{H} NMR** (75 MHz, CD_3CN) δ 157.3, 140.7, 139.3, 135.6, 134.8, 133.9, 133.9, 132.1, 130.6, 129.7, 129.6, 129.5, 128.2, 125.2, 122.2 (q, C-F, $^1J_{C\text{-}F}$ = 320.9 Hz), 115.8, 111.8, 72.5, 20.2; **^{19}F NMR** (282 MHz, CD_3CN) δ -79.3; **IR (ATR)** [cm^{-1}]: $\tilde{\nu}$

= 3088, 3061, 2936, 1496, 1449, 1254, 1150, 1028, 979, 759, 741, 633; **HR-MS-ESI(+)** calc. $C_{26}H_{21}OS^+$ $[M-TfO]^+$ 381.1308; found 381.1307.

5-{2-[(4-Fluorobenzyl)oxy]-5-methylphenyl}-5*H*-dibenzo[*b*,*d*]thiophen-5-ium Trifluoromethanesulfonate (470d)

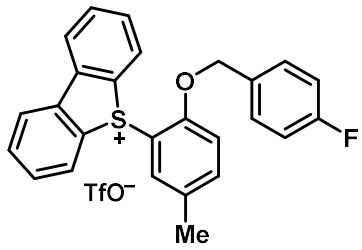

According to general procedure B, compound **470d** was obtained from 1-fluoro-4-[(4-methylbenzyl)oxy]benzene (**469d**) (1.08 g, 4.99 mmol, 1.00 equiv.) and corresponding amounts of other reagents in CH_2Cl_2 (50 mL) after flash-chromatography as a colorless solid (1.84 g, 3.35 mmol, 67%).

m.p. 193 °C; **^{1}H NMR** (300 MHz, CD_3CN) δ 8.04 – 7.91 (m, 4H), 7.82 (td, *J* = 7.6, 1.2 Hz, 2H), 7.67 (td, *J* = 7.7, 1.3 Hz, 2H), 7.58 (dd, *J* = 8.6, 2.2 Hz, 1H), 7.49 (d, *J* = 2.2 Hz, 1H), 7.17 (d, *J* = 8.6 Hz, 1H), 7.14 – 7.04 (m, 2H), 7.04 – 6.95 (m, 2H), 4.84 (s, 2H), 2.30 (s, 3H); **^{13}C{H} NMR** (75 MHz, CD_3CN) δ 163.8 (d, C-F, $^1J_{C\text{-}F}$ = 245.3 Hz), 157.1, 140.6, 139.4, 134.8, 134.7, 133.8, 132.0, 131.8 (d, C-F, $^3J_{C\text{-}F}$ = 8.5 Hz), 131.7 (d, C-F, $^4J_{C\text{-}F}$ = 3.2 Hz), 130.6, 128.2, 125.1, 122.2 (q, C-F, $^1J_{C\text{-}F}$ = 321.0 Hz), 116.4 (d, C-F, $^2J_{C\text{-}F}$ = 21.9 Hz), 115.7, 111.4, 71.6, 20.2; **^{19}F NMR** (282 MHz, CD_3CN) δ -79.3, -114.6; **IR (ATR)** [cm^{-1}]: $\tilde{\nu}$ = 3086, 3049, 2955, 2936, 1606, 1515, 1496, 1254, 1146, 1028, 978, 821, 753, 634; **HR-MS-ESI(+)** calc. $C_{26}H_{20}FOS^+$ $[M-TfO]^+$ 399.1213; found 399.1215.

5-{5-(*tert*-Butyl)-2-[(3,5-dichlorobenzyl)oxy]phenyl}-5*H*-dibenzo[*b*,*d*]thiophen-5-ium Trifluoromethane-sulfonate (470e)

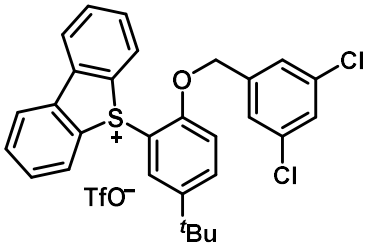

According to general procedure B, compound **470e** was obtained from 1-{[4-(*tert*-butyl)phenoxy]methyl}-3,5-dichlorobenzene (**469e**) (1.00 g, 3.23 mmol, 1.00 equiv.) and corresponding amounts of other reagents in CH_2Cl_2 (50 mL) after flash-chromatography as a colorless solid (1.78 g, 2.77 mmol, 86%).

m.p. 229 °C; **^{1}H NMR** (400 MHz, CD_3CN) δ 8.10 (d, *J* = 2.3 Hz, 1H), 7.96 (d, *J* = 8.0 Hz, 2H), 7.86 (dt, *J* = 7.9, 2.0 Hz, 3H), 7.83 – 7.78 (m, 2H), 7.67 (ddd, *J* = 8.4, 7.2, 1.5 Hz, 2H), 7.52 (t, *J* = 1.9 Hz, 1H), 7.10 (d, *J* = 8.8 Hz, 1H), 6.67 (d, *J* = 1.9 Hz, 2H), 4.58 (s, 2H), 1.37 (s, 9H); **^{13}C{H} NMR** (101 MHz, CD_3CN) δ 156.4, 146.8, 140.6, 138.6, 136.6, 135.6, 134.6, 134.4, 131.9, 130.5, 129.8, 128.6, 127.9, 124.6, 122.2 (q, C-F, $^1J_{C\text{-}F}$ = 321.0 Hz), 115.3, 110.1, 70.4, 35.5, 31.3; **^{19}F NMR** (376 MHz, CD_3CN) δ -79.23; **IR (ATR)** [cm^{-1}]: $\tilde{\nu}$ = 3077, 3010, 2957, 2904, 2894, 2870, 1573, 1493, 1431, 1254, 1151, 1028, 858, 800, 765, 708, 634, 574, 516, 483, 420; **HR-MS-ESI(+)** calc. $C_{29}H_{25}Cl_2OS^+$ $[M-TfO]^+$ 491.0998; found 491.1001.

5-[5-(*tert*-Butyl)-2-{[4-(methylsulfonyl)benzyl]oxy}phenyl]-5*H*-dibenzo[*b*,*d*]thiophen-5-ium Trifluoro-methanesulfonate (470f)

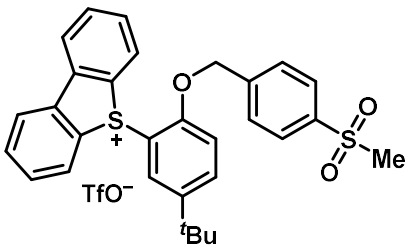

According to general procedure B, compound **470f** was obtained from 1-(*tert*-butyl)-4-{[4-(methylsulfonyl)benzyl]oxy}benzene (**469f**) (1.00 g, 3.14 mmol, 1.00 equiv.) and corresponding amounts of other reagents in CH_2Cl_2 (50 mL) after flash-chromatography as a colorless solid (1.70 g, 2.61 mmol, 83%).

m.p. 254 °C; **^{1}H NMR** (300 MHz, CD_3CN) δ 7.99 (dd, *J* = 8.2, 1.0 Hz, 2H), 7.92 – 7.83 (m, 6H), 7.80 (td, *J* = 7.8, 1.3 Hz, 2H), 7.68 (td, *J* = 7.7, 1.3 Hz, 2H), 7.16 (d, *J* = 8.8 Hz, 1H), 7.04 (d, *J* = 8.3 Hz, 2H), 4.84 (s, 2H), 3.17 (s, 3H), 1.33 (s, 9H); **^{13}C{H} NMR** (75 MHz, CD_3CN) δ 156.6, 147.0, 142.2, 141.2, 140.6, 136.4, 134.7, 133.4, 132.0, 130.6, 130.2, 128.4, 128.1, 124.9, 122.2 (q, C-F, $^1J_{C\text{-}F}$ = 320.9 Hz), 115.5, 110.7, 71.1, 44.4, 35.44, 31.2; **^{19}F NMR**

(282 MHz, CD_3CN) δ -79.26; **IR (ATR)** [cm^{-1}]: $\tilde{\nu}$ = 3087, 3077, 3064, 3052, 3014, 2962, 2943, 2926, 2909, 2871, 1492, 1257, 1146, 1030, 1001, 956, 863, 827, 760, 707, 635, 573, 550, 516, 477, 418; **HR-MS-ESI(+)** calc. $C_{30}H_{29}O_3S_2^+$ [M−TfO]$^+$ 501.1553; found 501.1553.

5-[2,3,4-Trimethyl-6-(naphthalen-1-ylmethoxy)phenyl]-5*H*-dibenzo[*b*,*d*]thiophen-5-ium Trifluorome-thanesulfonate (470g)

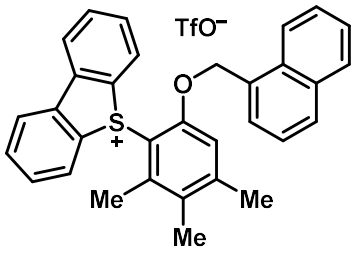

According to general procedure B, compound **470g** was obtained from 1-[(3,4,5-trimethylphenoxy)methyl]naphthalene (**469g**) (1.00 g, 3.62 mmol, 1.00 equiv.) and corresponding amounts of other reagents in CH_2Cl_2 (50 mL) after flash-chromatography as a colorless solid (1.20 g, 1.97 mmol, 54%).

m.p. 183 °C (decomp.); **^{1}H NMR** (500 MHz, CD_3CN) δ 8.03 – 7.92 (m, 2H), 7.73 (ddd, *J* = 8.0, 1.1, 0.6 Hz, 2H), 7.51 (ddd, *J* = 8.1, 6.7, 1.1 Hz, 1H), 7.41 (ddd, *J* = 8.0, 7.4, 1.2 Hz, 2H), 7.36 (dd, *J* = 8.3, 6.8 Hz, 1H), 7.29 (ddd, *J* = 7.4, 1.0 Hz, 2H), 7.15 (ddd, *J* = 8.3, 6.8, 1.3 Hz, 1H), 7.07 (s, 1H), 7.02 – 6.95 (m, 3H), 6.69 (dd, *J* = 6.9, 1.2 Hz, 1H), 4.88 (s, 2H), 2.92 (s, 3H), 2.45 (t, *J* = 0.6 Hz, 3H), 2.34 (s, 3H); **^{13}C{H} NMR** (126 MHz, CD_3CN) δ 157.4, 149.7, 145.9, 139.7, 134.4, 133.6, 132.6, 131.8, 131.2, 130.8, 130.2, 130.1, 129.6, 129.3, 127.9, 126.9, 126.4, 126.4, 123.9, 123.7, 122.2 (q, C-F, $^1J_{C\text{-}F}$ = 320.8 Hz), 114.5, 105.9, 69.7, 22.1, 19.1, 16.0; **^{19}F NMR** (471 MHz, CD_3CN) δ -79.34; **IR (ATR)** [cm^{-1}]: $\tilde{\nu}$ = 3061, 3013, 2926, 1582, 1448, 1257, 1146, 1070, 1029, 753, 635, 572, 515, 419; **HR-MS-ESI(+)** calc. $C_{32}H_{27}SO^+$ [M−TfO]$^+$ 459.1777; found 459.1774.

5-[5-(*tert*-Butyl)-2-{[4-(trifluoromethyl)benzyl]oxy}phenyl]-5*H*-dibenzo[*b*,*d*]thiophen-5-ium Trifluoromethanesulfonate (470h)

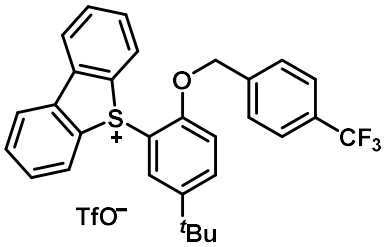

According to general procedure B, compound **470h** was obtained from 1-(*tert*-butyl)-4-{[4-(trifluoromethyl)benzyl]oxy}benzene (**469h**) (1.00 g, 3.24 mmol, 1.00 equiv.) and corresponding amounts of other reagents in CH_2Cl_2 (50 mL) after flash-chromatography as a colorless solid (1.75 g, 2.73 mmol, 84%).

m.p. 215 °C; **^{1}H NMR** (400 MHz, CD_3CN) δ 7.97 (dt, *J* = 8.0, 0.9 Hz, 2H), 7.92 – 7.87 (m, 3H), 7.84 (dd, *J* = 8.8, 2.5 Hz, 1H), 7.79 (td, *J* = 7.6, 1.0 Hz, 2H), 7.71 – 7.60 (m, 4H), 7.15 (d, *J* = 8.8 Hz, 1H), 6.99 (d, *J* = 7.9 Hz, 2H), 4.82 (s, 2H), 1.32 (s, 9H); **^{13}C{H} NMR** (101 MHz, CD_3CN) δ 156.7, 146.9, 140.6, 139.7, 136.4, 134.7, 133.3, 132.0, 131.0 (q, C-F, $^2J_{C\text{-}F}$ = 31.9 Hz), 130.5, 130.1, 128.1, 126.5 (q, C-F, $^3J_{C\text{-}F}$ = 3.9 Hz), 125.3 (q, C-F, $^1J_{C\text{-}F}$ = 272.1 Hz), 124.9, 122.2 (q, C-F, $^1J_{C\text{-}F}$ = 321.2 Hz), 115.4, 110.7, 71.3, 35.4, 31.2; **^{19}F NMR** (282 MHz, CD_3CN) δ -63.09, -79.34; **IR (ATR)** [cm^{-1}]: $\tilde{\nu}$ = 3098, 3072, 3040, 2967, 2906, 2871, 1497, 1327, 1255, 1113, 1065, 1030, 999, 831, 755, 706, 636, 571, 517, 483, 418; **HR-MS-ESI(+)** calc. $C_{30}H_{26}F_3OS^+$ [M−TfO]$^+$ 491.1651; found 491.1659.

5-(5-chloro-2-((3,5-dichlorobenzyl)oxy)phenyl)-5H-dibenzo[b,d]thiophen-5-ium trifluoromethanesulfonate (470i)

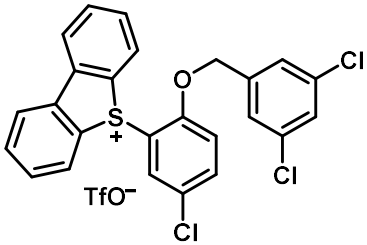

According to general procedure B, compound **470i** was obtained from 1,3-dichloro-5-((4-chlorophenoxy)methyl)benzene (**469i**) (1.00 g, 3.48 mmol, 1.00 equiv.) and corresponding amounts of other reagents in CH_2Cl_2 (50 mL) after flash-chromatography as a colorless solid (0.21 g, 0.35 mmol, 10%).

m.p. 220 °C; **^{1}H NMR** (300 MHz, CD_3CN) δ 8.06 – 7.96 (m, 3H), 7.93 – 7.76 (m, 5H), 7.68 (t, *J* = 7.6 Hz, 2H), 7.53 (t, *J* = 1.9 Hz, 1H), 7.18 (d, *J*

= 9.0 Hz, 1H), 6.76 (s, 2H), 4.67 (s, 2H); **^{13}C{H} NMR** (75 MHz, CD_3CN) δ 157.7, 140.8, 138.8, 138.3, 136.0, 135.7, 134.8, 132.1, 130.0, 129.6, 128.6, 128.3, 127.5, 124.8, 122.2 (q, C-F, $^1J_{C\text{-}F}$ = 320.6 Hz), 117.2, 112.5, 71.1; **^{19}F NMR** (282 MHz, CD_3CN) δ -79.25; **IR (ATR)** [cm^{-1}]: $\tilde{\nu}$ = 3101, 3060, 1702, 1571, 1481, 1429, 1378, 1279, 1251, 1225, 1145, 1028, 997, 873, 843, 822, 796, 751, 705, 679, 653, 634, 572, 532, 515, 497, 478, 418; **HR-MS-ESI(+)** calc. $C_{25}H_{16}Cl_3OS^+$ $[M-TfO]^+$ 468.9982; found 468.9981.

5-(5-methyl-2-((4-nitrobenzyl)oxy)phenyl)-5H-dibenzo[b,d]thiophen-5-ium trifluoromethanesulfonate (470j)

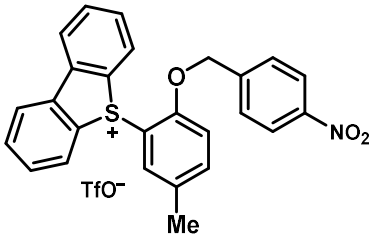

According to general procedure B, compound **470j** was obtained from 1-methyl-4-[(4-nitrobenzyl)oxy]benzene (**469j**) (0.22 g, 0.91 mmol, 1.00 equiv.) and corresponding amounts of other reagents in CH_2Cl_2 (50 mL) after flash-chromatography as a colorless solid (0.405 g, 0.704 mmol, 78%).

^{1}H NMR (400 MHz, $CDCl_3$) δ 8.16 (d, *J* = 8.7 Hz, 4H), 7.97 (dd, *J* = 7.8, 1.3 Hz, 2H), 7.79 (td, *J* = 7.6, 1.2 Hz, 2H), 7.65 (td, *J* = 7.7, 1.2 Hz, 2H), 7.43 (t, *J* = 7.8 Hz, 3H), 7.12 (d, *J* = 8.7 Hz, 2H), 5.22 (s, 2H), 2.23 (s, 3H); **^{13}C NMR** (101 MHz, $CDCl_3$) δ 156.2, 148.2, 142.0, 139.3, 138.1, 134.3, 134.0, 131.6, 131.2, 130.0, 129.1, 128.8, 124.0, 123.7, 121.0 (q, *J* = 320.6 Hz), 115.3, 112.9, 71.3, 20.6; **^{19}F NMR** (282 MHz, CD_3CN) δ -79.34; **IR (ATR)** [cm^{-1}]: $\tilde{\nu}$ = 3578, 3512, 3081, 3059, 3015, 2959, 2931, 2855, 1607, 1524, 1496, 1349, 1250, 1153, 1029, 981, 854, 817, 761, 741, 708, 635, 570, 516, 490, 474, 418; **HR-MS-ESI(+)** calc. $C_{26}H_{20}NO_3S^+$ $[M-TfO]^+$ 426.1158, found 426.1160.

4-{[2-(5*H*-Dibenzo[*b*,*d*]thiophen-5-ium-5-yl)-4-methylphenoxy]methyl}pyridin-1-ium Bis(trifluoromethanesulfonate) (470k)

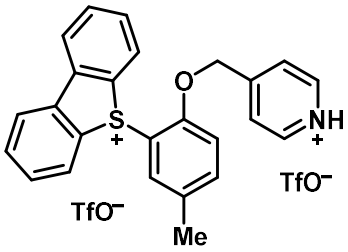

According to general procedure B, compound **470k** was obtained from 4-[(*p*-tolyloxy)methyl]pyridine (**469k**) (4.01 g, 20.13 mmol, 1.00 equiv.) and corresponding amounts of other reagents in CH_2Cl_2 (100 mL), but without addition of pyridine as an external base, after flash-chromatography as a pale violet solid (7.65 g, 11.22 mmol, 56%).

m.p. 188 °C (decomp.); **^{1}H NMR** (300 MHz, CD_3CN) δ 13.66 (t, *J* = 50.0 Hz, 1H), 8.73 (t, *J* = 6.7 Hz, 2H), 8.19 (dd, *J* = 7.8, 0.6 Hz, 2H), 8.08 (dt, *J* = 8.1, 0.8 Hz, 2H), 7.91 (td, *J* = 7.7, 1.1 Hz, 2H), 7.86 (d, *J* = 6.5 Hz, 2H), 7.73 (ddd, *J* = 8.7, 7.5, 1.3 Hz, 2H), 7.57 (ddd, *J* = 8.6, 2.1, 0.7 Hz, 1H), 7.18 (d, *J* = 8.7 Hz, 1H), 7.15 (d, *J* = 1.3 Hz, 1H), 5.39 (s, 2H), 2.23 (s, 3H); **^{13}C{H} NMR** (75 MHz, CD_3CN) δ 158.0, 156.5, 142.7, 140.7, 139.2, 135.6, 135.3, 132.6, 132.5, 131.0, 128.8, 126.3, 125.4, 122.1 (q, C-F, $^1J_{C\text{-}F}$ = 320.3 Hz), 116.1, 113.4, 69.9, 20.2; **^{19}F NMR** (282 MHz, CD_3CN) δ -79.32; **IR (ATR)** [cm^{-1}]: $\tilde{\nu}$ = 3103, 3092, 3071, 3033, 2921, 2886, 2858, 2836, 1613, 1493, 1448, 1237, 1153, 1060, 1025, 813, 760, 710, 634, 572, 514, 490, 474, 420; **HR-MS-ESI(+)** calc. $C_{25}H_{20}NOS$ $[M-2TfO-H]^+$ 382.1260; found 382.1263.

4-{[2-(5*H*-Dibenzo[*b*,*d*]thiophen-5-ium-5-yl]-4-methylphenoxy}methyl)pyridine 1-oxide Trifluorometha-nesulfonate (470k')

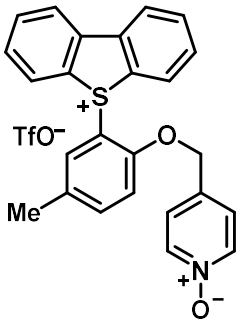

To the stirred mixture of 4-{[2-(5*H*-dibenzo[*b*,*d*]thiophen-5-ium-5-yl)-4-methylphenoxy]methyl}pyridin-1-ium bis(trifluoro-methanesulfonate) (**470k**) (264 mg, 387.3 μmol, 1.00 equiv.) and NaOAc (35 mg, 426.6 μmol, 1.10 equiv.) in CH_2Cl_2 (20 mL) *m*CPBA (95.5 mg of 77% p/w, 73.5 mg, 426 μmol, 1.10 equiv.) was added. The reaction mixture was stirred for 4 h at ambient temperature. The CH_2Cl_2 solution was washed with a saturated aqueous solution of $NaHCO_3$ and dried over Na_2SO_4. All volatile compounds were removed under reduced pressure to give the target compound as a colorless solid (208 mg, 380 μmol, 98%).

m.p. 196 °C (decomp.); **^{1}H NMR** (600 MHz, CD_3CN) δ 8.12 – 8.08 (m, 4H), 7.99 (ddd, *J* = 8.1, 1.0, 0.5 Hz, 2H), 7.86 (td, *J* = 7.6, 1.0 Hz, 2H), 7.69 (ddd, *J* = 8.0, 7.4, 1.2 Hz, 2H), 7.60 – 7.57 (m, 1H), 7.44 (s, 1H), 7.14 (d, *J* = 8.6 Hz, 1H), 6.96 (d, *J* = 6.4 Hz, 2H), 4.87 (s, 2H), 2.29 (s, 3H); **^{13}C{H} NMR** (101 MHz, CD_3CN) δ 156.8, 140.6, 140.0, 139.5, 135.0, 134.5, 134.4, 133.6, 132.2, 130.7, 128.4, 127.0, 125.1, 122.1 (q, C-F, $^1J_{C\text{-}F}$ = 320.7 Hz), 115.8, 111.8, 69.9, 20.2; **^{19}F NMR** (565 MHz, CD_3CN) δ -79.30; **IR (ATR)** [cm^{-1}]: $\tilde{\nu}$ = 3114, 3087, 3059, 2950, 2899, 1496, 1449, 1263, 1151, 1028, 981, 848, 808, 755, 707, 632, 561, 516, 475, 418; **HR-MS-ESI(+)** calc. $C_{25}H_{20}NO_2S$ $[M-TfO]^+$ 398.1209; found 398.1211.

5-{5-(*tert*-Butyl)-2-[(2,6-dimethylbenzyl)oxy]phenyl}-5*H*-dibenzo[*b*,*d*]thiophen-5-ium Trifluoromethane-sulfonate (470l)

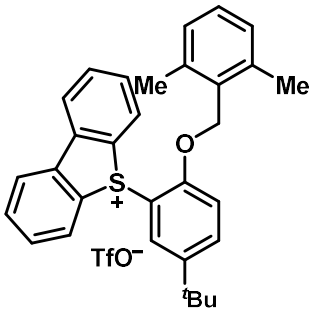

According to general procedure B, compound **470l** was obtained from 2-{[4-(*tert*-butyl)phenoxy]methyl}-1,3-dimethylbenzene (**469l**) (2.00 g, 7.45 mmol, 1.00 equiv.) and corresponding amounts of other reagents in CH_2Cl_2 (50 mL) after flash-chromatography as a colorless solid (2.50 g, 4.16 mmol, 56%).

m.p. 208 °C; **^{1}H NMR** (300 MHz, CD_3CN) δ 8.28 (d, *J* = 2.5 Hz, 1H), 7.93 (dd, *J* = 8.8, 2.5 Hz, 1H), 7.88 (dt, *J* = 7.8, 0.7 Hz, 2H), 7.70 (td, *J* = 7.6, 1.2 Hz, 2H), 7.60 (td, *J* = 7.7, 1.3 Hz, 2H), 7.52 (dd, *J* = 7.6, 1.3 Hz, 2H), 7.23 (t, *J* = 7.6 Hz, 1H), 7.19 (d, *J* = 8.9 Hz, 1H), 6.94 (d, *J* = 7.6 Hz, 2H), 4.64 (s, 2H), 1.53 (s, 6H), 1.43 (s, 9H); **^{13}C{H} NMR** (75 MHz, CD_3CN) δ 157.1, 146.1, 140.5, 139.3, 136.8, 135.8, 134.5, 131.7, 131.2, 129.9 (2C), 129.2, 127.4, 124.7, 122.2 (d, C-F, $^1J_{C\text{-}F}$ = 321.2 Hz), 114.8, 108.8, 66.4, 35.4, 31.4, 19.2; **^{19}F NMR** (282 MHz, CD_3CN) δ -79.25; **IR (ATR)** [cm^{-1}]: $\tilde{\nu}$ = 3090, 3071, 3042, 2963, 2952, 2909, 2870, 1447, 1255, 1146, 1030, 977, 839, 752, 635, 572, 516, 483, 417; **HR-MS-ESI(+)** calc. $C_{31}H_{31}OS^+$ $[M-TfO]^+$ 451.2090; found 451.2095.

5-(5-(tert-butyl)-2-((2,6-dichlorobenzyl)oxy)phenyl)-5H-dibenzo[b,d]thiophen-5-ium trifluoromethanesulfonate (470m)

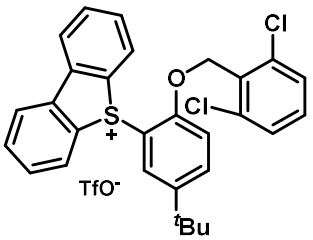

According to general procedure B, compound **470m** was obtained from 2-[(4-(tert-butyl)phenoxy)methyl]-1,3-dichlorobenzene (**469m**) (0.71 g, 2.30 mmol, 1.00 equiv.) and corresponding amounts of other reagents in CH_2Cl_2 (50 mL) after flash-chromatography as a colorless solid (1.28 g, 2.00 mmol, 87%).

^{1}H NMR (300 MHz, CD_3CN) δ 8.27 (d, *J* = 2.5 Hz, 1H), 7.97 – 7.86 (m, 3H), 7.80 – 7.68 (m, 2H), 7.69 – 7.55 (m, 4H), 7.44 (dd, *J* = 8.9, 7.1 Hz, 1H), 7.34 – 7.28 (m, 2H), 7.20 (d, *J* = 8.8 Hz, 1H), 4.86 (s, 2H), 1.42 (s, 9H); **^{13}C NMR** (75 MHz, CD_3CN) δ 156.4, 146.7, 140.3, 137.6, 136.8,

135.8, 134.7, 132.6, 132.0, 130.3, 129.9, 129.6, 127.6, 124.4, 122.2 (d, *J* = 321.0 Hz), 114.7, 109.1, 66.6, 35.5, 31.3; **^{19}F NMR** (282 MHz, CD_3CN) δ -79.26; **IR (ATR)** [cm^{-1}]: $\tilde{\nu}$ = 3087, 3071, 2966, 2904, 2870, 1440, 1255, 1146, 1029, 994, 752, 707, 635, 573, 516, 482, 418; **HR-MS-ESI(+)** calc. $C_{29}H_{25}Cl_2OS^+$ $[M-TfO]^+$ 491.0998, found 491.0998.

5-(4'-{[4-(Trifluoromethyl)benzyl]oxy}-[1,1'-biphenyl]-4-yl)-5*H*-dibenzo[*b*,*d*]thiophen-5-ium Trifluoro-methanesulfonate (470n)

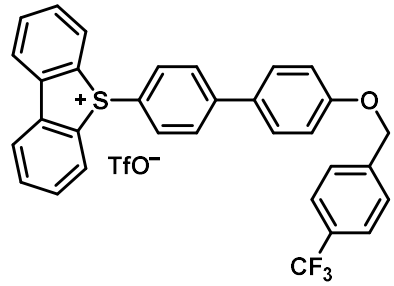

According to general procedure B, compound **470n** was obtained from 4-{[4-(trifluoromethyl)benzyl]oxy}-1,1'-biphenyl (**469n**) (1.00 g, 3.05 mmol, 1.00 equiv.) and corresponding amounts of other reagents in CH_2Cl_2 (50 mL) after flash-chromatography as a colorless solid (1.33 g, 2.01 mmol, 66%).

m.p. 217 °C; **^{1}H NMR** (400 MHz, CD_3CN) δ 8.36 (d, *J* = 7.9 Hz, 2H), 8.09 (d, *J* = 8.1 Hz, 2H), 8.00 – 7.91 (m, 2H), 7.80 – 7.68 (m, 6H), 7.66 – 7.55 (m, 6H), 7.09 (d, *J* = 8.7 Hz, 2H), 5.22 (s, 2H). **^{13}C{H} NMR** (101 MHz, CD_3CN) δ 160.51, 148.05, 142.74 (q, C-F, $^4J_{C\text{-}F}$ = 1.4 Hz), 140.44, 135.48, 133.19, 132.72, 132.09, 131.65, 130.31 (q, C-F, $^2J_{C\text{-}F}$ = 32.2 Hz), 130.21, 129.78, 128.90, 128.85, 126.41 (q, C-F, $^3J_{C\text{-}F}$ = 3.8 Hz), 125.63, 125.39 (q, C-F, $^1J_{C\text{-}F}$ = 271.4 Hz), 124.89, 122.19 (q, C-F, $^1J_{C\text{-}F}$ = 320.8 Hz), 116.52, 69.86. **^{19}F NMR** (376 MHz, CD_3CN) δ -63.01, -79.24. **IR (ATR)** [cm^{-1}]: $\tilde{\nu}$ = 3089, 2928, 2879, 1583, 1485, 1327, 1254, 1152, 1112, 1065, 1028, 821, 758, 705, 635, 610, 572, 512, 418. **HR-MS-ESI(+)** calc. $C_{32}H_{22}F_3OS^+$ $[M-TfO]^+$ 511.1338; found 511.1339.

5-{4'-[(3,5-Dichlorobenzyl)oxy]-[1,1'-biphenyl]-4-yl}-5*H*-dibenzo[*b*,*d*]thiophen-5-ium Trifluoromethane-sulfonate (470o)

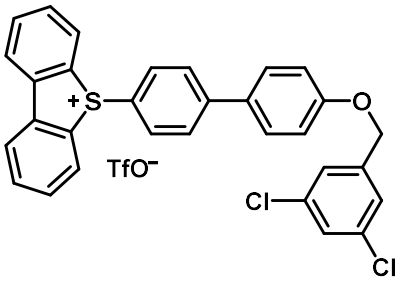

According to general procedure B, compound **470o** was obtained from 4-[(3,5-dichlorobenzyl)oxy]-1,1'-biphenyl (**469o**) (1.00 g, 3.04 mmol, 1.00 equiv.) and corresponding amounts of other reagents in CH_2Cl_2 (50 mL) after flash-chromatography as a colorless solid (1.50 g, 2.27 mmol, 75%).

m.p. 107 °C (decomp.); **^{1}H NMR** (400 MHz, CD_3CN) δ 8.36 (dd, *J* = 7.9, 1.2 Hz, 2H), 8.09 (dd, *J* = 8.1, 1.0 Hz, 2H), 7.95 (td, *J* = 7.7, 1.0 Hz, 2H), 7.78 (d, *J* = 8.7 Hz, 2H), 7.73 (td, *J* = 7.8, 1.2 Hz, 2H), 7.60 (dd, *J* = 8.9, 2.2 Hz, 4H), 7.44 – 7.39 (m, 3H), 7.07 (d, *J* = 8.8 Hz, 2H), 5.11 (s, 2H); **^{13}C{H} NMR** (101 MHz, CD_3CN) δ 160.26, 148.02, 142.19, 140.44, 135.77, 135.49, 133.18, 132.73, 132.09, 131.78, 130.23, 129.79, 128.90, 128.68, 126.85, 125.63, 124.92, 122.19 (q, C-F, $^1J_{C\text{-}F}$ = 320.8 Hz), 116.52, 69.11; **^{19}F NMR** (376 MHz, CD_3CN) δ -79.25; **IR (ATR)** [cm^{-1}]: $\tilde{\nu}$ = 3087, 3064, 3012, 2923, 2904, 2853, 1572, 1520, 1484, 1450, 1252, 1153, 1029, 850, 816, 797, 757, 706, 660, 635, 572, 516, 413; **HR-MS-ESI(+)** calc. $C_{31}H_{21}Cl_2OS^+$ $[M-TfO]^+$ 511.0685; found 511.0680.

5-(5-methyl-2-(p-tolyloxy)phenyl)-5H-dibenzo[b,d]thiophen-5-ium trifluoromethanesulfonate (470p)

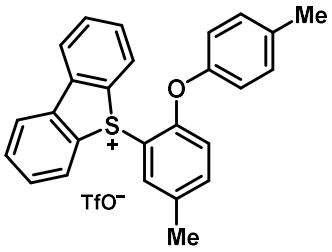

According to general procedure B, compound **470p** was obtained from Di-*p*-tolyl ether (8.00 g, 40.35 mmol, 1.00 equiv.) and corresponding amounts of other reagents in CH_2Cl_2 (100 mL) after recrystallization from THF/hexane as a colorless solid (9.83 g, 18.53 mmol, 46%).

^{1}H NMR (400 MHz, CDCl3) δ 8.20 (d, *J* = 7.9 Hz, 2H), 8.09 (d, *J* = 7.7 Hz, 2H), 7.77 (td, *J* = 7.6, 1.2 Hz, 2H), 7.64 (td, *J* = 7.7, 1.3 Hz, 2H), 7.61 (d, *J* = 2.2 Hz, 1H), 7.32 (dd, *J* = 8.6, 2.4 Hz, 1H), 7.03 (d, *J* = 8.5 Hz, 2H), 6.67 (d, *J* = 8.5 Hz, 1H), 6.52 (d, *J* = 8.5 Hz, 2H), 2.31 (s, 3H), 2.27 (s, 3H); **^{13}C NMR** (101 MHz, CDCl3) δ 155.8, 151.7, 139.7, 137.9, 135.5, 135.3, 134.1, 133.3, 131.5, 130.7, 129.7, 128.4, 124.0, 121.0 (q, *J* = 320.9 Hz), 119.2, 118.3, 113.5, 20.8, 20.6; **^{19}F NMR** (376 MHz, CDCl3) δ -78.11; **IR (ATR)** [cm^{-1}]: $\tilde{\nu}$ = 3087, 3064, 3046, 3033, 3011, 2993, 2964, 2934, 1487, 1448, 1250, 1147, 1027, 754, 634, 515, 472; **HR-MS-ESI(+)** calc. $C_{26}H_{21}OS^+$ $[M-TfO]^+$ 381.1308, found 381.1313.

5,5'-({[1,2-Phenylenebis(methylene)]bis(oxy)}bis[5-(*tert*-butyl)-2,1-phenylene])bis(5*H*-dibenzo[*b*,*d*]thio-phen-5-ium) Bis(trifluoromethanesulfonate) (470q)

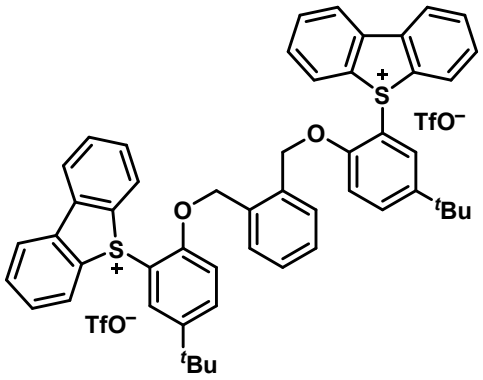

According to general procedure B, compound **470q** was obtained from 1,2-bis{[4-(*tert*-butyl)phenoxy]methyl}benzene (**469q**) (1.00 g, 2.48 mmol, 1.00 equiv.) and corresponding amounts of other reagents in CH_2Cl_2 (100 mL) after flash-chromatography as a colorless solid (1.83 g, 1.71 mmol, 69%).

m.p. 236 °C (decomp.); **^{1}H NMR** (400 MHz, CD_3CN) δ 8.10 (d, *J* = 2.5 Hz, 2H), 7.88 – 7.84 (m, 4H), 7.82 (dd, *J* = 8.8, 2.5 Hz, 2H), 7.65 (pd, *J* = 7.4, 1.5 Hz, 8H), 7.53 – 7.43 (m, 4H), 7.37 (dd, *J* = 5.6, 3.3 Hz, 2H), 6.65 (dd, *J* = 5.5, 3.4 Hz, 2H), 6.61 (d, *J* = 8.9 Hz, 2H), 3.68 (s, 4H), 1.36 (s, 18H); **^{13}C{H} NMR** (126 MHz, CD_3CN) δ 156.3, 146.5, 140.3, 136.5, 135.0, 134.5, 133.8, 131.9, 131.7, 130.8, 130.3, 127.7, 124.6, 122.1 (q, C-F, $^1J_{C\text{-}F}$ = 320.8 Hz), 115.0, 109.4, 68.8, 35.4, 31.3; **^{19}F NMR** (377 MHz, CD_3CN) δ -79.31; **IR (ATR)** [cm^{-1}]: $\tilde{\nu}$ = 3086, 2958, 2905, 2890, 2870, 1493, 1254, 1142, 1028, 984, 826, 754, 635, 567, 516, 482, 418; **HR-MS-ESI(+)** calc. $C_{26}H_{24}OS^+$ $[M-2TfO]^{2+}$ 384.1542; found 384.1544.

5,5'-[{[1,4-Phenylenebis(methylene)]bis(oxy)}bis(5-methyl-2,1-phenylene)]bis(5*H*-dibenzo[*b*,*d*]thiophen-5-ium) Bis(trifluoromethanesulfonate) (470r)

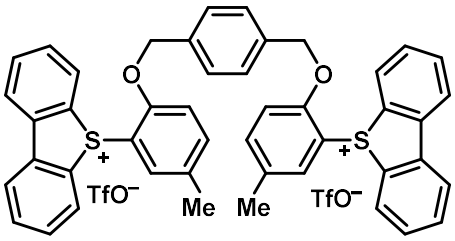

According to general procedure B, compound **470r** was obtained from 1,4-bis[(*p*-tolyloxy)methyl]benzene (**469r**) (1.00 g, 3.14 mmol, 1.00 equiv.) and corresponding amounts of other reagents in CH_2Cl_2 (100 mL) after flash-chromatography and washing with CH_2Cl_2 as a brownish solid (1.27 g, 1.29 mmol, 41%).

m.p. 245 °C (decomp.); **^{1}H NMR** (400 MHz, CD_3CN) δ 8.04 – 7.94 (m, 8H), 7.81 (tt, J = 7.5, 1.0 Hz, 4H), 7.72 – 7.65 (m, 4H), 7.60 (dd, J = 8.6, 2.2 Hz, 2H), 7.39 – 7.33 (m, 2H), 7.23 (d, J = 8.6 Hz, 2H), 7.04 (s, 4H), 5.01 (s, 4H), 2.28 (s, 6H); **^{13}C{H} NMR** (151 MHz, CD_3CN) δ 157.3, 140.7, 139.3, 136.2, 134.9, 134.1, 133.8, 132.1, 130.7, 129.7, 128.3, 125.2, 122.2 (q, C-F, $^1J_{C\text{-}F}$ = 320.8 Hz), 115.8, 111.9, 72.1, 20.2; **^{19}F**

NMR (377 MHz, CD_3CN) δ -79.32; **IR (ATR)** [cm^{-1}]: $\tilde{\nu}$ = 3084, 3046, 2936, 2877, 2359, 1499, 1256, 1142, 1028, 753, 634, 572, 515, 482; **HR-MS-ESI(+)** calc. $C_{23}H_{18}OS^+$ [M−2TfO]$^{2+}$ 342.1073, found 342.1076.

5,5'-({[Naphthalene-1,4-diylbis(methylene)]bis(oxy)}bis[5-(*tert*-butyl)-2,1-phenylene])bis(5*H*-dibenzo[*b*,*d*]-thiophen-5-ium) Bis(trifluoromethanesulfonate) (470s)

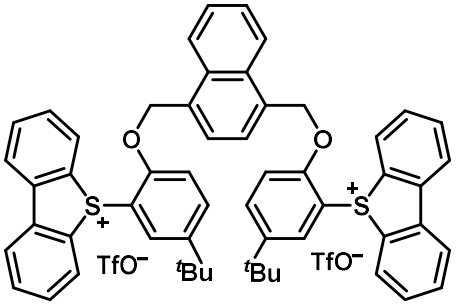

According to general procedure B, compound **470s** was obtained from 1,4-bis{[4-(*tert*-butyl)phenoxy]methyl}naphthalene (**469s**) (0.75 g, 1.66 mmol, 1.00 equiv.) and corresponding amounts of other reagents in CH_2Cl_2 (100 mL) after flash-chromatography as a colorless solid (1.20 g, 1.07 mmol, 65%).

m.p. 240 °C (decomp.); **^{1}H NMR** (600 MHz, CD_3CN) δ 7.97 (dd, *J* = 8.7, 2.5 Hz, 2H), 7.93 (s, 2H), 7.87 (ddd, *J* = 8.0, 1.1, 0.5 Hz, 4H), 7.49 (ddd, *J* = 8.0, 7.4, 1.2 Hz, 6H), 7.44 – 7.39 (m, 6H), 7.35 (dt, *J* = 6.5, 3.3 Hz, 2H), 7.23 (d, *J* = 7.7 Hz, 4H), 6.91 (s, 2H), 5.31 (s, 4H), 1.37 (s, 18H); **^{13}C{H} NMR** (101 MHz, CD_3CN) δ 157.1, 146.8, 140.3, 136.5, 134.3, 133.4, 132.6, 132.6, 131.6, 130.1, 128.6, 128.0, 127.6, 124.7, 124.2, 122.1 (q, C-F, $^1J_{C\text{-}F}$ = 321.0 Hz), 115.4, 110.6, 70.3, 35.4, 31.2; **^{19}F NMR** (565 MHz, CD_3CN) δ -79.32; **IR (ATR)** [cm^{-1}]: $\tilde{\nu}$ = 3087, 2958, 2870, 1495, 1254, 1223, 1145, 1028, 975, 854, 820, 752, 704, 635, 572, 516, 500, 479, 416; **HR-MS-ESI(+)** calc. $C_{28}H_{25}OS^+$ [M−2TfO]$^{2+}$ 409.1621; found 409.1625.

5,5'-([{[1,1'-Biphenyl]-2,2'-diylbis(methylene)}bis(oxy)]bis[5-(*tert*-butyl)-2,1-phenylene])bis(5*H*-dibenzo-[*b*,*d*]thiophen-5-ium) Bis(trifluoromethanesulfonate) (470t)

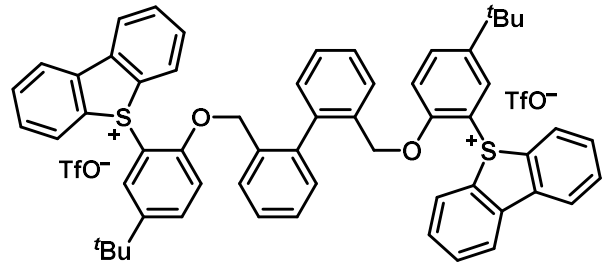

According to general procedure B, compound **470t** was obtained from 2,2'-bis{[4-(*tert*-butyl)phenoxy]-methyl}-1,1'-biphenyl (**469t**) (1.03 g, 2.15 mmol, 1.00 equiv.) and corresponding amounts of other reagents in CH_2Cl_2 (100 mL) after flash-chromatography as a colorless solid (1.58 g, 1.38 mmol, 64%).

m.p. 222 °C; **^{1}H NMR** (300 MHz, CD_3CN) δ 8.02 (dd, *J* = 7.7, 1.3 Hz, 2H), 7.99 – 7.78 (m, 12H), 7.74 (td, *J* = 7.6, 1.6 Hz, 2H), 7.71 – 7.60 (m, 4H), 7.26 (td, *J* = 7.5, 1.5 Hz, 2H), 7.16 (td, *J* = 7.5, 1.5 Hz, 2H), 6.72 (d, *J* = 8.9 Hz, 2H), 6.61 (dd, *J* = 7.6, 1.4 Hz, 2H), 6.15 (dd, *J* = 7.6, 1.4 Hz, 2H), 4.37 (d, *J* = 10.6 Hz, 2H), 4.27 (d, *J* = 10.5 Hz, 2H), 1.29 (s, 18H); **^{13}C{H} NMR** (126 MHz, CD_3CN) δ 156.5, 146.7, 140.7, 140.5, 140.0, 136.3, 134.9, 134.7, 133.6, 132.7, 132.2, 132.1, 131.3, 130.7, 130.5, 130.3, 129.3, 129.2, 128.2, 128.0, 125.5, 124.9, 122.2 (q, C-F, $^1J_{C\text{-}F}$ = 321.0 Hz), 115.1, 110.0, 69.9, 35.4, 31.2; **^{19}F NMR** (282 MHz, CD_3CN) δ -79.25; **IR (ATR)** [cm^{-1}]: $\tilde{\nu}$ = 3084, 2966, 2869, 1496, 1254, 1149, 1029, 975, 848, 756, 635, 571, 516, 482, 417; **HR-MS-ESI(+)** calc. $C_{29}H_{26}OS^+$ [M−2TfO]$^{2+}$ 422.1699; found 422.1700.

5,5'-{[{[Ethane-1,2-diylbis(4,1-phenylene)]bis(methylene)}bis(oxy)]bis(5-methyl-2,1-phenylene)}bis(5*H*-dibenzo[*b*,*d*]thiophen-5-ium) Bis(trifluoromethanesulfonate) (470u)

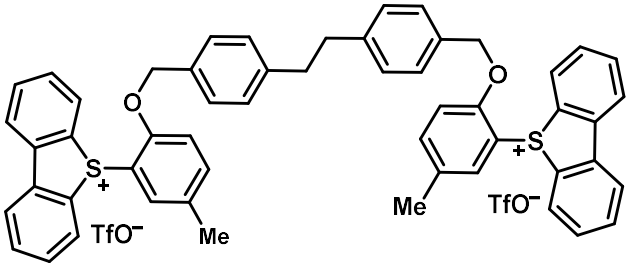

According to general procedure B, compound **470u** was obtained from 1,2-bis{4-[(*p*-tolyloxy)methyl]phenyl}ethane (**469u**) (1.10 g, 2.60 mmol, 1.00 equiv.) and corresponding amounts of other reagents in CH_2Cl_2 (100 mL) after flash-chromatography as a colorless solid (1.56 g, 1.43 mmol, 55%).

m.p. 231 °C (decomp.); **^{1}H NMR** (400 MHz, CD_3CN) δ 7.83 (dd, *J* = 8.0, 0.9 Hz, 4H), 7.80 – 7.72 (m, 8H), 7.58 (ddd, *J* = 8.1, 6.3, 2.5 Hz, 4H), 7.53 (dd, *J* = 8.6, 2.1 Hz, 2H), 7.33 (d, *J* = 7.5 Hz, 6H), 7.15 (d, *J* = 8.6 Hz, 2H), 6.96 (d, *J* = 7.7 Hz, 4H), 4.83 (s, 4H), 3.14 (s, 4H), 2.26 (s, 6H); **^{13}C{H} NMR** (101 MHz, CD_3CN) δ 157.3, 143.5, 140.5, 139.4, 134.8, 133.9, 133.8, 133.2, 132.0, 130.3, 130.0, 129.8, 128.1, 125.2, 122.2 (q, C-F, $^1J_{C\text{-}F}$ = 321.2 Hz), 115.7, 111.5, 72.4, 36.8, 20.2; **^{19}F NMR** (282 MHz, CD_3CN) δ -79.32; **IR (ATR)** [cm^{-1}]: $\tilde{\nu}$ = 3032, 3020, 2994, 2952, 2918, 2890, 2860, 1611, 1487, 1360, 1248, 1204, 1118, 1079, 958, 914, 880, 814, 777, 756, 714, 626, 585, 502, 476, 448; **HR-MS-ESI(+)** calc. $C_{27}H_{22}OS^+$ $[M-2OTf]^{2+}$ 394.1386; found 394.1383.

5-(2-(benzoyloxy)-5-(tert-butyl)phenyl)-5H-dibenzo[b,d]thiophen-5-ium trifluoromethanesulfonate (470v)

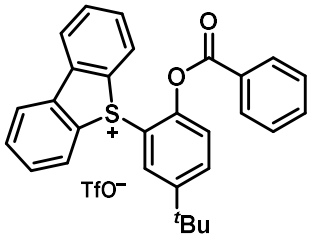

K_2CO_3 (0.27 g, 1.93 mmol, 3.00 equiv.) was added to a solution of 5-(5-(tert-butyl)-2-hydroxyphenyl)-5H-dibenzo[b,d]thiophen-5-ium trifluoromethanesulfonate[233] (0.31 g, 0.64 mmol, 1.00 equiv.) and benzoyl chloride (0.10 g, 0.71 mmol, 1.10 equiv.) in DCM (50 mL), and the reaction mixture was stirred for 24h. Afterwards, the solvent was removed *in vacuo*. Water was added to the residue, and the mixture was extracted with CH_2Cl_2 (3 × 50 mL). The combined organic phases were dried over $MgSO_4$. All volatile compounds were removed under reduced pressure, and the residue was purified by flash-chromatography (SiO_2, gradient elution: CH_2Cl_2; acetone:CH_2Cl_2 1:4) affording the target compound as a colorless solid (0.312 g, 0.53 mmol, 83%).

^{1}H NMR (300 MHz, CD_3CN) δ 8.11 – 8.00 (m, 3H), 7.96 (ddd, *J* = 8.6, 2.5, 1.1 Hz, 1H), 7.87 – 7.66 (m, 7H), 7.53 – 7.40 (m, 4H), 7.37 (dd, *J* = 8.7, 1.1 Hz, 1H), 1.38 (d, *J* = 1.2 Hz, 9H); **^{13}C NMR** (75 MHz, CD_3CN) δ 164.4, 153.0, 149.1, 140.4, 136.0, 135.8, 135.1, 133.9, 132.5, 131.0, 130.9, 129.7, 128.6, 127.7, 127.2, 125.4, 122.2 (q, *J* = 320.8 Hz), 116.9, 36.0, 31.1; **^{19}F NMR** (282 MHz, CD_3CN) δ -79.29; **IR (ATR)** [cm^{-1}]: $\tilde{\nu}$ = 3087, 2970, 2911, 2871, 1743, 1449, 1253, 1219, 1139, 1029, 870, 760, 705, 634, 571, 553, 516, 485, 415; **HR-MS-ESI(+)** calc. $C_{29}H_{25}O_2S^+$ $[M-TfO]^+$ 437.1570, found 437.1573.

General procedure C:

Starting from Dibenzothiophenium trifluoromethanesulfonates

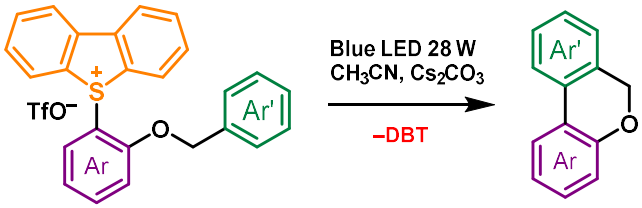

An oven-dried microwave tube (d = 17 mm, h = 82.5 mm) was equipped with a stirring bar, charged with the corresponding dibenzothiophenium trifluoromethanesulfonate (184 µmol, 1.00 equiv.), Cs_2CO_3 (65.8 mg, 202 µmol, 1.10 equiv.), *fac*-[Ir(ppy)$_3$] (1.21 mg, 1.8 µmol, 1 mol%) and sealed with a septum. The tube was evacuated and back-filled with nitrogen three times. Dry degassed CH_3CN (6 mL) was added under nitrogen. The suspension was stirred and irradiated by blue LEDs (28 Watt) for 4 h under N_2 at room temperature. Afterwards, the solvent was removed under reduced pressure, and the residue was purified by flash-chromatography (SiO_2, gradient elution: pentane; EtOAc:pentane 1:20) to give the target compound.

Starting from Bis(dibenzothiophenium) trifluoromethanesulfonates

An oven-dried microwave tube (d = 17 mm, h = 82.5 mm) was equipped with a stirring bar, charged with the corresponding dibenzothiophenium trifluoromethanesulfonate (92 µmol, 1.00 equiv.), Cs_2CO_3 (62.9 mg, 193.2 µmol, 2.10 equiv.), *fac*-[Ir(ppy)$_3$] (0.6 mg, 0.92 µmol, 1 mol%) and sealed with a septum. The tube was evacuated and back-filled with nitrogen three times. Dry degassed DMF (6 mL) was added under nitrogen. The suspension was stirred and irradiated with blue LEDs (28 Watt) for 2 h under N_2 at room temperature. Afterwards, the solvent was removed under reduced pressure and the residue was purified by flash-chromatography (SiO_2, gradient elution: pentane; EtOAc:pentane 1:20) to give the target compound.

6*H*-Benzo[*c*]chromenes:

2,9-Dimethyl-6*H*-benzo[*c*]chromene (471a)

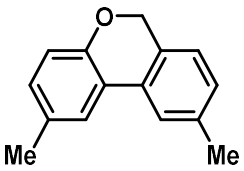

Compound **471a** (34.00 mg, 165 µmol, 90%) was obtained as a colorless solid from 5-{5-methyl-2-[(4-methylbenzyl)oxy]phenyl}-5*H*-dibenzo[*b*,*d*]thiophen-5-ium trifluorome-thanesulfonate (**470a**) according to general procedure C in MeCN.

Gram-scale: An oven-dried J Young Schlenk flask (d = 25 mm) was equipped with a stirring bar and charged with 5-{5-methyl-2-[(4-methylbenzyl)oxy]phenyl}-5*H*-dibenzo[*b*,*d*]thiophen-5-ium trifluoromethanesulfonate (**470a**) (1g, 1.84 mmol, 1.00 equiv.), Cs_2CO_3 (658 mg, 2.02 mmol, 1.10 equiv.), *fac*-[Ir(ppy)$_3$] (12 mg, 18.3 µmol, 1 mol%) and sealed. The tube was evacuated and back-filled with nitrogen three times. Dry degassed CH_3CN (60 mL) was added under nitrogen. The suspension was stirred and irradiated with blue LEDs (28 Watt) for 4 h under N_2 at room temperature. Afterwards, the solvent was removed under reduced pressure and the residue was purified by flash-chromatography (SiO_2, gradient elution: pentane; EtOAc:pentane 1:20) to give 2,9-dimethyl-6*H*-benzo[*c*]chromene (**471a**) as a colorless solid (347.3 mg, 1.65 mmol, 90%). Furthermore, 323.6 mg (1.76 mmol, 96%) of dibenzothiophene could be recovered.

m.p. 85 °C; **^{1}H NMR** (400 MHz, $CDCl_3$) δ 7.54 (d, *J* = 2.1 Hz, 1H), 7.52 (d, *J* = 1.6 Hz, 1H), 7.09 (dd, *J* = 7.7, 1.6 Hz, 1H), 7.06 – 7.01 (m, 2H), 6.89 (d, *J* = 8.1 Hz, 1H), 5.06 (s, 2H), 2.42 (s, 3H), 2.37 (s, 3H); **^{13}C{H}**

NMR (101 MHz, $CDCl_3$) δ 152.8, 138.1, 131.4, 130.2, 130.1, 128.9, 128.4, 124.7, 123.7, 122.9, 122.7, 117.2, 68.6, 21.7, 21.1.

Analytical data are in accordance with those previously published in the literature.[285]

(3*S*,4'*s*)-4'-{(3*S*,4'*s*)-4',5-Dimethyl-2*H*-spiro[benzofuran-3,1'-cyclohexane]-2',5'-dien-4'-yl}-4',5-dimethyl-2*H*-spiro[benzofuran-3,1'-cyclohexane]-2',5'-diene (471a')

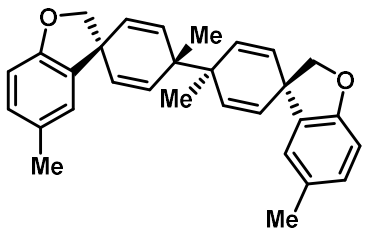

The synthesis was carried out using a modified literature procedure.[244]

An oven-dried microwave tube (d = 17 mm, h = 82.5 mm) was equipped with a stirring bar, charged with 5-{5-methyl-2-[(4-methylbenzyl)oxy]phenyl}-5*H*-dibenzo[*b*,*d*]thiophen-5-ium trifluorometha-nesulfonate (**470a**) (300 mg, 0.551 mmol, 1.00 equiv.) and $[Ru(bpy)_3]Cl_2 \bullet 6H_2O$ (20.6 mg, 27.6 μmol, 0.05 equiv.) and sealed with a septum. The tube was evacuated and back-filled with nitrogen three times. Dry degassed CH_3CN (15 mL) and DIPEA (356 mg, 2.75 mmol, 5 equiv.) were added under nitrogen. The solution was stirred and irradiated by blue LEDs (28 Watt) for 30 min under N_2 at room temperature. During this time a colorless crystalline solid was formed. The precipitate was filtered off, washed with small portions of CH_3CN and dried *in vacuo* to give the target compound as a crystalline colorless solid (35.70 mg, 84.4 μmol, 31%).

m.p. 172 °C; **^{1}H NMR** (400 MHz, $CDCl_3$) δ 6.95 (dd, *J* = 8.2, 1.3 Hz, 2H), 6.75 (d, *J* = 2.2 Hz, 2H), 6.72 (d, *J* = 8.1 Hz, 2H), 5.77 (d, *J* = 10.4 Hz, 4H), 5.73 (d, *J* = 10.4 Hz, 4H), 4.31 (s, 4H), 2.27 (s, 6H), 1.17 (s, 6H); **^{13}C{H} NMR** (101 MHz, $CDCl_3$) δ 157.3, 133.8, 131.2, 130.6, 129.5, 129.2, 125.2, 109.6, 82.45 48.1, 42.0, 25.0, 20.9; **IR (ATR)** [cm^{-1}]: $\tilde{\nu}$ = 3033, 3021, 2996, 2961, 2952, 2918, 2890, 2861, 1612, 1487, 1361, 1248, 1204, 1118, 1080, 958, 914, 880, 815, 777, 756, 714, 626, 585, 502, 476, 449; **HR-MS-ESI(+)** calc. $C_{30}H_{31}O_2^+$ $[M+H]^+$ 423.2319; found 423.2334.

2,9-Di-*tert*-butyl-6*H*-benzo[*c*]chromene (471b)

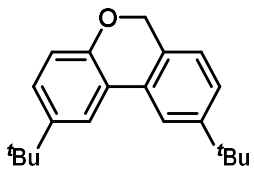

Compound **471b** (51.3 mg, 174 μmol, 94%) was obtained as a colorless solid from 5-[5-(*tert*-butyl)-2-{[4-(*tert*-butyl)benzyl]oxy}phenyl]-5*H*-dibenzo[*b,*d]-thiophen-5-ium trifluoromethanesul-fonate (**470b**) according to general procedure C in MeCN.

m.p. 71 °C; **^{1}H NMR** (300 MHz, $CDCl_3$) δ 7.75 (d, *J* = 2.4 Hz, 1H), 7.72 (d, *J* = 1.9 Hz, 1H), 7.32 (dd, *J* = 7.9, 1.9 Hz, 1H), 7.27 (dd, *J* = 8.5, 2.4 Hz, 1H), 7.13 – 7.06 (m, 1H), 6.93 (d, *J* = 8.5 Hz, 1H), 5.07 (s, 2H), 1.39 (s, 9H), 1.39 (s, 9H); **^{13}C{H} NMR** (101 MHz, $CDCl_3$) δ 152.8, 151.5, 144.8, 130.1, 129.0, 126.5, 124.7, 124.6, 122.7, 119.8, 118.8, 116.9, 68.5, 35.0, 34.5, 31.7, 31.6; **IR (ATR)** [cm^{-1}]: $\tilde{\nu}$ = 3056, 2958, 2903, 2867, 1737, 1614, 1496, 1408, 1362, 1261, 1202, 1123, 1017, 945, 882, 820, 743, 705, 606; **HR-MS-EI** calc. $C_{21}H_{26}O^+$ $[M]^+$ 294.1984; found 294.1978.

2-Methyl-6*H*-benzo[*c*]chromene (471c)

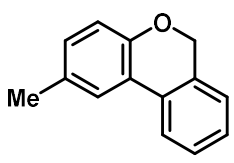

Compound **471c** (26.8 mg, 137 μmol, 74%) was obtained as a colorless solid from 5-[2-(benzyloxy)-5-methylphenyl]-5*H*-dibenzo[*b*,*d*]thiophen-5-ium trifluoromethanesulfonate (**470c**) according to general procedure C in MeCN.

^{1}H NMR (300 MHz, $CDCl_3$) δ 7.70 (d, *J* = 7.7 Hz, 1H), 7.54 (d, *J* = 2.1 Hz, 1H), 7.38 (td, *J* = 7.6, 1.4 Hz, 1H), 7.28 (t, *J* = 6.8 Hz, 1H), 7.15 (d, *J* = 8.3 Hz, 1H), 7.05 (dd, *J* = 8.2, 2.1 Hz, 1H), 6.90 (d, *J* = 8.2 Hz, 1H), 5.09 (s, 2H), 2.37 (s, 3H); **^{13}C{H} NMR** (75 MHz, $CDCl_3$) δ 152.8, 131.7, 131.5, 130.4, 130.2, 128.5, 127.7, 124.8, 123.8, 122.8, 122.1, 117.2, 68.7, 21.1; **IR (ATR)** [cm^{-1}]: $\tilde{\nu}$ = 3029, 2917, 1609,

1496, 1336, 1245, 1215, 1190,1037, 1024, 961, 941, 814, 769, 713, 583; **HR-MS-EI** calc. $C_{14}H_{12}O^+$ $[M]^+$ 196.0880; found 196.0883.

Analytical data are in accordance with those previously published in the literature.[285]

9-Fluoro-2-methyl-6*H*-benzo[*c*]chromene (471d)

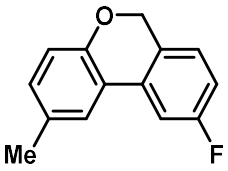

Compound **471d** (35.6 mg, 166 μmol, 90%) was obtained as a colorless oil from 5-{2-[(4-fluorobenzyl)oxy]-5-methylphenyl}-5*H*-dibenzo[*b*,*d*]thiophen-5-ium trifluoromethane-sulfonate (**470d**) according to general procedure C in MeCN.

^{1}H NMR (300 MHz, $CDCl_3$) δ 7.45 (d, *J* = 2.0 Hz, 1H), 7.37 (dd, *J* = 9.9, 2.5 Hz, 1H), 7.15 – 7.04 (m, 2H), 6.96 (td, *J* = 8.5, 2.5 Hz, 1H), 6.90 (d, *J* = 8.2 Hz, 1H), 5.05 (d, *J* = 1.0 Hz, 2H), 2.36 (d, *J* = 0.8 Hz, 3H); **^{13}C{H} NMR** (101 MHz, $CDCl_3$) δ 163.2 (d, C-F, $^1J_{C\text{-}F}$ = 244.6 Hz), 152.7, 132.6 (d, C-F, $^3J_{C\text{-}F}$ = 8.4 Hz), 131.7, 131.0, 127.3 (d, C-F, $^4J_{C\text{-}F}$ = 3.1 Hz), 126.4 (d, C-F, $^3J_{C\text{-}F}$ = 8.7 Hz), 124.0, 122.0 (d, C-F, $^4J_{C\text{-}F}$ = 2.5 Hz), 117.3, 114.3 (d, C-F, $^2J_{C\text{-}F}$ = 22.1 Hz), 109.1 (d, C-F, $^2J_{C\text{-}F}$ = 23.1 Hz), 68.2, 21.0; **^{19}F NMR** (282 MHz, $CDCl_3$) δ -113.66; **IR (ATR)** [cm^{-1}]: $\tilde{\nu}$ = 3074, 3041, 2963, 2920, 2858, 2736, 1727, 1602, 1577, 1505, 1426, 1313, 1274, 1245, 1205, 1168, 1130, 1101, 1037, 958, 937, 891, 816, 742, 698, 649, 634, 601, 536, 500, 436; **HR-MS-EI** calc. $C_{14}H_{11}FO^+$ $[M]^+$ 214.0788; found 214.0780.

2-(*tert*-Butyl)-8,10-dichloro-6*H*-benzo[*c*]chromene (471e)

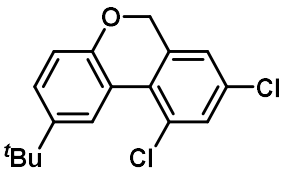

Compound **471e** (23.0 mg, 75 μmol, 41%) was obtained as a colorless solid from 5-{5-(*tert*-butyl)-2-[(3,5-dichlorobenzyl)oxy]phenyl}-5*H*-dibenzo[*b*,*d*]thiophen-5-ium trifluo-romethane-sulfonate (**470e**) according to general procedure C in MeCN.

^{1}H NMR (300 MHz, $CDCl_3$) δ 8.49 (d, *J* = 2.3 Hz, 1H), 7.46 (d, *J* = 2.1 Hz, 1H), 7.33 (dd, *J* = 8.5, 2.4 Hz, 1H), 7.12 (d, *J* = 2.3 Hz, 1H), 6.99 (d, *J* = 8.5 Hz, 1H), 4.90 (s, 2H), 1.37 (s, 9H); **^{13}C{H} NMR** (101 MHz, $CDCl_3$) δ 153.8, 144.6, 137.4, 132.8, 131.5, 131.2, 127.3, 127.2, 125.1, 124.0, 120.8, 116.7, 69.0, 34.7, 31.6; **IR (ATR)** [cm^{-1}]: $\tilde{\nu}$ = 2960, 2901, 2862, 1491, 1456, 1415, 1389, 1362, 1262, 1288, 1259, 1244, 1212, 1173, 1030, 860, 825, 803, 668, 620; **HR-MS-EI** calc. $C_{17}H_{16}Cl_2O^+$ $[M]^+$ 306.0573; found 306.0573.

2-(*tert*-Butyl)-9-(methylsulfonyl)-6*H*-benzo[*c*]chromene (471f) and 2-(*tert*-Butyl)-8-(methylsulfonyl)-6*H*-benzo[*c*]chromene (471f')

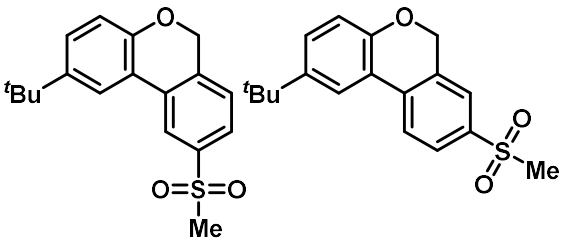

Compounds **471f$^{(\prime)}$** (31.0 mg, 98 μmol, 53% combined) were obtained as a colorless oil from 5-[5-(*tert*-butyl)-2-{[4-(methylsulfonyl)-benzyl]oxy}phenyl]-5*H*-dibenzo[*b*,*d*]-thiophen-5-ium trifluoromethanesulfonate (**470f**) according to general procedure C in MeCN. Flash-chromatography (SiO_2, pentane) afforded a 1:1 mixture of regioisomers **471f** and **471f'**, analytically pure samples of which were isolated by preparative HPLC.

Regioisomer 471f (left)

^{1}H NMR (300 MHz, $CDCl_3$) δ 8.24 (d, *J* = 1.8 Hz, 1H), 7.84 (dd, *J* = 7.9, 1.8 Hz, 1H), 7.76 (d, *J* = 2.4 Hz, 1H), 7.36 (dd, *J* = 8.6, 2.1 Hz, 2H), 6.96 (d, *J* = 8.6 Hz, 1H), 5.14 (s, 2H), 3.11 (s, 3H), 1.38 (s, 9H); **^{13}C{H} NMR** (75 MHz, $CDCl_3$) δ 152.8, 145.8, 141.0, 137.3, 132.5, 128.3, 126.2, 126.1, 120.9, 120.6, 120.3, 117.3, 68.2, 44.8, 34.7, 31.7; **IR (ATR)** [cm^{-1}]: $\tilde{\nu}$ = 3060, 2961, 2931, 2904, 2868, 2843, 1497, 1407, 1307, 1199,

1146, 1024, 960, 828, 770, 733, 635, 590, 562, 526; **HR-MS-ESI(+)** calc. $C_{18}H_{21}O_3S^+$ $[M+H]^+$ 317.1206; found 317.1208.

Regioisomer 471f' (right)

^{1}H NMR (300 MHz, $CDCl_3$) δ 7.99 – 7.83 (m, 2H), 7.76 (d, *J* = 2.4 Hz, 1H), 7.75 – 7.72 (m, 1H), 7.38 (dd, *J* = 8.5, 2.3 Hz, 1H), 6.97 (d, *J* = 8.6 Hz, 1H), 5.14 (s, 2H), 3.09 (s, 3H), 1.37 (s, 9H); **^{13}C{H} NMR** (75 MHz, $CDCl_3$) δ 153.4, 145.6, 139.0, 136.3, 132.7, 128.9, 127.6, 124.0, 122.9, 120.7, 120.6, 117.4, 68.1, 44.8, 34.6, 31.6; **IR (ATR)** [cm^{-1}]: $\tilde{\nu}$ = 3060, 2960, 2929, 2905, 2867, 1604, 1490, 1402, 1364, 1299, 1255, 1204, 1144, 1122, 1086, 1025, 959, 832, 771, 734, 645, 628, 552, 499; **HR-MS-ESI(+)** calc. $C_{18}H_{21}O_3S^+$ $[M+H]^+$ 317.1206; found 317.1204.

8,9,10-Trimethyl-5*H*-naphtho[1,2-*c*]chromene (471g)

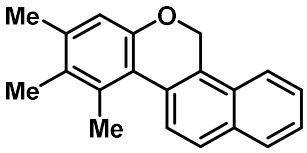

Compound **471g** (43,9 mg, 160 µmol, 87%) was obtained as a colorless oil from 5-[2,3,4-trimethyl-6-(naphthalen-1-ylmethoxy)phenyl]-5*H*-dibenzo[*b*,*d*]thiophen-5-ium trifluoromethanesulfonate (**470g**) according to general procedure C in MeCN.

^{1}H NMR (300 MHz, $CDCl_3$) δ 7.96 (dd, *J* = 8.3, 1.3 Hz, 1H), 7.92 – 7.78 (m, 3H), 7.57 (ddd, *J* = 8.5, 6.8, 1.6 Hz, 1H), 7.50 (ddd, *J* = 8.0, 6.8, 1.3 Hz, 1H), 6.86 (s, 1H), 5.44 (s, 2H), 2.63 (s, 3H), 2.36 (s, 3H), 2.26 (s, 3H); **^{13}C{H} NMR** (75 MHz, $CDCl_3$) δ 153.8, 137.9, 133.6, 132.1, 130.1, 129.4, 128.9, 128.9, 128.6, 127.2, 126.6, 125.6, 125.3, 122.8, 122.5, 115.6, 65.2, 21.2, 19.9, 15.7; **IR (ATR)** [cm^{-1}]: $\tilde{\nu}$ = 3057, 2845, 2914, 1600, 1513, 1469, 1378, 1284, 1185, 1135, 1083, 1057, 1019, 822, 758, 747, 570, 512, 440; **HR-MS-ESI(+)** calc. $C_{20}H_{19}O^+$ $[M+H]^+$ 275.1430; found 275.1423.

2-(*tert*-Butyl)-9-(trifluoromethyl)-6*H*-benzo[*c*]chromene (471h)

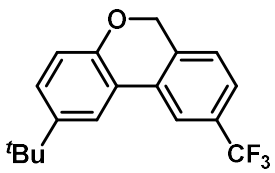

Compound **471h** (37.8 mg, 123.3 µmol, 67%) was obtained as a colorless solid from 5-[5-(*tert*-butyl)-2-{[4-(trifluoromethyl)benzyl]oxy}phenyl]-5*H*-dibenzo[*b*,*d*]thio-phen-5-ium trifluoromethanesulfonate (**470h**) according to general procedure C in MeCN.

^{1}H NMR (400 MHz, $CDCl_3$) δ 7.91 (s, 1H), 7.73 (d, *J* = 2.3 Hz, 1H), 7.53 (d, *J* = 7.8 Hz, 1H), 7.34 (dd, *J* = 8.6, 2.3 Hz, 1H), 7.27 (d, *J* = 7.8 Hz, 1H), 6.96 (d, *J* = 8.5 Hz, 1H), 5.12 (s, 2H), 1.38 (s, 9H); **^{13}C{H} NMR** (101 MHz, $CDCl_3$) δ 152.8, 145.5, 135.2, 131.6, 131.0 (q, C-F, $^2J_{C\text{-}F}$ = 32.4 Hz), 127.8, 125.3, 124.3 (q, C-F, $^1J_{C\text{-}F}$ = 272.2 Hz), 124.2 (q, C-F, $^3J_{C\text{-}F}$ = 4.0 Hz), 121.1, 120.1, 118.9 (q, C-F, $^3J_{C\text{-}F}$ = 3.8 Hz), 117.2, 68.2, 34.6, 31.7; **^{19}F NMR** (282 MHz, $CDCl_3$) δ -62.52; **IR (ATR)** [cm^{-1}]: $\tilde{\nu}$ = 2967, 2907, 2873, 2841, 1510, 1427, 1335, 1274, 1164, 1118, 1076, 1017, 888, 814; **HR-MS-EI** calc. $C_{18}H_{17}F_3O^+$ $[M]^+$ 306.1226; found 306.1216.

2,8,10-trichloro-6H-benzo[c]chromene (471i)

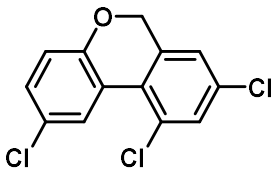

Compound **471i** (25.8 mg, 90 µmol, 49%) was obtained as a colorless solid from 5-(5-chloro-2-((3,5-dichlorobenzyl)oxy)phenyl)-5H-dibenzo[b,d]thiophen-5-ium trifluoromethanesulfonate (**470i**) according to general procedure C in MeCN.

m.p. 157 °C; **^{1}H NMR** (300 MHz, $CDCl_3$) δ 8.43 (d, *J* = 2.5 Hz, 1H), 7.45 (d, *J* = 2.2 Hz, 1H), 7.24 (dd, *J* = 8.6, 2.4 Hz, 1H), 7.12 (d, *J* = 2.2 Hz, 1H), 6.99 (d, *J* = 8.6 Hz, 1H), 4.90 (s, 2H); **^{13}C{H} NMR** (75 MHz, $CDCl_3$) δ 154.6, 137.1, 133.8, 131.8, 131.3, 130.0, 127.7, 127.0, 125.7, 124.1, 122.7, 118.8, 69.0; **IR (ATR)** [cm^{-1}]: $\tilde{\nu}$ = 3132, 3071, 2985, 2913, 2867, 1449, 1386, 1273, 1246, 1206,

1172, 1093, 1037, 883, 869, 849, 818, 756, 740, 697, 660, 641, 585, 538, 525, 487, 458, 422; **HR-MS-EI** calc. $C_{13}H_7Cl_3O^+$ $[M]^+$ 283.9557; found 283.9558.

5-Methyl-1'*H*,2*H*-spiro[benzofuran-3,4'-pyridin]-1'-oxyl (471k')

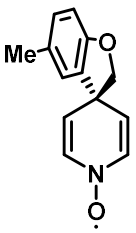

4-[{2-(5H-Dibenzo[*b*,*d*]thiophen-5-ium-5-yl)-4-methylphenoxy}methyl]pyridine 1-oxide trifluoromethanesulfonate (**470k'**) (18.1 mg, 33.1 μmol, 1.00 equiv.) was dissolved in CH_2Cl_2. A solution of cobaltocene (6.25 mg, 33.05 μmol, 1.00 equiv.) in CH_2Cl_2 was added. After stirring for 1 min the mixture was filtered into a J. Young EPR sample tube.

a(N) = 8.39 G, a(H) = 5.83 (2H), 1.99 (2H) G; g = 2.0054

5-**(*tert*-Butyl)-2',6'-dimethyl-[1,1'-biphenyl]-2-ol (471l)**

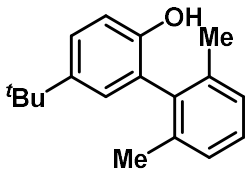

Compound **471l** (31.0 mg, 121.8 μmol, 66%) was obtained as a colorless oil from 5-{5-(*tert*-butyl)-2-[(2,6-dimethylbenzyl)oxy]phenyl}-5*H*-dibenzo[*b*,*d*]thiophen-5-ium tri-fluoromethanesulfonate (**470l**) according to general procedure C in MeCN.

^{1}H NMR (300 MHz, $CDCl_3$) δ 7.29 (ddd, J = 8.5, 2.6, 0.9 Hz, 1H), 7.25 – 7.14 (m, 3H), 7.03 (d, J = 3.2 Hz, 1H), 6.92 (d, J = 9.4 Hz, 1H), 4.44 (s, broad, 1H), 2.06 (s, 6H), 1.30 (d, J = 0.9 Hz, 9H); **^{13}C{H} NMR** (101 MHz, $CDCl_3$) δ 150.0, 143.7, 138.1, 135.6, 128.4, 128.1, 126.9, 125.9, 125.7, 114.6, 34.3, 31.8, 20.5; **IR (ATR)** [cm^{-1}]: $\tilde{\nu}$ = 3548, 3495, 2952, 2359, 2337, 498, 1466, 1458, 1207, 1172, 892, 822, 819, 771; **HR-MS-EI** calc. $C_{18}H_{22}O^+$ $[M]^+$ 254.1665; found 254.1666.

5-(*tert*-Butyl)-2-(methoxymethoxy)-2',6'-dimethyl-1,1'-biphenyl (471l')

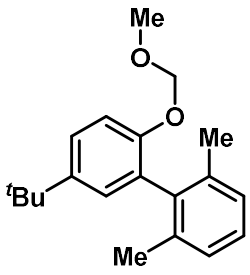

Compound **470l'** (31.0 mg, 103.8 μmol, 56%) was obtained as a colorless oil from 5-{5-(*tert*-butyl)-2-[(2,6-dimethylbenzyl)oxy]phenyl}-5*H*-dibenzo[*b*,*d*]thiophen-5-ium tri-fluoromethanesulfonate (**470l**) according to general procedure C in MeCN in the presence of MeOH (29.60 mg, 0.924 mmol, 5.00 equiv.).

^{1}H NMR (400 MHz, $CDCl_3$) δ 7.33 (dd, *J* = 8.6, 2.6 Hz, 1H), 7.21 – 7.11 (m, 4H), 7.09 (d, *J* = 2.5 Hz, 1H), 5.03 (s, 2H), 3.30 (s, 3H), 2.06 (s, 6H), 1.32 (s, 9H); **^{13}C{H} NMR** (75 MHz, $CDCl_3$) δ 152.0, 145.0, 139.0, 136.9, 130.1, 128.2, 127.1, 127.1, 125.0, 114.9, 94.9, 55.9, 34.4, 31.7, 20.7; **IR (ATR)** [cm^{-1}]: $\tilde{\nu}$ = 2958, 2904, 2869, 2824, 1499, 1225, 1143, 1077, 1005, 768; **HR-MS-ESI(+)** calc. $C_{20}H_{26}NaO_2^+$ $[M+Na]^+$ 321.1825; found 321.1834.

2,11-Di-*tert*-butyl-6,7-dihydrobenzo[2,1-*c*:3,4-*c*']dichromene (471q)

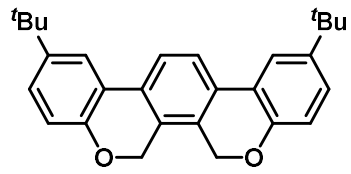

Compound **471q** (5.0 mg, 12.5 μmol, 14%) was obtained as a colorless oil from 5,5'-({[1,2-phenylenebis(methylene)]bis(oxy)}bis[5-(*tert*-butyl)-2,1-phenyle-ne])bis(5*H*-dibenzo[*b*,*d*]thio-phen-5-ium) bis-(trifluoromethanesulfonate) (**470q**) according to general procedure C in DMF.

^{1}H NMR (300 MHz, $CDCl_3$) δ 7.78 – 7.70 (m, 4H), 7.30 (dd, *J* = 8.5, 2.3 Hz, 2H), 6.95 (d, *J* = 8.5 Hz, 2H), 5.13 (s, 4H), 1.39 (s, 18H); **^{13}C{H} NMR** (101 MHz, $CDCl_3$) δ 152.2, 145.2, 130.0, 127.2, 126.9, 122.1, 121.9, 120.0, 116.8, 64.6, 34.6, 31.7; **IR (ATR)** [cm^{-1}]: $\tilde{\nu}$ = 3068, 3039, 2960, 2902, 2867, 1483, 1255, 1025, 828; **HR-MS-EI** calc. $C_{28}H_{30}O_2^+$ $[M]^+$ 398.2240; found 398.2238.

*Side product: 2-[(4-(tert-butyl)phenoxy)methyl]benzaldehyde (**471q'**)*

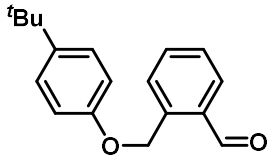

^{1}H NMR (300 MHz, $CDCl_3$) δ 10.21 (s, 1H), 7.90 (dd, *J* = 7.6, 1.5 Hz, 1H), 7.80 (d, *J* = 7.7 Hz, 1H), 7.64 (td, *J* = 7.6, 1.5 Hz, 1H), 7.52 (t, *J* = 7.6 Hz, 1H), 7.32 (d, *J* = 8.8 Hz, 2H), 6.95 (d, *J* = 8.8 Hz, 2H), 5.50 (s, 2H), 1.31 (s, 9H); **^{13}C NMR** (75 MHz, $CDCl_3$) δ 193.2, 156.4, 144.0, 140.0, 134.2, 133.7, 133.3, 128.0, 128.0, 126.5, 114.5, 67.7, 34.3, 31.7; **IR (ATR)** [cm^{-1}]: $\tilde{\nu}$ = 3038, 2961, 2903, 2867, 2738, 1693, 1513, 1242, 828, 756; **HR-MS-ESI(+)** calc. $C_{18}H_{21}O_2^+$ [M+H]$^+$ 269.1536, found 269.1533.

9,12-Dimethyl-2,5-dihydrobenzo[1,2-*c*:4,3-*c*']dichromene (471r) *and* 2,9-Dimethyl-6,13-dihydrobenzo[1,2-*c*:4,5-*c*']dichromene (471r')

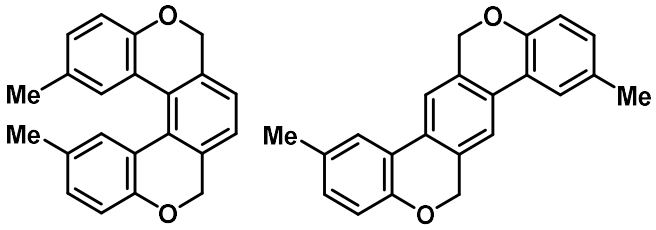

Compounds **471r**$^{(\prime)}$ (19.0 mg, 60.4 µmol, 65% combined) were obtained as a colorless oil from 5,5'-[{[1,4-phenylenebis(methylene)]bis(oxy)}bis(5-methyl-2,1-phenylene)]bis(5*H*-dibenzo[*b*,*d*]thiophen-5-ium) bis(trifluoromethanesulfonate) (**470r**) according to general procedure C in DMF. Flash-chromatography (SiO_2, pentane) afforded a 3:2 mixture of regioisomers **471r** and **471r'**, analytically pure samples of which were isolated by preparative HPLC.

Regioisomer 471r (left, major)

^{1}H NMR (300 MHz, $CDCl_3$) δ 7.35 (s, 2H), 7.04 (d, *J* = 1.3 Hz, 2H), 7.03 – 6.95 (m, 4H), 4.93 (s, 4H), 2.13 (s, 6H); **^{13}C{H} NMR** (101 MHz, $CDCl_3$) δ 154.4, 137.6, 130.4, 130.0, 129.4, 127.3, 123.5, 123.0, 117.5, 69.9, 20.7; **IR (ATR)** [cm^{-1}]: $\tilde{\nu}$ = 3048, 3025, 2973, 2965, 2919, 2893, 2836, 1496, 1252, 817; **HR-MS-ESI(+)** calc. $C_{22}H_{19}O_2^+$ [M+H]$^+$ 315.1380; found 315.1382.

Regioisomer 471r' (right, minor)

^{1}H NMR (400 MHz, $CDCl_3$) δ 7.52 (d, *J* = 2.1 Hz, 2H), 7.46 (s, 2H), 7.05 (dd, *J* = 8.2, 2.1 Hz, 2H), 6.90 (d, *J* = 8.2 Hz, 2H), 5.14 (s, 4H), 2.37 (s, 6H); **^{13}C{H} NMR** (101 MHz, $CDCl_3$) δ 152.8, 131.9, 131.6, 130.4, 129.8, 123.7, 122.4, 118.4, 117.3, 68.7, 21.1; **IR (ATR)** [cm^{-1}]: $\tilde{\nu}$ = 3023, 2960, 2919, 2903, 2841, 1501, 1238, 1012, 896, 809, 734, 585; **HR-MS-ESI(+)** calc. $C_{22}H_{19}O_2^+$ [M+H]$^+$ 315.1380; found 315.1372.

9,12-Di-*tert*-butyl-5,16-dihydronaphtho[1,2-*c*:4,3-*c*']dichromene (471s)

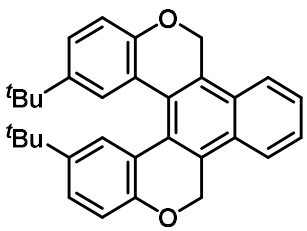

Compound **471s** (28.1 mg, 62.6 µmol, 68%) was obtained as a colorless solid from 5,5'-({[naphthalene-1,4-diylbis(methylene)]bis(oxy)}bis[5-(*tert*-butyl)-2,1-phe-nylene])bis(5*H*-dibenzo[*b*,*d*]-thiophen-5-ium) bis-(trifluoromethanesulfonate) (**470s**) according to general procedure C in DMF.

^{1}H NMR (300 MHz, $CDCl_3$) δ 7.90 – 7.79 (m, 2H), 7.57 – 7.48 (m, 2H), 7.27 (d, *J* = 2.8 Hz, 2H), 7.21 (dd, *J* = 8.6, 2.5 Hz, 2H), 7.09 (d, *J* = 8.5 Hz, 2H), 5.90 (d, *J* = 14.0 Hz, 2H), 5.07 (d, *J* = 14.0 Hz, 2H), 1.08 (s, 18H); **^{13}C{H} NMR** (101 MHz, $CDCl_3$) δ 152.9, 144.2, 133.2, 127.9, 126.7, 126.2, 125.9, 125.5, 124.0, 122.9, 117.2, 66.8, 34.3, 31.4; **IR (ATR)** [cm^{-1}]: $\tilde{\nu}$ = 2960, 2905, 1487, 1424, 1393, 1362, 1259, 1223, 1128, 1098, 1004, 903, 822, 795, 773, 708, 654, 586, 485; **HR-MS-EI** calc. $C_{32}H_{32}O_2^+$ [M]$^+$ 448.2397; found 448.2394.

2,2'-Di-*tert*-butyl-6*H*,6'H-7,7'-bibenzo[*c*]chromene (471t)

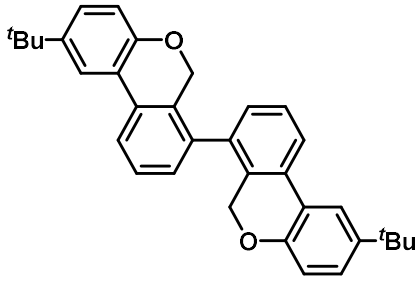

Compound **471t** (5.0 mg, 10.5 μmol, 11%) was obtained as a colorless oil from 5,5'-([{[1,1'-Biphenyl]-2,2'-diylbis(methylene)}bis(oxy)]bis[5-(*tert*-butyl)-2,1-phenylene])bis(5*H*-dibenzo-[*b*,*d*]thiophen-5-ium) bis-(trifluoromethanesulfonate) (**470t**) according to general procedure C in DMF after flash-chromatography (SiO_2, pentane).

^{1}H NMR (300 MHz, $CDCl_3$) δ 7.86 – 7.77 (m, 4H), 7.46 (t, *J* = 7.7 Hz, 2H), 7.32 (dd, *J* = 8.5, 2.3 Hz, 2H), 7.16 (d, *J* = 7.5 Hz, 2H), 6.93 (d, *J* = 8.5 Hz, 2H), 4.91 (d, *J* = 13.6 Hz, 2H), 4.84 (d, *J* = 13.5 Hz, 2H), 1.41 (s, 18H); **^{13}C{H} NMR** (75 MHz, $CDCl_3$) δ 152.7, 145.1, 136.3, 131.3, 130.0, 128.8, 128.0, 127.0, 122.4, 121.8, 120.3, 116.9, 66.3, 34.6, 31.7; **IR (ATR)** [cm^{-1}]: $\tilde{\nu}$ = 3066, 2961, 2902, 2867, 2838, 1591, 1500, 1254, 1023, 823, 795, 734, 677, 624, 421; **HR-MS-ESI(+)** calc. $C_{34}H_{34}NaO_2^+$ $[M+Na]^+$ 497.2451; found 497.2446.

1,2-Bis(2-methyl-6*H*-benzo[*c*]chromen-9-yl)ethane (471u)

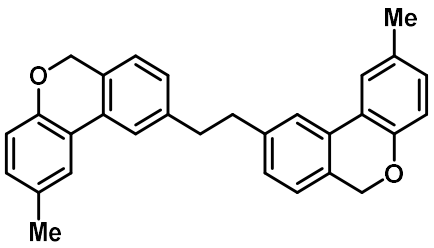

Compound **471u** (12.1 mg, 28.9 μmol, 31%) was obtained as a colorless oil from 5,5'-{[{[ethane-1,2-diylbis(4,1-phenylene)]-bis(methyle-ne)}bis(oxy)]bis(5-methyl-2,1-phenylene)}bis(5*H*-diben-zo[*b*,*d*]-thi-ophen-5-ium) bis-(trifluoromethanesulfonate) (**470u**) according to general procedure C in CH_3CN.

^{1}H NMR (300 MHz, $CDCl_3$) δ 7.51 (d, *J* = 5.9 Hz, 4H), 7.14 – 6.99 (m, 6H), 6.88 (d, *J* = 8.2 Hz, 2H), 5.07 (s, 4H), 3.01 (s, 4H), 2.35 (s, 6H); **^{13}C{H} NMR** (75 MHz, $CDCl_3$) δ 152.8, 141.9, 131.4, 130.4, 130.2, 129.6, 127.9, 124.8, 123.7, 122.8, 122.3, 117.2, 68.6, 38.2, 21.0; **IR (ATR)** [cm^{-1}]: $\tilde{\nu}$ = 3022, 2964, 2921, 2856, 2838, 1614, 1491, 1421, 1245, 1200, 1018, 908, 845, 816, 731; **HR-MS-ESI(+)** calc. $C_{30}H_{26}NaO_2^+$ $[M+Na]^+$ 441.1825; found 441.1828.

2,9-Dimethyl-dibenzo[*b*,*d*]pyrylium Tetrafluoroborate (472a)

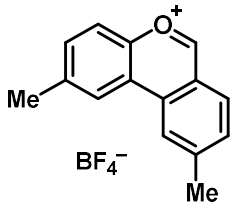

The synthesis was carried out using a modified literature procedure.[264]

An oven-dried Schlenk flask was equipped with a stirring bar and charged with 2,9-dimethyl-6*H*-benzo[*c*]chromene (**471a**) (100 mg, 475.5 μmol, 1.00 equiv.) and PCl_5 (65.9 mg, 316.5 μmol, 0.67 equiv.). The flask was evacuated and back-filled with nitrogen three times. Thionyl chloride (984 mg, 0.6 mL, 5.21 mmol) was added under nitrogen, and the reaction mixture was stirred under reflux for 5min using a pre-heated oil bath. After cooling to room temperature, a solution of fluoroboric acid in diethyl ether (50% p/w; 0.21 mL, 251 mg, 1.43 mmol, 3.00 equiv.) was added dropwise. After addition of dry degassed diethyl ether (1 mL), a yellow precipitate was formed. The latter was filtered off, washed several times with dry degassed diethyl ether and dried *in vacuo* to give the target compound as a yellow solid (90.6 mg, 306.0 μmol, 64%).

m.p. 207 °C (decomp.); **^{1}H NMR** (300 MHz, CD_3CN) δ 10.29 (s, 1H), 8.78 (d, *J* = 1.5 Hz, 1H), 8.72 – 8.63 (m, 2H), 8.21 (d, *J* = 8.8 Hz, 1H), 8.07 – 7.98 (m, 2H), 2.88 (s, 3H), 2.71 (s, 3H); **^{13}C NMR** (75 MHz, CD_3CN) δ 177.0, 162.7, 152.1, 143.3, 140.3, 137.3, 136.7, 134.8, 125.0, 124.3, 122.9, 122.1, 120.7, 24.6, 21.8; **^{19}F NMR** (282 MHz, CD_3CN) δ -151.66; **^{11}B NMR** (96 MHz, CD_3CN) δ -1.16; **IR (ATR)** [cm^{-1}]: $\tilde{\nu}$ = 3099, 3077, 3050, 1612, 1526, 1448, 1378, 1335, 1266, 1050, 934, 822, 806, 768, 680, 625, 517, 423; **HR-MS-ESI(+)** calc. $C_{15}H_{13}O^+$ $[M-BF_4]^+$ 209.0961; found 209.0958.

Dynamic NMR

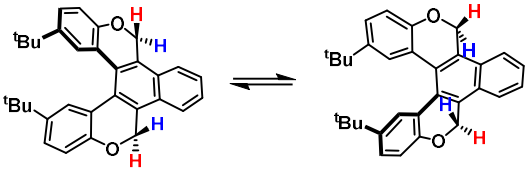

Bruker AV400

^{1}H NMR (400 MHz, DMSO-d_6, 298 K) δ 8.09 – 7.99 (m, 2H), 7.65 – 7.55 (m, 2H), 7.29 (dd, *J* = 8.5, 2.4 Hz, 2H), 7.14 (d, *J* = 2.3 Hz, 2H), 7.11 (d, *J* = 8.5 Hz, 2H), 6.05 (d, *J* = 14.5 Hz, 2H), 4.98 (d, *J* = 14.5 Hz, 2H), 1.04 (s, 18H); Δ*n*= 429 Hz, J_{AB}= 14.5 Hz

The NMR spectra of compound **471s** were recorded at different temperatures (298-423 K) in DMSO-d_6 in a J. Young NMR tube. At a temperature (T_c) of 150 °C (423 K) in a Bruker AV400 coalescence was achieved and the diastereotopic proton pairs exchanged due to stereoinversion. With the coalescence temperature in hand the Gibbs energy of activation ($\Delta G^{\ddagger}$ = 81.2 kJ·mol^{-1}) could be estimated via equations E1 and E2.

$$k_c = 2.22\sqrt{\Delta n^2 + 6J_{AB}^2} = 956\ s^{-1} \qquad (E1)$$

$$\Delta G^{\ddagger} = 19.14 T_c \left(10.32 + log\left(\frac{T_c}{k_c}\right)\right) = 81.2\ \frac{kJ}{mol} \qquad (E2)$$

T_c: coalescence temperature in K

J_{AB}: mutual coupling of exchanging nuclei in Hz

Δ*n*: separation between the peaks of exchanging nuclei in Hz

k_c: rate of exchange at coalescence temperature in s^{-1}

$\Delta G^{\ddagger}$: Gibbs energy of activation in J/mol

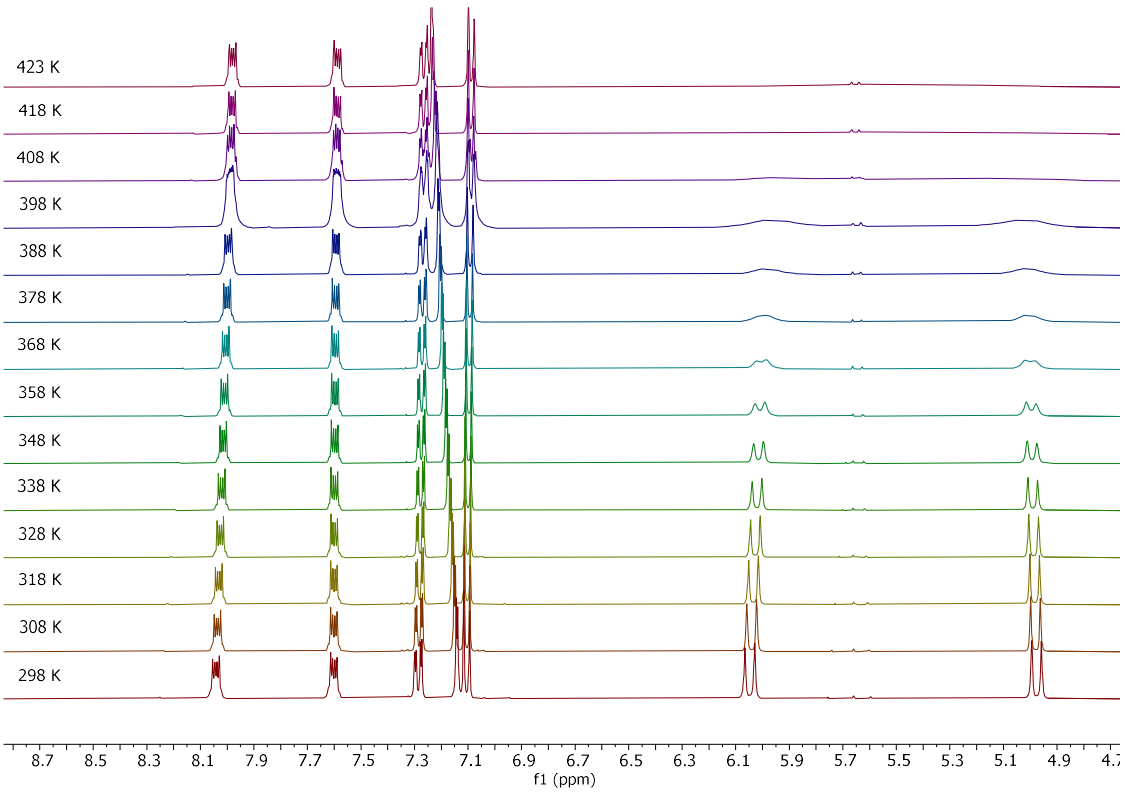

Stern–Volmer Quenching Experiment[286]

Under an atmosphere of nitrogen in a MBraun UNIlab plus glovebox samples of noted Quencher-concentrations were prepared by mixing a *fac*-[Ir(ppy)$_3$] (CH_3CN) stock solution with a dilution series of Quencher 5-{5-methyl-2-[(4-methylbenzyl)oxy]phenyl}-5*H*-dibenzo[*b*,*d*]thiophen-5-ium trifluoromethanesulfonate (**470a**) in CH_3CN. The fluorescence quenching of *fac*-[Ir(ppy)$_3$] (0.199 mM) was than recorded in a Jasco FP-8500 spectrofluorometer using a 10×2 mm quartz sample cell irradiating the sample at 372.8 nm.

*c*_Quencher [mM]	*I*_average [a.u.]	I_0/I	eq	*I*_scan1 [a.u.]	*I*_scan2 [a.u.]	*I*_scan3 [a.u.]
0.00	681.9	1.0	0.0	679.063	681.972	684.644
8.00	5.8	118.0	40.3	5.64911	6.10679	5.58716
4.00	13.9	49.1	20.1	14.3071	15.07	12.2684
2.00	24.3	28.1	10.1	21.3506	25.7425	25.7836
1.00	46.0	14.8	5.0	41.7912	47.2864	48.9637
0.50	98.2	6.9	2.5	97.1011	96.9008	100.597
0.25	118.9	5.7	1.3	127.114	116.71	112.731
0.12	211.8	3.2	0.6	228.186	208.303	198.922
0.06	279.4	2.4	0.3	297.61	274.644	265.817
0.03	479.4	1.4	0.2	492.109	475.044	471.188

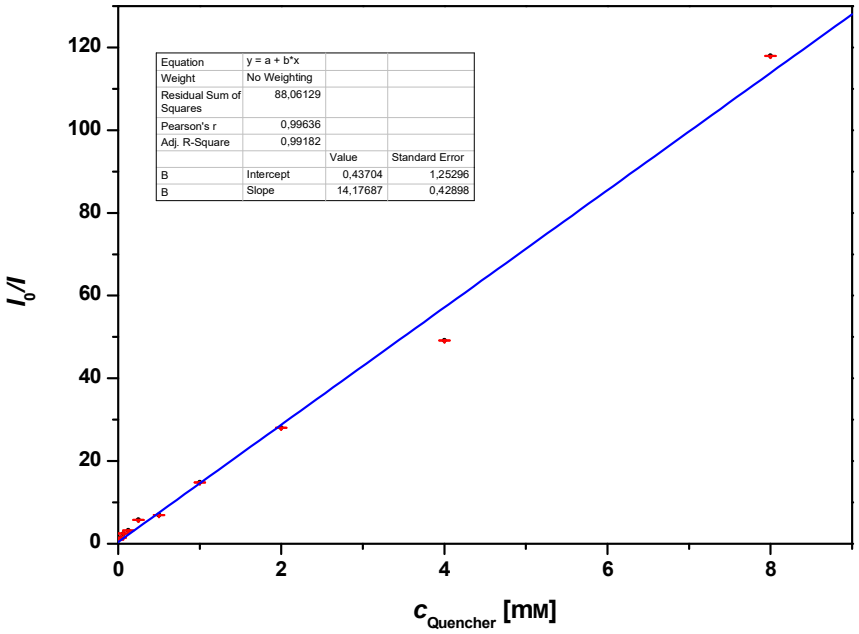

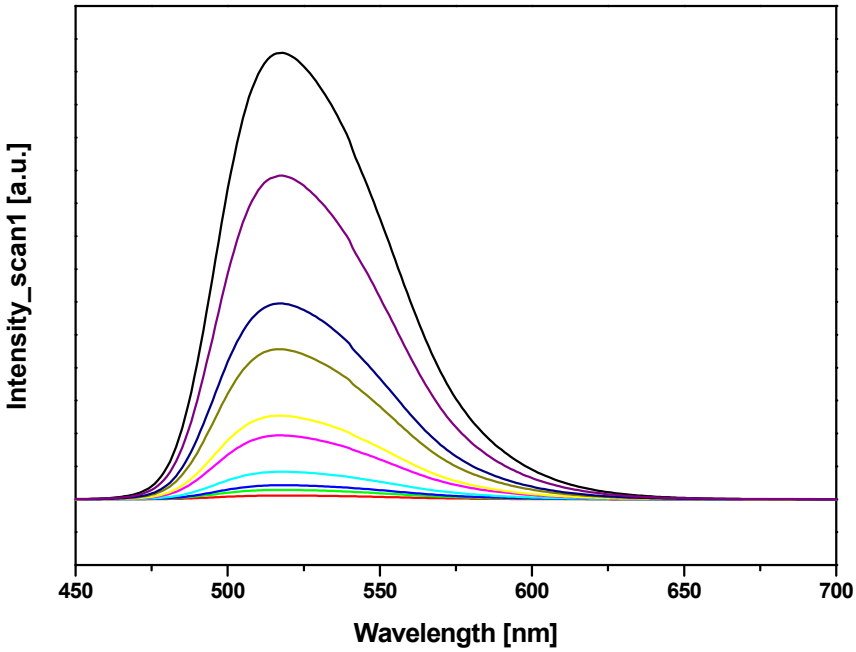

$\tau_f k_q$ = 14.177 (±0.43) $m^3 \cdot mol^{-1}$

Cyclic Voltammetry

5-{5-Methyl-2-[(4-methylbenzyl)oxy]phenyl}-5*H*-dibenzo[*b*,*d*]thiophen-5-ium Trifluoromethanesulfonate (470a)

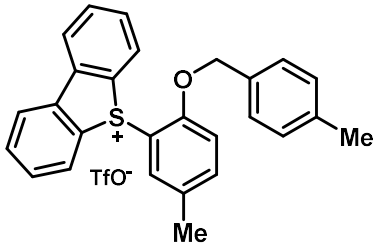

Cyclic voltammetry was measured with a VersaSTAT 4 potentiostat from Princeton Applied Research using the VersaStudio software (version 2.44.4). A standard three electrodes setup was used with a glassy carbon working electrode, a platinum counter electrode and a Ag/AgCl pseudo-reference electrode. Referencing was performed against $[Fe(Cp)_2]_{0/+}$. As electrolyte, a 0.1 M solution of $^nBu_4NPF_6$ in dry and degassed acetonitrile was used.

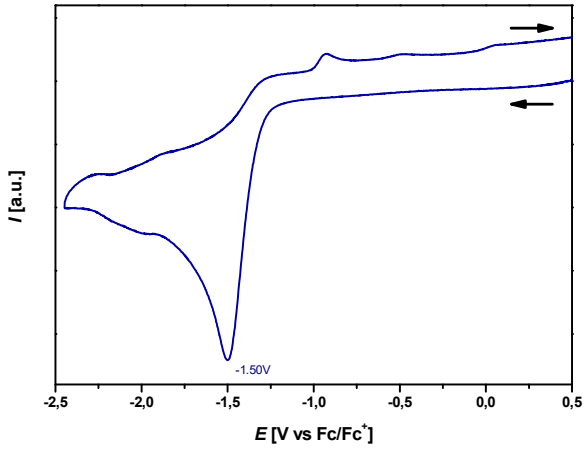

Scan rate: 100 mV/s

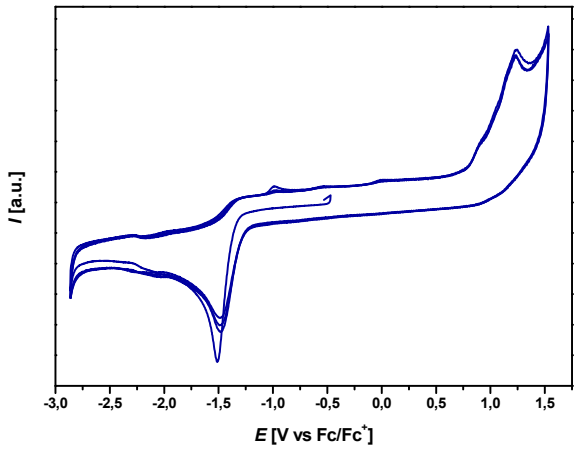

Scan rate: 100 mV/s

4-{[2-(5*H*-Dibenzo[*b*,*d*]thiophen-5-ium-5-yl]-4-methylphenoxy}methyl)pyridine 1-oxide Trifluorometha-nesulfonate (470k')

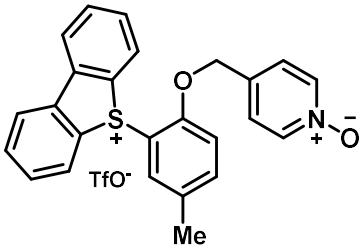

Cyclic voltammetry was measured with a VersaSTAT 4 potentiostat from Princeton Applied Research using the VersaStudio software (version 2.44.4). A standard three electrodes setup was used with a glassy carbon working electrode, a platinum counter electrode and a Ag/AgCl pseudo-reference electrode. Referencing was performed against $[Fe(Cp)_2]_{0/+}$. As electrolyte, a 0.1 M solution of $^nBu_4NPF_6$ in dry and degassed CH_2Cl_2 was used.

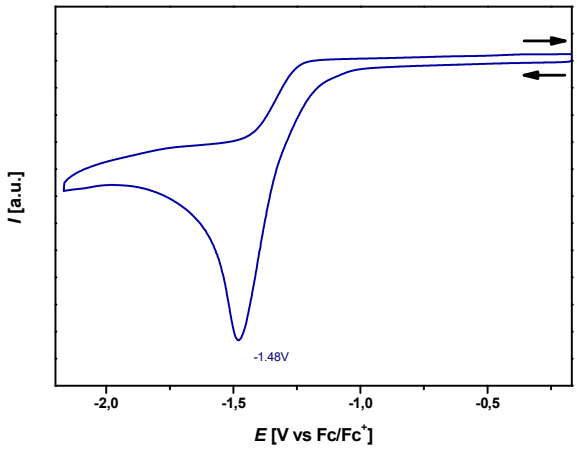

Scan rate: 100 mV/s

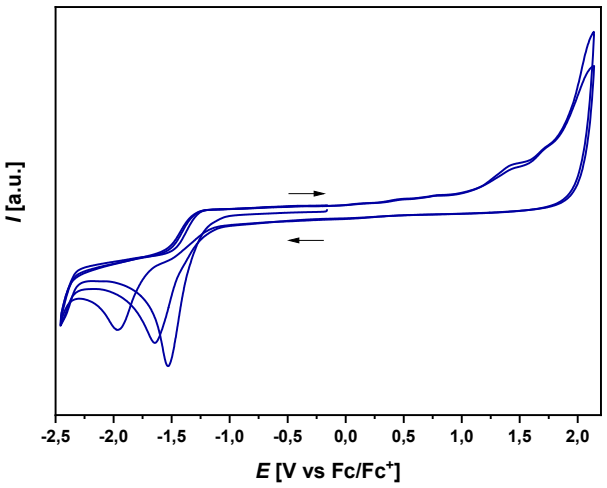

Scan rate: 100 mV/s

Quantum Yield Measurement

Samples were irradiated by a Jasco FP-8500 spectrofluorometer using a 10×2 mm quartz sample cell with stirring capability. The radiant flux was determined by standard ferrioxalate actinometry.[233,263]

Therefore, four stock solutions were prepared:

0.05 M H_2SO_4 stock solution

0.5 M H_2SO_4 stock solution

0.006 M ferrioxalate solution

Phenantroline-Buffer solution

A)

In a 1 l volumetric flask, 5.16 g of conc. H_2SO_4 (95% p/w) and 800 mL deionized water were added and mixed by shaking the flask. Then, deionized water was added until the 1 L graduation mark was reached.

B)

In a 1 l volumetric flask, 51.62 g of conc. H_2SO_4 (95% w/w) and 800 mL deionized water were added and mixed by shaking the flask. Then, deionized water was added until the 1 L graduation mark was reached.

C)

In a darkened room potassium ferrioxalate trihydrate ($K_3[Fe(C_2O_4)_3]\cdot 3H_2O$, 737 mg, 1.5 mmol) was added to a 250 mL volumetric flask covered with aluminum foil. Then, solution A was added until the 250 mL graduation mark was reached and homogeneity ensured by sonication.

D)

56 g of NaOAc and 250 mg of phenanthroline were added to a 250 mL volumetric flask covered with aluminum foil. Then, solution B was added until the 250 mL graduation mark was reached and homogeneity ensured by sonication.

Photon flux Measurement

Non-irradiated "blank" sample

A 10×2 mm quartz cuvette with stirring capability was charged with 1.1 mL of solution C and 0.2 mL of solution D and a stirring bar. After shaking the cuvette, the solution was stored in the dark for 1h. The UV/Vis spectrum was then taken and the absorbance measured at a narrow range (500-550 nm) of the electromagnetic radiation spectrum to identify the absorbance at λ = 510 nm. With the absorbance of the non-irradiated "blank" sample in hand, the difference in absorbance (ΔA) of the following irradiated samples can be calculated.

Irradiated samples

A 10×2 mm quartz cuvette with stirring capability was charged with 1.1 mL of solution C and a stirring bar. The sample was stirred at 400 rpm and irradiated for 10 s at λ = 436 nm (excitation bandwidth 5 nm). After irradiation, 0.2 mL of solution D was immediately added and the cuvette shaken and stored in the dark for 1h. The UV/Vis spectrum was then taken and the absorbance measured at a

narrow range (500-550 nm) of the electromagnetic radiation spectrum to identify the absorbance at λ = 510 nm. The same experiment was repeated for different irradiation times (20 s, 30 s, 40 s, 50 s).

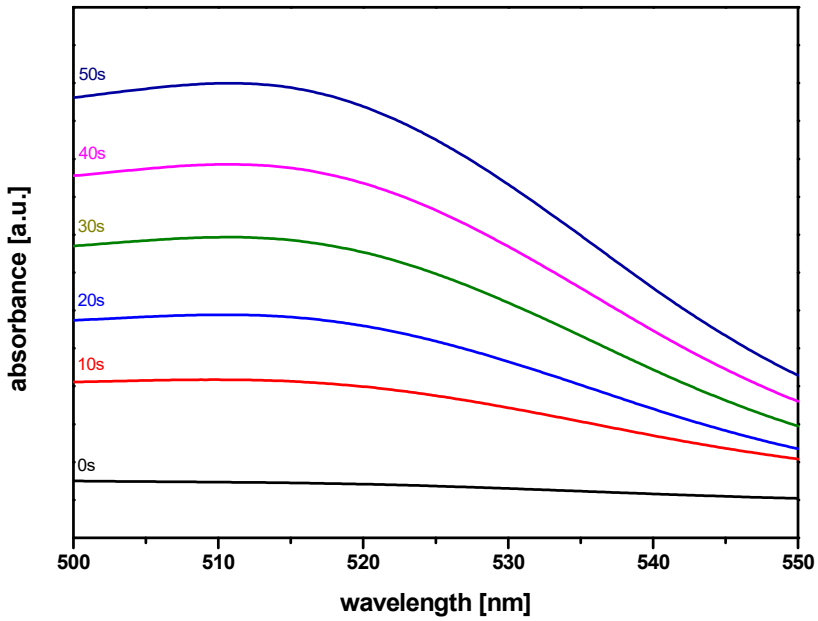

Fraction of light absorbed (f) by ferrioxalate solution

A 10×2 mm quartz cuvette with stirring capability was charged with 1.3 mL of solution C and a stirring bar. A UV/Vis spectrum was then taken and the absorbance measured at a narrow range (430-440 nm) of the electromagnetic radiation spectrum to identify the absorbance at λ = 436 nm. The same experiment was repeated with a cuvette filled with 1.3 mL of solution A (blank). The difference in absorbance A (0.2523 at λ = 436 nm) was calculated and used to determine the fraction of light absorbed f via eq. (E3).

$$f = 1 - 10^{-A} = 0.4406 \qquad (E3)$$

Conversion and photon flux were calculated using eq. E4 and E5:

$$n(Fe^{2+}) = \frac{V \cdot \Delta A}{l \cdot \varepsilon} \qquad (E4)$$

$$photon\ flux = \frac{n(Fe^{2+})}{\Phi \cdot t \cdot f} \qquad (E5)$$

V = total volume (0.0013 L)

ΔA = difference in absorbance (λ = 510 nm) between irradiated and non-irradiated sample

l = path length, cuvette was always placed with maximal path length in the optical path of UV/Vis and spectrofluorometer (1.000 cm)

ε = molar absorptivity at 510 nm (11100 l/(mol×cm))[287]

Φ = quantum yield for ferrioxalate actinometer (1.11 for a 0.006 M solution, λ = 436 nm)[287]

irradiation time [s]	ΔA	n Fe2+ [mol]	radiant flux [Einstein/s]
0	0	0	-
10	0.270	3.165E-08	6.47E-09
20	0.442	5.172E-08	5.29E-09
30	0.646	7.571E-08	5.16E-09
40	0.838	9.820E-08	5.02E-09
50	1.053	1.233E-07	5.04E-09
		average:	5.40E-09

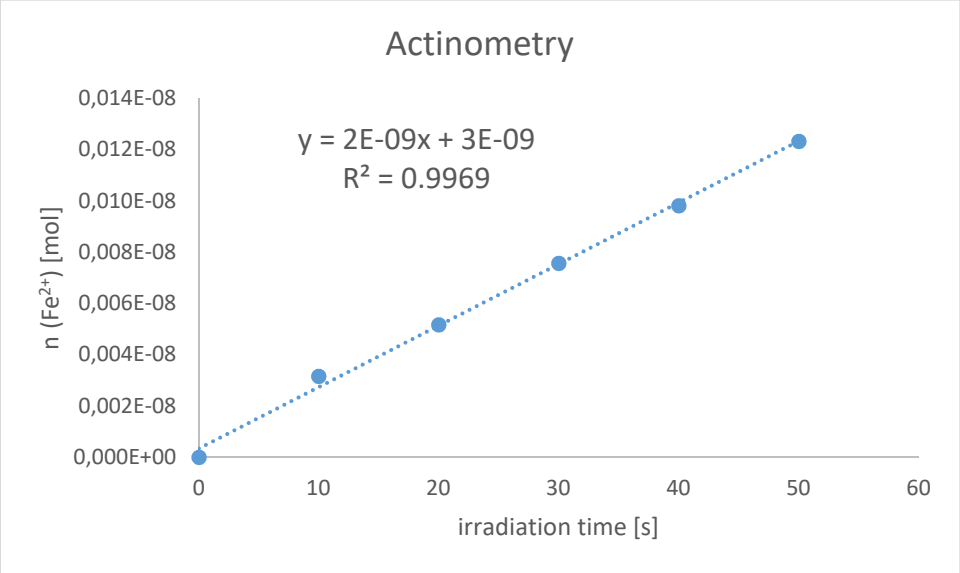

Determination of Quantum Yield

Fraction of light absorbed (f) by photocatalyst (fac-[Ir(ppy)$_3$]*) solution*

A 10×2 mm quartz cuvette with stirring capability was charged with 1.3 mL of a 3.06×10^{-4} M solution of *fac*-[Ir(ppy)$_3$] in acetonitrile (same concentration as in photoredox reaction) and a stirring bar. A UV/Vis spectrum was then taken and the absorbance measured at a narrow range (430-440 nm) of the electromagnetic radiation spectrum to identify the absorbance at λ = 436 nm. The same experiment was repeated with a cuvette filled with 1.3 mL of pure acetonitrile (blank). The difference in absorbance A (1.1153 at λ = 436 nm) was calculated and used to determine the fraction of light absorbed f via eq. (E3) (0.9233).

Photoredox reaction

An oven-dried J Young Schlenk flask (35 mL) was equipped with a stirring bar, charged with 5-{5-methyl-2-[(4-methylbenzyl)oxy]phenyl}-5*H*-dibenzo[*b*,*d*]thiophen-5-ium trifluoromethanesulfonate (**470a**) (501 mg, 0.92 mmol, 1.00 equiv.), *fac*-[Ir(ppy)$_3$] (6 mg, 9.1 μmol, 1 mol%) and sealed. The tube was evacuated and back-filled with nitrogen three times. Dry degassed CH_3CN (30 mL) was added under nitrogen. The mixture was sonicated until all solids dissolved and stored in the dark. 1.1 mL (3.37×10^{-5} mol **470a**) of the resulting solution was added to a 10×2 mm quartz cuvette with stirring capability equipped with a stirring bar and charged with Cs_2CO_3 (12.1 mg). The reaction mixture was stirred at 400 rpm and irradiated for 3600 s at λ = 436 nm (excitation bandwidth 5 nm) in a nitrogen

atmosphere. 0.1 mL reaction mixture was then taken by a syringe and thinned with 0.4 mL CH_2Br_2 (internal standard) solution in $CDCl_3$. Comparison of the relative integrals of the internal standard and product **471a** [CH_2 signal at 5.75 ppm ($CDCl_3$)] of the irradiated solution and the non-irradiated solution taken from the J Young Schlenk flask revealed a yield of 26% product **471a** ($0.26\times3.37\times10^{-5}$ mol mol = 0.87×10^{-5} mol in 1.1 mL solution). The experiment was repeated with different irradiation times (900s, 1800s, 2700s) and the resulting amounts of substance **471a** were plotted.

reaction time [s]	yield	amount of substance **471a** [mol]	quantum yield [%]
0	0	0.00E+00	-
900	0.06	2.02E-06	45.12
1800	0.12	4.05E-06	45.12
2700	0.19	6.41E-06	47.63
3600	0.26	8.77E-06	48.88
		average:	46.69

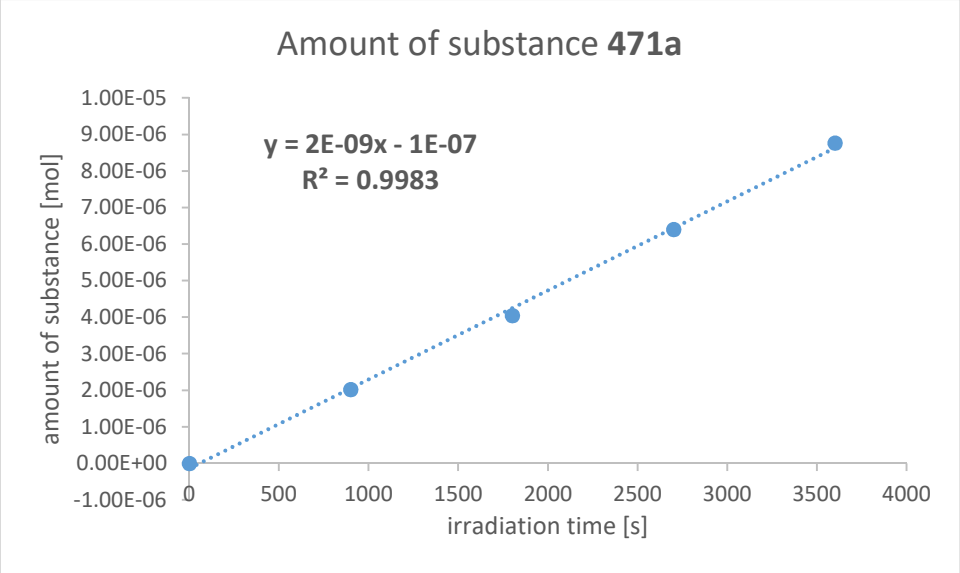

The quantum yield was determined using eq. (E6)

$$\Phi = \frac{n(product)}{flux \cdot t \cdot f} \cdot 100 = 47\% \qquad (E6)$$

n(product) = 1.05×10-5 mol

t = reaction time (3600s)

f = fraction of light absorbed by photocatalyst (0.9233)

flux = photon flux (5.40E-09 Einstein/s)

8 References

[1] Steinborn, *Grundlagen der metallorganischen Komplexkatalyse*, Springer Berlin Heidelberg, **2019**.

[2] W. C. Zeise, *Ann. Phys.* **1831**, *97*, 497.

[3] C. Wentrup, *Angewandte Chemie International Edition* **2020**, *59*, 8332.

[4] C. Elschenbroich, *Organometallics*, Wiley-VCH; [John Wiley, distributor], Weinheim, [Chichester], **2006**.

[5] a) J. S. Dewar, *Bulletin de la Societe Chimique de France* **1951**, *18*, C71-C79; b) J. Chatt, L. A. Duncanson, *Journal of the Chemical Society (Resumed)* **1953**, 2939.

[6] A. Fürstner, P. W. Davies, *Angewandte Chemie International Edition* **2007**, *46*, 3410.

[7] G. N. Lewis, *Valence and The structure of atoms and molecules*, The Chemical Catalog Company Inc, New York, **1923**.

[8] R. G. Pearson, *Journal of the American Chemical Society* **1963**, *85*, 3533.

[9] M. Benedetti, F. P. Fanizzi, L. Maresca, G. Natile, *Chemical Communications* **2006**, 1118.

[10] a) A. Leyva-Pérez, A. Corma, *Angewandte Chemie International Edition* **2012**, *51*, 614; b) P. Pyykkö, *Angewandte Chemie International Edition* **2004**, *43*, 4412; c) D. J. Gorin, F. D. Toste, *Nature* **2007**, *446*, 395.

[11] Y. Wang, M. E. Muratore, A. M. Echavarren, *Chem. Eur. J.* **2015**, *21*, 7332.

[12] R. J. Harris, R. A. Widenhoefer, *Chemical Society Reviews* **2016**, *45*, 4533.

[13] D. Benitez, N. D. Shapiro, E. Tkatchouk, Y. Wang, W. A. Goddard, F. D. Toste, *Nature Chemistry* **2009**, *1*, 482.

[14] W. Wang, G. B. Hammond, B. Xu, *Journal of the American Chemical Society* **2012**, *134*, 5697.

[15] A. Fürstner, *Accounts of Chemical Research* **2014**, *47*, 925.

[16] A. Fürstner, *Chemical Society Reviews* **2009**, *38*, 3208.

[17] T. J. Brown, M. G. Dickens, R. A. Widenhoefer, *Chemical Communications* **2009**, 6451.

[18] S. Flügge, A. Anoop, R. Goddard, W. Thiel, A. Fürstner, *Chem. Eur. J.* **2009**, *15*, 8558.

[19] M. García-Mota, N. Cabello, F. Maseras, A. M. Echavarren, J. Pérez-Ramírez, N. Lopez, *ChemPhysChem* **2008**, *9*, 1624.

[20] C. Nieto-Oberhuber, M. P. Muñoz, E. Buñuel, C. Nevado, D. J. Cárdenas, A. M. Echavarren, *Angewandte Chemie International Edition* **2004**, *43*, 2402.

[21] S. Oi, I. Tsukamoto, S. Miyano, Y. Inoue, *Organometallics* **2001**, *20*, 3704.

[22] C. Nieto-Oberhuber, S. López, M. P. Muñoz, D. J. Cárdenas, E. Buñuel, C. Nevado, A. M. Echavarren, *Angewandte Chemie International Edition* **2005**, *44*, 6146.

[23] a) C. Nieto-Oberhuber, S. López, M. P. Muñoz, E. Jiménez-Núñez, E. Buñuel, D. J. Cárdenas, A. M. Echavarren, *Chem. Eur. J.* **2006**, *12*, 1694; b) A. Escribano-Cuesta, P. Pérez-Galán, E. Herrero-Gómez, M. Sekine, A. A. C. Braga, F. Maseras, A. M. Echavarren, *Organic & Biomolecular Chemistry* **2012**, *10*, 6105.

[24] a) M. Mato, A. Franchino, C. García-Morales, A. M. Echavarren, *Chemical Reviews* **2021**, *121*, 8613; b) V. López-Carrillo, A. M. Echavarren, *Journal of the American Chemical Society* **2010**, *132*, 9292.

[25] C. A. Witham, P. Mauleón, N. D. Shapiro, B. D. Sherry, F. D. Toste, *Journal of the American Chemical Society* **2007**, *129*, 5838.

[26] S. M. Canham, D. J. France, L. E. Overman, *Journal of the American Chemical Society* **2010**, *132*, 7876.

[27] B. Baskar, H. J. Bae, S. E. An, J. Y. Cheong, Y. H. Rhee, A. Duschek, S. F. Kirsch, *Organic Letters* **2008**, *10*, 2605.

[28] R. Dorel, A. M. Echavarren, *Chemical Reviews* **2015**, *115*, 9028.

[29] C. Nevado, A. M. Echavarren, *Chem. Eur. J.* **2005**, *11*, 3155.

[30] A. S. K. Hashmi, T. M. Frost, J. W. Bats, *Journal of the American Chemical Society* **2000**, *122*, 11553.

[31] A. S. K. Hashmi, M. Rudolph, H.-U. Siehl, M. Tanaka, J. W. Bats, W. Frey, *Chem. Eur. J.* **2008**, *14*, 3703.
[32] Y. Chen, W. Yan, N. G. Akhmedov, X. Shi, *Organic Letters* **2010**, *12*, 344.
[33] A. Fürstner, V. Mamane, *The Journal of Organic Chemistry* **2002**, *67*, 6264.
[34] V. Mamane, P. Hannen, A. Fürstner, *Chem. Eur. J.* **2004**, *10*, 4556.
[35] R. Pertschi, D. Hatey, P. Pale, P. de Frémont, A. Blanc, *Organometallics* **2020**, *39*, 804.
[36] P. Ríos, A. Rodríguez, S. Conejero, *Chemical Communications* **2020**, *56*, 5333.
[37] N. J. Gunsalus, A. Koppaka, S. H. Park, S. M. Bischof, B. G. Hashiguchi, R. A. Periana, *Chemical Reviews* **2017**, *117*, 8521.
[38] A. Fürstner, P. W. Davies, T. Gress, *Journal of the American Chemical Society* **2005**, *127*, 8244.
[39] A. Amgoune, D. Bourissou, *Chemical Communications* **2011**, *47*, 859.
[40] Di You, H. Yang, S. Sen, F. P. Gabbaï, *Journal of the American Chemical Society* **2018**, *140*, 9644.
[41] H. Yang, F. P. Gabbaï, *Journal of the American Chemical Society* **2015**, *137*, 13425.
[42] Di You, F. P. Gabbaï, *Journal of the American Chemical Society* **2017**, *139*, 6843.
[43] Y.-H. Lo, F. P. Gabbaï, *Organometallics* **2018**, *37*, 2500.
[44] J. W. Dube, Y. Zheng, W. Thiel, M. Alcarazo, *Journal of the American Chemical Society* **2016**, *138*, 6869.
[45] M. Alcarazo, *Accounts of Chemical Research* **2016**, *49*, 1797.
[46] R. H. Crabtree, *The Organometallic Chemistry of the Transition Metals*, John Wiley & Sons, New York, NY, **2014**.
[47] C. Amatore, A. Jutand, G. Le Duc, *Chem. Eur. J.* **2011**, *17*, 2492.
[48] M. P. Mitoraj, A. Michalak, *Inorganic Chemistry* **2010**, *49*, 578.
[49] A. G. Orpen, N. G. Connelly, *Organometallics* **1990**, *9*, 1206.
[50] M. Alcarazo, *Chem. Eur. J.* **2014**, *20*, 7868.
[51] C. A. Tolman, *Chemical Reviews* **1977**, *77*, 313.
[52] C. A. Tolman, *Journal of the American Chemical Society* **1970**, *92*, 2953.
[53] O. Kühl, *Coordination Chemistry Reviews* **2005**, *249*, 693.
[54] U. Beckmann, D. Süslüyan, P. C. Kunz, *Phosphorus, Sulfur, and Silicon and the Related Elements* **2011**, *186*, 2061.
[55] D. W. Allen, B. F. Taylor, *Journal of the Chemical Society, Dalton Transactions* **1982**, 51.
[56] R. P. Pinnell, C. A. Megerle, S. L. Manatt, P. A. Kroon, *Journal of the American Chemical Society* **1973**, *95*, 977.
[57] T. E. Müller, D. M. P. Mingos, *Transition Metal Chemistry* **1995**, *20*, 533.
[58] R. Dorta, E. D. Stevens, N. M. Scott, C. Costabile, L. Cavallo, C. D. Hoff, S. P. Nolan, *Journal of the American Chemical Society* **2005**, *127*, 2485.
[59] H. Clavier, S. P. Nolan, *Chemical Communications* **2010**, *46*, 841.
[60] A. Poater, B. Cosenza, A. Correa, S. Giudice, F. Ragone, V. Scarano, L. Cavallo, *Eur. J. Inorg. Chem.* **2009**, *2009*, 1759.
[61] Di You, J. E. Smith, S. Sen, F. P. Gabbaï, *Organometallics* **2020**, *39*, 4169.
[62] A. S. K. Hashmi, *Angewandte Chemie International Edition* **2010**, *49*, 5232.
[63] J. Carreras, M. Patil, W. Thiel, M. Alcarazo, *Journal of the American Chemical Society* **2012**, *134*, 16753.
[64] R. L. LaLonde, Brenzovich, Jr., William E., D. Benitez, E. Tkatchouk, K. Kelley, Goddard, III, William A., F. D. Toste, *Chemical Science* **2010**, *1*, 226.
[65] Y. Chen, D. Wang, J. L. Petersen, N. G. Akhmedov, X. Shi, *Chemical Communications* **2010**, *46*, 6147.
[66] Z. J. Wang, D. Benitez, E. Tkatchouk, W. A. Goddard III, F. D. Toste, *Journal of the American Chemical Society* **2010**, *132*, 13064.

[67] P. Morán-Poladura, S. Suárez-Pantiga, M. Piedrafita, E. Rubio, J. M. González, *Journal of Organometallic Chemistry* **2011**, *696*, 12.
[68] J. P. Markham, S. T. Staben, F. D. Toste, *Journal of the American Chemical Society* **2005**, *127*, 9708.
[69] P. W. N. M. van Leeuwen, *Homogeneous Catalysis*, Springer Netherlands, Dordrecht, **2004**.
[70] C. W. Kohlpaintner, R. W. Fischer, B. Cornils, *Applied Catalysis A: General* **2001**, *221*, 219.
[71] C. Hinderling, C. Adlhart, P. Chen, *Angewandte Chemie International Edition* **1998**, *37*, 2685.
[72] D. M. Chisholm, J. Scott McIndoe, *Dalton Transactions* **2008**, 3933.
[73] T. Drews, D. Rusch, S. Seidel, S. Willemsen, K. Seppelt, *Chem. Eur. J.* **2008**, *14*, 4280.
[74] C. J. Rugen, M. Alcarazo, *Synlett* **2022**, *33*, 16.
[75] U. Zoller, *Tetrahedron* **1988**, *44*, 7413.
[76] N. Kuhn, J. Fahl, D. Bläser, R. Boese, *Z. anorg. allg. Chem.* **1999**, *625*, 729.
[77] M. Azouri, J. Andrieu, M. Picquet, P. Richard, B. Hanquet, I. Tkatchenko, *Eur. J. Inorg. Chem.* **2007**, *2007*, 4877.
[78] G. Bouhadir, R. W. Reed, R. Réau, G. Bertrand, *Heteroatom Chem.* **1995**, *6*, 371.
[79] J. J. Weigand, K.-O. Feldmann, F. D. Henne, *Journal of the American Chemical Society* **2010**, *132*, 16321.
[80] T. Johannsen, C. Golz, M. Alcarazo, *Angewandte Chemie International Edition* **2020**, *59*, 22779.
[81] I. V.Komarov, M. Yu.Kornilov, A. A. Tolmachev, A. A. Yurchenko, E. B. Rusanov, A. N. Chernega, *Tetrahedron* **1995**, *51*, 11271.
[82] N. Debono, Y. Canac, C. Duhayon, R. Chauvin, *Eur. J. Inorg. Chem.* **2008**, *2008*, 2991.
[83] A. A. Tolmachev, A. A. Yurchenko, A. S. Merculov, M. G. Semenova, E. V. Zarudnitskii, V. V. Ivanov, A. M. Pinchuk, *Heteroatom Chem.* **1999**, *10*, 585.
[84] E. Haldón, Á. Kozma, H. Tinnermann, L. Gu, R. Goddard, M. Alcarazo, *Dalton Transactions* **2016**, *45*, 1872.
[85] J. Petuškova, H. Bruns, M. Alcarazo, *Angewandte Chemie International Edition* **2011**, *50*, 3799.
[86] H. Tinnermann, C. Wille, M. Alcarazo, *Angewandte Chemie International Edition* **2014**, *53*, 8732.
[87] S. Kaye, J. M. Fox, F. A. Hicks, S. L. Buchwald, *Adv. Synth. Catal.* **2001**, *343*, 789.
[88] H. Tinnermann, L. D. M. Nicholls, T. Johannsen, C. Wille, C. Golz, R. Goddard, M. Alcarazo, *ACS Catalysis* **2018**, *8*, 10457.
[89] C. D. Mboyi, C. Maaliki, A. Mankou Makaya, Y. Canac, C. Duhayon, R. Chauvin, *Inorganic Chemistry* **2016**, *55*, 11018.
[90] M. Azouri, J. Andrieu, M. Picquet, H. Cattey, *Inorganic Chemistry* **2009**, *48*, 1236.
[91] C. Maaliki, C. Lepetit, Y. Canac, C. Bijani, C. Duhayon, R. Chauvin, *Chem. Eur. J.* **2012**, *18*, 7705.
[92] J. Carreras, G. Gopakumar, L. Gu, A. Gimeno, P. Linowski, J. Petuškova, W. Thiel, M. Alcarazo, *Journal of the American Chemical Society* **2013**, *135*, 18815.
[93] L. Gu, L. M. Wolf, A. Zieliński, W. Thiel, M. Alcarazo, *Journal of the American Chemical Society* **2017**, *139*, 4948.
[94] F. D. Henne, A. T. Dickschat, F. Hennersdorf, K.-O. Feldmann, J. J. Weigand, *Inorganic Chemistry* **2015**, *54*, 6849.
[95] A. Augurusa, M. Mehta, M. Perez, J. Zhu, D. W. Stephan, *Chemical Communications* **2016**, *52*, 12195.
[96] D. J. Brauer, K. W. Kottsieper, C. Liek, O. Stelzer, H. Waffenschmidt, P. Wasserscheid, *Journal of Organometallic Chemistry* **2001**, *630*, 177.
[97] Y. García-Rodeja, I. Fernández, *Organometallics* **2017**, *36*, 460.
[98] C. C. Brasse, U. Englert, A. Salzer, H. Waffenschmidt, P. Wasserscheid, *Organometallics* **2000**, *19*, 3818.
[99] A. Zieliński, X. Marset, C. Golz, L. M. Wolf, M. Alcarazo, *Angewandte Chemie International Edition* **2020**, *59*, 23299.

[100] L. Hu, D. Mahaut, N. Tumanov, J. Wouters, R. Robiette, G. Berionni, *The Journal of Organic Chemistry* **2019**, *84*, 11268.
[101] H. Shet, U. Parmar, S. Bhilare, A. R. Kapdi, *Organic Chemistry Frontiers* **2021**, *8*, 1599.
[102] D. Mahaut, G. Berionni, B. Champagne, *The Journal of Physical Chemistry A* **2022**, *126*, 2794.
[103] C. Jongsma, J. P. de Kleijn, F. Bickelhaupt, *Tetrahedron* **1974**, *30*, 3465.
[104] J. Kobayashi, T. Agou, T. Kawashima, *Chemistry Letters* **2003**, *32*, 1144.
[105] T. Agou, J. Kobayashi, T. Kawashima, *Chemistry Letters* **2004**, *33*, 1028.
[106] L. Hu, D. Mahaut, N. Tumanov, J. Wouters, L. Collard, R. Robiette, G. Berionni, *Dalton Transactions* **2021**, *50*, 4772.
[107] D. Hellwinkel, W. Schenk, *Angew. Chem. Int. Ed. Engl.* **1969**, *8*, 987.
[108] D. Hellwinkel, W. Schenk, W. Blaicher, *Chem. Ber.* **1978**, *111*, 1798.
[109] Y. Cao, J. W. Napoline, J. Bacsa, P. Pollet, J. D. Soper, J. P. Sadighi, *Organometallics* **2019**, *38*, 1868.
[110] H. Ube, Y. Yasuda, H. Sato, M. Shionoya, *Nature Communications* **2017**, *8*, 14296.
[111] Rot,, Nicolette, de Wijs,, Willem-Jan A., de Kanter,, Frans J. J., Dam,, Matheus A., Bickelhaupt,, Friedrich, Lutz,, Martin, Spek,, Anthony L., *Main Group Metal Chemistry* **1999**, *22*, 519.
[112] H. Tsuji, T. Inoue, Y. Kaneta, S. Sase, A. Kawachi, K. Tamao, *Organometallics* **2006**, *25*, 6142.
[113] S. Kawamorita, T. Miyazaki, H. Ohmiya, T. Iwai, M. Sawamura, *Journal of the American Chemical Society* **2011**, *133*, 19310.
[114] S. Kawamorita, T. Miyazaki, T. Iwai, H. Ohmiya, M. Sawamura, *Journal of the American Chemical Society* **2012**, *134*, 12924.
[115] S. Kawamorita, R. Murakami, T. Iwai, M. Sawamura, *Journal of the American Chemical Society* **2013**, *135*, 2947.
[116] T. Iwai, S. Konishi, T. Miyazaki, S. Kawamorita, N. Yokokawa, H. Ohmiya, M. Sawamura, *ACS Catalysis* **2015**, *5*, 7254.
[117] U. Christmann, R. Vilar, *Angewandte Chemie International Edition* **2005**, *44*, 366.
[118] S. Konishi, T. Iwai, M. Sawamura, *Organometallics* **2018**, *37*, 1876.
[119] M. W. Drover, K. Nagata, J. C. Peters, *Chemical Communications* **2018**, *54*, 7916.
[120] R. Suter, H. Sinclair, N. Burford, R. McDonald, M. J. Ferguson, E. Schrader, *Dalton Transactions* **2017**, *46*, 7681.
[121] a) P. L. Shutov, S. S. Karlov, K. Harms, D. A. Tyurin, A. V. Churakov, J. Lorberth, G. S. Zaitseva, *Inorganic Chemistry* **2002**, *41*, 6147; b) X. Liu, Y. Bai, J. Verkade, *Journal of Organometallic Chemistry* **1999**, *582*, 16.
[122] S. Hanf, A. L. Colebatch, P. Stehr, R. García-Rodríguez, E. Hey-Hawkins, D. S. Wright, *Dalton Transactions* **2020**, *49*, 5312.
[123] E. Larsen, G. N. LaMar, B. E. Wagner, J. E. Parks, R. H. Holm, *Inorganic Chemistry* **1972**, *11*, 2652.
[124] a) A. Fürstner, *Adv. Synth. Catal.* **2016**, *358*, 2362; b) B. D. Sherry, A. Fürstner, *Accounts of Chemical Research* **2008**, *41*, 1500; c) P. Chirik, R. Morris, *Accounts of Chemical Research* **2015**, *48*, 2495; d) P. J. Chirik, *Accounts of Chemical Research* **2015**, *48*, 1687.
[125] L. Tong, R. Zong, R. P. Thummel, *Journal of the American Chemical Society* **2014**, *136*, 4881.
[126] L. D. Wickramasinghe, R. Zhou, R. Zong, P. Vo, K. J. Gagnon, R. P. Thummel, *Journal of the American Chemical Society* **2015**, *137*, 13260.
[127] C. L. Diedrich, D. Haase, J. Christoffers, *Synthesis* **2008**, *2008*, 2199.
[128] a) L. Mao, T. Moriuchi, H. Sakurai, H. Fujii, T. Hirao, *Tetrahedron Letters* **2005**, *46*, 8419; b) F. Cottet, M. Marull, O. Lefebvre, M. Schlosser, *Eur. J. Org. Chem.* **2003**, *2003*, 1559.
[129] D. Basu, R. Gilbert-Wilson, D. L. Gray, T. B. Rauchfuss, A. K. Dash, *Organometallics* **2018**, *37*, 2760.
[130] D. Basu, A. K. Dash, T. B. Rauchfuss, R. G. Watson, WO2019018357 (A1), **2018**.

[131] 浩. 中沢, 昌. 神谷, 裕. 中島, 一. 佐藤, JP2020050637 (A), **2018**.
[132] Lavallo Vincent, Canac Yves, Donnadieu Bruno, Schoeller Wolfgang W., Bertrand Guy, *Science* **2006**, *312*, 722.
[133] A. J. Arduengo, H. V. R. Dias, R. L. Harlow, M. Kline, *Journal of the American Chemical Society* **1992**, *114*, 5530.
[134] R. G. Bryant, *Journal of Chemical Education* **1983**, *60*, 933.
[135] J.-C. Hierso, D. Armspach, D. Matt, *Comptes Rendus Chimie* **2009**, *12*, 1002.
[136] V. S. Dimitrov, J. A. Ladd, *Magn. Reson. Chem.* **1985**, *23*, 529.
[137] J. Petuškova, M. Patil, S. Holle, C. W. Lehmann, W. Thiel, M. Alcarazo, *Journal of the American Chemical Society* **2011**, *133*, 20758.
[138] Z. B. Maksić, B. Kovačević, *Journal of the Chemical Society, Perkin Transactions 2* **1999**, 2623.
[139] L. Gu, Y. Zheng, E. Haldón, R. Goddard, E. Bill, W. Thiel, M. Alcarazo, *Angewandte Chemie International Edition* **2017**, *56*, 8790.
[140] J. V. Obligacion, P. J. Chirik, *Nature Reviews Chemistry* **2018**, *2*, 15.
[141] K. Kamata, A. Suzuki, Y. Nakai, H. Nakazawa, *Organometallics* **2012**, *31*, 3825.
[142] P. Sobota, Z. Olejnik, J. Utko, T. Lis, *Polyhedron* **1993**, *12*, 613.
[143] a) I. Capel Berdiell, R. Kulmaczewski, O. Cespedes, M. A. Halcrow, *Chem. Eur. J.* **2018**, *24*, 5055; b) D.-Y. Wu, O. Sato, C.-Y. Duan, *Inorganic Chemistry Communications* **2009**, *12*, 325.
[144] a) L. Sacconi, *Pure and Applied Chemistry* **1968**, *17*, 95; b) P. Gütlich, *Spin Crossover in Transition Metal Compounds II*, Springer, Berlin, Heidelberg, **2004**.
[145] A. W. Addison, T. N. Rao, J. Reedijk, J. van Rijn, G. C. Verschoor, *Journal of the Chemical Society, Dalton Transactions* **1984**, 1349.
[146] S. E. Boiadjiev, D. A. Lightner, *Journal of the American Chemical Society* **2000**, *122*, 11328.
[147] Á. Kozma, T. Deden, J. Carreras, C. Wille, J. Petuškova, J. Rust, M. Alcarazo, *Chem. Eur. J.* **2014**, *20*, 2208.
[148] a) L. D. M. Nicholls, M. Alcarazo, *Chemistry Letters* **2018**, *48*, 1; b) V. Karthik, V. Gupta, G. Anantharaman, *Organometallics* **2015**, *34*, 3713.
[149] L. Yang, D. R. Powell, R. P. Houser, *Dalton Transactions* **2007**, 955.
[150] A. Okuniewski, D. Rosiak, J. Chojnacki, B. Becker, *Polyhedron* **2015**, *90*, 47.
[151] J. E. Parks, B. E. Wagner, R. H. Holm, *Journal of Organometallic Chemistry* **1973**, *56*, 53.
[152] S. F. Malysheva, A. V. Artem'ev, N. A. Belogorlova, A. O. Korocheva, N. K. Gusarova, B. A. Trofimov, *Russian Journal of General Chemistry* **2012**, *82*, 1307.
[153] S. F. Malysheva, V. A. Kuimov, N. A. Belogorlova, A. I. Albanov, N. K. Gusarova, B. A. Trofimov, *Eur. J. Org. Chem.* **2019**, *2019*, 6240.
[154] S. F. Malysheva, V. A. Kuimov, A. B. Trofimov, N. A. Belogorlova, Y. I. Litvintsev, A. M. Belogolova, N. K. Gusarova, B. A. Trofimov, *Mendeleev Communications* **2018**, *28*, 472.
[155] D. Shin, C. Switzer, *Chemical Communications* **2007**, 4401.
[156] M. Böttger, B. Wiegmann, S. Schaumburg, P. G. Jones, W. Kowalsky, H.-H. Johannes, *Beilstein journal of organic chemistry* **2012**, *8*, 1037.
[157] E. Conterosito, C. Magistris, C. Barolo, G. Croce, M. Milanesio, *Journal of Molecular Structure* **2016**, *1107*, 337.
[158] P. Gütlich, A. Hauser, H. Spiering, *Angew. Chem. Int. Ed. Engl.* **1994**, *33*, 2024.
[159] V. V. Pavlishchuk, A. W. Addison, *Inorganica Chimica Acta* **2000**, *298*, 97.
[160] L. A. Büldt, A. Prescimone, M. Neuburger, O. S. Wenger, *Eur. J. Inorg. Chem.* **2015**, *2015*, 4666.
[161] D. A. C. Brownson, C. E. Banks in *The Handbook of Graphene Electrochemistry* (Eds.: D. A. C. Brownson, C. E. Banks), Springer London, London, **2014**, pp. 23–77.
[162] N. G. Connelly, W. E. Geiger, *Chemical Reviews* **1996**, *96*, 877.
[163] M. N. Hopkinson, A. Tlahuext-Aca, F. Glorius, *Accounts of Chemical Research* **2016**, *49*, 2261.

[164] D. W. Thompson, A. Ito, T. J. Meyer, *Pure and Applied Chemistry* **2013**, *85*, 1257.
[165] M. A. Ischay, M. E. Anzovino, J. Du, T. P. Yoon, *Journal of the American Chemical Society* **2008**, *130*, 12886.
[166] B. Sahoo, M. N. Hopkinson, F. Glorius, *Journal of the American Chemical Society* **2013**, *135*, 5505.
[167] A. Hauser, N. Amstutz, S. Delahaye, A. Sadki, S. Schenker, R. Sieber, M. Zerara in *Optical Spectra and Chemical Bonding in Inorganic Compounds: Special Volume dedicated to Professor Jørgensen I* (Eds.: D. M. P. Mingos, T. Schönherr), Springer Berlin Heidelberg, Berlin, Heidelberg, **2004**, pp. 81–96.
[168] a) I. Krivokapic, M. Zerara, M. L. Daku, A. Vargas, C. Enachescu, C. Ambrus, P. Tregenna-Piggott, N. Amstutz, E. Krausz, A. Hauser, *Coordination Chemistry Reviews* **2007**, *251*, 364; b) H. A. Goodwin in *Topics in Current Chemistry* (Eds.: P. Gütlich, H. A. Goodwin), Springer Berlin Heidelberg, Berlin, Heidelberg, **2004**, pp. 23–47.
[169] T. Nishinaga, *Organic Redox Systems*. *Synthesis, Properties, and Applications*, John Wiley & Sons, New York, NY, **2016**.
[170] C. E. Schäffer in *Structure and Bonding*, Springer Berlin Heidelberg, Berlin, Heidelberg, **1968**, pp. 68–95.
[171] E. Cremades, J. Echeverría, S. Alvarez, *Chem. Eur. J.* **2010**, *16*, 10380.
[172] L. Falivene, Z. Cao, A. Petta, L. Serra, A. Poater, R. Oliva, V. Scarano, L. Cavallo, *Nature Chemistry* **2019**, *11*, 872.
[173] R. D. Shannon, *Acta Cryst A* **1976**, *32*, 751.
[174] M. Valigi, D. Gazzoli, *Zeitschrift für Physikalische Chemie* **1981**, *125*, 89.
[175] D. G. Gorenstein, *Progress in Nuclear Magnetic Resonance Spectroscopy* **1984**, *16*, 1.
[176] O. Kühl, *Phosphoros-31 NMR spectroscopy*. *A concise introduction for the synthetic organic and organometallic chemist*, Springer, Berlin, Heidelberg, **2008**.
[177] a) V. A. Blatov, A. P. Shevchenko, D. M. Proserpio, *Crystal Growth & Design* **2014**, *14*, 3576; b) J. K. Burdett, R. Hoffmann, R. C. Fay, *Inorganic Chemistry* **1978**, *17*, 2553.
[178] R. Hoffmann, B. F. Beier, E. L. Muetterties, A. R. Rossi, *Inorganic Chemistry* **1977**, *16*, 511.
[179] V. Y. Buško, I. V. Sukhno, M. B. Buzko, A. Polushin, V. T. Panyushkin, *Russian Journal of Inorganic Chemistry* **2008**, *53*, 1249.
[180] F. Renaud, C. Piguet, G. Bernardinelli, J.-C. G. Bünzli, G. Hopfgartner, *Journal of the American Chemical Society* **1999**, *121*, 9326.
[181] S. Serron, J. Huang, S. P. Nolan, *Organometallics* **1998**, *17*, 534.
[182] Z. L. Niemeyer, A. Milo, D. P. Hickey, M. S. Sigman, *Nature Chemistry* **2016**, *8*, 610.
[183] M. L. Kelty, A. J. McNeece, J. W. Kurutz, A. S. Filatov, J. S. Anderson, *Chemical Science* **2022**.
[184] S. R. Alvarado, I. A. Shortt, H.-J. Fan, J. Vela, *Organometallics* **2015**, *34*, 4023.
[185] a) H. Y. Liu, K. Eriks, A. Prock, W. P. Giering, *Organometallics* **1990**, *9*, 1758; b) T. Allman, R. G. Goel, *Canadian Journal of Chemistry* **1982**, *60*, 716.
[186] Z. Domínguez, J. Hernández, L. Silva-Gutiérrez, M. Salas-Reyes, M. Sánchez, G. Merino, *Phosphorus, Sulfur, and Silicon and the Related Elements* **2010**, *185*, 772.
[187] P. Serp, M. Hernandez, B. Richard, P. Kalck, *Eur. J. Inorg. Chem.* **2001**, *2001*, 2327.
[188] B. J. Dunne, R. B. Morris, A. G. Orpen, *Journal of the Chemical Society, Dalton Transactions* **1991**, 653.
[189] K. Sprenger, C. Golz, M. Alcarazo, *Eur. J. Org. Chem.* **2020**, *2020*, 6245.
[190] G. Mehler, P. Linowski, J. Carreras, A. Zanardi, J. W. Dube, M. Alcarazo, *Chem. Eur. J.* **2016**, *22*, 15320.
[191] D. Zhu, X. Cao, B. Yu, *Organic Chemistry Frontiers* **2015**, *2*, 360.

[192] T. Hartung, R. Machleid, M. Simon, C. Golz, M. Alcarazo, *Angewandte Chemie International Edition* **2020**, *59*, 5660.
[193] S. Kolle, *Tuning the donor properties of phosphines by metal encapsulation. Application in the synthesis of phenanthrenes*. Bachelor's thesis, Georg-August Universität Göttingen, Göttingen, **2019**.
[194] D. Wang, R. Cai, S. Sharma, J. Jirak, S. K. Thummanapelli, N. G. Akhmedov, H. Zhang, X. Liu, J. L. Petersen, X. Shi, *Journal of the American Chemical Society* **2012**, *134*, 9012.
[195] N. Mézailles, L. Ricard, F. Gagosz, *Organic Letters* **2005**, *7*, 4133.
[196] J. H. Teles, S. Brode, M. Chabanas, *Angewandte Chemie International Edition* **1998**, *37*, 1415.
[197] A. Guérinot, W. Fang, M. Sircoglou, C. Bour, S. Bezzenine-Lafollée, V. Gandon, *Angewandte Chemie International Edition* **2013**, *52*, 5848.
[198] J. Schießl, P. M. Stein, J. Stirn, K. Emler, M. Rudolph, F. Rominger, A. S. K. Hashmi, *Adv. Synth. Catal.* **2019**, *361*, 725.
[199] D. Belli Dell' Amico, D. Fioco, L. Labella, F. Marchetti, S. Samaritani, *Polyhedron* **2018**, *145*, 63.
[200] S. J. Pastine, S. W. Youn, D. Sames, *Organic Letters* **2003**, *5*, 1055.
[201] H. Tinnermann, *Design, Synthesis and Applications of new cationic ligands of the 15th main group elements*, Georg-August Universität Göttingen, Göttingen, **2017**.
[202] Nicewicz David A., MacMillan David W. C., *Science* **2008**, *322*, 77.
[203] J. M. R. Narayanam, J. W. Tucker, C. R. J. Stephenson, *Journal of the American Chemical Society* **2009**, *131*, 8756.
[204] C. K. Prier, D. A. Rankic, D. W. C. MacMillan, *Chemical Reviews* **2013**, *113*, 5322.
[205] M. C. Maust, C. M. Hendy, N. T. Jui, S. B. Blakey, *Journal of the American Chemical Society* **2022**, *144*, 3776.
[206] C. M. Hendy, G. C. Smith, Z. Xu, T. Lian, N. T. Jui, *Journal of the American Chemical Society* **2021**, *143*, 8987.
[207] E. Speckmeier, T. G. Fischer, K. Zeitler, *Journal of the American Chemical Society* **2018**, *140*, 15353.
[208] P.-Z. Wang, J.-R. Chen, W.-J. Xiao, *Organic & Biomolecular Chemistry* **2019**, *17*, 6936.
[209] B. P. Roberts, *Chemical Society Reviews* **1999**, *28*, 25.
[210] A. G. Condie, J. C. González-Gómez, C. R. J. Stephenson, *Journal of the American Chemical Society* **2010**, *132*, 1464.
[211] a) J. D. Bell, J. A. Murphy, *Chemical Society Reviews* **2021**, *50*, 9540; b) Q. Yang, L. Zhang, C. Ye, S. Luo, L.-Z. Wu, C.-H. Tung, *Angewandte Chemie International Edition* **2017**, *56*, 3694.
[212] D. B. Freeman, L. Furst, A. G. Condie, C. R. J. Stephenson, *Organic Letters* **2012**, *14*, 94.
[213] O. Baslé, N. Borduas, P. Dubois, J. M. Chapuzet, T.-H. Chan, J. Lessard, C.-J. Li, *Chem. Eur. J.* **2010**, *16*, 8162.
[214] H. Cano-Yelo, A. Deronzier, *Journal of the Chemical Society, Perkin Transactions 2* **1984**, 1093.
[215] H. Cano-Yelo, A. Deronzier, *Journal of Photochemistry* **1987**, *37*, 315.
[216] F. Strieth-Kalthoff, F. Glorius, *Chem* **2020**, *6*, 1888.
[217] F. Strieth-Kalthoff, M. J. James, M. Teders, L. Pitzer, F. Glorius, *Chemical Society Reviews* **2018**, *47*, 7190.
[218] M. Zhu, C. Zheng, X. Zhang, S.-L. You, *Journal of the American Chemical Society* **2019**, *141*, 2636.
[219] S. I. Kozhushkov, M. Alcarazo, *Eur. J. Inorg. Chem.* **2020**, *2020*, 2486.
[220] R. Li, N. Barel, V. Subramaniyan, O. Cohen, F. Tibika, Y. Tulchinsky, *Chemical Science* **2022**, *13*, 4770.
[221] R. Oost, J. D. Neuhaus, J. Merad, N. Maulide in *Modern Ylide Chemistry: Applications in Ligand Design, Organic and Catalytic Transformations* (Ed.: V. H. Gessner), Springer International Publishing, Cham, **2018**, pp. 73–115.

[222] K. Kafuta, A. Korzun, M. Böhm, C. Golz, M. Alcarazo, *Angewandte Chemie International Edition* **2020**, *59*, 1950.

[223] a) P. S. Engl, A. P. Häring, F. Berger, G. Berger, A. Pérez-Bitrián, T. Ritter, *Journal of the American Chemical Society* **2019**, *141*, 13346; b) M. H. Aukland, F. J. T. Talbot, J. A. Fernández-Salas, M. Ball, A. P. Pulis, D. J. Procter, *Angewandte Chemie International Edition* **2018**, *57*, 9785.

[224] a) J.-N. Zhao, M. Kayumov, D.-Y. Wang, A. Zhang, *Organic Letters* **2019**, *21*, 7303; b) L. Mu, C. R. Fischer, J. P. Holland, J. Becaud, P. A. Schubiger, R. Schibli, S. M. Ametamey, K. Graham, T. Stellfeld, L. M. Dinkelborg et al., *Eur. J. Org. Chem.* **2012**, *2012*, 889.

[225] U. Teruo, I. Sumi, *Tetrahedron Letters* **1990**, *31*, 3579.

[226] J.-A. Ma, D. Cahard, *The Journal of Organic Chemistry* **2003**, *68*, 8726.

[227] a) Y. Macé, C. Pradet, M. Popkin, J.-C. Blazejewski, E. Magnier, *Tetrahedron Letters* **2010**, *51*, 5388; b) Y. Macé, E. Magnier, *Eur. J. Org. Chem.* **2012**, *2012*, 2479.

[228] T. Koike, M. Akita, *Accounts of Chemical Research* **2016**, *49*, 1937.

[229] Y. Yasu, T. Koike, M. Akita, *Angewandte Chemie International Edition* **2012**, *51*, 9567.

[230] D. M. Hedstrand, W. H. Kruizinga, R. M. Kellogg, *Tetrahedron Letters* **1978**, *19*, 1255.

[231] T. J. van Bergen, D. M. Hedstrand, W. H. Kruizinga, R. M. Kellogg, *The Journal of Organic Chemistry* **1979**, *44*, 4953.

[232] P. Xu, Da Zhao, F. Berger, A. Hamad, J. Rickmeier, R. Petzold, M. Kondratiuk, K. Bohdan, T. Ritter, *Angewandte Chemie International Edition* **2020**, *59*, 1956.

[233] M. H. Aukland, M. Šiaučiulis, A. West, G. J. P. Perry, D. J. Procter, *Nature Catalysis* **2020**, *3*, 163.

[234] R. J. DeVoe, P. M. Olofson, M. R. V. Sahyun, *Photochemistry and Photophysics of 'Onium Salts*, **1992**.

[235] a) R. Sang, S. E. Korkis, W. Su, F. Ye, P. S. Engl, F. Berger, T. Ritter, *Angewandte Chemie International Edition* **2019**, *58*, 16161; b) F. Ye, F. Berger, H. Jia, J. Ford, A. Wortman, J. Börgel, C. Genicot, T. Ritter, *Angewandte Chemie International Edition* **2019**, *58*, 14615; c) C. Huang, J. Feng, R. Ma, S. Fang, T. Lu, W. Tang, D. Du, J. Gao, *Organic Letters* **2019**, *21*, 9688.

[236] J. W. Knapczyk, W. E. McEwen, *Journal of the American Chemical Society* **1969**, *91*, 145.

[237] J. V. Crivello, J. H. W. Lam, *The Journal of Organic Chemistry* **1978**, *43*, 3055.

[238] K. K. Andersen, N. E. Papanikolaou, *Tetrahedron Letters* **1966**, *7*, 5445.

[239] R. D. Miller, A. F. Renaldo, H. Ito, *The Journal of Organic Chemistry* **1988**, *53*, 5571.

[240] S. Imazeki, M. Sumino, K. Fukasawa, M. Ishihara, T. Akiyama, *Synthesis* **2004**, *2004*, 1648.

[241] C. A. Ramsden (Ed.) *Science of Synthesis: Houben-Weyl Methods of Molecular Transformations Vol. 31a*, Georg Thieme Verlag, Stuttgart, **2007**.

[242] S. Karreman, S. B. H. Karnbrock, S. Kolle, C. Golz, M. Alcarazo, *Organic Letters* **2021**, *23*, 1991.

[243] F. Berger, M. B. Plutschack, J. Riegger, W. Yu, S. Speicher, M. Ho, N. Frank, T. Ritter, *Nature* **2019**, *567*, 223.

[244] S. Donck, A. Baroudi, L. Fensterbank, J.-P. Goddard, C. Ollivier, *Adv. Synth. Catal.* **2013**, *355*, 1477.

[245] S. E. Braslavsky, *Pure and Applied Chemistry* **2007**, *79*, 293.

[246] D. H. Hey, C. W. Rees, A. R. Todd, *Journal of the Chemical Society C: Organic* **1967**, 1518.

[247] a) D. H. Hey, G. H. Jones, M. J. Perkins, *Journal of the Chemical Society, Perkin Transactions 1* **1972**, 1150; b) D. H. Hey, G. H. Jones, M. J. Perkins, *Journal of the Chemical Society C: Organic* **1971**, 116.

[248] D. C. Harrowven, M. I. Nunn, N. A. Newman, D. R. Fenwick, *Tetrahedron Letters* **2001**, *42*, 961.

[249] A. M. Rosa, A. M. Lobo, P. S. Branco, P. Sundaresan, *Tetrahedron* **1997**, *53*, 285.

[250] W. R. Bowman, E. Mann, J. Parr, *Journal of the Chemical Society, Perkin Transactions 1* **2000**, 2991.

[251] H. Ohno, H. Iwasaki, T. Eguchi, T. Tanaka, *Chemical Communications* **2004**, 2228.

[252] D. S. Roman, Y. Takahashi, A. B. Charette, *Organic Letters* **2011**, *13*, 3242.
[253] I. Fleming, *Frontier orbitals and organic chemical reactions*, Wiley, Chichester [u.a.], **1978**.
[254] A. Studer, M. Bossart, *Tetrahedron* **2001**, *57*, 9649.
[255] Q. Deng, L. Tan, Y. Xu, P. Liu, P. Sun, *The Journal of Organic Chemistry* **2018**, *83*, 6151.
[256] A. R. Flynn, K. A. McDaniel, M. E. Hughes, D. B. Vogt, N. T. Jui, *Journal of the American Chemical Society* **2020**, *142*, 9163.
[257] a) B. Galmés, A. Juan-Bals, A. Frontera, G. Resnati, *Chem. Eur. J.* **2020**, *26*, 4599; b) P. Politzer, J. S. Murray, T. Clark, *Physical Chemistry Chemical Physics* **2013**, *15*, 11178.
[258] P. Beak, T. A. Sullivan, *Journal of the American Chemical Society* **1982**, *104*, 4450.
[259] S. Takayasu, T. Suzuki, K. Shinozaki, *The Journal of Physical Chemistry B* **2013**, *117*, 9449.
[260] F. A. Neugebauer, S. Bamberger, *Chem. Ber.* **1974**, *107*, 2362.
[261] J. B. Gerken, S. S. Stahl, *ACS Central Science* **2015**, *1*, 234.
[262] M. A. Cismesia, T. P. Yoon, *Chemical Science* **2015**, *6*, 5426.
[263] J. Li, J. Chen, R. Sang, W.-S. Ham, M. B. Plutschack, F. Berger, S. Chabbra, A. Schnegg, C. Genicot, T. Ritter, *Nature Chemistry* **2020**, *12*, 56.
[264] G. Bringmann, B. Schöner, K. Peters, E.-M. Peters, H. G. von Schnering, *Liebigs Ann. Chem.* **1994**, *1994*, 439.
[265] Y. Li, H. Wang, X. Li, *Chemical Science* **2020**, *11*, 12249.
[266] R. Núñez-Franco, G. Jiménez-Osés, J. Jiménez-Barbero, F. Cabrera-Escribano, A. Franconetti, *Physical Chemistry Chemical Physics* **2022**, *24*, 1965.
[267] G. M. Sheldrick, *Acta crystallographica. Section A, Foundations of crystallography* **2008**, *64*, 112.
[268] O. V. Dolomanov, L. J. Bourhis, R. J. Gildea, J. A. K. Howard, H. Puschmann, *J Appl Crystallogr* **2009**, *42*, 339.
[269] T. Kottke, D. Stalke, *J Appl Crystallogr* **1993**, *26*, 615.
[270] M. Kalek, M. Jezowska, J. Stawinski, *Adv. Synth. Catal.* **2009**, *351*, 3207.
[271] R. García-Rodríguez, H. Liu, *Journal of the American Chemical Society* **2012**, *134*, 1400.
[272] Y. Yang, L. Eberle, F. F. Mulks, J. F. Wunsch, M. Zimmer, F. Rominger, M. Rudolph, A. S. K. Hashmi, *Journal of the American Chemical Society* **2019**, *141*, 17414.
[273] H. A. Muathen, N. A. M. Aloweiny, A. H. M. Elwahy, *J. Heterocyclic Chem.* **2009**, *46*, 656.
[274] R. J. Mayer, M. Breugst, N. Hampel, A. R. Ofial, H. Mayr, *The Journal of Organic Chemistry* **2019**, *84*, 8837.
[275] Y. Lin, M. Cai, Z. Fang, H. Zhao, *RSC Advances* **2016**, *6*, 85186.
[276] T. Yoshinaga, T. Iwata, M. Shindo, *Chemistry Letters* **2020**, *49*, 191.
[277] C. Sedano, R. Velasco, C. Feberero, S. Suárez-Pantiga, R. Sanz, *Organic Letters* **2020**, *22*, 6365.
[278] K. Debbabi, M. Beji, A. Baklouti, *Phosphorus, Sulfur, and Silicon and the Related Elements* **2005**, *180*, 1545.
[279] D. de Zani, M. Colombo, *Journal of Flow Chemistry* **2012**, *2*, 5.
[280] Z. Tang, J. Mayrargue, M. Alami, *Synthetic Communications* **2007**, *37*, 3367.
[281] D. E. Thorne, K. Engel, US4053607 (A), **1975**.
[282] D. W. Manley, J. C. Walton, *Organic Letters* **2014**, *16*, 5394.
[283] K. M. Vailonis, K. Gnanasekaran, X. B. Powers, N. C. Gianneschi, D. M. Jenkins, *Journal of the American Chemical Society* **2019**, *141*, 10177.
[284] A. Taladriz, A. Healy, E. J. Flores Pérez, V. Herrero García, C. Ríos Martínez, A. A. M. Alkhaldi, A. A. Eze, M. Kaiser, H. P. de Koning, A. Chana et al., *Journal of Medicinal Chemistry* **2012**, *55*, 2606.
[285] J.-Y. He, Q.-F. Bai, C. Jin, G. Feng, *Synlett* **2018**, *29*, 2311.
[286] J. R. Lakowicz, *Principles of fluorescence spectroscopy*, Springer, New York, NY, **2006**.

[287] C. G. Hatchard, C. A. Parker, E. J. Bowen, *Proceedings of the Royal Society of London. Series A. Mathematical and Physical Sciences* **1956**, *235*, 518.

9 Appendix

9.1 NMR Spectra

Compound **184**

^{1}H NMR (400 MHz, $CDCl_3$)

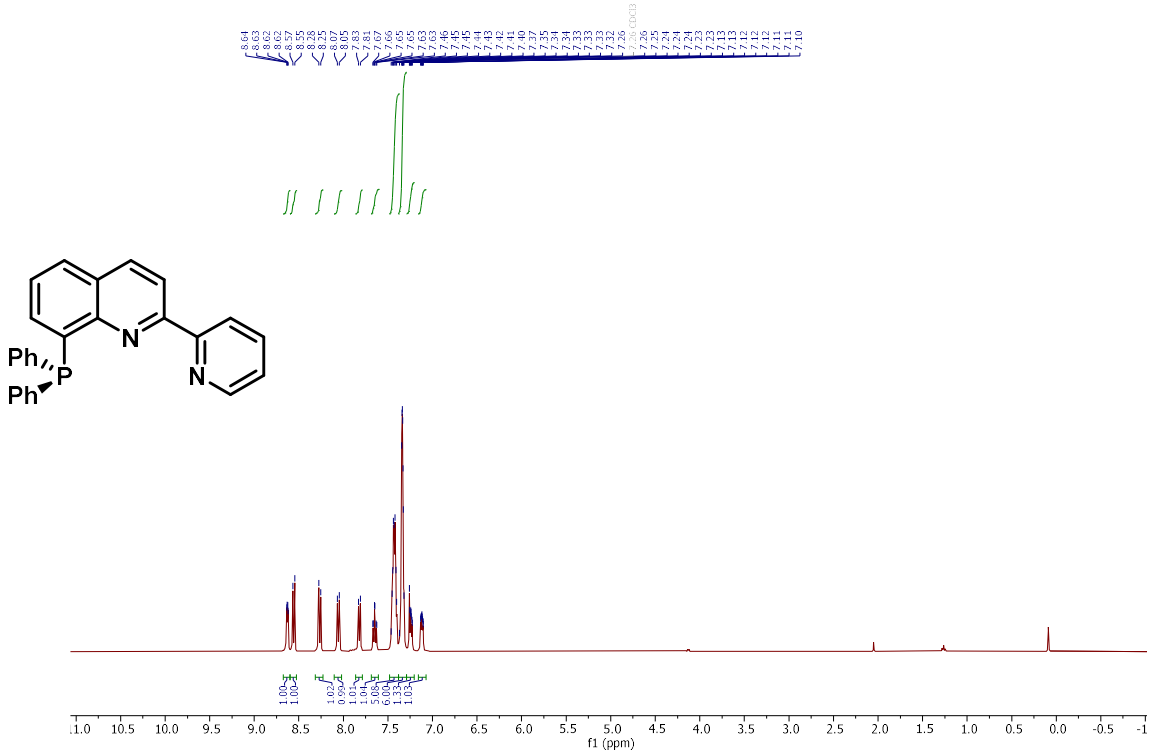

^{1}H NMR (300 MHz, $CDCl_3$)

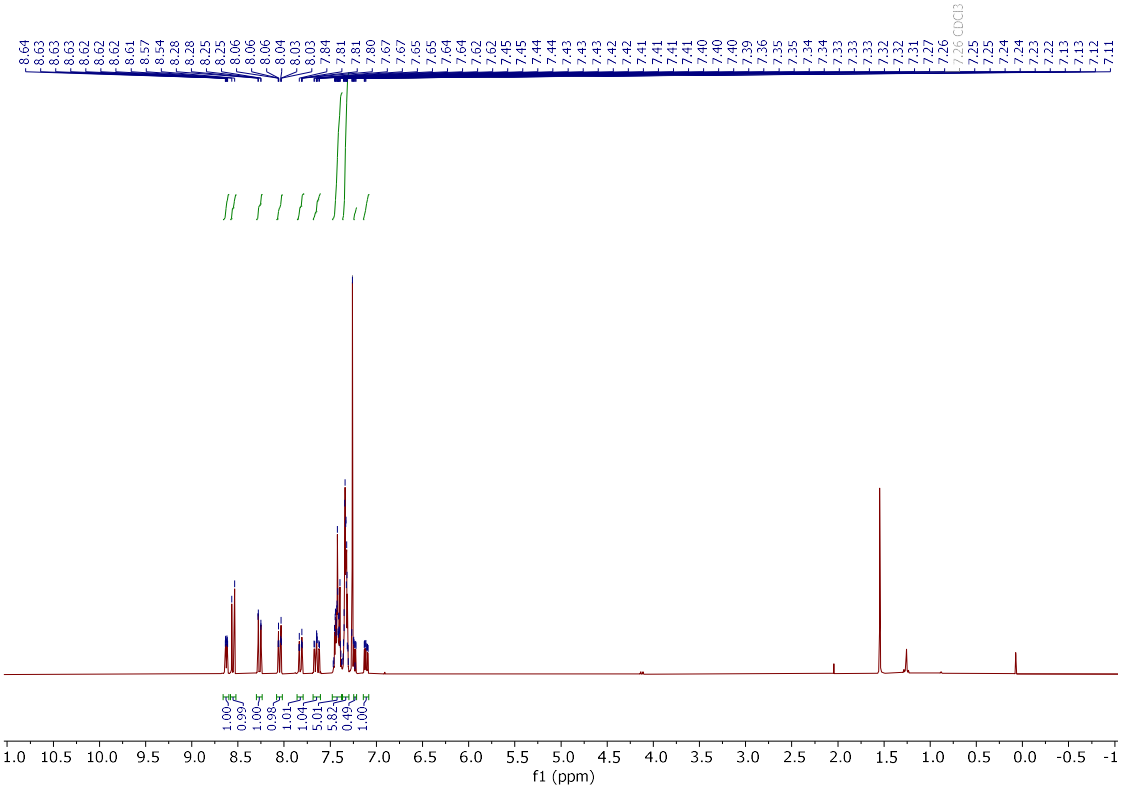

$^{13}C\{H\}$ NMR (101 MHz, $CDCl_3$)

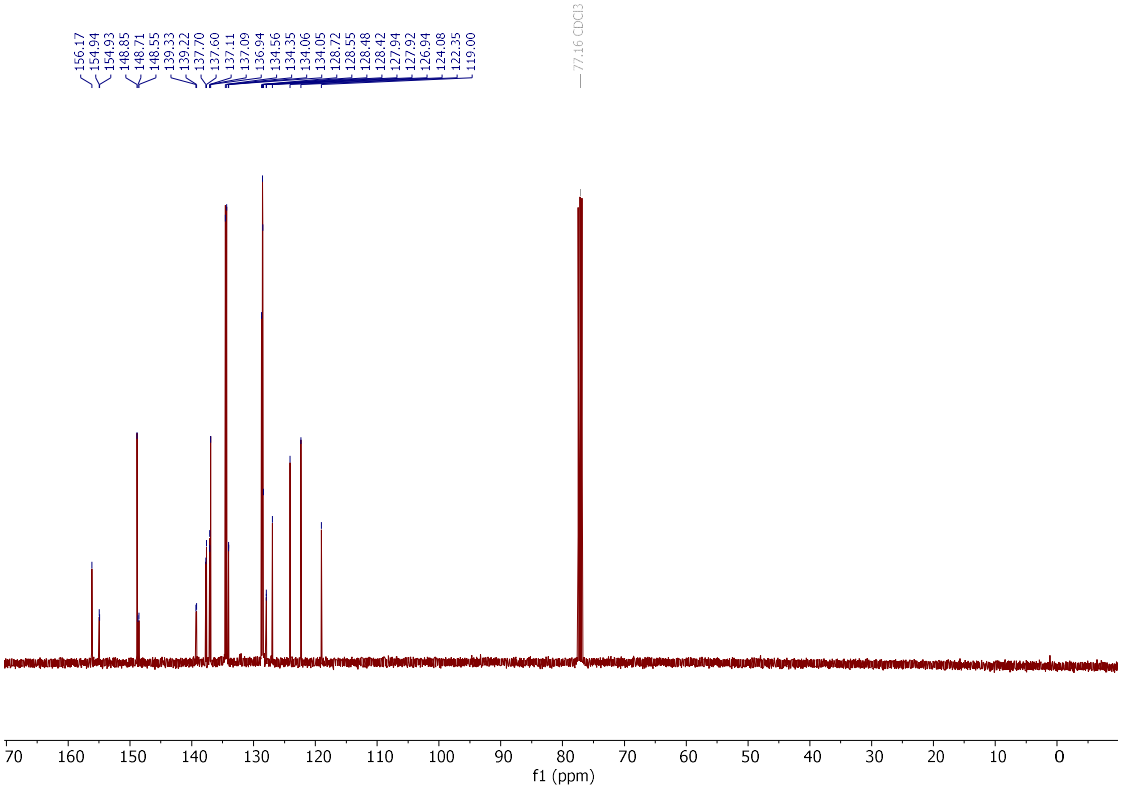

$^{31}P\{H\}$ NMR (121 MHz, $CDCl_3$)

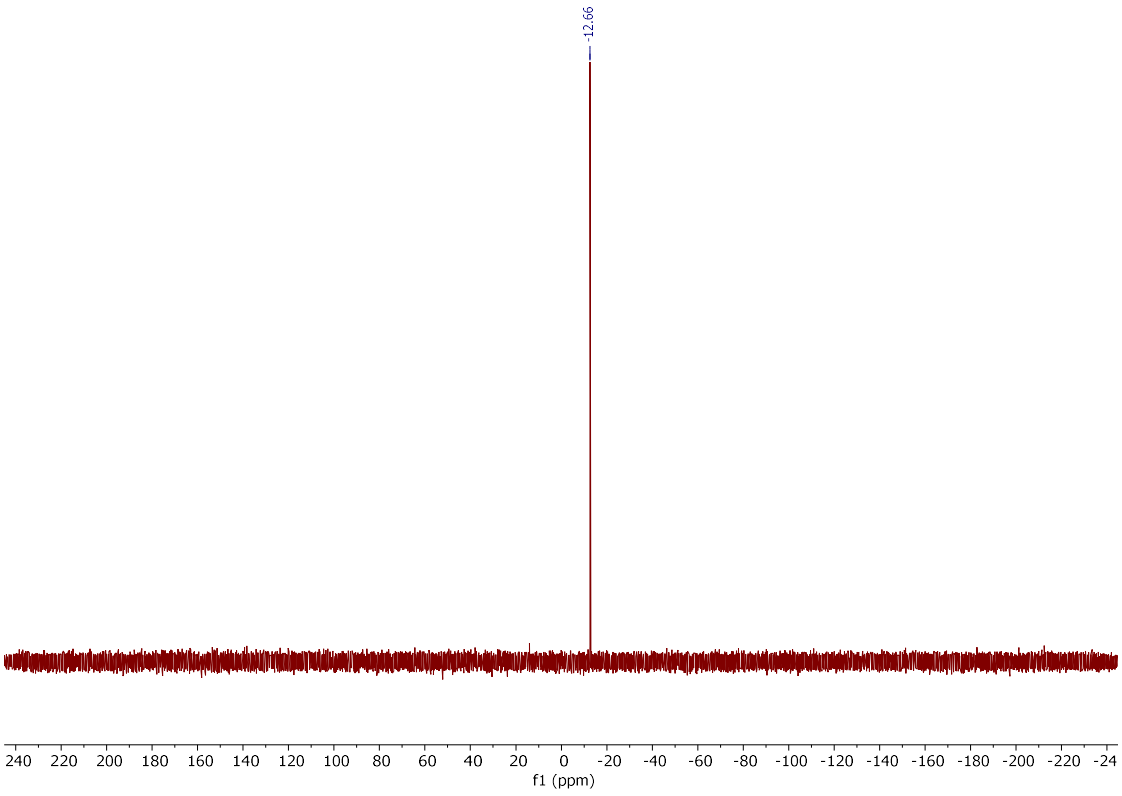

Compound **200**

^{1}H NMR (300 MHz, $CDCl_3$)

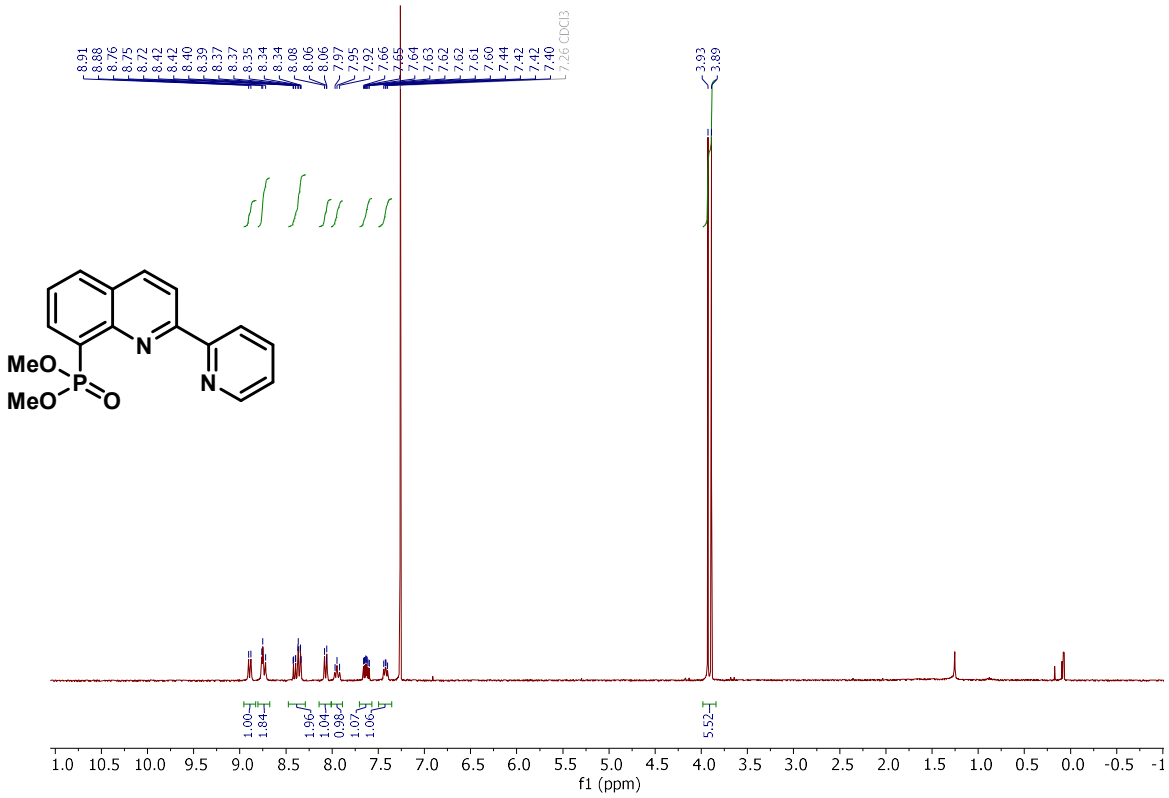

^{13}C{H} NMR (75 MHz, $CDCl_3$)

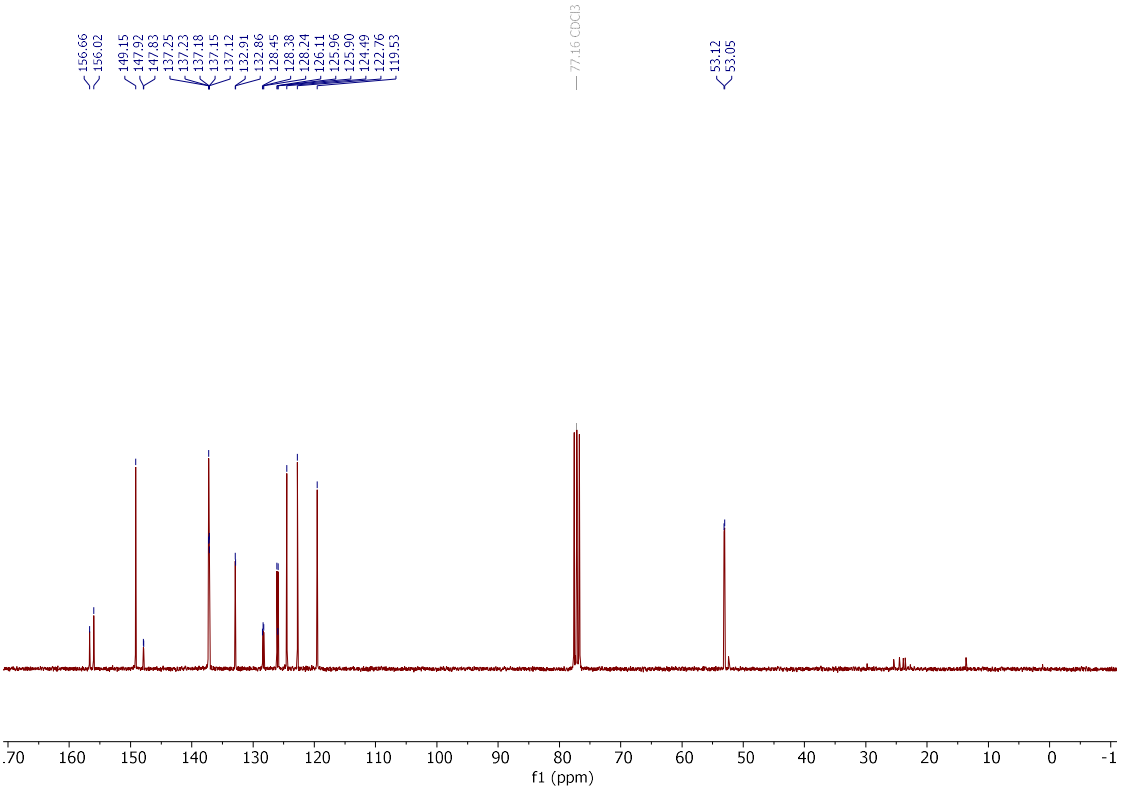

$^{31}P\{H\}$ NMR (121 MHz, $CDCl_3$)

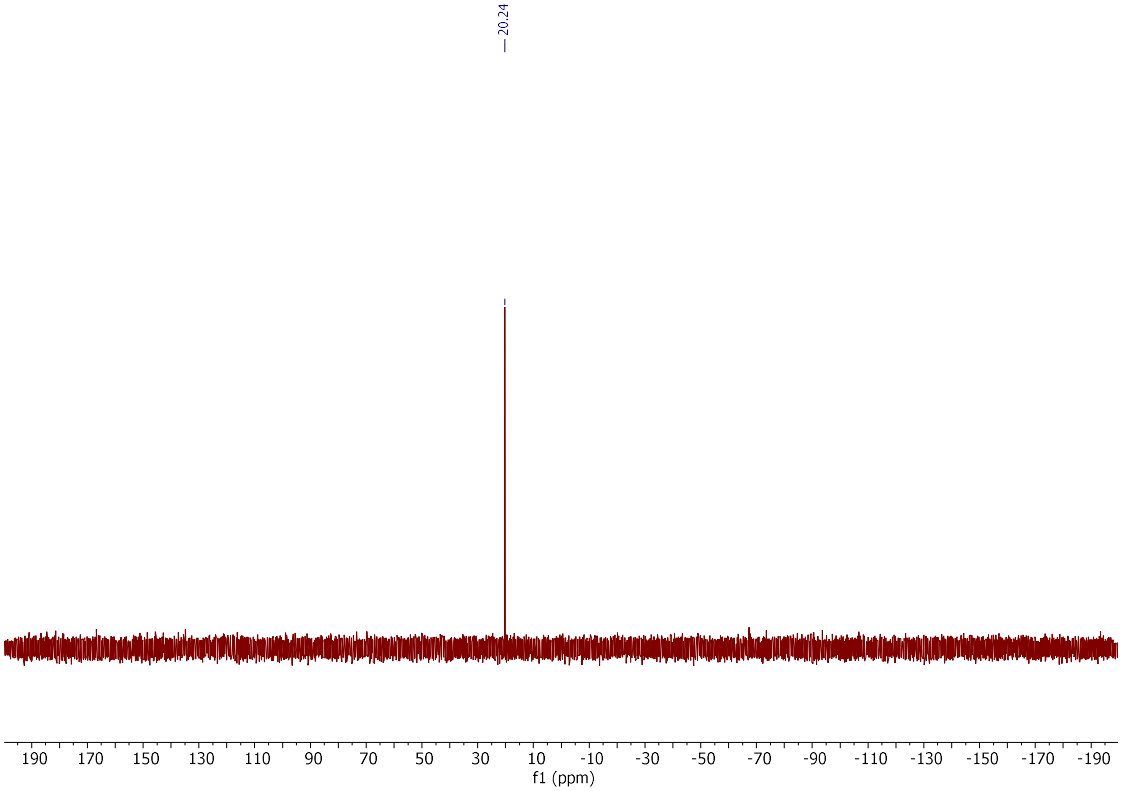

Compound **203**

^{1}H NMR (300 MHz, $CDCl_3$)

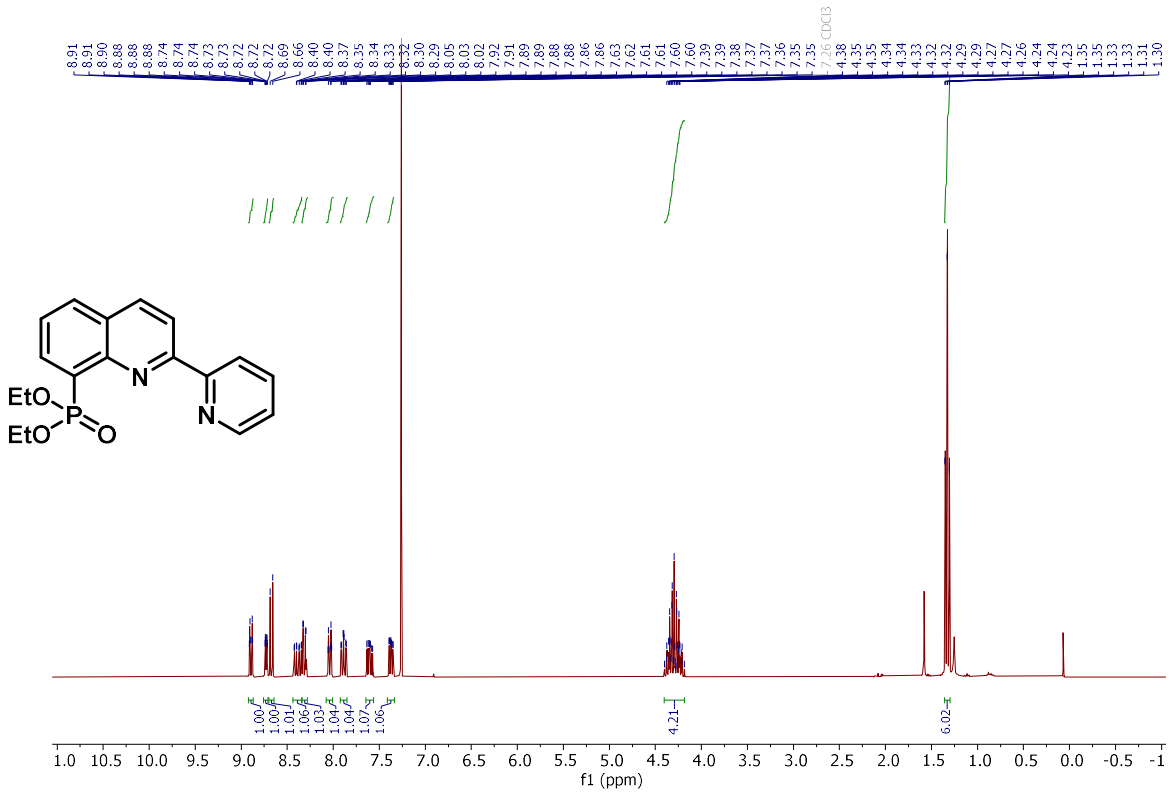

^{13}C{H} NMR (75 MHz, $CDCl_3$)

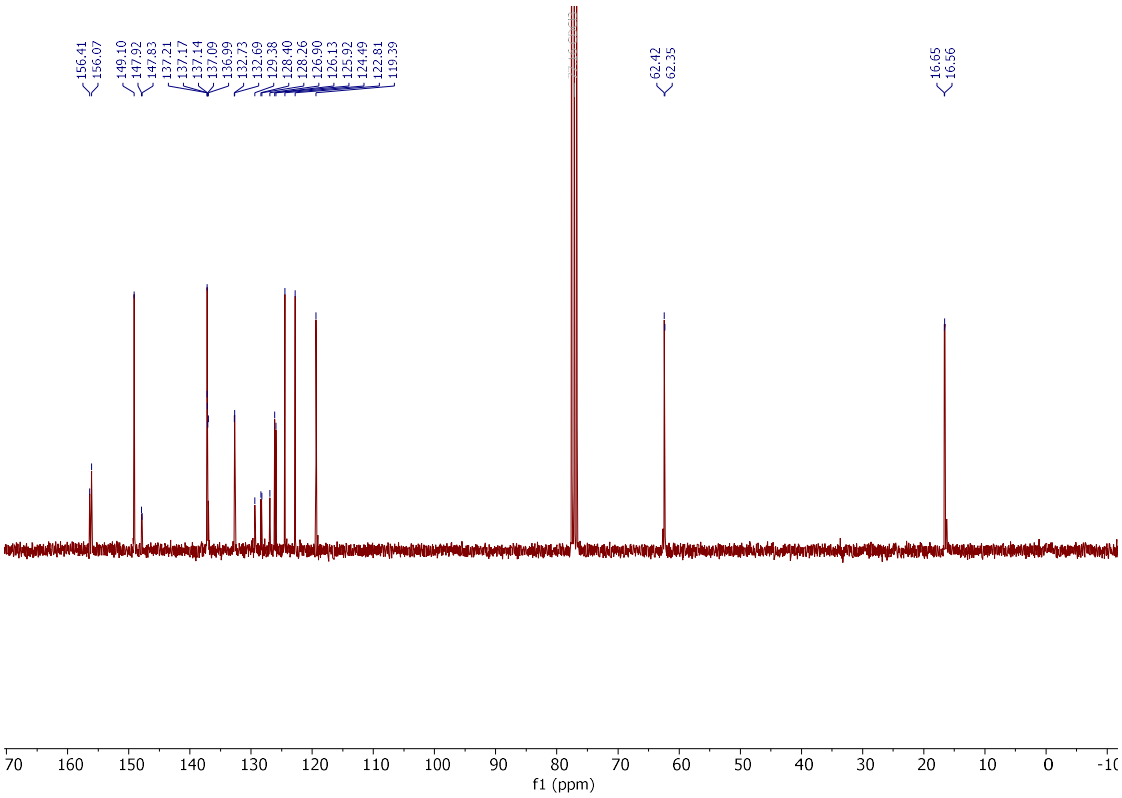

$^{31}P\{H\}$ NMR (121 MHz, $CDCl_3$)

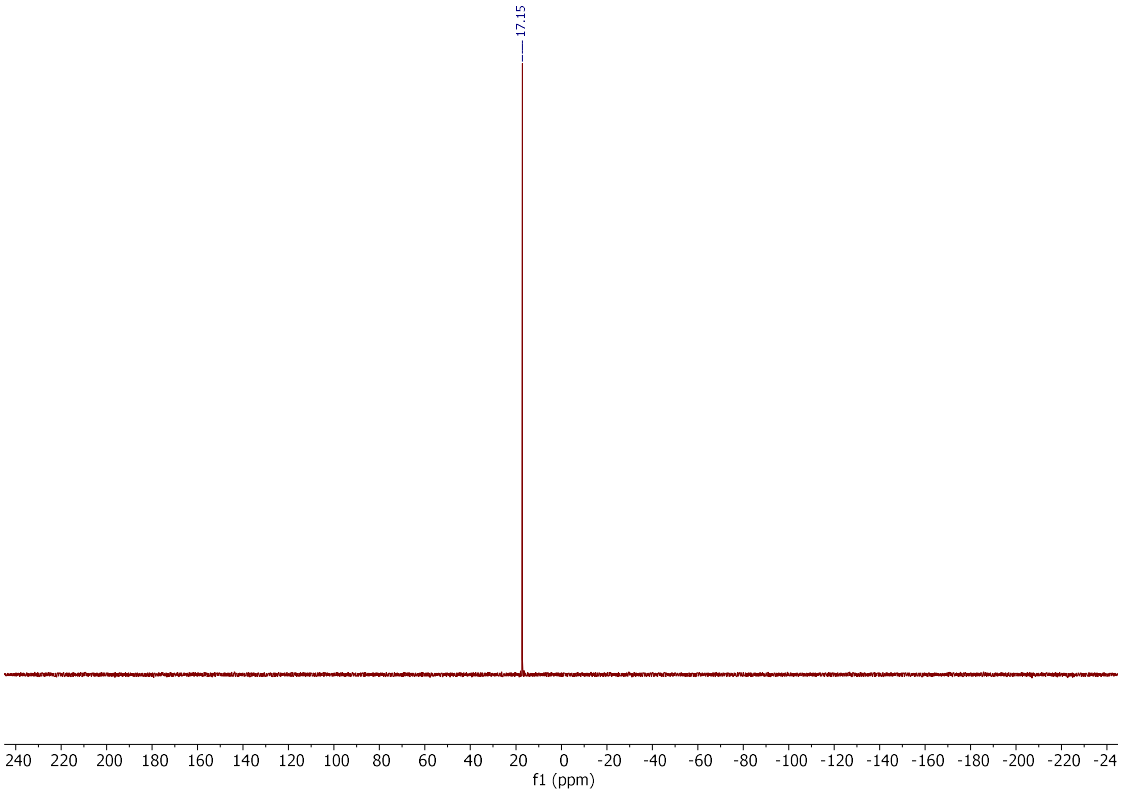

Compound **204**

^{1}H NMR (400 MHz, $CDCl_3$)

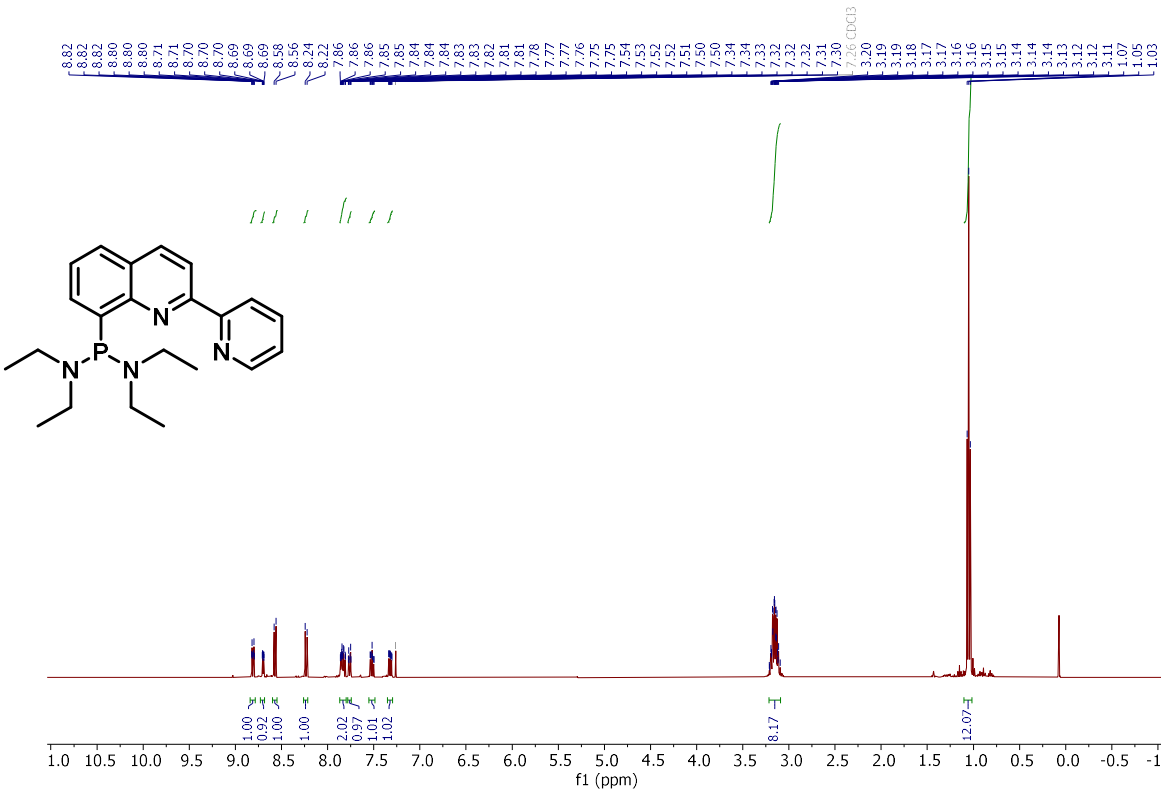

^{13}C{H} NMR (101 MHz, $CDCl_3$)

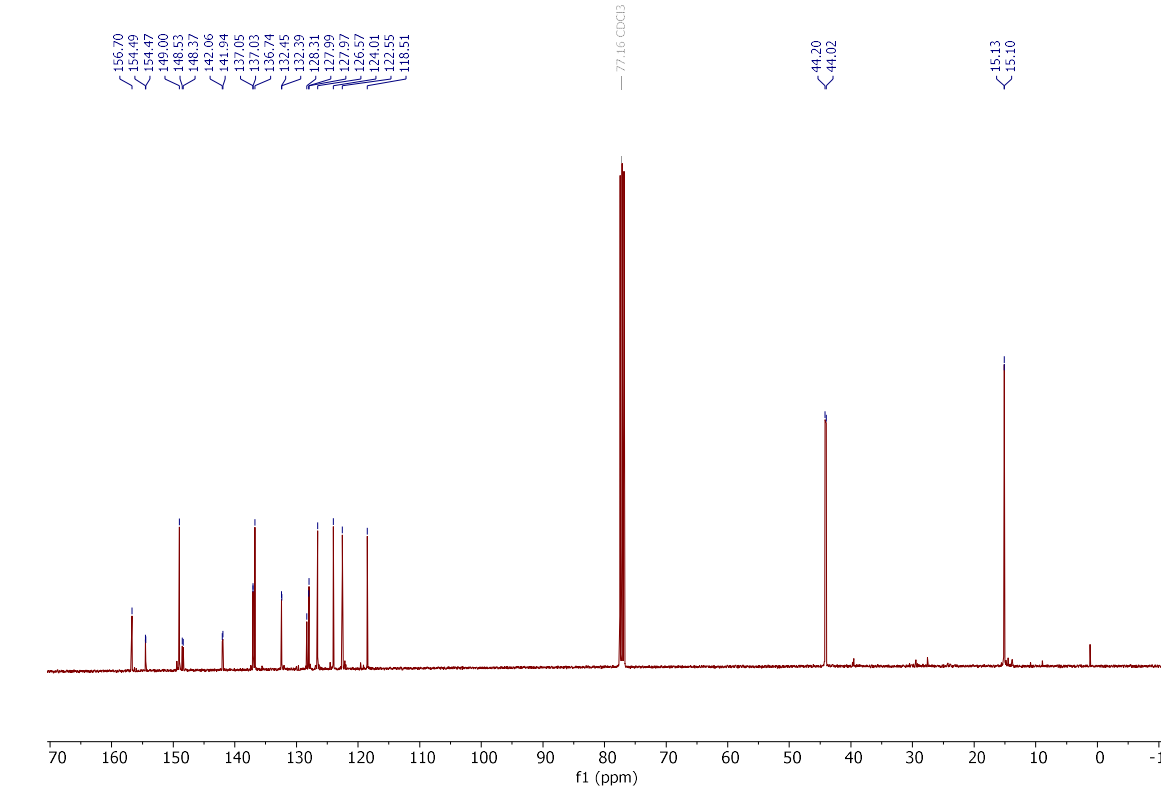

$^{31}P\{H\}$ NMR (162 MHz, $CDCl_3$)

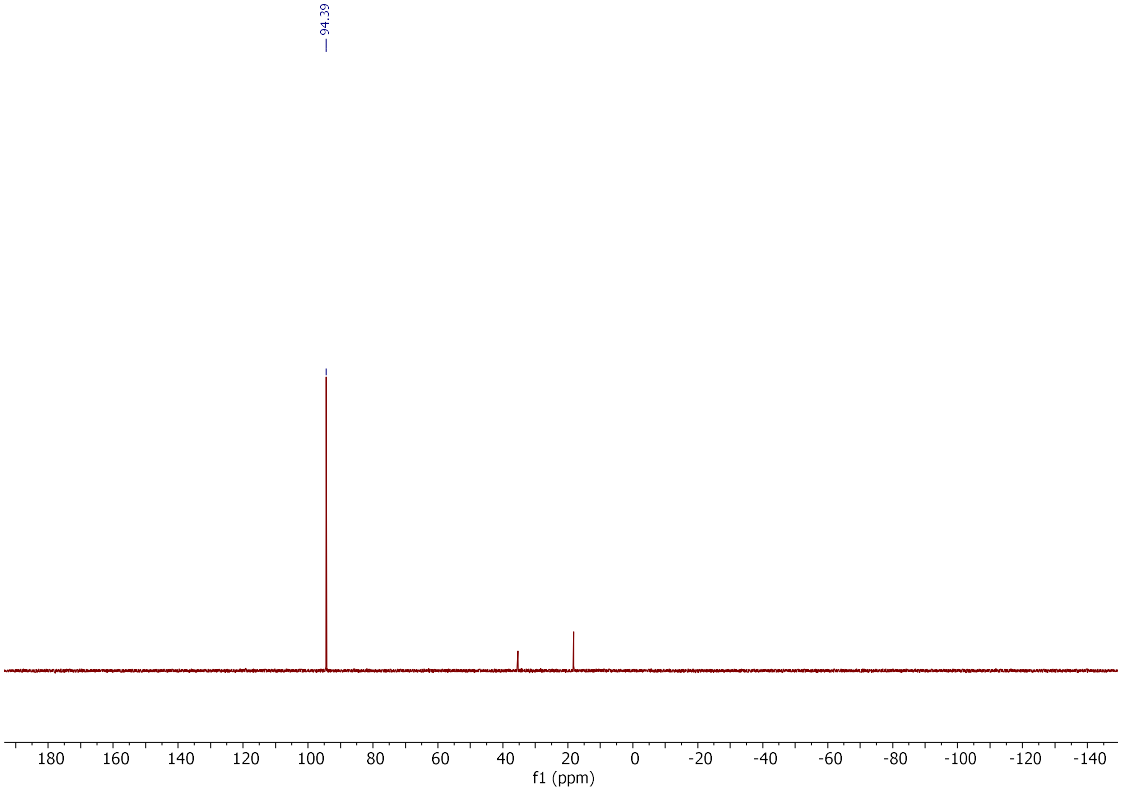

Compound **205**

^{1}H NMR (400 MHz, $CDCl_3$)

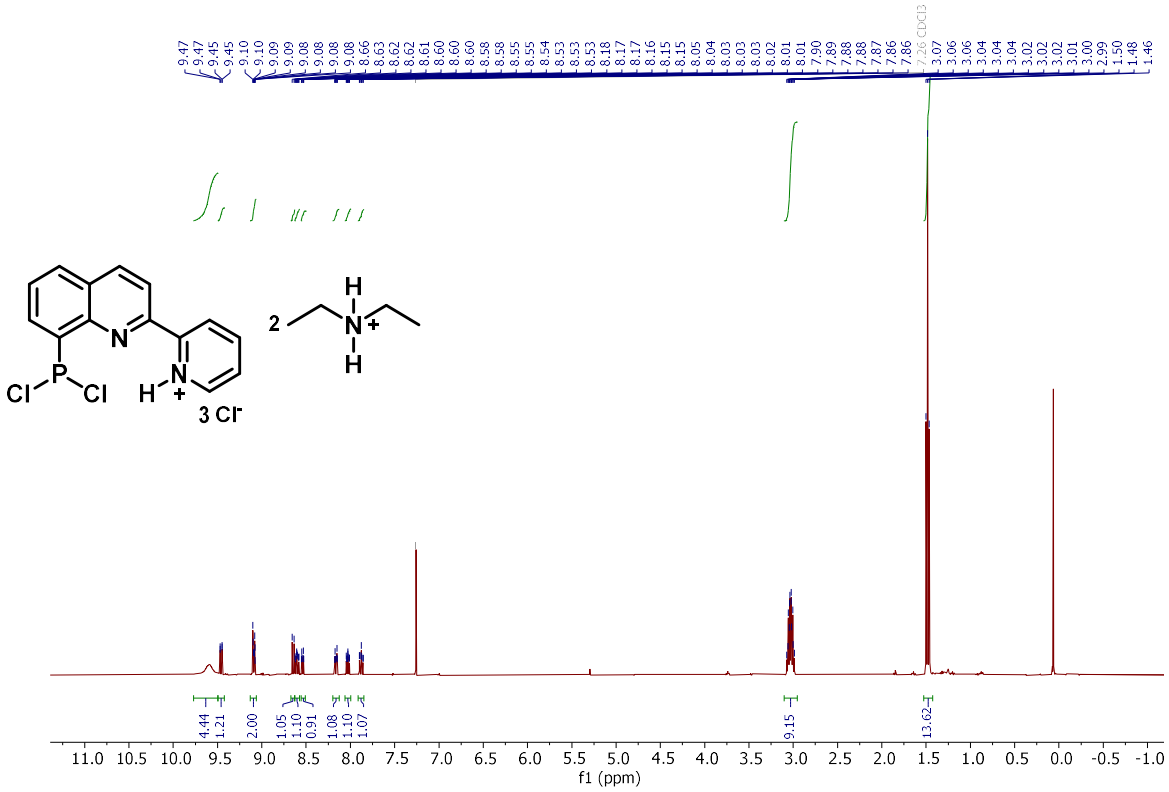

^{13}C{H} NMR (101 MHz, $CDCl_3$)

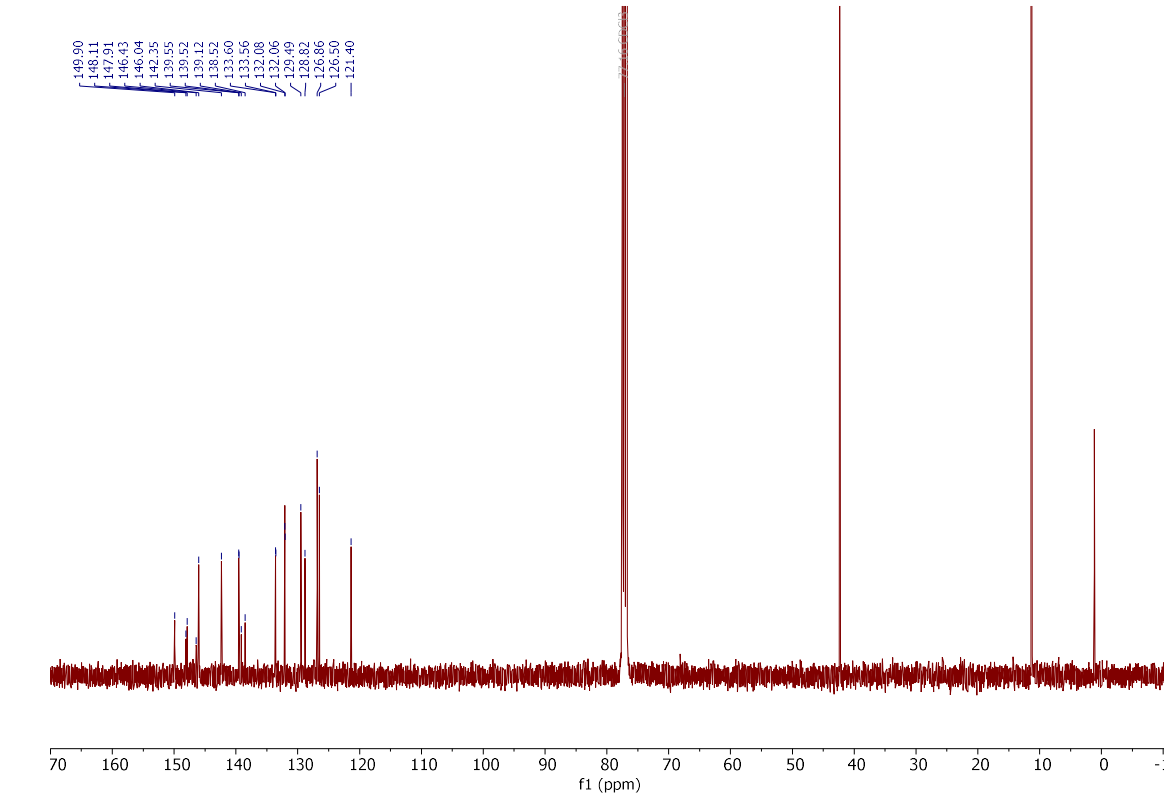

$^{31}P\{H\}$ NMR (162 MHz, $CDCl_3$)

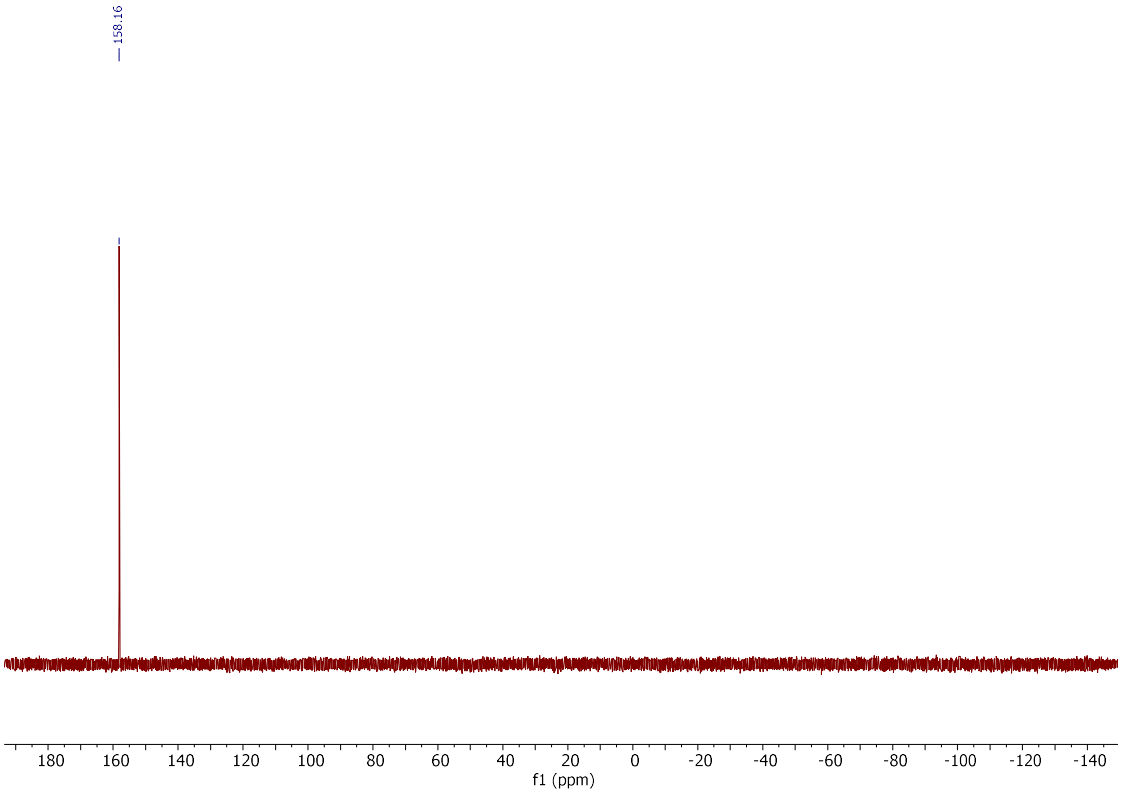

Compound **207**

^{1}H NMR (400 MHz, CD_3CN)

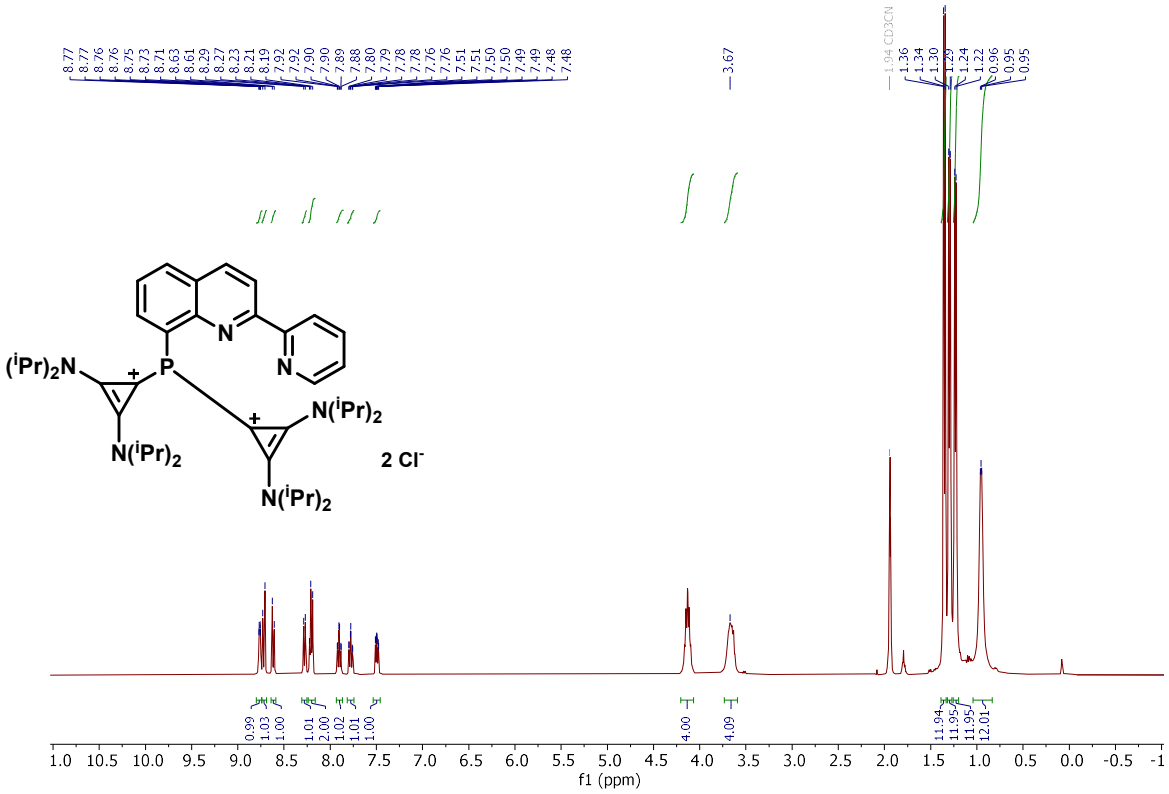

^{13}C{H} NMR (101 MHz, CD_3CN)

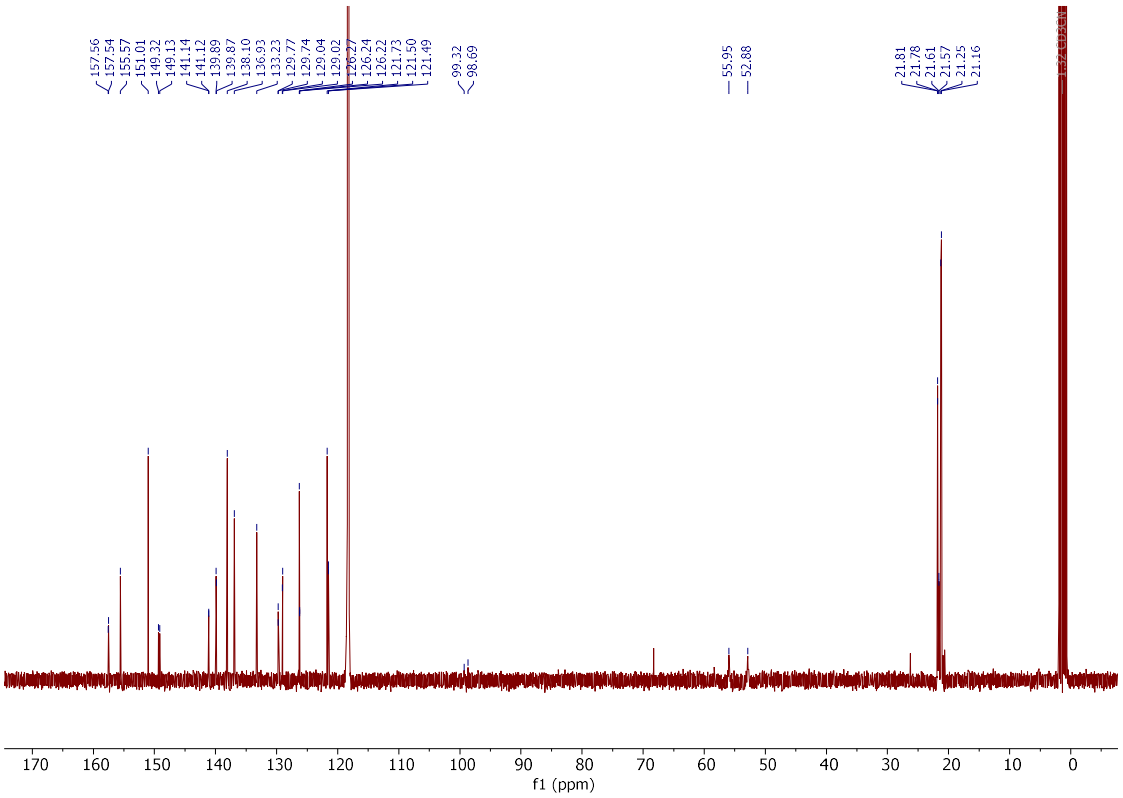

$^{31}P\{H\}$ NMR (162 MHz, CD_3CN)

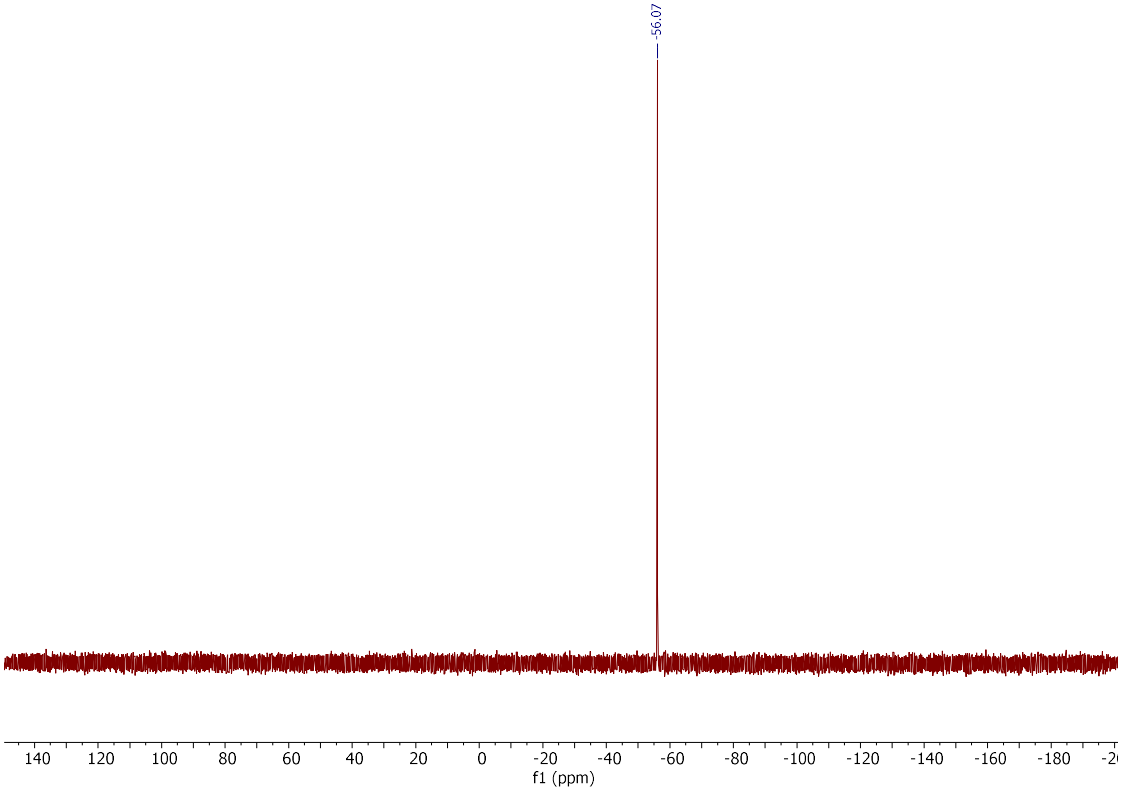

(^1H-^1H) COSY

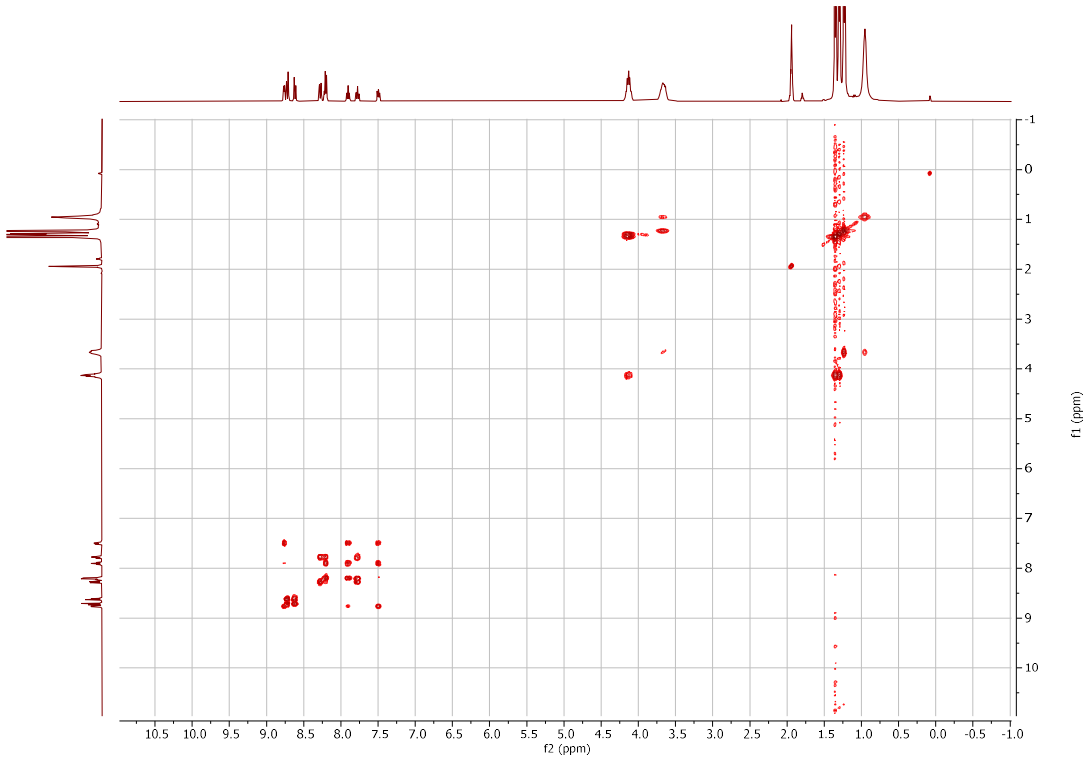

(^{1}H-^{13}C) HSQC

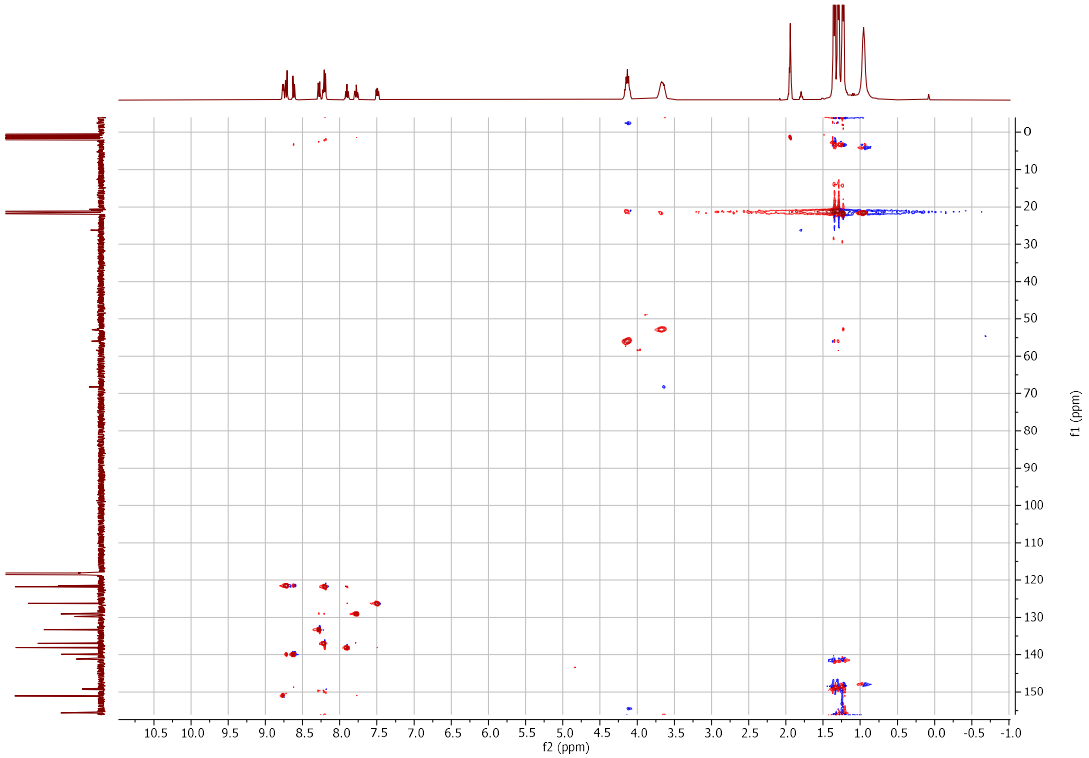

(^{1}H-^{13}C) HMBC

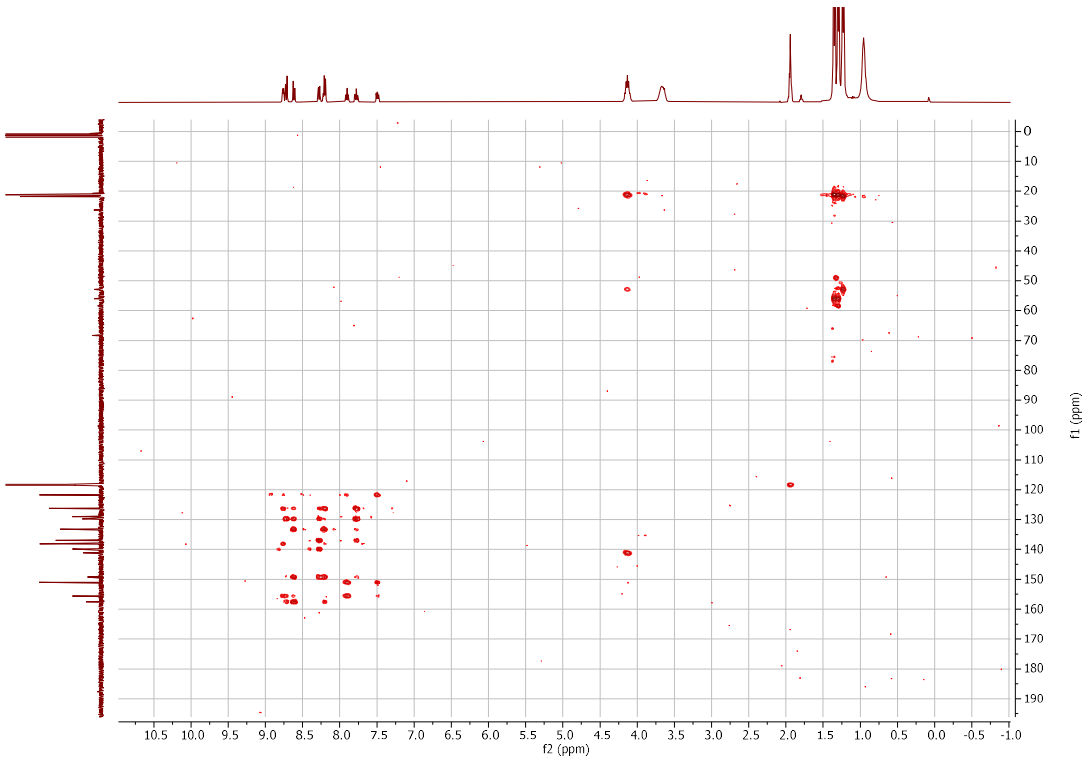

Compound **208**

^{1}H NMR (400 MHz, CD_3CN)

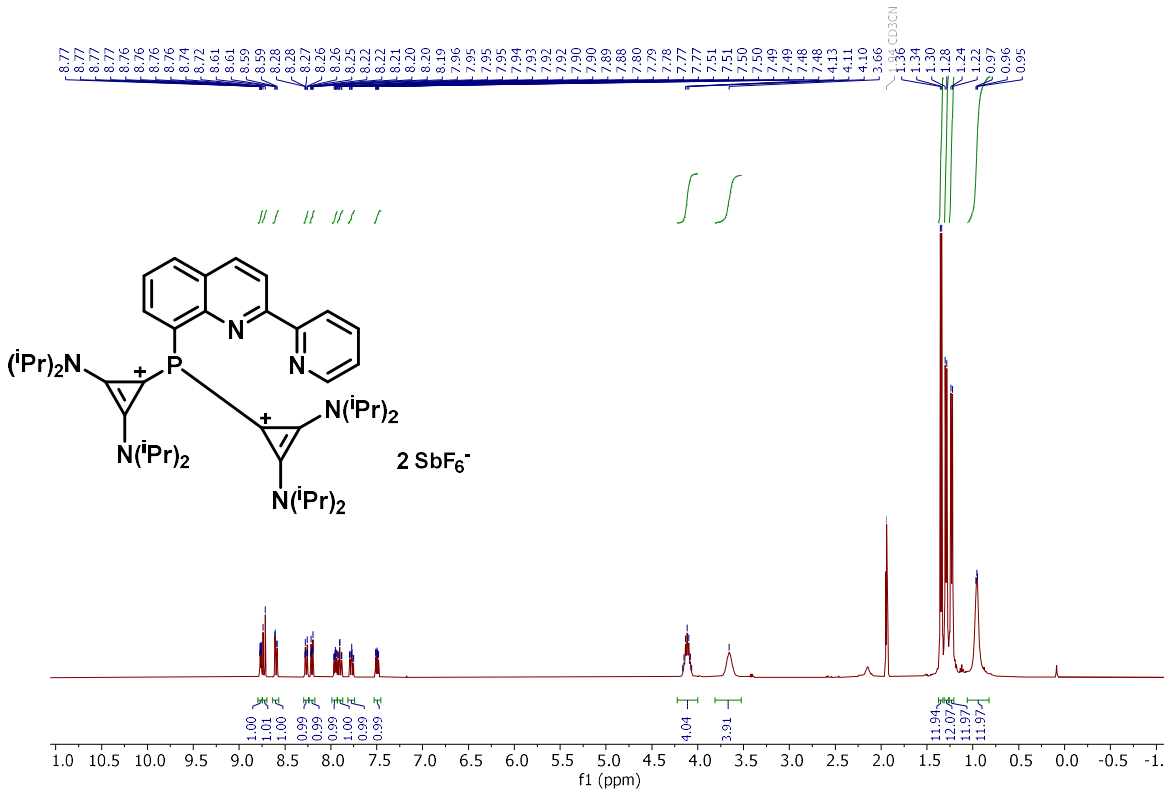

^{1}H NMR (300 MHz, CD_3CN)

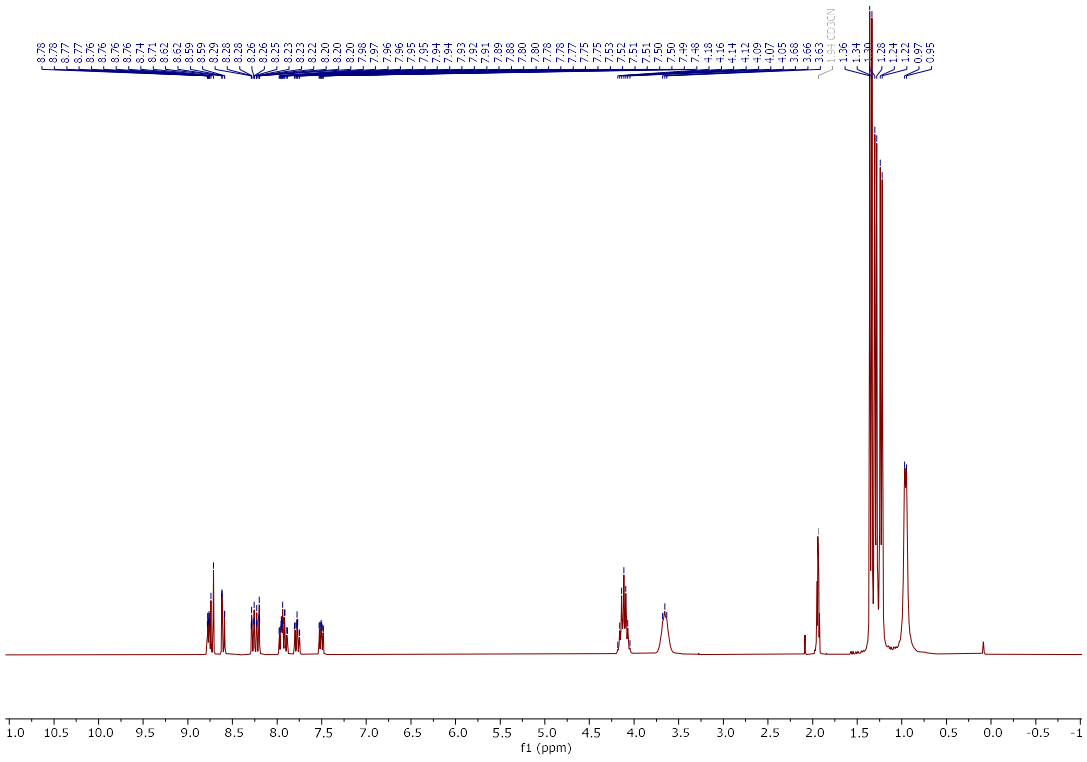

$^{13}C\{H\}$ NMR (101 MHz, CD_3CN)

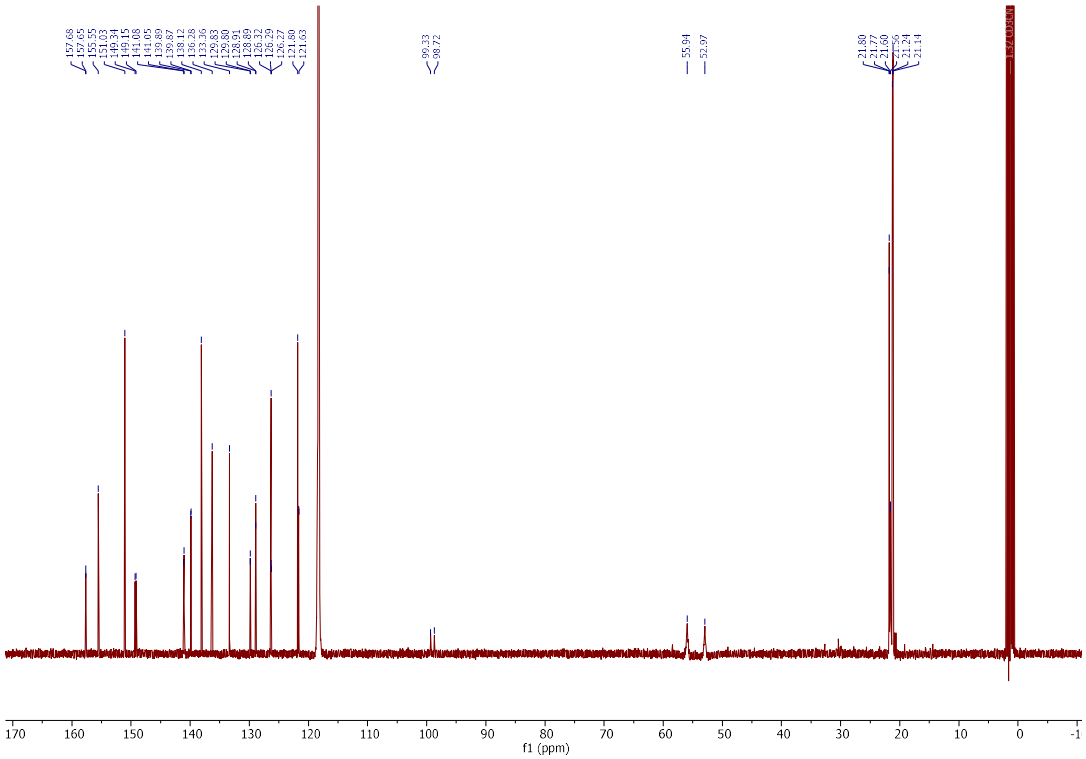

^{13}C NMR (75 MHz, CD_3CN)

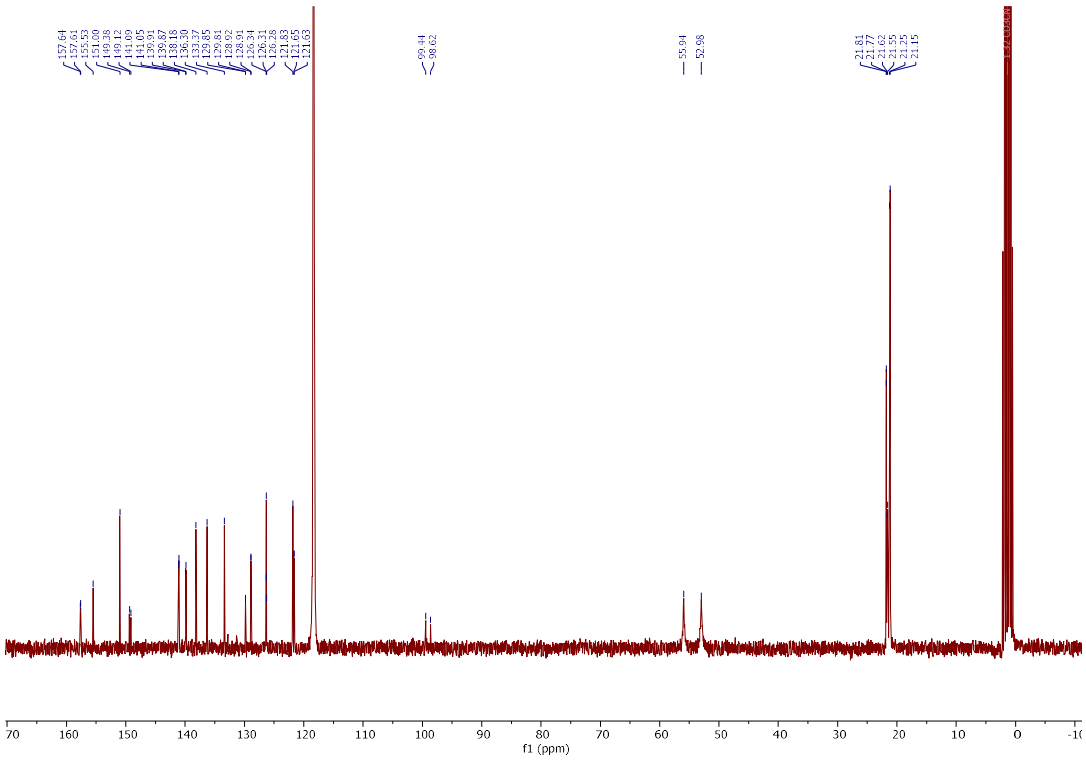

^{31}P{H} NMR (162 MHz, CD_3CN) δ -56.24

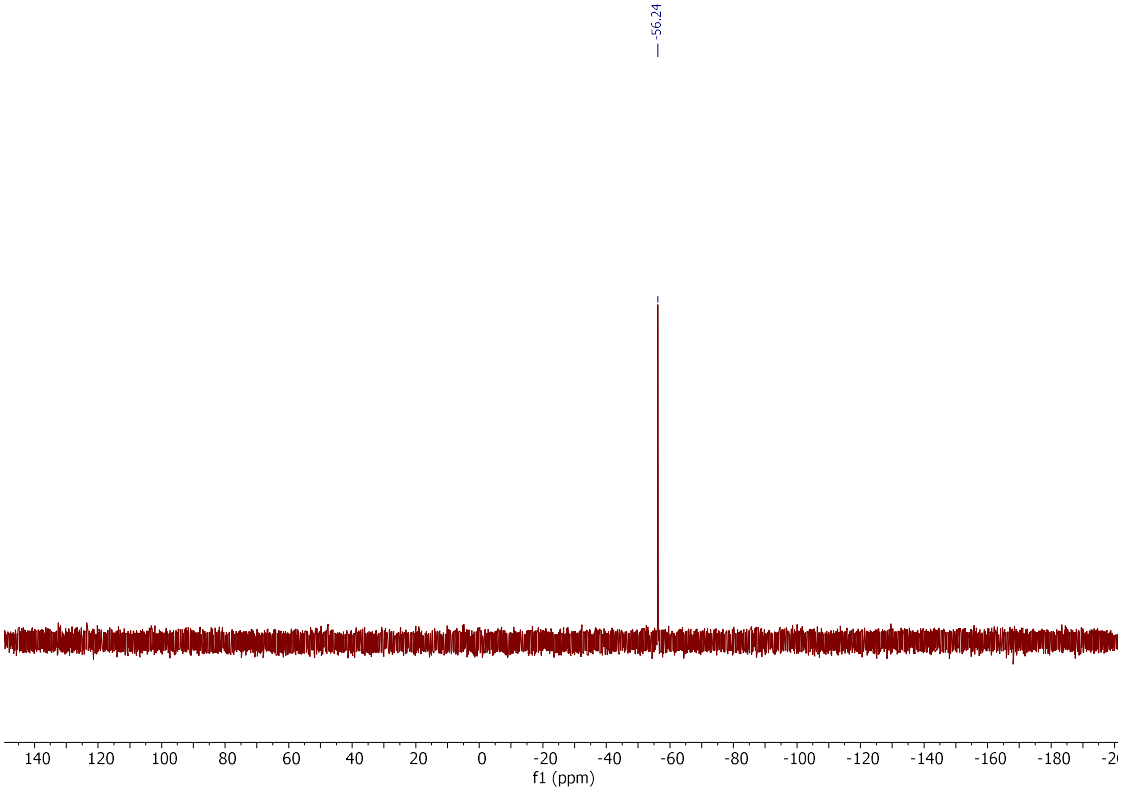

^{19}F NMR (282 MHz, CD_3CN)

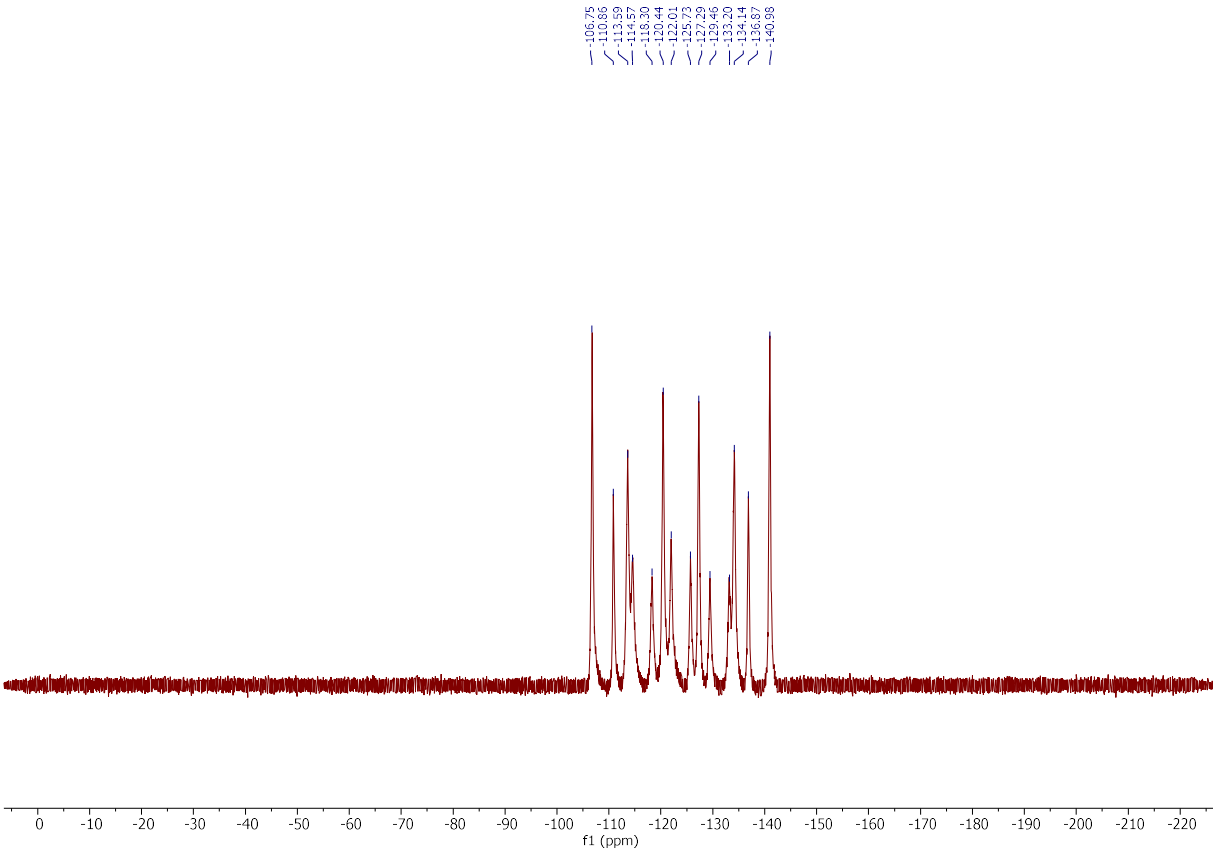

Compound **209a**

^{1}H NMR (400 MHz, CD_3CN)

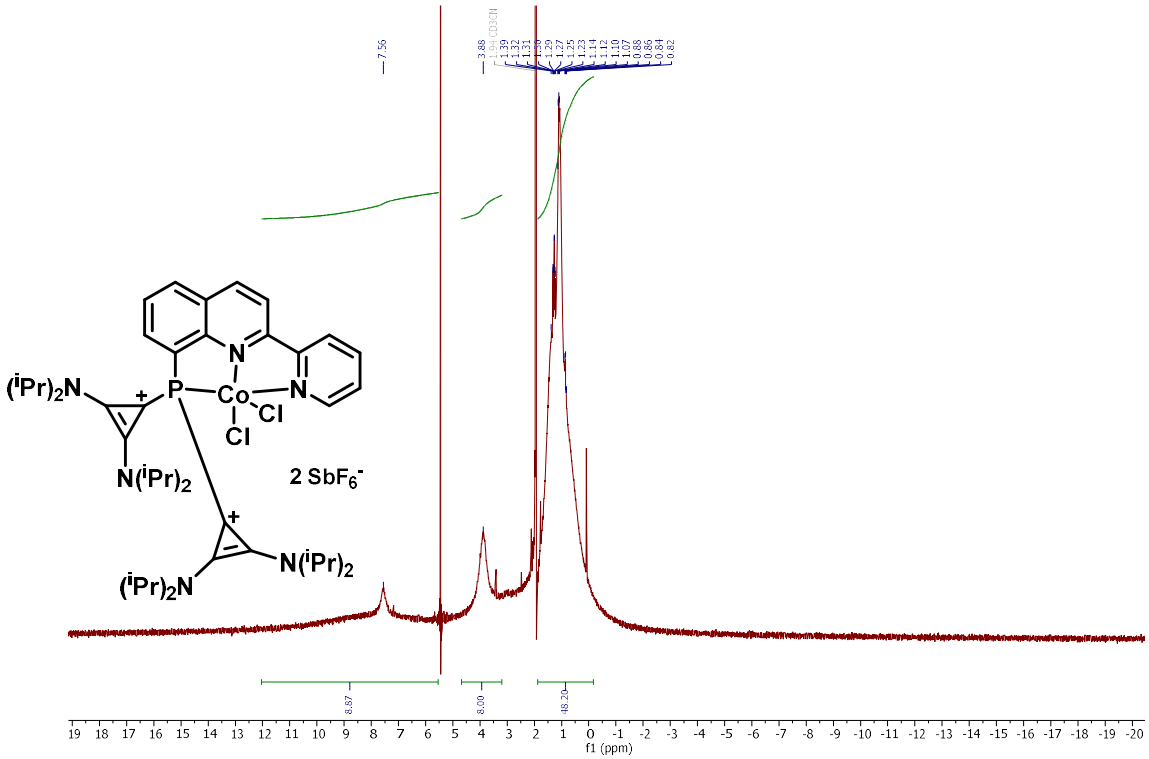

Compound **212**

^{1}H NMR (300 MHz, $CDCl_3$)

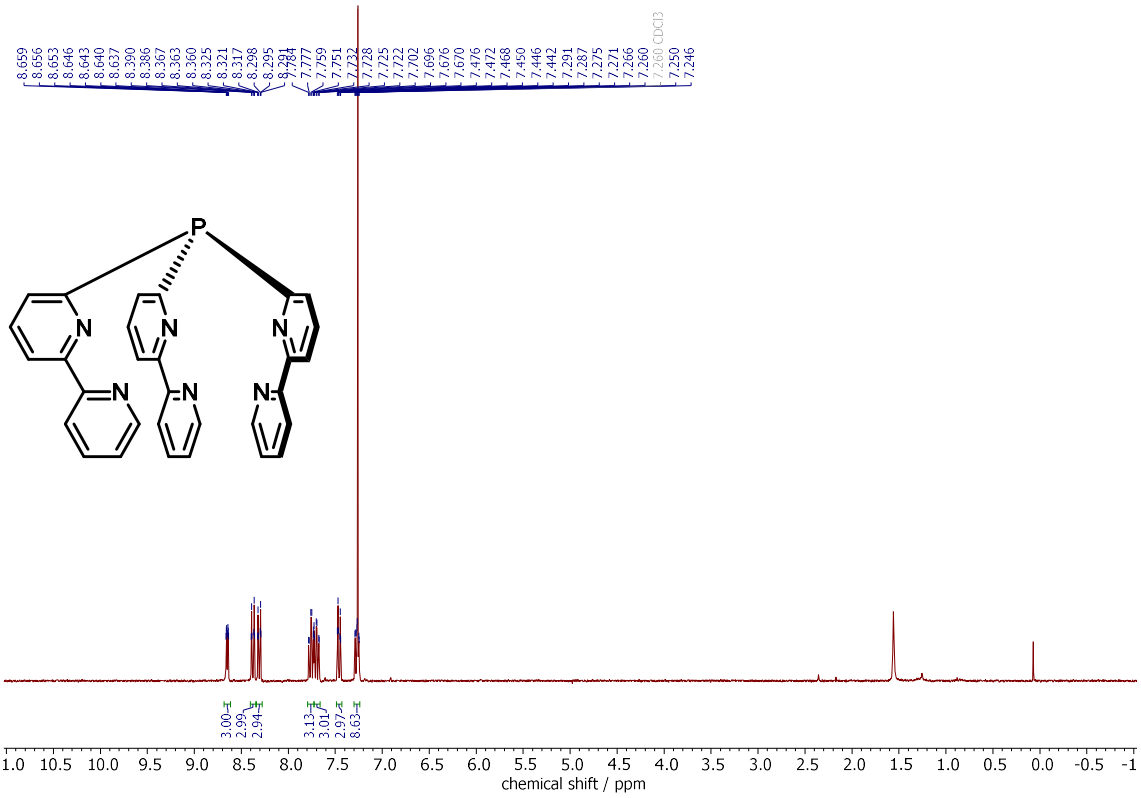

^{13}C{H} NMR (101 MHz, $CDCl_3$)

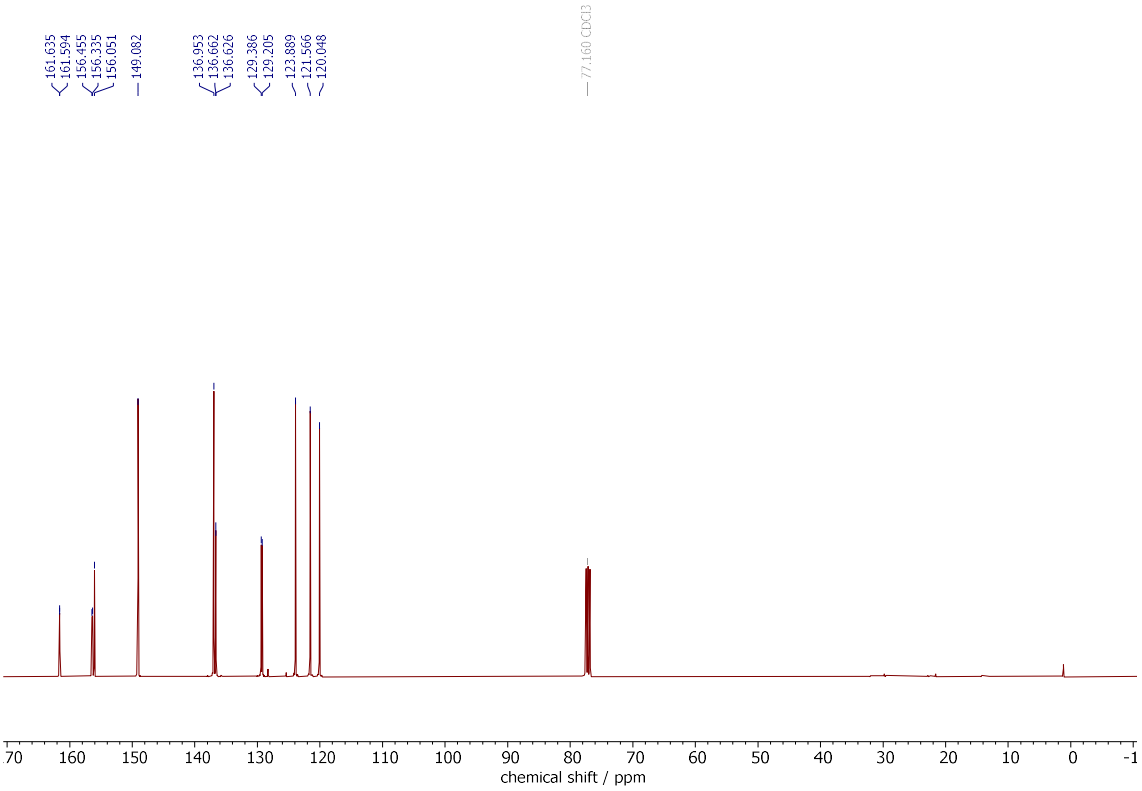

$^{31}P\{H\}$ NMR (121 MHz, $CDCl_3$)

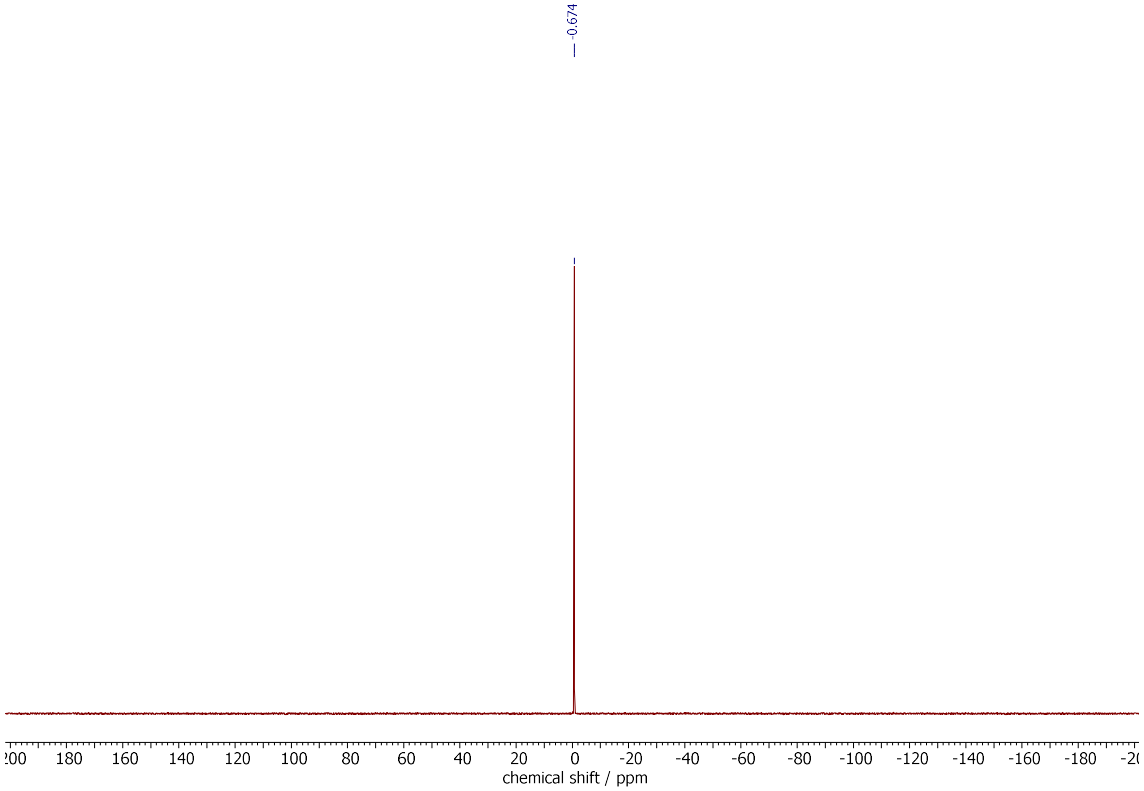

Compound **237**

^{1}H NMR (400 MHz, $CDCl_3$)

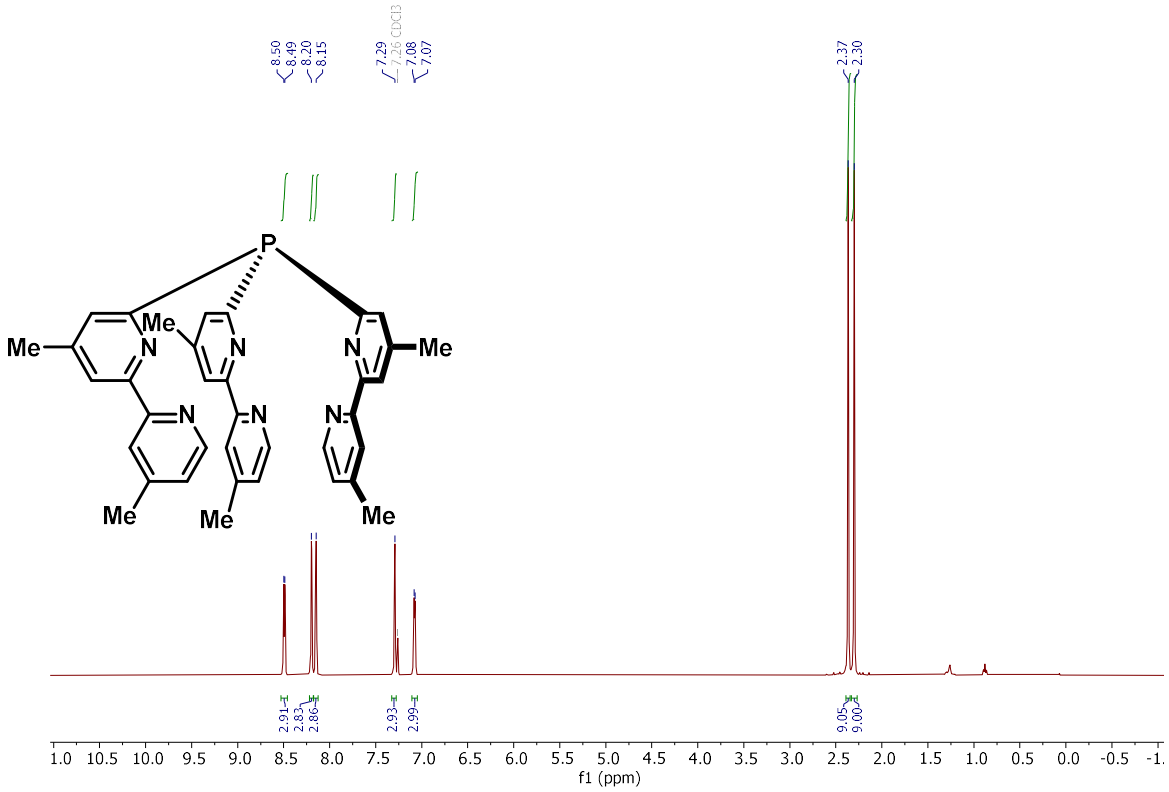

^{13}C{H} NMR (101 MHz, $CDCl_3$)

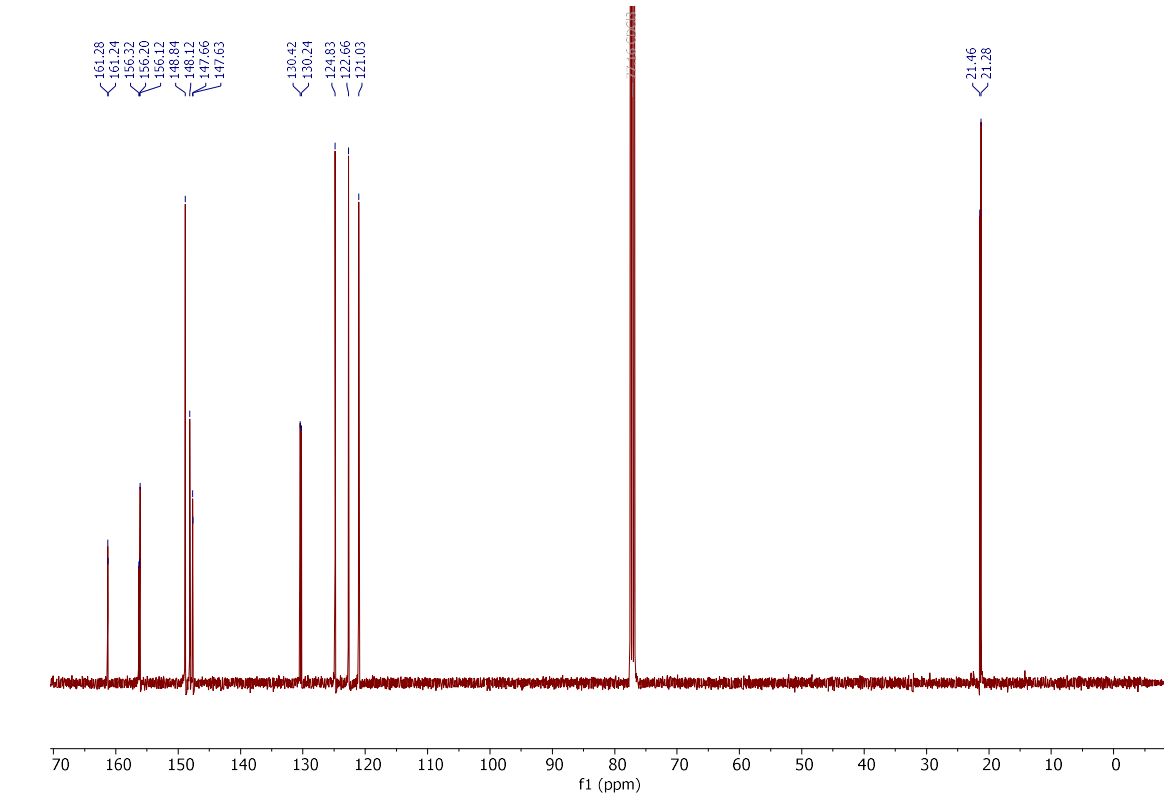

$^{31}P\{H\}$ NMR (162 MHz, $CDCl_3$)

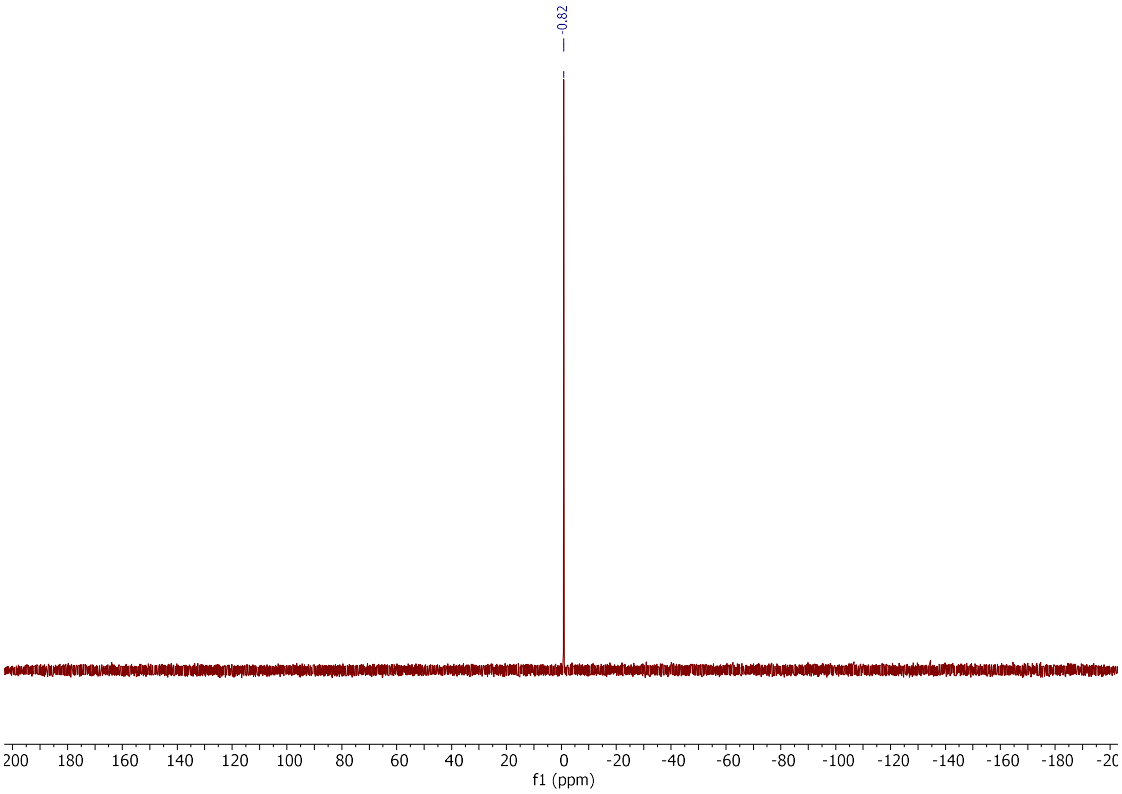

Compound **237x**

^{1}H NMR (300 MHz, $CDCl_3$)

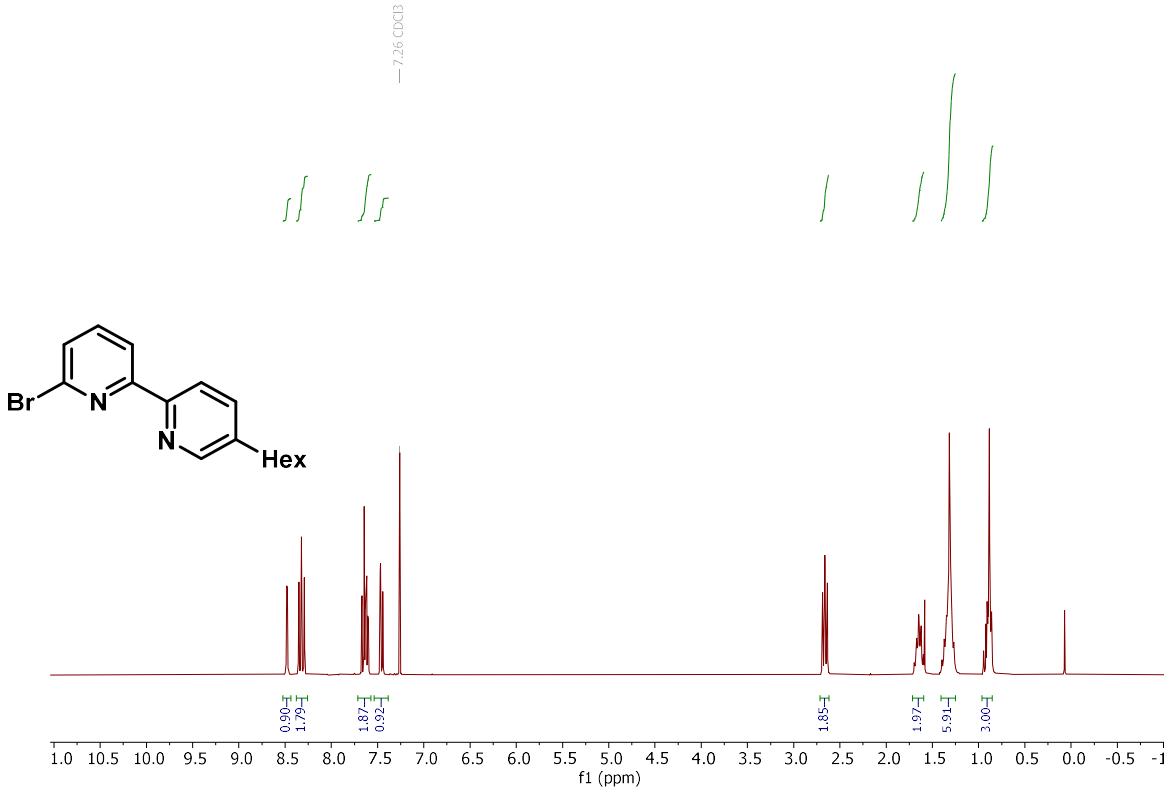

^{13}C NMR (75 MHz, $CDCl_3$)

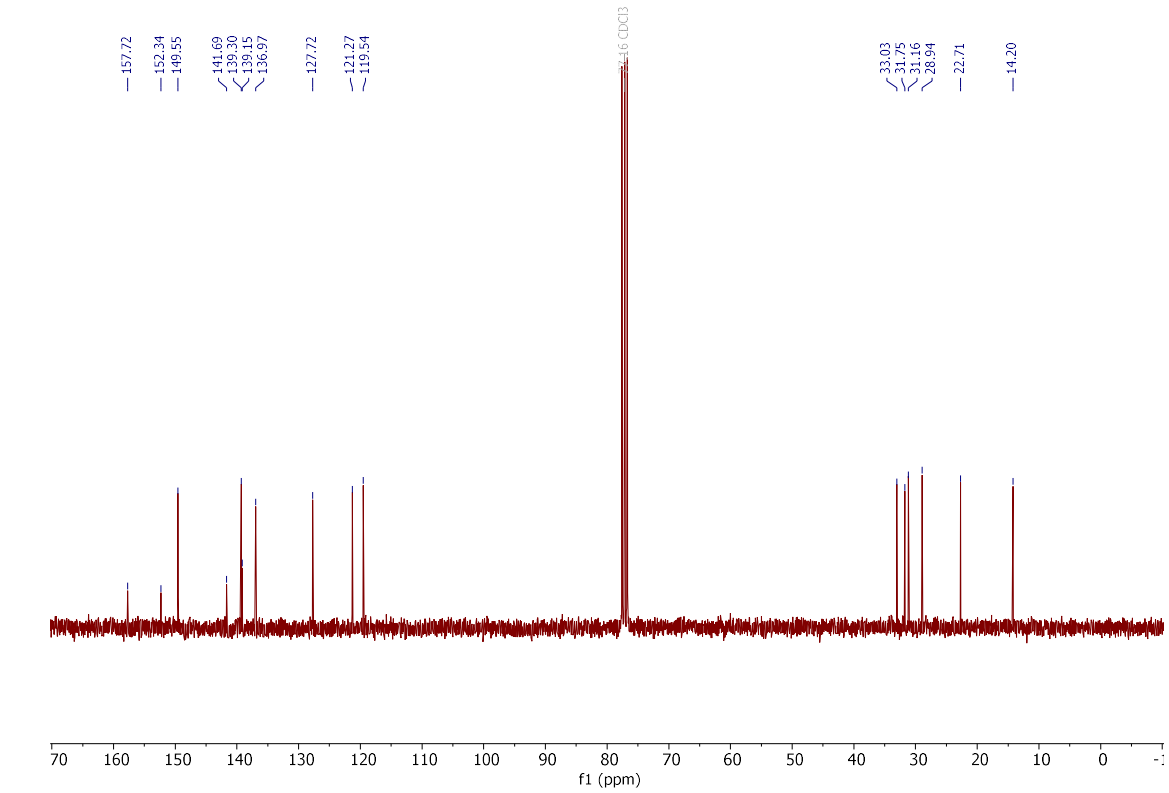

Compound **237y**

^{1}H NMR (400 MHz, $CDCl_3$)

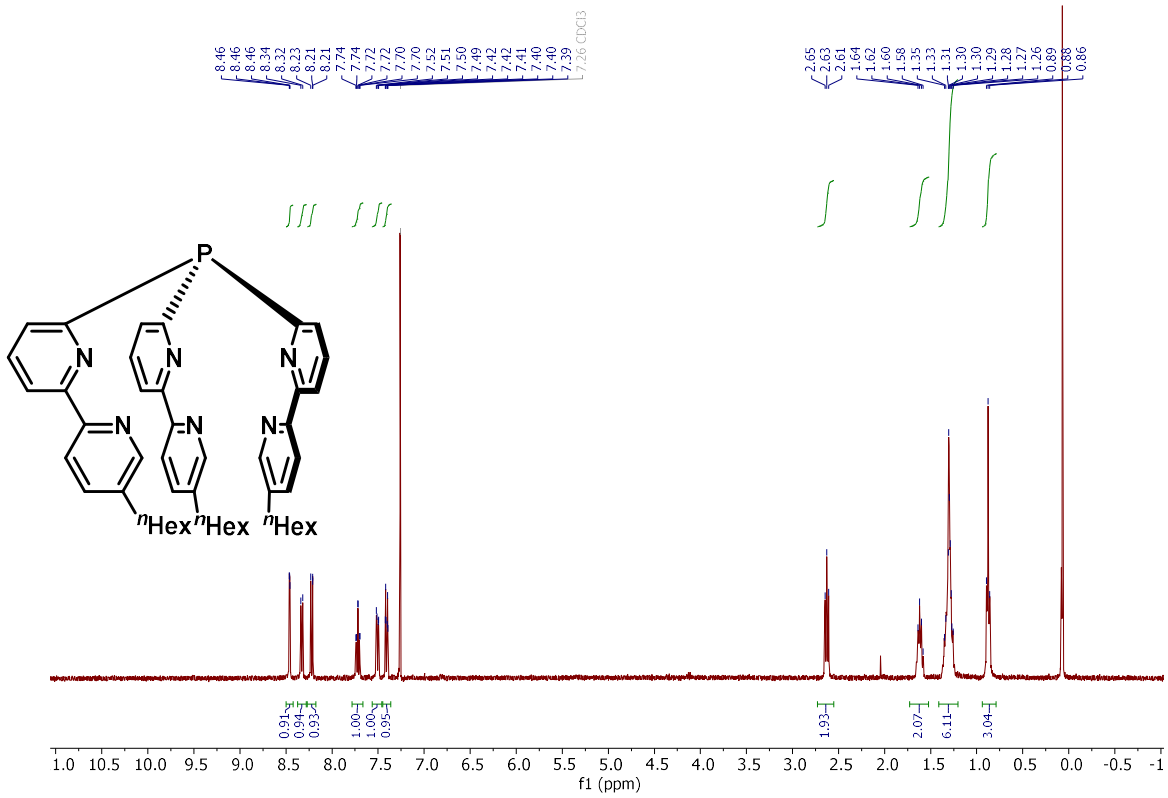

^{13}C{H} NMR (101 MHz, $CDCl_3$)

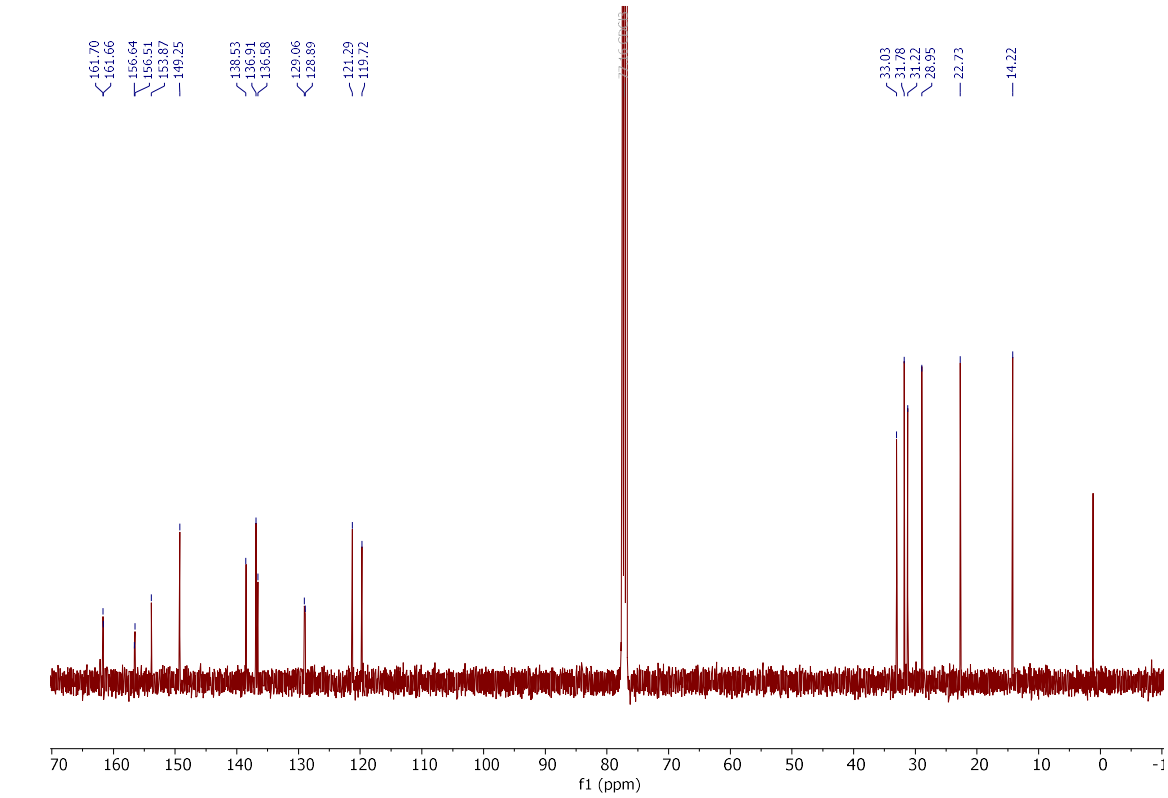

$^{31}P\{H\}$ NMR (162 MHz, $CDCl_3$)

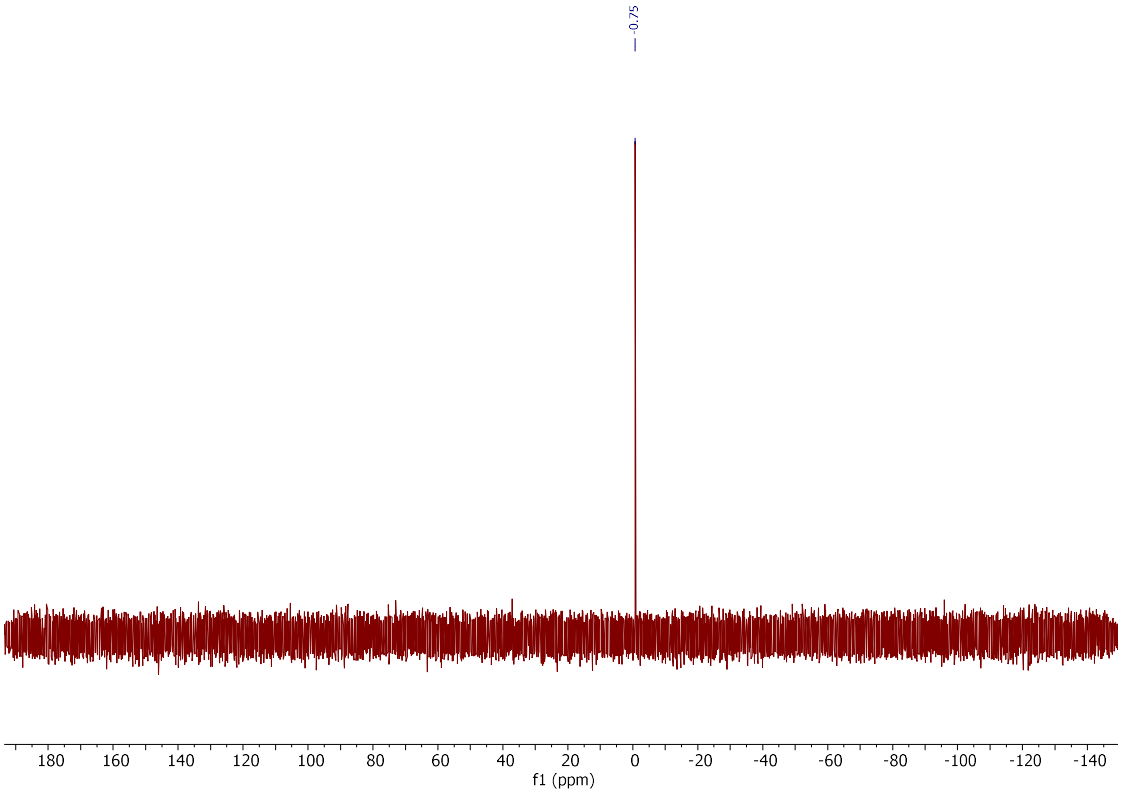

Compound **237z**

^{1}H NMR (300 MHz, CD_3CN)

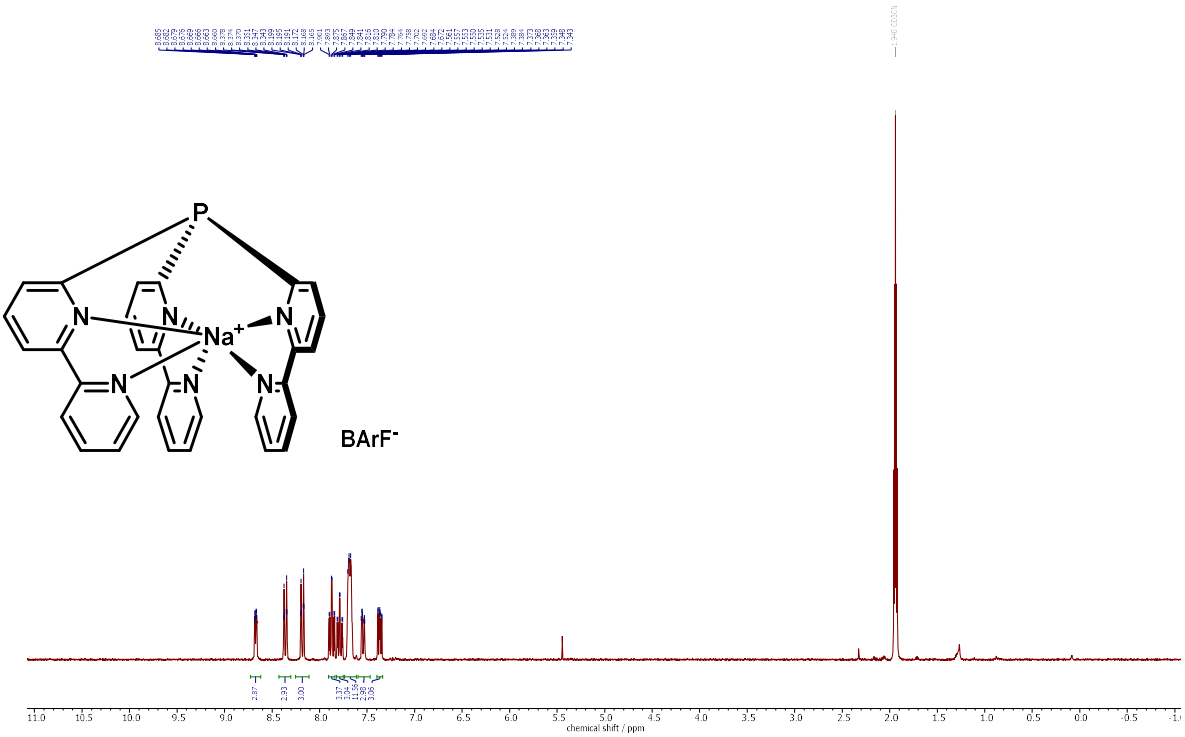

^{1}H NMR (400 MHz, $CDCl_3$)

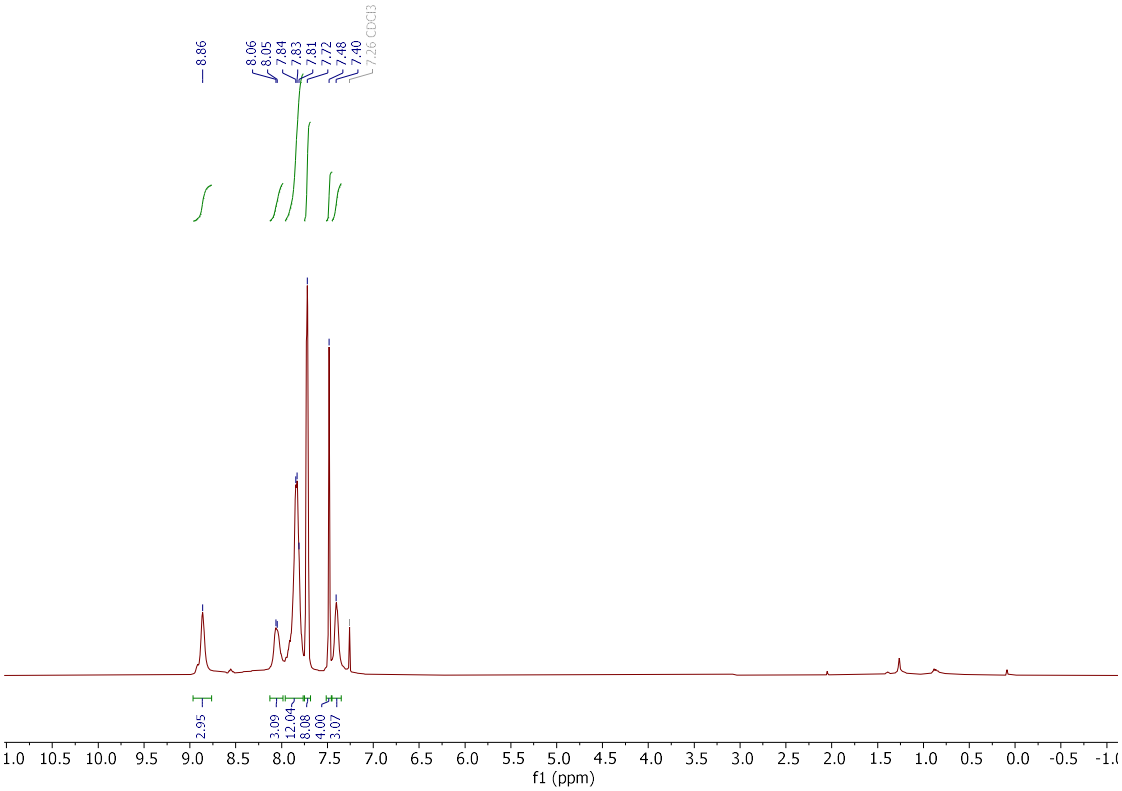

^{13}C NMR (101 MHz, CD_3CN)

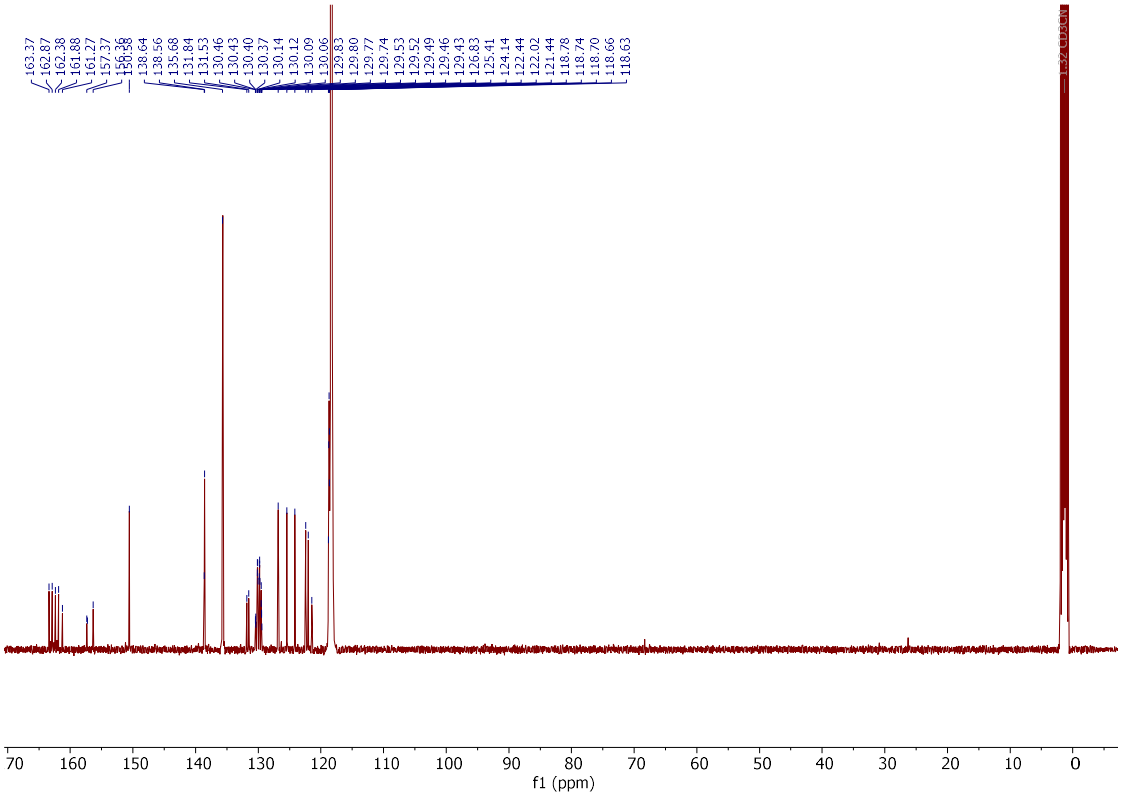

^{13}C NMR (101 MHz, $CDCl_3$)

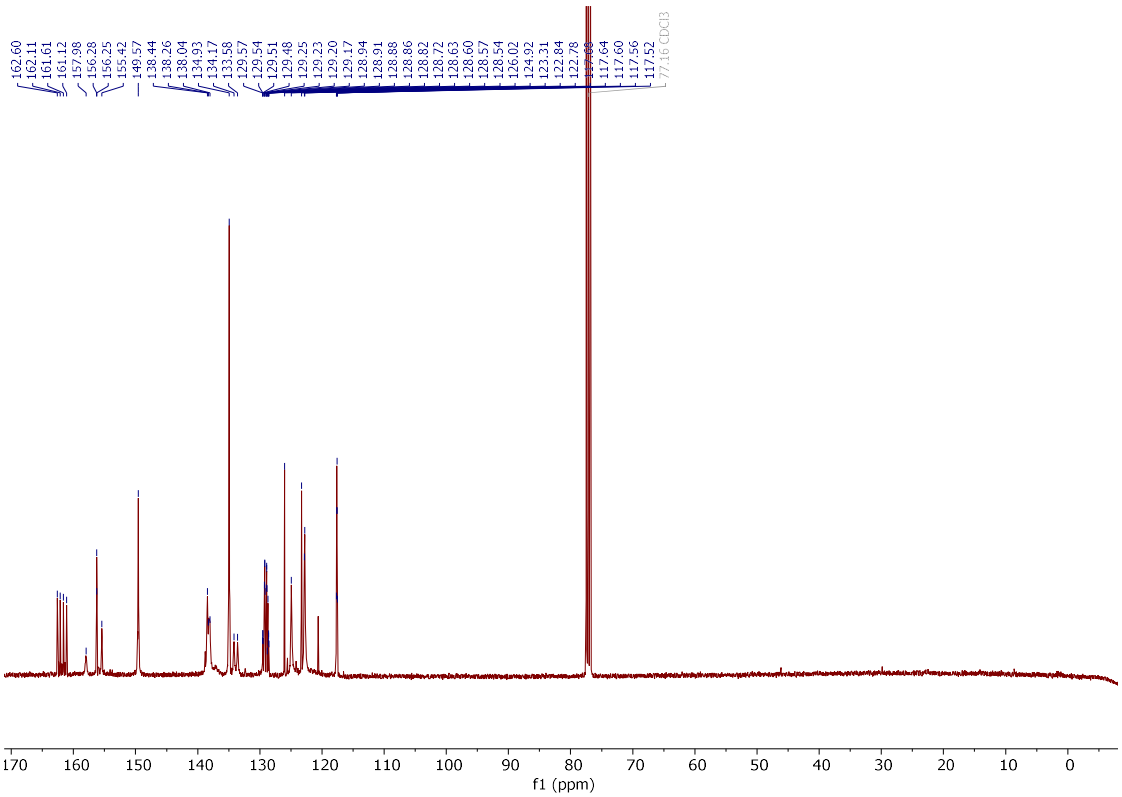

$^{31}P\{H\}$ NMR (121 MHz, CD_3CN)

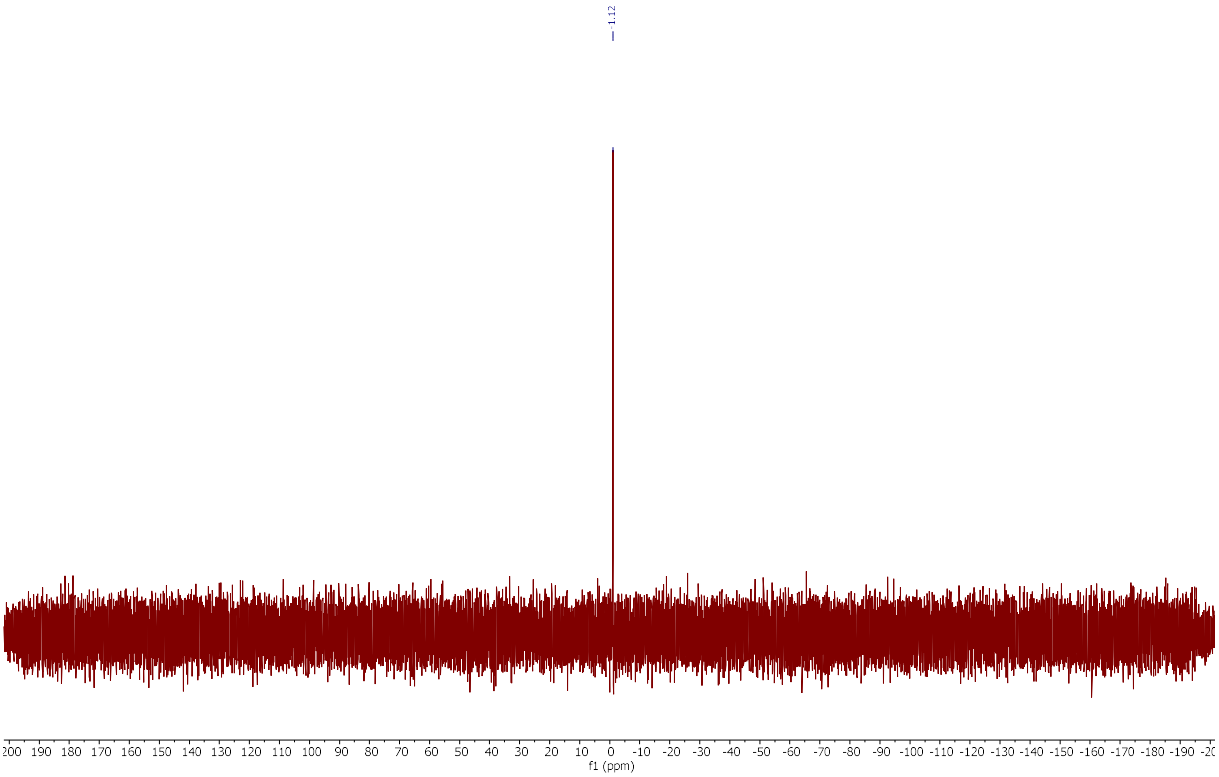

$^{31}P\{H\}$ NMR (121 MHz, $CDCl_3$)

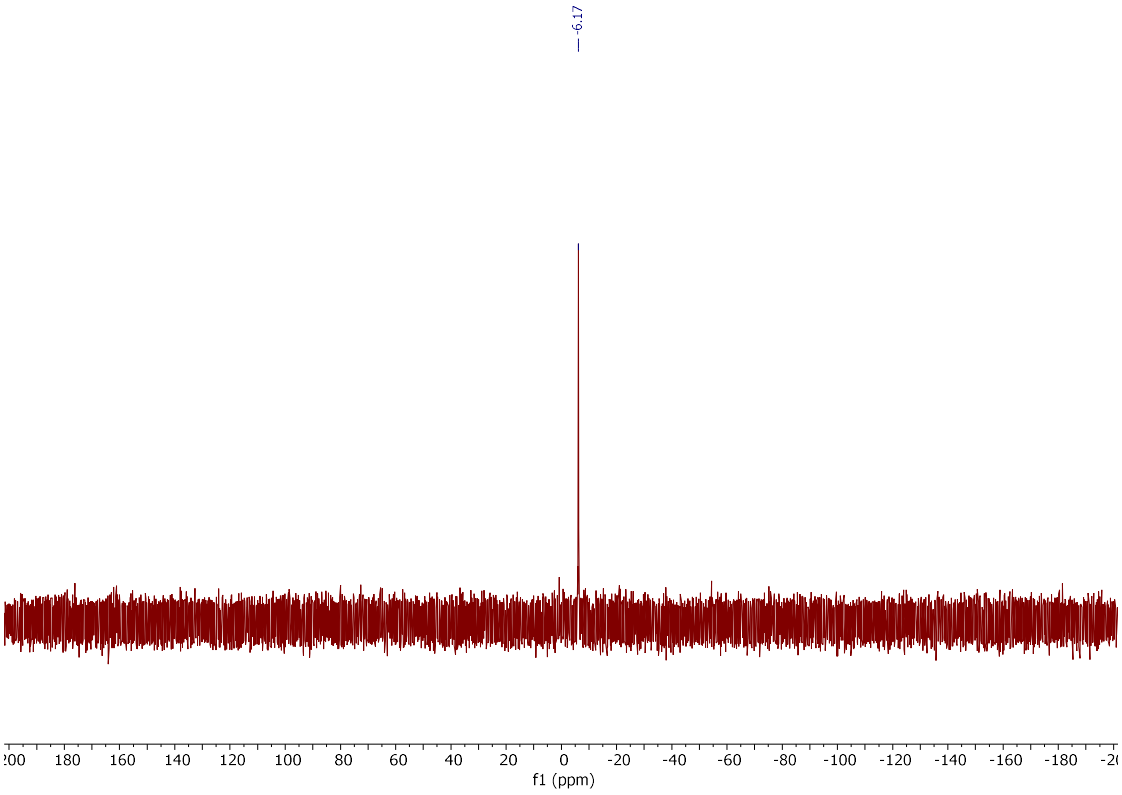

^{19}F NMR (282 MHz, CD_3CN)

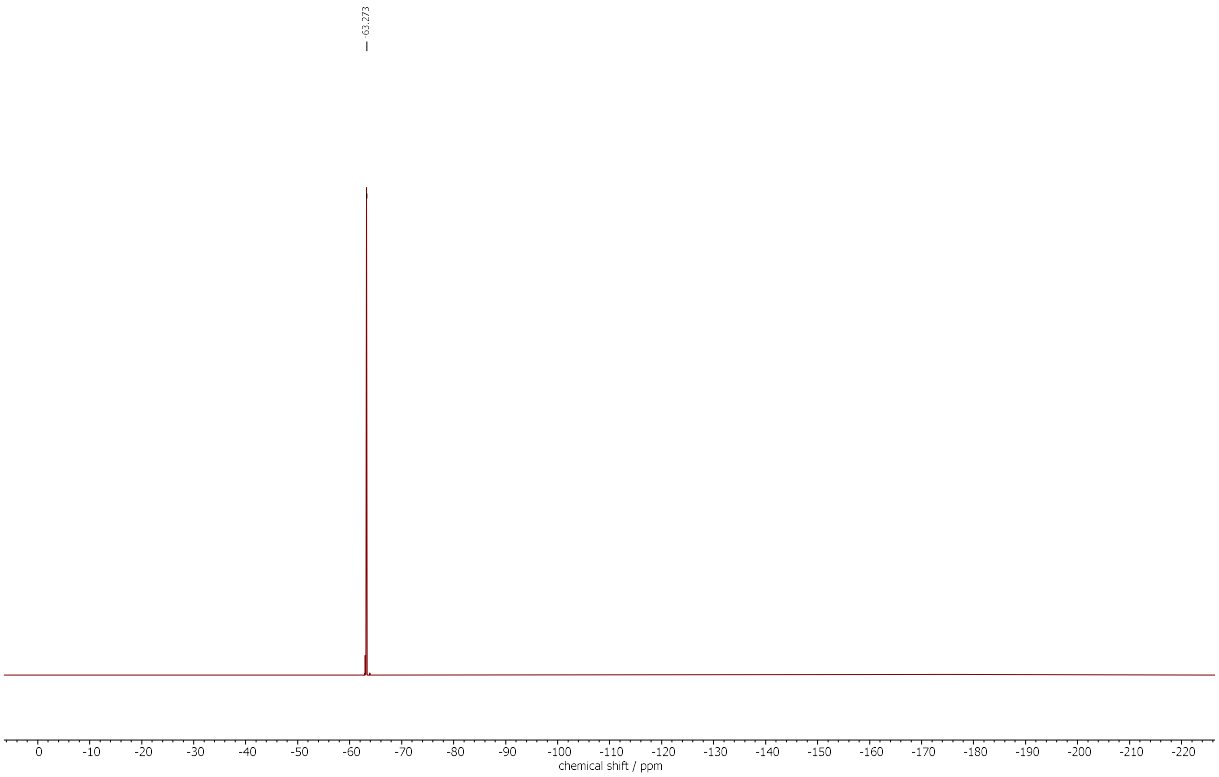

^{19}F NMR (377 MHz, $CDCl_3$)

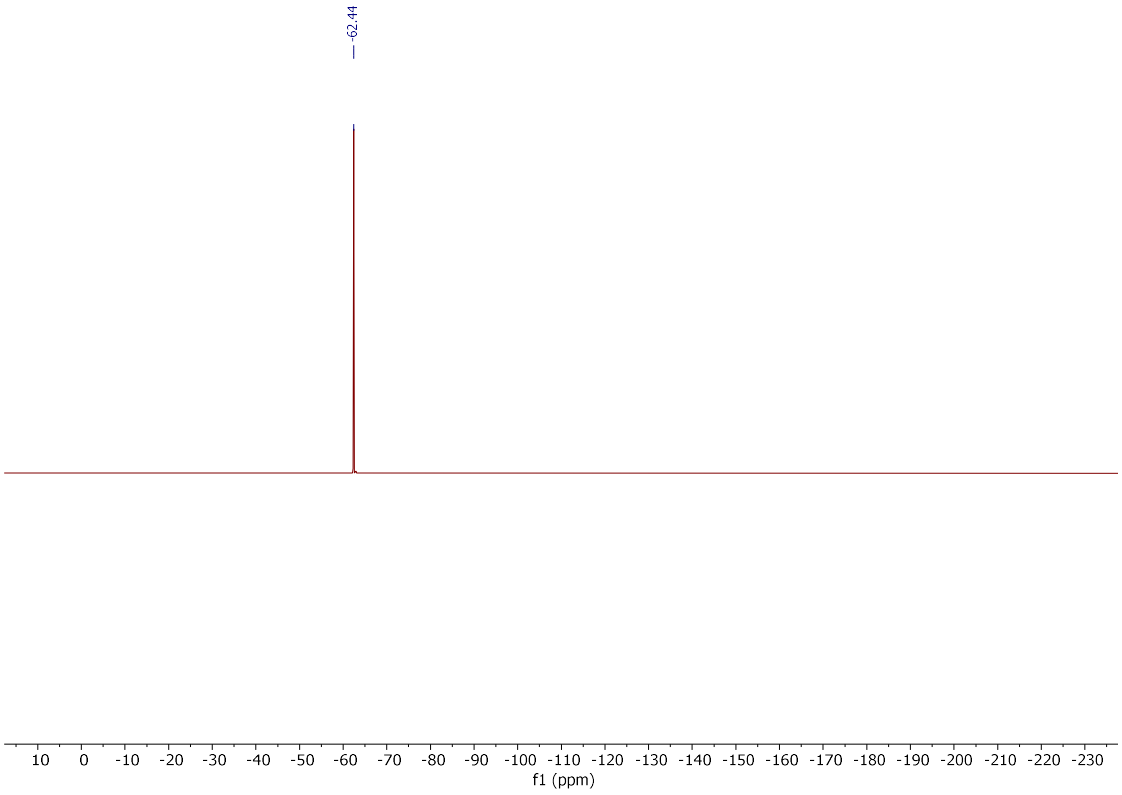

^{11}B NMR (96 MHz, CD_3CN)

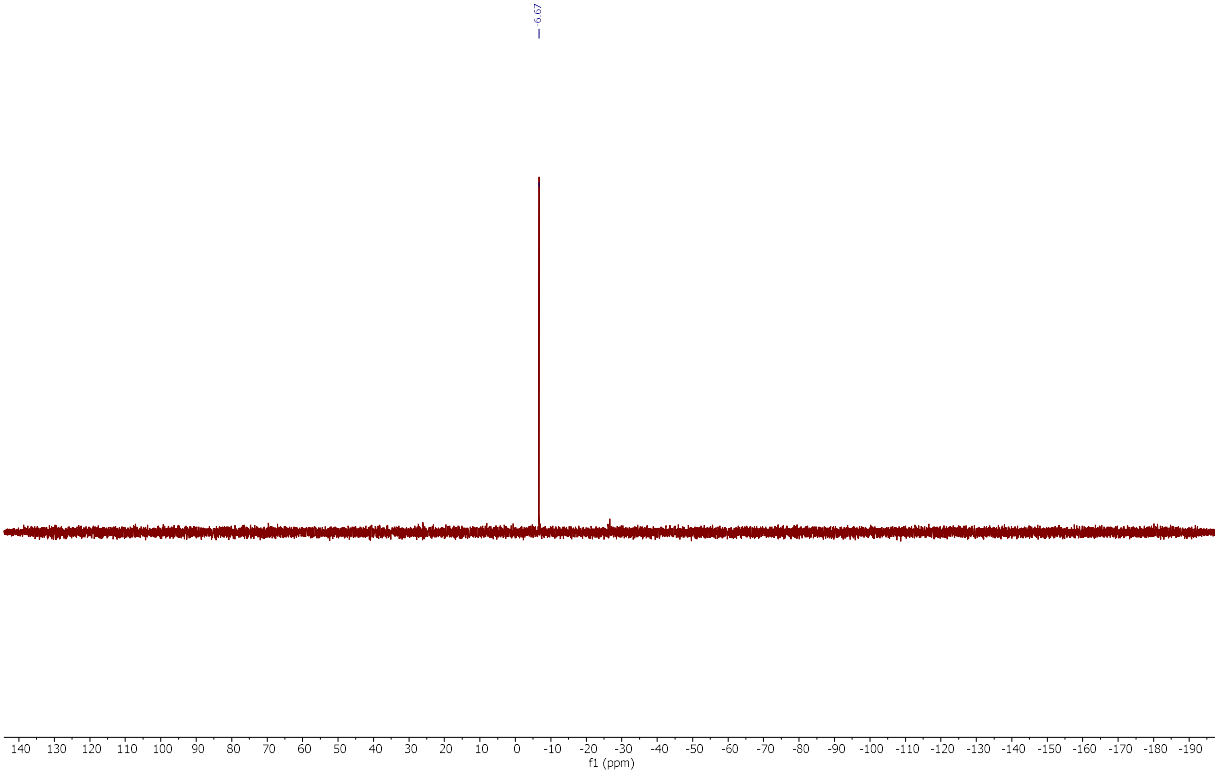

^{11}B NMR (96 MHz, $CDCl_3$)

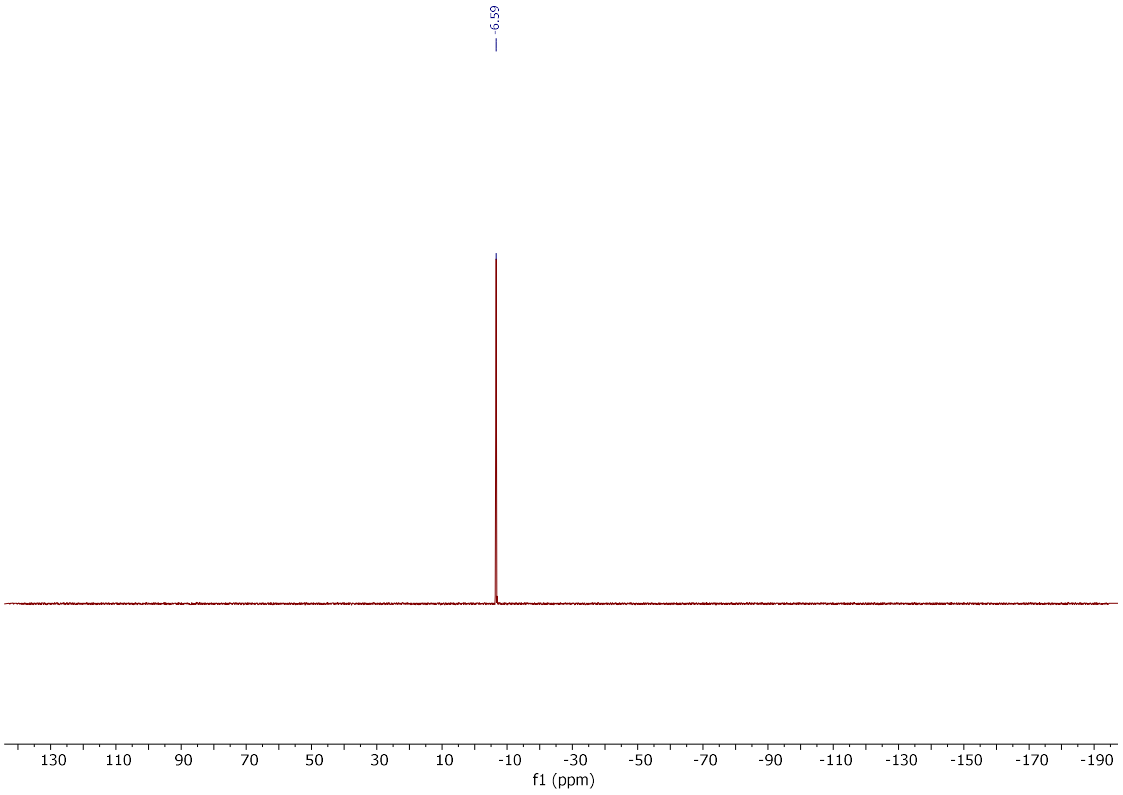

Compound **238**

^{1}H NMR (300 MHz, CD_3CN)

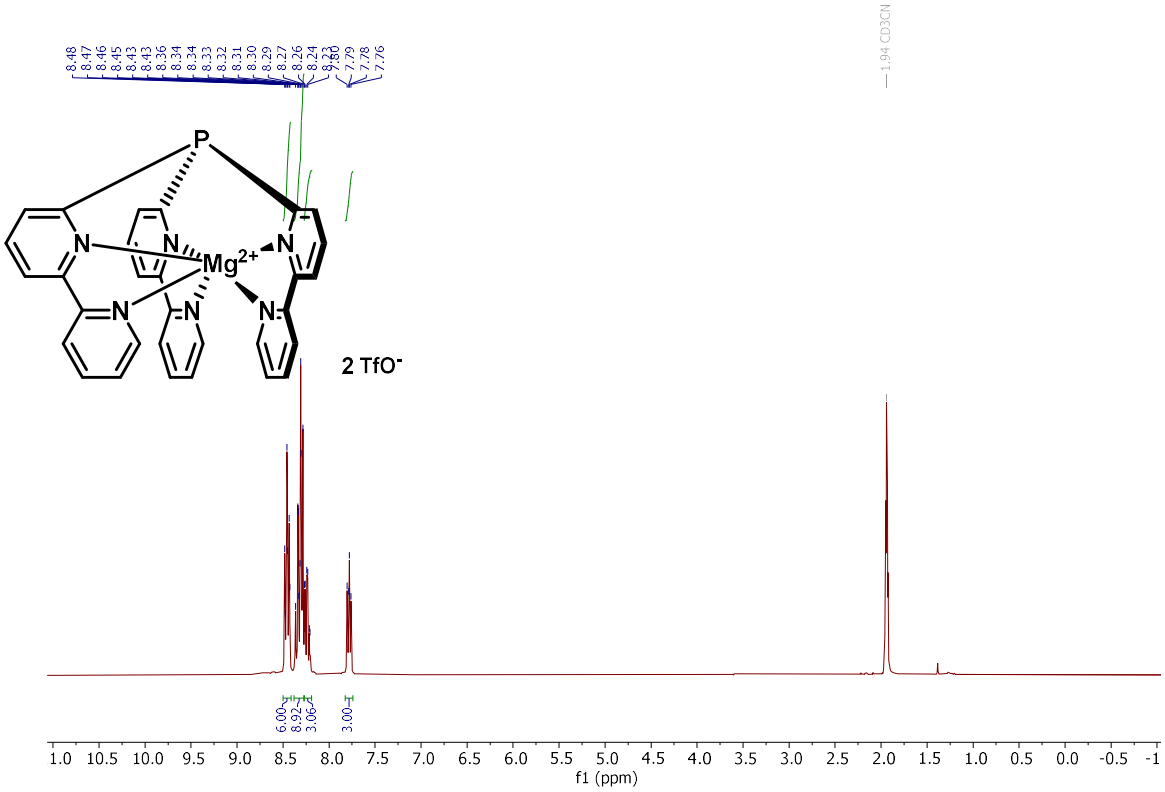

^{13}C{H} NMR (101 MHz, CD_3CN)

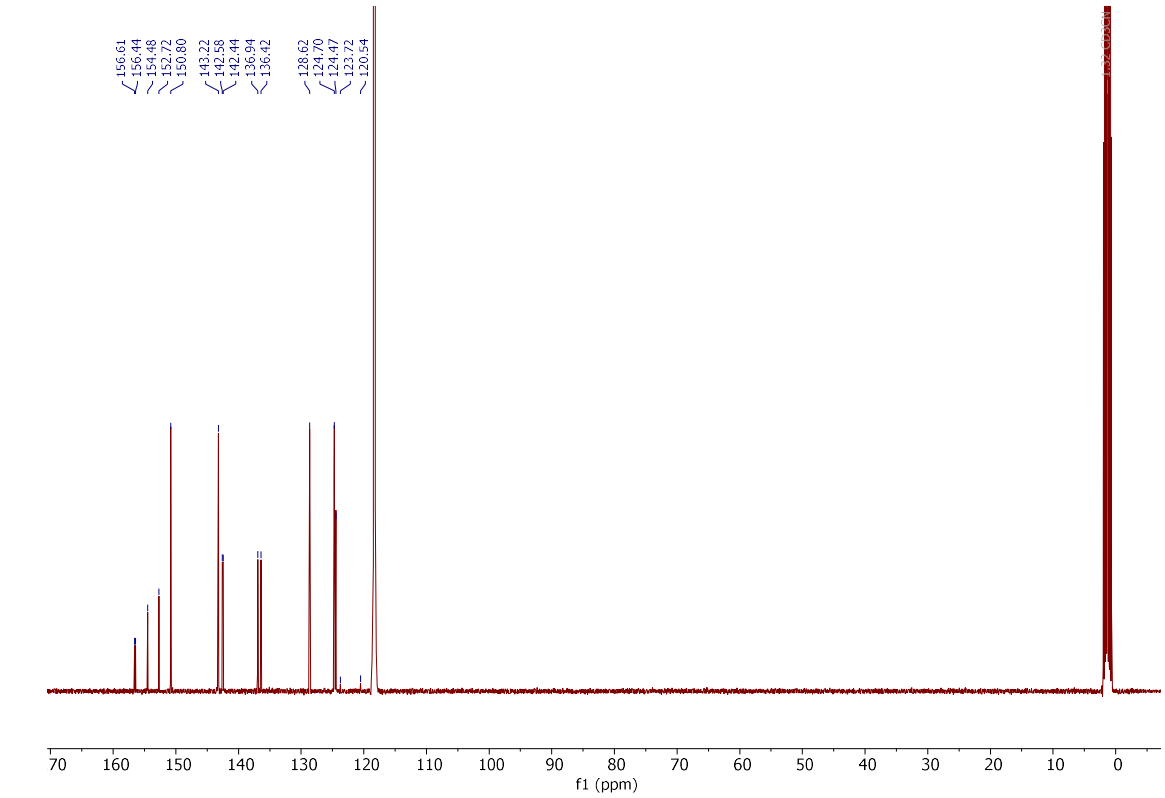

^{31}P{H} NMR (121 MHz, CD_3CN)

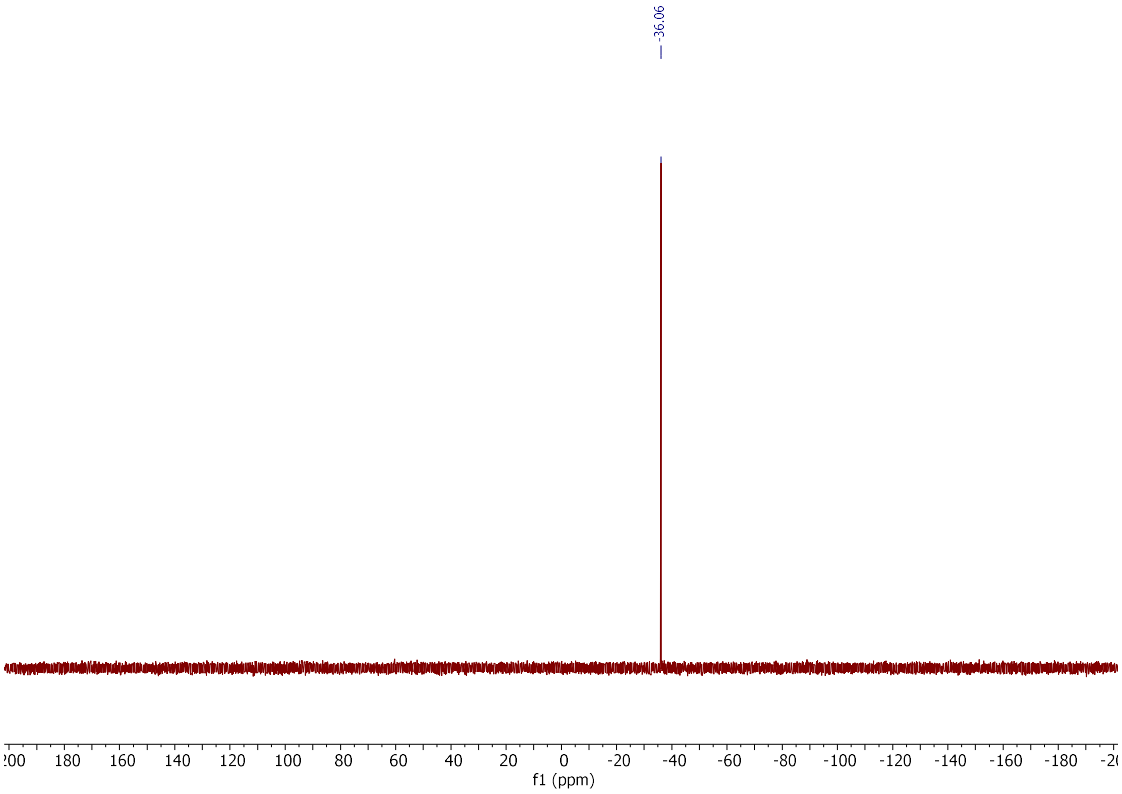

^{31}P NMR (162 MHz, CD_3CN)

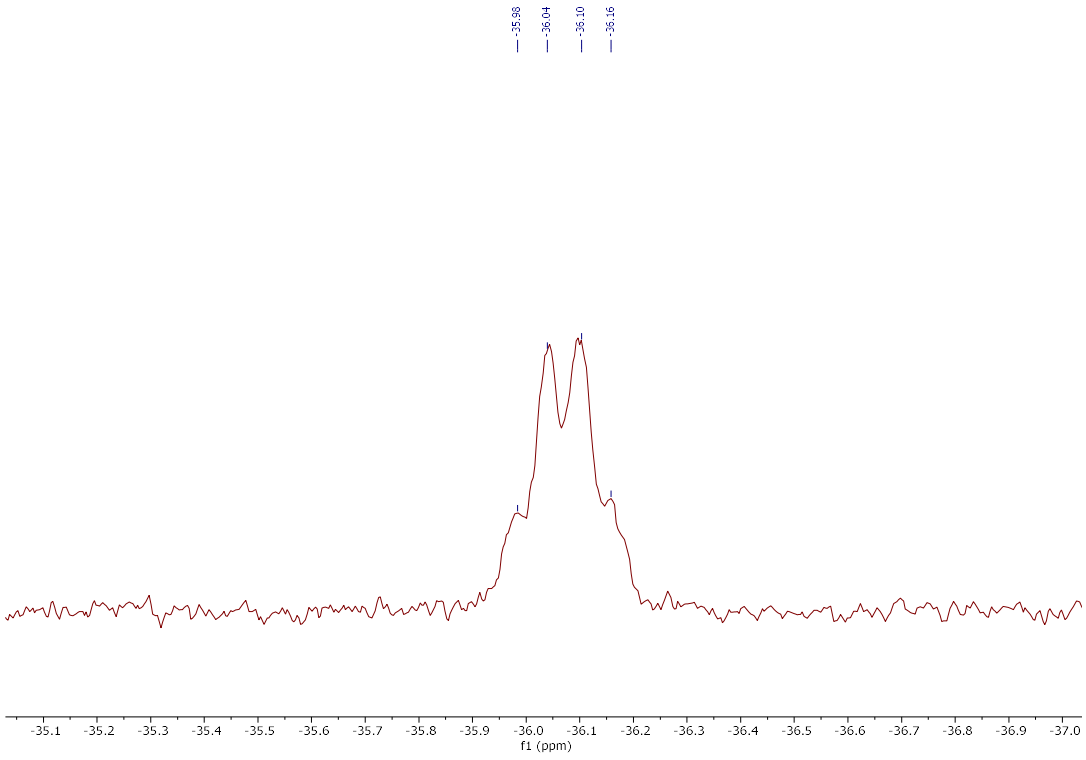

^{19}F NMR (282 MHz, CD_3CN)

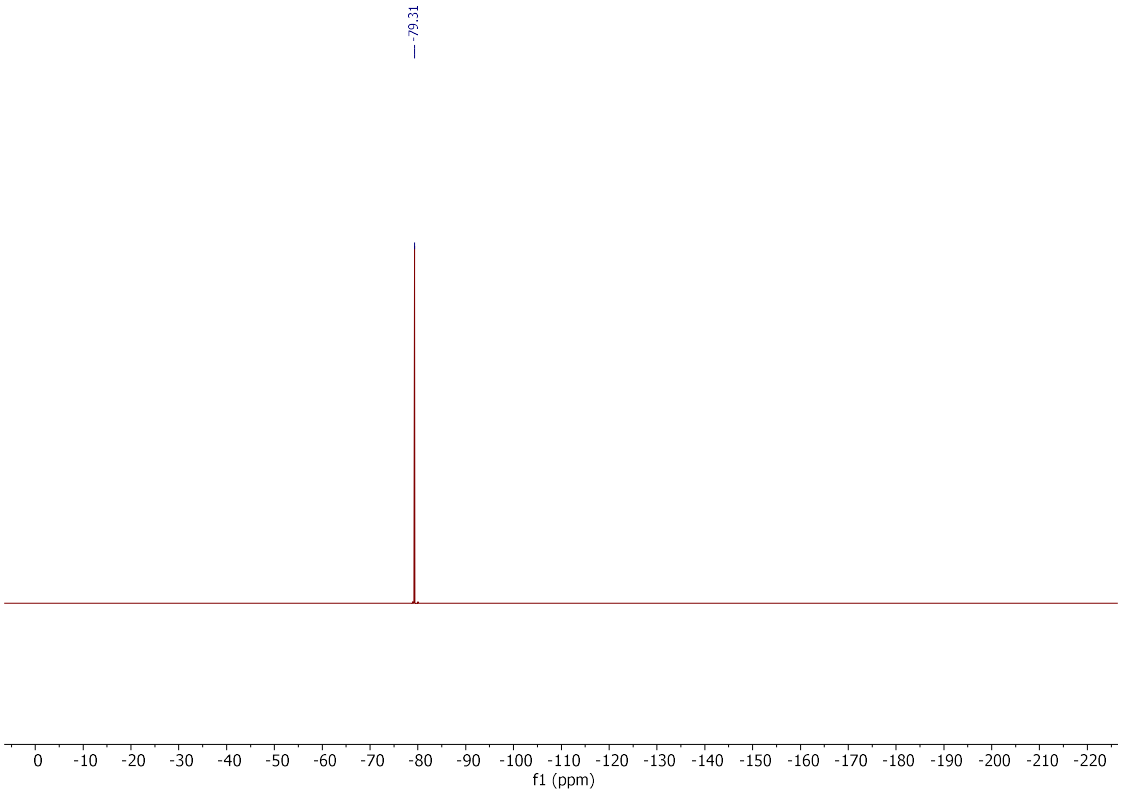

Compound **239**

^{1}H NMR (300 MHz, CD_3CN)

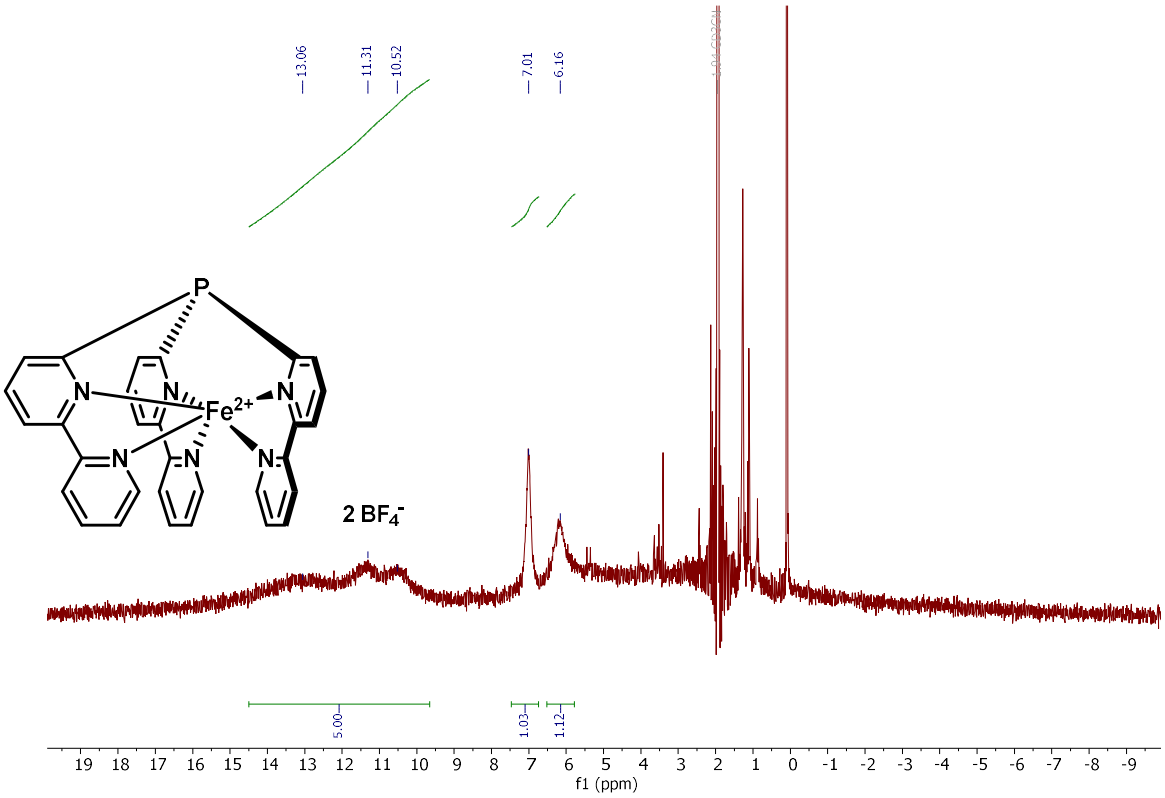

Compound **240**

^{1}H NMR (400 MHz, CD_3CN)

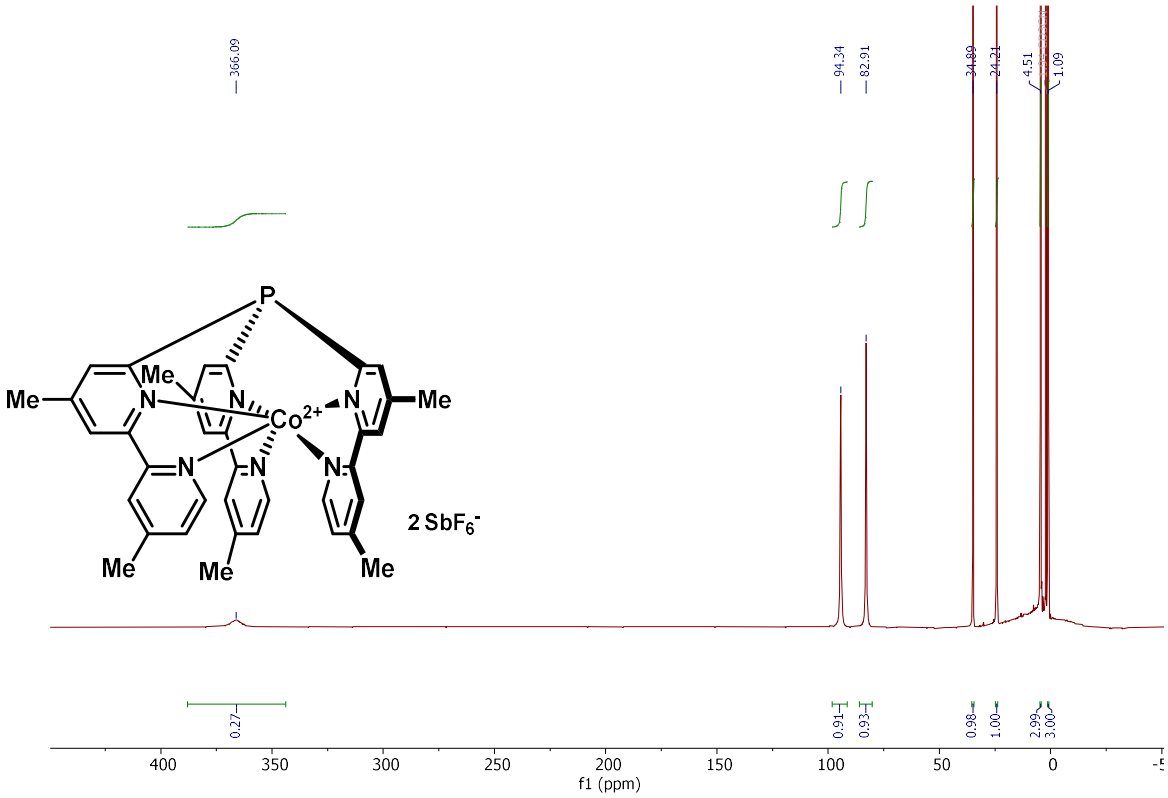

^{31}P{H} NMR (162 MHz, CD_3CN)

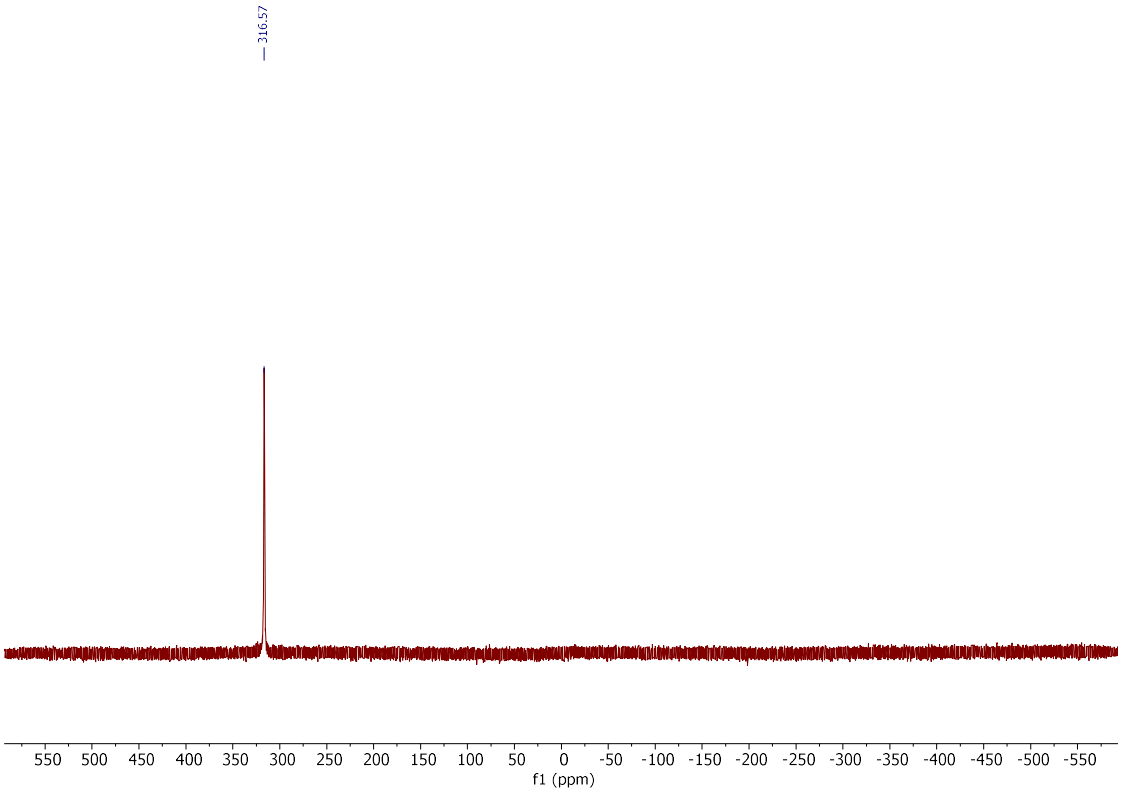

^{19}F NMR (377 MHz, CD_3CN)

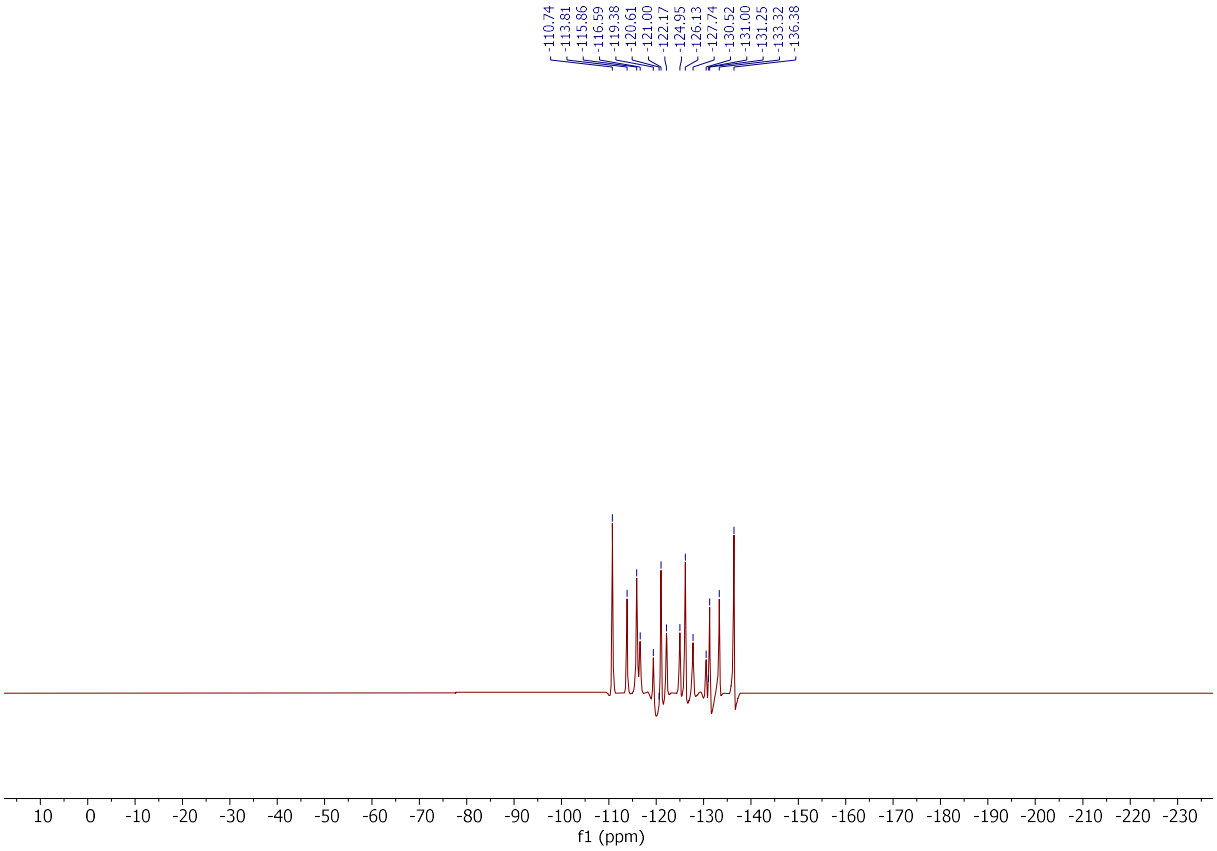

Compound **241**

^{1}H NMR (400 MHz, CD_3CN)

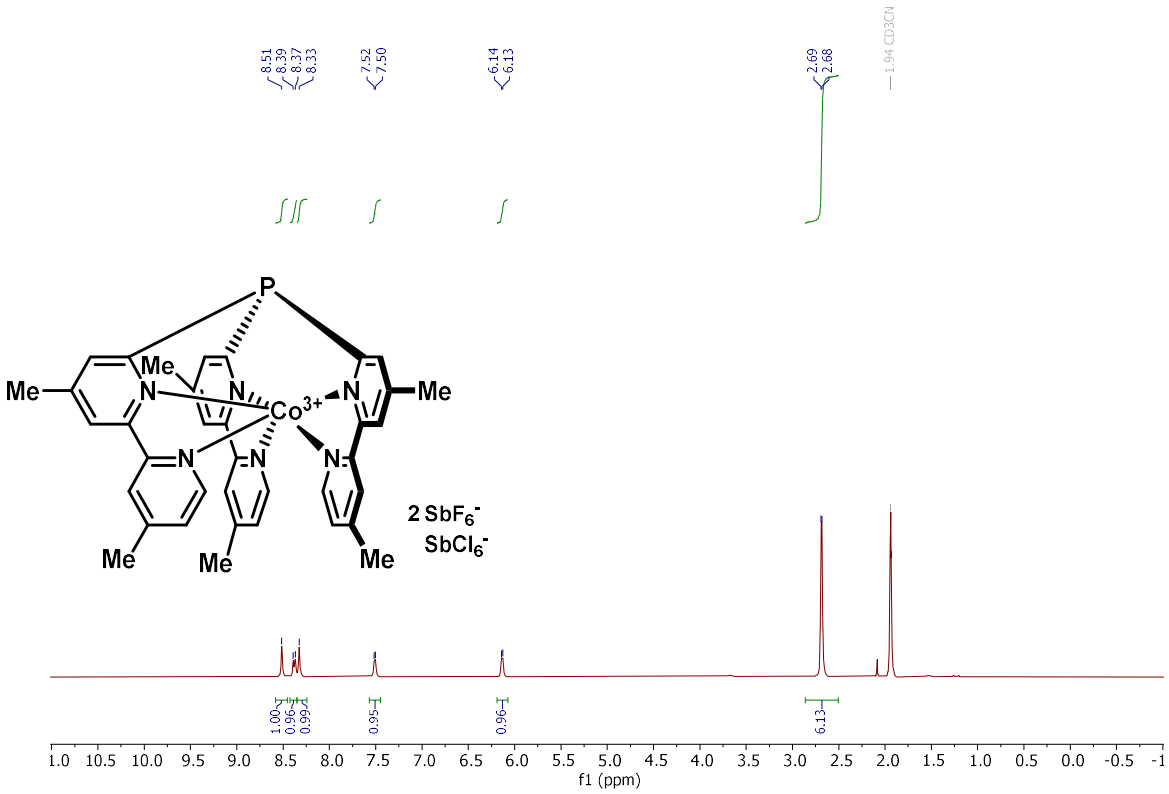

^{13}C{H} NMR (101 MHz, CD_3CN)

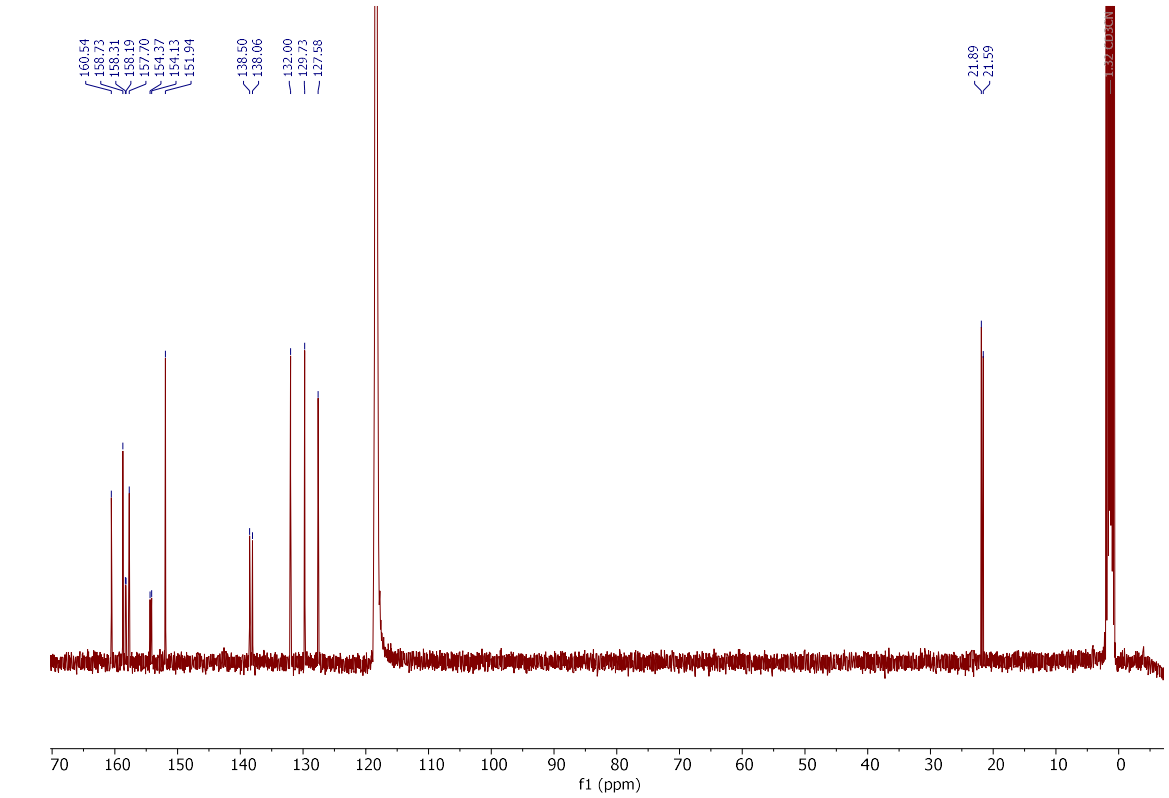

$^{31}P\{H\}$ NMR (162 MHz, CD_3CN)

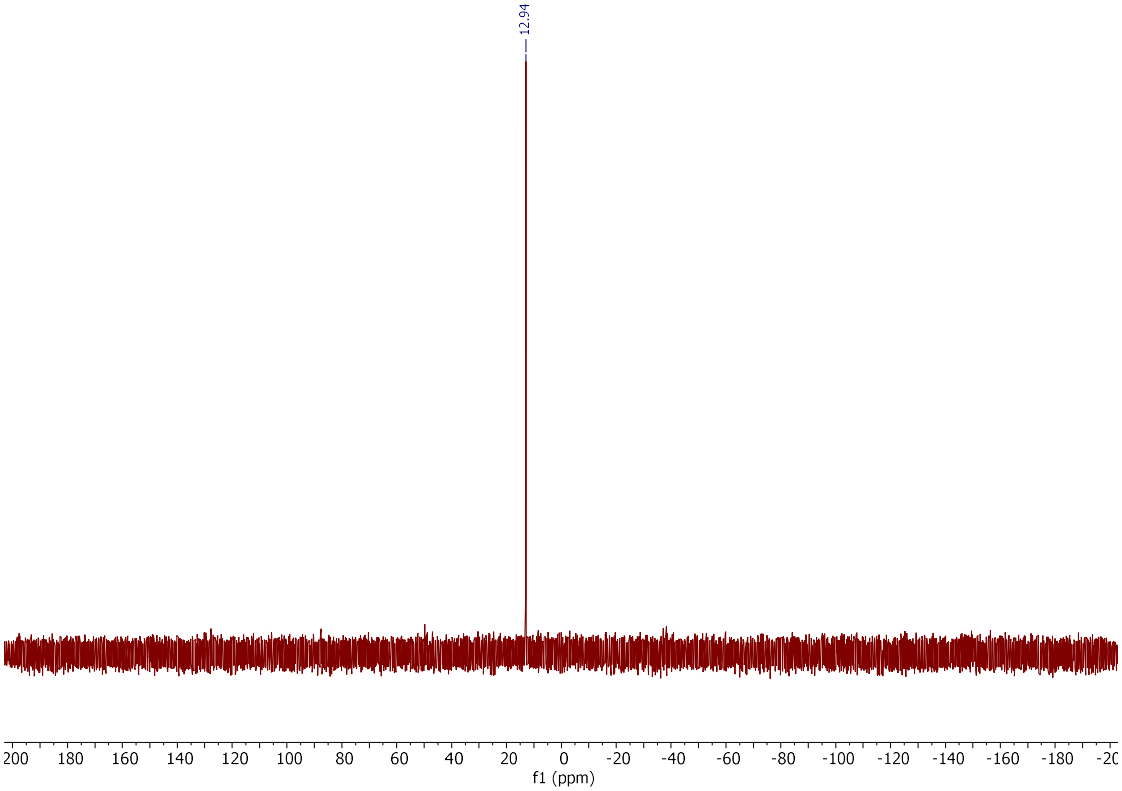

^{19}F NMR (377 MHz, CD_3CN)

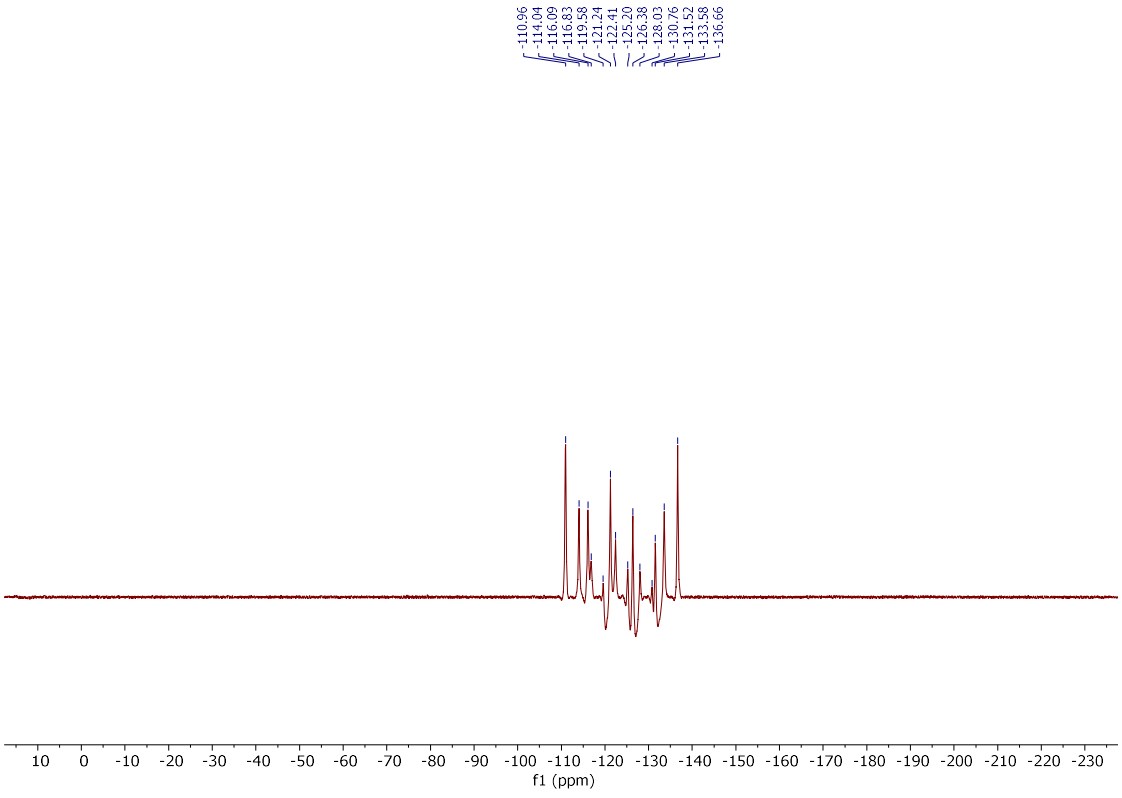

Compound **241b**

^{1}H NMR (400 MHz, CD_2Cl_2)

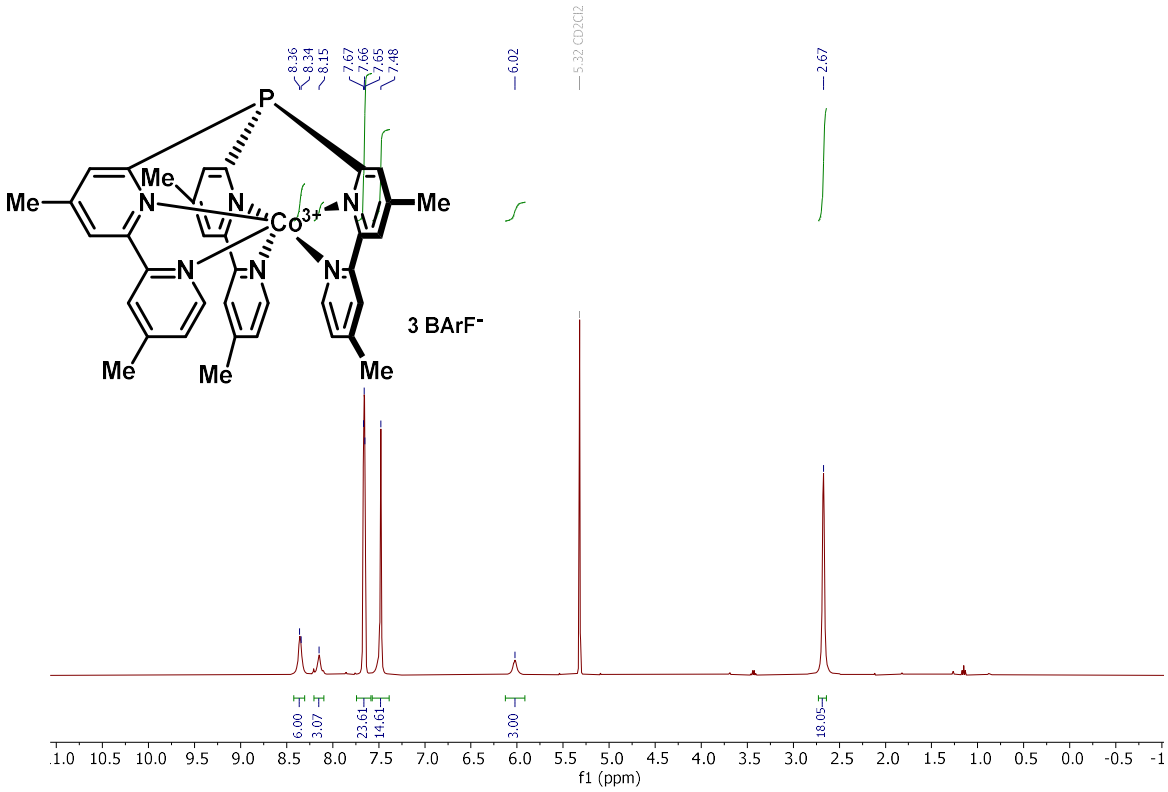

^{13}C{H} NMR (101 MHz, CD_2Cl_2)

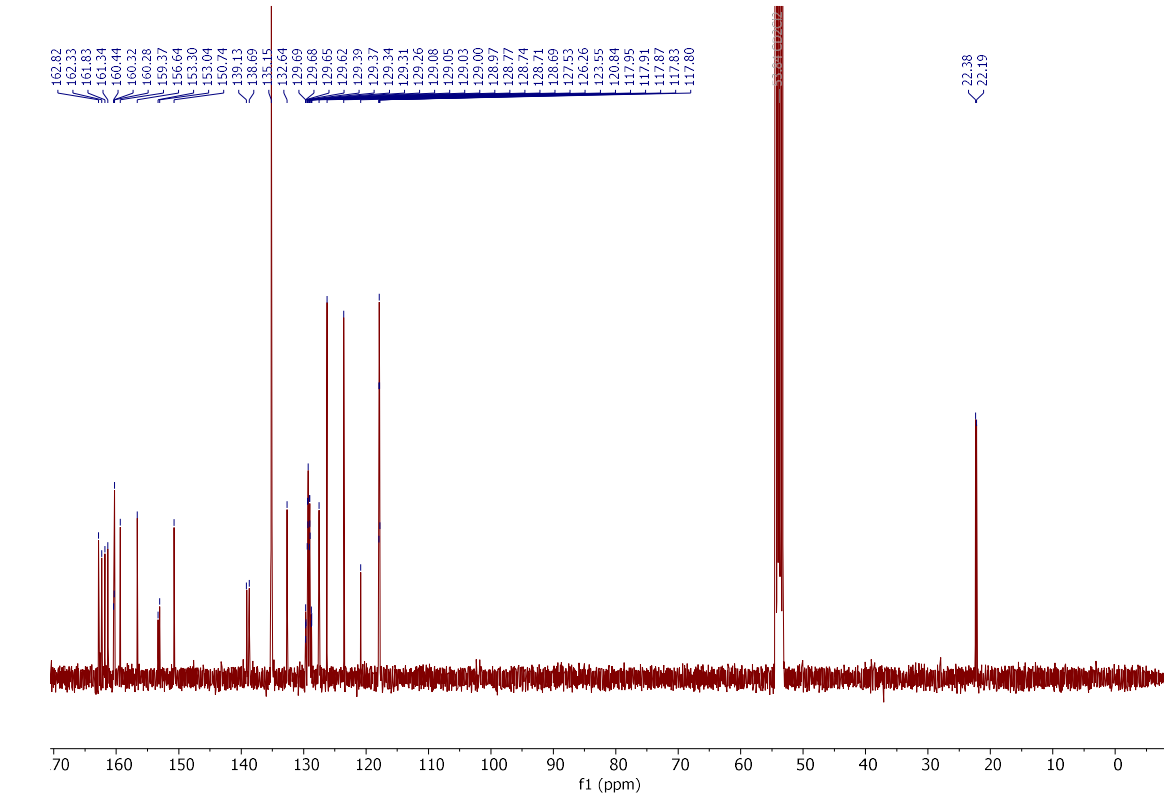

$^{31}P\{H\}$ NMR (162 MHz, CD_2Cl_2)

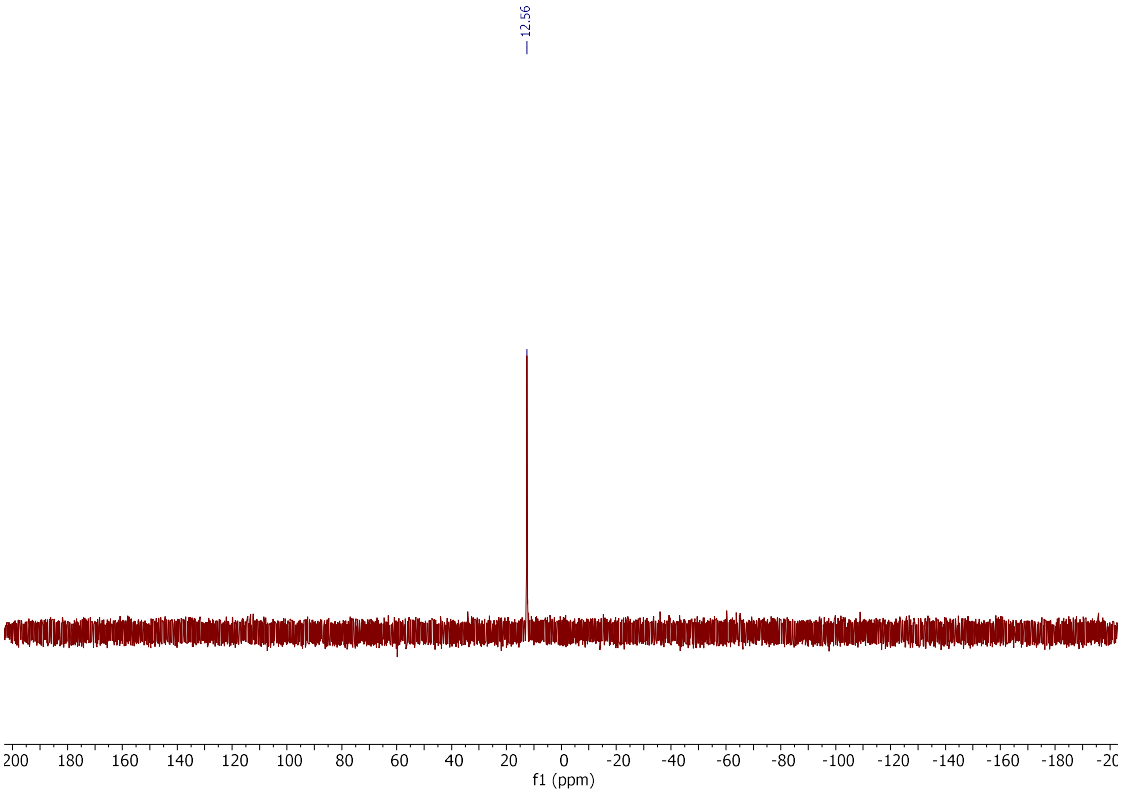

^{19}F NMR (377 MHz, CD_2Cl_2)

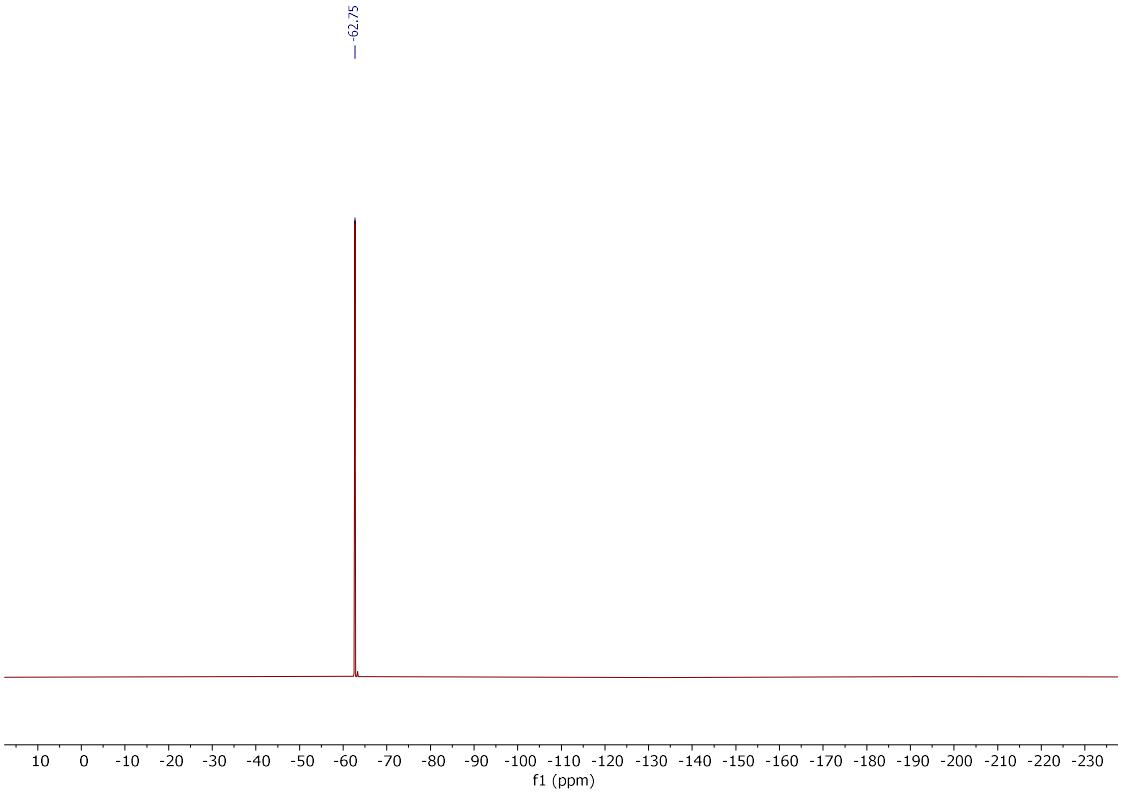

^{11}B NMR (96 MHz, CD_2Cl_2)

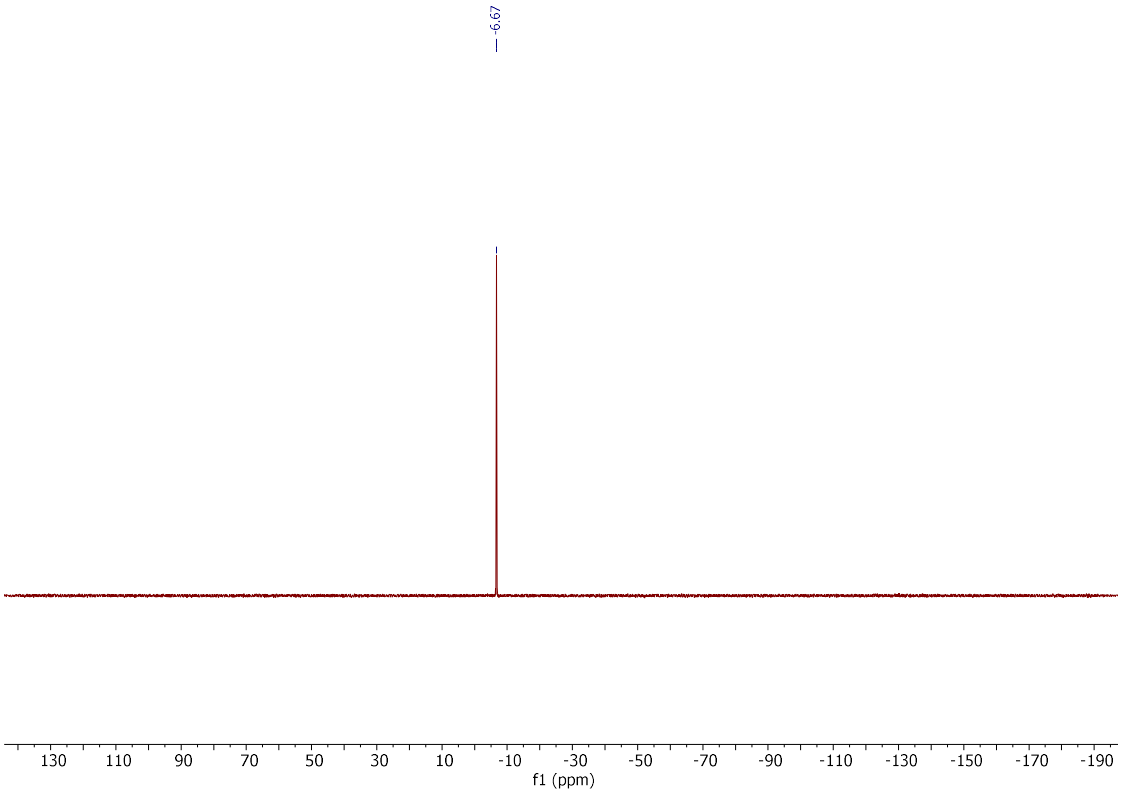

Compound **242**

^{1}H NMR (300 MHz, CD_3CN)

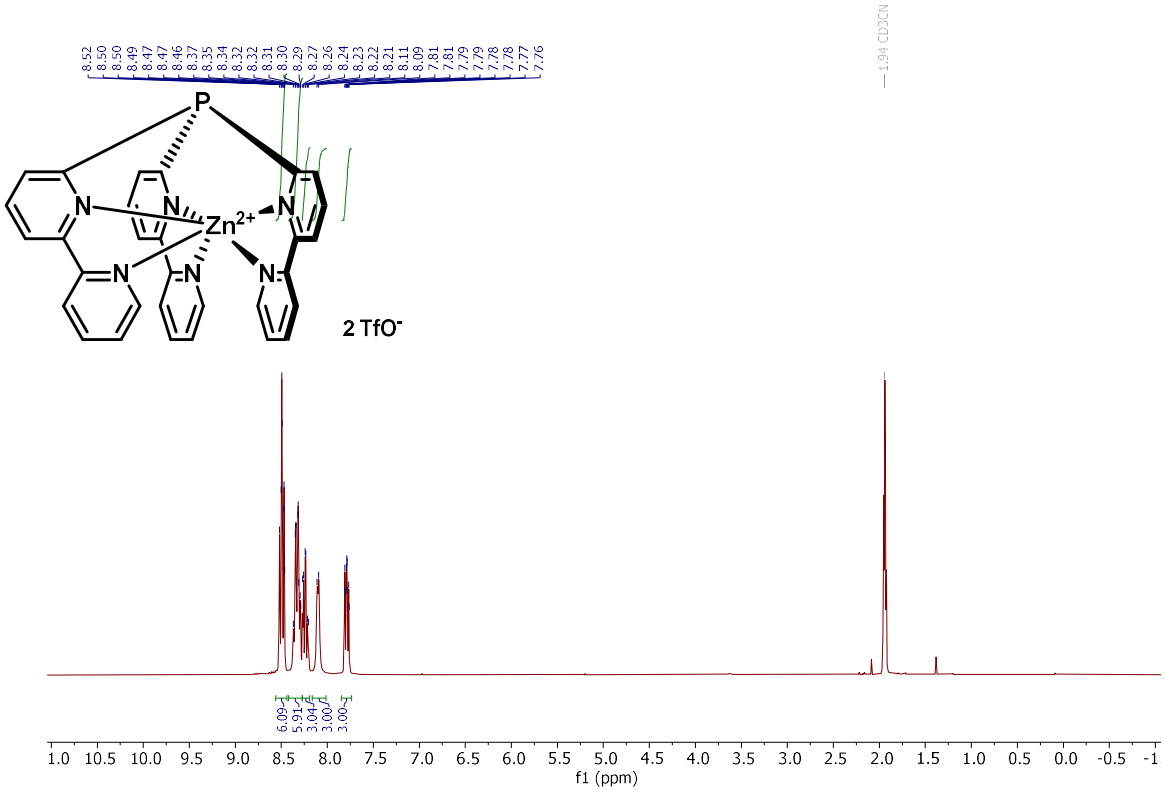

^{13}C{H} NMR (101 MHz, CD_3CN)

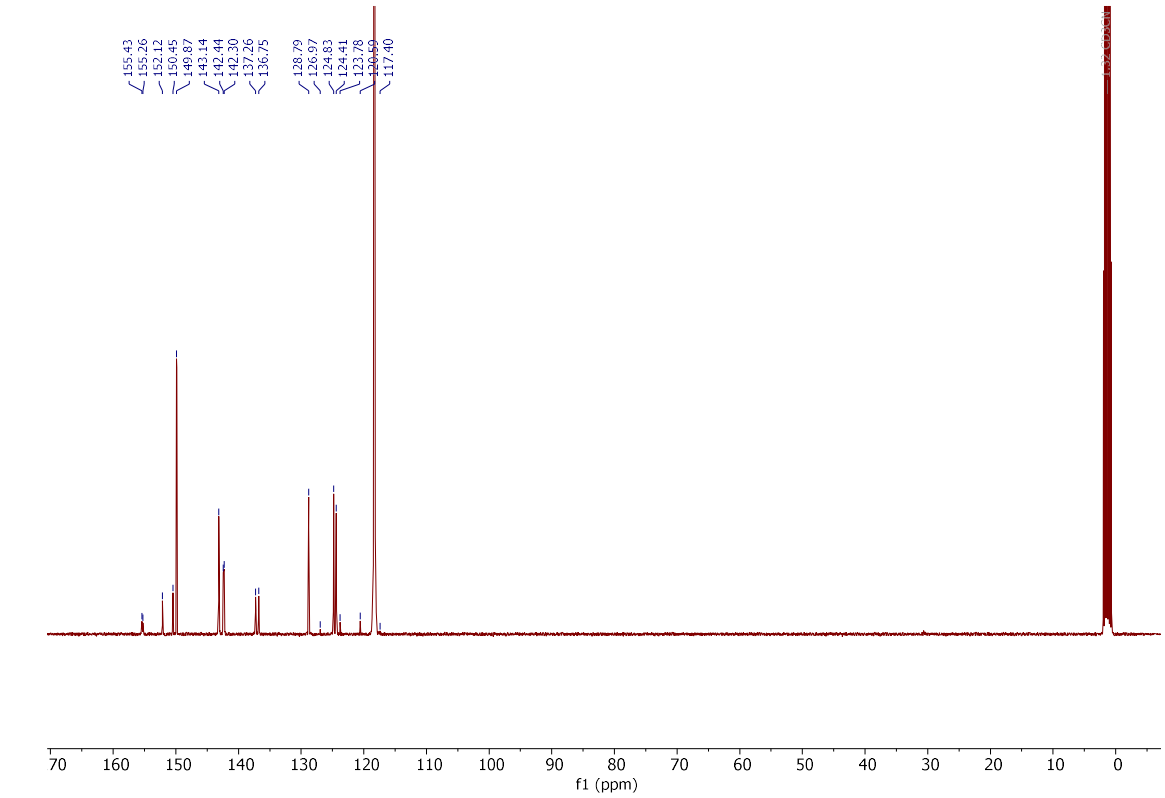

$^{31}P\{H\}$ NMR (121 MHz, CD_3CN)

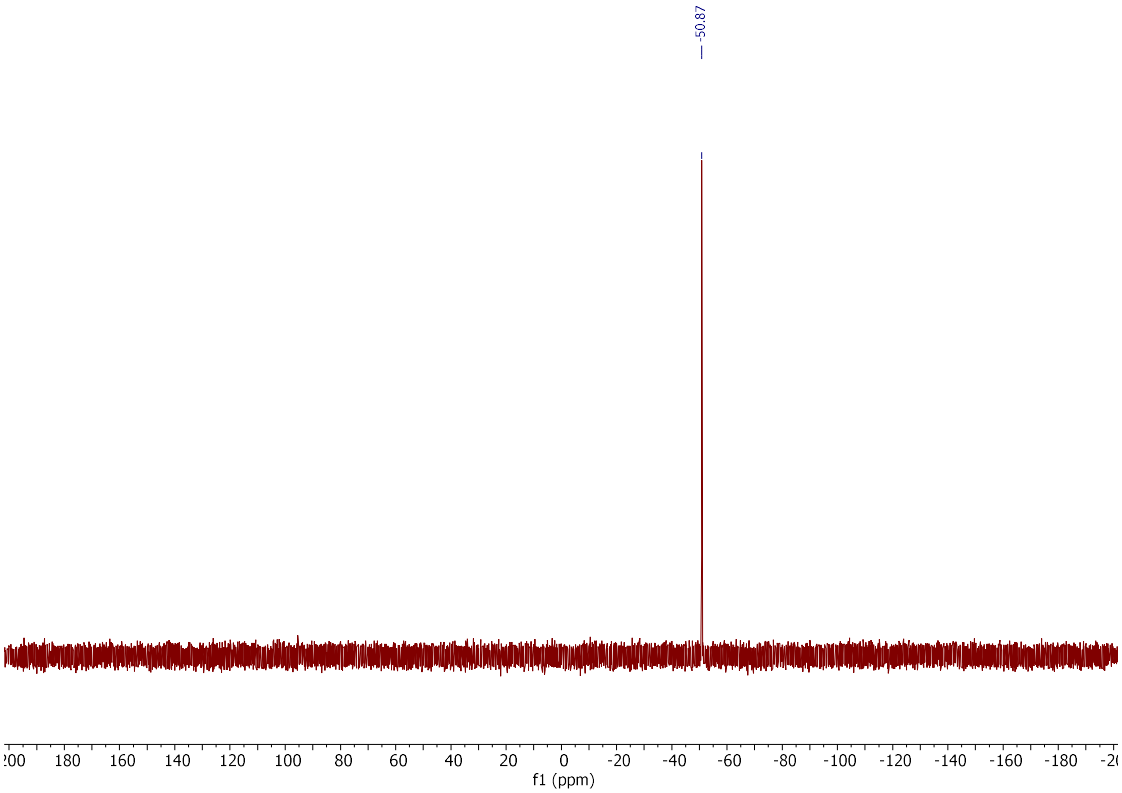

^{19}F NMR (282 MHz, CD_3CN)

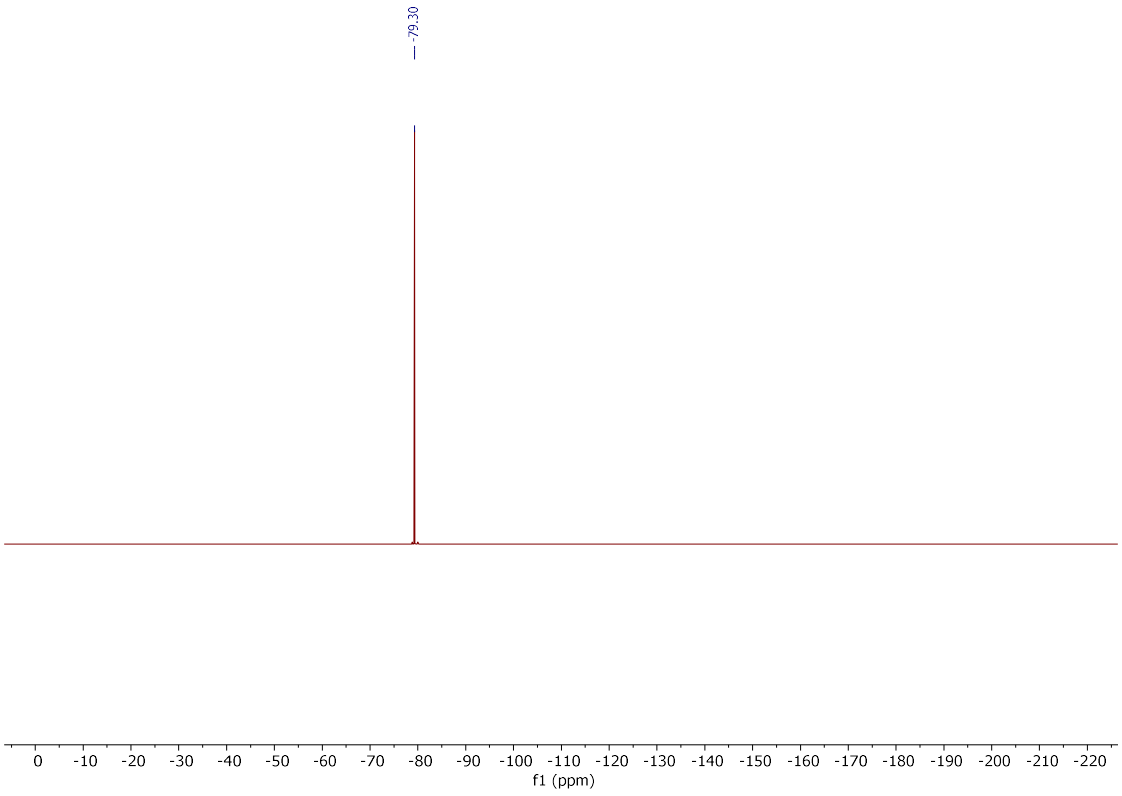

Compound **242b**

^{1}H NMR (600 MHz, CD_3CN)

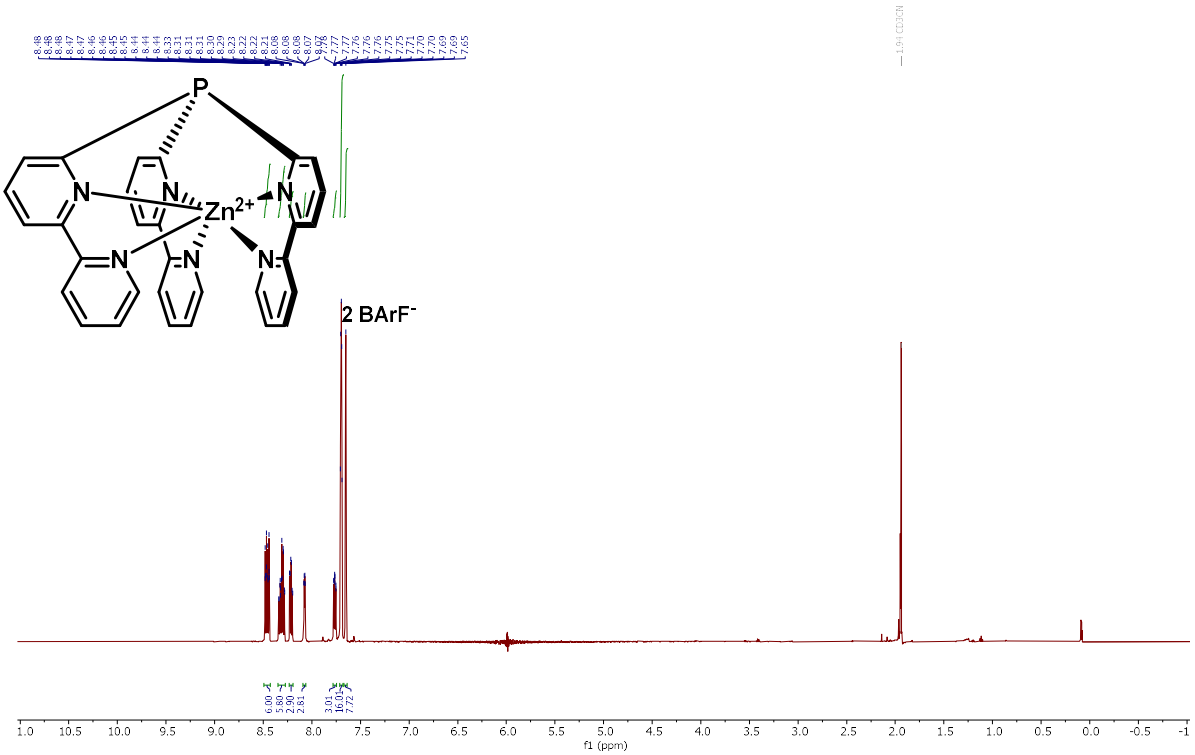

^{13}C{H} NMR (126 MHz, CD_3CN)

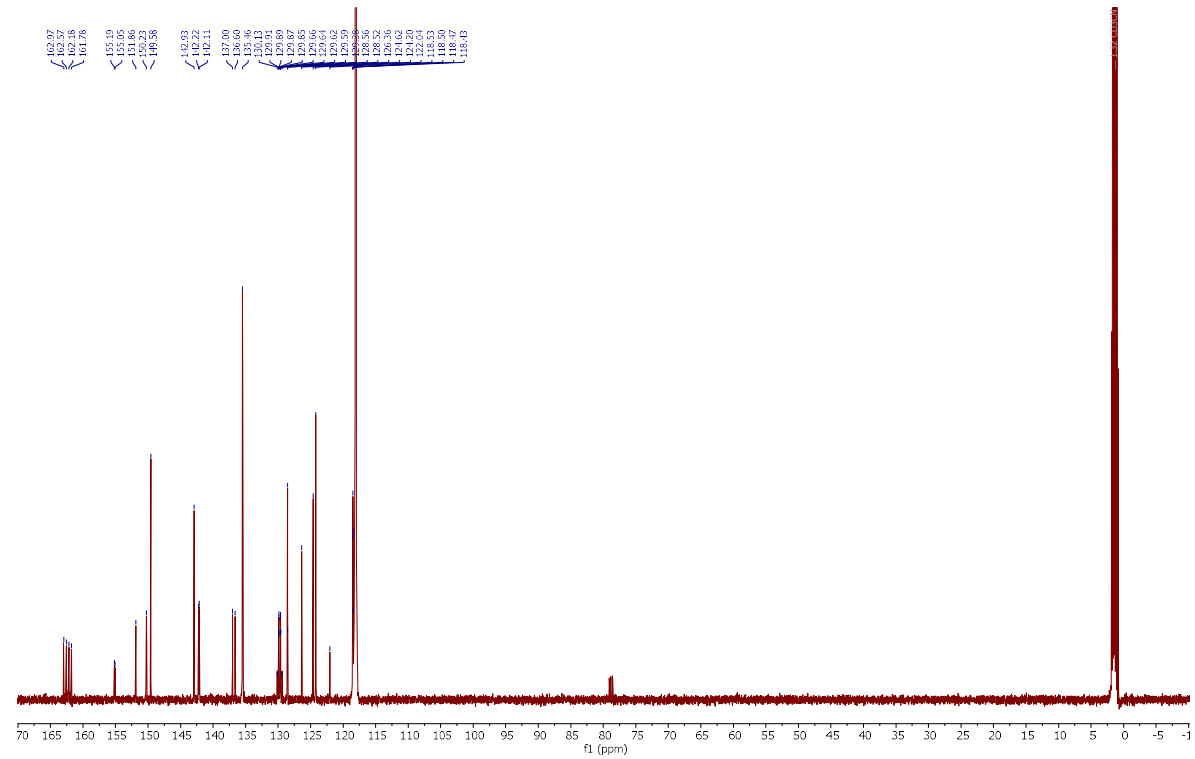

$^{31}P\{H\}$ NMR (121 MHz, CD_3CN)

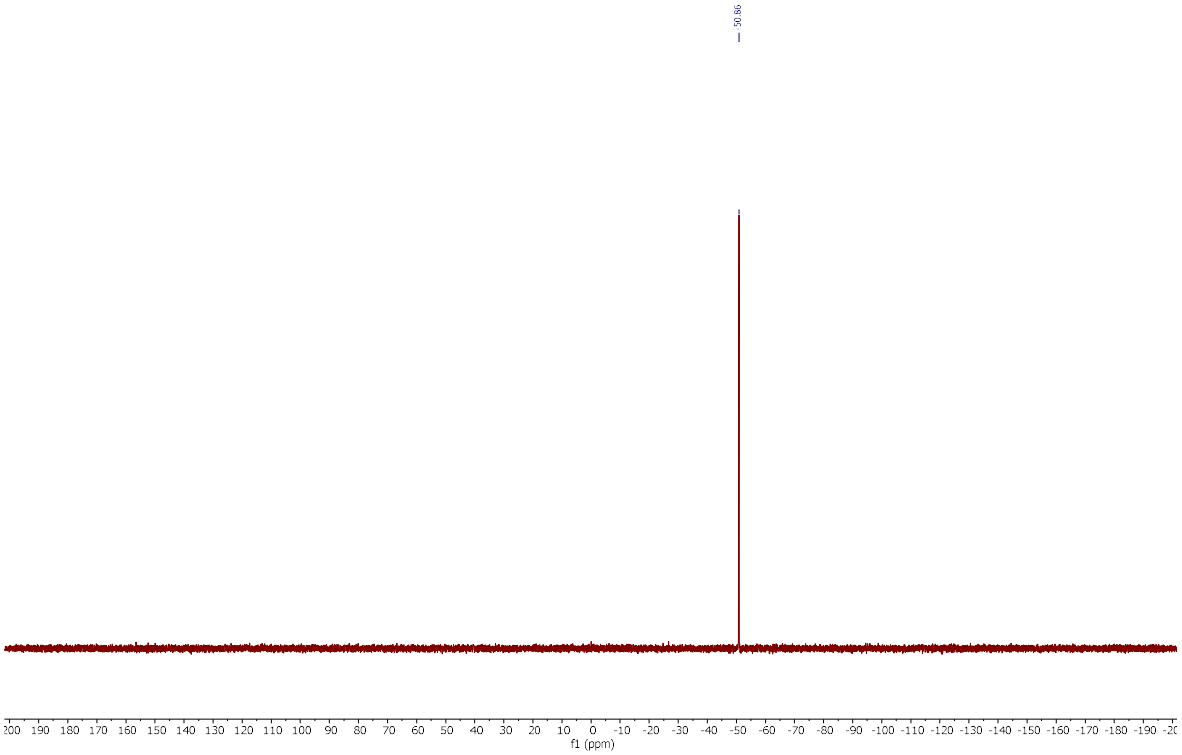

^{19}F NMR (282 MHz, CD_3CN)

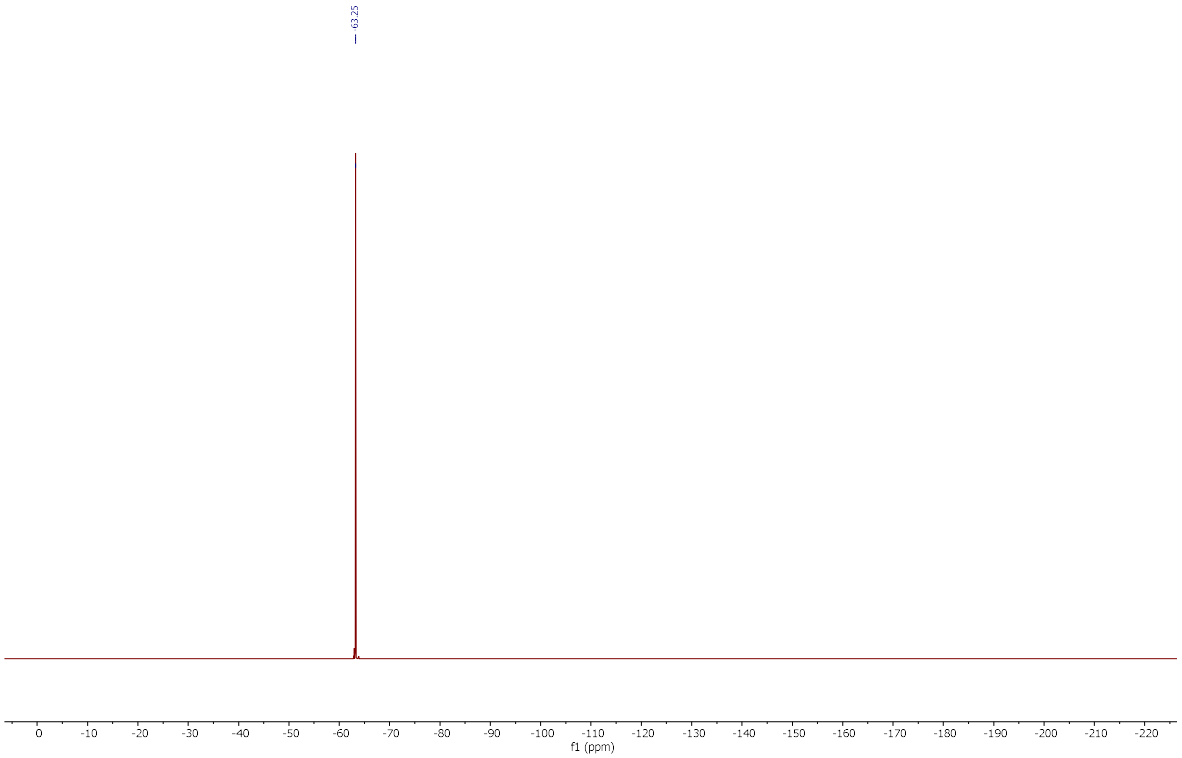

^{11}B NMR (96 MHz, CD_3CN)

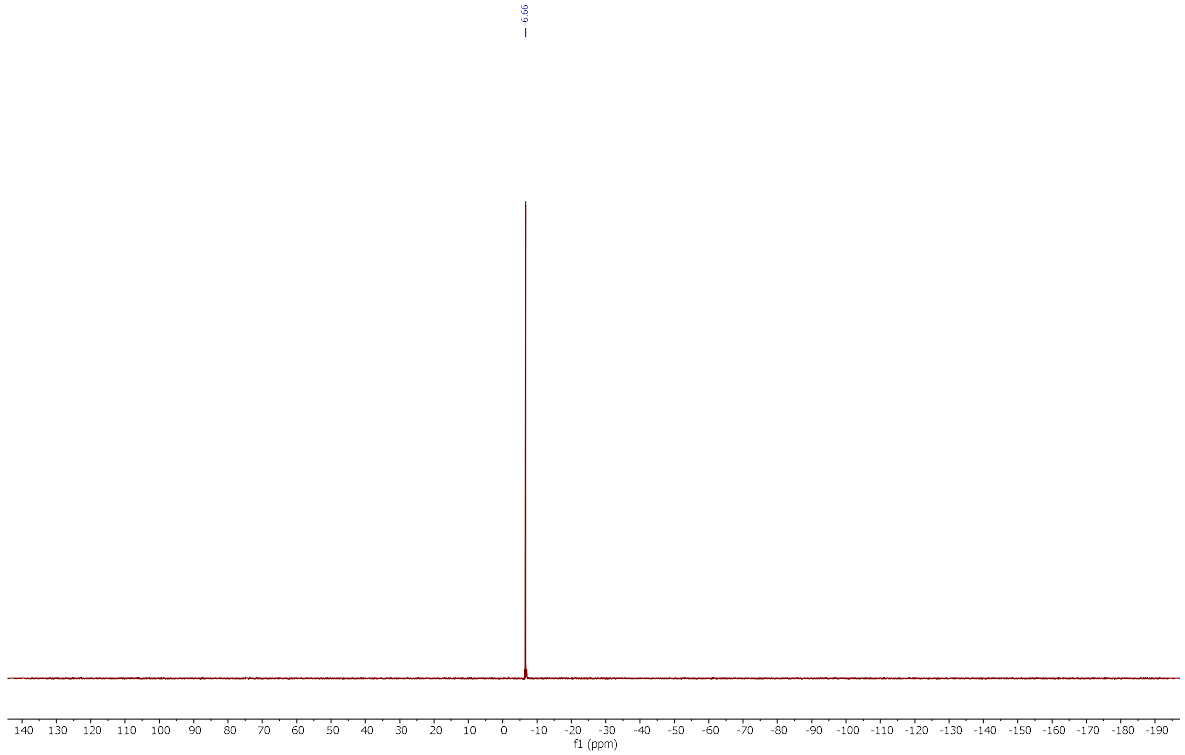

Compound **243**

^{1}H NMR (400 MHz, CD_3CN)

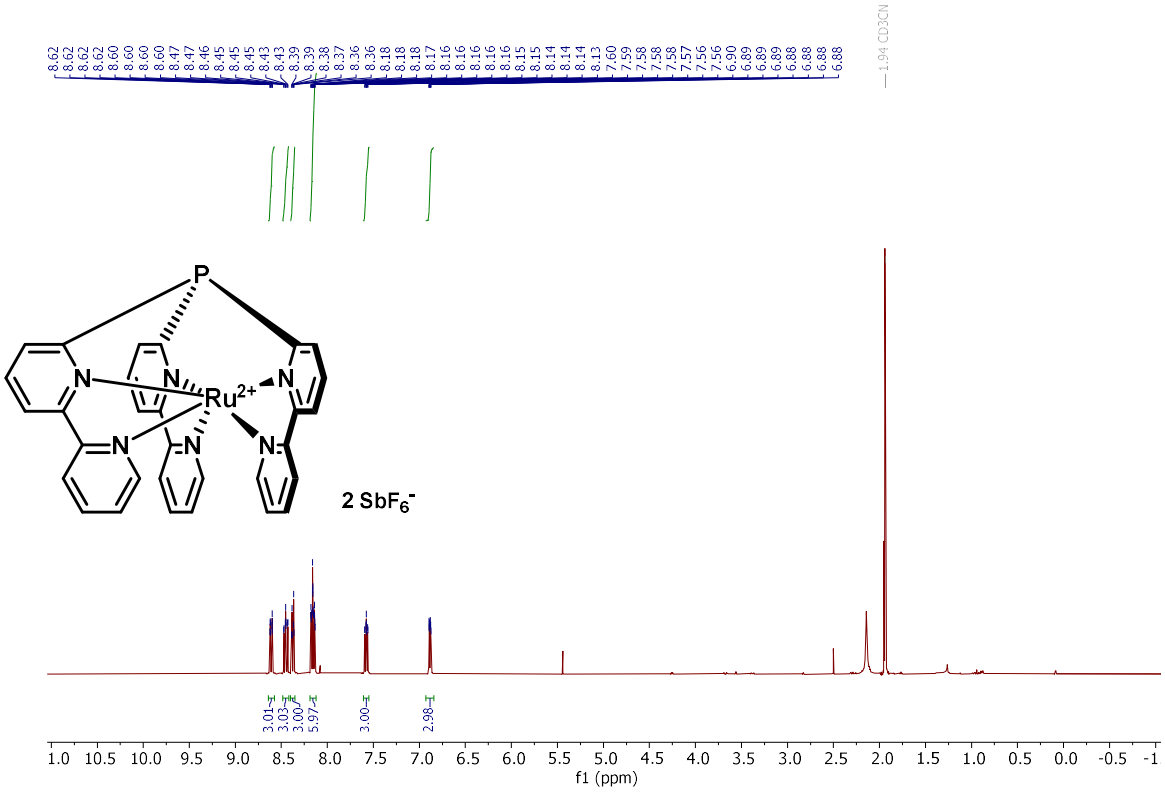

^{13}C{H} NMR (126 MHz, CD_3CN)

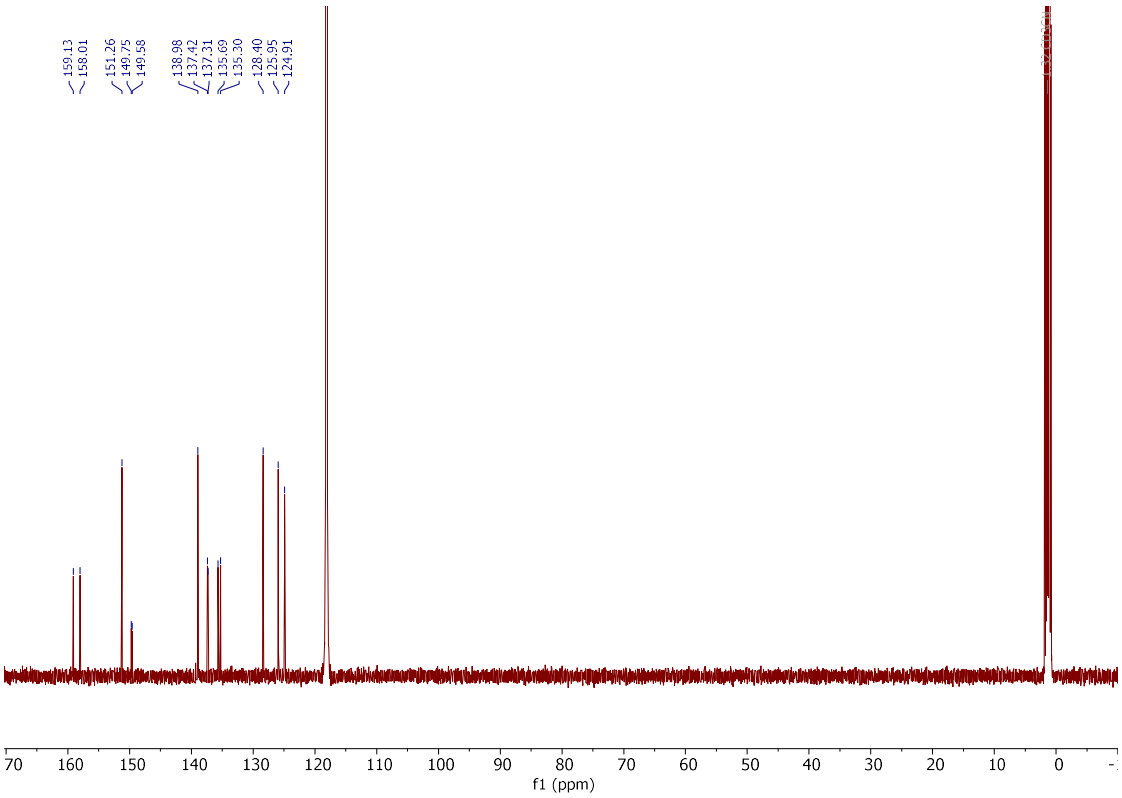

$^{31}P\{H\}$ NMR (162 MHz, CD_3CN)

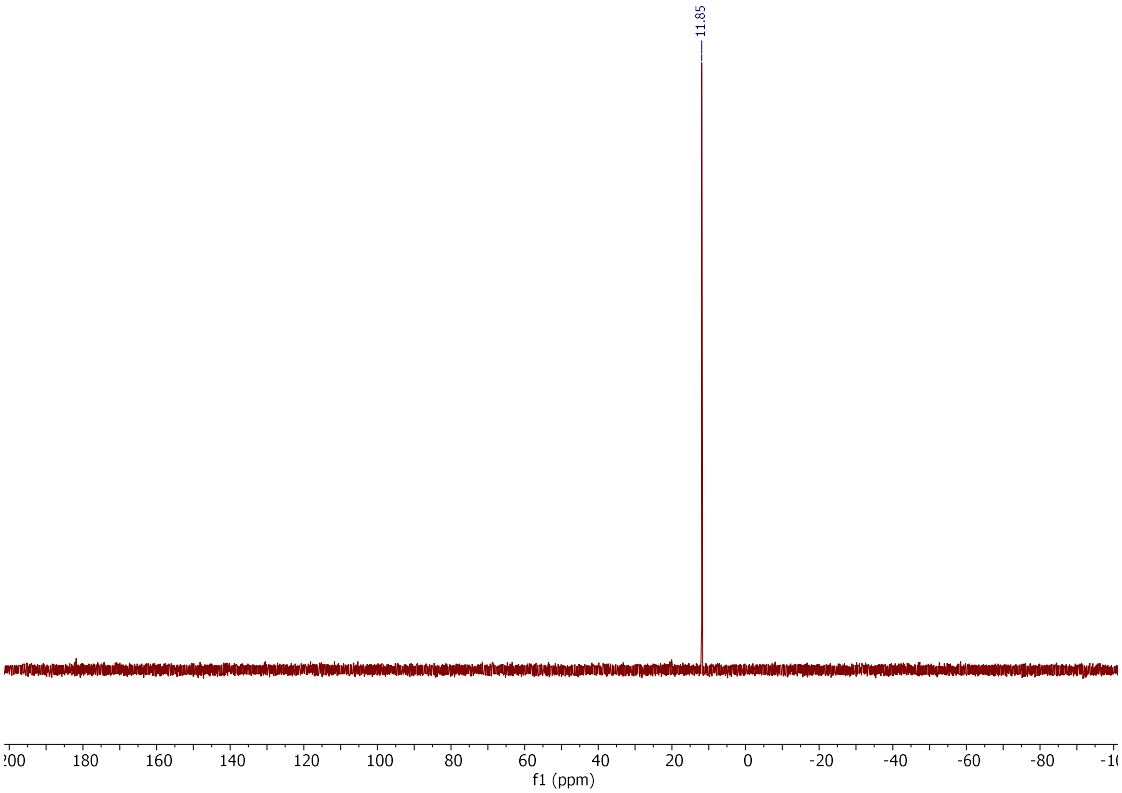

^{19}F NMR (376 MHz, CD_3CN)

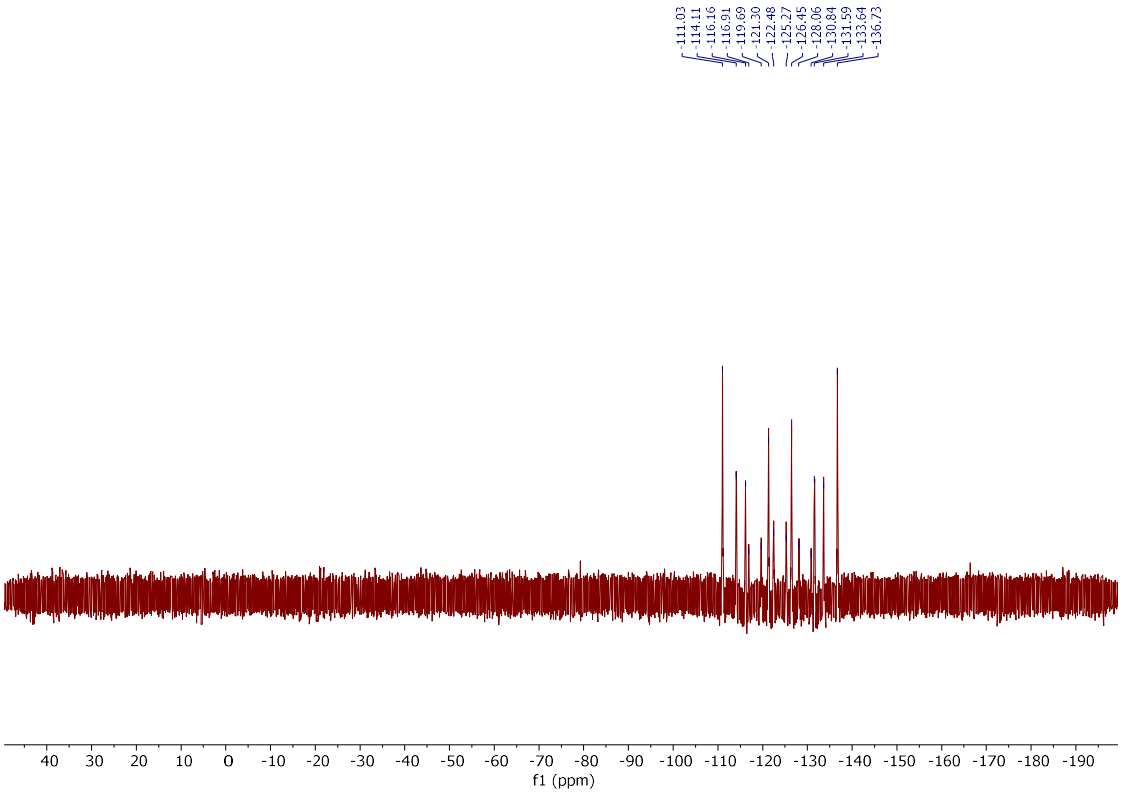

Compound **244**

^{1}H NMR (300 MHz, CD_3CN)

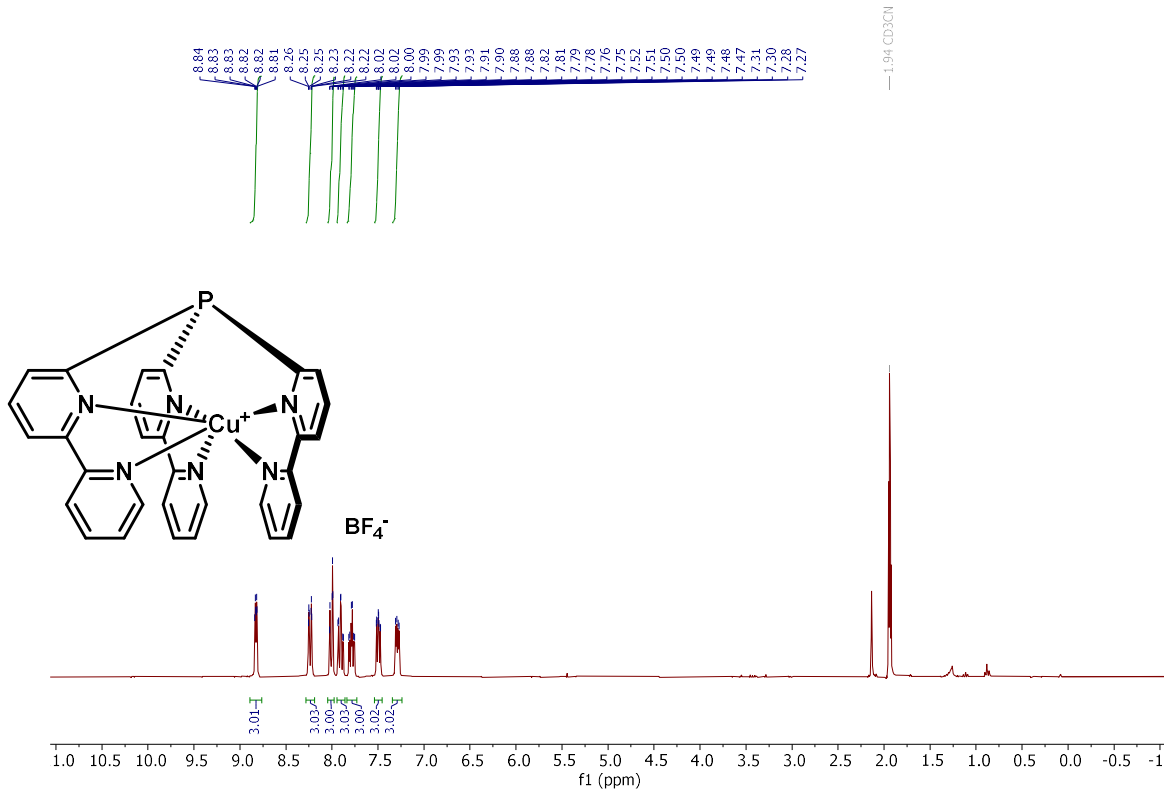

^{13}C NMR (101 MHz, CD_3CN)

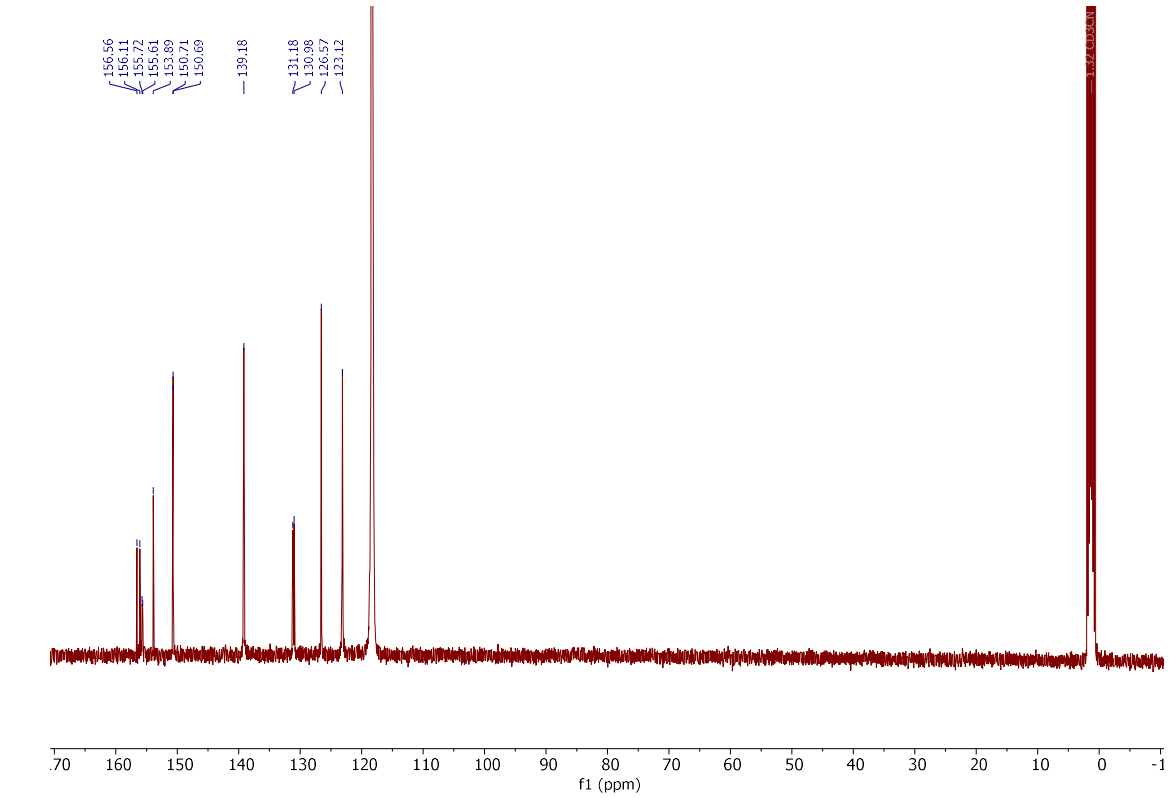

^{31}P{H} NMR (203 MHz, CD_3CN)

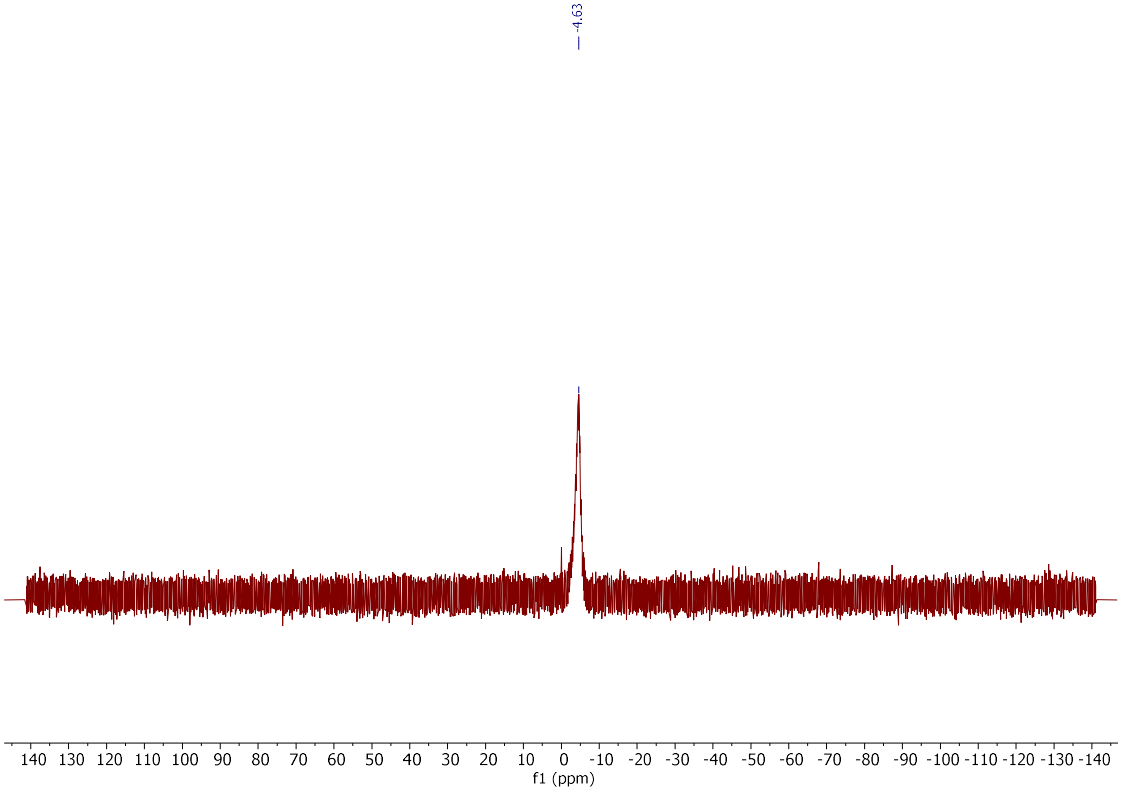

^{19}F NMR (376 MHz, CD_3CN)

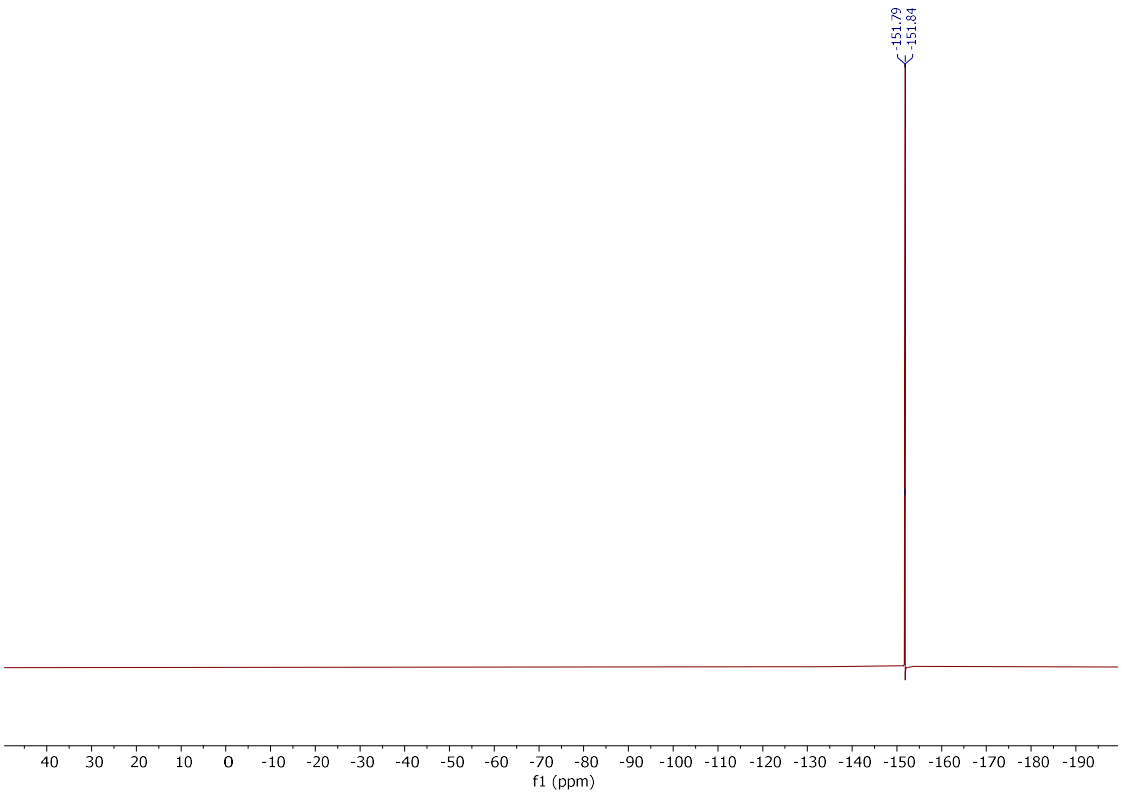

^{11}B NMR (96 MHz, CD_3CN)

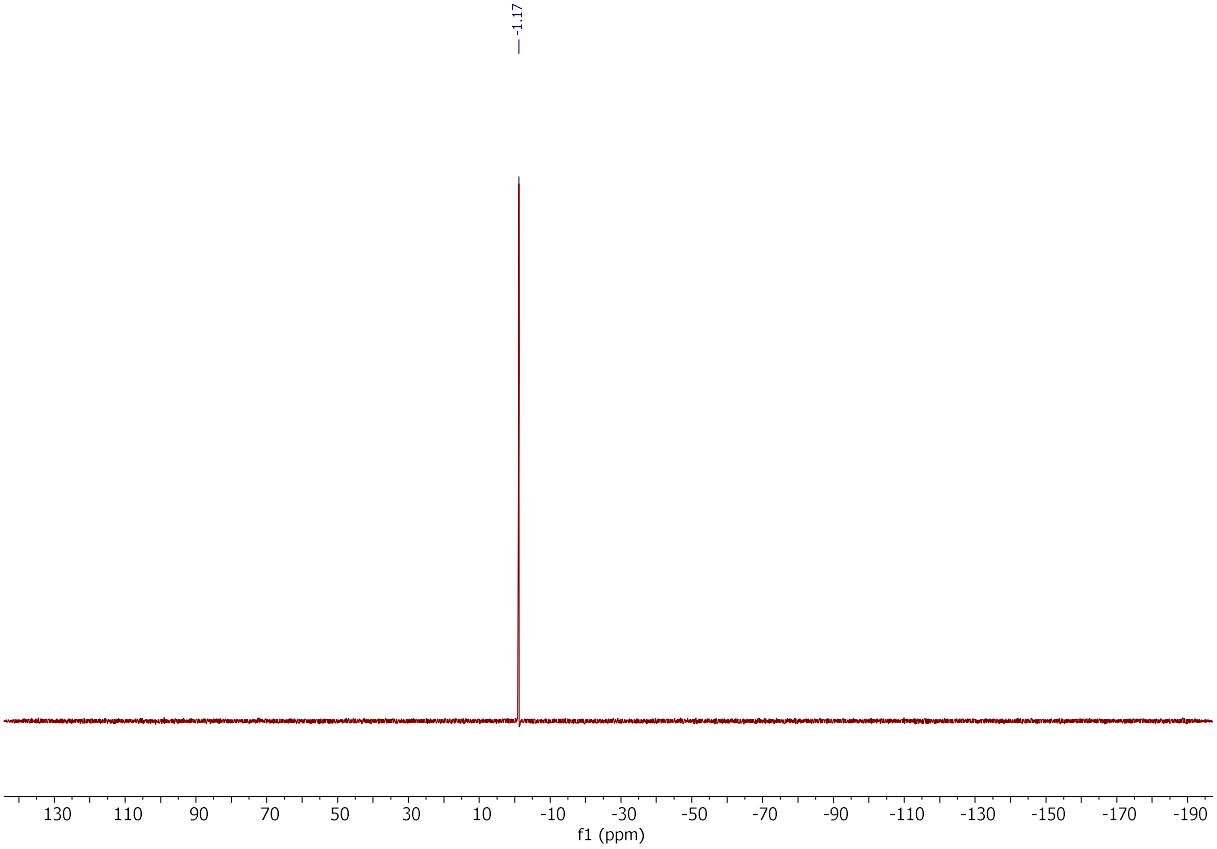

Compound **245**

^{1}H NMR (300 MHz, CD_3CN)

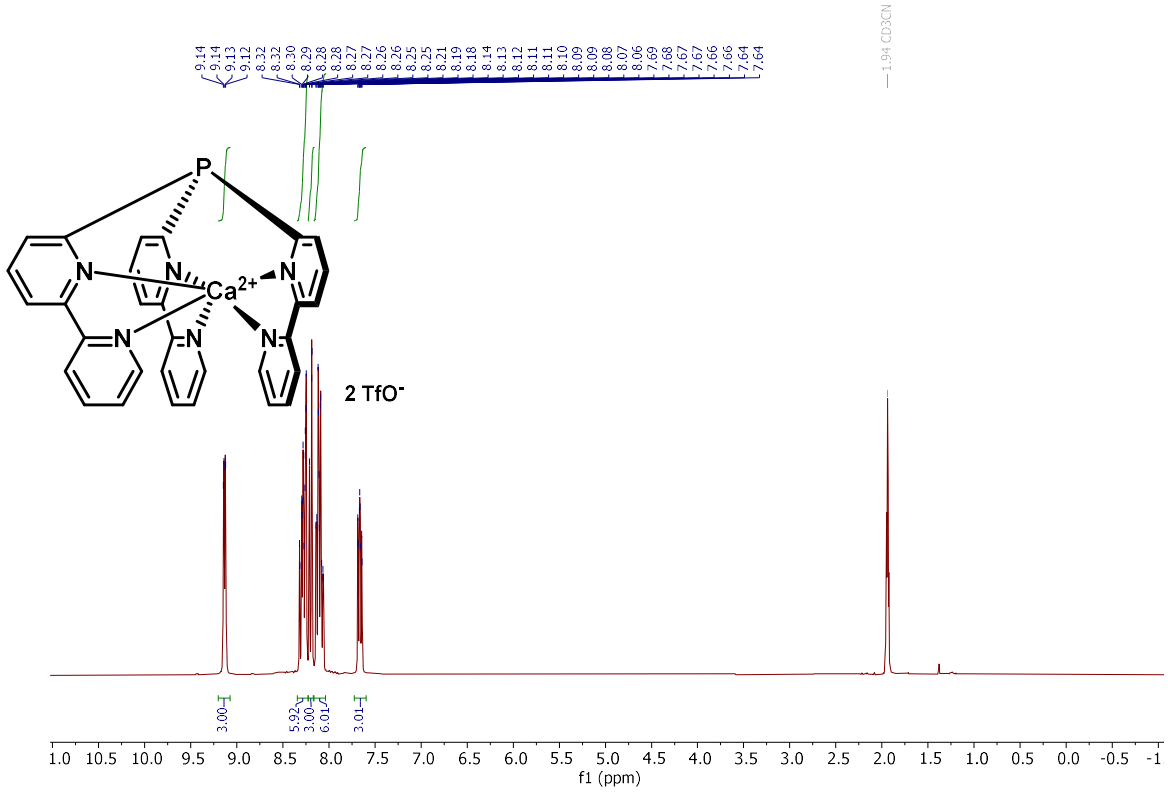

^{13}C{H} NMR (101 MHz, CD_3CN)

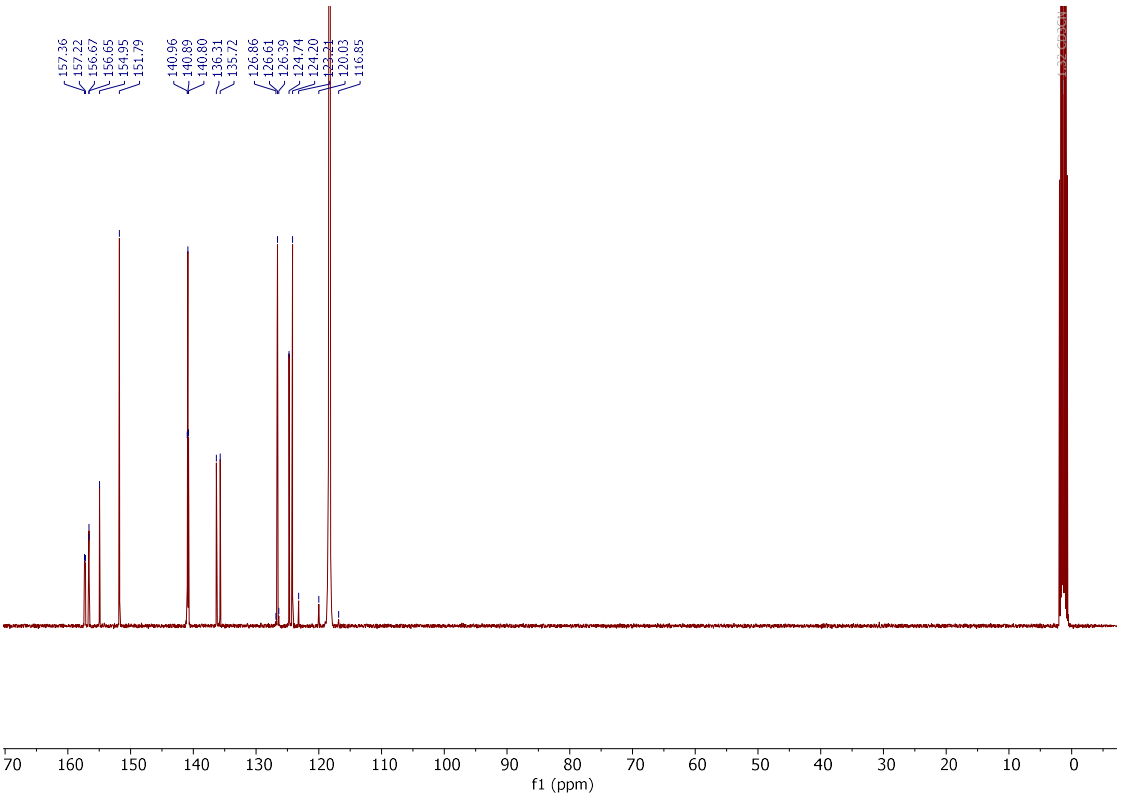

$^{31}P\{H\}$ NMR (121 MHz, CD_3CN)

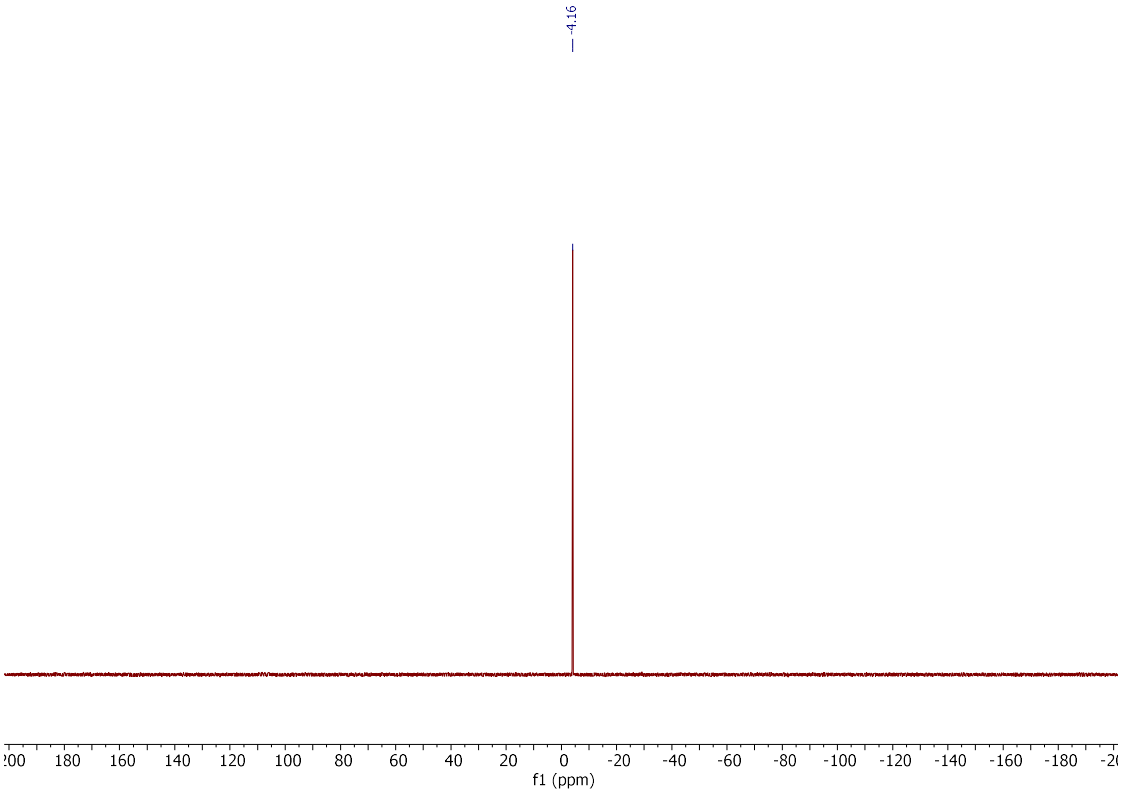

^{19}F NMR (282 MHz, CD_3CN)

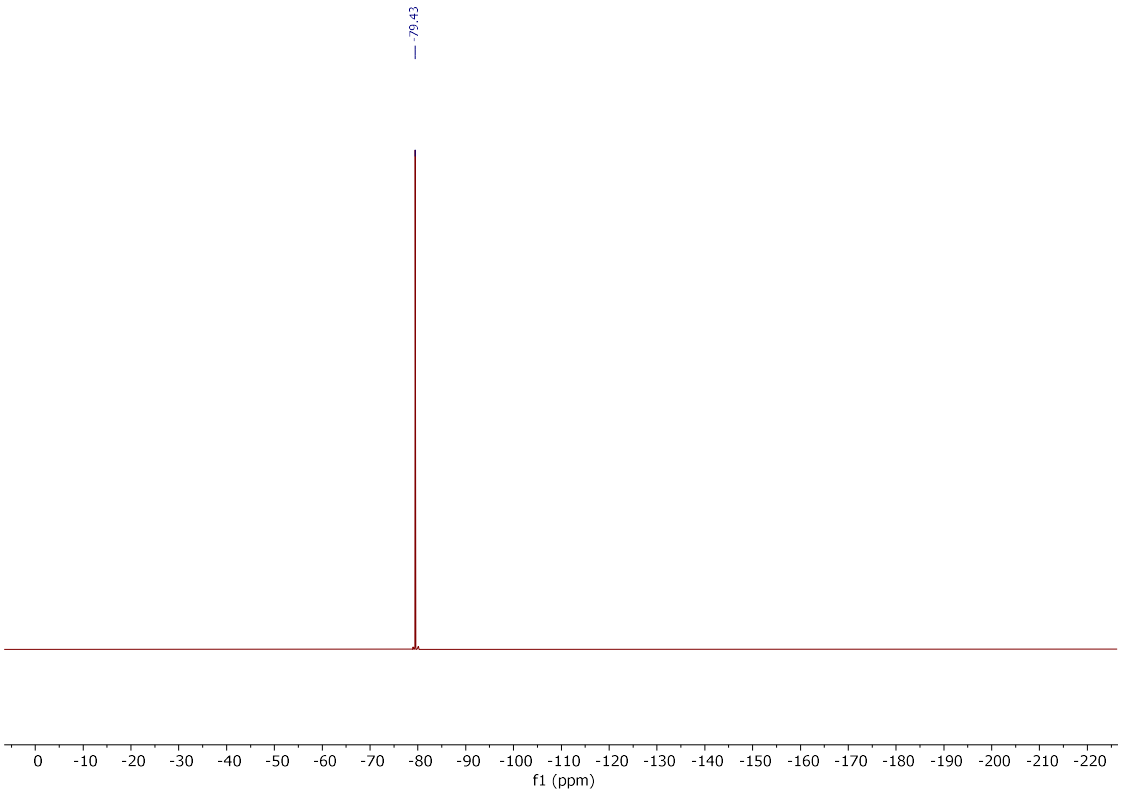

Compound **246**

^{1}H NMR (300 MHz, CD_3CN)

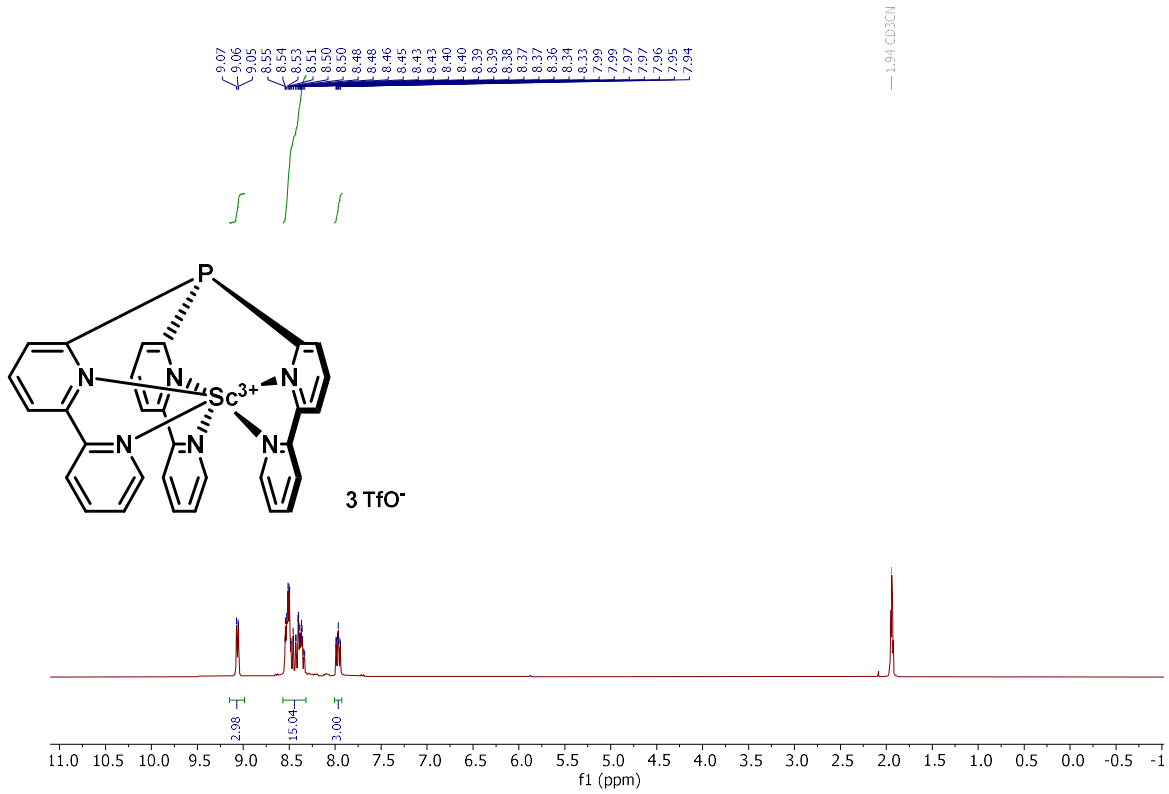

^{13}C{H} NMR (101 MHz, CD_3CN)

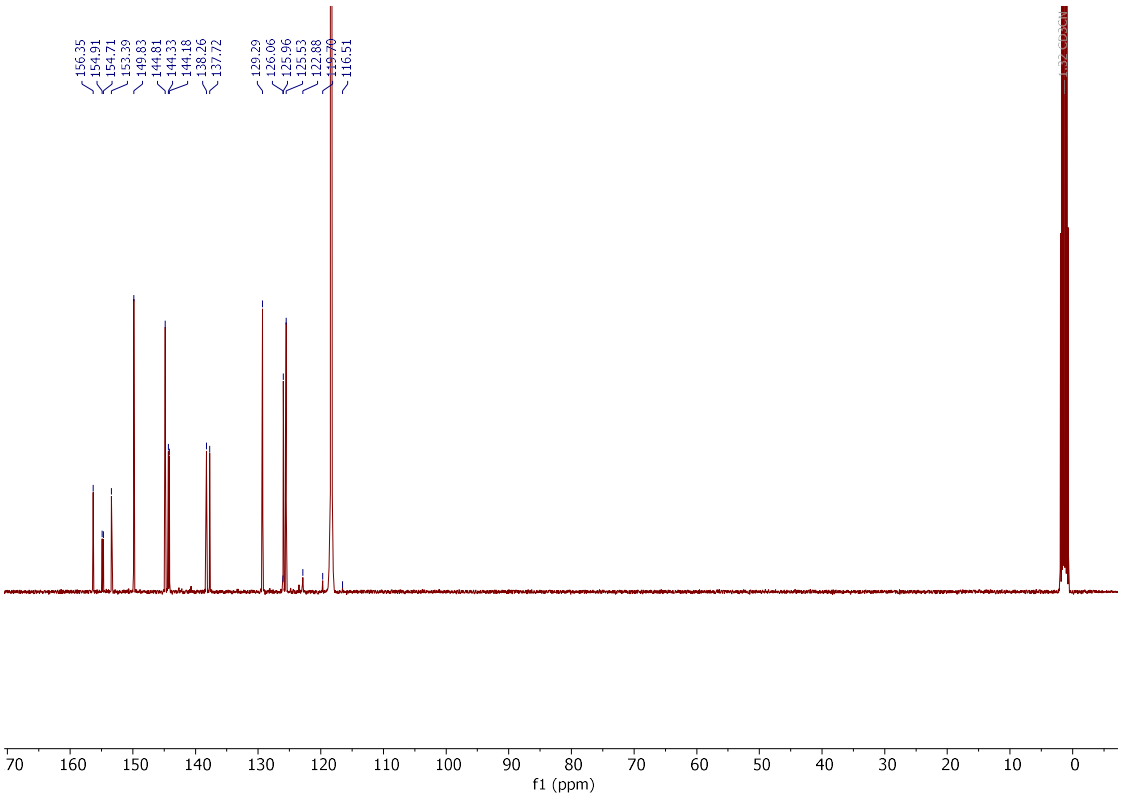

$^{31}P\{H\}$ NMR (162 MHz, CD_3CN)

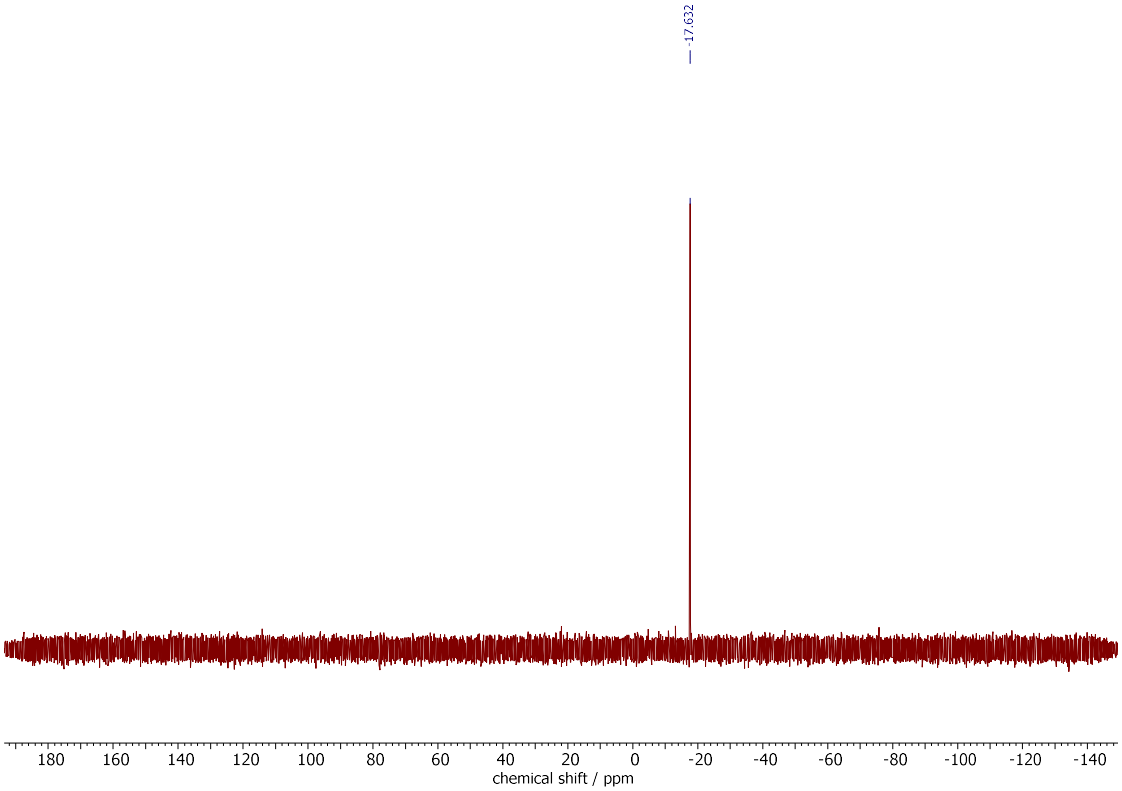

^{19}F NMR (282 MHz, CD_3CN)

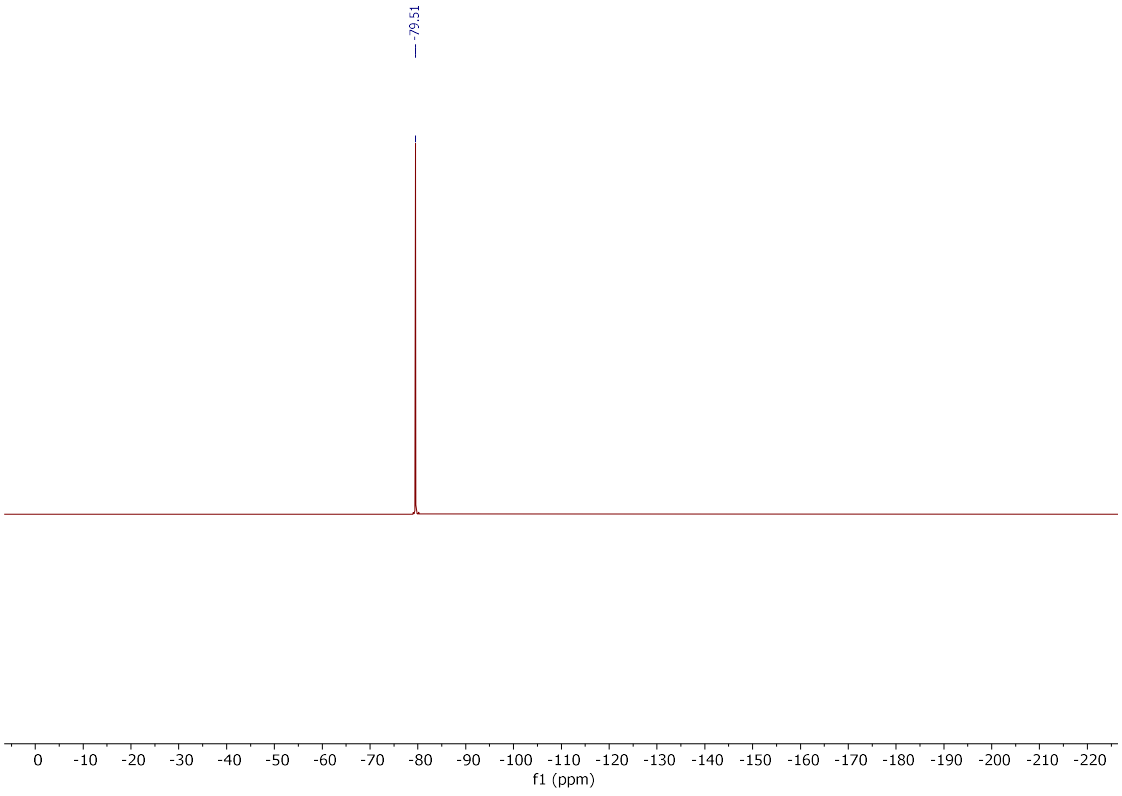

Compound **247**

^{1}H NMR (400 MHz, CD_3CN)

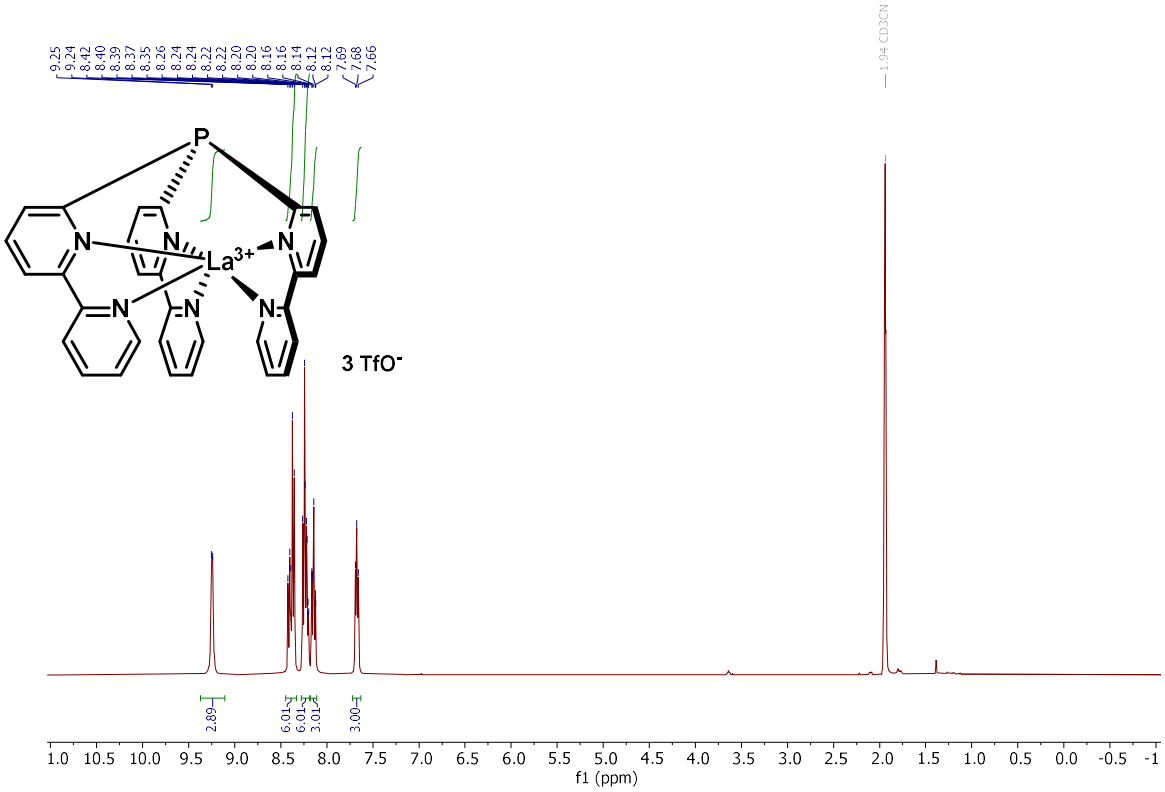

^{13}C{H} NMR (101 MHz, CD_3CN)

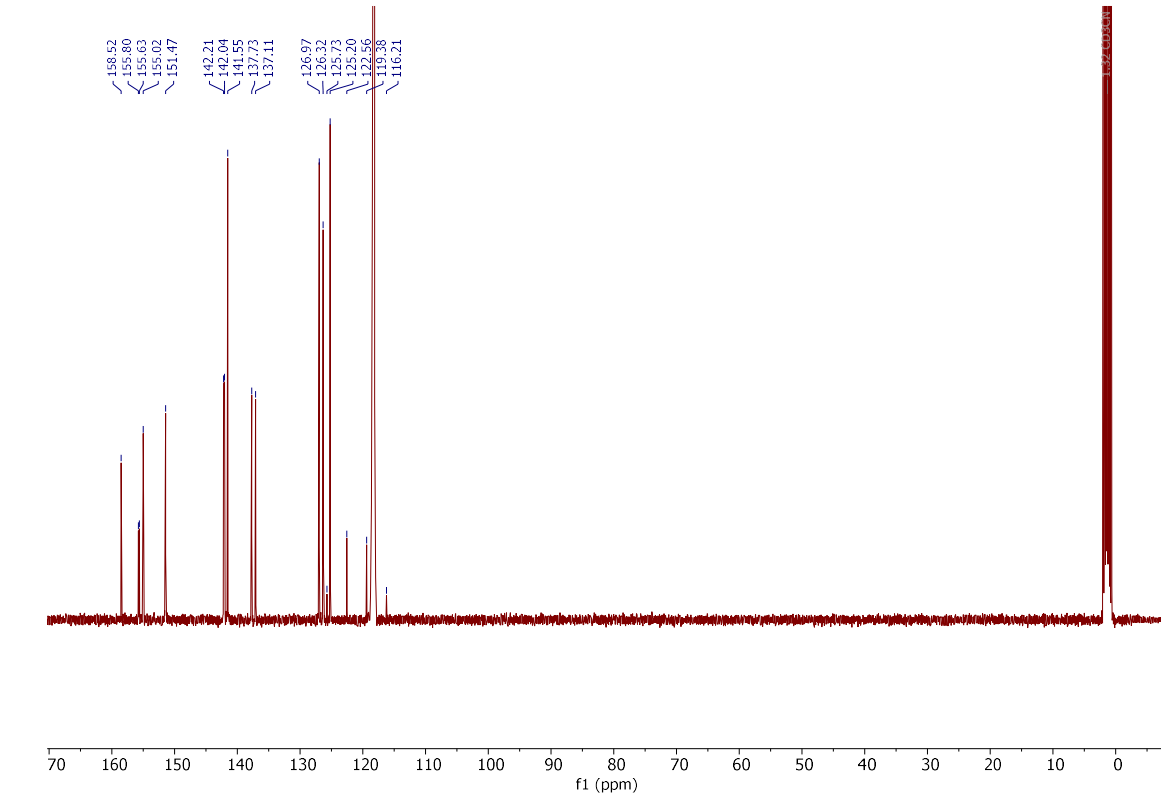

$^{31}P\{H\}$ NMR (162 MHz, CD_3CN)

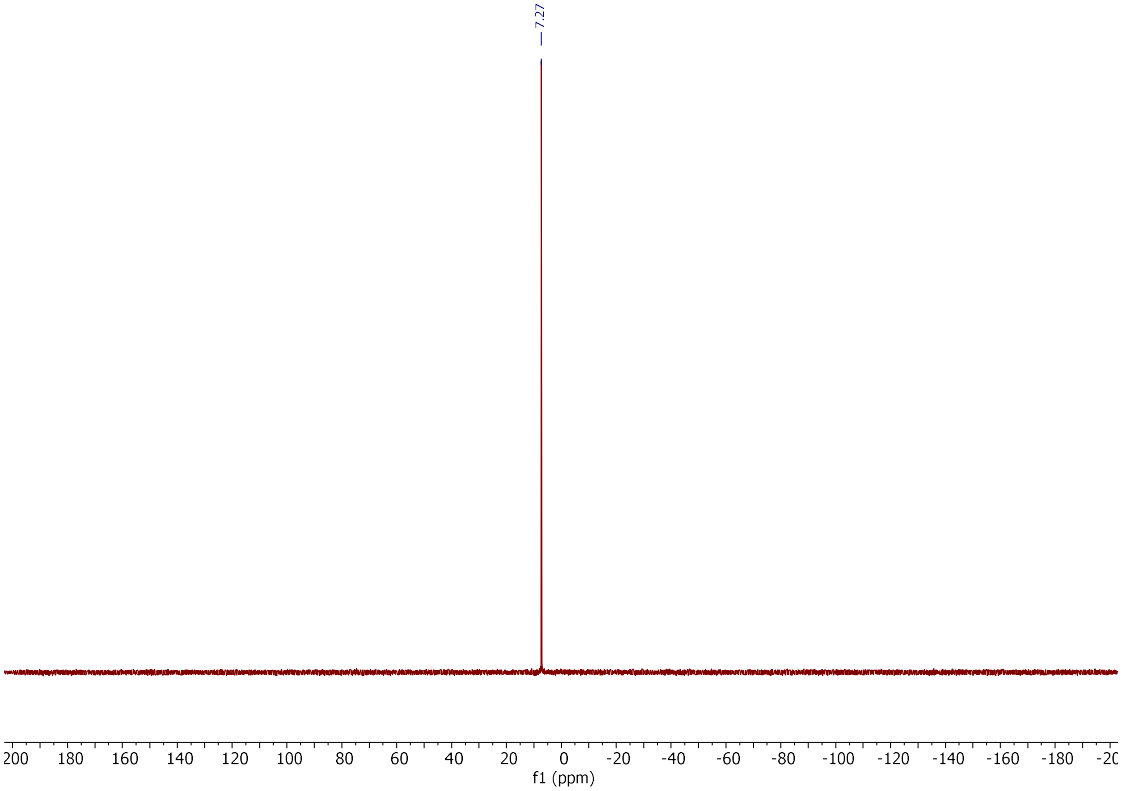

^{19}F NMR (377 MHz, CD_3CN)

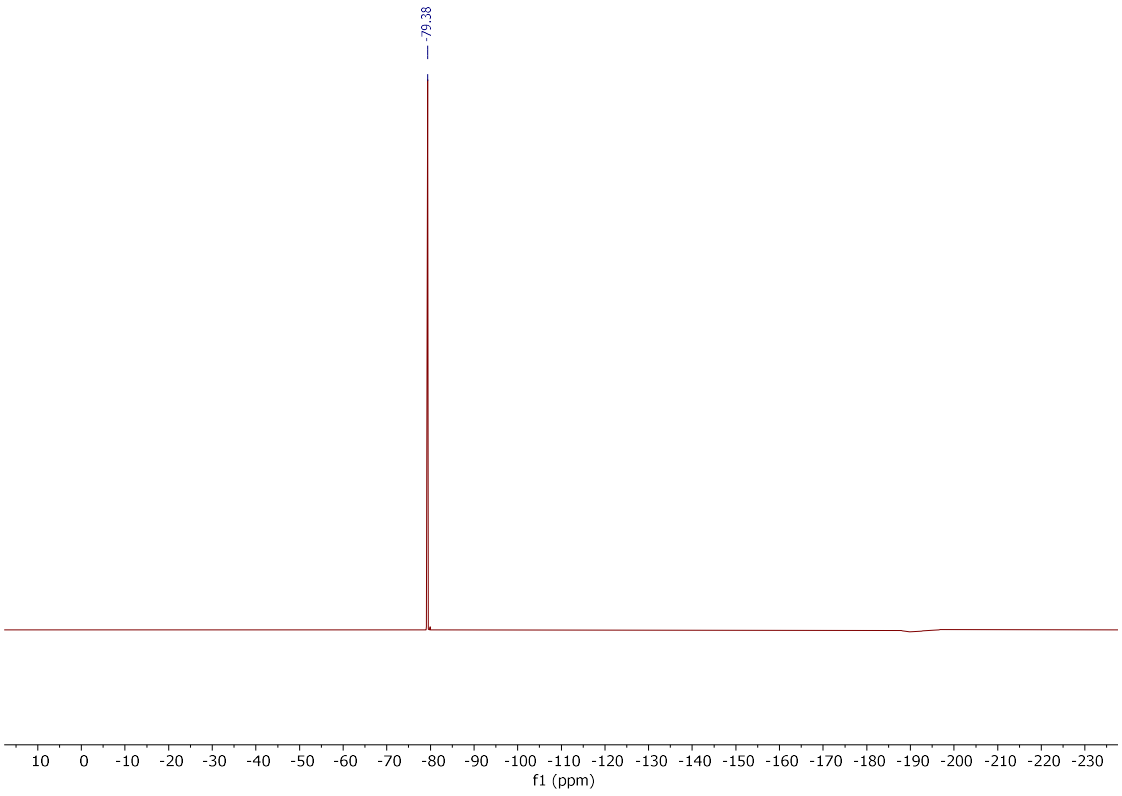

Compound **247b**

^{1}H NMR (300 MHz, CD_3CN)

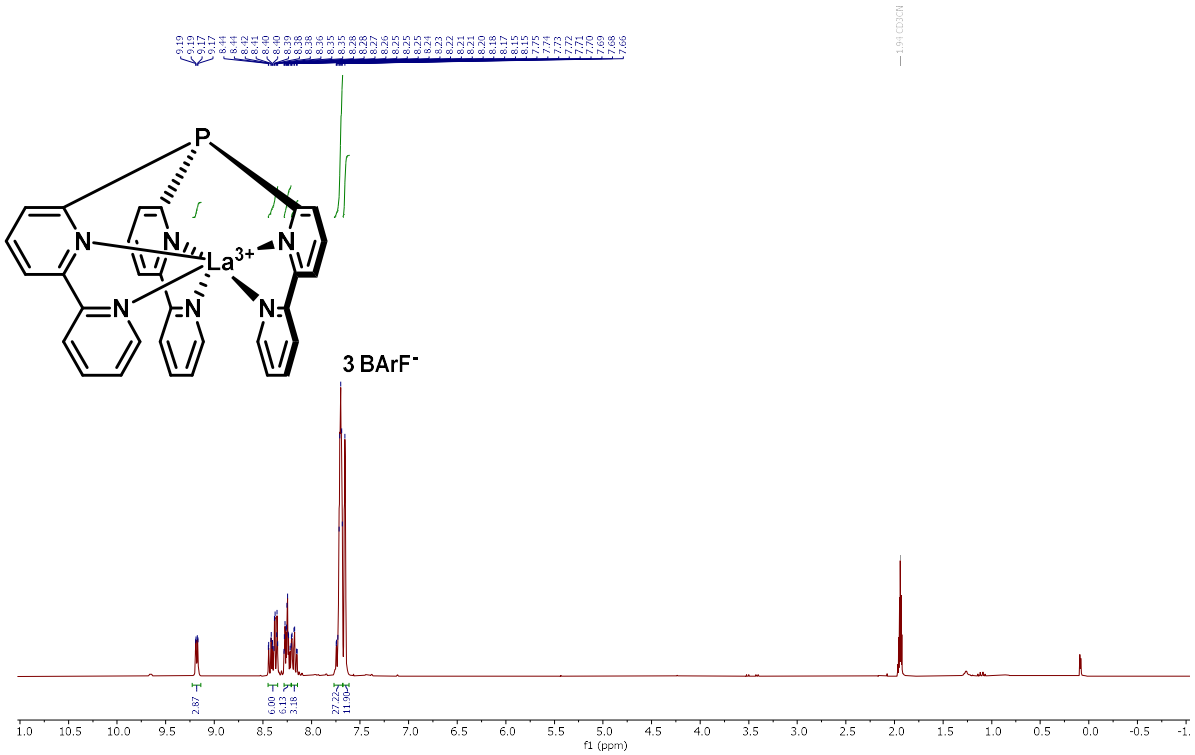

^{13}C{H} NMR (75 MHz, CD_3CN)

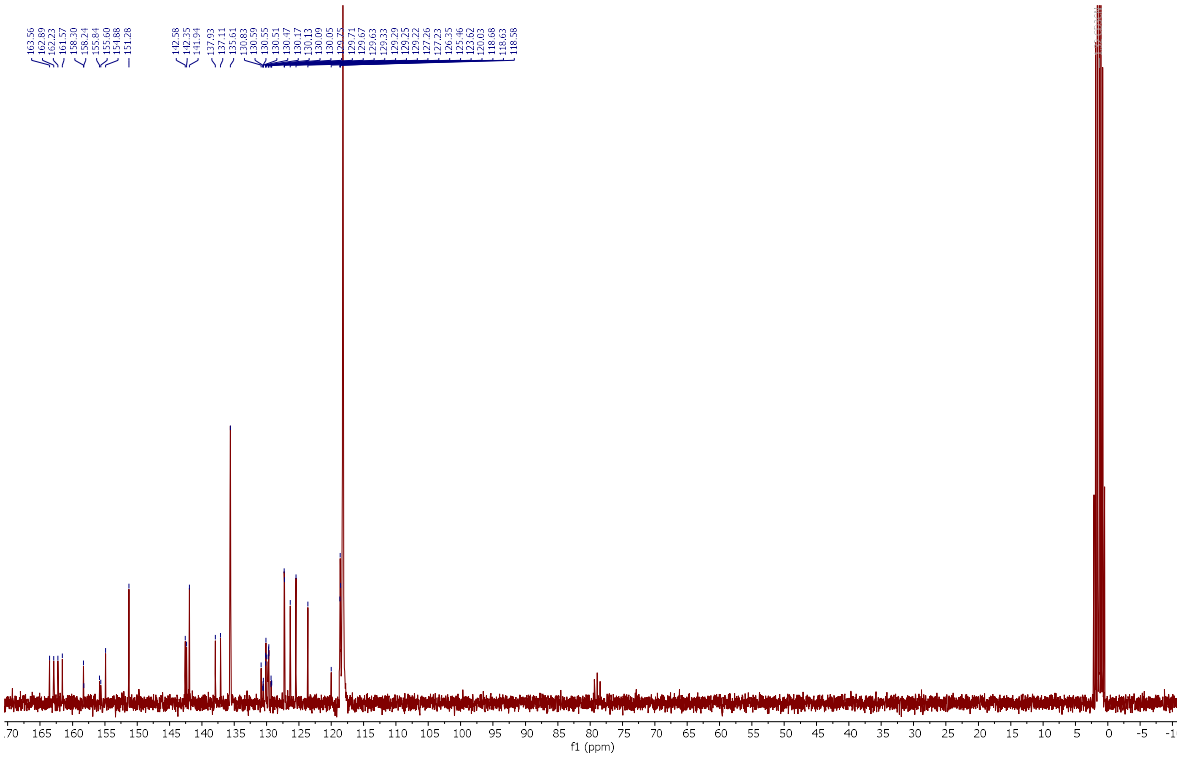

$^{31}P\{H\}$ NMR (121 MHz, CD_3CN)

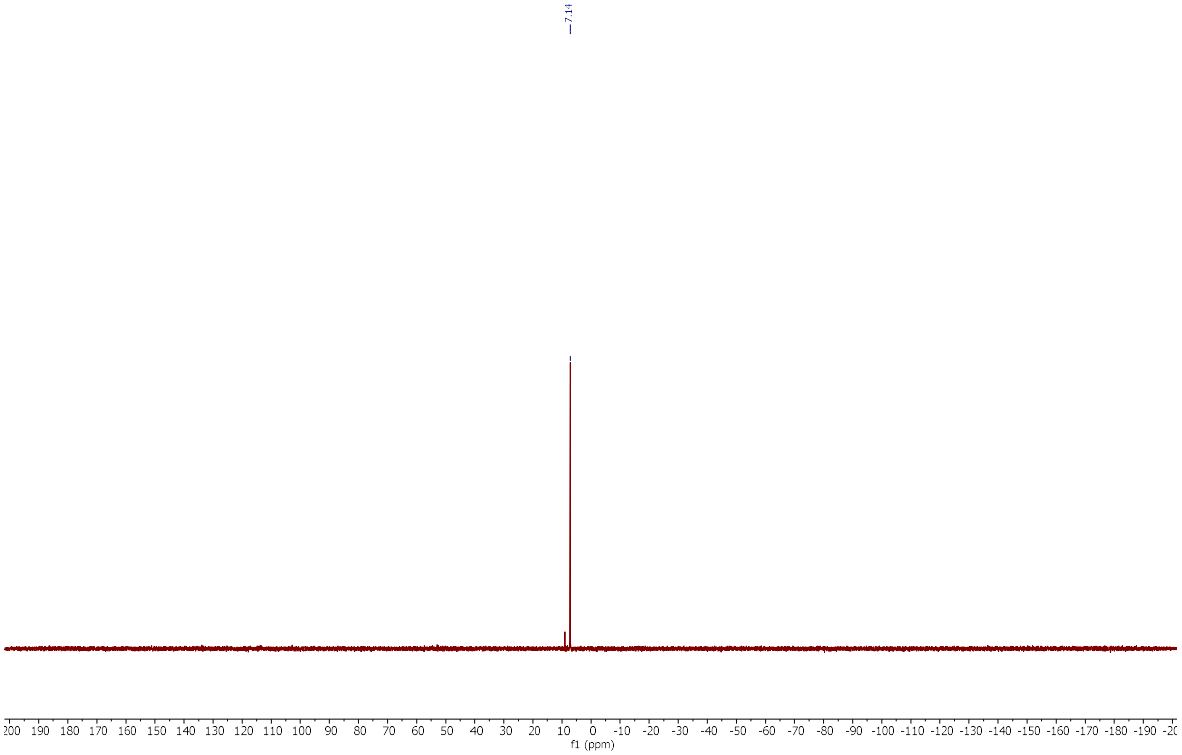

^{19}F NMR (282 MHz, CD_3CN)

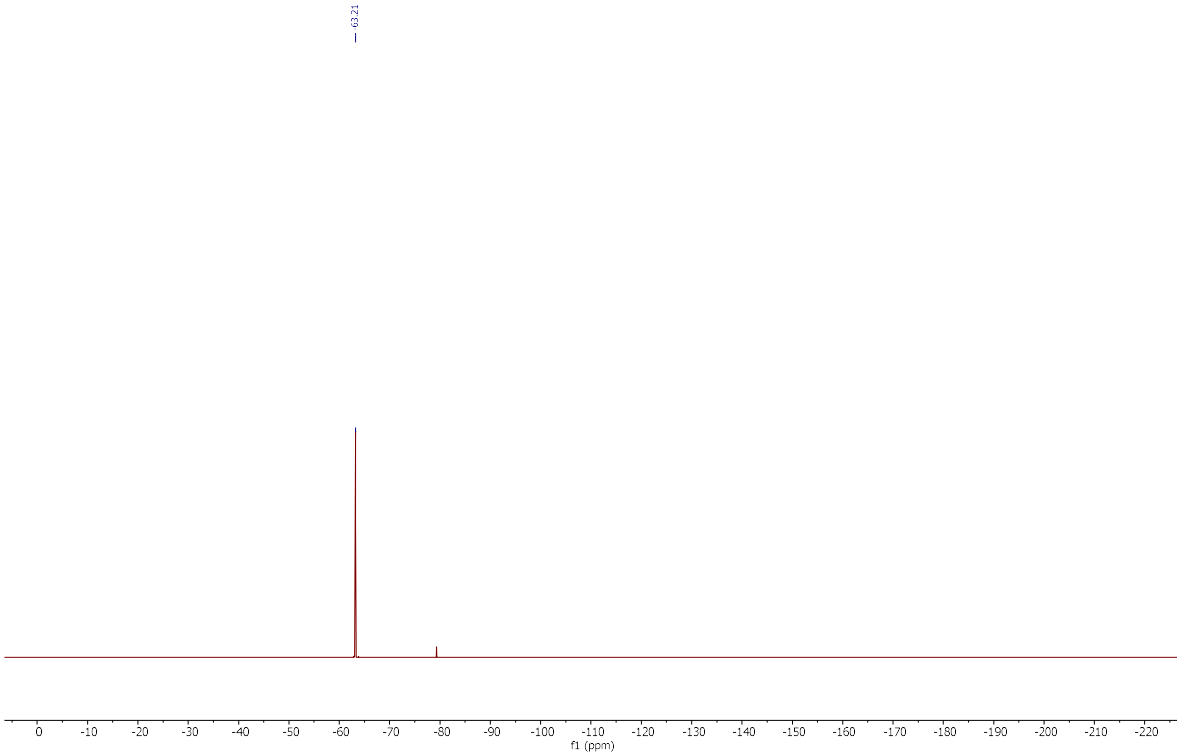

^{11}B NMR (96 MHz, CD_3CN)

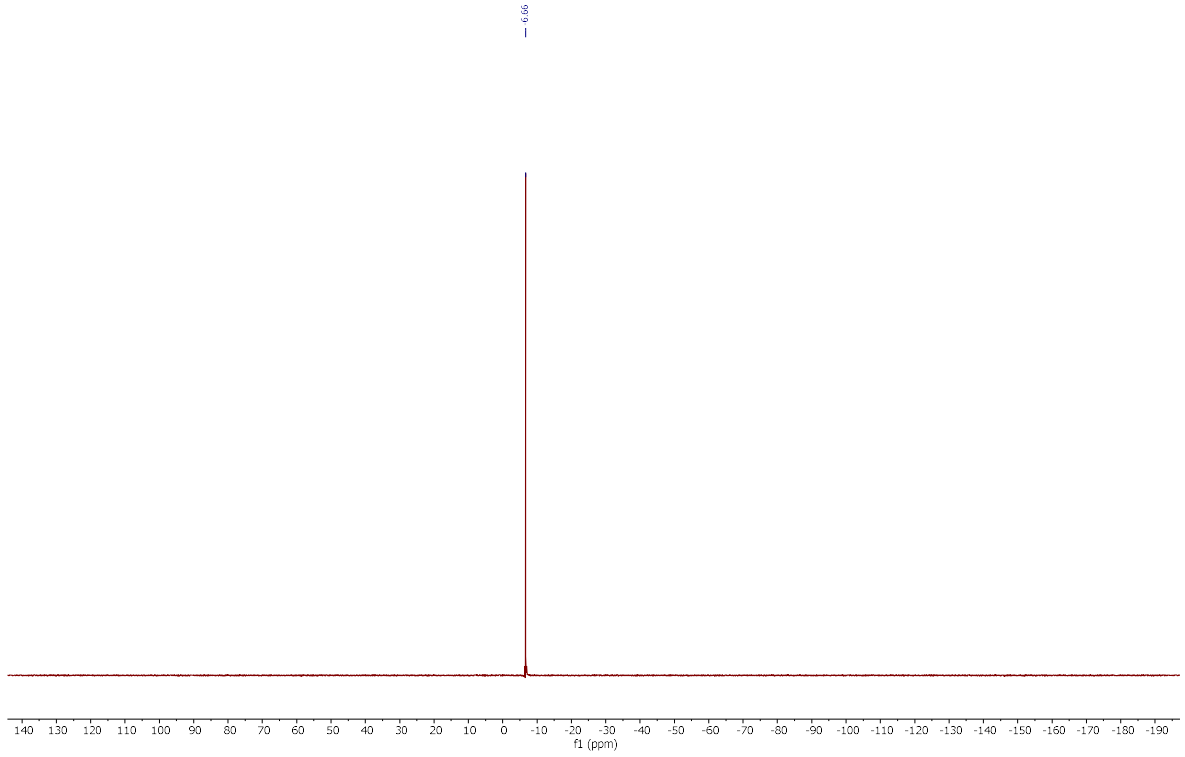

Compound **248**

^{1}H NMR (400 MHz, CD_2Cl_2)

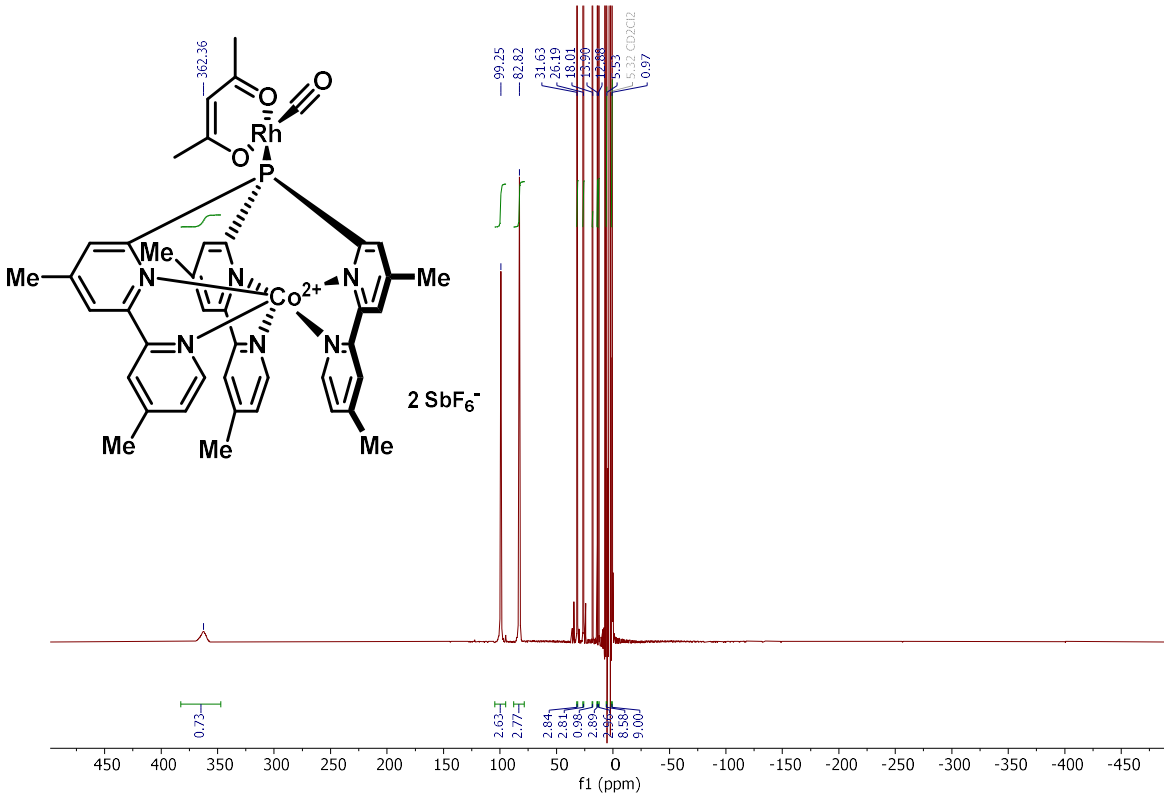

^{31}P{H} NMR (162 MHz, CD_2Cl_2)

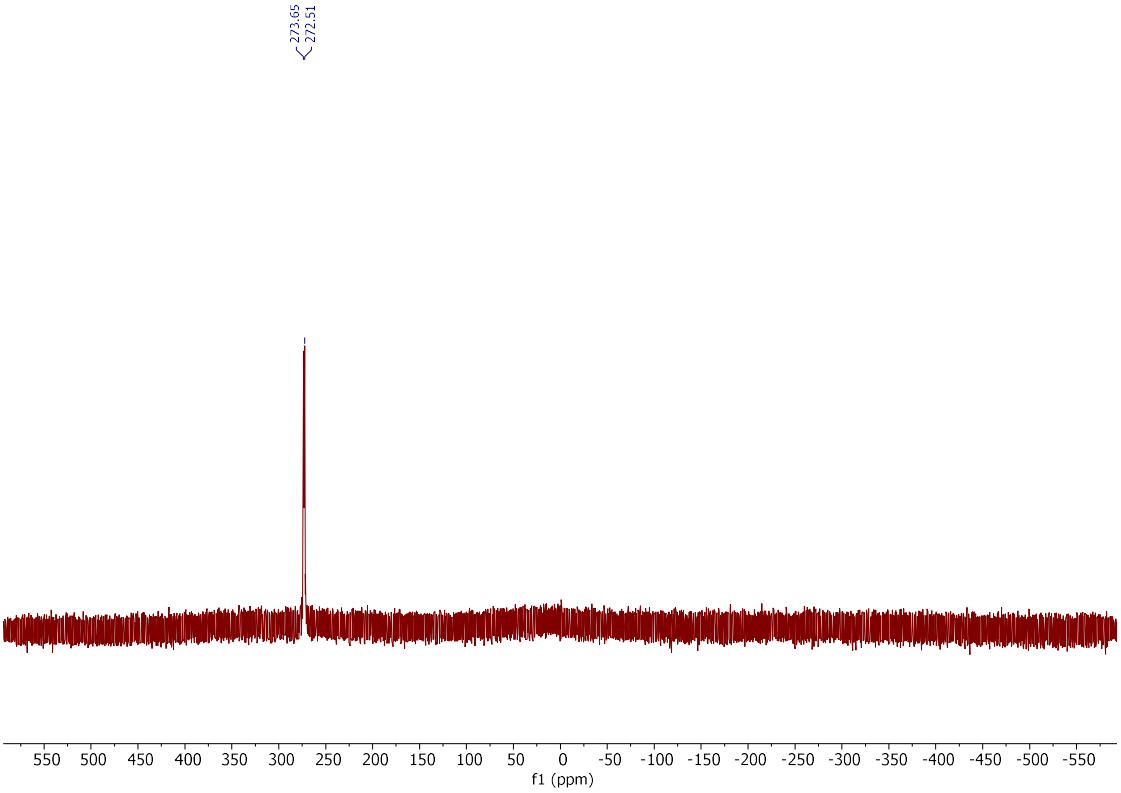

^{19}F NMR (377 MHz, CD_2Cl_2)

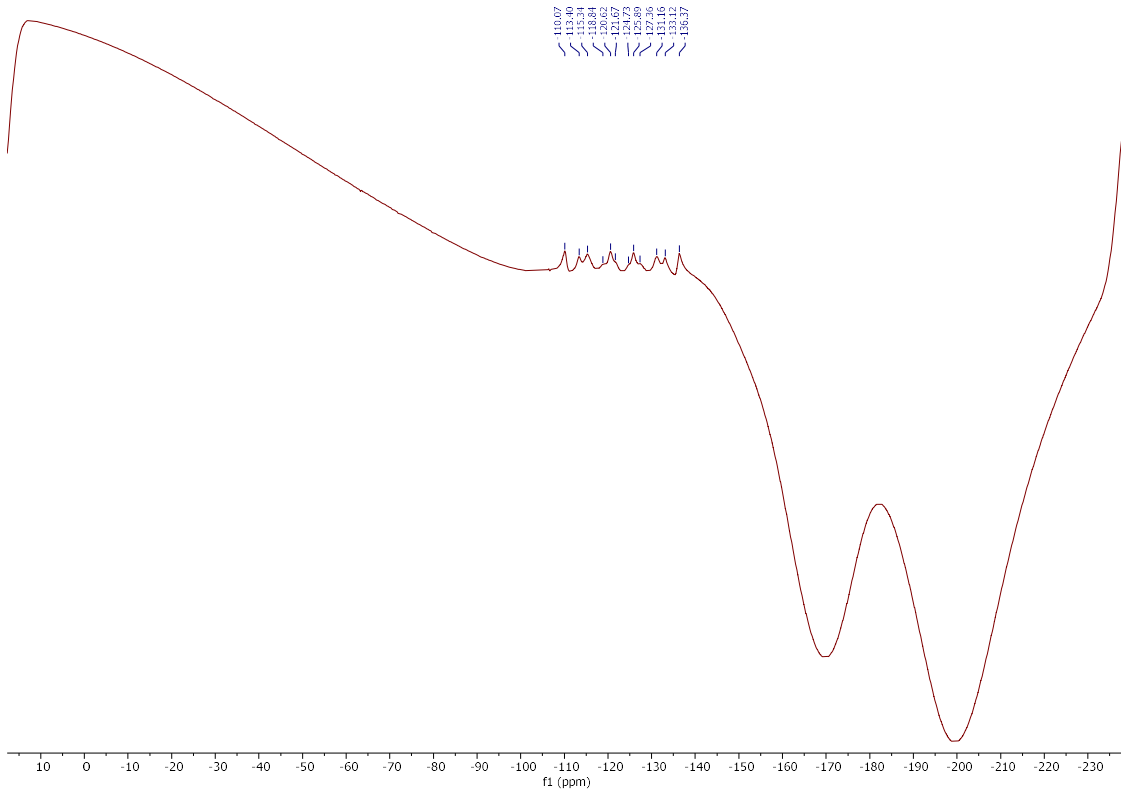

Compound **249**

^{1}H NMR (300 MHz, CD_2Cl_2)

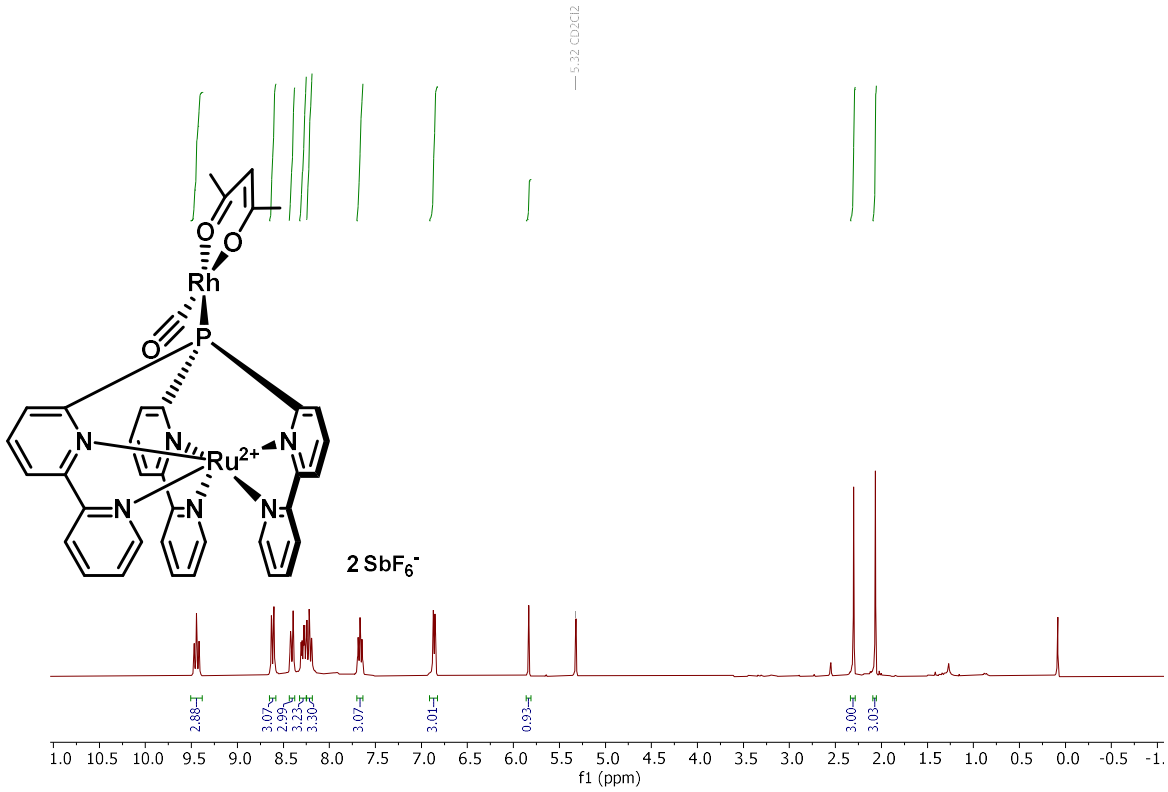

^{13}C{H} NMR (101 MHz, CD_2Cl_2)

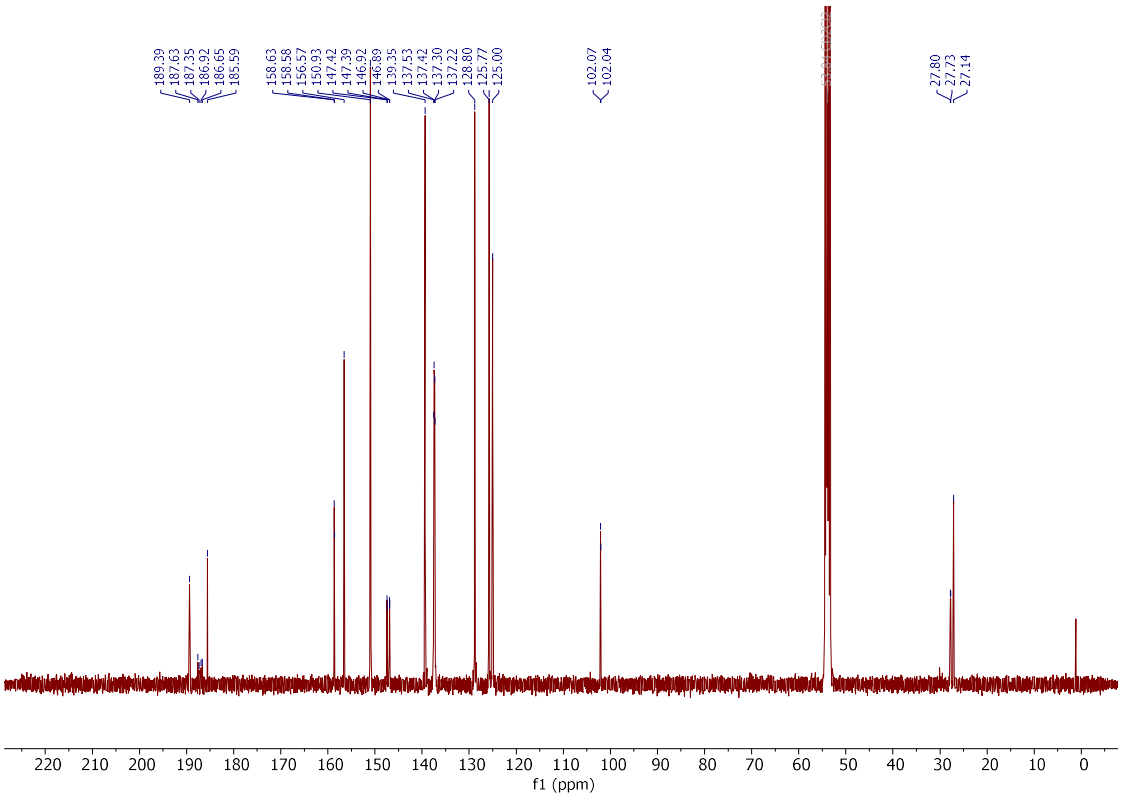

$^{31}P\{H\}$ NMR (162 MHz, CD_2Cl_2)

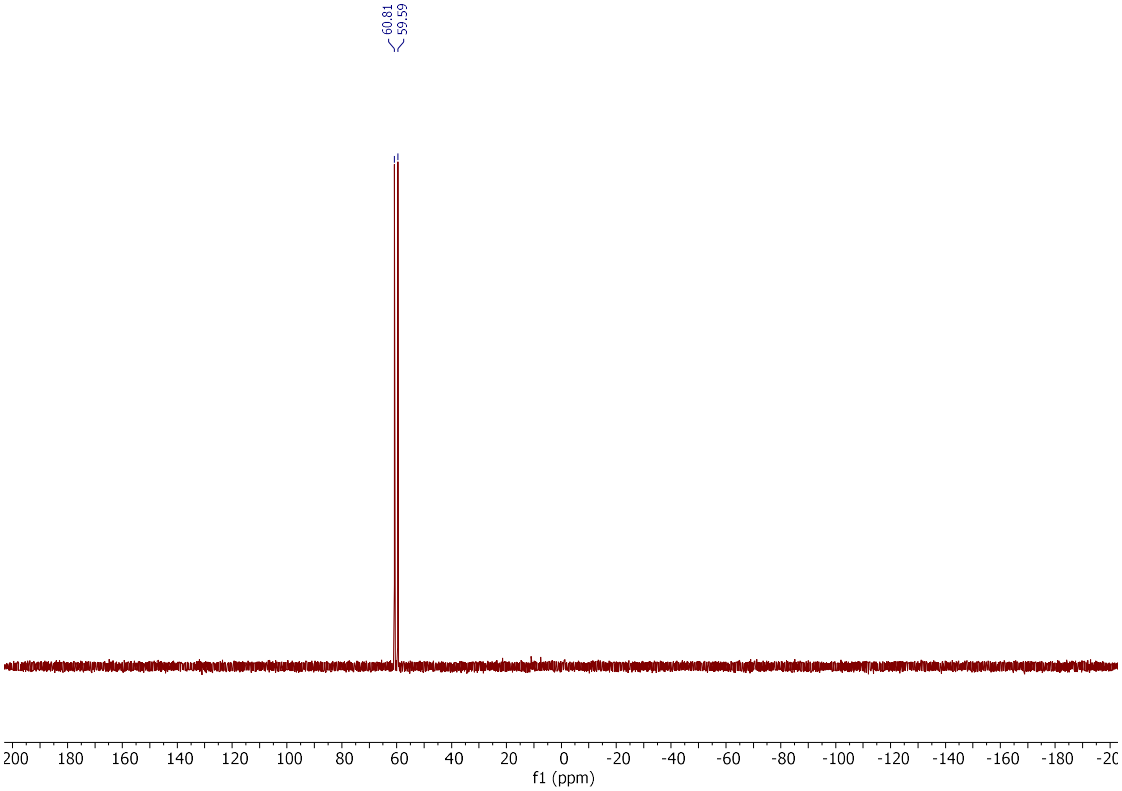

^{19}F NMR (376 MHz, CD_3CN)

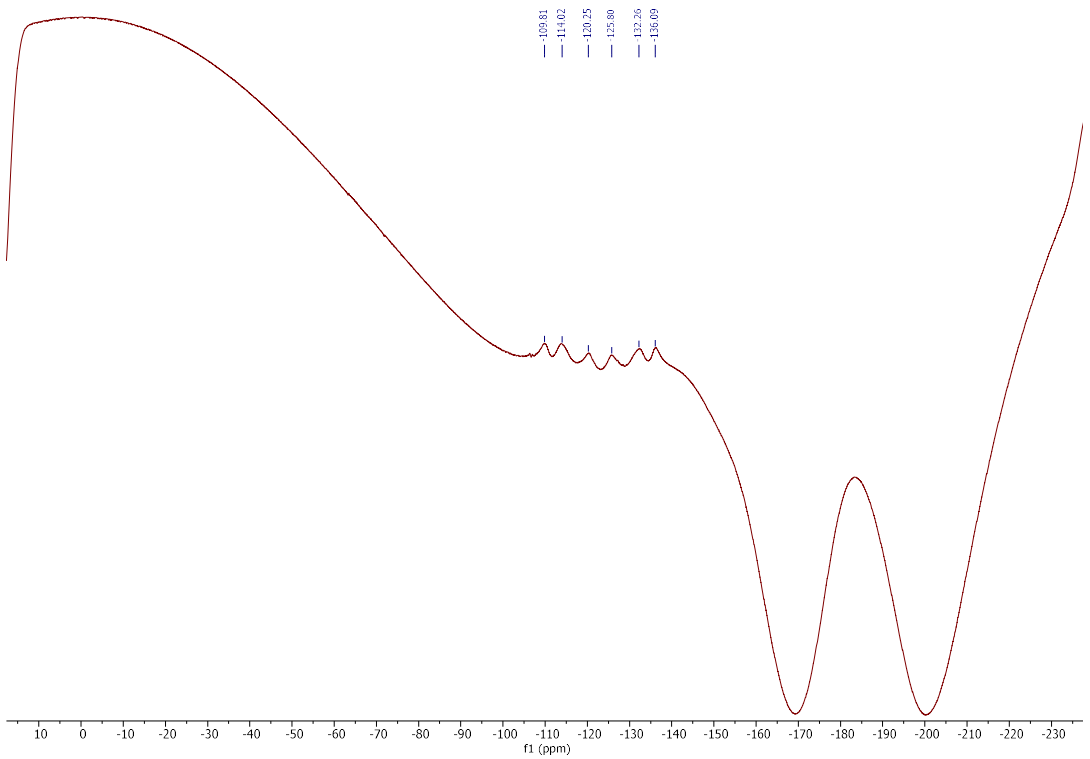

Compound **250**

^{1}H NMR (400 MHz, $CDCl_3$)

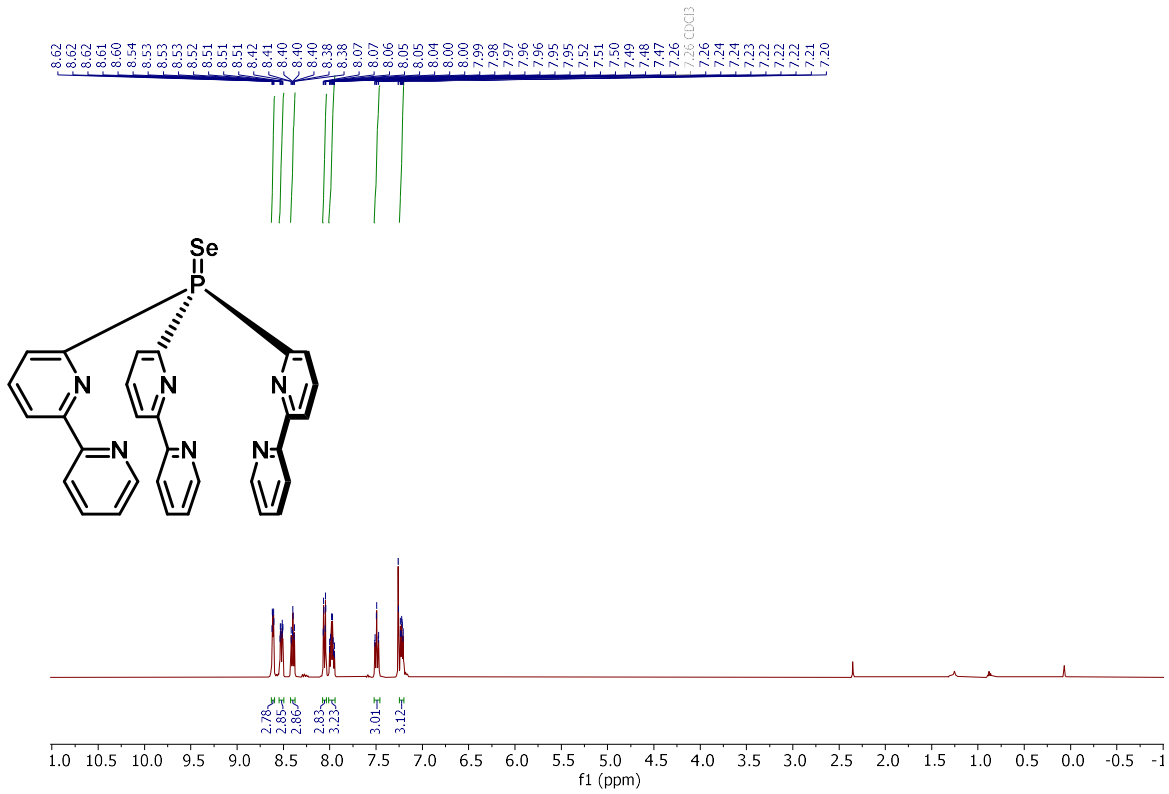

^{13}C{H} NMR (101 MHz, $CDCl_3$)

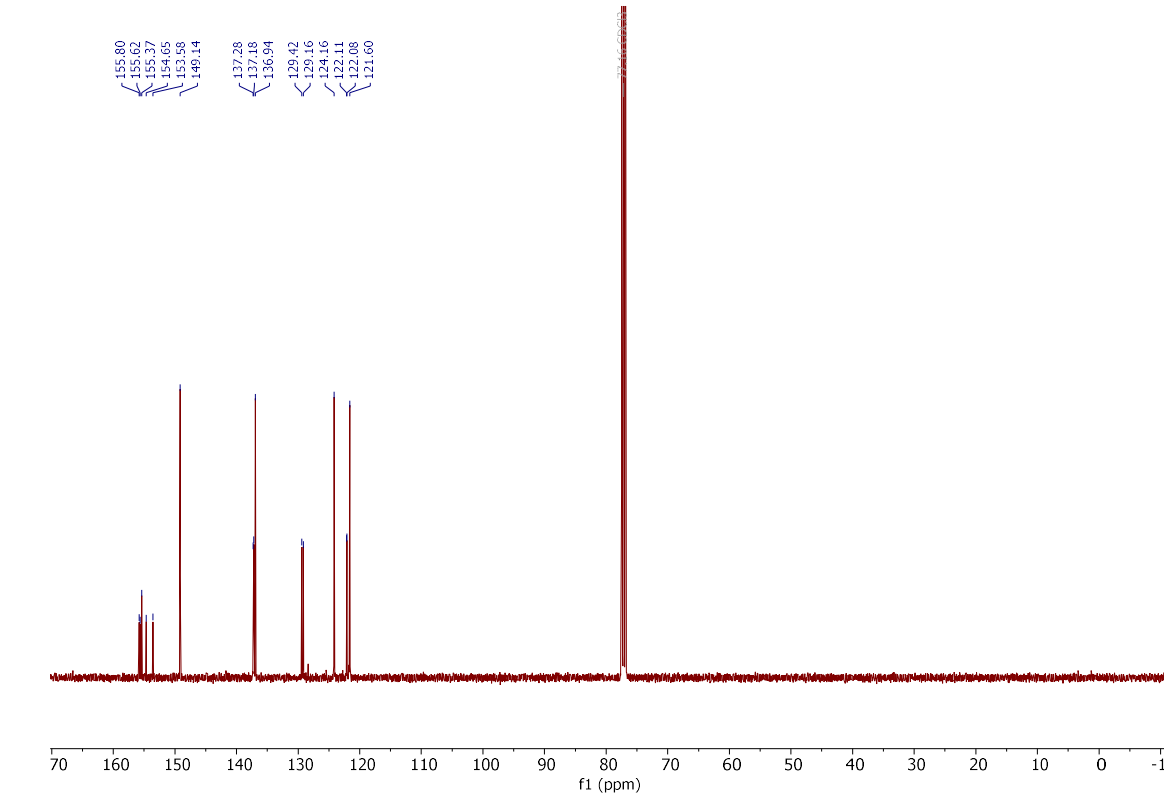

$^{31}P\{H\}$ NMR (162 MHz, CD_3CN)

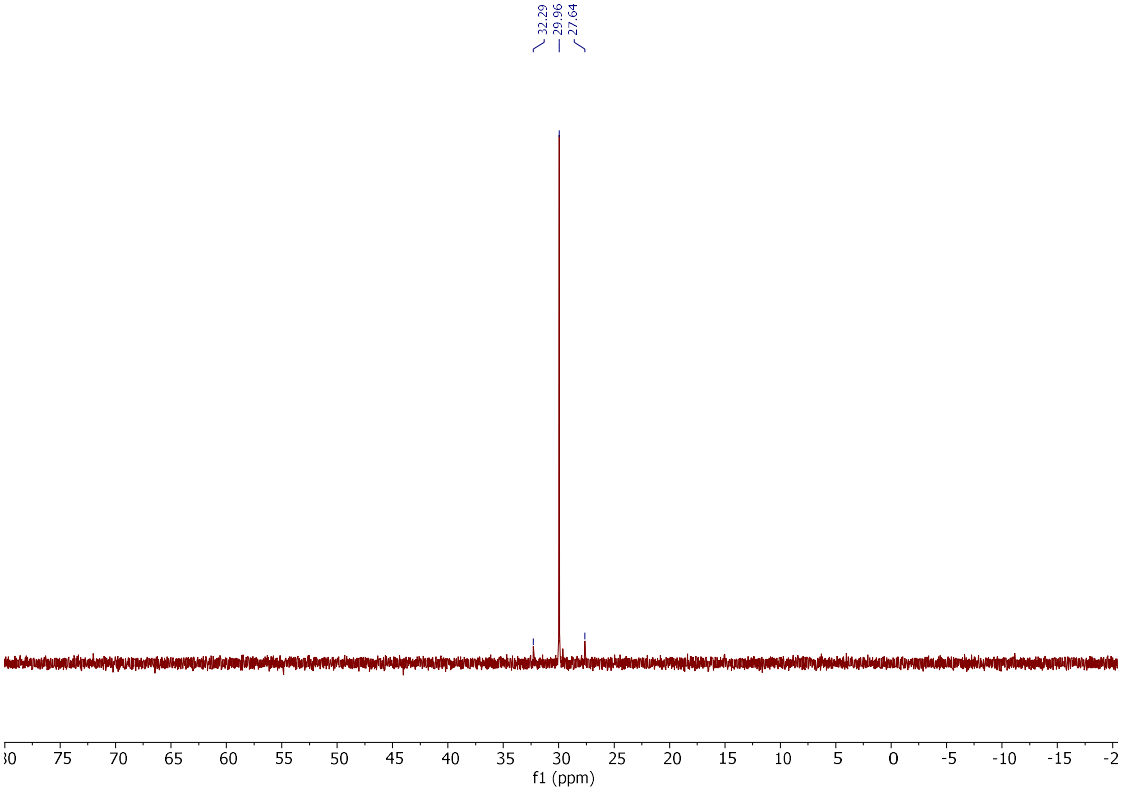

$^{31}P\{H\}$ NMR (162 MHz, $CDCl_3$)

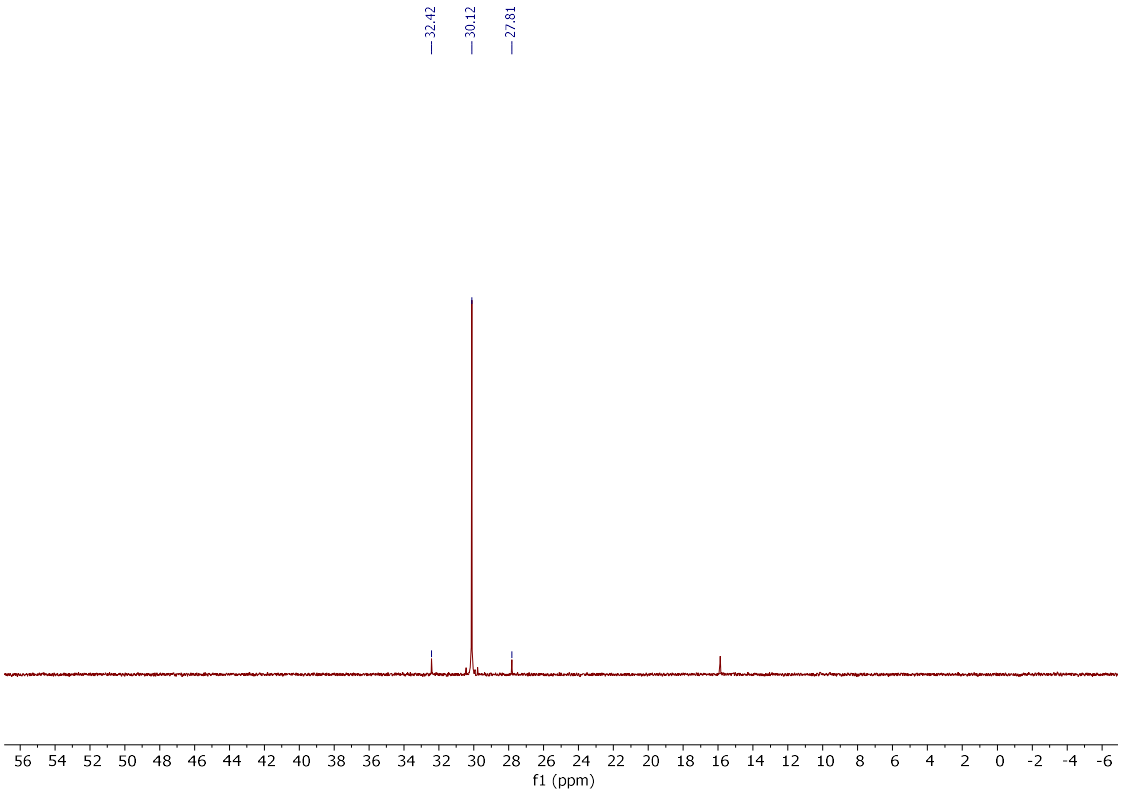

^{77}Se NMR (76 MHz, $CDCl_3$)

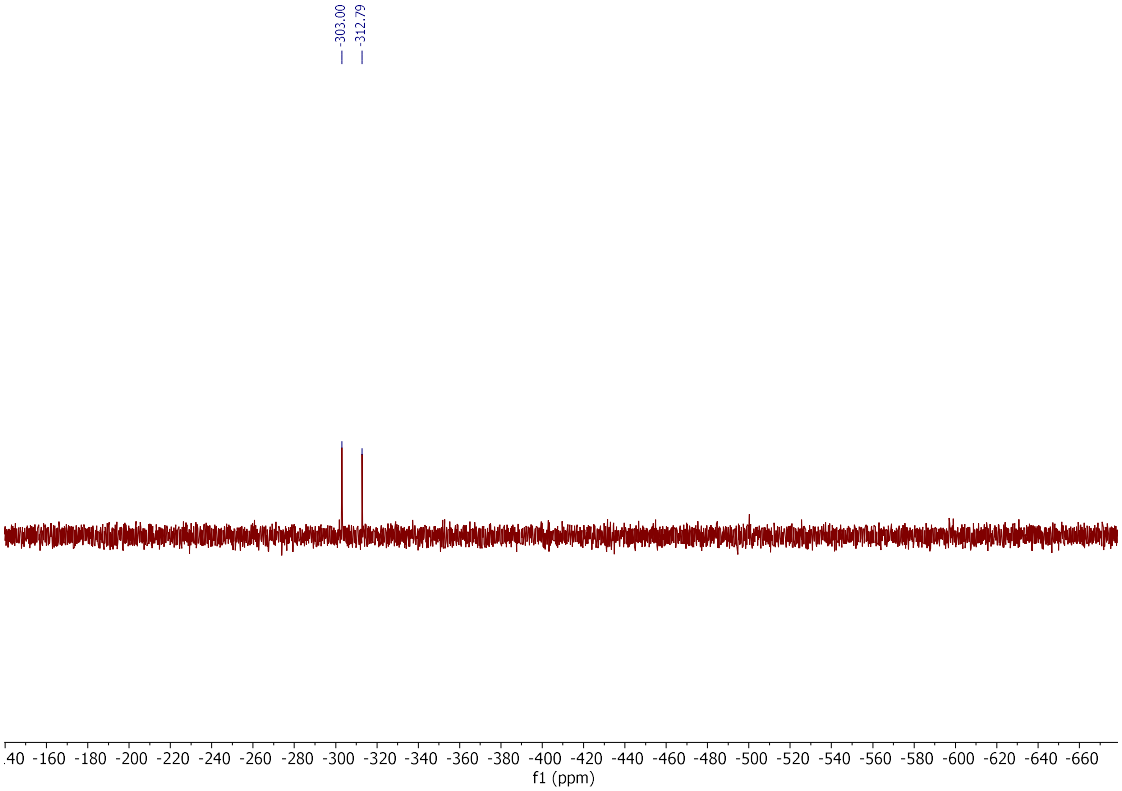

Compound **250x**

^{1}H NMR (400 MHz, CD_3CN)

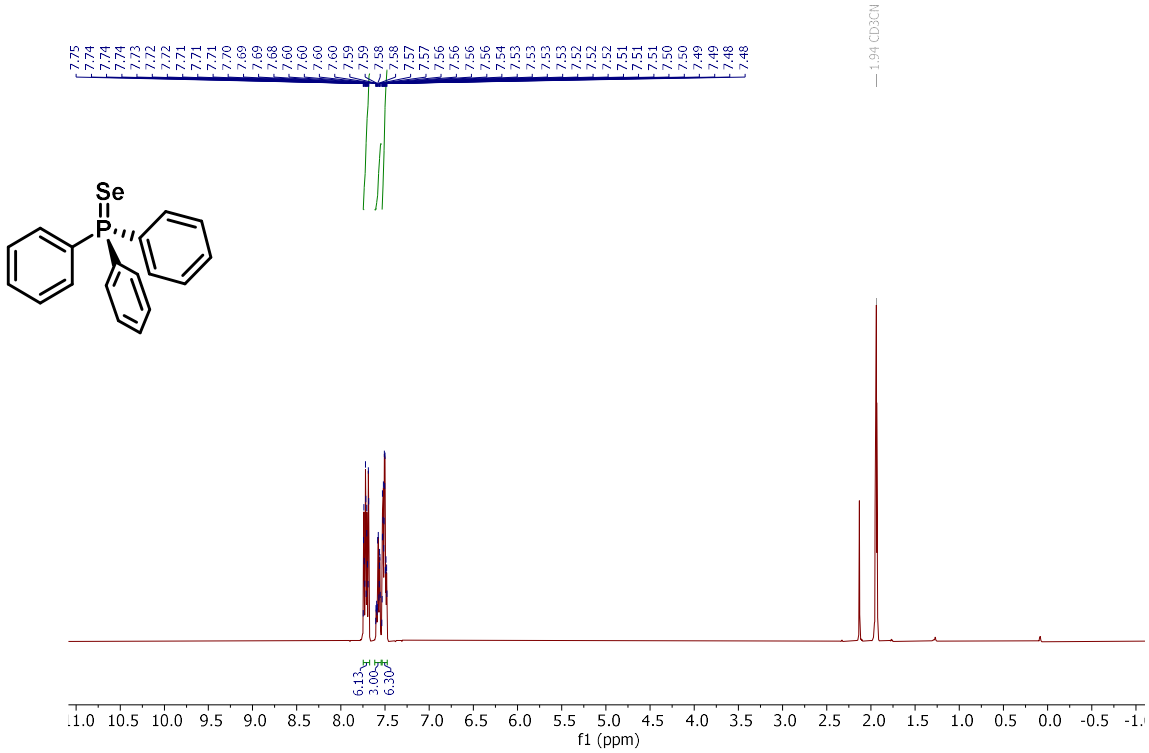

^{13}C NMR (101 MHz, CD_3CN)

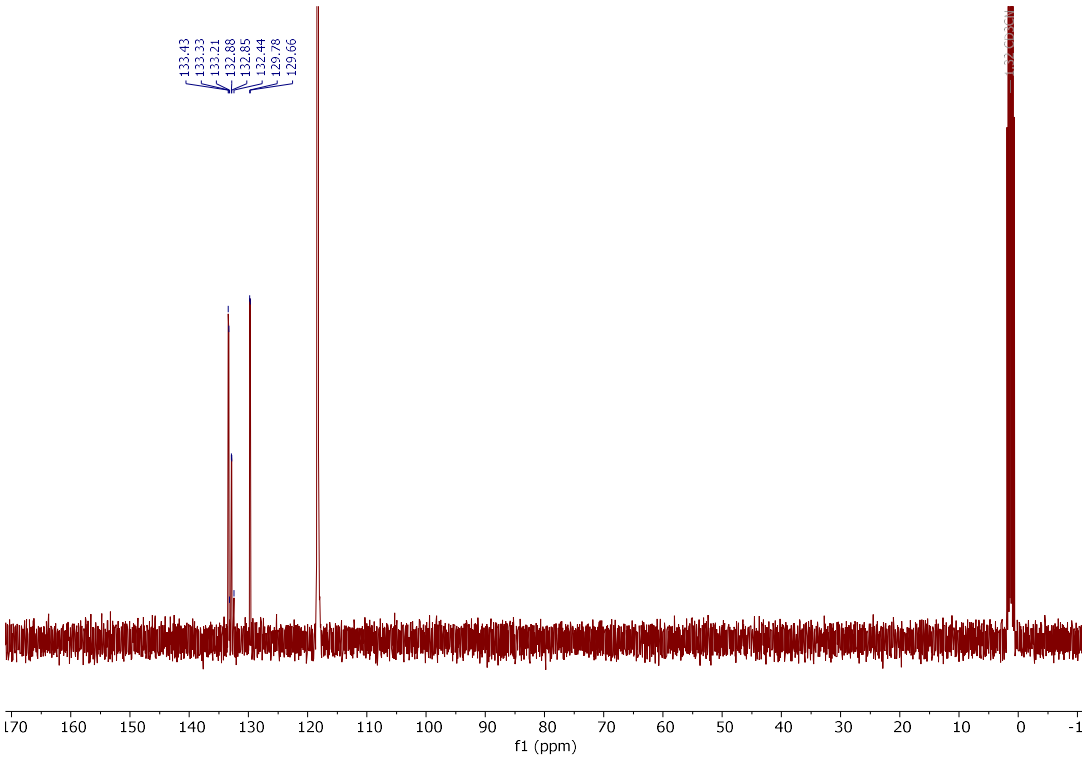

^{31}P NMR (162 MHz, CD_3CN)

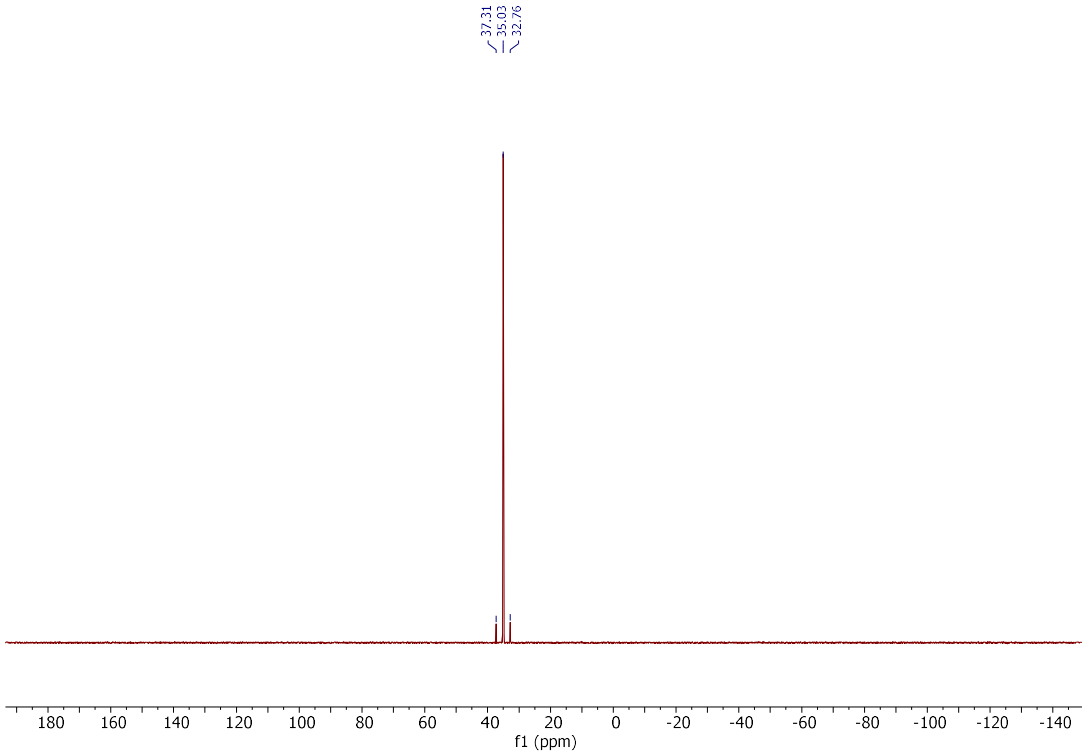

^{77}Se NMR (76 MHz, CD_3CN)

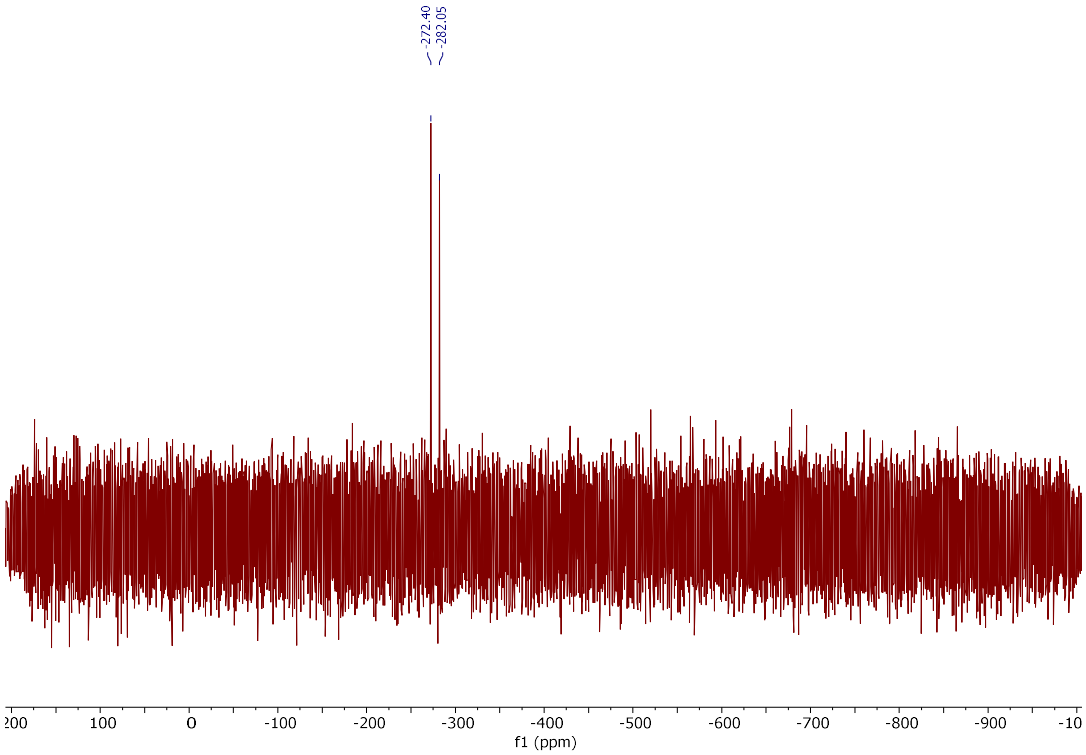

Compound **251**

^{1}H NMR (400 MHz, CD_3CN)

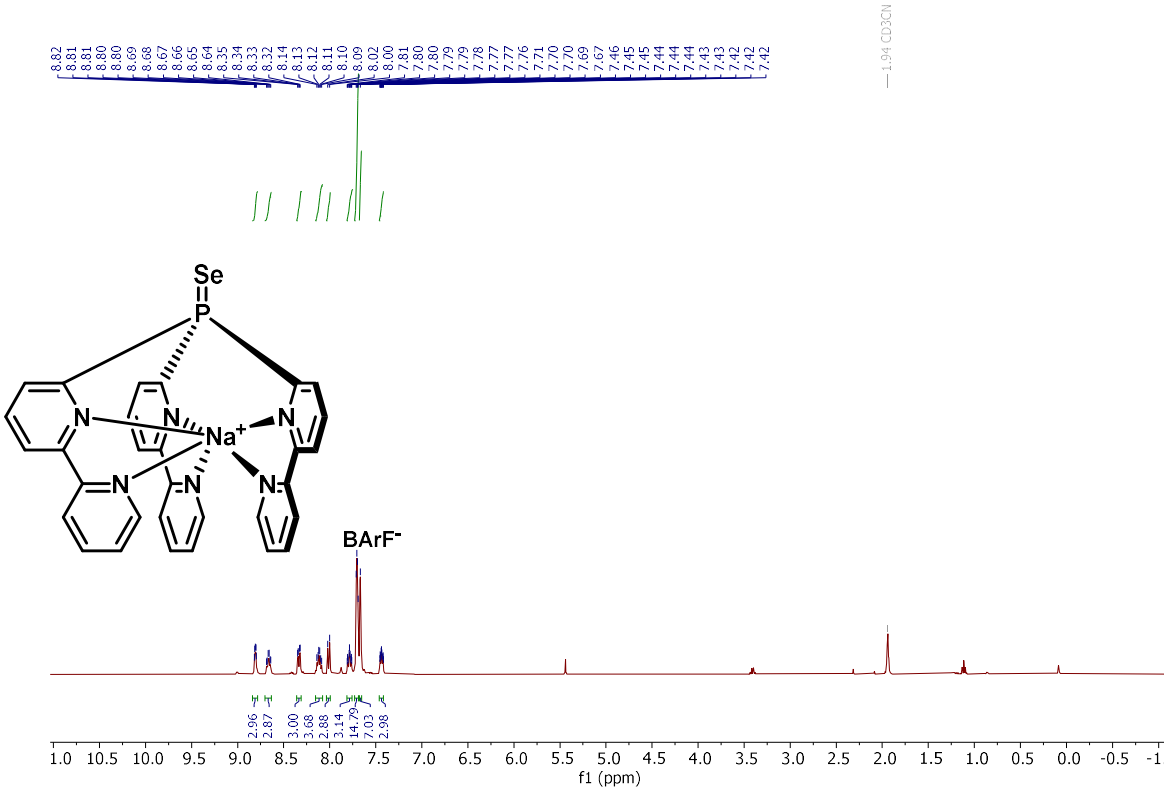

^{1}H NMR (400 MHz, $CDCl_3$)

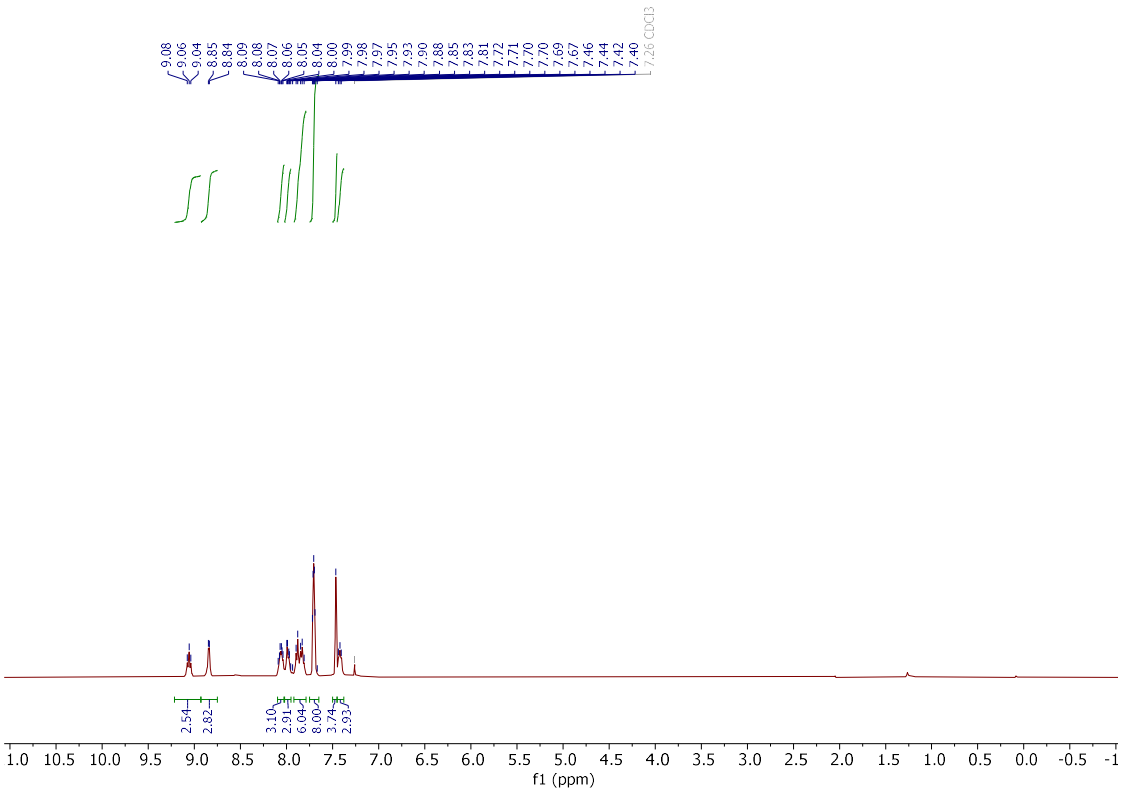

$^{13}C\{H\}$ NMR (101 MHz, CD_3CN)

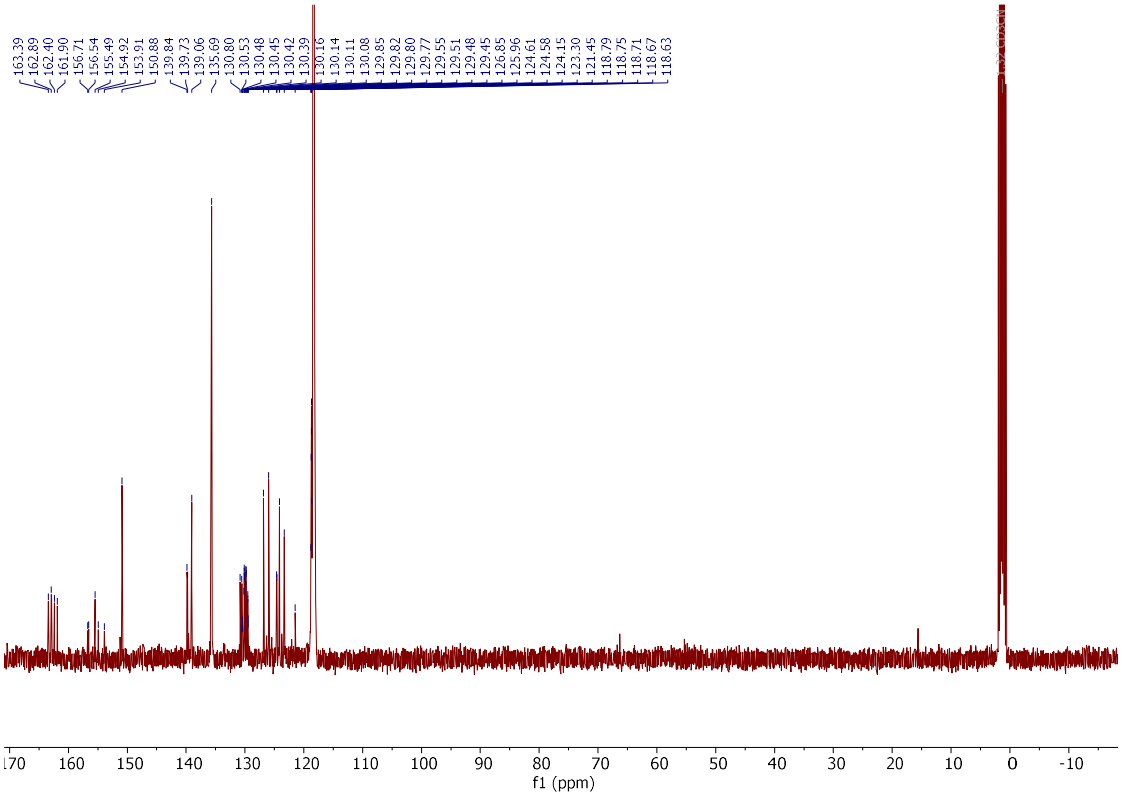

^{13}C NMR (101 MHz, $CDCl_3$)

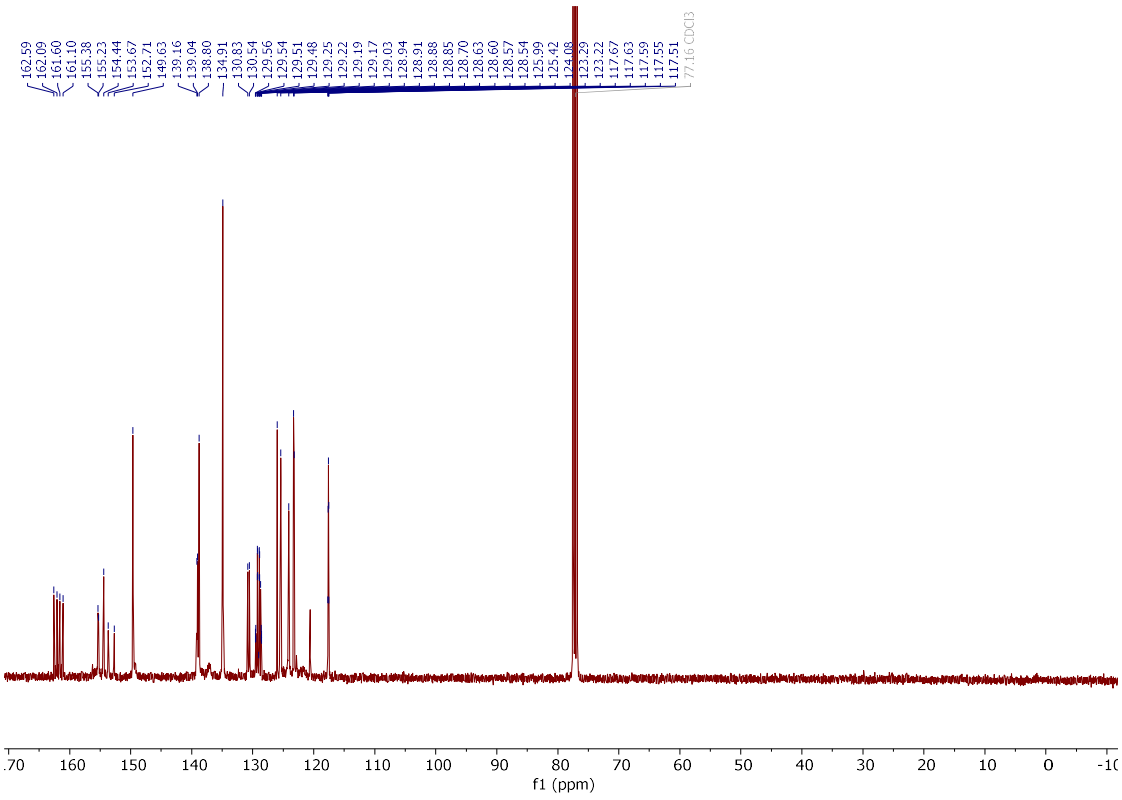

$^{31}P\{H\}$ NMR (162 MHz, CD_3CN)

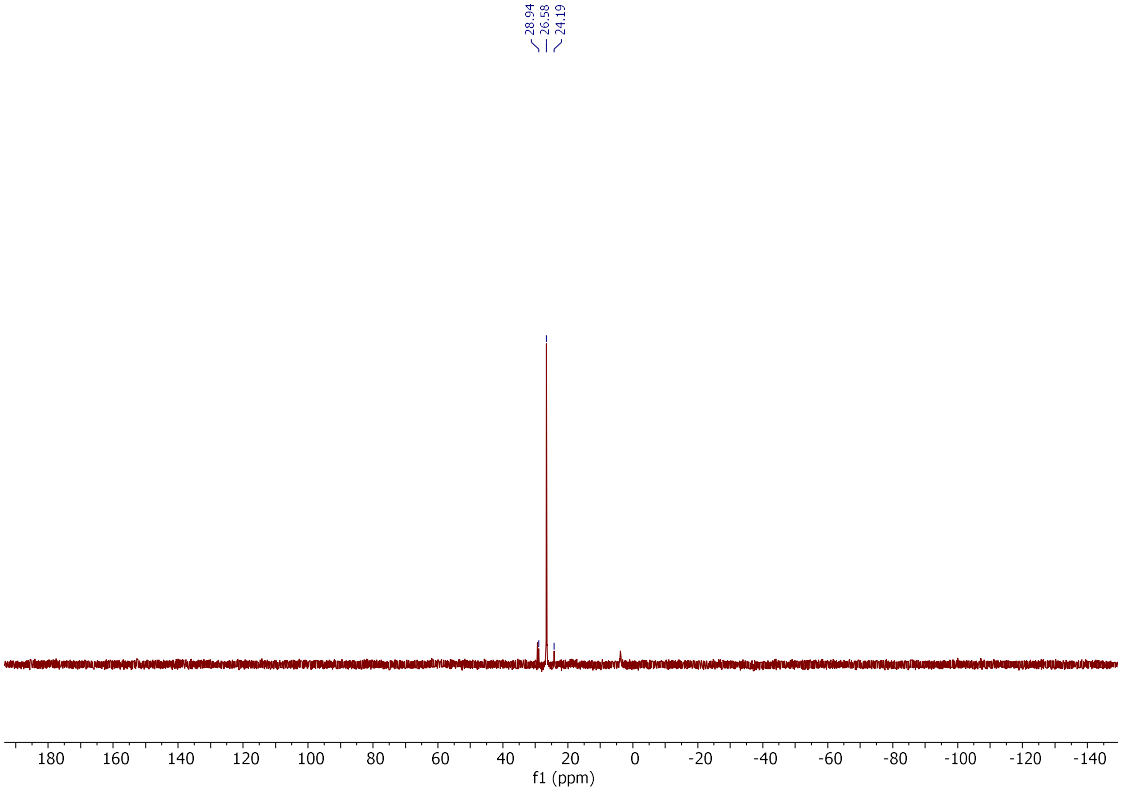

$^{31}P\{H\}$ NMR (162 MHz, $CDCl_3$)

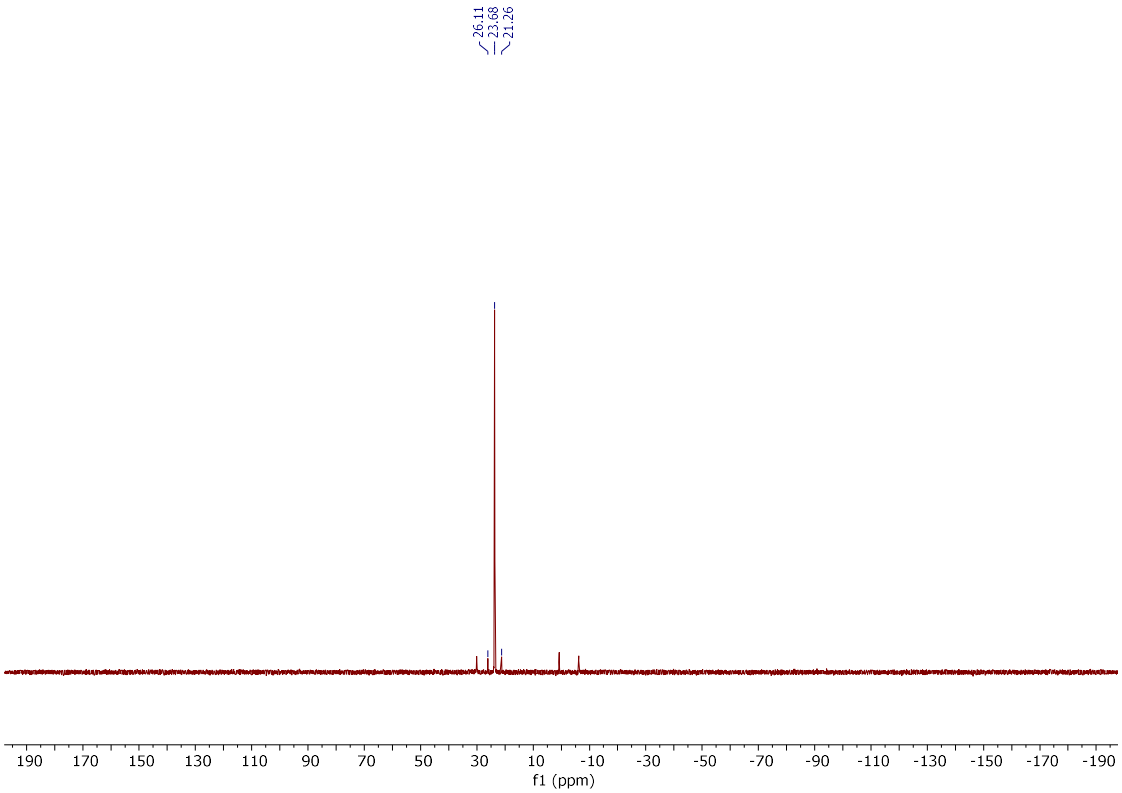

^{19}F NMR (377 MHz, CD_3CN)

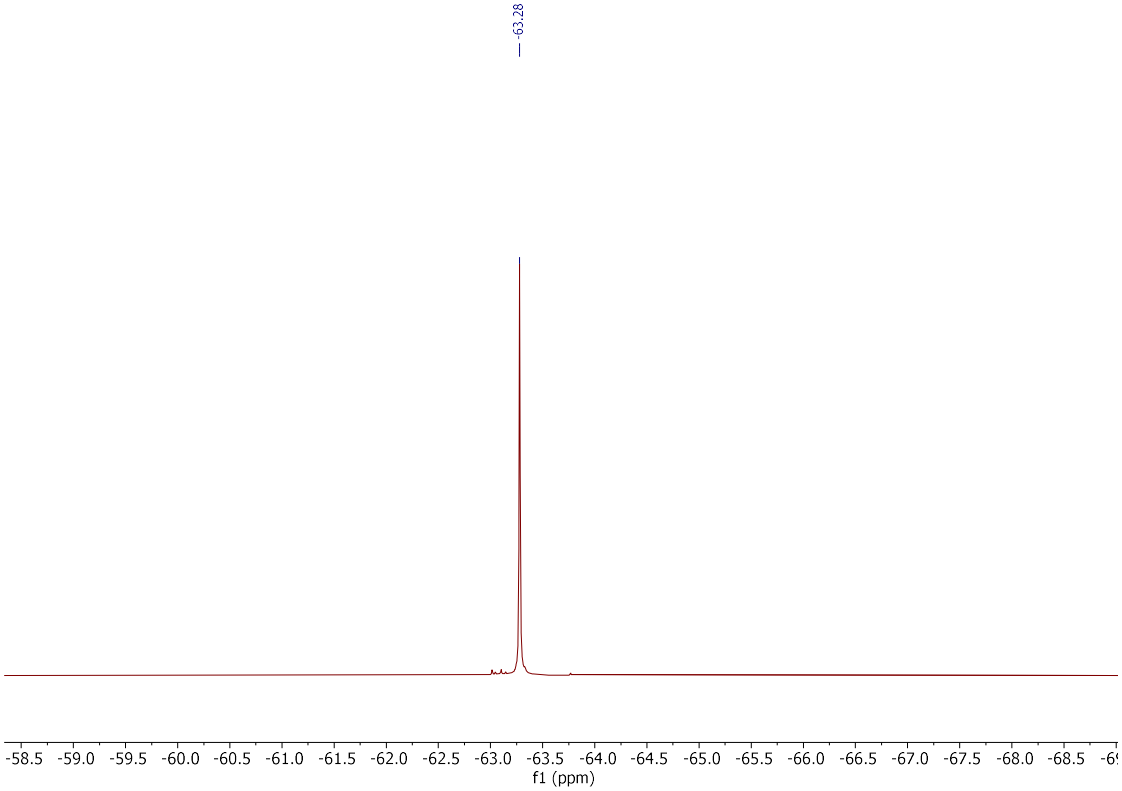

^{19}F NMR (376 MHz, $CDCl_3$)

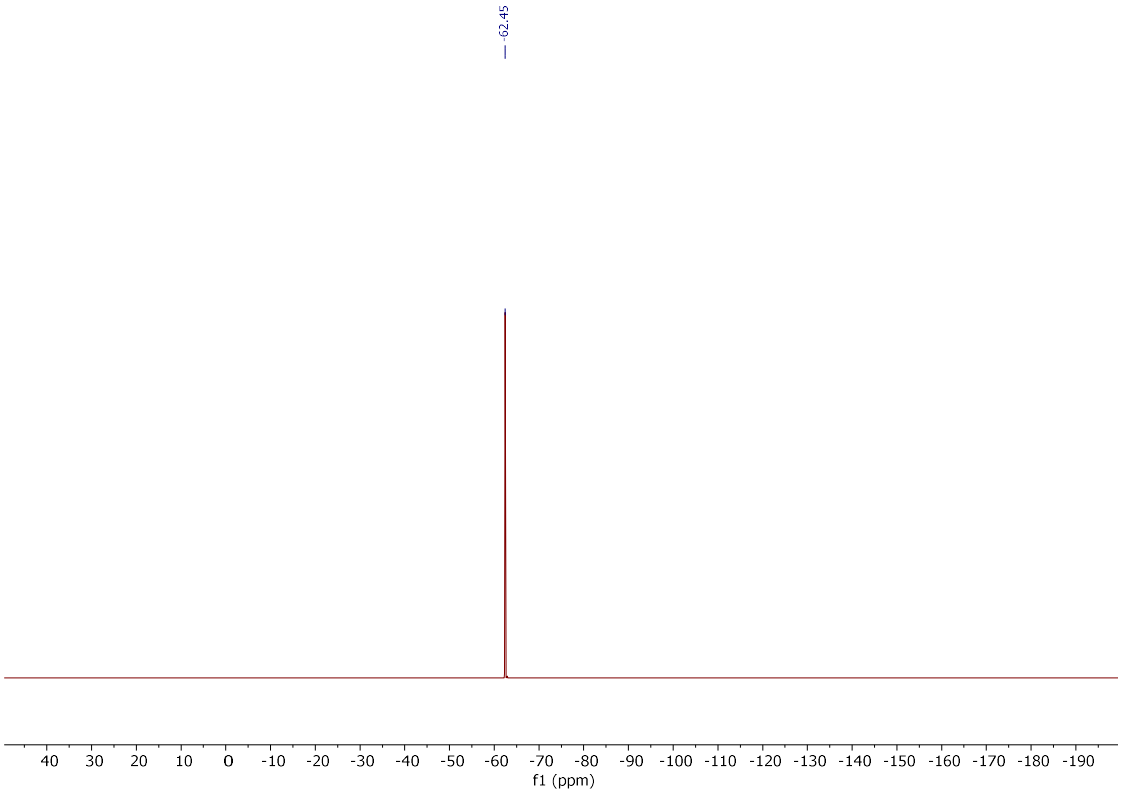

^{11}B NMR (128 MHz, CD_3CN)

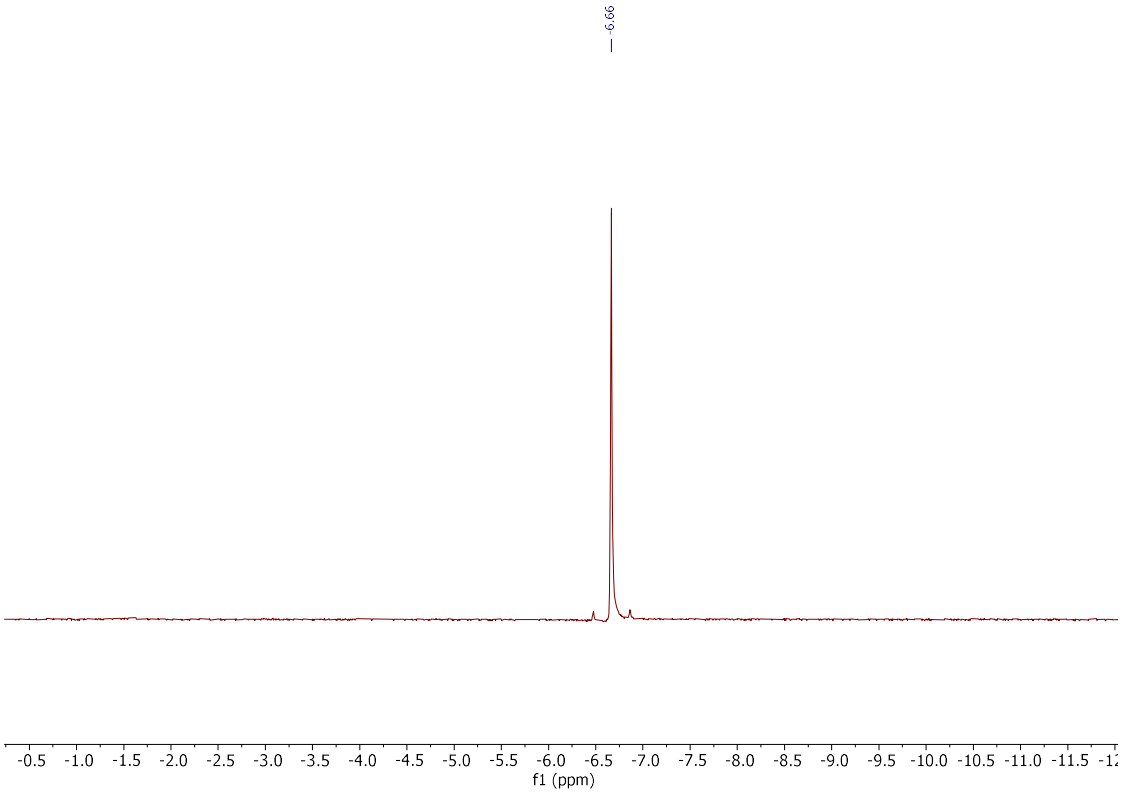

^{11}B NMR (96 MHz, $CDCl_3$)

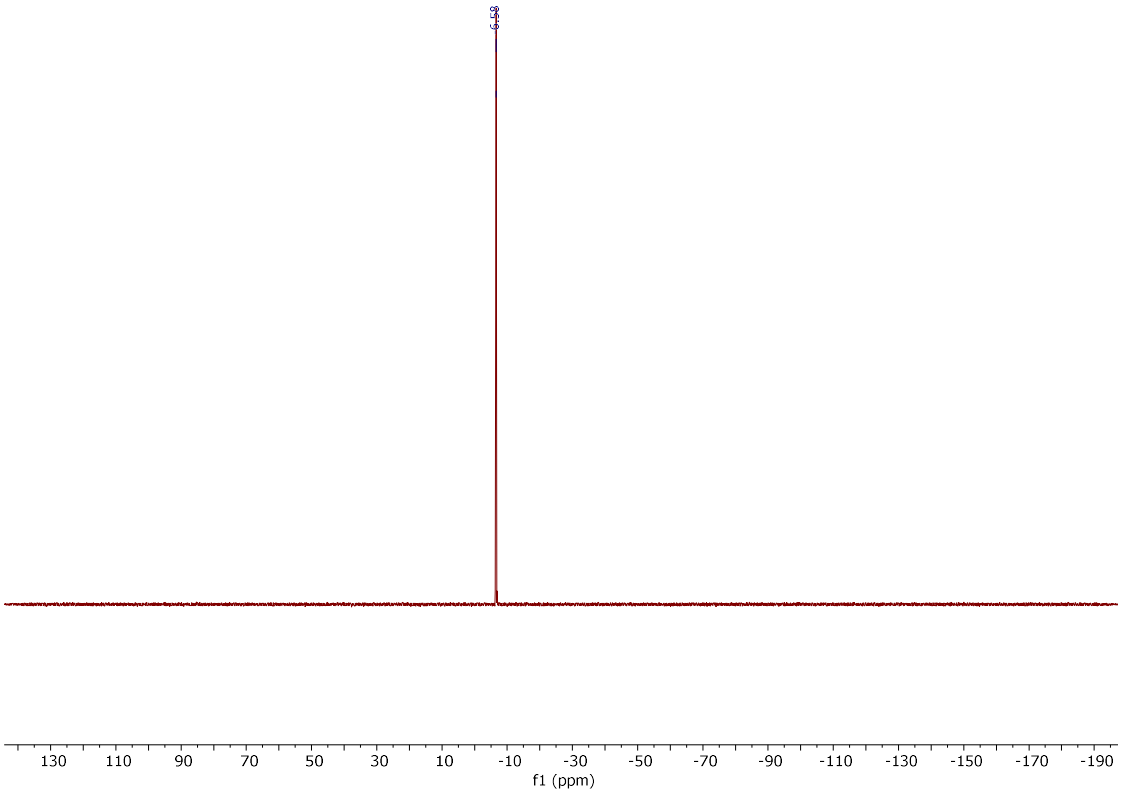

^{77}Se NMR (76 MHz, $CDCl_3$)

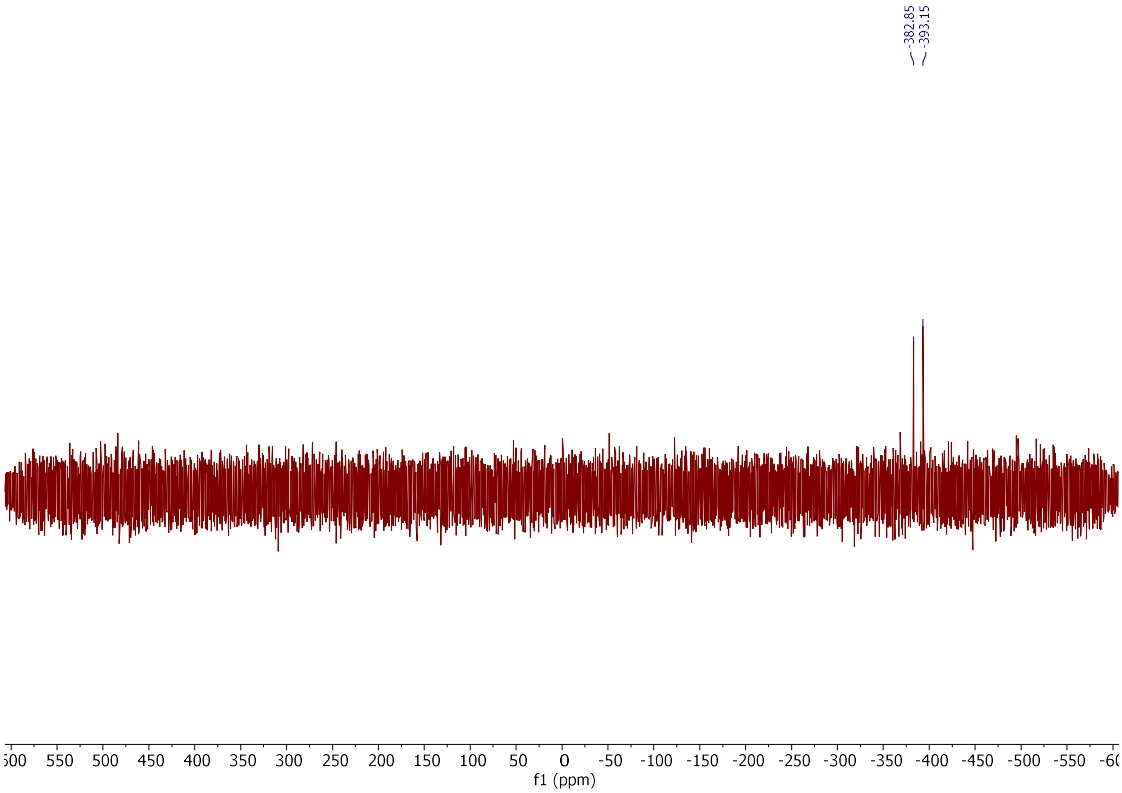

Compound **252**

^{1}H NMR (400 MHz, CD_3CN)

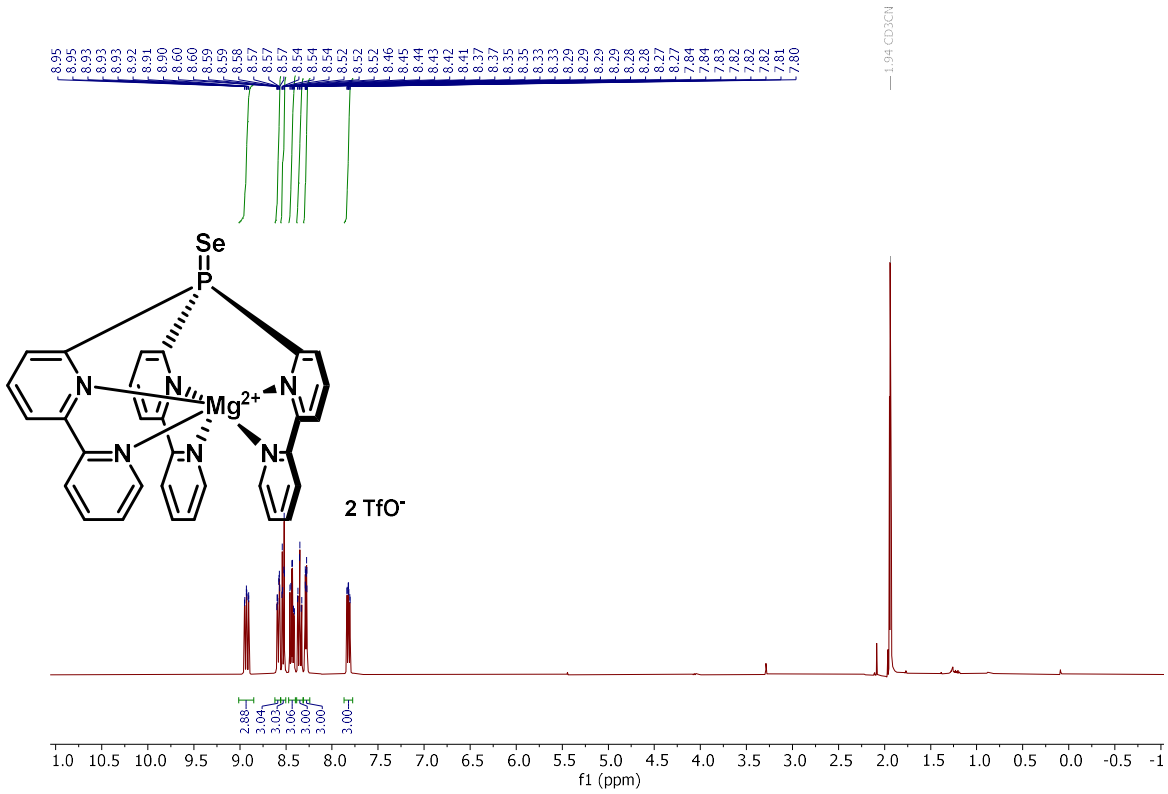

^{13}C{H} NMR (101 MHz, CD_3CN)

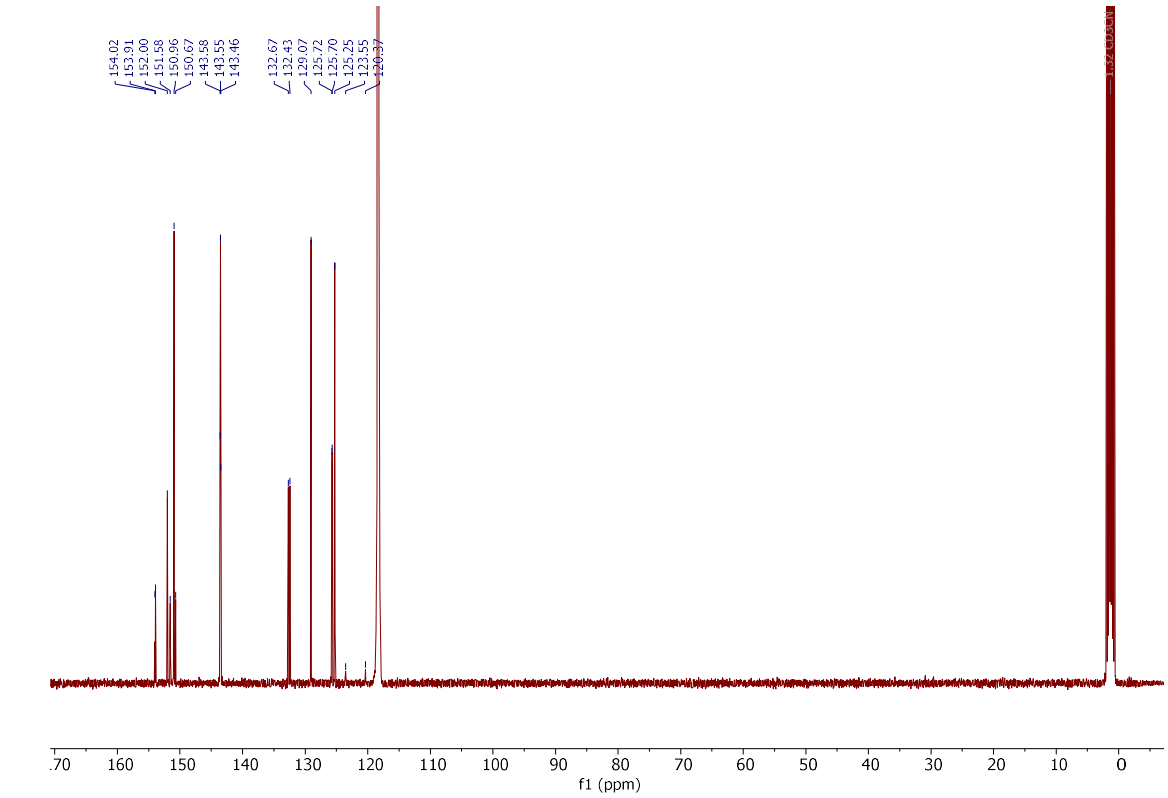

$^{31}P\{H\}$ NMR (162 MHz, CD_3CN)

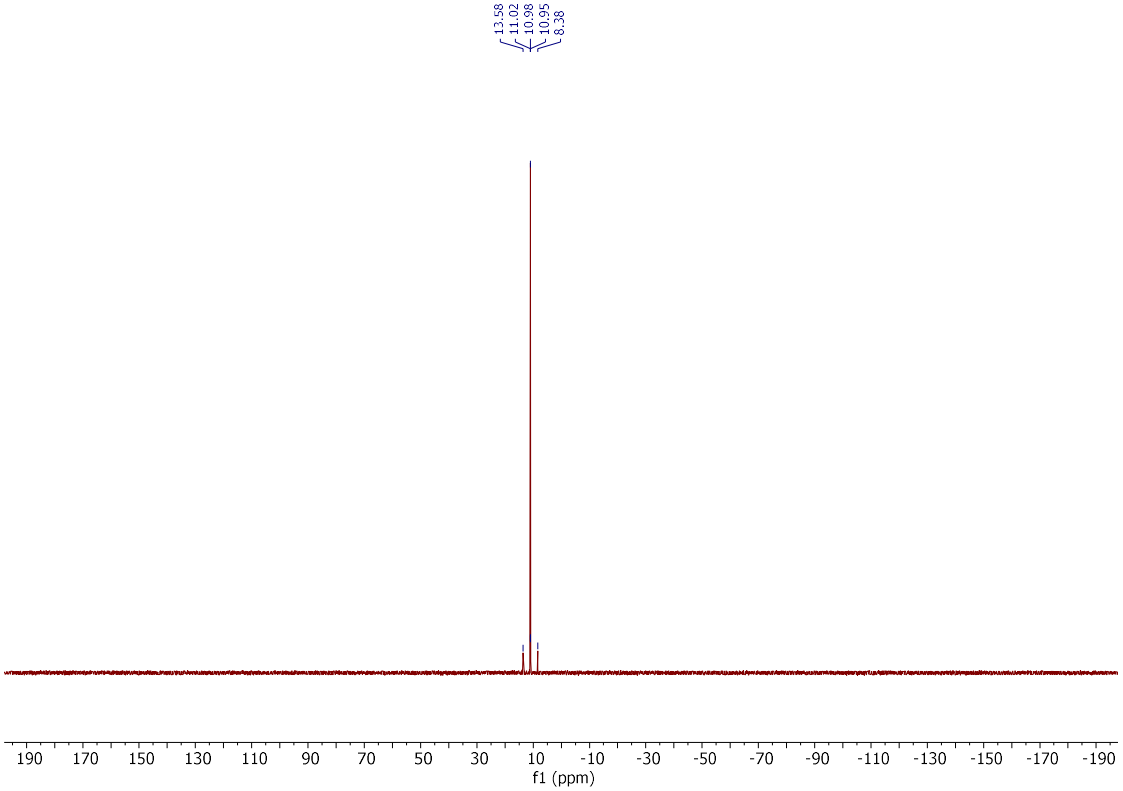

$^{31}P\{H\}$ NMR (162 MHz, CD_2Cl_2)

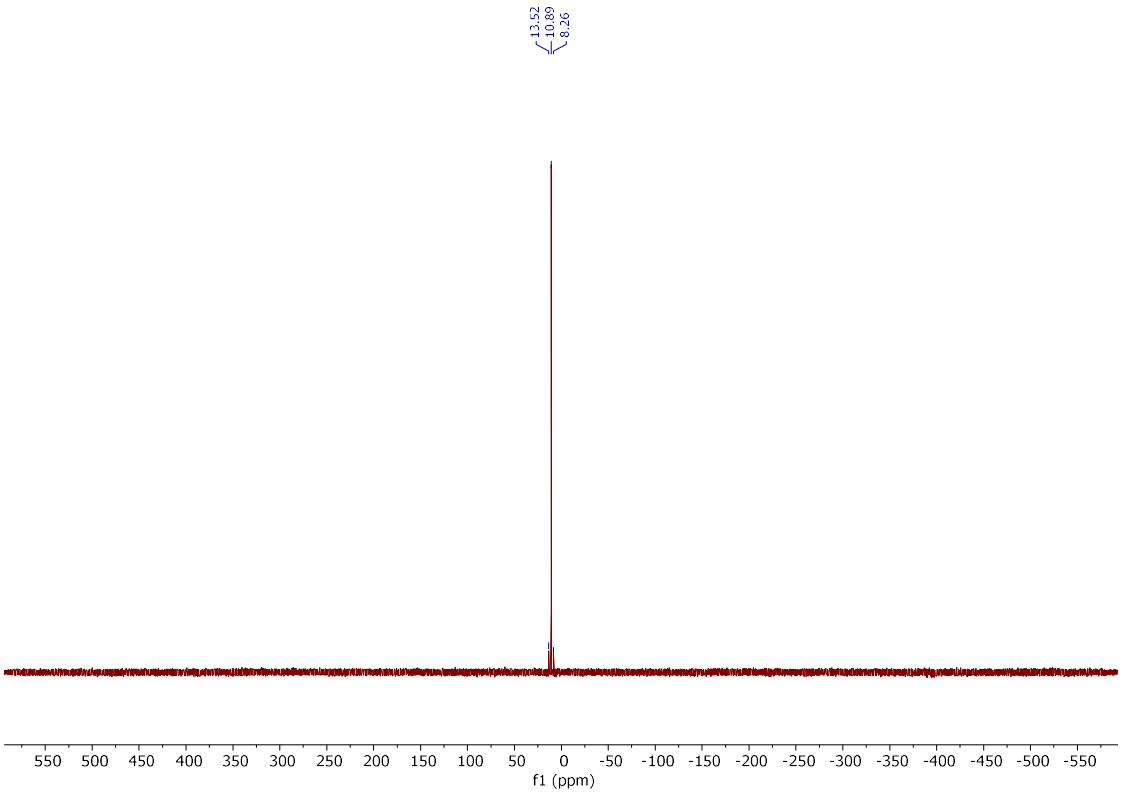

^{19}F NMR (376 MHz, CD_3CN)

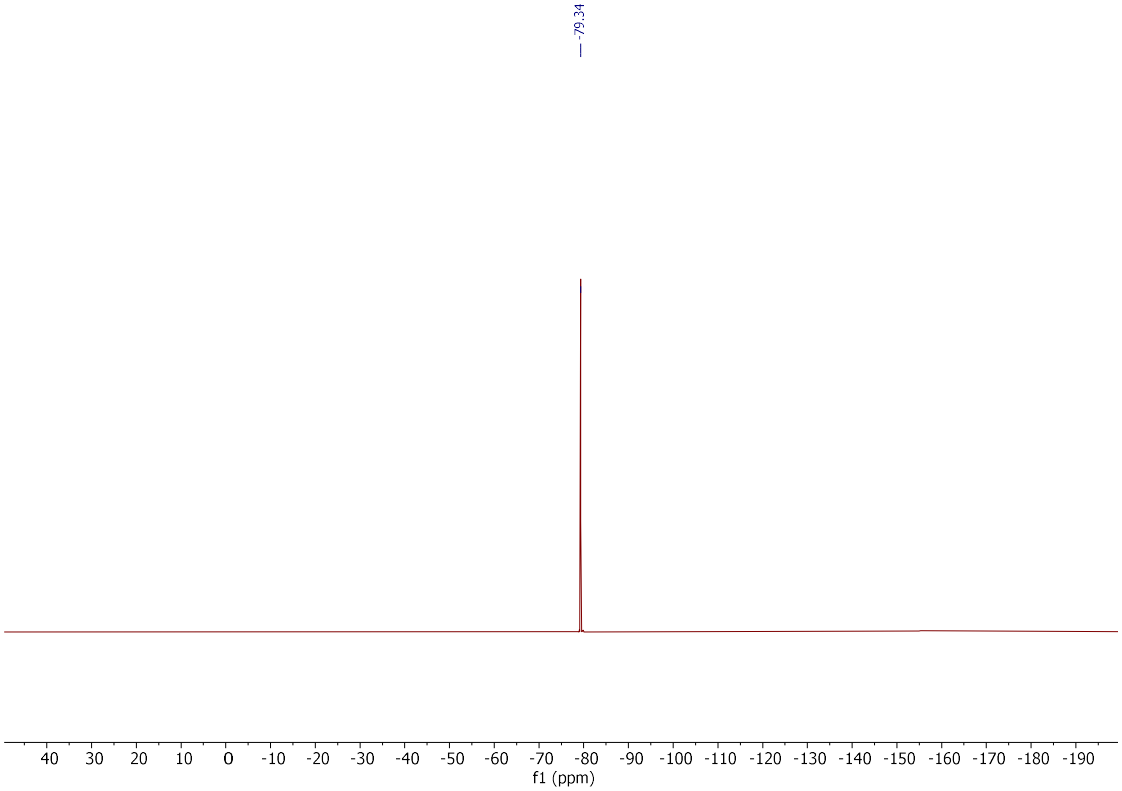

^{77}Se NMR (76 MHz, CD_3CN)

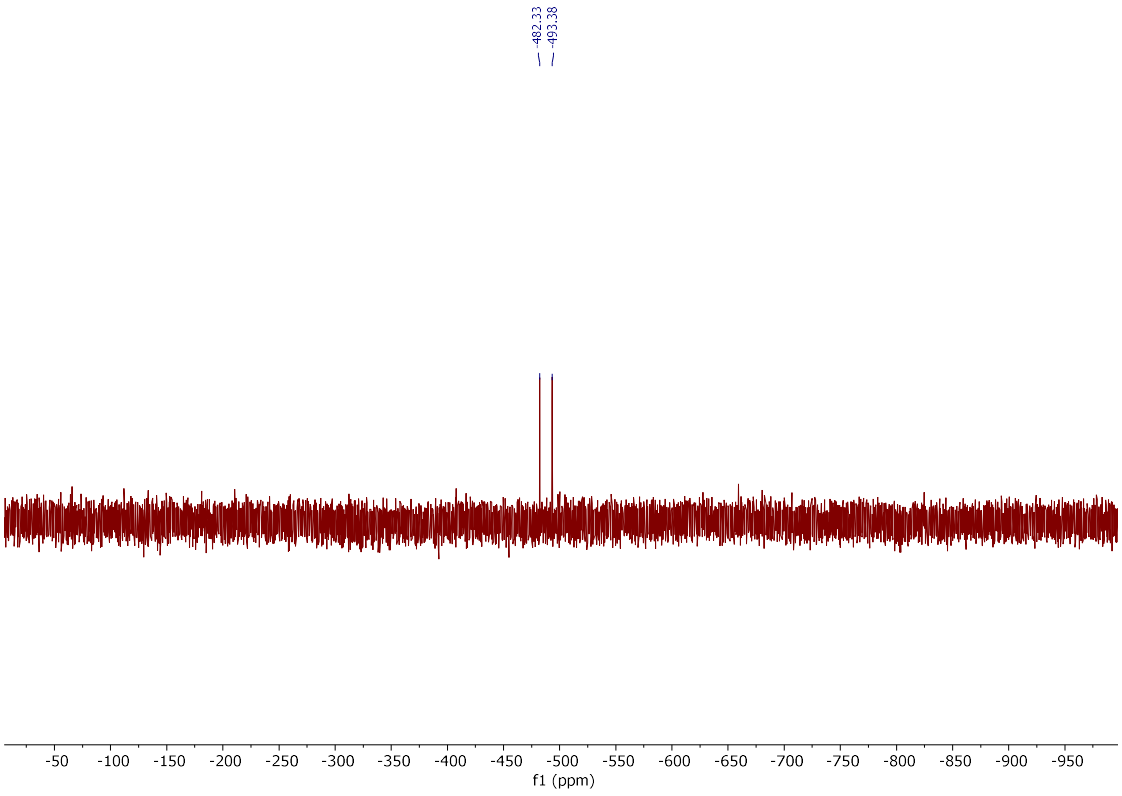

Compound **254**

^{1}H NMR (400 MHz, CD_3CN)

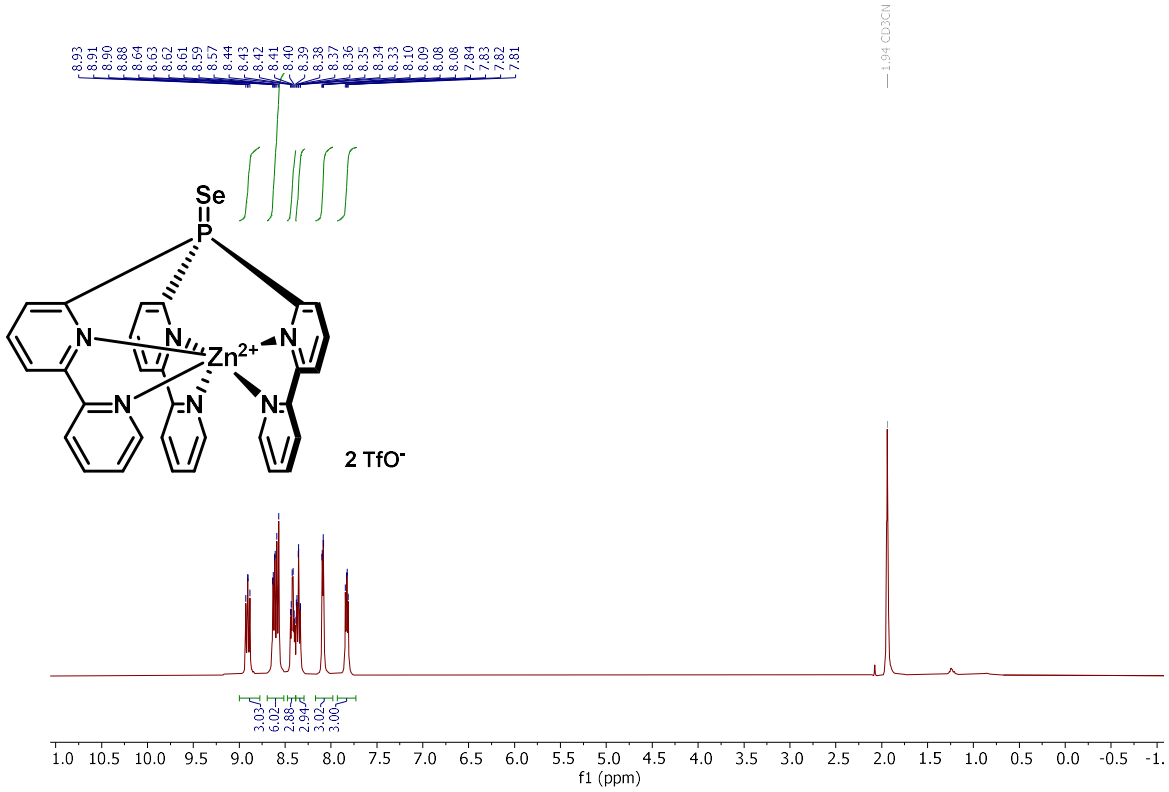

^{13}C{H} NMR (101 MHz, CD_3CN)

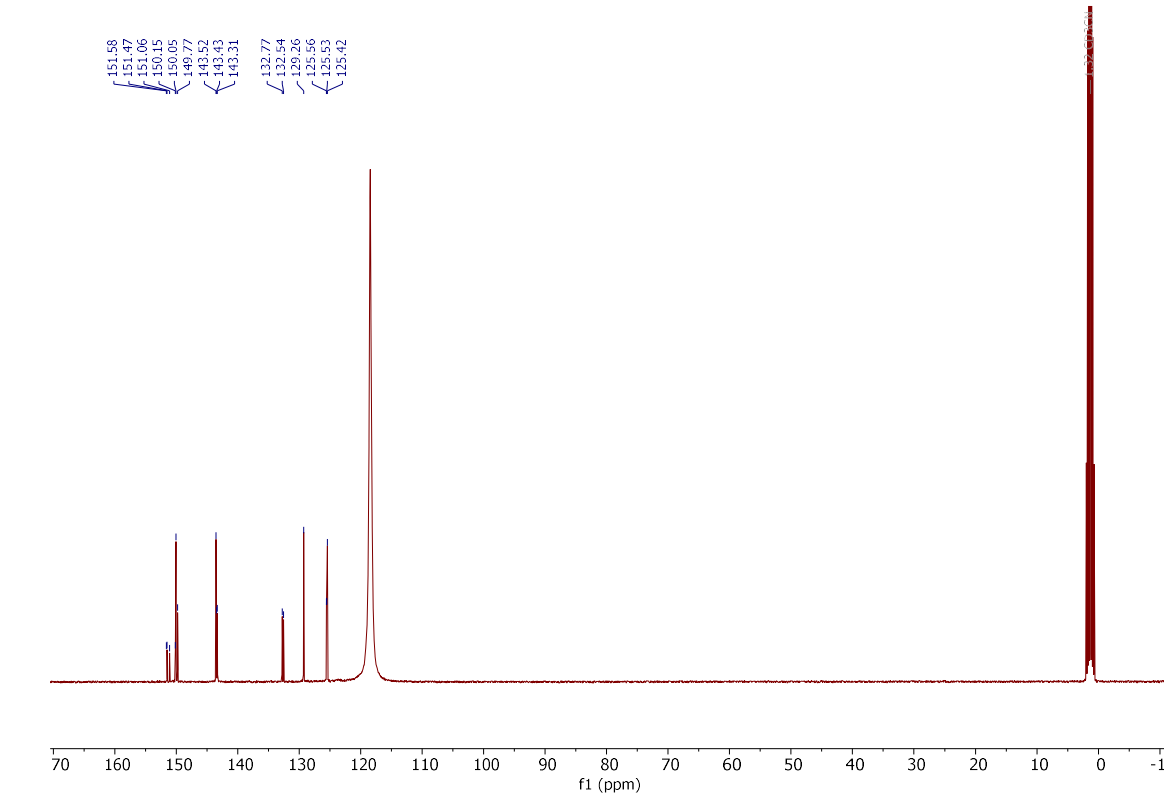

$^{31}P\{H\}$ NMR (162 MHz, CD_3CN)

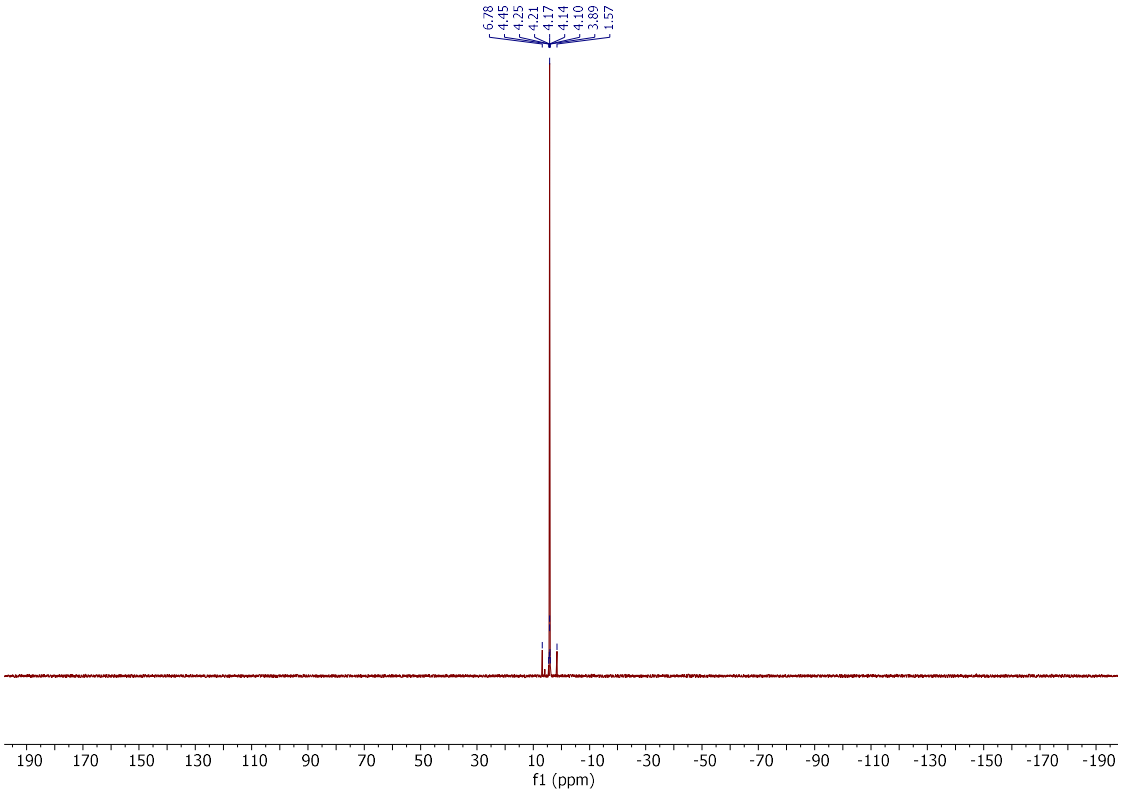

$^{31}P\{H\}$ NMR (162 MHz, CD_2Cl_2)

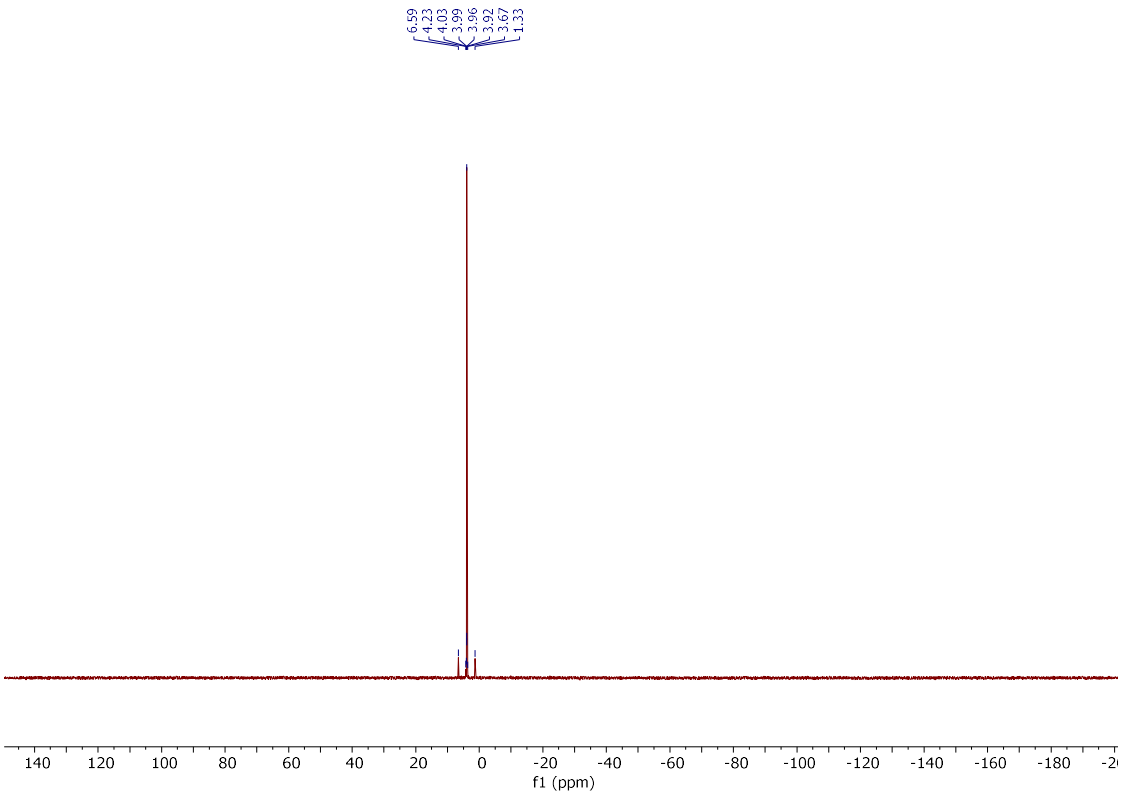

^{19}F NMR (376 MHz, CD_3CN)

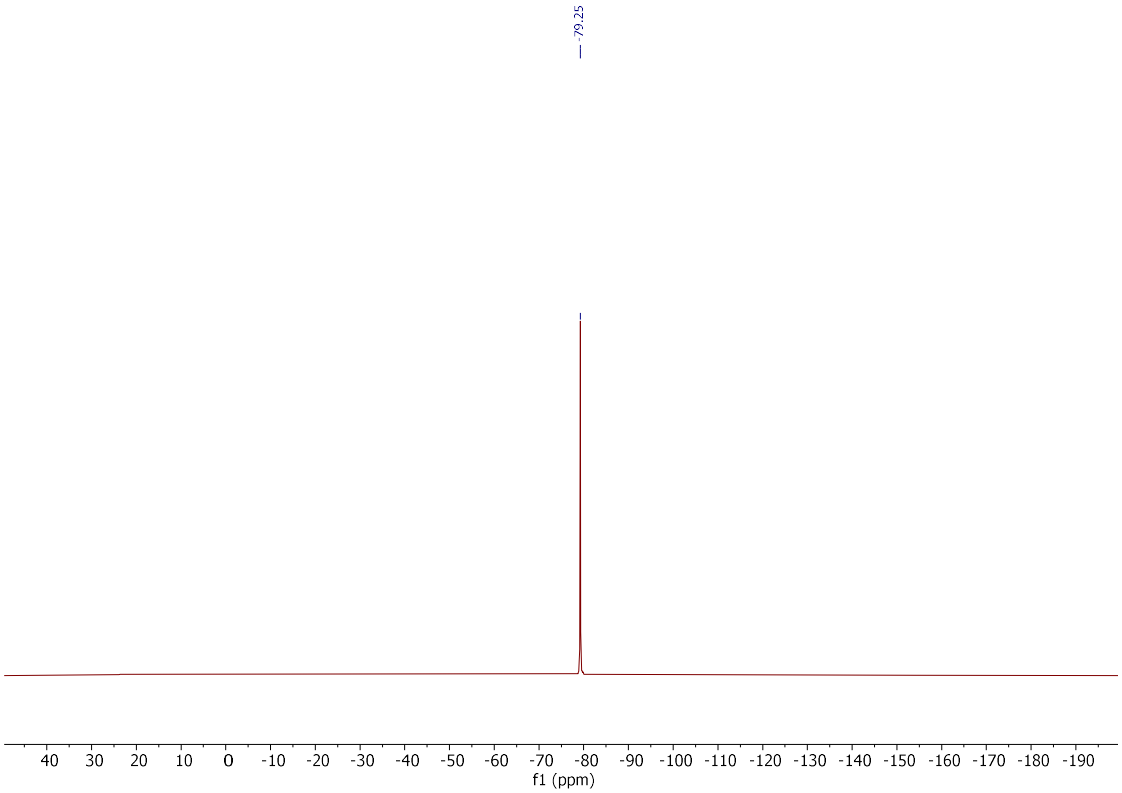

^{77}Se NMR (76 MHz, CD_3CN)

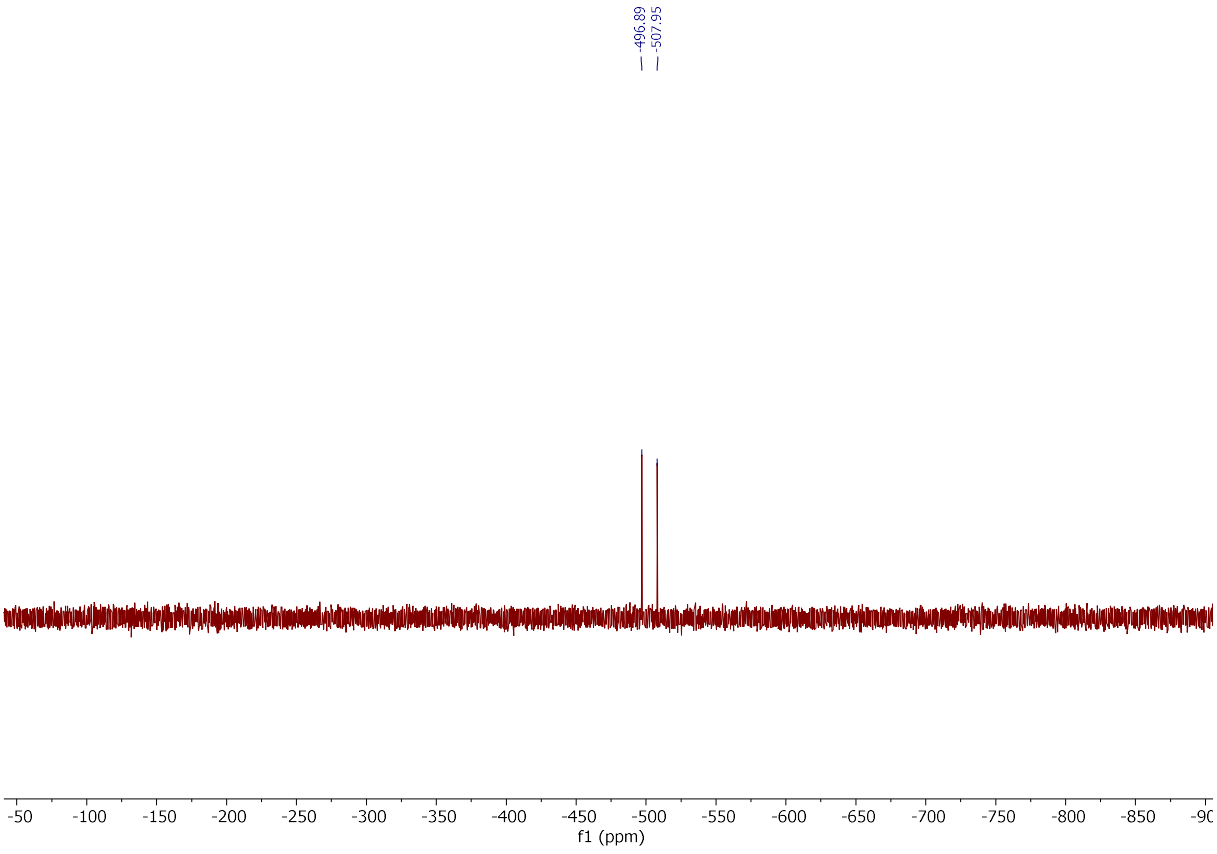

Compound **255**

^{1}H NMR (400 MHz, CD_3CN)

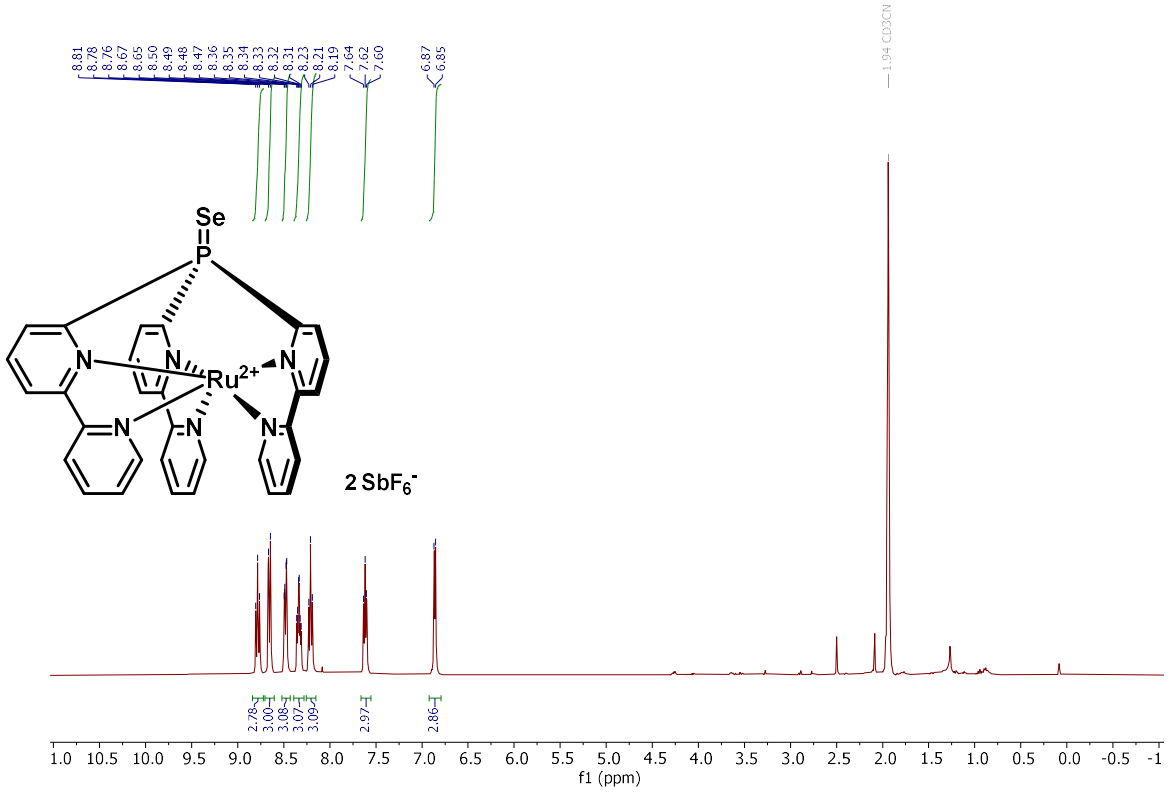

^{13}C{H} NMR (101 MHz, CD_3CN)

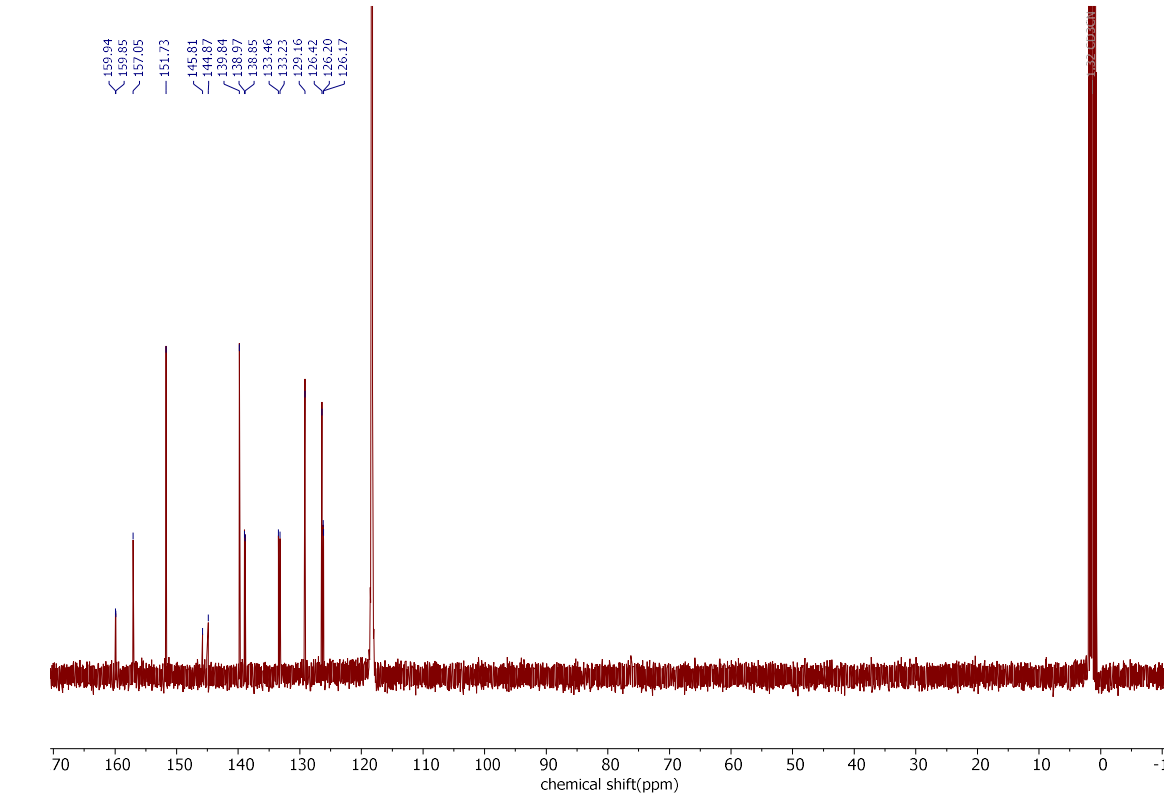

$^{31}P\{H\}$ NMR (162 MHz, CD_3CN)

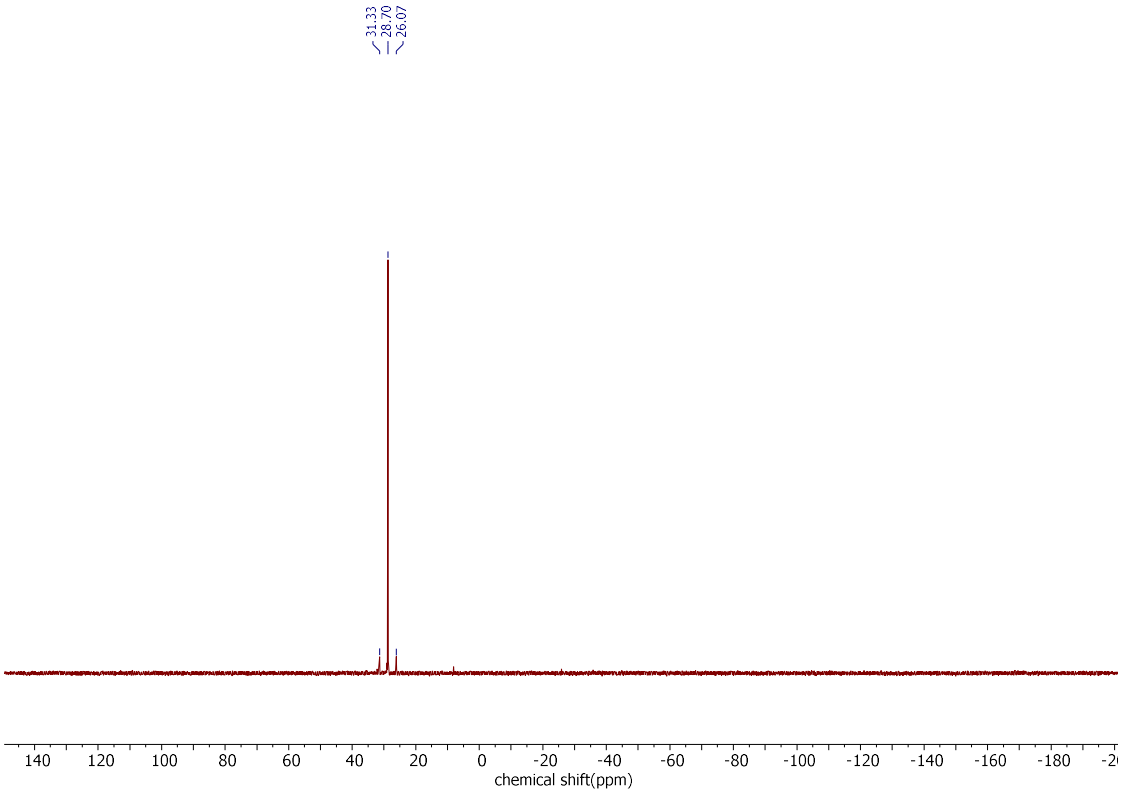

$^{31}P\{H\}$ NMR (162 MHz, CD_2Cl_2)

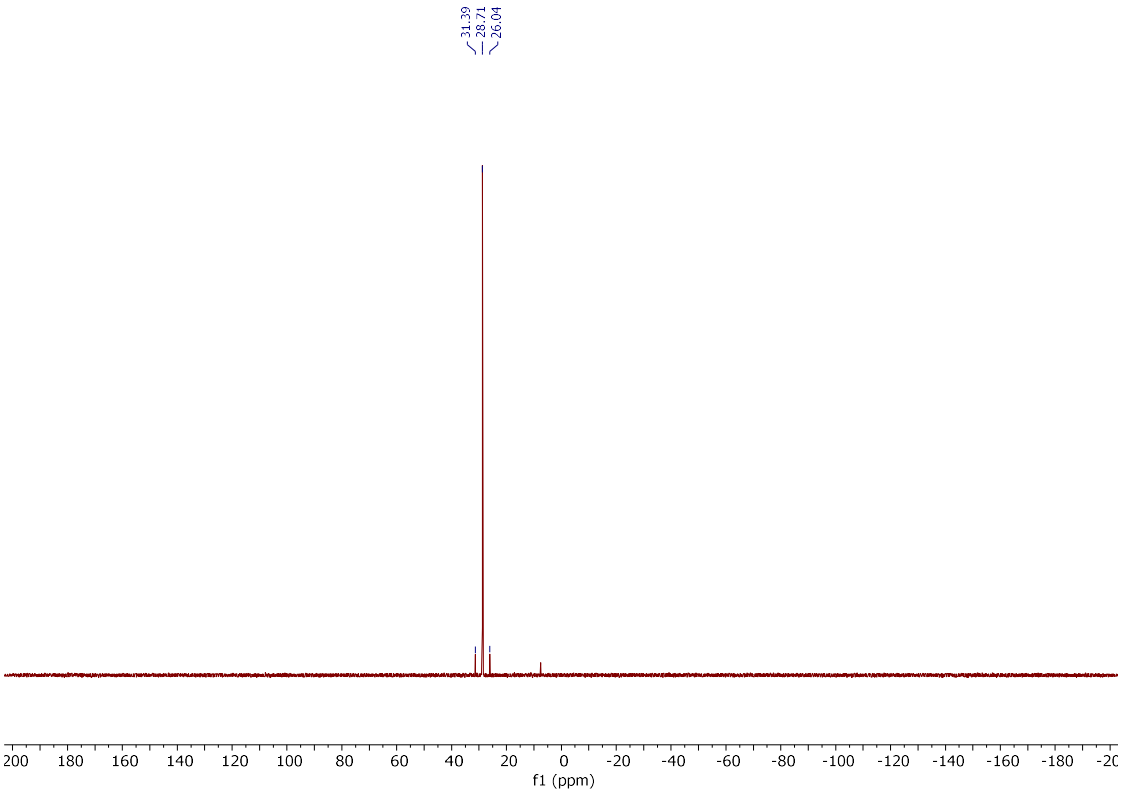

^{19}F NMR (377 MHz, CD_3CN)

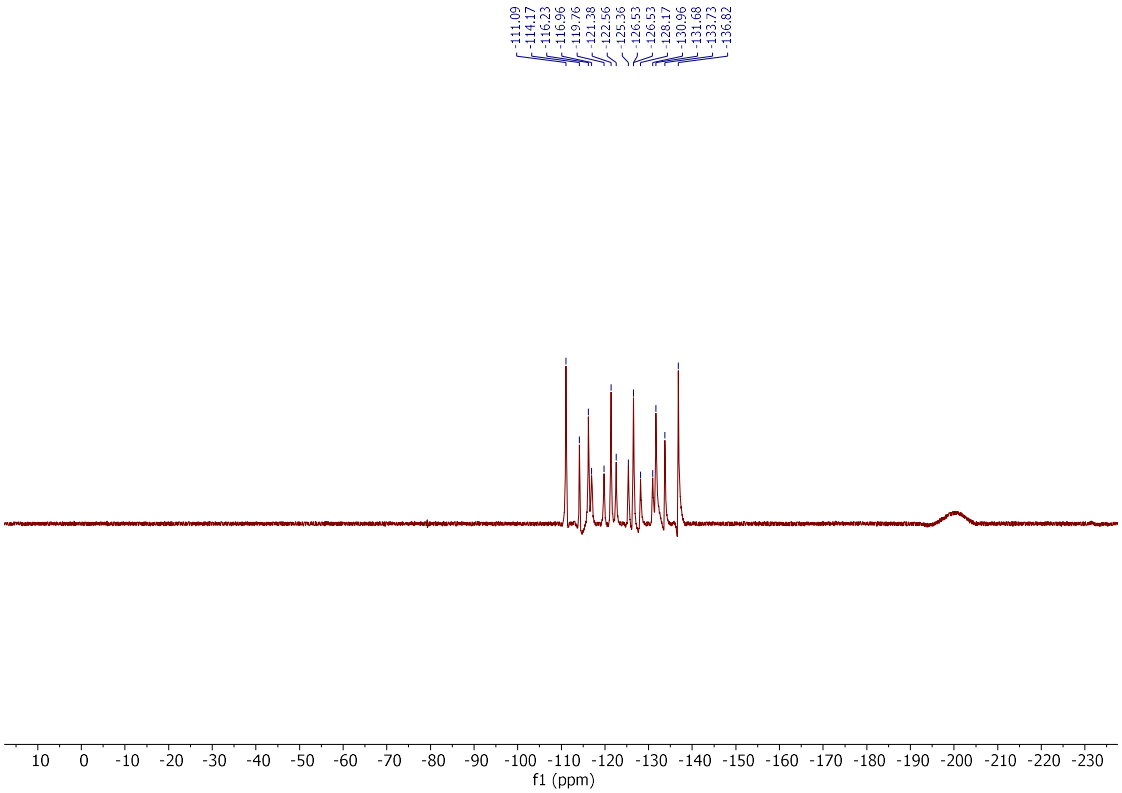

^{77}Se NMR (76 MHz, CD_3CN)

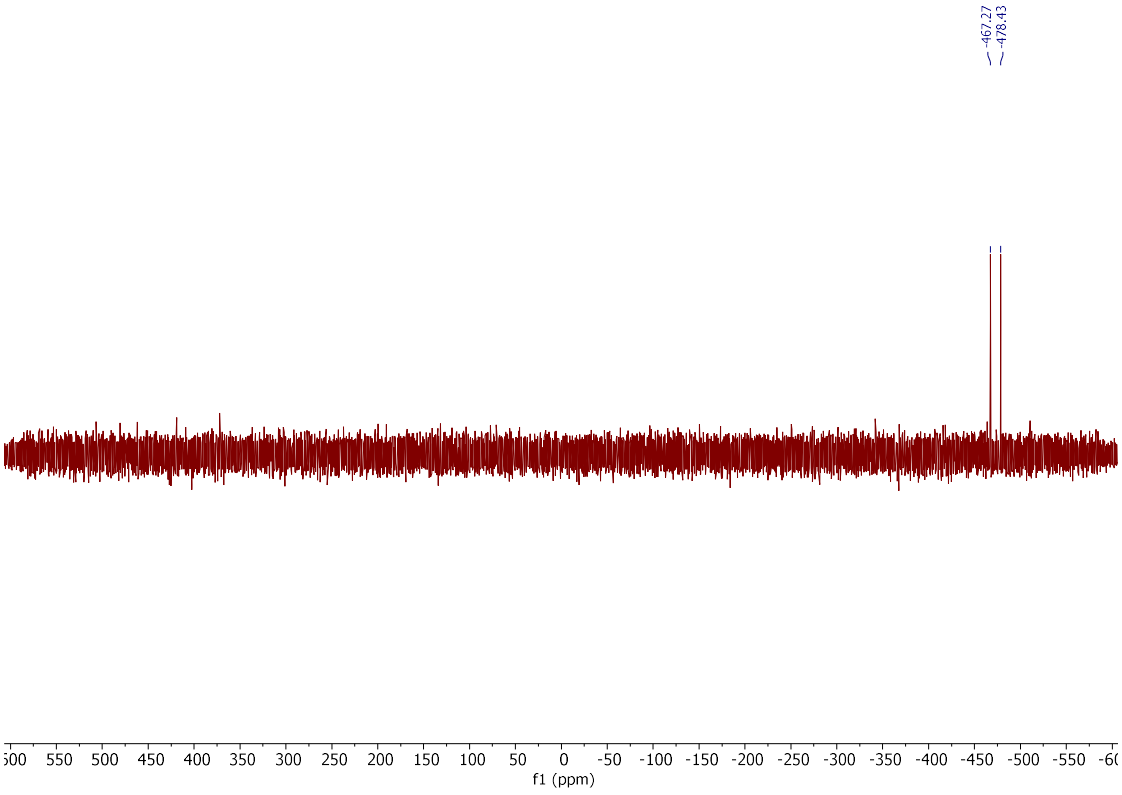

Compound **256**

^{1}H NMR (400 MHz, CD_3CN)

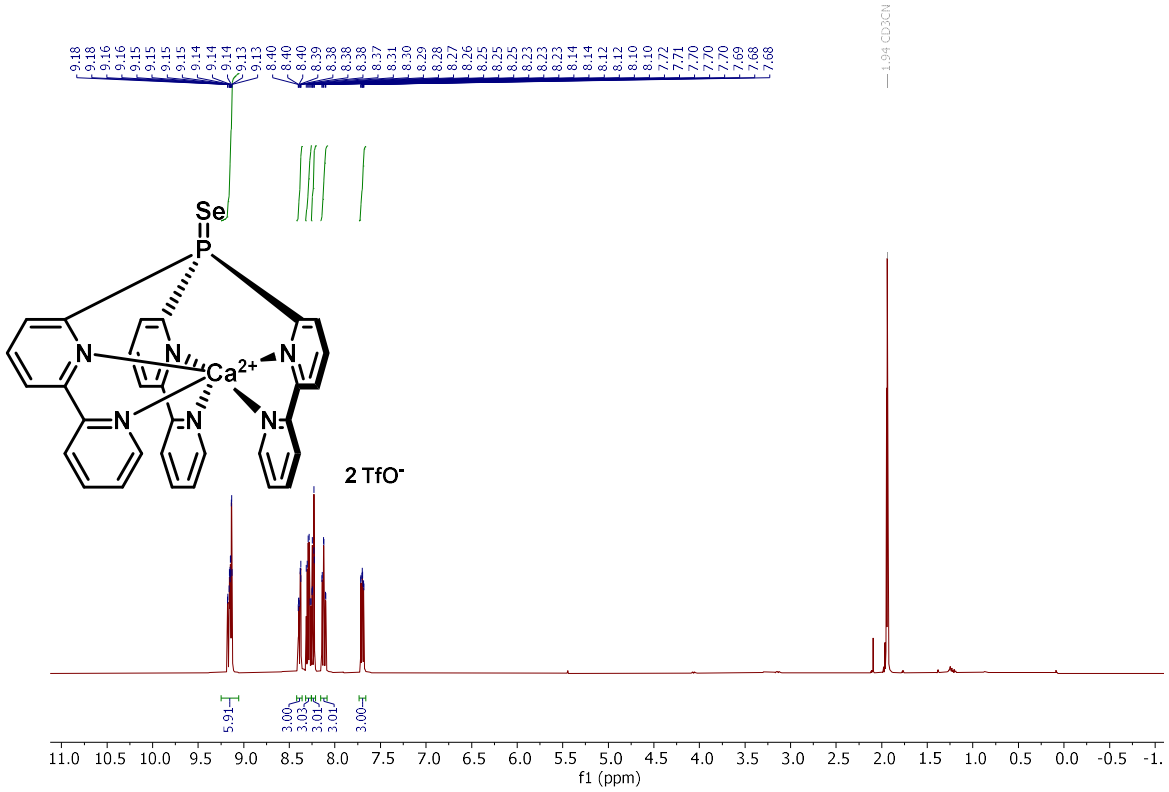

^{13}C{H} NMR (101 MHz, CD_3CN)

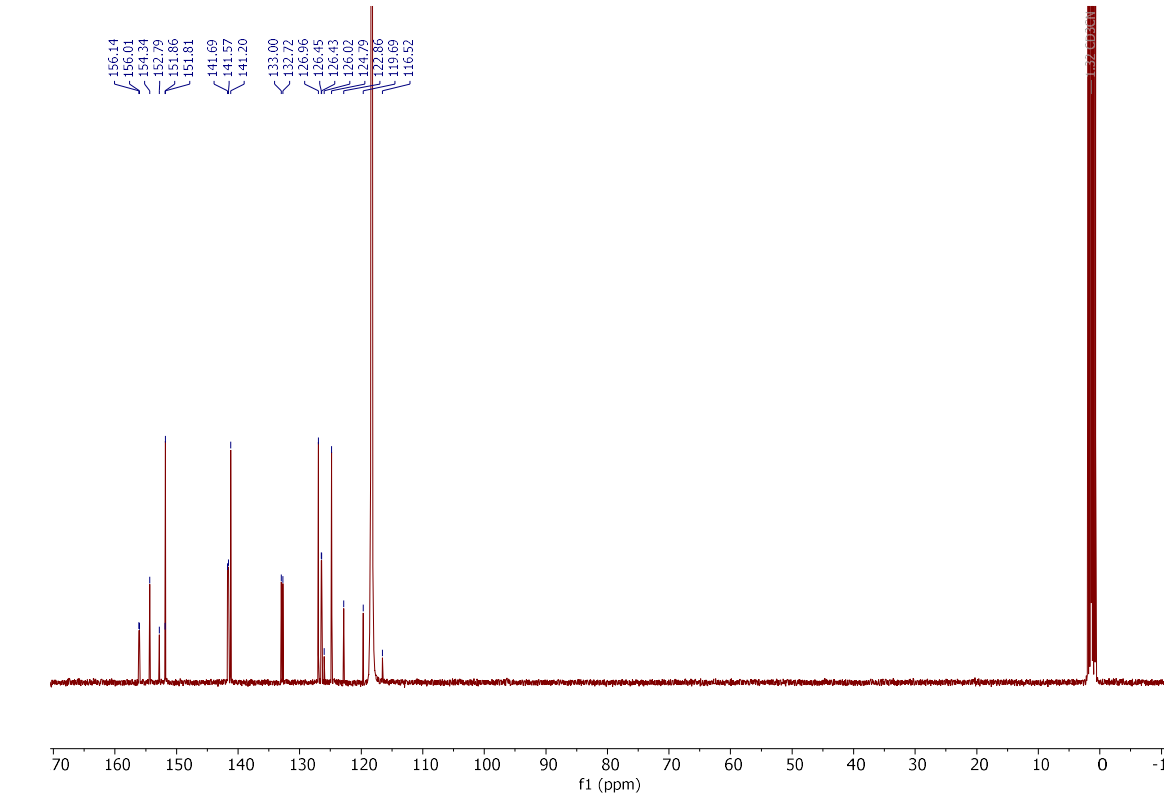

$^{31}P\{H\}$ NMR (162 MHz, CD_3CN)

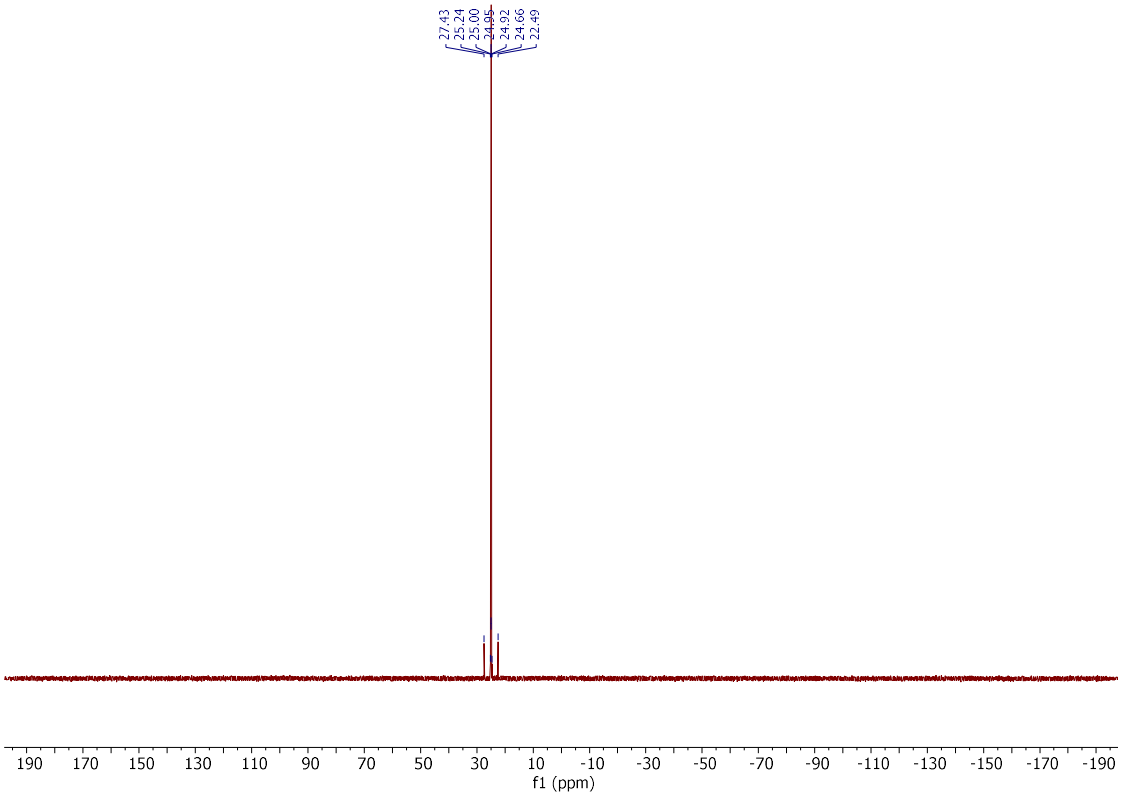

^{19}F NMR (376 MHz, CD_3CN)

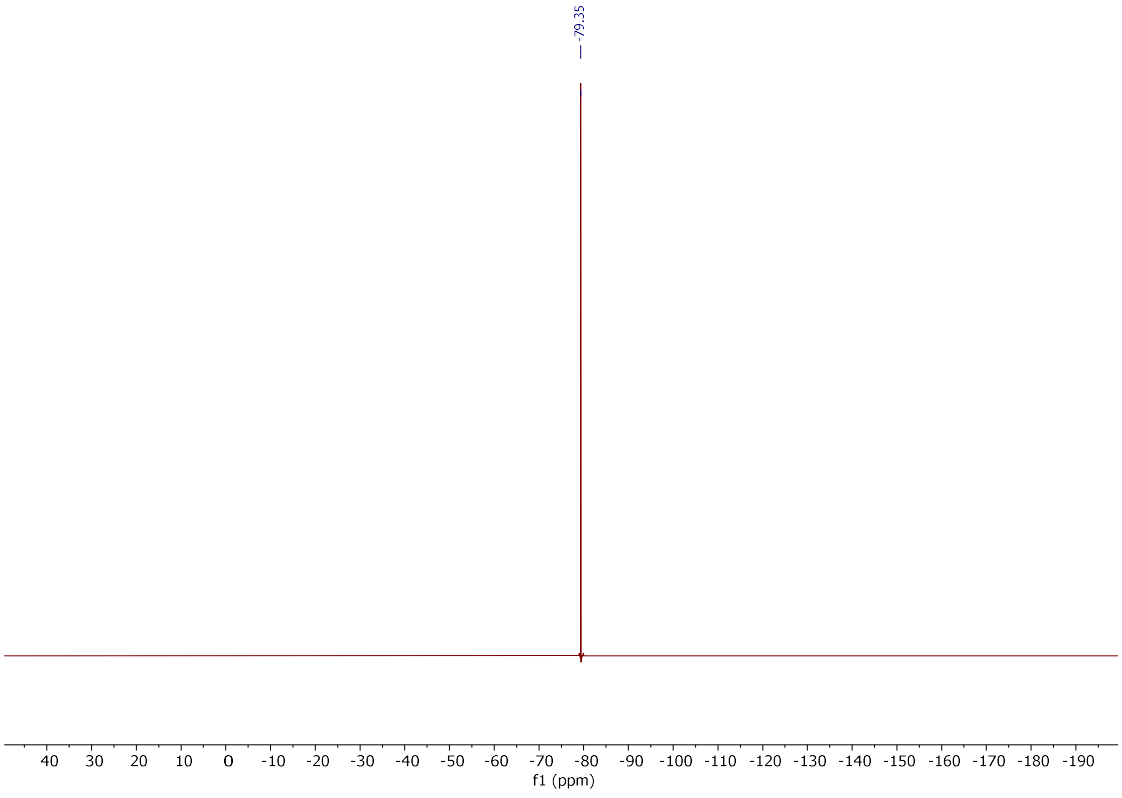

^{77}Se NMR (76 MHz, CD_3CN)

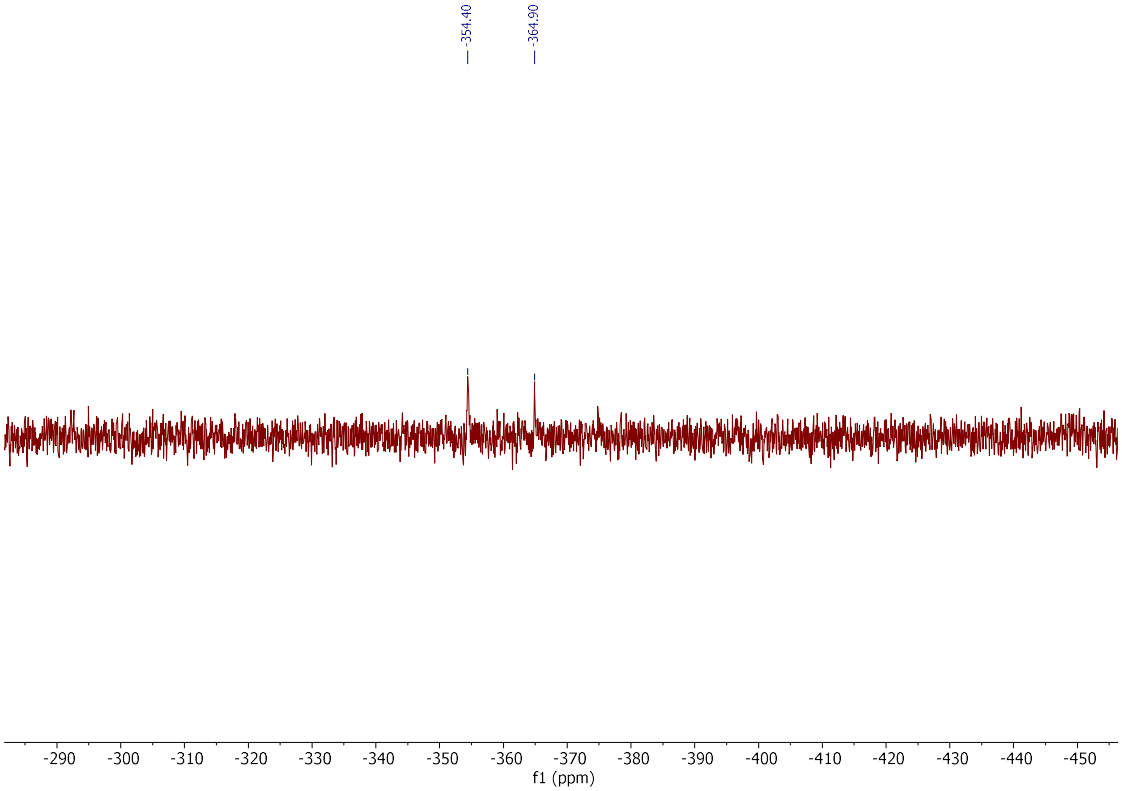

Compound **257**

^{1}H NMR (400 MHz, CD_3CN)

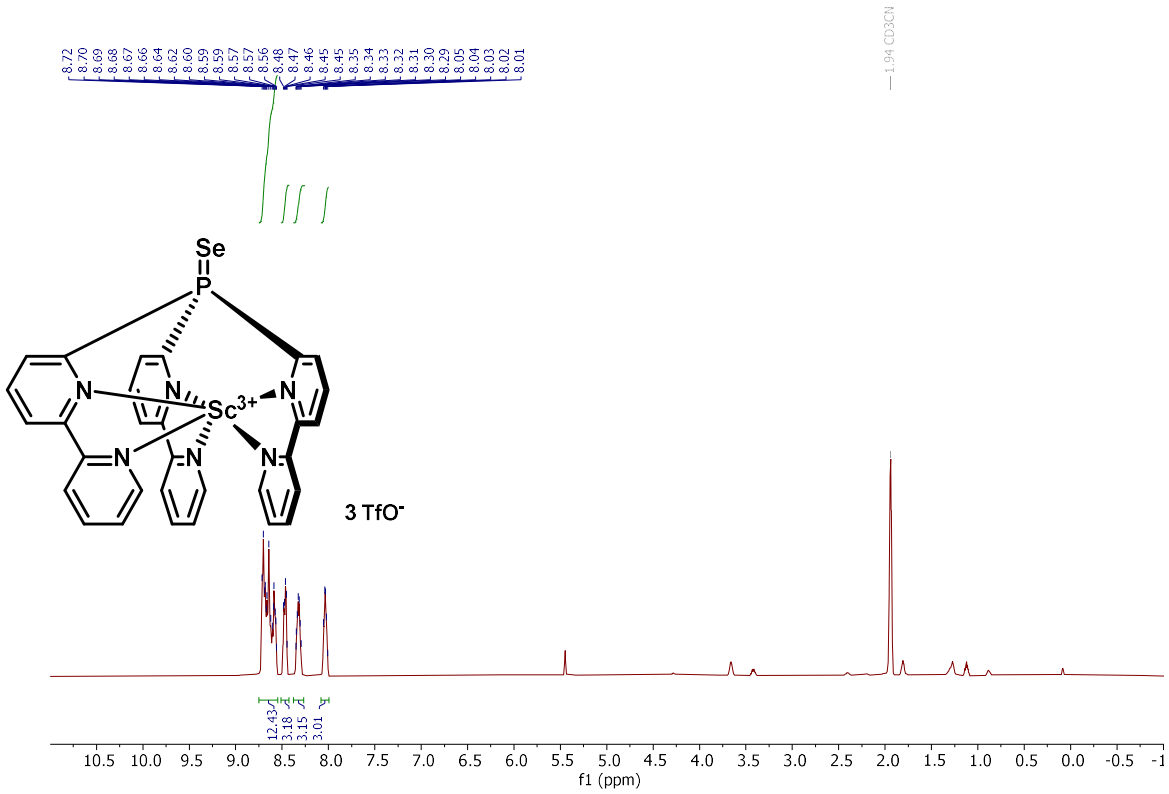

^{13}C{H} NMR (101 MHz, CD_3CN)

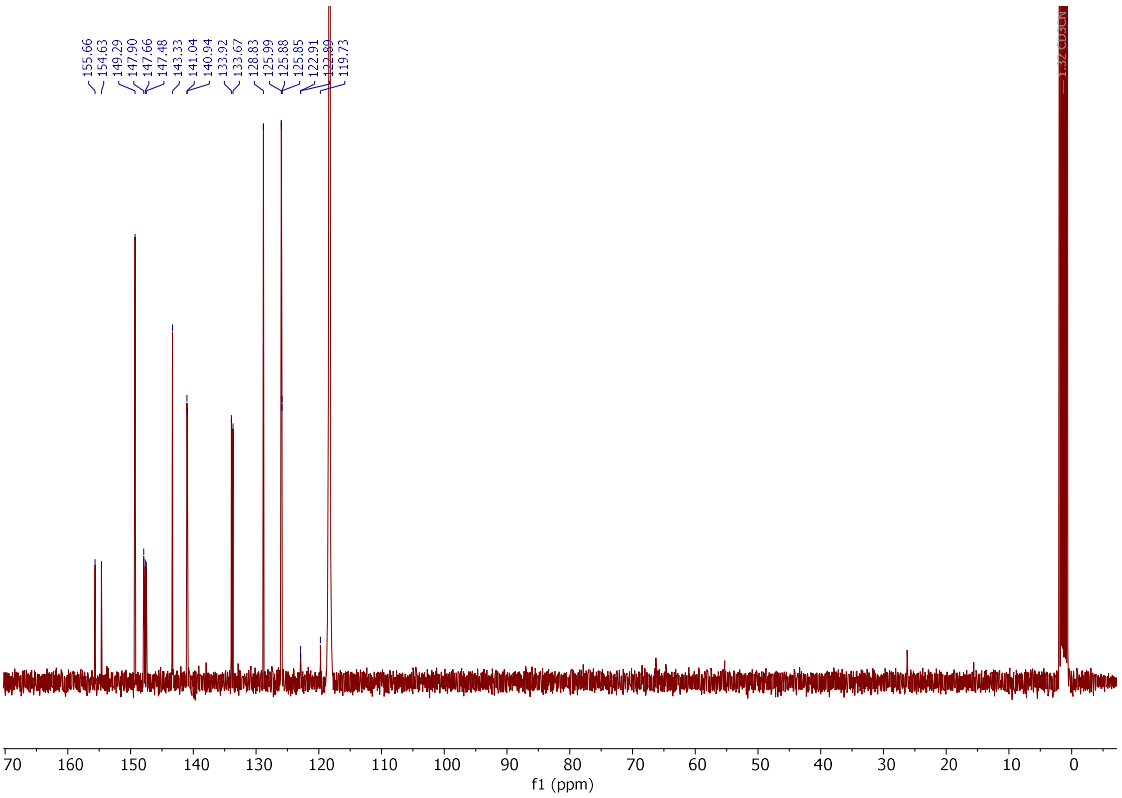

$^{31}P\{H\}$ NMR (162 MHz, CD_3CN)

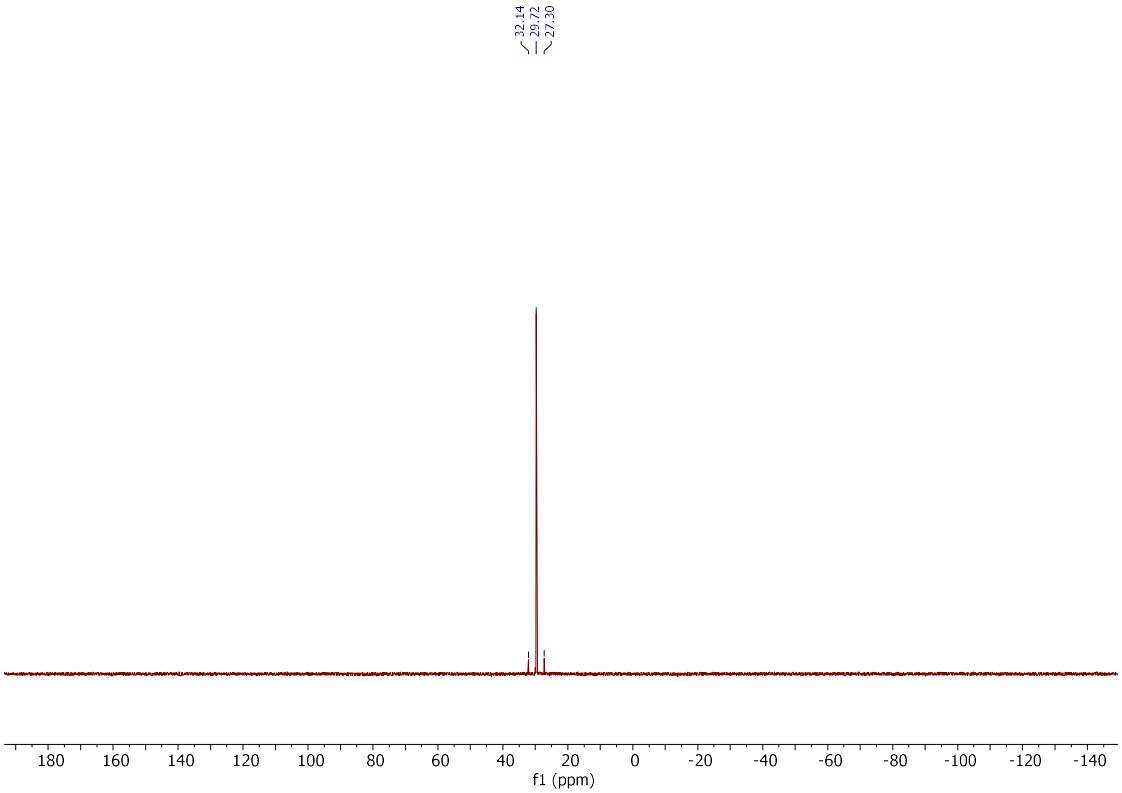

^{19}F NMR (282 MHz, CD_3CN)

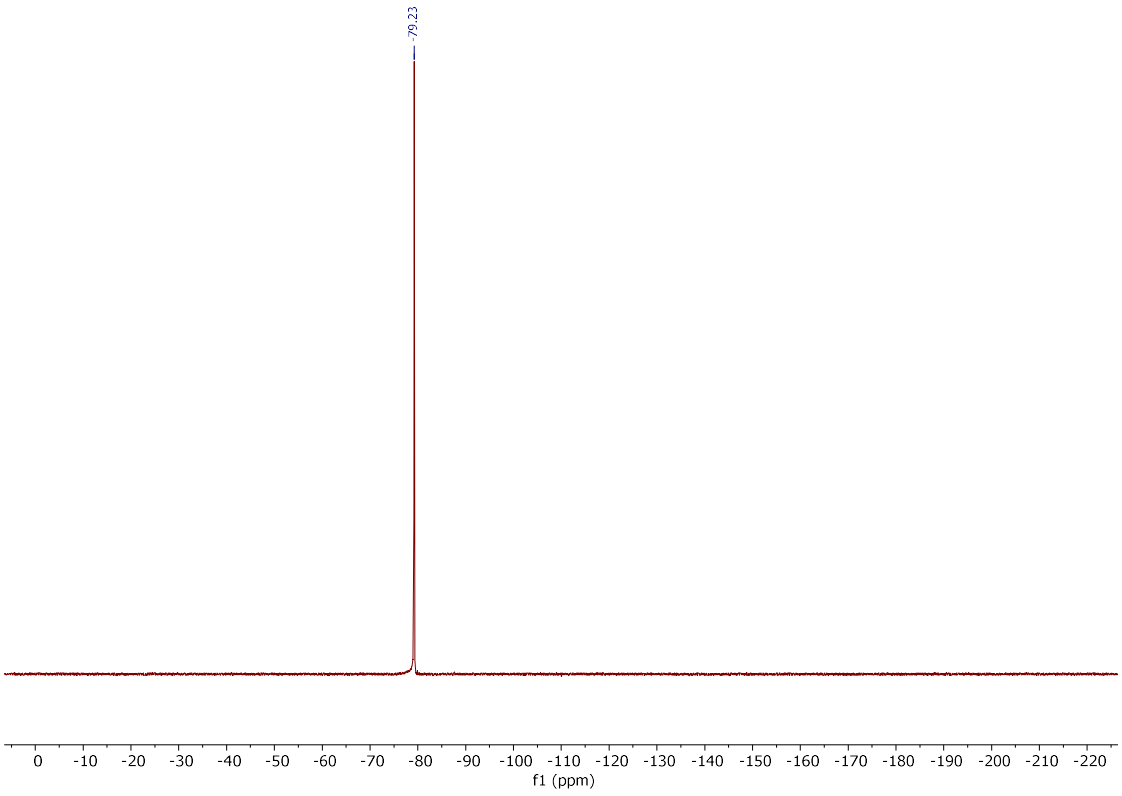

Compound **258**

^{1}H NMR (400 MHz, CD_3CN)

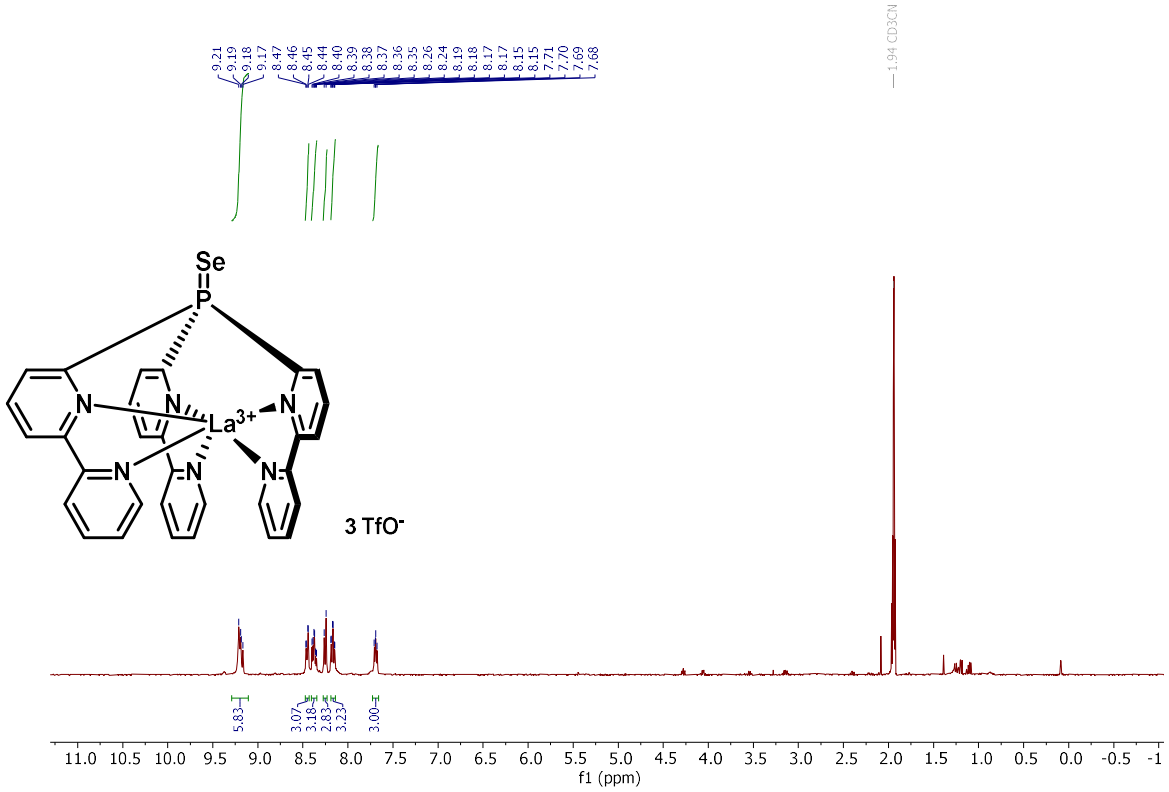

^{1}H NMR (400 MHz, CD_2Cl_2)

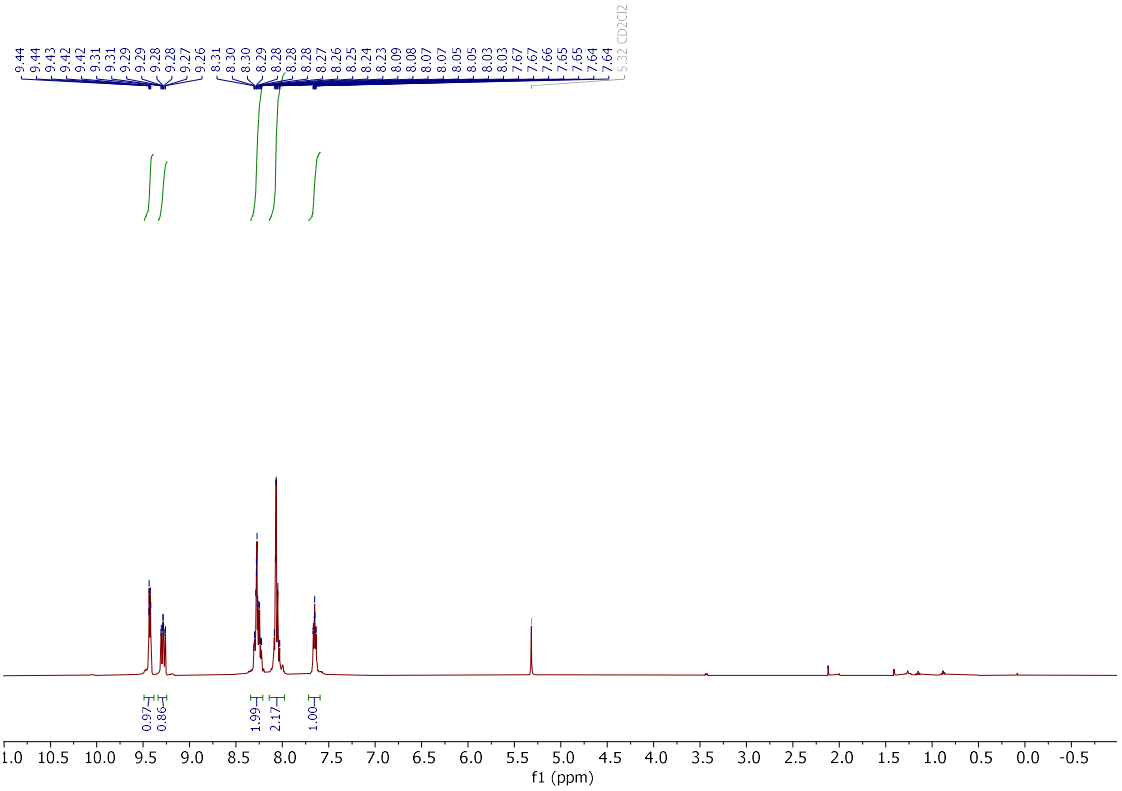

$^{13}C\{H\}$ NMR (101 MHz, CD_3CN)

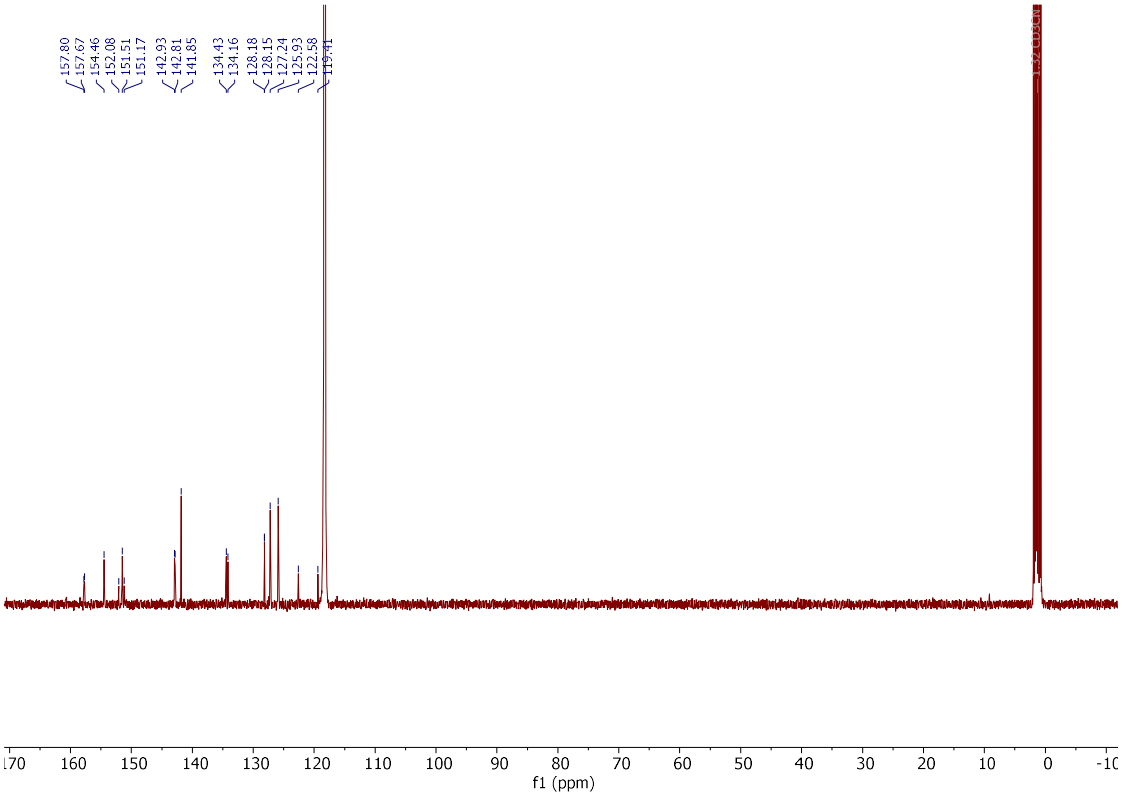

$^{31}P\{H\}$ NMR (162 MHz, CD_3CN)

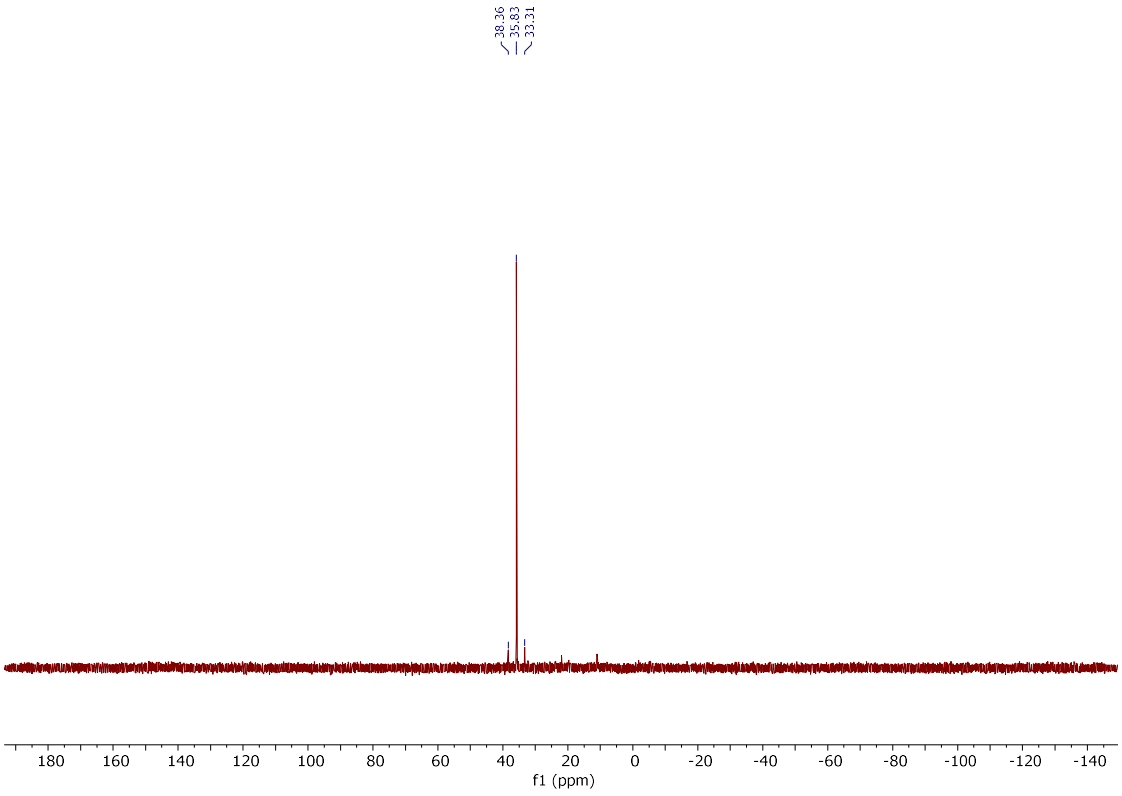

$^{31}P\{H\}$ NMR (162 MHz, CD_2Cl_2)

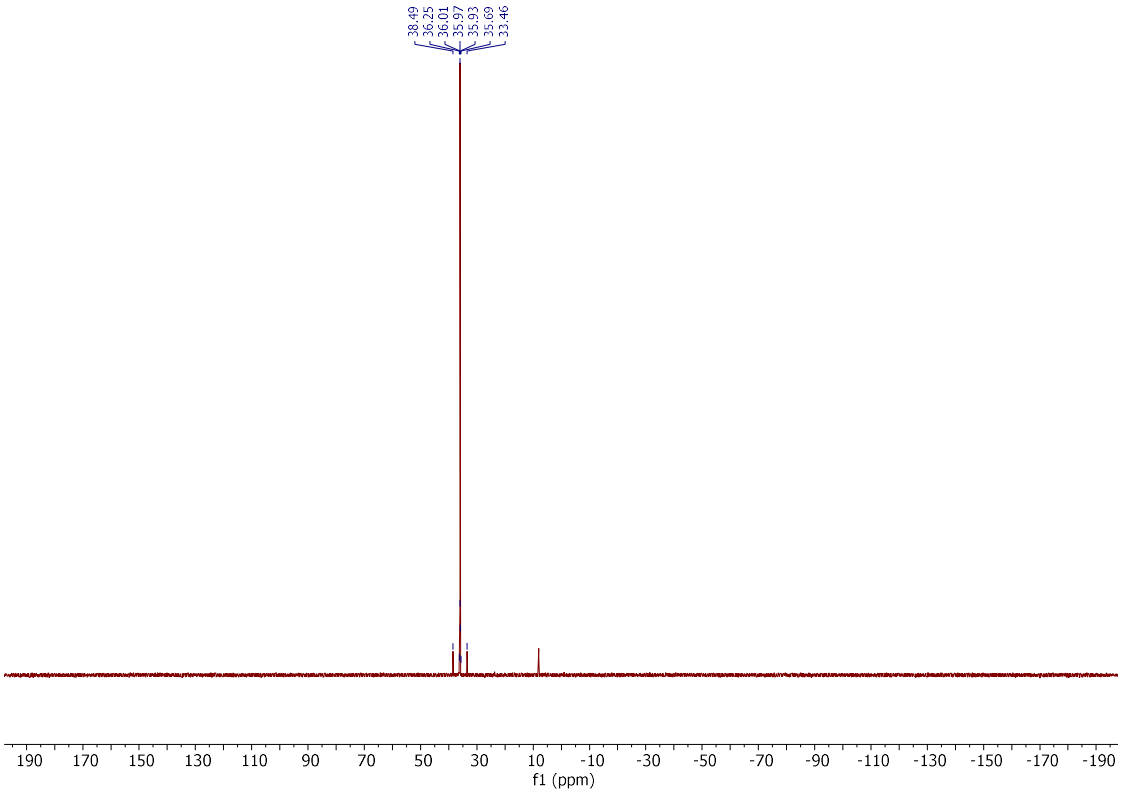

^{19}F NMR (376 MHz, CD_3CN)

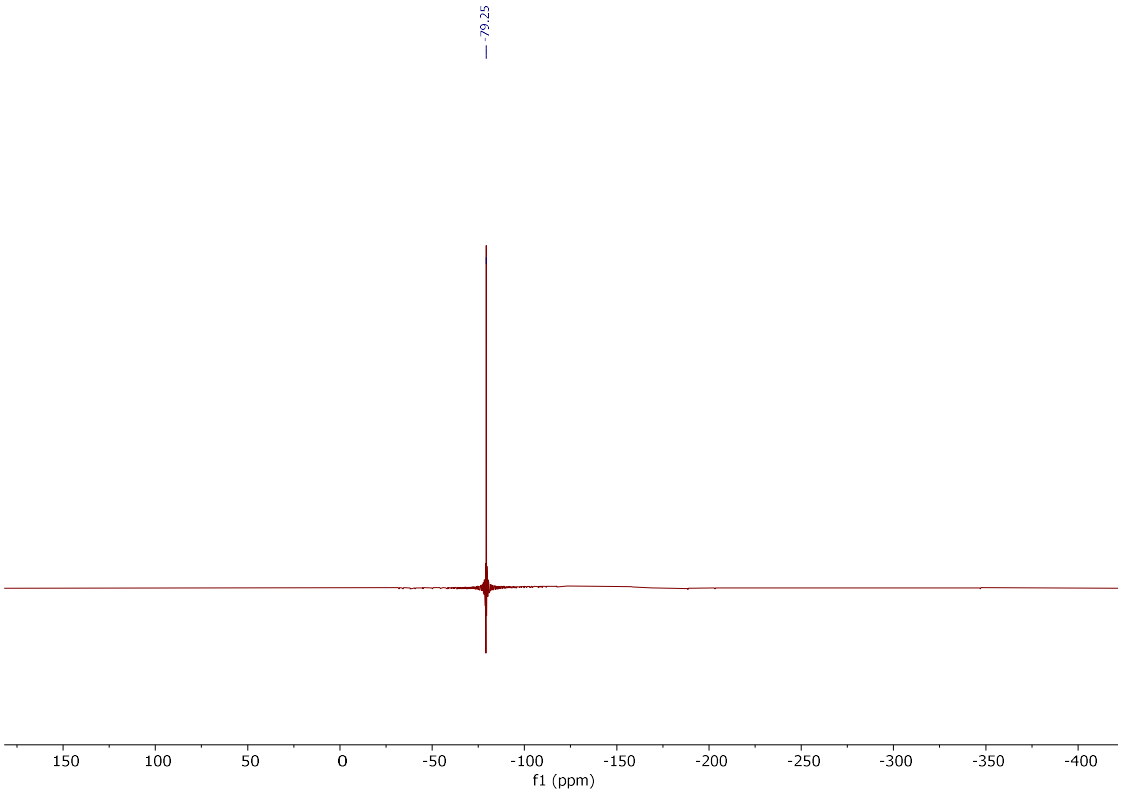

^{19}F NMR (376 MHz, CD_2Cl_2)

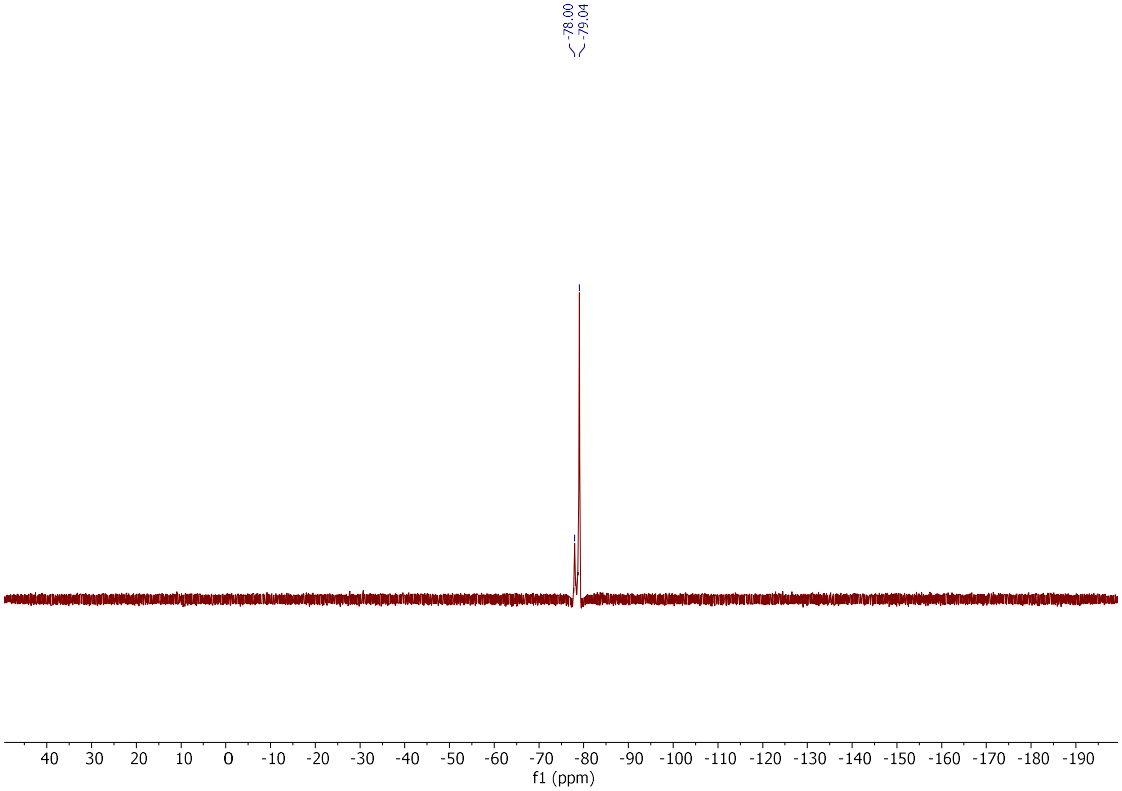

^{77}Se NMR (76 MHz, CD_3CN)

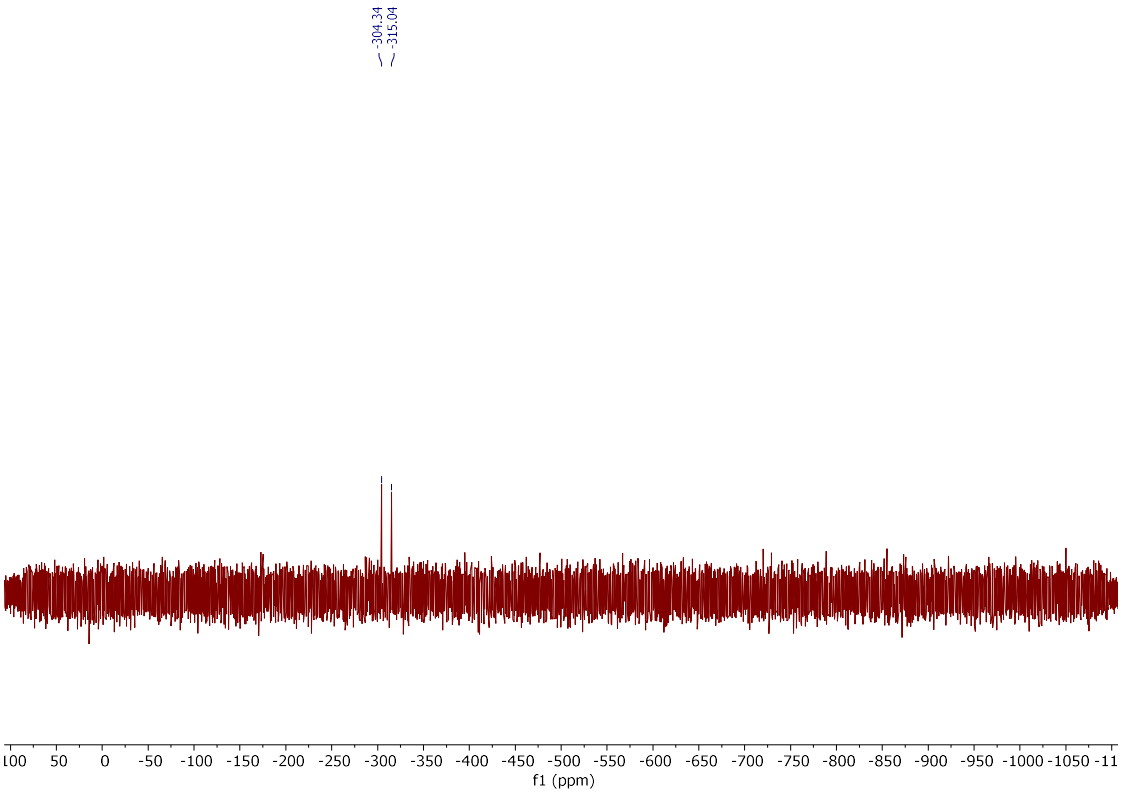

^{77}Se NMR (76 MHz, CD_2Cl_2)

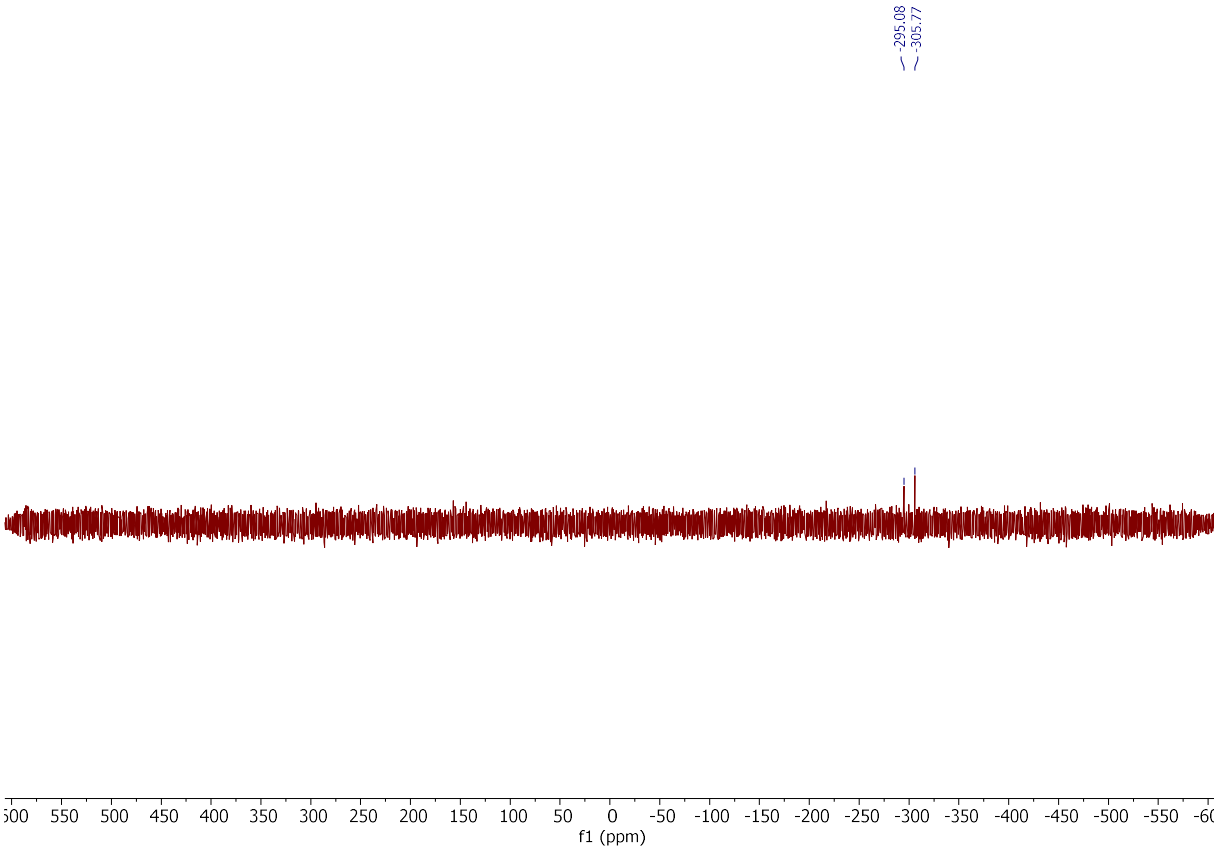

Compound **266**

^{1}H NMR (300 MHz, $CDCl_3$)

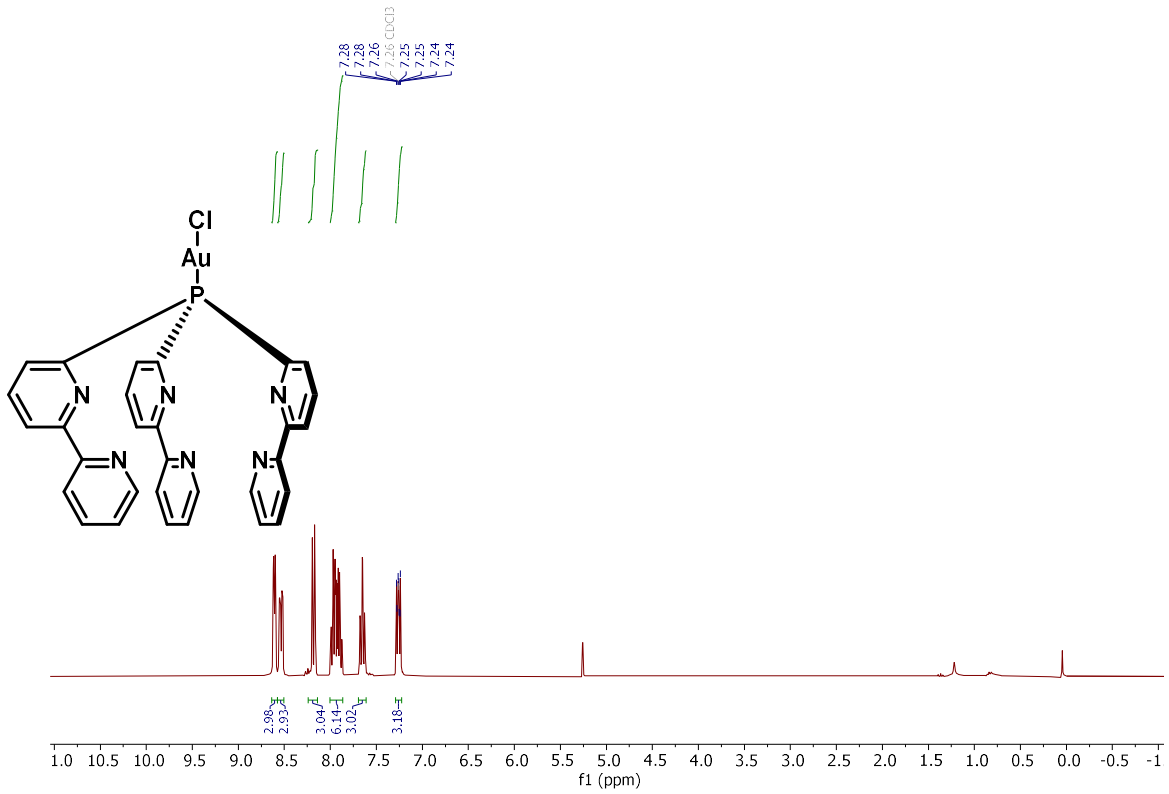

^{13}C{H} NMR (75 MHz, $CDCl_3$)

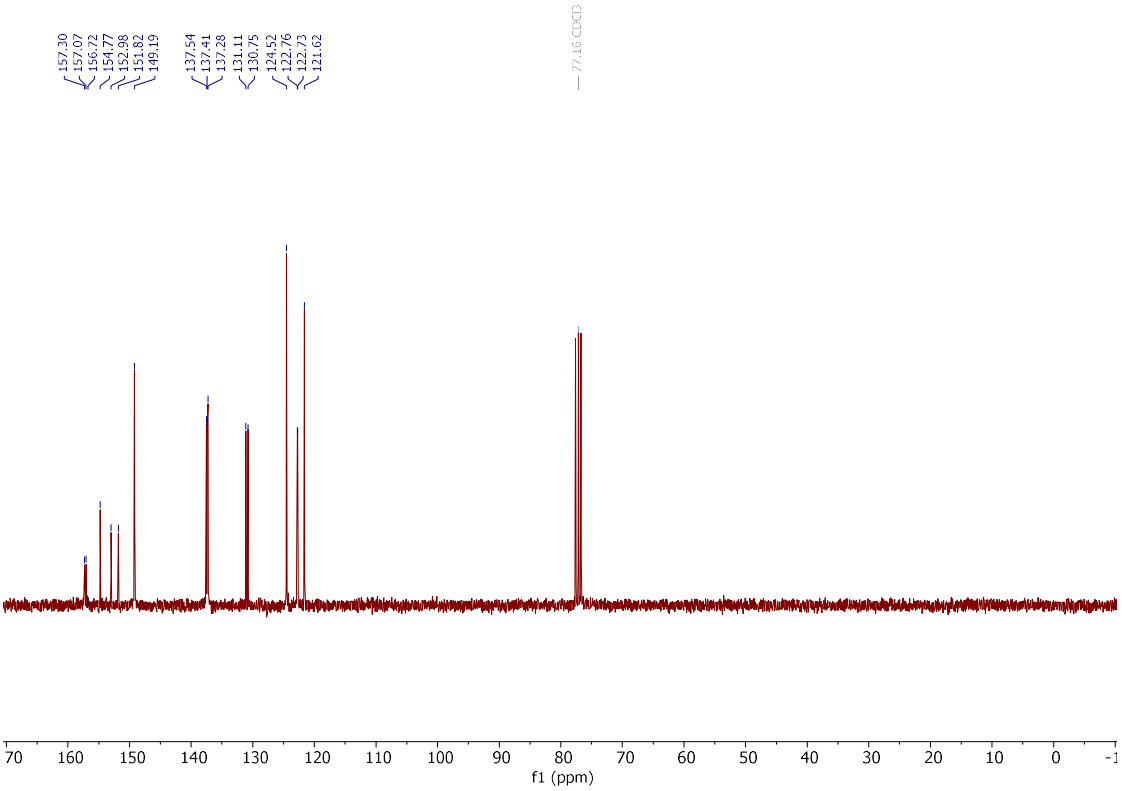

$^{31}P\{H\}$ NMR (162 MHz, $CDCl_3$)

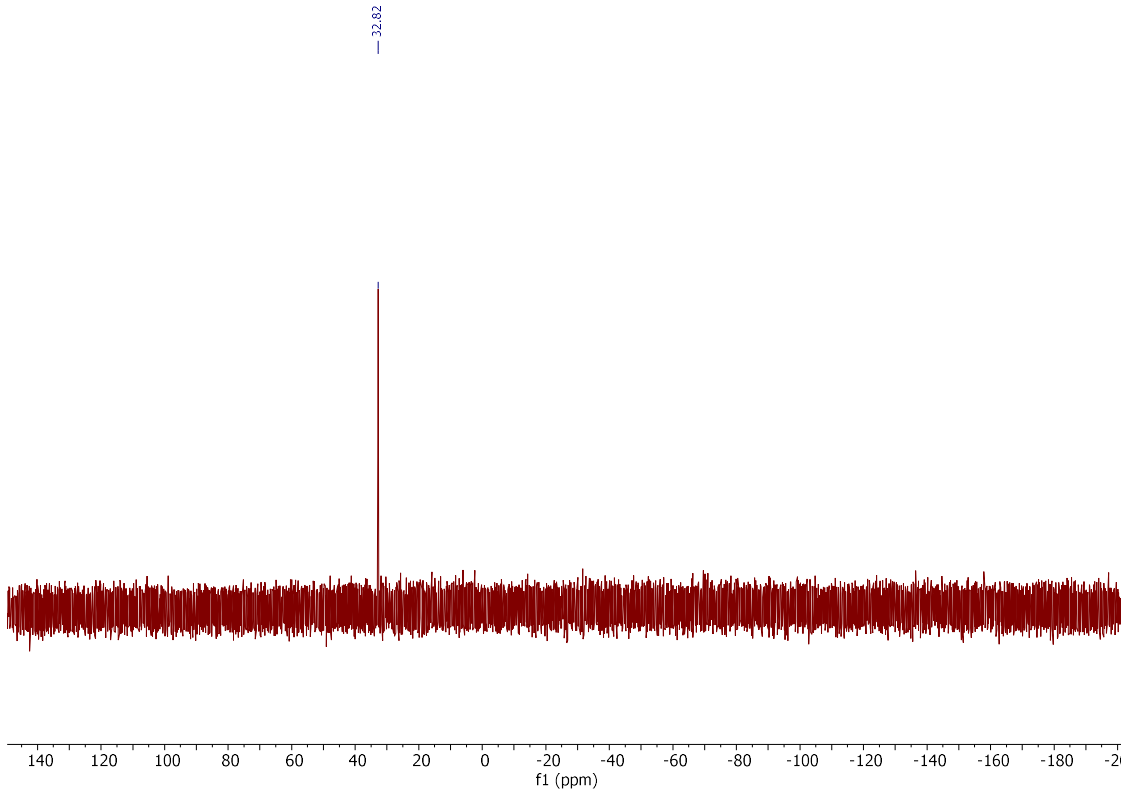

Compound **267**

^{1}H NMR (300 MHz, CD_3CN)

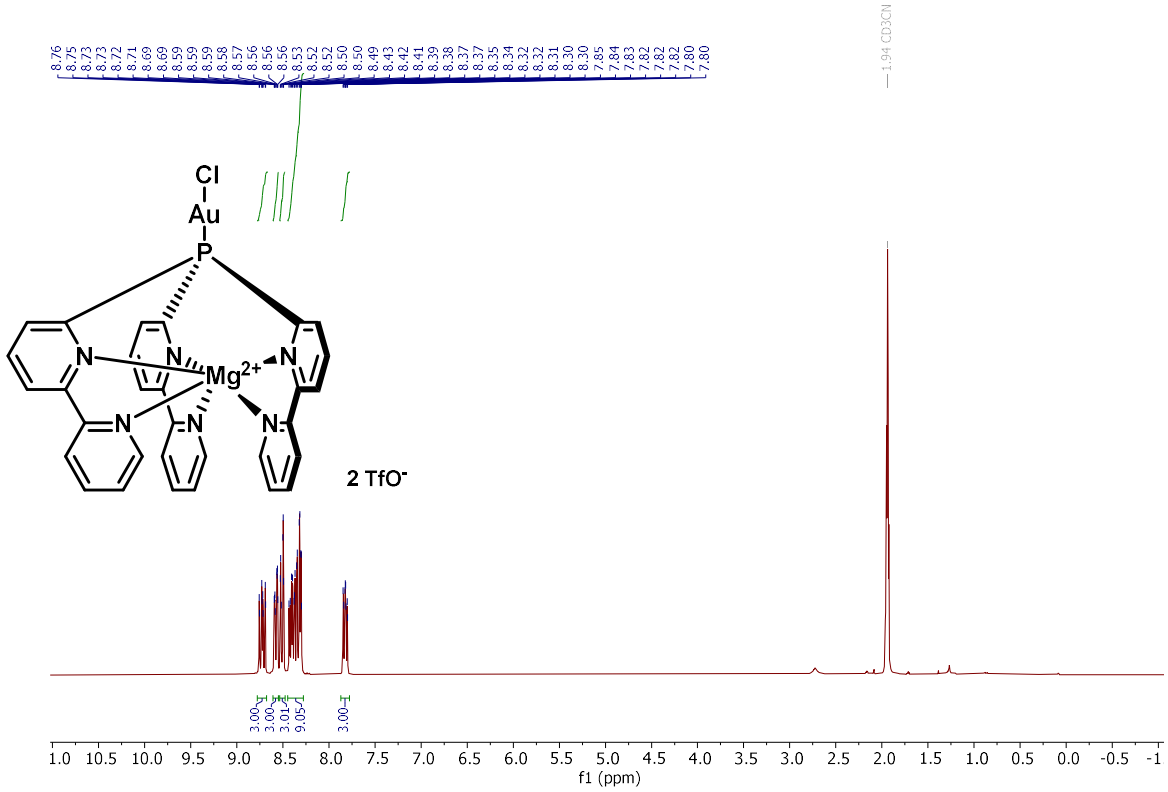

^{13}C{H} NMR (101 MHz, CD_3CN)

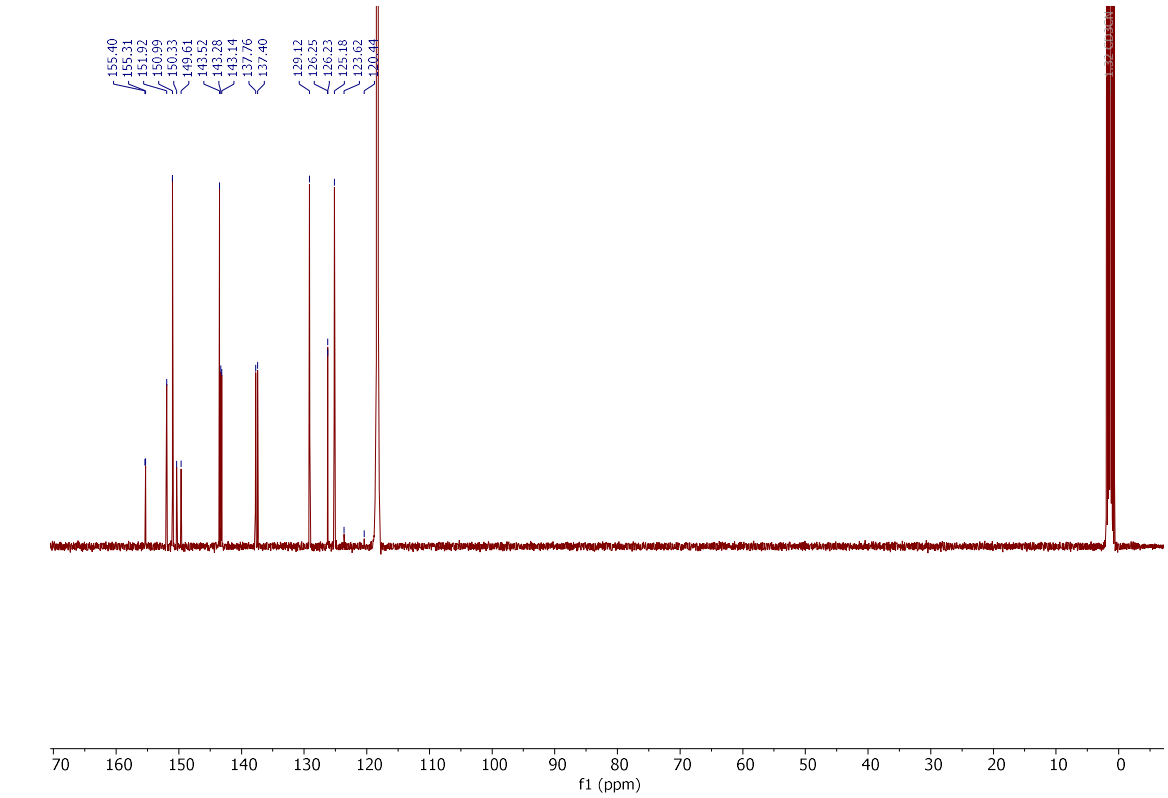

^{31}P{H} NMR (121 MHz, CD_3CN)

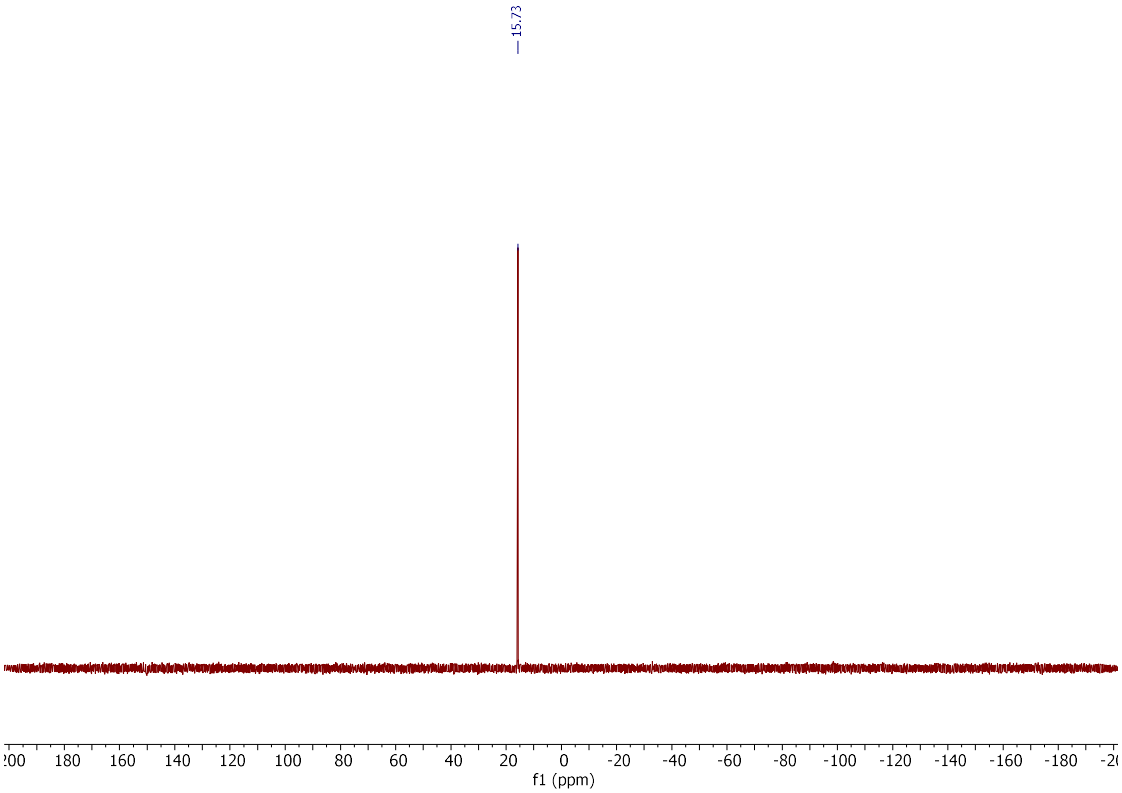

^{19}F NMR (282 MHz, CD_3CN)

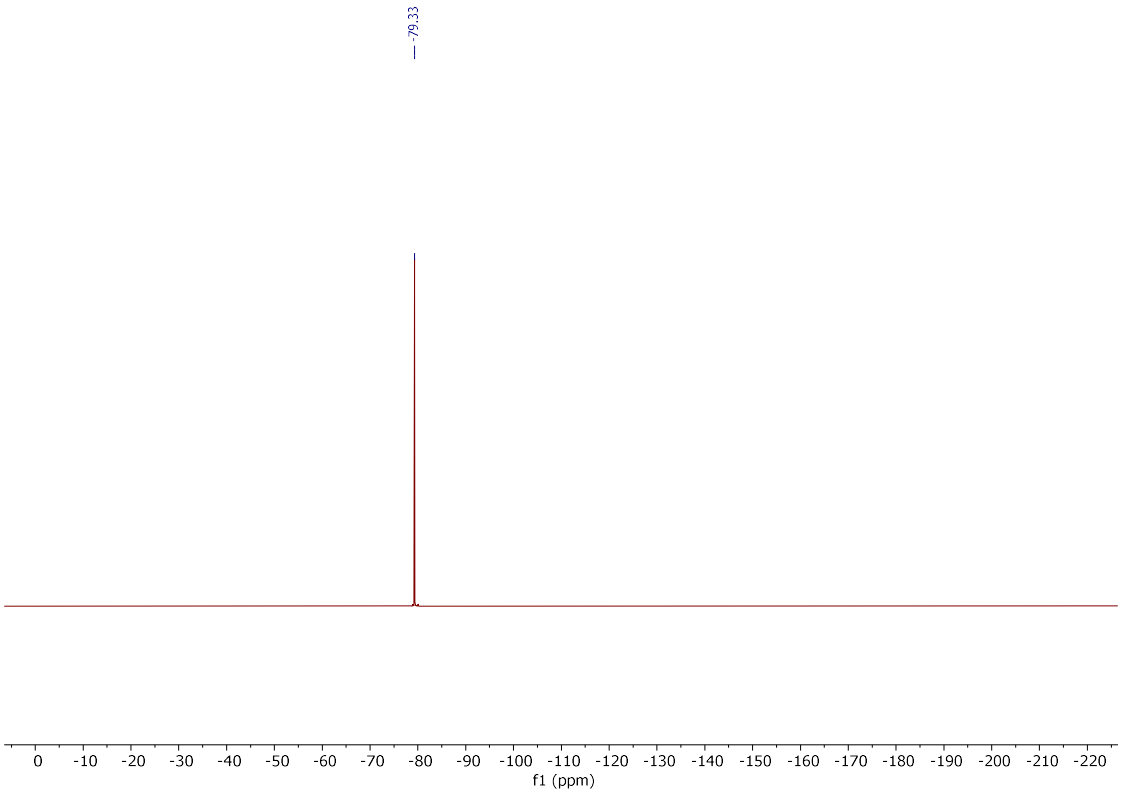

Compound **268**

^{1}H NMR (500 MHz, CD_3CN, 238K)

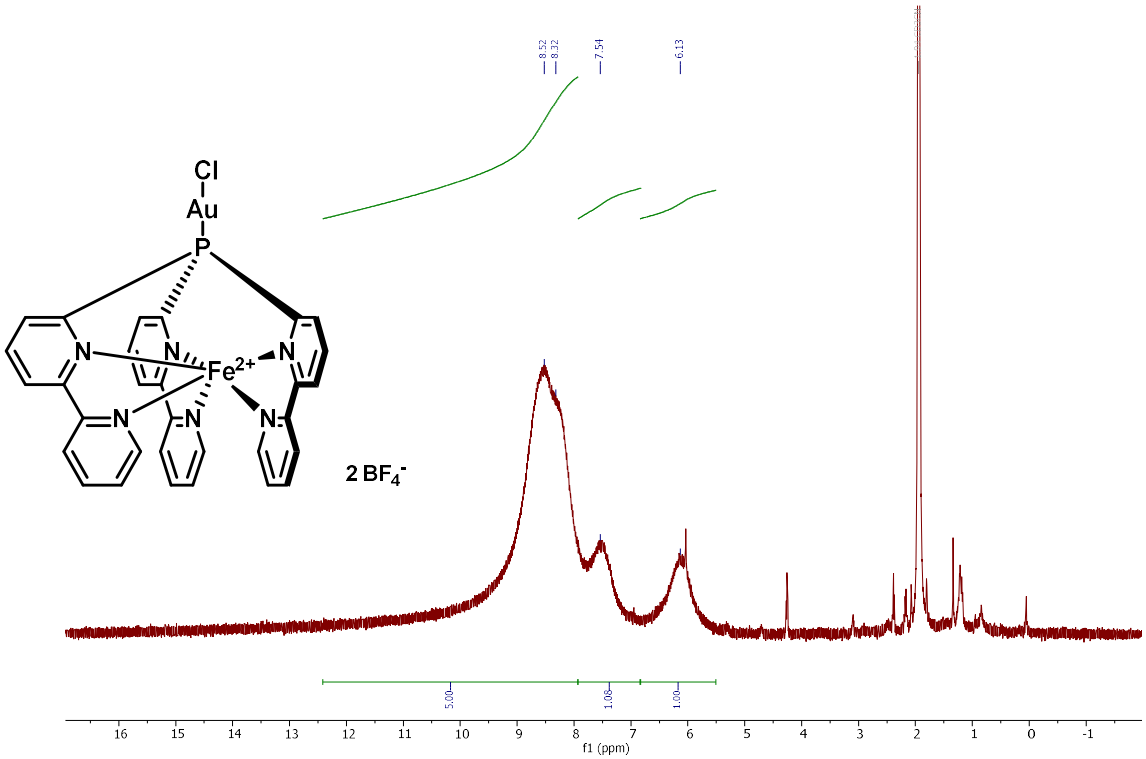

^{13}C NMR (126 MHz, CD_3CN, 238K)

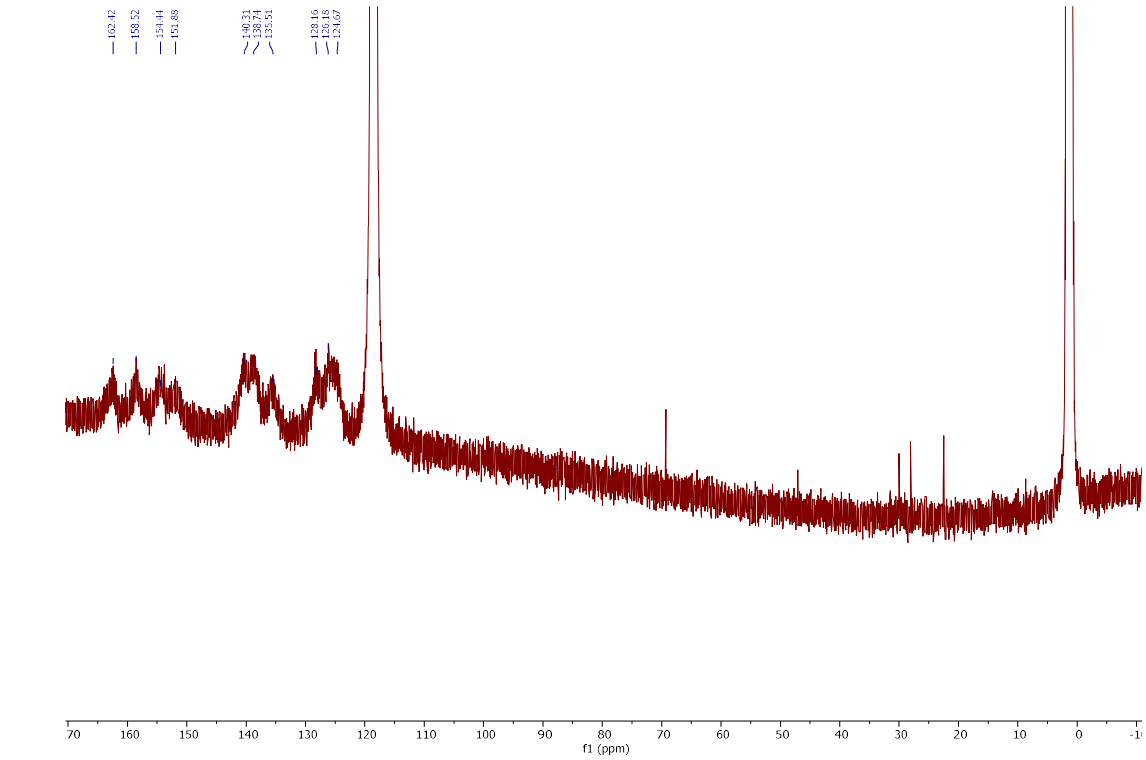

^{31}P NMR (203 MHz, CD_3CN, 238K)

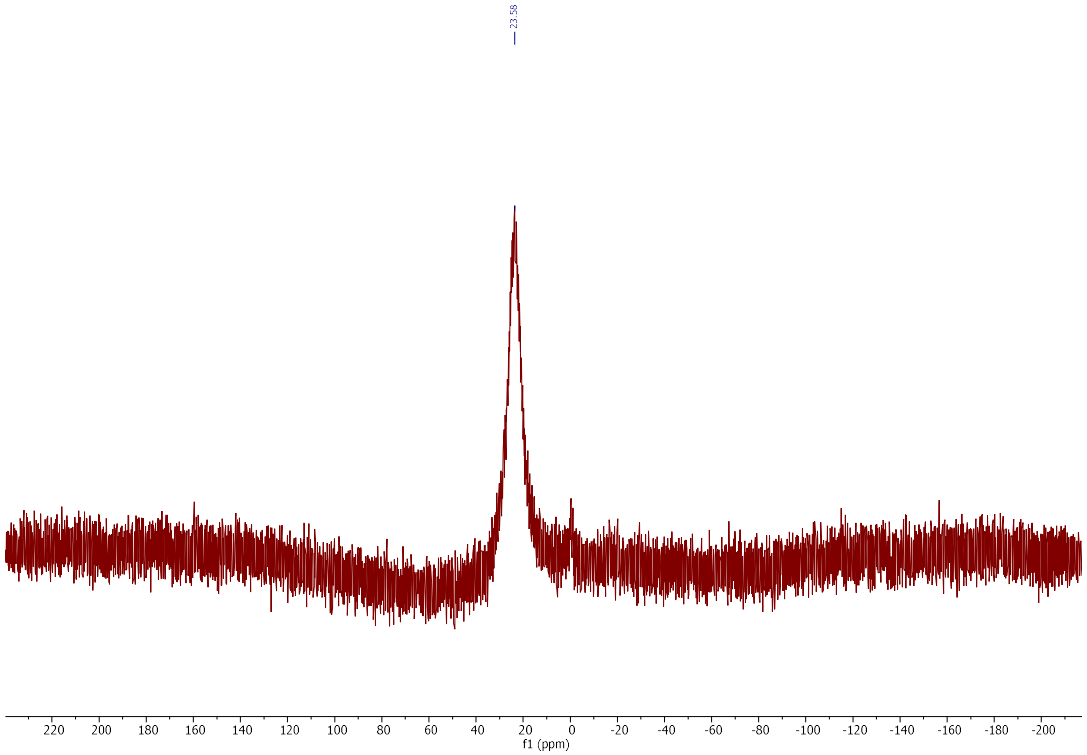

^{19}F NMR (471 MHz, CD_3CN, 238K)

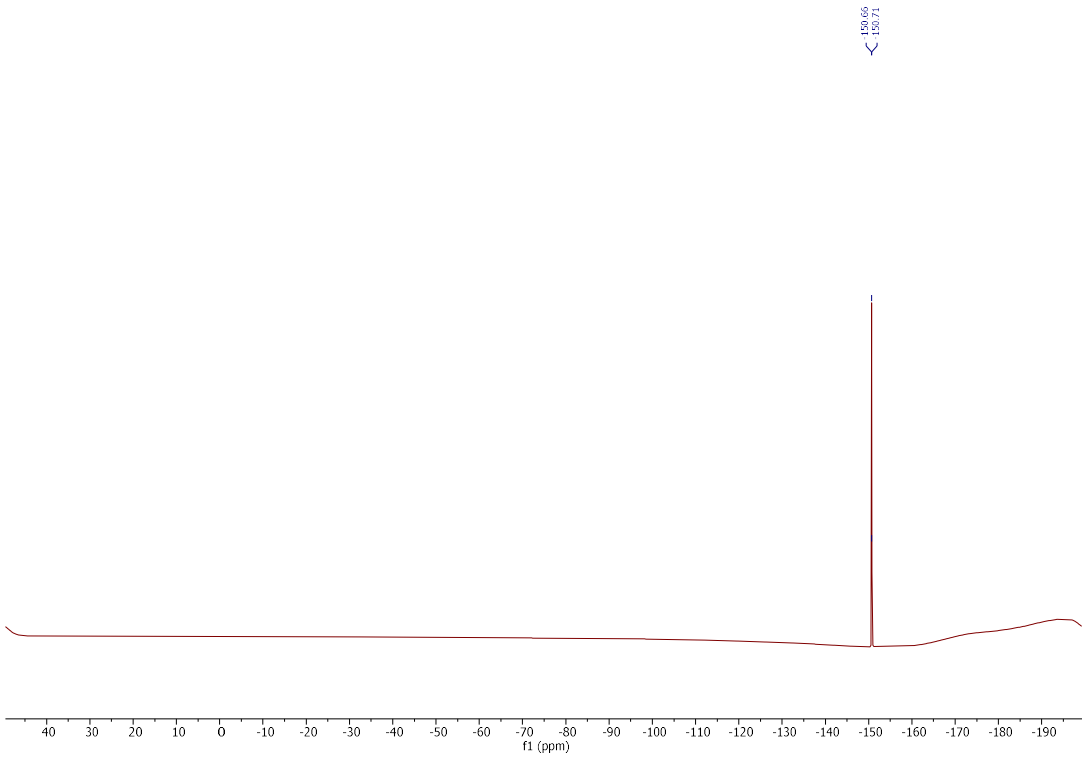

Compound **269**

^{1}H NMR (400 MHz, CD_3CN)

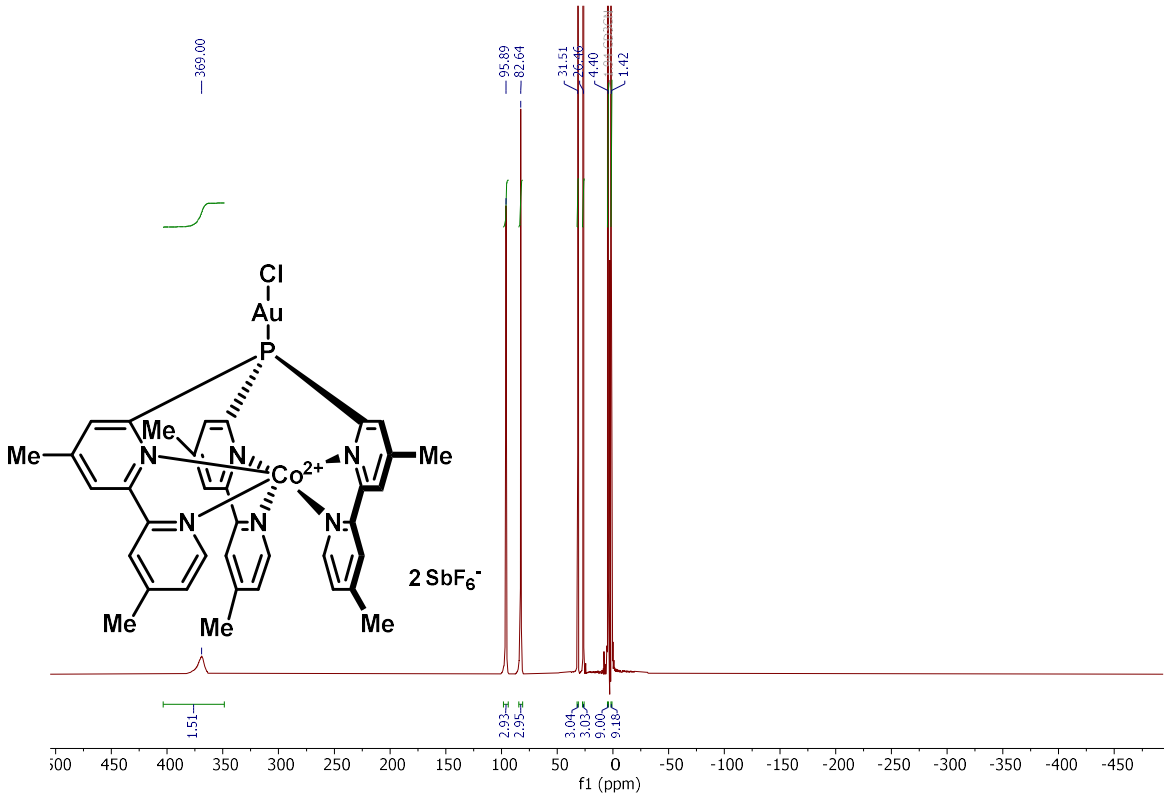

^{31}P{H} NMR (162 MHz, CD_3CN)

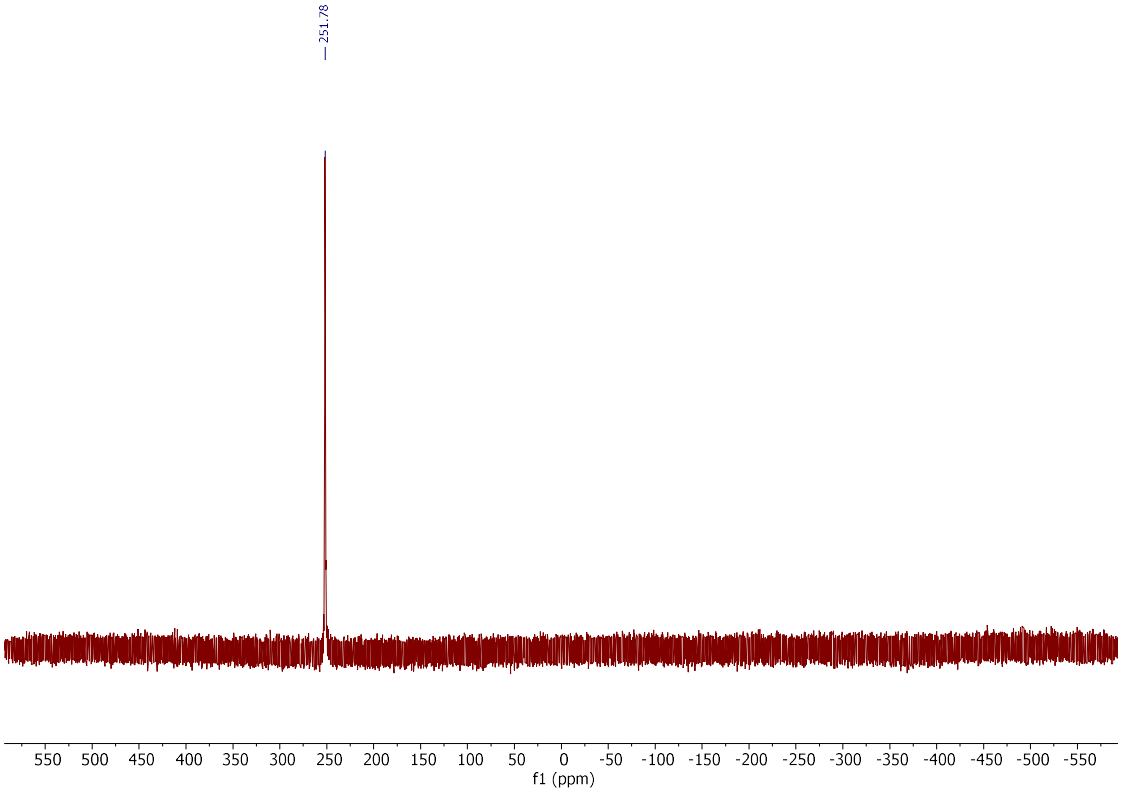

^{19}F NMR (376 MHz, CD_3CN)

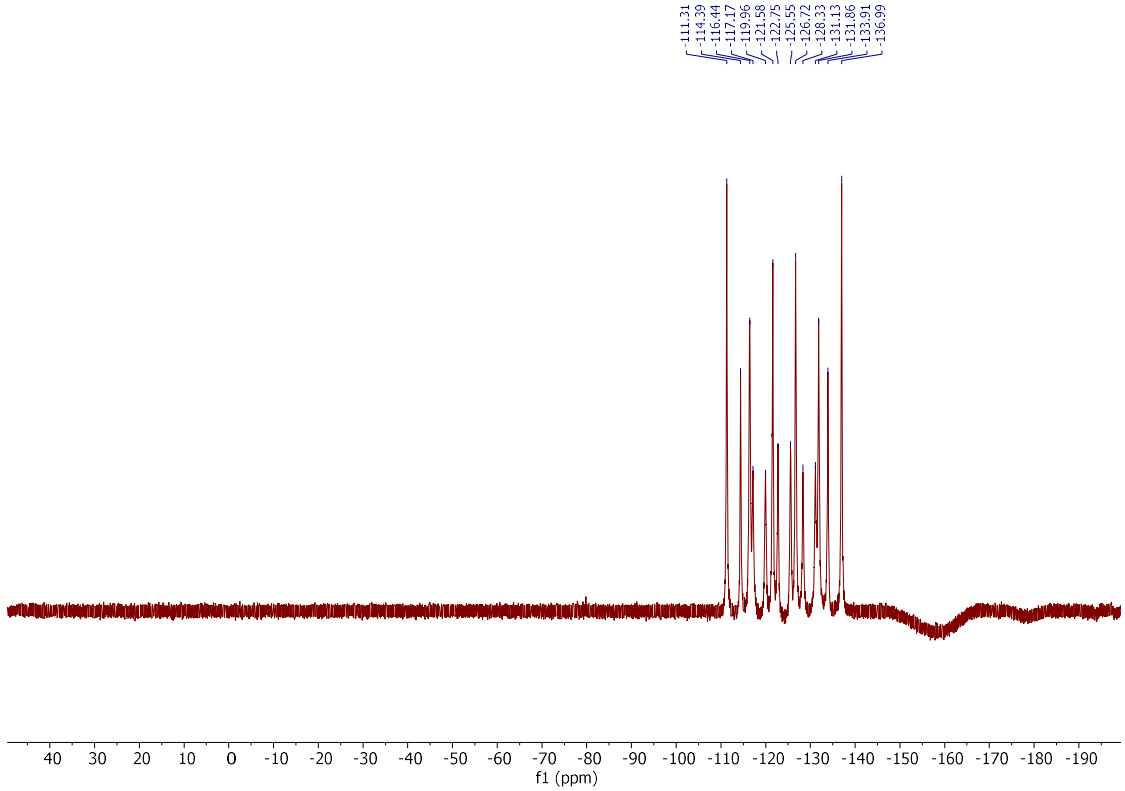

Compound **270**

^{1}H NMR (300 MHz, CD_3CN)

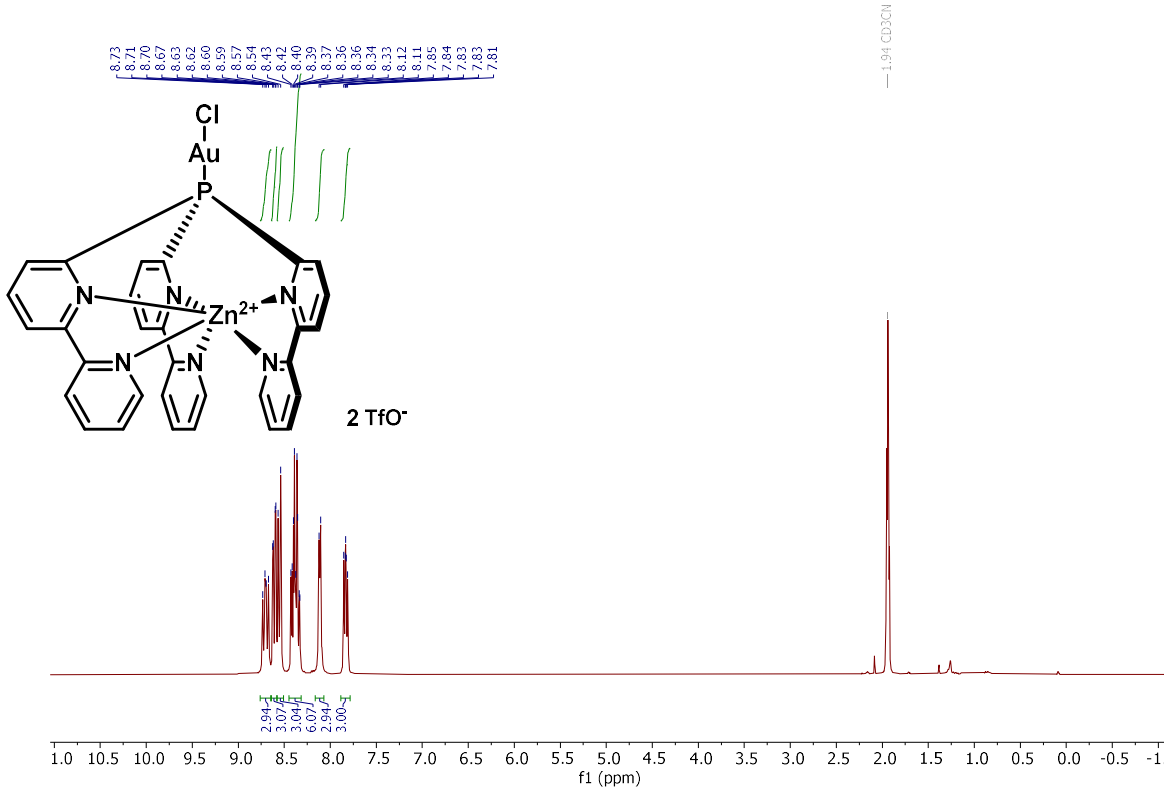

^{13}C{H} NMR (101 MHz, CD_3CN)

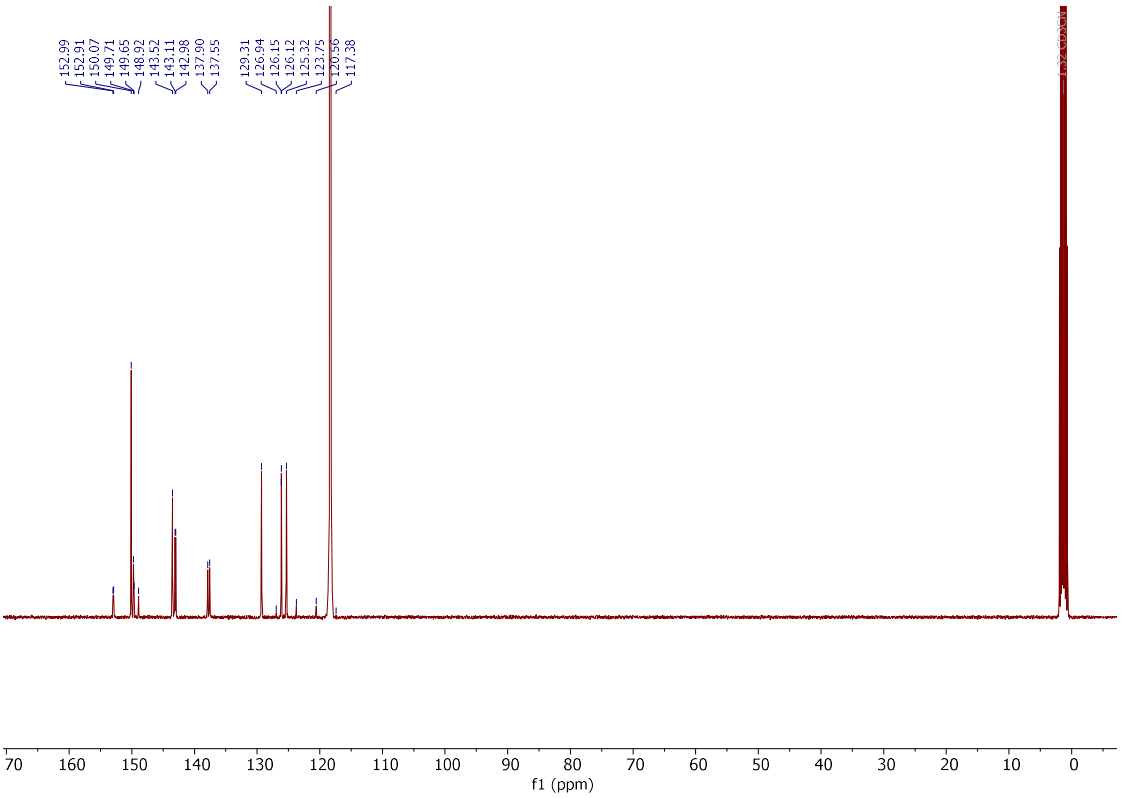

$^{31}P\{H\}$ NMR (121 MHz, CD_3CN)

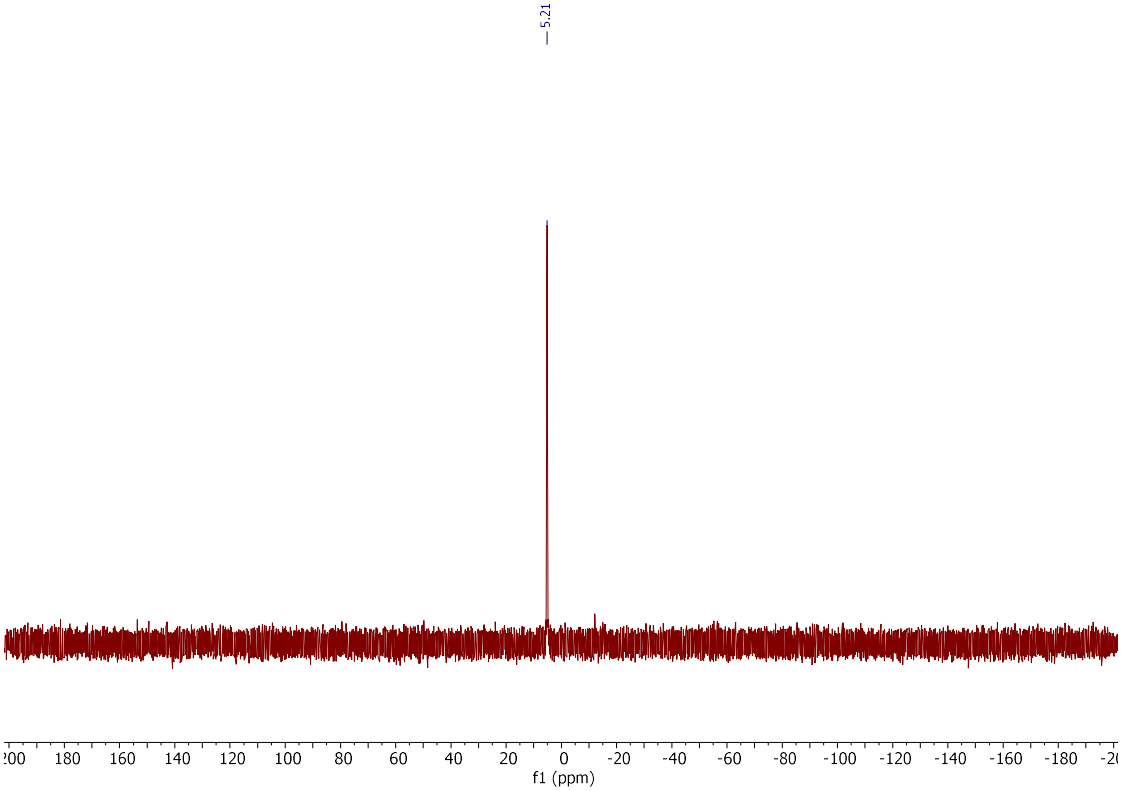

^{19}F NMR (282 MHz, CD_3CN)

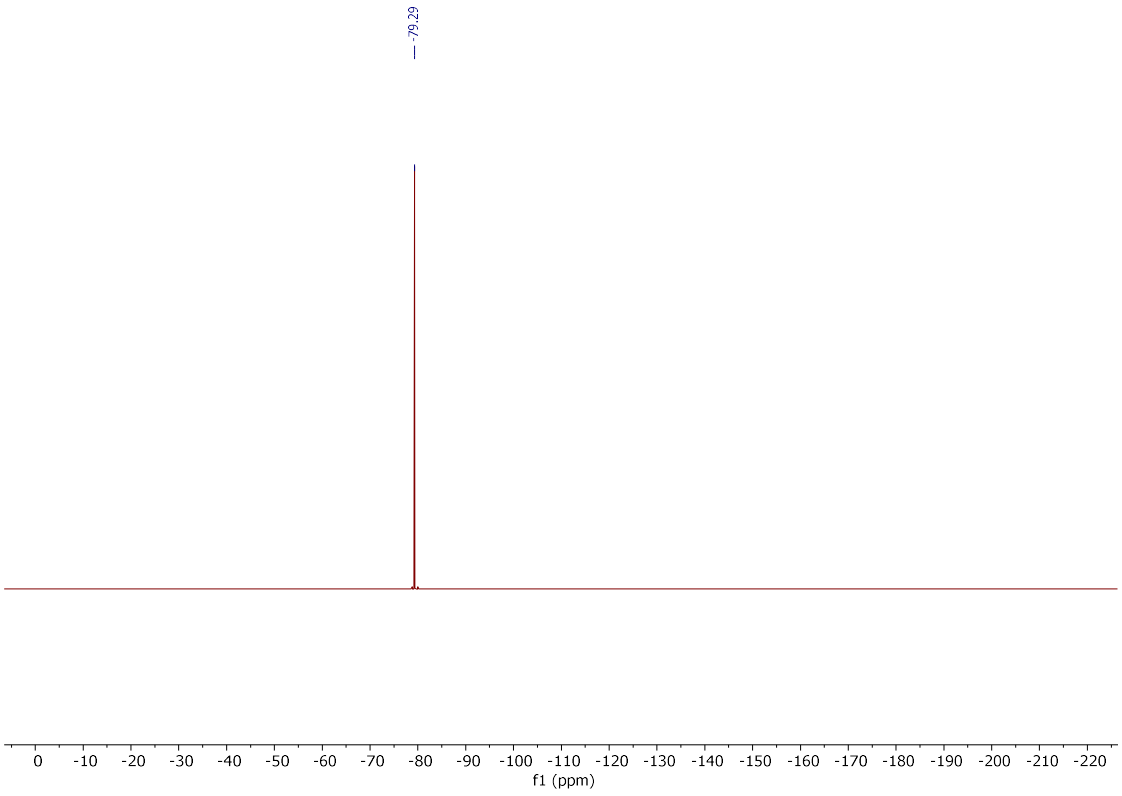

Compound **270b**

^{1}H NMR (300 MHz, CD_3CN)

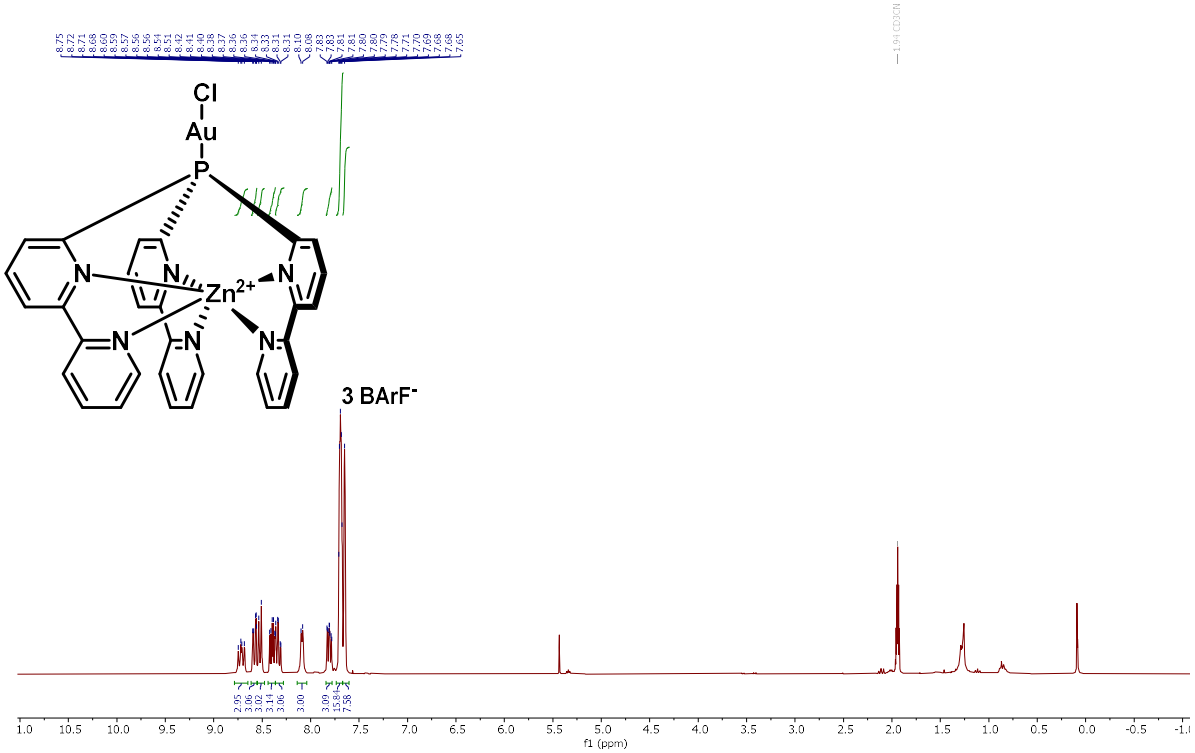

^{13}C{H} NMR (75 MHz, CD_3CN)

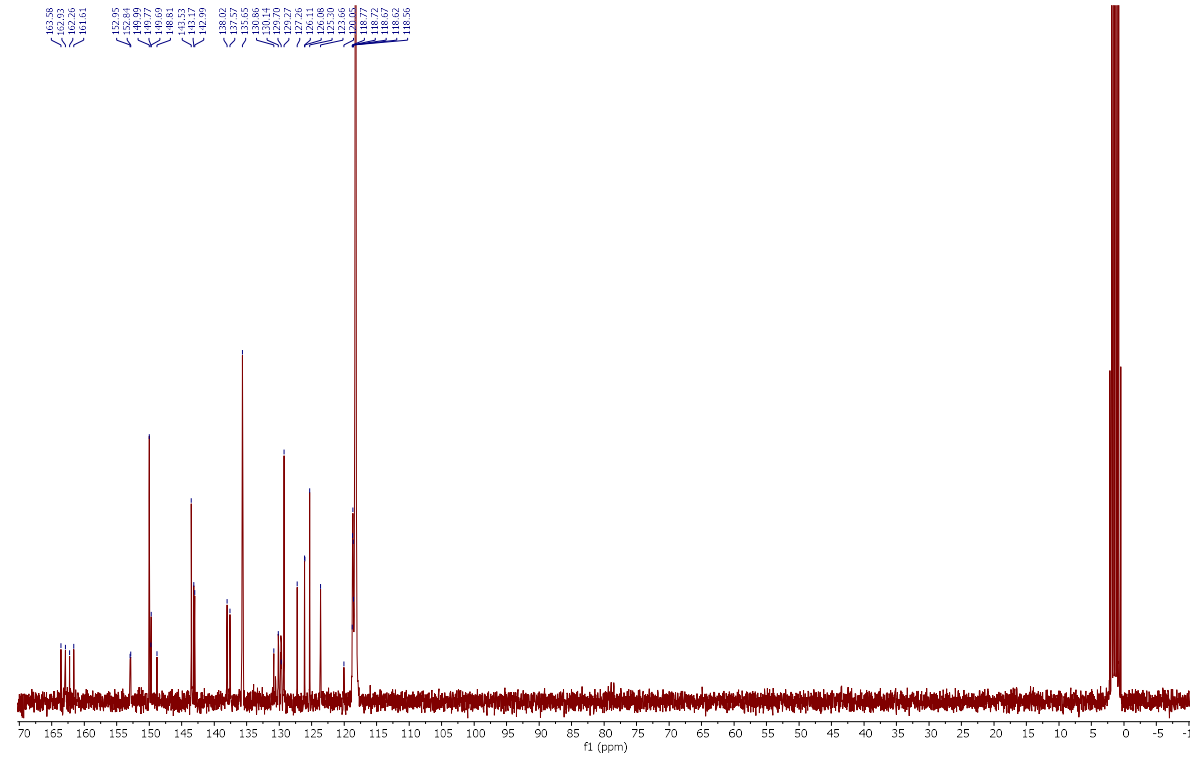

$^{31}P\{H\}$ NMR (121 MHz, CD_3CN)

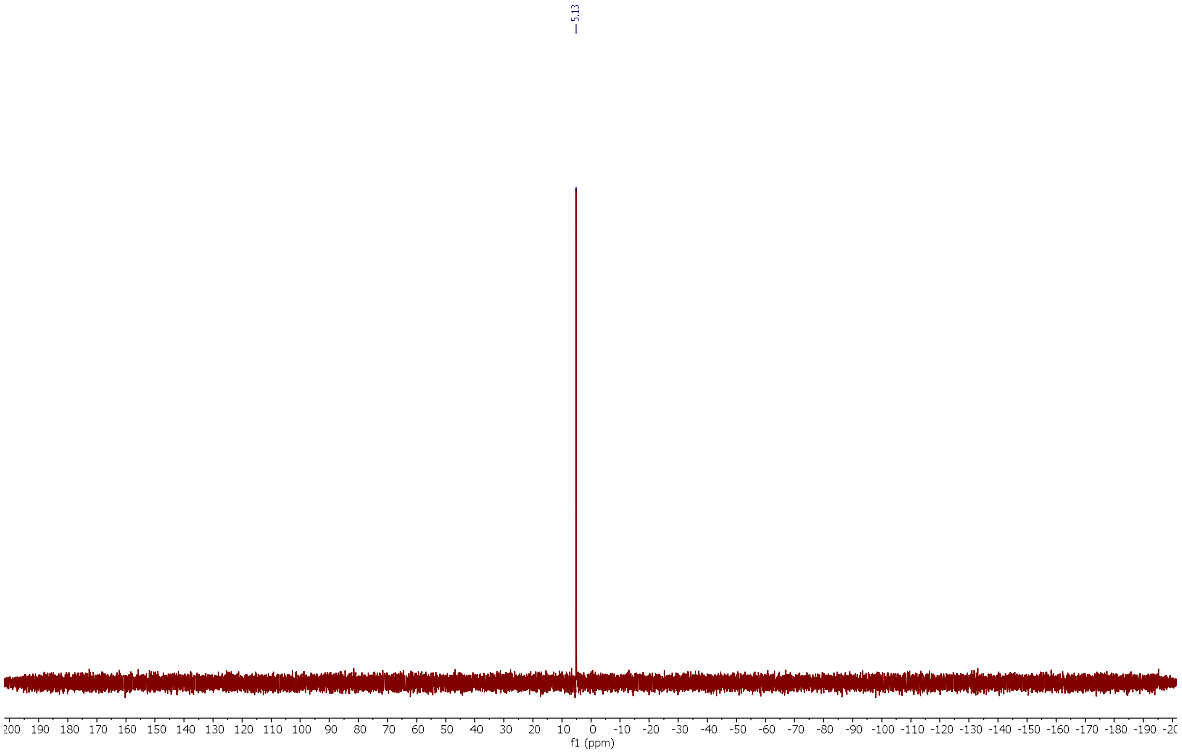

^{19}F NMR (282 MHz, CD_3CN)

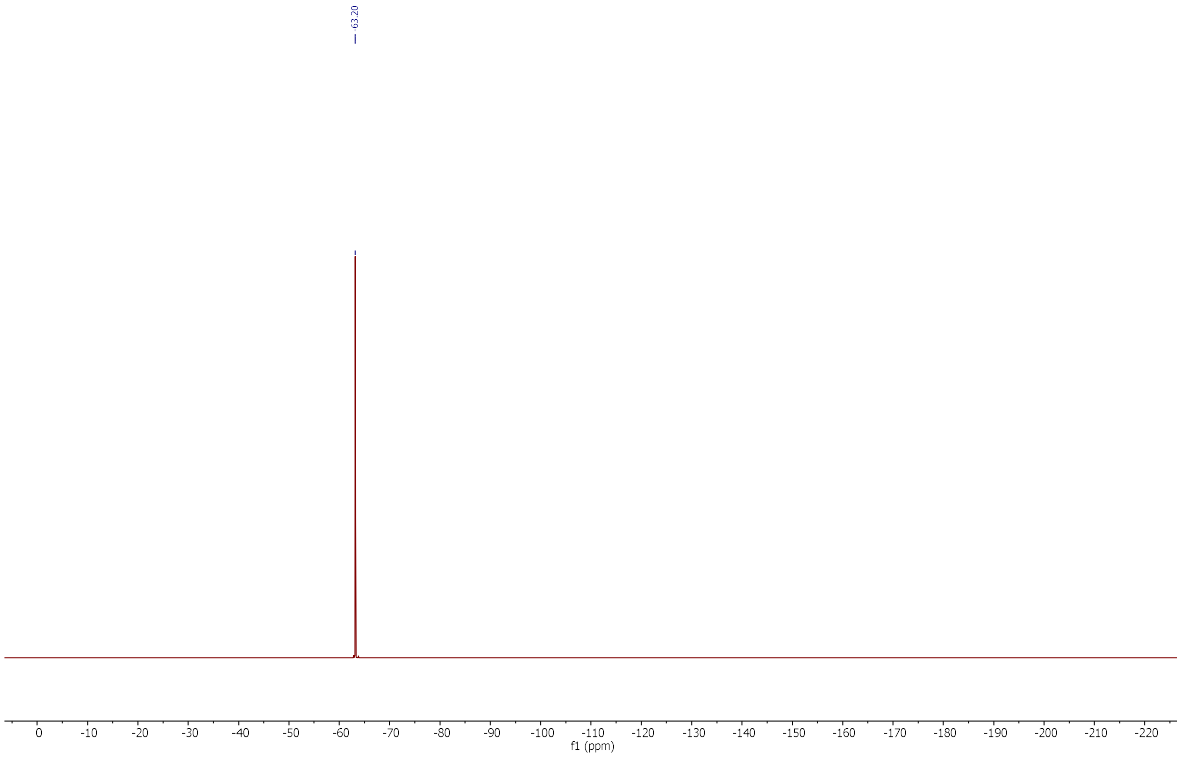

^{11}B NMR (96 MHz, CD_3CN)

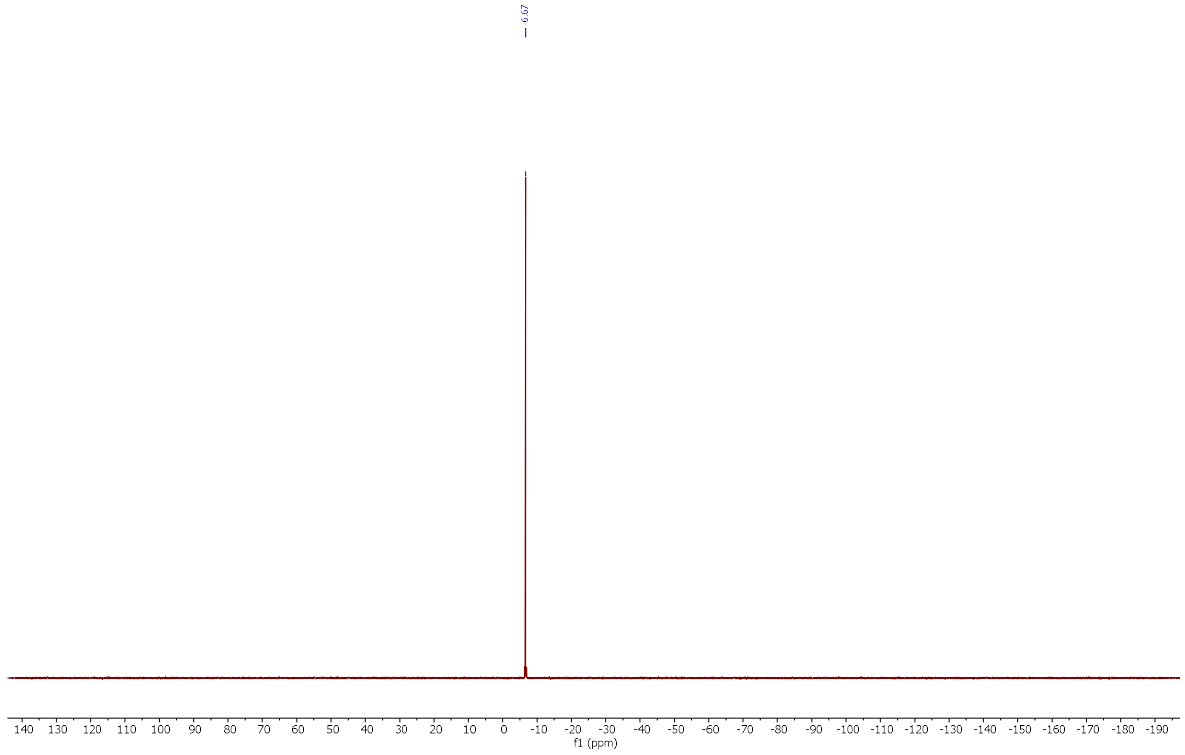

Compound **271**

^{1}H NMR (400 MHz, CD_3CN)

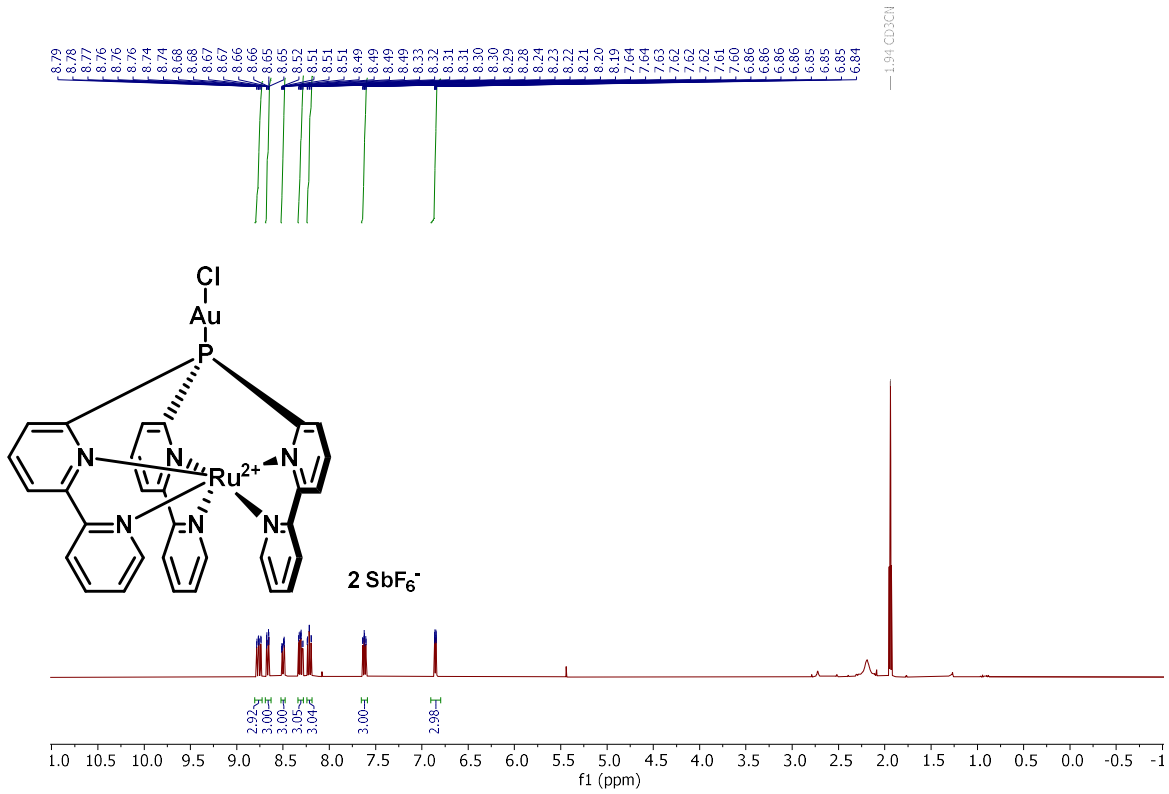

^{13}C{H} NMR (101 MHz, CD_3CN)

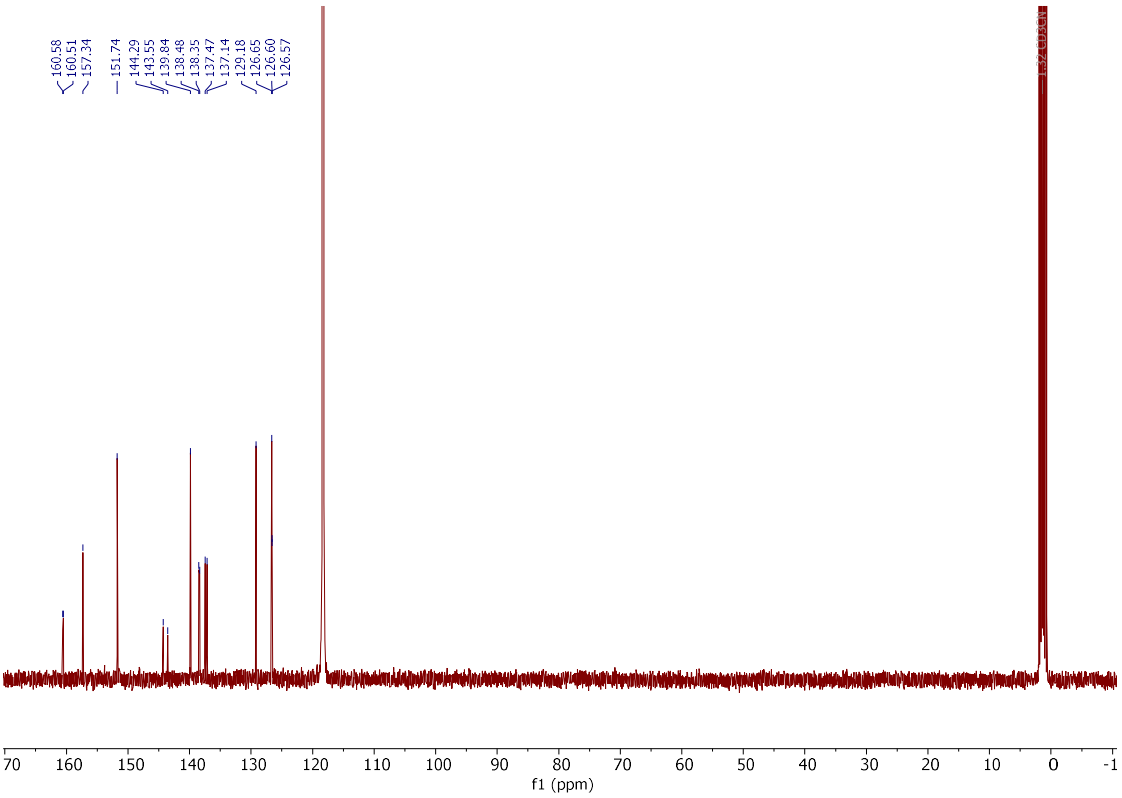

$^{31}P\{H\}$ NMR (162 MHz, CD_3CN)

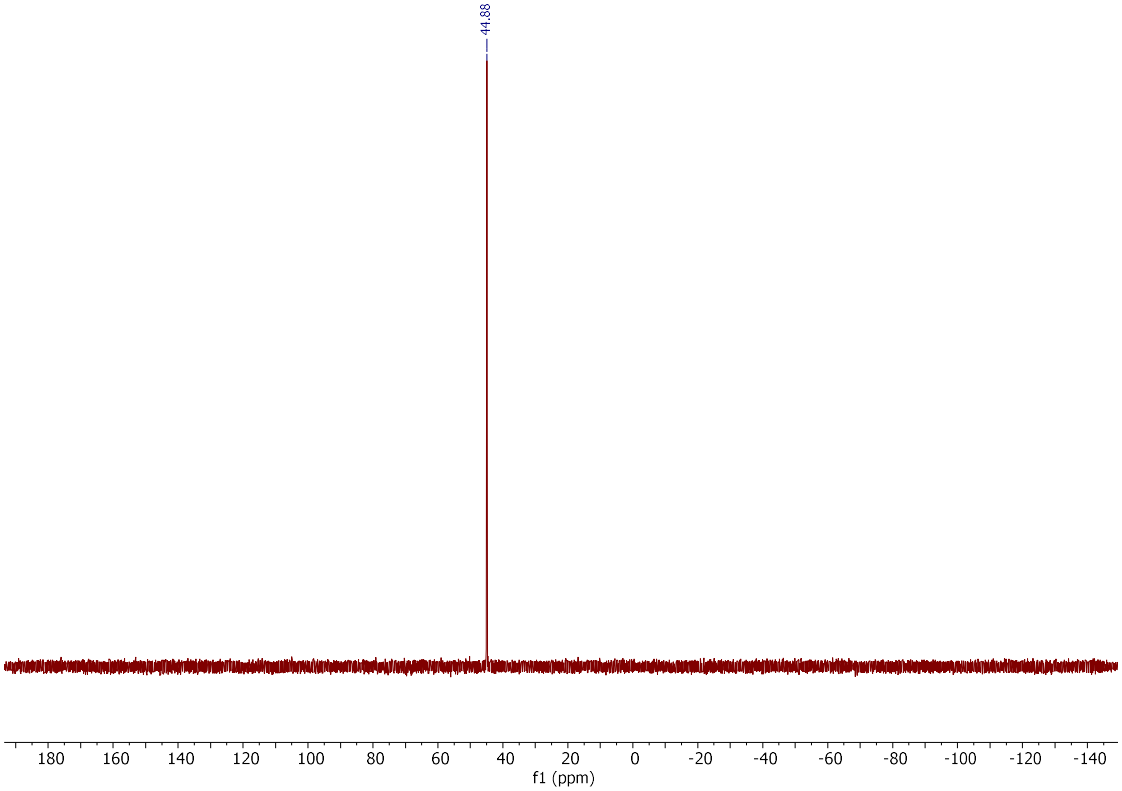

^{19}F NMR (376 MHz, CD_3CN)

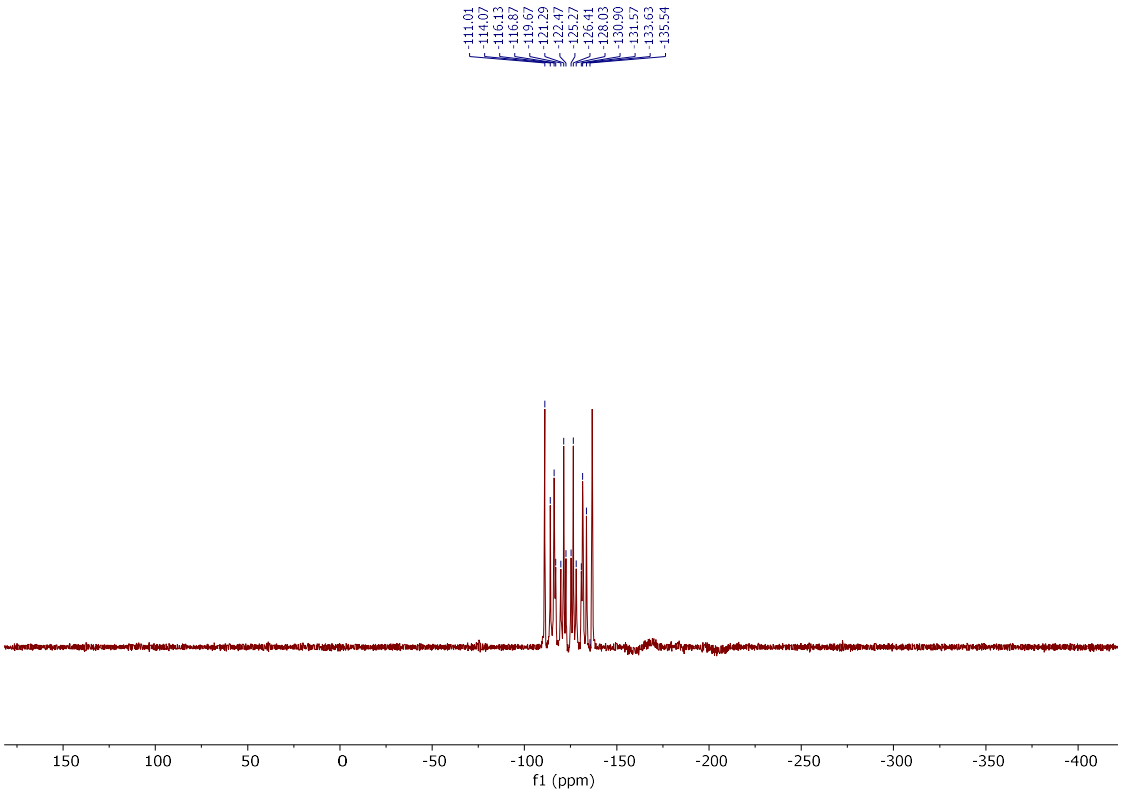

Compound **272**

^{1}H NMR (400 MHz, CD_3CN)

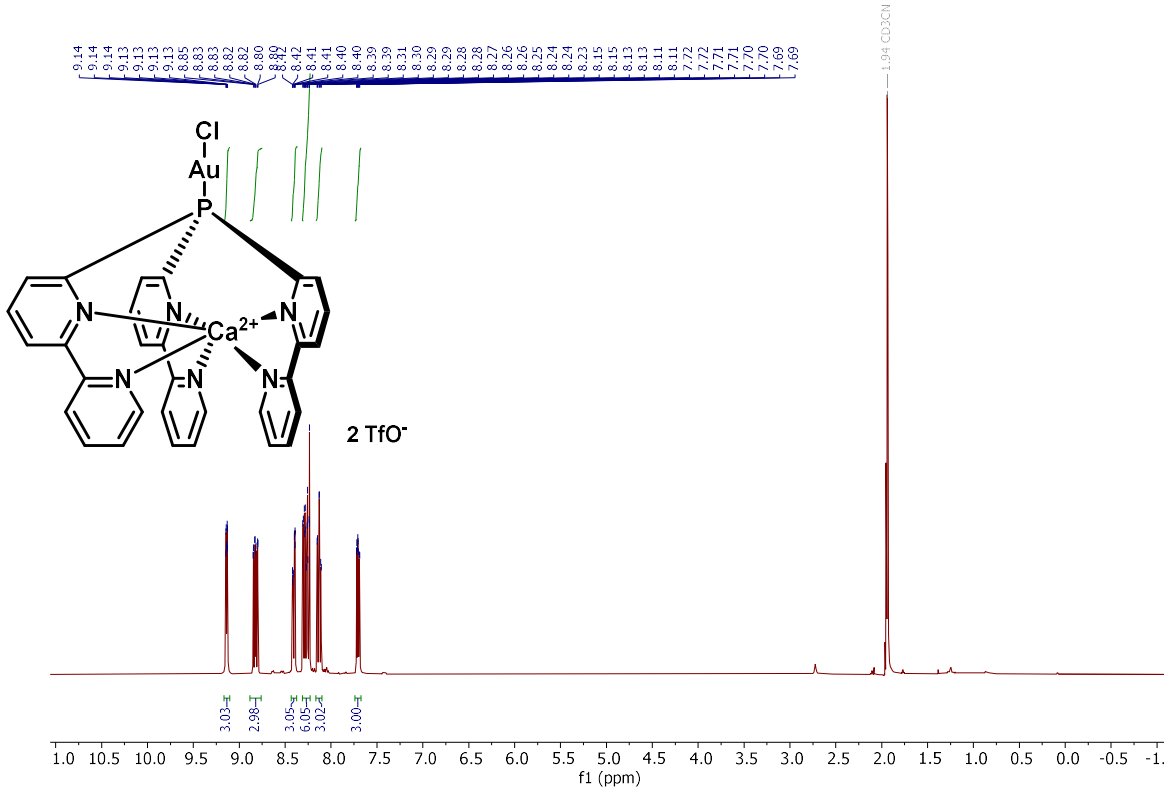

^{13}C{H} NMR (101 MHz, CD_3CN)

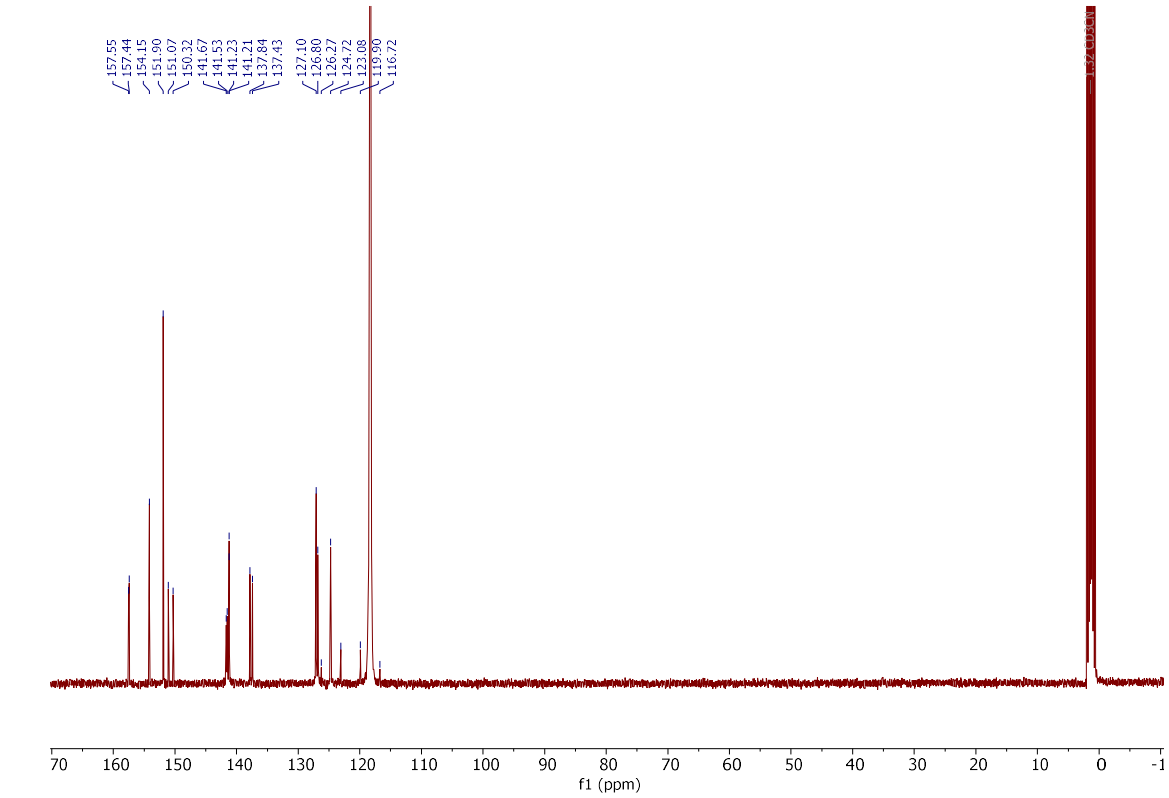

$^{31}P\{H\}$ NMR (162 MHz, CD_3CN)

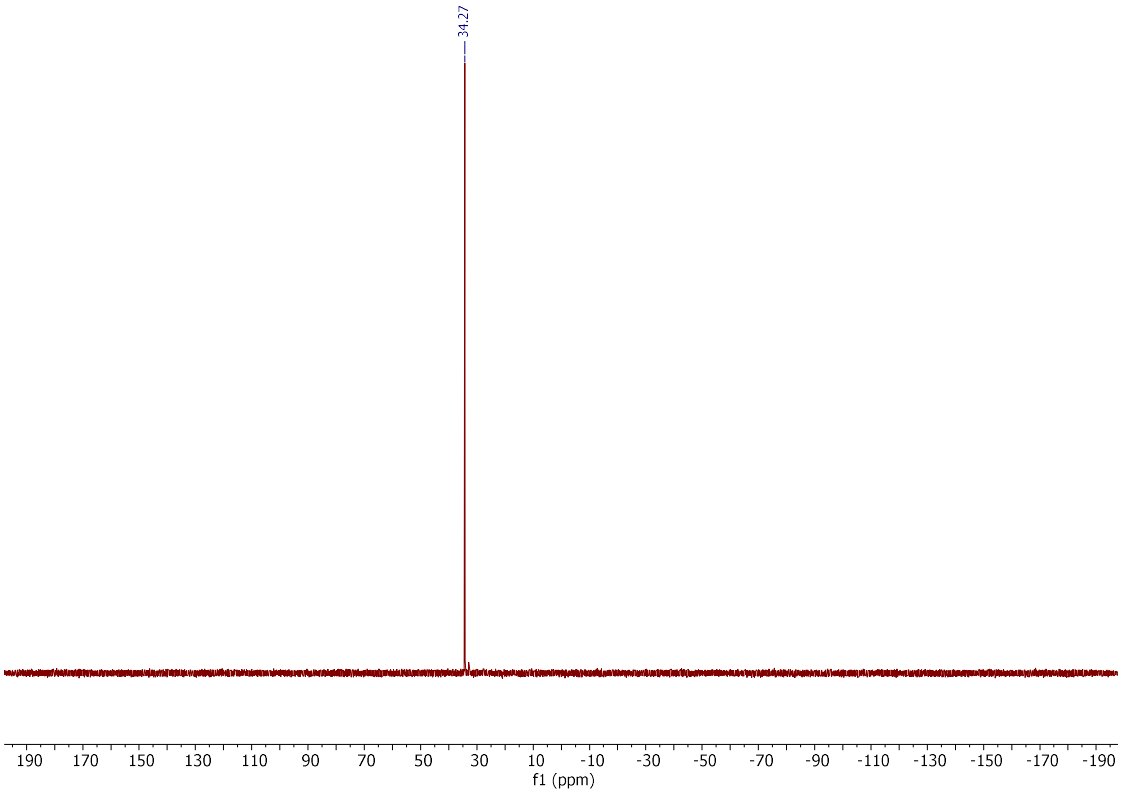

^{19}F NMR (376 MHz, CD_3CN)

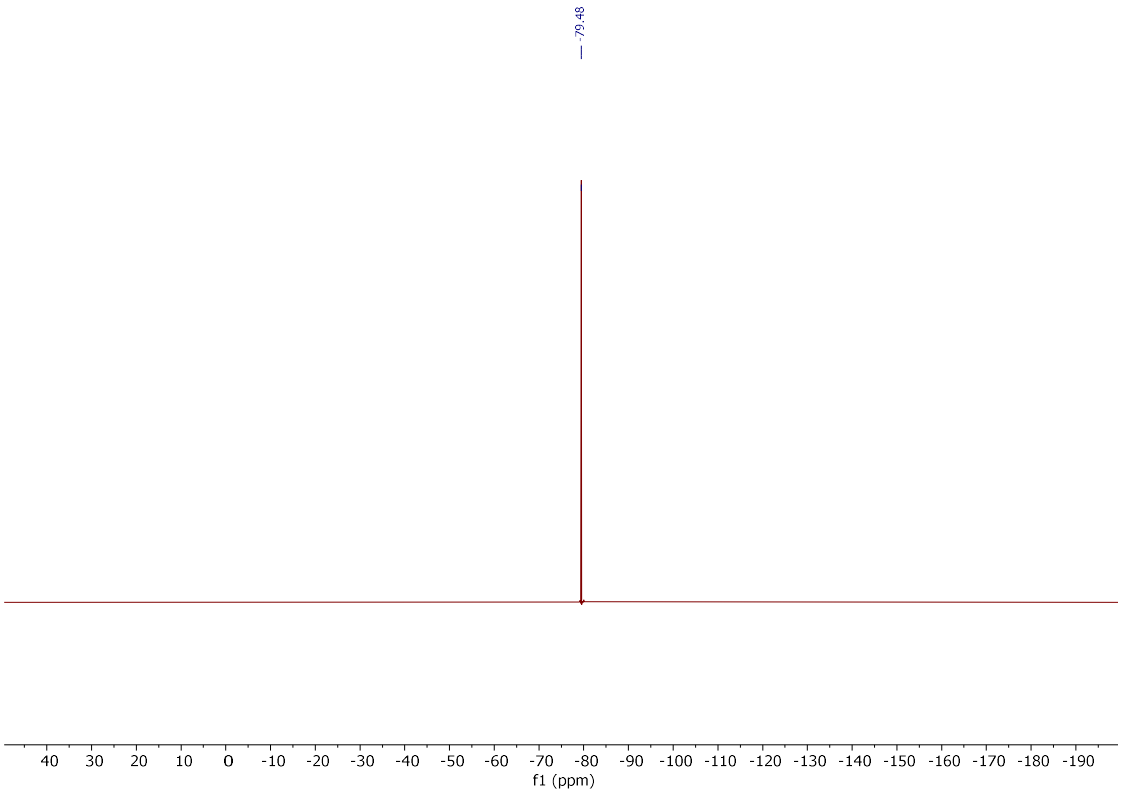

Compound **273**

^{1}H NMR (300 MHz, CD_2Cl_2)

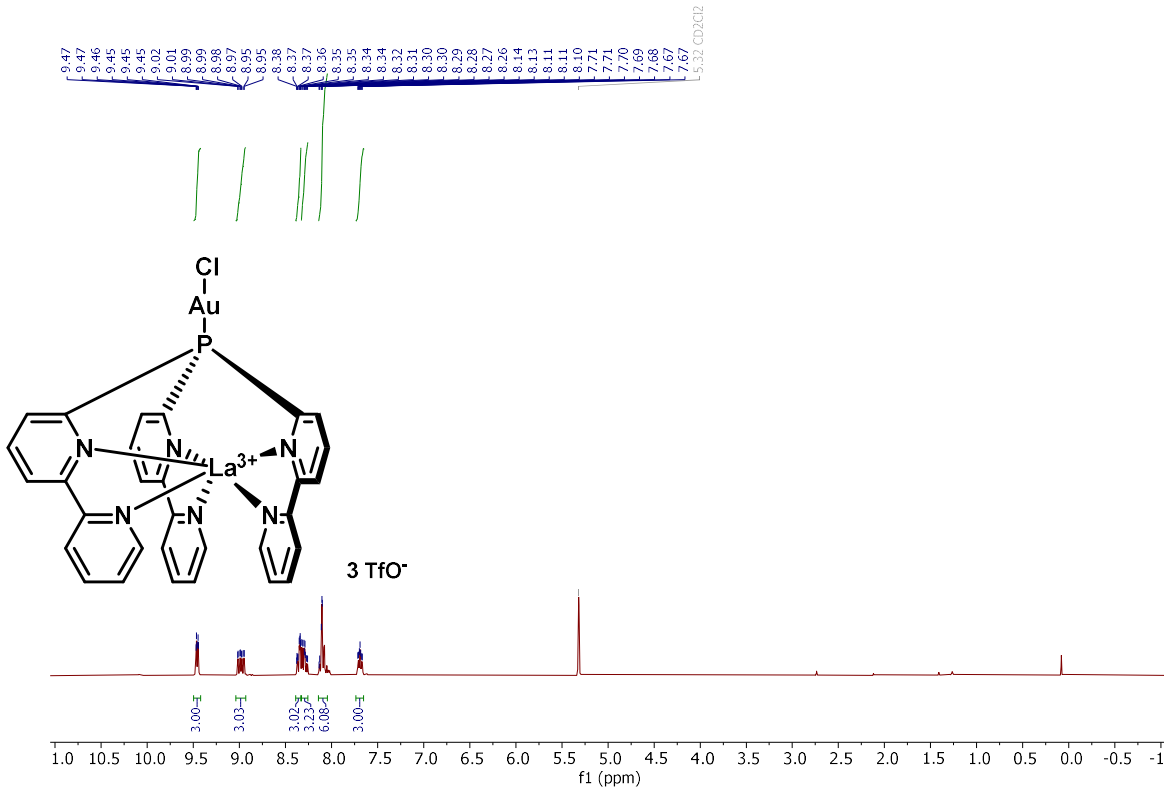

^{13}C{H} NMR (101 MHz, CD_2Cl_2)

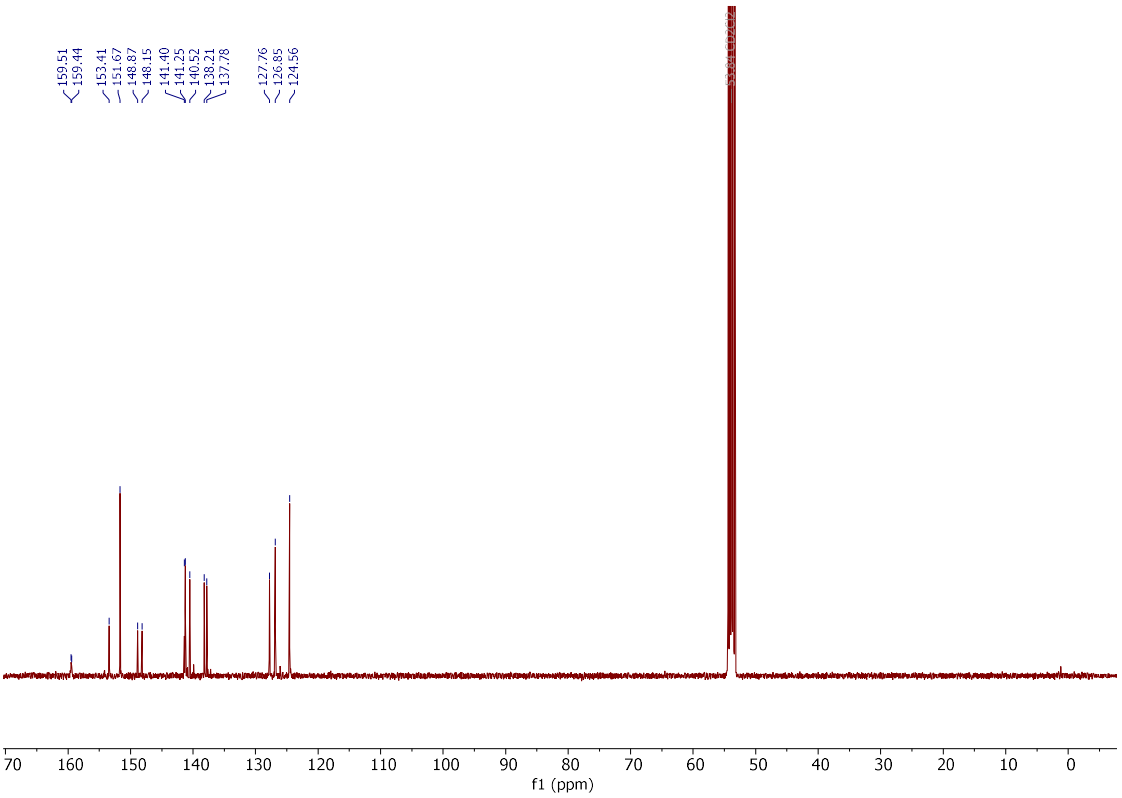

$^{31}P\{H\}$ NMR (121 MHz, CD_2Cl_2)

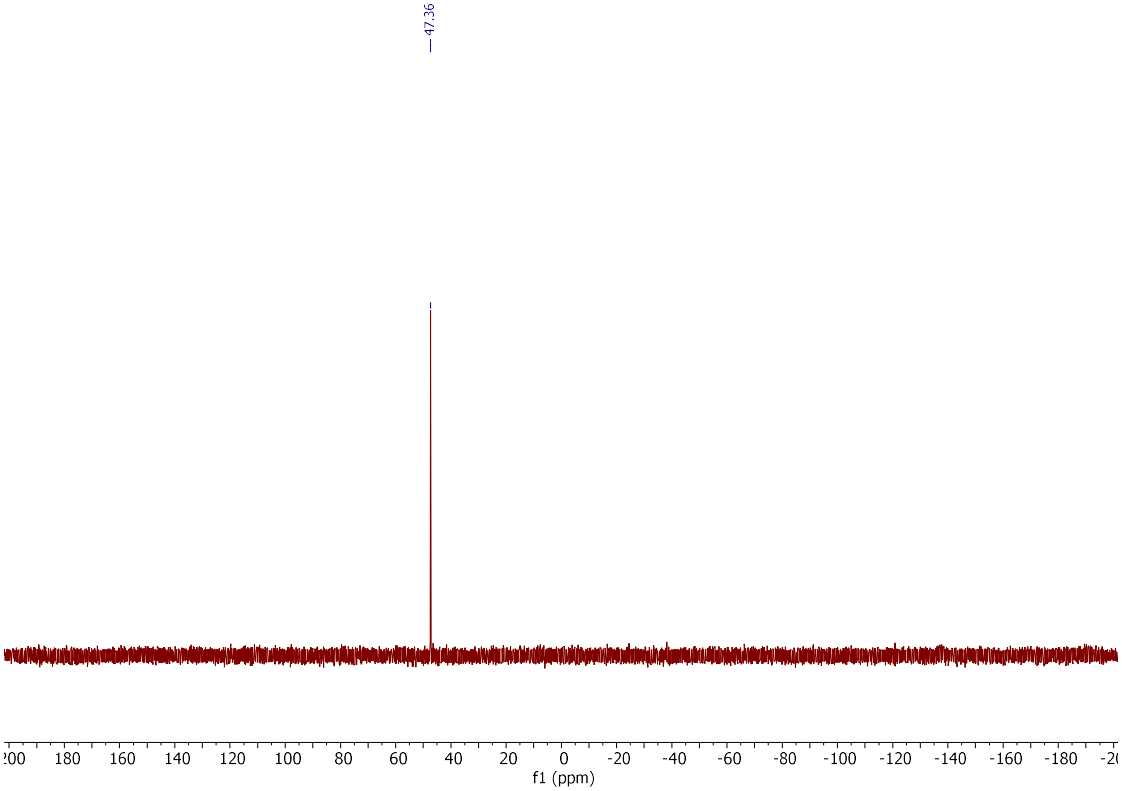

^{19}F NMR (282 MHz, CD_2Cl_2)

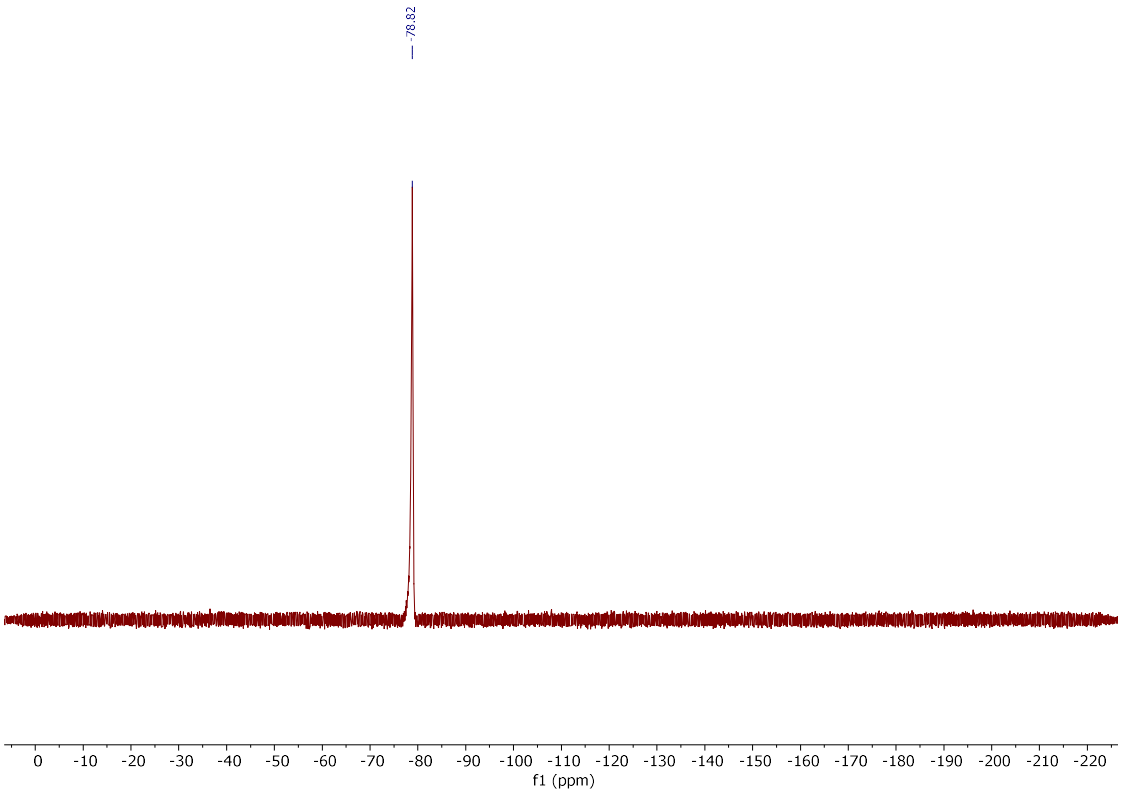

Compound **294**

^{1}H NMR (400 MHz, CD_3CN)

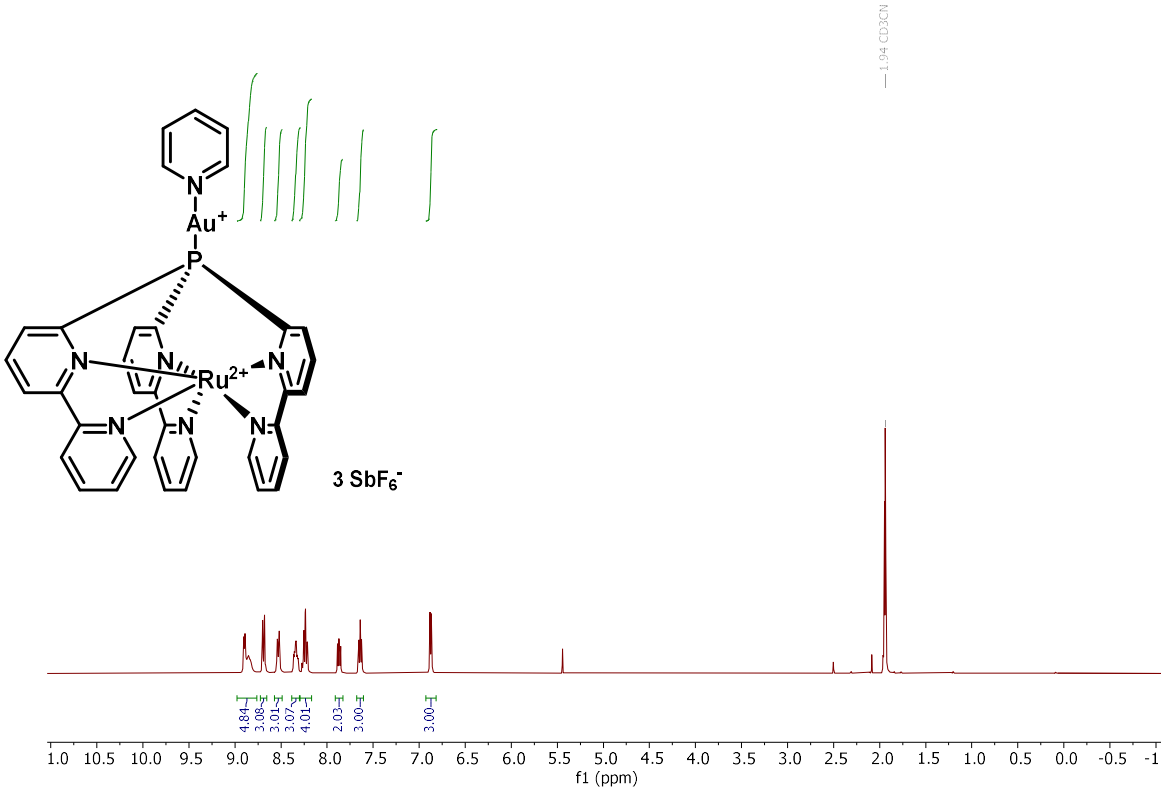

^{13}C{H} NMR (101 MHz, CD_3CN)

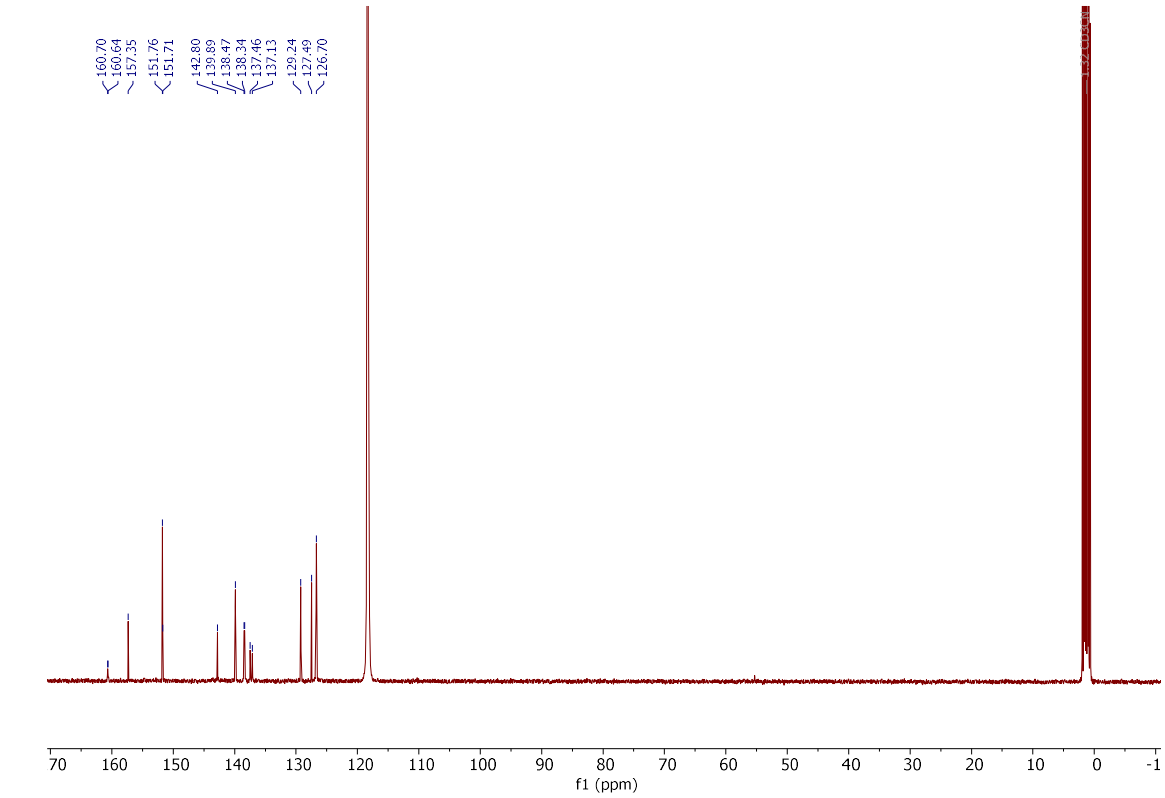

$^{31}P\{H\}$ NMR (162 MHz, CD_3CN)

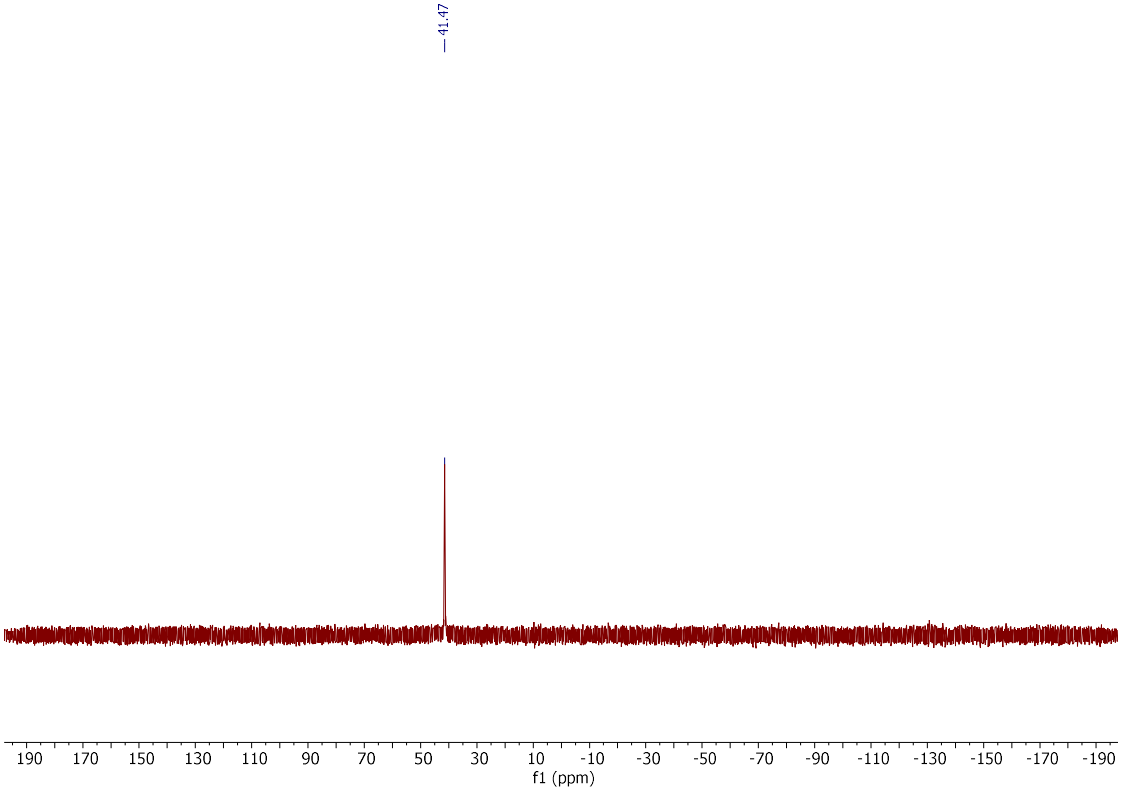

^{19}F NMR (376 MHz, CD_3CN)

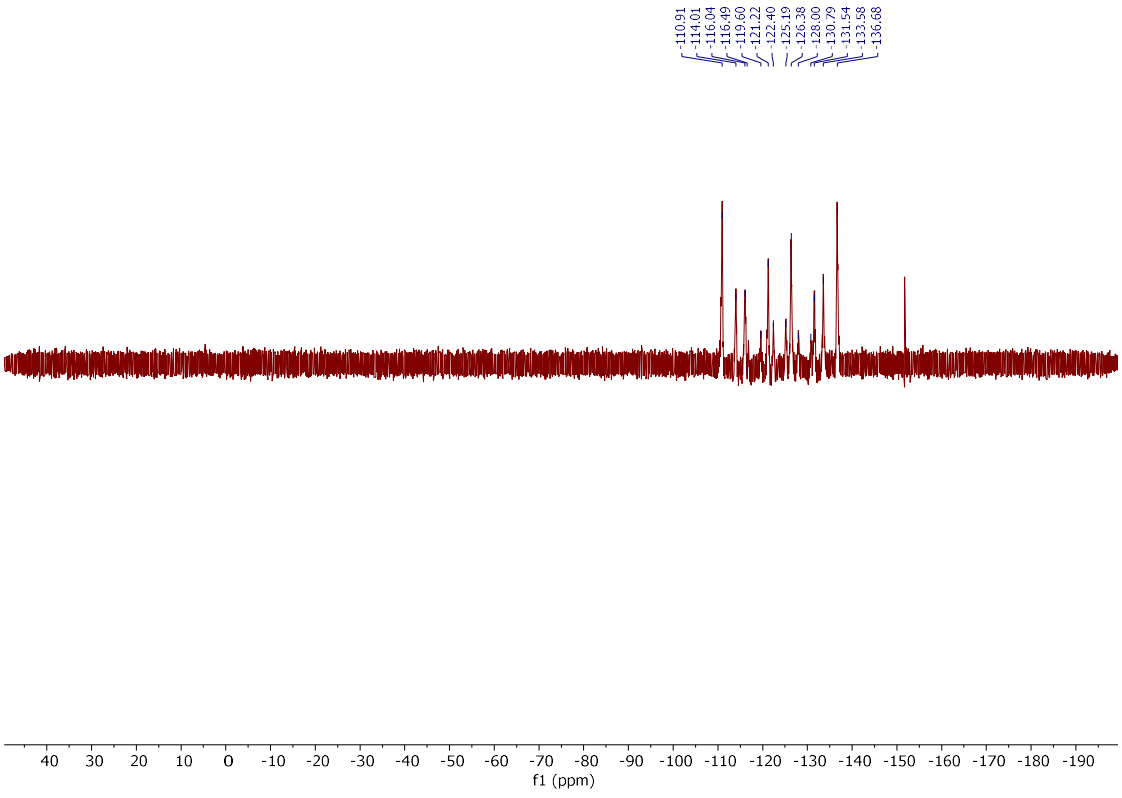

Compound **299**

^{1}H NMR (400 MHz, CD_3CN)

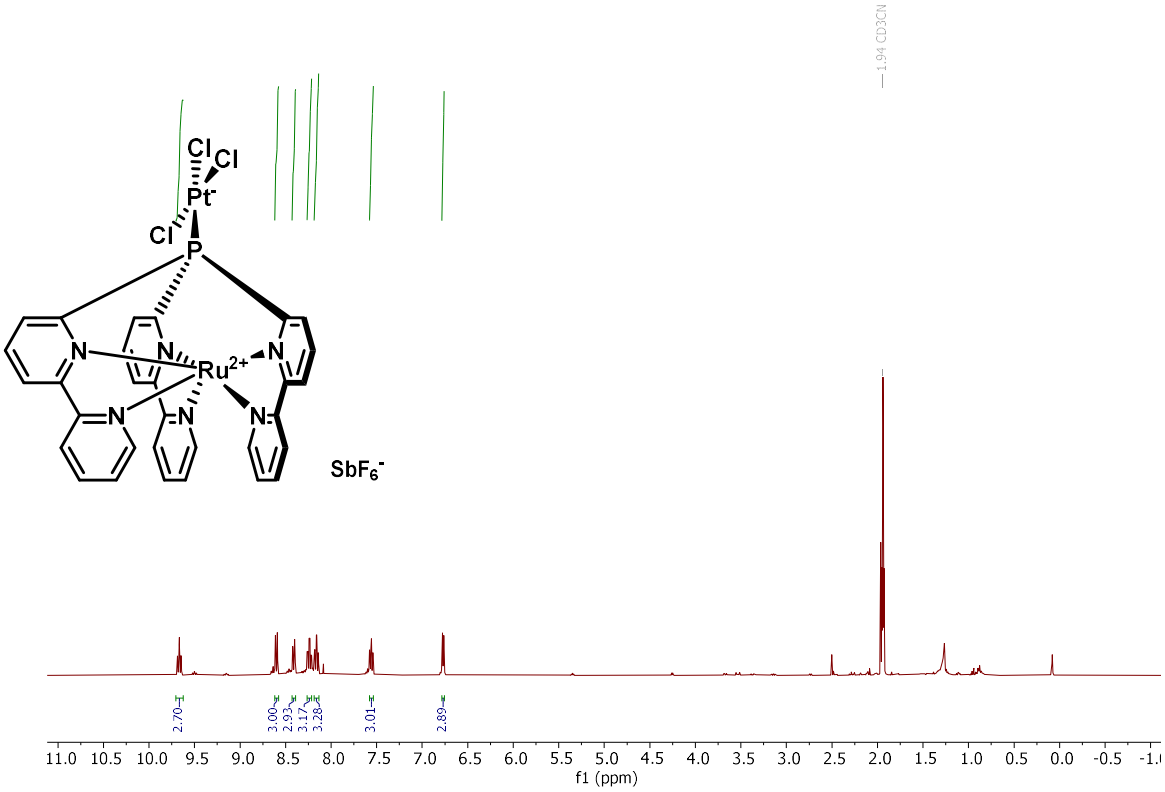

^{13}C{H} NMR (101 MHz, CD_3CN)

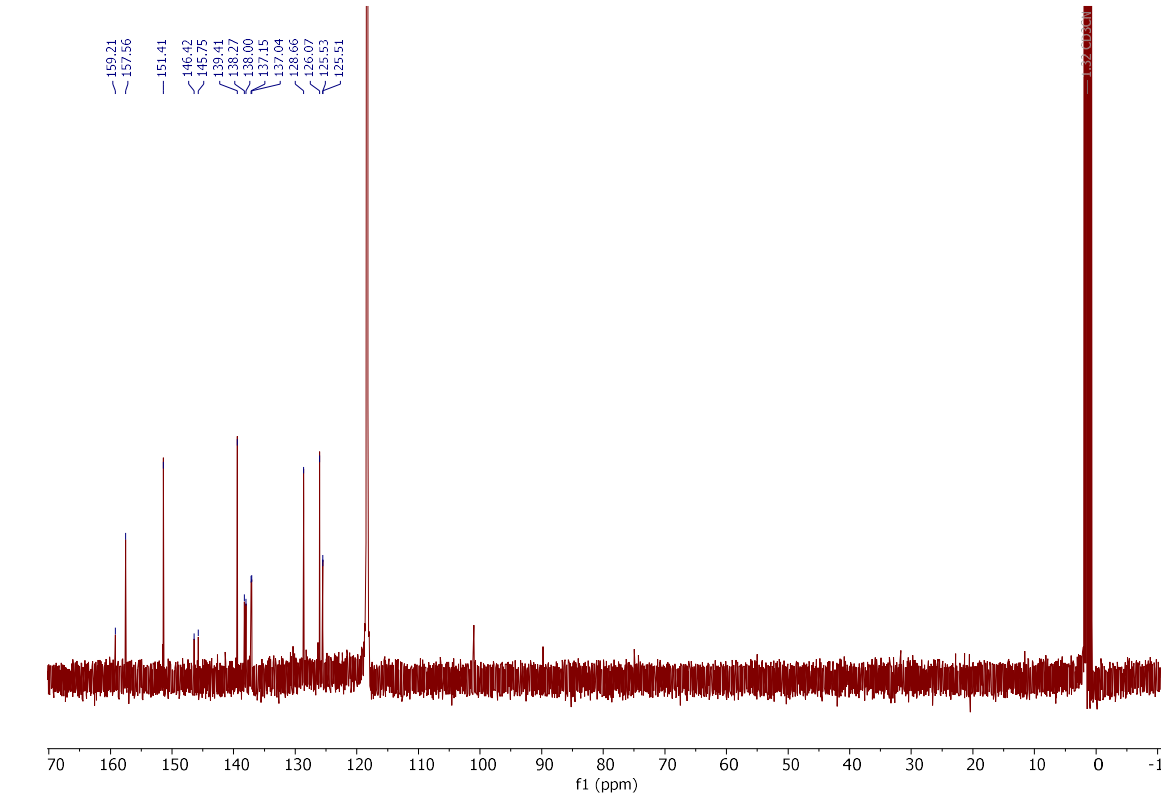

$^{31}P\{H\}$ NMR (162 MHz, CD_3CN)

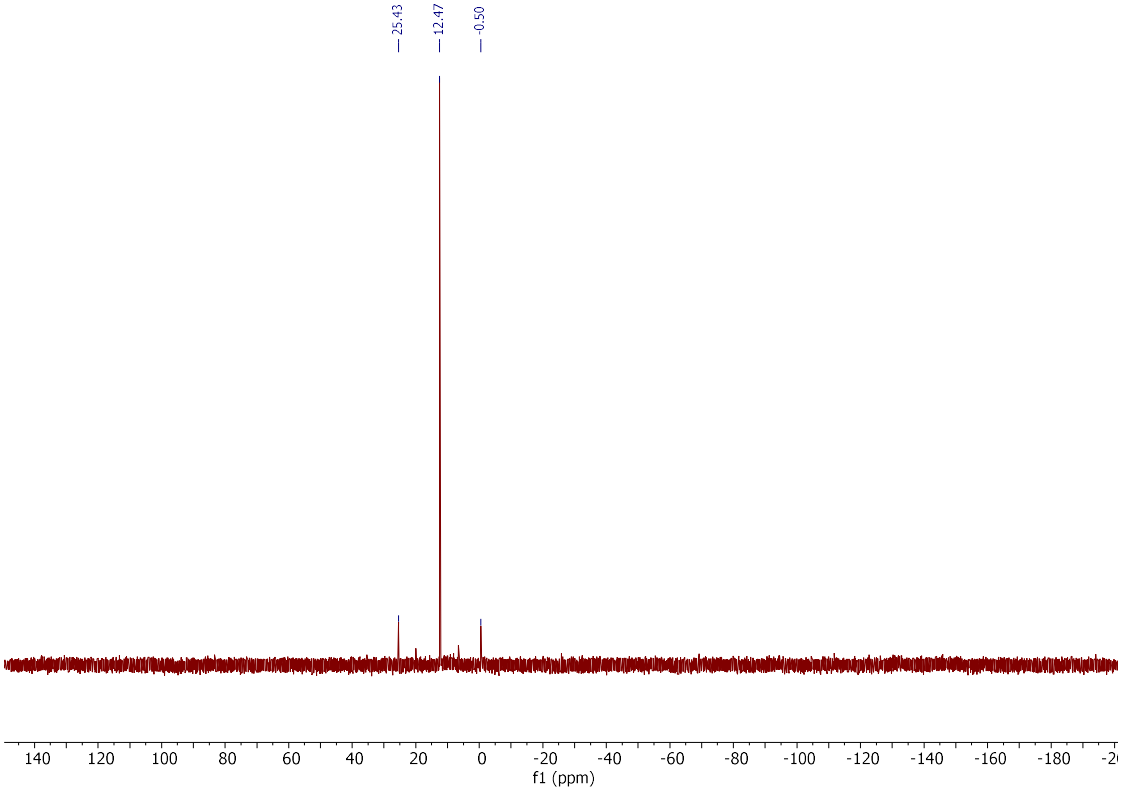

^{19}F NMR (282 MHz, CD_3CN)

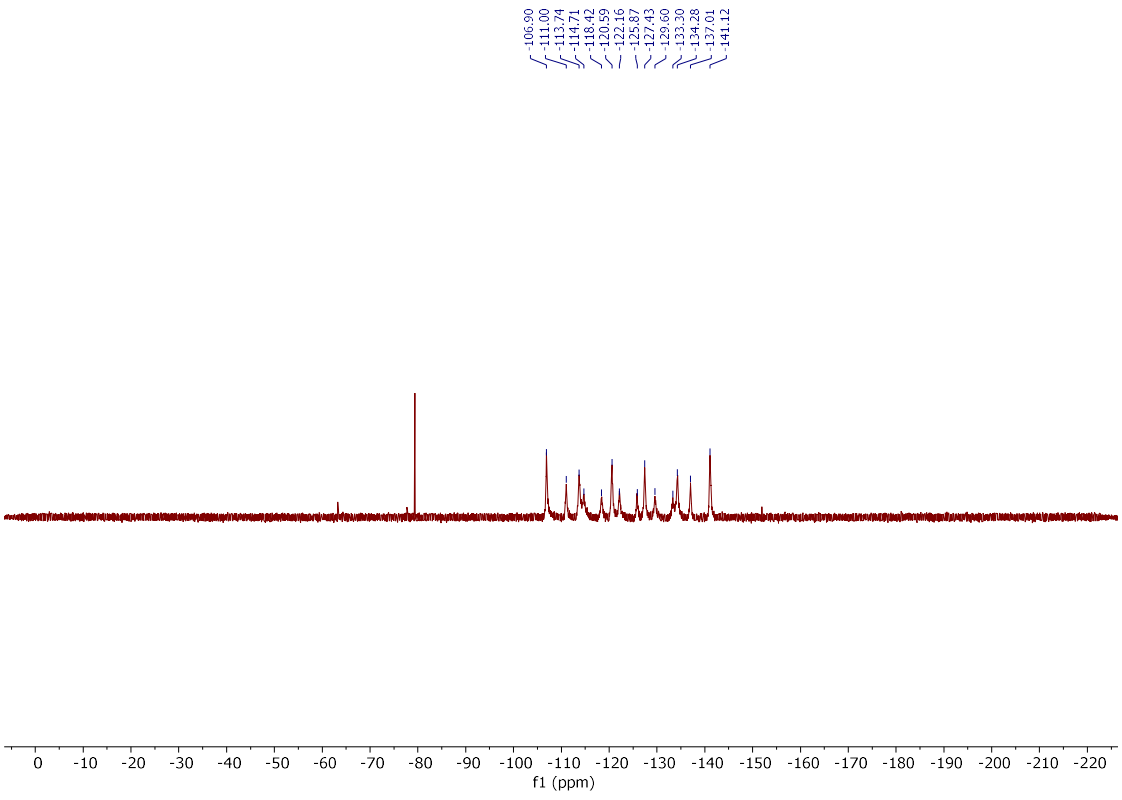

Compound **300**

^{1}H NMR (400 MHz, CD_3CN)

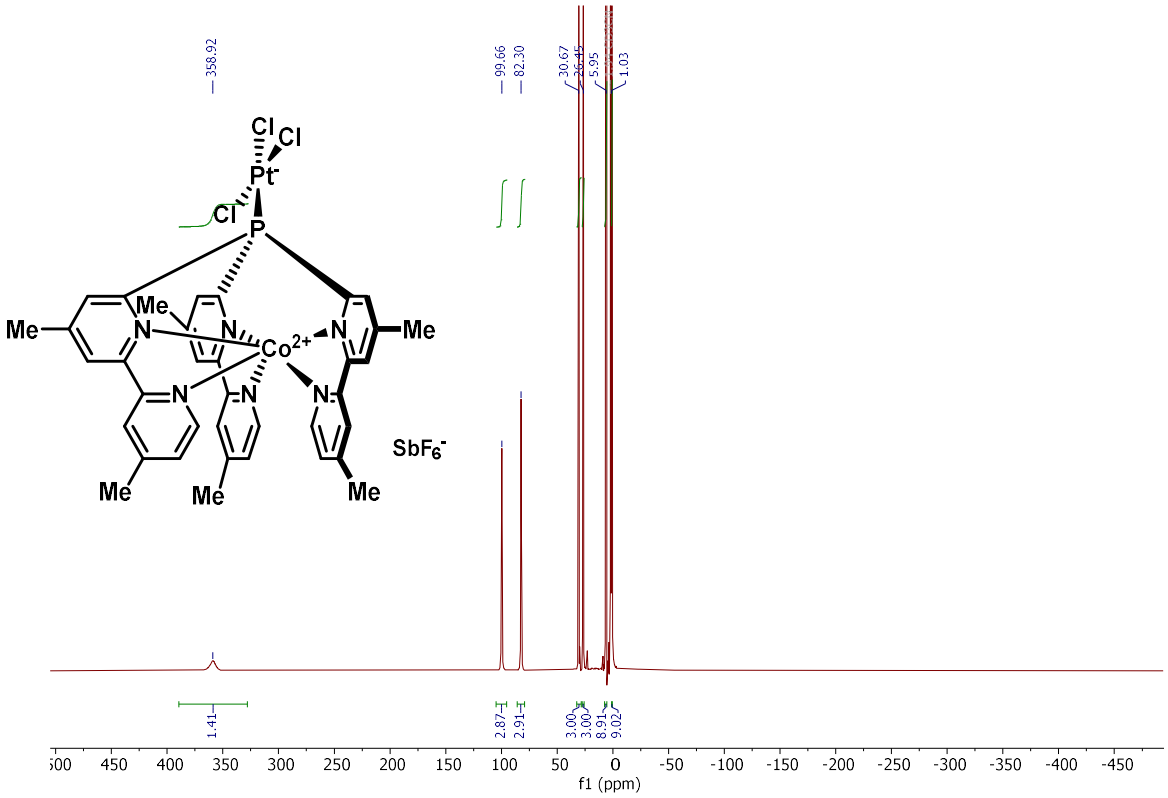

^{31}P{H} NMR (162 MHz, CD_3CN)

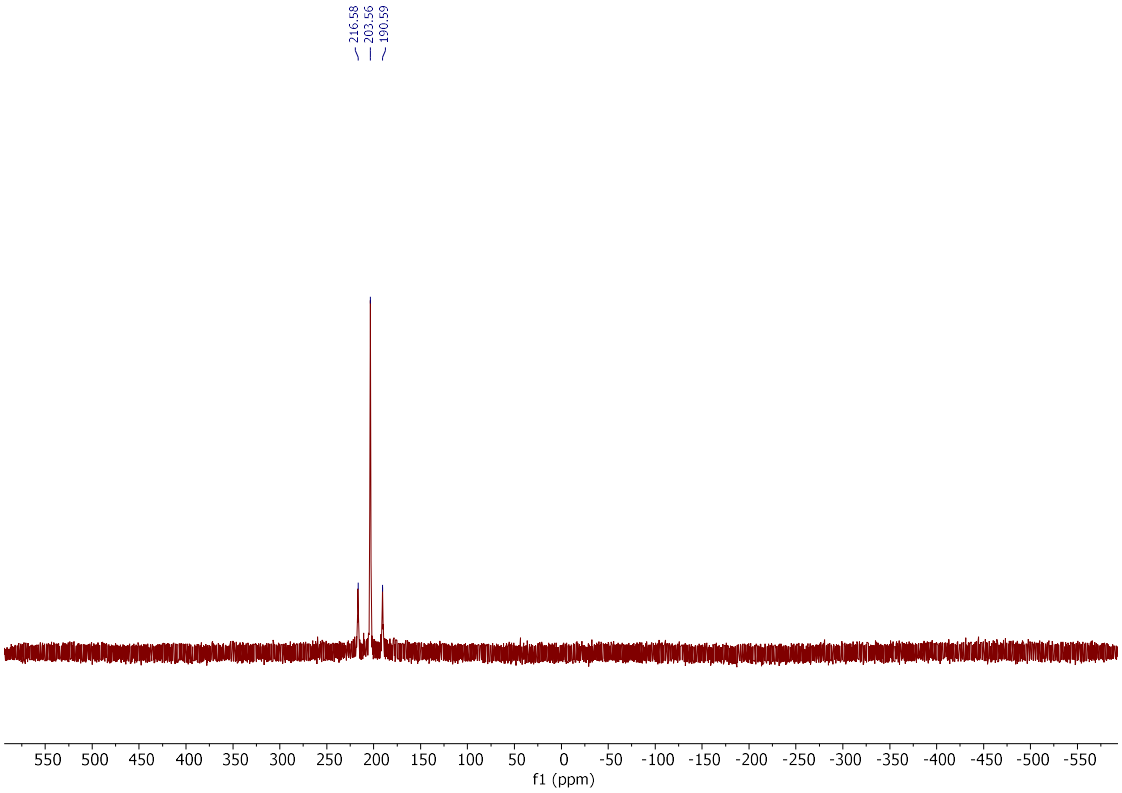

^{19}F NMR (376 MHz, CD_3CN)

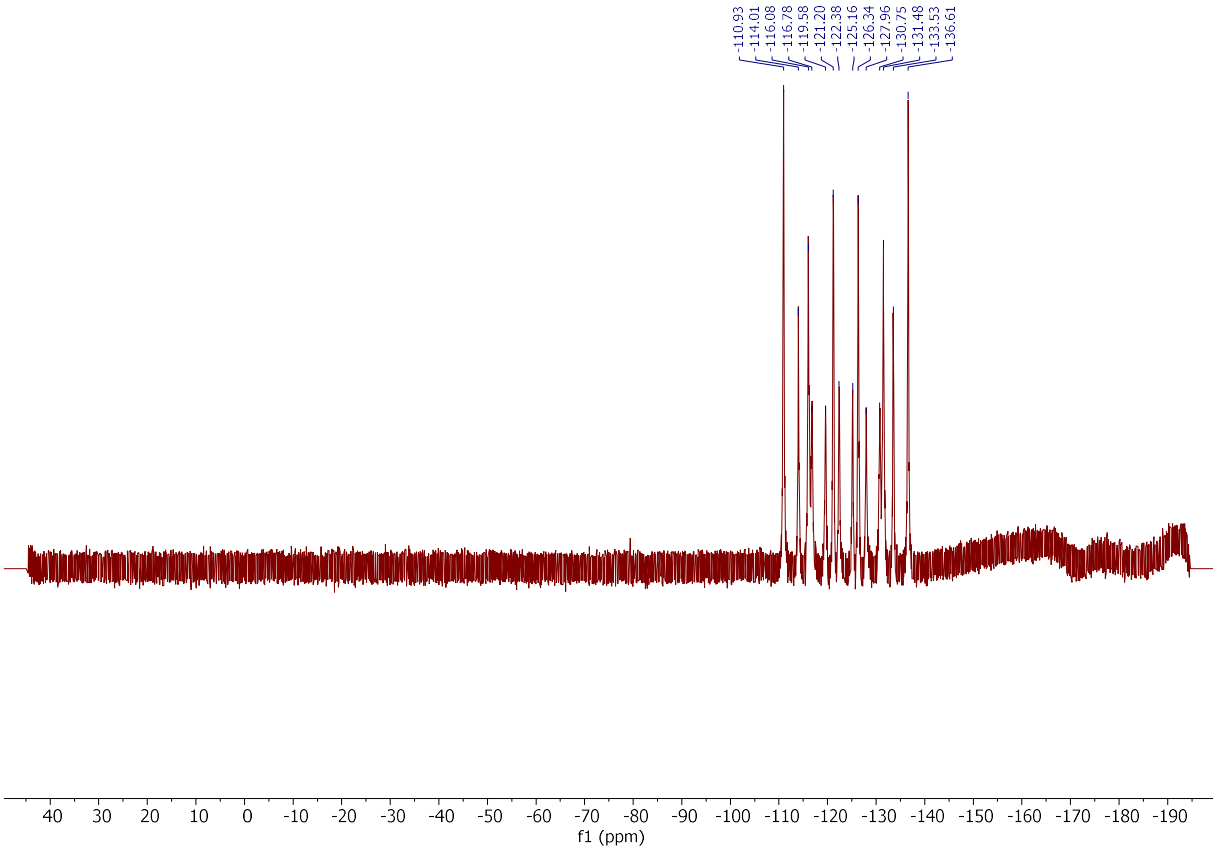

Compound **301**

^{1}H NMR (400 MHz, CD_3CN)

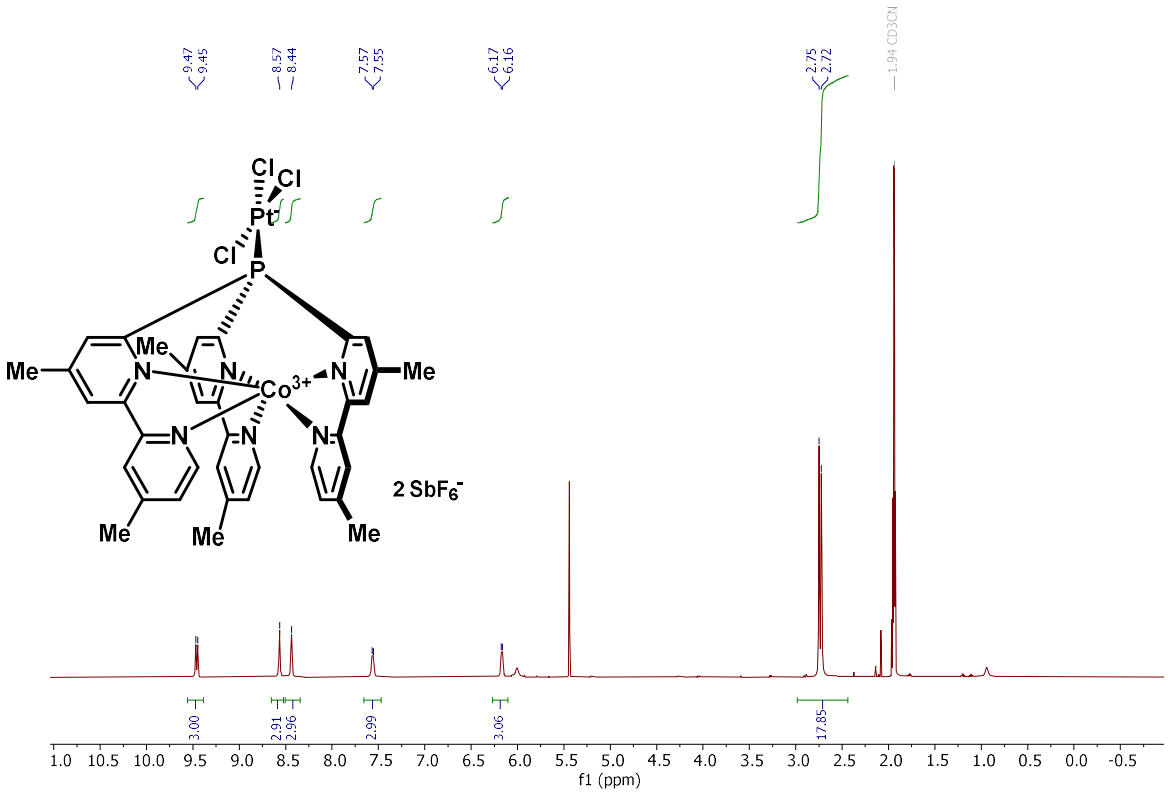

^{13}C NMR (101 MHz, CD_3CN)

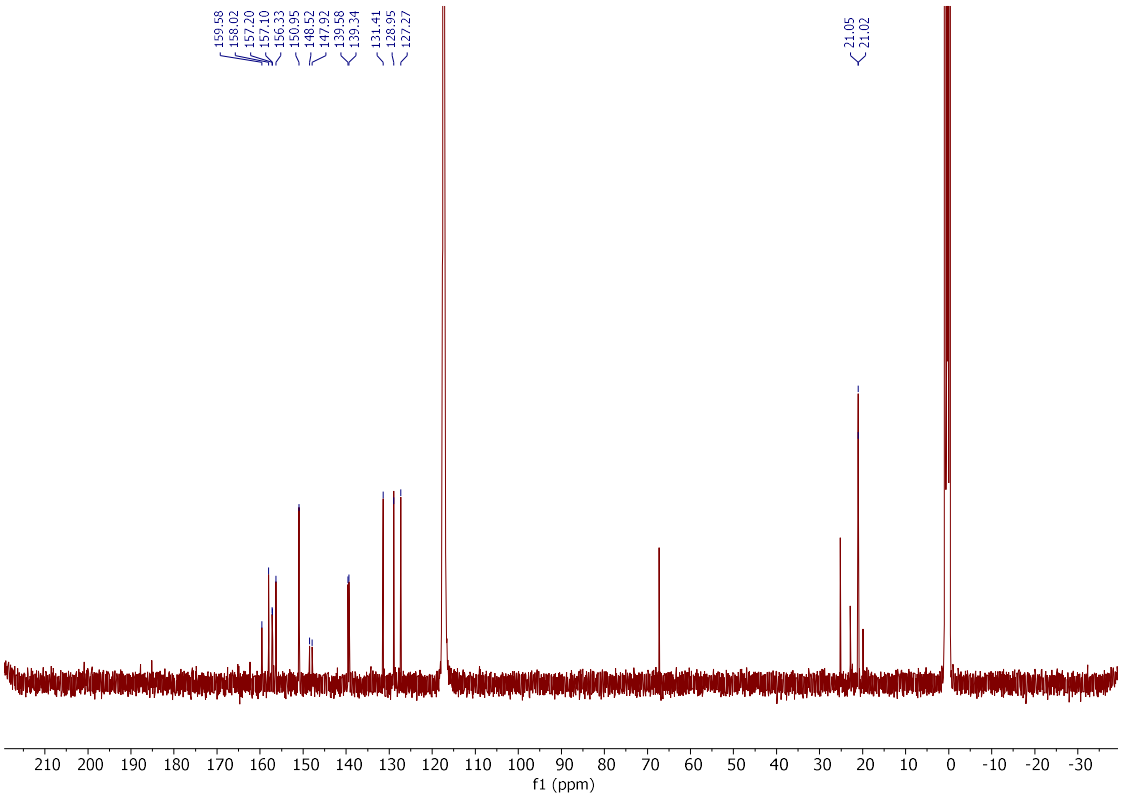

$^{31}P\{H\}$ NMR (162 MHz, CD_3CN)

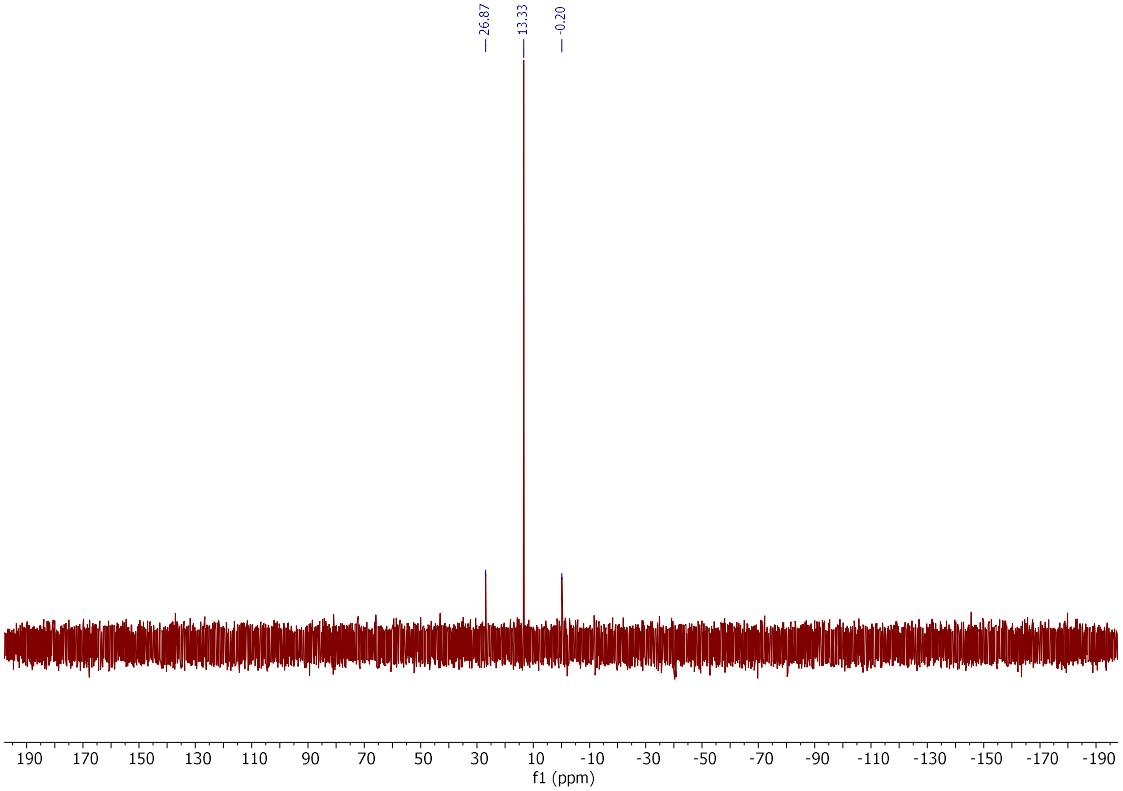

^{19}F NMR (376 MHz, CD_3CN)

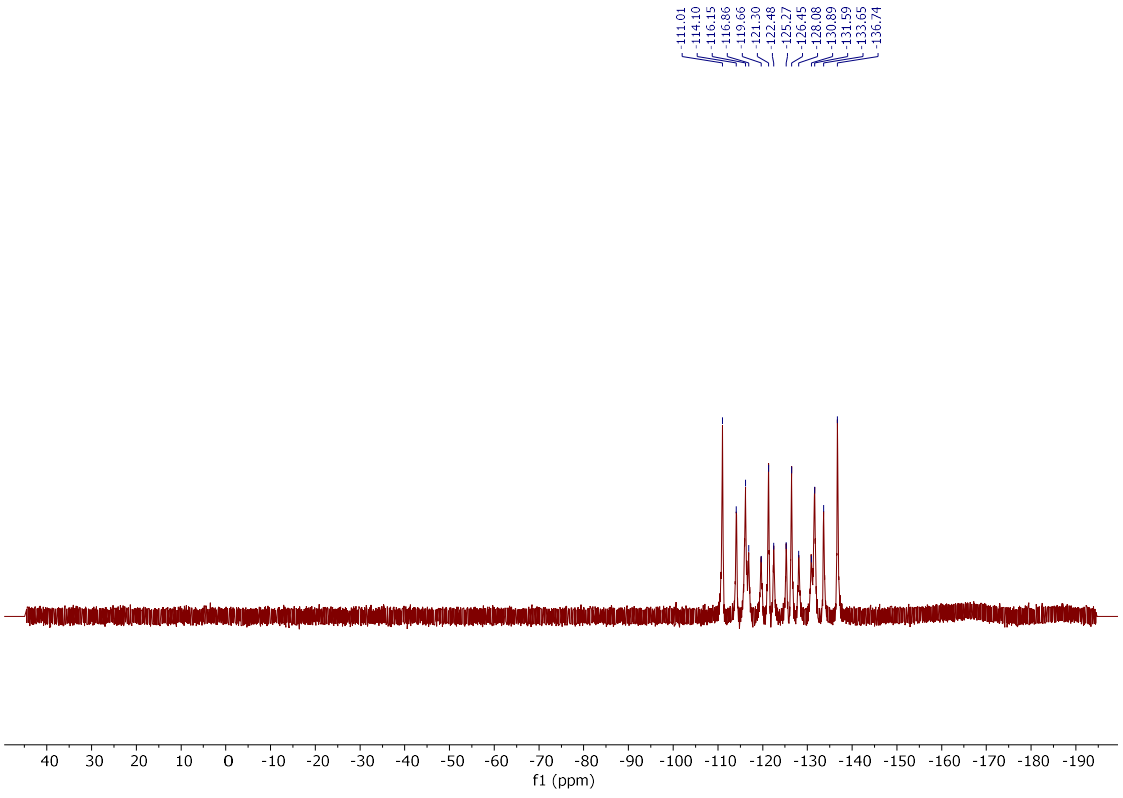

Benzyl ethers:

1-{[4-(tert-Butyl)phenoxy]methyl}-3,5-dichlorobenzene (**469e**)

^{1}H NMR (300 MHz, $CDCl_3$)

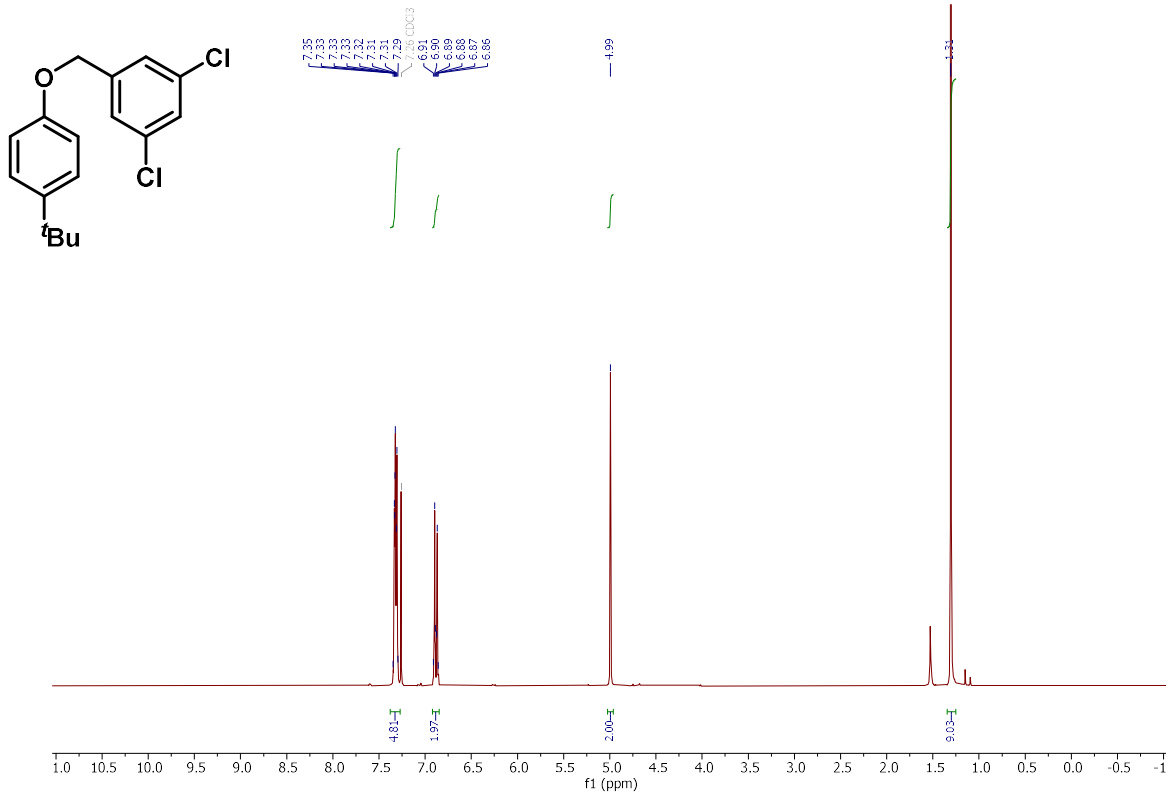

^{13}C{H} NMR (101 MHz, $CDCl_3$)

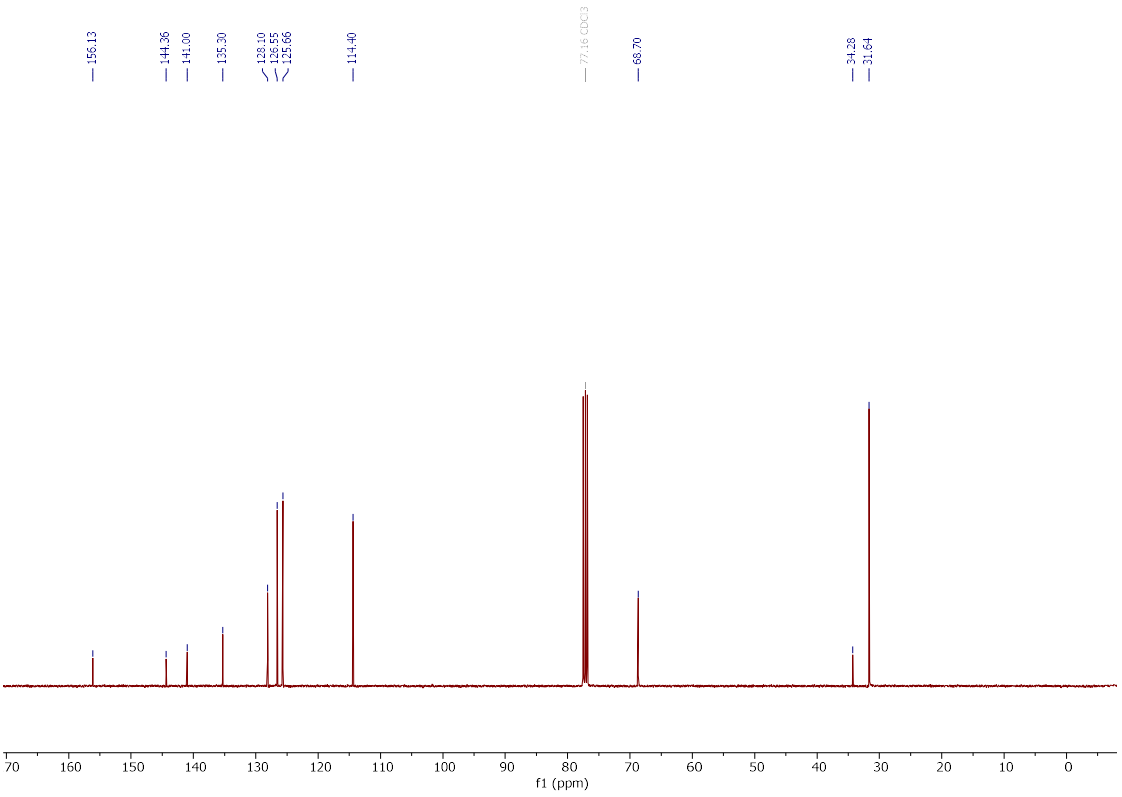

1-(*tert*-Butyl)-4-{[4-(methylsulfonyl)benzyl]oxy}benzene (**469f**)

^{1}H NMR (300 MHz, $CDCl_3$)

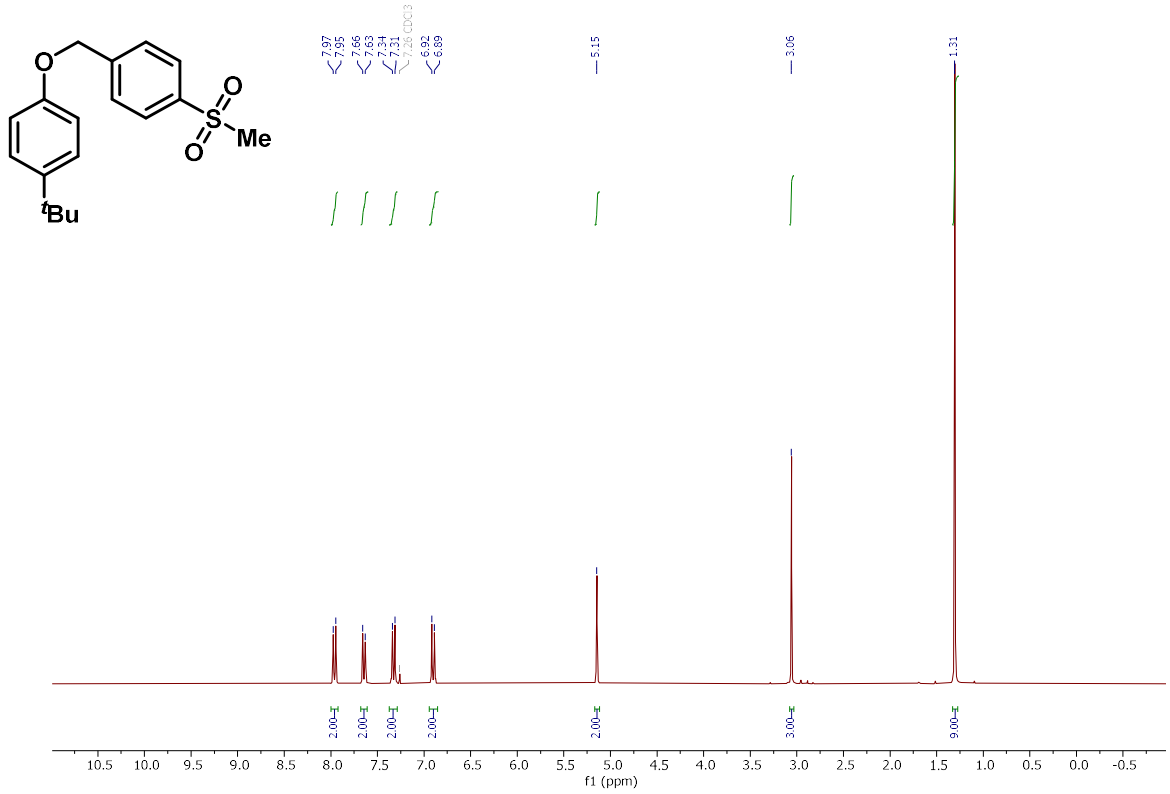

^{13}C{H} NMR (75 MHz, $CDCl_3$)

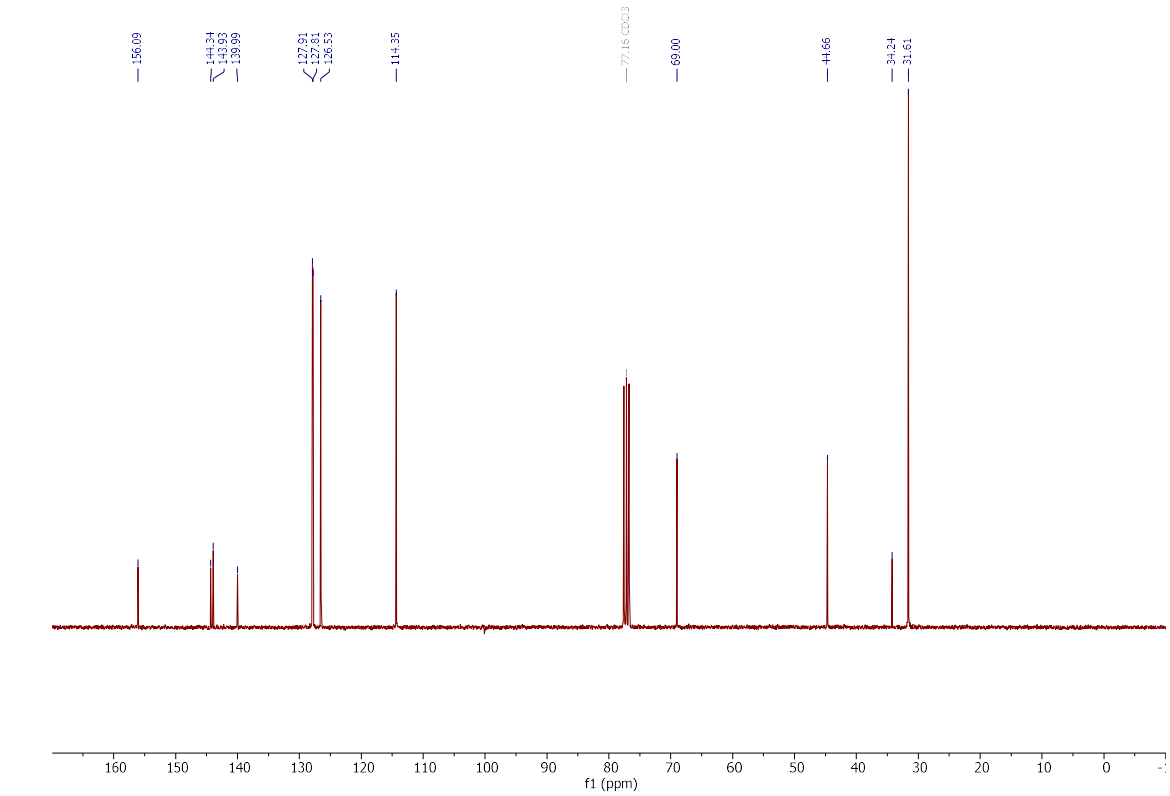

1-[(3,4,5-Trimethylphenoxy)methyl]naphthalene (**469g**)

^{1}H NMR (300 MHz, $CDCl_3$)

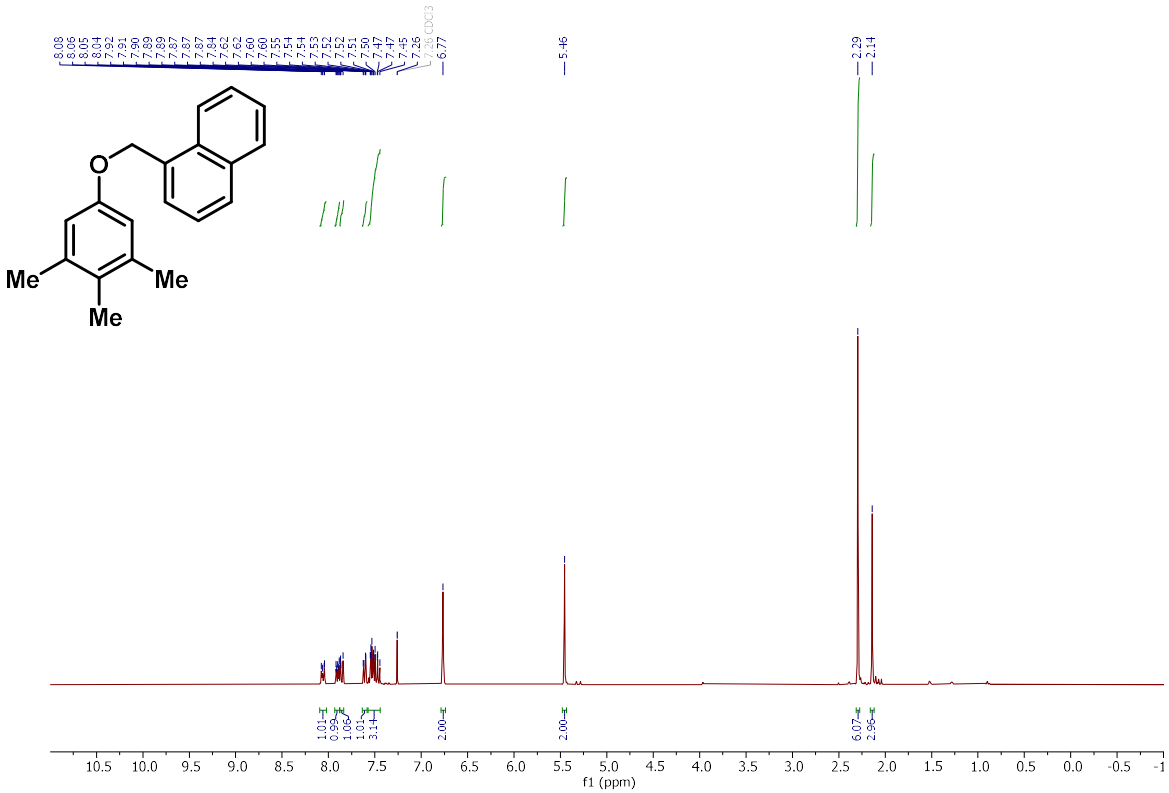

^{13}C{H} NMR (75 MHz, $CDCl_3$)

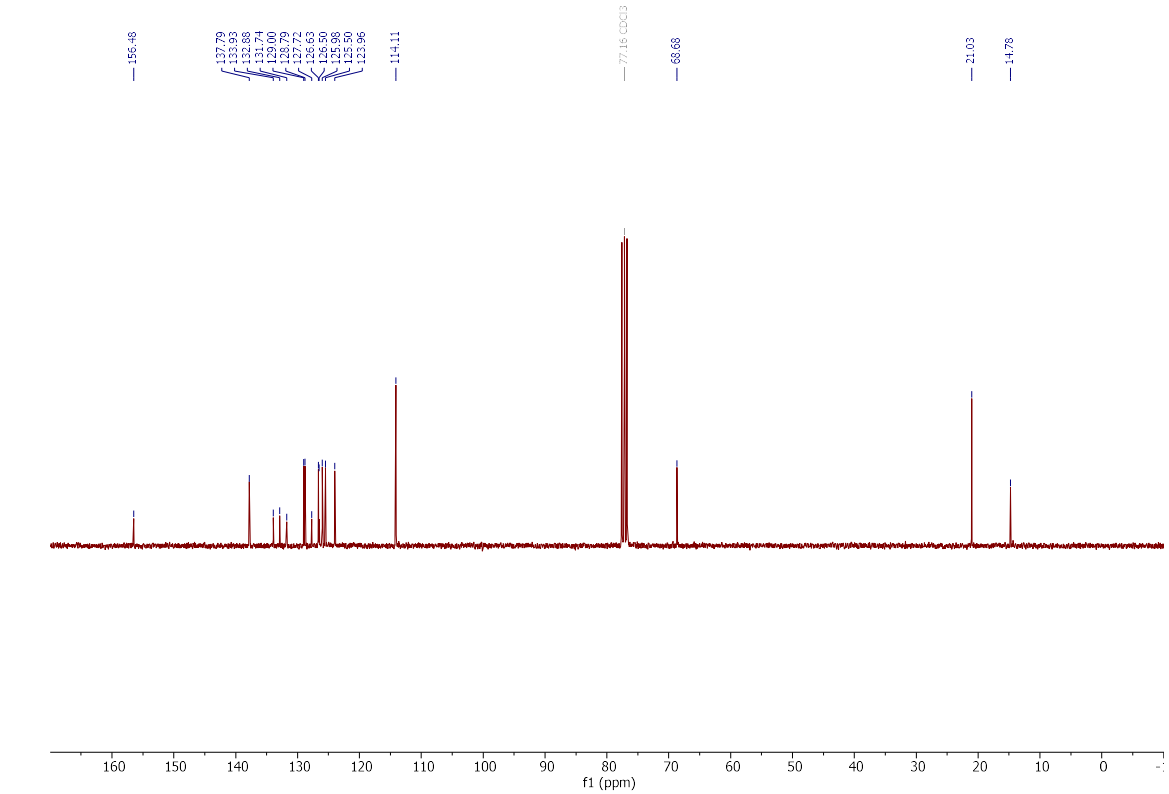

1-(*tert*-Butyl)-4-{[4-(trifluoromethyl)benzyl]oxy}benzene (**469h**)

^{1}H NMR (300 MHz, $CDCl_3$)

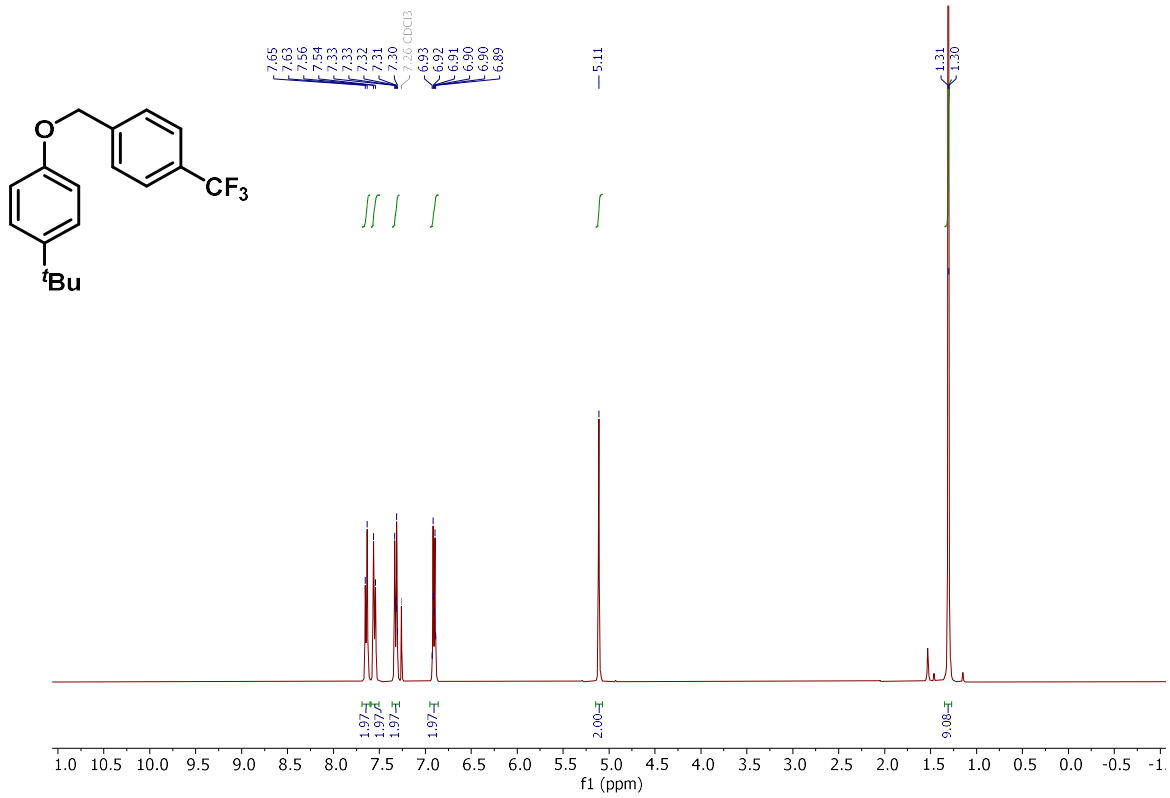

^{13}C{H} NMR (101 MHz, $CDCl_3$)

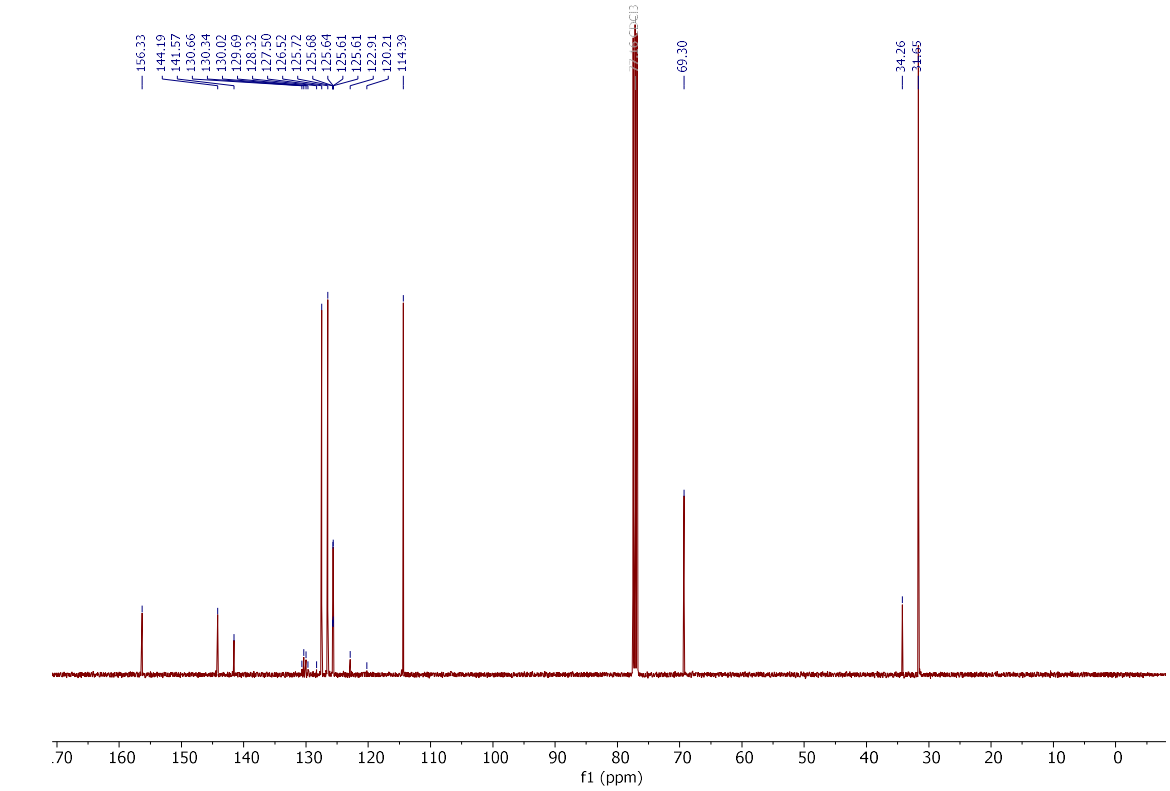

^{19}F NMR (377 MHz, $CDCl_3$)

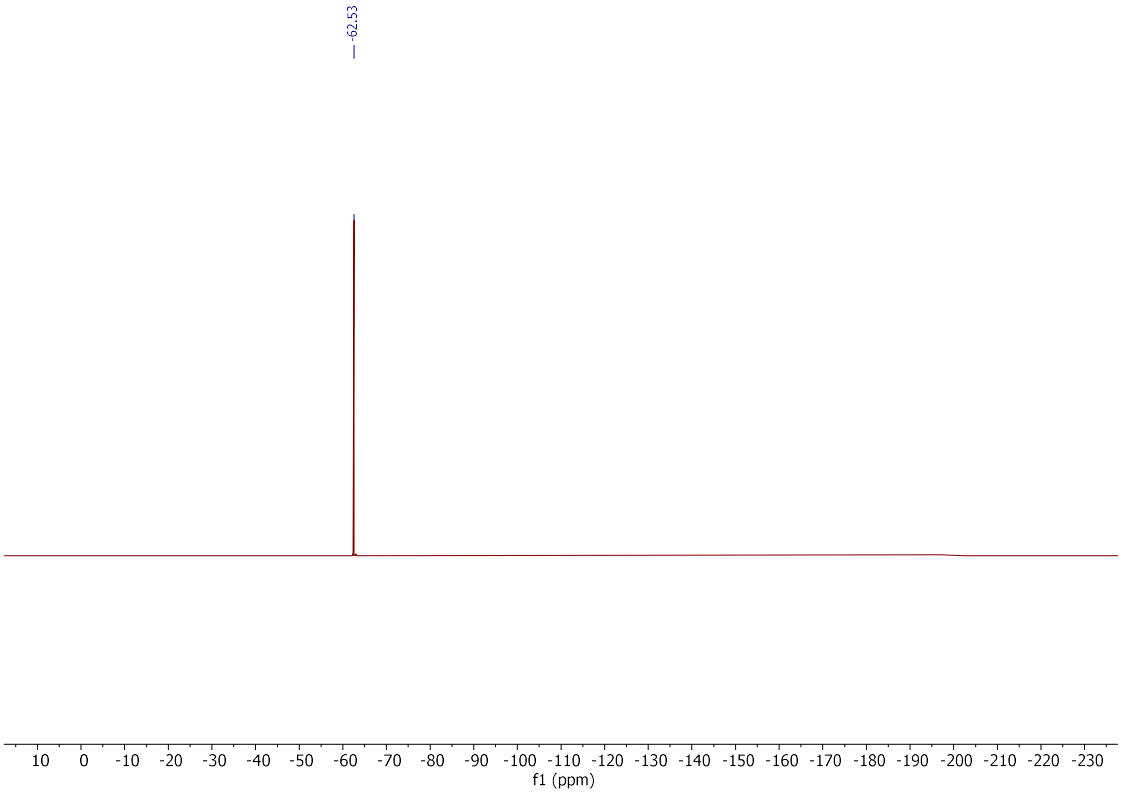

1,3-dichloro-5-((4-chlorophenoxy)methyl)benzene (**469i**)

^{1}H NMR (300 MHz, $CDCl_3$)

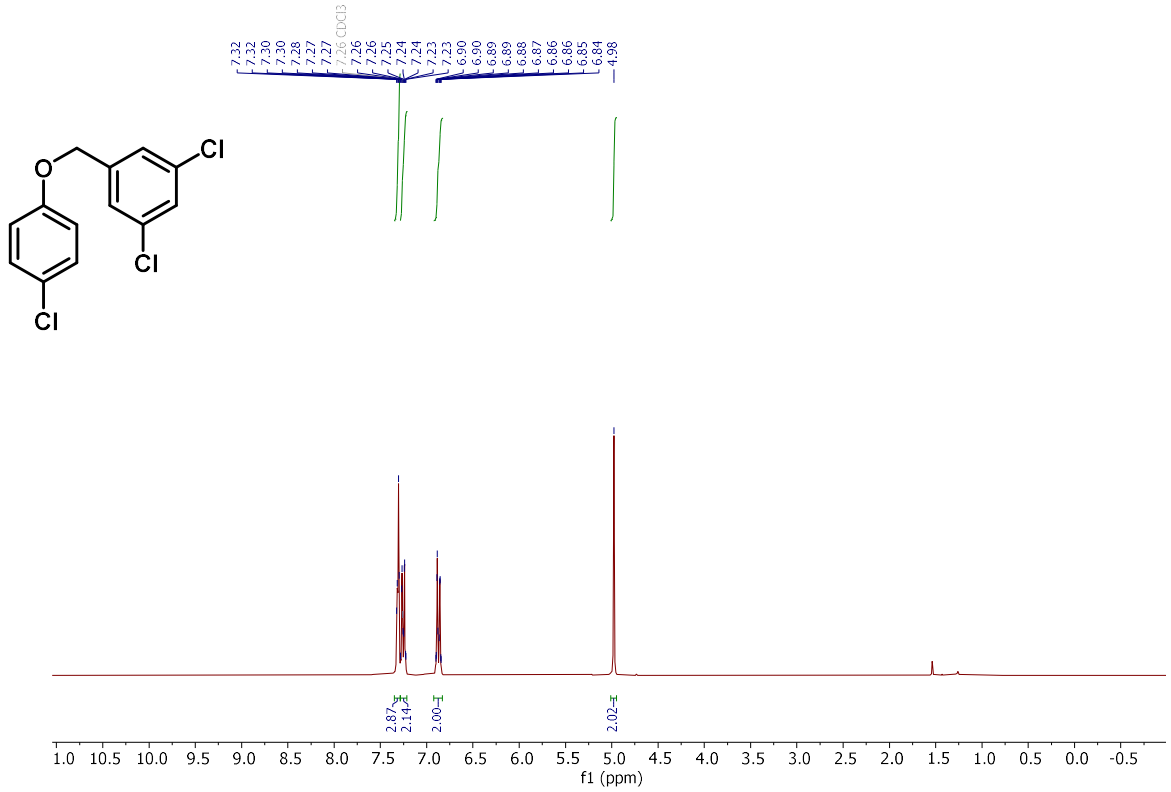

^{13}C{H} NMR (75 MHz, $CDCl_3$)

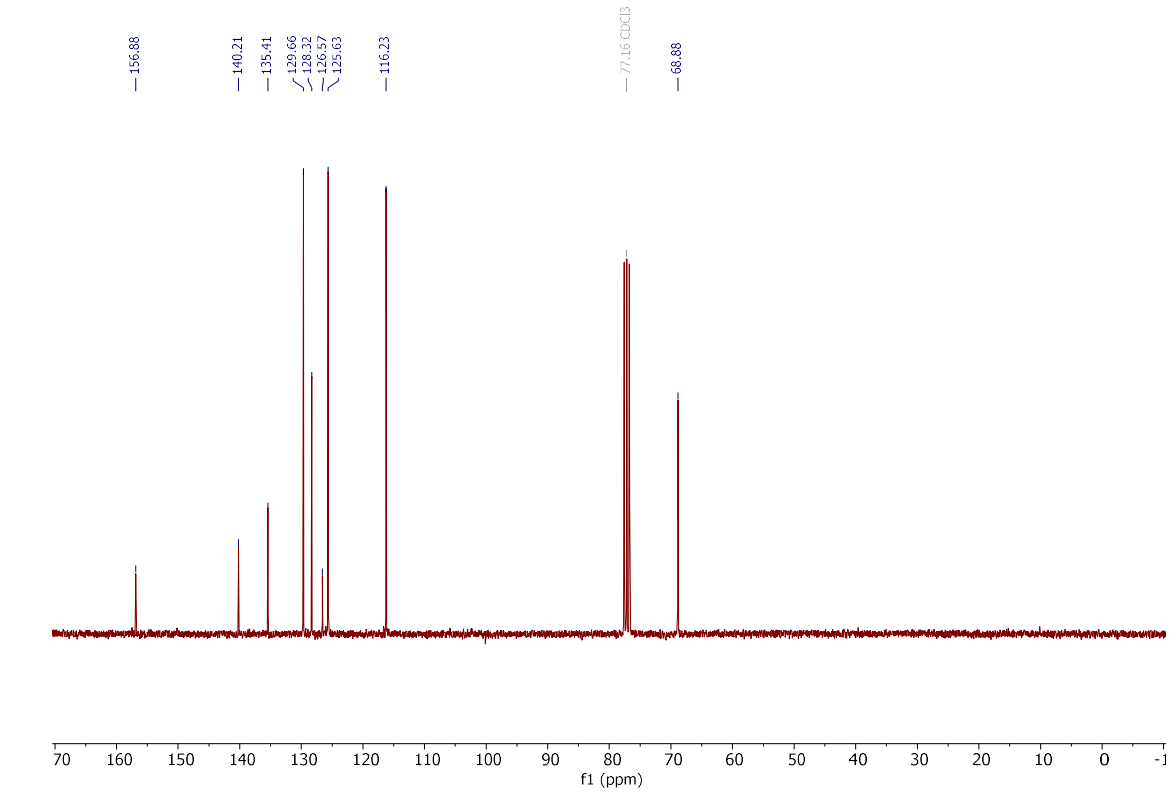

1-methyl-4-((4-nitrobenzyl)oxy)benzene (**469j**)

^{1}H NMR (400 MHz, CDCl3)

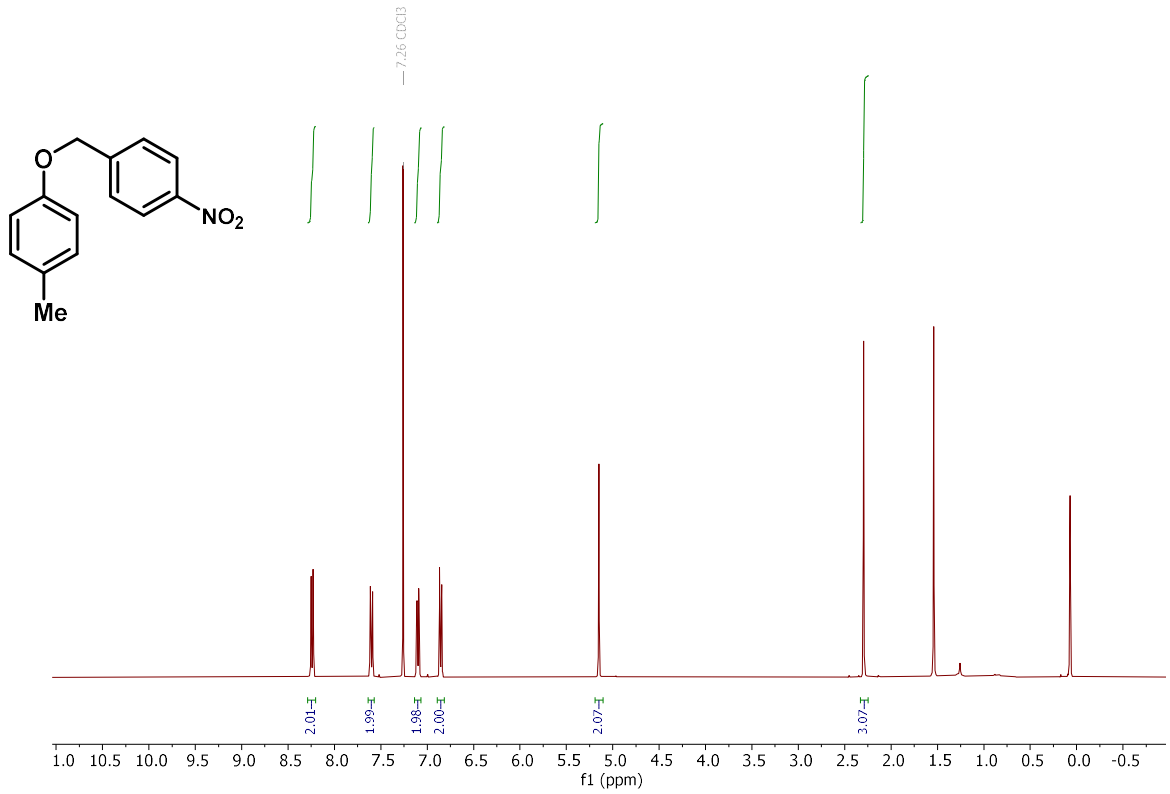

^{13}C NMR (101 MHz, CDCl3)

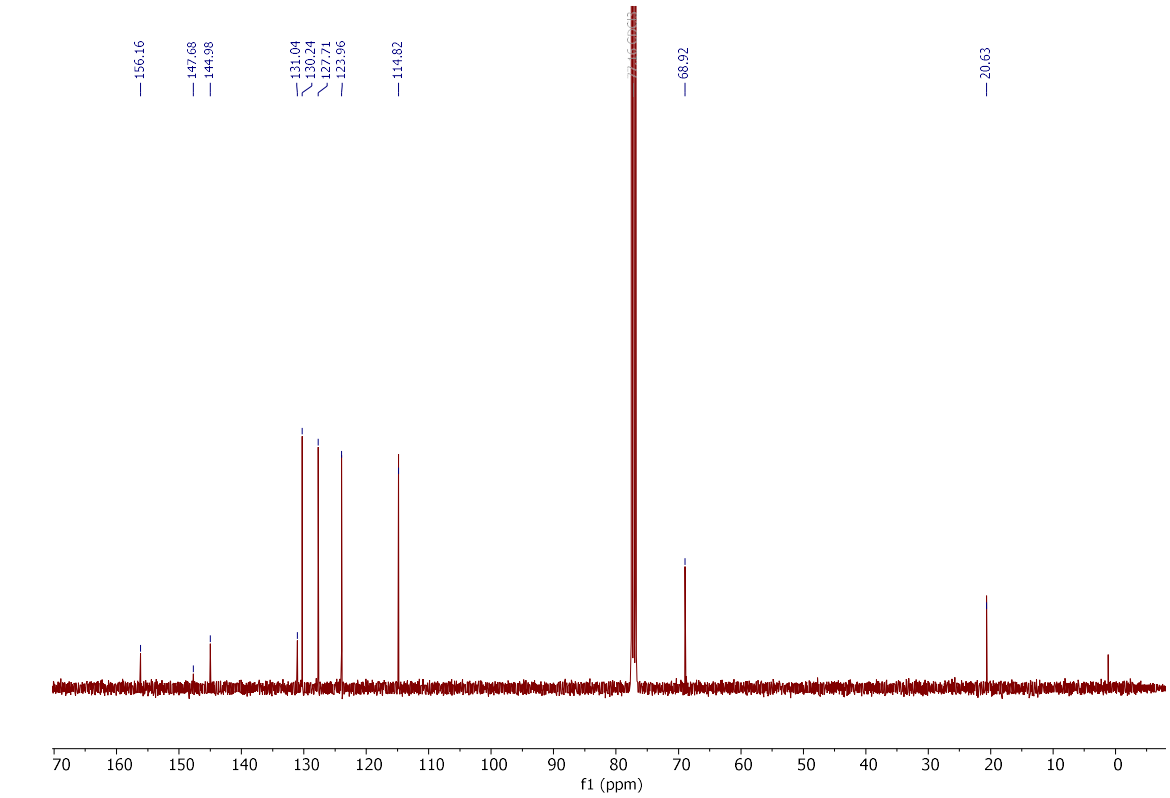

4-[(*p*-Tolyloxy)methyl]pyridine (**469k**)

^{1}H NMR (300 MHz, $CDCl_3$)

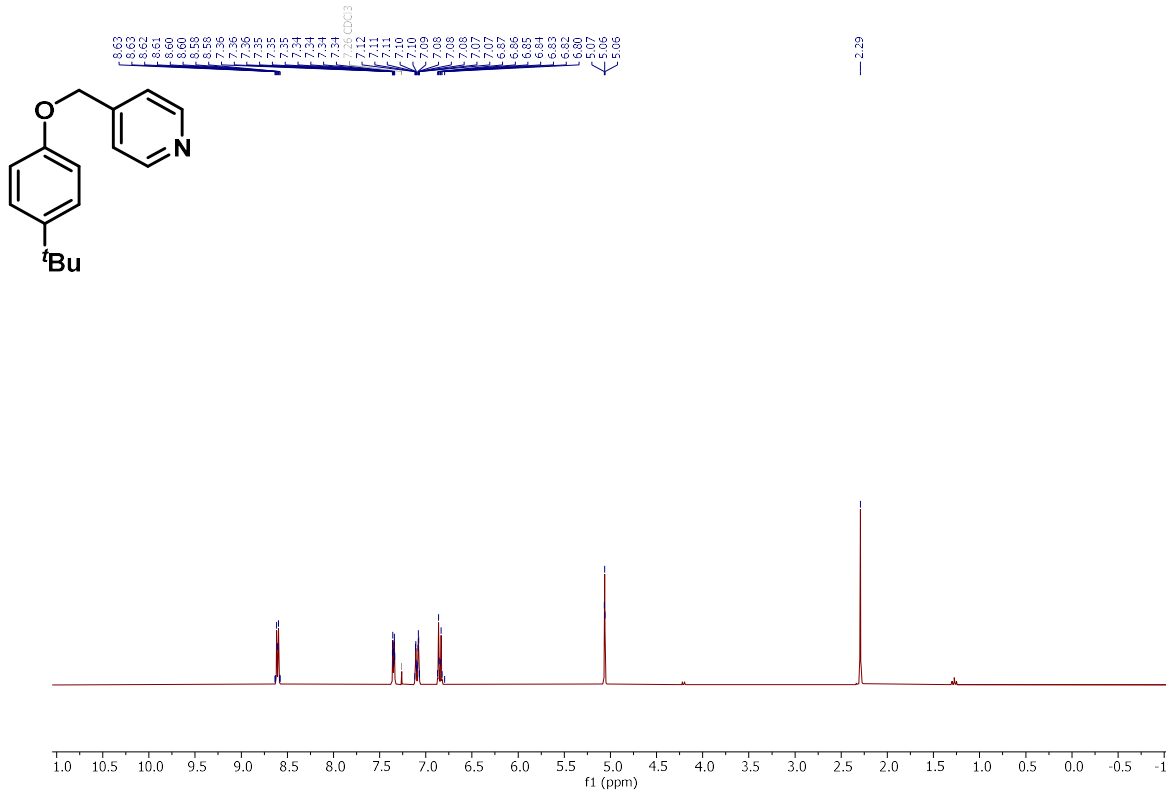

^{13}C{H} NMR (75 MHz, $CDCl_3$)

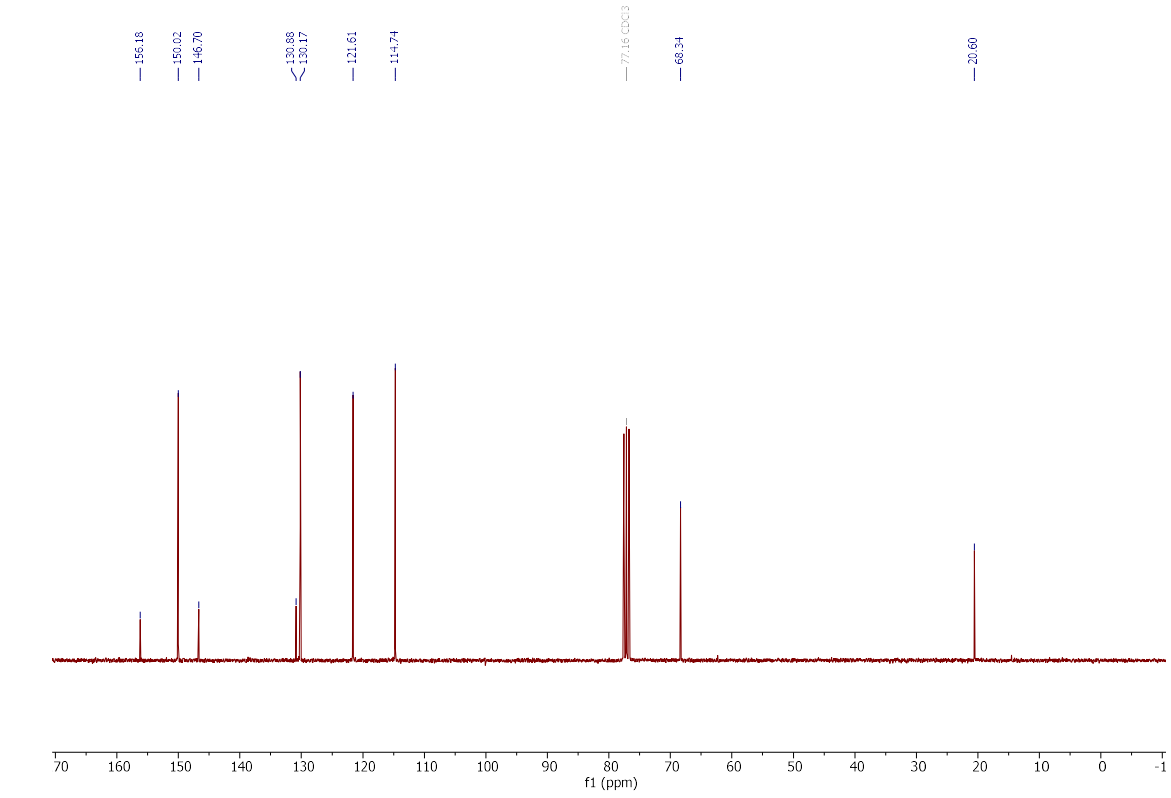

2-{[4-(*tert*-Butyl)phenoxy]methyl}-1,3-dimethylbenzene (**469l**)

^{1}H NMR (300 MHz, $CDCl_3$)

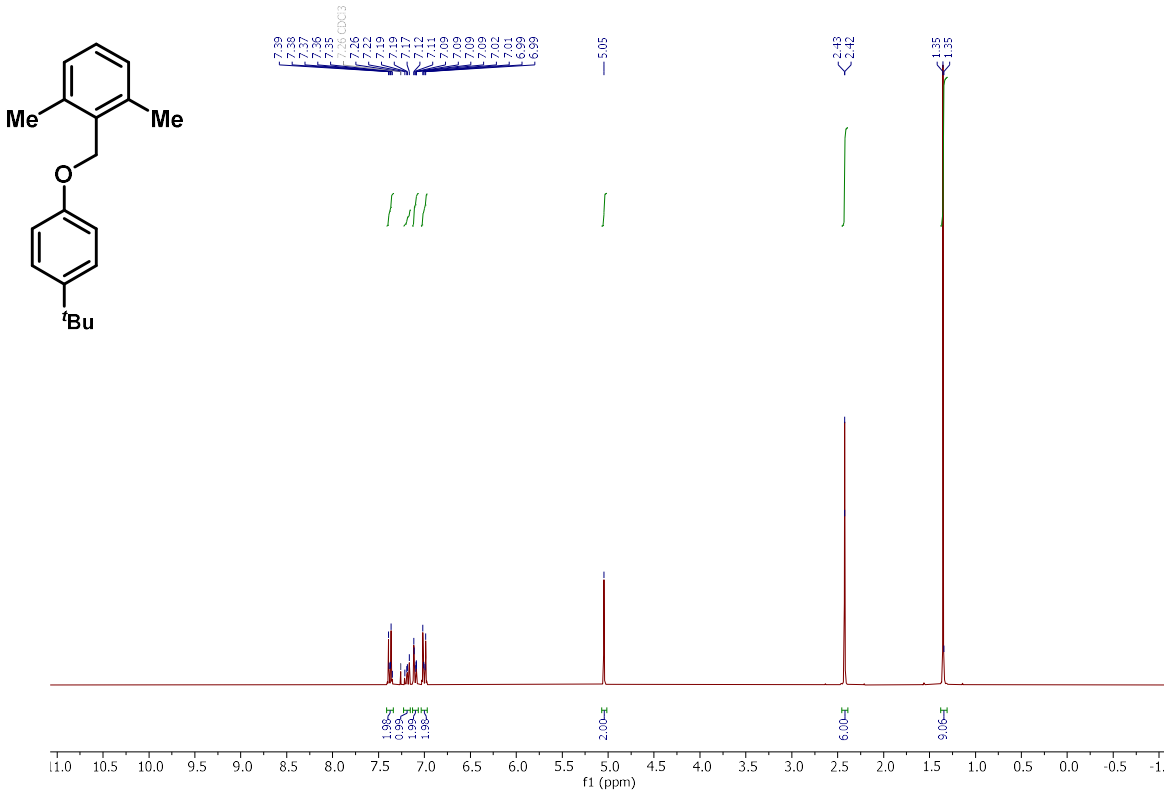

^{13}C{H} NMR (75 MHz, $CDCl_3$)

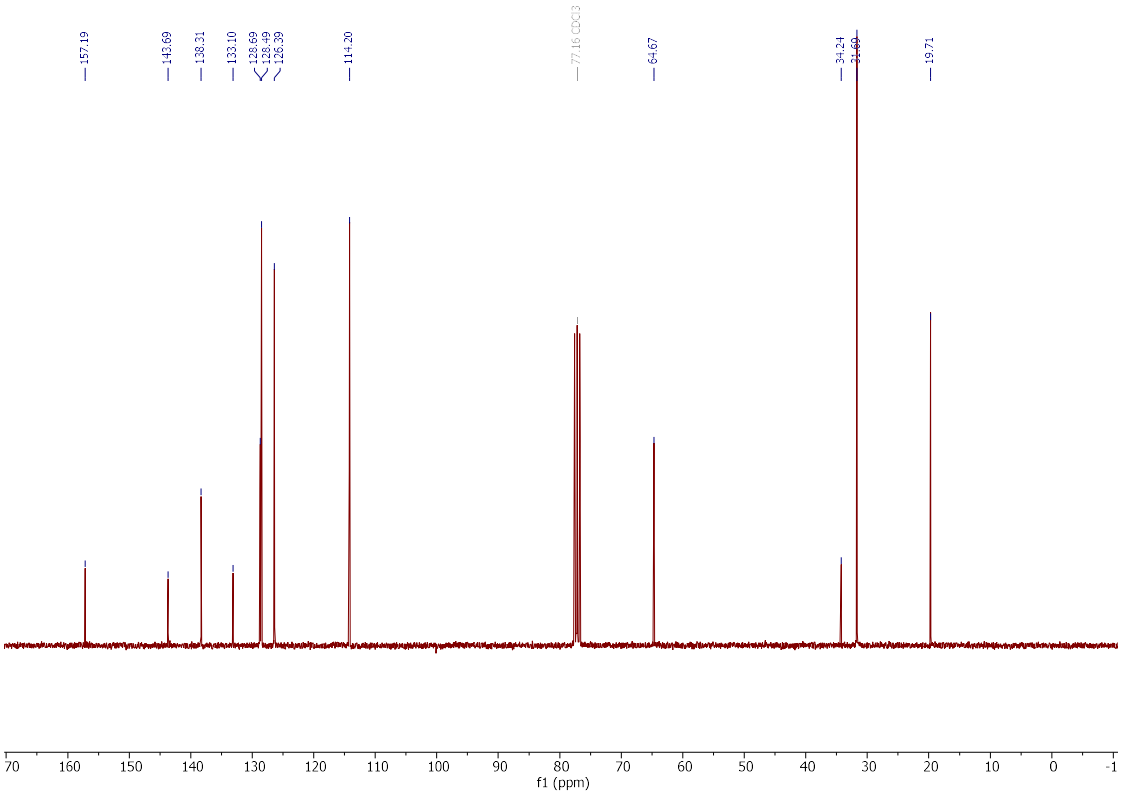

2-((4-(tert-butyl)phenoxy)methyl)-1,3-dichlorobenzene (**469m**)

^{1}H NMR (300 MHz, $CDCl_3$)

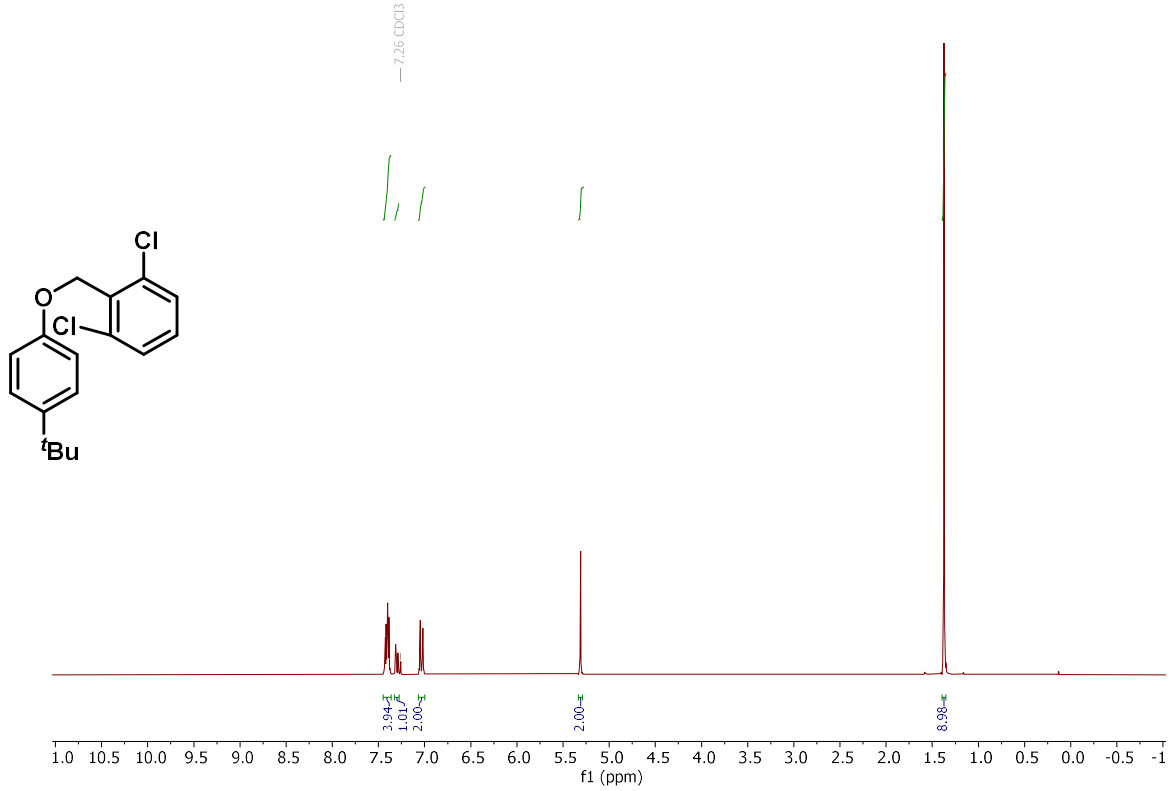

^{13}C NMR (75 MHz, $CDCl_3$)

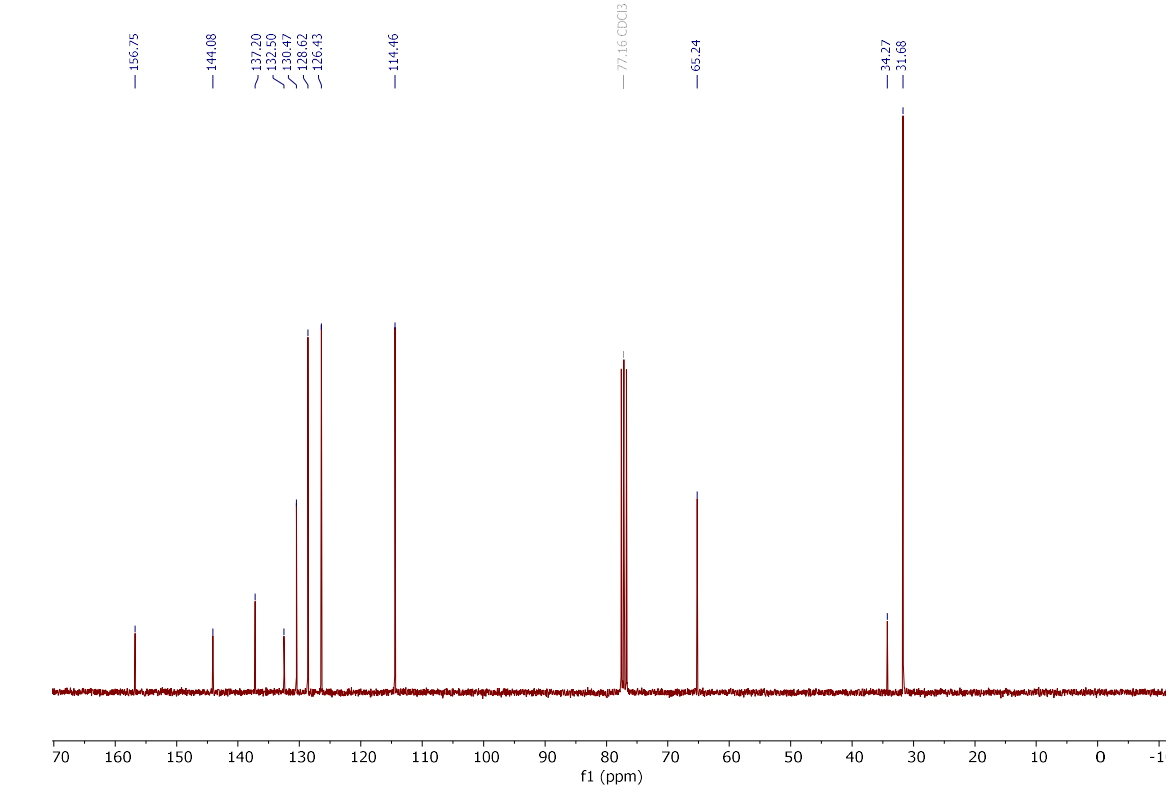

4-{[4-(Trifluoromethyl)benzyl]oxy}-1,1'-biphenyl (**469n**)

^{1}H NMR (400 MHz, $CDCl_3$)

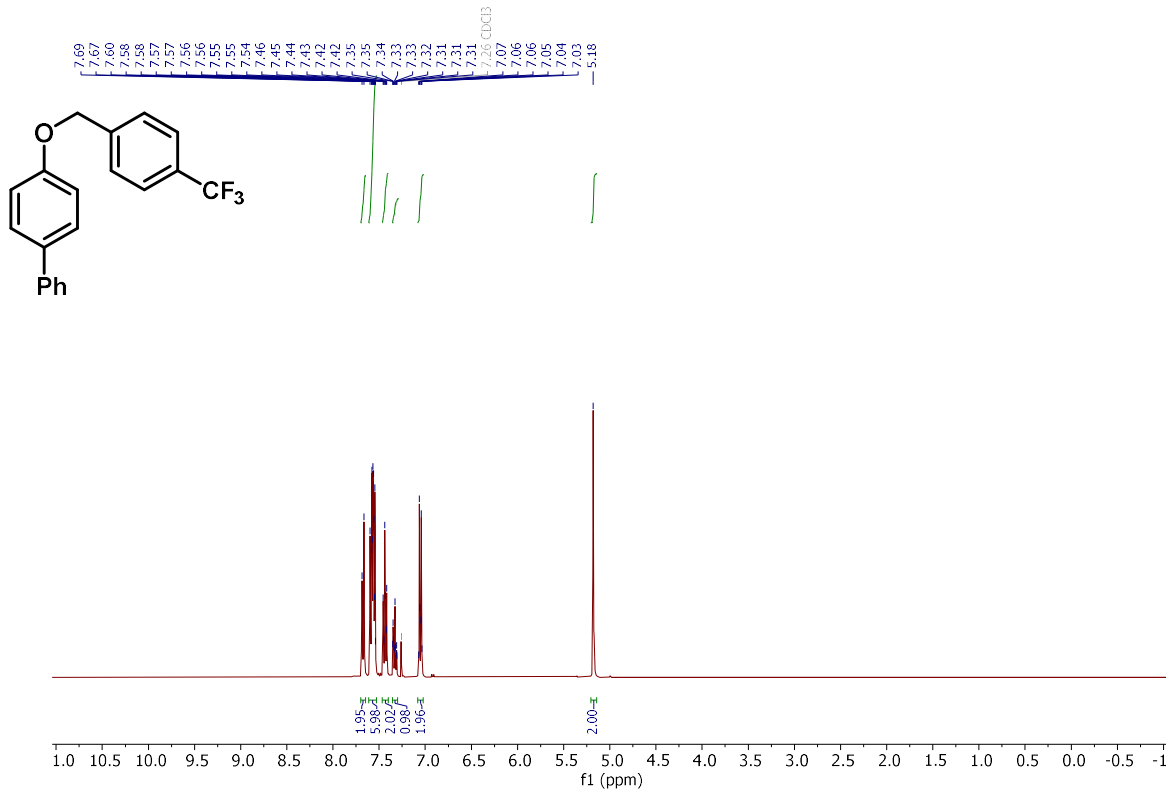

^{13}C{H} NMR (101 MHz, $CDCl_3$)

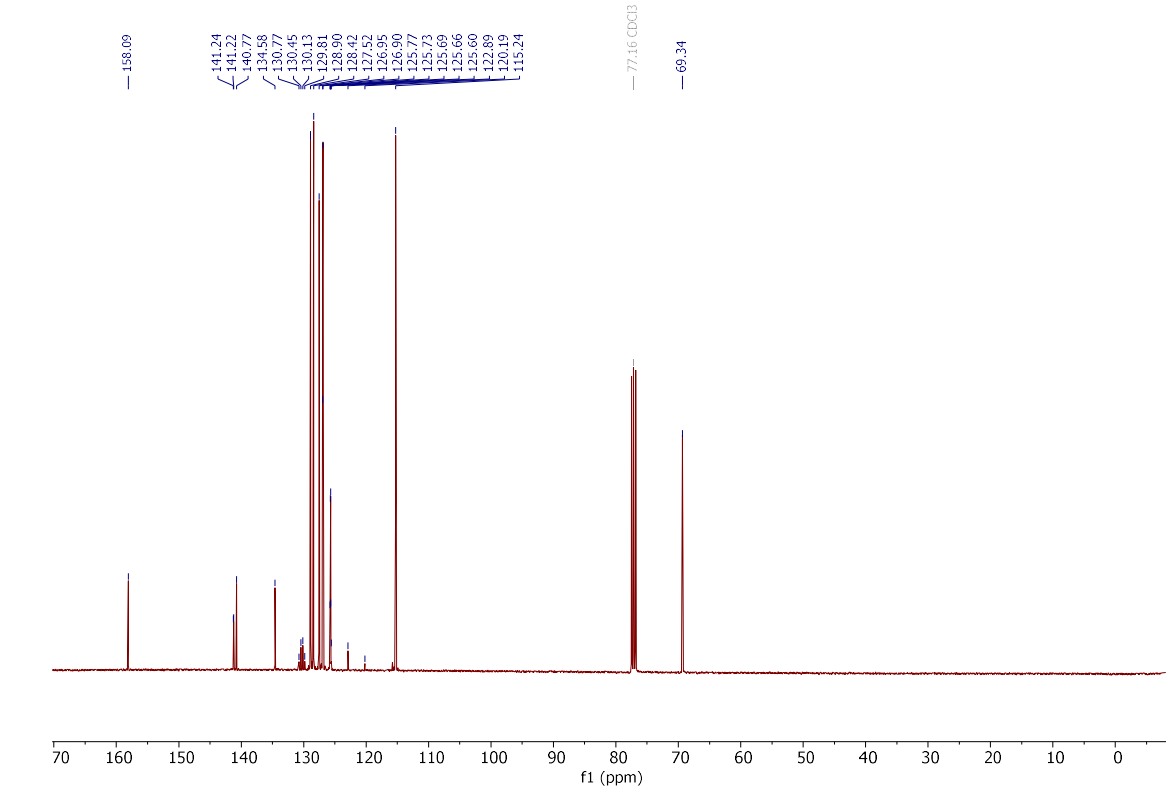

^{19}F NMR (377 MHz, $CDCl_3$)

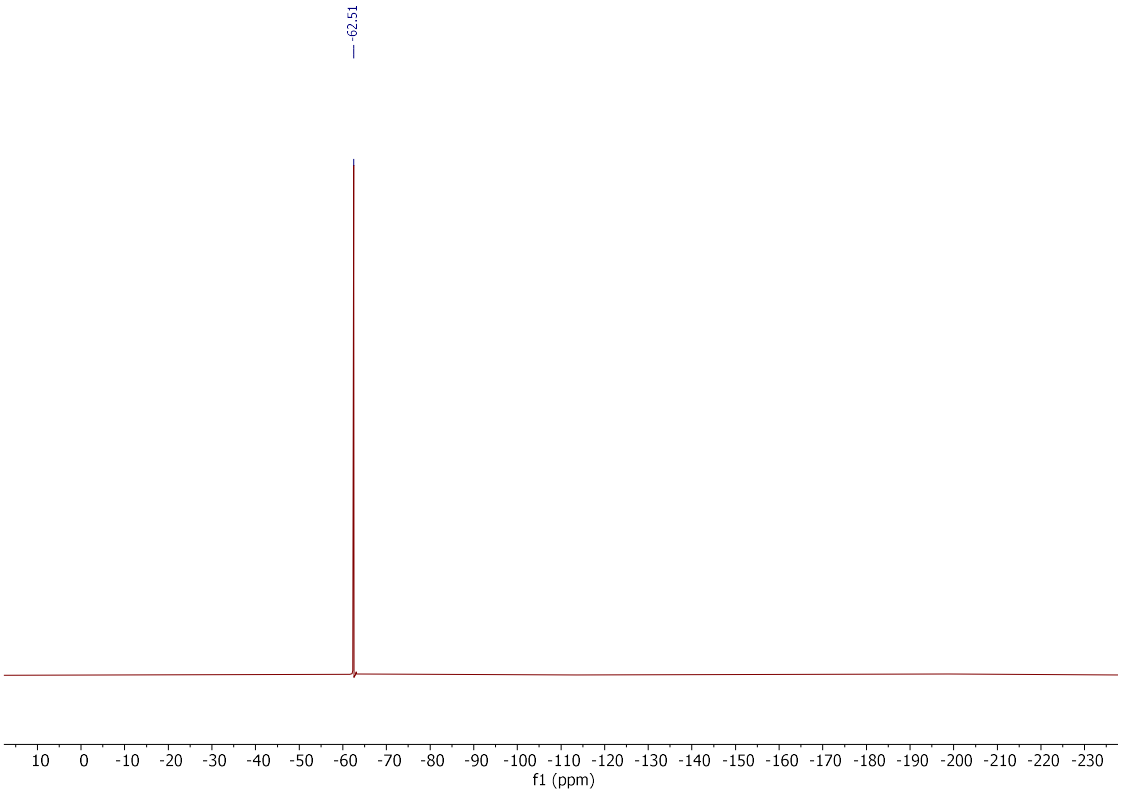

4-[(3,5-Dichlorobenzyl)oxy]-1,1'-biphenyl (**469o**)

^{1}H NMR (300 MHz, $CDCl_3$)

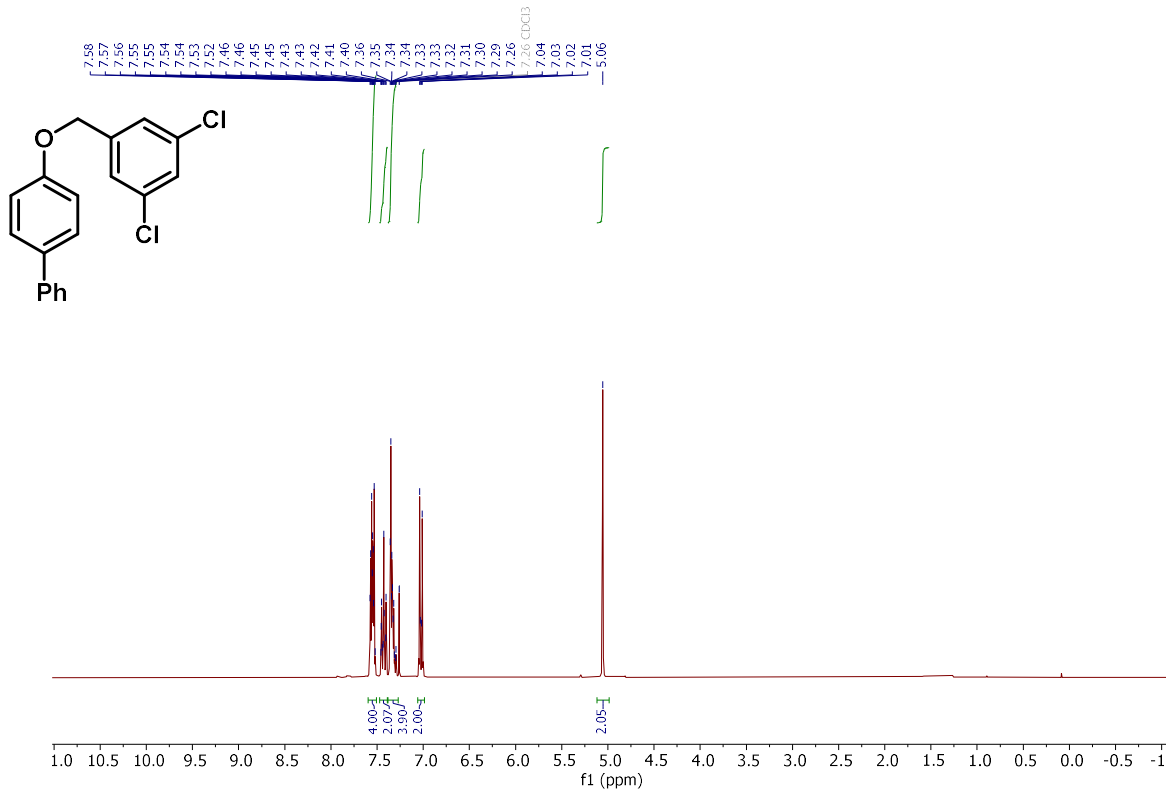

^{13}C{H} NMR (75 MHz, $CDCl_3$)

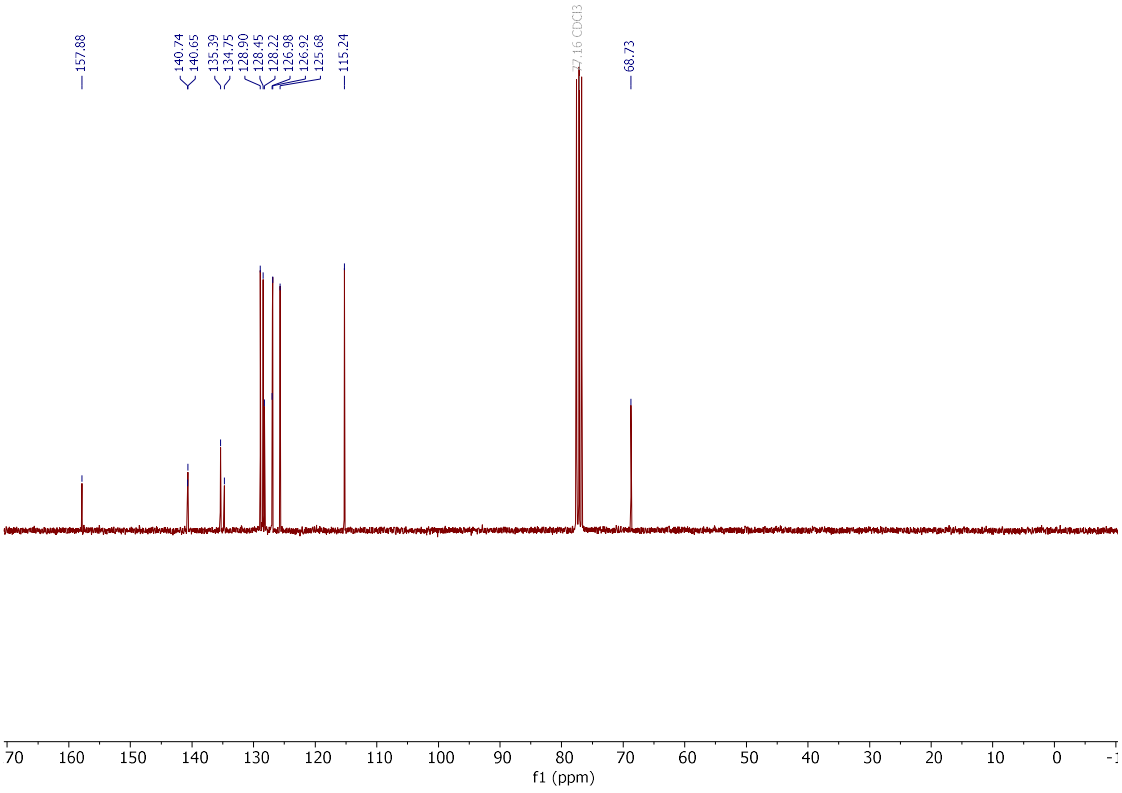

1,2-Bis{[4-(*tert*-butyl)phenoxy]methyl}benzene (**469q**)

^{1}H NMR (300 MHz, $CDCl_3$)

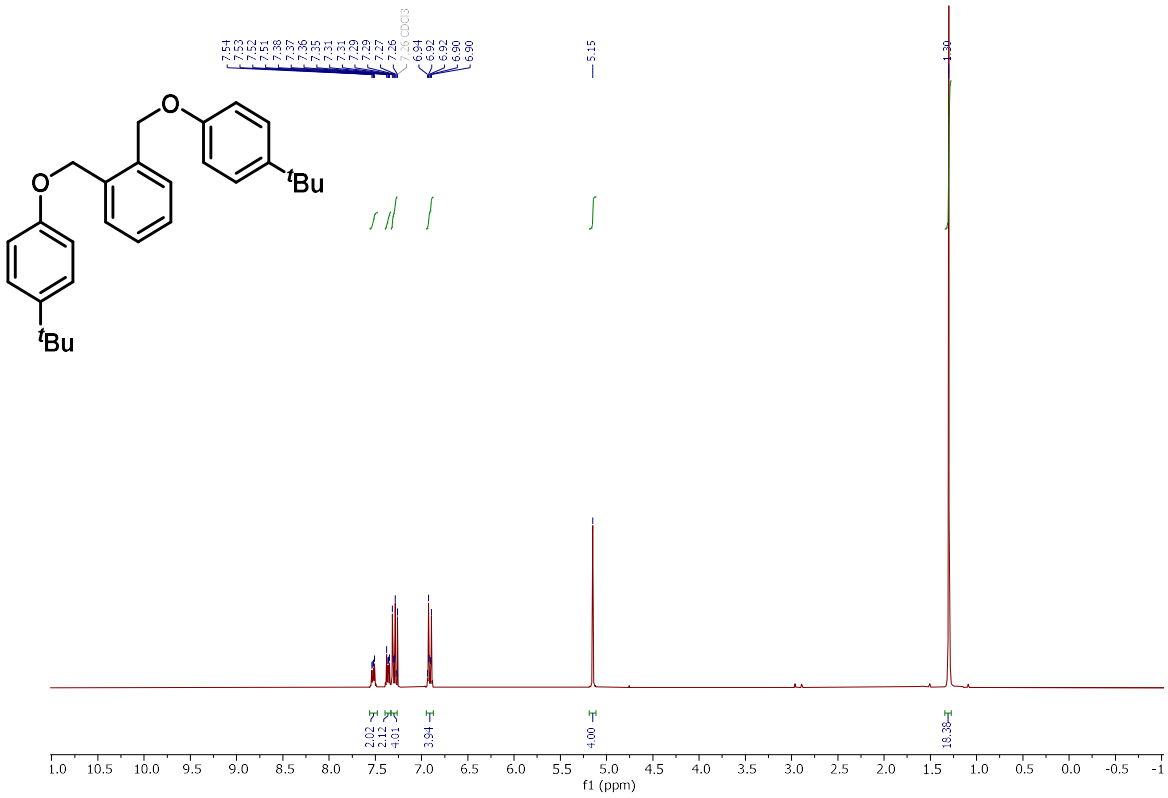

^{13}C{H} NMR (75 MHz, $CDCl_3$)

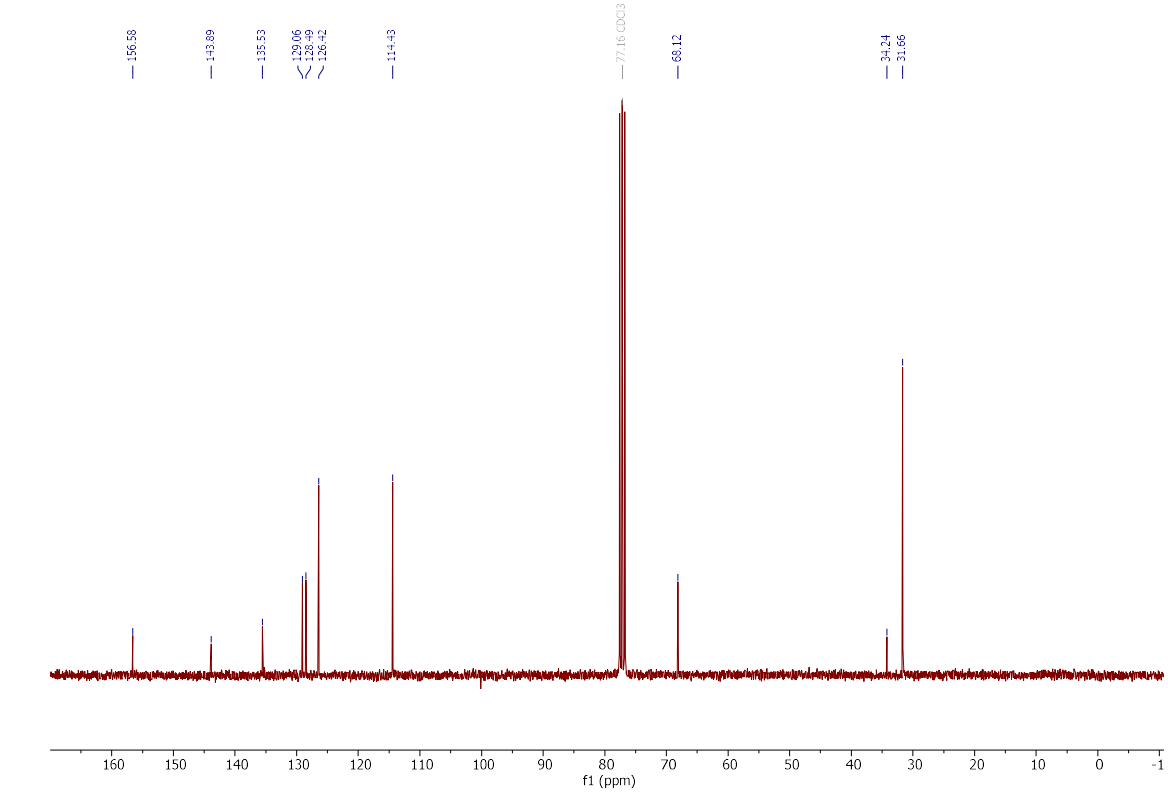

1,4-Bis{[4-(*tert*-butyl)phenoxy]methyl}naphthalene (**469s**)

^{1}H NMR (300 MHz, $CDCl_3$)

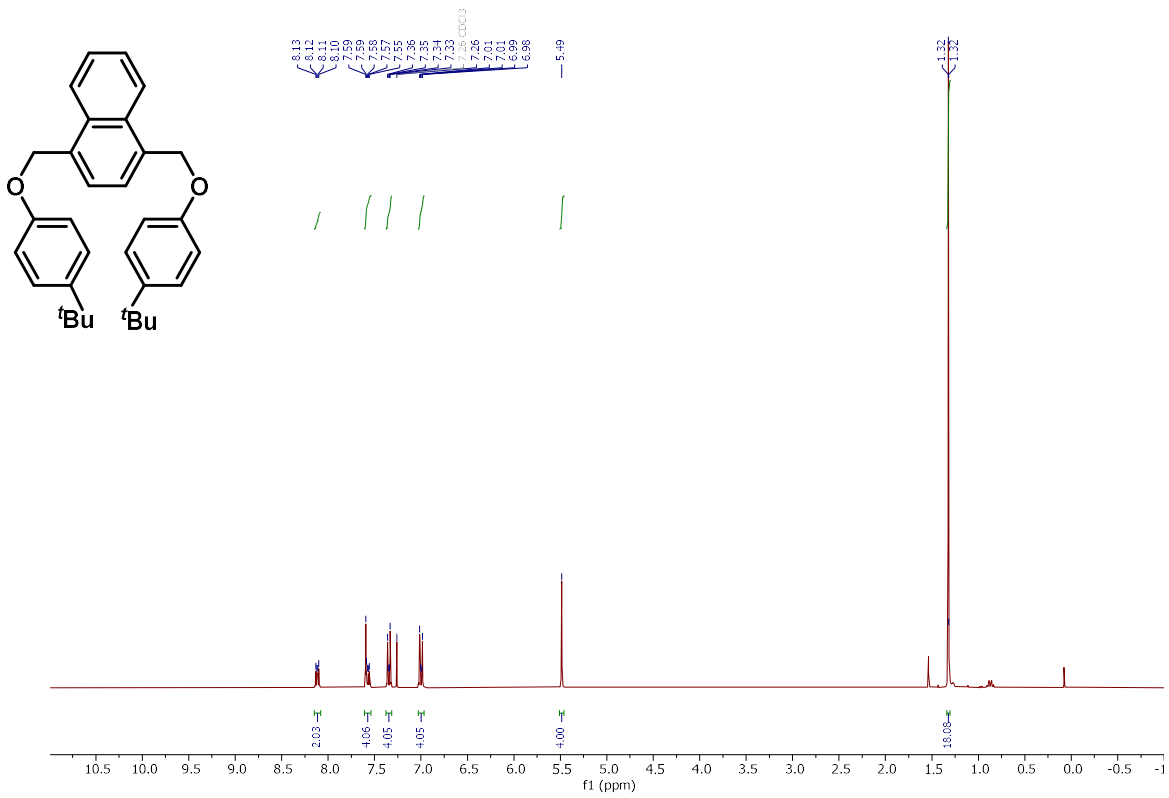

^{13}C{H} NMR (75 MHz, $CDCl_3$)

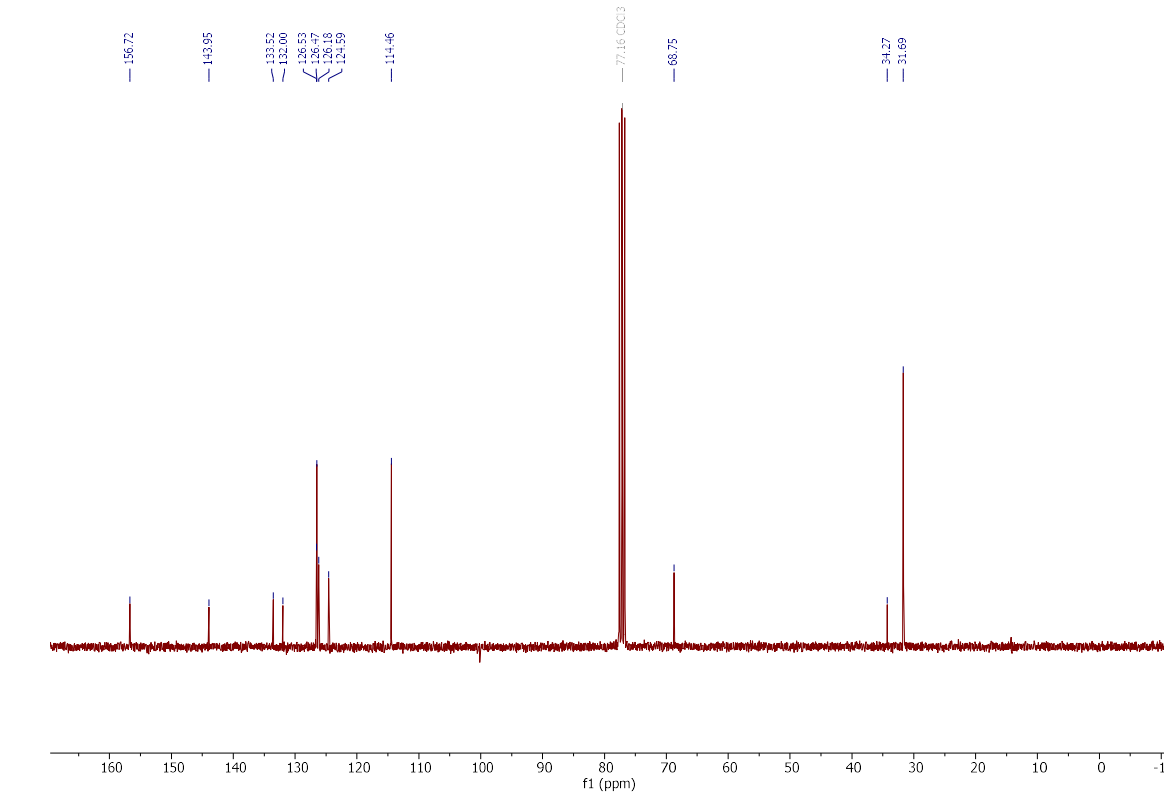

2,2'-Bis{[4-(*tert*-butyl)phenoxy]methyl}-1,1'-biphenyl (**469t**)

^{1}H NMR (300 MHz, $CDCl_3$)

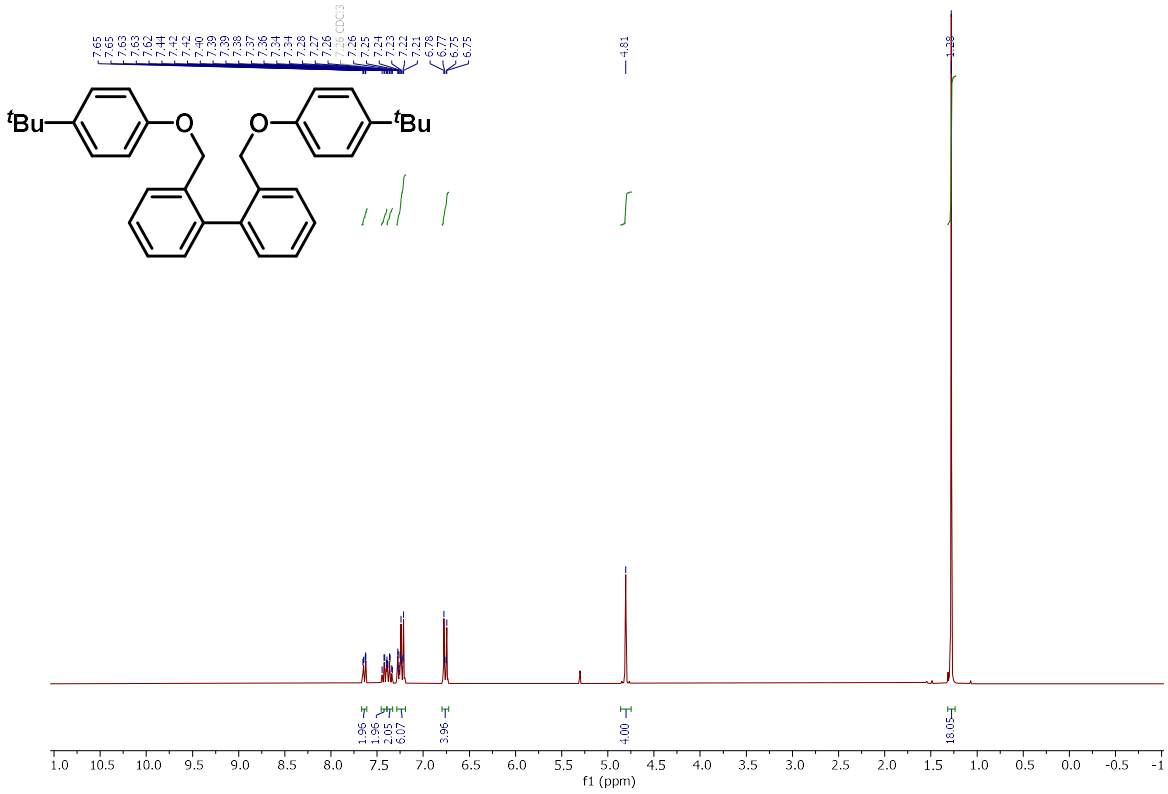

^{13}C{H} NMR (75 MHz, $CDCl_3$)

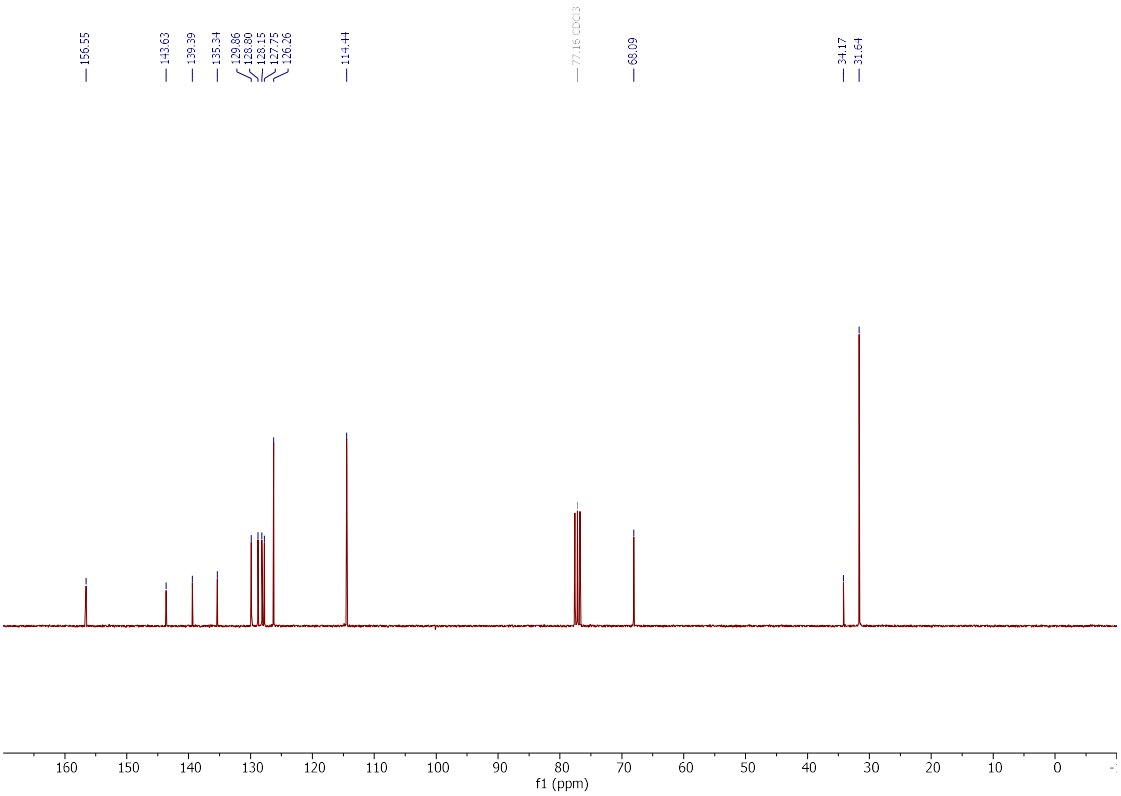

1,2-Bis{4-[(*p*-tolyloxy)methyl]phenyl}ethane (**469u**)

^{1}H NMR (300 MHz, $CDCl_3$)

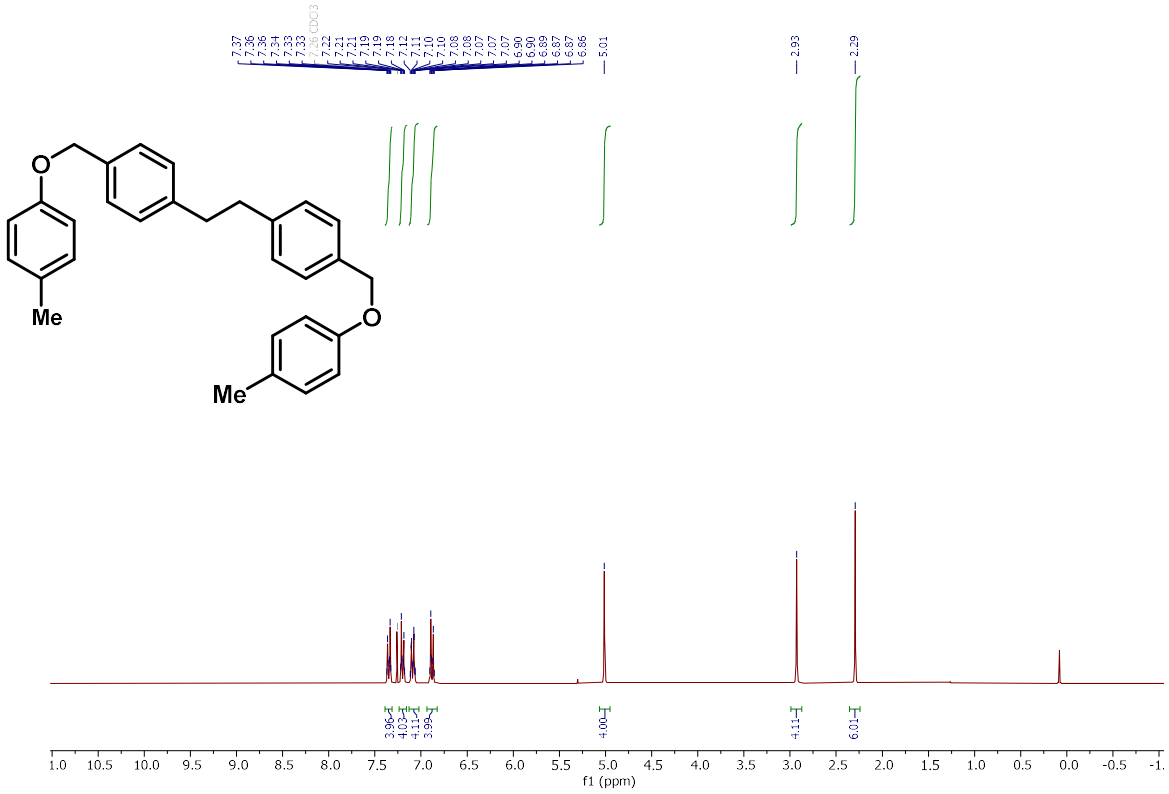

^{13}C{H} NMR (75 MHz, $CDCl_3$)

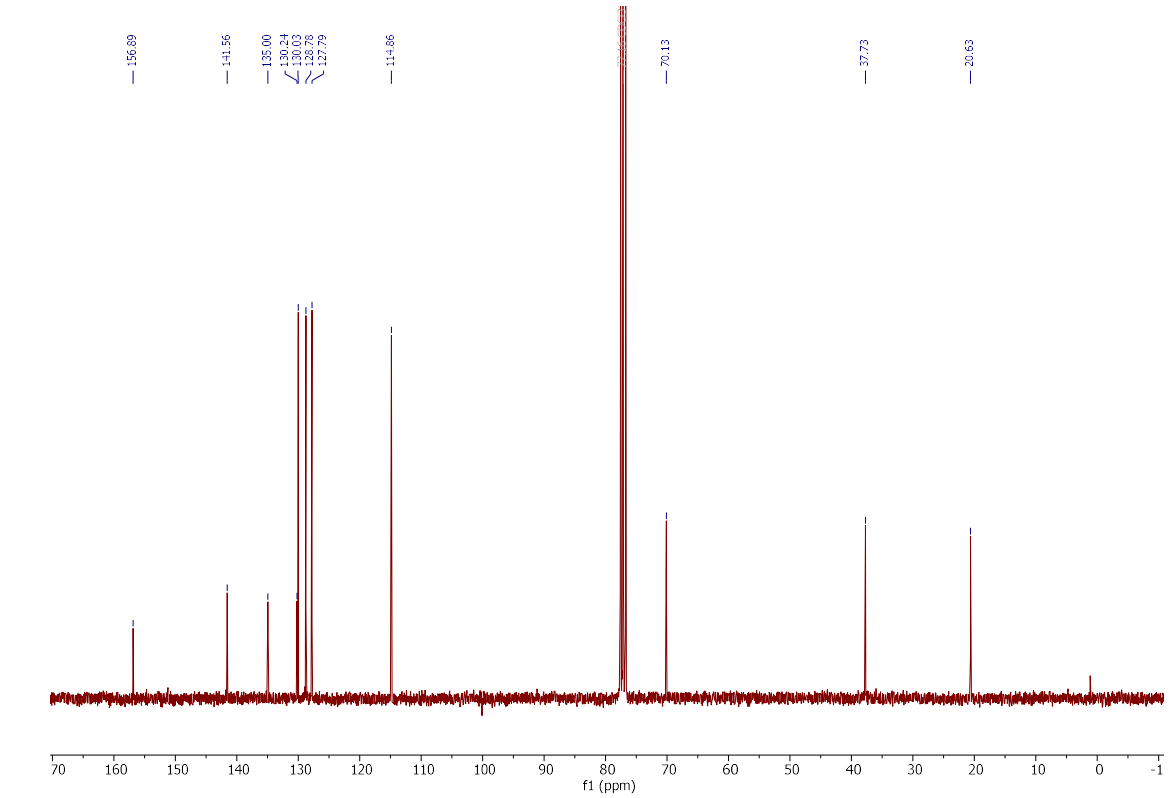

Dibenzothiophenium trifluoromethanesulfonates:

5-{5-Methyl-2-[(4-methylbenzyl)oxy]phenyl}-5*H*-dibenzo[*b*,*d*]thiophen-5-ium Trifluoromethanesulfonate (**470a**)

^{1}H NMR (400 MHz, $CDCl_3$)

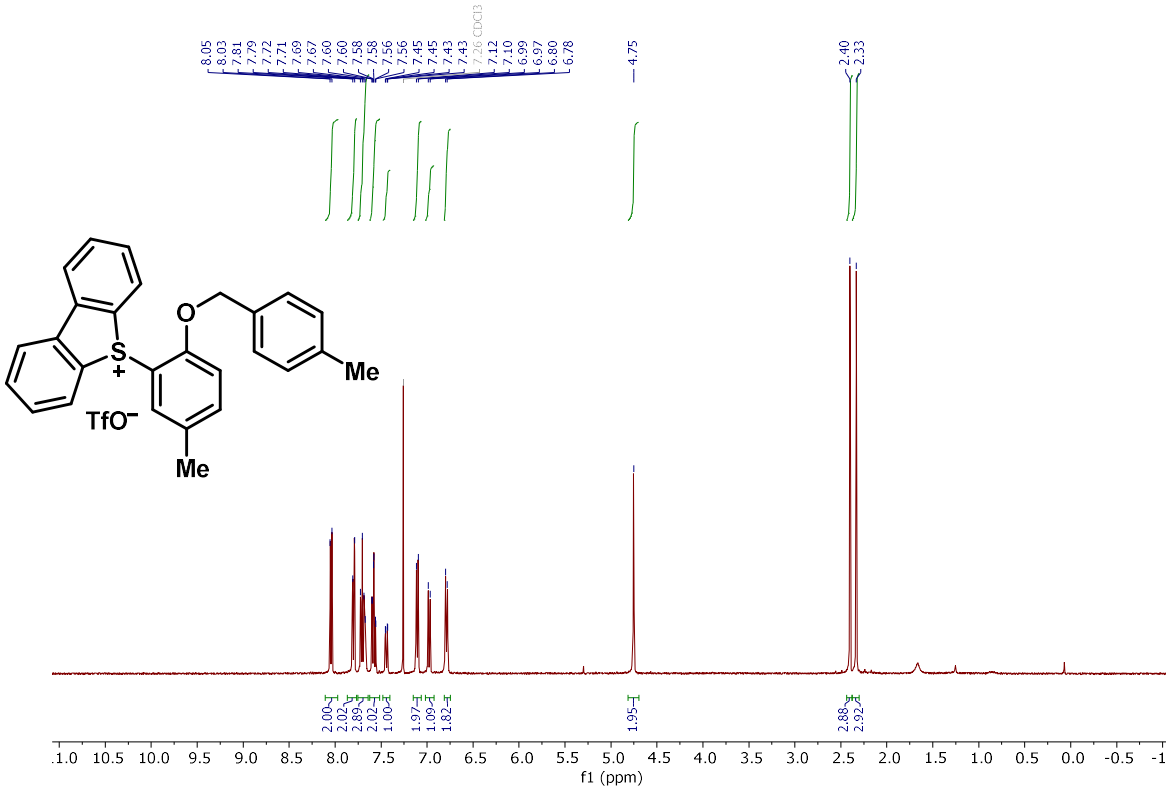

^{13}C{H} NMR (101 MHz, $CDCl_3$)

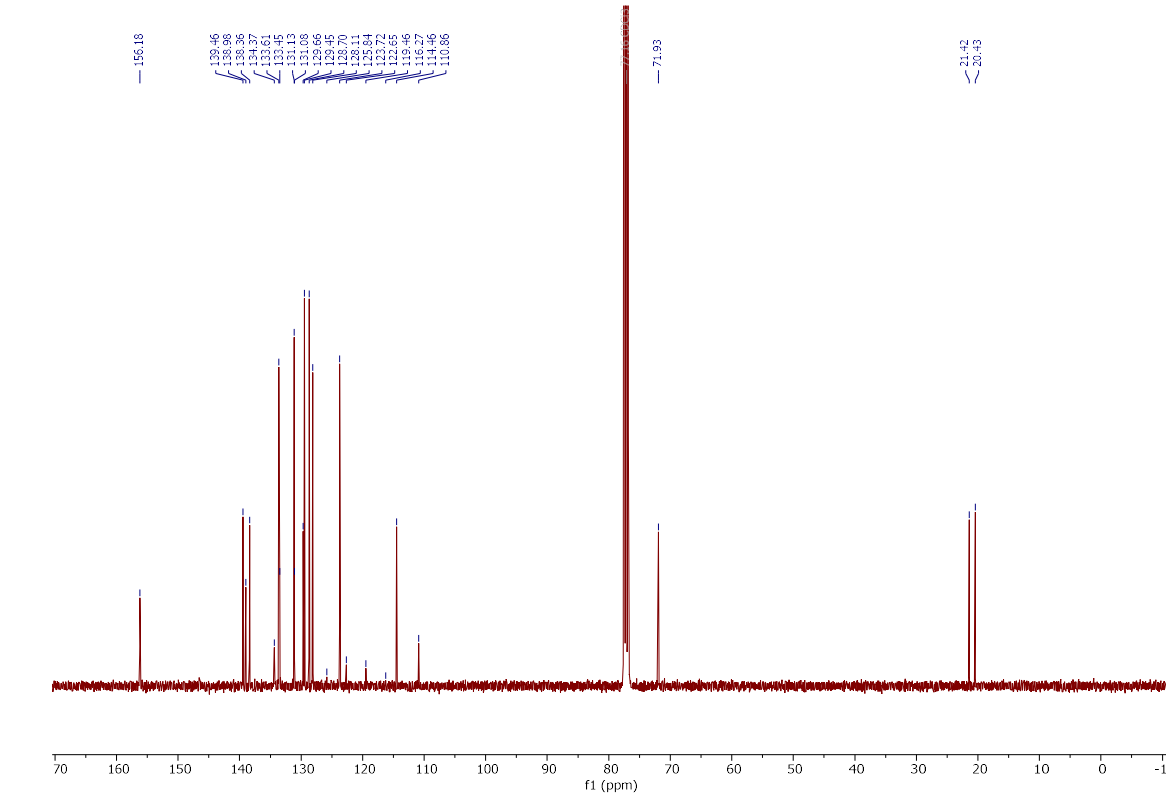

^{19}F NMR (376 MHz, $CDCl_3$)

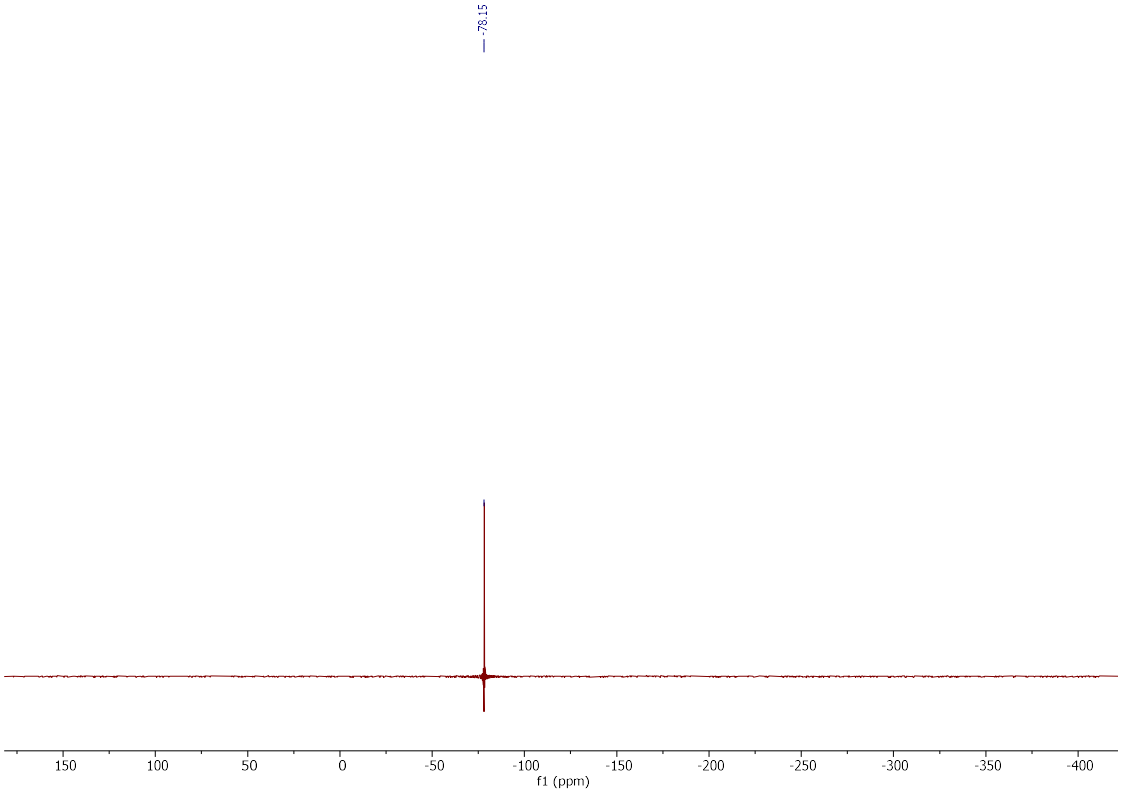

5-[5-(*tert*-Butyl)-2-{[4-(*tert*-butyl)benzyl]oxy}phenyl]-5*H*-dibenzo[*b,*d]thiophen-5-ium Trifluoromethane-sulfonate (**470b**)

^{1}H NMR (400 MHz, $CDCl_3$)

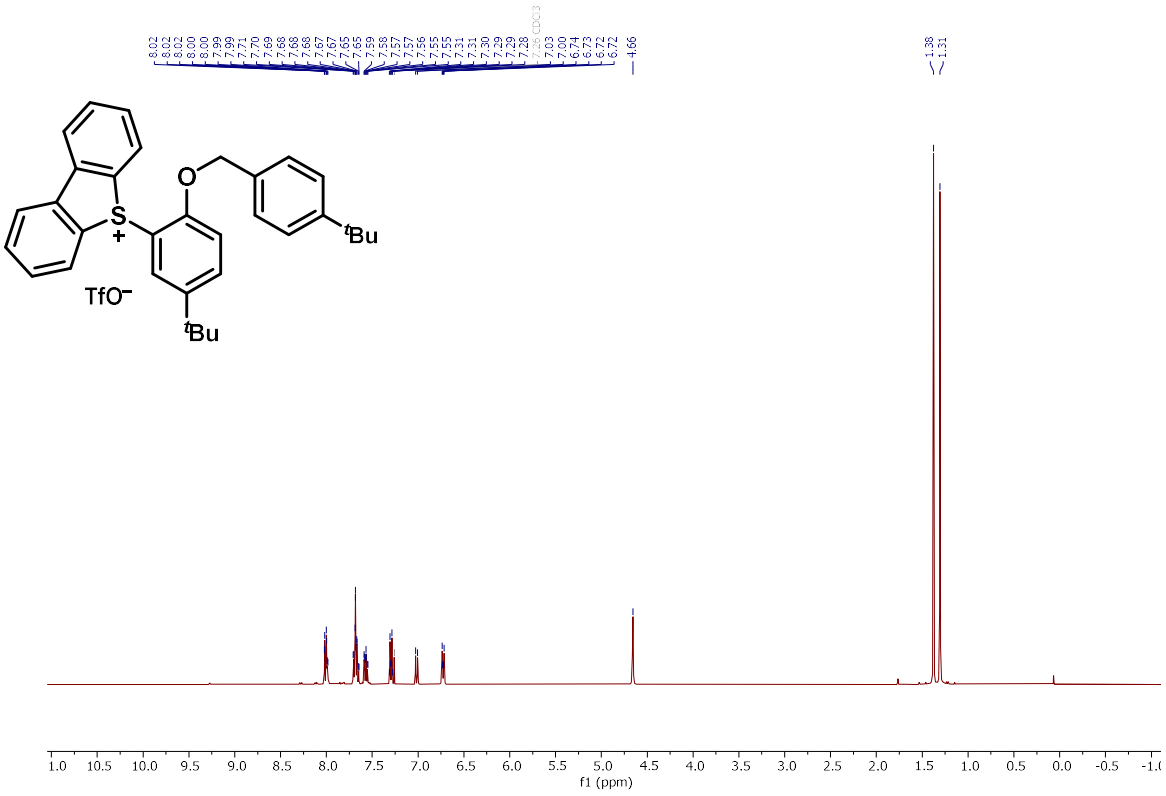

^{13}C{H} NMR (101 MHz, $CDCl_3$)

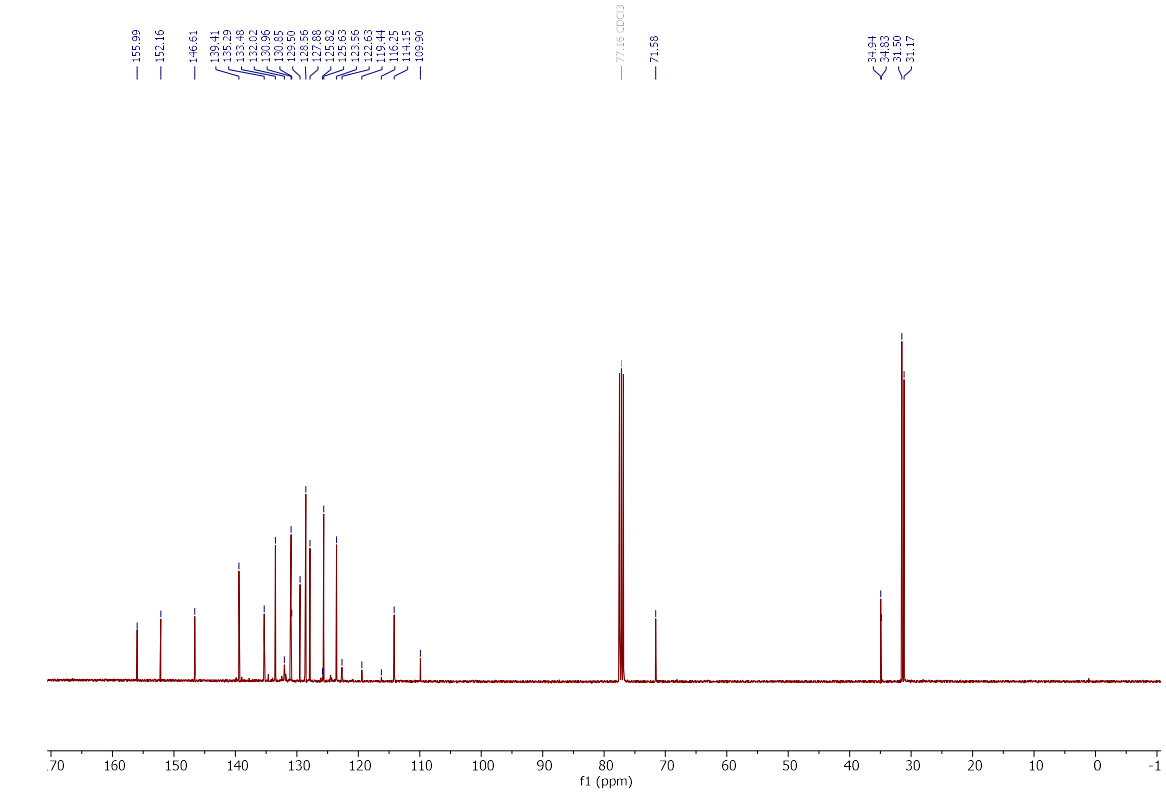

^{19}F NMR (282 MHz, CD_3CN)

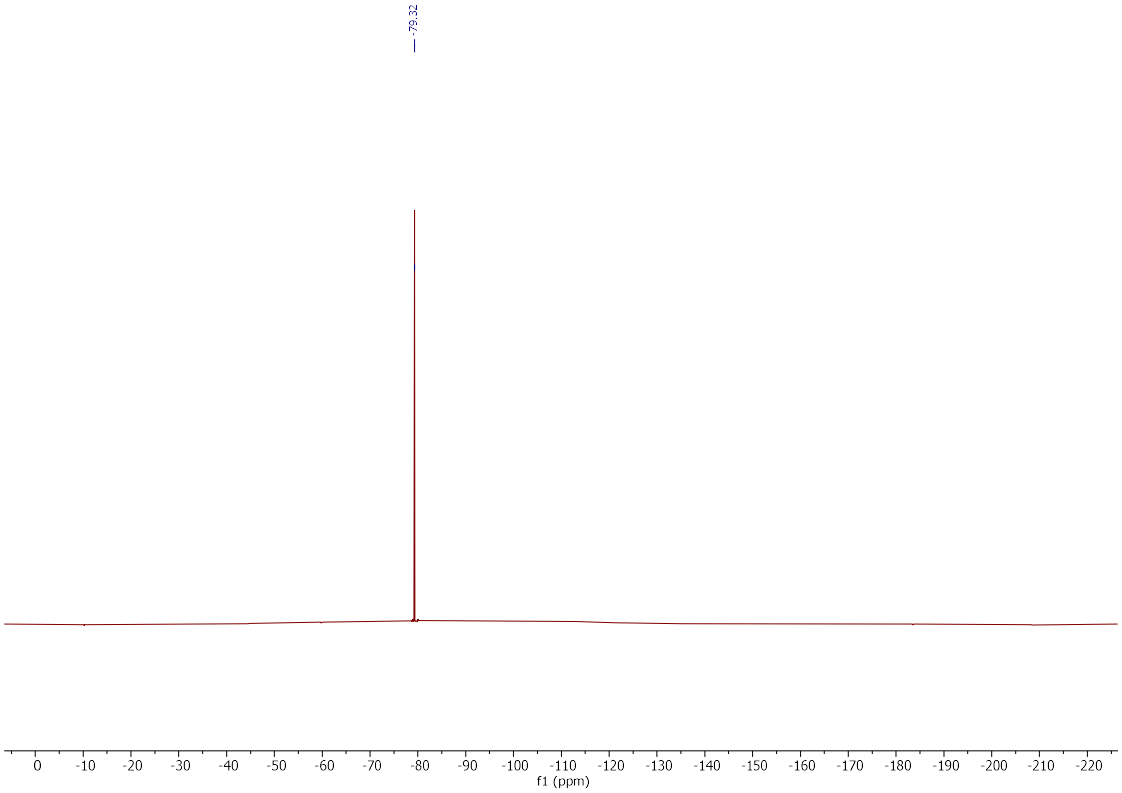

5-[2-(Benzyloxy)-5-methylphenyl]-5*H*-dibenzo[*b*,*d*]thiophen-5-ium Trifluoromethanesulfonate (**470c**)

^{1}H NMR (300 MHz, CD_3CN)

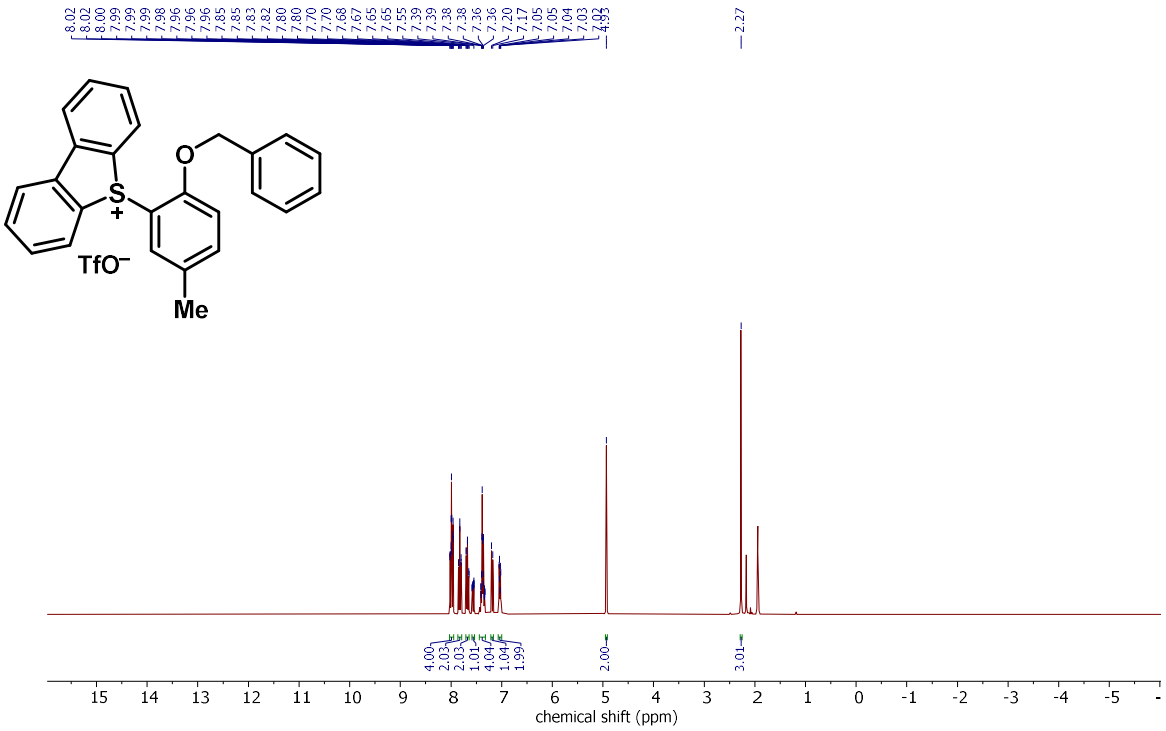

^{13}C{H} NMR (75 MHz, CD_3CN)

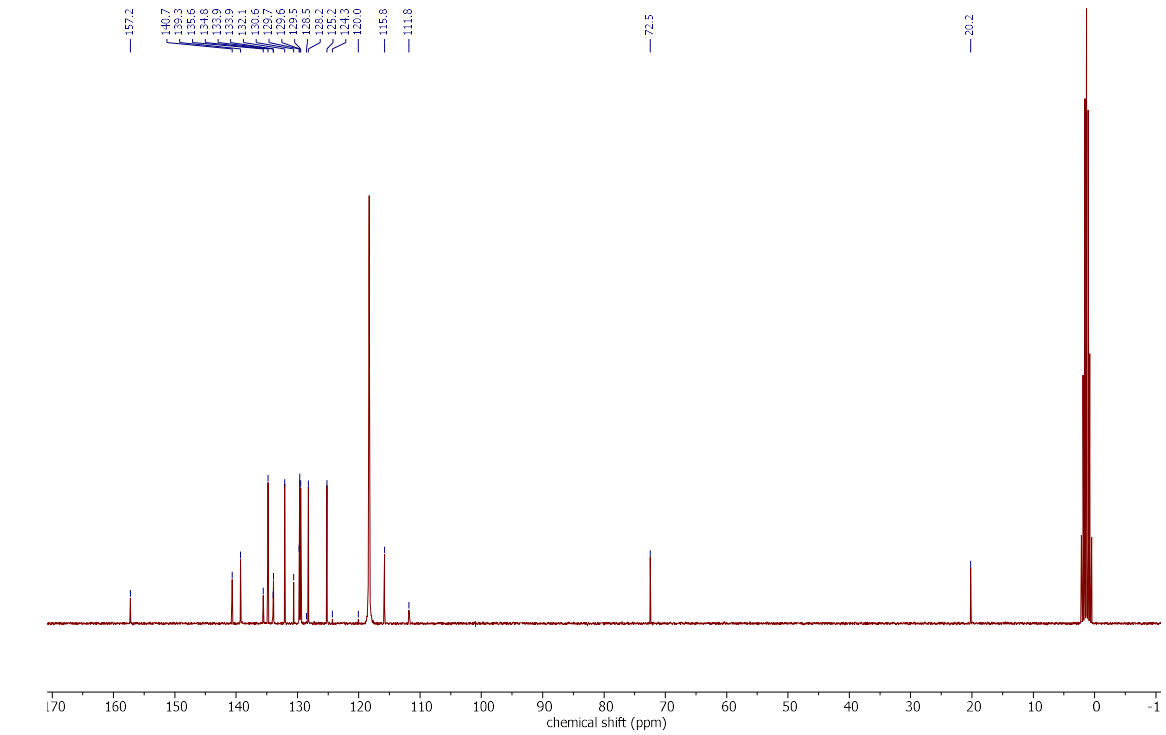

^{19}F NMR (282 MHz, CD_3CN)

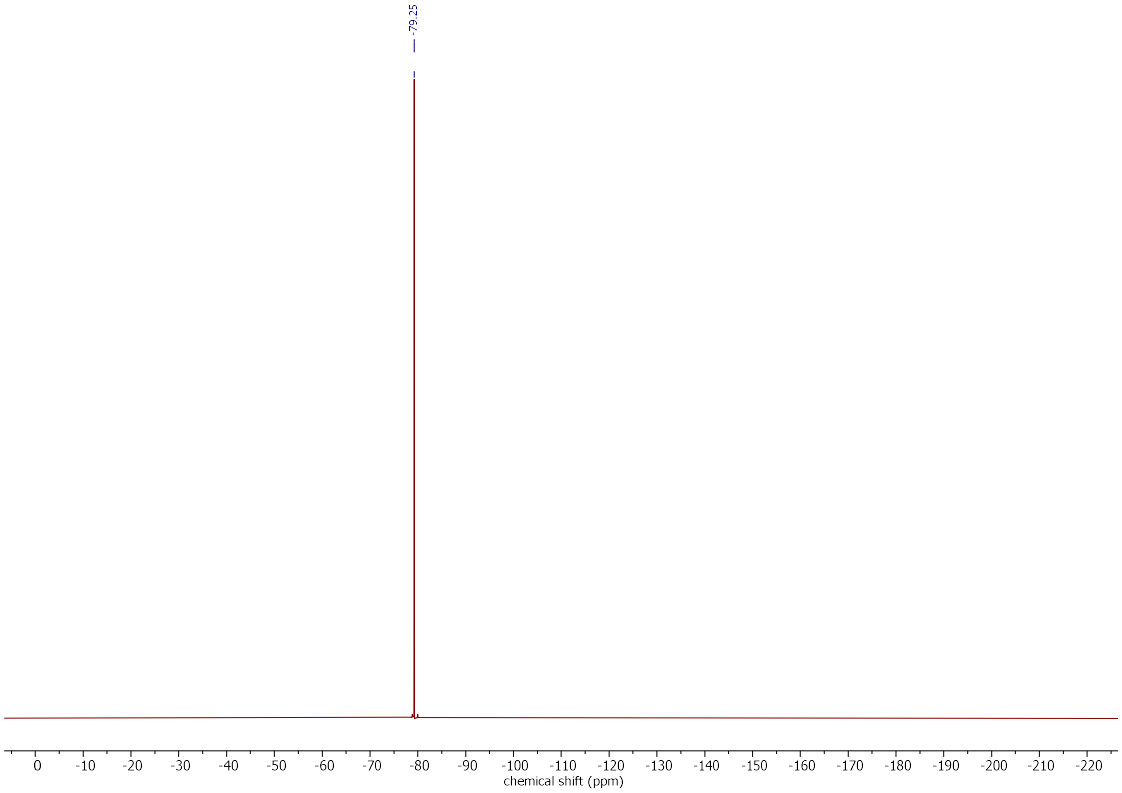

5-{2-[(4-Fluorobenzyl)oxy]-5-methylphenyl}-5H-dibenzo[b,d]thiophen-5-ium Trifluoromethanesulfonate (**470d**)

^{1}H NMR (300 MHz, CD_3CN)

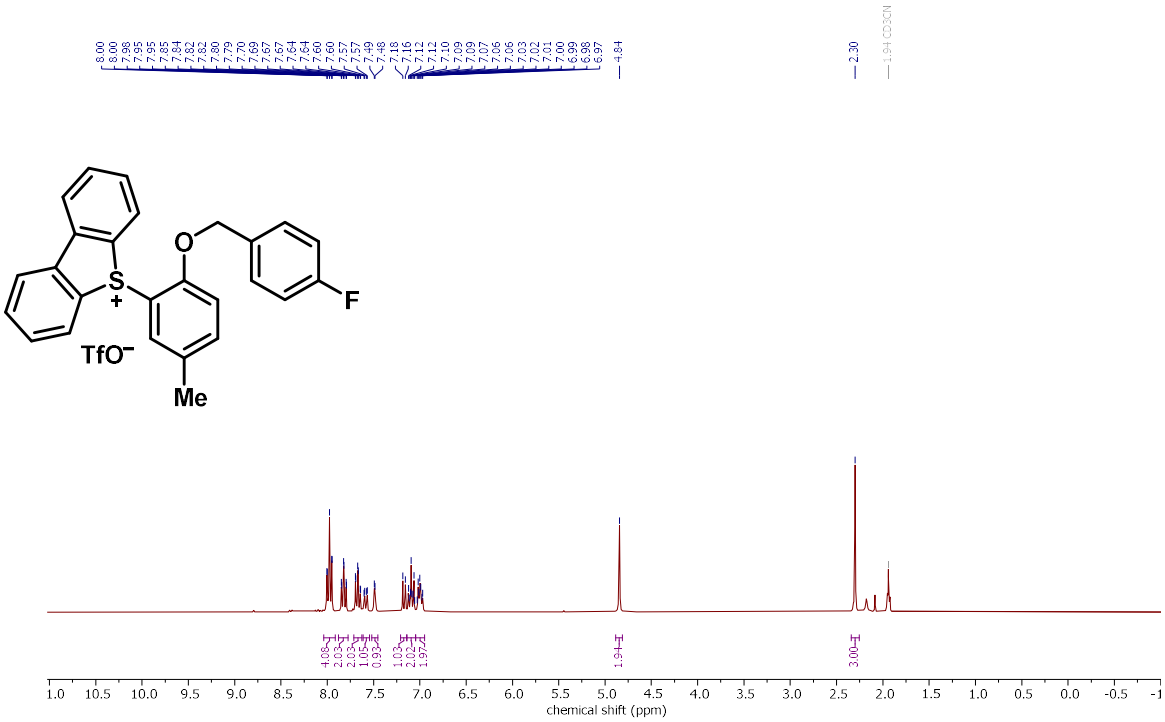

^{13}C{H} NMR (75 MHz, CD_3CN)

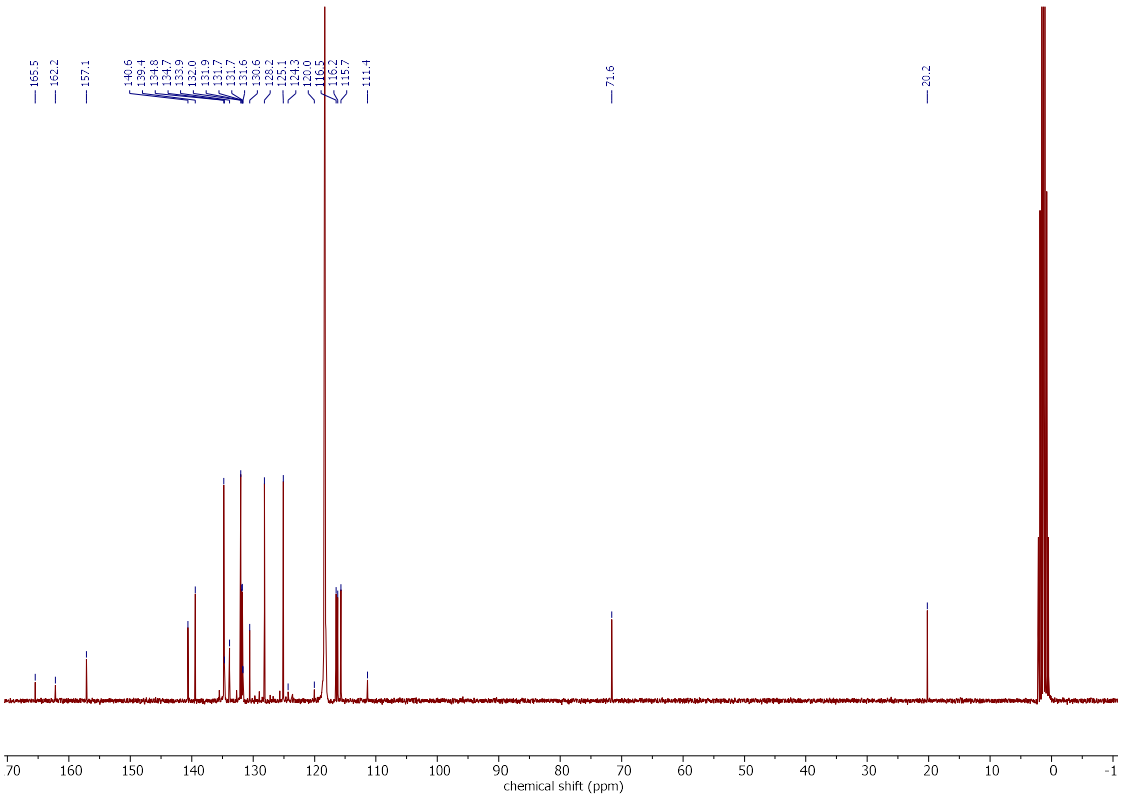

^{19}F NMR (282 MHz, CD_3CN)

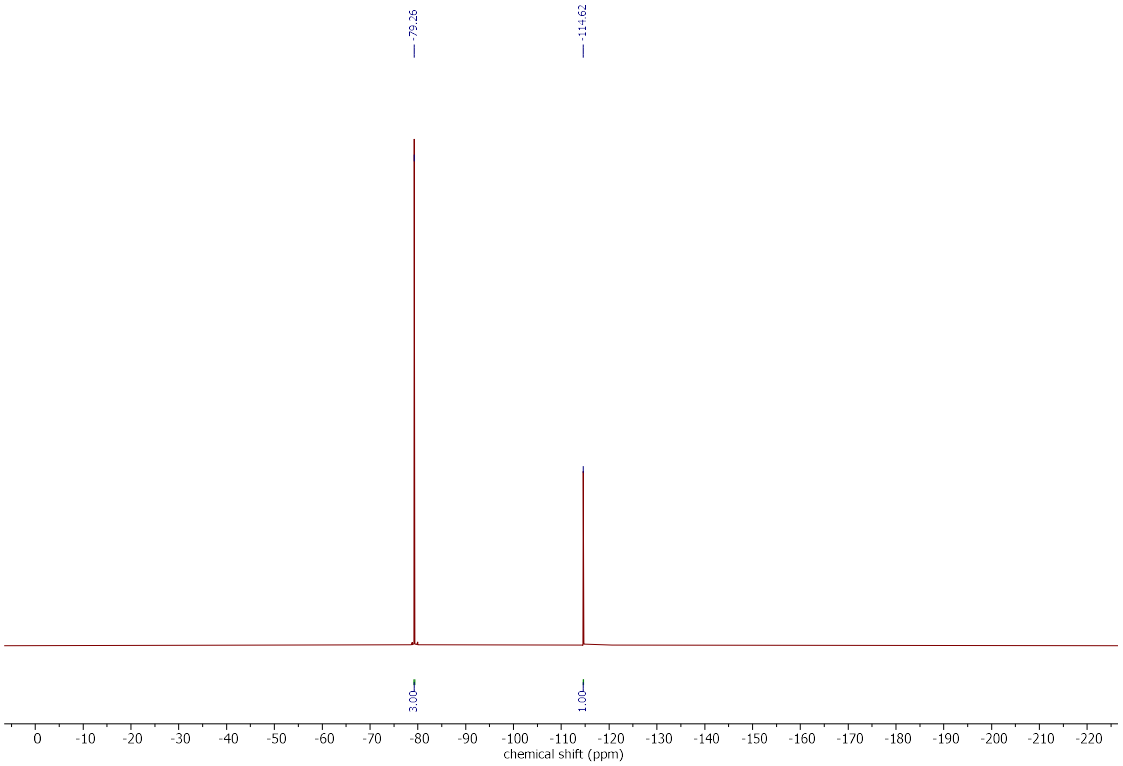

5-{5-(*tert*-Butyl)-2-[(3,5-dichlorobenzyl)oxy]phenyl}-5*H*-dibenzo[*b*,*d*]thiophen-5-ium Trifluoromethane-sulfonate (**470e**)

^{1}H NMR (400 MHz, CD_3CN)

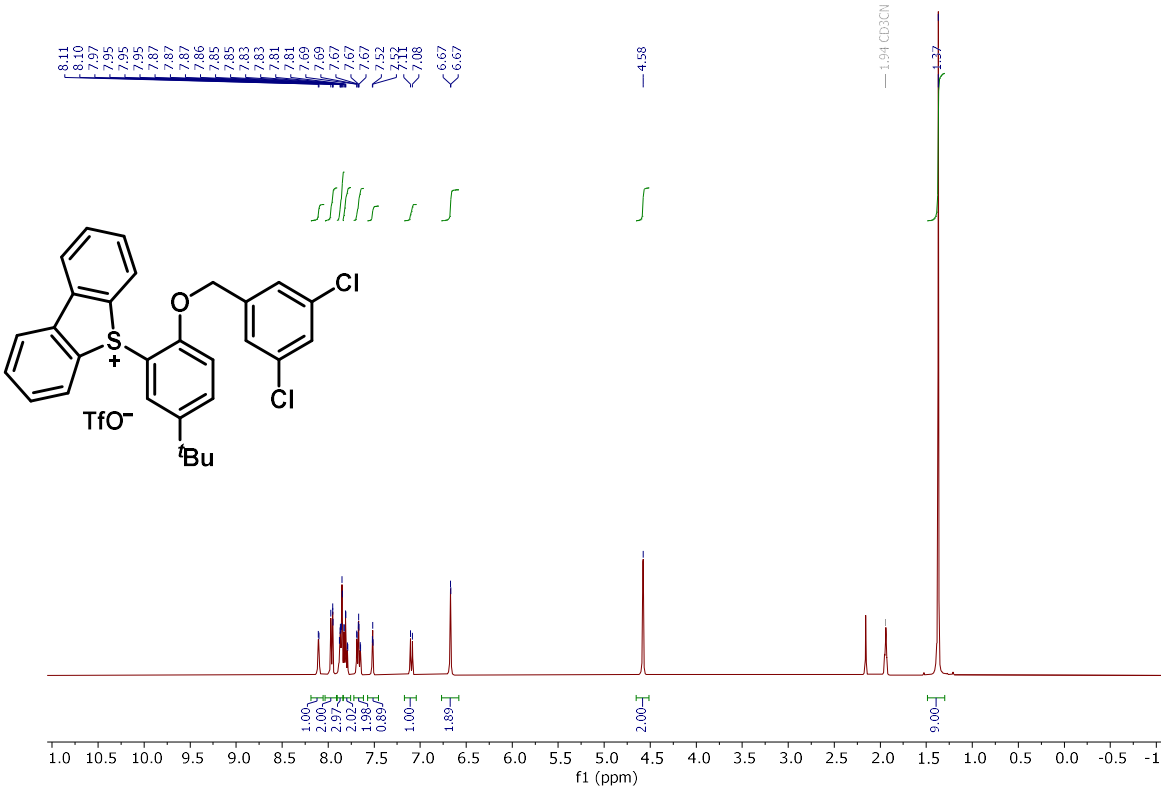

^{13}C{H} NMR (101 MHz, CD_3CN)

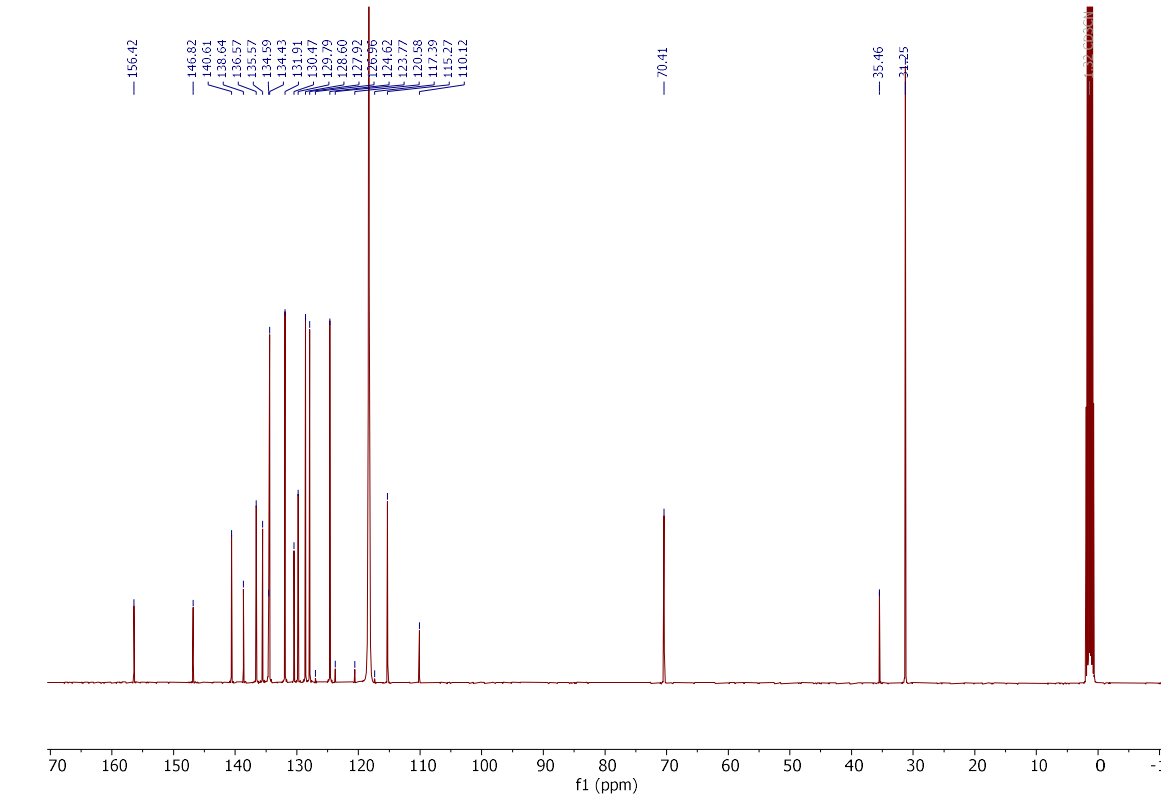

^{19}F NMR (376 MHz, CD_3CN)

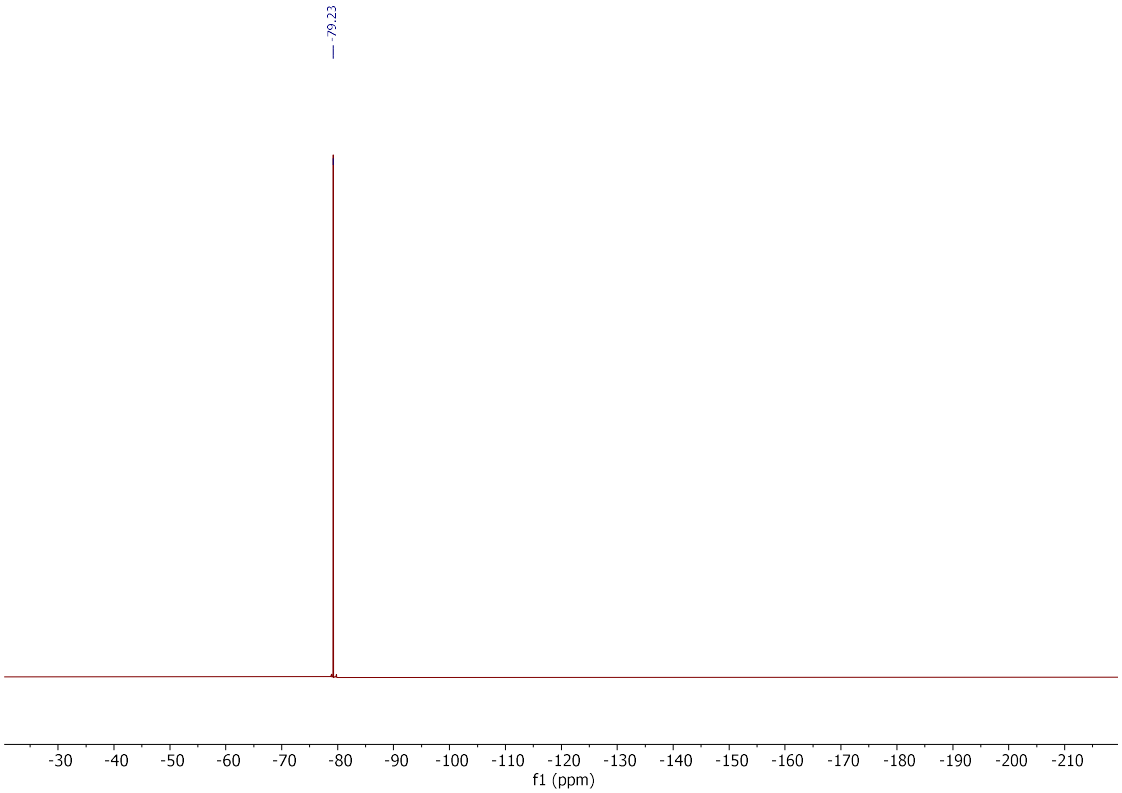

5-[5-(*tert*-Butyl)-2-{[4-(methylsulfonyl)benzyl]oxy}phenyl]-5*H*-dibenzo[*b*,*d*]thiophen-5-ium Trifluoromethanesulfonate (**470f**)

^{1}H NMR (300 MHz, CD_3CN)

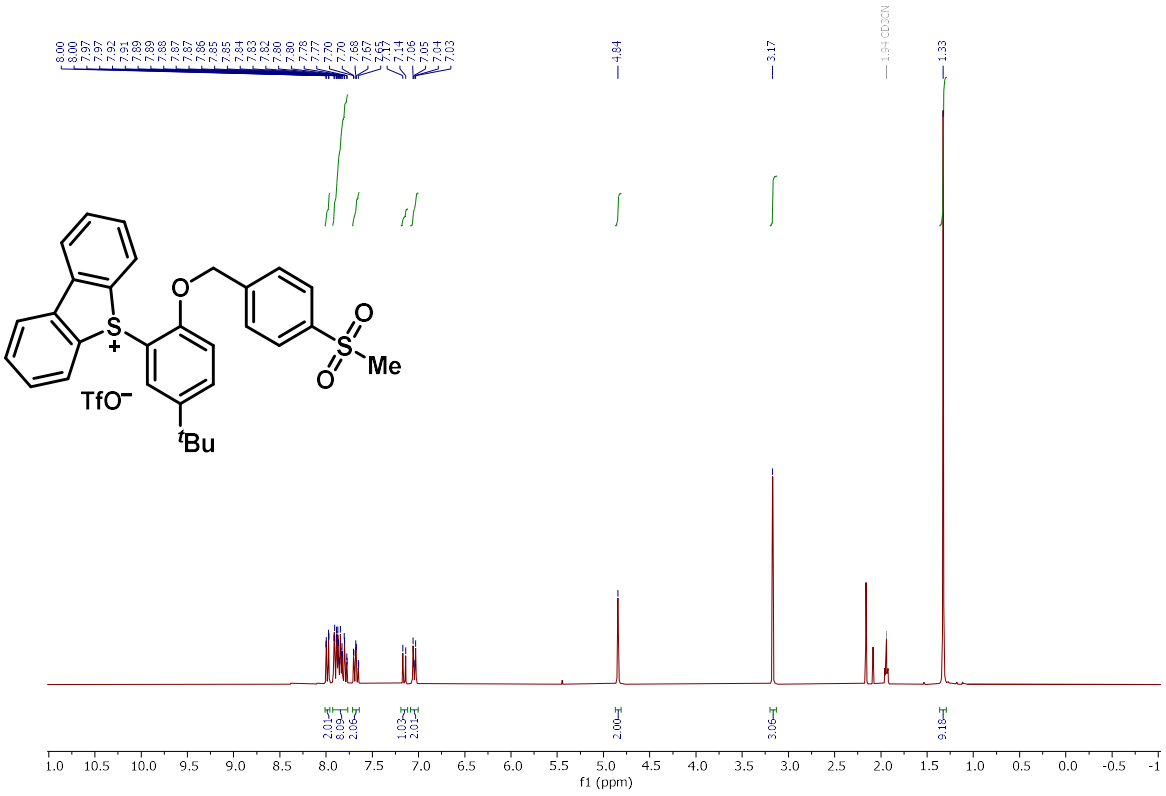

^{13}C{H} NMR (75 MHz, CD_3CN)

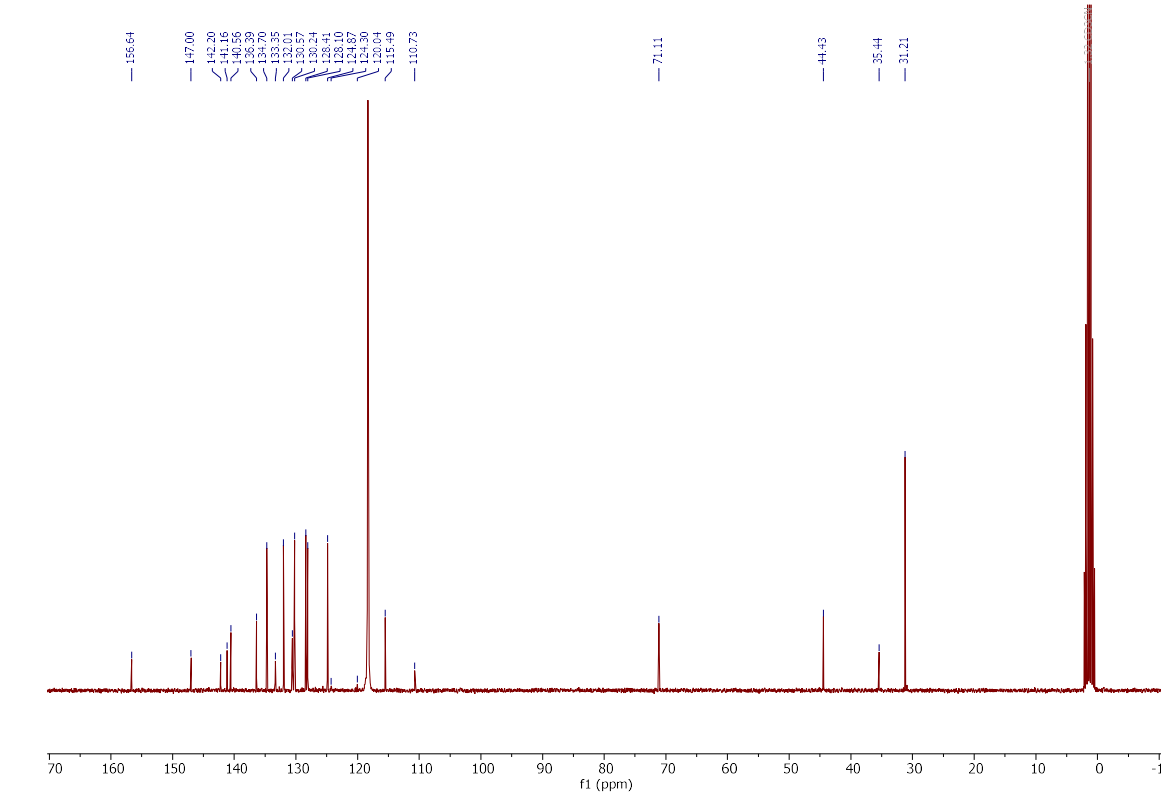

^{19}F NMR (282 MHz, CD_3CN)

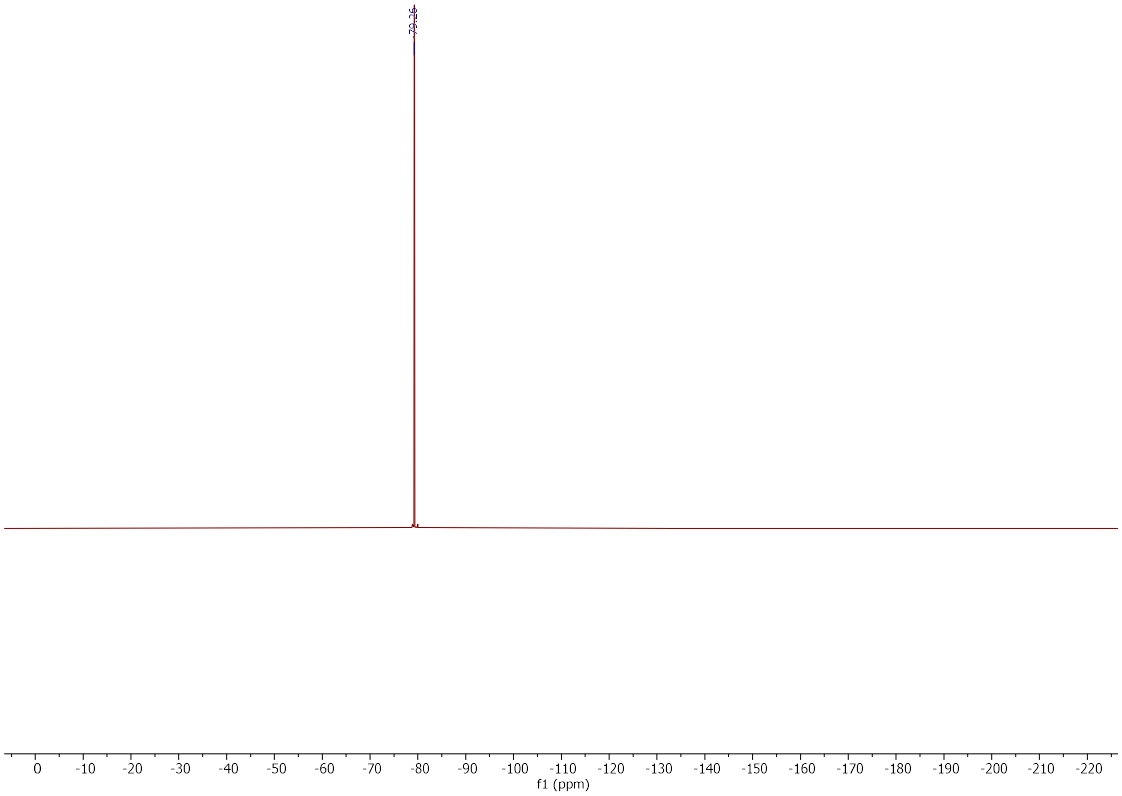

5-[2,3,4-Trimethyl-6-(naphthalen-1-ylmethoxy)phenyl]-5*H*-dibenzo[*b*,*d*]thiophen-5-ium Trifluorometha-nesulfonate (**470g**)

^{1}H NMR (500 MHz, CD_3CN)

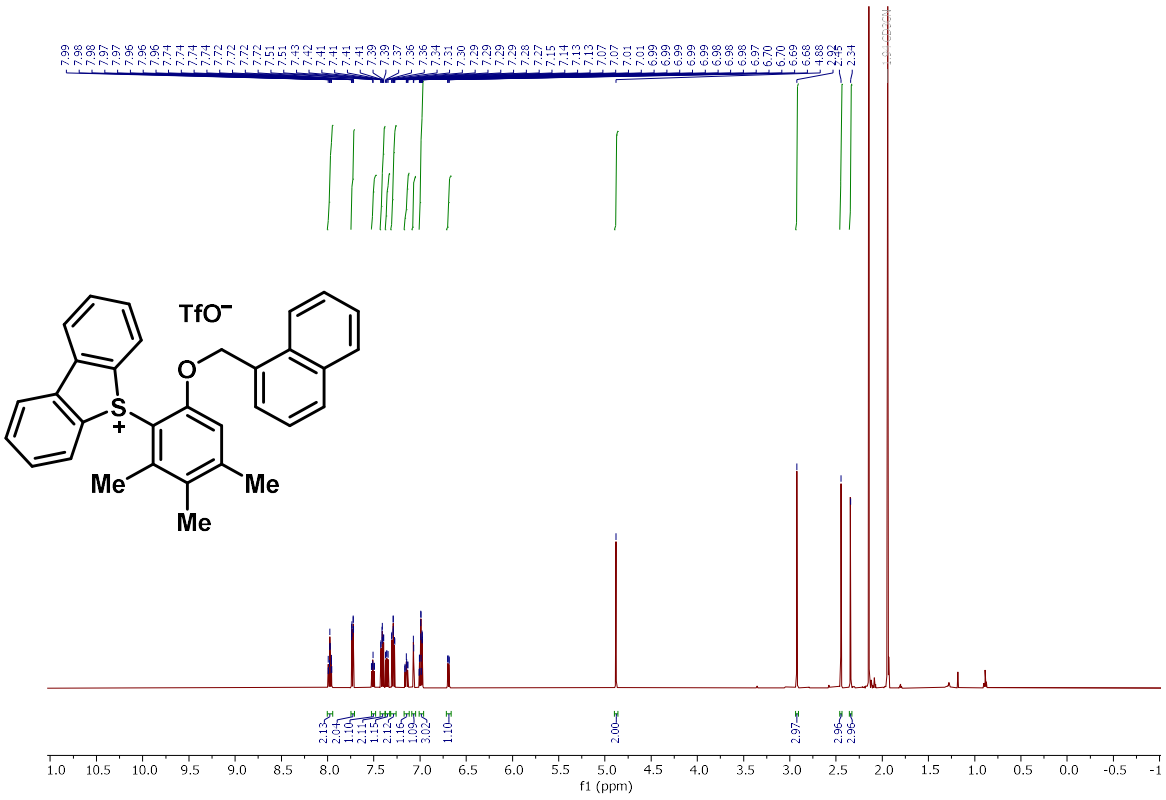

^{13}C{H} NMR (126 MHz, CD_3CN)

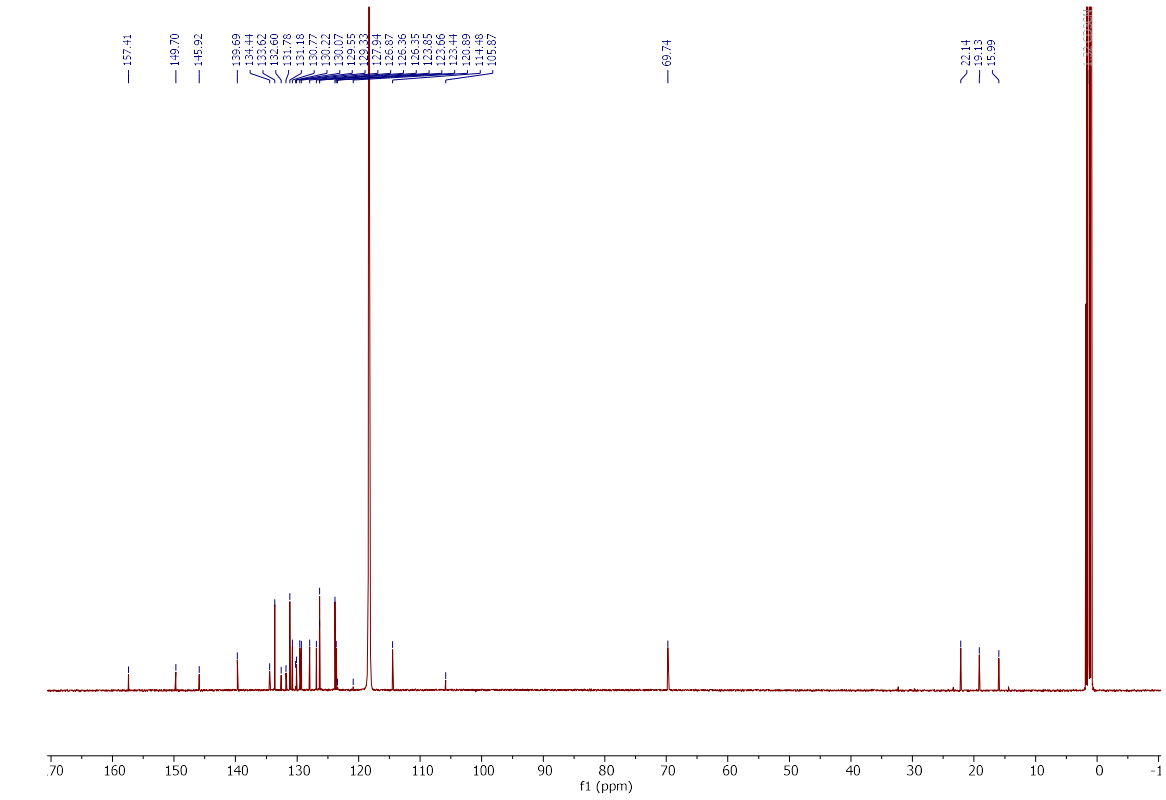

^{19}F NMR (471 MHz, CD_3CN)

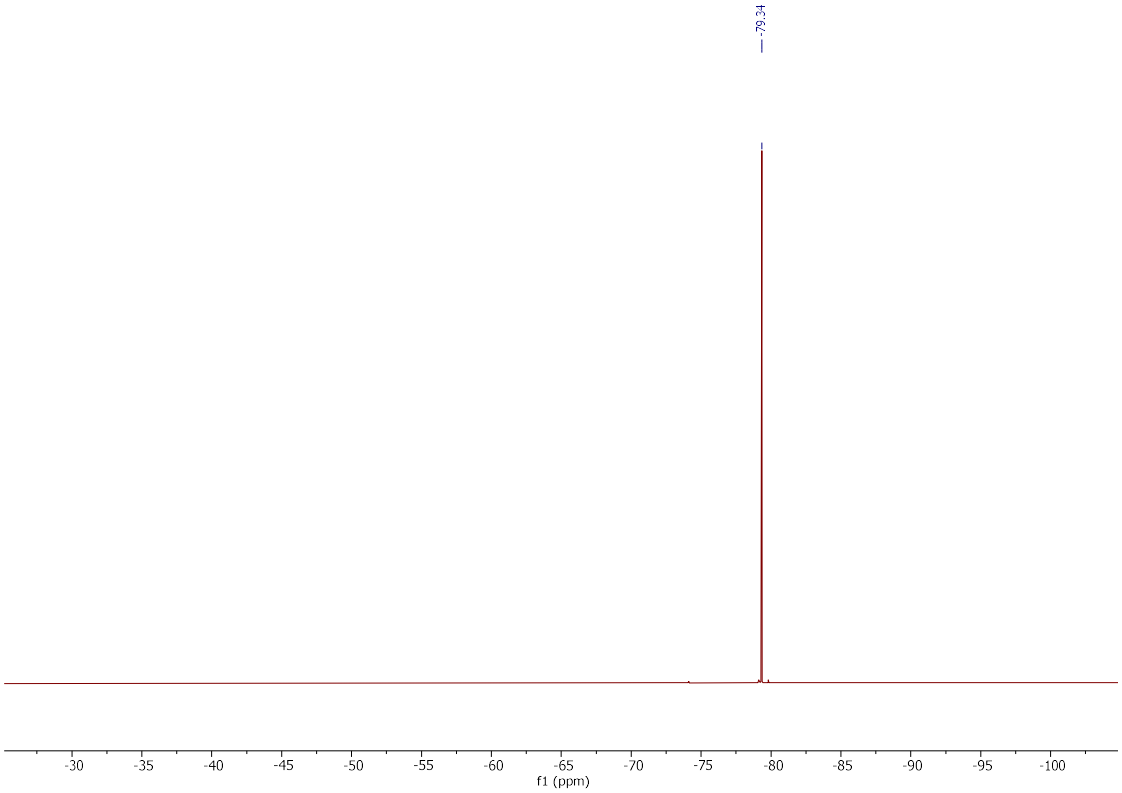

5-[5-(*tert*-Butyl)-2-{[4-(trifluoromethyl)benzyl]oxy}phenyl]-5*H*-dibenzo[*b*,*d*]thiophen-5-ium Trifluoromethanesulfonate (**470h**)

^{1}H NMR (400 MHz, CD_3CN)

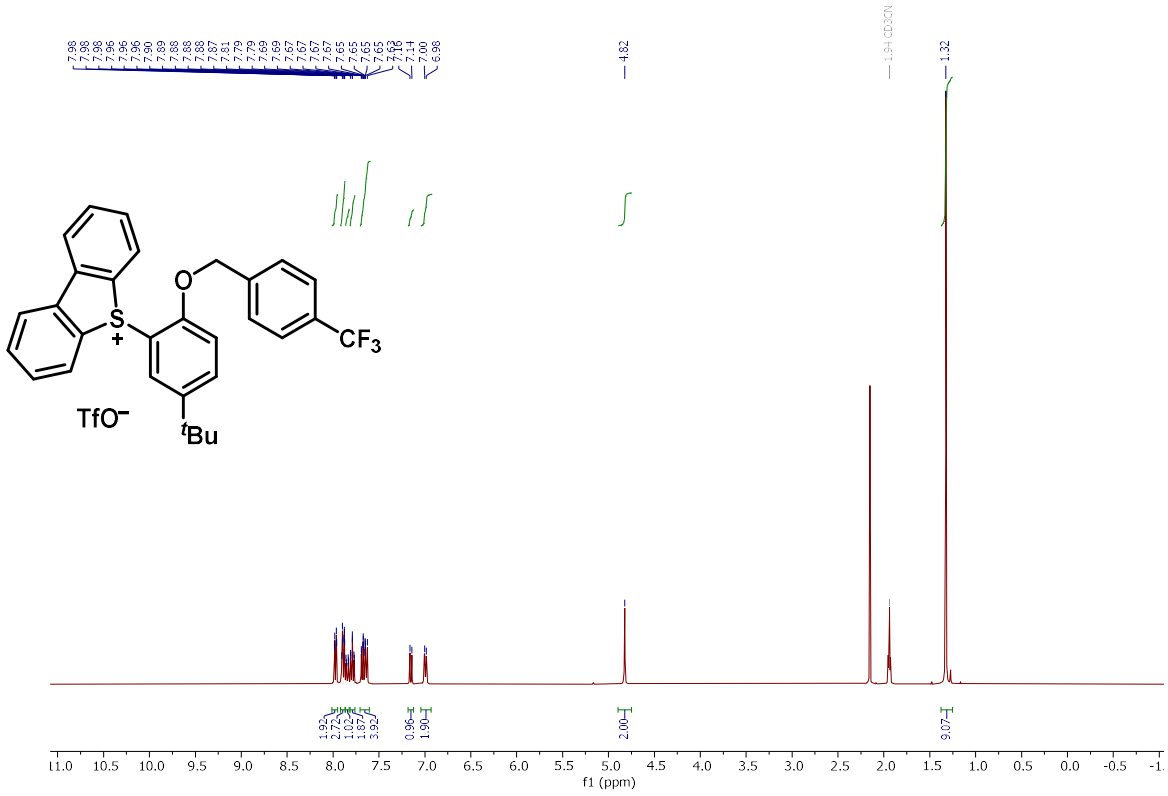

^{13}C{H} NMR (101 MHz, CD_3CN)

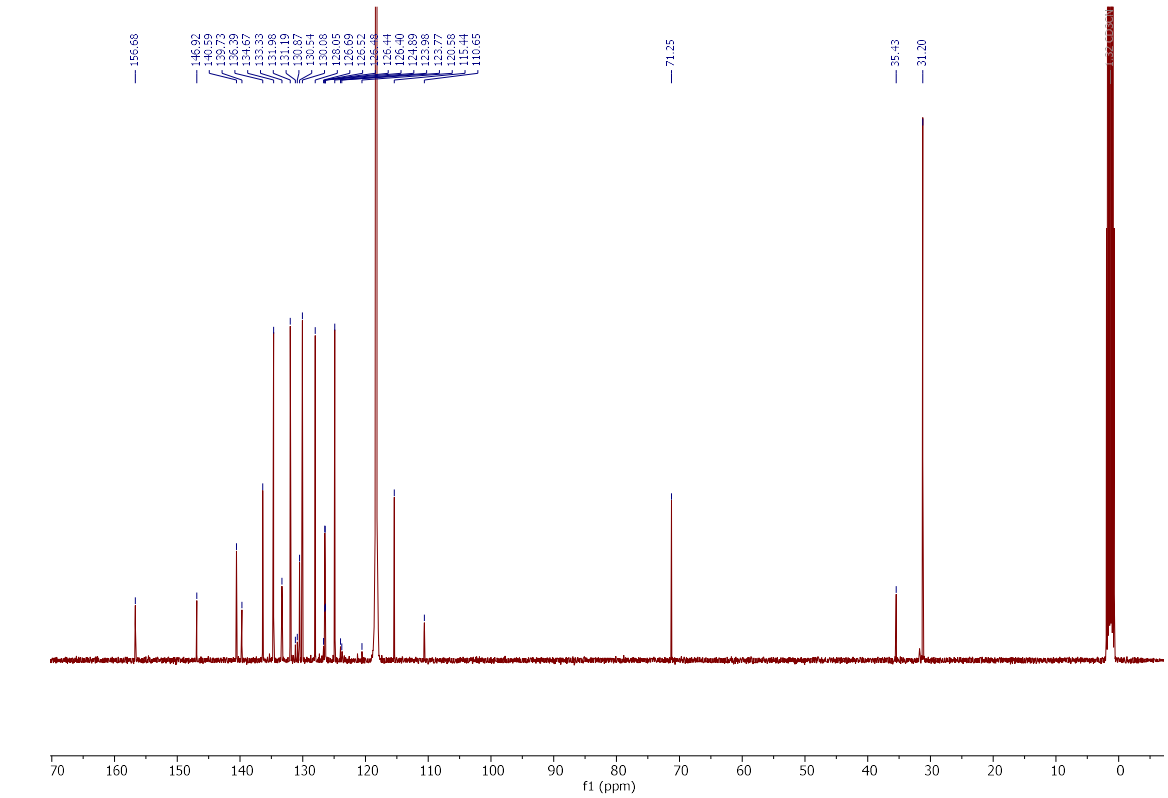

^{19}F NMR (282 MHz, CD_3CN)

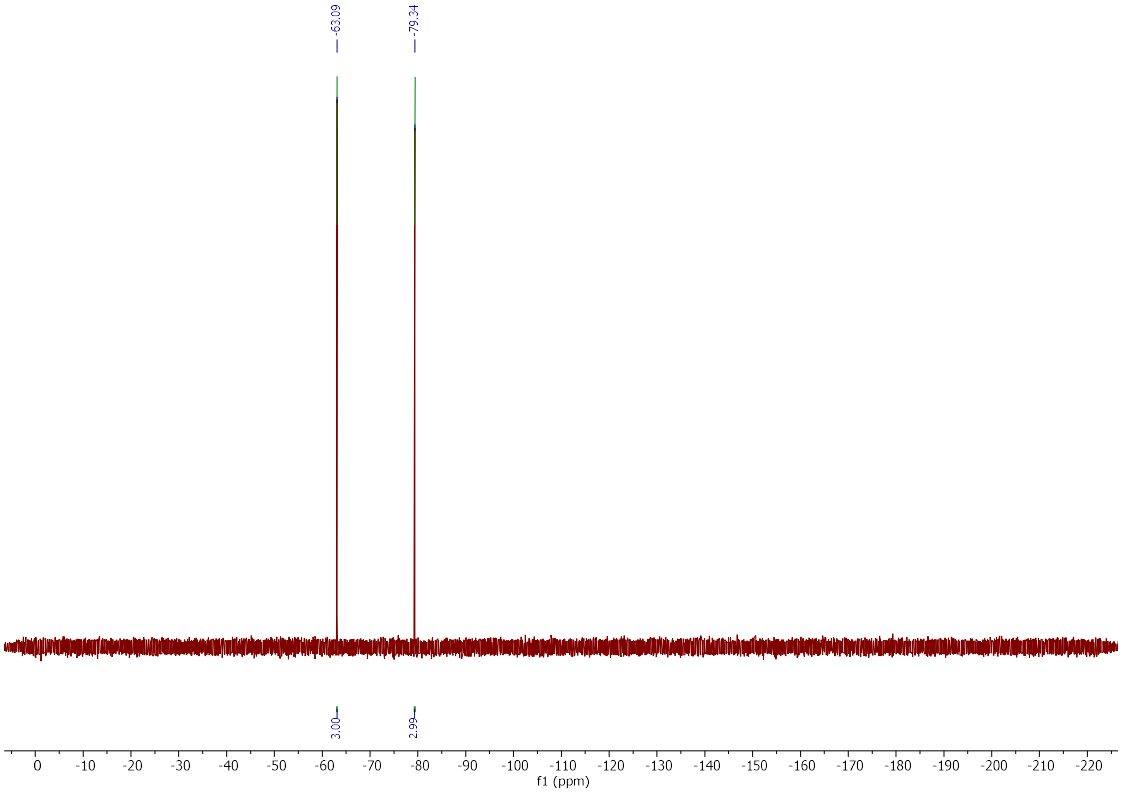

5-(5-chloro-2-((3,5-dichlorobenzyl)oxy)phenyl)-5H-dibenzo[b,d]thiophen-5-ium trifluoromethanesulfonate (**470i**)

^{1}H NMR (300 MHz, CD_3CN)

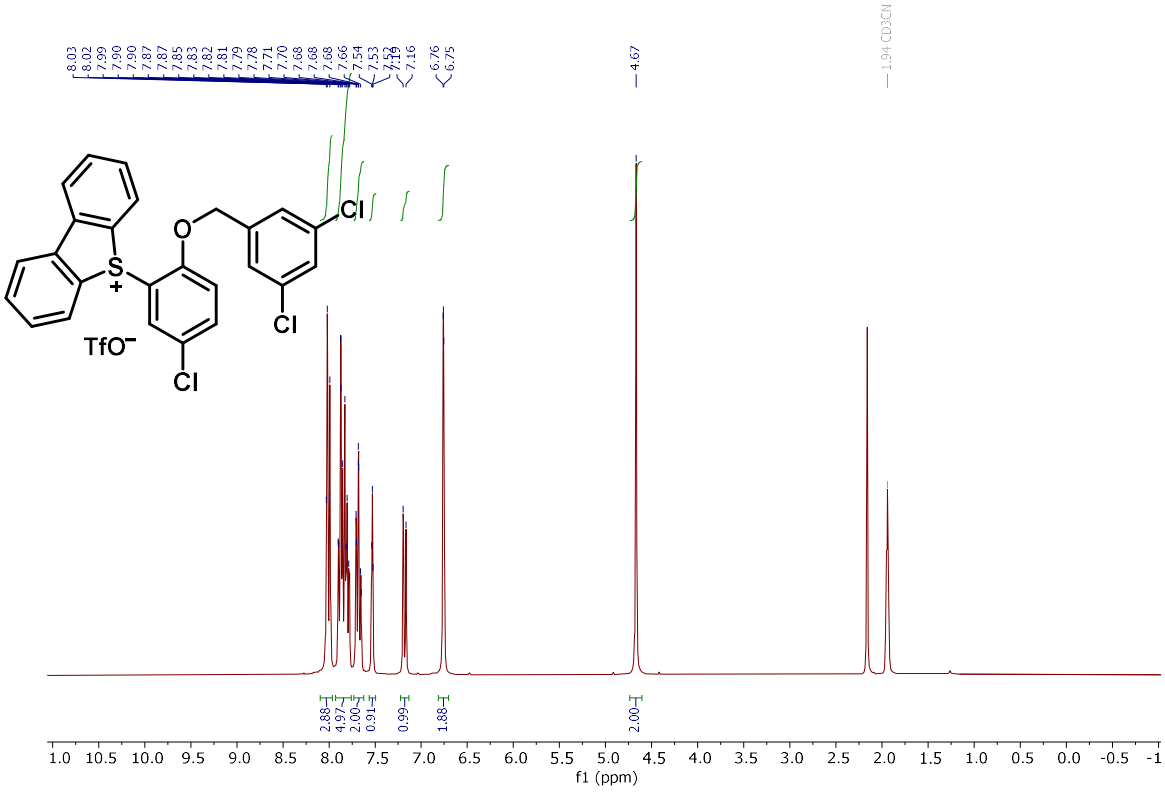

^{13}C{H} NMR (75 MHz, CD_3CN)

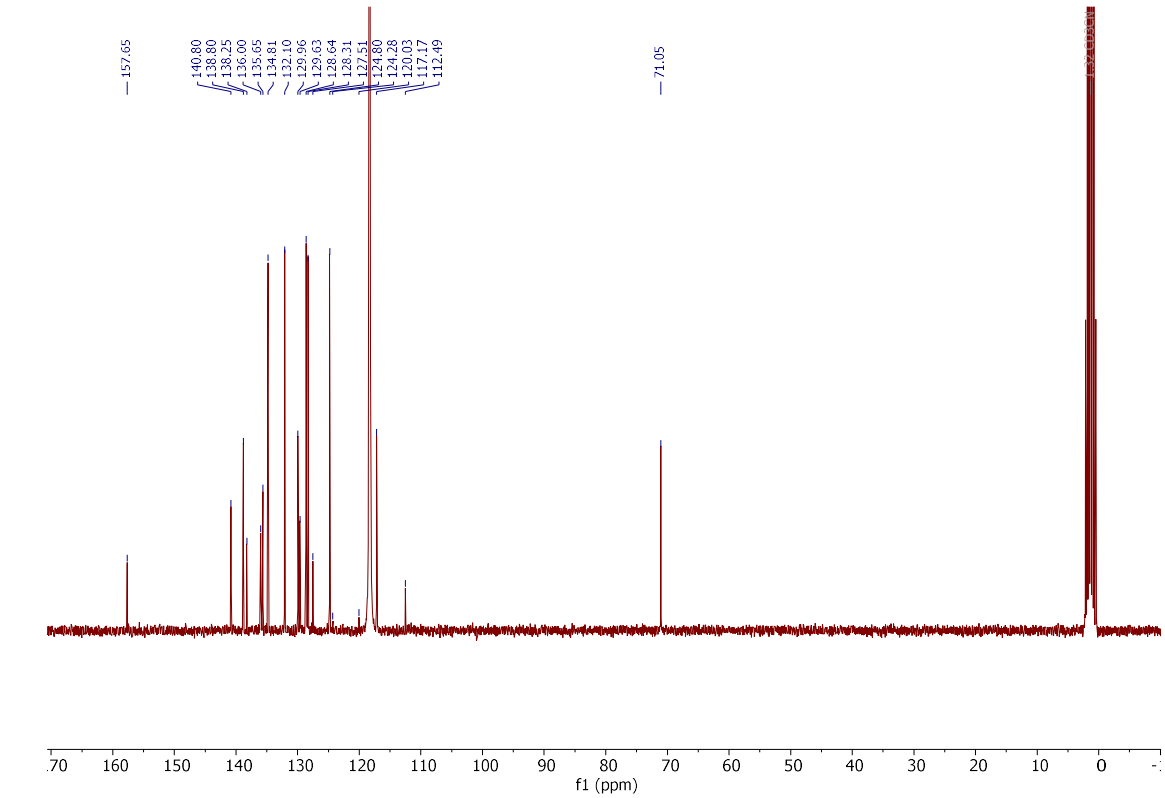

^{19}F NMR (282 MHz, CD_3CN)

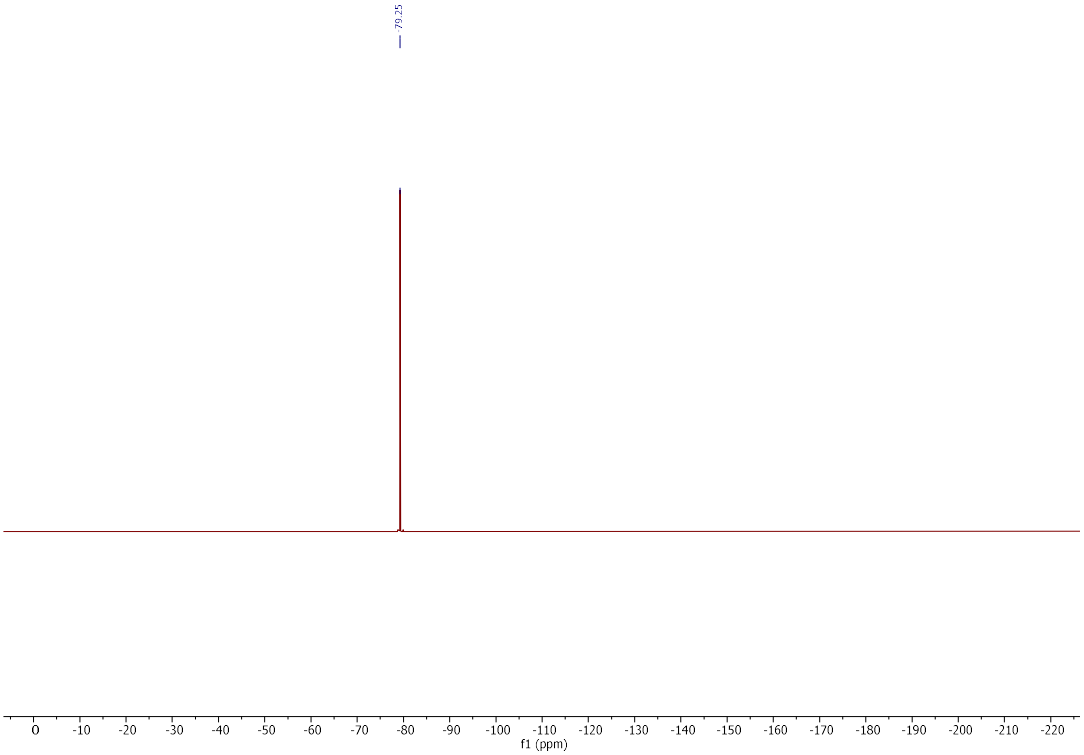

5-(5-methyl-2-((4-nitrobenzyl)oxy)phenyl)-5H-dibenzo[b,d]thiophen-5-ium trifluoromethanesulfonate (**470j**)

^{1}H NMR (400 MHz, $CDCl_3$)

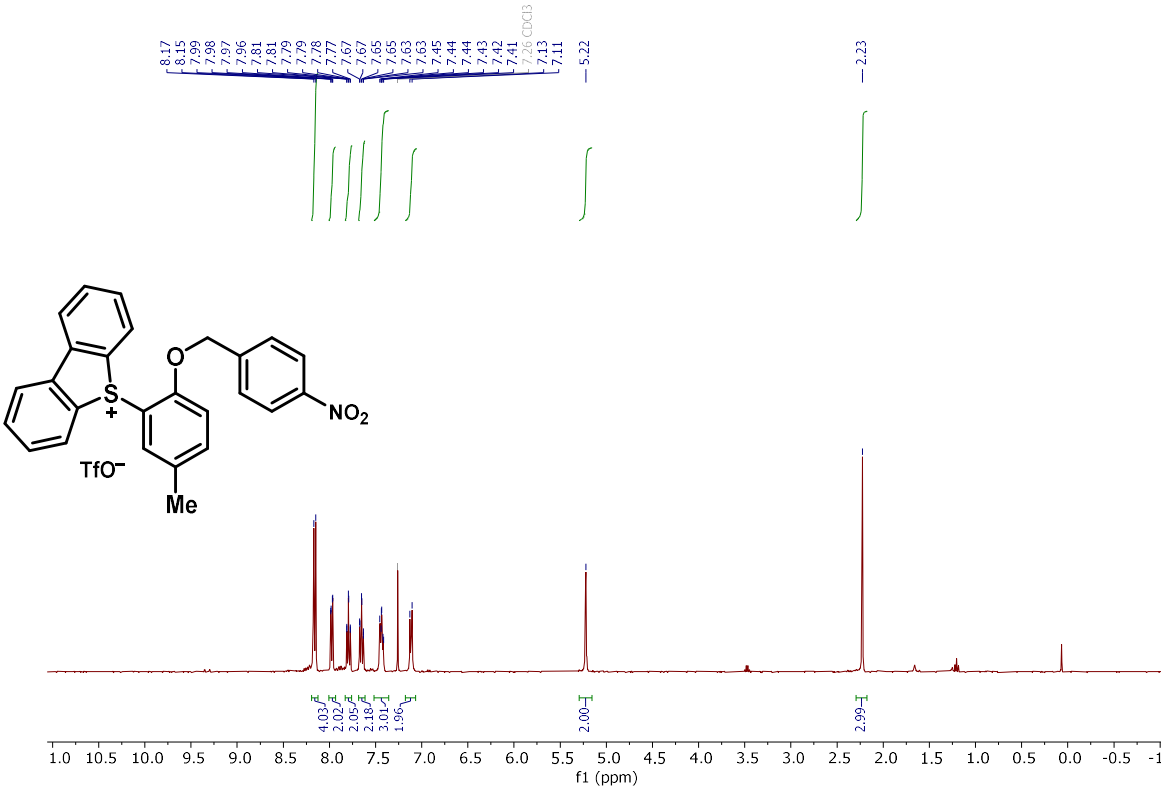

^{13}C NMR (101 MHz, $CDCl_3$)

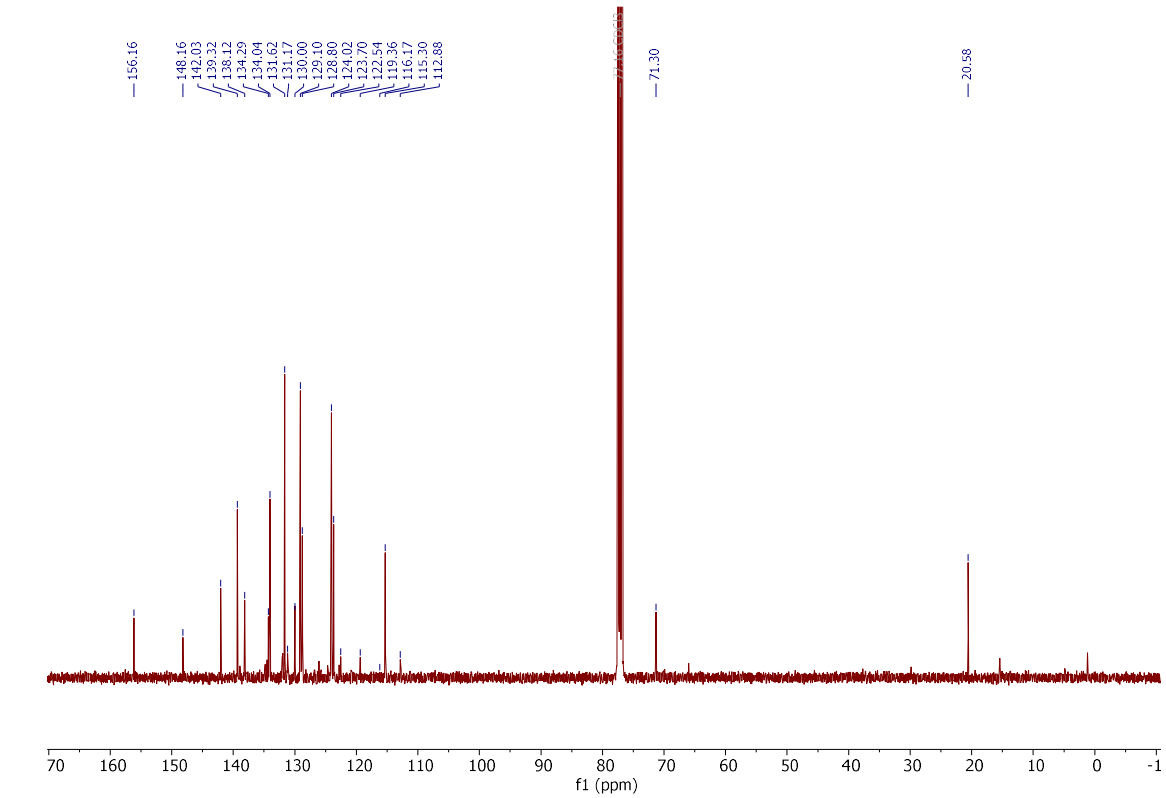

^{19}F NMR (282 MHz, CD_3CN)

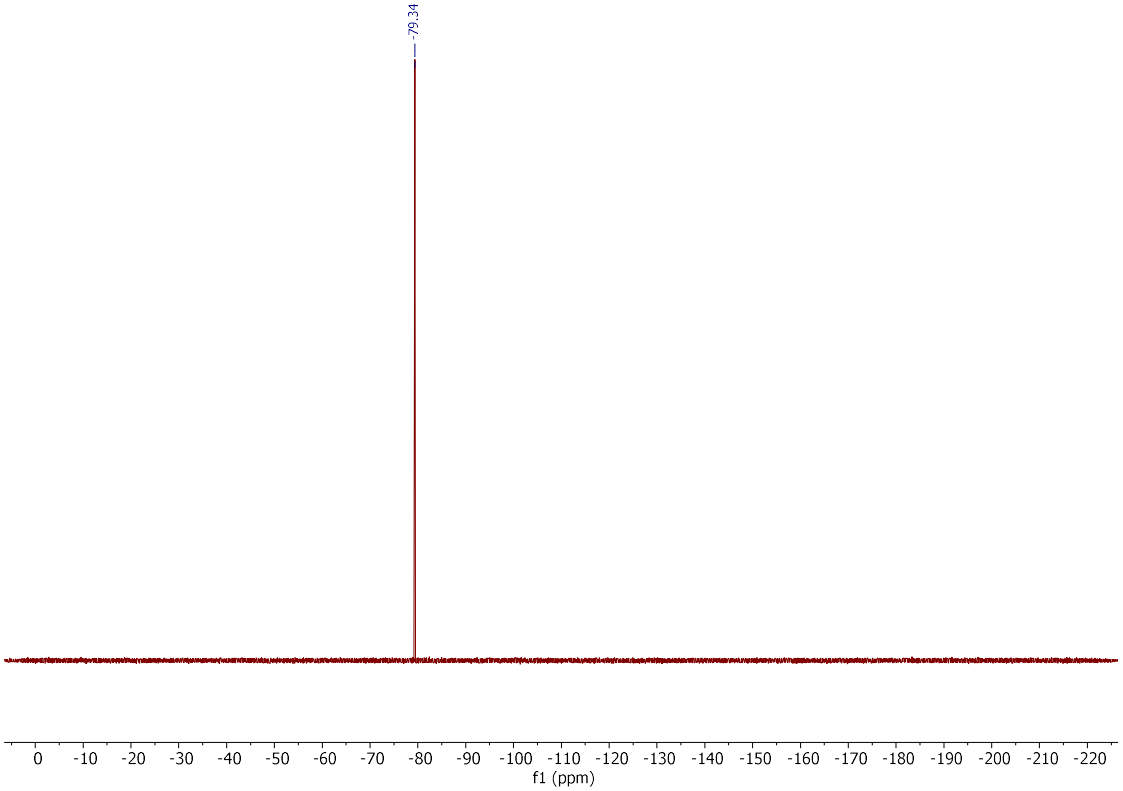

4-{[2-(5*H*-Dibenzo[*b*,*d*]thiophen-5-ium-5-yl)-4-methylphenoxy]methyl}pyridin-1-ium Bis(trifluoromethanesulfonate) (**470k**)

^{1}H NMR (300 MHz, CD_3CN)

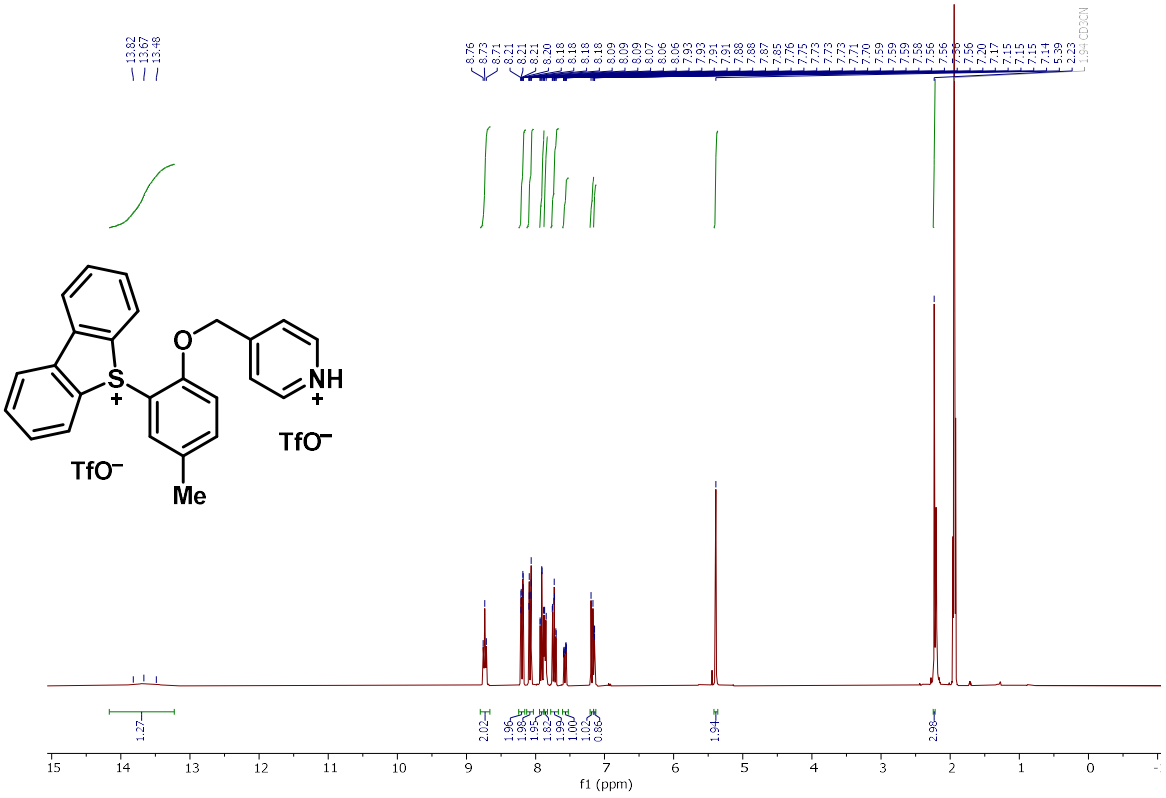

^{13}C{H} NMR (75 MHz, CD_3CN)

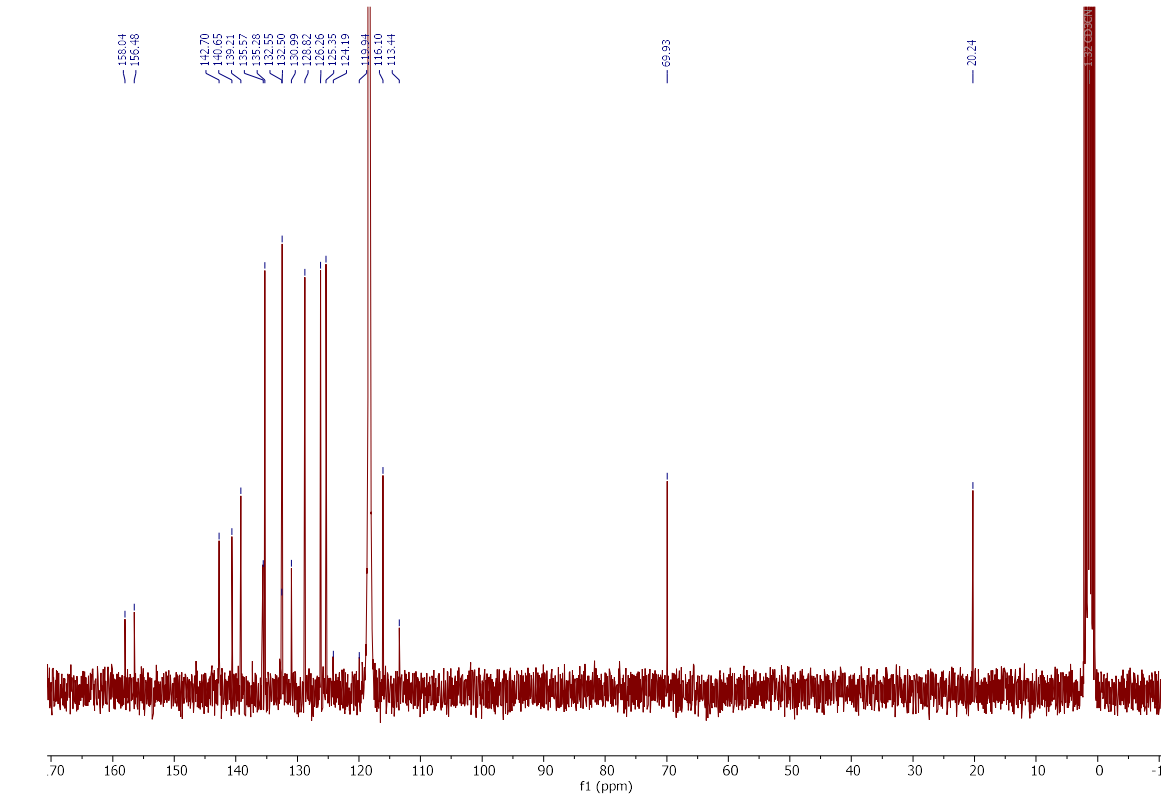

^{19}F NMR (282 MHz, CD_3CN)

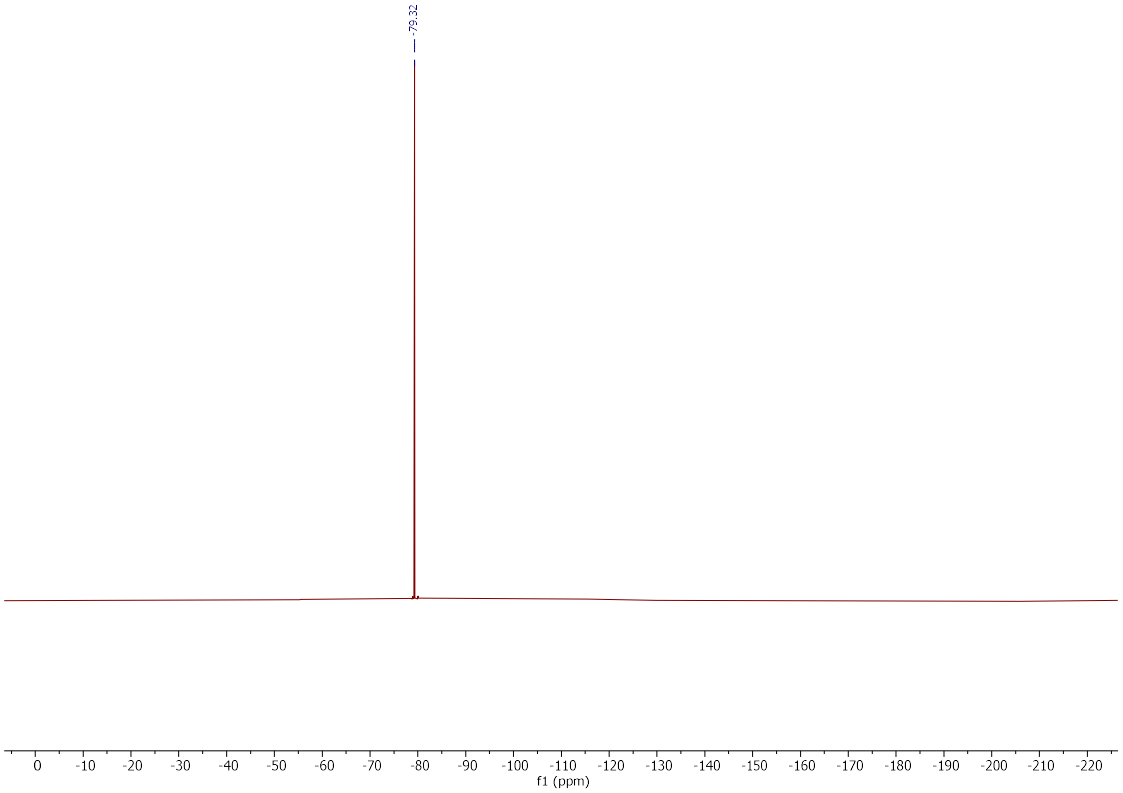

4-{[2-(5*H*-Dibenzo[*b*,*d*]thiophen-5-ium-5-yl]-4-methylphenoxy}methyl)pyridine 1-oxide Trifluorometha-nesulfonate (**470k'**)

^{1}H NMR (600 MHz, CD_3CN)

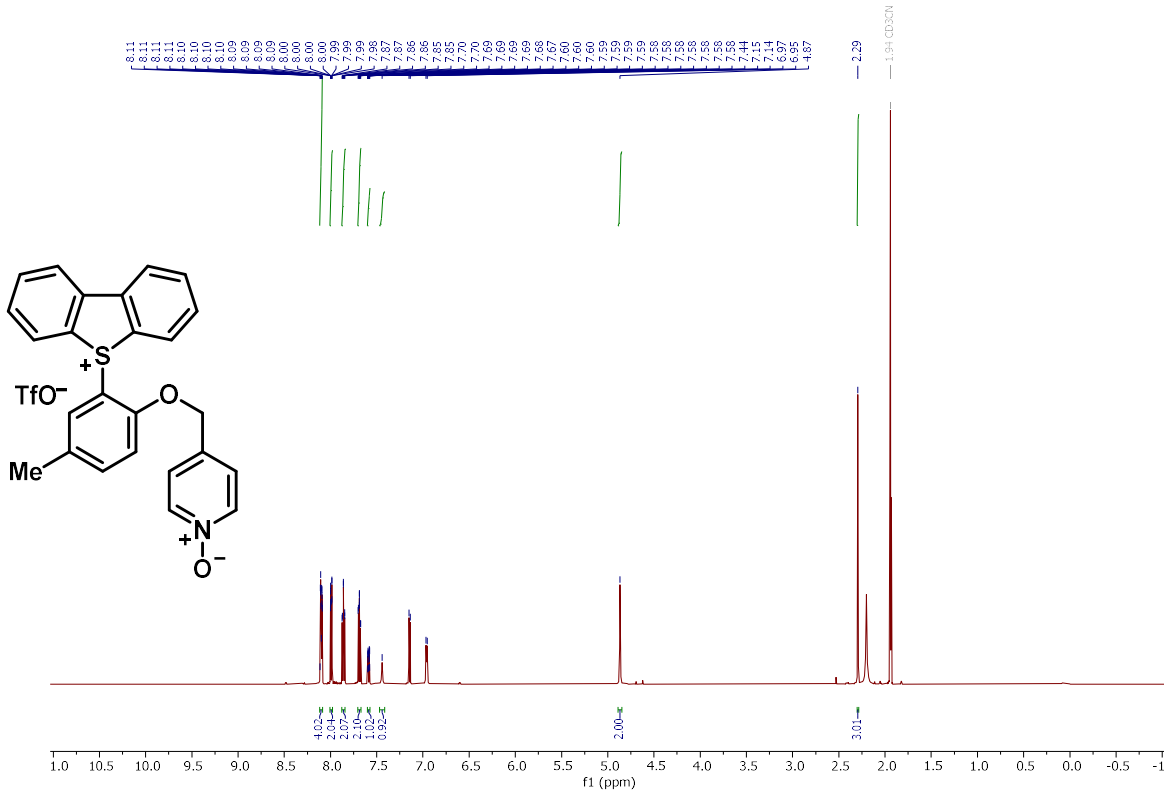

^{13}C{H} NMR (101 MHz, CD_3CN)

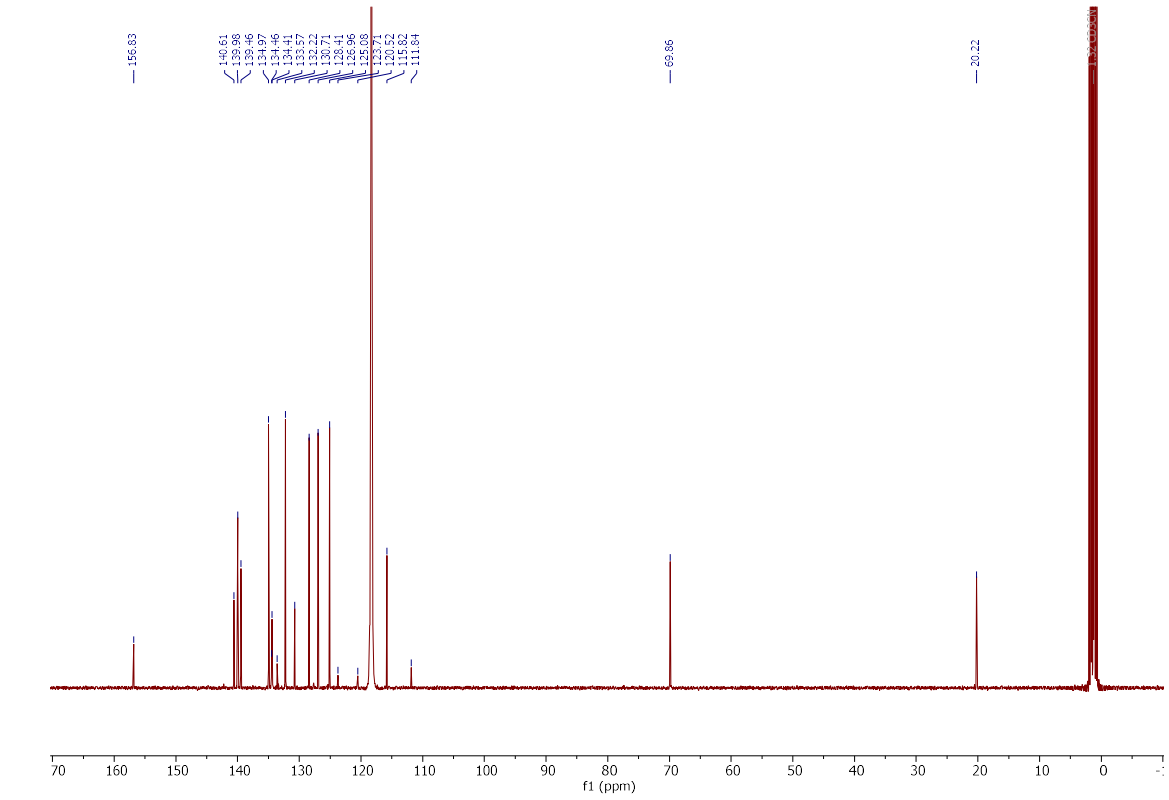

^{19}F NMR (565 MHz, CD_3CN)

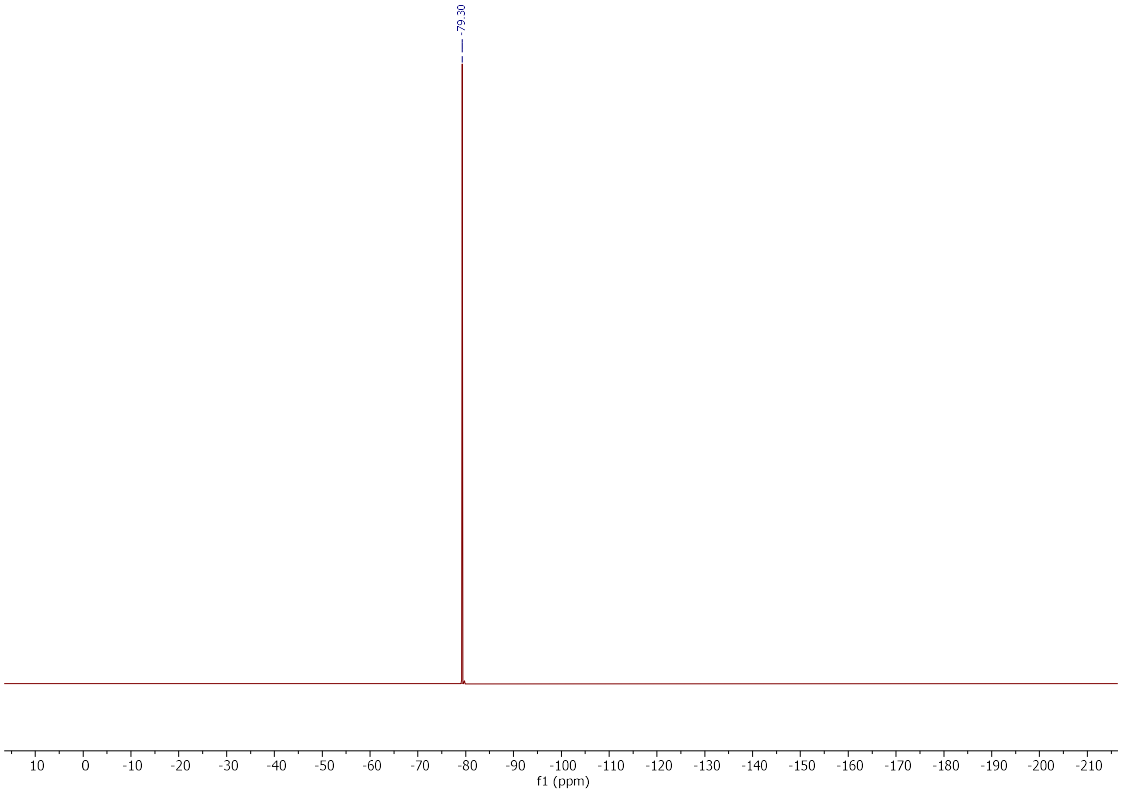

5-{5-(*tert*-Butyl)-2-[(2,6-dimethylbenzyl)oxy]phenyl}-5*H*-dibenzo[*b*,*d*]thiophen-5-ium Trifluoromethane-sulfonate (**470l**)

^{1}H NMR (300 MHz, CD_3CN)

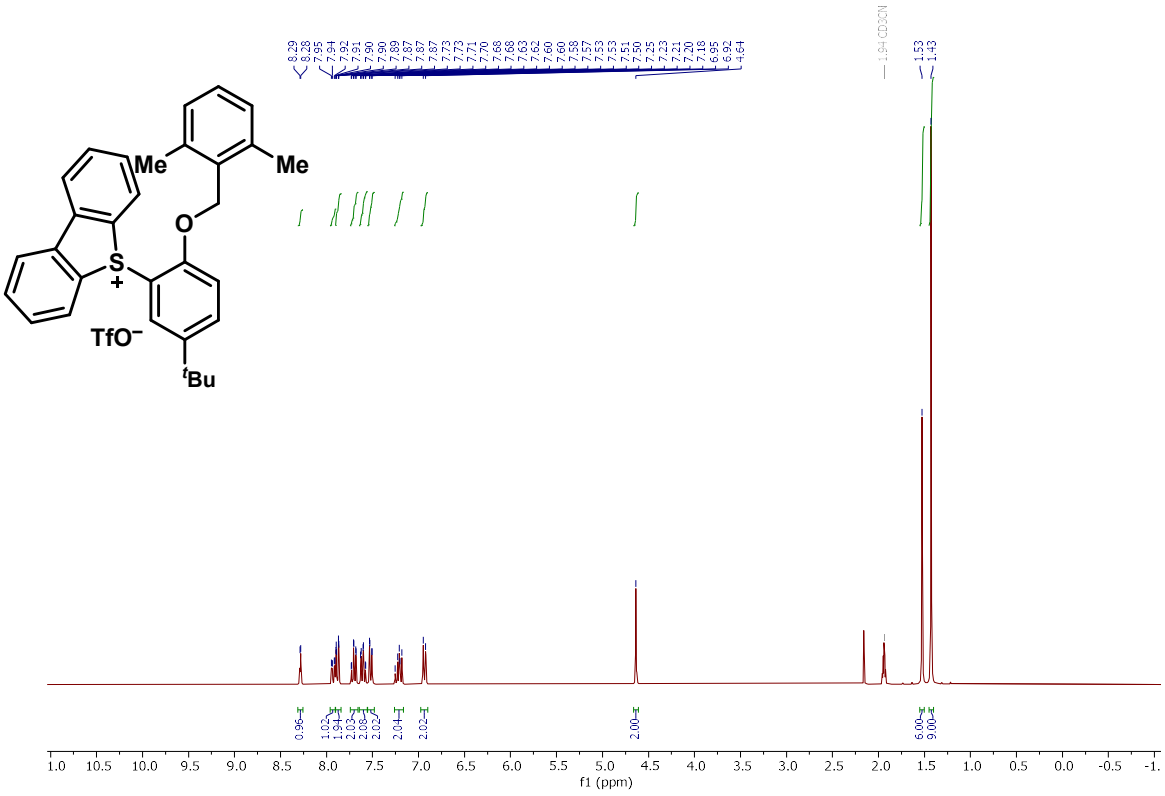

^{13}C{H} NMR (75 MHz, CD_3CN)

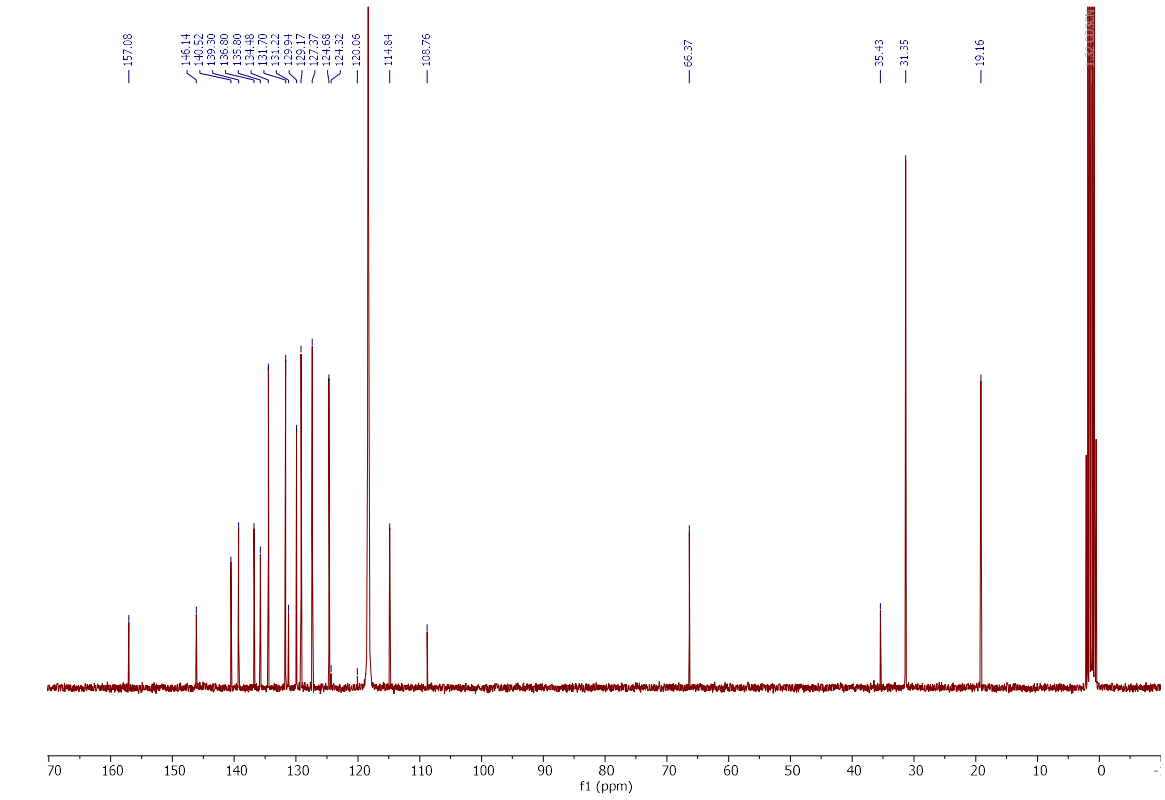

^{19}F NMR (282 MHz, CD_3CN)

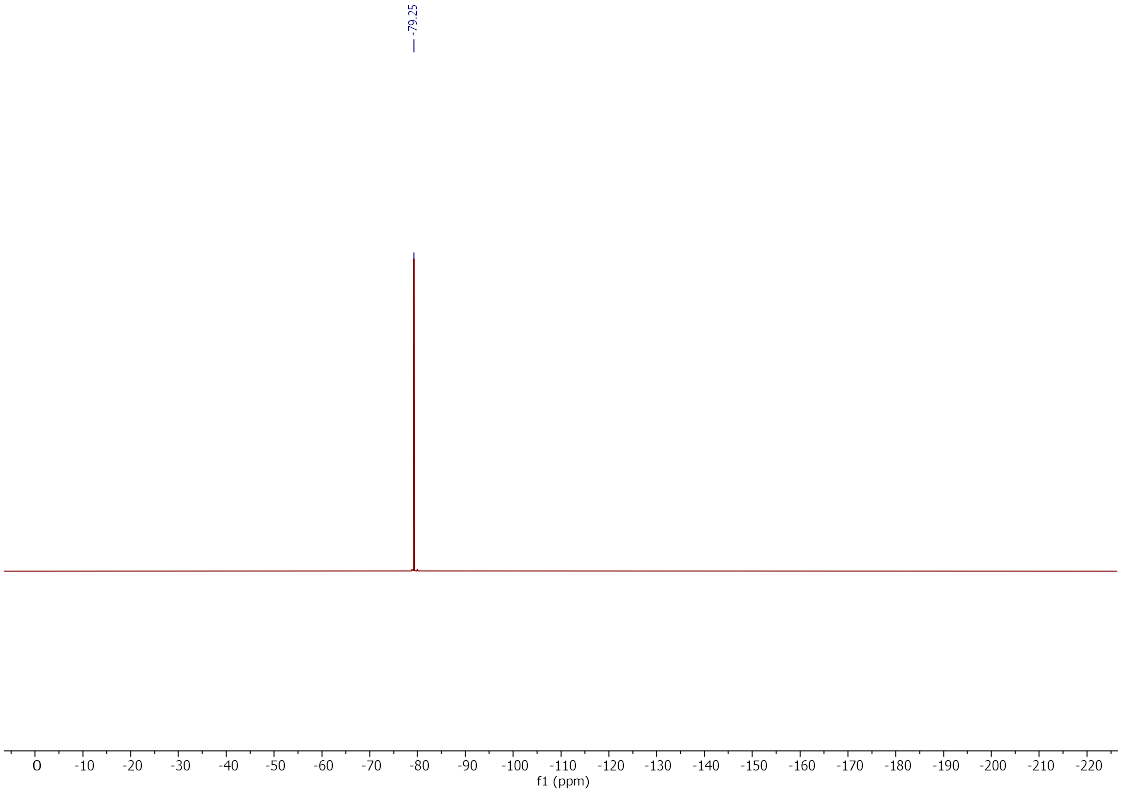

5-(5-(tert-butyl)-2-((2,6-dichlorobenzyl)oxy)phenyl)-5H-dibenzo[b,d]thiophen-5-ium trifluoromethanesulfonate (**470m**)

^{1}H NMR (300 MHz, CD_3CN)

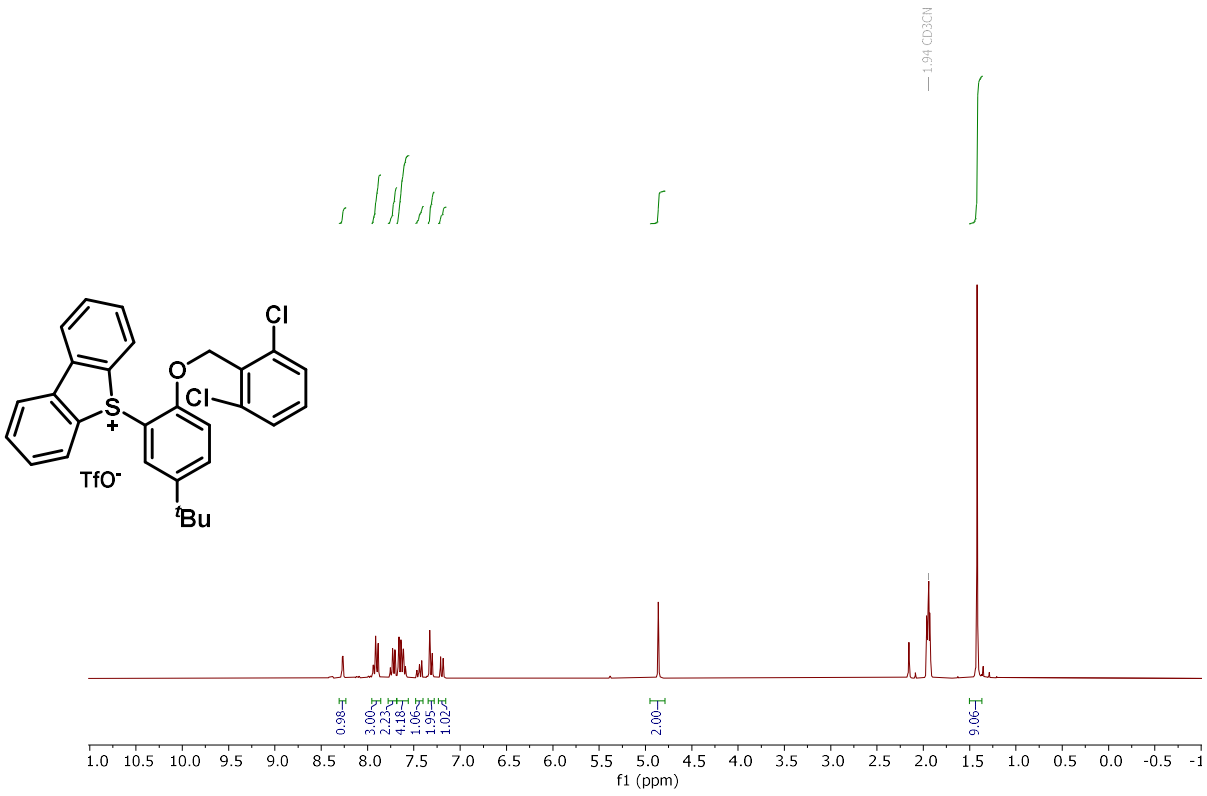

^{13}C NMR (75 MHz, CD_3CN)

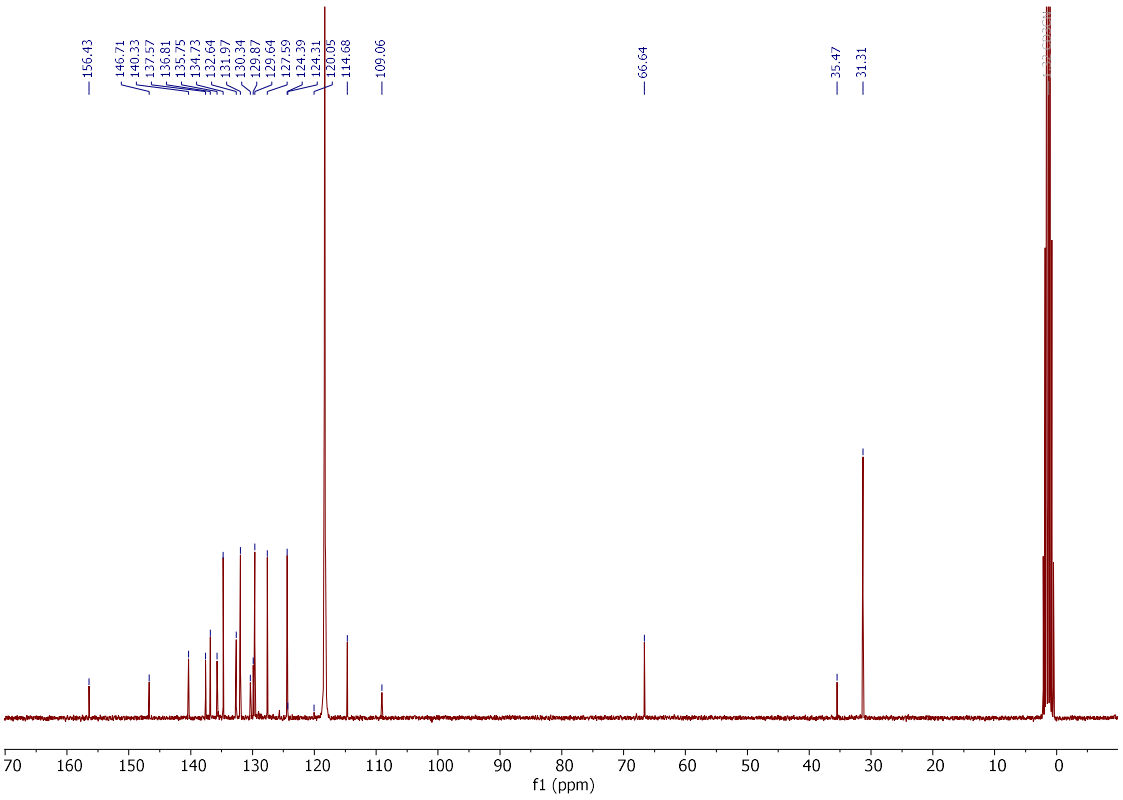

^{19}F NMR (282 MHz, CD_3CN)

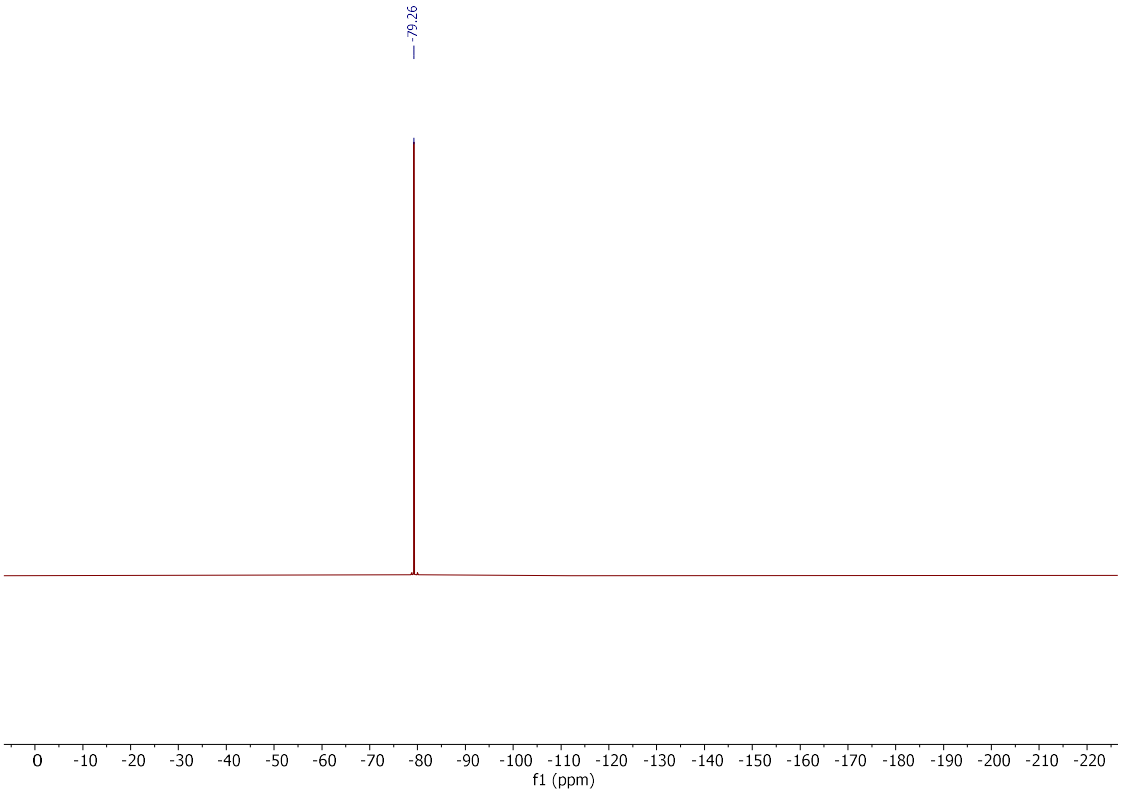

5-(4'-{[4-(Trifluoromethyl)benzyl]oxy}-[1,1'-biphenyl]-4-yl)-5*H*-dibenzo[*b*,*d*]thiophen-5-ium Trifluoromethanesulfonate (**470n**)

^{1}H NMR (400 MHz, CD_3CN)

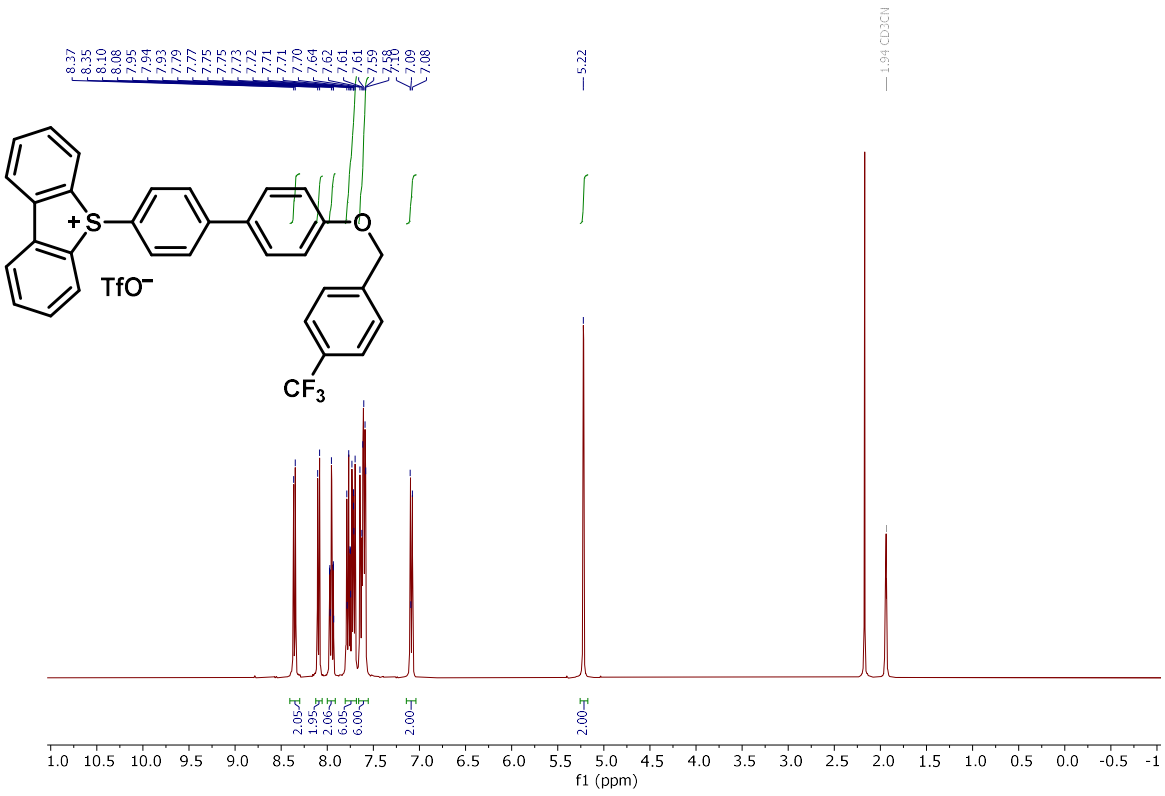

^{13}C{H} NMR (101 MHz, CD_3CN)

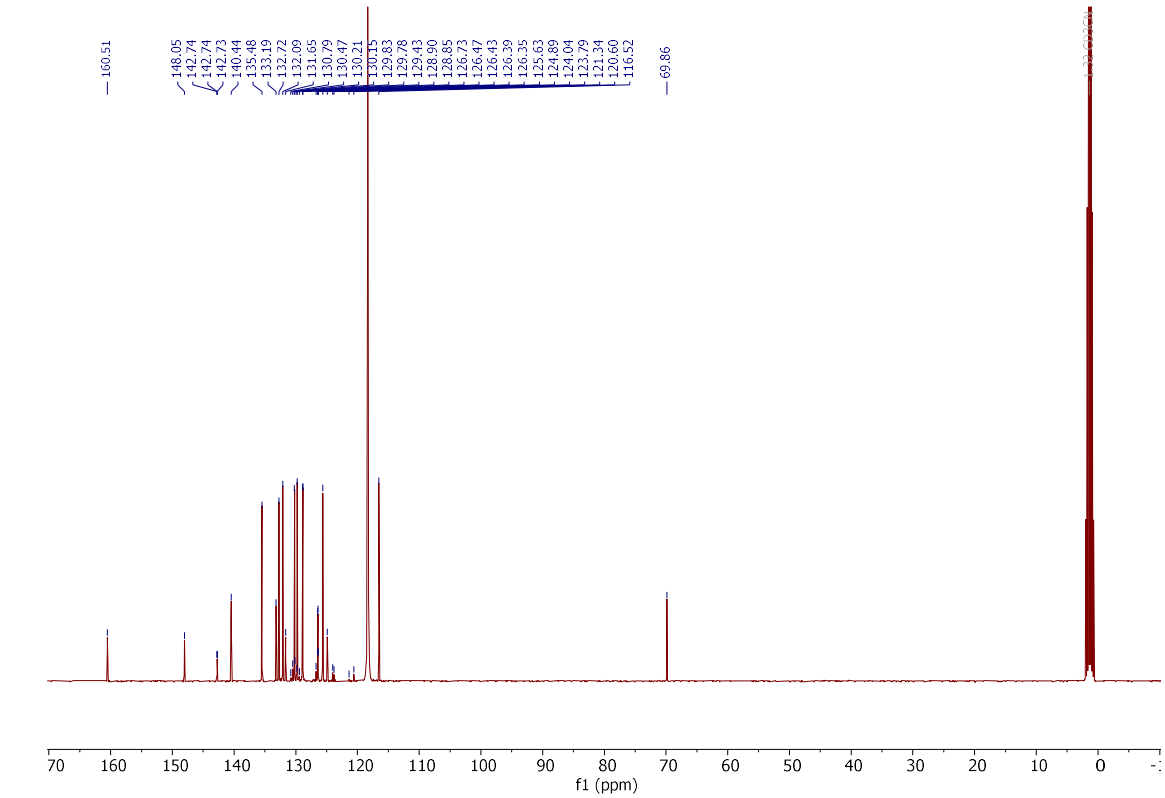

^{19}F NMR (376 MHz, CD_3CN)

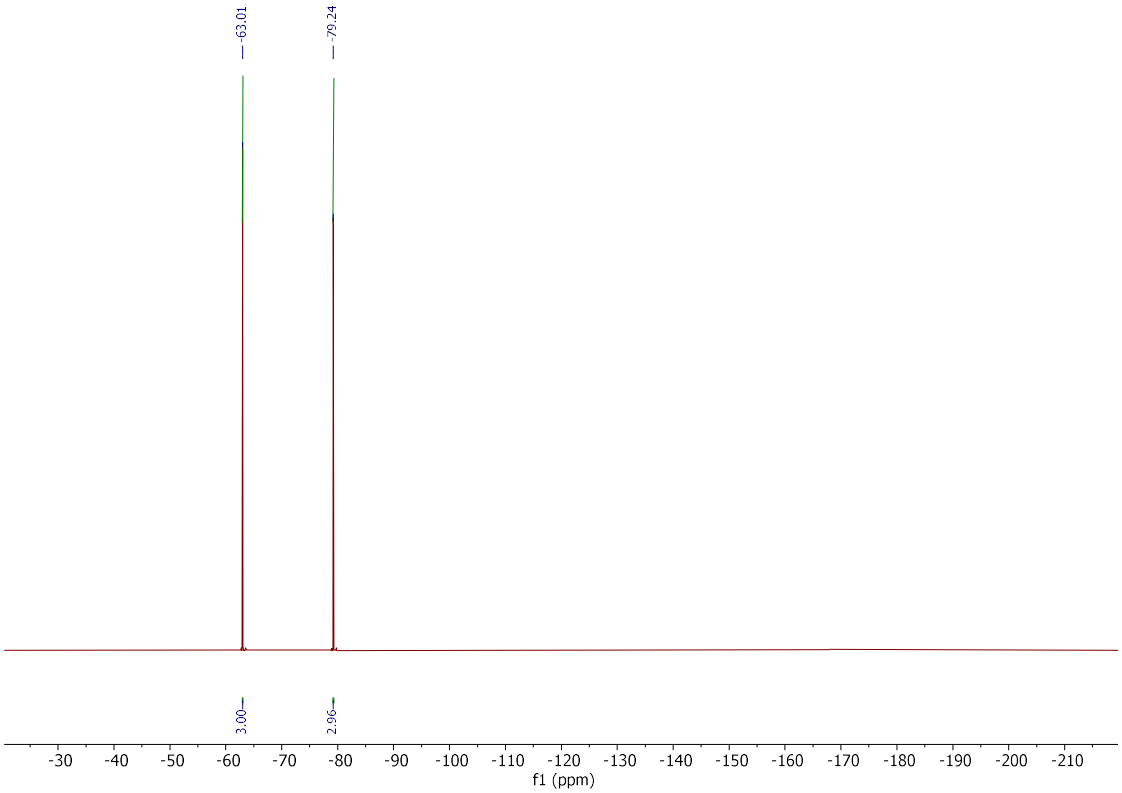

5-{4'-[(3,5-Dichlorobenzyl)oxy]-[1,1'-biphenyl]-4-yl}-5*H*-dibenzo[*b*,*d*]thiophen-5-ium Trifluoromethane-sulfonate (**470o**)

^{1}H NMR (400 MHz, CD_3CN)

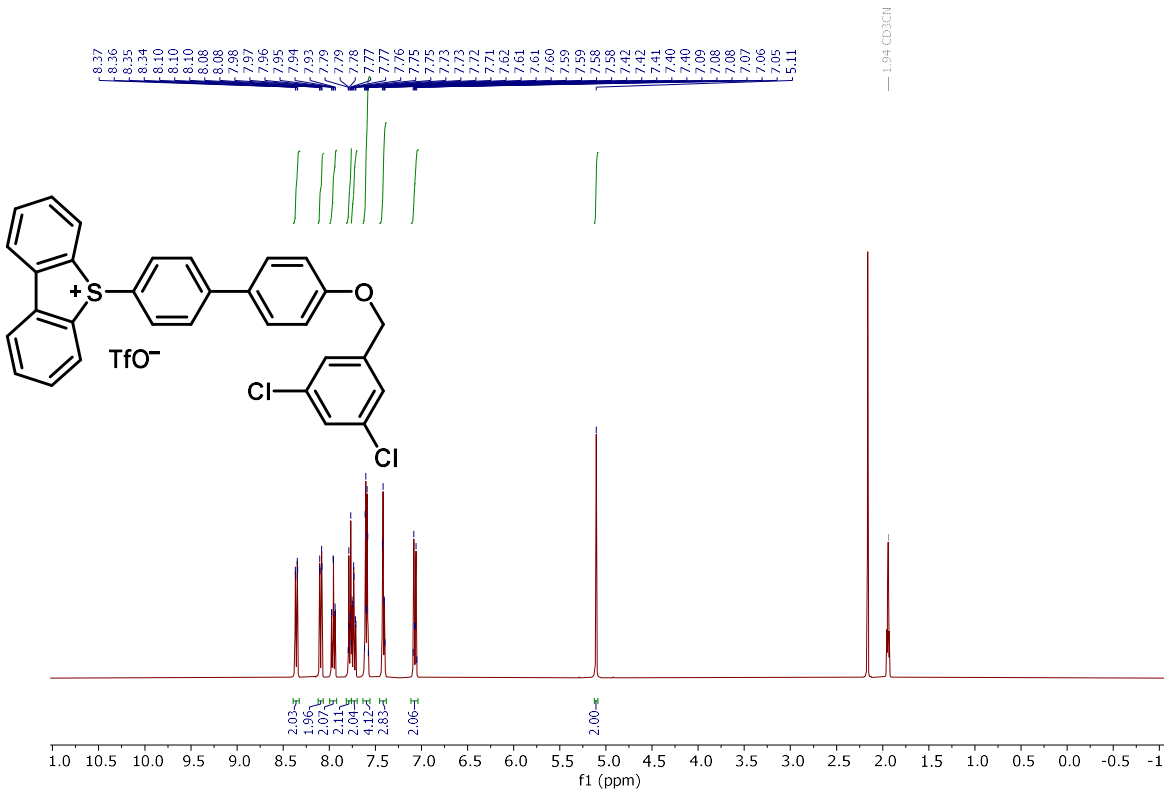

^{13}C{H} NMR (101 MHz, CD_3CN)

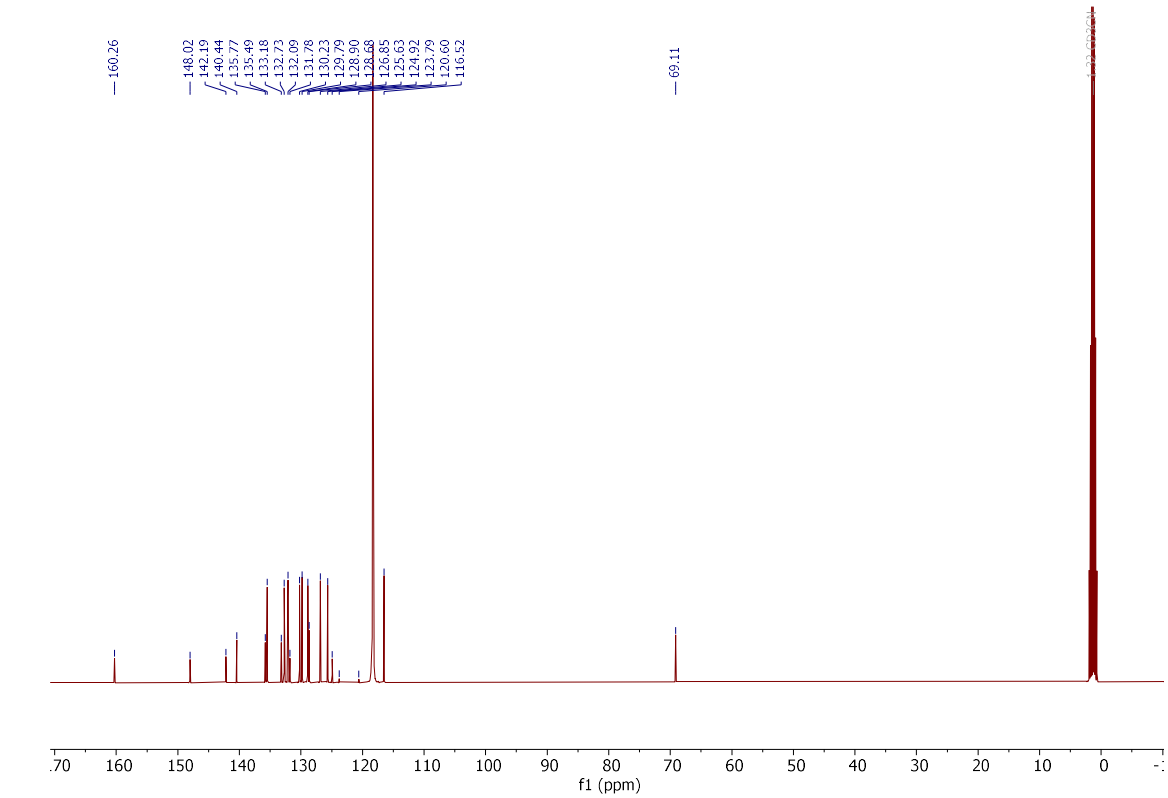

^{19}F NMR (376 MHz, CD_3CN)

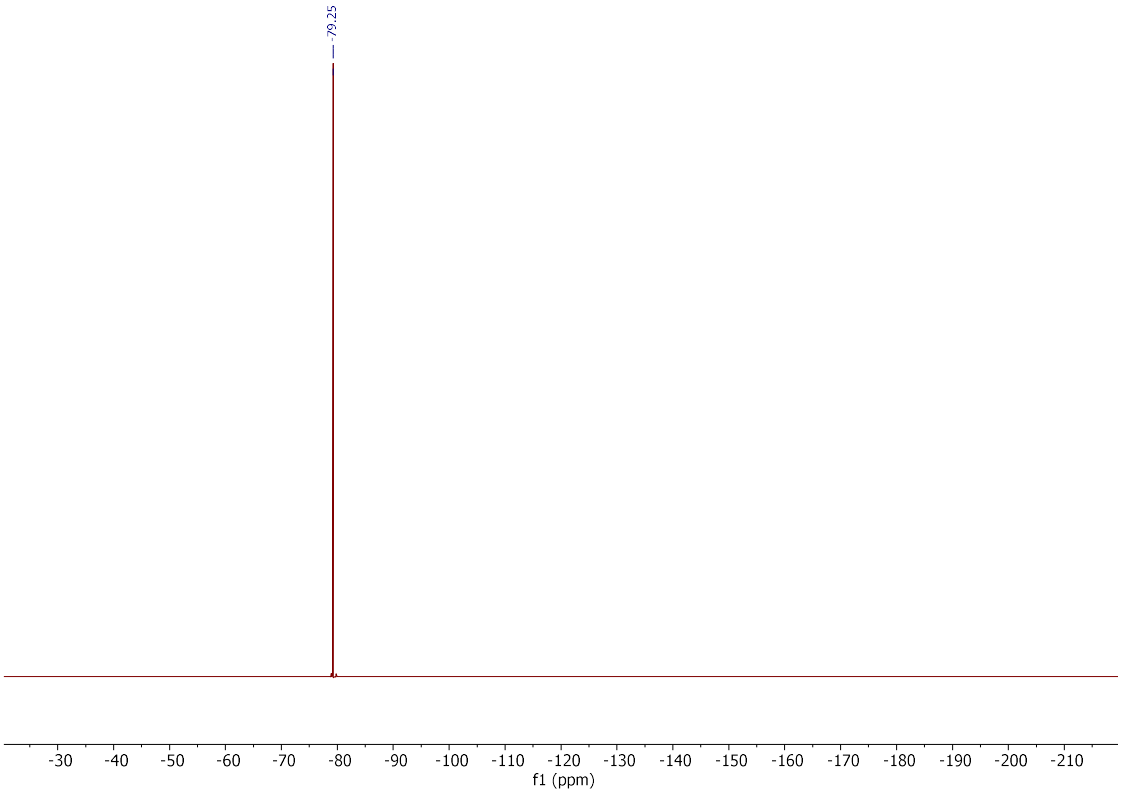

5-(5-methyl-2-(p-tolyloxy)phenyl)-5H-dibenzo[b,d]thiophen-5-ium trifluoromethanesulfonate (**470p**)

^{1}H NMR (400 MHz, $CDCl_3$)

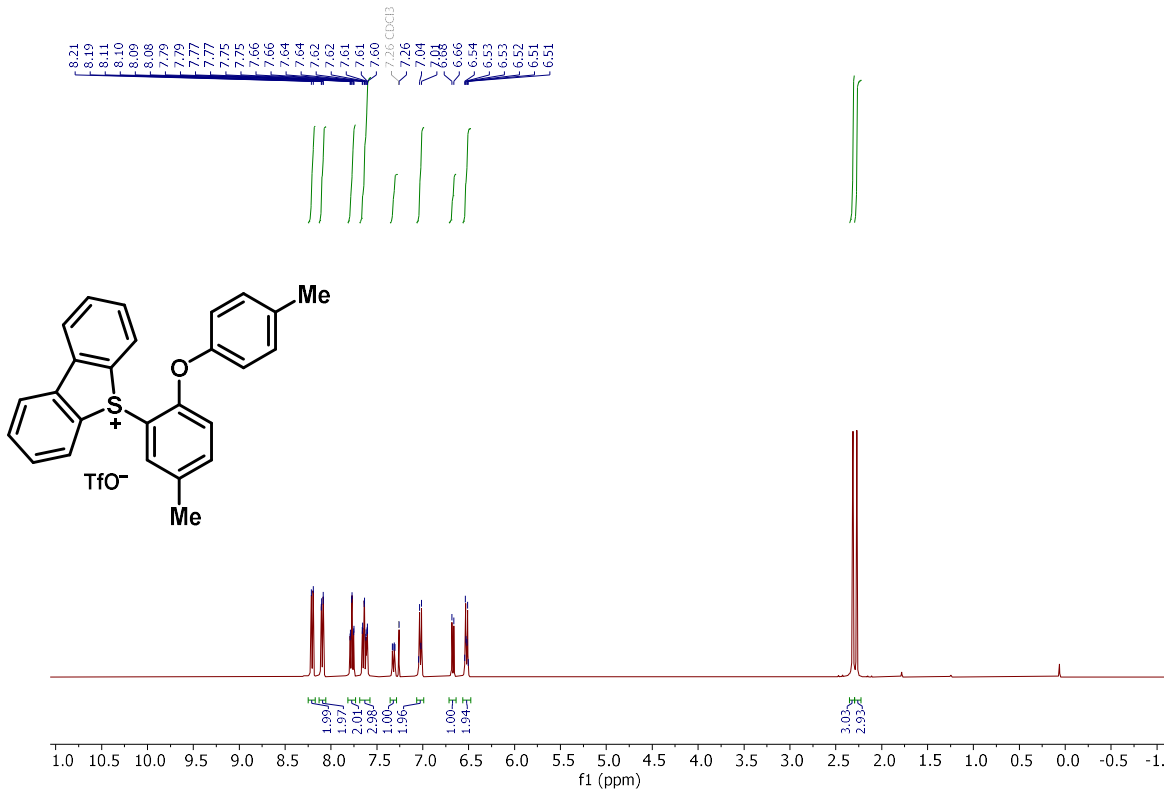

^{13}C NMR (101 MHz, $CDCl_3$)

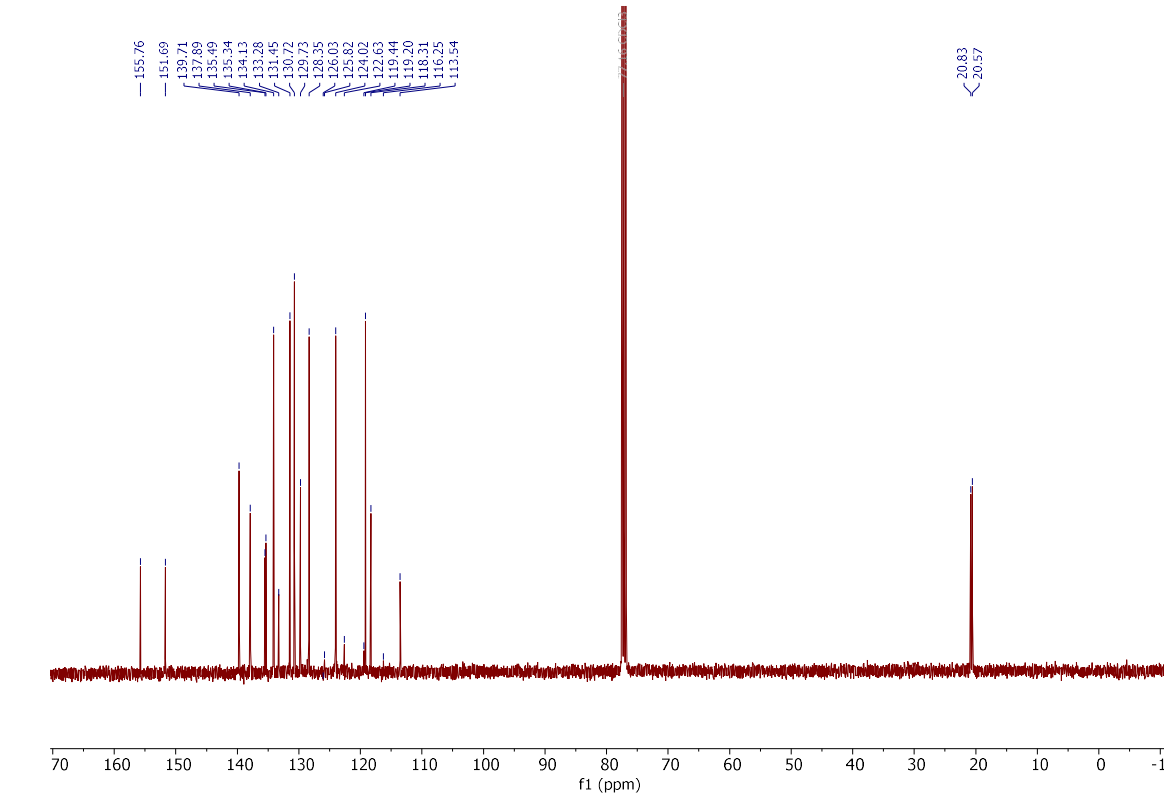

^{19}F NMR (376 MHz, $CDCl_3$)

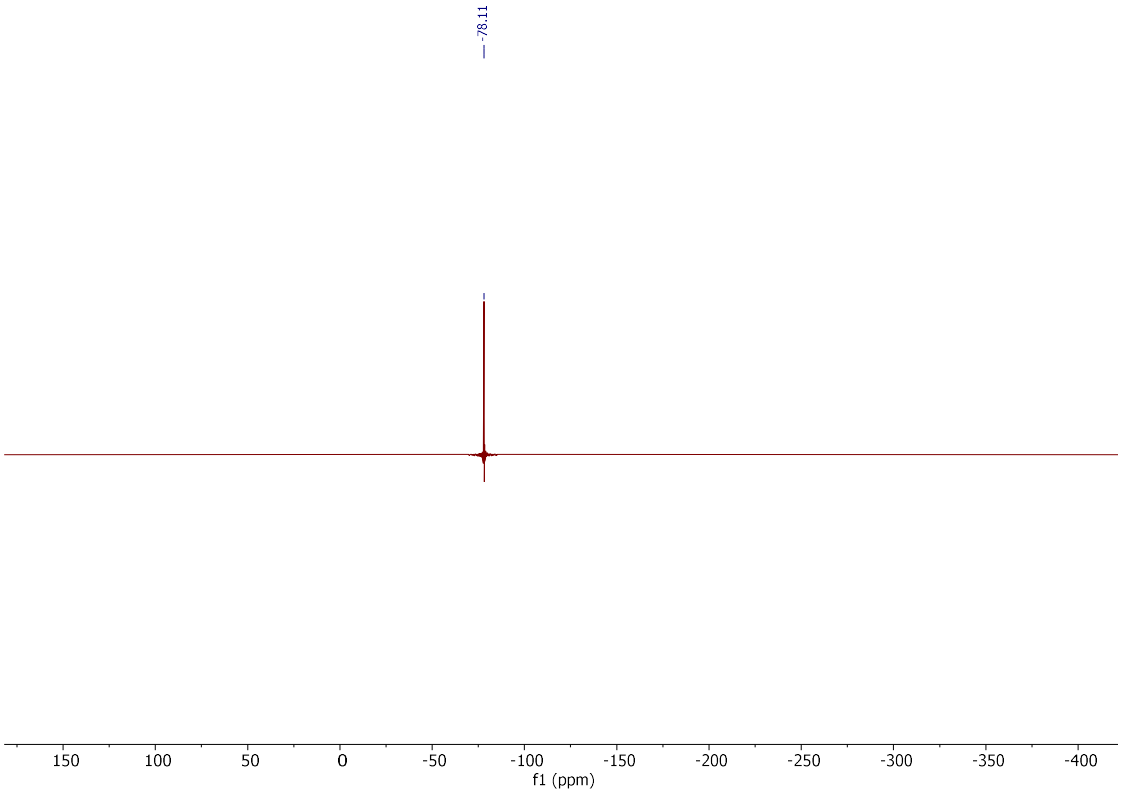

5,5'-({[1,2-Phenylenebis(methylene)]bis(oxy)}bis[5-(*tert*-butyl)-2,1-phenylene])bis(5*H*-dibenzo[*b*,*d*]thio-phen-5-ium) Bis(trifluoromethanesulfonate) (**470q**)

^{1}H NMR (400 MHz, CD_3CN)

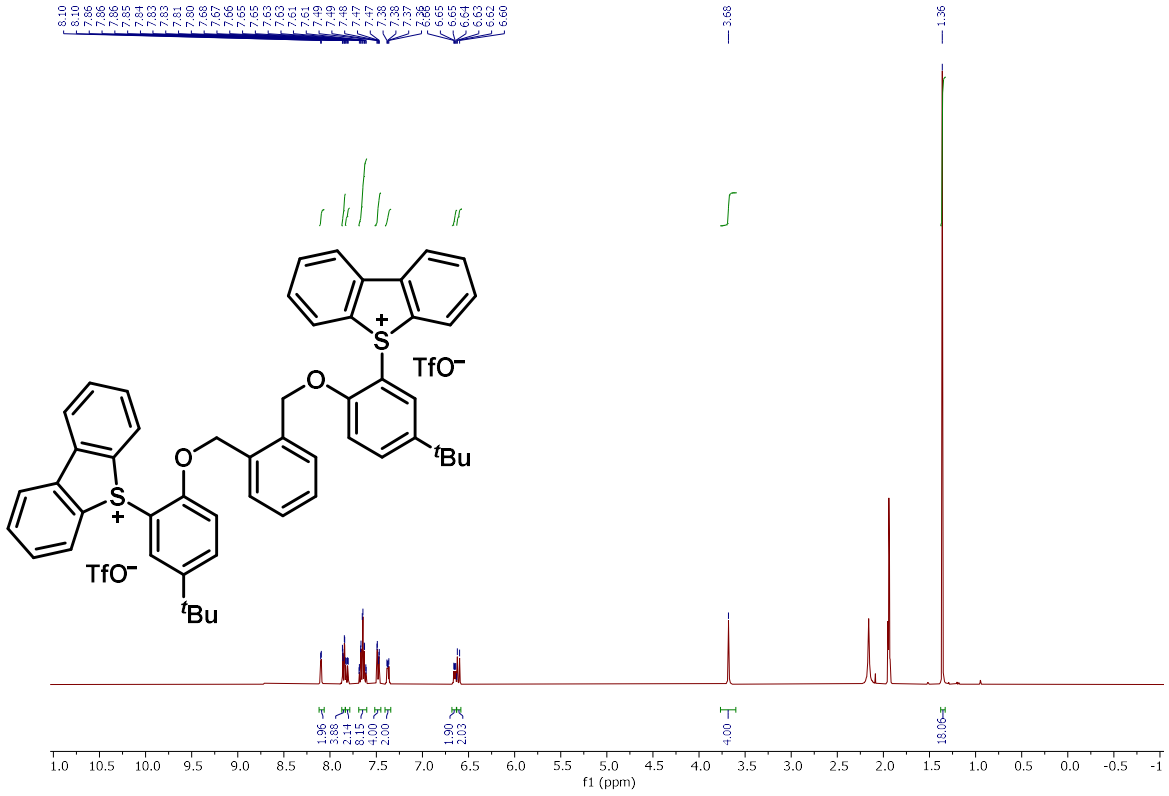

^{13}C{H} NMR (126 MHz, CD_3CN)

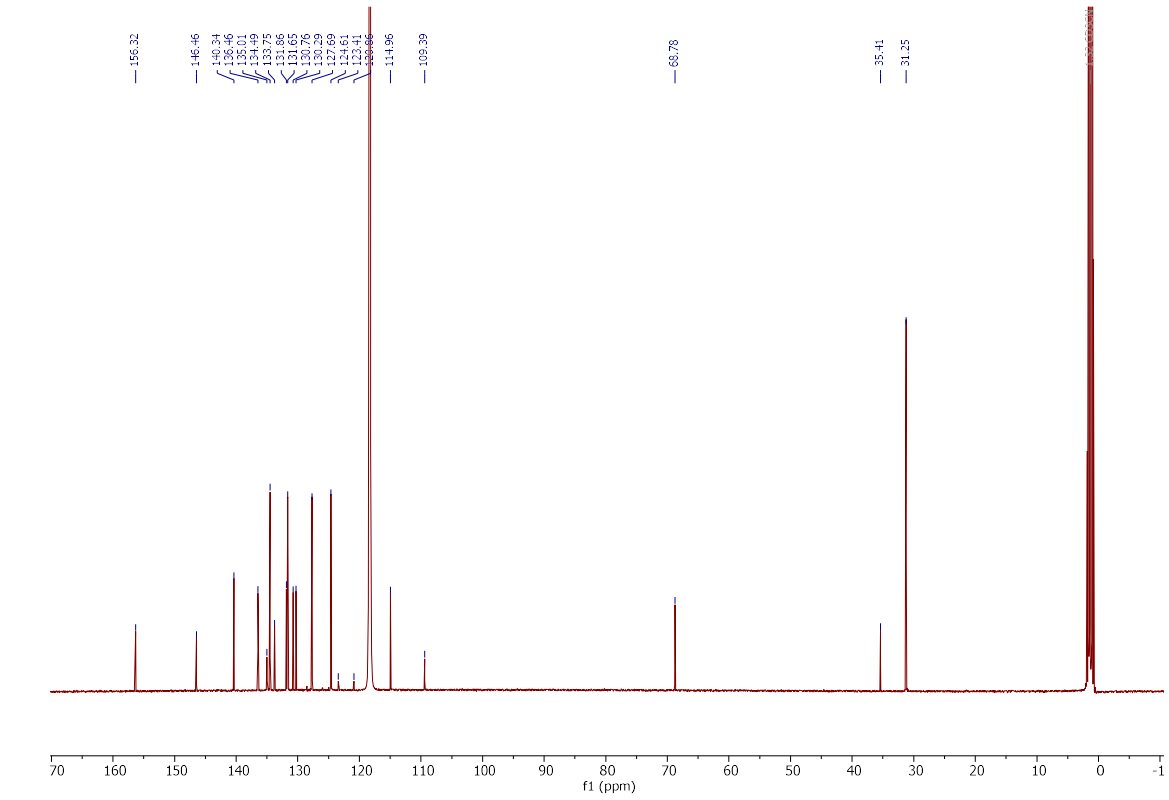

^{19}F NMR (377 MHz, CD_3CN)

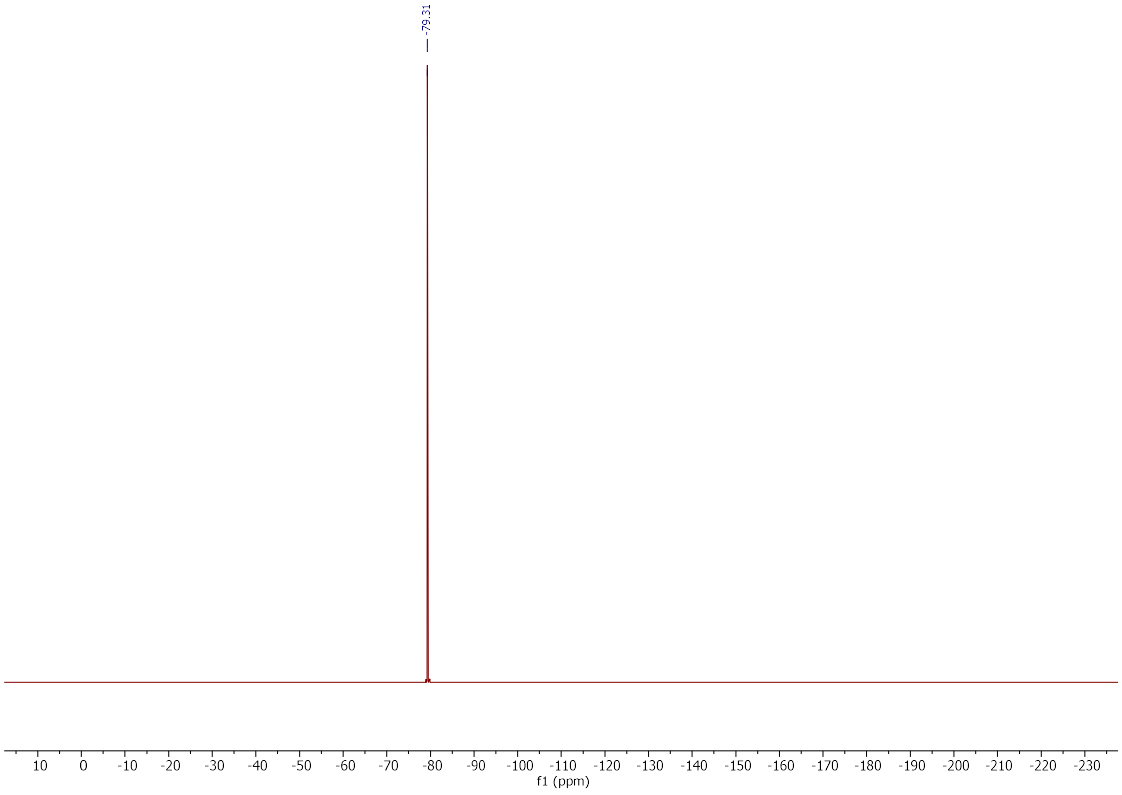

5,5'-[{[1,4-Phenylenebis(methylene)]bis(oxy)}bis(5-methyl-2,1-phenylene)]bis(5*H*-dibenzo[*b*,*d*]thiophen-5-ium) Bis(trifluoromethanesulfonate) (**470r**)

^{1}H NMR (400 MHz, CD_3CN)

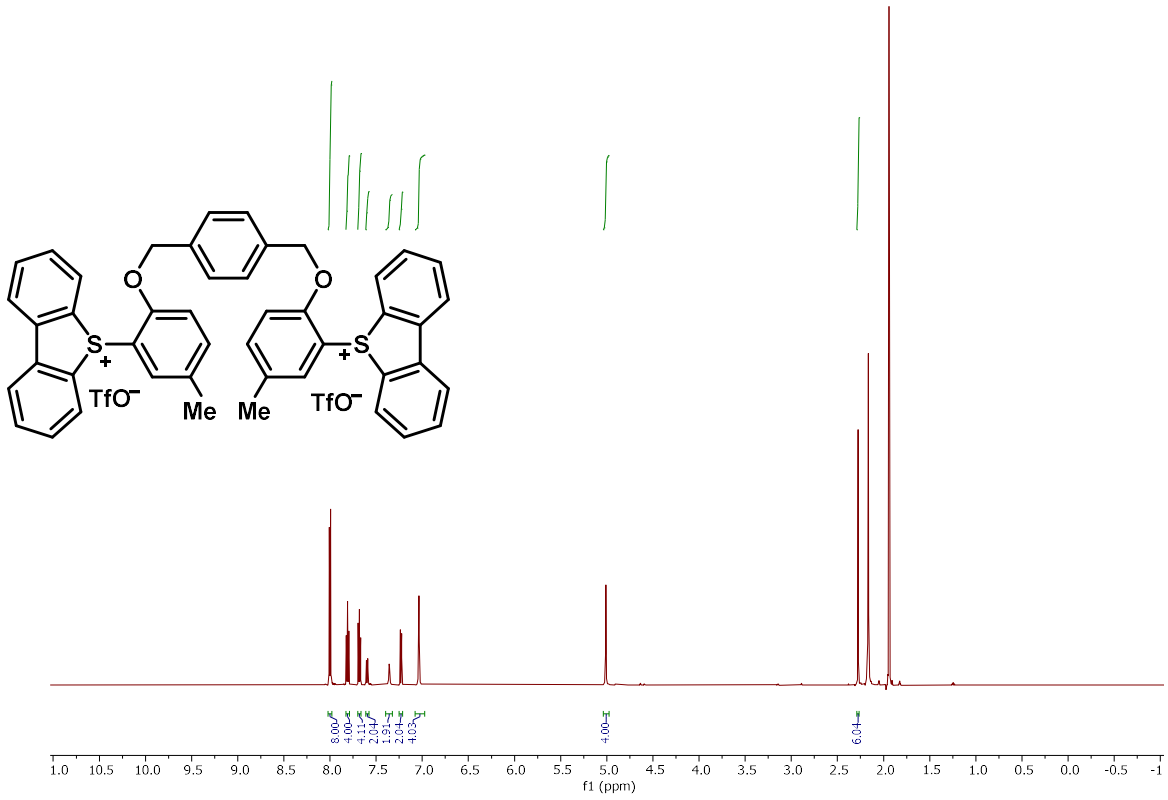

^{13}C{H} NMR (151 MHz, CD_3CN)

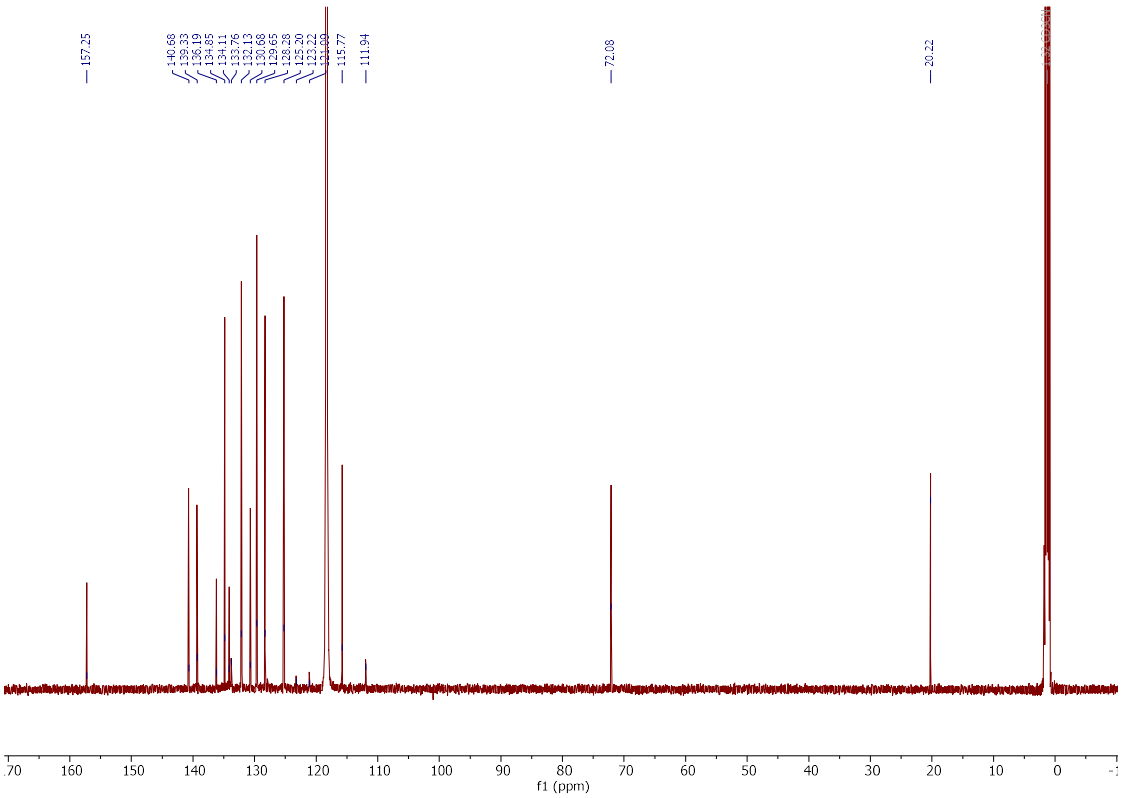

^{19}F NMR (377 MHz, CD_3CN)

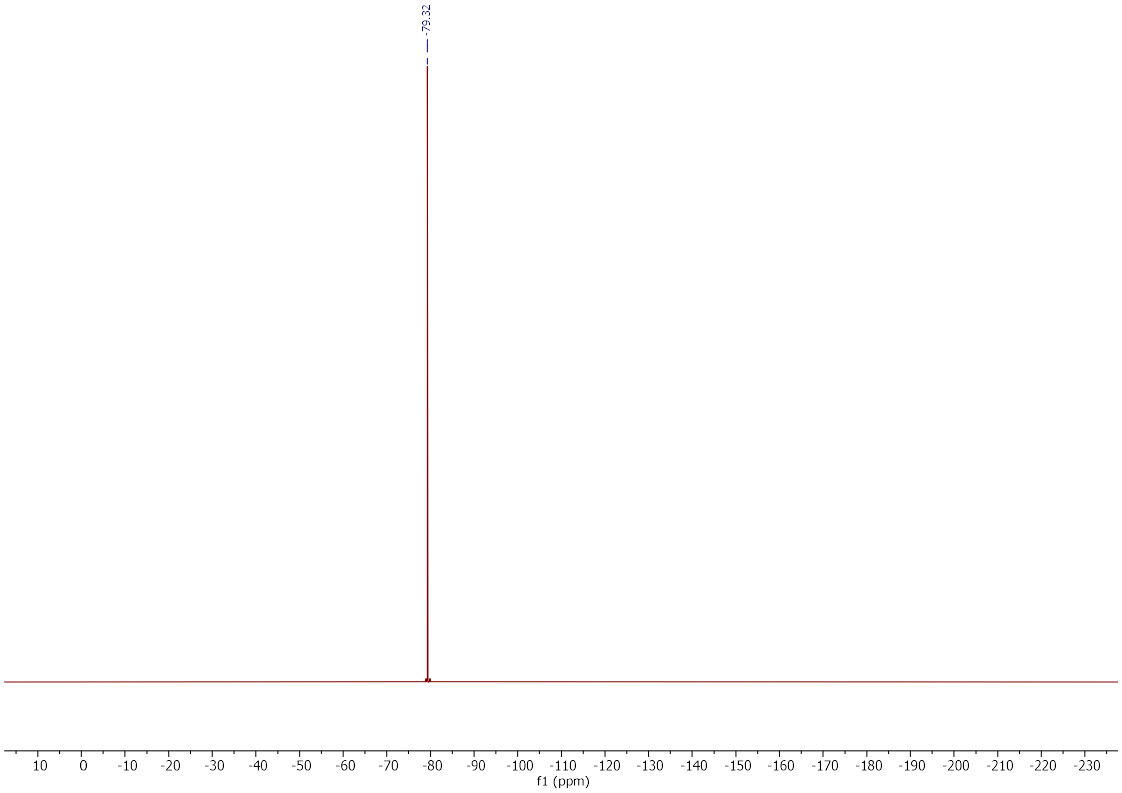

5,5'-({[Naphthalene-1,4-diylbis(methylene)]bis(oxy)}bis[5-(*tert*-butyl)-2,1-phenylene])bis(5*H*-dibenzo[*b*,*d*]-thiophen-5-ium) Bis(trifluoromethanesulfonate) (**470s**)

^{1}H NMR (600 MHz, CD_3CN)

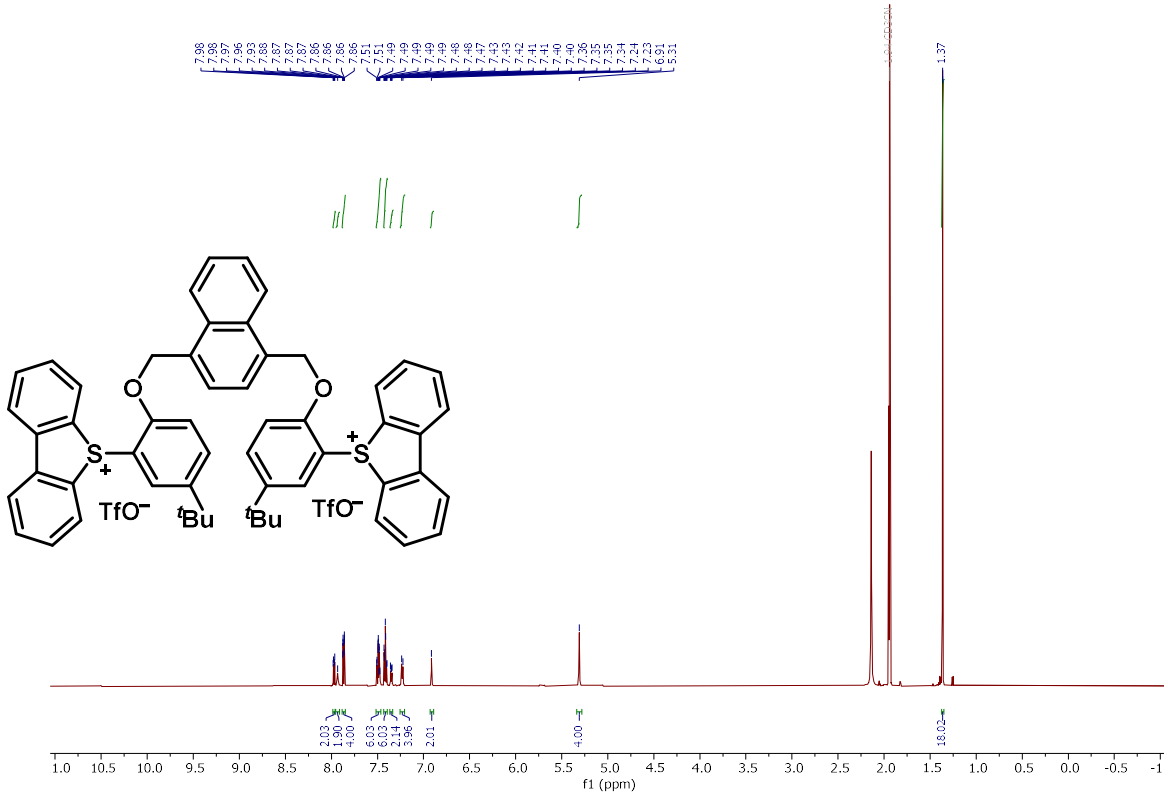

^{13}C{H} NMR (101 MHz, CD_3CN)

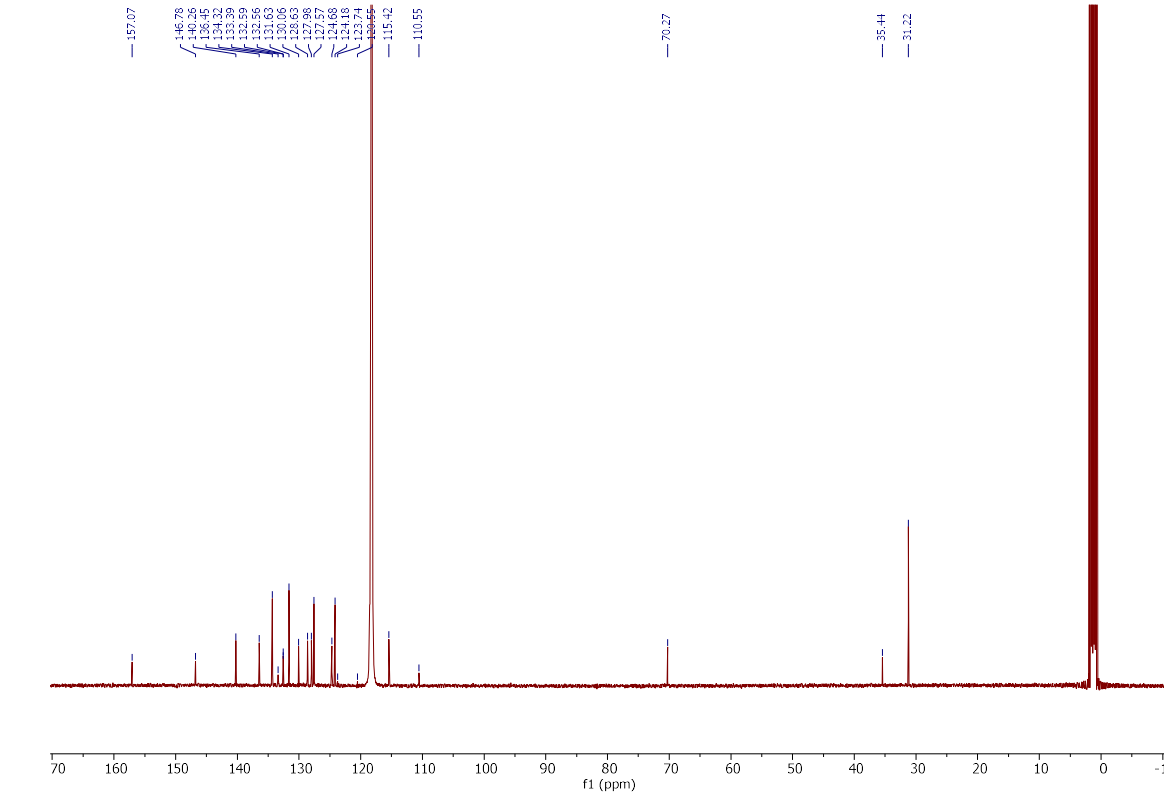

^{19}F NMR (565 MHz, CD_3CN)

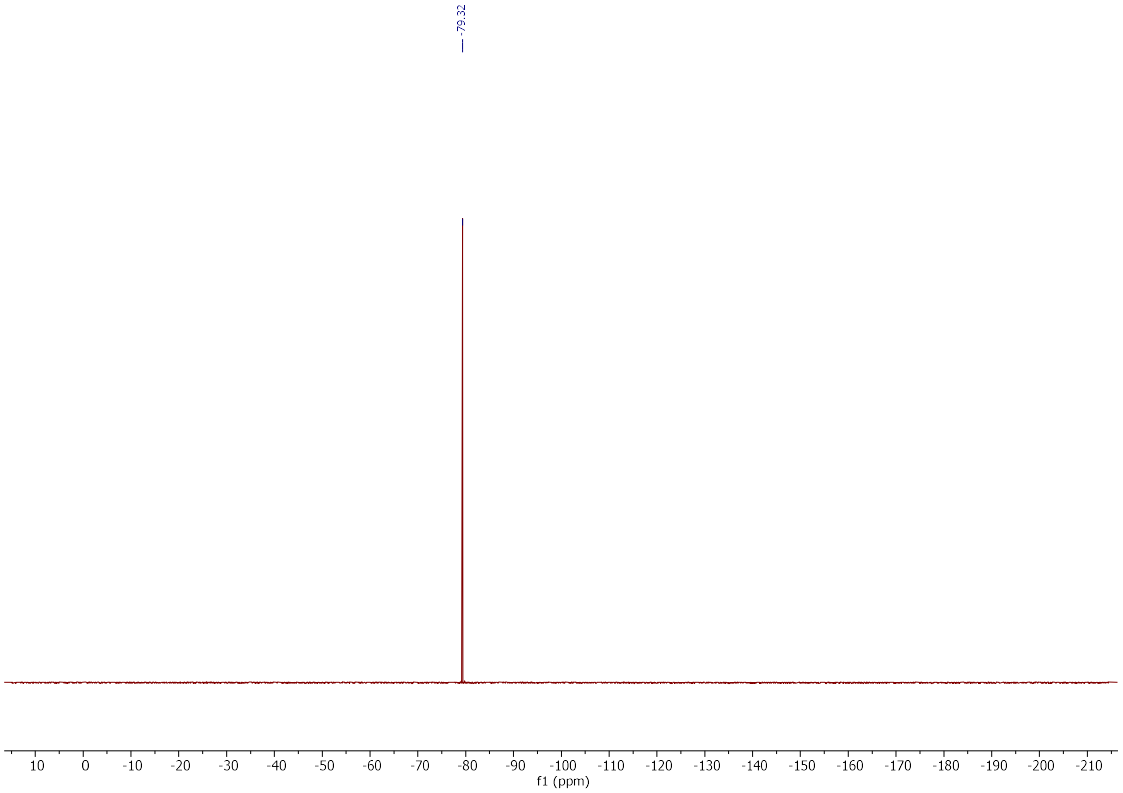

5,5'-([{[1,1'-Biphenyl]-2,2'-diylbis(methylene)}bis(oxy)]bis[5-(*tert*-butyl)-2,1-phenylene])bis(5*H*-dibenzo-[*b*,*d*]thiophen-5-ium) Bis(trifluoromethanesulfonate) (**470t**)

^{1}H NMR (300 MHz, CD_3CN)

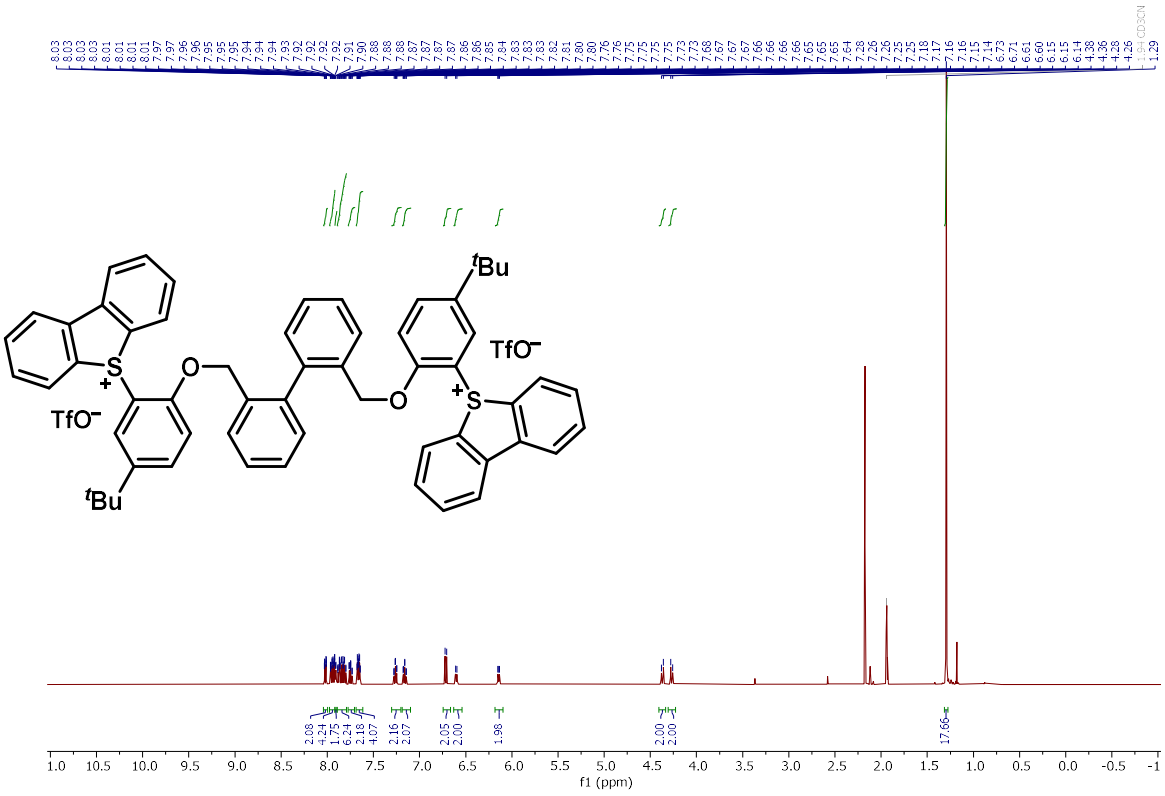

^{13}C{H} NMR (126 MHz, CD_3CN)

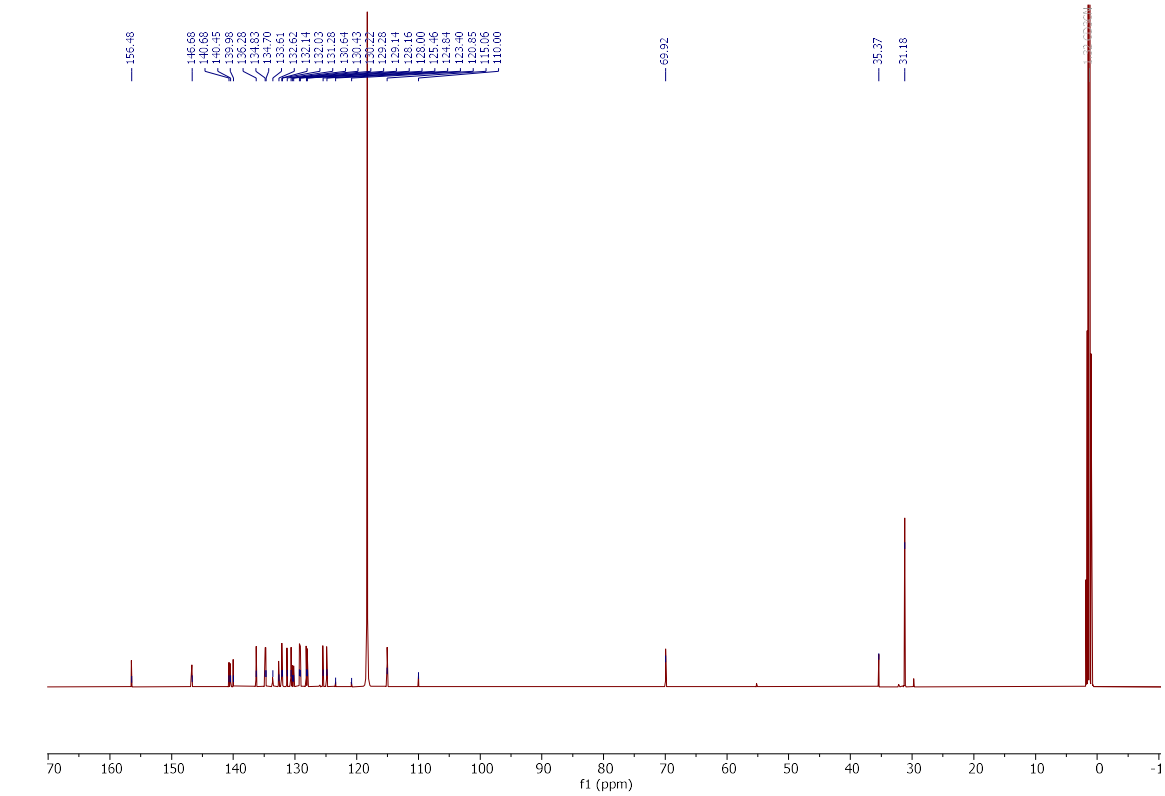

^{19}F NMR (282 MHz, CD_3CN)

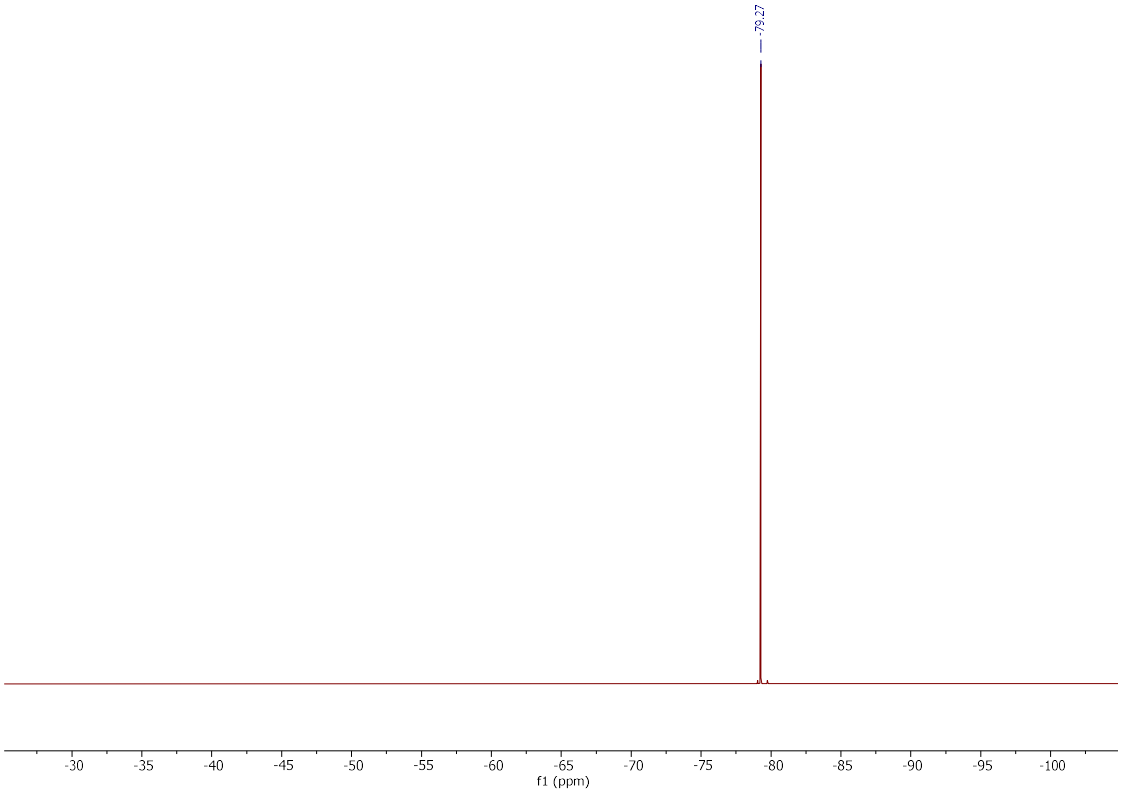

5,5'-{[{[Ethane-1,2-diylbis(4,1-phenylene)]bis(methylene)}bis(oxy)]bis(5-methyl-2,1-phenylene)}bis(5*H*-dibenzo[*b*,*d*]thiophen-5-ium) Bis(trifluoromethanesulfonate) (**470u**)

^{1}H NMR (400 MHz, CD_3CN)

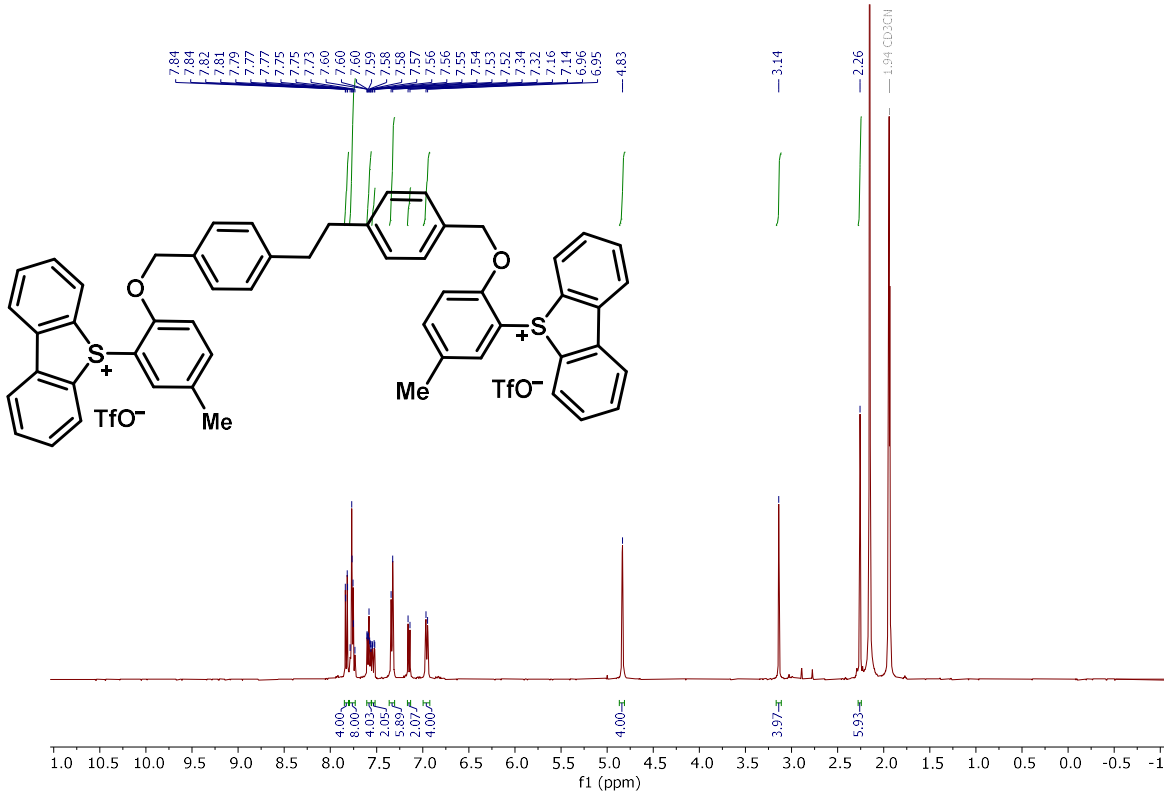

^{13}C{H} NMR (101 MHz, CD_3CN)

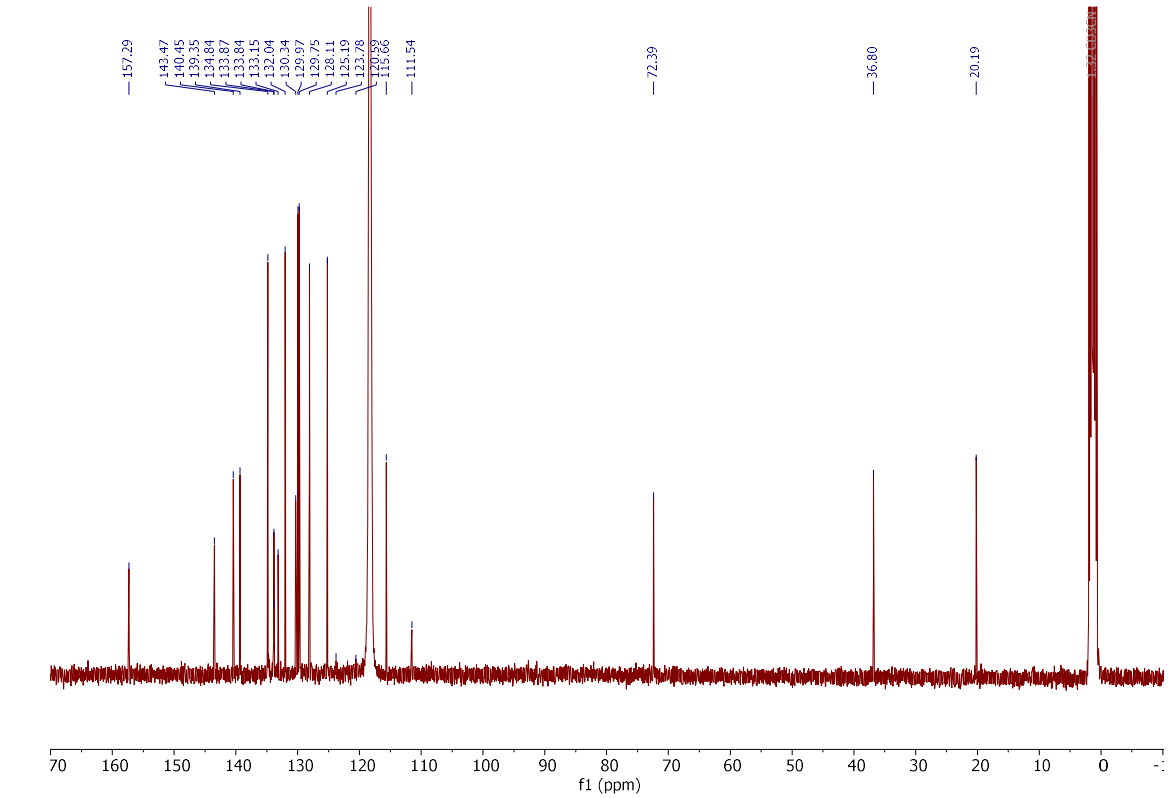

^{19}F NMR (282 MHz, CD_3CN)

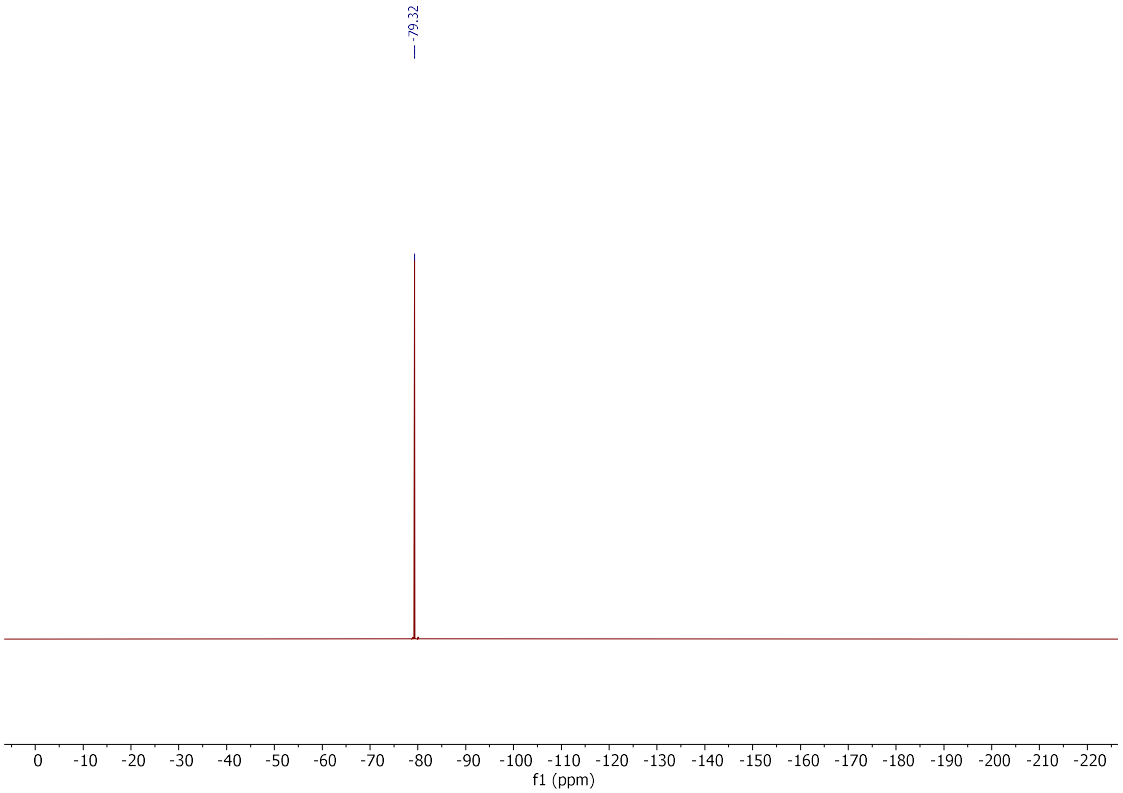

5-(2-(benzoyloxy)-5-(tert-butyl)phenyl)-5H-dibenzo[b,d]thiophen-5-ium trifluoromethanesulfonate (**470v**)

^{1}H NMR (300 MHz, CD_3CN)

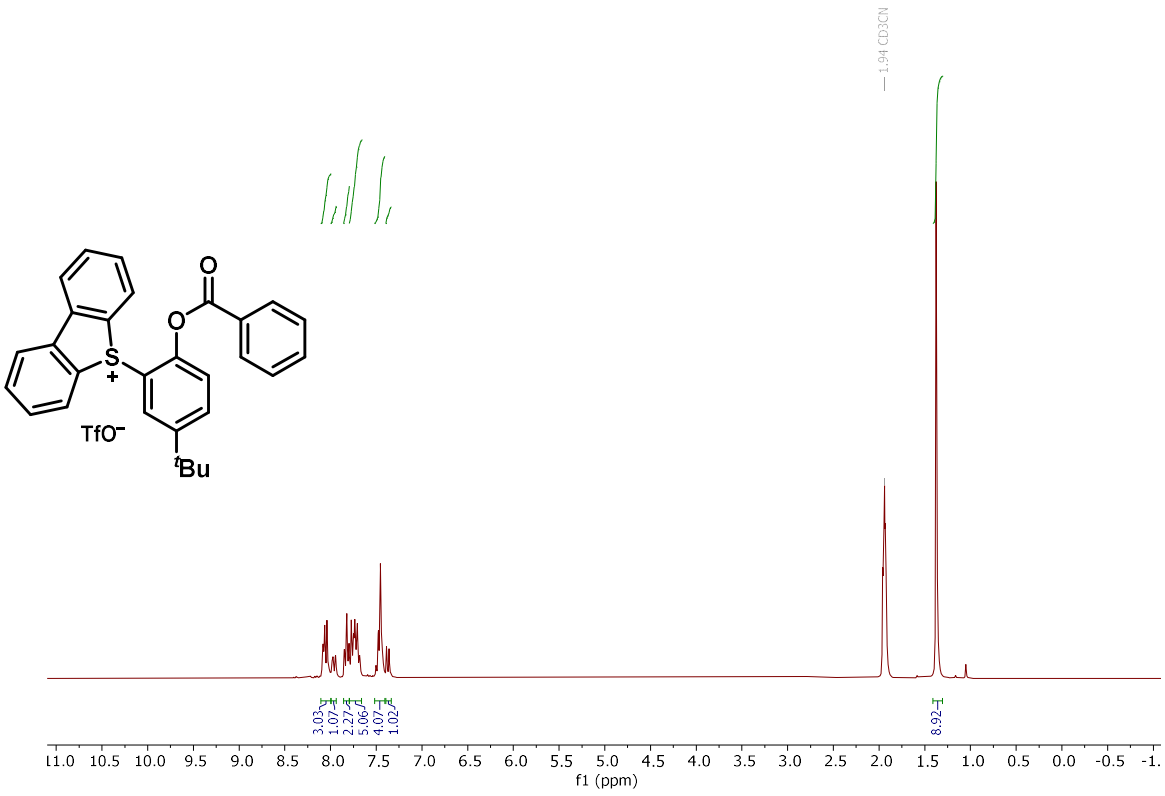

^{13}C NMR (75 MHz, CD_3CN)

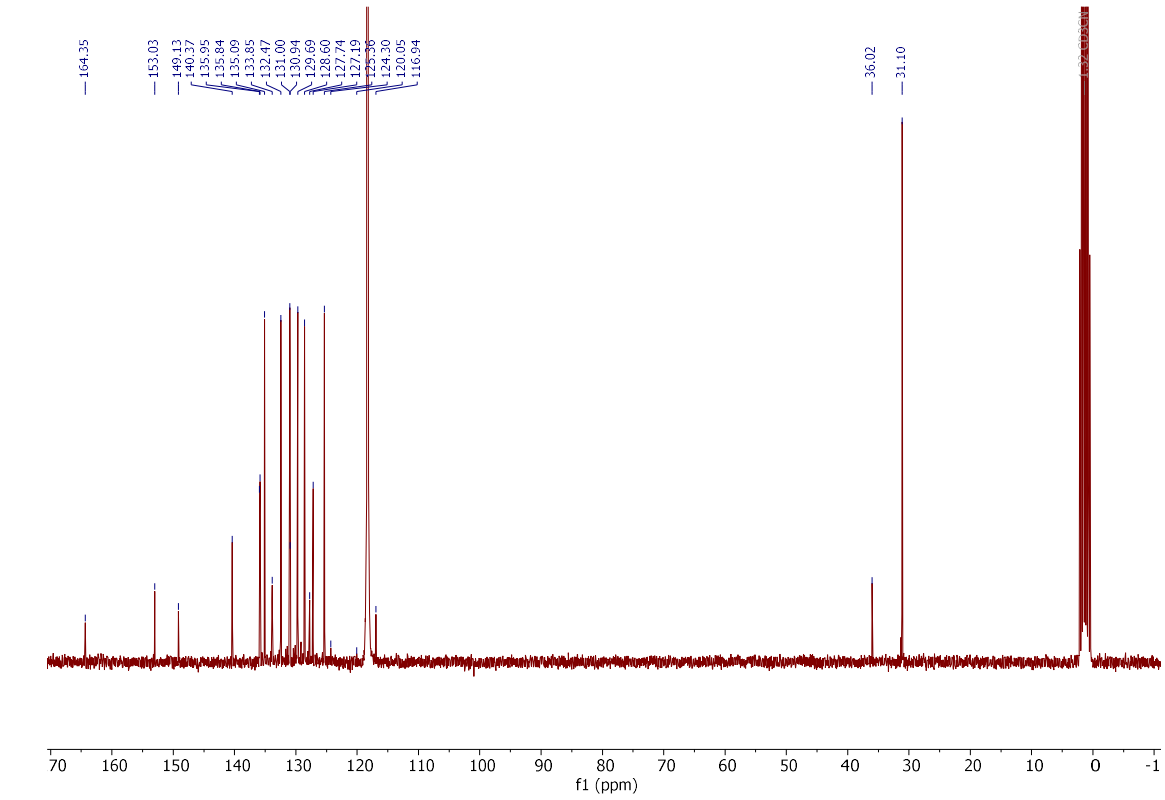

^{19}F NMR (282 MHz, CD_3CN)

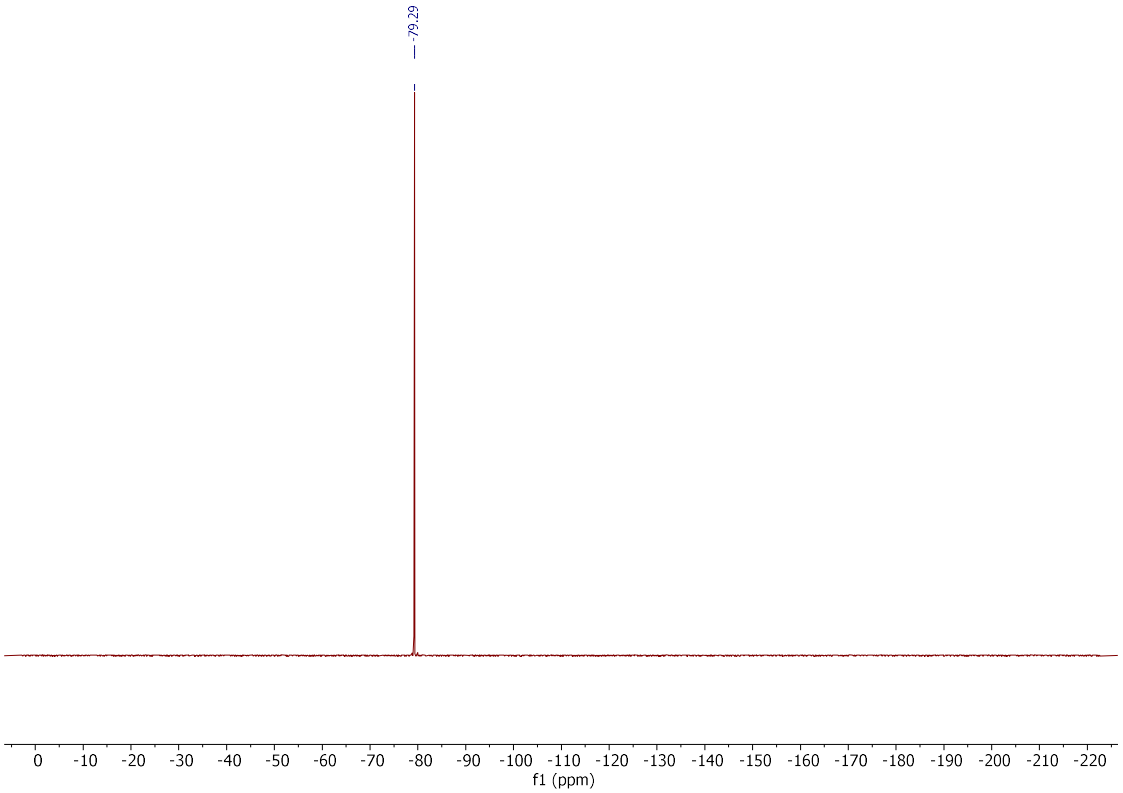

6H-Benzo[*c*]chromenes:

(3*S*,4'*s*)-4'-{(3*S*,4'*s*)-4',5-Dimethyl-2*H*-spiro[benzofuran-3,1'-cyclohexane]-2',5'-dien-4'-yl}-4',5-dimethyl-2*H*-spiro[benzofuran-3,1'-cyclohexane]-2',5'-diene (**471a'**)

^{1}H NMR (400 MHz, $CDCl_3$)

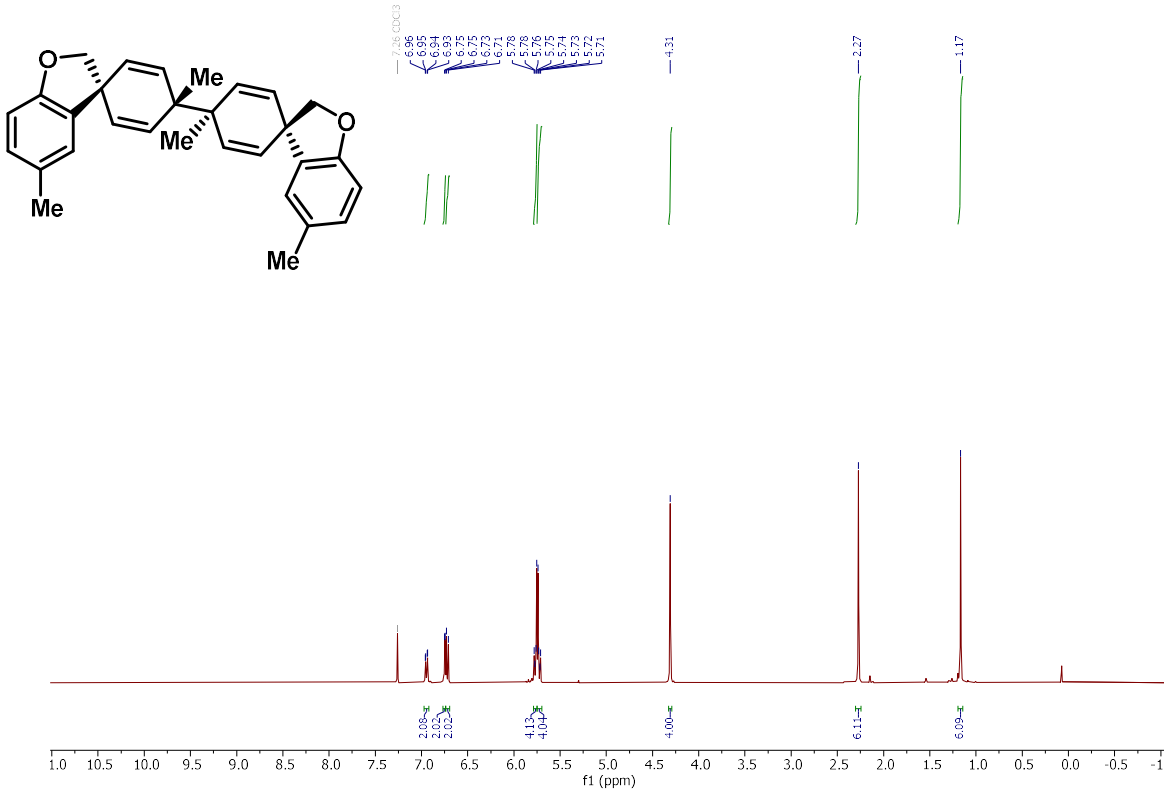

^{13}C{H} NMR (101 MHz, $CDCl_3$)

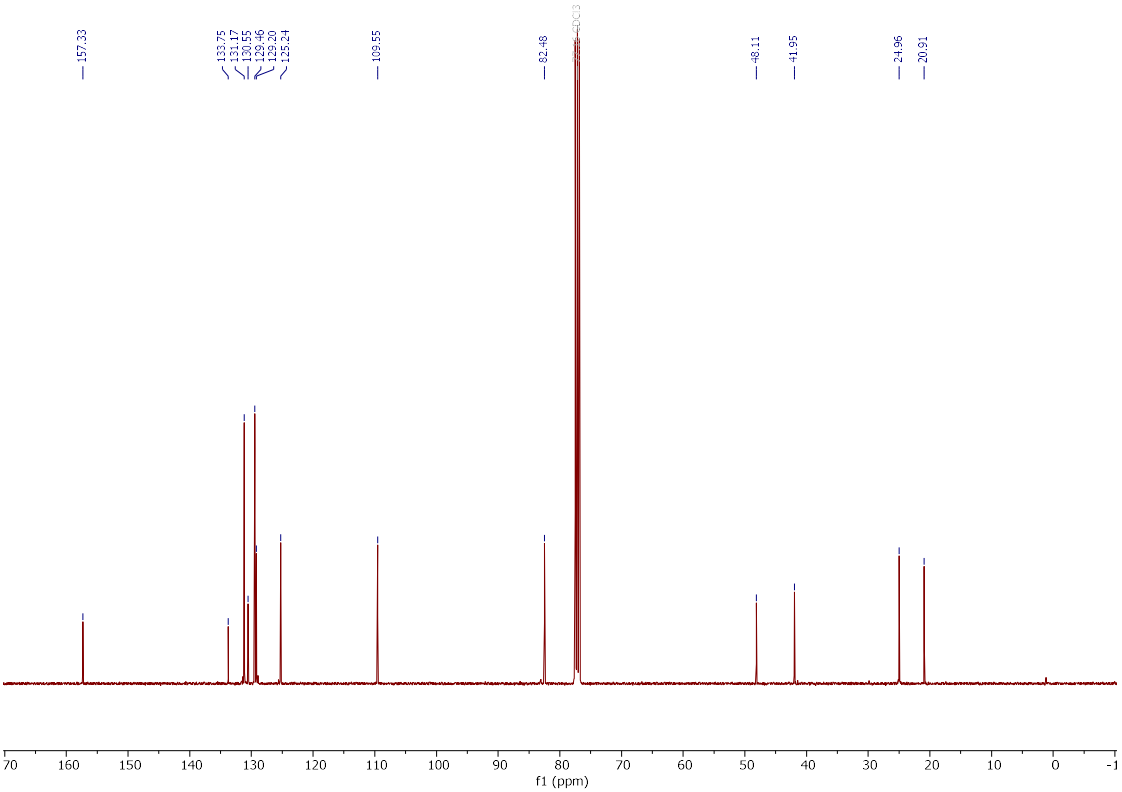

2,9-Di-*tert*-butyl-6*H*-benzo[*c*]chromene (**471b**)

^{1}H NMR (300 MHz, $CDCl_3$)

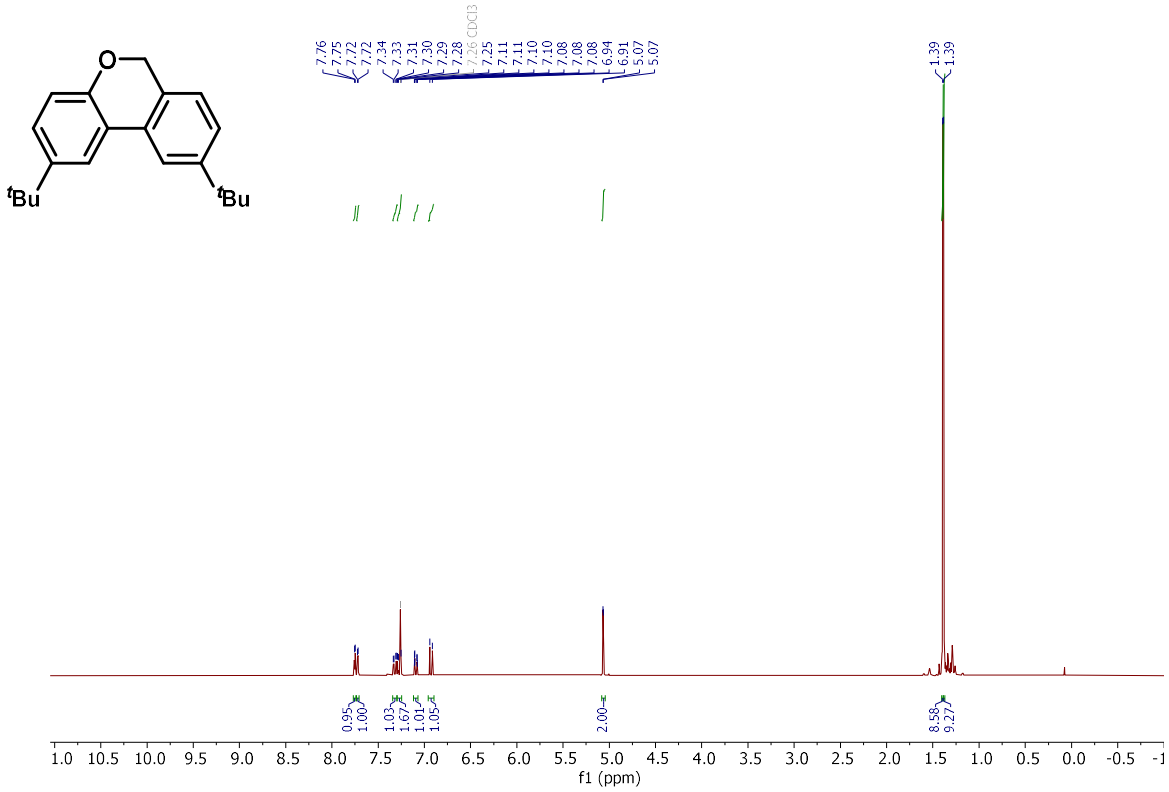

^{13}C{H} NMR (101 MHz, $CDCl_3$)

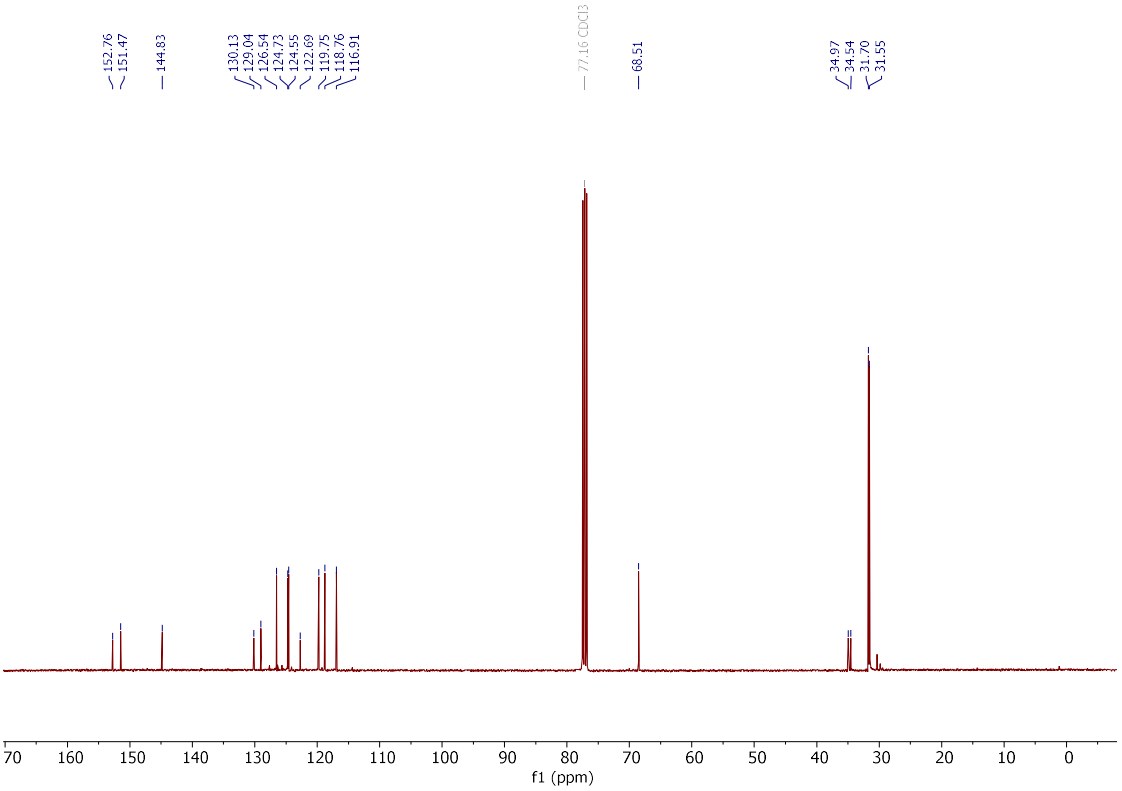

9-Fluoro-2-methyl-6*H*-benzo[*c*]chromene (**471d**)

^{1}H NMR (300 MHz, $CDCl_3$)

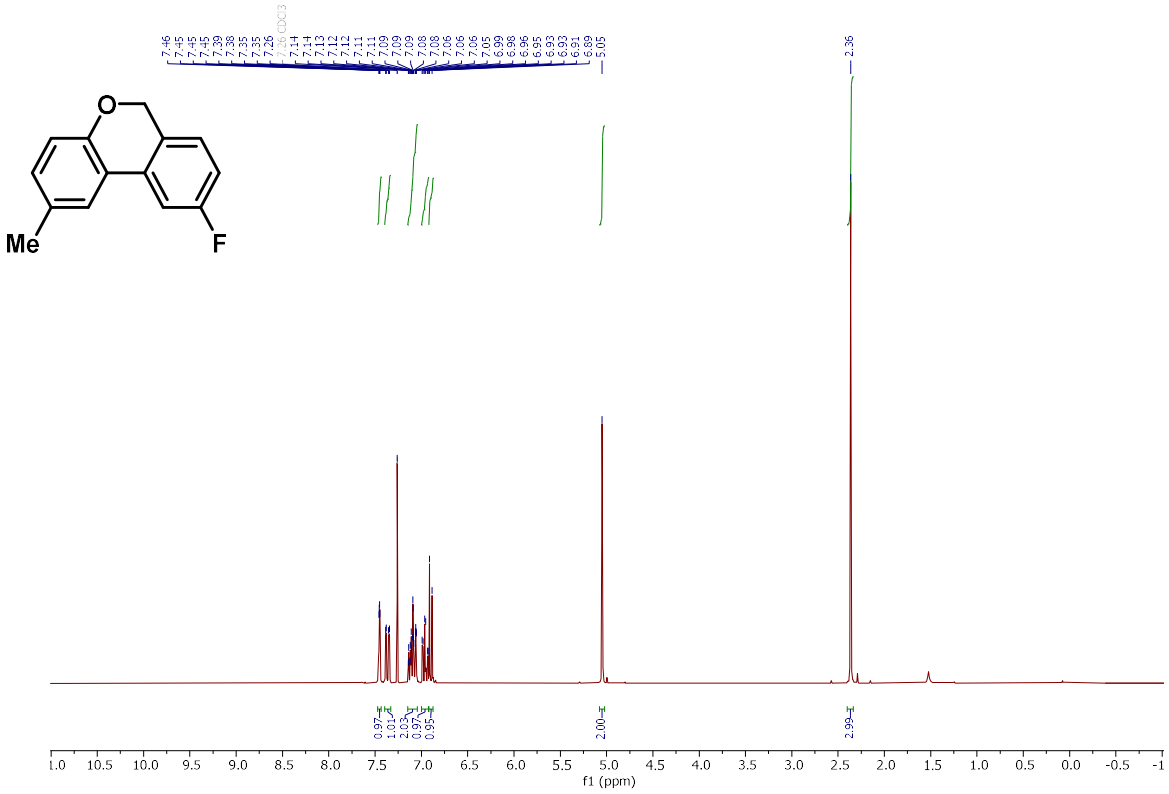

^{13}C{H} NMR (101 MHz, $CDCl_3$)

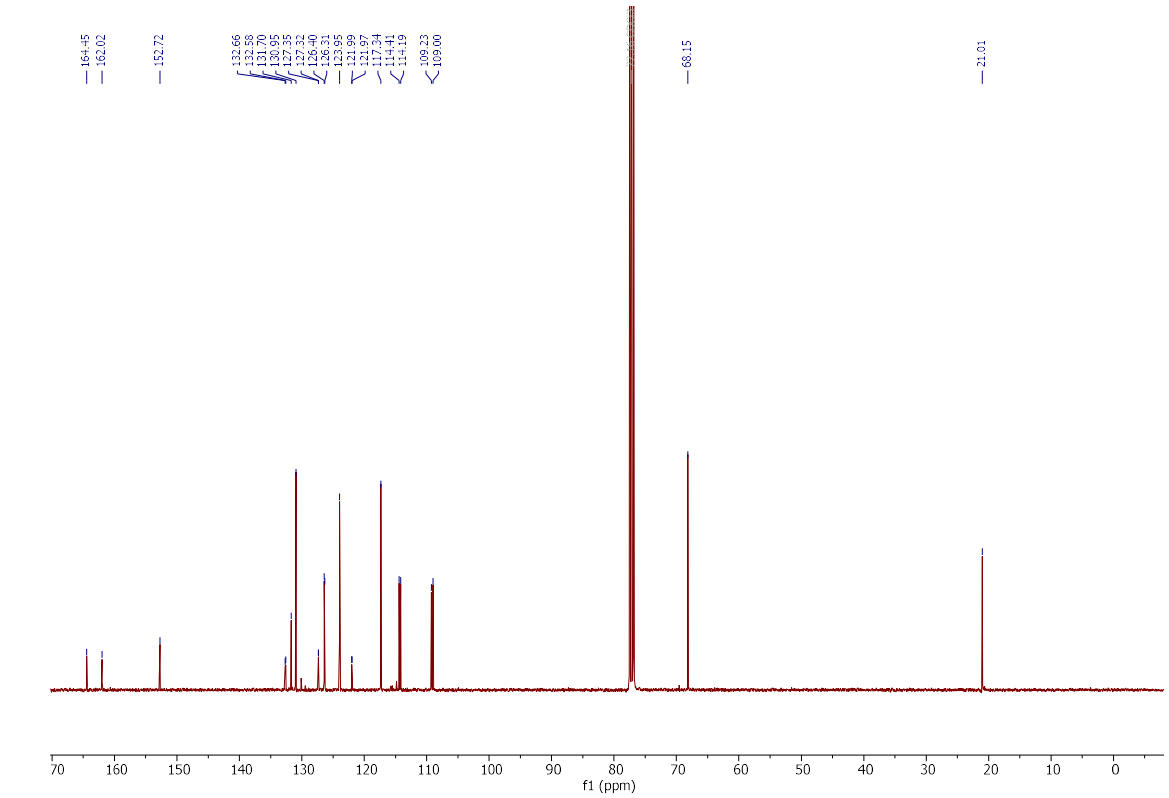

^{19}F NMR (282 MHz, $CDCl_3$)

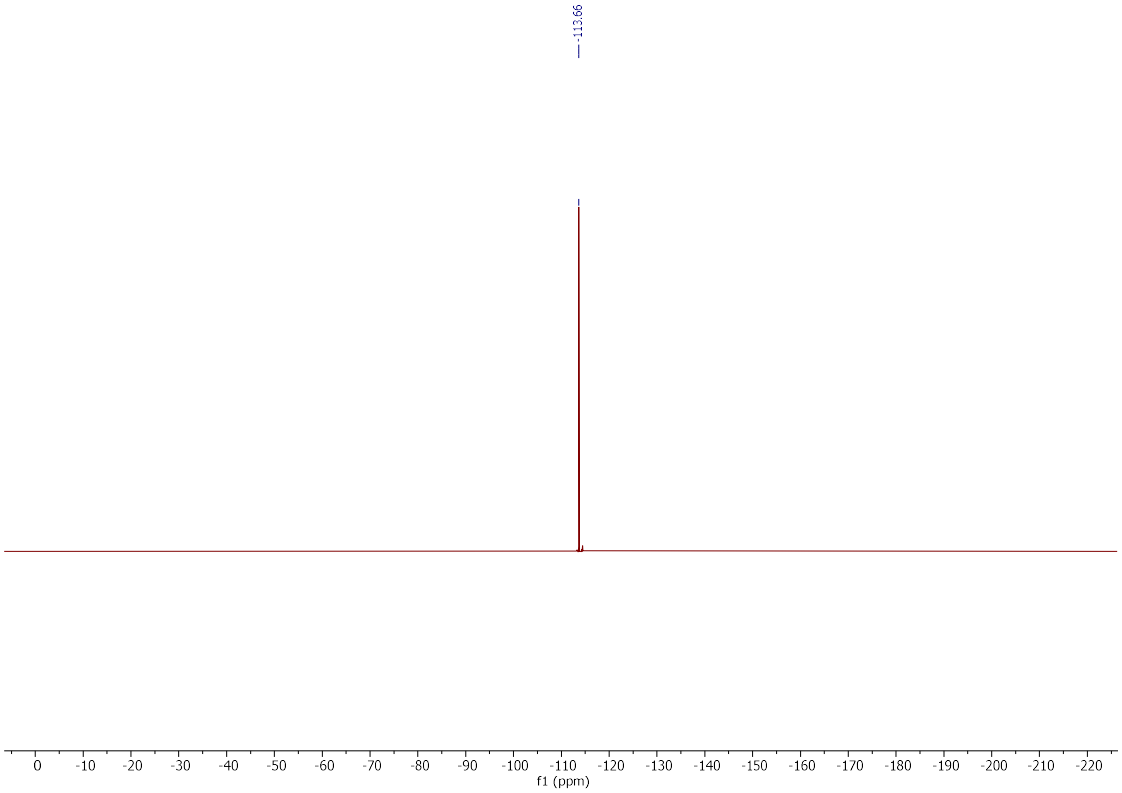

2-(*tert*-Butyl)-8,10-dichloro-6*H*-benzo[*c*]chromene (**471e**)

^{1}H NMR (300 MHz, $CDCl_3$)

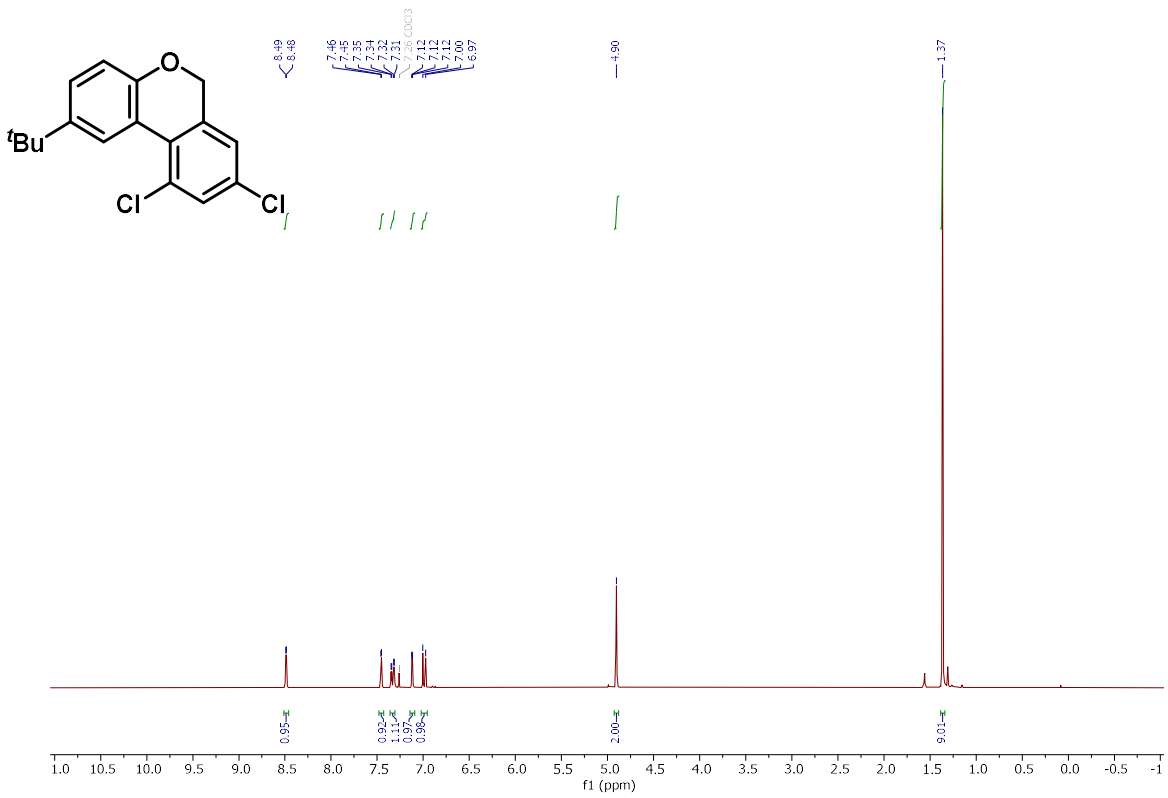

^{13}C{H} NMR (101 MHz, $CDCl_3$)

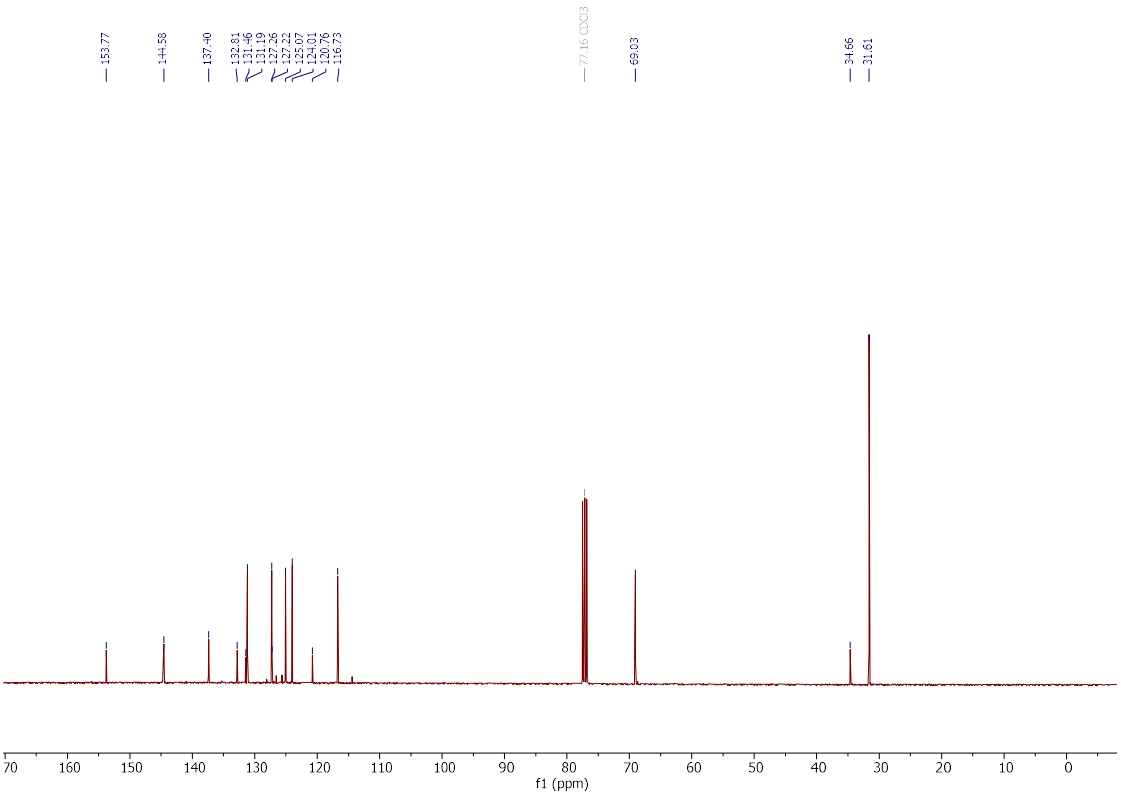

2-(*tert*-Butyl)-9-(methylsulfonyl)-6*H*-benzo[*c*]chromene (**471f**)

^{1}H NMR (300 MHz, $CDCl_3$)

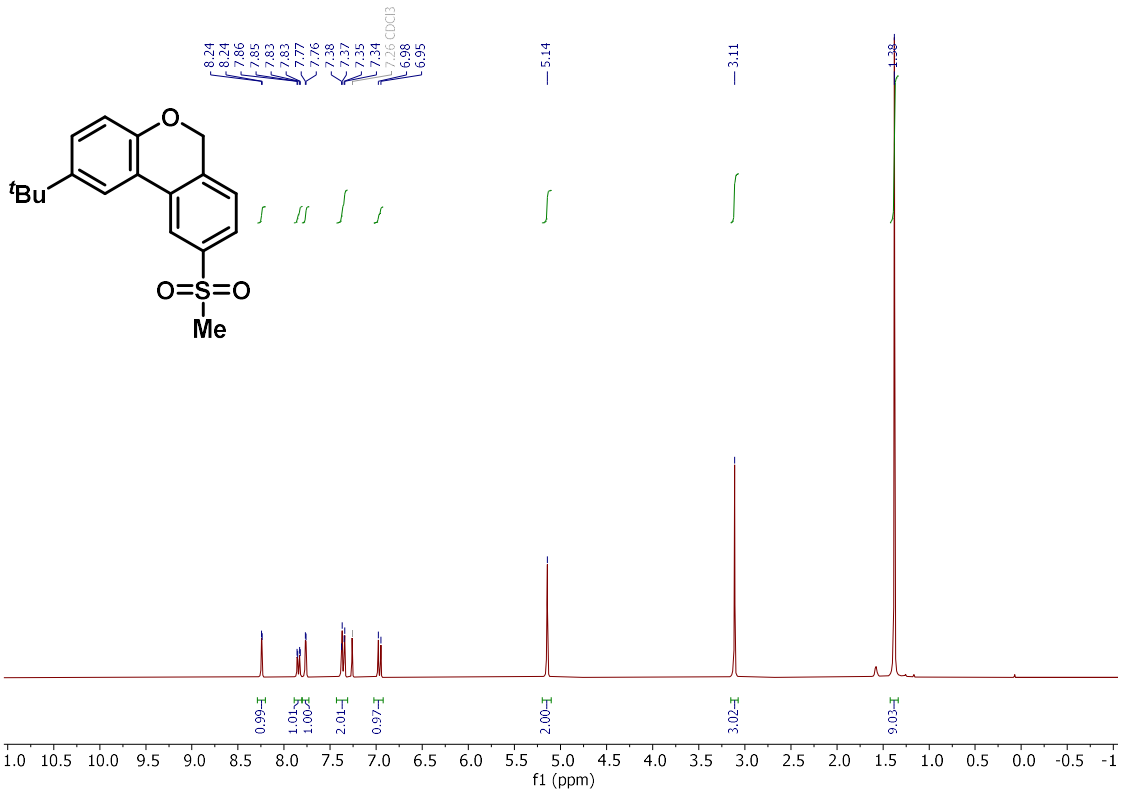

^{13}C{H} NMR (75 MHz, $CDCl_3$)

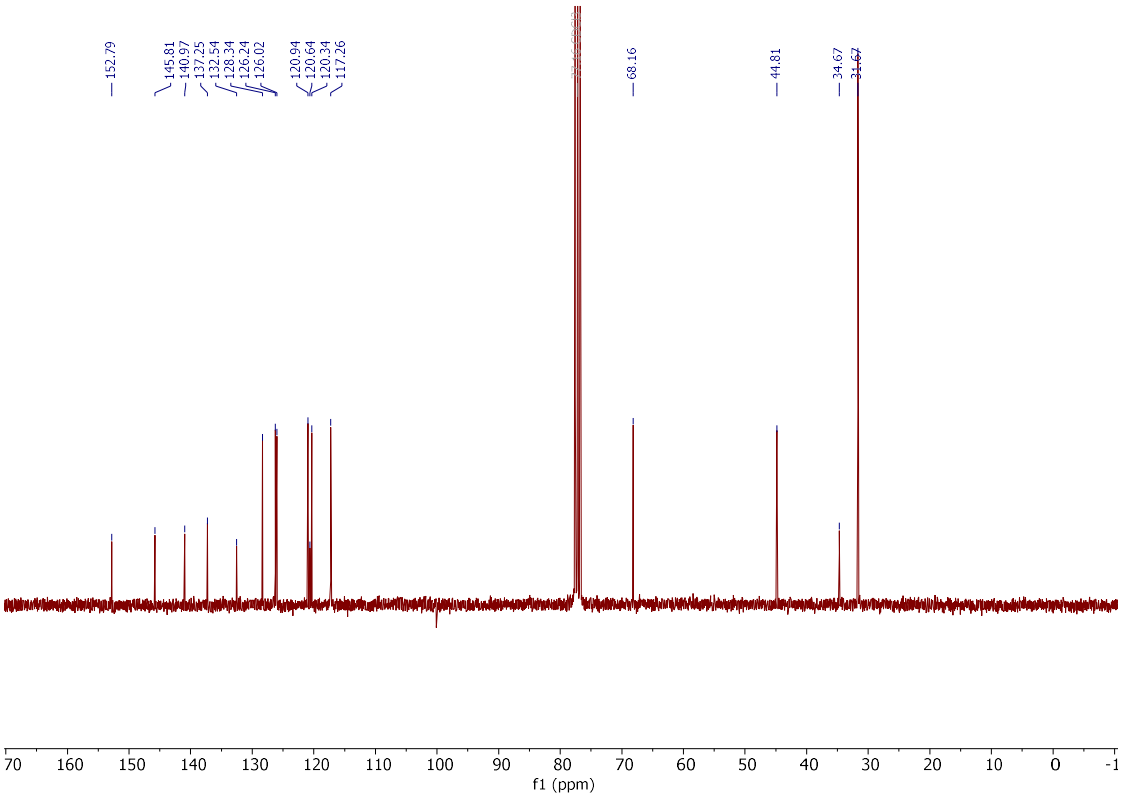

2-(*tert*-Butyl)-8-(methylsulfonyl)-6*H*-benzo[*c*]chromene (**471f'**)

^{1}H NMR (300 MHz, $CDCl_3$)

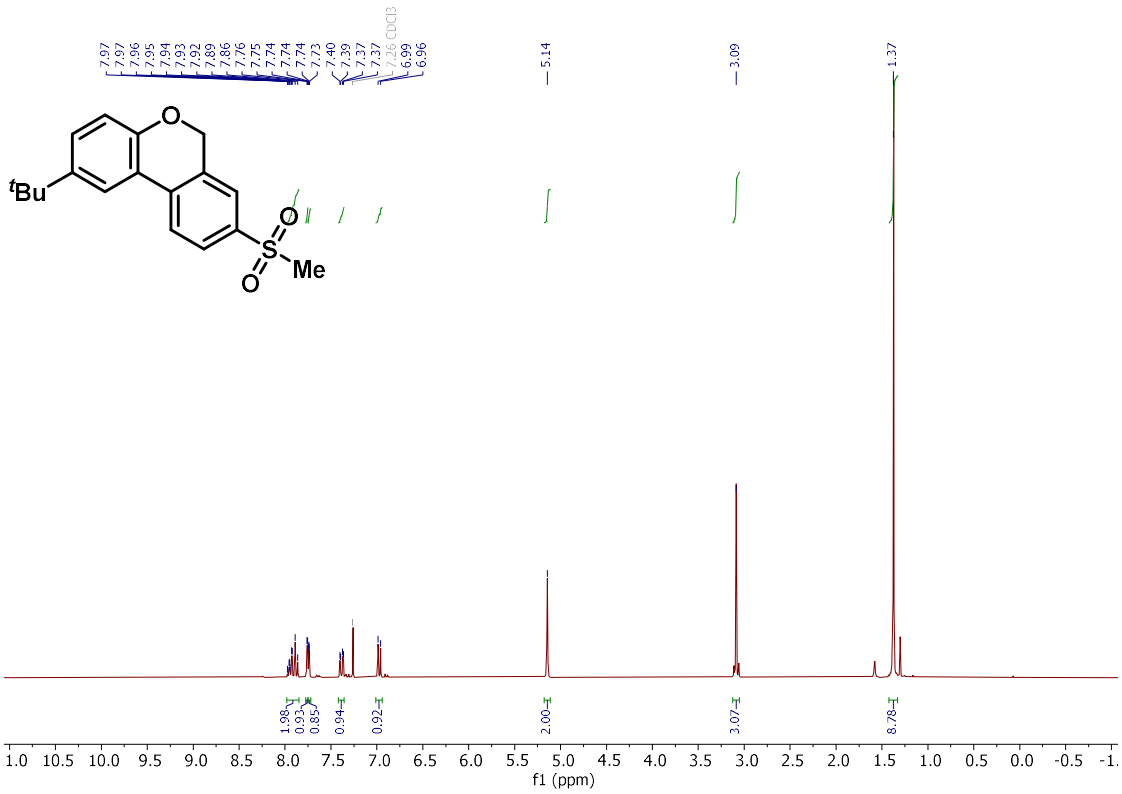

^{13}C{H} NMR (75 MHz, $CDCl_3$)

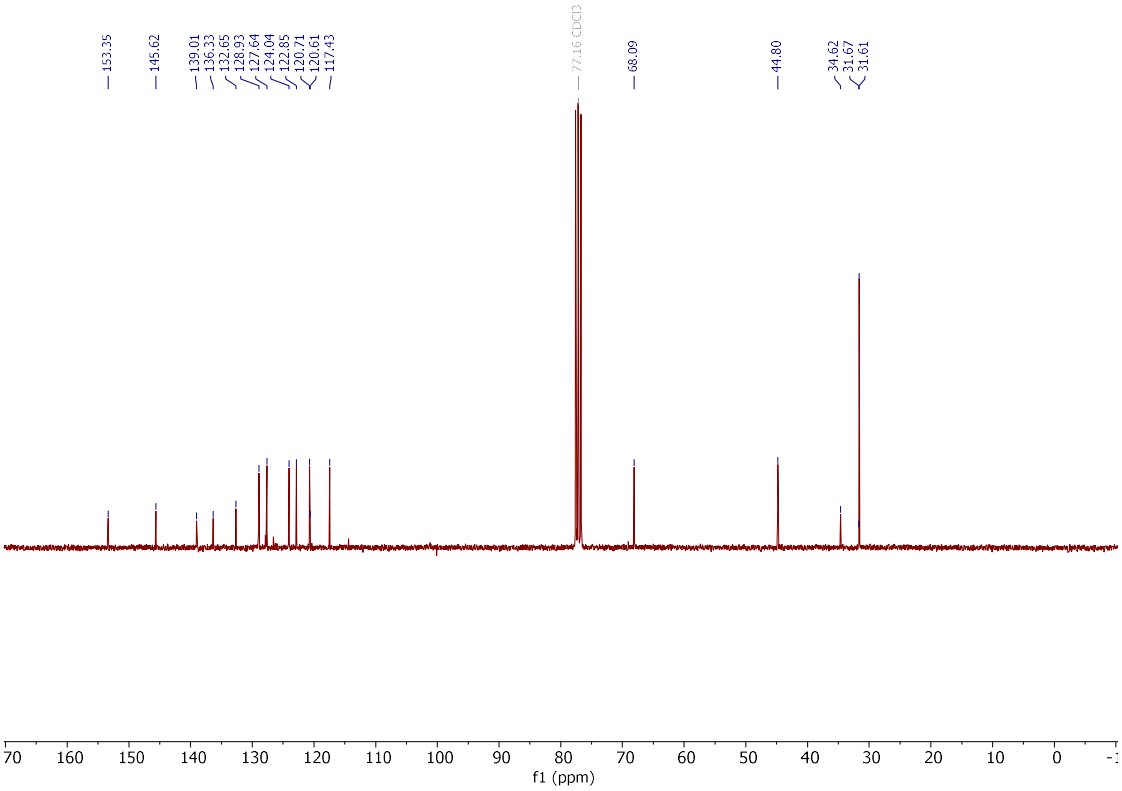

8,9,10-Trimethyl-5*H*-naphtho[1,2-*c*]chromene (**471g**)

^{1}H NMR (300 MHz, $CDCl_3$)

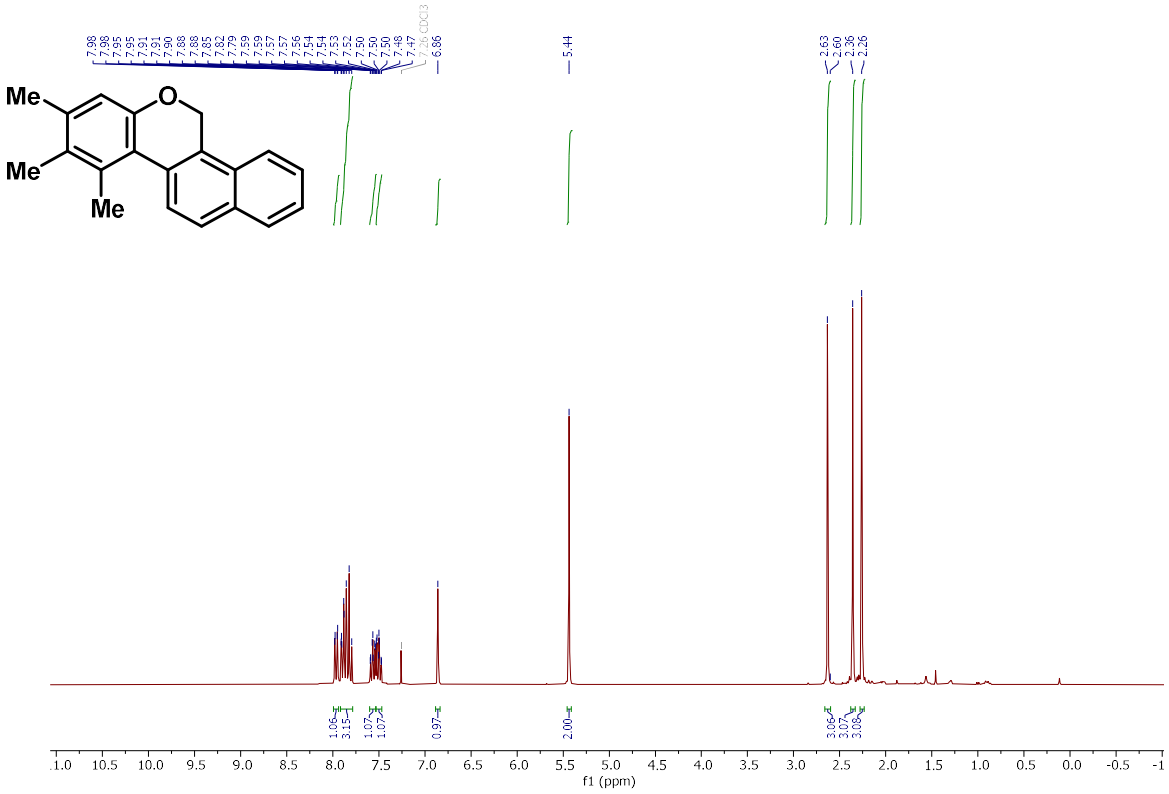

^{13}C{H} NMR (75 MHz, $CDCl_3$)

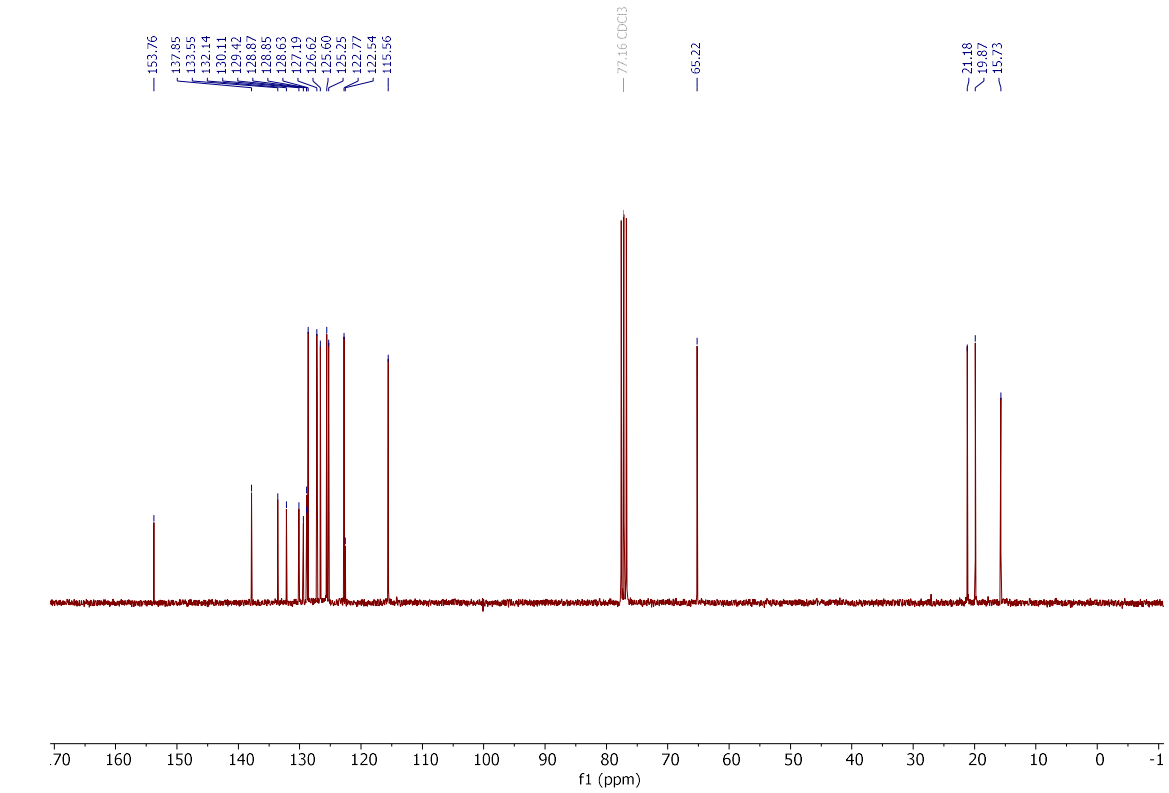

2-(*tert*-Butyl)-9-(trifluoromethyl)-6*H*-benzo[*c*]chromene (**471h**)

^{1}H NMR (400 MHz, $CDCl_3$)

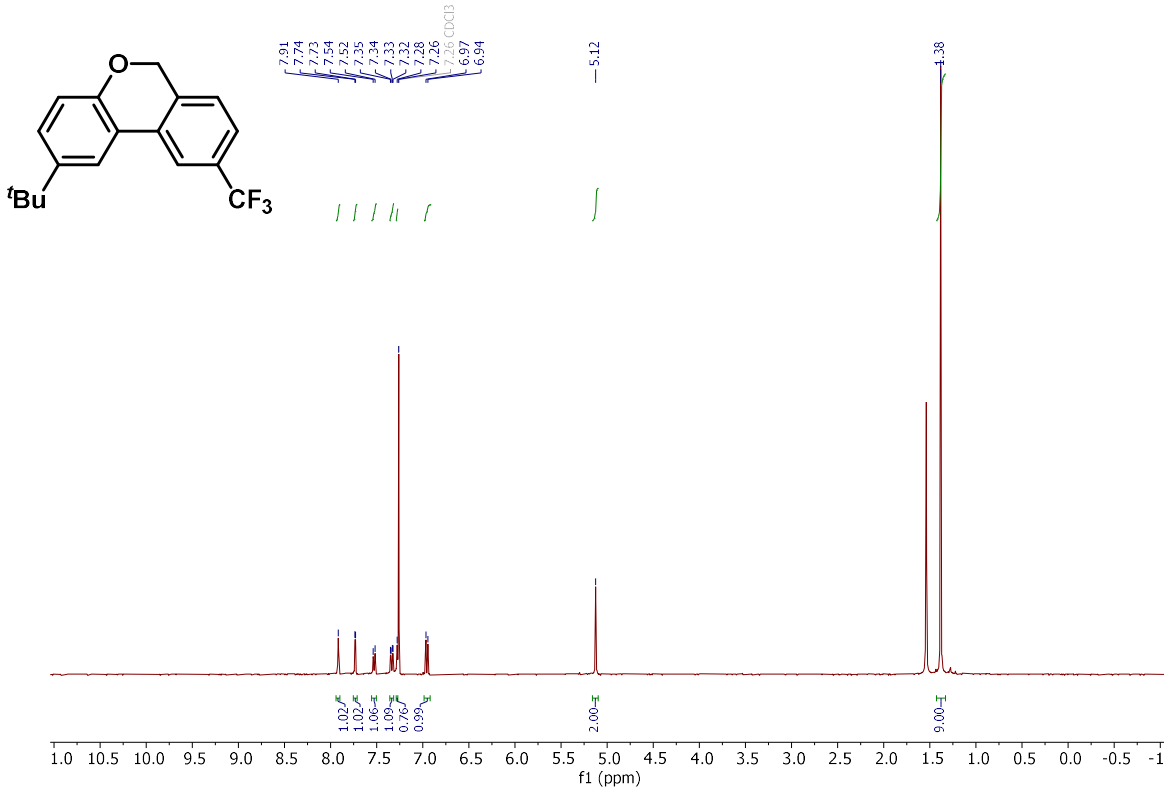

^{13}C{H} NMR (101 MHz, $CDCl_3$)

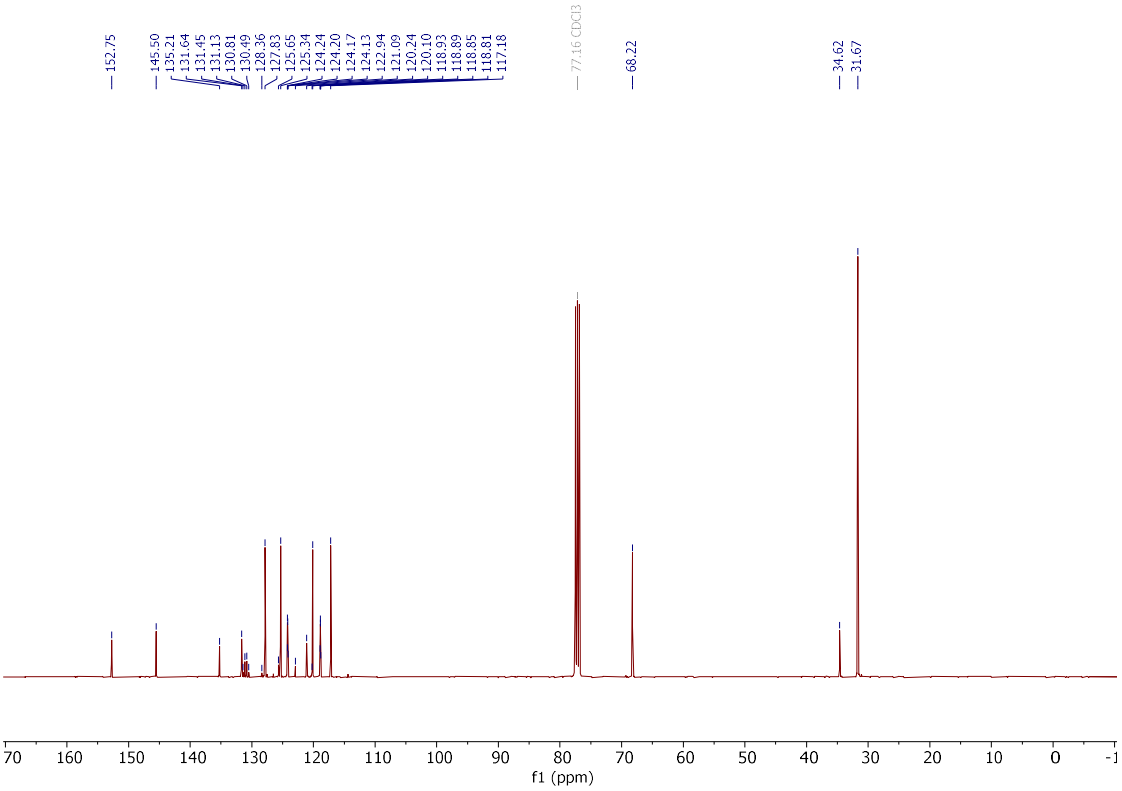

^{19}F NMR (282 MHz, $CDCl_3$)

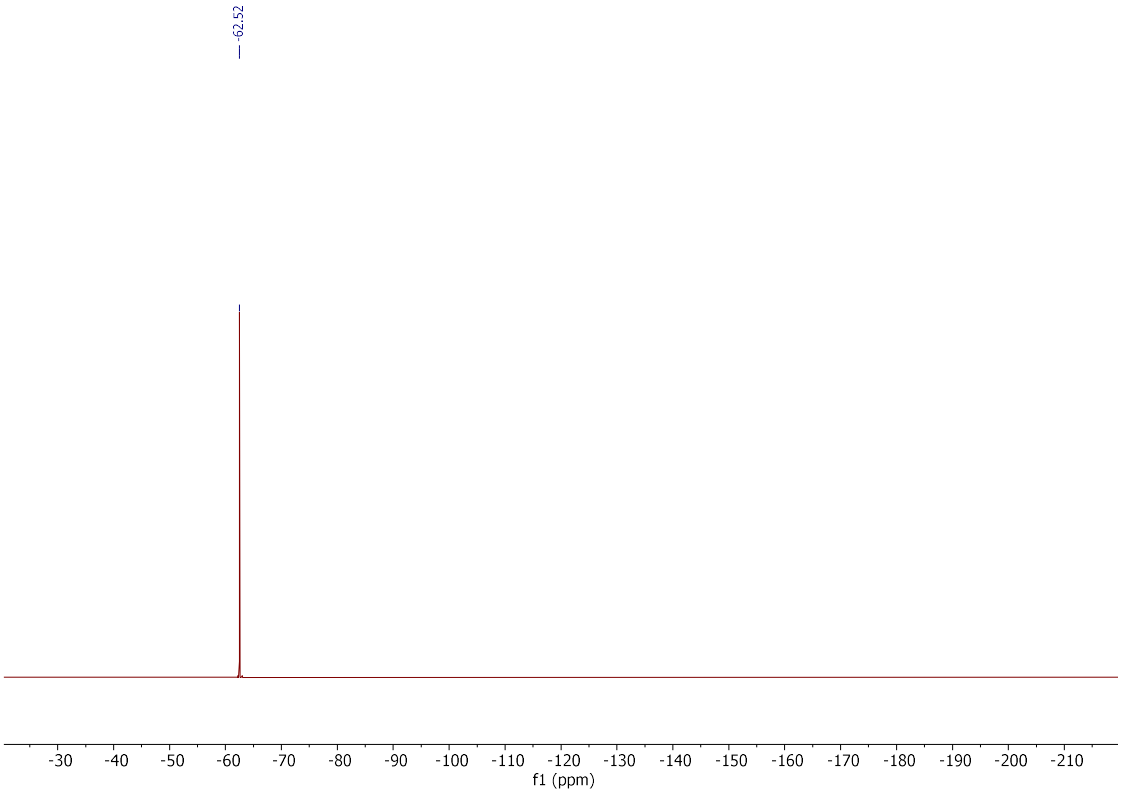

2,8,10-trichloro-6H-benzo[c]chromene (**471i**)

^{1}H NMR (300 MHz, $CDCl_3$)

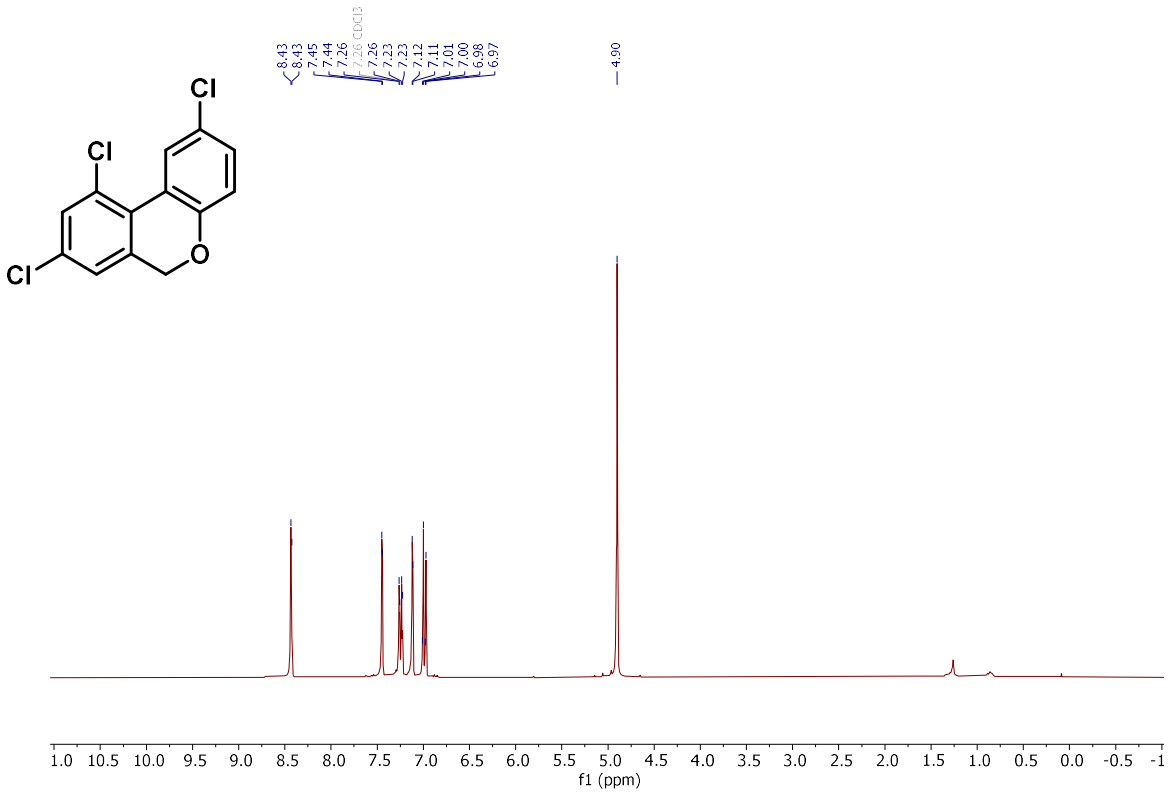

^{13}C{H} NMR (75 MHz, $CDCl_3$)

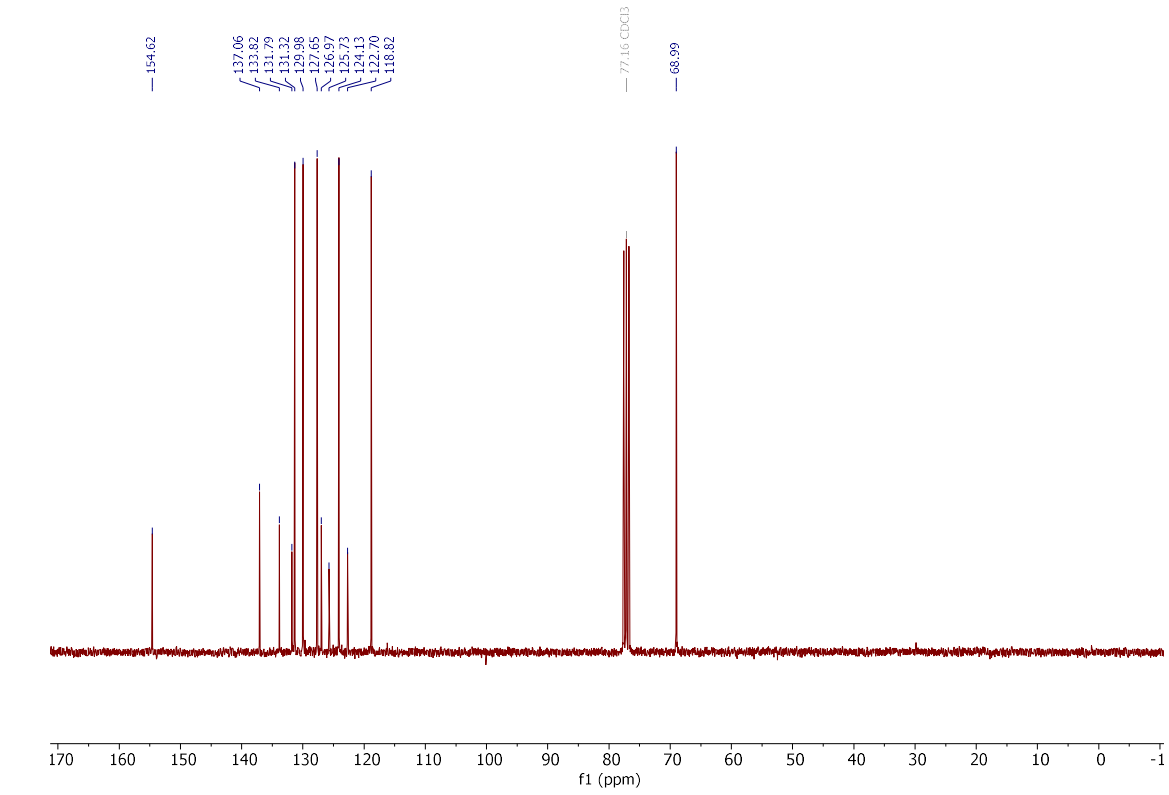

5-Methyl-1'*H*,2*H*-spiro[benzofuran-3,4'-pyridin]-1'-oxyl (**471k'**)

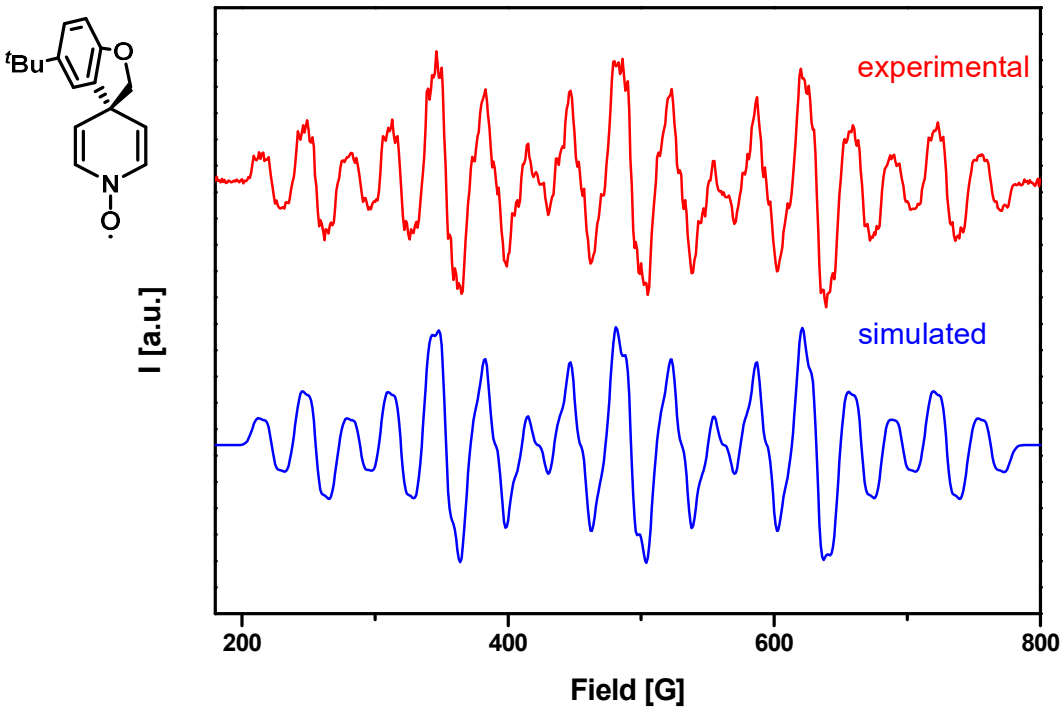

5-(*tert*-Butyl)-2',6'-dimethyl-[1,1'-biphenyl]-2-ol (**471l**)

^{1}H NMR (300 MHz, $CDCl_3$)

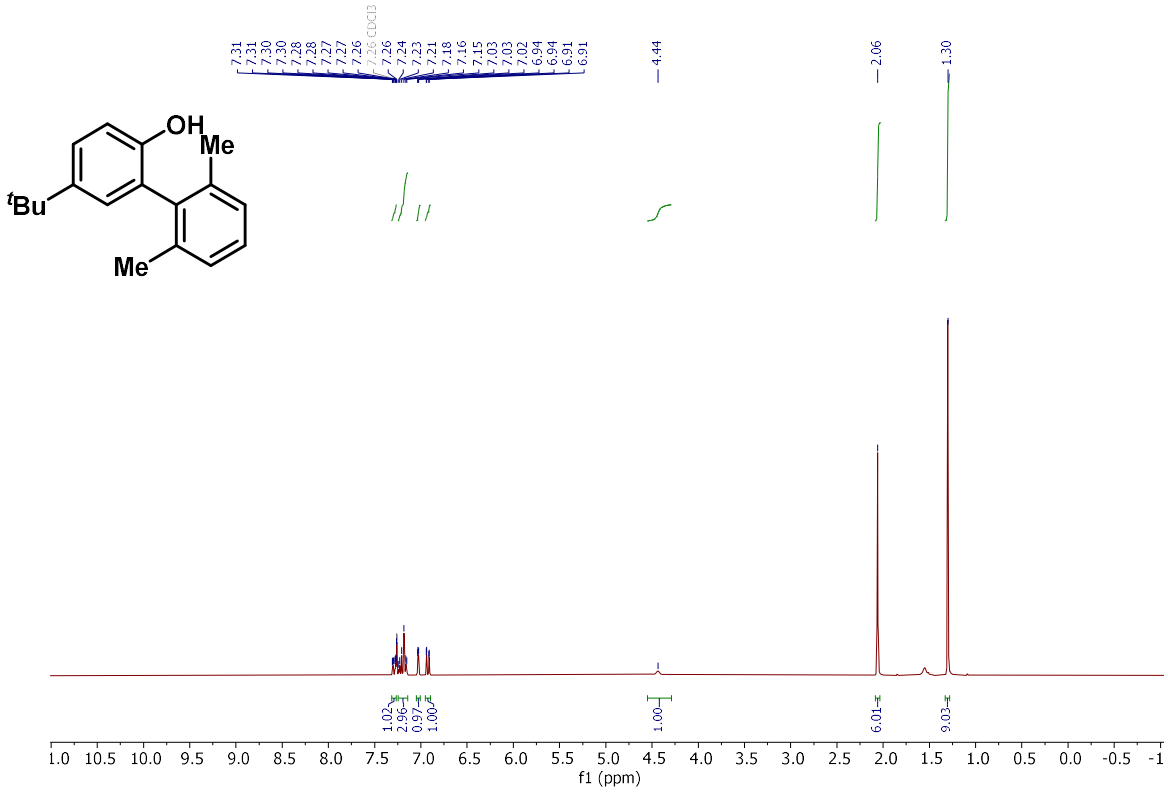

^{13}C{H} NMR (101 MHz, $CDCl_3$)

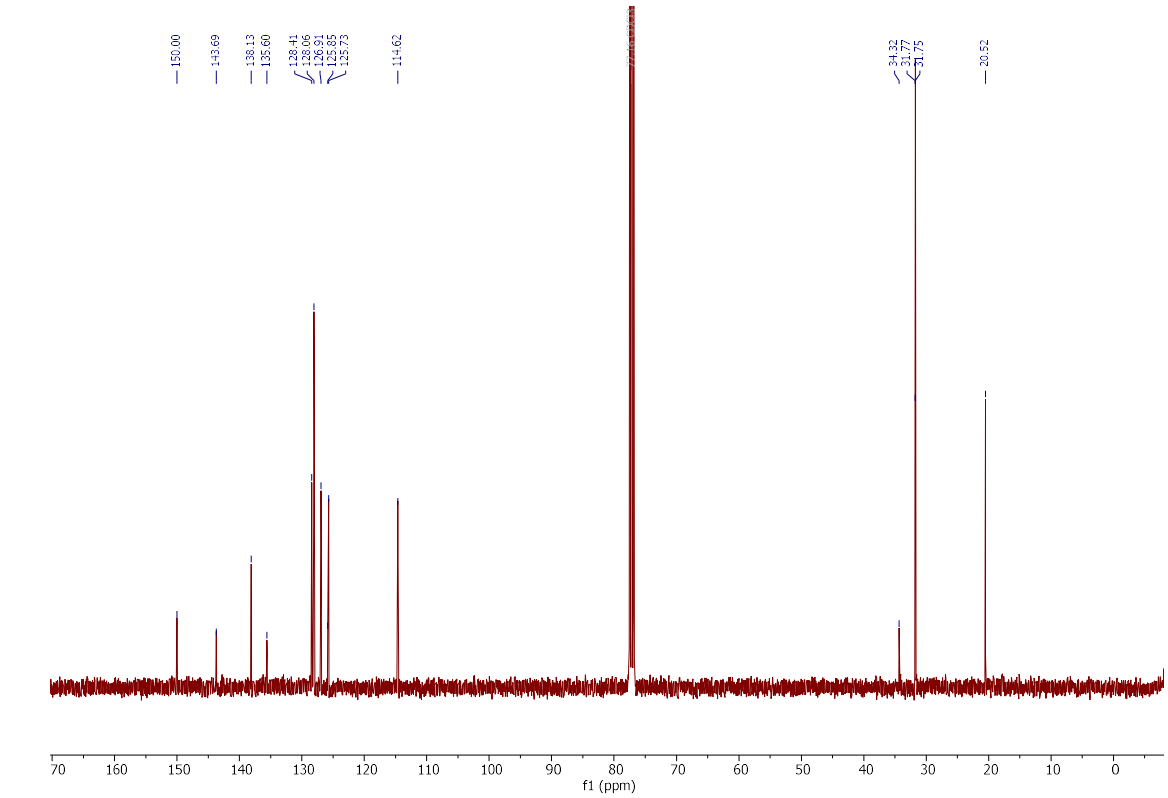

5-(*tert*-Butyl)-2-(methoxymethoxy)-2',6'-dimethyl-1,1'-biphenyl (**471l'**)

^{1}H NMR (400 MHz, $CDCl_3$)

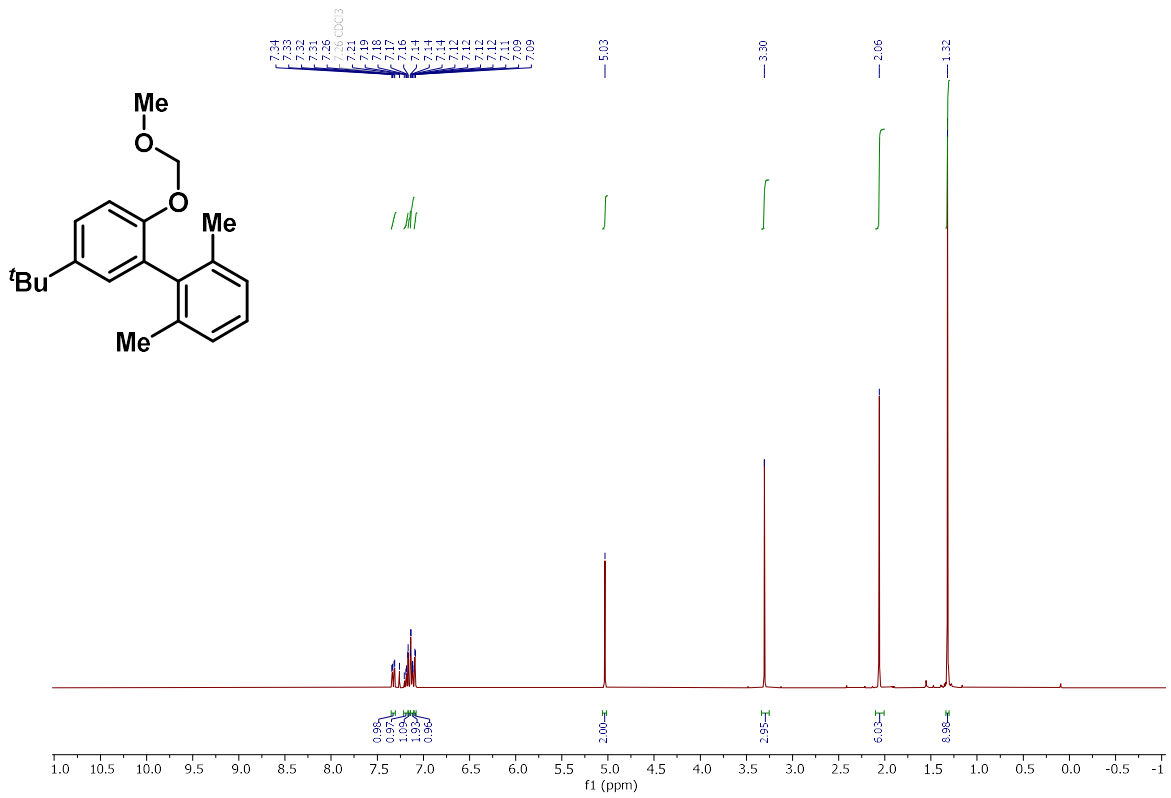

^{13}C{H} NMR (75 MHz, $CDCl_3$)

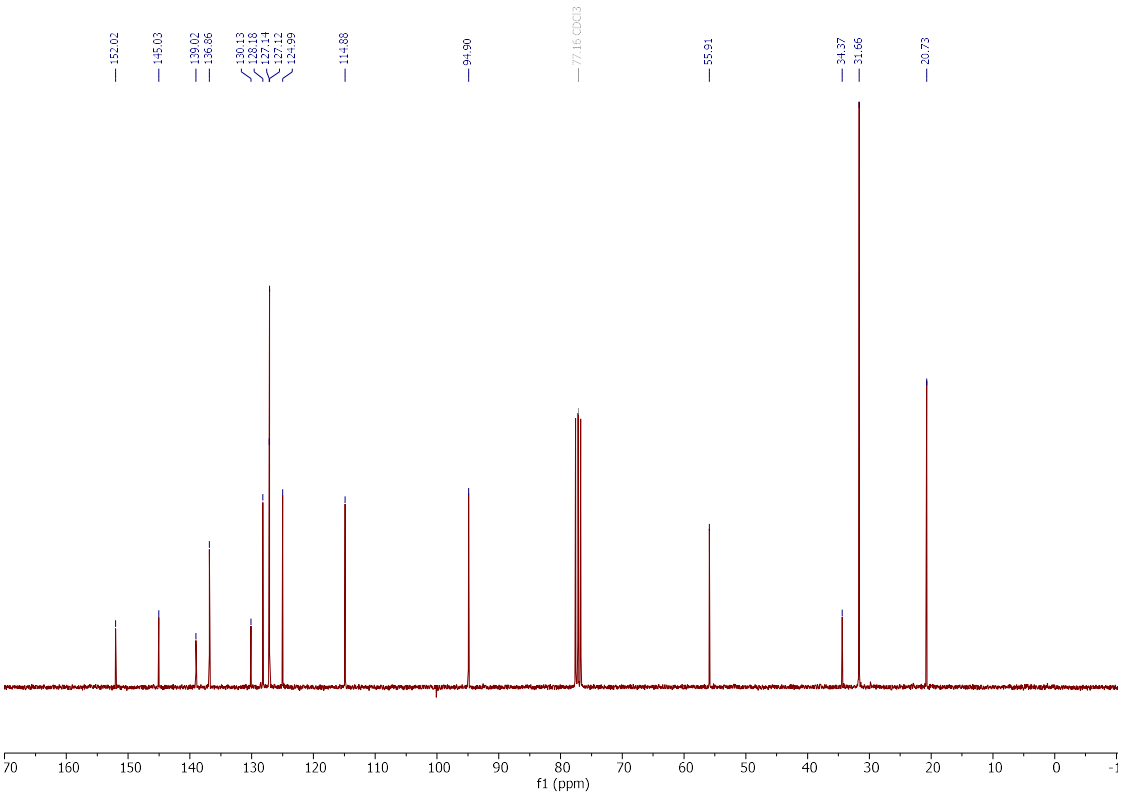

2,11-Di-*tert*-butyl-6,7-dihydrobenzo[2,1-*c*:3,4-*c*']dichromene (**471q**)

^{1}H NMR (300 MHz, $CDCl_3$)

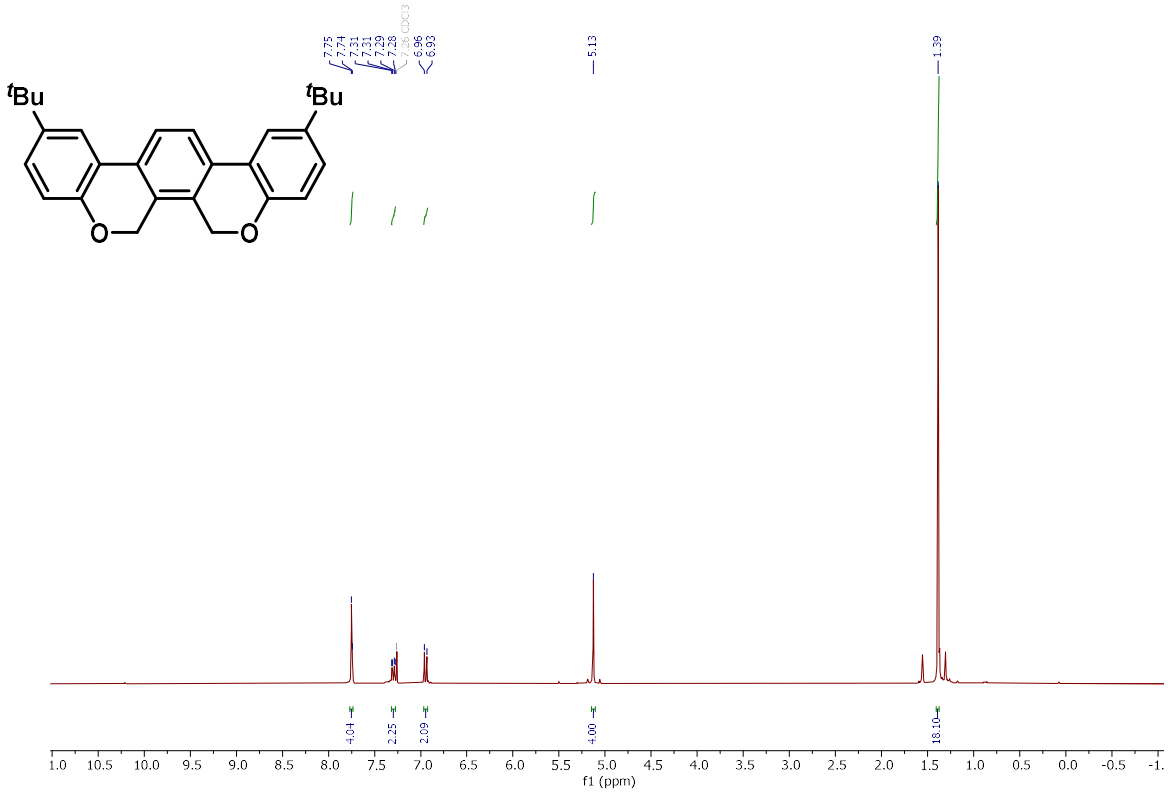

^{13}C{H} NMR (101 MHz, $CDCl_3$)

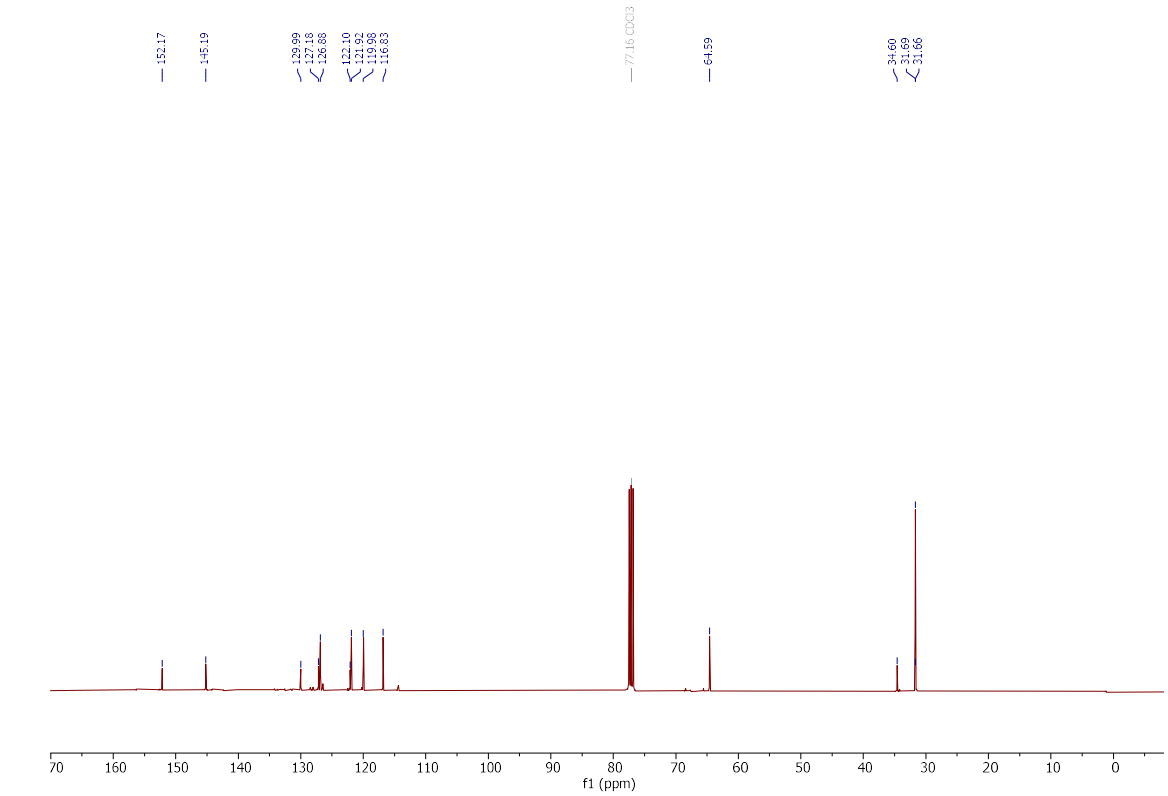

2-((4-(tert-butyl)phenoxy)methyl)benzaldehyde (**471q'**)

^{1}H NMR (300 MHz, $CDCl_3$)

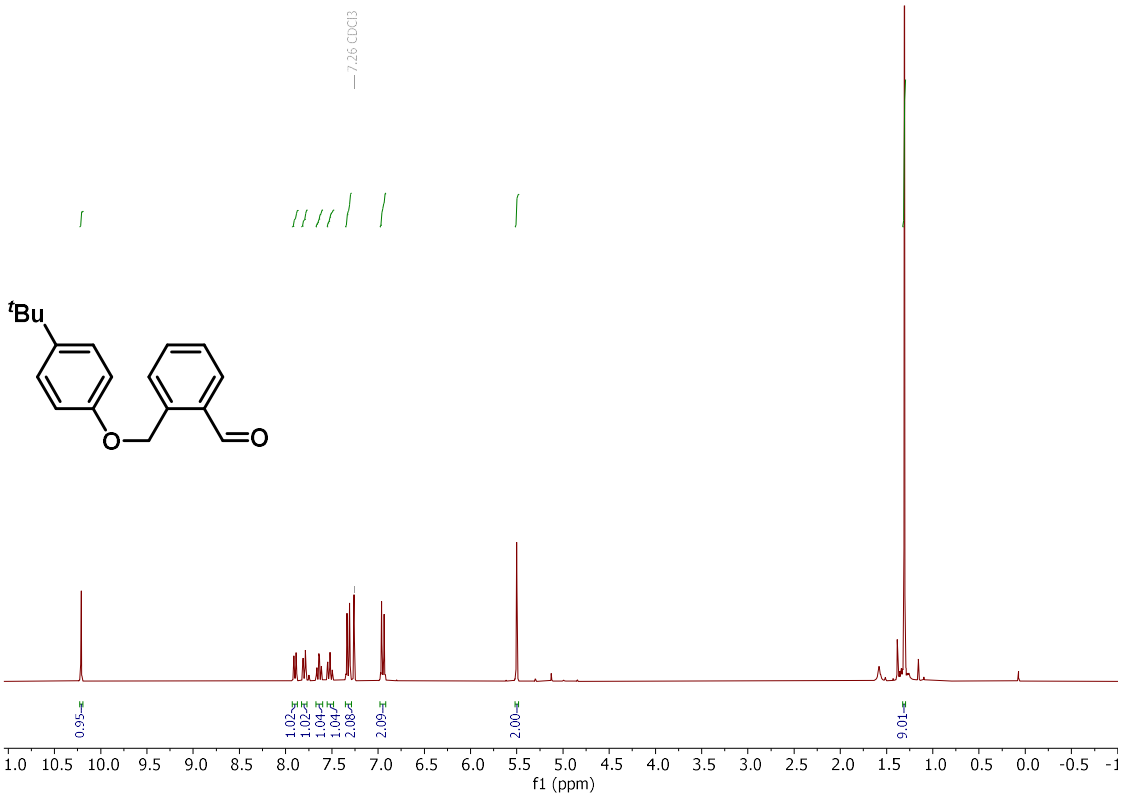

^{13}C NMR (75 MHz, $CDCl_3$)

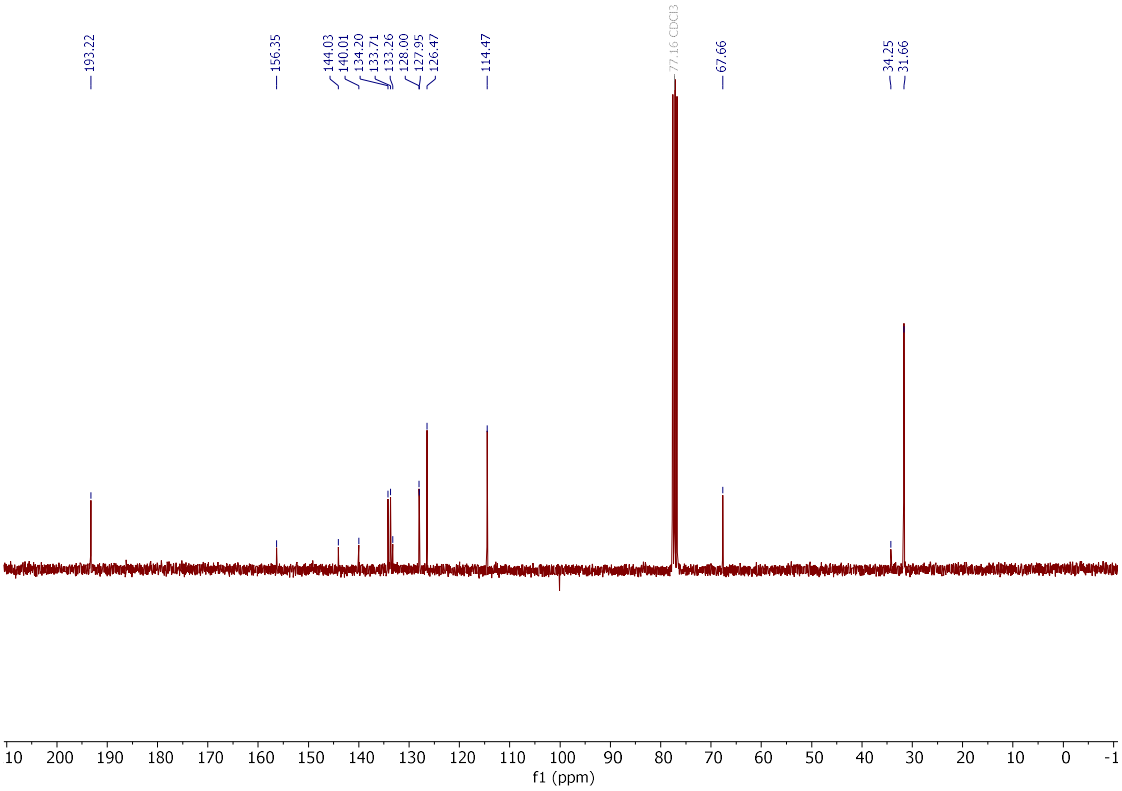

9,12-Dimethyl-2,5-dihydrobenzo[1,2-*c*:4,3-*c*']dichromene (**471r**)

^{1}H NMR (300 MHz, $CDCl_3$)

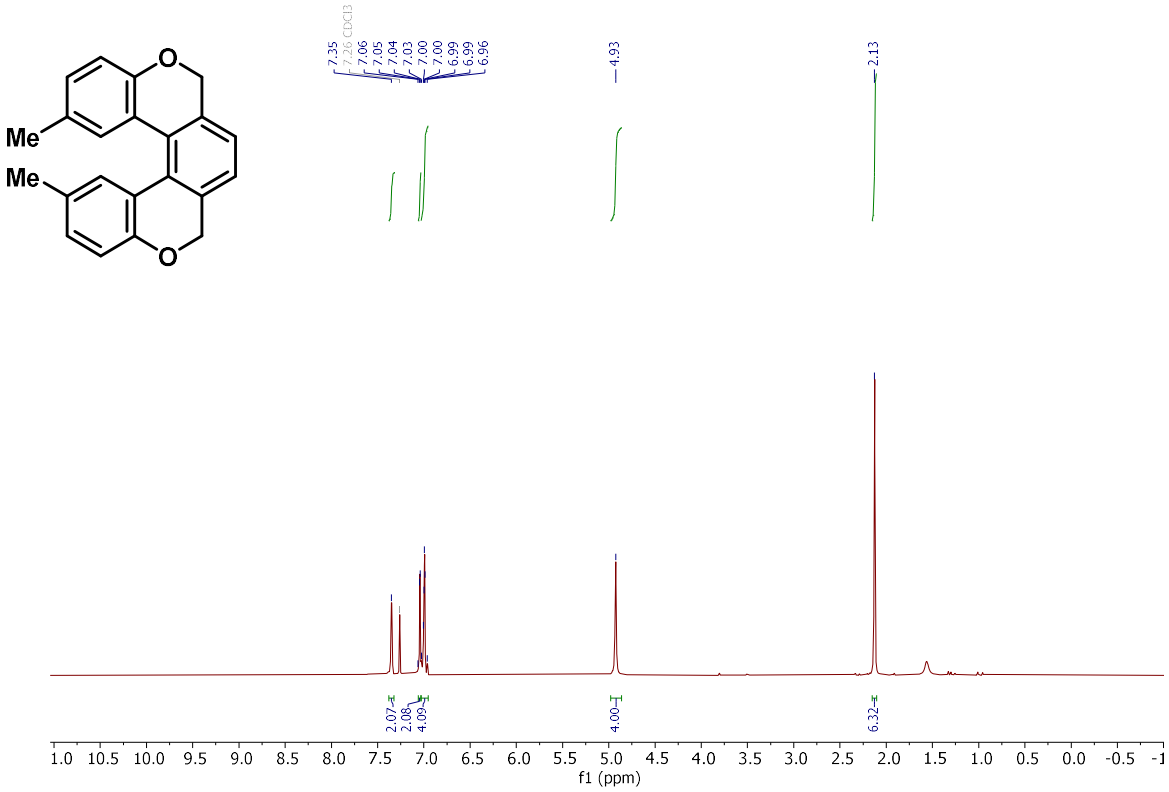

^{13}C{H} NMR (101 MHz, $CDCl_3$)

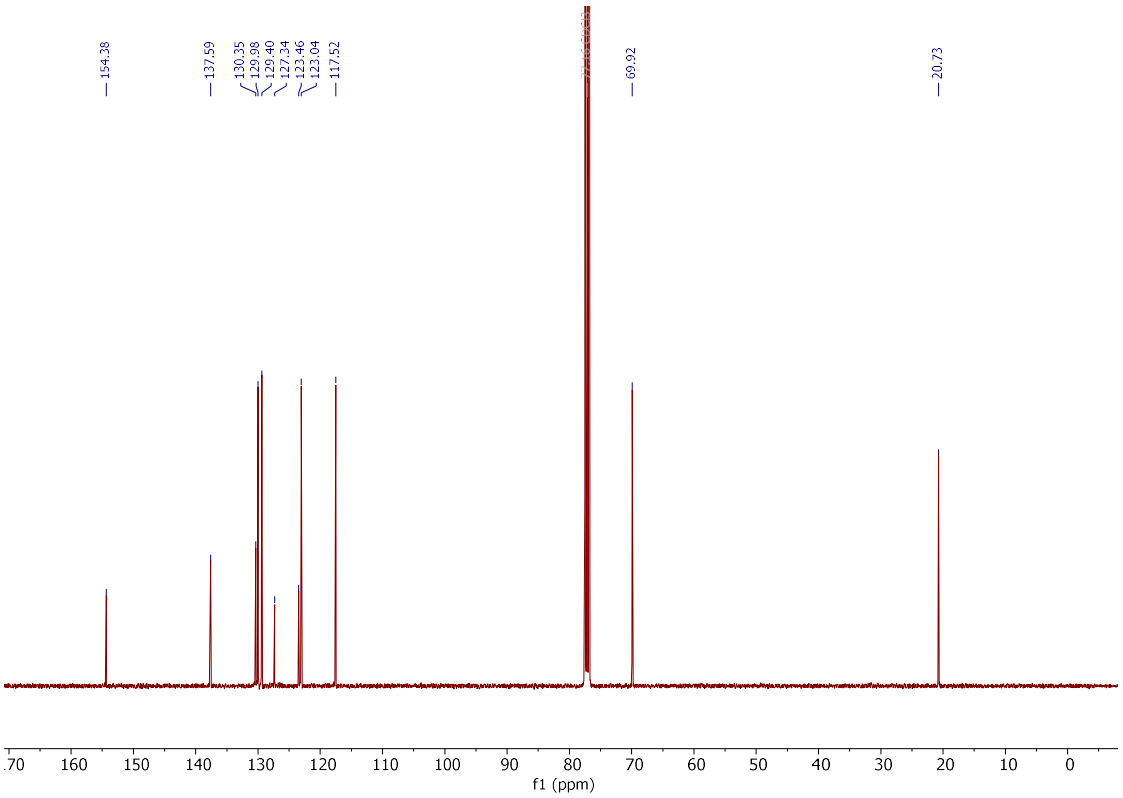

2,9-Dimethyl-6,13-dihydrobenzo[1,2-*c*:4,5-*c*']dichromene (**471r'**)

^{1}H NMR (400 MHz, $CDCl_3$)

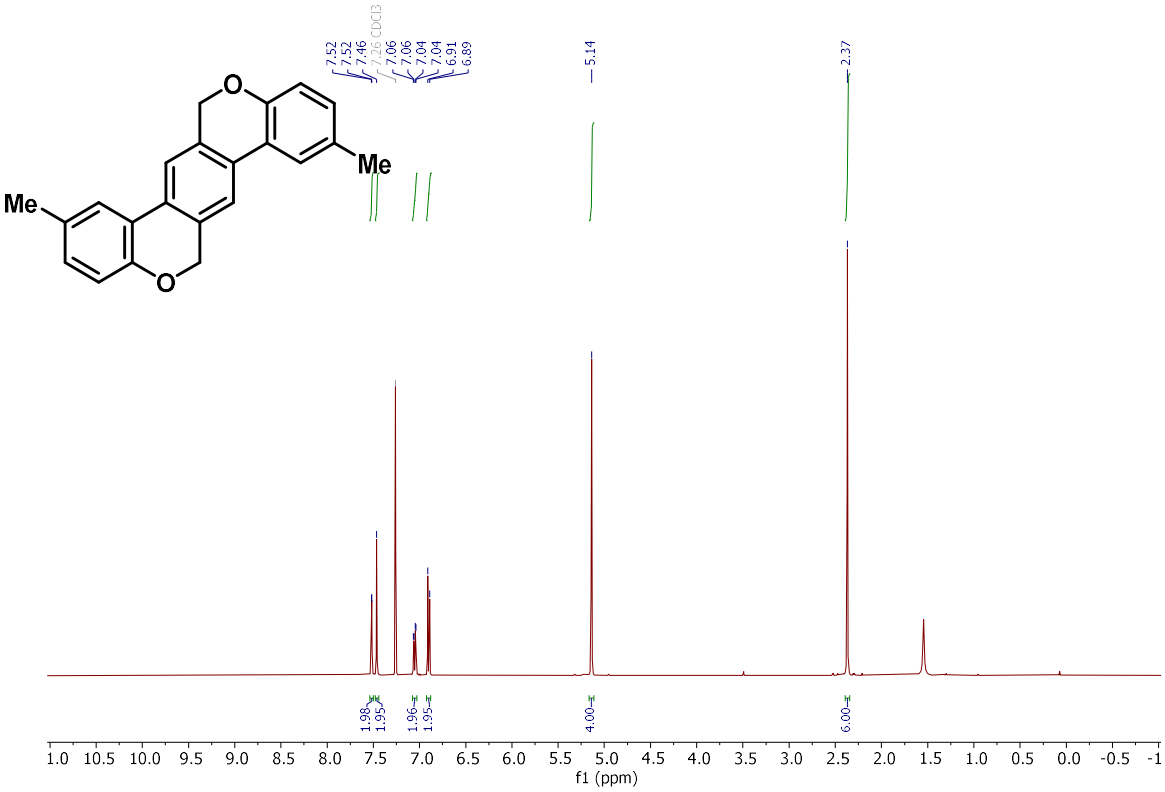

^{13}C{H} NMR (101 MHz, $CDCl_3$)

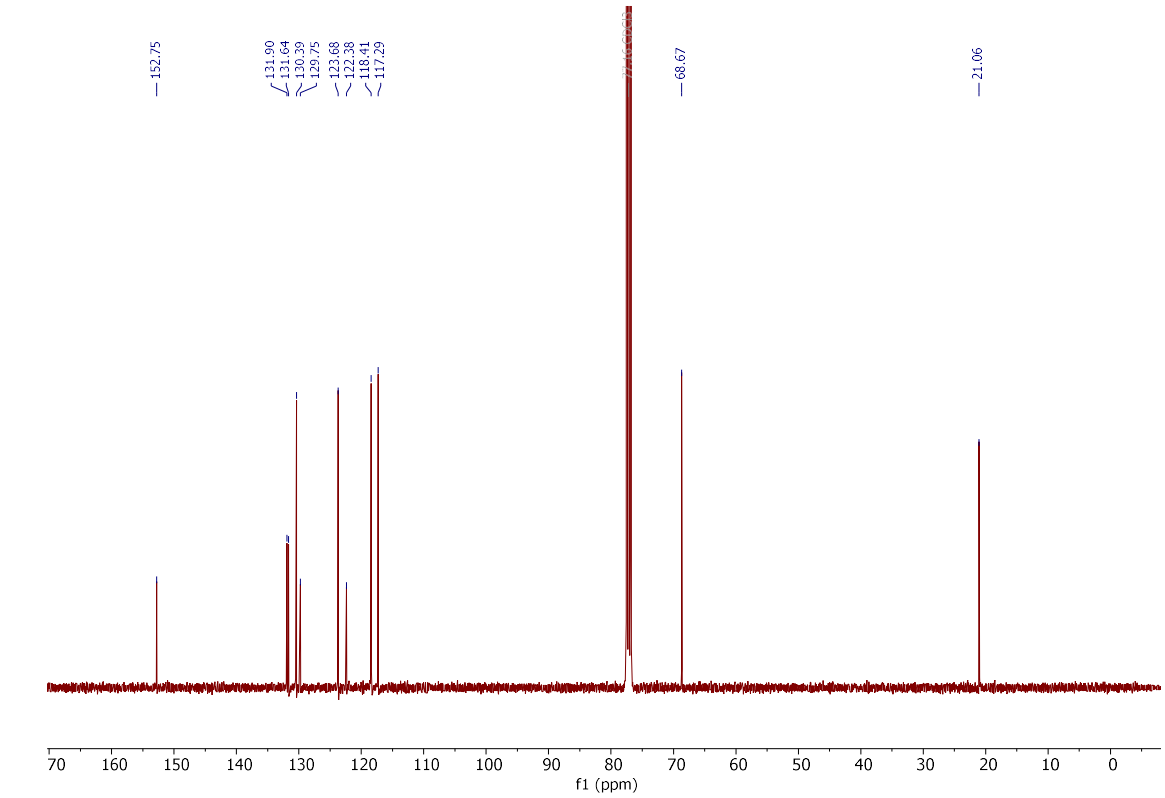

9,12-Di-*tert*-butyl-5,16-dihydronaphtho[1,2-*c*:4,3-*c*']dichromene (**471s**)

^{1}H NMR (300 MHz, $CDCl_3$)

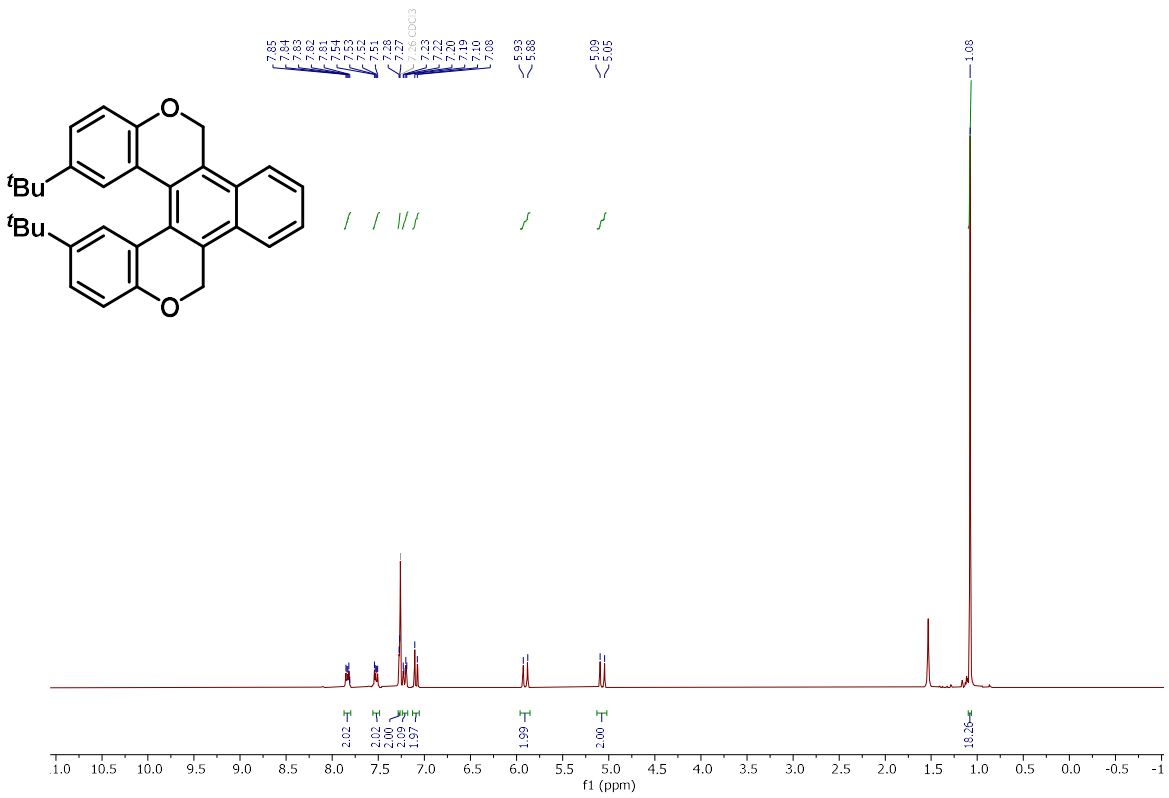

^{13}C{H} NMR (101 MHz, $CDCl_3$)

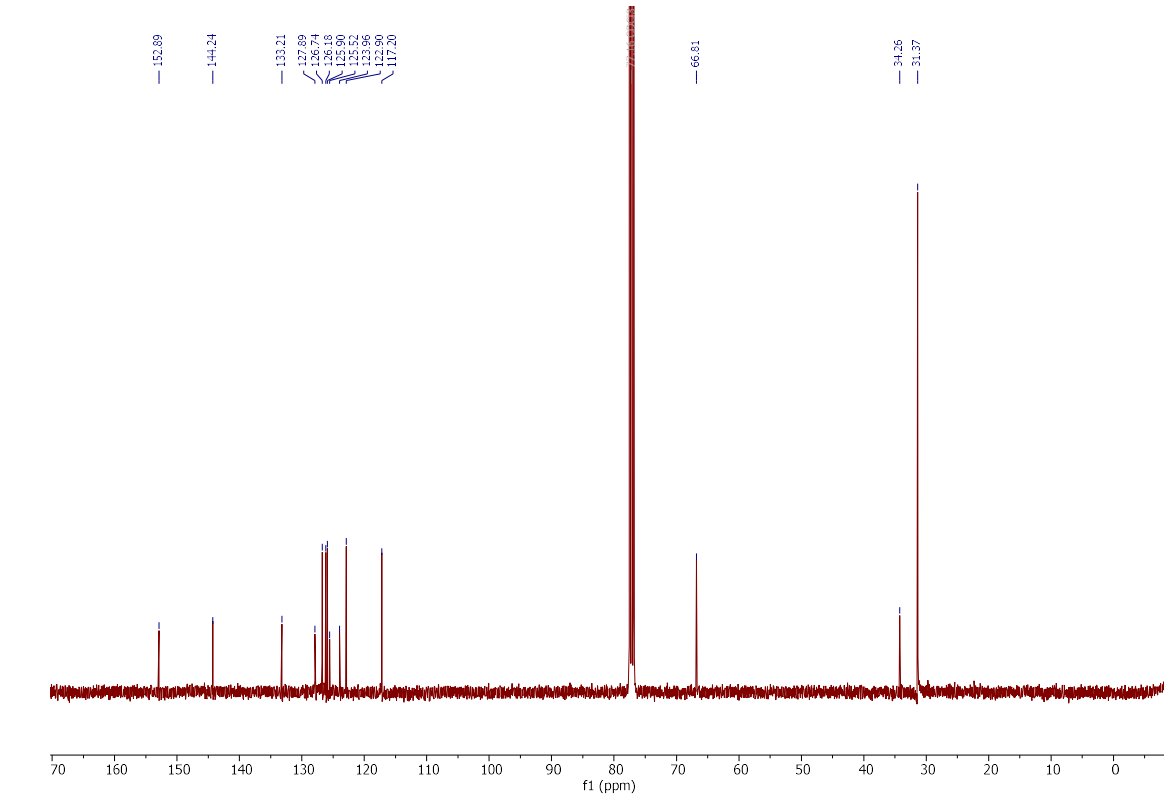

2,2'-Di-*tert*-butyl-6*H*,6'H-7,7'-bibenzo[*c*]chromene (**471t**)

^{1}H NMR (300 MHz, $CDCl_3$)

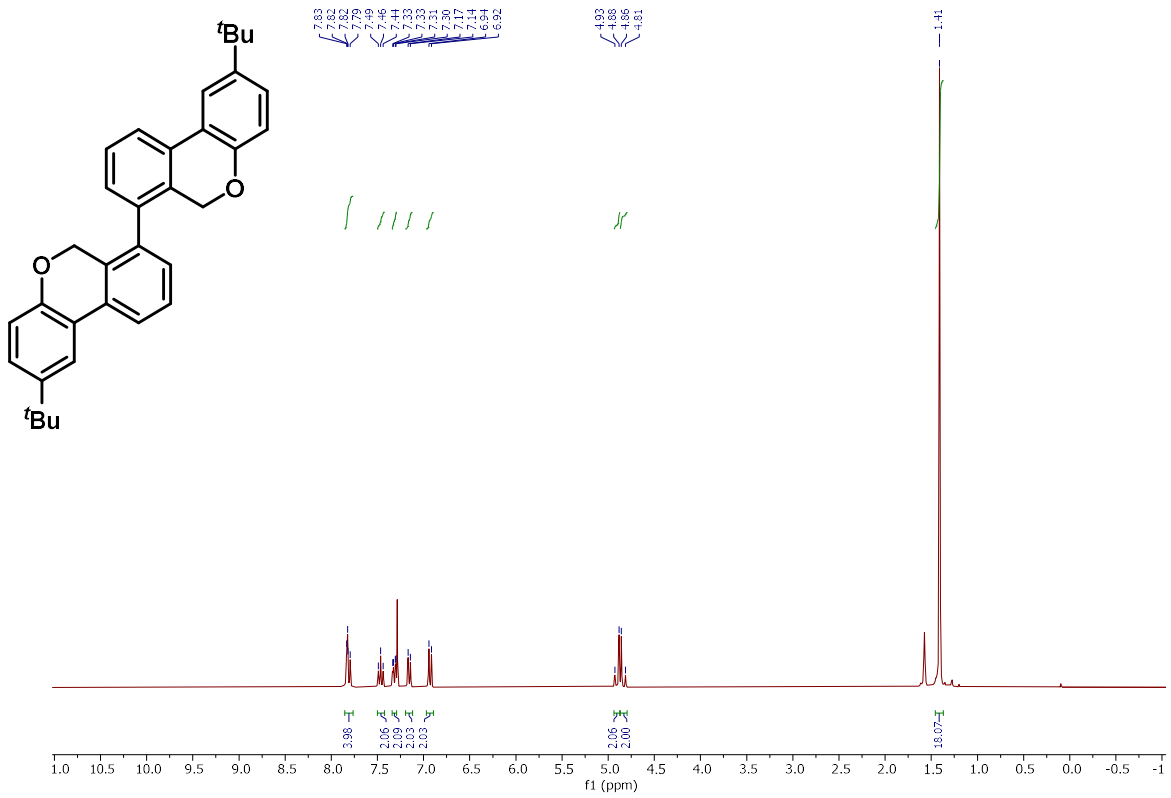

^{13}C{H} NMR (75 MHz, $CDCl_3$)

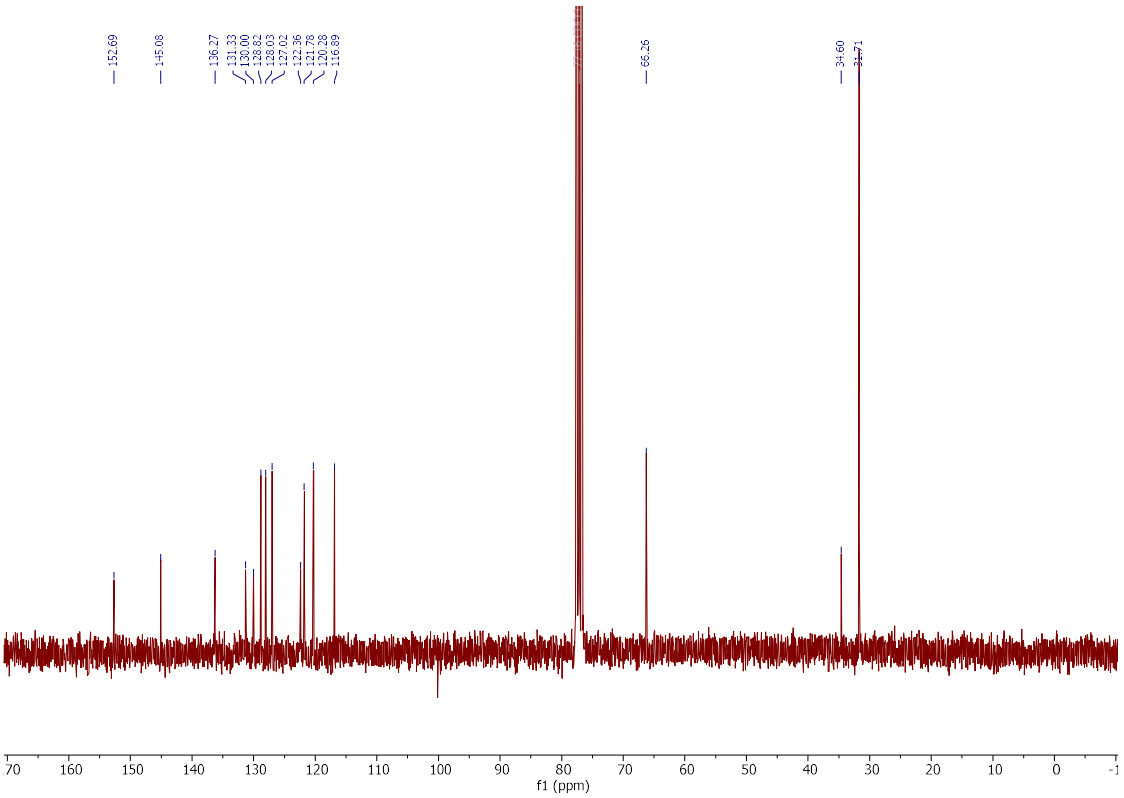

1,2-Bis(2-methyl-6*H*-benzo[*c*]chromen-9-yl)ethane (**471u**)

^{1}H NMR (300 MHz, $CDCl_3$)

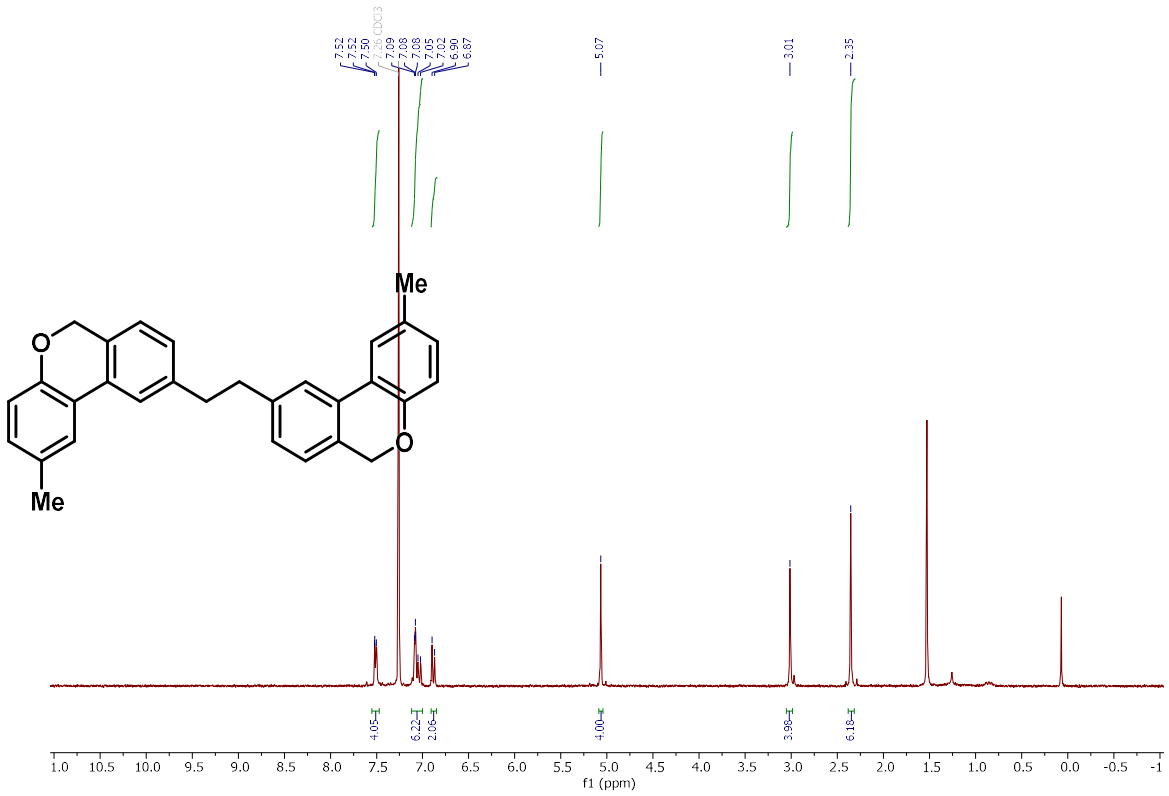

^{13}C{H} NMR (75 MHz, $CDCl_3$)

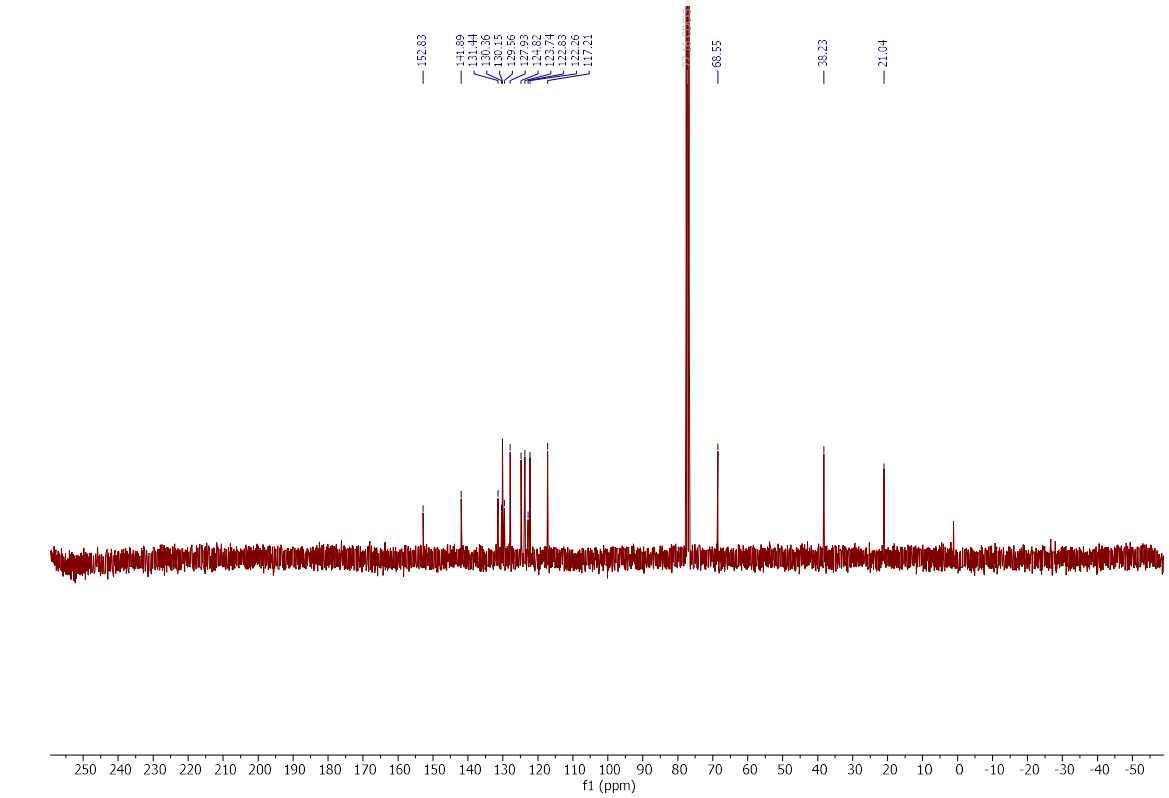

2,9-Dimethyl-dibenzo[*b*,*d*]pyrylium tetrafluoroborate (**472a**)

^{1}H NMR (300 MHz, CD_3CN)

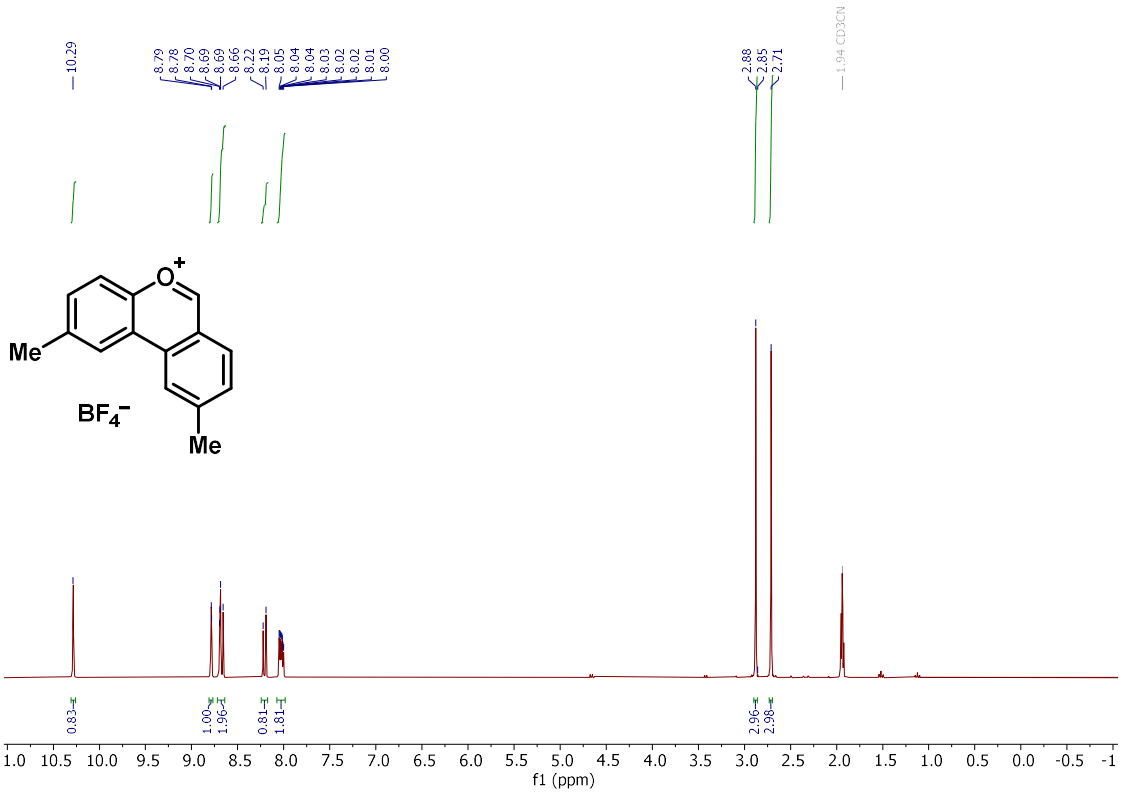

^{13}C NMR (75 MHz, CD_3CN)

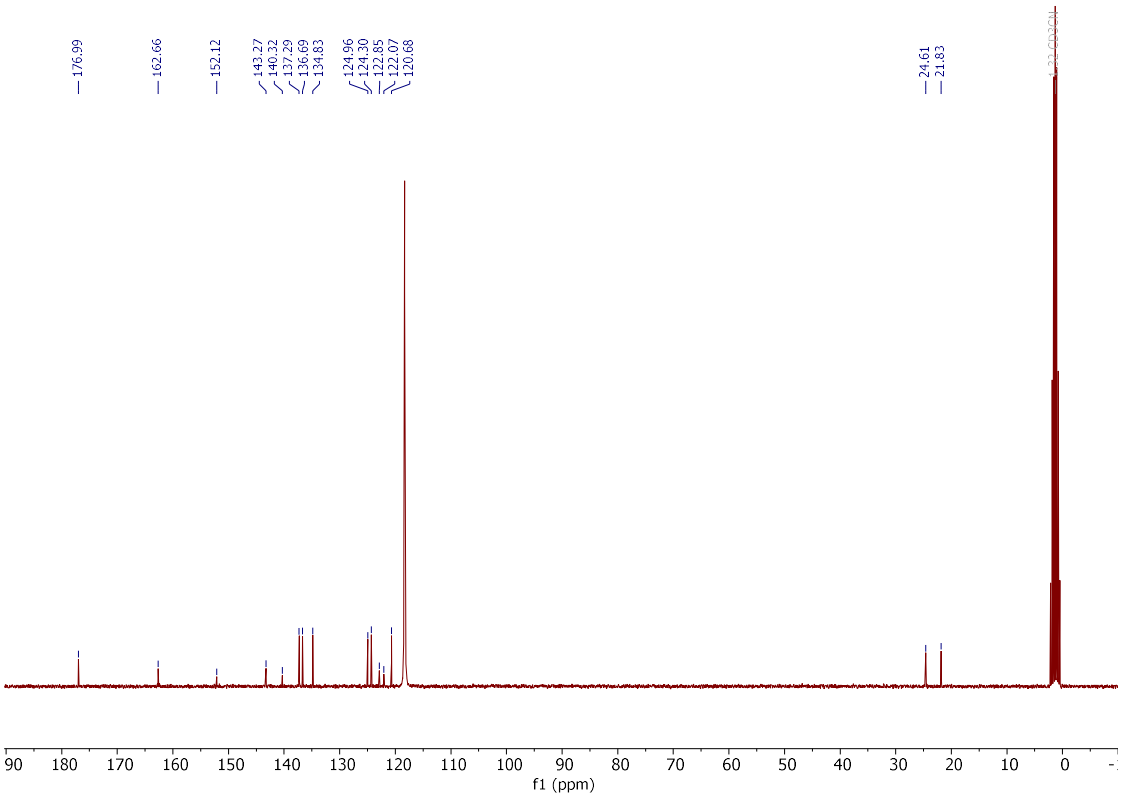

^{19}F NMR (282 MHz, CD_3CN)

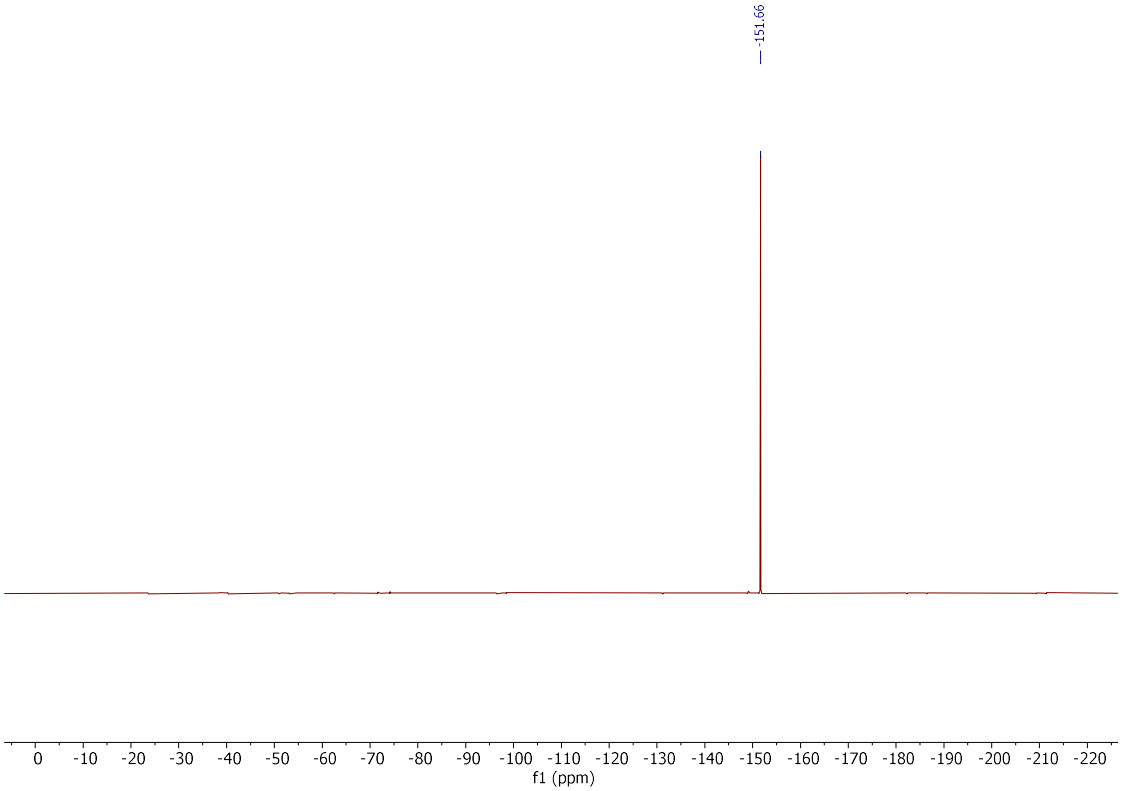

^{11}B NMR (96 MHz, CD_3CN)

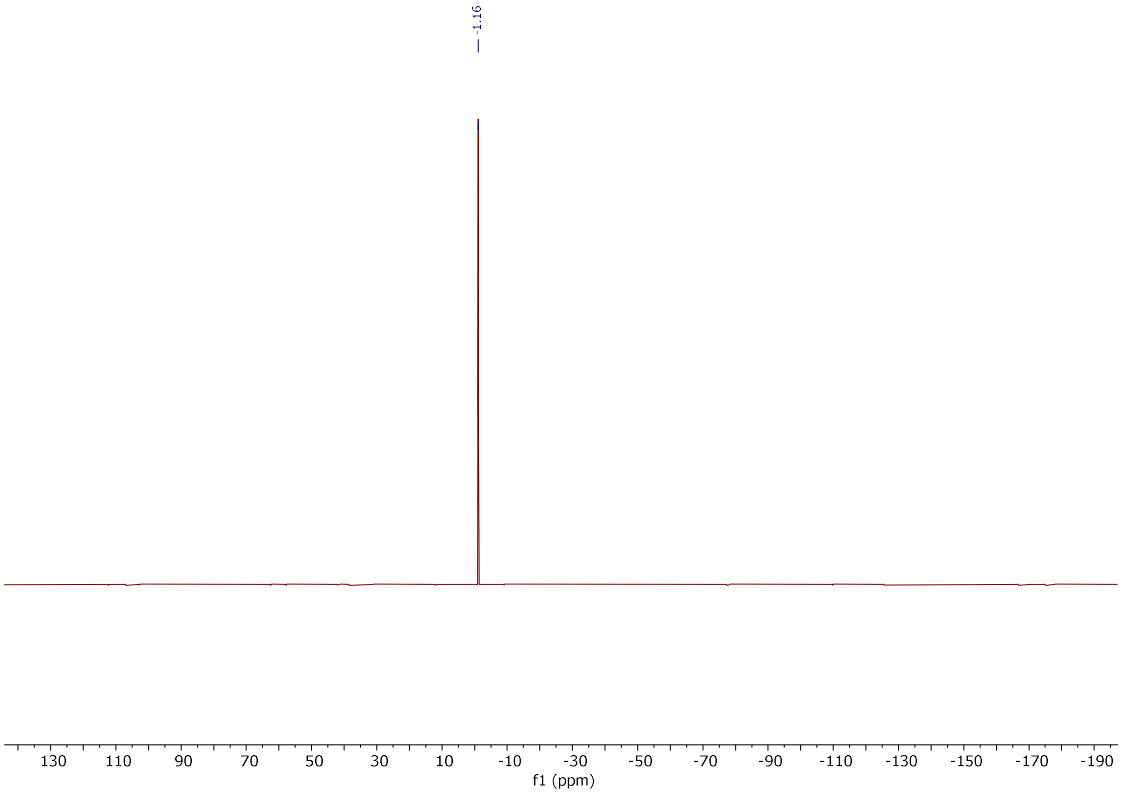

9.2 Crystal Data and Structure Refinement

Compound **208**

Single crystals suitable for X-ray analysis were obtained by slowly evaporating a DCM solution. (DCM)

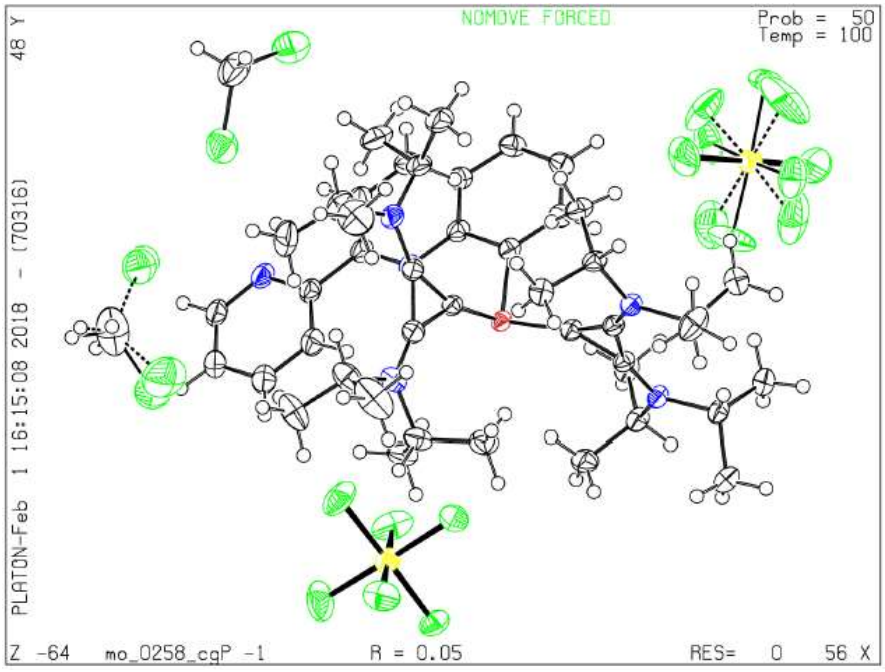

Identification code	mo_0258_CG_0m
Empirical formula	$C_{46}H_{69}Cl_4F_{12}N_6PSb_2$
Formula weight	1350.34
Temperature/K	99.99
Crystal system	triclinic
Space group	P-1
a/Å	13.7169(11)
b/Å	15.6969(13)
c/Å	15.9398(14)
α/°	118.339(5)
β/°	101.005(4)
γ/°	94.173(4)
Volume/Å^3	2911.7(4)
Z	2
ρ_{calc}g/cm^3	1.540
μ/mm^{-1}	1.214
F(000)	1360.0
Crystal size/mm^3	0.277 × 0.151 × 0.091
Radiation	MoKα (λ = 0.71073)
2Θ range for data collection/°	4.69 to 61.082
Index ranges	-17 ≤ h ≤ 19, -22 ≤ k ≤ 22, -22 ≤ l ≤ 22
Reflections collected	50911
Independent reflections	17723 [R_{int} = 0.0290, R_{sigma} = 0.0334]
Data/restraints/parameters	17723/24/706
Goodness-of-fit on F^2	1.047
Final R indexes [I>=2σ (I)]	R_1 = 0.0458, wR_2 = 0.1091
Final R indexes [all data]	R_1 = 0.0569, wR_2 = 0.1162
Largest diff. peak/hole / e Å^{-3}	2.12/-1.50

Compound **184**

Single crystals suitable for X-ray analysis were obtained by slowly evaporating a DCM solution. (DCM)

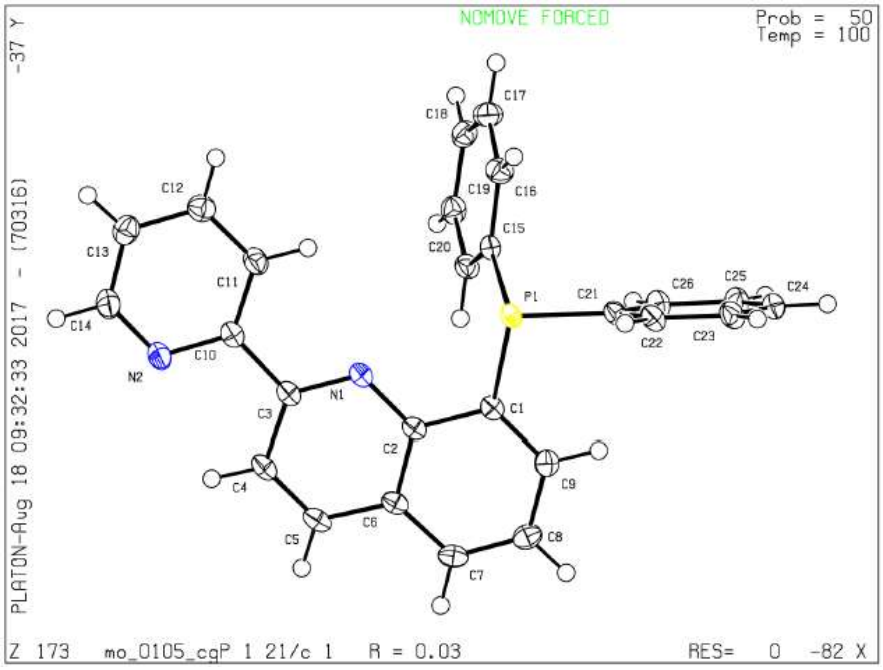

Identification code	mo_0105_CG_0m
Empirical formula	$C_{26}H_{19}N_2P$
Formula weight	390.40
Temperature/K	99.98
Crystal system	monoclinic
Space group	$P2_1/c$
a/Å	9.4673(7)
b/Å	9.4429(7)
c/Å	22.5342(17)
α/°	90
β/°	99.214(3)
γ/°	90
Volume/Å^3	1988.5(3)
Z	4
ρ_{calc}g/cm^3	1.304
μ/mm^{-1}	0.153
F(000)	816.0
Crystal size/mm^3	0.34 × 0.321 × 0.287
Radiation	MoKα (λ = 0.71073)
2Θ range for data collection/°	4.686 to 59.226
Index ranges	-13 ≤ h ≤ 13, -13 ≤ k ≤ 13, -31 ≤ l ≤ 31
Reflections collected	30026
Independent reflections	5587 [R_{int} = 0.0223, R_{sigma} = 0.0170]
Data/restraints/parameters	5587/0/262
Goodness-of-fit on F^2	1.044
Final R indexes [I>=2σ (I)]	R_1 = 0.0347, wR_2 = 0.0927
Final R indexes [all data]	R_1 = 0.0372, wR_2 = 0.0947
Largest diff. peak/hole / e Å^{-3}	0.48/-0.25

Compound **209a**

Single crystals suitable for X-ray analysis were obtained by slowly evaporating a DCM/THF solution. (DCM/THF)

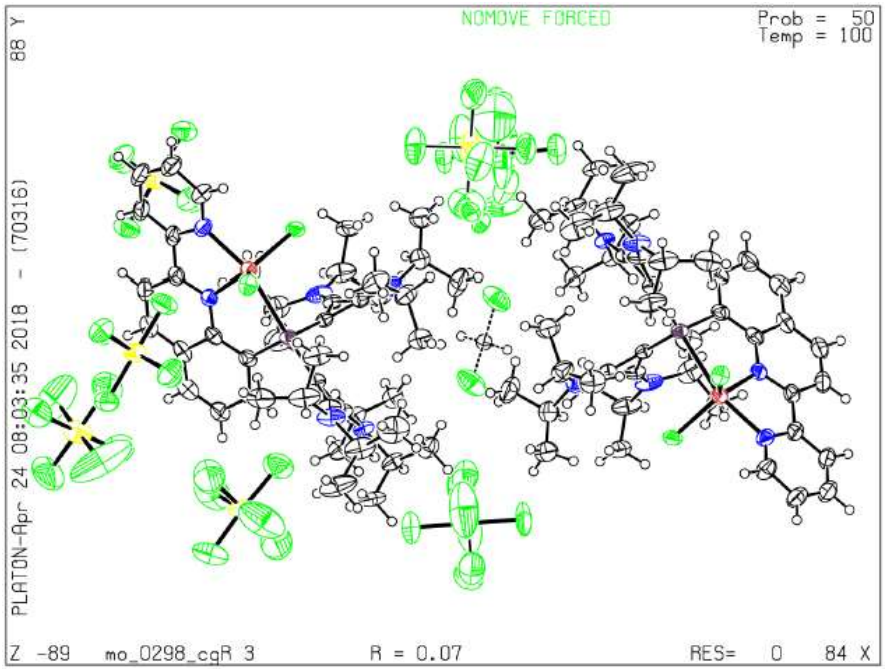

Identification code	mo_0298_CG_0m
Empirical formula	$C_{44.17}H_{65.33}Cl_{2.83}CoF_{12}N_6PSb_2$
Formula weight	1342.21
Temperature/K	100.01
Crystal system	trigonal
Space group	R3
a/Å	21.0339(13)
b/Å	21.0339(13)
c/Å	66.548(5)
α/°	90
β/°	90
γ/°	120
Volume/Å^3	25498(4)
Z	18
ρ_{calc}g/cm^3	1.573
μ/mm^{-1}	1.473
F(000)	12105.0
Crystal size/mm^3	0.286 × 0.196 × 0.024
Radiation	MoKα (λ = 0.71073)
2Θ range for data collection/°	4.286 to 59.274
Index ranges	-29 ≤ h ≤ 29, -28 ≤ k ≤ 28, -92 ≤ l ≤ 92
Reflections collected	84025
Independent reflections	31692 [R_{int} = 0.0266, R_{sigma} = 0.0342]
Data/restraints/parameters	31692/368/1342
Goodness-of-fit on F^2	1.033
Final R indexes [I>=2σ (I)]	R_1 = 0.0703, wR_2 = 0.2003
Final R indexes [all data]	R_1 = 0.0840, wR_2 = 0.2167
Largest diff. peak/hole / e Å^{-3}	3.25/-1.88
Flack parameter	0.28(2)

Compound **209b**

Single crystals suitable for X-ray analysis were obtained by slowly evaporating a DCM solution. (DCM)

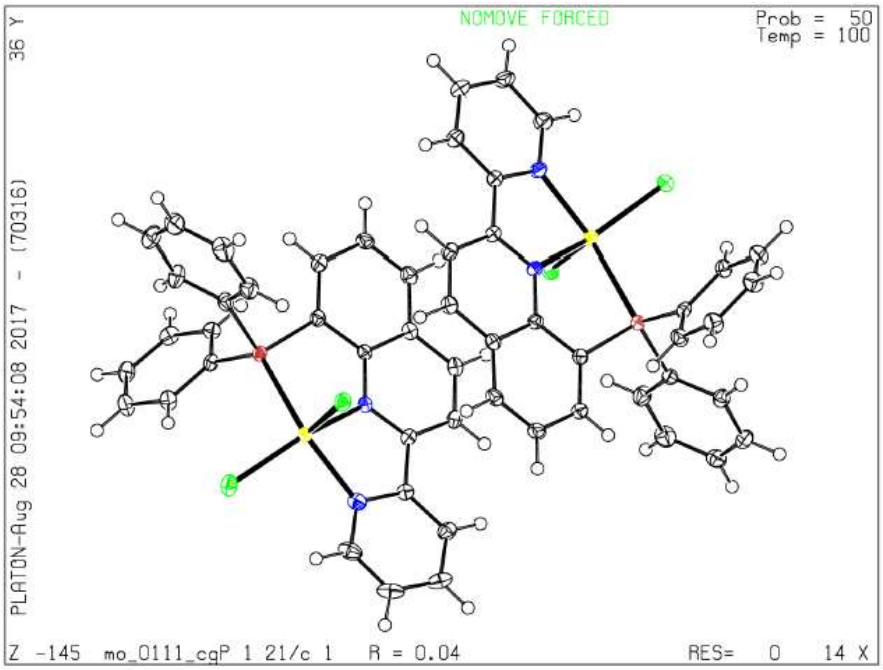

Identification code	mo_0111_CG_0m
Empirical formula	$C_{26}H_{19}Cl_2CoN_2P$
Formula weight	520.23
Temperature/K	99.96
Crystal system	monoclinic
Space group	$P2_1/c$
a/Å	16.018(6)
b/Å	15.183(6)
c/Å	18.598(5)
α/°	90
β/°	90.017(8)
γ/°	90
Volume/Å^3	4523(3)
Z	8
ρ_{calc}g/cm^3	1.528
μ/mm^{-1}	1.083
F(000)	2120.0
Crystal size/mm^3	0.108 × 0.051 × 0.011
Radiation	MoKα (λ = 0.71073)
2Θ range for data collection/°	4.296 to 59.236
Index ranges	-22 ≤ h ≤ 22, -21 ≤ k ≤ 20, -25 ≤ l ≤ 24
Reflections collected	64376
Independent reflections	12677 [R_{int} = 0.0478, R_{sigma} = 0.0395]
Data/restraints/parameters	12677/0/577
Goodness-of-fit on F^2	1.046
Final R indexes [I>=2σ (I)]	R_1 = 0.0379, wR_2 = 0.0755
Final R indexes [all data]	R_1 = 0.0582, wR_2 = 0.0817
Largest diff. peak/hole / e Å^{-3}	0.77/-1.14

Compound **210x**

Single crystals suitable for X-ray analysis were obtained by layering of a THF solution with pentane. (THF/pentane)

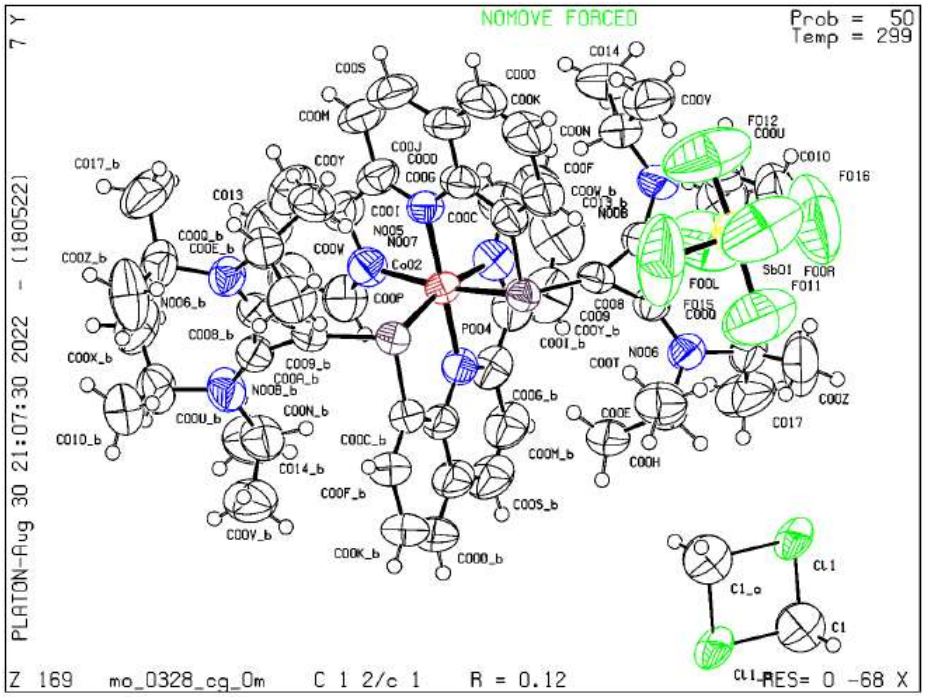

Identification code	mo_0328_CG_0m
Empirical formula	$C_{59}H_{76}Cl_2CoF_{12}N_8P_2Sb_2$
Formula weight	1560.54
Temperature/K	298.65
Crystal system	monoclinic
Space group	C2/c
a/Å	33.1838(18)
b/Å	11.2289(5)
c/Å	25.8131(15)
α/°	90
β/°	123.2400(10)
γ/°	90
Volume/Å^3	8044.7(7)
Z	4
ρ_{calc}g/cm^3	1.288
μ/mm^{-1}	1.041
F(000)	3148.0
Crystal size/mm^3	? × ? × ?
Radiation	MoKα (λ = 0.71073)
2Θ range for data collection/°	4.68 to 52.866
Index ranges	-41 ≤ h ≤ 41, -13 ≤ k ≤ 13, -32 ≤ l ≤ 30
Reflections collected	24706
Independent reflections	8170 [R_{int} = 0.0899, R_{sigma} = 0.0932]
Data/restraints/parameters	8170/312/401
Goodness-of-fit on F^2	1.250
Final R indexes [I>=2σ (I)]	R_1 = 0.1164, wR_2 = 0.3366
Final R indexes [all data]	R_1 = 0.1767, wR_2 = 0.3876
Largest diff. peak/hole / e Å^{-3}	1.41/-1.17

Compound **210b**

Single crystals suitable for X-ray analysis were obtained by layering of a THF solution with pentane. (THF/pentane)

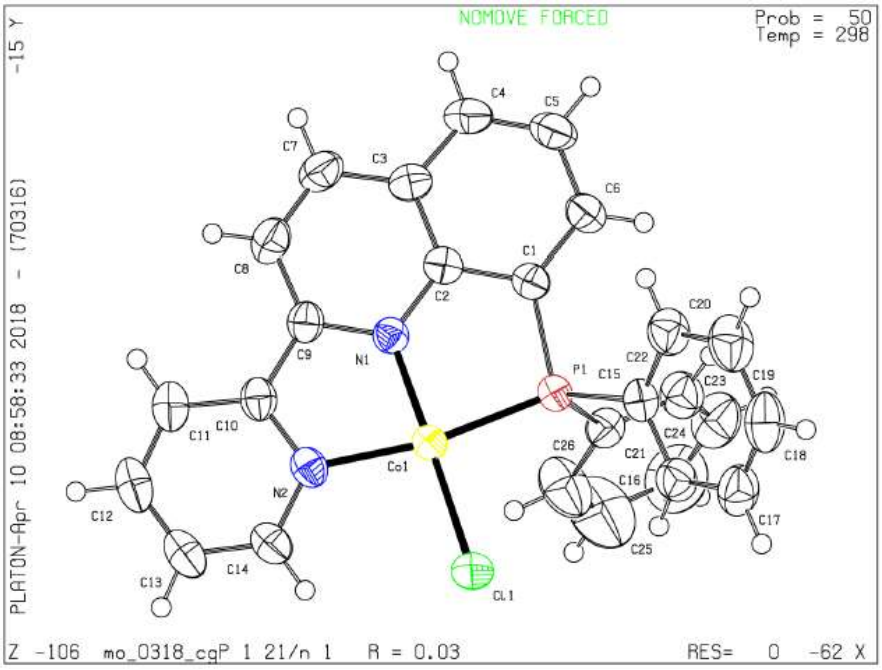

Identification code	mo_0318_CG_0m
Empirical formula	$C_{26}H_{19}ClCoN_2P$
Formula weight	484.78
Temperature/K	298.04
Crystal system	monoclinic
Space group	$P2_1/n$
a/Å	10.3651(9)
b/Å	16.8319(12)
c/Å	12.3935(11)
α/°	90
β/°	96.483(4)
γ/°	90
Volume/Å^3	2148.4(3)
Z	4
ρ_{calc}g/cm^3	1.499
μ/mm^{-1}	1.014
F(000)	992.0
Crystal size/mm^3	0.222 × 0.196 × 0.192
Radiation	MoKα (λ = 0.71073)
2Θ range for data collection/°	4.84 to 61.052
Index ranges	-14 ≤ h ≤ 14, -23 ≤ k ≤ 24, -17 ≤ l ≤ 17
Reflections collected	28704
Independent reflections	6552 [R_{int} = 0.0201, R_{sigma} = 0.0179]
Data/restraints/parameters	6552/0/280
Goodness-of-fit on F^2	1.046
Final R indexes [I>=2σ (I)]	R_1 = 0.0300, wR_2 = 0.0805
Final R indexes [all data]	R_1 = 0.0365, wR_2 = 0.0844
Largest diff. peak/hole / e Å^{-3}	0.46/-0.43

Compound **212**

Single crystals suitable for X-ray analysis were obtained from hot toluene. (toluene)

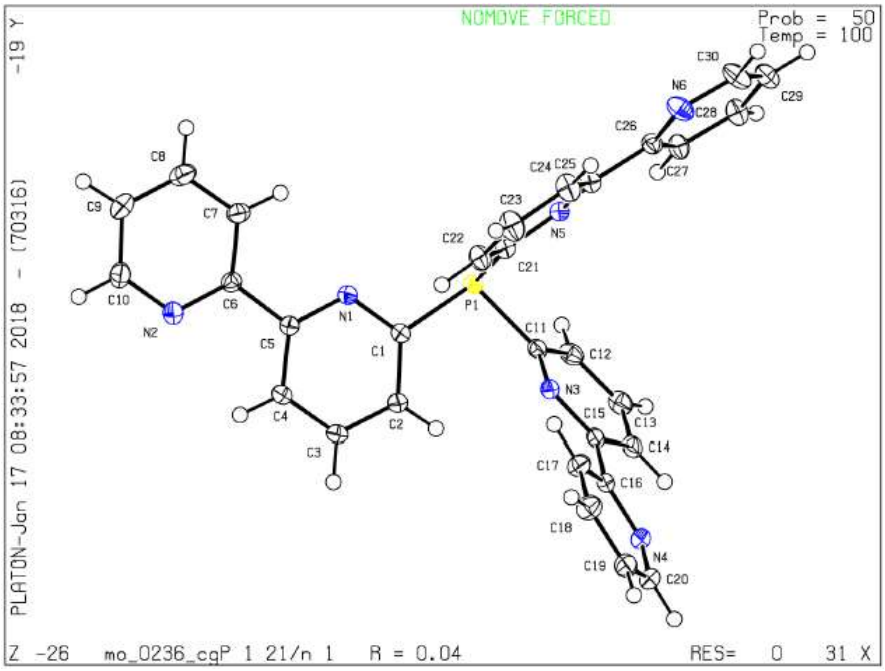

Identification code	mo_0236_CG_0m
Empirical formula	$C_{30}H_{21}N_6P$
Formula weight	496.50
Temperature/K	100.02
Crystal system	monoclinic
Space group	$P2_1/n$
a/Å	12.8993(14)
b/Å	11.5311(11)
c/Å	17.2403(19)
α/°	90
β/°	105.668(4)
γ/°	90
Volume/Å^3	2469.1(5)
Z	4
ρ_{calc}g/cm^3	1.336
μ/mm^{-1}	0.143
F(000)	1032.0
Crystal size/mm^3	0.286 × 0.214 × 0.056
Radiation	MoKα (λ = 0.71073)
2Θ range for data collection/°	4.3 to 63.046
Index ranges	-18 ≤ h ≤ 18, -16 ≤ k ≤ 16, -25 ≤ l ≤ 25
Reflections collected	80015
Independent reflections	8222 [R_{int} = 0.0252, R_{sigma} = 0.0139]
Data/restraints/parameters	8222/0/334
Goodness-of-fit on F^2	1.053
Final R indexes [I>=2σ (I)]	R_1 = 0.0370, wR_2 = 0.1015
Final R indexes [all data]	R_1 = 0.0409, wR_2 = 0.1056
Largest diff. peak/hole / e Å^{-3}	0.51/-0.25

Compound **238**

Single crystals suitable for X-ray analysis were obtained from MeCN and Et_2O by diffusion crystallization. (MeCN/Et2O)

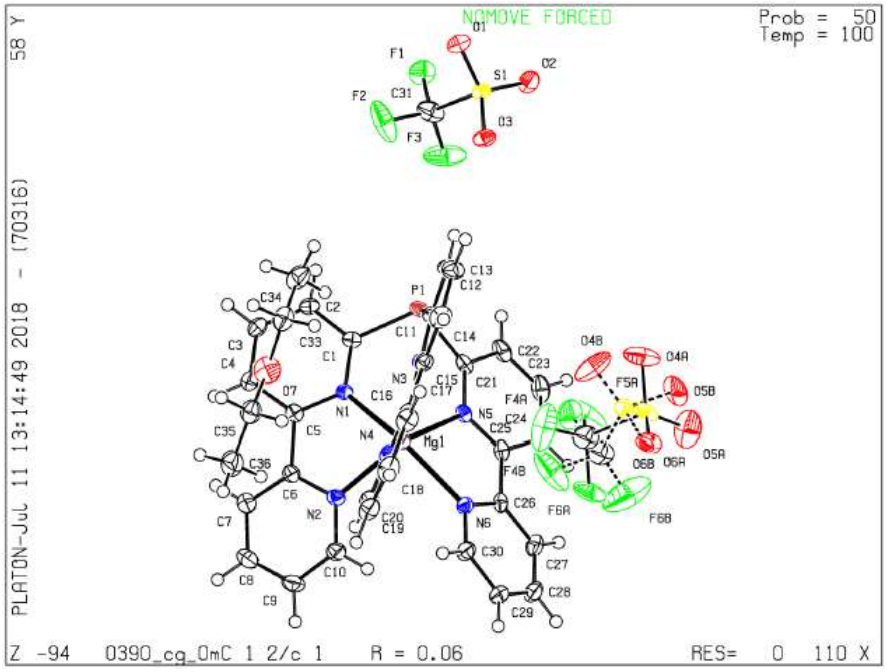

Identification code	0390_CG_0m
Empirical formula	$C_{68}H_{52}F_{12}Mg_2N_{12}O_{13}P_2S_4$
Formula weight	1712.01
Temperature/K	100.04
Crystal system	monoclinic
Space group	C2/c
a/Å	19.138(9)
b/Å	14.306(4)
c/Å	27.811(11)
α/°	90
β/°	105.757(15)
γ/°	90
Volume/Å^3	7328(5)
Z	4
ρ_{calc}g/cm^3	1.552
μ/mm^{-1}	0.293
F(000)	3496.0
Crystal size/mm^3	0.525 × 0.462 × 0.094
Radiation	MoKα (λ = 0.71073)
2Θ range for data collection/°	4.14 to 55.66
Index ranges	-24 ≤ h ≤ 25, -18 ≤ k ≤ 17, -36 ≤ l ≤ 29
Reflections collected	22385
Independent reflections	8657 [R_{int} = 0.0400, R_{sigma} = 0.0582]
Data/restraints/parameters	8657/160/601
Goodness-of-fit on F^2	1.023
Final R indexes [I>=2σ (I)]	R_1 = 0.0568, wR_2 = 0.1297
Final R indexes [all data]	R_1 = 0.0855, wR_2 = 0.1437
Largest diff. peak/hole / e Å^{-3}	1.54/-0.69

Compound **239**

Single crystals suitable for X-ray analysis were obtained from MeCN and Et_2O by diffusion crystallization. (MeCN/Et2O)

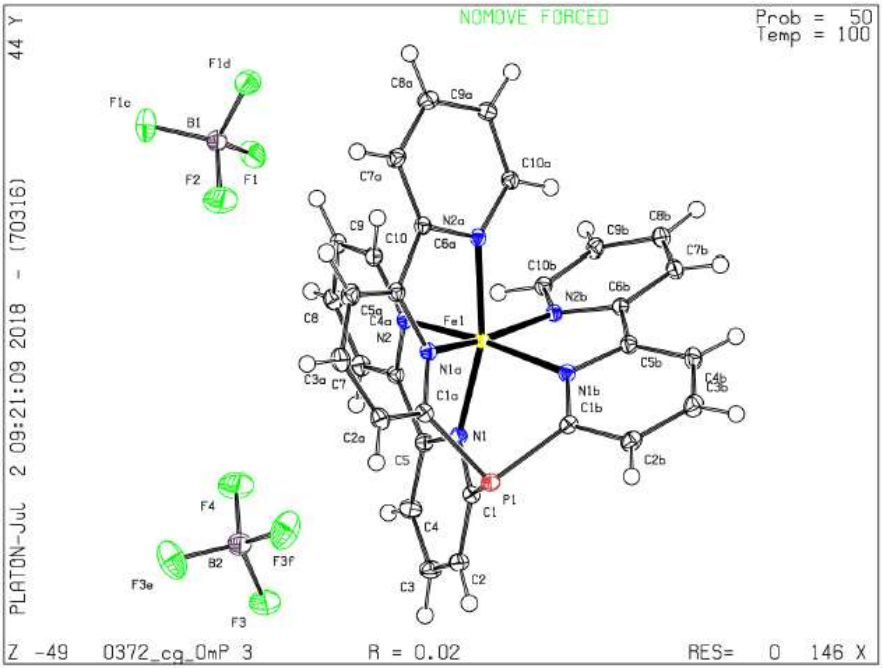

Identification code	0372_CG_0m
Empirical formula	$C_{30}H_{21}B_2F_8FeN_6P$
Formula weight	726.04
Temperature/K	99.99
Crystal system	trigonal
Space group	P3
a/Å	9.538(2)
b/Å	9.538(2)
c/Å	8.899(2)
α/°	90
β/°	90
γ/°	120
Volume/Å^3	701.2(3)
Z	0.9999
ρ_{calc}g/cm^3	1.719
μ/mm^{-1}	0.685
F(000)	366.0
Crystal size/mm^3	0.277 × 0.032 × 0.025
Radiation	MoKα (λ = 0.71073)
2Θ range for data collection/°	4.578 to 62.986
Index ranges	-14 ≤ h ≤ 14, -14 ≤ k ≤ 14, -13 ≤ l ≤ 13
Reflections collected	17503
Independent reflections	3119 [R_{int} = 0.0262, R_{sigma} = 0.0187]
Data/restraints/parameters	3119/1/146
Goodness-of-fit on F^2	1.086
Final R indexes [I>=2σ (I)]	R_1 = 0.0191, wR_2 = 0.0498
Final R indexes [all data]	R_1 = 0.0192, wR_2 = 0.0498
Largest diff. peak/hole / e Å^{-3}	0.44/-0.24
Flack parameter	0.003(3)

Compound **240**

Single crystals suitable for X-ray analysis were obtained from MeCN and Et_2O by diffusion crystallization. (MeCN/Et2O)

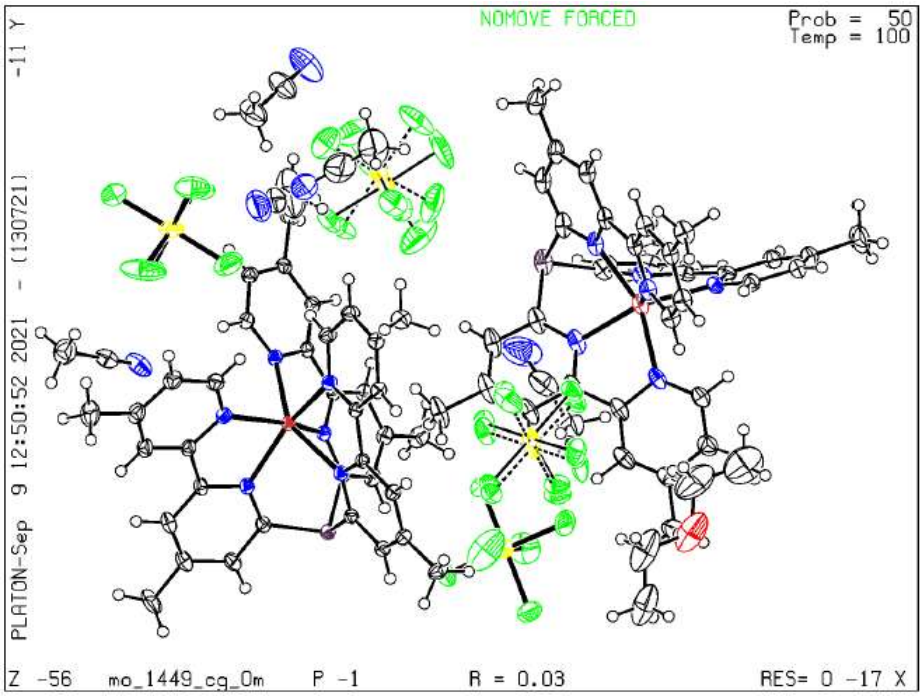

Identification code	mo_1449_CG_0m
Empirical formula	$C_{84}H_{88}Co_2F_{24}N_{16}OP_2Sb_4$
Formula weight	2460.50
Temperature/K	100.00
Crystal system	triclinic
Space group	P-1
a/Å	13.9725(6)
b/Å	17.4714(8)
c/Å	22.1473(9)
α/°	106.5790(10)
β/°	99.0290(10)
γ/°	107.9820(10)
Volume/Å^3	4747.3(4)
Z	2
ρ_{calc}g/cm^3	1.721
μ/mm^{-1}	1.598
F(000)	2432.0
Crystal size/mm^3	0.466 × 0.293 × 0.13
Radiation	MoKα (λ = 0.71073)
2Θ range for data collection/°	3.878 to 65.4
Index ranges	-21 ≤ h ≤ 21, -26 ≤ k ≤ 26, -33 ≤ l ≤ 33
Reflections collected	233866
Independent reflections	34498 [R_{int} = 0.0296, R_{sigma} = 0.0180]
Data/restraints/parameters	34498/94/1373
Goodness-of-fit on F^2	1.056
Final R indexes [I>=2σ (I)]	R_1 = 0.0313, wR_2 = 0.0750
Final R indexes [all data]	R_1 = 0.0371, wR_2 = 0.0784
Largest diff. peak/hole / e Å^{-3}	1.52/-1.89

Compound **241**

Single crystals suitable for X-ray analysis were obtained from MeCN and Et_2O by diffusion crystallization. (MeCN/Et2O)

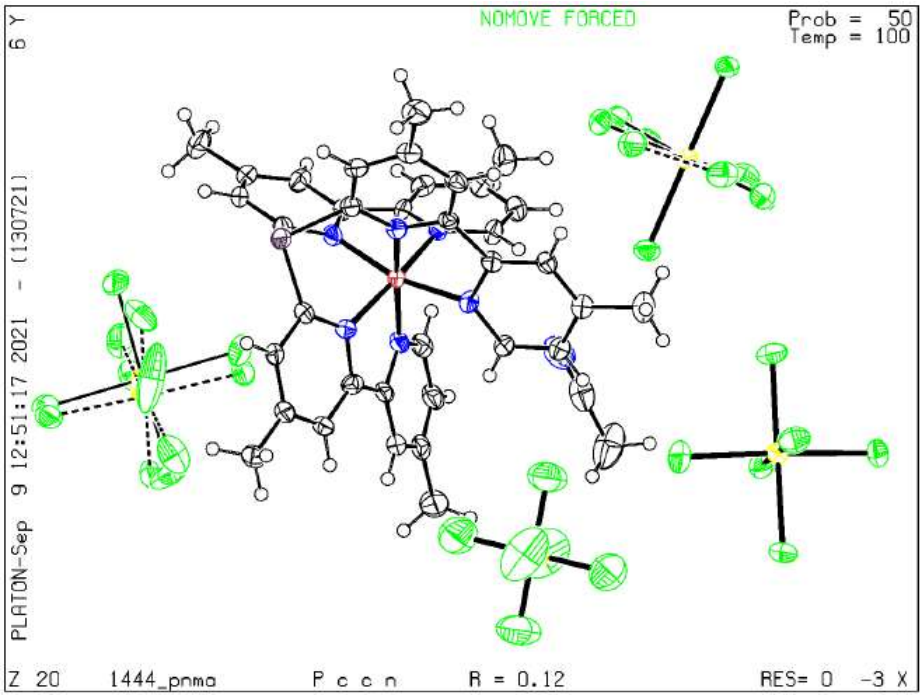

Identification code	1444_Pnma
Empirical formula	$C_{38}H_{36}Cl_{15}CoF_3N_7PSb_3$
Formula weight	1634.64
Temperature/K	100.00
Crystal system	orthorhombic
Space group	Pccn
a/Å	38.7202(18)
b/Å	19.7571(9)
c/Å	14.3388(7)
α/°	90
β/°	90
γ/°	90
Volume/Å^3	10969.2(9)
Z	8
ρ_{calc}g/cm^3	1.980
μ/mm^{-1}	2.567
F(000)	6320.0
Crystal size/mm^3	0.323 × 0.181 × 0.048
Radiation	MoKα (λ = 0.71073)
2Θ range for data collection/°	3.664 to 59.174
Index ranges	-53 ≤ h ≤ 53, -27 ≤ k ≤ 27, -19 ≤ l ≤ 19
Reflections collected	209333
Independent reflections	15342 [R_{int} = 0.0470, R_{sigma} = 0.0212]
Data/restraints/parameters	15342/250/705
Goodness-of-fit on F^2	1.262
Final R indexes [I>=2σ (I)]	R_1 = 0.1174, wR_2 = 0.2541
Final R indexes [all data]	R_1 = 0.1224, wR_2 = 0.2560
Largest diff. peak/hole / e Å^{-3}	2.46/-2.78

Compound **242**

Single crystals suitable for X-ray analysis were obtained from MeCN and Et_2O by diffusion crystallization. (MeCN/Et2O)

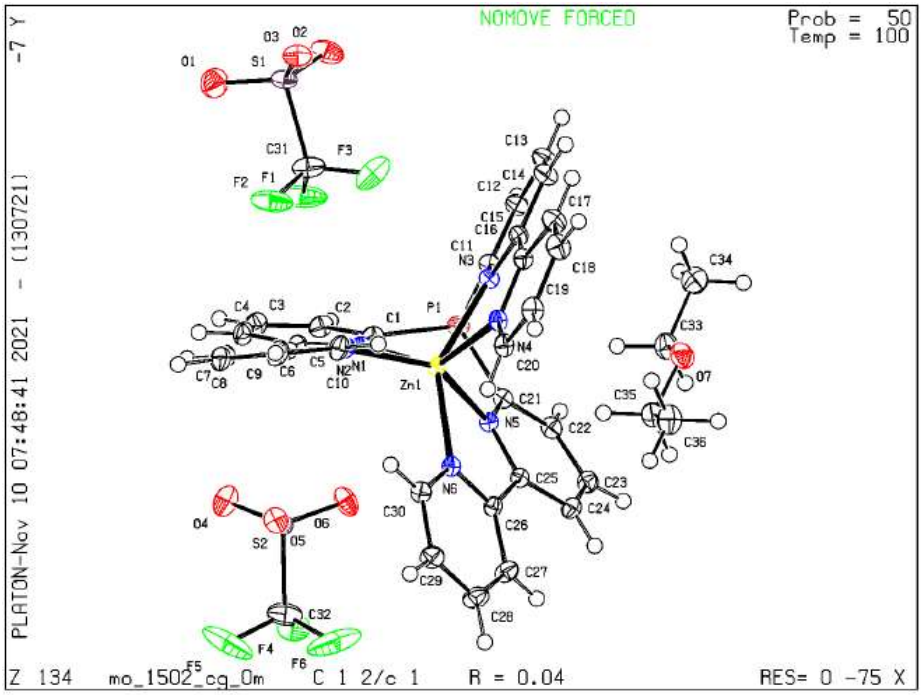

Identification code	mo_1502_CG_0m-finalcif
Empirical formula	$C_{68}H_{52}F_{12}N_{12}O_{13}P_2S_4Zn_2$
Formula weight	1794.13
Temperature/K	100.00
Crystal system	monoclinic
Space group	C2/c
a/Å	19.0320(11)
b/Å	14.2485(8)
c/Å	27.6486(14)
α/°	90
β/°	105.530(2)
γ/°	90
Volume/Å^3	7223.9(7)
Z	4
ρ_{calc}g/cm^3	1.650
μ/mm^{-1}	0.928
F(000)	3640.0
Crystal size/mm^3	0.352 × 0.189 × 0.178
Radiation	MoKα (λ = 0.71073)
2Θ range for data collection/°	4.154 to 65.22
Index ranges	-28 ≤ h ≤ 28, -21 ≤ k ≤ 20, -41 ≤ l ≤ 41
Reflections collected	93941
Independent reflections	13001 [R_{int} = 0.0265, R_{sigma} = 0.0157]
Data/restraints/parameters	13001/48/534
Goodness-of-fit on F^2	1.118
Final R indexes [I>=2σ (I)]	R_1 = 0.0366, wR_2 = 0.0941
Final R indexes [all data]	R_1 = 0.0392, wR_2 = 0.0955
Largest diff. peak/hole / e Å^{-3}	1.77/-0.94

Compound **243**

Single crystals suitable for X-ray analysis were obtained from MeCN and Et_2O by diffusion crystallization. (MeCN/Et2O)

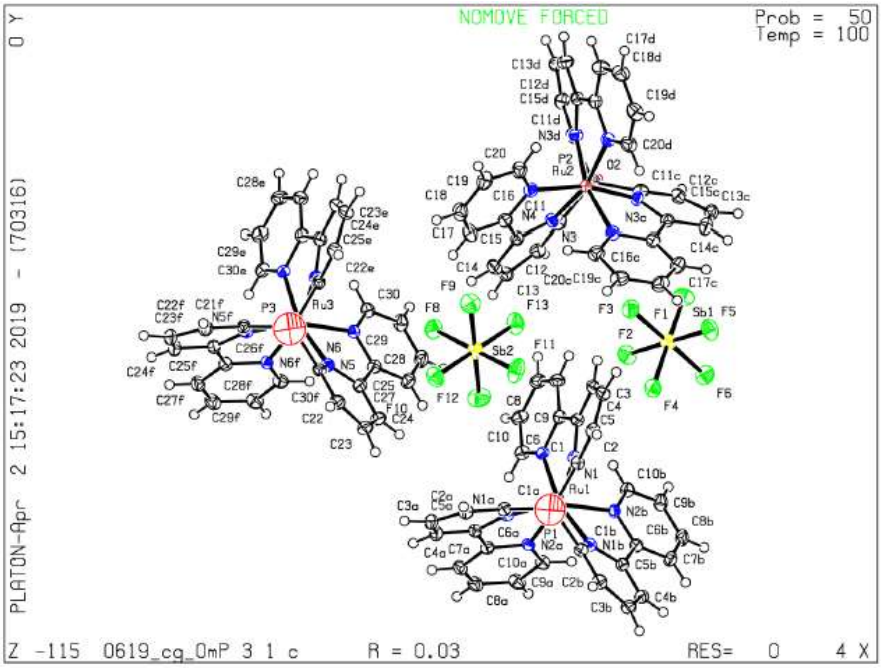

Identification code	0619_CG_0m_4
Empirical formula	$C_{30}H_{21}F_{12}N_6O_{0.2}PRuSb_2$
Formula weight	1072.29
Temperature/K	99.96
Crystal system	trigonal
Space group	P31c
a/Å	17.7830(12)
b/Å	17.7830(12)
c/Å	18.1227(13)
α/°	90
β/°	90
γ/°	120
Volume/Å^3	4963.2(8)
Z	6
ρ_{calc}g/cm^3	2.153
μ/mm^{-1}	2.223
F(000)	3082.0
Crystal size/mm^3	0.3 × 0.235 × 0.062
Radiation	MoKα (λ = 0.71073)
2Θ range for data collection/°	4.582 to 61.064
Index ranges	-25 ≤ h ≤ 25, -25 ≤ k ≤ 25, -25 ≤ l ≤ 25
Reflections collected	19575
Independent reflections	10101 [R_{int} = 0.0204, R_{sigma} = 0.0201]
Data/restraints/parameters	10101/19/482
Goodness-of-fit on F^2	1.052
Final R indexes [I>=2σ (I)]	R_1 = 0.0252, wR_2 = 0.0652
Final R indexes [all data]	R_1 = 0.0276, wR_2 = 0.0665
Largest diff. peak/hole / e Å^{-3}	2.62/-1.15
Flack parameter	0.504(19)

Compound **244**

Single crystals suitable for X-ray analysis were obtained from MeCN and Et_2O by diffusion crystallization. (MeCN/Et2O)

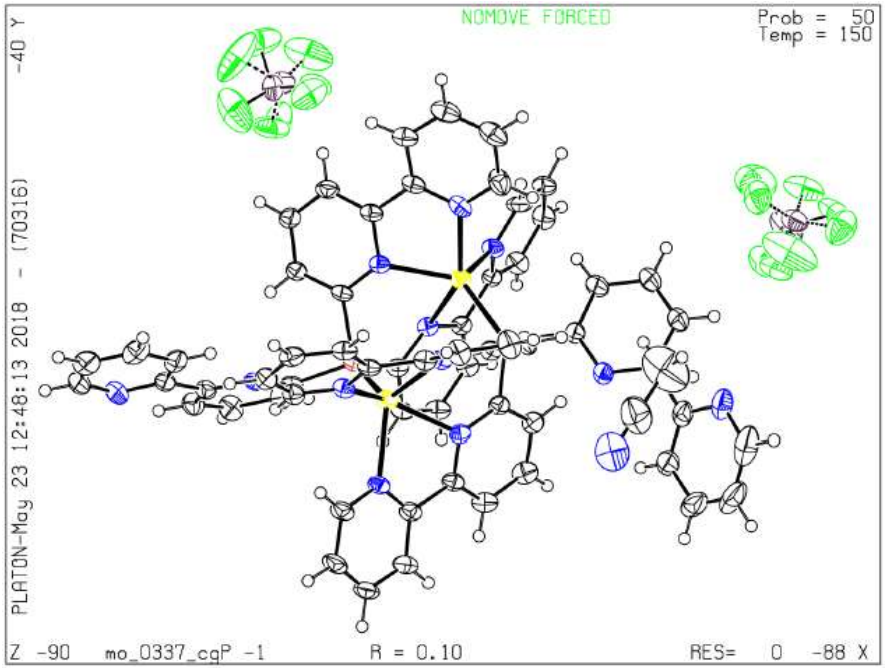

Identification code	mo_0337_CG_0m
Empirical formula	$C_{62}H_{45}B_2Cu_2F_8N_{13}P_2$
Formula weight	1334.75
Temperature/K	150.0
Crystal system	triclinic
Space group	P-1
a/Å	9.992(2)
b/Å	12.717(2)
c/Å	23.241(5)
α/°	84.103(6)
β/°	89.849(7)
γ/°	87.319(8)
Volume/Å^3	2934.4(10)
Z	2
ρ_{calc}g/cm^3	1.511
μ/mm^{-1}	0.859
F(000)	1356.0
Crystal size/mm^3	0.503 × 0.122 × 0.048
Radiation	MoKα (λ = 0.71073)
2Θ range for data collection/°	4.08 to 57.986
Index ranges	-13 ≤ h ≤ 13, -17 ≤ k ≤ 17, -31 ≤ l ≤ 31
Reflections collected	121147
Independent reflections	15435 [R_{int} = 0.0686, R_{sigma} = 0.0424]
Data/restraints/parameters	15435/220/877
Goodness-of-fit on F^2	1.098
Final R indexes [I>=2σ (I)]	R_1 = 0.0952, wR_2 = 0.2323
Final R indexes [all data]	R_1 = 0.1065, wR_2 = 0.2372
Largest diff. peak/hole / e Å^{-3}	1.42/-1.32

Compound **245**

Single crystals suitable for X-ray analysis were obtained from MeCN and Et_2O by diffusion crystallization. (MeCN/Et2O)

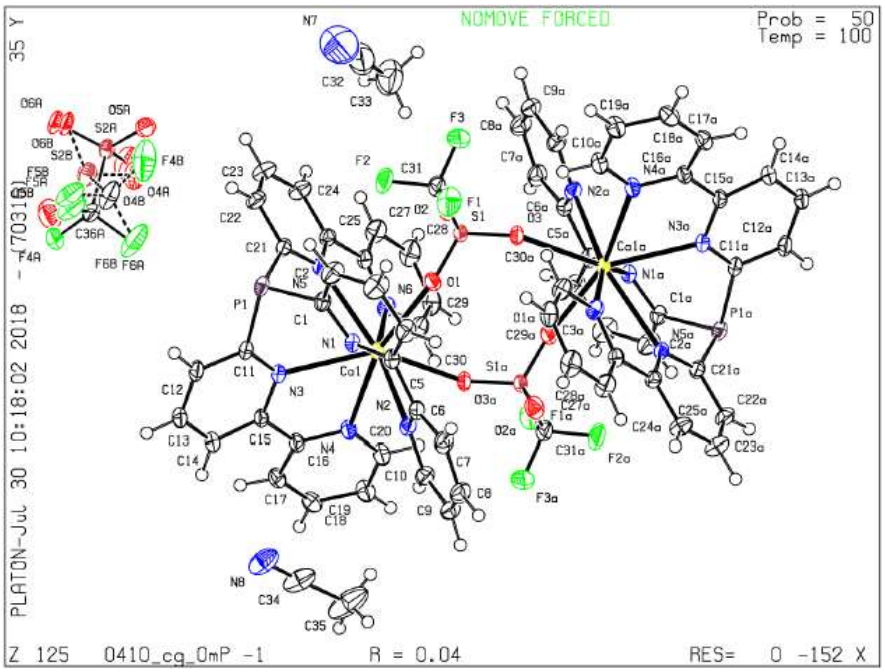

Identification code	0410_CG_0m
Empirical formula	$C_{36}H_{27}CaF_6N_8O_6PS_2$
Formula weight	916.82
Temperature/K	100
Crystal system	triclinic
Space group	P-1
a/Å	12.3954(14)
b/Å	13.5925(15)
c/Å	13.9772(14)
α/°	76.642(3)
β/°	64.708(3)
γ/°	69.307(3)
Volume/Å^3	1982.9(4)
Z	2
ρ_{calc}g/cm^3	1.536
μ/mm^{-1}	0.389
F(000)	936.0
Crystal size/mm^3	0.241 × 0.136 × 0.1
Radiation	MoKα (λ = 0.71073)
2Θ range for data collection/°	4.108 to 63.236
Index ranges	-18 ≤ h ≤ 18, -19 ≤ k ≤ 20, -20 ≤ l ≤ 20
Reflections collected	186985
Independent reflections	13262 [R_{int} = 0.0322, R_{sigma} = 0.0141]
Data/restraints/parameters	13262/126/604
Goodness-of-fit on F^2	1.054
Final R indexes [I>=2σ (I)]	R_1 = 0.0386, wR_2 = 0.1007
Final R indexes [all data]	R_1 = 0.0425, wR_2 = 0.1037
Largest diff. peak/hole / e Å^{-3}	1.42/-1.03

Compound **246**

Single crystals suitable for X-ray analysis were obtained from MeCN and Et_2O by diffusion crystallization. (MeCN/Et2O)

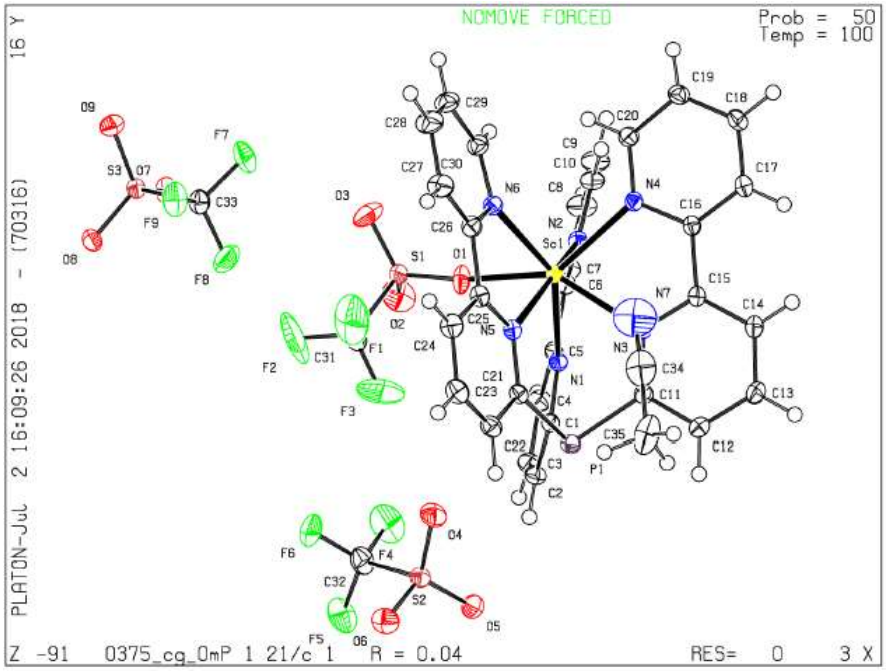

Identification code	0375_CG_0m
Empirical formula	$C_{35}H_{24}F_9N_7O_9PS_3Sc$
Formula weight	1029.72
Temperature/K	100.0
Crystal system	monoclinic
Space group	$P2_1/c$
a/Å	13.7123(4)
b/Å	16.5738(4)
c/Å	19.0349(4)
α/°	90
β/°	106.8050(10)
γ/°	90
Volume/Å^3	4141.22(18)
Z	4
ρ_{calc}g/cm^3	1.652
μ/mm^{-1}	0.471
F(000)	2080.0
Crystal size/mm^3	0.49 × 0.357 × 0.102
Radiation	MoKα (λ = 0.71073)
2Θ range for data collection/°	4.648 to 63.074
Index ranges	-20 ≤ h ≤ 20, -24 ≤ k ≤ 24, -28 ≤ l ≤ 22
Reflections collected	73236
Independent reflections	13807 [R_{int} = 0.0351, R_{sigma} = 0.0259]
Data/restraints/parameters	13807/0/587
Goodness-of-fit on F^2	1.050
Final R indexes [I>=2σ (I)]	R_1 = 0.0390, wR_2 = 0.1021
Final R indexes [all data]	R_1 = 0.0468, wR_2 = 0.1073
Largest diff. peak/hole / e Å^{-3}	1.05/-0.52

Compound **247**

Single crystals suitable for X-ray analysis were obtained from MeCN and Et_2O by diffusion crystallization. (MeCN/Et2O)

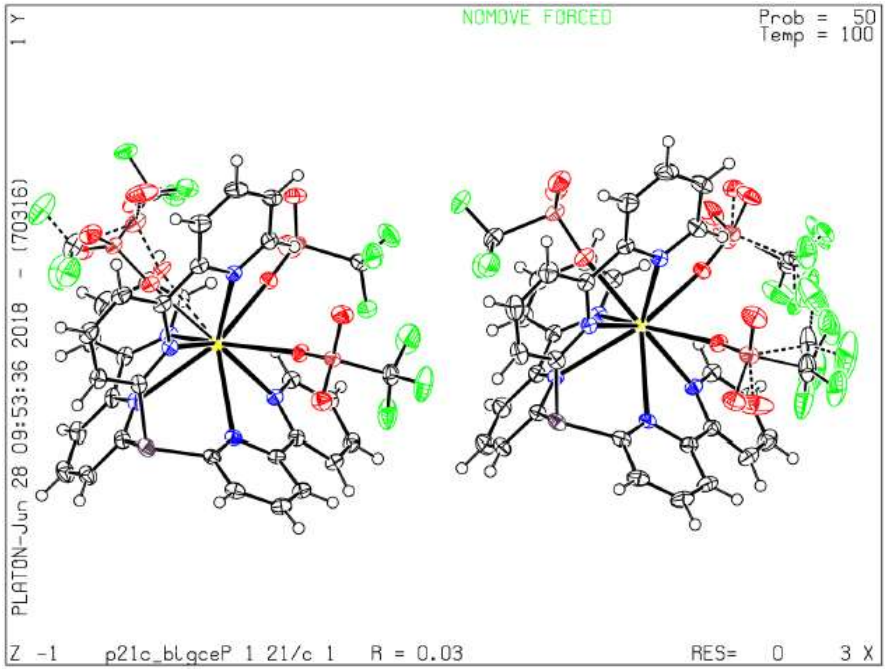

Identification code	P21c_bigcell
Empirical formula	$C_{33}H_{21}F_9LaN_6O_9PS_3$
Formula weight	1082.62
Temperature/K	100.03
Crystal system	monoclinic
Space group	$P2_1/c$
a/Å	22.8133(13)
b/Å	19.5884(10)
c/Å	17.8485(10)
α/°	90
β/°	106.423(2)
γ/°	90
Volume/Å^3	7650.6(7)
Z	8
ρ_{calc}g/cm^3	1.880
μ/mm^{-1}	1.430
F(000)	4272.0
Crystal size/mm^3	0.446 × 0.394 × 0.022
Radiation	MoKα (λ = 0.71073)
2Θ range for data collection/°	4.264 to 63.23
Index ranges	-33 ≤ h ≤ 33, -28 ≤ k ≤ 28, -26 ≤ l ≤ 26
Reflections collected	94756
Independent reflections	25511 [R_{int} = 0.0397, R_{sigma} = 0.0420]
Data/restraints/parameters	25511/103/1291
Goodness-of-fit on F^2	1.014
Final R indexes [I>=2σ (I)]	R_1 = 0.0325, wR_2 = 0.0709
Final R indexes [all data]	R_1 = 0.0455, wR_2 = 0.0768
Largest diff. peak/hole / e Å^{-3}	2.12/-1.20

Compound **250**

Single crystals suitable for X-ray analysis were obtained from hot toluene. (toluene)

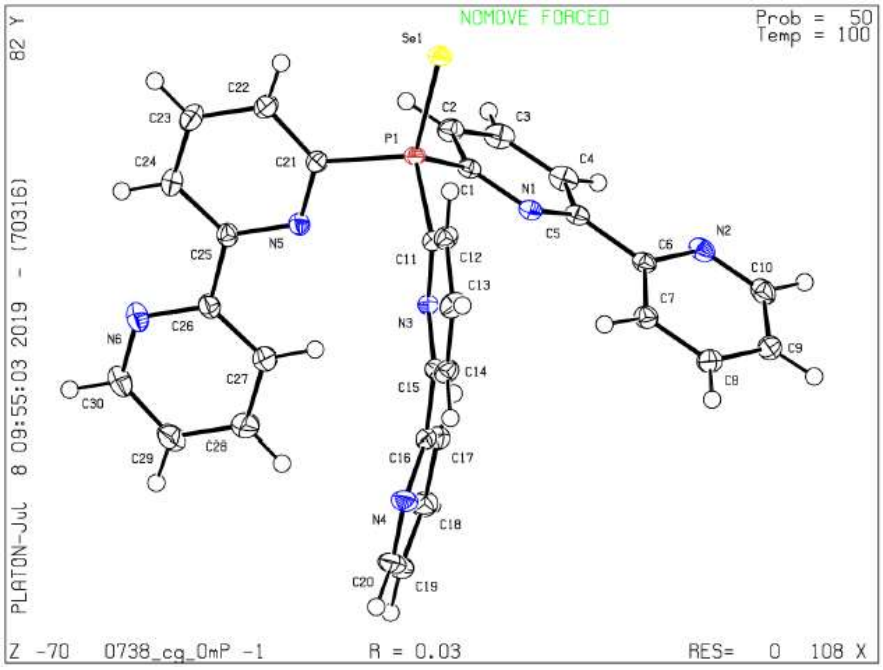

Identification code	0738_CG_0m
Empirical formula	$C_{30}H_{21}N_6PSe$
Formula weight	575.46
Temperature/K	100.01
Crystal system	triclinic
Space group	P-1
a/Å	8.4515(6)
b/Å	11.7706(8)
c/Å	13.5596(9)
α/°	91.842(2)
β/°	96.535(2)
γ/°	104.198(2)
Volume/Å^3	1296.67(15)
Z	2
ρ_{calc}g/cm^3	1.474
μ/mm^{-1}	1.542
F(000)	584.0
Crystal size/mm^3	0.311 × 0.268 × 0.198
Radiation	MoKα (λ = 0.71073)
2Θ range for data collection/°	4.83 to 65.182
Index ranges	-11 ≤ h ≤ 12, -17 ≤ k ≤ 17, -19 ≤ l ≤ 18
Reflections collected	23695
Independent reflections	7809 [R_{int} = 0.0168, R_{sigma} = 0.0195]
Data/restraints/parameters	7809/0/343
Goodness-of-fit on F^2	1.072
Final R indexes [I>=2σ (I)]	R_1 = 0.0250, wR_2 = 0.0698
Final R indexes [all data]	R_1 = 0.0274, wR_2 = 0.0711
Largest diff. peak/hole / e Å^{-3}	0.49/-0.46

Compound **252**

Single crystals suitable for X-ray analysis were obtained from MeCN and Et_2O by diffusion crystallization. (MeCN/Et_2O)

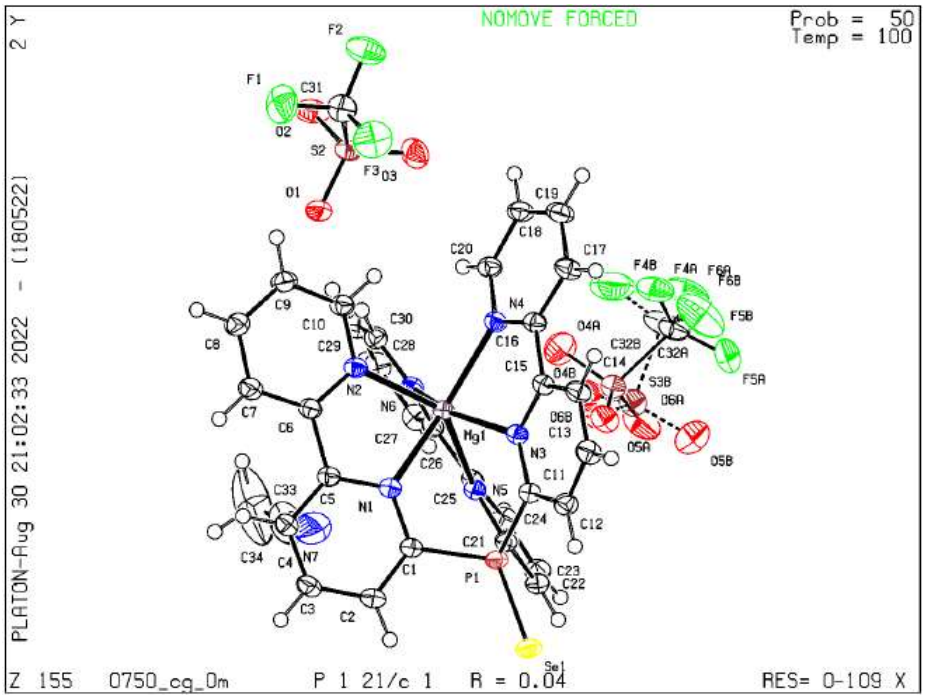

Identification code	0750_CG_0m
Empirical formula	$C_{34}H_{24}F_6MgN_7O_6PS_2Se$
Formula weight	1070.95
Temperature/K	100.03
Crystal system	monoclinic
Space group	$P2_1/c$
a/Å	17.9189(6)
b/Å	17.8810(6)
c/Å	14.2629(5)
α/°	90
β/°	110.7900(10)
γ/°	90
Volume/Å^3	4272.4(3)
Z	4
ρ_{calc}g/cm^3	1.665
μ/mm^{-1}	1.138
F(000)	2171.0
Crystal size/mm^3	0.408 × 0.192 × 0.122
Radiation	MoKα (λ = 0.71073)
2Θ range for data collection/°	5.07 to 61.114
Index ranges	-25 ≤ h ≤ 25, -25 ≤ k ≤ 24, -20 ≤ l ≤ 19
Reflections collected	129994
Independent reflections	13016 [R_{int} = 0.0286, R_{sigma} = 0.0165]
Data/restraints/parameters	13016/72/597
Goodness-of-fit on F^2	1.099
Final R indexes [I>=2σ (I)]	R_1 = 0.0383, wR_2 = 0.1009
Final R indexes [all data]	R_1 = 0.0441, wR_2 = 0.1036
Largest diff. peak/hole / e Å^{-3}	0.52/-0.61

Compound **253**

Single crystals suitable for X-ray analysis were obtained from MeCN and Et_2O by diffusion crystallization. (MeCN/Et_2O)

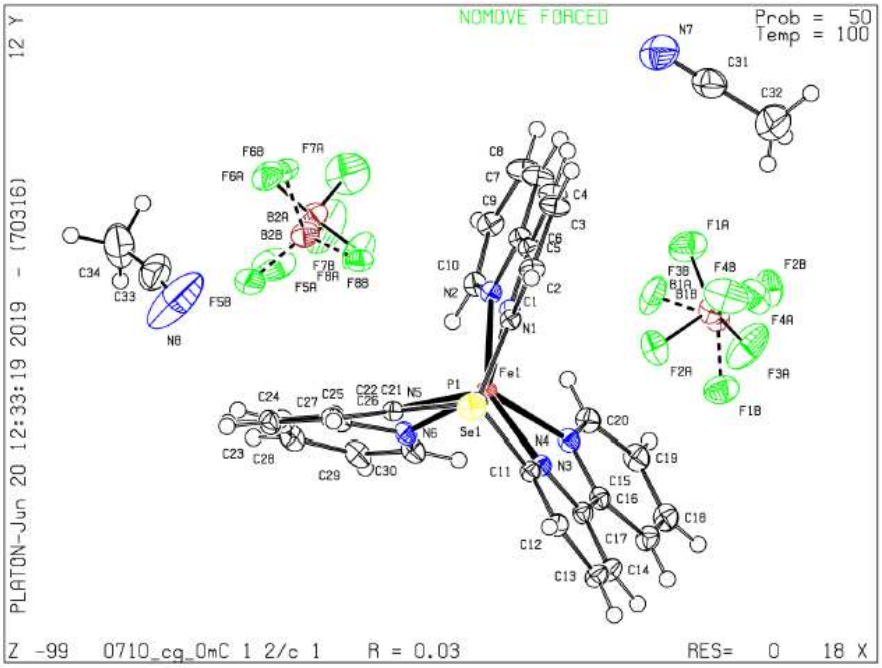

Identification code	0710_CG_0m
Empirical formula	$C_{33}H_{25.5}B_2F_8FeN_{7.5}PSe$
Formula weight	866.51
Temperature/K	99.99
Crystal system	monoclinic
Space group	C2/c
a/Å	21.8613(10)
b/Å	12.4042(6)
c/Å	25.4288(13)
α/°	90
β/°	101.743(2)
γ/°	90
Volume/Å^3	6751.3(6)
Z	8
ρ_{calc}g/cm^3	1.705
μ/mm^{-1}	1.656
F(000)	3464.0
Crystal size/mm^3	0.599 × 0.368 × 0.338
Radiation	MoKα (λ = 0.71073)
2Θ range for data collection/°	4.284 to 63.058
Index ranges	-27 ≤ h ≤ 32, -17 ≤ k ≤ 18, -34 ≤ l ≤ 37
Reflections collected	68833
Independent reflections	10771 [R_{int} = 0.0233, R_{sigma} = 0.0162]
Data/restraints/parameters	10771/200/590
Goodness-of-fit on F^2	1.057
Final R indexes [I>=2σ (I)]	R_1 = 0.0264, wR_2 = 0.0670
Final R indexes [all data]	R_1 = 0.0289, wR_2 = 0.0683
Largest diff. peak/hole / e Å^{-3}	0.46/-0.61

Compound **254**

Single crystals suitable for X-ray analysis were obtained from MeCN and Et_2O by diffusion crystallization. (MeCN/Et_2O)

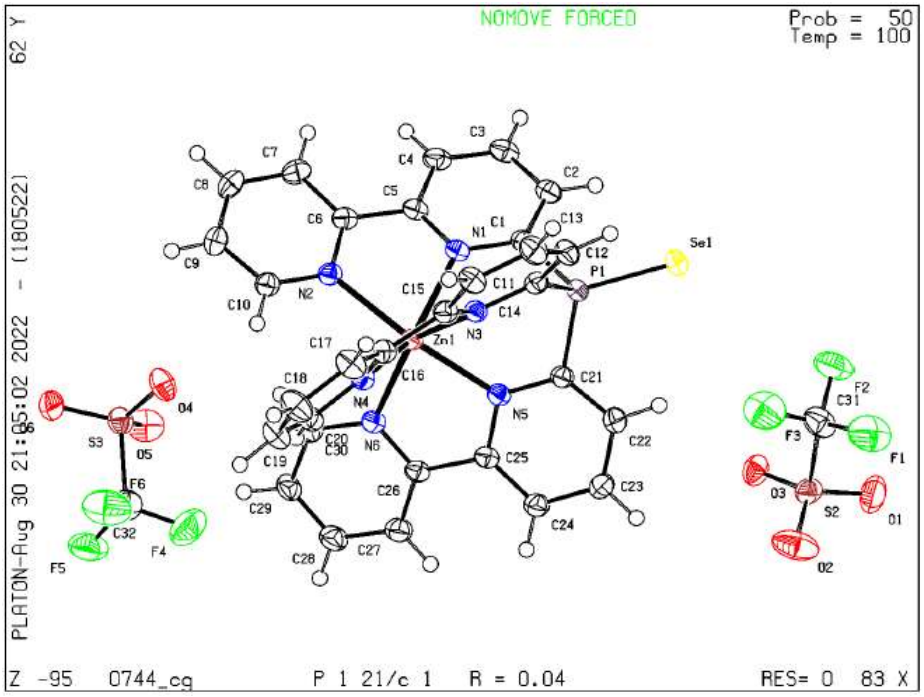

Identification code	0744_CG
Empirical formula	$C_{32}H_{21}F_6N_6O_6PS_2SeZn$
Formula weight	1112.01
Temperature/K	100.0
Crystal system	monoclinic
Space group	$P2_1/c$
a/Å	17.9209(7)
b/Å	17.9062(7)
c/Å	14.2484(6)
α/°	90
β/°	110.6650(10)
γ/°	90
Volume/Å^3	4278.1(3)
Z	4
ρ_{calc}g/cm^3	1.727
μ/mm^{-1}	1.669
F(000)	2243.0
Crystal size/mm^3	0.233 × 0.181 × 0.128
Radiation	MoKα (λ = 0.71073)
2Θ range for data collection/°	4.858 to 54.236
Index ranges	-22 ≤ h ≤ 22, -22 ≤ k ≤ 22, -18 ≤ l ≤ 18
Reflections collected	100373
Independent reflections	9434 [R_{int} = 0.0303, R_{sigma} = 0.0154]
Data/restraints/parameters	9434/0/496
Goodness-of-fit on F^2	1.087
Final R indexes [I>=2σ (I)]	R_1 = 0.0403, wR_2 = 0.0967
Final R indexes [all data]	R_1 = 0.0444, wR_2 = 0.0986
Largest diff. peak/hole / e Å^{-3}	0.89/-0.61

Compound **256**

Single crystals suitable for X-ray analysis were obtained from MeCN and Et_2O by diffusion crystallization. (MeCN/Et_2O)

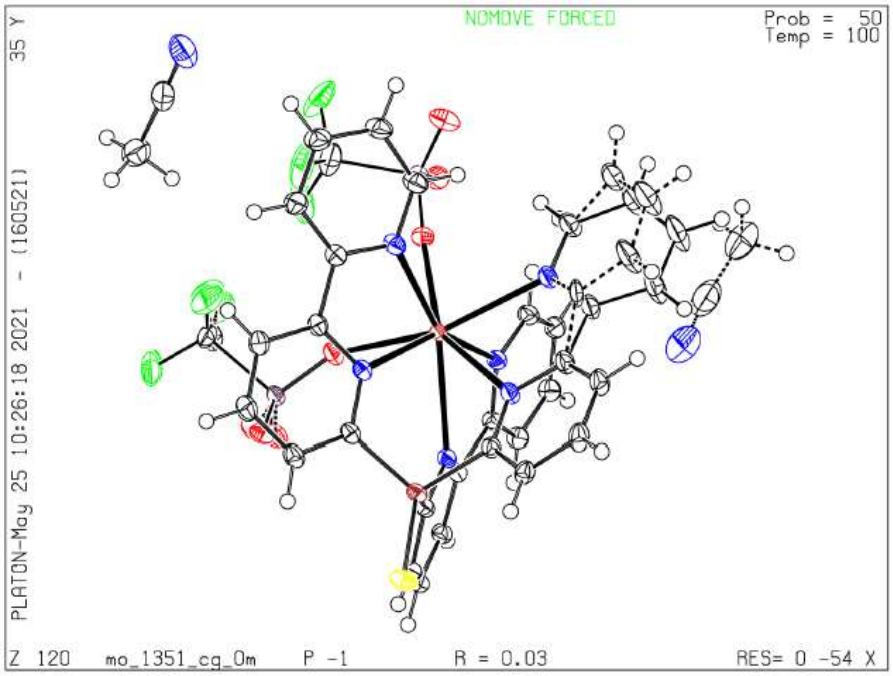

Identification code	mo_1351_CG_0m
Empirical formula	$C_{34.13}H_{24.4}CaF_{5.93}N_{7.07}O_6PS_{1.98}Se$
Formula weight	955.53
Temperature/K	100.0
Crystal system	triclinic
Space group	P-1
a/Å	11.9266(8)
b/Å	12.0896(9)
c/Å	13.8290(7)
α/°	103.091(2)
β/°	97.731(2)
γ/°	95.302(2)
Volume/Å^3	1908.8(2)
Z	2
ρ_{calc}g/cm^3	1.662
μ/mm^{-1}	1.352
F(000)	961.0
Crystal size/mm^3	0.261 × 0.222 × 0.174
Radiation	MoKα (λ = 0.71073)
2Θ range for data collection/°	4.046 to 65.218
Index ranges	-18 ≤ h ≤ 18, -18 ≤ k ≤ 18, -20 ≤ l ≤ 20
Reflections collected	283398
Independent reflections	13931 [R_{int} = 0.0193, R_{sigma} = 0.0068]
Data/restraints/parameters	13931/85/646
Goodness-of-fit on F^2	1.039
Final R indexes [I>=2σ (I)]	R_1 = 0.0256, wR_2 = 0.0714
Final R indexes [all data]	R_1 = 0.0268, wR_2 = 0.0722
Largest diff. peak/hole / e Å^{-3}	1.71/-0.57

Compound **258**

Single crystals suitable for X-ray analysis were obtained from MeCN and Et_2O by diffusion crystallization. (MeCN/Et_2O)

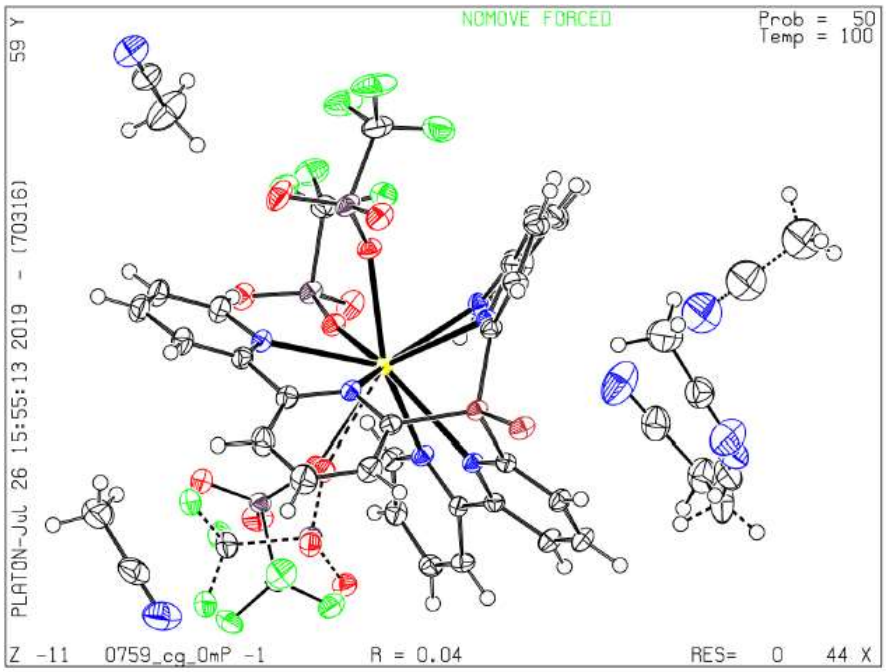

Identification code	0759_CG_0m_4
Empirical formula	$C_{41}H_{33}F_9LaN_{10}O_9PS_3Se$
Formula weight	1325.79
Temperature/K	100.01
Crystal system	triclinic
Space group	P-1
a/Å	11.8645(5)
b/Å	14.0467(6)
c/Å	15.9396(8)
α/°	79.8440(10)
β/°	89.095(2)
γ/°	71.4750(10)
Volume/Å^3	2477.03(19)
Z	2
ρ_{calc}g/cm^3	1.778
μ/mm^{-1}	1.854
F(000)	1312.0
Crystal size/mm^3	0.304 × 0.117 × 0.052
Radiation	MoKα (λ = 0.71073)
2Θ range for data collection/°	4.498 to 64.908
Index ranges	-17 ≤ h ≤ 17, -20 ≤ k ≤ 20, 0 ≤ l ≤ 23
Reflections collected	15747
Independent reflections	15747 [R_{int} = ?, R_{sigma} = 0.0354]
Data/restraints/parameters	15747/188/800
Goodness-of-fit on F^2	1.053
Final R indexes [I>=2σ (I)]	R_1 = 0.0387, wR_2 = 0.0793
Final R indexes [all data]	R_1 = 0.0500, wR_2 = 0.0850
Largest diff. peak/hole / e Å^{-3}	1.32/-0.74

Compound **266**

Single crystals suitable for X-ray analysis were obtained by slowly evaporating a Et_2O solution. (Et_2O)

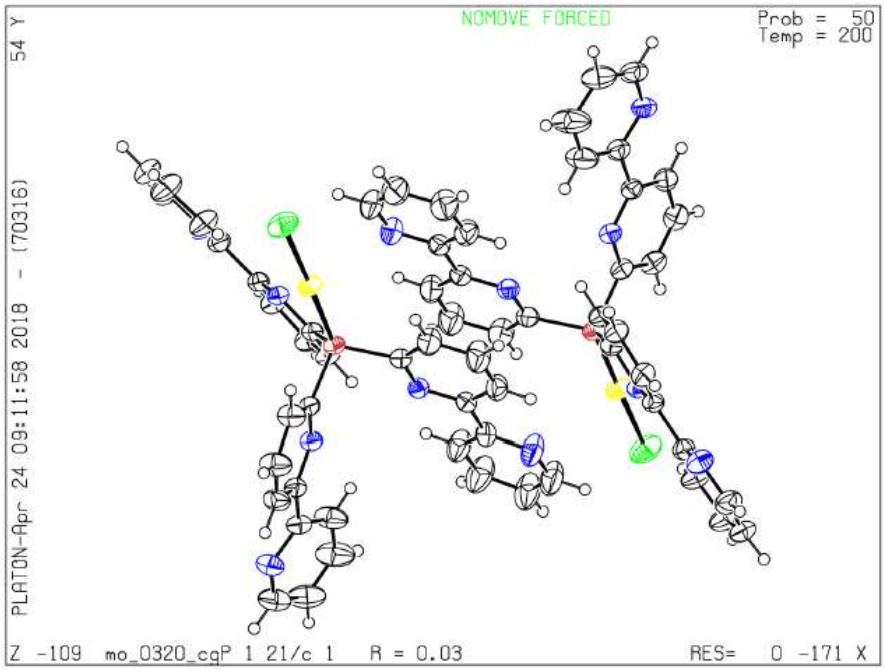

Identification code	mo_0320_CG_0m
Empirical formula	$C_{30}H_{21}AuClN_6P$
Formula weight	728.91
Temperature/K	199.98
Crystal system	monoclinic
Space group	$P2_1/c$
a/Å	10.6032(4)
b/Å	27.4329(9)
c/Å	23.9847(11)
α/°	90
β/°	90.679(2)
γ/°	90
Volume/Å^3	6976.1(5)
Z	8
ρ_{calc}g/cm^3	1.388
μ/mm^{-1}	4.365
F(000)	2832.0
Crystal size/mm^3	0.285 × 0.253 × 0.159
Radiation	MoKα (λ = 0.71073)
2Θ range for data collection/°	4.118 to 61.344
Index ranges	-15 ≤ h ≤ 15, -39 ≤ k ≤ 39, -34 ≤ l ≤ 33
Reflections collected	82508
Independent reflections	21377 [R_{int} = 0.0256, R_{sigma} = 0.0251]
Data/restraints/parameters	21377/0/703
Goodness-of-fit on F^2	1.088
Final R indexes [I>=2σ (I)]	R_1 = 0.0275, wR_2 = 0.0762
Final R indexes [all data]	R_1 = 0.0366, wR_2 = 0.0789
Largest diff. peak/hole / e Å^{-3}	0.82/-1.29

Compound **267**

Single crystals suitable for X-ray analysis were obtained from MeCN and Et_2O by diffusion crystallization. (MeCN/Et2O)

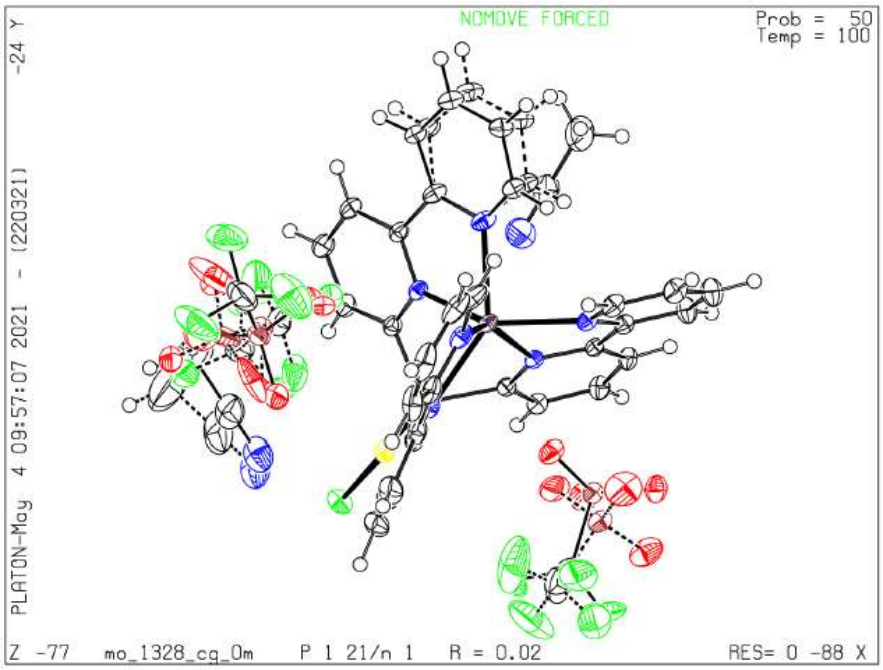

Identification code	mo_1328_CG_0m
Empirical formula	$C_{36}H_{27}AuClF_6MgN_8O_6PS_2$
Formula weight	1133.47
Temperature/K	100.0
Crystal system	monoclinic
Space group	$P2_1/n$
a/Å	14.0320(5)
b/Å	14.4151(5)
c/Å	20.3948(7)
α/°	90
β/°	91.9850(10)
γ/°	90
Volume/Å^3	4122.8(2)
Z	4
ρ_{calc}g/cm^3	1.826
μ/mm^{-1}	3.872
F(000)	2224.0
Crystal size/mm^3	0.32 × 0.19 × 0.052
Radiation	MoKα (λ = 0.71073)
2Θ range for data collection/°	4.052 to 66.34
Index ranges	-21 ≤ h ≤ 21, -22 ≤ k ≤ 22, -31 ≤ l ≤ 31
Reflections collected	237732
Independent reflections	15601 [R_{int} = 0.0303, R_{sigma} = 0.0138]
Data/restraints/parameters	15601/579/774
Goodness-of-fit on F^2	1.029
Final R indexes [I>=2σ (I)]	R_1 = 0.0219, wR_2 = 0.0536
Final R indexes [all data]	R_1 = 0.0244, wR_2 = 0.0546
Largest diff. peak/hole / e Å^{-3}	1.06/-0.96

Compound **268**

Single crystals suitable for X-ray analysis were obtained from MeCN and Et_2O by diffusion crystallization. (MeCN/Et2O)

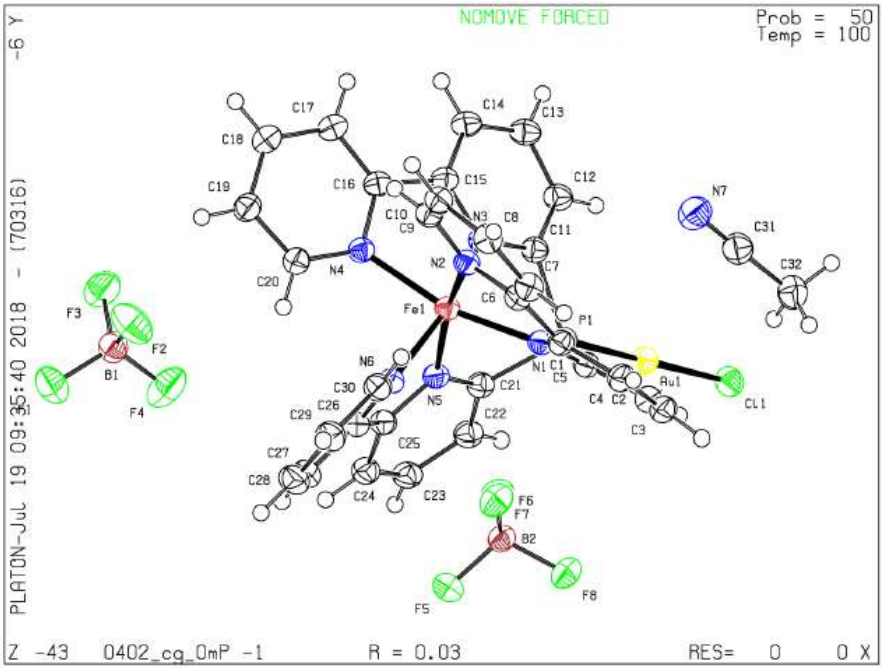

Identification code	0402_CG_0m
Empirical formula	$C_{32}H_{24}AuB_2ClF_8FeN_7P$
Formula weight	999.44
Temperature/K	100.01
Crystal system	triclinic
Space group	P-1
a/Å	11.6881(7)
b/Å	12.3876(9)
c/Å	12.9242(7)
α/°	89.801(3)
β/°	72.710(4)
γ/°	68.357(3)
Volume/Å^3	1648.82(19)
Z	2
ρ_{calc}g/cm^3	2.013
μ/mm^{-1}	5.097
F(000)	968.0
Crystal size/mm^3	0.221 × 0.192 × 0.056
Radiation	MoKα (λ = 0.71073)
2Θ range for data collection/°	4.18 to 65.382
Index ranges	-17 ≤ h ≤ 17, -18 ≤ k ≤ 18, -19 ≤ l ≤ 19
Reflections collected	120907
Independent reflections	12084 [R_{int} = 0.0238, R_{sigma} = 0.0113]
Data/restraints/parameters	12084/0/479
Goodness-of-fit on F^2	1.097
Final R indexes [I>=2σ (I)]	R_1 = 0.0324, wR_2 = 0.0829
Final R indexes [all data]	R_1 = 0.0330, wR_2 = 0.0835
Largest diff. peak/hole / e Å^{-3}	2.90/-0.38

Compound **270**

Single crystals suitable for X-ray analysis were obtained from MeCN and Et_2O by diffusion crystallization. (MeCN/Et2O)

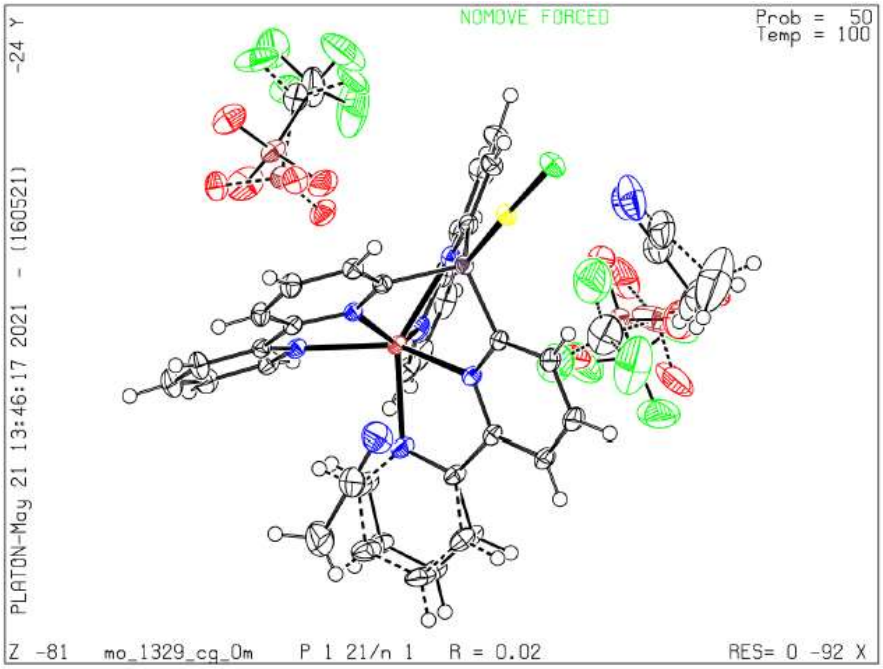

Identification code	mo_1329_CG_0m
Empirical formula	$C_{36}H_{27}AuClF_6N_8O_6PS_2Zn$
Formula weight	1174.53
Temperature/K	100.0
Crystal system	monoclinic
Space group	$P2_1/n$
a/Å	13.9820(5)
b/Å	14.4313(6)
c/Å	20.4194(8)
α/°	90
β/°	92.3160(10)
γ/°	90
Volume/Å^3	4116.8(3)
Z	4
ρ_{calc}g/cm^3	1.895
μ/mm^{-1}	4.431
F(000)	2296.0
Crystal size/mm^3	0.151 × 0.126 × 0.104
Radiation	MoKα (λ = 0.71073)
2Θ range for data collection/°	4.058 to 66.342
Index ranges	-20 ≤ h ≤ 21, -22 ≤ k ≤ 22, -30 ≤ l ≤ 31
Reflections collected	226250
Independent reflections	15512 [R_{int} = 0.0255, R_{sigma} = 0.0125]
Data/restraints/parameters	15512/501/773
Goodness-of-fit on F^2	1.043
Final R indexes [I>=2σ (I)]	R_1 = 0.0217, wR_2 = 0.0549
Final R indexes [all data]	R_1 = 0.0242, wR_2 = 0.0560
Largest diff. peak/hole / e Å^{-3}	1.79/-0.91

Compound **272**

Single crystals suitable for X-ray analysis were obtained from MeCN and Et_2O by diffusion crystallization. (MeCN/Et2O)

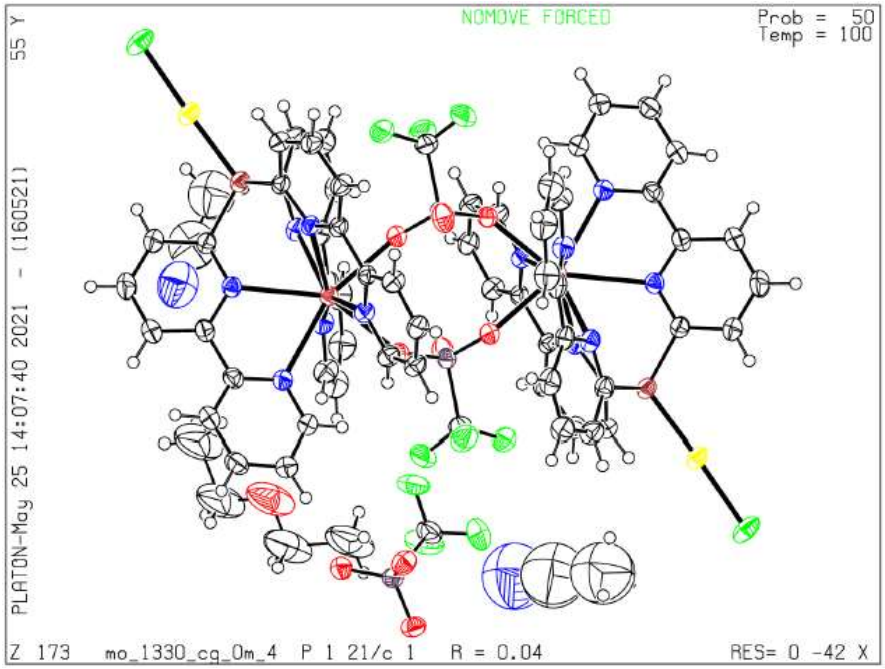

Identification code	mo_1330_CG_0m_4
Empirical formula	$C_{36}H_{29}AuCaClF_6N_7O_{6.5}PS_2$
Formula weight	1145.25
Temperature/K	100.0
Crystal system	monoclinic
Space group	$P2_1/c$
a/Å	11.5902(13)
b/Å	14.7946(14)
c/Å	25.274(3)
α/°	90
β/°	91.069(3)
γ/°	90
Volume/Å^3	4333.0(8)
Z	4
ρ_{calc}g/cm^3	1.756
μ/mm^{-1}	3.788
F(000)	2252.0
Crystal size/mm^3	0.307 × 0.147 × 0.076
Radiation	MoKα (λ = 0.71073)
2Θ range for data collection/°	4.24 to 61.05
Index ranges	-16 ≤ h ≤ 16, 0 ≤ k ≤ 21, 0 ≤ l ≤ 36
Reflections collected	16970
Independent reflections	16970 [R_{int} = ?, R_{sigma} = 0.0283]
Data/restraints/parameters	16970/132/600
Goodness-of-fit on F^2	1.129
Final R indexes [I>=2σ (I)]	R_1 = 0.0398, wR_2 = 0.1261
Final R indexes [all data]	R_1 = 0.0448, wR_2 = 0.1301
Largest diff. peak/hole / e Å^{-3}	1.92/-0.64

Compound **470a**

Single crystals suitable for X-ray analysis were obtained from DCM and Et_2O by diffusion crystallization. (DCM/Et_2O)

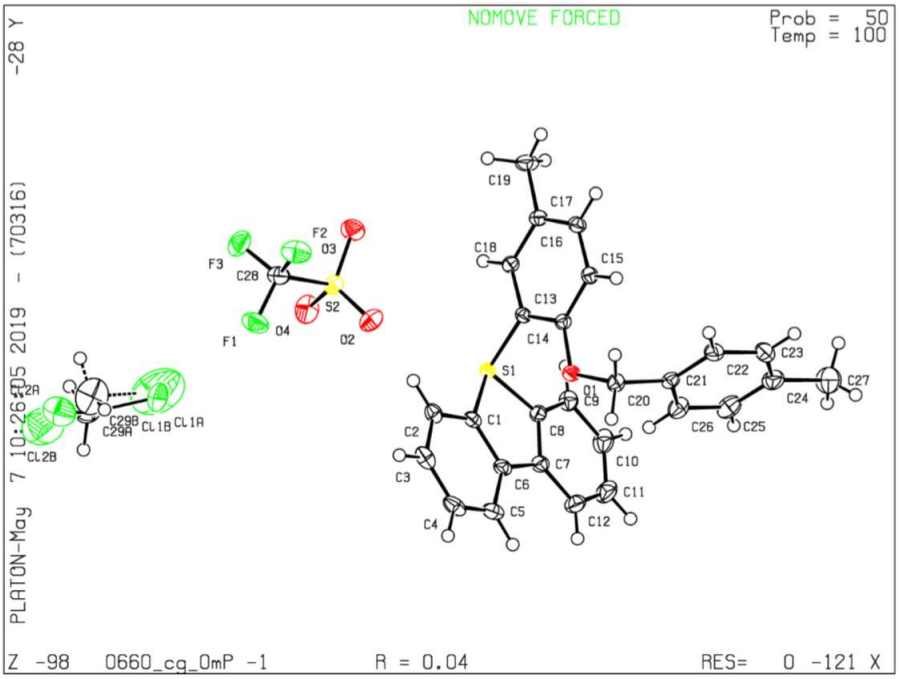

CCDC-Nr.	2051252
Empirical formula	$C_{29}H_{25}Cl_2F_3O_4S_2$
Formula weight	629.51
Temperature/K	100
Crystal system	Triclinic
Space group	P-1
a/Å	10.3968(8)
b/Å	10.5814(7)
c/Å	13.6257(9)
α/°	91.537(3)
β/°	102.506(3)
γ/°	102.648(2)
Volume/Å^3	1423.58(17)
Z	2
ρ_{calc}g/cm^3	1.469
μ/mm^{-1}	0.429
F(000)	648
Crystal size/mm^3	0.343 × 0.315 × 0.265
Radiation	MoKα (λ = 0.71073)
2Θ range for data collection/°	4.546 to 57.446
Index ranges	-14 ≤ h ≤ 14, -14 ≤ k ≤ 14, -18 ≤ l ≤ 18
Reflections collected	61800
Independent reflections	7347 [R_{int} = 0.0222, R_{sigma} = 0.0131]
Data/restraints/parameters	7347/32/391
Goodness-of-fit on F^2	1.025
Final R indexes [I>=2σ (I)]	R_1 = 0.0370, wR_2 = 0.0969
Final R indexes [all data]	R_1 = 0.0383, wR_2 = 0.0980
Largest diff. peak/hole / e Å^{-3}	0.76/-0.61

Compound **470e**

Single crystals suitable for X-ray analysis were obtained from MeCN and Et_2O by diffusion crystallization. (MeCN/Et_2O)

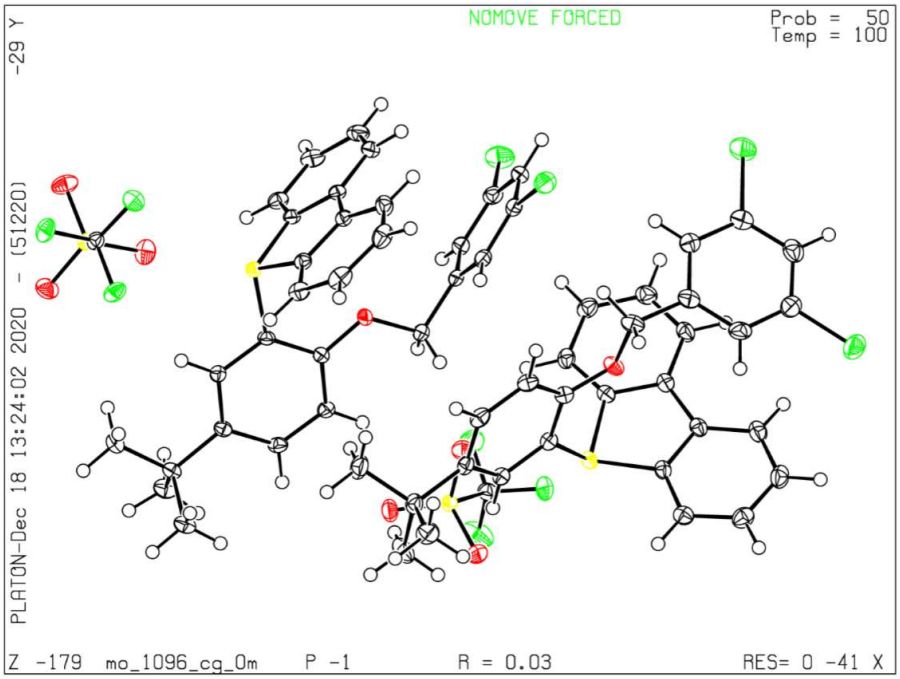

CCDC-Nr.	2051254
Empirical formula	$C_{30}H_{25}Cl_2F_3O_4S_2$
Formula weight	641.52
Temperature/K	100
Crystal system	Triclinic
Space group	P-1
a/Å	12.288(2)
b/Å	13.457(2)
c/Å	17.735(2)
α/°	87.935(5)
β/°	88.466(5)
γ/°	81.486(5)
Volume/Å^3	2898.0(8)
Z	4
ρ_{calc}g/cm^3	1.47
μ/mm^{-1}	0.423
F(000)	1320
Crystal size/mm^3	0.516 × 0.138 × 0.098
Radiation	MoKα (λ = 0.71073)
2Θ range for data collection/°	4.106 to 59.292
Index ranges	-17 ≤ h ≤ 17, -18 ≤ k ≤ 18, -24 ≤ l ≤ 20
Reflections collected	76807
Independent reflections	16230 [R_{int} = 0.0375, R_{sigma} = 0.0310]
Data/restraints/parameters	16230/0/745
Goodness-of-fit on F^2	1.052
Final R indexes [I>=2σ (I)]	R_1 = 0.0336, wR_2 = 0.0741
Final R indexes [all data]	R_1 = 0.0448, wR_2 = 0.0811
Largest diff. peak/hole / e Å^{-3}	0.41/-0.43

Compound **470f**

Single crystals suitable for X-ray analysis were obtained from MeCN and Et_2O by diffusion crystallization. (MeCN/Et_2O)

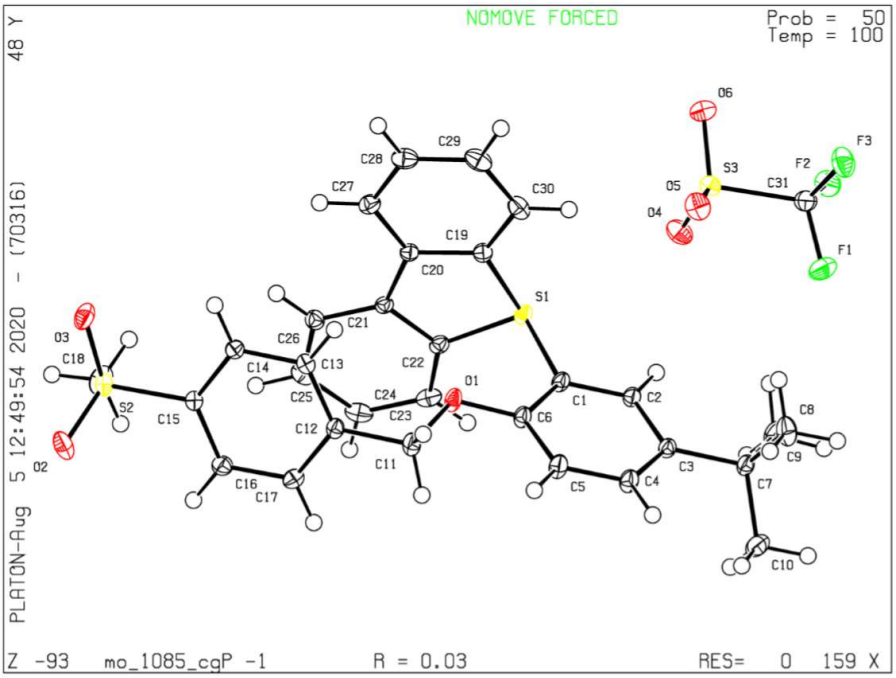

CCDC-Nr.	2051253
Empirical formula	$C_{31}H_{29}F_3O_6S_3$
Formula weight	650.72
Temperature/K	100
Crystal system	Triclinic
Space group	P-1
a/Å	10.4015(5)
b/Å	11.4555(5)
c/Å	14.4789(8)
α/°	99.272(2)
β/°	106.979(2)
γ/°	111.023(2)
Volume/Å^3	1470.30(13)
Z	2
ρ_{calc}g/cm^3	1.47
μ/mm^{-1}	0.316
F(000)	676
Crystal size/mm^3	0.412 × 0.345 × 0.228
Radiation	MoKα (λ = 0.71073)
2Θ range for data collection/°	3.99 to 68.674
Index ranges	-15 ≤ h ≤ 16, -18 ≤ k ≤ 15, -22 ≤ l ≤ 22
Reflections collected	80472
Independent reflections	10974 [R_{int} = 0.0210, R_{sigma} = 0.0154]
Data/restraints/parameters	10974/0/392
Goodness-of-fit on F^2	1.032
Final R indexes [I>=2σ (I)]	R_1 = 0.0289, wR_2 = 0.0771
Final R indexes [all data]	R_1 = 0.0322, wR_2 = 0.0793
Largest diff. peak/hole / e Å^{-3}	0.54/-0.42

Compound **470h**

Single crystals suitable for X-ray analysis were obtained from MeCN and Et_2O by diffusion crystallization. (MeCN/Et_2O)

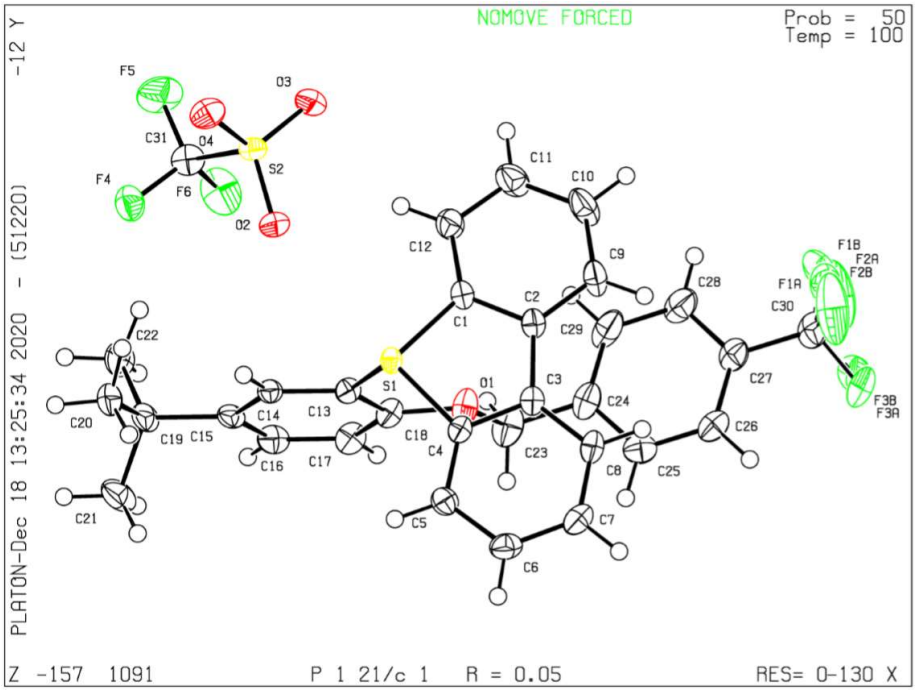

CCDC-Nr.	2051255
Empirical formula	$C_{31}H_{26}F_6O_4S_2$
Formula weight	640.64
Temperature/K	100
Crystal system	Monoclinic
Space group	$P2_1/c$
a/Å	12.7942(18)
b/Å	18.753(3)
c/Å	12.5933(19)
α/°	90
β/°	106.529(4)
γ/°	90
Volume/Å^3	2896.6(7)
Z	4
ρ_{calc}g/cm^3	1.469
μ/mm^{-1}	0.259
F(000)	1320
Crystal size/mm^3	0.473 × 0.133 × 0.116
Radiation	MoKα (λ = 0.71073)
2Θ range for data collection/°	4.344 to 56.032
Index ranges	-16 ≤ h ≤ 16, -24 ≤ k ≤ 24, -16 ≤ l ≤ 16
Reflections collected	54576
Independent reflections	6957 [R_{int} = 0.0494, R_{sigma} = 0.0308]
Data/restraints/parameters	6957/39/420
Goodness-of-fit on F^2	1.22
Final R indexes [I>=2σ (I)]	R_1 = 0.0537, wR_2 = 0.1158
Final R indexes [all data]	R_1 = 0.0587, wR_2 = 0.1178
Largest diff. peak/hole / e Å^{-3}	0.39/-0.46

Compound **470j**

Single crystals suitable for X-ray analysis were obtained from MeCN and Et_2O by diffusion crystallization. (MeCN/Et_2O)

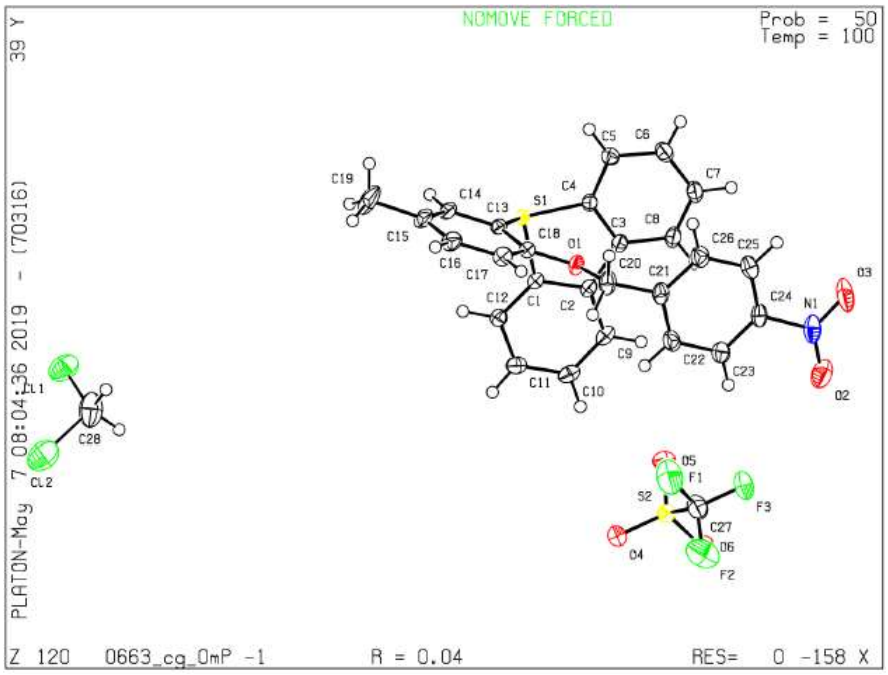

Identification code	0663_CG_0m
Empirical formula	$C_{27.5}H_{21}ClF_3NO_6S_2$
Formula weight	618.02
Temperature/K	99.98
Crystal system	triclinic
Space group	P-1
a/Å	8.5295(9)
b/Å	11.5788(15)
c/Å	14.6028(18)
α/°	72.127(4)
β/°	81.483(3)
γ/°	76.786(4)
Volume/Å^3	1331.5(3)
Z	2
ρ_{calc}g/cm^3	1.541
μ/mm^{-1}	0.367
F(000)	634.0
Crystal size/mm^3	0.622 × 0.499 × 0.036
Radiation	MoKα (λ = 0.71073)
2Θ range for data collection/°	4.924 to 59.244
Index ranges	-11 ≤ h ≤ 11, -16 ≤ k ≤ 16, -20 ≤ l ≤ 20
Reflections collected	96536
Independent reflections	7486 [R_{int} = 0.0228, R_{sigma} = 0.0123]
Data/restraints/parameters	7486/0/380
Goodness-of-fit on F^2	1.060
Final R indexes [I>=2σ (I)]	R_1 = 0.0443, wR_2 = 0.1297
Final R indexes [all data]	R_1 = 0.0461, wR_2 = 0.1317
Largest diff. peak/hole / e Å^{-3}	0.71/-0.85

Compound **470l**

Single crystals suitable for X-ray analysis were obtained from MeCN and Et_2O by diffusion crystallization. (MeCN/Et_2O)

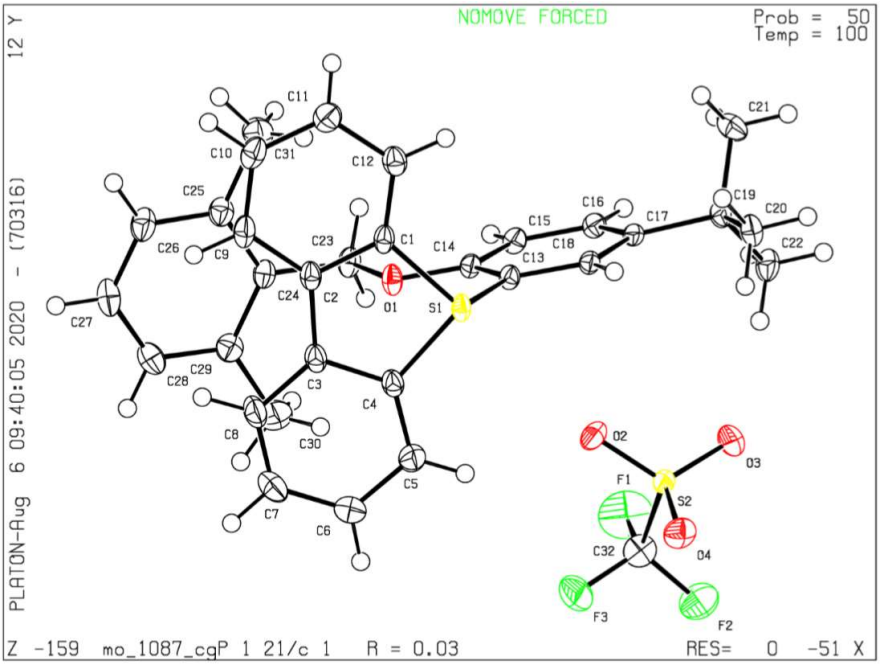

CCDC-Nr.	2051256
Empirical formula	$C_{32}H_{31}F_3O_4S_2$
Formula weight	600.69
Temperature/K	100
Crystal system	Monoclinic
Space group	$P2_1/c$
a/Å	12.2978(7)
b/Å	17.7425(9)
c/Å	13.6378(6)
α/°	90
β/°	95.691(2)
γ/°	90
Volume/Å^3	2961.0(3)
Z	4
ρ_{calc}g/cm^3	1.347
μ/mm^{-1}	0.234
F(000)	1256
Crystal size/mm^3	0.354 × 0.325 × 0.299
Radiation	MoKα (λ = 0.71073)
2Θ range for data collection/°	4.592 to 61.034
Index ranges	-17 ≤ h ≤ 17, -25 ≤ k ≤ 23, -19 ≤ l ≤ 19
Reflections collected	73673
Independent reflections	9040 [R_{int} = 0.0269, R_{sigma} = 0.0162]
Data/restraints/parameters	9040/0/375
Goodness-of-fit on F^2	1.031
Final R indexes [I>=2σ (I)]	R_1 = 0.0336, wR_2 = 0.0871
Final R indexes [all data]	R_1 = 0.0392, wR_2 = 0.0914
Largest diff. peak/hole / e Å^{-3}	0.45/-0.41

Compound **470n**

Single crystals suitable for X-ray analysis were obtained from MeCN and Et_2O by diffusion crystallization. (MeCN/Et_2O)

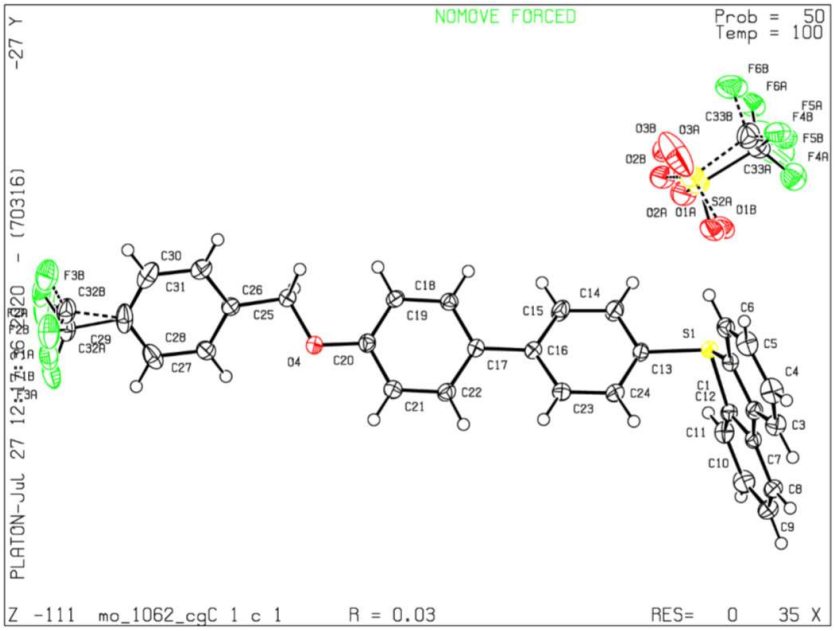

CCDC-Nr.	2051257
Empirical formula	$C_{33}H_{22}F_6O_4S_2$
Formula weight	660.62
Temperature/K	100
Crystal system	Monoclinic
Space group	Cc
a/Å	10.9573(10)
b/Å	18.3080(16)
c/Å	14.6355(12)
α/°	90
β/°	101.241(3)
γ/°	90
Volume/Å^3	2879.6(4)
Z	4
ρ_{calc}g/cm^3	1.524
μ/mm^{-1}	0.263
F(000)	1352
Crystal size/mm^3	0.408 × 0.261 × 0.25
Radiation	MoKα (λ = 0.71073)
2Θ range for data collection/°	4.394 to 59.284
Index ranges	-15 ≤ h ≤ 15, -25 ≤ k ≤ 24, -20 ≤ l ≤ 20
Reflections collected	28697
Independent reflections	8020 [R_{int} = 0.0204, R_{sigma} = 0.0215]
Data/restraints/parameters	8020/182/516
Goodness-of-fit on F^2	1.047
Final R indexes [I>=2σ (I)]	R_1 = 0.0311, wR_2 = 0.0789
Final R indexes [all data]	R_1 = 0.0318, wR_2 = 0.0803
Largest diff. peak/hole / e Å^{-3}	0.36/-0.19
Flack parameter	0.011(10)

Compound **470p**

Single crystals suitable for X-ray analysis were obtained from MeCN and Et_2O by diffusion crystallization. (MeCN/Et_2O)

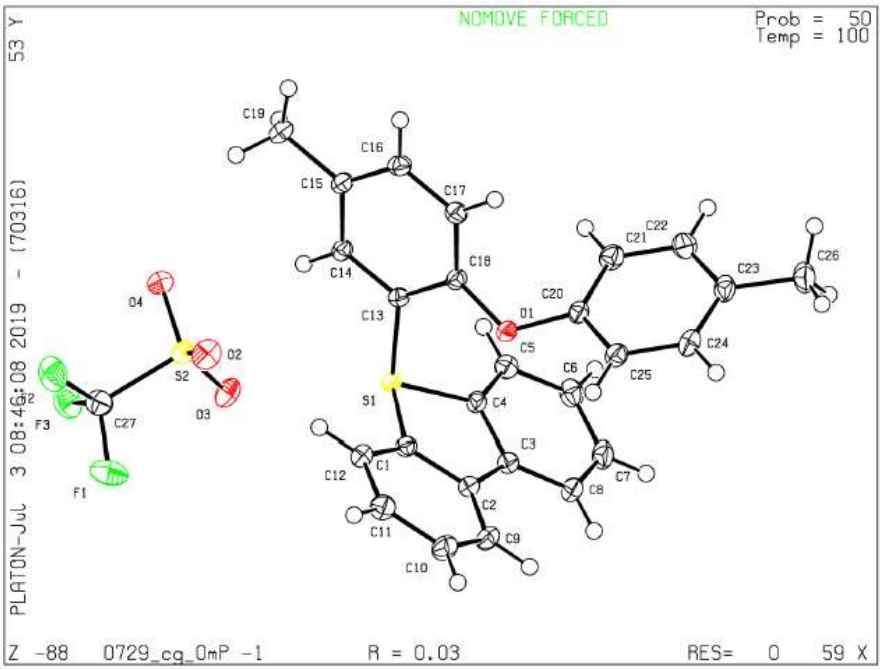

Identification code	0729_CG_0m
Empirical formula	$C_{27}H_{21}F_3O_4S_2$
Formula weight	530.56
Temperature/K	99.99
Crystal system	triclinic
Space group	P-1
a/Å	8.4140(7)
b/Å	11.8431(13)
c/Å	13.3560(12)
α/°	69.169(4)
β/°	80.816(4)
γ/°	73.350(4)
Volume/Å^3	1189.3(2)
Z	2
ρ_{calc}g/cm^3	1.482
μ/mm^{-1}	0.281
F(000)	548.0
Crystal size/mm^3	0.581 × 0.251 × 0.082
Radiation	MoKα (λ = 0.71073)
2Θ range for data collection/°	5.522 to 57.55
Index ranges	-11 ≤ h ≤ 11, -16 ≤ k ≤ 16, -18 ≤ l ≤ 18
Reflections collected	26453
Independent reflections	6150 [R_{int} = 0.0234, R_{sigma} = 0.0205]
Data/restraints/parameters	6150/0/327
Goodness-of-fit on F^2	1.049
Final R indexes [I>=2σ (I)]	R_1 = 0.0304, wR_2 = 0.0806
Final R indexes [all data]	R_1 = 0.0334, wR_2 = 0.0835
Largest diff. peak/hole / e Å^{-3}	0.44/-0.40

Compound **471a'**

Single crystals suitable for X-ray analysis were obtained directly from reaction mixture during synthesis in MeCN. (MeCN) The crystals underwent phase transition upon cooling just below 150 K at which the crystal breaks. Crystal mounting was done at 250 K and the data collection was carried out at 150 K, instead of 100 K.

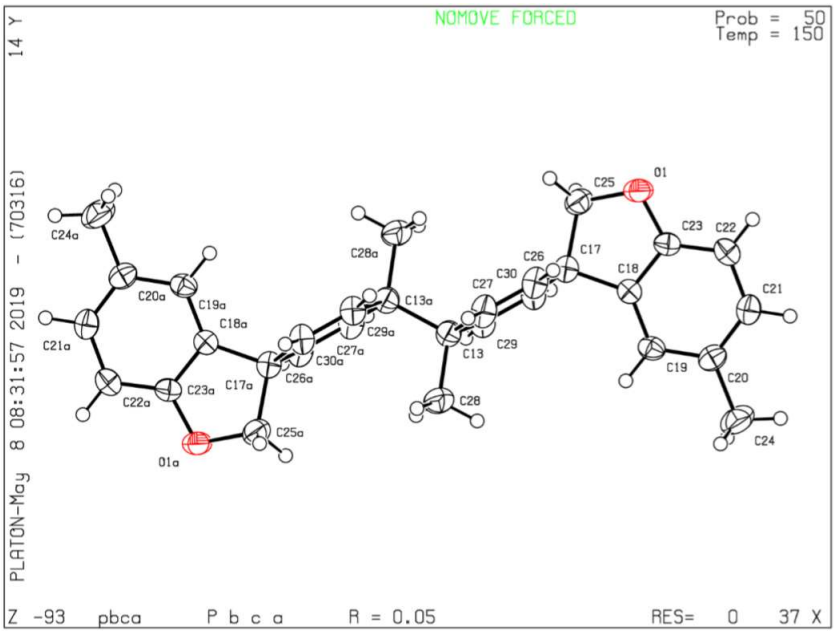

CCDC-Nr.	2051258
Empirical formula	$C_{15}H_{15}O$
Formula weight	211.27
Temperature/K	150
Crystal system	Orthorhombic
Space group	Pbca
a/Å	13.2616(3)
b/Å	8.2331(2)
c/Å	21.3930(5)
α/°	90
β/°	90
γ/°	90
Volume/Å^3	2335.78(9)
Z	8
ρ_{calc}g/cm^3	1.202
μ/mm^{-1}	0.073
F(000)	904
Crystal size/mm^3	0.413 × 0.313 × 0.076
Radiation	MoKα (λ = 0.71073)
2Θ range for data collection/°	4.892 to 55.784
Index ranges	-17 ≤ h ≤ 17, -10 ≤ k ≤ 10, -28 ≤ l ≤ 28
Reflections collected	39949
Independent reflections	2783 [R_{int} = 0.0253, R_{sigma} = 0.0103]
Data/restraints/parameters	2783/0/147
Goodness-of-fit on F^2	1.086
Final R indexes [I>=2σ (I)]	R_1 = 0.0511, wR_2 = 0.1467
Final R indexes [all data]	R_1 = 0.0559, wR_2 = 0.1512
Largest diff. peak/hole / e Å^{-3}	0.41/-0.20

Compound **471b**

Single crystals suitable for X-ray analysis were obtained from hot MeOH. (MeOH)

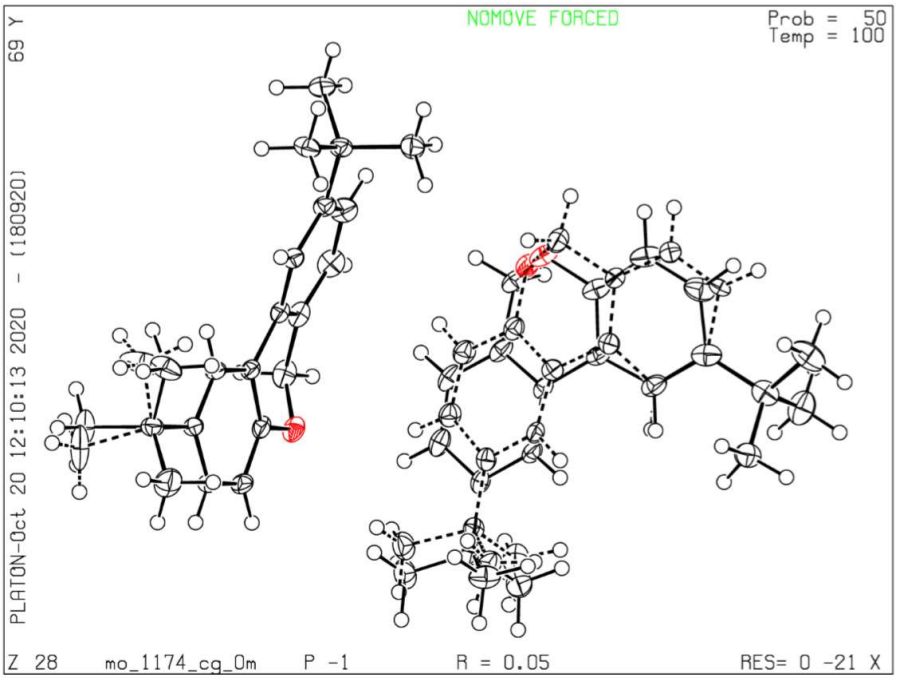

CCDC-Nr.	2051259
Empirical formula	$C_{21}H_{26}O$
Formula weight	294.42
Temperature/K	100
Crystal system	Triclinic
Space group	P-1
a/Å	5.8629(10)
b/Å	16.941(3)
c/Å	17.277(3)
α/°	92.461(5)
β/°	90.992(8)
γ/°	92.986(5)
Volume/Å^3	1711.8(5)
Z	4
ρ_{calc}g/cm^3	1.142
μ/mm^{-1}	0.068
F(000)	640
Crystal size/mm^3	0.453 × 0.344 × 0.06
Radiation	MoKα (λ = 0.71073)
2Θ range for data collection/°	4.72 to 63.146
Index ranges	-8 ≤ h ≤ 8, -24 ≤ k ≤ 24, -25 ≤ l ≤ 22
Reflections collected	117019
Independent reflections	11374 [R_{int} = 0.0274, R_{sigma} = 0.0187]
Data/restraints/parameters	11374/135/579
Goodness-of-fit on F^2	1.145
Final R indexes [I>=2σ (I)]	R_1 = 0.0506, wR_2 = 0.1249
Final R indexes [all data]	R_1 = 0.0567, wR_2 = 0.1284
Largest diff. peak/hole / e Å^{-3}	0.36/-0.23

Compound **471r**

Single crystals suitable for X-ray analysis were obtained from hot MeOH. (MeOH)

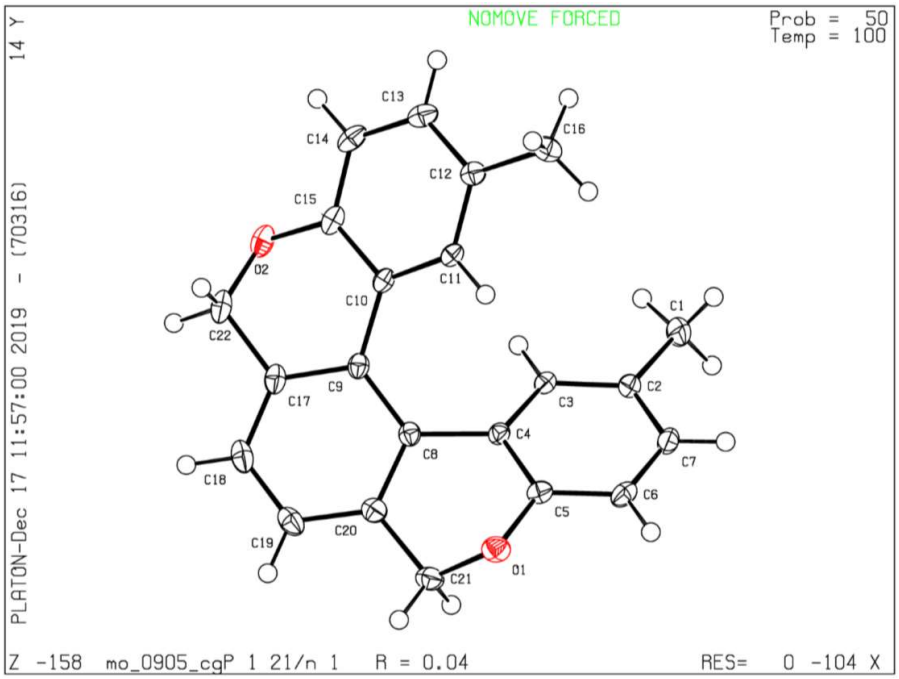

CCDC-Nr.	2051261
Empirical formula	$C_{22}H_{18}O_2$
Formula weight	314.36
Temperature/K	100
Crystal system	Monoclinic
Space group	$P2_1/n$
a/Å	10.6570(8)
b/Å	9.3242(8)
c/Å	16.6165(11)
α/°	90
β/°	101.178(3)
γ/°	90
Volume/Å^3	1619.8(2)
Z	4
ρ_{calc}g/cm^3	1.289
μ/mm^{-1}	0.081
F(000)	664
Crystal size/mm^3	0.231 × 0.219 × 0.195
Radiation	MoKα (λ = 0.71073)
2Θ range for data collection/°	4.2 to 57.406
Index ranges	-14 ≤ h ≤ 14, -12 ≤ k ≤ 12, -22 ≤ l ≤ 22
Reflections collected	72705
Independent reflections	4173 [R_{int} = 0.0212, R_{sigma} = 0.0081]
Data/restraints/parameters	4173/0/219
Goodness-of-fit on F^2	1.033
Final R indexes [I>=2σ (I)]	R_1 = 0.0410, wR_2 = 0.1084
Final R indexes [all data]	R_1 = 0.0427, wR_2 = 0.1102
Largest diff. peak/hole / e Å^{-3}	0.39/-0.31

Compound **471r'**

Single crystals suitable for X-ray analysis were obtained from hot toluene. (PhMe)

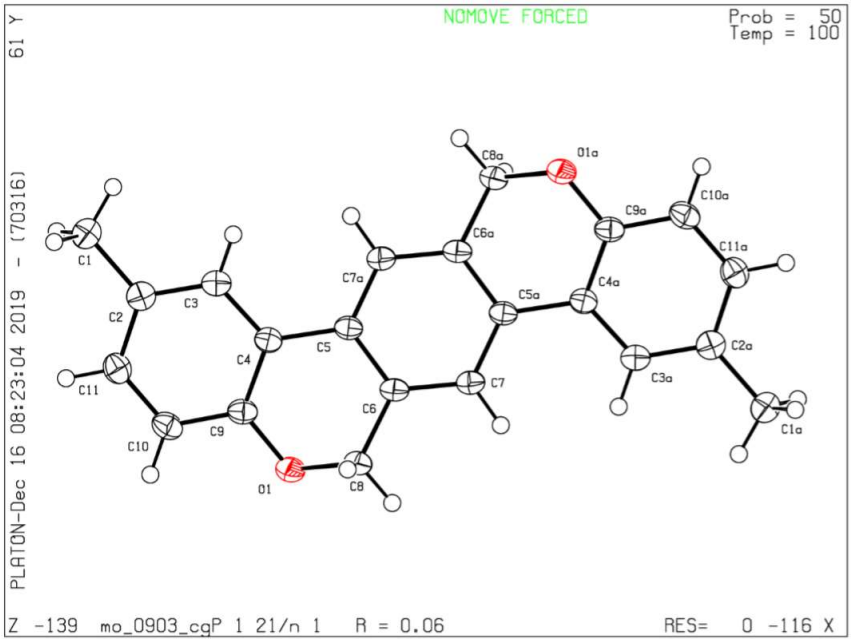

CCDC-Nr.	2051262
Empirical formula	$C_{22}H_{18}O_2$
Formula weight	314.36
Temperature/K	100
Crystal system	Monoclinic
Space group	$P2_1/n$
a/Å	8.1303(10)
b/Å	7.7477(9)
c/Å	12.6640(16)
α/°	90
β/°	99.953(4)
γ/°	90
Volume/Å^3	785.71(17)
Z	2
ρ_{calc}g/cm^3	1.329
μ/mm^{-1}	0.084
F(000)	332
Crystal size/mm^3	0.186 × 0.053 × 0.038
Radiation	MoKα (λ = 0.71073)
2Θ range for data collection/°	5.55 to 57.436
Index ranges	-10 ≤ h ≤ 10, -10 ≤ k ≤ 10, -17 ≤ l ≤ 17
Reflections collected	37879
Independent reflections	2028 [R_{int} = 0.0277, R_{sigma} = 0.0105]
Data/restraints/parameters	2028/0/111
Goodness-of-fit on F^2	1.114
Final R indexes [I>=2σ (I)]	R_1 = 0.0551, wR_2 = 0.1346
Final R indexes [all data]	R_1 = 0.0607, wR_2 = 0.1378
Largest diff. peak/hole / e Å^{-3}	0.32/-0.20

Compound **471s**

Single crystals suitable for X-ray analysis were obtained from MeCN and H_2O by diffusion crystallization. (MeCN/H_2O)

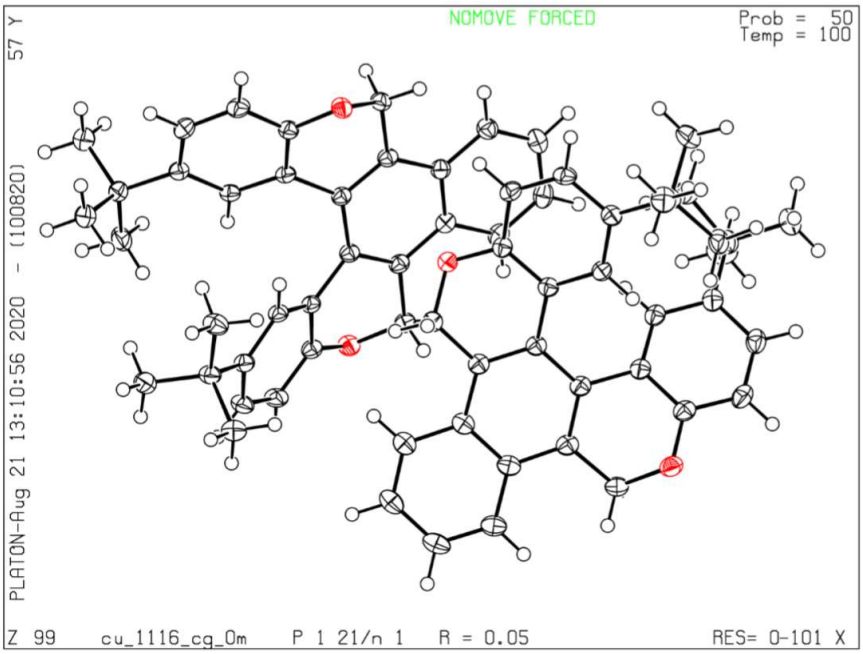

CCDC-Nr.	2051260
Empirical formula	$C_{32}H_{32}O_2$
Formula weight	448.57
Temperature/K	100
Crystal system	Monoclinic
Space group	$P2_1/n$
a/Å	8.0674(12)
b/Å	17.459(3)
c/Å	35.358(5)
α/°	90
β/°	93.039(6)
γ/°	90
Volume/Å^3	4973.3(13)
Z	8
ρ_{calc}g/cm^3	1.198
μ/mm^{-1}	0.564
F(000)	1920
Crystal size/mm^3	0.329 × 0.15 × 0.088
Radiation	CuKα (λ = 1.54178)
2Θ range for data collection/°	5.646 to 159.88
Index ranges	-10 ≤ h ≤ 9, -22 ≤ k ≤ 22, -44 ≤ l ≤ 44
Reflections collected	123599
Independent reflections	10779 [R_{int} = 0.0468, R_{sigma} = 0.0251]
Data/restraints/parameters	10779/0/626
Goodness-of-fit on F^2	1.132
Final R indexes [I>=2σ (I)]	R_1 = 0.0508, wR_2 = 0.1271
Final R indexes [all data]	R_1 = 0.0543, wR_2 = 0.1288
Largest diff. peak/hole / e Å^{-3}	0.29/-0.24

Compound **472a**

Single crystals suitable for X-ray analysis were obtained from MeCN and Et_2O by diffusion crystallization. (MeCN/Et_2O) Non-merohedral twinning was detected for these crystals. Final refinement against hklf5 data with refined batch scale factor of 0.50298 and twin domain transformation matrix (-1 0 0 / 0 -1 0 / 0.348 0 1).

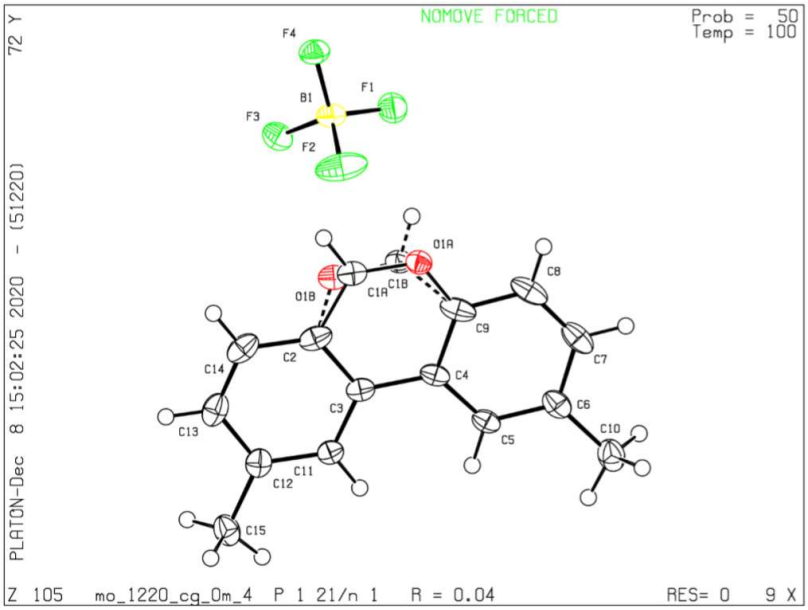

CCDC-Nr.	2051263
Empirical formula	$C_{15}H_{13}BF_4O$
Formula weight	296.06
Temperature/K	100
Crystal system	Monoclinic
Space group	$P2_1/n$
a/Å	6.9285(6)
b/Å	18.8834(14)
c/Å	10.2997(6)
α/°	90
β/°	96.754(2)
γ/°	90
Volume/Å^3	1338.20(17)
Z	4
ρ_{calc}g/cm^3	1.47
μ/mm^{-1}	0.127
F(000)	608
Crystal size/mm^3	0.364 × 0.19 × 0.076
Radiation	MoKα (λ = 0.71073)
2Θ range for data collection/°	4.314 to 59.164
Index ranges	-9 ≤ h ≤ 9, 0 ≤ k ≤ 26, 0 ≤ l ≤ 14
Reflections collected	3776
Independent reflections	3776 [R_{int} = ?, R_{sigma} = 0.0130]
Data/restraints/parameters	3776/69/212
Goodness-of-fit on F^2	1.08
Final R indexes [I>=2σ (I)]	R_1 = 0.0389, wR_2 = 0.1148
Final R indexes [all data]	R_1 = 0.0433, wR_2 = 0.1190
Largest diff. peak/hole / e Å^{-3}	0.37/-0.26